



PdFe

Electron diffraction pattern showing a grid of bright spots on a dark background. Two red arrows point to specific spots in the upper left quadrant. A black circular spot with a horizontal line extending to the right is visible in the lower right quadrant.



SiN (30)

High-resolution transmission electron microscopy (HRTEM) image showing a cross-section of a SiN layer. The layer exhibits a clear lattice structure with distinct horizontal lines representing atomic planes.

KAZAN EAST MAG 2022

# EAST MAG




Pb (20)

HRTEM image showing a cross-section of a Pb layer. The lattice structure is visible with horizontal atomic planes.



Cu (2)

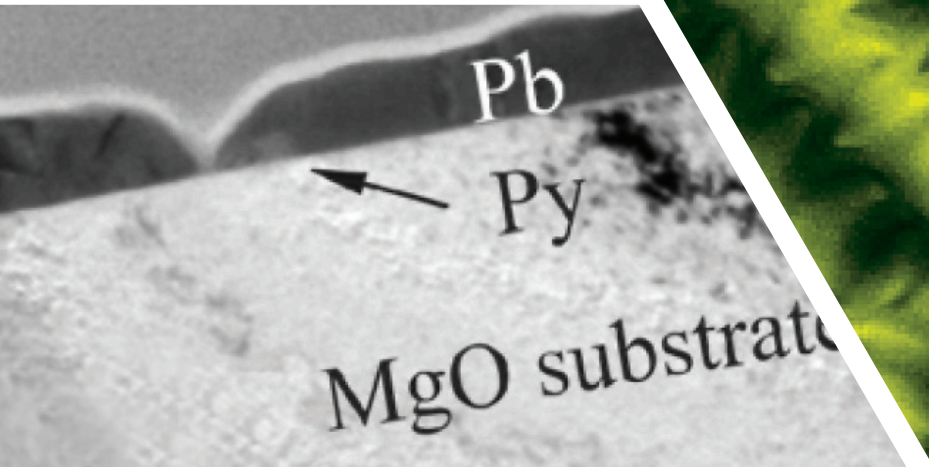
HRTEM image showing a cross-section of a Cu layer. The lattice structure is visible with horizontal atomic planes.



Heusler (12)

HRTEM image showing a cross-section of a Heusler layer. The lattice structure is visible with horizontal atomic planes.

## ABSTRACTS VOLUME II



Pb

Py

MgO substrate

HRTEM image showing a cross-section of a Pb layer on top of a Py layer, which is on an MgO substrate. The layers are clearly visible with distinct lattice structures.

Py

MgO substrate

VIII Euro-Asian Symposium «Trends in MAGnetism»

August 22–26, 2022, Kazan, Russia

Zavoisky Physical-Technical Institute FRC Kazan SC RAS



**BOOK OF ABSTRACTS**

VOLUME II

Symposium is supported by:



Ministry of Science  
and Higher Education  
of the Russian Federation



Ministry of Education and Science  
of the Republic of Tatarstan



Federal Research Center  
"Kazan Scientific Center of  
the Russian Academy of Sciences"



Zavoisky Physical-Technical  
Institute FRC KazanSC RAS



Kazan Federal University



Academy of Sciences  
of the Republic of Tatarstan

Symposium is sponsored by:



Government  
of the Republic of Tatarstan



"MTEON" Ltd

**ORGANIZING COMMITTEE**

Vladimir V. USTINOV (Ekaterinburg)  
Alexey A. KALACHEV (Kazan)  
Kev M. SALIKHOV (Kazan)  
Lenar R. TAGIROV (Kazan)  
Rushana M. EREMINA (Kazan)  
Sergey M. KHANTIMEROV (Kazan)  
Dmitrii A. TAYURSKII (Kazan)  
Marat R. GAFUROV (Kazan)  
Sergey M. AKHMIN (Kazan)  
Sufia A. ZIGANSHINA (Kazan)  
Andrey A. KAMASHEV (Kazan)  
Ivan V. YATSYK (Kazan)

Symposium General Chairman  
Organizing Committee Chairman  
Organizing Committee Co-Chairman  
Organizing Committee Co-Chairman  
Program Committee Chairman  
Local Committee Chairman  
Local Committee Co-Chairman  
Local Committee Co-Chairman  
Publication Committee Chairman  
Symposium Chief Secretary  
Symposium Secretary  
Symposium Secretary

**PROGRAM COMMITTEE**

Nikolay G. BEBENIN (Ekaterinburg)  
Alexander V. BELUSHKIN (Dubna)  
Mikhail V. EREMIN (Kazan)  
Nikolay V. ERSHOV (Ekaterinburg)  
Andrey A. FRAERMAN (Nizhny  
Novgorod)  
Zukhra V. GAREEVA (Ufa)  
Andrei A. GIPPIUS (Moscow)  
Oksana A. GOLOVNAYA (Ekaterinburg)  
Alexander A. GOLUBOV (Dolgoprudny)  
Alexander B. GRANOVSKY (Moscow)  
Sergey V. GRIGORIEV (Gatchina)  
Alexey O. IVANOV (Ekaterinburg)  
Alexandra M. KALASHNIKOVA (Saint  
Petersburg)  
Leonid N. KOROTKOV (Voronezh)  
Alexander I. KURBAKOV (Gatchina)  
Ivan V. LEONOV (Ekaterinburg)  
Alexander S. MEL'NIKOV (Nizhny  
Novgorod)

Mikhail A. MILYAEV (Ekaterinburg)  
Elena V. MOSTOVSHCHIKOVA  
(Ekaterinburg)  
Alexander A. MUKHIN (Moscow)  
Alexey V. OGNEV (Vladivostok)  
Sergei G. OVCHINNIKOV (Krasnoyarsk)  
Alexander P. PYATAKOV (Moscow)  
Yuriy L. RAIKHER (Perm)  
Valeria V. RODIONOVA (Kaliningrad)  
Alexander V. SADOVNIKOV (Saratov)  
Anatolie S. SIDORENKO (Chisinau)  
Alexander I. SMIRNOV (Moscow)  
Sergey V. STRELTSOV (Ekaterinburg)  
Gregory B. TEITELBAUM (Kazan)  
Alexander N. VASILIEV (Moscow)  
Evgeniia L. VAVILOVA (Kazan)  
Roman V. YUSUPOV (Kazan)  
Anatoly E. YERMAKOV (Ekaterinburg)  
Svetlana V. YURTAEVA (Kazan)

**PUBLICATION COMMITTEE**

Sergey G. L'VOV (KPTI FRC KazSC RAS)  
Olga B. YANDUGANOVA (KPTI FRC KazSC RAS)

Polina A. AGZAMOVA (IMP UB RAS)

**LOCAL COMMITTEE**

Tatiana P. GAVRILOVA (KPTI FRC KazSC RAS)  
Ilshat I. FAZLIZHANOV (KPTI FRC KazSC RAS)  
Andrey A. KAMASHEV (KPTI FRC KazSC RAS)  
Ivan V. YATSYK (KPTI FRC KazSC RAS)  
Alexei V. SHESTAKOV (KPTI FRC KazSC RAS)  
Raisa R. GUSEVA (KPTI FRC KazSC RAS)  
Valentina I. KHABIBULLINA (KPTI FRC KazSC RAS)  
Valentina V. PUSHKOVA (KPTI FRC KazSC RAS)  
Alla M. AKHMETGALIEVA (KPTI FRC KazSC RAS)  
Olga O. KUPRIYANOVA (KPTI FRC KazSC RAS)  
Yuriy V. OLADOSHKIN (KPTI FRC KazSC RAS)  
Dilyara V. ILMATOVA (KPTI FRC KazSC RAS)  
Ranis R. GARIPOV (KPTI FRC KazSC RAS)  
Rodion F. LIKEROV (KPTI FRC KazSC RAS)  
Daniil V. POPOV (KPTI FRC KazSC RAS)  
Roman V. YUSUPOV (IP KFU)

Igor V. YANILKIN (IP KFU)  
Airat G. KIIAMOV (IP KFU)  
Ruslan G. BATULIN (IP KFU)  
Anna S. MOROZOVA (KPTI FRC KazSC RAS)  
Albina R. GAFAROVA (KPTI FRC KazSC RAS)  
Amir I. GUMAROV (IP KFU)  
Iskander R. VAKHITOV (IP KFU)  
Almaz L. ZINNATULLIN (IP KFU)  
Mikhail A. CHEROSOV (IP KFU)  
Evgenii M. BEGISHEV (KPTI FRC KazSC RAS)  
Alsu R. SAKHBIIEVA (IP KFU)  
Marina S. YATSYK (IP KFU)  
German A. NOVIKOV (KPTI FRC KazSC RAS)  
Tatiana N. ENDEROVA (KPTI FRC KazSC RAS)  
Diana E. ZHELEZNYAKOVA (KPTI FRC KazSC RAS)

## TOPICS

Plenary lectures

Section A. Spintronics and magnetic nanostructures

Section B. Spin dynamics and magnetic resonances

Section C. Low dimensional magnetism

Section D. Domain walls, vortices and skyrmions

Section E. Magnetotransport, magnetooptics and magnetophotonics

Section F. Magnetoelastic, magnetocaloric and shape memory effects

Section G. Frustrated and disordered magnetism

Section H. Magnetism of strongly correlated electron systems

Section I. Magnetism and superconductivity

Section J. Soft and hard magnetic materials

Section K. Magnetic semiconductors, multiferroics, topological insulators

Section L. Magnetic soft matter

Section M. Magnetism in biology and medicine

Section N. Instruments and techniques for studying magnetism

Section O. MAX materials

# Contents

## Section G.

<b>Frustrated and disordered magnetism</b> . . . . .	<b>1</b>
<b>G.01</b>	
CONCENTRATIONAL TRANSITION IN $\text{Cu}_2(\text{Mn,Ga})\text{BO}_5$ SOLID SOLUTIONS <i>E. Eremin, M. Molocheev, A. Veligzhanin, M. Pavlovsky, V. Kuchesheva-Titova,      L. Bezmaternykh, E. Moshkina</i> . . . . .	<b>2</b>
<b>G.02</b>	
MAGNETIC BEHAVIOR OF LANTHANIDES (La-Tb) IN LINEAR-CHAIN COORDINATION POLYMERS <i>N.V. Lomova, F.F. Chausov, L.V. Dobysheva, A.I. Ulyanov, N.N. Zverev</i> . . . . .	<b>4</b>
<b>G.03</b>	
THERMALLY STABLE SKYRMION CRISTALL IN TRIANGULAR FRUSTRATED ANTIFERROMAGNETIC/FERROELECTRIC BILAYER <i>I.F. Sharafullin, A.G. Nugumanov, A.H. Baisheva, A.R. Yuldasheva, H.T. Diep</i> . . . . .	<b>6</b>
<b>G.04</b>	
MAGNETIC PHASE DIAGRAM AND POSSIBLE KITAEV-LIKE BEHAVIOR OF HONEYCOMB-LATTICE ANTIMONATE $\text{Na}_3\text{Co}_2\text{SbO}_6$ <i>E. Vavilova, T. Vasilchikova, D. Mikhailova</i> . . . . .	<b>8</b>
<b>G.05</b>	
ORBITAL ORDERING AND FRUSTRATED ANISOTROPY IN $\text{PbMnBO}_4$ <i>S.N. Martynov</i> . . . . .	<b>9</b>
<b>G.06</b>	
EXACT DETERMINATION OF THE SINGLE ION AND PAIR INTERACTIONS PARAMETERS IN THE MAGNET WITH COMPETING DIPOLAR AND EXCHANGE INTERACTIONS $\text{LiGdF}_4$ <i>V.N. Glazkov, S.S. Sosin, A.F. Iafarova, O.A. Morozov, R.G. Batulin,      I.V. Romanova</i> . . . . .	<b>10</b>
<b>G.07</b>	
RESEARCH BY DEEP NEURAL NETWORKS OF FRUSTRATED SPIN GLASS SYSTEMS <i>D.Yu. Kapitan, P.D. Andriushchenko, V.Yu. Kapitan, A.O. Korol</i> . . . . .	<b>11</b>
<b>G.08</b>	
A NEURAL NETWORK APPROACH TO THE STUDY OF COMPLEX FRUSTRATED SYSTEMS <i>A.O. Korol, V.Yu. Kapitan, D.Yu. Kapitan, E.V. Vasiliev</i> . . . . .	<b>13</b>
<b>G.09</b>	
MAGNETIC PROPERTIES OF PEROVSKITE $\text{Sr}_2\text{MnTiO}_6$ <i>D.V. Popov, I.V. Yatsyk, A.V. Shestakov, R.G. Batulin, T.I. Chupakhina,      R.M. Eremina</i> . . . . .	<b>15</b>

G.P1	STUDY OF THE EFFECT OF Cr ON ELECTRIC AND MAGNETIC PROPERTIES OF Co-RICH AMORPHOUS FERROMAGNETIC MICROWIRES UNDER JOULE HEATING <i>A.E. Sarakueva, V.S. Mashera, M.N. Churyukanova, I.V. Kozlov, V.I. Odintsov, G.N. Elmanov, S.A. Gudoshnikov</i> . . . . .	17
G.P2	ON THE MAGNETIC STATE OF Co IN CHALCOGENIDES $Co_{1-x}Ch$ <i>D.F. Akramov, D.A. Shishkin, S.N. Mozgovykh, K.N. Mikhalev, A.Y. Germov, N.V. Selezneva</i> . . . . .	19
G.P3	SPECTRAL PROPERTIES OF HEISENBERG ANTIFERROMAGNET $S = 1/2$ ON THE TRIANGULAR LATTICE IN A MAGNETIC FIELD <i>A.S. Martynov, A.A. Khudaiberdyev, D.M. Dzebisashvili</i> . . . . .	20
G.P4	PHASE TRANSITIONS AND CRITICAL PHENOMENA IN THE 4-STATE 2D SITE-DILUTED POTTS MODEL ON A SQUARE LATTICE <i>A.K. Murtazaev, A.B. Babaev, G.Ya. Ataeva, Ya.K. Abuev, M.A. Babaev</i> . . . . .	21
G.P5	ANISOTROPY OF THE MAGNETIC PROPERTIES OF $SrY_2O_4:Er^{3+}$ SINGLE CRYSTAL <i>M.A. Cherosov, A.G. Kiiamov, R.G. Batulin, I.F. Gilmutdinov, A.G. Ivanova, D.S. Uvin, R.V. Yusupov, D.A. Tayurskii</i> . . . . .	22
G.P6	NON-STOICHIOMETRY AND UNCONVENTIONAL SPIN-GLASS IN FRUSTRATED SYSTEM $Li_{0.8}Ni_{0.6}Sb_{0.4}O_2$ <i>E. Vavilova, T. Salikhov, M. Iakovleva, T. Vasilchikova, E. Zvereva, I. Shukaev, V. Nalbandyan, A. Vasiliev</i> . . . . .	23
G.P7	NMR STUDY OF SPIN DYNAMICS IN THE ALTERNATING CHAIN SYSTEM $Li_3Cu_2SbO_6$ WITH DEFECTS <i>E. Vavilova, T. Salikhov, T. Vasilchikova, V. Nalbandyan, A. Vasiliev, E. Zvereva</i> . . . . .	24
G.P8	PECULIARITIES AND COMPARISON OF $Cu_2MBO_5$ ( $M = Fe, Mn, Cr$ ) LUDWIGITES CRYSTALLIZATION IN $Bi_2O_3-MoO_3-Na_2O-B_2O_3$ MULTICOMPONENT FLUXES <i>M.S. Molokeev, A.F. Bovina, K.A. Shabanova, D. Kokh, D.A. Velikanov, E.V. Eremin, L.N. Bezmaternykh, E.M. Moshkina</i> . . . . .	25
G.P9	THERMAL EXPANSION AND RESISTIVITY ANOMALIES IN $Cu_2FeBO_5$ LUDWIGITE <i>Yu.S. Gokhfeld, L.A. Solovyov, S.N. Vereshchagin, A.A. Borus, I.A. Gudim, N.V. Kazak</i> . . . . .	27
G.P10	MAGNETIC SPECIFIC HEAT OF $SrDy_2O_4$ SINGLE CRYSTAL <i>A.G. Kiiamov, R.G. Batulin, M.A. Cherosov, I.F. Gilmutdinov, A.G. Ivanova, R.V. Yusupov, D.A. Tayurskii</i> . . . . .	29



G.P11	PHASE DIAGRAM OF THE FRUSTRATED FOUR-STATE POTTS MODEL WITH COMPETING EXCHANGE INTERACTIONS <i>D.R. Kurbanova, M.K. Ramazanov, M.A. Magomedov, A.K. Murtazaev</i> . . . . .	30
G.P12	PHASE TRANSITION IN THREE-STATE ANTIFERROMAGNETIC POTTS MODEL ON THE BODY-CENTERED CUBIC LATTICE <i>D.R. Kurbanova, M.K. Ramazanov, M.A. Magomedov, K.Sh. Murtazaev, A.K. Murtazaev</i> . . . . .	32
G.P13	INFLUENCE OF A MAGNETIC FIELD ON AN ANTIFERROMAGNET WITH COMPETING EXCHANGE INTERACTIONS <i>K.Sh. Murtazaev, A.K. Murtazaev, M.K. Ramazanov, M.A. Magomedov</i> . . . . .	34
G.P14	MAGNETIC GRÜNEISEN PARAMETER OF THE 1D DILUTE ISING MODEL <i>A.V. Shadrin, Y.D. Panov</i> . . . . .	36
G.P15	SPERMAGNETIC PHASE TRANSITIONS IN GdFeCo AMORPHOUS ALLOYS: H-T PHASE DIAGRAMS <i>S.V. Solov'yov</i> . . . . .	38
G.P16	HEAT CAPACITY AND PHASE TRANSITION OF DIPOLE SUPERSPIN ICE ON A TRIMERIZED TRIANGULAR LATTICE <i>V.S. Strongin, M.A. Chesnokov, I.N. Nalivaiko, K.S. Soldatov, I.A. Titovets, K.V. Nefedev</i> . . . . .	40
G.P17	SOLID-STATE SYNTHESIS AND SPECIFIC HEAT OF STRONTIUM SAMARATE $SrSm_2O_4$ <i>Y. Tian, A.G. Kiiamov, R.G. Batulin, M.A. Cherosov, I.F. Gilmutdinov, A.G. Ivanova, R.V. Yusupov, D.A. Tayurskii</i> . . . . .	42
G.P18	GROUND AND LOW-ENERGY STATES OF DIPOLE SUPERSPIN ICE ON A TRIMERIZED TRIANGULAR LATTICE <i>I.A. Titovets, M.A. Chesnokov, I.N. Nalivaiko, V.S. Strongin, K.S. Soldatov, K.V. Nefedev</i> . . . . .	43
G.P19	EXACT SOLUTION EDVARD-SANDERSON SPIN GLASS FOR NEAREST NEIGHBORS <i>V. Trukhin, K. Nefedev</i> . . . . .	45
G.P20	STUDY OF A COMPLEX INCOMMENSURABLE MAGNETIC STRUCTURE $Ho_3Co$ <i>A.A. Vaulin, A.F. Gubkin</i> . . . . .	47
G.P21	MAGNETIC PROPERTIES AND HYSTERESIS BEHAVIOR OF A 2D DILUTE ISING MAGNET WITH FRUSTRATION <i>D.N. Yasinskaya, V.A. Ulitko, Y.D. Panov</i> . . . . .	49

## Section H.

<b>Magnetism of strongly correlated electron systems . . . . .</b>	<b>51</b>
<b>H.I1</b>	
MODELLING OF THE ELECTRONIC STRUCTURE, MAGNETIC STATE AND LATTICE STABILITY OF STRONGLY CORRELATED ELECTRON SYSTEMS <i>I. Leonov . . . . .</i>	<b>52</b>
<b>H.I2</b>	
CHANGE IN ANISOTROPY OF CHARGE SUBSYSTEM IN LAYERED COBALTITES LnBaCo <sub>2</sub> O <sub>5+Δ</sub> <i>E.V. Mostovshchikova, S.V. Naumov, B.A. Gizhevskii, M.S. Udintseva,     V.R. Galakhov. . . . .</i>	<b>53</b>
<b>H.O1</b>	
MAGNETIC PROPERTIES OF CaCu <sub>3</sub> Ti <sub>4</sub> O <sub>12</sub> :Fe SOLID SOLUTIONS <i>T.P. Gavrilova, A.R. Yagfarova, I.F. Gilmutdinov, I.V. Yatsyk, F.G. Vagizov,     J.A. Deeva, T.I. Chupakhina, R.M. Eremina. . . . .</i>	<b>56</b>
<b>H.O2</b>	
DESTRUCTION OF THE LONG-RANGE CHARGE ORDERING STATE VIA Fe DOPING IN THE PEROVSKITE MANGANITE La <sub>0.5</sub> Sr <sub>0.5</sub> MnO <sub>3</sub> <i>I.M. Usatyy, V.S. Zakhvalinskii, O.N. Ivanov . . . . .</i>	<b>58</b>
<b>H.O3</b>	
ELECTRONIC TRANSITIONS IN THE Co <sub>3</sub> BO <sub>5</sub> <i>N.V. Kazak, A. Arauzo, J. Bartolomé, A.A. Borus, V.V. Yumashev,     S.G. Ovchinnikov. . . . .</i>	<b>61</b>
<b>H.O4</b>	
CRITICAL PHENOMENA IN THE DYNAMIC SPIN-FLUCTUATION THEORY OF METALLIC MAGNETISM <i>N.B. Melnikov, A.S. Gulenko, B.I. Reser . . . . .</i>	<b>63</b>
<b>H.O5</b>	
SPIN INDUCED ELECTRIC POLARIZATION IN Fe <sub>2</sub> Mo <sub>3</sub> O <sub>8</sub> <i>K.V. Vasin, M.V. Eremin, A.R. Nurmukhametov . . . . .</i>	<b>65</b>
<b>H.O6</b>	
MAGNETIC PROPERTIES OF La <sub>0.81</sub> Sr <sub>0.19</sub> Mn <sub>0.9</sub> Fe <sub>0.1-x</sub> Zn <sub>x</sub> O <sub>3</sub> (x = 0, x = 0.05) <i>R.M. Eremina, I.V. Yatsyk, Z.Y. Seidov, F.G. Vagizov, V.A. Shustov, A.G. Badelin,     V.K. Karpasyuk, D.S. Abdinov, M.M. Tagiev, S.Kh. Estemirova,     H.-A. Krug von Nidda . . . . .</i>	<b>67</b>
<b>H.O7</b>	
MANY-BODY EFFECTS IN MAGIC ANGLE TWISTED BILAYER GRAPHENE <i>A.O. Sboychakov, A.V. Rozhkov, A.L. Rakhmanov, F. Nori . . . . .</i>	<b>68</b>
<b>H.O8</b>	
ELECTRONIC STATES OF Co IONS IN LnBaCo <sub>2</sub> O <sub>5+δ</sub> COBALTITES (Ln = RARE EARTH, 0 ≤ δ ≤ 1): SOFT X-RAY ABSORPTION STUDIES <i>V.R. Galakhov, M.S. Udintseva, S.V. Naumov, B.A. Gizhevskii. . . . .</i>	<b>69</b>
<b>H.O9</b>	
SYNTHESIS ASPECTS AND MAGNETIC MICROSTRUCTURE OF TERNARY ORDERED Fe-Al-M (M = Ga, B, Sn, V, Mn) ALLOYS <i>E.V. Voronina, A.F. Abdullin, A.G. Ivanova, L.V. Dobysheva, A.V. Korolyov,     A.K. Arzhnikov . . . . .</i>	<b>72</b>

H.O10	ENTANGLEMENT AND THE EXTERNAL FIELDS IN THE KUGEL-KHOMSKII MODEL <i>V.E. Valiulin, A.V. Mikheyenkov, N.M. Chtchelkatchev, K.I. Kugel</i> . . . . .	74
H.O11	ON THE GENERAL CONDITIONS FOR ITINERANT FERROMAGNETISM FOR NON-DEGENERATE HUBBARD MODEL ON A THREE-DIMENSIONAL LATTICE <i>P.A. Igoshev, A.A. Katanin</i> . . . . .	76
H.O12	ANISOTROPIC MAGNETORESISTANCE IN $RB_{12}$ (R – Ho, Er, Tm) ANTIFERROMAGNETS WITH DYNAMIC CHARGE STRIPES <i>K. Krasikov, V. Glushkov, S. Demishev, A. Bogach, A. Azarevich, N. Shitsevalova, V. Filipov, S. Gabani, K. Flachbart, N. Sluchanko</i> . . . . .	78
H.P1	MAGNETIC STATE OF $Fe_xMn_{1-x}S$ , UNDER HYDROSTATIC AND CHEMICAL PRESSURE <i>G. Abramova, M. Boehm, J. Schefer, A. Piovano, Yu. Knyazev, O. Bajukov, S.P. Kubrin</i> . . . . .	79
H.P2	AB INITIO STUDY OF PHYSICAL PROPERTIES OF MAGNETIC TETRABORATE CRYSTALS $FeB_4O_7$ AND $MnB_4O_7$ <i>A.S. Shinkorenko</i> . . . . .	81
H.P3	COMPETITIVE EFFECTS OF SUBSTITUTIONS IN $La_{1-x}Sr_xMn_{0.9}(Mg_yGe_z)_{0.1}O_{3+y}$ SYSTEM <i>A.G. Badelin, I.M. Derzhavin, S.Kh. Estemirova, V.K. Karpasyuk</i> . . . . .	82
H.P4	NEGATIVE PHOTOCONDUCTIVITY OF THE HETEROSTRUCTURE $Ba_{0.8}Sr_{0.2}TiO_3/LaMnO_3$ <i>A.O. Chibirev, A.V. Leontiev, N.N. Garig'yanov, M.I. Bannikov, R.F. Mamin</i> . . . . .	84
H.P5	DIAMIC AND STATIC PROPERTIES OF A NON-HEISENBERG FERRIMANET WITH A SINGLE-ION ANISOTROPY <i>O.A. Kosmachev, Ya.Yu. Matyunina, Yu.A. Fridman</i> . . . . .	85
H.P6	ANISOTROPIC THERMAL EXPANSION IN $Co_3BO_5$ LUDWIGITE <i>Yu.S. Gokhfeld, N.V. Kazak, M.S. Molokeev, V.A. Dudnikov, L.A. Solovyov, S.G. Ovchinnikov</i> . . . . .	87
H.P7	A THEORY OF MAGNETIC PHASE SEPARATION IN METALS AND ITS IMPACT ONTO THE MAGNETOCALORICAL EFFECT <i>P.A. Igoshev</i> . . . . .	89
H.P8	MAGNETIC PROPERTIES OF $Fe_{1.21}Ga_{0.79}O_3$ <i>I.V. Yatsyuk, R.M. Eremina, E.M. Moshkina</i> . . . . .	91

H.P9	IMPURITY FERROMAGNETISM IN Pd-Fe AND Pd-Co ALLOYS <i>A.Y. Korableva, I.I. Gumarova, A.I. Gumarov, I.V. Yanilkin, R.I. Khaibullin</i> . . . . .	92
H.P10	HYPERFINE INTERACTIONS IN HIGH-PRESSURE-SYNTHESIZED COMPOUNDS OF 3d-METALS WITH RARE-EARTH AND ALKALINE-EARTH ELEMENTS <i>M.V. Magnitskaya, A.V. Bokov, D.A. Salamatin, N.M. Chtchelkatchev, V.I. Krylov, A.V. Tsvyashchenko</i> . . . . .	93
H.P11	CHARGE SUBSYSTEM RESPONSE TO PHASE TRANSITIONS IN DOUBLE MANGANITES $\text{LnBaMn}_2\text{O}_6$ <i>E.V. Mostovshchikova, E.V. Sterkhov, S.A. Uporov, S.V. Pryanichnikov, Ya.Ya. Pyzhyanov, S.G. Titova</i> . . . . .	95
H.P12	CHARGE ORDERING AND MAGNETIC TRANSITIONS IN $\text{Fe}_{1.75}\text{V}_{0.25}\text{Bo}_4$ WARWICKITE <i>N. Belskaya, N. Kazak, D. Velikanov, S. Gromilov, A. Sukhikh, V. Rudenko, S. Ovchinnikov</i> . . . . .	98
H.P13	ALTERATION OF MAGNETIC PROPERTIES OF $(\text{Mg}_{1-x}\text{Ni}_x)_3\text{Si}_2\text{O}_5(\text{OH})_4$ ( $x = 0.67, 1$ ) NANOSCROLLS AFTER HYDROGEN TREATMENT <i>N. Belskaya, A. Krasilin, E. Khrapova, D. Chikurov, M. Volkov</i> . . . . .	100
H.P14	METAL-INSULATOR TRANSITION AND MAGNETIC PROPERTIES $\text{NdBaCo}_2\text{O}_{5+\delta}$ , $0.37 \leq \delta \leq 0.65$ <i>N.I. Solin, S.V. Naumov</i> . . . . .	102
H.P15	EFFECT OF THE ELECTRON-PHONON INTERACTION ON THE FORMATION OF THE EXCITON PHASE IN STRONGLY CORRELATED SYSTEMS WITH THE SPIN CROSSOVER <i>Yu.S. Orlov, S.V. Nikolaev, V.I. Kuz'min, S.G. Ovchinnikov</i> . . . . .	104
H.P16	LIGHT-INDUCED ULTRAFAST QUANTUM RELAXATION DYNAMICS OF MAGNETICALLY ORDERED SPIN CROSSOVER SYSTEMS <i>Yu.S. Orlov, S.V. Nikolaev, S.G. Ovchinnikov</i> . . . . .	106
H.P17	STRAIN-INDUCED CHARGE ORDERING IN Pr-Sr MANGANITES ( $x \leq 0.4$ ) <i>Yu.E. Samoshkina, M.V. Rautskii, D.S. Neznakhin, E.A. Stepanova, N.V. Andreev, V.I. Chichkov, A.V. Chernichenko</i> . . . . .	107
H.P18	MAGNETIC INTERACTIONS IN $\text{FeBO}_3$ UNDER HIGH PRESSURE <i>S.I. Polukeev, V.A. Gavrichkov, S.G. Ovchinnikov</i> . . . . .	108
H.P19	NMR STUDY OF ELECTRONIC STATES IN CHALCOGENIDES $\text{Cr}_x\text{NbSe}_2$ ( $x \leq 0.5$ ) <i>V.V. Ogloblichev, N.V. Baranov, Yu.V. Piskunov, A.Y. Germov, N.M. Nosova, E.M. Sherokalova, N.V. Selezneva</i> . . . . .	110

H.P20	A SIMPLE EXACTLY SOLVABLE SPIN-REORIENTATION MODEL IN RARE-EARTH ORTHOFERRITES <i>E.V. Vasinovich, A.S. Moskvina, A.V. Shadrin</i> . . . . .	112
H.P21	CHARGE AND MAGNETIC CORRELATIONS IN GRAPHENE NANOFOLDS WITH SCREENED LONG-RANGE COULOMB POTENTIAL <i>V.S. Protsenko, A.A. Katanin</i> . . . . .	114
H.P22	MAGNETIC AND ELECTRONIC PROPERTIES OF $Mn_3Z$ ( $Z = Ga, Ge, In, Sn$ ): AB INITIO STUDIES <i>M.A. Zagrebin, M.A. Obambi, V.D. Buchelnikov</i> . . . . .	117
H.P23	PRESSURE EFFECT ON THE ELECTRONIC AND MAGNETIC PROPERTIES OF NOVEL IRON OXIDE $Fe_4O_5$ <i>V.S. Zhandun, N.V. Kazak</i> . . . . .	120
H.P24	THE SPIN-STATE TRANSITION IN $ACo_2O_4$ OXIDES ( $A = Be, Mg, Ca, Cd, Zn$ ) <i>V.S. Zhandun</i> . . . . .	121
H.P25	SYNTHESIS AND MAGNETIC PROPERTIES OF NANOSTRUCTURAL COMPOSITE $(CaCu_3Ti_4O_{12})_{1-x}(SrFe_{12}O_{19})_x$ ( $x = 0.01, 0.03, 0.07$ AND $0.1$ ) <i>Yu. A. Deeva, T.I. Chupakhina, T.P. Gavrilova, R.M. Eremina</i> . . . . .	122
H.P26	SPIN DYNAMICS AND MAGNETIC PROPERTIES IN RARE-EARTH ORTHOFERRITES $TmFeO_3$ AND $TbFeO_3$ <i>S.A. Skorobogatov, K.A. Shaykhutdinov, D.A. Balaev, M.S. Pavlovskii, A.A. Krasikov, K.Yu. Terentjev</i> . . . . .	125
<b>Section I.</b>		
<b>Magnetism and superconductivity</b> . . . . .		127
I.11	MULTITERMINAL JOSEPHSON STRUCTURES WITH QUASIPARTICLE INJECTION <i>V.V. Ryazanov, T.E. Golikova, I.V. Bobkova, A.M. Bobkov</i> . . . . .	128
I.12	MAGNETOCHIRAL EFFECT IN SUPERCONDUCTING HYBRID STRUCTURES <i>A.S. Mel'nikov, A.A. Kopasov, A.G. Kutlin</i> . . . . .	129
I.13	PROXIMITY EFFECT AT SUPERCONDUCTOR/ANTIFERROMAGNET INTERFACES <i>G.A. Bobkov, I.V. Bobkova, A.M. Bobkov, Akashdeep Kamra</i> . . . . .	131
I.14	FUNCTIONAL BASE ELEMENTS FOR ARTIFICIAL NEURAL NETWORK <i>A. Sidorenko, N. Klenov, I. Soloviev, S. Bakurskiy, A. Vakhrushev, V. Boian, A. Prepelitsa, A. Iacunin, M. Lupu, A. Denisov</i> . . . . .	133

I.I5	SUPERCONDUCTIVITY, MAGNETIC INTERACTIONS, AND DISORDER IN IRON-BASED MATERIALS <i>M.M. Korshunov, V.A. Shestakov, L.V. Begunovich, Yu.N. Togushova . . . . .</i>	134
I.O1	THE MAGNETIC FLUX STRUCTURE $\text{EuFe}_2\text{As}_2$ SINGLE CRYSTALS DOPED BY RUBIDIUM <i>M.S. Sidelnikov, A.V. Palnichenko, A.A. Avtandilyan, K.S. Pervakov, V.A. Vlasenko, I.A. Golovchanskiy, V.M. Pudalov, V.S. Stolyarov, L.Ya. Vinnikov . . . . .</i>	135
I.O2	SUPERCONDUCTING HYBRID SPIN-VALVE WITH SPIN-ORBIT INTERACTION <i>A. Neilo, N. Klenov, I. Soloviev, M. Kupriyanov, S. Bakurskiy. . . . .</i>	137
I.O3	MAGNON-COOPARONS IN MAGNET-SUPERCONDUCTOR HYBRIDS <i>I.V. Bobkova, A.M. Bobkov, A. Kamra, W. Belzig . . . . .</i>	138
I.O4	TRANSPORT AND MICROWAVE STUDIES OF MAGNETIC FLUCTUATION IMPACT ON THE CONDUCTIVITY AND SUPERCONDUCTING TRANSITION OF IRON CHALCOGENIDES <i>I. Gimazov, D. Chareev, A. Vasiliev, A. Sadakov, Yu. Talanov . . . . .</i>	140
I.O5	SPIRAL AND FERRO-MAGNETS IN THE INVERSE PROXIMITY EFFECT <i>N.G. Pugach, D.V. Seleznev, V.O. Yagovtsev, N.A. Gusev . . . . .</i>	141
I.O6	PROXIMITY INDUCED SUPERCONDUCTIVITY IN ORGANIC DIELECTRIC <i>K.Yu. Arutyunov, K.A. Belyaev, A.N. Lachinov, A.P. Yusupov . . . . .</i>	142
I.O7	DYNAMICAL PROPERTIES OF SUPERCONDUCTOR/FERROMAGNETIC-INSULATOR HYBRID STRUCTURES UNDER FERROMAGNETIC RESONANCE CONDITION <i>Y.V. Turkin, N.G. Pugach . . . . .</i>	143
I.O8	MAJORANA AND SUBGAP VORTEX-BOUND STATES IN SPIN-SINGLET CHIRAL SUPERCONDUCTORS WITH NONCOLLINEAR SPIN ORDERING <i>A.O. Zlotnikov . . . . .</i>	144
I.O9	SUPERCONDUCTING BIO-INSPIRED NEURONS FOR SPIKING NETWORKS <i>A.E. Schegolev, N.V. Klenov, I.I. Soloviev, M.Yu. Kupriyanov . . . . .</i>	146
I.O10	MODEL OF CHARGE TRIPLETS FOR UNCONVENTIONAL HTSC SYSTEMS <i>A.S. Moskvina, Yu.D. Panov . . . . .</i>	148
I.O11	PECULIAR PROPERTIES OF $0-\pi$ TRANSITION IN SF-F-FS VARIABLE THICKNESS BRIDGES <i>V.I. Ruzhickiy, S.V. Bakurskiy, N.V. Klenov, I.I. Soloviev, M.Yu. Kupriyanov, A.A. Golubov. . . . .</i>	151

I.P1	EFFECT OF WEAK HUBBARD REPULSION ON SPECTRUM AND TRANSPORT IN HIGHER-ORDER TOPOLOGICAL SUPERCONDUCTOR <i>S.V. Aksenov, A.D. Fedoseev, M.S. Shustin, A.O. Zlotnikov</i> . . . . .	153
I.P2	BROADENED YU-SHIBA-RUSINOV STATES IN DIRTY SUPERCONDUCTING FILMS <i>S.S. Babkin, A.A. Lyublinskaya, I.S. Burmistrov</i> . . . . .	155
I.P3	MAGNETIC AND THERMAL PROPERTIES OF POLYCRYSTALLINE YBCO SUPERCONDUCTOR <i>D.Z. Gabadulin, A.G. Kiiamov, M.A. Cherosov, R.G. Batulin</i> . . . . .	156
I.P4	QUASICLASSICAL THEORY OF PROXIMITY EFFECT AT SUPERCONDUCTOR/ANTIFERROMAGNET INTERFACES <i>G.A. Bobkov, I.V. Bobkova, A.M. Bobkov, V.M. Gordeeva, Akashdeep Kamra</i> . . . . .	157
I.P5	MODELLING OF THE SUPERCONDUCTING TRIPLET SPIN VALVE WITH SEVERAL SUPERCONDUCTOR LAYERS <i>R.R. Gaifullin, R.G. Deminov, V.N. Kushnir, M.Yu. Kupriyanov, A.A. Golubov, L.R. Tagirov</i> . . . . .	159
I.P6	GAP STRUCTURE OF MULTIBAND SUPERCONDUCTORS WITH A SPIN-FLUCTUATION INTERACTION <i>A.E. Karakozov, M.V. Magnitskaya</i> . . . . .	162
I.P7	EFFECTIVE INTERACTIONS IN HIGHER-ORDER TOPOLOGICAL SUPERCONDUCTORS WITH STRONG ELECTRON CORRELATIONS <i>S.V. Aksenov, A.D. Fedoseev, M.S. Shustin, A.O. Zlotnikov</i> . . . . .	164
I.P8	QUANTUM MONTE-CARLO STUDY OF HARDCORE BOSONS IN TWO DIMENSIONS <i>V.S. Ryumshin, V.A. Ulitko, Y.D. Panov</i> . . . . .	166
I.P9	INDUCEMENT OF SUPERCONDUCTIVITY IN ANTIFERROMAGNETIC IRON TELLURIDE BY DOPING WITH TITANIUM CHALCOGENIDES <i>E.V. Kislov, N.V. Selezneva, N.V. Baranov</i> . . . . .	167
I.P10	CRITICAL TEMPERATURE OF SUPERCONDUCTOR/FERROMAGNET NANOSTRUCTURE NEAR A MAGNETIC SKYRMION <i>Yu.N. Proshin, V.E. Zayceva, V.A. Tumanov</i> . . . . .	169
I.P11	CLASSICAL MONTE CARLO ALGORITHM FOR SIMULATION OF A PSEUDOSPIN MODEL FOR CUPRATES <i>V.A. Ulitko, Yu.D. Panov, A.S. Moskvina</i> . . . . .	171

I.P12

SUPERCURRENT-INDUCED LONG-RANGE TRIPLE CORRELATIONS AND CONTROLLABLE JOSEPHSON EFFECT IN SUPERCONDUCTOR/FERROMAGNET HYBRIDS WITH EXTRINSIC SOC

*A.A. Mazanik, I.V. Bobkova . . . . .* 173

**Section J.**

**Soft and hard magnetic materials . . . . .** 174

J.I1

FIELD-INDUCED MAGNETIC PHASE TRANSITIONS IN HIGHLY ANISOTROPIC  $RFe_5Al_7$  FERRIMAGNETS

*N.V. Mushnikov, E.V. Rosenfeld, D.I. Gorbunov, A.V. Andreev . . . . .* 175

J.I2

SELECTIVE LASER SINTERING OF HIGH-COERCIVITY PERMANENT MAGNETS

*A.S. Volegov, S.V. Andreev, N.V. Selezneva, N.M. Nosova, I.A. Ryzhikhin, N.V. Kudrevatykh, V.E. Maltseva . . . . .* 178

J.I3

INVESTIGATION OF NANOPARTICLES OF MATERIALS WITH HIGH MAGNETIC ANISOTROPY IN STRONG PULSED MAGNETIC FIELDS

*D.A. Balaev . . . . .* 179

J.O1

MAGNETIC STRUCTURES IN  $(La_{1-x}Tb_x)Mn_2Si_2$

*P.A. Borisova, V.P. Glazkov, Haneen M. Alsafi, M.A. Semkin, E.G. Gerasimov, P.B. Terentev, N.V. Mushnikov, A.N. Pirogov . . . . .* 181

J.O2

INVESTIGATION OF THE ULTRA-HIGH FIELD-INDUCED PHASE TRANSITION IN THE  $(Nd,Dy)_2Fe_{14}B$

*N.V. Kostyuchenko, I.S. Tereshina, O.M. Surdin, D.A. Maslov, I.S. Strelkov, R.V. Kozabaranov, A.S. Korshunov, Yu.B. Kudasov, V.V. Platonov, I.V. Makarov, A.I. Bykov, A.V. Filippov, S.V. Galanova, A.K. Zvezdin . . . . .* 183

J.O3

SUPERPARAMAGNETISM AND HYSTERESIS CHARACTERISTICS OF COMPOSITES  $Fe_3O_4-Fe_{3-x}Ti_xO_4$ : MICROMAGNETIC MODELING

*P.V. Kharitonskii, A.Yu. Ralin, E.S. Sergienko, N.A. Zolotov, K.G. Gareev, Yu.A. Anikieva . . . . .* 185

J.O4

HIGH FREQUENCY MAGNETOIMPEDANCE (MI) IN AMORPHOUS MICROWIRES WITH DIFFERENT ANISOTROPY NEAR THE CURIE TEMPERATURE

*J. Alam, A. Zedan, D. Mosharov, M.G. Nematov, N.A. Yudanov, L.V. Panina, V.G. Kostishin . . . . .* 188

J.O5

ELECTROMAGNETIC PROPERTIES OF COMPOSITE MATERIAL BASED ON ABC100.30 IRON CAPSULATED BY PHOSPHORUS OXIDE

*O.F. Demidenko, A.O. Larin, G.A. Govor, A.L. Zhaludkevich, T.V. Shoukavaya, A.R. Normirzaev . . . . .* 190



J.O6	ACID ETCHING EFFECTS ON THERMAL STABILITY OF $\Delta E$ -EFFECT IN Cr-DOPED IRON-BASED AMORPHOUS RIBBONS <i>E.A. Golygin, Y.S. Chen, J.G. Lin, A.A. Gavriluk</i> . . . . .	192
J.O7	NANOSTRUCTURED FeNi-C FILMS REDUCED BY CARBOHYDRATES: SYNTHESIS AND MAGNETIC PROPERTIES <i>E.A. Chekanova, E.A. Denisova, S.V. Komogortsev, O.A. Li, R.S. Iskhakov, D.A. Velikanov, A.L. Suhachev, I.V. Nemtsev</i> . . . . .	194
J.O8	INFLUENCE OF HYDROGENATION ON THE STRUCTURAL AND MAGNETIC PROPERTIES OF $Tb(Fe,Co)_{11}Ti$ <i>A.A. Makurenkova, N.Y. Pankratov, I.S. Tereshina, M. Zhelezny, S.A. Nikitin</i> . . . . .	197
J.O9	MAGNETIC PROPERTIES AND ELECTRONIC STRUCTURE OF Gd(Co,Ru)Si TERNARY INTERMETALLICS <i>A.V. Lukoyanov, R.D. Mukhachev, S.P. Platonov, A.G. Kuchin</i> . . . . .	198
J.O10	INVESTIGATION OF THE MAGNETIC PROPERTIES OF AMORPHOUS IRON-BASED MICROWIRES WITH A PARTIALLY CRYSTALLIZED SURFACE LAYER <i>A.A. Fuks, A.S. Aronin, O.I. Aksenov</i> . . . . .	200
J.O11	SYNTHESIS AND MAGNETIC PROPERTIES OF Co, Ni AND COMPOUNDS OF CoFe, NiFe NANOWIRES <i>A.E. Driagina, A.N. Gorkovenko, N.A. Kulesh, V.O. Vas'kovskiy</i> . . . . .	202
J.O12	MAGNETOCALORIC EFFECT IN $R_2Fe_{10}Al_7$ COMPOUND <i>N.Yu. Pankratov, A.Yu. Karpenkov, S.A. Nikitin, I.S. Tereshina</i> . . . . .	204
J.P1	MAGNETIC STRUCTURE OF $Tb(Ni_{0.9}Mn_{0.1})_2Si_2$ <i>Haneen M. Alsafi, E.G. Gerasimov, A.E. Teplykh, P.B. Terentev, N.V. Mushnikov, A.N. Pirogov</i> . . . . .	206
J.P2	MAGNETISM IN $Fe_3Se_4$ UNDER THE ISOTROPIC COMPRESSION <i>L.V. Begunovich, M.M. Korshunov, S.G. Ovchinnikov</i> . . . . .	208
J.P3	MODELING AND ANALYSIS OF FREQUENCY DEPENDENCES OF SOFT MAGNETIC AMORPHOUS WIRES IMPEDANCE <i>D.A. Bukreev, M.S. Derevyanko, A.A. Moiseev, V.O. Kudryavtcev, A.V. Semirov</i> . . . . .	209
J.P4	EFFECT OF SURFACE LAYER TEMPERATURE ON MAGNETIC HYSTERESIS PROPERTIES OF Nd-Fe-B PERMANENT MAGNETS <i>A.S. Cherepanova, V.E. Maltseva, S.V. Andreev, A.S. Volegov</i> . . . . .	211

J.P5	MAGNETIC PROPERTIES OF HIGH-ENTROPY CERAMICS $(\text{SmEuGd})_{1-x}\text{M}_x\text{MnO}_3$ (M = LaBa, SrBa and SrBaCa) WITH PEROVSKITE STRUCTURE <i>N.A. Cherkasova, V.E. Zhivulin, S.V. Taskaev, D.A. Vinnik, O.V. Zaitseva, E.A. Trofimov, D.A. Zhrebtsov, S.A. Gudkova</i> . . . . .	213
J.P6	INTERLAYER COUPLING AND COERCIVITY OF SANDWICH STRUCTURES PRODUCED BY CHEMICAL DEPOSITION <i>A.V. Chzhan, V.A. Orlov</i> . . . . .	215
J.P7	TEMPERATURE DEPENDENCE OF ELECTRIC IMPEDANCE OF THE COBALT-BASED SOFT MAGNETIC WIRE NEAR THE FERROMAGNETIC PHASE TRANSITION <i>M.S. Derevyanko, D.A. Bukreev, A.A. Moiseev, A.V. Semirov</i> . . . . .	217
J.P8	MANUFACTURING OF PERMANENT MAGNETS BASED ON $\text{SmFe}_{11}\text{Ti}$ PHASE BY SELECTIVE LASER SINTERING <i>D.S. Neznakhin, V.E. Maltseva, S.V. Andreev, N.V. Selezneva, E.I. Patrakov, O.A. Golovnia, A.S. Volegov</i> . . . . .	220
J.P9	MAGNETIC STATE OF $\text{Fe}_{0.33}\text{TiS}_2$ WITH TRIANGULAR NETWORK OF INTERCALATED Fe ATOMS <i>E.M. Sherokalova, N.V. Selezneva, A.S. Volegov, N.V. Baranov</i> . . . . .	222
J.P10	PHASE TRANSITIONS UPON SINTERING OF Nd-Dy-Fe-B POWDERS STUDIED BY IN-SITU DSC <i>O.A. Golovnia, L.A. Stashkova, A.V. Protasov, A.V. Ogurtsov, M.K. Sharin, A.G. Popov, K.A. Kruchinina, A.V. Shitov</i> . . . . .	223
J.P11	MAGNETIC PROPERTIES OF IRON-DOPED $\text{WTe}_2$ , A WEYL SEMIMETAL <i>A.Sh. Khachatryan, E.V. Charnaya, V.V. Marchenkov</i> . . . . .	225
J.P12	TUNING THE MAGNETIC PROPERTIES OF NANOWIRES MADE OF IRON GROUP METALS <i>D.R. Khairtdinova, I.M. Doludenko, S.A. Lukkareva, D.L. Zagorskiy, L.V. Panina</i> . . . . .	226
J.P13	MAGNETIC PROPERTIES AND MICROSTRUCTURE OF $\text{Sm}_2\text{Fe}_{17}\text{N}_3$ POWDERS AFTER MILLING IN DIFFERENT TYPE MILLS <i>D.A. Kolodkin, A.G. Popov</i> . . . . .	229
J.P14	CANTED FERROMAGNETS IN DOPED GdTsi SYSTEMS <i>A.G. Kuchin, S.P. Platonov, R.D. Mukhachev, A.V. Lukoyanov, A.S. Volegov, V.S. Gaviko, M.Yu. Yakovleva</i> . . . . .	231

J.P15	MAGNETIC PROPERTIES AND STRUCTURE OF THE ALLOY Fe <sub>63.5</sub> Ni <sub>10</sub> Cu <sub>1</sub> Nb <sub>3</sub> Si <sub>13.5</sub> B <sub>9</sub> WITH INDUCED MAGNETIC ANISOTROPY <i>V.A. Lukshina, N.V. Dmitrieva, E.G. Volkova, D.A. Shishkin</i> . . . . .	233
J.P16	MAGNETIC CHARACTERISTICS OF NdFeB 3D-PRINTED PERMANENT MAGNETS OBTAINED BY SELECTIVE LASER SINTERING <i>V.E. Maltseva, A.N. Urzhumtsev, S.V. Andreev, A.S. Volegov</i> . . . . .	235
J.P17	MAGNETIC PROPERTIES AND MAGNETIC HYSTERESIS IN HIGH-COERCIVE Fe <sub>0.25</sub> TaS <sub>2</sub> : EFFECT OF Se FOR S SUBSTITUTION <i>N.M. Nosova, N.V. Baranov, E.M. Sherokalova, A.S. Volegov</i> . . . . .	237
J.P18	STRUCTURAL TRANSITIONS AND MAGNETIC RESPONSE OF SUPRAMOLECULAR MAGNETIC POLYMER-LIKE STRUCTURES WITH BIDISPERSE MONOMERS <i>E.S. Pyanzina, E.V. Novak, M. Gupalo, S.S. Kantorovich</i> . . . . .	238
J.P19	DESIGN OF LAMINATED NANOCOMPOSITES FOR MICROWAVES <i>A.V. Osipov, S.Y. Bobrovskii, A.N. Lagarkov, S.A. Maklakov, S.S. Maklakov, K.N. Rozanov, I.A. Ryzhikov, P.A. Zezyulina</i> . . . . .	239
J.P20	NEGATIVE ANISOTROPY IN Ni-Fe FILMS <i>P.A. Savin, O.A. Adanakova, V.N. Lepalovskij, E.V. Kudyukov, V.O. Vas'kovskiy</i> . . . . .	240
J.P21	DETERMINATION OF THE 3d-4f ELECTRONIC STATES DISTRIBUTION IN THE VALENCE BAND IN COMPOUNDS WITH LAVES PHASE STRUCTURE ErCo <sub>2</sub> AND ErCo <sub>2</sub> Mn <sub>0.4</sub> BY RESONANT PHOTOEMISSION <i>E.A. Ponomareva, V.I. Grebennikov, E.G. Gerasimov, P.B. Terent'yev, A.A. Inishev, N.V. Mushnikov, T.V. Kuznetsova</i> . . . . .	242
J.P22	MICROSTRUCTURE AND MAGNETIC PROPERTIES OF STRIP-CASTED (Sm,Zr) (Fe,Co) <sub>10</sub> Ti <sub>0.7</sub> ALLOY <i>A.V. Protasov, O.A. Golovnya, A.G. Popov, A.S. Volegov, V.S. Gaviko, A.V. Shitov</i> . . . . .	243
J.P23	Cu DOPED HARD MAGNETIC POWDERS BASED ON Nd(FeCo)B. MICROMAGNETIC PROPERTIES AND STRUCTURE <i>A.V. Ognev, V.Yu. Samardak, V.N. Kharitonov, A.A. Belov, O.O. Shichalin, E.K. Papynov, A.S. Samardak</i> . . . . .	245
J.P24	MAGNETIC PROPERTIES OF Mn-DOPED Fe <sub>3+x</sub> Si <sub>1-x</sub> FILMS SYNTHESIZED ON SOI SUBSTRATE BY LOW TEMPERATURE ANNEALING <i>A.V. Lukyanenko, A.S. Tarasov, I.A. Tarasov, M.V. Rautskii, I.A. Yakovlev, N.N. Kosyrev, V.A. Komarov, L.V. Shanidze, S.N. Varnakov, S.G. Ovchinnikov, G.S. Patrin, N.V. Volkov</i> . . . . .	248

J.P25	CORRELATION OF THE CHEMICAL COMPOSITION AND MAGNETIC PROPERTIES OF Ni-Zn-Co FERRITE <i>D.A. Vinnik, D.P. Sherstyuk, V.E. Zhivulin, D.A. Zherebtsov, S.A. Gudkova, N.S. Perov, Yu.A. Alekhina, K.A. Astapovich, A.V. Trukhanov</i> . . . . .	250
J.P26	STUDY OF ALIGNMENT DEGREE OF Nd-Dy-Fe-B SINTERED MAGNETS BY DIFFERENT METHODS <i>A.V. Shitov, O.A. Golovnia, V.S. Gaviko, A.G. Popov, D.Yu. Vasilenko</i> . . . . .	253
J.P27	EFFECT OF ION SUBSTITUTIONS ON THE MAGNETIC PROPERTIES OF BARIUM HEXAFERRITE <i>I.A. Solizoda, V.E. Zhivulin, E.A. Trofimov, S.V. Taskaev, D.A. Vinnik</i> . . . . .	256
J.P28	INVESTIGATION OF THE MAGNETIC AND DIELECTRIC PROPERTIES OF BARIUM-TITANIUM HEXAFERRITE <i>S.V. Trukhanov, T.I. Zubar, V.A. Turchenko, An.V. Trukhanov, L. Matzui, O. Yakovenko, D.A. Vinnik, A.Yu. Starikov, V.E. Zhivulin, A.V. Trukhanov</i> . . . . .	258
J.P29	INFLUENCE OF THERMAL TREATMENTS ON THE MAGNETIC PROPERTIES OF SOFT MAGNETIC MATERIALS PRODUCED BY SLS METHOD FROM IRON POWDER <i>E.A. Stepanova, D.A. Razueva, V.E. Maltseva, S.V. Andreev, A.S. Volegov</i> . . . . .	260
J.P30	PREDICTIONS OF THE MAGNETIC PROPERTIES OF NANOCRYSTALLINE FINEMET-TYPE ALLOYS USING MACHINE LEARNING <i>K.A. Stepanova, V.A. Kataev</i> . . . . .	262
J.P31	EASY PLANE TYPE OF MAGNETIC ANISOTROPY IN LAYERED GdMn <sub>2</sub> Si <sub>2</sub> COMPOUND WITH EASY AXIS TYPE OF MAGNETOCRYSTALLINE ANISOTROPY <i>P.B. Terentev, E.G. Gerasimov, A.F. Gubkin, N.V. Mushnikov</i> . . . . .	264
J.P32	MAGNETIZATION REVERSAL PROCESSES IN Nd <sub>2</sub> Fe <sub>14</sub> B AND Sm(Co, Fe, Zr, Cu) <sub>6,63</sub> PERMANENT MAGNETS <i>A.N. Urzhumtsev, V.E. Maltseva, A.S. Volegov</i> . . . . .	265
J.P33	STRUCTURAL FEATURES OF MAGNETIC METAL-DIELECTRIC FILMS (CoFeB + SiO <sub>2</sub> ) <i>L.N. Kotov, V.A. Ustyugov, V.S. Vlasov</i> . . . . .	267
J.P34	UNIQUE MAGNETIC PROPERTIES OF NANOCRYSTALLINE CO-BASED GLASS-COATED HYBRID ALLOY <i>V. Kolesnikova, N. Andreev, A. Omelyanchik, I. Baraban, M. Gorshenkov, V. Rodionova</i> . . . . .	269
J.P35	APPLICATION OF MACHINE VISION IN DILATOMETRY TECHNIQUE <i>V. Rodionov, D. Borov</i> . . . . .	270

J.P36	SYNTHESIS OF HIGH-ENTROPY PHASE WITH THE MAGNETOPLUMBITE STRUCTURE BY THE NITRATE-CITRATE METHOD <i>V.E. Zhivulin, N.A. Cherkasova, D.A. Vinnik, O.V. Zaitseva, D.A. Zhrebtsov, E.A. Trofimov</i> . . . . .	271
J.P37	EFFECT OF PLASTIC DEFORMATION ON THE MAGNETIC PROPERTIES OF RAPIDLY QUENCHED CoFeNbSiB WIRES <i>N.A. Lyu-yu, N.V. Morozova, E.A. Golygin, A.V. Gavrilyuk, S.M. Zubritskii, A.A. Gavrilyuk</i> . . . . .	273
J.P38	STRUCTURE AND MORPHOLOGY OF TITANIUM DIOXIDE ENCAPSULATED IRON POWDER <i>A.L. Zhaludkevich, O.F. Demidenko, A.O. Larin, G.A. Govor, U.T. Berdiev, U.B. Suleimanov, F.F. Hasanov</i> . . . . .	275
J.P39	BEHAVIOR OF ELECTRICAL RESISTANCE OF FERROMAGNETIC MICROWIRES HEATED BY EXTERNAL SOURCE AND DIRECT CURRENT <i>A.A. Pahomova, A.A. Samokhvalov, A.T. Morchenko</i> . . . . .	277
<b>Section K.</b>		
<b>Magnetic semiconductors, multiferroics, topological insulators . . .</b>		
K.I1	MAGNETOELECTRIC EFFECT IN PARAMAGNETIC RARE-EARTH LANGASITES <i>A.A. Mukhin, V.Yu. Ivanov, A.M. Kuzmenko, A.Yu. Tikhonovskii</i> . . . . .	280
K.I2	EFFECT OF BaTiO <sub>3</sub> AND Zn <sub>0.25</sub> Co <sub>0.75</sub> Fe <sub>2</sub> O <sub>4</sub> FILLERS ON MECHANICAL AND MAGNETOELECTRIC PROPERTIES OF PVDF-TrFE-BASED COMPOSITES <i>K.V. Sobolev, V.G. Kolesnikova, A.S. Omelyanchik, Yu.A. Alekhina, L.A. Makarova, V.N. Antipova, K.V. Levada, A.A. Amirov, V.V. Rodionova</i> . . . . .	283
K.I3	TERAHERTZ INDUCED DYNAMICS OF ANTIFERROMAGNETS <i>E.A. Mashkovich</i> . . . . .	286
K.O1	MAGNETOELECTRIC COUPLING IN FeCr <sub>2</sub> O <sub>4</sub> , FeV <sub>2</sub> O <sub>4</sub> , DyCrO <sub>4</sub> AND Fe <sub>2</sub> Mo <sub>3</sub> O <sub>8</sub> <i>M.V. Eremin</i> . . . . .	289
K.O2	TEMPERATURE BEHAVIOR OF MAGNETIC AND MAGNETOELECTRIC PROPERTIES IN Fe LANGASITES <i>A.Yu. Tikhonovskii, V.Yu. Ivanov, A.M. Kuzmenko, Yu.F. Popov, G.P. Vorobev, A.A. Mukhin</i> . . . . .	290
K.O3	DETECTION OF ELECTRIC POLARIZATION IN TERBIUM ORTHOFERRITE <i>V.Yu. Ivanov, A.M. Kuzmenko, A.A. Mukhin</i> . . . . .	292

K.O4	THE ROLE OF MANGANESE SUBSTITUTION IN CHANGING THE MAGNETIC AND DIELECTRIC PROPERTIES OF BULK MAGNETOELECTRICS $\text{BiFe}_{1-x}\text{Mn}_x\text{O}_3$ ( $x = 0.05$ and $0.15$ ) <i>T.N. Tarasenko, V.I. Mikhaylov, Z.F. Kravchenko, V.V. Burkhovetskiy, A.I. Izotov, Yu.A. Legenkii, A.M. Zyvulko, K.I. Yanushkevich, S.S. Aplesnin . . . . .</i>	294
K.O5	EFFECT OF DOPING IMPURITIES ON THE SENSITIVITY OF DIAMAGNETIC CdTe CRYSTALS TO PULSED MAGNETIC ACTION <i>I.S. Volchkov, P.L. Podkur, M.D. Pavlyuk, V.B. Kvarталov, V.M. Kanevskii . . . . .</i>	297
K.O6	MAGNETIC RESONANCE IN Ho-DOPED RARE-EARTH LANGASITE <i>A.M. Kuzmenko, A.A. Mukhin, V.Yu. Ivanov, A.Yu. Tikhanovskii, L. Weymann, A. Shuvaev, A. Pimenov . . . . .</i>	299
K.O7	POLYMER MAGNETOELECTRIC COMPOSITES BASED ON PVDF <i>A.A. Amirov, V.V. Rodionova, A.M. Aliev . . . . .</i>	301
K.O8	NÉEL TRANSITION TEMPERATURES AS A FUNCTION OF LATTICE PARAMETER FOR LITHIUM METAL ORTHOPHOSPHATES <i>M.A. Semkin . . . . .</i>	303
K.O9	EFFECTIVE MASS ANISOTROPY AND SPIN-ORBIT COUPLING IN 2D ELECTRON GAS OF GaN/AlN HIGH-ELECTRON-MOBILITY TRANSISTOR HETEROSTRUCTURES <i>N.K. Chumakov, I.S. Ezubchenko, I.A. Chernykh, I.V. Belov, M.L. Zanaevskiy, L.L. Lev, V.N. Strocov, V.G. Valeyev . . . . .</i>	305
K.P1	FERROMAGNETISM AND TWO MAGNETIC PHASES IN COBALT ION IMPLANTED RUTILE: EFFECT OF SUBSTRATE TEMPERATURE <i>E.M. Begishev, I.R. Vakhitov, N.M. Lyadov, V.I. Nuzhdin, V.F. Valeev, V.V. Bazarov, D.M. Kuzina, R.I. Khaibullin . . . . .</i>	308
K.P2	FREQUENCY DEPENDENCES OF ELECTRICAL RESISTANCE OF MANGANITES WITH MANGANESE REPLACEMENT BY $(\text{Ni}_{0.5}^{2+}\text{Ge}_{0.5}^{4+})$ COMBINATION <i>A.G. Badelin, I.M. Derzhavin, V.K. Karpasyuk, E.A. Korneeva, D.I. Merkulov . . . . .</i>	310
K.P3	DIRECT AND REVERS MAGNETOELECTRIC EFFECT IN $\text{NdFe}_3(\text{BO}_3)_4$ <i>E.V. Eremin, A.L. Freydmann, I.A. Gudim . . . . .</i>	312
K.P4	MAGNETIC FIELD SPECTRUM ANALYZER USING MAGNETOELECTRIC EFFECT OF FREQUENCY MIXING IN COMPOSITE FERROMAGNET-PIEZOELECTRIC STRUCTURE <i>L.Y. Fetisov, D.V. Chashin, D.V. Saveliev, D.A. Burdin, Y.K. Fetisov, F.A. Fedulov . . . . .</i>	313
K.P5	MAGNETOELECTRIC FREQUENCY DOUBLER <i>F.A. Fedulov, D.V. Saveliev, L.Y. Fetisov . . . . .</i>	316

K.P6	THE INFLUENCE OF RARE EARTH ION SUBSTITUTION ON MAGNETOELECTRIC PROPERTIES IN ORTHOROMBIC SINGLE CRYSTALS $Dy_{1-x}Ho_xMnO_3$ <i>I.N. Horoshiy, M.I. Kolkov, K.Yu. Terent'ev, A.L. Freydmann</i> . . . . .	318
K.P7	MAGNETIC PROPERTIES OF TWIN TRIGONAL OXIBORATE WITH HUNTITE STRUCTURE. EFFECT OF ANNEALING <i>I.A. Gudim, E.V. Eremin, V.R. Kuchesheva-Titova</i> . . . . .	320
K.P8	THE PHENOMENON OF MAGNETIC COMPENSATION IN THE MULTICOMPONENT $(Sm, Gd, Y)Fe_2$ COMPOUNDS <i>M.R. Khomenko, N.Yu. Pankratov, Z.S. Umhaeva, I.M. Aliev, A.Yu. Karpenkov, I.S. Tereshina</i> . . . . .	322
K.P9	MAGNETOELECTRIC EFFECT IN YIG-GGG-PZT STRUCTURE <i>K.V. Lambrianidj, D.A. Burdin, Y.K. Fetisov, N.A. Ekonomov, D.V. Chashin</i> . . . . .	325
K.P10	INFLUENCE OF SPACERS AND NANOSTRUCTURING ON THE MAGNETOELECTRIC PROPERTIES OF METAL/PVDF FILM COMPOSITES <i>K.G. Balymov, E.V. Kudyukov, A.A Feshenko, M.A. Kalinin, V.O. Vas'kovskiy</i> . . . . .	327
K.P11	SYNTHESIS AND MAGNETIC PROPERTIES OF $TbCr_3(BO_3)_4$ SINGLE CRYSTALS <i>A.I. Pankrats, I.A. Gudim, M.S. Molokeev, N.V. Mikhashenok</i> . . . . .	329
K.P12	STRONTIUM IRIDATE THIN FILMS – MATERIAL FOR SUPERCONDUCTING CRYOELECTRONICS AND SPINTRONICS <i>I.E. Moskal, Yu.V. Kisilinski, A.M. Petrzhik, K.Y. Constantinian, A.V. Shadrin, G.A. Ovsyannikov</i> . . . . .	331
K.P13	SENSITIVITY OF $Cd_{1-x}Zn_xTe$ DIAMAGNETIC SEMICONDUCTOR CRYSTALS ( $x = 0.06; 0.03; 0$ ) TO THE INFLUENCE OF A PULSED MAGNETIC FIELD <i>P.L. Podkur, I.S. Volchkov, V.B. Kvartalov, M.V. Pavluyk, V.M. Kanevskii</i> . . . . .	333
K.P14	STRUCTURAL, MAGNETIC AND TRANSPORT PROPERTIES THULIUM-SUBSTITUTED MANGANESE SELENIDE <i>O.B. Romanova, S.S. Aplesnin, L.V. Udod, K.I. Yanushkevich, A.I. Galays, A.M. Zhivulko</i> . . . . .	335
K.P15	FEATURES OF THE ELECTRONIC STATE OF $Cu^+$ IONS IN DELAFOSSITE COMPOUNDS $CuBO_2$ ( $B = Al, Cr, Fe$ ) ACCORDING TO NMR- AND NQR-DATA <i>A.G. Smolnikov, V.V. Ogloblichev, A.F. Sadykov, Yu.V. Piskunov, R.V. Skoryunov</i> . . . . .	337
K.P16	REFLECTION AND MAGNETOREFLECTION SPECTRUM OF THE $MnFe_2O_4$ FERRITE-SPINEL <i>E.A. Surzhikov, Yu.P. Sukhorukov, S.V. Naumov, A.V. Telegin</i> . . . . .	339

K.P17	ROOM TEMPERATURE FERROMAGNETISM IN ORGANIC-INORGANIC LEAD IODIDE PEROVSKITE SINGLE CRYSTALS <i>I.V. Zhevstovskikh, T.B. Charikova, A.S. Klepikova, M.R. Popov, E.A. Stepanova, O.I. Semenova</i> . . . . .	340
K.P18	TOPOLOGICAL FEATURES IN BAND STRUCTURE OF GdNiSb COMPOUND <i>S.T. Baidak, A.V. Lukoyanov</i> . . . . .	342
K.P19	MAGNETOELECTRIC EFFECT IN A HEMATITE-PIEZOELECTRIC HETEROSTRUCTURE <i>V.V. Borichok, D.A. Burdin, Y.K. Fetisov, N.A. Ekonomov, D.V. Chashin</i> . . . . .	343
K.P20	EFFECT OF A MELT-SOLUTION ON THE MAGNETIC PROPERTIES OF A SINGLE CRYSTAL WITH THE HUNTITE STRUCTURE <i>V.R. Kuchesheva-Titova, I.A. Gudim, E.V. Eremin</i> . . . . .	345
K.P21	IRON OXIDATION STATE IN $\text{La}_{0.7}\text{Sr}_{1.3}\text{Fe}_{0.7}\text{Ti}_{0.3}\text{O}_4$ AND $\text{La}_{0.5}\text{Sr}_{1.5}\text{Fe}_{0.5}\text{Ti}_{0.5}\text{O}_4$ LAYERED PEROVSKITES: DIELECTRIC AND MAGNETIC PROPERTIES <i>T.P. Gavrilova, T.I. Chupakhina, Yu.A. Deeva, I.F. Gilmutdinov, M.A. Cherosov, I.V. Yatsyk, F.G. Vagizov, A.R. Yagfarova, R.M. Eremina</i> . . . . .	347
K.P22	FABRICATION AND ANALYZIS OF 2D COMPOSITE MATERIALS BASED ON PIEZOELECTRIC POLYMERS AND FERROMAGNETIC NANOPARTICLES <i>S.A. Vorontcov, K.V. Sobolev, V.G. Kolesnikova, A. Omelyanchik, V.V. Rodionova, K. Levada</i> . . . . .	349
<b>Section L.</b>		
<b>Magnetic soft matter</b> . . . . .		350
L.I1	TISSUE-MIMETIC MAGNETOACTIVE ELASTOMERS BASED ON BOTTLEBRUSH POLYMER MATRICES <i>S.A. Kostrov, S.S. Sheiko, E.Yu. Kramarenko</i> . . . . .	351
L.I2	MATHEMATICAL AND COMPUTER MODELLING OF THE EFFECTS OF INTERACTIONS, STRUCTURE FORMATION, AND POLYDISPERSITY ON THE DYNAMIC MAGNETIC SUSCEPTIBILITY AND MAGNETIC RELAXATION OF FERROFLUIDS <i>A.O. Ivanov, P.J. Camp</i> . . . . .	352
L.O1	MAGNETIC PROPERTIES OF MAGNETIC ELASTOMERS FILLED WITH SPHERICAL AND FLAKE-LIKE PARTICLES <i>A.B. Dobroserdova, S.S. Kantorovich</i> . . . . .	353



L.02	MAGNETICALLY INDUCED STRUCTURAL TRANSITIONS IN LIQUID CRYSTALS DOPED WITH CARBON NANOTUBES: BRIDGING FROM MOLECULAR-STATISTICAL TO CONTINUUM THEORY <i>D.A. Petrov</i> . . . . .	354
L.03	MAGNETIC AND STRUCTURAL EQUILIBRIUM PROPERTIES OF A SUSPENSION OF MAGNETIC MULTICORE NANOPARTICLES <i>A.A. Kuznetsov, E.V. Novak, E.S. Pyanzina, S.S. Kantorovich</i> . . . . .	356
L.04	FORMATION OF RING-SHAPED DEPOSITS DURING THE EVAPORATION OF DROPS OF MAGNETIC COLLOIDS IN MAGNETIC AND ELECTRIC FIELDS <i>S.A. Semenova, A.S. Drozdov, Yu.I. Dikansky</i> . . . . .	358
L.05	DYNAMIC RESPONSE OF AN ENSEMBLE OF INTERACTING MAGNETIC PARTICLES: THE INFLUENCE OF AC MAGNETIC FIELD AMPLITUDE <i>E.A. Elfimova, M.S. Rusanov, V.C. Zverev</i> . . . . .	360
L.06	MAGNETIC PROPERTIES OF FRACTIONED FERROFLUID <i>S.A. Kunikin, A.G. Ispiryay, N.V. Gorkovenko, D.I. Dmitryevskaya</i> . . . . .	361
L.07	DYNAMICS OF MULTIPHASE MAGNETIC FLUID SYSTEMS UNDER VARIOUS EXTERNAL INFLUENCES <i>P.A. Ryapolov, E.V. Shel'deshova, E.A. Sokolov, D.A. Kalyuzhnaya, A.O. Vasilyeva</i> . . . . .	363
L.08	SUPERPARAMAGNETIC EFFECTS IN LONGITUDINAL DYNAMIC MAGNETIC SUSCEPTIBILITY OF UNIAXIAL NANOPARTICLES SUSPENDED IN A LIQUID <i>A.V. Lebedev, M.A. Koskov, I.S. Poperechny</i> . . . . .	364
L.09	MODELING OF THE PSEUDO-PLASTICITY EFFECT INDUCED BY FORCED DEFORMATION OF A MAGNETOACTIVE ELASTOMER UNDER EXTERNAL FIELD <i>O.V. Stolbov, Yu.L. Raikher</i> . . . . .	366
L.010	GMI DETECTION OF EPOXY COMPOSITES WITH VARIOUS CONCENTRATIONS OF IRON OXIDE MICROPARTICLES <i>G.Yu. Melnikov, L. Media Ranero, A.P. Safronov, A. Larrañaga, A.V. Svalov, G.V. Kurlyandskaya</i> . . . . .	368
L.011	DYNAMIC REMAGNETIZATION OF CLUSTERED FERROGELS <i>A.Y. Zubarev</i> . . . . .	370
L.012	SUSPENSION AGGREGATION KINETICS IN A UNIFORM STATIONARY MAGNETIC FIELD <i>A.R. Zakinyan</i> . . . . .	372
L.013	STRAIN-MAGNETO-OPTICS OF MAGNETOSTRICTIVE FERRITE-SPINELS <i>Yu.P. Sukhorukov, A.V. Telegin, N.G. Bebenin, S.V. Naumov, E.A. Surzhikov</i> . . . . .	374

L.O14	THE INFLUENCE OF THE SHEAR FLOW AND TOPOLOGY ON THE MAGNETORHEOLOGICAL PROPERTIES OF CLUSTERS FORMED BY STOCKMAYER SUPRACOLLOIDAL MAGNETIC POLYMERS <i>V.S. Zverev, E.V. Novak, I. Novikau, S.S. Kantorovich</i> . . . . .	375
L.O15	SPHERICAL MAGNETIZABLE BODY IN A DROP OF FERROFLUID IN A UNIFORM HORIZONTAL MAGNETIC FIELD <i>K.L. Sogomonyan, A.S. Vinogradova, O.A. Sharova, D.A. Pelevina, V.A. Naletova</i> . . . . .	376
L.P1	THE DYNAMIC MAGNETIC RESPONSE OF IMMOBILIZED SUPERPARAMAGNETIC NANOPARTICLES TO AN AC FIELD WITH ARBITRARY AMPLITUDE <i>A.V. Ambarov, E.A. Elfimova, V.S. Zverev</i> . . . . .	378
L.P2	TEMPERATURE DEPENDENCE OF THE MAGNETO-OPTICAL EFFECT IN A MAGNETIC EMULSION <i>S.S. Belykh, C.V. Yerin, V.V. Fursova</i> . . . . .	380
L.P3	THEORETICAL STUDY OF THE MAGNETIC PROPERTIES OF THE DIMER <i>A.Yu. Zubarev, D.N. Chirikov</i> . . . . .	382
L.P4	MATHEMATICAL MODELING OF THE POLYMER FERROCOMPOSITE MAGNETIC PROPERTIES TAKING INTO ACCOUNT DIPOLAR INTERACTIONS <i>D.I. Radushnov, A.Yu. Solovyova, E.A. Elfimova</i> . . . . .	385
L.P5	DEFORMATION OF A STRUCTURED MAGNETICALLY ACTIVE ELASTOMER WITH MAGNETICALLY HARD INCLUSIONS IN A 2D FORMULATION <i>A.A. Ignatov, O.V. Stolbov, V.V. Rodionova</i> . . . . .	387
L.P6	PROBLEM OF MAGNETOSTATIC SKYRMION STABILIZATION IN FERROMAGNET/X (X = PARAMAGNET, SUPERCONDUCTOR) HYBRID SYSTEMS <i>M.A. Kuznetsov, K.R. Mukhamatchin, A.A. Fraerman</i> . . . . .	389
L.P7	THE SPECIFIC LOSS POWER IN THE SYSTEMS OF MOBILE AND IMMOBILIZED MAGNETIC PARTICLES IN APPLIED AC MAGNETIC FIELD <i>A.A. Kuznetsova, E.A. Elfimova, A.V. Ambarov</i> . . . . .	392
L.P8	THE MAGNETIC CHARACTERISTICS INHOMOGENEITY OF AMORPHOUS COBALT-BASED ALLOY IN AS-QUENCHED STATE <i>E.S. Nekrasov, N.A. Skulkina</i> . . . . .	394
L.P9	DEMAGNETIZING FACTOR CONTRIBUTION TO THE FUNCTIONAL PROPERTIES OF COBALT-BASED AMORPHOUS RIBBONS WITH HIGH GIANT MAGNETIC IMPEDANCE <i>A.A. Pasynkova, A.V. Timofeeva, V.A. Lukshina, G.V. Kurlyandskaya</i> . . . . .	396

L.P10	MAGNETOACTIVE ELASTOMERS WITH MAGNETICALLY HARD PARTICLES: THE EFFECT OF PARTICLE/MATRIX ADHESION FAILURE ON THE MAGNETIZATION <i>M.V. Vaganov, D.Yu. Borin, S. Odenbach, Yu.L. Raikher</i> . . . . .	398
L.P11	NUMERICAL CALCULATION OF THE CUBIC TERM OF THE DYNAMIC SUSCEPTIBILITY OF INTERACTING AND MOVING MAGNETIC PARTICLES <i>M.S Rusanov, E.A. Elfimova, V.C Zverev</i> . . . . .	400
L.P12	COMPUTER SIMULATION OF JOINT MAGNETIC-STRUCTURAL-MECHANICAL RESPONSE OF MAGNETOSENSITIVE VESICLES <i>A.V. Ryzhkov</i> . . . . .	402
L.P13	DYNAMICS OF MAGNETIC FLUIDS AND BIDISPERSE MAGNETIC SYSTEMS UNDERGOING OSCILLATORY SHEAR <i>E.V. Shel'deshova, P.A. Ryapolov</i> . . . . .	404
L.P14	MAGNETIC PROPERTIES OF Fe-Ga ALLOYS <i>V.A. Lukshina, D.A. Shishkin, N.V. Ershov, A.R. Kuznetsov, Yu.N. Gornostyrev</i> . . . . .	405
L.P15	ORIENTATIONAL TRANSITIONS IN A LIQUID CRYSTAL SUSPENSION OF SPIRAL MAGNETIC PARTICLES UNDER WEAK SEGREGATION <i>D.P. Sokolchik, D.V. Makarov</i> . . . . .	407
L.P16	DYNAMICS OF NONMAGNETIC DROPS AND GAS BUBBLES IN A MICROCHANNEL WITH A MAGNETIC FLUID IN AN INHOMOGENEOUS MAGNETIC FIELD <i>E.A. Sokolov, D.A. Kalyuzhnaya, A.O. Vasilyeva, P.A. Ryapolov</i> . . . . .	408
L.P17	SPECTRA OF BIREFRINGENCE AND DICHROISM IN MAGNETIC COLLOIDS WITH SIZE-SORTED NANOPARTICLES <i>E.I. Shevchenko, V.I. Vivchar, C.V. Yerin</i> . . . . .	409
L.P18	MATHEMATICAL AND COMPUTER MODELING OF THE SYSTEMS OF THE IMMOBILIZED PARTICLES LOCATED IN THE NODES OF THE SIMPLE CUBIC LATTICE OR DISTRIBUTED RANDOMLY <i>S.A. Sokolsky, A.Yu. Solovyova, E.A. Elfimova</i> . . . . .	411
L.P19	ON THE THEORY OF MAGNETICALLY INDUCED FLOWS IN THROMBOSED CHANNELS <i>A.Yu. Musikhin, A.Yu. Zubarev</i> . . . . .	413

**Section M.**

<b>Magnetism in biology and medicine</b> . . . . .	<b>414</b>
<b>M.I1</b>	
MULTIFUNCTIONAL MAGNETORHEOLOGICAL MATERIALS AND THEIR APPLICATION PROSPECTS <i>N.S. Perov, L.A. Makarova, D.A. Isaev, Iu.A. Alekhina, M.F. Khajrullin, E.Yu. Kramarenko</i> . . . . .	<b>415</b>
<b>M.O1</b>	
REGISTRATION OF MAGNETIC NANOPARTICLES IN AQUEOUS USING MAGNETOMETERS <i>L.P. Ichkitidze, M.V. Belodedov, A.Yu. Gerasimenko, D.V. Telyshev, S.V. Selishchev</i> . . . . .	<b>417</b>
<b>M.O2</b>	
“MAGNETIC CORE-GOLD SHELL” NANOSTRUCTURES FOR PHOTOTHERMAL THERAPY <i>A. Shumskaya, A. Rogachev, I. Korolkov, M. Zdorovets, A. Kozlov, A. Ognev, V.K. Belyaev, V.V. Rodionova, L.V. Panina</i> . . . . .	<b>419</b>
<b>M.O3</b>	
EVALUATION OF CYTOTOXICITY OF GOLD COMPOSITES SUPPLEMENTED WITH METAL-DOPED CFO NANOPARTICLES USING JURKAT CELL LINE <i>A.V. Motorzhina, S.E. Pshenichnikov, V.V. Malashchenko, S. Jovanović, L.S. Litvinova, L.V. Panina, V.V. Rodionova, K.V. Levada</i> . . . . .	<b>421</b>
<b>M.O4</b>	
MAGNETIC NANOPARTICLES Fe <sub>3</sub> O <sub>4</sub> , Fe <sub>3</sub> O <sub>4</sub> @SiO <sub>2</sub> , Fe <sub>3</sub> O <sub>4</sub> @C, and Fe <sub>3</sub> O <sub>4</sub> @C@C FOR THE ORGANIC DYES ADSORPTION <i>O.S. Ivanova, I.S. Edelman, A.E. Sokolov, E.S. Svetlitsky, Chun-Rong Lin, Ying-Zhen Chen</i> . . . . .	<b>424</b>
<b>M.P1</b>	
EFFECT OF PLASMA TREATMENT ON THE MORPHO-MECHANICAL AND ADHESIVE PROPERTIES OF MAGNETOELECTRIC NANOCOMPOSITES FOR BIOMEDICAL APPLICATIONS <i>V. Antipova, K. Sobolev, E. Korepanova, S. Vorontcov, V. Malashchenko, V.V. Shupletsova, L. Litvinova, K. Levada, V. Rodionova</i> . . . . .	<b>427</b>
<b>M.P2</b>	
REMOVAL OF NONMAGNETIC PARTICLES FROM WATER BY USING MAGNETIC SYSTEM <i>M.S. Filinkova, Iu.A. Bakhteeva, I.V. Medvedeva, I.V. Byzov, S.V. Zhakov, M.A. Uimin</i> . . . . .	<b>429</b>
<b>M.P3</b>	
THE EFFECTIVENESS OF USING MAGNETIC PARTICLES IN CANCER HYPERTHERMIA <i>L.P. Ichkitidze, G.Yu. Galechian, A.Yu. Gerasimenko, D.V. Telyshev</i> . . . . .	<b>431</b>
<b>M.P4</b>	
MAGNETIC STUDY OF THE DEFORMED MEDICAL GRADE 316L STEEL, MANUFACTURED WITH A LASER 3D PRINTER <i>N.V. Kazantseva, Yu.N. Koemets, I.V. Ezhov, D.I. Davydov, D.A. Shishkin, M.B. Rigmant, A.V. Kochnev</i> . . . . .	<b>433</b>

M.P5	HEAT RELEASE BY FERRIHYDRITE NANOPARTICLES AT FERROMAGNETIC RESONANCE <i>S.V. Stolyar, O.A. Li, V.P. Ladygina, E.D. Nikolaeva, A.M. Vorotynov, D.A. Velikanov, V. F. Pyankov, R.S. Iskhakov.</i> . . . . .	434
M.P6	COBALT FERRITE/GOLD NANOCOMPOSITE AS A POTENTIAL AGENT FOR PHOTOTHERMAL TREATMENT <i>A.V. Motorzhina, S.E. Pshenichnikov, S. Jovanovic, A.A. Anikin, V.V. Rodionova, L.V. Panina, K.V. Levada.</i> . . . . .	435
M.P7	CALCULATION OF TUNNEL MAGNETORESISTANCE OF MAGNETIC TUNNEL JUNCTION FOR MAGNETIC BIOSENSORS <i>V.A. Paskal, N.Kh. Useinov</i> . . . . .	436
M.P8	CYTOTOXIC EFFECTS OF NANOCOMPOSITES OF GOLD AND GALLIUM-DOPED CFO NANOPARTICLES <i>S.E. Pshenichnikov, A.V. Motorzhina, V.V. Malashchenko, S. Jovanović, L.S. Litvinova, L.V. Panina, V.V. Rodionova, K.V. Levada</i> . . . . .	437
M.P9	SYNTHESIS, OPTICAL AND MAGNETIC PROPERTIES OF Au-Fe <sub>3</sub> O <sub>4</sub> NANOHYBRIDS <i>N.V. Volkov, T.E. Smoliarova</i> . . . . .	440
M.P10	AMINATED MAGNETIC NANOPARTICLES FUNCTIONALIZED WITH ANTIBODIES FOR CELL SEPARATION <i>A.V. Tyumentseva, R.N. Yaroslavtsev, S.V. Stolyar, S.V. Komogortsev, D.A. Velikanov, Yu.V. Gerasimova, Yu.V. Knyazev</i> . . . . .	442
M.P11	A STUDY OF THE ANTI-TUMOUR ACTIVITY OF MAGNETIC HYPERTHERMIA USING BIOCOMPATIBLE IRON OXIDE NANOPARTICLES IN VIVO <i>D.E. Yakobson, M.N. Zharkov, V.P. Ageev, V.I. Shlyapkina, O.A. Kulikov, G.B. Sukhorukov, N.A. Pyataev</i> . . . . .	444
M.P12	MAGNETIC PROPERTIES OF Fe <sub>3</sub> O <sub>4</sub> -Au NANOCOMPOSITES <i>R.N. Yaroslavtsev, S.V. Stolyar, D.A. Velikanov, M.N. Volochaev</i> . . . . .	446
M.P13	AMOUNT OF MAGNETIC MATERIAL AND SIZE AS MAIN PARAMETERS OF DRUG CARRIERS FOR EFFECTIVE MAGNETIC TARGETING IN BLOOD MICROCIRCULATORY SYSTEM: THEORY AND EXPERIMENT IN VITRO/IN VIVO <i>M.A. Pyataev, N.A. Pyataev, D.E. Yakobson, V.P. Ageev, O.A. Kulikov, G.B. Sukhorukov, M.N. Zharkov</i> . . . . .	448
M.P14	DIAGNOSTIC TECHNIQUE FOR THE CROHN'S DISEASE USING FERROMAGNETIC Fe <sub>3</sub> O <sub>4</sub> -Au NANOPARTICLES <i>Z.A. Grigoreva, Ch.A. Gritsenko, E.V. Levada, V.V. Rodionova, M.V. Efremova</i> . . . . .	450

M.P15	THE MANIFESTATION OF STOICHIOMETRY DEVIATION IN SILICA-COATED MAGNETITE NANOPARTICLES <i>S.V. Stolyar, D.A. Velikanov, A.V. Tyumentseva, S.V. Komogortsev, R.N. Yaroslavtsev, Yu.V. Gerasimova, M.V. Rautskii, R.S. Iskhakov . . . . .</i>	451
M.P16	INVESTIGATION OF MAGNETITE NANOPARTICLES FOR MAGNETIC HYPERTHERMIA <i>S.V. Stolyar, O.A. Li, D.A. Velikanov, E.D. Nikolaeva, A.M. Vorotynov, V.F. Pyankov, R.S. Iskhakov . . . . .</i>	454
M.P17	CHARACTERISTICS OF EMR SIGNALS IN FAST-GROWING TARTARY BUCKWHEAT CALLUS CULTURES <i>S.V. Yurtaeva, I.V. Yatsyk, A.I. Valieva, E.A. Gumerova, N.I. Rumyantseva . . . . .</i>	456
 <b>Section N.</b>		
<b>Instruments and techniques for studying magnetism . . . . .</b>		<b>458</b>
N.O1	Co-BASED AMORPHOUS MATERIALS: TOWARD HIGH FREQUENCY FUNCTIONAL COMPOSITES <i>G.V. Kuryandskaya, I. Orue, A.A. Pasyukova, A.V. Timofeeva, S.O. Volchkov, A. Larrañaga . . . . .</i>	459
N.O2	MAGNETIC NANOSTRUCTURES OF THE CORE/SHELL TYPE AND GRO-FERRITE NANOCOMPOSITES FOR BIOMEDICINE: SYNTHESIS AND CHARACTERIZATIONS <i>A.S. Kamzin . . . . .</i>	461
N.O3	MAGNETIC NON-DESTRUCTIVE TESTING USING A SCANNING GMI MAGNETOMETER <i>S.A. Gudoshnikov, G.E. Danilov, V.P. Tarasov, Yu.B. Grebenshchikov, V.I. Odintsov, A.V. Popova, S.N. Venediktov . . . . .</i>	462
N.P1	SCANNING GMI MAGNETOMETER FOR MEASURING STRAY MAGNETIC FIELDS OF AMORPHOUS FERROMAGNETIC MICROWIRES <i>G.E. Danilov, V.P. Tarasov, Yu.B. Grebenshchikov, V.I. Odintsov, S.A. Gudoshnikov . . . . .</i>	464
N.P2	DEVELOPMENT OF NON-CONTACT MECHANICAL STRESS SENSORS BASED ON NONLINEAR PROCESSES OF MAGNETIZATION REVERSAL IN AMORPHOUS MICROWIRES <i>O.V. Lutsenko, N.A. Yudanov, S.A. Evstigneeva, L.V. Panina . . . . .</i>	466
N.P3	DEVELOPMENT OF MAGNETIC CODING SYSTEM BASED ON FERROMAGNETIC MICROWIRE IN A GLASS-SHELL BASED ON Co ALLOY <i>S.E. Medar, S.A. Evstigneeva, N.A. Yudanov, L.V. Panina . . . . .</i>	468

N.P4	NON-DESTRUCTIVE MAGNETO-OPTICAL ELLIPSOMETRY TESTING OF MAX MATERIALS <i>O.A. Maximova, S.A. Lyaschenko, S.N. Varnakov, S.G. Ovchinnikov.</i> . . . . .	469
N.P5	STRESS-SENSITIVE MAGNETIC PARAMETERS OF EUTECTOID STEEL WITH DIFFERENT PEARLITE MORFOLOGY <i>E.A. Schapova, A.N. Stashkov, A.P. Nichipuruk</i> . . . . .	471
N.P6	MAGNETIC PROPERTIES OF 3D-PRINTING 09G2S STEEL BEFORE AND AFTER LOW-CYCLE TESTS <i>A.N. Stashkov, E.A. Schapova, A.P. Nichipuruk</i> . . . . .	472
N.P7	THE AUTOMATION OF THE SE/X-2544 EPR SPECTROMETER <i>D.A. Velikanov</i> . . . . .	474
<b>Section O.</b>		
<b>MAX materials</b> . . . . .		477
O.01	HIGH TEMPERATURE PERFORMANCE EVOLUTION IN $(Cr_{1-x}Mn_x)_2AlC$ MAX-PHASE UPON MANGANESE DOPING <i>K.V. Sobolev, M.V. Gorshenkov, V.V. Rodionova</i> . . . . .	478
O.02	THE FORMATION OF FERROMAGNETIC ORDER IN THE Fe-DOPED MAX PHASE $Mn_2GaC$ <i>O.N. Draganyuk, N.G. Zamkova, V.S. Zhandun</i> . . . . .	480
O.P1	AUGER ELECTRON SPECTROSCOPY OF THE Cr-Mn BASE MAX-PHASE SURFACE <i>T.A. Andryushchenko, S.A. Lyaschenko, S.N. Varnakov, U. Wiedwald, M. Farle</i> . . . . .	482
O.P2	OPTICAL AND MAGNETOOPTICAL SPECTROSCOPY OF Mn-Cr BASED MAX-PHASES <i>S.A. Lyaschenko, O.A. Maximova, S.G. Ovchinnikov, S.N. Varnakov, T.A. Andryushchenko, D.V. Shevtsov, U. Wiedwald, M. Farle</i> . . . . .	484
O.P3	UHV SYSTEM FOR PRODUCING AND STUDYING OF MAX PHASES BY IN SITU SPECTRAL MAGNETO-OPTICAL ELLIPSOMETRY IN A WIDE TEMPERATURE RANGE <i>D.V. Shevtsov, S.A. Lyaschenko, S.N. Varnakov, S.G. Ovchinnikov, O.A. Maximova</i> . . . . .	485
<b>Sponsors</b> . . . . .		487
MTEON LIMITED. . . . .		488
<b>Author Index</b> . . . . .		489

Section G.  
Frustrated and disordered magnetism

---



## CONCENTRATIONAL TRANSITION IN $\text{Cu}_2(\text{Mn,Ga})\text{BO}_5$ SOLID SOLUTIONS

*E. Eremin*<sup>1,2,3</sup>, *M. Molokeev*<sup>1,3</sup>, *A. Velizhanin*<sup>4</sup>, *M. Pavlovsky*<sup>1</sup>, *V. Kuchesheva-Titova*<sup>1,3</sup>,  
*L. Bezmaternykh*<sup>1</sup>, *E. Moshkina*<sup>1\*</sup>

<sup>1</sup>Kirensky Institute of Physics, Federal Research Center KSC SB RAS, Krasnoyarsk, Russia

<sup>2</sup>Siberian State University of Science and Technologies, Krasnoyarsk, Russia

<sup>3</sup>Siberian Federal University, Krasnoyarsk, Russia

<sup>4</sup>National Research Centre “Kurchatov Institute”, Moscow, Russia

\*E-mail: [ekoles@iph.krasn.ru](mailto:ekoles@iph.krasn.ru)

Copper-containing ludwigites can be highlighted as a separate subclass among the family due to the lower symmetry relatively natural mineral ludwigite structure ( $Pnma \rightarrow P2_1/c$ ). That is caused by Jahn-Teller effect of  $\text{Cu}^{2+}$  cation gives rise the monoclinic distortions of metal-oxygen octahedra. Like other copper-containing ludwigites,  $\text{Cu}_2\text{GaBO}_5$  and  $\text{Cu}_2\text{MnBO}_5$  have a monoclinic structure. However, the type of monoclinic distortion and the direction of the monoclinic axis in these compounds is different: the monoclinic angle of  $\text{Cu}_2\text{MnBO}_5$  ( $\sim 92^\circ$ ) [1] is noticeably lower than that of  $\text{Cu}_2\text{GaBO}_5$  ( $\sim 97^\circ$ ) [2]. Magnetic properties of  $\text{Cu}_2\text{GaBO}_5$  and  $\text{Cu}_2\text{MnBO}_5$  are also significantly different from each other.  $\text{Cu}_2\text{GaBO}_5$  is an antiferromagnet with a magnetic ordering temperature  $T_N = 4.1$  K [2, 3]. Ludwigite  $\text{Cu}_2\text{MnBO}_5$  is a ferrimagnet with a magnetic ordering temperature  $T_C = 92$  K [1, 4]. Thus, the concentrational transition in  $\text{Cu}_2\text{GaBO}_5$ - $\text{Cu}_2\text{MnBO}_5$  solid solutions is expected.

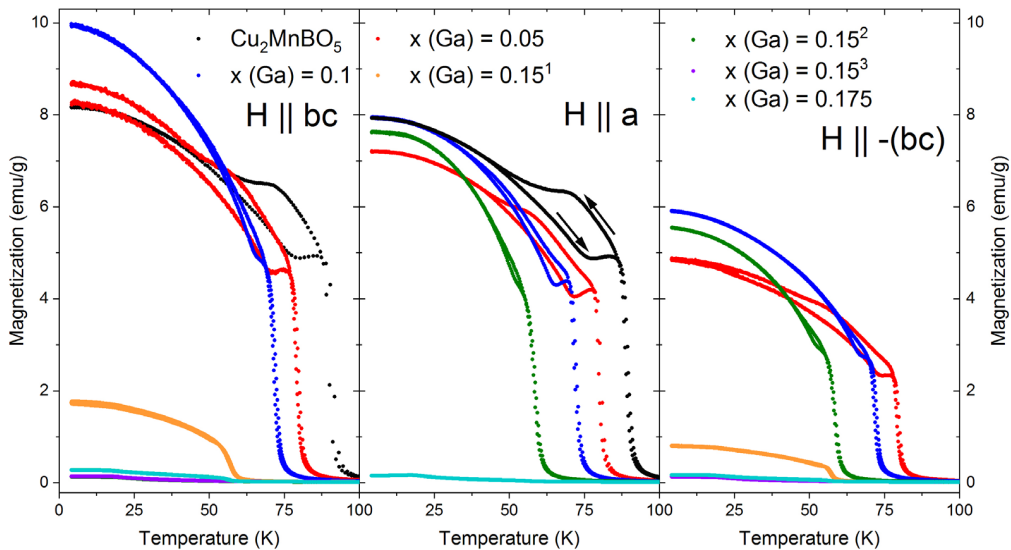


Figure 1. Thermal dependencies of the magnetization of  $\text{Cu}_2\text{Mn}_{1-x}\text{Ga}_x\text{BO}_5$  solid solutions obtained at  $H = 200$  Oe in the modes of FC (cooling in nonzero magnetic field) and FH (heating in nonzero magnetic field). The concentrations  $x$  correspond to the initial ratio of the components in the fluxes (the boundary  $x = 0.15$  is characterized by the phase boundary and by the high sensibility to the small content changes, that is the reason of 0.15<sup>1</sup>, 0.15<sup>2</sup>, 0.15<sup>3</sup> – the samples obtained with the same ratio of the components in the flux).

Single crystals of  $\text{Cu}_2\text{Mn}_{1-x}\text{Ga}_x\text{BO}_5$  solid solutions have been synthesized by flux technique. It was obtained four single crystal samples with the concentration  $x = 0.05, 0.10, 0.15, 0.175$  that corresponds to the initial ratio of the components in the fluxes. The critical concentration of the magnetic ordering type change has been estimated and it belongs to  $x = 0.15 \div 0.175$  range, as it was shown by the powder X-ray diffraction and magnetic properties measurements. The change of trivalent cations sites occupations depending on the substitution degree has been studied using XANES and EXAFS element-sensitive techniques. Non-monotonic behavior of the magnetic properties has been found in the  $0.05 \div 0.15$  concentration range (Fig. 1). The concentration phase boundary is blurred – there are the concentration range with two phase transitions inherited from the both parent compounds  $\text{Cu}_2\text{GaBO}_5$  and  $\text{Cu}_2\text{MnBO}_5$ . The evolution of the thermal hysteresis below the  $T_c$  in the  $\text{Cu}_2\text{MnBO}_5$ -like phase is also studied.

*The study was supported by the Russian Science Foundation (grant No. 21-72-00130).*

1. S. Sofronova, E. Moshkina, I. Nazarenko, Yu. Seryotkin, S.A. Nepijko, V. Ksenofontov, K. Medjanik, A. Veligzhanin, L. Bezmaternykh, Crystal growth, structure, magnetic properties and theoretical exchange interaction calculations of  $\text{Cu}_2\text{MnBO}_5$ , *J. Magn. Mag. Mater*, **420**, 309–316 (2016).
2. R.M. Eremina, T.P. Gavrilova, E.M. Moshkina, I.F. Gilmudtinov, R.G. Batulin, V.V. Gurzhiy, V. Grinenko, D.S. Inosov, Structure, magnetic and thermodynamic properties of heterometallic ludwigites:  $\text{Cu}_2\text{GaBO}_5$  and  $\text{Cu}_2\text{AlBO}_5$ , *J. Magn. Mag. Mater*, **515**, 167262 (2020).
3. A.A. Kulbakov, R. Sarkar, O. Janson, S. Dengre, T. Weinhold, E.M. Moshkina, P.Y. Portnichenko, H. Luetkens, F. Yokaichiya, A.S. Sukhanov, R.M. Eremina, Ph. Schlender, A. Schneidewind, H.-H. Klauss, D.S. Inosov, Destruction of long-range magnetic order in an external magnetic field and the associated spin dynamics in  $\text{Cu}_2\text{GaBO}_5$  and  $\text{Cu}_2\text{AlBO}_5$  ludwigites, *Phys. Rev. B*, **103**, 024447 (2021).
4. E. Moshkina, C. Ritter, E. Eremin, S. Sofronova, A. Kartashev, A. Dubrovskiy, L. Bezmaternykh, Magnetic structure of  $\text{Cu}_2\text{MnBO}_5$  ludwigite: thermodynamic, magnetic properties and neutron diffraction study, *J. Phys.: Condens. Matter*, **29**, 245801 (2017).

## MAGNETIC BEHAVIOR OF LANTHANIDES (La-Tb) IN LINEAR-CHAIN COORDINATION POLYMERS

*N.V. Lomova, F.F. Chausov\**, *L.V. Dobyshcheva, A.I. Ulyanov, N.N. Zverev*

Udmurt Federal Research Center, Ural Br. of Rus. Ac. Sci., Izhevsk, Russia

\*E-mail: [chaus@udman.ru](mailto:chaus@udman.ru)

Many lanthanide compounds have unusual physicochemical properties: record values of the magnetic moment, luminescence, and other properties valuable for practice [1]. Complex compounds of lanthanides are used as diagnostic drugs, photo-, X-ray, and electroluminophores, and as other functional materials. One of the ligands which forms very interesting for study and application complexes with lanthanides, is nitrilo-*tris*(methylenephosphonic acid)  $H_6\{N(CH_2PO_3)_3\}$  (NTP).

The purpose of this work is to study the magnetic moment of light lanthanide atoms (La-Tb) in linear chain complex compounds with NTP, with different chain pitch and different symmetry of the nearest environment of the rare-earth (RE) atom in  $[Ln\{N(CH_2PO_3)_3\}_2H_3] \cdot nH_2O$  (I) и  $[Na(H_2O)_6]_2[LnNa_6H(H_2O)_{10}\{NTP\}_2] \cdot 3H_2O$  (II). The compounds I and II were obtained and characterized according to the methods worked out earlier.

Unlike 3d-metals, where the orbital momentum of the 3d-shell in the condensed phase is frozen by interaction with the crystal field, the total magnetic moment  $\mu_j$  of RE complex compounds can be described by the vector addition of the orbital  $\mu_L$  and spin  $\mu_S$  magnetic moments [2]. Most often, in RE compounds,  $\mu_L$  and  $\mu_S$  are added in the same way as in a free atom. Therefore, the calculated values of  $\mu_j$  for isolated RE ions almost equal the effective magnetic moments  $\mu_{eff}$  measured in condensed phases.

To determine the total magnetic moment of rare-earth atoms, the magnetic susceptibility  $\chi$  of the samples was measured using a vibrating magnetometer, the effective magnetic moment  $\mu_{eff}$  was estimated with the Curie law [3], magnetic moments of non-RE atoms being considered zero [4].

To determine  $\mu_S$ , the method of X-ray photoelectron spectroscopy (XPS) was used. The s-state spectra demonstrate doublets due to the fact that two final states are possible in which the spin of the remaining s electron is parallel or anti-parallel to the total momentum. The intensity and position of the maxima of the two peaks are governed by the number of 4f-electrons and, consequently, by the spin magnetic moment of the RE atom.  $\mu_S$  can be estimated from the intensity ratio of the doublet components in the 3s-, 4s-, or 5s-lines of the photoelectron spectra of transition metals as  $I_2/I_1 = (S + 1)/S$ , where  $S$  is the total spin of unpaired electrons in the initial (non-ionized) state [5]. The spin magnetic moment of the atom in Bohr magnetons  $\mu_B$  is found then as  $2\sqrt{S(S+1)}$ .

The effective magnetic moments  $\mu_I$  and  $\mu_{II}$  for the I and II compounds is compared in Fig. 1 with the calculated values of  $\mu_{Ln^{3+}}$  and  $\mu_{Ln^{2+}}$  for isolated Ln ions, determined in a standard way [3].

The formation of the magnetic moments in the systems under study are investigated with the DFT calculations using a full-potential linearized augmented plane wave (FP-LAPW) method realized in the WIEN2k program package [6].

**Conclusion.** Magnetic moments of the lanthanide atoms (La-Tb) in complex compounds with NTP with different symmetry of the RE nearest environment have been obtained using vibrational magnetometry and XPS.

The effective magnetic moments of the RE elements in complex compounds are in a good agreement with the calculated values of  $Ln^{3+}$  ions. Distinctions are observed only for La and Eu in the complex I and for Tb in the complex II.

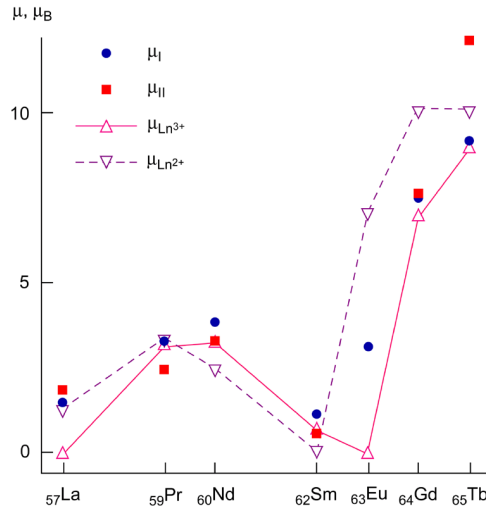


Figure 1. Dependence of the effective magnetic moments  $\mu_I$  and  $\mu_{II}$  on the RE atomic number for the I and II coordination compounds, and the calculated values of  $\mu_{Ln^{3+}}$  and  $\mu_{Ln^{2+}}$  for isolated Ln ions.

The differences in the effective magnetic moment between compounds I and II cannot be explained by solely the behavior of the spin magnetic moment. Probably, the differences are due to the behavior of the orbital angular momentum  $\mu_L$  in different coordination environments.

*This study was carried out within State Task of the Ministry of Science and Higher Education of Russian Federation (state registrations #121030100002-0 and #121030100003-7). The work was performed with the equipment of the Centre for Shared Usage “Center of physical and physical-chemical methods of analysis and research of properties and characteristics of surfaces, nanostructures, materials, and samples” of the UdmFRC UB RAS. The calculations have been partly performed using “Uran” supercomputer of IMM UB RAS.*

1. E.M. Saviczkiy, V.F. Terekhova, Metallovedenie redkozemel'nykh metallov (Metal Science of Rare Earth Metals), Nauka, Moscow (1975) [in Russian].
2. N.V. Kudrevatykh, A.S. Volegov, Magnetizm redkozemel'nykh metallov i ih intermetallicheskih soedinenij (Magnetism of Rare Earth Metals and Intermetallic Compounds of their), Izdatel'stvo Ural'skogo Universiteta, Ekaterinburg (2015) [in Russian].
3. S.V. Vonsovskii, Magnetism, Nauka, Moscow (1971) [in Russian].
4. L.V. Dobysheva, F.F. Chausov, and N.V. Lomova, Materials Today Comm., **29**, 102892 (2021).
5. I.N. Shabanova, N.V. Lomova, and A.Z. Men'shikov, Zhurnal strukt. Him., **43**, 85 (2002) [in Russian].
6. P. Blaha, K. Schwarz, F. Tran, R. Laskowski, G.K.H. Madsen, and L.D. Marks, WIEN2k: an APW+lo program for calculating the properties of solids, J. Chem. Phys., **152**, 074101, (2020).

## THERMALLY STABLE SKYRMION CRISTALL IN TRIANGULAR FRUSTRATED ANTIFERROMAGNETIC/FERROELECTRIC BILAYER

*I.F. Sharafullin\**<sup>1</sup>, *A.G. Nugumanov*<sup>1</sup>, *A.H. Baisheva*<sup>1</sup>, *A.R. Yuldasheva*<sup>1</sup>, *H.T. Diep*<sup>2</sup>

<sup>1</sup>Institute of Physics and Technology, Bashkir State University, Ufa, Russia

<sup>2</sup>Laboratoire de Physique Théorique et Modélisation, CY Cergy Paris University, Cergy-Pontoise cedex, France

\*E-mail: [SharafullinIF@yandex.ru](mailto:SharafullinIF@yandex.ru)

The increasing interest in skyrmions results from the fact that skyrmions may play an important role in technological application devices [1, 2]. We note that skyrmion crystals have been experimentally observed in various materials [3]. The single skyrmions and skyrmion crystals can form in magnetic films due to the Dzyaloshinskii-Moriya interaction [1]. The skyrmions can be created without the Dzyaloshinskii-Moriya (DM) interaction provided that competing interactions between far neighbors have to be included to make the system over-frustrated [1–3]. In this work, we investigate the possibility of an existence of such skyrmion crystals on the frustrated triangular lattice taking into account the DM interaction in addition to the frustrating antiferromagnetic interaction between nearest-neighbors (NN) and an interface magnetoelectric coupling between antiferromagnetic and ferroelectric layers. When the DM vector lies in the lattice plane and in a range of a magnetoelectric coupling, we show that our model presents a skyrmion crystal composed of three interpenetrating skyrmion crystals resulting from the NN triangular antiferromagnet over-frustrated by the DM interaction. We consider a bilayer with triangular lattice of lateral dimension  $L$ . The total number of sites  $N$  is given by  $N = L \times L$ . We show using steepest descent method that in the absence of DM interaction and very weak interface (magnetoelectric) coupling the antiferromagnetic interaction on a triangular lattice causes a 120-degree structure in the  $xy$  plan. In the absence of antiferromagnetic and ferroelectric exchange interactions, unlike the bipartite square lattice where one can arrange the NN spins to be perpendicular with each order in the  $xy$  plane, the triangular lattice cannot fully satisfy the DM interaction for each bond, namely with the perpendicular spins at the ends. The ground state of the model including the effects of exchange interactions, in-plane DM interactions

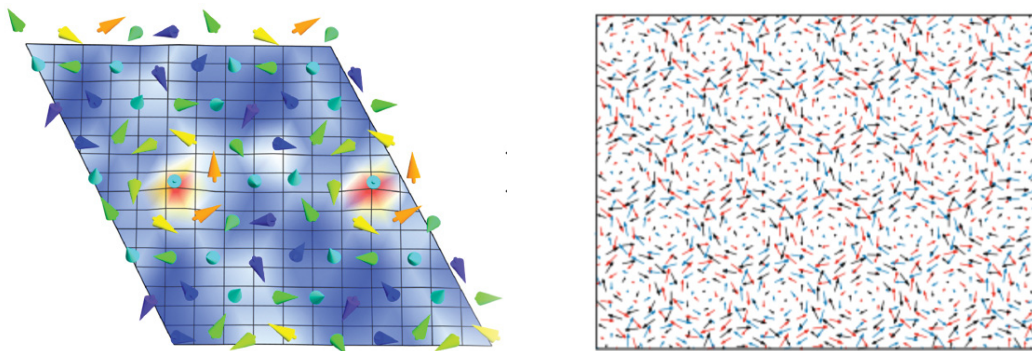


Figure 1. Zoom of stable ground state of the magnetic layer of a AFM/FE bilayer with parameters  $J = -1.0$ ,  $J = 1.0$ ,  $D = -0.75$ ,  $J = 3.4$  and three interpenetrating antiferromagnetic skyrmion sublattices distinguished by three colors.

and interface coupling is calculated using the local energy minimization. In the ground state we observe the skyrmion crystal composed of three interpenetrating skyrmion sublattices (Fig. 1).

The perfect skyrmion crystal formed from interface coupling  $J = 3.0$  as seen in Fig. 1. By using the Monte Carlo simulations we study the phase transition of the skyrmion crystal shown above when we increase the temperature  $T$ . Our conclusion is that the observed ground state in form of three interpenetrating antiferromagnetic skyrmion sublattices is stable up to a finite temperature  $T = 0.570$  in the unit of exchange energy.

*The authors thanks for the support of the State assignment of Russian Federation for the implementation of scientific research by laboratories (Order MN-8/1356 of 09/20/2021).*

1. H.T. Diep, Theory of Magnetism: Application to Surface Physics, World Scientific: Singapore (2014).
2. I.F. Sharafullin and H.T. Diep, Symmetry, **12**, 26–41 (2020).
3. M. Mohylna, M. Zukovic, M. Journal of Magnetism and Magnetic Materials, **546**, 168840 (2022).

**MAGNETIC PHASE DIAGRAM AND POSSIBLE KITAEV-LIKE BEHAVIOR OF HONEYCOMB-LATTICE ANTIMONATE  $\text{Na}_3\text{Co}_2\text{SbO}_6$** 

*E. Vavilova*<sup>1\*</sup>, *T. Vasilchikova*<sup>2</sup>, *D. Mikhailova*<sup>3</sup>

<sup>1</sup>Zavoisky Physical-Technical Institute, FRC Kazan Scientific Center, Russian Academy of Sciences, Kazan, Russia

<sup>2</sup>Faculty of Physics, Moscow State University, Moscow, Russia

<sup>3</sup>IFW Dresden, Dresden, Germany

\*E-mail: [jenia.vavilova@gmail.com](mailto:jenia.vavilova@gmail.com)

As materials demonstrating the Kitaev model physics, as a rule, Mott insulators with 5d ions with pseudospin 1/2 are considered. Recent theoretical studies [1, 2] suggest that 3d cobalt compounds may also contain the Kitaev-Heisenberg pseudospin 1/2 model and associated physics. One of the most likely candidates is the honeycomb compound  $\text{Na}_3\text{Co}_2\text{SbO}_6$ . We studied a powder sample of this compound using DC and AC magnetometry, thermodynamic studies, and magnetic resonance. A phase diagram of  $\text{Na}_3\text{Co}_2\text{SbO}_6$  was proposed based on the results of the experiments in a wide range of magnetic fields and temperatures. The results demonstrate the transformation of the magnetic structure and the suppression of the AFM order under the external field, the gradual development of the saturation phase at low temperatures, as well as signs of gap spin-liquid behavior in certain parts of the phase diagram.

The authors are grateful to V. Nalbandyan for providing the high-quality samples and to B. Büchner and H.-J. Grafe for the opportunity to carry out the high field NMR measurements. The authors use some of the data obtained by E. Zvereva.

*E.V. would like to thank financial support from the government assignment for FRC Kazan scientific Center of RAS.*

1. Huimei Liu and G. Khaliullin, Phys. Rev. B, **97**, 014407 (2018).

2. H. Liu, J. Chaloupka and G. Khaliullin, Phys. Rev. Lett., **125**, 047201 (2020).

## ORBITAL ORDERING AND FRUSTRATED ANISOTROPY IN $\text{PbMnBO}_4$

*S.N. Martynov*

Kirensky Institute of Physics, KSC SB RAS, Krasnoyarsk, Russia  
 E-mail: [unonav@iph.krasn.ru](mailto:unonav@iph.krasn.ru)

A distribution of  $\text{Mn}^{3+}$  orbital electron function in the lattice of four-sublattice chain ferromagnet  $\text{PbMnBO}_4$  is studied. Based on the structure data of the  $\text{O}^{2-}$ -octahedron distortions a mixing of the 3d  $e_g$ -functions is calculated in the framework of Kanamori approach [1]. The relation between the local second order single-ion anisotropy parameters  $D$  and  $E$  is obtained from the coefficients of entangled functions. An alternating orbital order leads to frustration of local single-ion anisotropies and reduction of the contribution in the total ground state anisotropy. The energy of ground state is calculated numerically in the classical spin approximation for the model with Hamiltonian

$$H = J_1 \sum_{i,j} \mathbf{S}_{i,j} \mathbf{S}_{i+1,j} + J_2 \sum_{i,j} \mathbf{S}_{i,j} \mathbf{S}_{i,j+1} + \sum_i (DS_{zi}^2 + E(S_{xi}^2 - S_{yi}^2)) + \sum_i a(S_{xi}^4 + S_{yi}^4 + S_{zi}^4) + \sum_{i,j} \mathbf{d}_j (-1)^i [\mathbf{S}_{i,j} \times \mathbf{S}_{i+1,j}] + A \sum_{i,j} S_{i,j}^b S_{i+1,j}^b, \quad (1)$$

where  $J_1$  and  $J_2$  – intra- and interchain Heisenberg exchange interactions, accordingly,  $a$  – the parameter of cubic single-ion anisotropy,  $\mathbf{d}_j$  – the vector of antisymmetric exchange in the  $j$ -chain, located in the mirror plane between the nearest  $\text{Mn}^{3+}$ -ions, and  $A$  – the parameter of the dipole-dipole interaction between spins in the chains. The chains are parallel to orthorhombic axis  $\mathbf{b}$ . The spatial distribution of the local single-ion anisotropy axes leads to the noncollinearity of magnetic sublattices. In the magnetic phases with the total ferromagnetic moment along the orthorhombic axes  $\mathbf{a}$  and  $\mathbf{b}$  ( $Pnm'a'$  and  $Pn'ma'$ -symmetries, accordingly) the chirality parameter  $\mathbf{K} = [\mathbf{S}_{i,j} \times \mathbf{S}_{i+1,j}]$  has the different sign. As a result the Dzyaloshinskii-Moriya interaction become frustrated in the one of phases depending on the sign of  $\mathbf{d}_j$  and the contribution from the interaction in energy of the ground states has different sign too. The result was also obtained for two-sublattice model by exact analytic analysis [2]. For four-sublattice model (1) the phase boundary between nearest magnetic  $Pnm'a'$  and  $Pn'ma'$ -phases on the plane of antisymmetric exchange components  $d_a$  and  $d_c$  is calculated numerically for the different values of single-ion anisotropy parameters  $D$  and  $a$ . The calculations shown insufficiency of the single-ion anisotropy for existence of the experimentally observed ground state in  $\text{PbMnBO}_4$  [3] with the total ferromagnetic moment directed along the orthorhombic axes  $\mathbf{a}$  (a magnetic symmetry  $Pnm'a'$ ). The state can be realized only with sizable Dzyaloshinskii-Moriya interaction between the spins in the chains.

1. J. Kanamori, J. Appl. Phys., **31**, 14S–23S (1960).
2. S.N. Martynov, Fizika Tverdogo Tela, **63**, 1090–1097 (2021) (Physics of Solid State, **63**, 1253–1261 (2021)).
3. A. Pankrats, K. Sablina, M. Eremin, A. Balaev, M. Kolkov, V. Tugarinov, A. Bovina, J. Magn. Magn. Matter., **414**, 82–89 (2016).



## EXACT DETERMINATION OF THE SINGLE ION AND PAIR INTERACTIONS PARAMETERS IN THE MAGNET WITH COMPETING DIPOLAR AND EXCHANGE INTERACTIONS $\text{LiGdF}_4$

*V.N. Glazkov*<sup>1\*</sup>, *S.S. Sosin*<sup>1</sup>, *A.F. Iafarova*<sup>1,2</sup>, *O.A. Morozov*<sup>3</sup>, *R.G. Batulin*<sup>3</sup>, *I.V. Romanova*<sup>3</sup>

<sup>1</sup>P. Kapitza Institute for Physical Problems RAS, Moscow, Russia

<sup>2</sup>Faculty of Physics, HSE University, Moscow Russia

<sup>3</sup>Institute of Physics, Kazan Federal University, Kazan, Russia

\*E-mail: [glazkov@kapitza.ras.ru](mailto:glazkov@kapitza.ras.ru)

Rare earth tetrafluorides  $\text{Li}(\text{Re})\text{F}_4$ , known for a long time as an optical media for lasers [1], provides an example of unusual sort of magnetic frustration: various interactions have similar strength and final choice of the ordered phase depends on a minute balance of these interactions.

For example,  $\text{LiHoF}_4$  is an example of a dipolar Ising ferromagnet with Curie temperature  $T_C = 1.53$  K, while  $\text{LiErF}_4$  is an XY-antiferromagnet with Neel temperature  $T_N = 0.38$  K and  $\text{LiGdF}_4$  remains disordered down to at least 0.4 K [2].

Understanding of the physics of the magnet with competing exchange interaction, dipolar coupling and single-ion anisotropy requires accurate determination of the interactions parameters. To achieve this goal we have grown samples of  $\text{LiGd}_x\text{Y}_{1-x}\text{F}_4$  with  $x = 0.01, 0.05, 1$  and we have studied their magnetic properties via magnetization measurements and electron spin resonance (ESR) spectroscopy.

Magnetization measurements on concentrated  $\text{LiGdF}_4$  reveals highly anisotropic Curie-Weiss temperature, which varies from  $(1.6 \pm 0.2)$  K for the field applied along tetragonal  $c$  axis to almost fully compensated  $(0.2 \pm 0.2)$  K for the field applied in the (001) plane.

Electron spin resonance spectroscopy of diluted samples with  $x = 0.01$  and  $0.05$  reveals complicated ESR spectra with the resolved fine structure of  $S = 7/2$   $\text{Gd}^{3+}$  ions. Besides of the ESR fine structure series of additional weak absorption lines are observed in diluted samples which can be interpreted as absorption signal of exchange and dipolar coupled pairs of  $\text{Gd}^{3+}$  ions.

To analyze these results numerically we model ESR absorption via exact diagonalization of the spin Hamiltonian for a single spin and for the coupled spins and fit measured spectra and their frequency-field and angular dependencies. Some of the spectral components appears to be highly sensitive to the value of exchange coupling parameter, which allows to determine both the parameters of single-ion anisotropy and exchange coupling parameter reliably.

Single ion anisotropy parameters up to fourth order are determined, main contribution comes from the easy-axis type second order term in spin Hamiltonian  $DS_z^2$  with  $D/h = -2.00$  GHz and agrees with the known values [3]. Exchange integral is determined to be antiferromagnetic  $J/h \approx 1.4$  GHz. Both interactions are comparable to the strength of dipolar coupling of neighboring  $\text{Gd}^{3+}$  ions  $(7\mu_B)^2/(hr^3) \approx 12$  GHz.

*The work was supported by Russian Science Foundation Grant 22-12-00259, work of I.V. Romanova was supported by V.Potinin Foundation “Academic mobility” program.*

1. R.Burkhalter, Prog. Cryst. Growth, **42**, 1 (2001).
2. P. Beauvillain et al., Phys. Rev. B, **18**, 3360 (1978); C. Kraemer et al., Science, **336**, 1416 (2012).
3. S. Misra et al., Phys. Rev. B, **32**, 4738 (1985).

**RESEARCH BY DEEP NEURAL NETWORKS  
 OF FRUSTRATED SPIN GLASS SYSTEMS**

*D.Yu. Kapitan<sup>1,2\*</sup>, P.D. Andriushchenko<sup>1</sup>, V.Yu. Kapitan<sup>2</sup>, A.O. Korol<sup>2</sup>*

<sup>1</sup>ITMO University, St. Petersburg, Russian Federation

<sup>2</sup>Far Eastern Federal University, Vladivostok, Russian Federation

\*E-mail: [kapitan.diu@dvfu.ru](mailto:kapitan.diu@dvfu.ru)

Spin glasses are distinguished by the presence of frustrations, i.e., the strong competition of magnetic interactions, and disorder – the freezing of atoms upon cooling. Due to these key features, spin glasses have long relaxation times, a rough energy landscape, and macroscopic degeneracy of ground states. This leads to the fact that numerical simulation and, even more so, analytical description of such systems is a difficult task. Therefore, to describe the physics of spin glass, numerical probabilistic methods, such as various variations of the Monte Carlo method [1–3], are most often used at present.

Simultaneously with the development of numerical Monte Carlo methods the exponential growth of computing power led to the second revolution of neural networks and to the emergence of completely new approaches to the architecture and training of neural networks, allowing to reduce the training time and increase the dimensionality of the solved tasks dramatically.

In this study, we use supervised machine learning techniques to solve the problem of regression of the basic thermodynamic characteristics  $\langle E \rangle$ ,  $\langle M \rangle$  (average energy and magnetization) as a function of temperature  $T$  for spin glass models with periodic boundary conditions on a square lattice with size  $N = L \times L$ , where each Ising spin has four neighbors with exchange integral  $J_i = \pm 1$ .

In this work we proposed a method for calculating the values of thermodynamic averages of the frustrated spin glass model using deep neural networks. Special architectures of neural networks that mimic the structure of spin lattices were proposed, allowing to obtain a higher rate of learning and prediction accuracy.

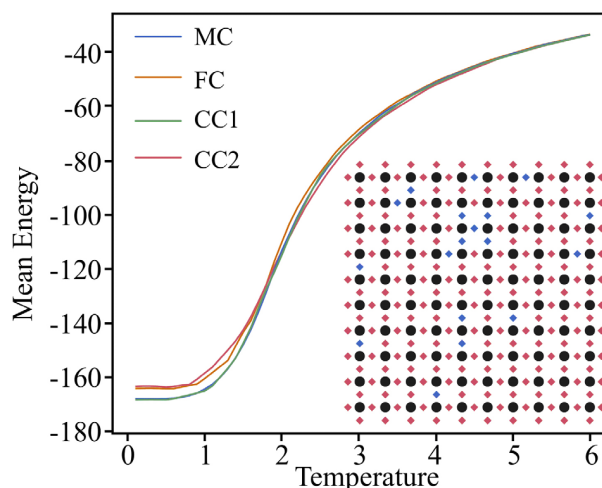


Figure 1. Example of mean energy calculation.

Table 1. Comparison of the RMSE results of average energy and magnetization, calculated with different deep neural network architectures for spin glass models with sizes  $N = 6 \times 6$ ,  $N = 10 \times 10$ .

Architectures	RMSE $\langle E \rangle$		RMSE $\langle M \rangle$	
	$6 \times 6$	$10 \times 10$	$6 \times 6$	$10 \times 10$
FC	1.9991	3.7660	0.0601	0.0491
CC1	1.4854	2.6071	0.0642	0.0443
CC2	1.7674	3.0173	0.0673	0.0581

Figure 1 shows an example of the average energy calculation using the replica-exchange Monte-Carlo(MC), as well as using different deep neural networks (two custom architectures –CC1,CC2; and the fully-connected network – FC). The configuration of the calculated spin glass model is shown in the corner of the figure. The black circles indicate spins, and the red and blue rhombuses indicate bonds.

Both networks were compared on 4500 unique spin configurations. Due to results on test dataset shown in Table 1, custom neural network shows more accurate predictions. As an error metric we used root mean square error.

The results of the research show a decrease in the root mean square error of the proposed architectures compared to the basic solution of fully-connected neural networks. At the same time, the use of trained neural networks allows to reduce simulation time compared to other classical methods. The validity of the results is confirmed by comparison with numerical simulation with the replica-exchange Monte Carlo method.

*The presented results were obtained within the framework of the state task of the Ministry of Science and Higher Education of the Russian Federation (No. 0657-2020-0005).*

1. P. Andriushchenko, K. Soldatov, A. Peretyatko et al., Physical Review E, **99**(2), 022138 (2019).
2. K. Soldatov, A. Peretyatko, P. Andriushchenko et al., Physics Letters A, **383**(12), 1229 (2019).
3. A. Makarov, K. Makarova, Yu. Shevchenko et al., JETP Letters, **110**, 702 (2019).

## A NEURAL NETWORK APPROACH TO THE STUDY OF COMPLEX FRUSTRATED SYSTEMS

*A.O. Korol<sup>1,2\*</sup>, V.Yu. Kapitan<sup>1,2</sup>, D.Yu. Kapitan<sup>1,2</sup>, E.V. Vasiliev<sup>1,2</sup>*

<sup>1</sup>Far Eastern Federal University (FEFU), Vladivostok, Russia

<sup>2</sup>Institute of Applied Mathematics (IAM), FEB RAS, Vladivostok, Russia

\*E-mail: [korol.ao@dvfu.ru](mailto:korol.ao@dvfu.ru)

The problem of modeling spin glass and spin ice is determined by the high difficulty of obtaining configurations with the lowest possible energy level due to its frustrated nature. Now there is no universal algorithm for direct generation of ground states. However, there are traditional methods for studying spin systems in statistical physics, among which the most effective are Monte Carlo simulations [1], consisting of stochastic sampling over the state space and calculating estimates of physical quantities. The Metropolis algorithm as one of the Monte Carlo methods is a general method used to study the thermodynamic properties of substances consisting of interacting particles. Monte Carlo methods continue to evolve, i.e., a new hybrid multi-spin method (HMM) has recently been proposed. HMM [2] uses a quasimarkov chain of random events. Combining canonical and multicanonical sampling of the Gibbs distribution in a single computational scheme makes it possible to determine the temperature dependences of the incremental number of excitations and entropy increments of the hexagonal lattice of artificial spin ice and calculate the configuration of the ground state.

Modern machine learning methods provide an additional paradigm to the above-mentioned approach. Machine learning in statistical physics began to be applied relatively recently but has already established itself as an excellent tool for classifying and interpreting massive datasets [3]. In this study, the Edwards-Anderson spin-glass model [4] on a square two-dimensional lattice of Ising spins with a bimodal distribution of bonds was studied. In the present work, we used a combination of our hybrid multi-spin method and restricted Boltzmann machine (RBM) to predict the ground states for the spin glass model. The spin glass modeling problem is determined by the high complexity of obtaining configurations with the lowest possible energy level (ground state) due to

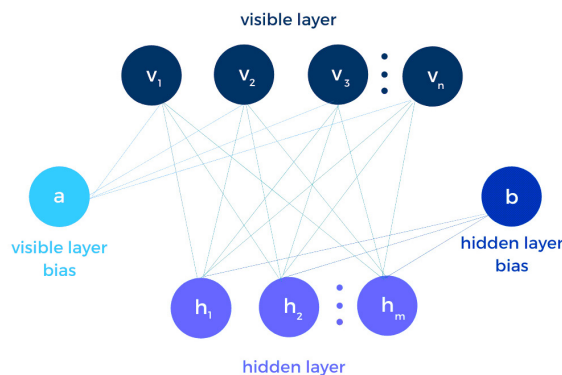


Figure 1. RBM architecture.

Table 1. Comparison of the results of different modeling methods.

Results	Brute-force method	Transfer-matrix method	Hybrid multi-spin method	Restricted Boltzmann machine
Lattice size	$E_{\min}$			
4×4	-1.5	-1.5	—	-1.5
6×6	-1.3	-1.3	—	-1.3
10×10	—	-1.4	-1.4	-1.4
20×20	—	-1.38	-1.34	-1.38
30×30	—	—	-1.334	-1.342

microscopic degeneracies and frustrations. The developed neural network consists of one visible layer ( $v_1, \dots, v_n$ ), one hidden layer ( $h_1, \dots, h_n$ ) and corresponding bias vectors  $a$  for visible and  $b$  for hidden layer (Fig. 1). The output layer is not required for this architecture because predictions are made differently than in conventional feed-forward neural networks. RBM assumes unsupervised learning – the network takes a set of data as input and has no clear instructions about what to do with it. The neural network tries to find correlations in the data on its own, extracting useful features and analyzing them. For training we use the Contrastive Divergence algorithm with Gibbs sampling. Also, we made research on configurations with different spin excess at energy maxima and minima on different lattices of spin glass and spin ice models. The proposed neural network methods showed more accurate results compared to various implementations of the Monte Carlo algorithm (Table 1). Values were tested using exact solution methods on relatively small systems. For lattices with larger amount of spins, the transfer matrix method was used.

*This work was supported by a grant from the RSF, project no. 21-72-00058.*

1. D.P. Landau, K. Binder, A guide to Monte Carlo simulations in statistical physics, Cambridge university press, 2014.
2. A.G. Makarov et al., On the Numerical Calculation of Frustrations in the Ising Model, JETP Letters, **110**, no. 10, 702–706 (2019).
3. Butler K.T. et al., Machine learning for molecular and materials science, Nature, **559**, no. 7715, 547–555 (2018).
4. S.F. Edwards, P.W. Anderson, Theory of spin glasses, Journal of Physics F: Metal Physics, **5**, no. 5, 965 (1975).

## MAGNETIC PROPERTIES OF PEROVSKITE $\text{Sr}_2\text{MnTiO}_6$

D.V. Popov<sup>1</sup>, I.V. Yatsyk<sup>1,2</sup>, A.V. Shestakov<sup>1</sup>, R.G. Batulin<sup>2</sup>, T.I. Chupakhina<sup>3</sup>, R.M. Eremina<sup>1,2\*</sup>

<sup>1</sup>Zavoisky Physical-Technical Institute, FRC Kazan Scientific Center, Russian Academy of Sciences, Kazan, Russia

<sup>2</sup>Institute of Physics, Kazan Federal University, Kazan, Russia

<sup>3</sup>Institute of Solid State Chemistry of the Russian Academy of Sciences (UB), Ekaterinburg, Russia

\*E-mail: REremina@yandex.ru

Perovskite based layered oxides have been widely investigated in recent times owing to their interesting electronic and magnetic properties including colossal magnetoresistance, metal-insulator transition, giant magnetoelectricity and multiferroic behavior [1]. Properties of these compounds strongly depend on the composition, number of layers oxygen deficiency, etc. Perovskites may be useful for different kind of device applications. Perovskite  $\text{Sr}_2\text{MnTiO}_6$  of a particular interest, because it has dielectric properties [2] to addition to aforementioned ones.

The aim of this work is investigation of magnetic properties of  $\text{Sr}_2\text{MnTiO}_6$  compound. Temperature dependences of magnetization were measured in zero field cooling (ZFC) and field cooling (FC) regimes at range 2–300 K using PPMS-9 device in Kazan Federal University. The inverse magnetic susceptibilities are presented in Fig. 1 for magnetic fields 500 Oe, 1000 Oe, 10000 Oe. Linear part of susceptibility was approximated using Curie-Weiss law above 100 K. The fitting parameters were obtained. Curie-Weiss temperature is negative –400 K which indicates the antiferromagnetic nature of isotropic exchange interactions between the spins of manganese ions in  $\text{Sr}_2\text{MnTiO}_6$  compound.

The experimental effective magnetic moment was obtained from Curie parameter  $\mu_{\text{eff}} = 4.27 \mu_B$ ,  $\mu_{\text{eff}} = \sqrt{(3k \cdot C)/N_A}$ , respectively. Theoretical effective magnetic moment were calculated assuming

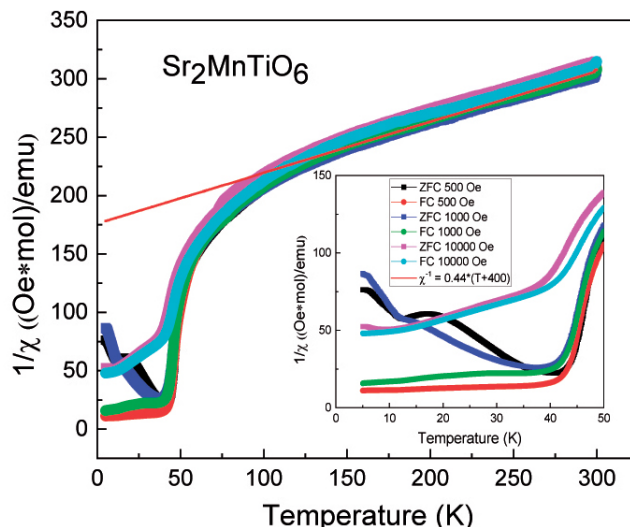


Figure 1. Temperature dependence of reverse magnetic susceptibility for  $\text{Sr}_2\text{MnTiO}_6$ .

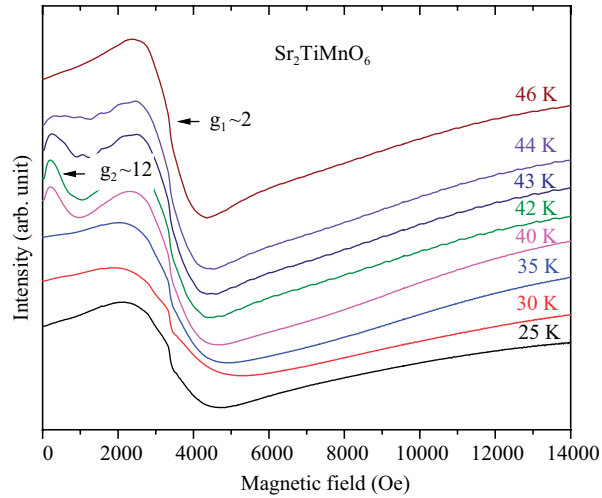


Figure 2. ESR spectra for  $\text{Sr}_2\text{MnTiO}_6$  for temperatures 25–46 K.

that the contribution is given only spins  $\text{Mn}^{4+}$  with  $S = 3/2$ . The calculated value  $\mu_{\text{eff}} = 3.87\mu_B$  is less than the value obtained in the experiment. We believe that manganese with two different valence  $\text{Mn}^{4+}$  with  $S = 3/2$  and  $\text{Mn}^{3+}$  with  $S = 2$  are in the sample. Using the relation  $\mu_{\text{eff}}^{\text{Theory}} = g \cdot (\sum [N \cdot S(S + 1)])^{1/2}$  we estimated concentration of  $\text{Mn}^{3+}$  and  $\text{Mn}^{4+}$  ions as 0.35 and 0.65, respectively.

In addition, EPR spectra were measured at temperatures 4.5–600 K using a Bruker spectrometer. Figure 2 shows obtained ESR spectra in temperature range 25–46 K where two ESR lines with effective  $g$ -values  $g_1 \sim 2$  and  $g_2 \sim 12$  were observed which connected with phase separation in  $\text{Sr}_2\text{MnTiO}_6$ . We do not associate the observation of the second line with  $g_2 \sim 12$  with the presence of an impurity in the sample, but we assume the formation of correlated regions of one valence manganese during the transition to the paramagnetic state of regions where manganese of another valence predominates.

*This work is supported by RSF-22-42-02014.*

1. S. Chowki et al.: AIP Conference Proceedings, **1731**, 090040 (2016).
2. I. Álvarez-Serrano et al.: Journal of the American Ceramic Society, **93**, 2311 (2010).

## STUDY OF THE EFFECT OF Cr ON ELECTRIC AND MAGNETIC PROPERTIES OF Co-RICH AMORPHOUS FERROMAGNETIC MICROWIRES UNDER JOULE HEATING

*A.E. Sarakueva*<sup>1\*</sup>, *V.S. Mashera*<sup>1</sup>, *M.N. Churyukanova*<sup>1</sup>, *I.V. Kozlov*<sup>1</sup>, *V.I. Odintsov*<sup>2</sup>,  
*G.N. Elmanov*<sup>3</sup>, *S.A. Gudoshnikov*<sup>1,2</sup>

<sup>1</sup>National University of Science and Technology “MISiS”, Moscow, Russia

<sup>2</sup>Pushkov Institute of Terrestrial Magnetism, Ionosphere and Radio Wave Propagation, Russian Academy of Sciences, (IZMIRAN), Troitsk, Moscow, Russia

<sup>3</sup>National Research Nuclear University “MEPhI”, Moscow, Russia

\*E-mail: [aida96570@mail.ru](mailto:aida96570@mail.ru)

Co-rich amorphous glass-coated ferromagnetic microwires (AFM) obtained by quenching from a melt by the Taylor-Ulitovsky method, are a promising material for many technical applications. The unique electrical and soft magnetic properties of AFMs are determined by the metal core composition, the technological conditions of manufacture, and their perfect cylindrical shape [1]. Based on such microwires, miniature magnetic, strain-sensitive and temperature sensors are being developed.

The purpose of this work was to study the electrical and magnetic properties of several series of AFMs with different compositions of the metal core  $\text{Co}_{(73-x)}\text{Fe}_4\text{Cr}_x\text{Si}_{12}\text{B}_{11}$  (Cr: 2%, 4%, 6%, 8%) during their heat treatment by the Joule heating method. Thermal treatment was carried out on an AKS-2 unit, which provides controlled heating of the AFM sample by a DC current of a given value and continuous control of its electrical resistance during annealing [2]. The data processing program made it possible to obtain graphs of the dependence of the AFM resistance on the power and heating temperature [3]. Figure 1 shows the temperature dependencies of the change in the resistance of AFM samples with different Cr contents during annealing when they are heated to complete crystallization. Supported by data obtained from the method of differential scanning calorimetry, these curves made it possible to control the state of the AFM during their heat treatment.

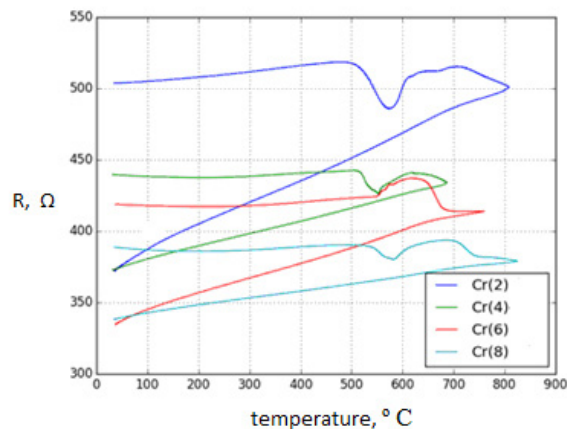


Figure 1. Temperature dependences of the AFM resistance with different Cr content.



In the course of studies of the electrical properties of AFMs, it was found that after heating above 650–700 °C, all AFMs crystallize. For all crystallized AFM samples, a decrease in resistance by 10–18% is observed compared to their initial amorphous state value. At the same time, the temperature dependencies  $R(T)$  become linear with characteristic values of the temperature coefficient of resistance (TCR) decreasing with increasing Cr content. During annealing in the temperature range up to 450 °C (amorphous state), the temperature dependencies of the AFM resistance (samples Cr (4%) Cr (6%) and Cr (8%)) exhibited an anomalous resistance minimum, while the Cr (2%) has no minimum in the  $R(T)$  graph. The anomalous minimum of resistances for Cr (4%), Cr (6%) and Cr (8%) samples is in the temperature range of 210–300 °C, and in the industrial temperature range (up to 100 °C) AFM is characterized by a negative TCR.

In the course of studying the magnetic properties of AFMs, it was found that in the initial (amorphous) state, all AFMs are characterized by either a quasi-linear hysteresis loop with anisotropy fields from 100 A/m to 500 A/m, or a bistable hysteresis loop with nucleation fields from 50 A/m to 200 A/m. In this case, no certain dependence of the AFM magnetic properties on the chromium content was observed. After heating above 650 °C, all crystallized AFMs were characterized by the wide hysteresis loops with a coercive force of more than 20000 A/m.

*Support by RSF, grant 20-19-00607, is acknowledged.*

1. V.S. Larin, A.V. Torkunov, A.P. Zhukov, J. Gonzales, M. Vazques, L.V. Panina, J. Magn. Magn Mater., **249**, 39–45 (2002).
2. A.V. Popova, V.I. Odintsov, S.A. Menshov, E.V. Kostitsyna, V.P. Tarasov, V. Zhukova, A. Zhukov, S.A. Gudoshnikov, Intermetallics, **99**, 39–43 (2018).
3. S.A. Gudoshnikov, V.I. Odintsov, B.Ya. Liubimov, S.A. Menshov, M.N. Churyukanova, S.D. Kaloshkin, G.N. Elmanov, Measurement, **182**, 109783 (2021).

ON THE MAGNETIC STATE OF Co IN CHALCOGENIDES Co<sub>1-x</sub>Ch

*D.F. Akramov*<sup>1,2\*</sup>, *D.A. Shishkin*<sup>2</sup>, *S.N. Mozgovykh*<sup>1</sup>, *K.N. Mikhalev*<sup>2</sup>, *A.Y. Germov*<sup>2</sup>,  
*N.V. Selezneva*<sup>1</sup>

<sup>1</sup>Institute of Natural Sciences and Mathematics, Ural Federal University, Ekaterinburg, Russia

<sup>2</sup>Institute of Metal Physics of Ural Branch of Russian Academy of Sciences, Ekaterinburg, Russia

\*E-mail: [Akramov.danil@urfu.ru](mailto:Akramov.danil@urfu.ru)

The chalcogenides of 3d-transition (M) metals with composition M<sub>1-x</sub>Ch (Ch = S, Se) have a layered hexagonal structure of the NiAs type. The magnetic properties of such compounds depend on the type of atoms M and on the concentration and ordering of vacancies in the cationic sublattice. For example, in Fe<sub>7</sub>Ch<sub>8</sub> compounds the magnetic moments of the iron atoms are directed parallel inside each cationic layer, while between the layers they are oriented antiparallel. The presence of cationic vacancies leads to decompensation of the magnetizations of the layers and, thus, to the occurrence of a ferrimagnetic state in Fe<sub>7</sub>Ch<sub>8</sub> [1]. However, the Co<sub>7</sub>S<sub>8</sub> and Co<sub>7</sub>Se<sub>8</sub> compounds do not possess a long-range magnetic order and exhibits Pauli paramagnetism [2]. This behaviour is suggested to result from a strong decrease in the interplanar distance *c* compared with Fe<sub>7</sub>Ch<sub>8</sub> and a strong overlap of the electron orbitals of cobalt atoms in Co<sub>7</sub>Ch<sub>8</sub> [3]. There are scarce and contradictory data in literature on the presence and properties of the Co<sub>7</sub>Te<sub>8</sub> compound.

The present work aims to study the crystal structure, magnetic and transport properties of Co<sub>7</sub>(Se<sub>1-y</sub>Te<sub>y</sub>)<sub>8</sub> and Co<sub>7-x</sub>Te<sub>8</sub>. Polycrystalline samples were obtained by solid-phase ampoule synthesis with quenching from *T* = 800 °C. X-ray attestation was carried out using Bruker D8 ADVANCE diffractometer in the temperature range of 298–750 K. Magnetization measurements were carried out by a Lake Shore VSM 7407 vibrating magnetometer in the temperature range 300–1273 K and magnetic fields up to 17 kOe. The <sup>59</sup>Co NMR measurements were carried out on a Bruker Avance 500 spectrometer.

For the Co<sub>7</sub>(Se<sub>1-y</sub>Te<sub>y</sub>)<sub>8</sub> system, it was found that the substitution of tellurium for selenium leads to a significant increase in the parameter *a* and a slight increase in the parameter *c* and, therefore, to a strong distortion of the anionic octahedron. Changes in the unit cell parameters are anisotropic, which is probably due to the higher polarizability of tellurium atoms compared to selenium and the strong bond between cobalt atoms. According to NMR data, the Co atoms in the Co<sub>7</sub>(Se<sub>1-y</sub>Te<sub>y</sub>)<sub>8</sub> system are in the low-spin state, and the replacement of selenium by tellurium does not significantly affect the magnetic state of the Co atoms.

An X-ray diffraction study showed that the Co<sub>6.5</sub>Te<sub>8</sub> and Co<sub>6.68</sub>Te<sub>8</sub> compounds with a lower cobalt content compared to the 7:8 stoichiometry are single-phase and crystallize in a hexagonal system with the space group *P-3m1*. It has been found that a decrease in the cobalt content in Co<sub>7</sub>Te<sub>8</sub> does not lead to an increase in the *c* parameter, as might be expected. A reversible anomalous increase in the magnetic susceptibility of the Co<sub>6.5</sub>Te<sub>8</sub> compound has been found in the temperature range from 600 K to 750 K. A similar anomaly is observed in the Co<sub>6.68</sub>Te<sub>8</sub> compound at temperatures from 650 K to 1000 K, but it is irreversible. High-temperature X-ray diffraction studies of Co<sub>6.5</sub>Te<sub>8</sub> and Co<sub>6.68</sub>Te<sub>8</sub> have revealed the phase separation in these compounds above 600 K. It is shown that deviation from stoichiometry does not lead to a change in the magnetic state of cobalt in Co<sub>7</sub>Te<sub>8</sub>.

*This work was supported by the Russian Science Foundation (project no. 22-12-00220).*

1. M. Kawaminami et al., J. Phys. Soc. Japan, **29**, 649 (1970).
2. V.L. Miller et al., J. Solid State Chem., **178**, 1508 (2005).
3. N.V. Baranov et al., J. Condens. Matter Phys., **27**, 286003 (2015).

## SPECTRAL PROPERTIES OF HEISENBERG ANTIFERROMAGNET $S = 1/2$ ON THE TRIANGULAR LATTICE IN A MAGNETIC FIELD

*A.S. Martynov, A.A. Khudaiberdyev, D.M. Dzebisashvili*

Kirensky Institute of Physics, KSC SB RAS, Krasnoyarsk, Russia

E-mail: [zldgin2@mail.ru](mailto:zldgin2@mail.ru)

A new approach for investigation of the spectral properties of a frustrated antiferromagnet on a square lattice in an external magnetic field was proposed in a recent paper [1]. The approach preserves the translational and axial symmetries of the system. In our work the proposed formalism is used for study the spectral properties of a frustrated antiferromagnet with spin  $S = 1/2$  on a triangular lattice in an external magnetic field. The dynamical structure factor of the model and spin-spin correlation functions are calculated for the different values of temperature and magnetic field. The influence of temperature and field on the dispersion and intensity of three branches of the spin wave spectrum is investigated. The obtained results are compared with the results of the spin-wave theory and the bond operator theory [2], as well as with the results of inelastic neutron scattering in the triangular antiferromagnet  $\text{Ba}_3\text{CoSbO}_9$  [3].

1. P.S. Savchenkov, A.F. Barabanov, J. Magn. Magn. Mat., **521**, 167505 (2021).
2. A.V. Syromiatnikov, Phys. Rev. B, **105**, 144414 (2022).
3. D. Macdougall, S. Williams, D. Prabhakaran, R. Bewley, D. Voneshen, R. Coldea, Phys. Rev. B, **102**, 064421 (2020).

## PHASE TRANSITIONS AND CRITICAL PHENOMENA IN THE 4-STATE 2D SITE-DILUTED POTTS MODEL ON A SQUARE LATTICE

*A.K. Murtazaev*<sup>1,2</sup>, *A.B. Babaev*<sup>2,3</sup>, *G.Ya. Ataeva*<sup>1</sup>, *Ya.K. Abuev*<sup>1\*</sup>, *M.A. Babaev*<sup>4</sup>

<sup>1</sup>H. Amirkhanov Institute of Physics of the Daghestan Federal Research Centre of the Russian Academy of Sciences, Makhachkala, Russia

<sup>2</sup>Department of Mathematics and Informatics, Dagestan Federal Scientific Center, Russian Academy of Sciences, Makhachkala, Russia

<sup>3</sup>Daghestan State Pedagogical Universities, Makhachkala, Russia

<sup>4</sup>Daghestan State Universities, Makhachkala, Russia

\*E-mail: [b\\_albert78@mail.ru](mailto:b_albert78@mail.ru)

To date, it is known that the structure defects as non-magnetic impurities affect the thermal and magnetic characteristics of spin systems, for which the Harris criterion is realized [1]. On the other side, impurities can influence on a phase transition order in the case of spin systems experiencing a first-order transition in the homogeneous state [2]. A stabilizing role of impurities in implementation of the second-order transition using Monte Carlo method has been indicated in a recent work [3]. The Potts model is well suited to study this case.

In this regard, the main goal of this work is to study the effect of non-magnetic impurities on phase transitions and critical behavior in the standard 4-state ( $q = 4$ ) two-dimensional Potts model on a square lattice at a spin concentration of  $p = 1.00, 0.90$ . The estimations are performed using the Monte-Carlo cluster Wolff algorithm [4]. As for the 2D site-diluted 4-state Potts model there are still no reliable data on the effect of non-magnetic impurities on the phase transitions, the universality class of critical behavior is not established, and there is no information about the dependence of the critical exponents of the concentration of nonmagnetic impurities, especially when the disorder is realized as quenched non-magnetic impurities. The reliable fact is only that, in the pure system, there is a second-order phase transition [5].

The Hamiltonian of the 2D diluted Potts model can be represented as follows [5]:

$$H = -\frac{1}{2}J \sum_{i,j} \rho_i \rho_j \delta(S_i, S_j), \quad S_i = 1, 2, 3, 4, \quad (1)$$

where  $\delta(S_i, S_j) = \begin{cases} 1, & \text{if } S_i = S_j, \\ 0, & \text{if } S_i \neq S_j. \end{cases}$  and  $\rho_i = \begin{cases} 1, & \text{if a site occupied by a magnetic atom} \\ 0, & \text{if a site occupied by a nonmagnetic impurity} \end{cases}$ .

For all analyzed systems in which a second-order transition occurs, we estimate the static critical exponents of the magnetization  $\beta$ , the susceptibility  $\gamma$ , and the heat capacity  $\alpha$  on the basis of the finite-size scaling theory [6]. The data from our investigations indicate that the second-order phase transition takes place in the considered Potts model on a square lattice, in accordance with the predictions of analytical theories [5]. The inclusion of nonmagnetic impurities causes a change in the universality class of the critical behavior of the two-dimensional 4-state Potts model on a square lattice.

1. A.B. Harris, J. Phys. C, **7**, 1671 (1974).
2. M. Aizenman. J. Wehr, Phys. Rev. Lett., **62**, 2503 (1989).
3. A.K. Murtazaev, A.B. Babaev, Materials Letters, **258**, 126771 (2020).
4. U. Wolff, Phys. Lett., **62**, 361 (1989).
5. F.Y. Wu, Rev. Mod. Phys., **54**, 235 (1982).
6. M.E. Fisher, M.N. Barber, Phys. Rev. Lett., **28**, 1516 (1972).

## ANISOTROPY OF THE MAGNETIC PROPERTIES OF $\text{SrY}_2\text{O}_4:\text{Er}^{3+}$ SINGLE CRYSTAL

*M.A. Cherosov\**, A.G. Kiiamov, R.G. Batulin, I.F. Gilmutdinov, A.G. Ivanova, D.S. Uvin,  
R.V. Yusupov, D.A. Tayurskii

Institute of Physics, Kazan Federal University, Kazan, Russia

\*E-mail: [mcherosov@gmail.com](mailto:mcherosov@gmail.com)

The crystal space group of the  $\text{SrLn}_2\text{O}_4$  (Ln = lanthanide ion) is orthorhombic Pnam. Ln atoms have two inequivalent sites. Compounds  $\text{SrLn}_2\text{O}_4$  consist of a network of linked hexagons and triangles which leads to unusual magnetic properties at low temperatures [1].

Here we present the results of a magnetization measurements with a magnetic field applied along the principal crystallographic axes of  $\text{SrY}_2\text{O}_4:\text{Er}$  0.5 at.% single crystal. A single crystal was grown by the optical floating zone technique.  $\text{Y}_2\text{O}_3$  (Alfa Aesar, 99.99%),  $\text{Er}_2\text{O}_3$  (Alfa Aesar, 99.9%) and  $\text{SrCO}_3$  (Alfa Aesar, 99.99%) oxides were used as starting materials. A synthesized product was examined at each stage with powder X-ray diffraction (Bruker D8 ADVANCE, Cu  $K_\alpha$ ) for corresponding to the expected  $\text{SrY}_2\text{O}_4$  structure and the absence of excess crystalline phases. A single crystal growth took place in an optical floating zone furnace FZ-T-4000-H-VII-VPO-PC (Crystal Systems Corp., Japan) equipped with four 1 kW halogen lamps in an air flow of 0.5 l/min at ambient pressure at a rate of 3 mm/h. The grown crystal was pinkish in color and was of high optical quality.

Magnetization measurements were performed using a Quantum Design VSM magnetometer (PPMS-9) within the temperature range 2–300 K. The dependence of the magnetization on the magnetic field at low temperatures shows c-axis is a hard axis. The temperature dependence of the susceptibility in a magnetic field of 9 T gives three different Curie-Weiss temperatures for the three principal crystallographic axes.

*This paper has been supported by the Kazan Federal University Strategic Academic Leadership Program (PRIORITY-2030). The magnetization measurements were carried out utilizing equipment of the PCR Federal Center of Shared Facilities (Kazan Federal University).*

1. O.A. Petrenko, *Low Temp. Phys.*, **40**, 2, 106–112 (2014).

**NON-STOICHIOMETRY AND UNCONVENTIONAL SPIN-GLASS  
IN FRUSTRATED SYSTEM  $\text{Li}_{0.8}\text{Ni}_{0.6}\text{Sb}_{0.4}\text{O}_2$** 

*E. Vavilova*<sup>1\*</sup>, *T. Salikhov*<sup>1</sup>, *M. Iakovleva*<sup>1</sup>, *T. Vasilchikova*<sup>2</sup>, *E. Zvereva*<sup>2</sup>, *I. Shukaev*<sup>3</sup>,  
*V. Nalbandyan*<sup>3</sup>, *A. Vasiliev*<sup>2</sup>

<sup>1</sup>Zavoisky Physical-Technical Institute, FRC Kazan Scientific Center, Russian Academy of Sciences,  
Kazan, Russia

<sup>2</sup>Faculty of Physics, Moscow State University, Moscow, Russia

<sup>3</sup>Faculty of Chemistry, Southern Federal University, Rostov-on-Don, Russia

\*E-mail: [jenia.vavilova@gmail.com](mailto:jenia.vavilova@gmail.com)

Structural and magnetic properties of  $\text{Li}_{0.8}\text{Ni}_{0.6}\text{Sb}_{0.4}\text{O}_2$  were studied by means of X-ray diffraction, magnetic susceptibility, specific heat, and nuclear magnetic resonance measurements. The formation of a new phase, which is Sb-enriched and Li-deficient with respect to the structurally honeycomb-ordered  $\text{Li}_3\text{Ni}_2\text{SbO}_6$  was proved by powder X-ray diffraction data. The structural modification leads to a drastic change of the magnetic properties in comparison to the stoichiometric partner. A combination of the bulk static susceptibility, heat capacity and  $^7\text{Li}$  NMR studies indicates a complicated step-by-step transformation of the magnetic system. We observe a development of a cluster spin glass, where the Ising-like  $\text{Ni}^{2+}$  magnetic moments demonstrate a 2D correlated slow short-range dynamics already at 12 K, whereas the formation of 3D short range static ordered clusters occurs far below the spin-glass freezing temperature at  $T \sim 4$  K.

*E.V. would like to thank financial support from the government assignment for FRC Kazan scientific Center of RAS.*

## NMR STUDY OF SPIN DYNAMICS IN THE ALTERNATING CHAIN SYSTEM $\text{Li}_3\text{Cu}_2\text{SbO}_6$ WITH DEFECTS

*E. Vavilova*<sup>1\*</sup>, *T. Salikhov*<sup>1</sup>, *T. Vasilchikova*<sup>2</sup>, *V. Nalbandyan*<sup>3</sup>, *A. Vasiliev*<sup>2</sup>, *E. Zvereva*<sup>2</sup>

<sup>1</sup>Zavoisky Physical-Technical Institute, FRC Kazan Scientific Center, Russian Academy of Sciences, Kazan, Russia

<sup>2</sup>Faculty of Physics, Moscow State University, Moscow, Russia

<sup>3</sup>Faculty of Chemistry, Southern Federal University, Rostov-on-Don, Russia

\*E-mail: [jenia.vavilova@gmail.com](mailto:jenia.vavilova@gmail.com)

In a hexagonal layered compound  $\text{Li}_3\text{Cu}_2\text{SbO}_6$  a quasi-one-dimensional magnetic structure arises as a result of the interplay of lattice distortion, an orbital arrangement, and frustration. However, as it often happens in structures containing lithium and copper ions, the Li and Cu atoms are partially mixed in  $\text{Li}_3\text{Cu}_2\text{SbO}_6$ . Since the Li ion acts as a non-magnetic defect, the lithium substitution results in a segmentation of the Cu-chains into fragments of different length and gives rise to uncompensated spins at the segment ends. Huge Curie-like contribution of unpaired Cu moments and clusters masks the component from the gapped spin matrix in bulk magnetic susceptibility. NMR as a local technique makes it possible to prove a clearly pronounced gapped behavior of a spin system with a spin gap value of about 90 K. The approximation using the AF-FM and non-interacting dimers models give an acceptable description of the experiments at temperatures above 40 K and make it possible to estimate the exchange interaction in the system.

*The authors are grateful to S. Nishimoto for discussions and theoretical support. E.V. would like to thank financial support from the government assignment for FRC Kazan scientific Center of RAS.*

**PECULIARITIES AND COMPARISON OF  $\text{Cu}_2\text{MBO}_5$  ( $\text{M} = \text{Fe}, \text{Mn}, \text{Cr}$ ) LUDWIGITES CRYSTALLIZATION IN  $\text{Bi}_2\text{O}_3\text{-MoO}_3\text{-Na}_2\text{O-B}_2\text{O}_3$  MULTICOMPONENT FLUXES**

*M.S. Molokeev<sup>1,2,3</sup>, A.F. Bovina<sup>1</sup>, K.A. Shabanova<sup>4,5</sup>, D. Kokh<sup>4,5</sup>, D.A. Velikanov<sup>1</sup>, E.V. Eremin<sup>1,2,4</sup>, L.N. Bezmaternykh<sup>1</sup>, E.M. Moshkina<sup>1\*</sup>*

<sup>1</sup>Kirensky Institute of Physics, Federal Research Center KSC SB RAS, Krasnoyarsk, Russia

<sup>2</sup>Siberian Federal University, Krasnoyarsk, Russia

<sup>3</sup>Far Eastern State Transport University, Khabarovsk, Russia

<sup>4</sup>Siberian State University of Science and Technologies, Krasnoyarsk, Russia

<sup>5</sup>Federal Research Center KSC SB RAS, Krasnoyarsk, Russia

\*E-mail: [ekoles@iph.krasn.ru](mailto:ekoles@iph.krasn.ru)

Copper-containing ludwigites  $\text{Cu}_2\text{M}^{3+}\text{BO}_5$  ( $\text{M}$  – transition metals) can be highlighted as a separate subclass among the family due to the lower symmetry relatively natural mineral ludwigite structure ( $Pnma \rightarrow P2_1/c$ ). That is caused by Jahn-Teller effect of  $\text{Cu}^{2+}$  cation gives rise the monoclinic distortions of metal-oxygen octahedra. These compounds with a different cations in trivalent subsystem are the objects of the number of the recent studies [1–3]. The ludwigite structure is quasi-two-dimensional one and these materials are characterized by the strong growth anisotropy [4]. One of the most efficient technique to obtain the single crystals of ludwigite of different composition is flux growth. Recently, single crystals of a number of ludwigites, including copper-containing, have been grown using this method [3–5].

The present work presents the results of study and comparison of the flux growth conditions and peculiarities of different Cu-containing ludwigites, including  $\text{Cu}_2\text{FeBO}_5$ ,  $\text{Cu}_2\text{MnBO}_5$  and  $\text{Cu}_2\text{CrBO}_5$ . The main focus is the interaction of the solvent and dissolved crystal forming oxides and the study of the influence of the solvent to the high-temperature crystallizing phase. The flux systems based on the  $\text{Bi}_2\text{O}_3\text{-MoO}_3$  mixture diluted by the  $\text{Na}_2\text{O}$  and  $\text{Na}_2\text{B}_4\text{O}_7$  are under study.

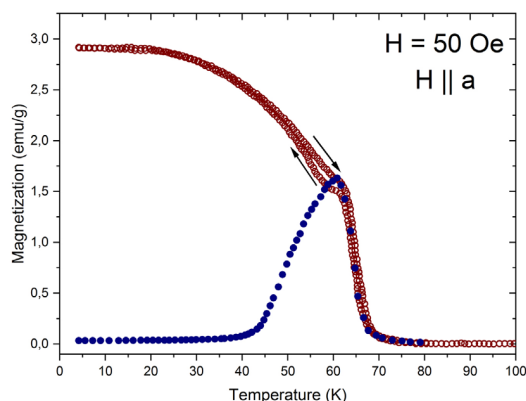


Figure 1. Thermal dependency of the magnetization of  $\text{Cu}_2\text{Mn}_{1-x}\text{Cr}_x\text{BO}_5$  ( $x \approx 10\%$ ) obtained in  $H = 50$  Oe, applied along the  $a$  axis in the ZFC (heating of the sample in nonzero magnetic field after cooling in zero magnetic field – blue color), FC (cooling in nonzero magnetic field – wine color) and FH (heating in nonzero magnetic field after cooling in the magnetic field of the same magnitude – wine color) modes.



The crystal structure of the studied compounds has been examined by powder and single crystal X-ray diffraction. All the Cu-containing ludwigites under study have different magnetic properties. Thus, the problem of the magnetic structure alteration between the compounds with different trivalent cations is of interest. So the part of the work is devoted to solid solutions crystallization study and the investigation of the evolution of its structure and magnetic properties. The Fig. 1 presents the thermal dependency of the magnetization of  $\text{Cu}_2\text{Mn}_{1-x}\text{Cr}_x\text{BO}_5$  ( $x \approx 10\%$ ) obtained in  $H = 50$  Oe, applied along the  $a$  axis in the ZFC (heating of the sample in nonzero magnetic field after cooling in zero magnetic field), FC (cooling in nonzero magnetic field) and FH (heating in nonzero magnetic field after cooling in the magnetic field of the same magnitude) modes.

*The study was supported by RSF-KRFS (grant No. 22-12-20019).*

1. F. Damay, J. Sottmann, F. Lainé, L. Chaix, M. Poienar, P. Beran, E. Elkaim, F. Fauth, L. Nataf, A. Guesdon, A. Maignan, C. Martin. *Phys. Rev. B*, **101**, 094418 (2020).
2. M.A.V. Heringer, D.L. Mariano, D.C. Freitas, E. Baggio-Saitovitch, M.A. Continentino, D.R. Sanchez. *Phys. Rev. Mater*, **4**, 064412 (2020).
3. E. Moshkina, C. Ritter, E. Eremin, S. Sofronova, A. Kartashev, A. Dubrovskiy, L. Bezmaternykh, *J. Phys.: Condens. Matter*, **29**, 245801 (2017).
4. E.M. Moshkina, T.P. Gavrilova, I.F. Gilmutdinov, A.G. Kiiamov, R.M. Eremina, *Journal of Crystal Growth*, **545**, 125723 (2020).
5. E. Moshkina, Y. Seryotkin, A. Bovina, M. Molokeyev, E. Eremin, N. Belskaya, L. Bezmaternykh, *Journal of Crystal Growth*, **503**, 1–8 (2018).
6. F. Damay, J. Sottmann, F. Fauth, E. Suard, A. Maignan, C. Martin, *Appl. Phys. Lett.*, **118**, 192903 (2021).

**THERMAL EXPANSION AND RESISTIVITY ANOMALIES  
IN  $\text{Cu}_2\text{FeBO}_5$  LUDWIGITE**

*Yu.S. Gokhfeld<sup>1\*</sup>, L.A. Solovyov<sup>2</sup>, S.N. Vereshchagin<sup>2</sup>, A.A. Borus<sup>1</sup>, I.A. Gudim<sup>1</sup>, N.V. Kazak<sup>1</sup>*

<sup>1</sup>Kirensky Institute of Physics, Federal Research Center KSC SB RAS, Krasnoyarsk, Russia

<sup>2</sup>Institute of Chemistry and Chemical Technology, Federal Research Center KSC SB RAS Krasnoyarsk, Russia

\*E-mail: [gokhfeld@kirensky.krasn.ru](mailto:gokhfeld@kirensky.krasn.ru)

$\text{Cu}_2\text{FeBO}_5$  belongs to the ludwigite family of borates. The material demonstrates a complex magnetic behavior, its magnetic ground state is a subject of long-standing discussion [1, 2]. Here, we focus on the structural and electronic properties of  $\text{Cu}_2\text{FeBO}_5$  at high temperatures.

Single crystals of  $\text{Cu}_2\text{FeBO}_5$  were grown using the flux method [3]. The crystals were crushed in agate mortar, pressed as a pellet and annealed in air at 1113 K for 60 hours. X-ray powder diffraction (XRPD) data were collected on a PANalytical X'Pert PRO diffractometer using a copper monochromator with  $\text{CuK}\alpha$  radiation. The measurements were performed in the temperature interval of 300–1000 K using an Anton Paar HTK 1200N camera. The crystal lattice parameters were refined

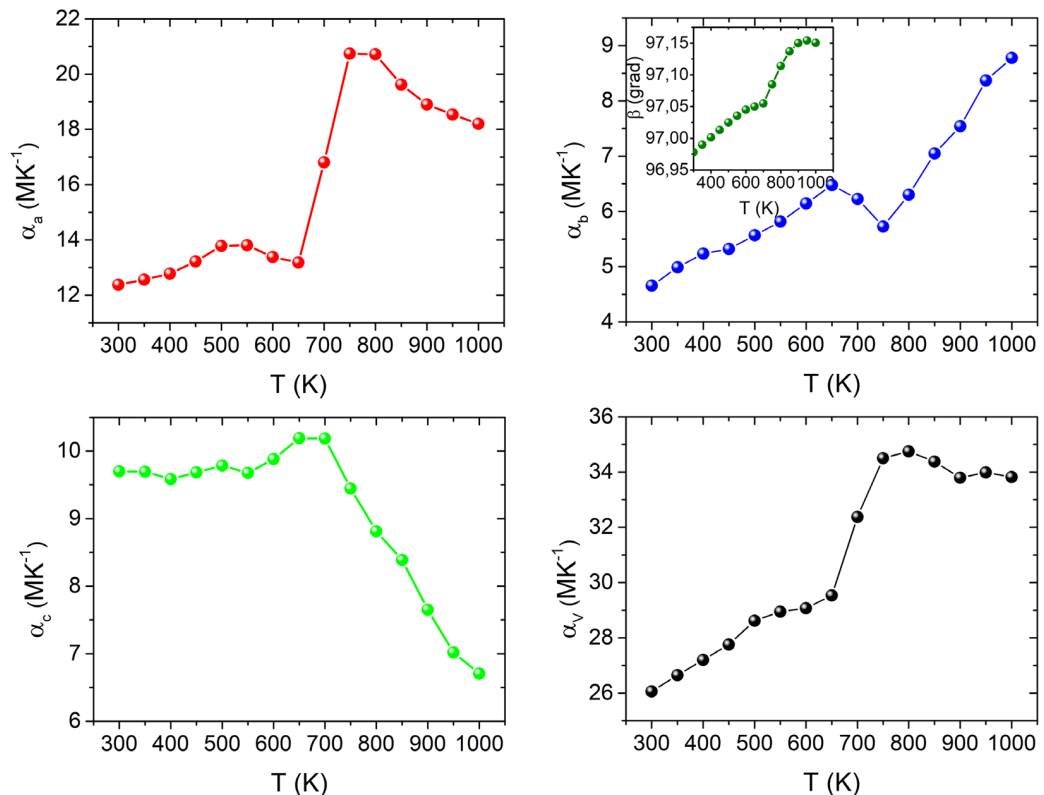


Figure 1. Thermal expansion coefficients of lattice parameters and unit cell volume of  $\text{Cu}_2\text{FeBO}_5$  as a function of the temperature.

by the derivative difference minimization method [4]. The electrical resistivity was measured with a standard four-point configuration in the temperature range of 550–800 K using an experimental setup for thermopower and resistivity measurements [5]. For this experiment, a  $\text{Cu}_2\text{FeBO}_5$  sample in the form of a regular parallelepiped of 15 mm length and 1.9 mm thickness was cut from a pellet.

The mass change (TG) and heat flux (DSC) measurements in air (20%  $\text{O}_2$  + Ar and 100% Ar) revealed no changes in weight or thermal effects in a wide temperature range 373–1000 K. That is  $\text{Cu}_2\text{FeBO}_5$  is thermally stable in the temperature range of interest. At room temperature the monoclinic crystal structure (space group  $P21/c$ ) with lattice parameters  $a = 3.11888(3)$  Å,  $b = 12.0226(1)$  Å,  $c = 9.4861(1)$  Å,  $\beta = 96.9780(7)^\circ$ ,  $V = 353.068(6)$  Å<sup>3</sup> was found, which is in a good agreement with earlier reported data [2].

On heating the crystal symmetry is preserved and the monoclinic angle  $\beta$  progressively increases, showing a clear kink at  $T = 700$  K (inset to Fig. 1). The expansion of the crystal structure is minimal in  $bc$ -plane and maximal along the  $a$ -axis, i.e. parallel and perpendicular, respectively, to the planes of the  $\text{BO}_3$  groups (Fig. 1). There is a strong coupling between the  $a$ - and  $c$ -lattice parameters: at  $T > 650$  K a rapid increase in  $a$  is accompanied by a decrease in  $c$ .

The electrical resistance at room temperature is too large to be accurately measured. So, we conclude that the  $\text{Cu}_2\text{FeBO}_5$  is an insulator. Above 550 K does the resistance become such that it can be reliably measured with  $\rho(T = 550 \text{ K}) \approx 10^6$  Ohm · cm. As temperature increases the resistivity rapidly decreases, changing by about 2 orders of magnitude up to 800 K (Fig. 2). The resistivity shows complex temperature dependence. A linear dependence  $\ln(\rho) \sim 1/T$  demonstrates two inflection points at  $\sim 625$  and 700 K corresponding to the changes in the slope. The activation energies at the  $T$  ranges of 550–625 K and 625–700 K were found to be  $E_a = 0.78$  eV and 1.45 eV, respectively. Above 700 K the  $\ln(\rho)$  curve is strongly nonlinear.

In summary, the study of thermal expansion of  $\text{Cu}_2\text{FeBO}_5$  revealed a strong anisotropy inherent to ludwigites. The thermal expansion anomaly at 700 K coincides with the electrical resistivity feature, indicating a strong relationship between crystalline and electronic subsystems.

*Support by RFBR 20-02-00559 and 21-52-12033 HHIIO\_a is acknowledged.*

1. M.A. Continentino, J.C. Fernandes, R.B. Guimarés et al., Eur. Phys. J. B, **9**, 613–618 (1999).
2. G.A. Petrakovskii, L.N. Bezmaternykh, D.A. Velikanov et al., Phys. Solid State, **51**, 2077 (2009).
3. E.M. Moshkina, M.S. Platonov, Yu.V. Seryotkin et al., J. Magn. Magn. Mater, **464**, 1–10 (2018).
4. L.A. Solovyov, J. Appl. Crystallogr., **37**, 743 (2004).
5. A.T. Burkov, A. Heinrich, P.P. Konstantinov et al., Meas. Sci. Technol., **12**, 264 (2001).

MAGNETIC SPECIFIC HEAT OF SrDy<sub>2</sub>O<sub>4</sub> SINGLE CRYSTAL

*A.G. Kiiamov\**, *R.G. Batulin*, *M.A. Cherosov*, *I.F. Gilmutdinov*, *A.G. Ivanova*, *R.V. Yusupov*,  
*D.A. Tayurskii*

Institute of Physics, Kazan Federal University, Kazan, Russia

\*E-mail: [AiratPhD@gmail.com](mailto:AiratPhD@gmail.com)

SrDy<sub>2</sub>O<sub>4</sub> belongs to the family of rare-earth strontium oxides with the general chemical composition SrLn<sub>2</sub>O<sub>4</sub> (where Ln is a lanthanide ion). It crystallizes in the form of calcium ferrite, with the space group *Pnam* (Space group #62) and each unit cell contains a total of eight Ln atoms that are divided into two inequivalent *4c* sites (*4c1* and *4c2*) at the center of distorted, edge-sharing, oxygen octahedra [1]. Magnetic properties of SrDy<sub>2</sub>O<sub>4</sub> have been studied within the context of geometrically frustrated magnetism [2]. In magnetically frustrated systems, competing interactions can inhibit long range order at low temperatures and enforce highly degenerate ground states. SrDy<sub>2</sub>O<sub>4</sub> shows no indications of long-range order down to low temperatures in zero magnetic field, suggesting a possible spin liquid ground state [3].

Here we present the investigation of the magnetic specific heat of SrDy<sub>2</sub>O<sub>4</sub> single crystal. In the present study, single crystals of magnetic SrDy<sub>2</sub>O<sub>4</sub> oxide and its nonmagnetic analogue SrY<sub>2</sub>O<sub>4</sub> have been synthesized by the floating zone technique. SrCO<sub>3</sub> (Alfa Aesar, 99.99%), Y<sub>2</sub>O<sub>3</sub> (Alfa Aesar, 99.99%) and Dy<sub>2</sub>O<sub>3</sub> (Alfa Aesar, 99.9%) oxides were used as starting materials. The thoroughly ground and mixed stoichiometric composition was initially sintered at 1050 °C for 8 hours for both compounds. The synthesized powders were examined with powder X-ray diffraction (Bruker D8 ADVANCE, Cu K $\alpha$ ) and found to be a phase-pure material with lattice parameters and space group symmetry corresponding to the structure of SrDy<sub>2</sub>O<sub>4</sub> and SrY<sub>2</sub>O<sub>4</sub>, respectively. The data were analyzed by a standard Rietveld refinement using the FullProf software [4]. Since all diffraction peaks were well described within the known (SrDy<sub>2</sub>O<sub>4</sub> or SrY<sub>2</sub>O<sub>4</sub>) structure model, it can be argued that the samples contain no impurity phases. The refinement does not fully describe the observed peak intensities. It can result from a combined effect of strain of the sample when crushed into powder and texture.

Cylindrical rods were formed from the powders using a hydrostatic press, and this rod was used as the ingot for the crystal growth. The single crystals were grown in an air flow of 0.5 l/min at ambient pressure using an optical floating zone furnace FZ-T-4000-H-VII-VPO-PC (Crystal Systems Corp., Japan) equipped with four 1 kW halogen lamps at a rate of 3 mm/h. The feed and seed rods were counterrotated at a rate of 15 rpm to obtain a homogeneous molten zone for both crystals.

Specific heat measurements are conducted at a commercial PPMS from Quantum Design (USA). The temperature dependence of the specific heat of single crystals of SrDy<sub>2</sub>O<sub>4</sub> and SrY<sub>2</sub>O<sub>4</sub> were measured in zero field. The lattice contribution to the specific heat of SrDy<sub>2</sub>O<sub>4</sub> has been modeled by using the temperature dependence of heat capacity of its non-magnetic analogue SrY<sub>2</sub>O<sub>4</sub>. The magnetic specific heat of SrDy<sub>2</sub>O<sub>4</sub> has been estimated as a difference between the total and the lattice specific heats. The magnetic specific heat should be helpful for the eventual development of realistic models of the magnetic interactions in the SrDy<sub>2</sub>O<sub>4</sub> compound and whole family of SrLn<sub>2</sub>O<sub>4</sub> compounds.

*The reported study was funded by Priority-2030 Program. The specific heat and x-ray diffraction measurements were carried out utilizing equipment of the PCR Federal Center of Shared Facilities (Kazan Federal University).*

1. A. Fennell et al., *Physical Review B*, **89**, 224511 (2014).
2. T. Cheffings et al., *J. Phys.: Condens. Matter*, **25**, 256001(2013).
3. L. Balents, *Nature*, **464**, 199–208 (2010).
4. J. Rodriguez-Carvajal, *Phys. B Condens. Matter*, **192**, 55–56 (1993).

## PHASE DIAGRAM OF THE FRUSTRATED FOUR-STATE POTTS MODEL WITH COMPETING EXCHANGE INTERACTIONS

*D.R. Kurbanova\**, *M.K. Ramazanov*, *M.A. Magomedov*, *A.K. Murtazaev*

Institute of Physics, Daghestan Federal Research Centre RAS, Makhachkala, Russia

\*E-mail: [d\\_kurbanova1990@mail](mailto:d_kurbanova1990@mail)

Low-dimensional lattice models describe a large class of real physical systems such as layered magnets, liquid helium films, superconducting films, and adsorbed films. A common feature of these systems is frustration, which is the competition due to geometric or energy constraints. Magnetic materials with triangular lattices are highly frustrated owing to their special geometry. When the temperature is decreased, the ordering process in such systems occurs much more slowly than that in ordinary frustrated systems. Such behavior is caused by the fact that not only states with non-trivial global degeneracy, but also locally degenerate states are possible in systems with a lower coordination number [1–4].

In present work, on basis Wang-Landau Monte Carlo algorithm, we investigate the exchange interaction competition influence on phase transitions, thermodynamic properties, and magnetic structures of the ground state for two-dimensional four-state Potts model on a triangular lattice the first and second nearest neighbor interactions. 4-state Potts model is a possible model for the behavior of some classes of adsorbed gases on graphite [5]. This model is also interesting because  $q = 4$  is the boundary value of the interval  $2 \leq q \leq 4$ , where a second-order phase transition is observed, and a first-order transition occurs in the range of  $q > 4$  [6]. In addition, ambiguous pseudocritical behavior was observed in the considered model [7].

The Hamiltonian of the 4-state Potts model with first and second nearest-neighbor interactions can be presented as

$$H = -J_1 \sum_{\langle i,j \rangle, i \neq j} S_i S_j - J_2 \sum_{\langle i,k \rangle, i \neq k} S_i S_k, \quad (1)$$

where  $J_1$  and  $J_2$  are the parameters of the exchange ferromagnetic ( $J_1 > 0$ ) and antiferromagnetic ( $J_2 < 0$ ) interactions for the first and second nearest-neighbors. The calculations were carried out for systems with periodic boundary conditions and linear dimensions  $L \times L = N$ ,  $L = 12 \div 120$  in the range  $-2.0 \leq J_2 \leq 0.0$ . The advantage of the Wang-Landau algorithm is that the density of states  $g(E)$  in the system is independent of the temperature. Knowing the density of states of the system, we can calculate the temperature dependence of any thermodynamic parameter [8–10]. We determined the order of the phase transitions by using the density of states (DOS) difference  $\ln g(E + \Delta E) - \ln g(E)$  and histogram analysis [11, 12].

A phase diagram of the critical temperature dependence on the value of the next-nearest-neighbor interaction is shown in Fig. 1. The diagram demonstrates several different phases: ferromagnetic (FM), paramagnetic (PM), stripe (in the range of  $-1.0 < J_2 \leq -0.5$ ) and Phase 1 (stripe-triplet). The critical temperature value  $T_c = 1.444(1)$ , which we have been obtained for  $J_2 = 0.0$ , coincides within the error with the data of [6]. When  $J_2 = -1.0$ , the critical temperature is zero and there is no phase transition [13]. This is explained by the fact that the competition between the exchange interactions of the first and second nearest-neighbors at a given point creates a strong frustration. Frustrations

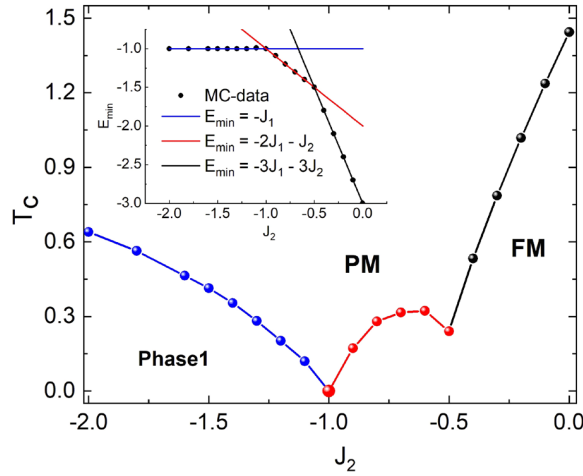


Figure 1. Phase diagram of the 4-state Potts model on a triangular lattice with first  $J_1$  and second  $J_2$  nearest-neighbor interactions. The inset depicts the ground state energy  $E_{\min}$  versus  $J_2$ : ferromagnetic phase (FM):  $E_{\min} = -3J_1 - 3J_2$ , stripe phase:  $E_{\min} = -2J_1 - J_2$ , stripe-triplet phase (Phase 1):  $E_{\min} = -J_1$ .

disturb the order of the system and lead to the disappearance of phase transition. The phase transition analysis, carried out for the entire considered interval  $J_2$ , shows that the phase transition from the ferromagnetic to the paramagnetic phase is a second-order transition, and the transition of the stripe and stripe-triplet phases to the paramagnetic phase is of the first-order. The inset also shows the ground state energy corresponding to different regions of the phase diagram: ferromagnetic phase –  $E_{\min} = -3J_1 - 3J_2$ , stripe phase –  $E_{\min} = -2J_1 - J_2$ , stripe-triplet phase –  $E_{\min} = -J_1$ .

The magnetic structures of the ground state were determined for different values of the second nearest-neighbor interaction: a triplet or mixed stripe-triplet state for Phase 1, disordered highly degenerate state at frustration, a weakly degenerate multilayer state for a stripe phase, and an ordered ferromagnetic state for a ferromagnetic phase. We can conclude that the ground state of the system can be both strongly degenerate, which indicates the presence of frustration in the system, and weakly degenerate, depending on the ratios of exchange interactions for the first and second nearest-neighbors.

1. G. Toulouse, *Commun. Phys.*, **2**, 115 (1977).
2. J. Villain, *J. Phys.*, **10**, 4793 (1977); **46**, 1840 (1985).
3. H.T. Diep, *Frustrated Spin Systems*, World Scientific Publishing Co. Pte. Ltd., Singapore (2004).
4. Zh. Fu, W. Guo, H.W.J. Blöte, *Phys. Rev. E*, **101**, 012118 (2020).
5. E. Domany, M. Schick, J.S. Walker, *Phys. Rev. Lett.*, **38**, 1148 (1977).
6. F.Y. Wu, *Rev. Mod. Phys.*, **54**, 235 (1982).
7. N. Schreiber, R. Cohen, S. Haber, *Phys. Rev. E*, **97**, 032106 (2018).
8. D.P. Landau and K. Binder, *Monte Carlo Simulations in Statistical Physics*, Cambridge University Press, Cambridge, 2000.
9. F. Wang and D.P. Landau, *Phys. Rev. E*, **64**, 056101 (2001).
10. C. Zhou, R.N. Bhatt, *Phys. Rev. E*, **72**, 025701(R) (2005).
11. F. Wang, D.P. Landau, *Phys. Rev. Lett.*, **86**, 2050 (2001); *Phys. Rev. E*, **64**, 056101 (2001).
12. Y. Komura, Y. Okabe, *Phys. Rev. E*, **85**, 010102 (2012).
13. D.R. Kurbanova, A.K. Murtazaev, M.K. Ramazanov, M.A. Magomedov, T.A. Taaev, *JETP*, **131**, 951–955 (2020).

## PHASE TRANSITION IN THREE-STATE ANTIFERROMAGNETIC POTTS MODEL ON THE BODY-CENTERED CUBIC LATTICE

*D.R. Kurbanova\**, *M.K. Ramazanov*, *M.A. Magomedov*, *K.Sh. Murtazaev*, *A.K. Murtazaev*

Institute of Physics, Daghestan Federal Research Centre RAS, Makhachkala, Russia

\*E-mail: [d\\_kurbanova1990@mail](mailto:d_kurbanova1990@mail)

Since its introduction, the Potts model has played a significant role in statistical physics [1, 2] and in applications to various condensed-matter systems [3]. Depending on the number of spin states  $q$  and spatial dimension, the Potts model demonstrates a temperature phase transition of the first or second order. Originally, most studies of the Potts model focused on ferromagnetic interactions, and for that case the critical properties and phase diagram are well known [2, 4]: at  $q > 4$ , the system exhibits a first-order phase transition, whereas at  $q \leq 4$ , the transition is continuous. For the three-dimensional case, it is known that at  $q > 3$ , a first-order phase transition is observed in the system [5]. Ferromagnetic Potts models are by now fairly well understood, thanks to universality; but the behavior of antiferromagnetic Potts models depends strongly on the microscopic lattice structure, so that many basic questions must be investigated case by case [6–9]: Is there a phase transition at finite temperature, and if so, of what order? What is the nature of the low-temperature phase(s)? If there is a critical point, what are the critical exponents and the universality classes?

In present work, on basis Wang-Landau Monte Carlo algorithm [10–11], we investigate the exchange interaction competition influence on phase transitions and thermodynamic properties of the three-dimensional 3-state antiferromagnetic Potts model on a body-centered cubic lattice.

The Hamiltonian of the 3-state Potts model with first and second nearest-neighbor interactions can be presented as

$$H = -J_1 \sum_{\langle i,j \rangle, i \neq j} S_i S_j - J_2 \sum_{\langle i,k \rangle, i \neq k} S_i S_k = -J_1 \sum_{\langle i,j \rangle, i \neq j} \cos \theta_{i,j} - J_2 \sum_{\langle i,k \rangle, i \neq k} \cos \theta_{i,k}, \quad (1)$$

where  $J_1$  and  $J_2$  are the parameters of the exchange ferromagnetic ( $J_1 > 0$ ) and antiferromagnetic ( $J_2 < 0$ ) interactions for the first and second nearest-neighbors. The calculations were carried out for systems with periodic boundary conditions and linear dimensions  $L \times L = N$ ,  $L = 12 \div 120$  in the range  $-2.0 \leq J_2 \leq 0.0$ . The advantage of the Wang-Landau algorithm is that the density of states in the system is independent of the temperature. Knowing the density of states of the system, we can calculate the temperature dependence of any thermodynamic parameter [8–10]. We determined the

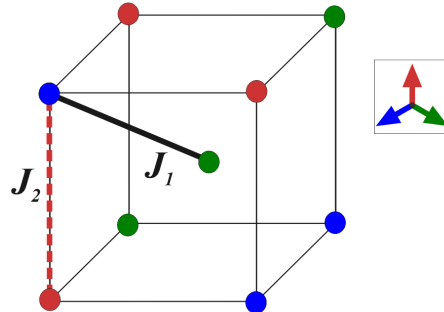


Figure 1. Schematics and color drawing of three feasible spin directions.

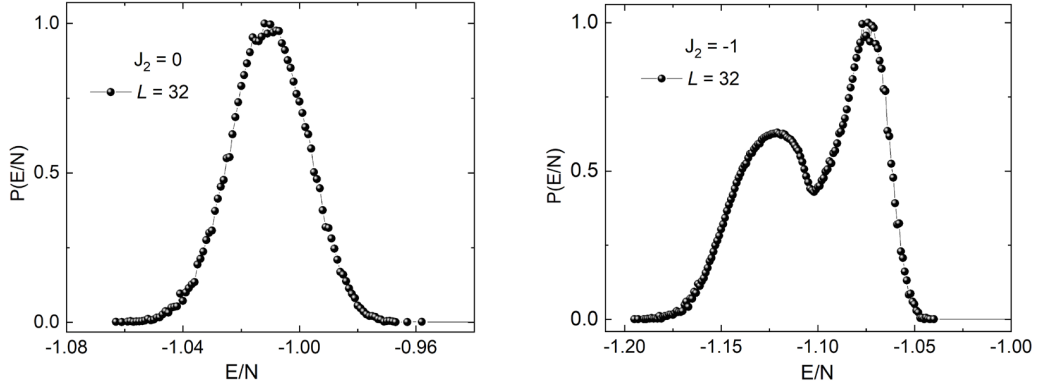


Figure 2. Energy histograms at  $J_2 = 0$  and  $-1$  with linear dimensions  $L = 32$ .

order of the phase transitions by using the density of states (DOS) difference  $\ln g(E + \Delta E) - \ln g(E)$  and histogram analysis [11].

A schematic and color representation of the model are shown in Fig. 1. The spins marked by circles of the same color, have the same direction. The figure also shows the interactions for the first and second nearest-neighbors.

The directions of the vectors are specified such that equality holds:

$$\theta_{i,j} = \begin{cases} 0, & \text{if } S_i = S_j \\ 120^\circ, & \text{if } S_i \neq S_j \end{cases} \Rightarrow \cos \theta_{i,j} = \begin{cases} 1, & \text{if } S_i = S_j \\ -1/2, & \text{if } S_i \neq S_j \end{cases}. \quad (2)$$

According to equation (2), for two spins  $S_i$  и  $S_j$  the energy of pairwise exchange interaction is  $E_{ij} = -J_1$  if  $S_i = S_j$ . In the case where  $S_i \neq S_j$ , the energy is  $E_{ij} = J_1/2$ . Thus, the energy of pairwise interaction of spins is equal to one value when they are in the same direction, and takes on a different value when the directions of the spins do not coincide.

A nature of phase transitions is estimated using the methods of the histogram analysis and the fourth order Binder cumulants. It was found that a second-order phase transition is observed in the model under study. Accounting for the interaction of second nearest neighbors leads to a change in the type of phase transition. Figure 2 presents energy histograms for  $J_2 = 0$  and  $J_2 = -1$  with linear dimensions  $L = 32$ . The bimodal energy distribution is observed in the system at  $J_2 = -1$ . This is in accordance with first-order behavior.

*This research was supported by the grant of the President of the Russian Federation for state support of young Russian scientists – PhD (№ MK-5223.2022.1.2).*

1. G. Toulouse, Commun. Phys., **2**, 115 (1977).
2. F.Y. Wu, Rev. Mod. Phys., **54**, 235 (1982).
3. D. Louis, D. Lacour, M. Hehn, V. Lomakin, T. Hauet and F. Montaigne, Nat. Mat. **17**, 1076 (2018).
4. R.J. Baxter, J. Phys. C, **6**, 445 (1973).
5. N. Schreiber, R. Cohen, S. Haber, Phys. Rev. E, **97**, 032106 (2018)
6. Zh. Fu, W. Guo, H.W.J. Blöte, Phys. Rev. E, **101**, 012118 (2020).
7. M.K. Ramazanov, A.K. Murtazaev, M.A. Magomedov, Physica A, **521**, 543 (2019).
8. Ch. Yamaguchi, Y. Okabe, J. Phys. A, **34**, 8781 (2001).
9. R. Kotecky, J. Salas, A.D. Sokal, Phys. Rev. Lett., **101**, 030601 (2008).
10. D.P. Landau and K. Binder, Monte Carlo Simulations in Statistical Physics, Cambridge University Press, Cambridge, 2000.
11. F. Wang and D.P. Landau, Phys. Rev. E, **64**, 056101 (2001).



## INFLUENCE OF A MAGNETIC FIELD ON AN ANTIFERROMAGNET WITH COMPETING EXCHANGE INTERACTIONS

*K.Sh. Murtazaev*<sup>1\*</sup>, *A.K. Murtazaev*<sup>1,2</sup>, *M.K. Ramazanov*<sup>1,2</sup>, *M.A. Magomedov*<sup>1,2</sup>

<sup>1</sup>Institute of Physics, Dagestan Federal Research Center, Russian Academy of Sciences, Makhachkala, Russia

<sup>2</sup>Dagestan Federal Research Center, Russian Academy of Sciences. Makhachkala, Russia

\*E-mail: [skurban@mail.ru](mailto:skurban@mail.ru)

The study of phase transitions (PT) and critical phenomena of frustrated spin systems is currently one of the most urgent and complex problems in the field of condensed matter physics [1, 2]. This is due to the fact that the ground state of the system is strongly degenerate in the presence of frustrations. Strictly and consistently, based on microscopic Hamiltonians, such systems can be studied by Monte Carlo (MC) methods [3–7]. The replica algorithm of the MC method is certainly a powerful tool for solving such problems. Therefore, in this study, a highly efficient replica exchange algorithm of the MC method was used.

The Hamiltonian of the antiferromagnetic Ising model on a body-centered cubic (bcc) lattice, taking into account the interaction of the first and second nearest neighbors, as well as the magnetic field, has the following form:

$$H = -J_1 \sum_{\langle i,j \rangle} S_i \cdot S_j - J_2 \sum_{\langle i,l \rangle} S_i \cdot S_l - h \sum_i S_i,$$

where  $J_1$  and  $J_2$  are the constants of the exchange antiferromagnetic interaction of the first ( $J_1 = -1$ ) and second ( $J_2 = -1$ ) nearest neighbors,  $S_{i,j,l} = \pm 1$  is the Ising spin,  $h$  is the magnitude of the magnetic field (the magnitude of the magnetic field is given in units of  $|J_1|$ ).

Calculations were carried out for systems with periodic boundary conditions and linear dimensions  $2 \times L \times L \times L \times L = 12 \div 60$ , where  $L$  – grating size, The magnitude of the values of the external

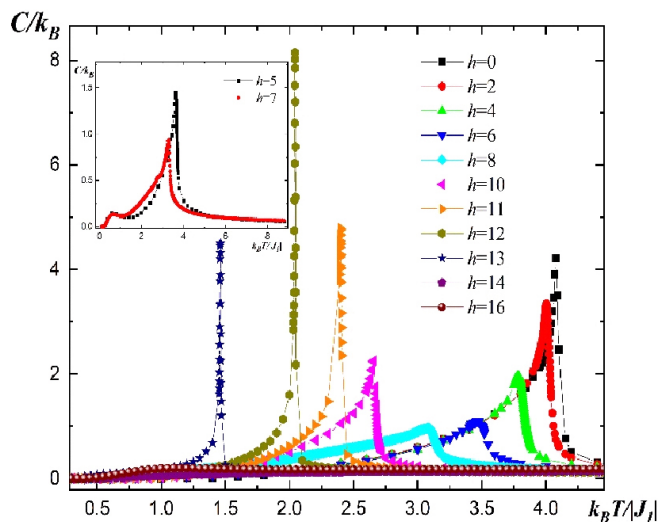


Figure 1. Dependence of heat capacity  $C/k_B$  on temperature  $k_B T/|J_1|$ .

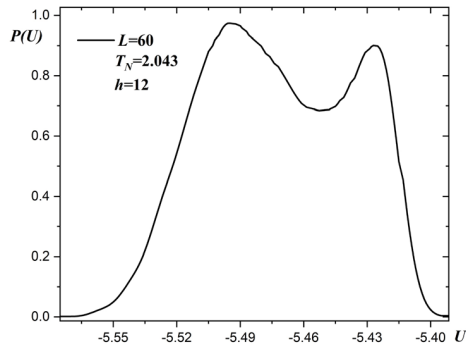


Figure 2. Histogram of energy distribution at  $h = 12.0$ .

magnetic field varied in the range  $0.0 \leq h \leq 18.0$ . The histogram method and the Binder cumulant method were used to analyze the nature and nature of the phase transition [8, 9].

Figure 1 shows that with an increase in the values of  $h$ , there is a shift in the heat capacity maxima towards lower temperatures. The shift of the heat capacity maxima towards lower temperatures is due to the competition between the internal spin (molecular) field, which builds the antiferromagnetic ordering, and the external magnetic field, which in turn builds the ordering in the direction of the field. For some fields in the region of low temperatures, small second maxima are observed. Note that the double peaks are associated with an intermediate, partially disordered antiferromagnetic phase. At magnetic field values of  $11.0 \leq h \leq 13.0$ , sharper peaks are observed in the critical region. Sharper pico is usually characteristic of AF of the first kind.

Figure 2 shows that the energy distribution histogram for systems with linear size  $L = 60$  at  $h = 12.0$  has two maxima. This indicates that the system has a PT of the first kind. The graph is plotted at the critical temperature  $T_N = 2.043$ . Distribution probability histograms were constructed for all field values in the range  $0.0 \leq h \leq 18.0$ . near critical temperatures.

The antiferromagnetic Ising model on a body-centered cubic lattice with competition of exchange spin interactions in magnetic fields is studied on the basis of the replica algorithm of the MC method. The range of magnetic field values  $0.0 \leq h \leq 18.0$  is considered. The results of our studies show that, in the magnetic field range  $0.0 \leq h \leq 10.0$ , a PT of the second kind occurs, and in the range  $11.0 \leq h \leq 13.0$ , a PT of the first kind occurs. A further increase in the value of the magnetic field suppresses the phase transition.

*The reported study was funded by RFBR according to the research project № 20-32-90079 also the work was supported by a grant from the Foundation for the Development of Theoretical Physics and Mathematics “BASIS”.*

1. A.Z. Patashinsky, V.L. Pokrovsky, Fluctuation theory of phase transitions. Science, M. (1982).
2. Sh. Ma, Modern theory of critical phenomena. Mir M. (1980).
3. A.K. Murtazaev, M.K. Ramazanov, F.A. Kassan-Ogly, D.R. Kurbanov, JETP, **147**, 1 (2015).
4. F.A. Kassan-Ogly, A.K. Murtazaev, A.K. Zhuravlev, M.K. Ramazanov, A.I. Proshkin, J. Mag. Mag. Mater., **384**, 247 (2015).
5. A.K. Murtazaev, M.K. Ramazanov, JETP Lett., **101** (2015).
6. A.K. Murtazaev, M.K. Ramazanov, M.K. Badiev, JETP., **142**, 2 (2012).
7. A.K. Murtazaev, M.K. Ramazanov, M.K. Badiev, Physica B: Condensed Matter, **476**, 1 (2015).
8. A.K. Murtazaev, M.K. Ramazanov, K.Sh. Murtazaev, M.A. Magomedov, M.K. Badiev, PSS, **62**, 2 (2020).
9. K.Z. Binder, Phys., **43**, 119 (1981).

## MAGNETIC GRÜNEISEN PARAMETER OF THE 1D DILUTE ISING MODEL

*A.V. Shadrin\**, *Y.D. Panov*

Institute of Natural Sciences and Mathematics, Ural Federal University, Ekaterinburg, Russia

\*E-mail: [shadrin.anton@urfu.ru](mailto:shadrin.anton@urfu.ru)

The dilute Ising model is one of the basic models in the theory of magnetic systems with quenched or annealed disorder [1]. Despite the absence of ordering at finite temperatures, one-dimensional spin systems exhibit a number of interesting phenomena such as magnetization plateaus, pseudophases, and pseudo-transitions. Previously, we considered the features of local distributions in our model [2] and we showed the behavior of the system in a magnetic field [3]. In this work we concentrate on a magnetic Grüneisen parameter  $\Gamma_{\text{mag}}$ .

We use the  $S = 1$  pseudospin formalism to describe our system. For a given lattice site, the states with the pseudospin projections  $S_z = \pm 1$  correspond to the two magnetic states with the conventional spin projections  $S_z = \pm 1/2$ . The state with  $S_z = 0$  corresponds to charged nonmagnetic state. The Hamiltonian of the system is

$$H = -J \sum_i S_{z,i} S_{z,i+1} + V \sum_i P_{0,i} P_{0,i+1} - h \sum_i S_{z,i} - \mu \sum_i P_{0,i} \quad (1)$$

where  $S_{z,i}$  is a  $z$ -projection of the on-site pseudospin operator,  $P_{0,i} = 1 - S_{z,i}^2$  is the projection operator on  $S_z = 0$  state,  $J$  is the exchange constant,  $V$  is the intersite density-density interaction,  $h$  is the external magnetic field,  $\mu$  is the chemical potential.

We use the transfer-matrix method applied to the Hamiltonian (1) to explore the ground state and the evolution of our system with the temperature. We get the dependences of thermodynamic quantities on temperature and concentration of impurities, which allow us to calculate the magnetic Grüneisen parameter  $\Gamma_{\text{mag}}$ . We explore the ground state diagram of the system in the external magnetic field and the magnetic entropy change caused by the frustration in the ground state. We discuss peculiarities of behavior of our system in ferromagnetic and antiferromagnetic cases and show how hidden frustration affects on  $\Gamma_{\text{mag}}$ .

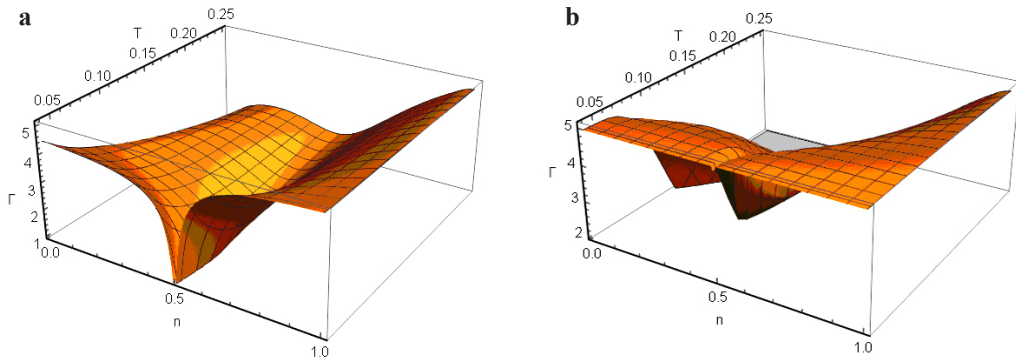


Figure 1. Magnetic Grüneisen parameter **a** for  $J = 0.5$  V,  $h = 0.2$  V, **b** for  $J = -0.5$  V,  $h = 0.2$  V.

1. S. Katsura, B. Tsujiyama, Ferro- and Antiferromagnetism of Dilute Ising Model, in: C. Domb (Ed.), Proceedings of the Conference on Phenomena in the Neighborhood of Critical Points, National Bureau of Standards, Washington, D.C., pp. 219–224 (1965).
2. Y.D. Panov, Local distributions of the 1D dilute Ising model. Journal of Magnetism and Magnetic Materials, **514**, 167224 (2020).
3. A.V. Shadrin, Y.D. Panov, Thermodynamic features of the 1D dilute Ising model in the external magnetic field, Journal of Magnetism and Magnetic Materials, **546**, 168804 (2022).

**SPERIMAGNETIC PHASE TRANSITIONS IN GdFeCo AMORPHOUS ALLOYS: H-T PHASE DIAGRAMS**

*S.V. Solov'yov*

Moscow Institute of Physics and Technology, Dolgoprudnyj, Moscow oblast, Russia  
 E-mail: [solovyov.sv@mipt.ru](mailto:solovyov.sv@mipt.ru)

An emergence of ultrafast magnetization reversal phenomena had initiated a wave of intensive fundamental and applied studies of underlying physics and materials, which could be promising for magnetic recording applications. One of the first materials which has shown an ultrafast switching by laser pulses was a quite well-known “rare earth”-“transition metal” (RE-TM) type ferrimagnetic amorphous alloy GdFeCo [1], which magnetic properties can be widely tuned due to a variety of stoichiometric compositions. Like other amorphous compounds, these alloys are characterized by the absence of long-range order of atomic structure, which turns out into microscopic stochasticity of magnetic properties causing the sperimagnetic magnetic structure. Such ferrimagnetic alloys were studied and used for the magneto-optical recording technology and now they are perspective not only for ultrafast switching applications, but also for creating spintronic devices, which is caused by high resonant frequencies in comparison to resonant frequencies of transition metal films and high velocity of domain wall motion induced by spin-polarized current [2].

In our work we describe a body of amorphous RE-TM type ferrimagnet as a grid of  $N$  interacting particles of quite small volume  $V_0$ . We suggest that magnetic properties of particles inside their volume are uniform. Particles are composed from RE and TM ions with concentrations  $n_{RE}$  and  $n_{TM}$ , which depend on the stoichiometric coefficient  $x$  of the formula  $Gd_x(FeCo)_{1-x}$ . Exchange interactions in RE-TM type ferrimagnets obey the interaction hierarchy, which could be described as an inequality of exchange integrals of d- and f-sublattices:  $J_{d-d} > J_{f-d} > J_{f-f}$ . In our work we take into account only d-d and f-d exchange interactions, and the d-d exchange is ferrimagnetic, and the f-d exchange is antiferromagnetic, which in some circumstances leads to a presence of compensa-

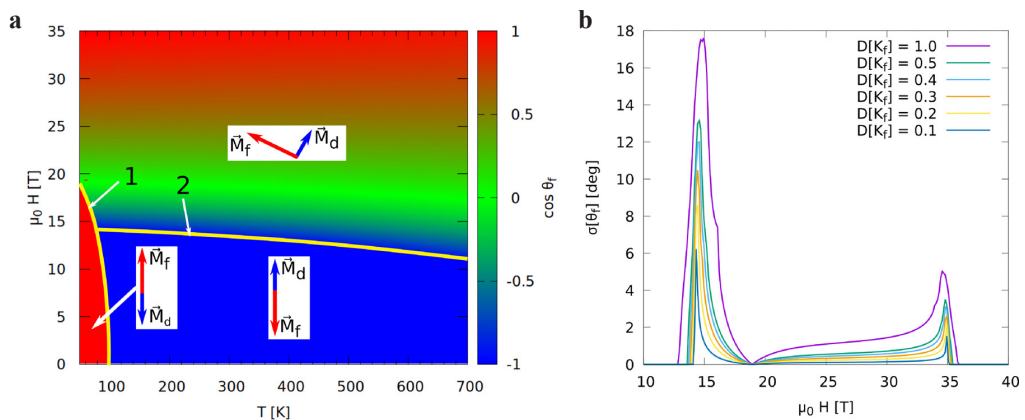


Figure 1. **a**  $H$ - $T$  phase diagram of magnetic states described as a cosine of equilibrium value of  $\theta_f$  for the composition  $x = 0.24$ . Insets show relative orientation of f- and d-sublattices, when the magnetic field is top oriented. **b** Dependencies of standard deviation for the angle  $\theta_f$  on the magnetic field for different variance of the uniaxial anisotropy constant  $K_f$ .

tion point and some peculiarities of magnetic phase transitions [3]. One of the features of GdFeCo and other amorphous ferrimagnets of RE-TM type films is the presence of perpendicular magnetic anisotropy which can be described within the framework stochastic anisotropy model [4]. The system of interacting ferrimagnet particles can be described with the use of the Hamiltonian, which includes the d-d and f-d exchange Heisenberg-like interactions, stochastic uniaxial magnetic anisotropy for the f-sublattice, and the Zeeman interaction of f- and d-sublattices with the external magnetic field.

For the purpose of simplicity we consider a case, when the external magnetic field and the axes of magnetic anisotropy within the particles are align in parallel with the  $Oz$  axis, and the magnetic moments of f- and d-sublattices are oriented in same plane with the  $Oz$  axis. In this case we can describe magnetic states of every particle using only two polar angles  $\theta_d$  and  $\theta_f$ . Stochasticity of magnetic properties is described by random values of magnetic anisotropy constants for every particle. The description of thermal properties is done by the use of the Gibbs distribution function and the molecular field theory for d-sublattice. Because in this approach the magnetic moments of the d-sublattice are connected through the molecular field the Hamiltonian of the system can be presented as a sum of single-particle Hamiltonians, and the integral of distribution function becomes a product of integrals of only two variables  $\theta_d$  and  $\theta_f$  for every particle.

The suggested model allows to describe the magnetic phases and phase transitions in amorphous ferrimagnet in external magnetic field for different temperatures and RE ions concentrations. We calculated  $H$ - $T$  phase diagrams for a variety of compositions from  $x = 0.20$  to  $x = 0.30$ . The diagram for the composition with  $x = 0.24$ , which is plotted in Fig. 1a, where two collinear and one tilted phases are presented by a cosine of  $\theta_f$ . Phases are divided by critical lines 1 and 2, which correspond to a first and a second order phase transitions. In the intersection of critical lines there is a tricritical point for this composition. If we take into account random uniaxial anisotropy constant for f-sublattice, random deviations from the equilibrium direction of magnetization take place and form sperimagnetic structure, which can be described by standard deviation of angles  $\theta_f$  or  $\theta_d$ . We calculated standard deviation of the angle  $\theta_f$  for the composition  $x = 0.24$  and temperature  $T = 200$  K, which is plotted in Fig. 1b. It is shown, that the most deviation takes place close to the critical lines and the sperimagnetic structure almost completely exists within the tilted phase borders.

Investigation of magnetic phases and peculiarities of phase transitions in GdFeCo alloys, especially in the vicinity of the compensations point, are important for possible applications in magnetic recording and spintronics, and for development of theoretical and experimental understanding of these materials. The presented model allows to describe equilibrium magnetic states for uniform and non-uniform stochastic magnetic anisotropy, which in the last case leads to the emergence of sperimagnetic structure, and we shown, that the sperimagnetic structure is almost completely limited to the tilted phase borders. The most deviation of magnetization from the equilibrium state takes place close to the critical lines of phase transitions.

1. C.D. Stanciu, F. Hansteen, A.V. Kimel, A. Kirilyuk, A. Tsukamoto, A. Itoh, and Th. Rasing, Phys. Rev. Lett., **99**, 047601 (2007).
2. V.V. Yurlov, K.A. Zvezdin, P.N. Skirdkov, A.K. Zvezdin, Phys. Rev. B, **103**, 134442 (2021).
3. M.D. Davydova, K.A. Zvezdin, J. Becker, A.V. Kimel, and A.K. Zvezdin, Phys. Rev. B, **100** (6), 064409 (2019).
4. G.V. Sayko, S.N. Utochkin, A.K. Zvezdin, JMMM, **113**, 1-3, 194–200 (1992).

## HEAT CAPACITY AND PHASE TRANSITION OF DIPOLE SUPERSPIN ICE ON A TRIMERIZED TRIANGULAR LATTICE

*V.S. Strongin*<sup>1,2\*</sup>, *M.A. Chesnokov*<sup>1</sup>, *I.N. Nalivaiko*<sup>1</sup>, *K.S. Soldatov*<sup>1,2</sup>, *I.A. Titovets*<sup>1</sup>, *K.V. Nefedev*<sup>1,2</sup>

<sup>1</sup>Far Eastern Federal University, Vladivostok, Russky Island, Russian Federation

<sup>2</sup>Institute of Applied Mathematics, Far Eastern Branch, Russian Academy of Science, Vladivostok, Russian Federation

\*E-mail: [strongin.vs@dvfu.ru](mailto:strongin.vs@dvfu.ru)

Artificial spin ice is a nanomagnetic, multiferroic, artificial material consisting of nanoparticles of elongated shape. The magnetic moment of a particle consists of many spins, therefore it is called a superspin or macrosin. The behavior of the magnetic moment of nanoparticles makes it possible to use the Ising model, since there are only two possible mutually exclusive orientations for it – “up” or “down”. Initially, artificial spin ice was understood as two-dimensional artificial analogues of spin ice on a pyrochlore lattice. Currently, research on artificial spin ice is relevant. Thermodynamic properties of systems are investigated. Theoretical work is usually aimed at confirming experimental observations. However, the most fundamental issue is the development of algorithms that could allow calculating a complete group of events based on a sample from the state space. Currently, there are no theories and, consequently, technical, software capabilities for accurate calculation of the statistical sum of a large number (>40) of interacting particles of a fully connected model. Therefore, interest in the topic of artificial spin systems is constantly growing.

The paper will investigate the properties of a trimerized triangular lattice which combines elements of two systems – an artificial kagome lattice and triangular spin ice. The nanomagnetic vertices (or trimmers) in it are located periodically at an angle of 60°. The resulting array is shown in Fig. 1.

The thermodynamic properties will be strongly influenced by the lattice parameters  $a$  and  $b$  (Fig. 2) since the physical properties of the system directly depend on them. The smaller the  $b$ , the closer the trimmers are to each other, and the greater the competitive interaction between the dipoles in the system. From certain values of  $b$  competitive interactions reduce to zero, and the system becomes an array of subsystems [1].

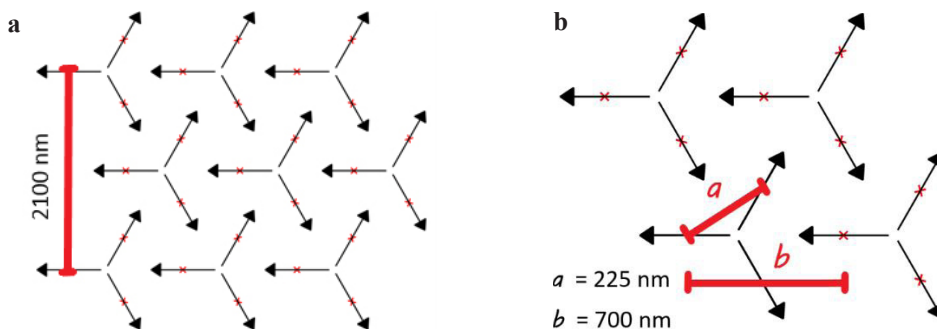


Figure 1. **a** Trimerized triangular lattice. **b** Lattice parameters  $a$  and  $b$  [1].

The energy of the dipole-dipole interaction of a system of dipoles on a trimerized lattice is calculated using the formula (2.1):

$$E_{ij} = \frac{(\vec{m}_i \vec{m}_j)}{|\vec{r}_{ij}|^3} - 3 \frac{(\vec{m}_i \vec{r}_{ij})(\vec{m}_j \vec{r}_{ij})}{|\vec{r}_{ij}|^5}, \quad (1)$$

where  $i, j$  – the numbers of the interacting dipoles,  $\mathbf{r}$  is the vector between the centers of the magnetic moments of the interacting dipoles,  $\mathbf{m}$  is the value of the magnetic moment vector.

To determine the thermodynamic properties of the system under study we used The Metropolis method. The main idea of this method is the equal formation of a sample of the state space with a given probability of the distribution of states. At each step of the sampling process, a configuration with a given probability is accepted (or rejected):

$$P(E_i \rightarrow E_j) = \min\left(\frac{P(E_j)}{P(E_i)}, 1\right). \quad (2)$$

When numerically calculating the temperature behavior of the system, the probability of the configuration energy is determined according to the canonical Gibbs distribution:

$$P(E_i) = \min\left(\frac{\exp(-E_i/k_B T)}{Z}\right). \quad (3)$$

Combine Eqs. (1) and (2), we get

$$P(E_i \rightarrow E_j) = \min\left(\frac{\exp(-E_j/k_B T)}{\exp(-E_i/k_B T)}, 1\right) = \min\left(\exp\left[-\frac{E_j - E_i}{k_B T}\right], 1\right) = \min\left(\exp\left[-\frac{\Delta E}{k_B T}\right], 1\right), \quad (4)$$

where  $\Delta E$  is the change in the energy level of the system as a result of configuration change,  $T$  is the absolute temperature. In the process of sampling, a certain characteristic (order parameter or spin excess) is determined for each selected configuration. Based on the obtained characteristics, the standard deviation and the mathematical mean are determined, based on which the thermodynamic quantities are calculated [2].

It is expected that a system with relatively low values of parameter  $b$  will be able to phase transition. It is necessary to determine from which  $b$  and by which dynamics the system loses this opportunity as  $b$  increases. To do this, the heat capacity of the system will be determined, so it can be used to judge the presence of a phase transition. The heat capacity directly depends on the energy of the system obtained by the Metropolis method.

The most important task in the study of artificial spin systems is to find the ground state of the system: a configuration in which the total energy of the system is minimal. It is necessary to try to find the minimum energy by the Metropolis method for various  $b$ , compare with the already available results and use other methods (e.g. a greedy algorithm) to search for lower-energy configurations or an exact solution by parallel full search, if possible.

1. K. Hofhuis et al., Geometrical frustration and competing orders in the dipolar trimerized triangular lattice, *Physical Review B*, **104**, no. 1, 014409 (2021).
2. Ю.А. Шевченко, Термодинамические свойства фрустрированных спиновых систем (2017).



## SOLID-STATE SYNTHESIS AND SPECIFIC HEAT OF STRONTIUM SAMARATE $\text{SrSm}_2\text{O}_4$

*Y. Tian\**, A.G. Kiiamov, R.G. Batulin, M.A. Cherosov, I.F. Gilmudinov, A.G. Ivanova, R.V. Yusupov, D.A. Tayurskii

Institute of Physics, Kazan Federal University, Kazan, Russia

\*E-mail: [Rockland1922@hotmail.com](mailto:Rockland1922@hotmail.com)

Here we present the investigation of the specific heat of strontium samarate  $\text{SrSm}_2\text{O}_4$ . Polycrystalline samples of  $\text{SrSm}_2\text{O}_4$  were prepared by the solid-state synthesis technique, which includes the thermal treatment of equimolar mixture of strontium carbonate and samarium oxide. The thoroughly ground and mixed stoichiometric composition was initially sintered at 1100 °C for 10 hours. The synthesized powder was examined with powder X-ray diffraction (Bruker D8 ADVANCE,  $\text{Cu K}\alpha$ ). The powder X-ray diffraction pattern of  $\text{SrSm}_2\text{O}_4$  is presented in Fig. 1. The data were analyzed by a standard Rietveld refinement using the FullProf software [1]. Since all diffraction peaks were well described within the known structure model of  $\text{SrSm}_2\text{O}_4$  [2]. The refinement does not fully describe the observed peak intensities. It can result from a combined effect of strain of the sample when crushed into powder and texture. Thus, we conclude that the composition of our  $\text{SrSm}_2\text{O}_4$  samples exhibits only small deviations from the stoichiometry and no foreign phases.

Specific heat measurements are conducted at a commercial PPMS from Quantum Design (USA). At the low temperatures the temperature dependence of specific heat does not show the cubic dependence on temperature, that indicates on the presence of magnetic correlations between magnetic ions and probably on magnetic order.

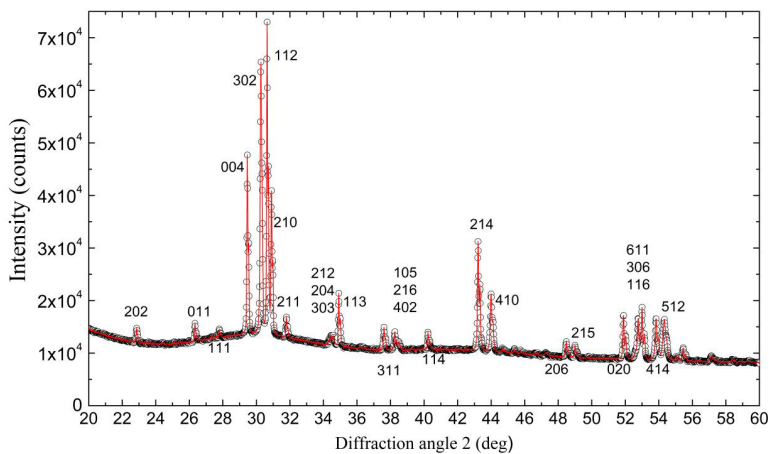


Figure 1. Powder X-ray diffraction pattern of  $\text{SrSm}_2\text{O}_4$ .

*The reported study was funded by Priority-2030 Program. The specific heat and X-ray diffraction measurements were carried out utilizing equipment of the PCR Federal Center of Shared Facilities (Kazan Federal University).*

1. J. Rodriguez-Carvajal, Phys. B Condens. Matter, **192**, 55–56 (1993).
2. S. Arul Antony, Materials Letters, **51**, 414–419 (2001).

## GROUND AND LOW-ENERGY STATES OF DIPOLE SUPERSPIN ICE ON A TRIMERIZED TRIANGULAR LATTICE

*I.A. Titovets*<sup>1\*</sup>, *M.A. Chesnokov*<sup>1</sup>, *I.N. Nalivaiko*<sup>1</sup>, *V.S. Strongin*<sup>1,2</sup>, *K.S. Soldatov*<sup>1,2</sup>,  
*K.V. Nefedev*<sup>1,2</sup>

<sup>1</sup>Far Eastern Federal University, Vladivostok, Russky Island, Russian Federation

<sup>2</sup>Institute of Applied Mathematics, Far Eastern Branch, Russian Academy of Science, Vladivostok, Russian Federation

\*E-mail: [titovetc.iaa@dvfu.ru](mailto:titovetc.iaa@dvfu.ru)

Artificial spin ice is a nanomagnet, multiferroic, an artificial nanomaterial consisting of nanoparticles of elongated shape. The magnetic moment of a particle consists of many atom spins; therefore, it is called a superspin or macrospin. The behavior of the magnetic moment of a nanoparticle makes it possible to use the Ising model, since due to the shape anisotropy energy, there are only two possible mutually exclusive moment orientations – “up” or “down”. Initially, artificial spin ice was understood as two-dimensional artificial analogues of spin ice on a pyrochlore lattice. Currently, research on artificial spin ice is relevant. The thermodynamic properties of the systems are investigated. Theoretical work is usually aimed at confirming experimental observations. Important questions are the search for the ground state of the system, low-energy states – configurations with the lowest energy of interaction in the system of dipoles, and the multiplicity of their degeneracy. The question of calculating the probability density of all possible states (configurations) has great fundamental and theoretical significance due to the fact, that it also allows to obtain information about the degree of frustration in the system. Currently, there are no theories and, consequently, technical, software capabilities for accurate calculation of the statistical sum of a large number (>40) of interacting particles of a fully connected model. Therefore, interest in the topic of artificial spin systems is constantly growing.

The paper will investigate the properties of a trimerized triangular lattice which combines elements of two systems – an artificial kagome lattice and triangular spin ice. The nanomagnetic vertices (or trimmers) in it are located periodically at an angle of 60°. The resulting array is shown in Fig. 1.

The thermodynamic properties will be strongly influenced by the lattice parameters  $a$  and  $b$  (Fig. 2) since the physical properties of the system directly depend on them. The smaller the  $b$ , the closer the trimmers are to each other, and the greater the competitive interaction between the

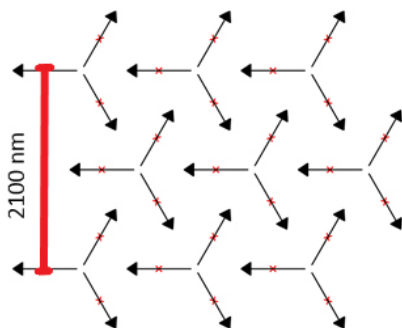


Figure 1. Trimerized triangular lattice.

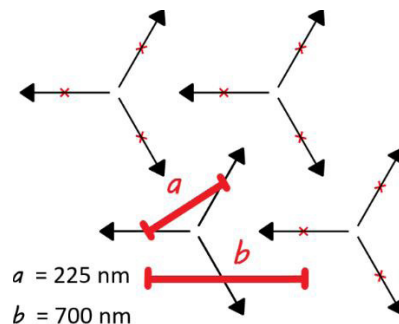


Figure 2. Lattice parameters  $a$  and  $b$  [1].

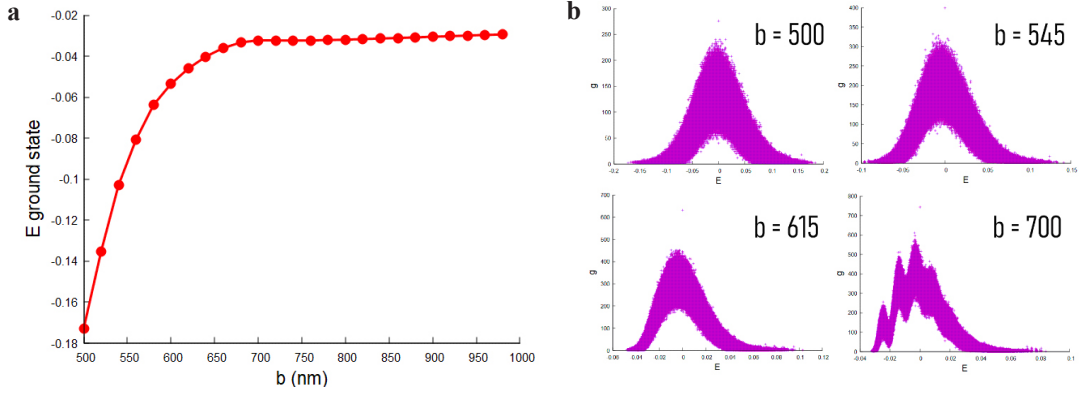


Figure 3. **a** Dynamics of change in the energy of the ground states depending on  $b$ . **b** Density of states for various  $b$ .

dipoles in the system. From certain values of  $b$  competitive interactions reduce to zero, and the system becomes an array of subsystems [1].

The energy of the dipole-dipole interaction of dipoles  $i$  and  $j$  on a trimerized lattice is calculated using the formula (2.1):

$$E_{ij} = \frac{(\vec{m}_i \vec{m}_j)}{|\vec{r}_{ij}|^3} - 3 \frac{(\vec{m}_i \vec{r}_{ij})(\vec{m}_j \vec{r}_{ij})}{|\vec{r}_{ij}|^5}, \quad (2.1)$$

where  $\vec{r}_{ij}$  is the vector between the centers of the magnetic moments of the interacting dipoles,  $\vec{m}_i$  is the value of the magnetic moment vector.

The brute force method was used for the calculations which is the only way to get accurate results, since it considers each of the possible lattice configurations. However, this method suffers from an exponential increase in computational time as  $N$  increases, and is only efficient in small systems ( $N < 40$ ). It can be used to obtain accurate results and then scale them up for comparison with results obtained with approximate methods for larger systems.

It was expected that a system with relatively low values of the parameter  $b$  would be able to phase transition. The larger the  $b$  parameter, the farther the trimers are from each other, which in turn affects the interaction energy of many parts. The ground state was searched and the density of states was calculated by using brute force method for a small lattice.

Figure 3 shows the dynamics of changes in the energy of the ground state for of the same sized and shaped lattices with different parameters  $b$ . As can be seen, from certain values of  $b$ , the system is divided into subsystems, the total interaction energy of which tends to zero. In such states, the system is not capable to phase transition.

Also, the density of states was calculated for lattices of the same size and shape with different parameters  $b$ . The same values of  $b$  were used as in Article G.P16. The change in the shape of the graphs as  $b$  increases not only shows the change in the minimum energy, but also indicates a disproportionate distribution of states with different  $b$ . This means that the systems have different frustration rates, which is consistent with the results from Article G.P16.

1. K. Hofhuis et al., Geometrical frustration and competing orders in the dipolar trimerized triangular lattice, Physical Review B, **104**, no. 1, 014409 (2021).

## EXACT SOLUTION EDVARD-SANDERSON SPIN GLASS FOR NEAREST NEIGHBORS

*V. Trukhin*<sup>1\*</sup>, *K. Nefedev*<sup>1,2</sup>

<sup>1</sup>Far Eastern Federal University, Vladivostok, Russia

<sup>2</sup>Institute of Applied Mathematics, Far Eastern Branch, Russian Academy of Science, Vladivostok, Russian Federation

\*E-mail: [trukhin.vo@dvfu.ru](mailto:trukhin.vo@dvfu.ru)

Despite the fact that the study of spin ice began in the middle of the last century, active research in this area continues [1, 2]. One of the main problems is the lack of methods for calculating the partition function  $Z$  for a relatively large number of spins. The exact solution for at least a small number of spins makes it possible to evaluate the correctness of probabilistic solution methods (such as Metropolis [3]) and can be used in joint methods with them. The main problem in finding an exact solution is the exponential growth in the number of states depending on the size of the system. However, the possibility of a significant reduction in the number of computational cycles by optimizing the enumeration algorithm is noted.

Let's consider system of three spins. For this system, we get the solution of Ising's formula for finding the partition function of a one-dimensional chain is as follows:

$$e^{3\beta-3\beta h} + 3e^{\beta(-h)-\beta} + 3e^{\beta h-\beta} + e^{3\beta+3\beta h} . \quad (1)$$

Adding the second chain of three spins, so as to obtain a flat 2 by 3 lattices, we obtain:

$$\begin{aligned} & e^{3\beta-3h\beta} (e^{3\beta-3h\beta+3\beta} + e^{-\beta-h\beta+\beta} + e^{-\beta-h\beta+\beta} + e^{-\beta-h\beta+\beta} + e^{-\beta+h\beta-\beta} + e^{-\beta+h\beta-\beta} + e^{-\beta+h\beta-\beta} + e^{3\beta+3h\beta-3\beta}) + \\ & e^{-\beta-h\beta} (e^{3\beta-3h\beta+\beta} + e^{-\beta-h\beta+3\beta} + e^{-\beta-h\beta-\beta} + e^{-\beta-h\beta-\beta} + e^{-\beta+h\beta+\beta} + e^{-\beta+h\beta+\beta} + e^{-\beta+h\beta-3\beta} + e^{3\beta+3h\beta-\beta}) + \\ & e^{-\beta-h\beta} (e^{3\beta-3h\beta+\beta} + e^{-\beta-h\beta-\beta} + e^{-\beta-h\beta+3\beta} + e^{-\beta-h\beta-\beta} + e^{-\beta+h\beta+\beta} + e^{-\beta+h\beta-3\beta} + e^{-\beta+h\beta+\beta} + e^{3\beta+3h\beta-\beta}) + \\ & e^{-\beta-h\beta} (e^{3\beta-3h\beta+\beta} + e^{-\beta-h\beta-\beta} + e^{-\beta-h\beta-\beta} + e^{-\beta-h\beta+3\beta} + e^{-\beta+h\beta-3\beta} + e^{-\beta+h\beta+\beta} + e^{-\beta+h\beta+\beta} + e^{3\beta+3h\beta-\beta}) + \\ & e^{-\beta+h\beta} (e^{3\beta-3h\beta-\beta} + e^{-\beta-h\beta+\beta} + e^{-\beta-h\beta+\beta} + e^{-\beta-h\beta-3\beta} + e^{-\beta+h\beta+3\beta} + e^{-\beta+h\beta-\beta} + e^{-\beta+h\beta-\beta} + e^{3\beta+3h\beta+\beta}) + \\ & e^{-\beta+h\beta} (e^{3\beta-3h\beta-\beta} + e^{-\beta-h\beta-3\beta} + e^{-\beta-h\beta+\beta} + e^{-\beta-h\beta+\beta} + e^{-\beta+h\beta-\beta} + e^{-\beta+h\beta-3\beta} + e^{-\beta+h\beta+\beta} + e^{3\beta+3h\beta+\beta}) + \\ & e^{3\beta+3h\beta} (e^{3\beta-3h\beta-3\beta} + e^{-\beta-h\beta-\beta} + e^{-\beta-h\beta-\beta} + e^{-\beta-h\beta-\beta} + e^{-\beta+h\beta+\beta} + e^{-\beta+h\beta+\beta} + e^{-\beta+h\beta+\beta} + e^{3\beta+3h\beta+3\beta}) . \quad (2) \end{aligned}$$

This approach is applicable to lattices of various shapes. However, let's look at the method itself using the example of a rectangular lattice.

At the beginning, all configurations of the chain of spins of two types are bit-encoded: the left and right parts. Then the energies within the systems are calculated for each elementary chain. The energy of the two combined chains will be as follows:

$$E_{\text{sum}} = E_{\text{left}} + E_{\text{right}} + E_{\text{unif}} , \quad (3)$$

where  $E_{\text{left}}$ ,  $E_{\text{right}}$  are the energies of the left and right chains, respectively,  $E_{\text{unif}}$  is the unification energy for a given configuration of the left and right chains:

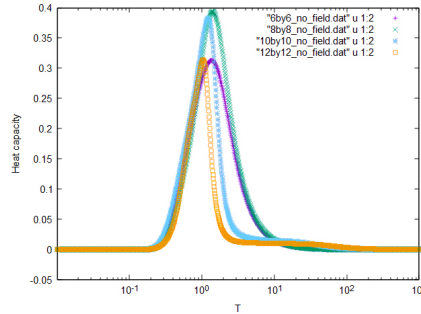


Figure 1. Heat capacity of four spin ice lattices: 6 by 6, 8 by 8, 10 by 10 and 12 by 12.

$$E_{\text{unif}} = -\sum_i^n J_{i,j} S_{ik} S_{il} \quad (4)$$

where  $S_i$  – the value of the  $i$ -th spin variable of the left lattice of  $k$ -th configuration of boundary,  $S_j$  – the value of the  $j$ -th spin variable of right lattice of  $l$ -th configuration,  $n$  – number of spins in a one-dimensional chain.  $J_{ij}$  – exchange integral between the  $i$ -th spins of the  $j$ -th column.

The method was applied to calculate the Evards-Andesen spin ice lattices of various sizes (Fig. 1). The exchange integrals were randomized between 1 and  $-1$ , but their sum remained equal to 0. This exact method of calculation gives a significant gain in time for calculating the partition function by exhaustive search and can be effectively used in hybrid methods for finding the heat capacity of flat lattices of various shapes [4, 5].

*The results of studies related to the development of a theoretical model, samples and physical experiments were obtained within the framework of the state task of the Ministry of Education and Science of Russia (No. 0657-2020-0005). The results of research related to the development of algorithms, programming, coding and implementation of a parallel calculation scheme were obtained at the expense of the grant of the President of the Russian Federation for state support of the leading scientific schools of the Russian Federation (NSh-2559.2022.1.2).*

1. P. Schiffer, C. Nisoli, Artificial spin ice: Paths forward, Applied Physics Letters, **118**, no. 11, 110501 (2021).
2. F. Caravelli, C. Nisoli, Logical gates embedding in artificial spin ice, New Journal of Physics, **22**, no. 10, 103052 (2020).
3. N. Metropolis, S. Ulam, The monte carlo method, Journal of the American statistical association, **44**, no. 247, 335–341 (1949).
4. A.G. Makarov, On the numerical calculation of frustrations in the ising model, JETP Letters, **110**, no. 10, 702–706 (2019).
5. K. Makarova et al., Low-energy states, ground states, and variable frustrations of the finite-size dipolar Cairo lattices, Physical Review E, **103**, no. 4, 042129 (2021).

**STUDY OF A COMPLEX INCOMMENSURABLE  
MAGNETIC STRUCTURE  $\text{Ho}_3\text{Co}$**

*A.A. Vaulin*<sup>1\*</sup>, *A.F. Gubkin*<sup>1,2</sup>

<sup>1</sup>M.N. Mikheev Institute of Metal Physics, UB RAS, Ekaterinburg, Russia

<sup>2</sup>Institute of Natural Sciences, Ural Federal University, Ekaterinburg, Russia

\*E-mail: [artavaulin@gmail.com](mailto:artavaulin@gmail.com)

The binary rare-earth intermetallic compound  $\text{R}_3\text{T}$  (R – rare-earth metal, T – 3d transition metal) crystallize in a low symmetry orthorhombic structure of the  $\text{Fe}_3\text{C}$  type with the space group  $Pnma$ . In this structure, T atoms occupy 4c Wyckoff site located in the centers of the trigonal prisms which are formed by Ho atoms occupying 4c and 8d Wyckoff sites. Co atoms do not possess a magnetic moment in the  $\text{R}_3\text{T}$  compounds. The competition between RKKY-type exchange interactions and crystal electric field gives rise to complex magnetic structures and to unusual magnetization processes in  $\text{R}_3\text{T}$ . Among the others,  $\text{Ho}_3\text{Co}$  exhibits a complex magnetic phase diagram with two successive magnetic phase transitions at  $T_N = 22$  K and  $T_I = 9$  K [1]. The neutron powder diffraction data (NPD) previously reported for  $\text{Ho}_3\text{Co}$  [1] revealed that in the temperature range  $T_I < T < T_N$  the magnetic ordering is associated with a combination of an incommensurate and commensurate propagation vectors  $\mathbf{k}_{\text{IC}} = (0.15\ 0\ 0)$  and  $\mathbf{k}_{\text{C}} = (0\ 0\ 0)$ . The higher order harmonics of  $\mathbf{k}_{\text{IC}}$  were observed below  $T_I$ . However, the magnetic structure of this compound has not yet been fully established in detail. In this work, we used magnetic superspace groups approach [2] to solve the complex magnetic structure emerging in  $\text{Ho}_3\text{Co}$  just below the Neel temperature.

Figure 1 shows the NPDs for  $\text{Ho}_3\text{Co}$  in the paramagnetic state at  $T = 50$  K as well as in the antiferromagnetic state at  $T = 15$  K. The Rietveld refinement of the magnetic structure at  $T = 15$  K was carried out using the program JANA2006 [3]. Our analysis of the NPD pattern confirmed that the low temperature magnetic structure at  $T = 15$  K exhibits both incommensurate and commensurate components. This coexistence implies superposition of two irreducible representations (ireps) associated with the propagation vectors  $\mathbf{k}_{\text{IC}} = (\mu\ 0\ 0)$  and  $\mathbf{k}_{\text{C}} = (0\ 0\ 0)$ , respectively. All

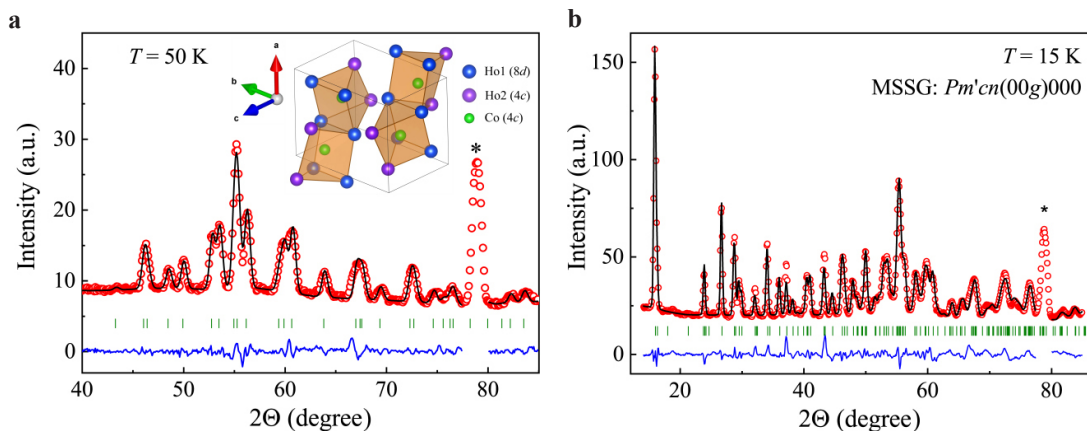


Figure 1. Neutron powder diffraction patterns for  $\text{Ho}_3\text{Co}$  measured in a paramagnetic state at  $T = 50$  K (a) and below the Neel temperature at  $T = 15$  K (b). The best fit result at  $T = 15$  K provided by a model of the magnetic superspace group  $Pm'cn(00g)000$  is shown as a solid line through the symbols.

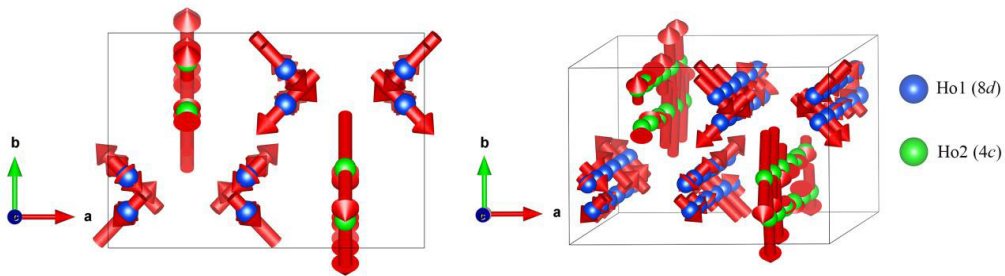


Figure 2. Visualization of the magnetic structure of the  $\text{Ho}_3\text{Co}$  compound at  $T = 15$  K. Magnetic moments of Ho atoms occupying 8d and 4c Wyckoff sites (blue and green atoms) are ordered in skew transverse waves propagating along the  $c$ -axis.

possible ireps associated with  $\mathbf{k}_C$  and  $\mathbf{k}_{IC}$  as well as isotropy subgroups arising from coupling of two primary order parameters were established by ISODISTORT [4]. In total, 64 possible intersections (isotropy subgroups) obtained from the superpositions of four  $mSM$  and eight  $mGM$  ireps have been obtained. It has been found by Rietveld refinement that magnetic superspace group  $Pm'cn(00g)000$  corresponding to the superposition of the  $mGM4-[\mathbf{k}_C]$  and  $mSM4[\mathbf{k}_C]$  ireps and order parameter direction  $(a|b,0)$  can describe the complex incommensurate antiferromagnetic structure of  $\text{Ho}_3\text{Co}$  at  $T = 15$  K (see Fig. 1b).

The schematic visualization of the constrained magnetic structure is shown in Fig. 2. In this magnetic structure, magnetic moments of Ho atoms occupying 8d and 4c Wyckoff sites form skew transverse spin waves propagating along the  $c$ -axis. Additional magnetic peaks indexed by third harmonic  $3\mathbf{k}_{IC}$  were found on the neutron diffraction pattern measured at the low temperature  $T = 1.5$  K. The odd harmonics peaks indicate squaring-up of the transverse spin wave component developing on the cooling. This process reflects a general tendency of the amplitude modulated magnetic structures to minimize their entropy on cooling by a transition towards equal momentum magnetic structure of anti-phase domains

*This work was supported by RFBR grant № 20-32-90047 and Ministry of Education and Science (themes “Flux”, № AAAA18-118020190112-8 and “Alloys”, № AAAA-A19-119070890020-3).*

1. A. Podlesnyak, A. Daoud-Aladine et al., J. Magn. Magn. Mater, **565**, 272–276 (2004).
2. J.M. Perez-Mato et al., J. Phys.: Condens. Matter, **24** (16), 163201 (2012).
3. V. Petricek et al., Z. Kristallogr. Cryst. Mater, **229**, 345 (2014).
4. H.T. Stokes, B.J. Campbell, Acta Cryst., **A73** (1) (2017).

## MAGNETIC PROPERTIES AND HYSTERESIS BEHAVIOR OF A 2D DILUTE ISING MAGNET WITH FRUSTRATION

*D.N. Yasinskaya\**, *V.A. Ulitko*, *Y.D. Panov*

Ural Federal University, Ekaterinburg, Russia

\*E-mail: [daria.iasinskaia@urfu.ru](mailto:daria.iasinskaia@urfu.ru)

Pseudospin formalism is one of the most effective approaches to study complex systems with various degrees of freedom. (Pseudo)spin models are widely used to describe many actual physical systems [1], in particular, anisotropic dilute magnets, metamagnets, binary alloys, superconductors. Various extensions of the Ising, Heisenberg, Blume-Emery-Griffiths, and Blume-Capel models are the most popular models for describing such systems. The flexibility of these models makes it possible to include various interactions, anisotropy, and fields in the Hamiltonian. The addition of competing interactions leads to frustration of the system. Frustrated systems with two or more competing interactions have a wide variety of phases with unconventional properties and complex symmetry [2]. In addition, it is possible to introduce impurities or defects into the system. This expands the possibilities of describing real physical systems that always have disorder.

We consider the Blume-Emery-Griffiths-type spin-pseudospin model with mixed spin  $S = 1/2$  and pseudospin  $S = 1$  [3]. Two pseudospin projections  $S_z = \pm 1$  are associated with two charge states, and  $S_z = 0$  is a magnetic doublet with two spin projections  $S_z = \pm 1/2$ . The Hamiltonian of the static spin-pseudospin model includes Ising spin exchange coupling ( $J$ ), external magnetic field ( $h$ ), on-site ( $\Delta$ ) and inter-site ( $V$ ) density-density correlations, which have the form of single-ion pseudospin anisotropy and Ising exchange coupling in the pseudospin formalism. The chemical potential  $\mu$  is necessary to take into account the constant charge density  $n = 1/(N \sum_i S_{iz})$ .

$$H = \Delta \sum_i S_{iz}^2 + V \sum_{\langle ij \rangle} S_{iz} S_{jz} + J \sum_{\langle ij \rangle} (1 - S_{iz}^2) S_{iz} S_{jz} (1 - S_{jz}^2) - h \sum_i S_{iz} - \mu \sum_i S_{iz} \quad (1)$$

We performed computer simulations of the spin-pseudospin model using the classical Monte Carlo method and the modified Metropolis algorithm on a 2D square lattice with periodic boundary

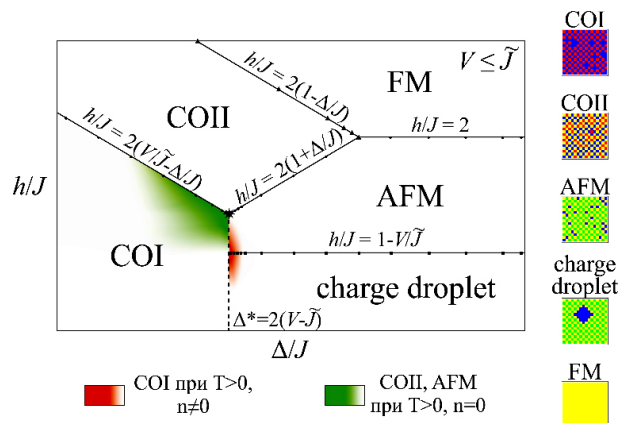


Figure 1. Ground state magnetic phase diagram. CO – charge order, AFM – antiferromagnetic, FM – ferromagnetic. Reentrant phase transitions and order-order transitions are observed near the frustration area.



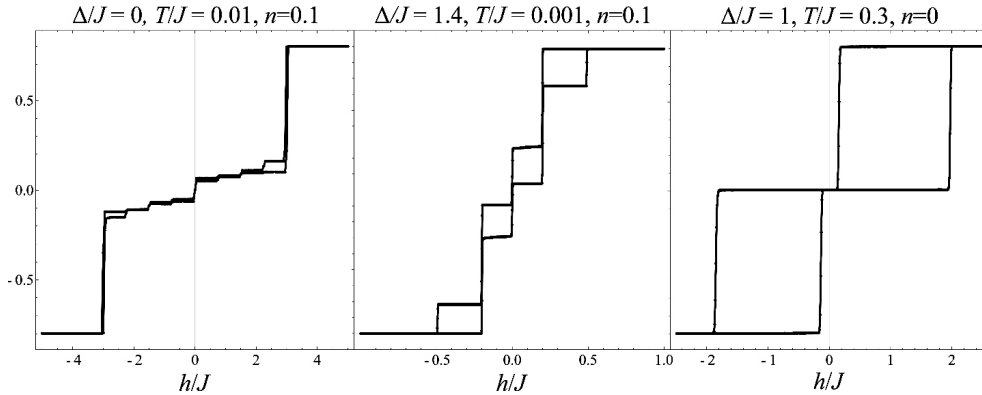


Figure 1. Ground state magnetic phase diagram. CO – charge order, AFM – antiferromagnetic, FM – ferromagnetic. Reentrant phase transitions and order-order transitions are observed near the frustration area.

conditions. Phase diagrams were constructed and critical fields of metamagnetic transitions were obtained (Fig. 1). Near the frustration area, the system in the magnetic field undergoes a series of order-order phase transitions. This effect is caused by a combination of frustration, magnetic field and impurities. Each of these factors favors different orderings, as a result, at finite temperatures, one can observe orderings that do not correspond to the energy minimum in the ground state.

The study of the magnetic hysteresis properties showed single loops in the region of AFM ordering. The effect of anisotropy, temperature, and impurities on the shape and parameters of hysteresis loops was also studied. In the case of strong spin exchange coupling ( $V \leq \tilde{J}$ ) both single and double hysteresis loops were found in the region of charge ordering. But at ( $V > \tilde{J}$ ) there are hysteresis loops with many windows (8-windowed, 6-windowed, 4-windowed, double and single loops). Some of these loops are presented in Fig. 2. In [4] it was shown that Blume-Capel model with effective spin-S might have 2S-windowed hysteresis loops, and the rising of crystal field dilution results in decreasing number of windowed hysteresis loops [5].

Thus, frustration and non-magnetic impurities strongly affect the magnetic properties of the spin-pseudospin model of a 2D dilute magnet with frustration.

*This work was supported by the Ministry of Science and Higher Education of the Russian Federation, project FEUZ-2020-0054.*

1. V.V. Hovhannisyan et al., Phys. Rev. E., **96**, 062103 (2017).
2. H.T. Diep et al. (ed.), Frustrated spin systems. World Scientific (2013).
3. Y.D. Panov et al., J. Supercond. Novel Magn., **29**, 1077–1083 (2016).
4. Ü Akıncı, Physica A., **484**, 130–138 (2017).
5. Ü Akıncı, Phys. Lett. A., **380**, 1352–1357 (2016).

Section H.  
**Magnetism of strongly correlated  
electron systems**

---

## MODELLING OF THE ELECTRONIC STRUCTURE, MAGNETIC STATE AND LATTICE STABILITY OF STRONGLY CORRELATED ELECTRON SYSTEMS

*I. Leonov*

M.N. Miheev Institute of Metal Physics, Russian Academy of Sciences, Ekaterinburg, Russia

E-mail: [ivan.v.leonov@yandex.ru](mailto:ivan.v.leonov@yandex.ru)

The electronic and magnetic phase transitions in strongly correlated electron systems have been among the main research topics of materials science and condensed matter physics over the last several decades. In such materials the complex interplay between electronic correlations and the spin, charge, orbital, and lattice degrees of freedom leads to a wealth of ordering phenomena and formation of complex quantum phases, which makes these compounds highly attractive for technological applications. In spite of intensive research over several past decades, a theoretical understanding of the electronic structure, magnetism, and phase stability of such compounds near the Mott or quantum phase transitions still remains elusive. In this talk, I will discuss an application of the novel computational scheme – DFT+dynamical mean-field theory (DFT+DMFT) to explore the electronic structure, magnetic state, and phase equilibria of correlated materials. In particular, I will discuss our recent applications of DFT+DMFT to study the Mott insulator-to-metal phase transitions under pressure in the prototypical oxide materials, such as the late transition-metal oxides, MnO, FeO, CoO, NiO [1], and Fe<sub>2</sub>O<sub>3</sub>[2], the formation of a charge- and bond-disproportionated state in perovskite oxides CaFeO<sub>3</sub> [3] and BiNiO<sub>3</sub> [4], and the electronic structure of unconventional superconductors Fe(Se,Te,S) [5] and infinite-layer RNiO<sub>2</sub> [6]. Our results demonstrate that electronic correlations are critically important to determine the electronic structure, magnetic state, and lattice stability of correlated materials, e.g., in the vicinity of the Mott or quantum phase transitions.

1. I. Leonov, Phys. Rev. B, **92**, 085142 (2015); I. Leonov, L. Pourovskii, A. Georges, I.A. Abrikosov, Phys. Rev. B, **94**, 155135 (2016); I. Leonov, A.O. Shorikov, V.I. Anisimov, I.A. Abrikosov, Phys. Rev. B, **101**, 245144 (2020); I. Leonov, S. Biermann, Phys. Rev. B, **103**, 165108 (2021); E. Koemets, I. Leonov, M. Bykov, E. Bykova, S. Chariton et al., Phys. Rev. Lett., **126**, 106001 (2021).
2. E. Greenberg, I. Leonov, S. Layek, Z. Konopkova, M.P. Pasternak et al., Phys. Rev. X **8**, 031059 (2018); I. Leonov, G. Kh. Rozenberg, I.A. Abrikosov, npj Comput. Mater., **5**, 90 (2019).
3. I. Leonov, Phys. Rev. B, **105**, 035157 (2022).
4. I. Leonov, A.S. Belozerov, S.L. Skornyakov, Phys. Rev. B, **100**, 161112(R) (2019).
5. S.L. Skornyakov, I. Leonov, Phys. Rev. B, **100**, 235123 (2019); S.L. Skornyakov, V.I. Anisimov, D. Vollhardt, I. Leonov, Phys. Rev. B, **97**, 115165 (2018); Phys. Rev. B, **96**, 035137 (2017); I. Leonov, S.L. Skornyakov, V.I. Anisimov, D. Vollhardt, Phys. Rev. Lett., **115**, 106402 (2015).
6. I. Leonov, S. L. Skornyakov, and S. Y. Savrasov, Phys. Rev. B, **101**, 241108(R) (2020); X. Wan, V. Ivanov, G. Resta, I. Leonov, and S. Y. Savrasov, Phys. Rev. B, **103**, 075123 (2021); I. Leonov, J. Alloys Comp. **883**, 160888 (2021).

**CHANGE IN ANISOTROPY OF CHARGE SUBSYSTEM  
IN LAYERED COBALTITES  $\text{LnBaCo}_2\text{O}_{5+\delta}$**

*E.V. Mostovshchikova\**, *S.V. Naumov*, *B.A. Gizhevskii*, *M.S. Udintseva*, *V.R. Galakhov*

M.N. Miheev Institute of Metal Physics, UB RAS, Ekaterinburg, Russia

\*E-mail: [mostovsikova@imp.uran.ru](mailto:mostovsikova@imp.uran.ru)

Layered cobaltites  $\text{LnBaCo}_2\text{O}_{5+\delta}$  (Ln is a rare earth ion,  $\delta$  can vary from 0 to 1) are ones of the representatives of the materials with high electronic and oxygen-ionic conductivity that makes them attractive to practical application. Besides, the layered cobaltites are interesting due to possibility to vary oxygen content in wide range from  $\delta = 0$  to 1. At that the local environment and charge state of cobalt ions changes: for  $\delta = 1$  coexisting  $\text{Co}^{3+}$  and  $\text{Co}^{4+}$  ions have octahedral coordination; for  $\delta = 0$   $\text{Co}^{3+}$  and  $\text{Co}^{2+}$  ions are in pyramidal coordination; if  $\delta = 0.5$  all cobalt ions are in trivalent state and in octahedral and pyramidal position ordered in *ab* plane. The wide range of varying oxygen content ( $0 \leq \delta \leq 1$ ) and the possibility of  $\text{Co}^{3+}$  ion to be in one of the three spin state (low-spin state,  $S = 0$ , intermediate-spin state,  $S = 1$  and high-spin state with  $S = 2$ ) make the phase diagram of the cobaltites rich. The structure of  $\text{LnBaCo}_2\text{O}_{5+\delta}$  with alternate Ln-O and Ba-O layers causes strong anisotropy of the properties of the cobaltites [1]. The evolution of this anisotropy with change of the oxygen content or of a rare earth element especially in the charge subsystem is still studied insufficiently, because it requires using single crystalline samples for investigation.

In the present work, we compare the optical properties and soft X-ray absorption spectra of  $\text{LnBaCo}_{1.95}\text{O}_{5+\delta}$  single crystals with Ln = Eu, Tb and  $\delta = 0.44, 0.2, \text{ and } 0$ . The oxygen content  $\delta = 0.44$  for this crystals with slight cobalt deficiency corresponds to absence of divalent cobalt ions, which is confirmed by soft X-ray absorption studies. The reflection spectra  $R(\lambda)$  from (001) and (120) planes were measured in near IR range, where the interaction of the light with the charge carriers dominates.

It is found that the anisotropy of the charge subsystem manifests itself in the reflection spectra measured from different planes. Cobaltite with Ln = Eu and  $\delta = 0.4$  had at room temperature Drude-like behavior of  $R(\lambda)$  both for (001) and (120) planes, but the charge carriers parameters

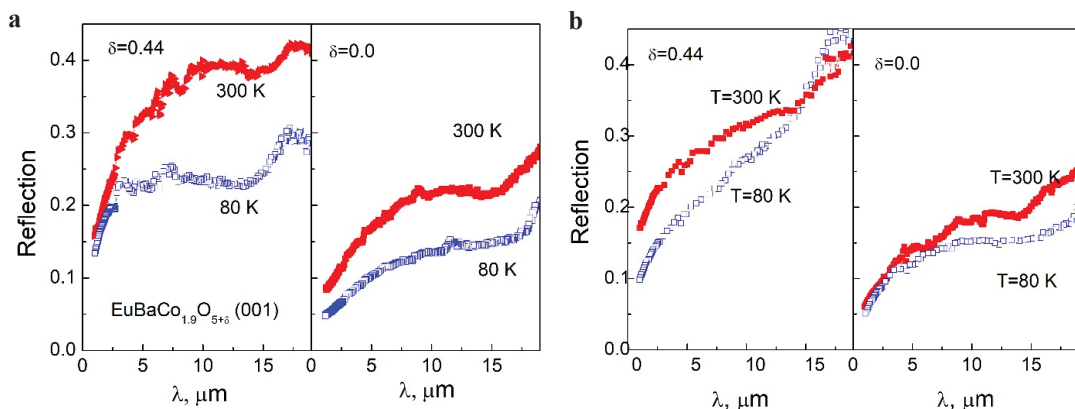


Figure 1. Reflection spectra of  $\text{EuBaCo}_{1.9}\text{O}_{5.4}$  from (001) and (120) planes measured at 300 K and 80 K.

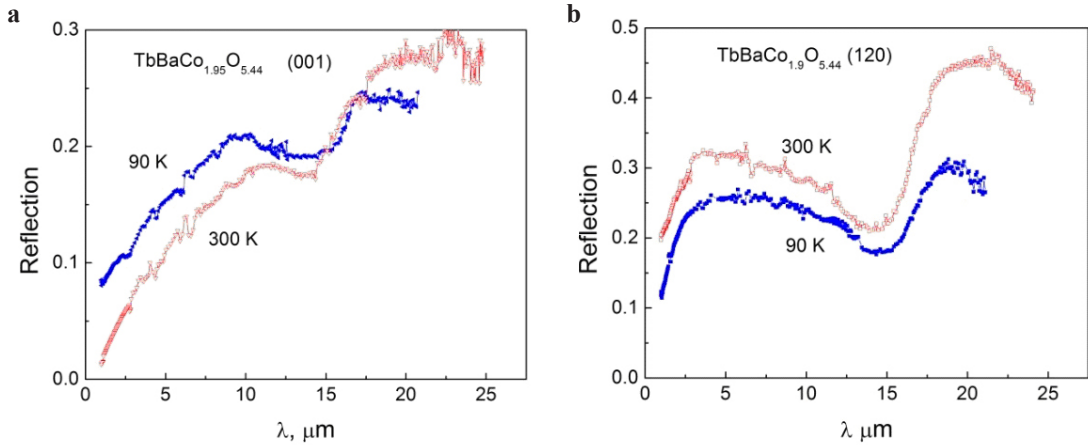


Figure 2. Reflection spectra of  $\text{TbBaCo}_{1.95}\text{O}_{5.44}$  from (001) and (120) planes measured at 300 K and 80 K.

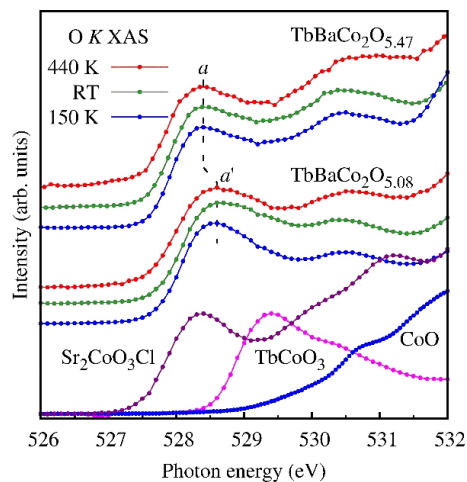


Figure 3. O *K* X-ray absorption spectra of  $\text{TbBaCo}_2\text{O}_{5+\delta}$ ,  $\delta = 0.47$  and  $0.08$ , measured at 150, 300, and 440 K. For comparison, spectra of  $\text{Sr}_2\text{CoO}_3\text{Cl}$  (high-spin  $\text{Co}^{3+}$  ions in  $\text{CoO}_5$  pyramids),  $\text{TbCoO}_3$  (low-spin  $\text{Co}^{3+}$  ions in  $\text{CoO}_6$  octahedra), and  $\text{CoO}$  (high-spin  $\text{Co}^{2+}$  ions in  $\text{CoO}_6$  octahedra) are shown.

differ [2]. Cooling resulted in evolution of the  $R(\lambda)$  spectra: for (001) plane it became typical for materials with localized carriers like polarons (Fig. 1a), while for (120) the form of  $R(\lambda)$  curve retained as in materials with delocalized states (Fig. 1b). A decrease in the oxygen content results in a decrease in the reflectivity both for (001) and (120) planes. This is in agreement with our results of measurements of O *K* X-ray absorption spectra which show an increase of the energy band gap.

In contrast to  $\text{EuBaCo}_{1.95}\text{O}_{5+d}$ , cobaltite  $\text{TbBaCo}_{1.95}\text{O}_{5.44}$  has different character for (001) and (120) planes, which is like in materials with itinerant charge carriers and in materials with polarons, respectively, and such forms kept at cooling down to 90 K (Fig. 2). It indicates that the size of the rare earth ions is important for forming anisotropy of the different strengths. The parameters of the charge carriers are determined from fitting of the reflection spectra by using the Drude formulae

and the formulae for polaronic charge carriers. The evolution in the charge carriers' subsystem is discussed also on the base of data of soft X-ray absorption (Fig. 3). We can suppose that the shift of the peak in the O *K*-edge absorption spectrum with a decrease in the relative oxygen content (appearance of Co<sup>2+</sup> ions and an increase in the relative fraction of CoO<sub>5</sub> structural fragments) is related to the change in the position of the bottom of the conduction band of cobaltites for about 0.2 eV.

*The research was carried out within the state assignment of Ministry of Science and Higher Education of the Russian Federation (topics "Electron", No. 122021000039-4 and "Spin", No. 122021000036-3) and supported in part by RFBR (project No. 20-02-00461)*

1. A.A. Taskin, A.N. Lavrov, Y. Ando, PRB, **71**, 134414 (2005).
2. E.V. Mostovshchikova, S.V. Naumov, N.I. Solin et al., JETP Lett., **104**, 236–240 (2016).

MAGNETIC PROPERTIES OF  $\text{CaCu}_3\text{Ti}_4\text{O}_{12}:\text{Fe}$  SOLID SOLUTIONS

*T.P. Gavrilova*<sup>1\*</sup>, *A.R. Yagfarova*<sup>1</sup>, *I.F. Gilmudinov*<sup>1,2</sup>, *I.V. Yatsyk*<sup>1</sup>, *F.G. Vagizov*<sup>2</sup>,  
*J.A. Deeva*<sup>3</sup>, *T.I. Chupakhina*<sup>3</sup>, *R.M. Eremina*<sup>1</sup>

<sup>1</sup>Zavoisky Physical-Technical Institute, FRC Kazan Scientific Center, Russian Academy of Sciences, Kazan, Russia

<sup>2</sup>Institute of Physics, Kazan Federal University, Kazan, Russia

<sup>3</sup>Institute of Solid State Chemistry of RAS (UB), Ekaterinburg, Russia

\*E-mail: [tatyana.gavrilova@gmail.com](mailto:tatyana.gavrilova@gmail.com)

Calcium copper titanate  $\text{CaCu}_3\text{Ti}_4\text{O}_{12}$  (CCTO) with the perovskite-type structure is already known as the giant dielectric permittivity material. CCTO has a high value of the dielectric constant  $\epsilon = 10^3\text{--}10^5$  and moderate dielectric loss ( $\tan \delta \sim 0.15$ ) in a wide temperature range (40–450 K) for frequencies up to 10 MHz, that allows to use it in wide potential applications as well as Fe-substituted CCTO [1]. The magnetic properties of the pure CCTO are also well known. It undergoes the phase transition into the antiferromagnetically ordered phase below  $T_N = 25$  K with a Weiss constant of  $\Theta_W \sim -30$  K, that was confirmed by some researchers through magnetometry, neutron scattering, Raman spectroscopy and electron spin resonance methods. The recent XANES spectra investigation of  $\text{CaCu}_{3-x}\text{Ti}_{4-x}\text{Fe}_{2x}\text{O}_{12}$  ( $x = 0.1\text{--}0.7$ ) shows that features in the XAS spectrum is comparable with the respective valence states are 2+ and 3+ for Cu and Fe ions, respectively [2]. At the same time the introducing of Fe ions in CCTO structure can also lead to manifestation of an unusual valence state of copper ions  $\text{Cu}^{3+}$  [3]. These results show that, the valence state of ions and magnetic properties are sensitive to the doping or sample preparation process. In this work, we present the thorough examinations of magnetic properties of CCTO:Fe solid solutions using Mössbauer spectroscopy, electron spin resonance and magnetometry methods, in order to reveal the relationship between the dopant concentration and magnetism in investigated samples.

$\text{CaCu}_3\text{Ti}_4\text{O}_{12}:\text{Fe}$  solid solutions were prepared by the standard solid-state synthesis technique. According to this technology the stoichiometric amount of pure calcium carbonate  $\text{CaCO}_3$ , copper oxide CuO and titan oxide  $\text{TiO}_2$  were taken. To obtain  $\text{CaCu}_3\text{Ti}_4\text{O}_{12}:\text{Fe}$  (1; 3%) solid solutions 1 or 3 wt.% of iron with a natural isotope content of  $^{56}\text{Fe}$  and  $^{57}\text{Fe}$  was added to the above mentioned components. XRD measurement showed the decrease of the  $a$  lattice parameter with increasing Fe concentration together with the cell volume. Based on Mössbauer spectroscopy, electron spin resonance and magnetometry experimental data we have concluded that Fe ions substitute  $\text{Ti}^{4+}$  and  $\text{Cu}^{2+}$  positions in octahedral and planar oxygen environment, respectively. Such type of substitution leads to the appearance of three types of iron magnetic centers: divalent  $\text{Fe}^{2+}$  centers in planar environment and trivalent  $\text{Fe}^{3+}$  centers in symmetrical and distorted octahedral positions that strongly effects to the magnetic properties of the investigated samples.

The highest value of the antiferromagnetic interaction one can observe in  $\text{CaCu}_3\text{Ti}_4\text{O}_{12}:\text{Fe}$  (3%) sample where the highest value of the Weiss constant and the maximum of ZFC-FC splitting (the divergence between temperature dependencies of magnetization measured in zero-field cooling and field cooling regimes) was observed. At low temperatures  $T < T_N$  the paramagnetic phase in  $\text{CaCu}_3\text{Ti}_4\text{O}_{12}:\text{Fe}$  (1; 3%) goes into magnetically ordered state (canted antiferromagnetic or ferrimagnetic state), that confirms by the significant drop in the integral intensity of electron spin resonance spectra when the temperature decreases. At the same time, the isothermal magnetization measurements as a function of the external magnetic field above the Néel temperature  $T_N$  showed that weak ferromagnetic interactions exist in  $\text{CaCu}_3\text{Ti}_4\text{O}_{12}:\text{Fe}$  (3%) sample that leads to the appearance of hysteresis loops in M-H curves and possible canted antiferromagnetic ordering with uncompensated

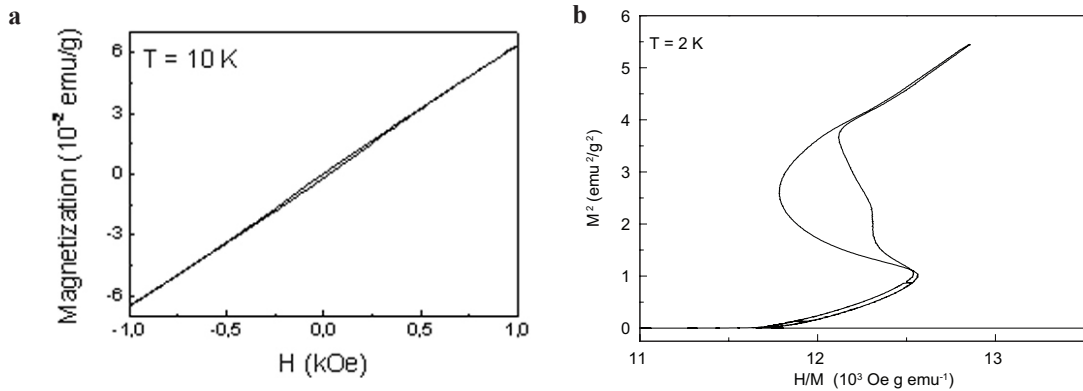


Figure 1. **a** Magnetization as a function of the external magnetic field in  $\text{CaCu}_3\text{Ti}_4\text{O}_{12}:\text{Fe}$  (3%) solid solution measured at  $T = 10$  K. **b** Arrott plot below the magnetic phase transition temperature in  $\text{CaCu}_3\text{Ti}_4\text{O}_{12}:\text{Fe}$  (3%) solid solution in the range of magnetic field up to 3 T.

residual magnetic moment. Below the magnetic phase transition temperature hysteresis loops became more visible (Fig. 1a). Based on our previous studies of other compounds with perovskite structure one can expect the appearance of the electronic phase separation in  $\text{CaCu}_3\text{Ti}_4\text{O}_{12}:\text{Fe}$  (3%) sample (the existence of ferromagnetically regions inside the antiferromagnetically ordered bulk material) at low temperatures [4, 5].

Figure 1b shows the Arrott plot ( $M^2$  vs.  $H/M$ ) for magnetic fields up to 3 T which is used to indicate the presence of magnetic phase transitions. It can be seen that there are multiple positive and negative slopes in the Arrott plot in  $\text{CaCu}_3\text{Ti}_4\text{O}_{12}:\text{Fe}$  (3%) sample. The change in the slope of the Arrott plot curve can be an indication of the field-induced phase transition or metamagnetic transitions with multiple values of the upper and lower critical fields indicating a significant competition between antiferromagnetic and ferromagnetic moments.

We suggest that two factors simultaneously effect on the magnetic properties of  $\text{CaCu}_3\text{Ti}_4\text{O}_{12}:\text{Fe}$  (3%) sample. This effect appears in the significant ZFC-FC splitting, the highest value of the Weiss constant and clearly visible metamagnetic transition and can be related with the simultaneous existence of the significant amount of  $\text{Fe}^{3+}$  ions in the distorted octahedral positions and  $\text{Fe}^{2+}$  ions.

1. K. Pal, R. Jana, A. Dey, P.P. Ray, Md M. Seikh, A. Gayen, Chem. Phys. Lett., **709**, 110–115 (2018).
2. P.Y. Raval, P.R. Pansara, C.-L. Chen, C.-L. Dong, A. Kandasami, K.B. Modi, J. Mater. Sci: Mater. Electron, **32**, 13630–13638 (2021).
3. U.M. Meshiya, P.Y. Raval, P.R. Pansara, M. Nehra, N. Jakhar, S. Kumar, K.B. Modia, D.-K. Lim, R.K. Singhal, Ceramics International, **46**, 2147–2154 (2020).
4. R.M. Eremina, T.P. Gavrilova, I.V. Yatsyk, R.B. Zaripov, A.A. Sukhanov, V.A. Shustov, N.M. Lyadov, V.I. Chichkov, N.V. Andreev, Applied Magnetic Resonance, **47**, 869–879 (2016).
5. E.O. Bykov, T.P. Gavrilova, I.V. Yatsyk, I.F. Gilmudtinov, V.V. Parfenov, A.I. Kurbakov, R.M. Eremina, Ceramics International, **45**, 10286–10294 (2019).



## DESTRUCTION OF THE LONG-RANGE CHARGE ORDERING STATE VIA Fe DOPING IN THE PEROVSKITE MANGANITE $\text{La}_{0.5}\text{Sr}_{0.5}\text{MnO}_3$

*I.M. Usatyy<sup>1</sup>, V.S. Zakhvalinskii<sup>1\*</sup>, O.N. Ivanov<sup>2</sup>*

<sup>1</sup>Belgorod State National Research University, Belgorod, Russia

<sup>2</sup>V.G. Shukhov Belgorod State Technological University, Belgorod, Russia

\*E-mail: [zakhvalinskii@bsu.edu.ru](mailto:zakhvalinskii@bsu.edu.ru)

Various properties of mixed-valence manganites with general chemical formula  $\text{R}_{1-x}\text{A}_x\text{MnO}_3$  (R = La, Pr, Nd, Sm – rare earth elements, A = Sr, Ca – divalent alkaline earth elements) with a perovskite structure, have been the subject of extensive research for several decades. Compounds near the doping level  $x \approx 1/2$ , which exhibit charge-orbital ordering (CO), are under meticulous study, since it is assumed that percolation paths of the coexisting metallic phases causes the CMR effect [1]. The compound  $\text{La}_{0.5}\text{Sr}_{0.5}\text{MnO}_3$  (LSMO-5) exhibits paramagnetic-ferromagnetic (PM-FM) transition at Curie temperature ( $T_C$ ) and CO state at  $T_{CO}$ , however, at Neel temperature ( $T_N$ ) LSMO-5 undergoes first order transition to low-temperature AFM phase which coexists with both FM and CO phases [2]. Indeed, these compounds tend to be AFM systems at low temperatures and compete slightly with the FM and CO phases in close proximity.

$\text{La}_{0.5}\text{Sr}_{0.5}\text{Mn}_{1-y}\text{Fe}_y\text{O}_3$  ceramic samples with  $x = 0.5$  and  $y = 0, 0.02, 0.05, 0.08,$  and  $0.10$ , denoted below by # 5-0, # 5-2, # 5-5, # 5-8 and # 5-10, respectively, were synthesized using the standard solid-phase reaction method. In accordance with the results of X-ray phase analysis, it was found that all samples were single-phase compounds and corresponded to the  $R-3c$  space group. One can see that Fe doping does not lead to any significant systematic change of the crystal lattice parameters, there is a direct substitution of  $\text{Mn}^{3+}$  ions for  $\text{Fe}^{3+}$  ions with same ionic radii [3].

We investigated the effect of Fe doping on the magnetotransport properties of the polycrystalline samples of  $\text{La}_{0.5}\text{Sr}_{0.5}\text{Mn}_{1-y}\text{Fe}_y\text{O}_3$  ( $0 \leq y \leq 0.10$ ) (Fig. 1).

Doping with low Fe concentration (10%) strongly affects electrical transport and magnetization. In this range, the Curie and Neel temperature decreases monotonously as a function of Fe doping. Long range charge order (CO) is disrupted even for the lowest doping level studied (~2%). For Fe concentration up to 5% a ferromagnetic state develops at low temperature with metallic-like conduction and decreases by further Fe doping. For the sample without iron,  $T_C$  is around 350 K, which is in good agreement with the known literature data [4, 5]. A specific feature of # 5-0 sample is that below  $T_C$ , there is a manifestation of a weak peak in the  $d\chi_{ac}/dT$  curve at  $T_{CO} \sim 319$  K, which is associated with the beginning of the transition to the CO state. The temperature dependence of the ac magnetic susceptibility  $\chi_{ac}(T)$  in LSMFO-5 samples, measured at a frequency of 10 kHz in a magnetic field of 1 G. All samples are PM at high temperatures, and with the decrease of the temperature, two magnetic transitions PM-FM and FM-AFM were observed for all studied samples. The temperature dependence of resistivity  $\rho(T)$  in the region of the CO phase obeys the Efros-Shklovskii variable range hopping conduction mechanism. The behavior of  $\rho(T)$  is determined by the complex structure of the density of localized states near the Fermi level, which includes both the soft Coulomb gap  $\Delta \approx 0.28\text{--}0.36$  eV and hard gap  $\delta v$  calculated and discussed by us. The found values of the localization radius of charge carriers  $\alpha \approx 2.0, 1.1,$  and  $1.0$  for samples with  $y = 0.02, 0.05,$  and  $0.10$ , respectively, satisfy the condition for the formation of small lattice polarons under conditions of strong electron-phonon interaction, as well as the increase in the spin disorder of the lattice, which in turn, is associated with the formation of local FM regions around Fe. The applied magnetic field significantly reduces the disorder potential and a change of the dominant type of

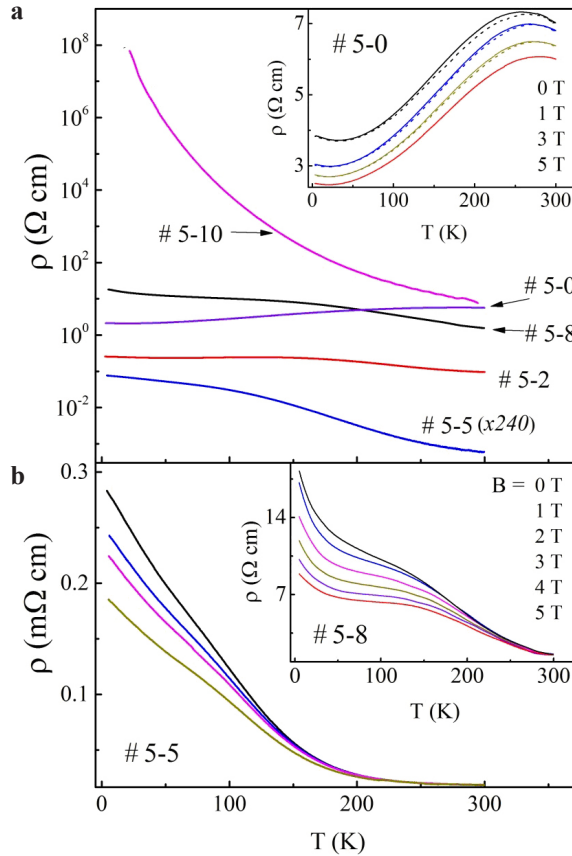


Figure 1. **a** Temperature dependence of the resistivity for  $\text{La}_{0.5}\text{Sr}_{0.5}\text{Mn}_{1-y}\text{Fe}_y\text{O}_3$  samples under zero magnetic field. For # 5-5, the values of  $\rho$  were increased 240 times (in brackets). Inset:  $\rho$  versus  $T$  plots at  $B \geq 0$  for # 5-0, where thermal hysteresis was observed (dashed lines); **b**  $\rho$  versus  $T$  plots at  $B \geq 0$  for # 5-5 and # 5-8 (inset).

hopping conductivity is also observed. Analysis of the field dependence of  $\rho$  at fixed temperatures indicated the presence of colossal magnetoresistance (CMR) in the Fe-doped sample with  $y = 0.1$  and its absence for samples with  $y = 0.02$  and  $0$ . The pronounced behavior of CMR in the sample with  $y = 0.1$  is associated with the increased competition between the FM and AFM regions, which confirms the important role of the coexistence of phases underlying the CMR phenomenon.

The introduction of Fe causes the destruction of the long-range CO state, increasing the fraction of FM and decreasing the resistivity at Fe concentrations of  $\leq 5\%$ . Then, upon further Fe doping, tendencies change and the dominant mechanism is the suppression of the DE interaction in the FM phase, which leads to a sharp increase of resistivity. The temperature dependence of the resistivity in the region of the CO phase corresponds to the mechanism of SE-VRH conductivity. The behavior of the resistivity is determined by the complex structure of the density of localized states near the Fermi level, including the soft Coulomb gap  $\Delta \approx 0.33$  eV, as well as the hard gap  $\delta_v \approx 0.07$  and  $0.03$  for samples with  $y = 0.02$  and  $0.05$ , respectively, and the absence of the hard gap in the sample with  $y = 0.1$ . The calculated values of the localization radius of charge carriers  $\alpha \approx 2.0$ ,

1.1, and 1.0 Å for  $y = 0.02$ , 0.05, and 0.10, respectively, satisfy the condition for the formation of small polarons. From the analysis of the obtained microparameters, we conclude that Fe doping leads to an increase of magnetic disorder, which is associated with the formation of local FM regions around Fe in the CO matrix.

1. M. Uehara, S. Mori, C.H. Chen, S.-W. Cheong, *Nature*, **399**, 560–563 (1999).
2. S.I. Patil, S.M. Bhagat, Q.Q. Shu, S.E. Lofland, S.B. Ogale, V.N. Smolyaninova, X. Zhang, B.S. Palmer, R.S. Decca, F.A. Brown, H.D. Drew, R.L. Greene, I.O. Troyanchuk, W.H. McCarroll, *Phys. Rev. B*, **62**, 9548–9554 (2000).
3. K.H. Ahn, X.W. Wu, K. Liu, C.L. Chien, *Physical Review B*, **54**, 15299–15302 (1996).
4. Y. Moritomo, T. Akimoto, A. Nakamura, K. Ohoyama, M. Ohashi, *Phys. Rev. B*, **58**, 5544–5549 (1998).
5. M. Izumi, T. Manako, Y. Konishi, M. Kawasaki, Y. Tokura, *Phys. Rev. B*, **61**, 12187–12195 (2000).

**ELECTRONIC TRANSITIONS IN THE  $\text{Co}_3\text{BO}_5$**

*N.V. Kazak*<sup>1\*</sup>, *A. Arauzo*<sup>2,3</sup>, *J. Bartolomé*<sup>2</sup>, *A.A. Borus*<sup>1</sup>, *V.V. Yumashev*<sup>4</sup>, *S.G. Ovchinnikov*<sup>1</sup>

<sup>1</sup>Kirensky Institute of Physics, FRC KSC SB RAS, Krasnoyarsk, Russia

<sup>2</sup>Instituto de Nanociencia y Materiales de Aragón (INMA), CSIC-Universidad de Zaragoza and Departamento de Física de la Materia Condensada, Zaragoza, Spain

<sup>3</sup>Servicio de Medidas Físicas, Universidad de Zaragoza, Zaragoza, Spain

<sup>4</sup>Institute of Chemistry and Chemical Technology, FRC KSC SB RAS, Krasnoyarsk, Russia

\*E-mail: [nat@iph.krasn.ru](mailto:nat@iph.krasn.ru)

The  $\text{Co}_3\text{BO}_5$  is extensively investigated for last two decades due to unusual magnetic and electronic properties. The compound presents a strongly anisotropic ferrimagnet with cobalt magnetic moments nearly directed along the *b*-axis and  $T_N = 42$  K [1]. Below room temperature the contribution to the magnetic behavior is due to the high-spin  $\text{Co}^{2+}$  ions, while the  $\text{Co}^{3+}$  ions are in low-spin state [2].  $\text{Co}_3\text{BO}_5$  is crystallized in the ludwigite orthorhombic structure (sp. gr. *Pbam* (No. 55)). The divalent and trivalent metal ions occupy four non-equivalent octahedral sites M1 (2a), M2 (2b), M3 (4g), and M4 (4h).

The single-crystalline X-ray diffraction measurements at high temperatures revealed a sharp increase in the bond-lengths at the M4 site at  $\sim 500$  K which was attributed to the transition from low- to high-spin state of  $\text{Co}^{3+}$  ion [3]. This electronic transition correlates well with the observation of an anomaly of the heat capacity and thermal expansion. The latter is assumed to affect the electronic state of  $\text{Co}^{3+}$  triggering the spin-state crossover.

In the present work, we report the experimental study of the electrical resistivity and magnetic susceptibility at temperatures up to 1000 K. The temperature-induced change in the effective magnetic moment with net increase  $(\mu_{\text{eff}}(\text{HT})^2 - \mu_{\text{eff}}(\text{LT})^2)^{0.5} \sim 3.8 \pm 0.5 \mu_B$  was found corresponding to the  $\text{Co}^{3+}$  spin-state crossover.

The electrical resistivity of the  $\text{Co}_3\text{BO}_5$  at  $T = 200$  K is extremely large,  $\sim 10^{10}$  Ohm·cm. However, it rapidly decreases with the heating and reaches a value of  $\sim 10^{-1}$  Ohm·cm at the  $T = 820$  K.

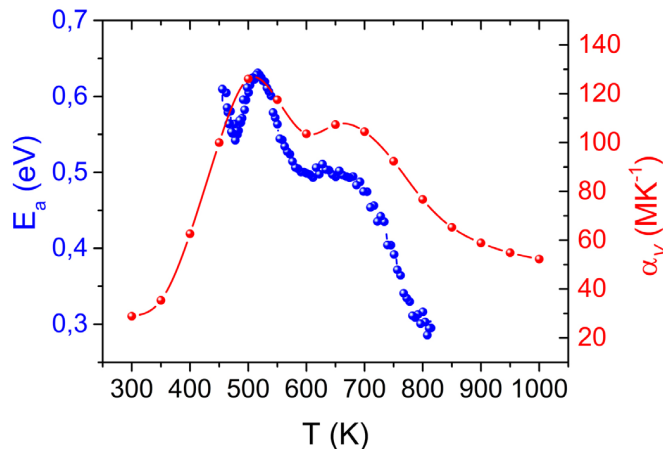


Figure 1. The activation energy and volume thermal expansion coefficient of  $\text{Co}_3\text{BO}_5$  as a function of the temperature.

A significant reduction of the activation energy from  $E_a = 0.82 \pm 0.02$  eV at 200 K to  $0.28 \pm 0.02$  eV at 820 K has been found, indicating that the system undergoes a semiconductor-semiconductor transition [4]. The important finding is that the energy gap is strongly temperature-dependent and is related to anomalous thermal expansion. In fact, the energy gap follows the volume thermal expansion over the entire temperature range (Fig. 1).

Thus, the strong interrelation between the lattice and electron degrees of freedom inherent in ludwigites which is manifested in the  $\text{Fe}_3\text{BO}_5$  as the charge-ordering and structural transitions at  $T_{\text{CO}} = 283$  K [5], here, in the  $\text{Co}_3\text{BO}_5$ , is manifested in the high sensitivity of the electronic subsystem to the thermal expansion.

*We are grateful to the RFBR (project no. 20-02-00559) for supporting this work.*

1. J. Bartolomé, A. Arauzo, N.V. Kazak et al., Phys. Rev. B, **83**, 144426 (2011).
2. D.C. Freitas, C.P.C. Medrano, D.R. Sanchez et al., Phys. Rev. B, **94**, 174409 (2016).
3. N.V. Kazak, M.S. Platunov, Yu.V. Knyazev et al., Phys. Rev. B, **103**, 094445 (2021).
4. N. Kazak, A. Arauzo, J. Bartolomé et al., Dalton Transactions, **51**, 6345 (2022).
5. M. Mir, R.B. Guimarães, J.C. Fernandes et al., Phys. Rev. Lett., **87**, 147201 (2001).

## CRITICAL PHENOMENA IN THE DYNAMIC SPIN-FLUCTUATION THEORY OF METALLIC MAGNETISM

*N.B. Melnikov<sup>1\*</sup>, A.S. Gulenko<sup>1</sup>, B.I. Reser<sup>2</sup>*

<sup>1</sup>Lomonosov Moscow State University, Moscow, Russia

<sup>2</sup>Mikheev Institute of Metal Physics, UrB RAS, Ekaterinburg, Russia

\*E-mail: [melnikov@cs.msu.ru](mailto:melnikov@cs.msu.ru)

Most of the first-principles calculations in metals either neglect nonlocal spin correlations or describe correlations through adiabatic spin dynamics and effective Hamiltonians with classical spins. These approaches have limitations in describing the magnetic shortrange order near the Curie point, and hence produce almost no deviation of the inverse susceptibility from the Curie-Weiss law.

We use the dynamic spin fluctuation theory (DSFT), which takes into account both quantum nature and nonlocal character of spin fluctuations [1]. We estimate the region of critical temperatures in ferromagnetic metals by investigating the paramagnetic susceptibility and correlation function of Fe, Co and Ni near the Curie point [2].

The numerical continuation method developed in [3] and further adjustments of the MAGPROP program for calculations near the Curie point made in [4] allowed us to improve the precision in the DSFT calculations above  $T_C$ . Results of the susceptibility calculations in the DSFT are presented in Fig. 1 in the example of Fe. The point (or rather an interval) where the scaling law  $\chi^{-1} \propto (T - T_C)^\gamma$ , and Curie-Weiss law come close to each other indicates the end of the critical region. In Fe the critical region extends to the end of the  $\alpha$ -Fe phase. The results of the inverse susceptibility in a log-log scale over this temperature range show reasonable agreement with the scaling law fitted to experiment.

Estimation of the critical exponent  $\nu$ , describing the power-law temperature dependence of the correlation radius  $r_c$  above  $T_C$ , requires calculating the spin-density correlator  $\langle s_q s_{-q} \rangle$ . In the static (classical) approximation, we obtain the Lorentzian form

$$\langle s_q s_{-q} \rangle \propto (\kappa^2 + q^2)^{-1}. \quad (1)$$

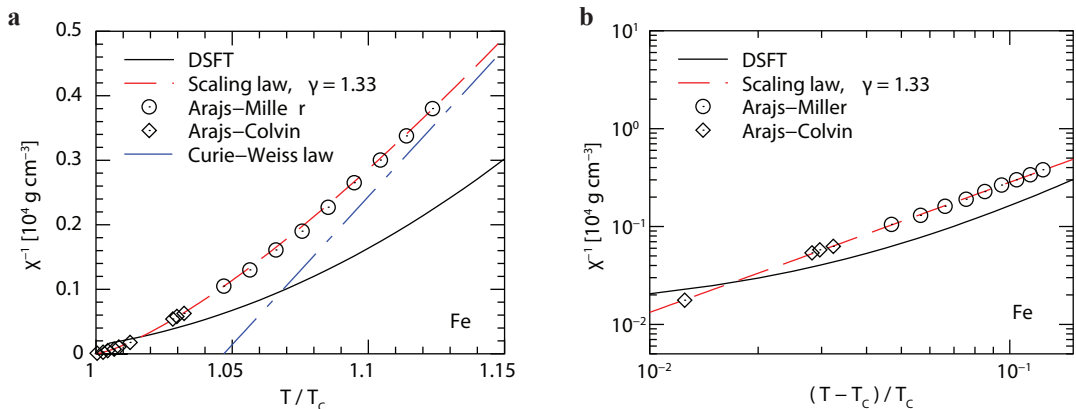


Figure 1. **a** Inverse susceptibility of Fe calculated in the DSFT compared to experiment [5, 6]. The red dotted line is the scaling law fitted to experiment near the Curie point and blue dash-dotted line is the straight line of the Curie-Weiss law. **b** The same but in a log-log scale.

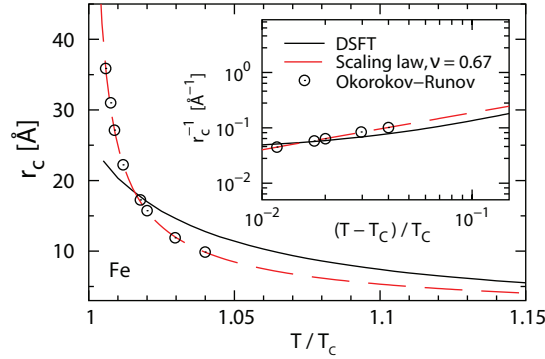


Figure 2. Correlation radius of Fe calculated in the DSFT compared to experiment [7]. The inset shows the reciprocal correlation radius in a log-log scale.

In the DSFT, this approximation holds only for  $q$  smaller than the peak position of the function  $q^2 \langle s_{q,s-q} \rangle$ . The peak position  $q_{\max}(T)$  is about  $0.2 \text{ \AA}^{-1}$  at  $1.01T_C$  in all three ferromagnetic metals. Using the mean-square fit for (1) over the specific interval  $0 \leq q \leq q_{\max}(T)$  for each temperature  $T$ , we obtain the reciprocal correlation radius  $\kappa(T)$ . Next, we fit the temperature dependence of the reciprocal correlation radius  $\kappa(T)$  by the power law  $\kappa \propto (T - T_C)^v$  in a log-log scale to obtain  $v$ .

Figure 2 shows good agreement of the correlation radius with experiment. The inset of Fig. 2 shows that  $r_c^{-1}$  depends linearly on reduced temperature in a log-log scale in the temperature range from about  $1.05T_C$  to  $1.15T_C$ , just as the inverse susceptibility (Fig. 1). The straight line obtained by the mean-square fit of the calculated  $r_c^{-1}$  vs.  $(T - T_C)/T_C$  in a log-log scale has almost the same slope as the linear mean-square fit of the experimental results.

To conclude, we have shown that the inverse paramagnetic susceptibility and reciprocal correlation radius follow the scaling laws up to  $1.1-1.15T_C$  and then switch to the linear law in the 3d ferromagnetic metals. The critical exponents  $\gamma$  and  $v$  for Fe, Co and Ni calculated in the dynamic spin fluctuation theory are in good agreement with experiment.

*The research was carried out within the state assignment of Ministry of Science and Higher Education of the Russian Federation (theme “Quantum” No. AAAA-A18118020190095-4).*

1. N.B. Melnikov, B.I. Reser, Dynamic Spin-Fluctuation Theory of Metallic Magnetism. Springer, Berlin, 2018.
2. N.B. Melnikov, A.S. Gulenko, B.I. Reser, J. Magn. Magn. Mater., submitted (2022).
3. G.V. Paradezhenko, N.B. Melnikov, B.I. Reser, Comp. Math. Math. Phys., **60**, 404 (2020).
4. N.B. Melnikov, G.V. Paradezhenko, B.I. Reser, J. Magn. Magn. Mater., **525**, 167559 (2021).
5. S. Arajs, D.S. Miller, J. Appl. Phys., **31**, 986 (1960).
6. S. Arajs, R.V. Colvin, J. Appl. Phys., **35**, 2424 (1964).
7. A.I. Okorokov, V.V. Runov, Physica B, **297**, 239 (2001).

## SPIN INDUCED ELECTRIC POLARIZATION IN $\text{Fe}_2\text{Mo}_3\text{O}_8$

*K.V. Vasin\**, *M.V. Eremin*, *A.R. Nurmukhametov*

Kazan Federal University, Kazan, Russia

\*E-mail: [krikus.ms@gmail.com](mailto:krikus.ms@gmail.com)

The  $\text{Fe}_2\text{Mo}_3\text{O}_8$  is known as polar dielectric, which exhibits a collinear antiferromagnetic order (AFM) below  $T_N = 60$  K and shows the strong magnetoelectric (ME) coupling. As it was shown in ref. [1] the polarization induced by the magnetic order jumps of a huge value of  $0.125$  uC/cm<sup>2</sup> under transition from AFM to ferromagnetic FIM phase, when an external magnetic field applied along the  $c$ -axis. Here we report the results of our research on the microscopic origin of this interesting phenomena.

Two sites are occupied by  $\text{Fe}^{2+}$  ions in  $\text{Fe}_2\text{Mo}_3\text{O}_8$ : tetrahedral (A) and octahedral (B) coordinated by  $\text{O}^{2-}$ . The electron configuration at Fe sites is  $3d^6$  and the ground term corresponds to  $^5D$  and  $S = 2$ . The starting Hamiltonian is written as

$$H = \sum B_q^{(k)} C_q^{(k)} + I_{\text{mol}} S_z + \lambda LS + \mu_B (L + gS) H_0, \quad (1)$$

where  $B_q^{(k)}$  crystal field parameters were calculated using Hartree-Fock wavefunctions for the free ions. The electrostatic interaction of 3d electrons with a spatially distributed charge density of 2p- and 2s-electrons of oxygen ions and exchange interaction are taken into account similar to how it has been done for  $\text{FeCr}_2\text{O}_4$  in ref [2]. In the process of calculation, it turned out that the crystal field parameter  $B(20)$  is determined by the sum of contributions of approximately the same value, but with the different signs. In this regard, its value, and the values of  $I_{\text{mol}}$  was adjusted according to the energy intervals for A and B sites probed by TRMOKE spectroscopy [3] and the magnetic moments, which were measured by Mössbauer spectroscopy [4]. Note that the obtained exchange (molecular) field parameters are close to those reported in [5] as a result of the analysis of the magnetic susceptibilities and the critical temperatures ( $T_N$ ) of the  $\text{Fe}_{(1-x)}\text{Zn}_x\text{Mo}_3\text{O}_8$ . They are also close by the magnitude to the theoretical estimates of the exchange integrals for  $\text{FeZnMo}_3\text{O}_8$  obtained in ref. [6]. The resulting sets of parameters we used are given in Table 1 and Fig. 1a. As for the spin-orbit coupling parameters, they are like their typical values for Fe in oxides;  $\lambda^{(A)} = -70$  cm<sup>-1</sup> and  $\lambda^{(B)} = -85$  cm<sup>-1</sup>. The effective Hamiltonian of the interaction of 3d electrons with the electric field of the electromagnetic wave [7] is written as follows

$$\hat{H}_E = \sum_{ptk} \{E^{(1)} U^{(k)}\}_t D_t^{(1k)p}, \quad (2)$$

where the curly brackets denote the Kronecker product of two spherical tensors. The parameters  $D_t^{(1k)p}$  were estimated using the structural data reported in [8]. Their values are given in Table 1.

Table 1. Crystal field parameters  $B_q^k$  and  $D_t^{(1k)p}$  for  $\text{Fe}^{2+}$  ions in A-site and B-site.

cm <sup>-1</sup>	A-site	B-site	a.u.	A-site	B-site	a.u.	A-site	B-site	a.u.	A-site	B-site
$B_0^{(4)}$	5500	-10500	$D_0^{(12)3}$	-3.38	0.53	$D_3^{(12)3}$	0.81	0.30	$D_0^{(12)1}$	0.79	-1.61
$B_3^{(4)}$	6000	-11500	$D_0^{(14)3}$	7.22	-1.78	$D_3^{(14)3}$	-1.27	-1.41			
$B_0^{(2)}$	1202	1020	$D_0^{(14)5}$	-0.26	-0.03	$D_3^{(14)5}$	0.19	0.17			



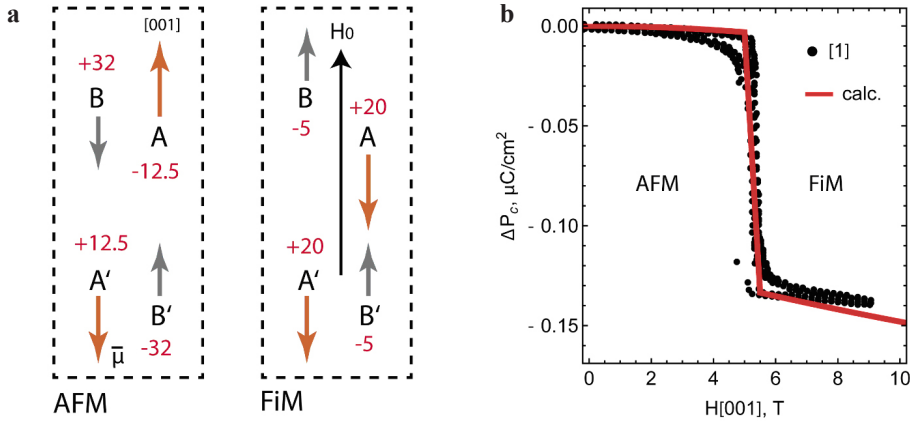


Figure 1. **a** The spin-reorientation of the magnetic moments and the corresponding values of the  $J_{\text{mol}}^{(A/B)}$  in  $\text{cm}^{-1}$  fitted using the field dependency of the polarization [1] and measured magnetic moments [5]. **b** Calculated changes of the polarization under the spin reorientation.

Combining the operator (2) with (1) in the second order of perturbation theory we have derived an analytical expression for effective Hamiltonian of coupling orbital and spin with an external static electric field. The calculated dependence of the electric polarization component from the applied external magnetic field along the  $c$ -axis of the crystal is shown in Fig. 1b.

It should be noted that to interpret the experimental data shown in Fig. 1b, the authors of [1] suggested the exchange striction mechanism. In fact, one believed that during the magnetic phase transition there is an abrupt change in the crystal lattice parameters and, therefore, the ionic dipole moments should change as well. The role of the electronic mechanism was not discussed. However, according to the recently obtained data on the temperature dependence of the lattice constant  $c$  there is a weak kink, corresponding to shifts of all lattice ions on the order of  $0.002 \text{ \AA}$ , i.e., 20 times smaller than assumed in ref. [1]. In this regard, we are inclined to believe that the scenario ionic polarization proposed in [1] is not suitable for explanation of the jump of electric polarization in  $\text{Fe}_2\text{Mo}_3\text{O}_8$ . Our calculations show the microscopic picture of this phenomena originates from the different electronic states of  $\text{Fe}^{2+}$  ions, which have a different interaction with an electric field. Fitting the field dependency of the electric polarization averaged over 4 magnetic domains we have found the different values of the superexchange fields acting on iron spins for AFM and FiM phases as it is shown Fig. 1a. Then we estimated the corresponding values of the resulting polarization.

By looking on the Fig. 1b one can clearly see that the suggested electronic mechanism reproduces well the jump of the polarization of  $\text{Fe}_2\text{Mo}_3\text{O}_8$ .

*We are grateful to Dr Joachim Deisenhofer for stimulating discussion of the terahertz spectroscopy and polarization data. This work was supported by the RSF (Project No. 19-12-00244).*

1. Yazhong Wang, L. Gheorghe, Pascut, Bin Gao et al., Scientific Rep., **5**, 12268 (2015).
2. K.V. Vasin, M.V. Eremin, J. of Phys. Con. Mat., **33**, 22 (2021).
3. Y.M. Sheu et al., Phys. Rev. X, **9**, 031038 (2019).
4. S. Reschke et al., Phys. Rev. B, **102**, 094307 (2020).
4. F. Varret, H. Czeskleba, F. Hartmann-Boutron, and P. Imbert, J. Phys., **33**, 549 (1972).
5. D. Bertrand, H. Kerner-Czeskleba, Le J. Physique, **36**, 379 (1975).
6. S.V. Streltsov, D.-J. Huang, I.V. Solovyev et al., JETP Letters, **109**, 12 (2019).
7. M.V. Eremin, Phys. Rev. B, **100**, 140404 (2019).
8. S. Reschke, A.A. Tsirlin, N. Khan et al., Phys. Rev. B, **102**, 094307 (2020).

## MAGNETIC PROPERTIES OF $\text{La}_{0.81}\text{Sr}_{0.19}\text{Mn}_{0.9}\text{Fe}_{0.1-x}\text{Zn}_x\text{O}_3$ ( $x = 0$ , $x = 0.05$ )

R.M. Eremina<sup>1</sup>, I.V. Yatsyk<sup>1</sup>, Z.Y. Seidov<sup>2\*</sup>, F.G. Vagizov<sup>3</sup>, V.A. Shustov<sup>2</sup>, A.G. Badelin<sup>4</sup>,  
V.K. Karpasyuk<sup>4</sup>, D.S. Abdinov<sup>2</sup>, M.M. Tagiev<sup>5</sup>, S.Kh. Estemirova<sup>6</sup>, H.-A. Krug von Nidda<sup>7</sup>

<sup>1</sup>Zavoisky Physical-Technical Institute, Federal Research “Kazan Scientific Center of RAS”,  
Kazan, Russia

<sup>2</sup>Institute of Physics, Azerbaijan National Academy of Sciences, Baku, Azerbaijan

<sup>3</sup>Institute of Physics, Kazan Federal University, Kazan, Russia

<sup>4</sup>Astrakhan State University, Astrakhan, Russia

<sup>5</sup>Azerbaijan State University of Economics, Baku, Azerbaijan

<sup>6</sup>Institute for Metallurgy, Ural Division of RAS, Ekaterinburg, Russia

<sup>7</sup>EP V, EKM, Institute of Physics, University of Augsburg, Augsburg, Germany

\*E-mail: [zsyu@rambler.ru](mailto:zsyu@rambler.ru)

Magnetic properties of polycrystalline  $\text{La}_{0.81}\text{Sr}_{0.19}\text{Mn}_{0.9}\text{Fe}_{0.1-x}\text{Zn}_x\text{O}_3$  ( $x = 0$ ,  $x = 0.05$ ) have been investigated by means of electron spin resonance, magnetic susceptibility, and Mössbauer measurements. Both samples show a clear ferromagnetic transition. The Curie temperature  $T_C$  decreases on increasing Fe content. Mössbauer studies indicate that Fe in these compounds is in the trivalent high-spin state. The temperature evolution of the Mössbauer spectra at low temperatures ( $T < T_C$ ) is typical for ferromagnetic clusters with a wide distribution in size and magnetic correlation length. The inverse susceptibility of all the samples deviates from the Curie-Weiss law above  $T_C$ , indicating the presence of fluctuations on approaching magnetic order. An anomalous downturn of the inverse susceptibility for  $x = 0.05$  significantly above  $T_C$  and the concomitant observation of ferromagnetic resonance signals coexisting with the paramagnetic resonance up to approximately room temperature, is caused by a Griffiths-like behavior. This regime is characterized by the coexistence of ferromagnetic entities within the globally paramagnetic phase

*The work of Z.Y. Seidov, M.M. Tagiev and D.S. Abdinov was supported by the Science Development Foundation under the President of the Republic Azerbaijan Grant EIF-BGM-4-RFTF-1/2017-21/03/1-M-03. Electron spin resonance measurements (I.V. Yatsyk, V.A. Shustov, R.M. Eremina) were performed with the financial support from the government assignment for FRC Kazan Scientific Center of RAS.*

MANY-BODY EFFECTS IN MAGIC ANGLE TWISTED  
BILAYER GRAPHENE*A.O. Sboychakov*<sup>1\*</sup>, *A.V. Rozhkov*<sup>1</sup>, *A.L. Rakhmanov*<sup>1</sup>, *F. Nori*<sup>2</sup><sup>1</sup>Institute for Theoretical and Applied Electrodynamics, Russian Academy of Sciences,  
Moscow, Russia<sup>2</sup>Theoretical Quantum Physics Laboratory, RIKEN, Wako-shi, Saitama, Japan\*E-mail: [sboycha@mail.ru](mailto:sboycha@mail.ru)

Recent progress in technologies of constructing heterostructures described by superlattice periodicity opens a new era in designing the 2D devices with tuned physical properties. One example of 2D materials with superstructure is the twisted bilayer graphene – material described by nonzero angle of rotation  $\theta$  (twist angle) between two graphene layers [1]. Low-energy electronic properties of this system depend substantially on the twist angle. At the so called magic angle  $\theta_c \sim 1^\circ$ , the electronic spectrum near the Fermi level is described by the flat bands. This, in turn, makes the Fermi liquid is very susceptible to interactions generating ordered quantum states at low temperatures. Many-body insulating states and the superconductivity in doped magic angle twisted bilayer graphene have been observed recently in [2–3]. The structure of the insulating state as well as the symmetry of the superconducting order parameter is not yet known. In our study, we predict that non-superconducting ordered state is the spin density wave. The developed theory allows us to correctly describe the dependence of the conductivity of the system versus doping [4]. We predict that near half-filling (two extra electrons or holes per supercell) our spin density wave phase obeys the properties of the electron nematic state: the symmetry of both the order parameter and the electron spectrum is lower than that dictated by the geometry of the system [5]. Recently, electron nematicity in twisted bilayer graphene has been observed experimentally [6].

*Support by Russian Science Foundation (grant No 22-22-00464) is acknowledged.*

1. A.V. Rozhkov, A.O. Sboychakov, A.L. Rakhmanov, and F. Nori, Phys. Rep., **648**, 1 (2016).
2. Y. Cao, V. Fatemi, S. Fang, K. Watanabe, T. Taniguchi, E. Kaxiras, and P. Jarillo-Herrero, Nature, **556**, 43 (2018).
3. Y. Cao et al., Nature, **556**, 80 (2018).
4. A.O. Sboychakov, A.V. Rozhkov, A.L. Rakhmanov, and F. Nori, Phys. Rev. B, **100**, 045111 (2019).
5. A.O. Sboychakov, A.V. Rozhkov, A.L. Rakhmanov, and F. Nori, Phys. Rev. B, **102**, 155142 (2020).
6. A. Kerelsky et al., Nature, **572**, 95 (2019).

**ELECTRONIC STATES OF Co IONS IN  $\text{LnBaCo}_2\text{O}_{5+\Delta}$  COBALTITES ( $\text{Ln} = \text{RARE EARTH}$ ,  $0 \leq \Delta \leq 1$ ): SOFT X-RAY ABSORPTION STUDIES***V.R. Galakhov\**, *M.S. Udintseva*, *S.V. Naumov*, *B.A. Gizhevskii*

M.N. Mikheev Institute of Metal Physics, Ural Branch of the Russian Academy of Sciences, Ekaterinburg, Russia

\*E-mail: [galakhov@ifmlrs.uran.ru](mailto:galakhov@ifmlrs.uran.ru)

$\text{LnBaCo}_2\text{O}_{5+\delta}$  layered cobaltites of rare-earth elements ( $0 \leq \delta \leq 1$ ) are most promising for novel cathodes for solid-oxide fuel cells, since they have a high level of both electronic and oxygen-ionic conductivity and have high activity for the oxygen reaction in many energy storage and conversion processes. Furthermore, these materials are interesting for studying the spin states of cobalt ions: (i) these compounds have two types of structural complexes ( $\text{CoO}_6$  octahedra with  $\text{Co}^{3+}$  ions) and  $\text{CoO}_5$  pyramids ( $\text{Co}^{3+}$  and  $\text{Co}^{2+}$  ions in pyramids of cobaltites with  $\delta \leq 0.5$ ); (ii) metal-insulator transition (MIT) in these cobaltites, (iii) spin transition associated with the MIT occurs at quite easily attainable temperatures (for example, 360 K for  $\text{EuBaCo}_2\text{O}_{5.5}$  [1]). The problem of spin states of  $\text{Co}^{3+}$  ions in octahedra and pyramids of these cobaltites (high spin, intermediate spin, and low spin) above and below the metal-insulator transition is a subject of intense discussion [2]. In this paper, we considered the above two issues: (i) the response of cobaltites to external influences (plastic deformation by torsion under pressure and milling in a vibratory mill) and (ii) the change in the spin states of cobalt ions with temperature. The main experimental method is soft X-ray absorption spectroscopy. X-ray absorption spectroscopy studies of cobaltites at the Co  $L_{2,3}$  and O  $K$  was performed at the Russian-German beamline at BESSY-II (Berlin) in surface-sensitive total electron-yield mode. Co  $L_{2,3}$  X-ray absorption spectra appear due to the  $2p^63d^n \rightarrow 2p^53d^{n+1}$  electron transition. They are determined by the Coulomb and exchange interactions between a Co 2p hole and Co 3d electrons and by the crystal field. Oxygen  $K$  spectra are due to transition from O 1s core level to the O 2p states which are hybridized with Co 3d states.

It was shown that in  $\text{CO}_2\text{--O}_2$  atmosphere at temperatures of 500–700 °C, orthorhombic  $\text{GdBaCo}_2\text{O}_{5.5}$  decomposes into the tetragonal phase of  $\text{GdBaCo}_2\text{O}_{5.5}$ ,  $\text{GdCoO}_3$ ,  $\text{BaCO}_3$ , and probably  $\text{Co}_3\text{O}_4$  [3]. A mechanical impact is similar to a thermal impact in terms of the resulting effect. Severe plastic deformation (uniaxial compression and torsion under pressure) was applied to  $\text{GdBaCo}_2\text{O}_{5.5}$ . We have carried out phase analysis of  $\text{EuBaCo}_2\text{O}_{5.5}$  powders subjected to mechanical impact (milling in a ball mill) with help using soft X-ray absorption spectra. It is shown that this kind of deformation leads to the nanostructural state of cobaltite. At a sufficiently high degree of deformation (at a pressure of 7 GPa and an angle of rotation of the anvils relative to each other of 180°), a new phase with ions appears in cobaltite, close to CoO [4]. Cobaltite  $\text{EuBaCo}_2\text{O}_{5.5}$  was subjected to less intense deformation: milling in a ball mill. It leads to the decomposition of the sample into  $\text{Co}_3\text{O}_4$ ,  $\text{BaCO}_3$ , and  $\text{EuCoO}_3$  [5].

To reveal the changes of the spin states of cobalt ions during the transition of the system from the semiconductor to the metallic state, we measured the O  $K$  and Co  $L_{2,3}$  spectra at room temperature and 440 K of cobaltites  $\text{EuBaCo}_2\text{O}_{5.5}$  and  $\text{EuBaCo}_2\text{O}_{5.25}$ . Fig. 1 shows O  $K$  and Co  $L_3$  X-ray absorption spectra of  $\text{EuBaCo}_2\text{O}_{5.25}$  and  $\text{EuBaCo}_2\text{O}_{5.5}$  measured at room temperature and at 440 K. For comparison, spectra of  $\text{Sr}_2\text{CoO}_3\text{Cl}$  (high-spin  $\text{Co}^{3+}$  ions in  $\text{CoO}_5$  pyramids),  $\text{EuCoO}_3$  (low-spin  $\text{Co}^{3+}$  ions in  $\text{CoO}_6$  octahedra), and CoO (high-spin  $\text{Co}^{2+}$  ions in  $\text{CoO}_6$  octahedra) are shown. According to the O  $K$  spectra (left part of Fig. 1), the substitution of  $\text{Co}^{2+}$  ions for some  $\text{Co}^{3+}$  ions with a decrease of the oxygen content in the chemical formula of a cobaltite and, hence, an increase of

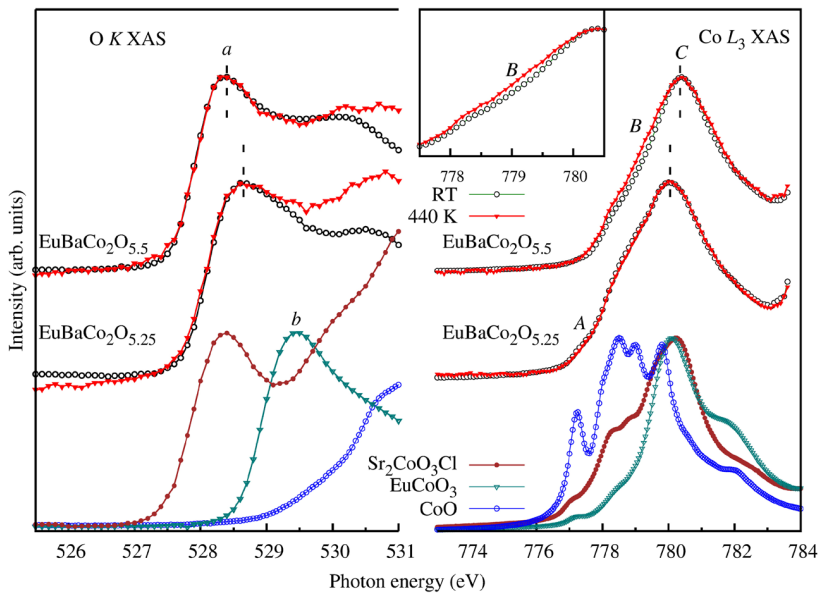


Figure 1. O K and Co L<sub>3</sub> X-ray absorption spectra of EuBaCo<sub>2</sub>O<sub>5.5</sub> and EuBaCo<sub>2</sub>O<sub>5.25</sub> measured at room temperature and at 440 K. For comparison, spectra of Sr<sub>2</sub>CoO<sub>3</sub>Cl (high-spin Co<sup>3+</sup> ions in CoO<sub>5</sub> pyramids), EuCoO<sub>3</sub> (low-spin Co<sup>3+</sup> ions in CoO<sub>6</sub> octahedra), and CoO (high-spin Co<sup>2+</sup> ions in CoO<sub>6</sub> octahedra) are shown.

the relative fraction of CoO<sub>5</sub> pyramids with respect to the number of CoO<sub>6</sub> octahedra leads to an increase of the band gap by about 0.3 eV.

Charge and spin state of Co ions were estimated from the Co L X-ray spectra (right part of Fig. 1). The feature *A* is the fingerprint of divalent cobalt ions. The absence of this feature in the spectra of EuBaCo<sub>2</sub>O<sub>5.5</sub> means that this sample is free from Co<sup>2+</sup> ions. A comparison of spectra of EuBaCo<sub>2</sub>O<sub>5.5</sub> and Sr<sub>2</sub>CoO<sub>3</sub>Cl shows that feature *B* of the spectrum of EuBaCo<sub>2</sub>O<sub>5.5</sub> cobaltite is determined by the high-spin states of Co<sup>3+</sup> ions in the pyramids. However, in accordance with the multiplet calculations, feature *B* corresponds also to high-spin states of Co<sup>3+</sup> ions in octahedra. Consequently, feature *B* in the spectrum of EuBaCo<sub>2</sub>O<sub>5.5</sub> is determined by the contributions of high-spin Co<sup>3+</sup> ions both in octahedra and in pyramids. The shift of the *C* maximum of the spectrum of EuBaCo<sub>2</sub>O<sub>5.25</sub> to lower photon energies indicates the appearance of Co<sup>2+</sup> ions in the sample, which, based on the structural data and electrical neutrality, should be in CoO<sub>5</sub> pyramids. Feature *A* appears, indicating the presence of Co<sup>2+</sup> ions, while feature *B* becomes more intense. Note, feature *B* also displays the Co<sup>2+</sup> states of the ions located in the pyramids. One can suggest that above the metal-insulator transition point, some of the low-spin Co<sup>3+</sup> ions in octahedra of EuBaCo<sub>2</sub>O<sub>5.5</sub> are converted into high-spin ions. In contrast, no change of the spin state in EuBaCo<sub>2</sub>O<sub>5.25</sub> was detected.

*The authors thank Dr. D.A. Smirnov (Dresden University of Technology, Germany) and Dr. A.A. Makarova for kindly measured some of the spectra at BESSY. The work was performed within the framework of State assignment from the Ministry of Science and Higher Education of the Rus-*

sian Federation (topics “Electron”, No. 122021000039-4 and “Spin”, No. 122021000036-3) and partially supported by the Russian Foundation for Basic Research (project No. 20-02-00461). The X-ray spectra were measured with partial financial support from Bilateral Program “Russian-German Laboratory at BESSY”.

1. C. Martin, A. Maignan, D. Pelloquin, N. Nguyen, B. Raveau, Appl. Phys. Lett., **71**, 1421–1423 (1997).
2. V.R. Galakhov, Phys. Met. Metallogr., **122**, 83–114 (2021).
3. A. Tarancón, J. Peña-Martínez, D. Marrero-López, A. Morata, J.C. Ruiz-Morales, and P. Núñez, Solid State Ionics, **179**, 2372–2378 (2008).
4. V.V. Mesilov, M.S. Udintseva, S.N. Shamin, S.V. Naumov, S.V. Telegin, B.A. Gizhevskii, and V.R. Galakhov, Phys. Solid State, **59**, 829–834 (2017).
5. V.R. Galakhov, M.S. Udintseva, V.V. Mesilov, B.A. Gizhevskii, S.V. Naumov, S.V. Telegin, and D.A. Smirnov, Appl. Surf. Sci., **493**, 1048–1054 (2019).

## SYNTHESIS ASPECTS AND MAGNETIC MICROSTRUCTURE OF TERNARY ORDERED Fe-Al-M (M = Ga, B, Sn, V, Mn) ALLOYS

*E.V. Voronina*<sup>1\*</sup>, *A.F. Abdullin*<sup>1</sup>, *A.G. Ivanova*<sup>1</sup>, *L.V. Dobysheva*<sup>2</sup>, *A.V. Korolyov*<sup>3</sup>,  
*A.K. Arzhnikov*<sup>2</sup>

<sup>1</sup>Institute of Physics, Kazan Federal University, Kazan, Russia

<sup>2</sup>UdmFRC UrB RAS, Izhevsk, Russia

<sup>3</sup>IMP UrB RAS, Ekaterinburg, Russia

\*E-mail: [Elena.Voronina@kpfu.ru](mailto:Elena.Voronina@kpfu.ru)

With the long history of experimental and theoretical research dating back to the first half of the last century, multicomponent compounds based on iron-aluminum are still of interest both from the point of view of developing practical applications and as a model for studying magnetic phenomena in strongly correlated electron systems. There is a large amount of experimental information about electronic, magnetic, mechanical, etc. properties of binary alloys Fe-Al [1]. Fe-Al based materials with additions of gallium or boron are important for technical applications due to their magnetoelastic properties and good mechanical strength [2, 3]. This kind of alloys are promising as materials for sensors and transducers, since, in addition to high magnetostriction, these alloys are inexpensive and can be machined. A series of compounds based on Fe<sub>2</sub>VAl with few percent of the tungsten reveals a high thermoelectric performance [4]. The small addition of the third element to binary compound significantly improves their functional characteristics and understanding the effect of such admixture is very important. The ordered Fe-Al alloys containing more than 30 at.% of Al turned out to be good model objects for studying the origin and stabilization of magnetic nano-sized inhomogeneity, in particular, incommensurate spin density waves or spin spiral waves.

Nanocrystalline metastable ternary solid solutions Fe<sub>65</sub>Al<sub>35-x</sub>M<sub>x</sub> and Fe<sub>65-y</sub>Al<sub>35</sub>M<sub>y</sub> with  $x, y = 0, 3, 5, 10$  at.% and M = B, Ga, Sn, V, Mn were prepared by mechanical alloying of elemental constituents. These disordered powders were then used as precursors to obtain ordered compounds through the required heat treatment. The structural phase transformations in the process of synthesis of ternary B2 or D0<sub>3</sub> intermetallics were characterized by X-ray diffraction and Mössbauer spectroscopy techniques. Single-phase metastable Fe-Al-B and Fe-Al-Sn powders showed a pronounced tendency to separate into several phases during heat treatment.

We calculated the formation energy to evaluate the phase stability of a certain composition ternary alloys. Calculations were performed using the full-potential linearized augmented plane wave (FP LAPW) technique contained in the WIEN2k software package [5]. Ternary systems with V or Mn additions were found to have the minimum energy. Ternary compounds Fe-Al-B and Fe-Al-Sn are the least stable and their formation is energetically unfavorable. The formation of the Fe<sub>2</sub>B phase reduces the total energy of the Fe-Al-B system, the same as the mixture of Fe-Al and FeSn<sub>2</sub> phases gives a lower energy for the Fe-Al-Sn system. The results of the study describe adequately the main experimental features of the synthesis of ternary intermetallics from mechanically alloyed solid solutions.

The magnetic state of ternary Fe-Al-M compounds was characterized based on an analysis of Mössbauer and magnetometric data (over the range of temperature 4.2–80 K and of external magnetic field 0–7 T). The Ga admixture leads to a small increase in the Fe atom magnetic moment (MM) and <sup>57</sup>Fe hyperfine field (HFF), whereas the boron addition heightens these characteristics significantly. For 3d-admixtures, we observed a sharp fall of hyperfine magnetic splitting when replacing Fe with V and some increase of HFF under substitution of Fe with Mn.

We carried out comparative *ab initio* calculations for the  $^{57}\text{Fe}$  HFF, magnetic moments and lattice parameters of various periodic Fe-Al-M systems with the replacement of one Al or Fe atom by Ga, Mn, V and B for *bcc* supercells of different Al content. The substitution of gallium for aluminum in most of the considered structures causes an increment in the distance between iron atoms, leading to the growth in the Fe MM and to the increase of the Fermi-contact contribution to HFF. When B atoms are added to Fe-Al, the local symmetry inside the cell reduces, leading to an increase in the distances between Fe atoms, and, as a result, to a growth of local magnetic characteristics. The  $^{57}\text{Fe}$  HFF values, calculated under the assumption that boron atoms occupy as lattice sites as interstices, made it possible to explain and approximate the Fe-Al-B Mössbauer spectra. For the Fe-Al-V compounds, the HFF decrease is explained by the antiferromagnetic orientation of the V atoms magnetic moments. For the Fe-Al-Mn system, both ferromagnetic and antiferromagnetic states turned out to be possible, each state having a proper equilibrium size of the unit cell.

The average and local magnetic characteristics of ordered Fe-Al-M (M = Ga, B, and V) alloys have been analyzed in terms of the phase separation into two magnetic phases: a ferromagnetic one and a spin density wave. It was found that the relative fraction of the spin density wave decreases as temperature and external magnetic field rises, resulting in growth of the ferromagnetic phase fraction. Disorder of any kind (chemical or topological defects, doping-induced disorder) makes highly unstable the ordering of magnetic moments like spin density wave. To study the dependence of the total energy on the formation of a spin spiral in a perfectly ordered Fe-Al-M (M = V, Mn, Ga, B) supercell, *ab initio* calculations [6] were carried out for noncollinear spin ordering and are under discussion.

*Support by ESRF is acknowledged.*

1. D.G. Morris (ed.), *Intermetallics*, Special Iss., **13**, 1255–1342 (2005).
2. J.B. Restorff et al., *J. Appl. Phys.*, **111**, 023905-1–023905-12 (2012).
3. C. Bormio-Nunes, O. Hubert, *JMMM*, **393**, 404–418 (2015).
4. B. Hinterleitner, I. Knapp, M. Poner, Yongpeng Shi, H. Müller et al., *Nature*, **576**, 85–90 (2019).
5. P. Blaha, K. Schwarz, G.K.H. Madsen, D. Kvasnicka, J. Luitz, R. Laskowski, F. Tran and L.D. Marks, WIEN2k, An Augmented Plane Wave + Local Orbitals Program for Calculating Crystal Properties, Karlheinz Schwarz, Techn. Universität Wien, Austria (2018).
6. R. Laskowski, G.K.H. Madsen, P. Blaha and K. Schwarz, *PRB*, **69**, 140408-1–140408-4 (2004).



## ENTANGLEMENT AND THE EXTERNAL FIELDS IN THE KUGEL-KHOMSKII MODEL

*V.E. Valiulin*<sup>1,2</sup>, *A.V. Mikheyenkov*<sup>1,2\*</sup>, *N.M. Chtchelkatchev*<sup>1,2</sup>, *K.I. Kugel*<sup>3,4</sup>

<sup>1</sup>Moscow Institute of Physics and Technology (National Research University), Dolgoprudny, Russia

<sup>2</sup>Vereshchagin Institute of High Pressure Physics, RAS, Moscow (Troitsk), Russia

<sup>3</sup>Institute for Theoretical and Applied Electrodynamics, Russian Academy of Sciences, Moscow, Russia

<sup>4</sup>National Research University Higher School of Economics, Moscow, Russia

\*E-mail: [mikheen@bk.ru](mailto:mikheen@bk.ru)

We use the of exact diagonalization method to study the entanglement between two subsystems for a finite chain with the Hamiltonian [1]

$$H = J \cdot \sum S_i S_j + I \cdot \sum T_i T_j + K \cdot \sum (S_i S_j)(T_i T_j) . \quad (1)$$

$S_i$  and  $T_i$  are spin and pseudospin operators ( $S = 1/2$ ,  $T = 1/2$ ), all sums are over the nearest neighbor bonds. Aside from the Hamiltonian (1), related models are considered in which the inter-subsystem interaction has Ising form for one or both subsystems. Such expressions arise in various physical realizations of the spin-pseudospin model (see, e.g. [2]). To characterize the degree of entanglement at zero temperature, one of the most popular criteria is used – Concurrence. Since the exact density matrix is calculated, any other criterion can of course be defined.

In all cases, the entanglement for zero external field is calculated (these results for some models are already known, see [3] and references therein), as well as the influence of external fields, in one or in both subsystems. The variant with staggered field has also been studied (it leads to interesting and non-intuitive results). A comparison is made with the previous (semi-analytical) works of the authors.

*At zero temperature.* As it was mentioned above, we use Concurrence to be the entanglement measure. It is shown, in particular, that at zero temperature an external field can both reduce entanglement (it is intuitively obvious) but also surprisingly enhance it. It is essential that, depending on the physical realization of the model, the external field can be of different nature, not only magnetic.

The examples of the calculated entanglement are shown in Fig. 1.

In addition, an (empirical) local criterion for determining the entanglement region is proposed, which does not require cumbersome calculations of the exact density matrix.

*At non-zero temperature.* At non-zero temperature, Concurrence is not an adequate quantitative measure of entanglement, so other measures are commonly used. Widely adopted Logarithmic Negativity is chosen here. As  $T \rightarrow 0$ , these two measures are mutually consistent. Note that, since all measures of entanglement come from an exact density matrix (corresponding to the ground state or to temperature), it is not difficult to convert one measure to another.

Among the finite temperature effects, let us note two surprises.

First, the entanglement can be nonmonotonic. Namely, there are ranges of the model parameters, where entanglement is absent at zero temperature, but then, with an increase in temperature, it appears, passes through a maximum, and again vanishes.

And, secondly, the entanglement can be also robust under effect of temperature within a wide range of parameters, forming the “stability islands”.

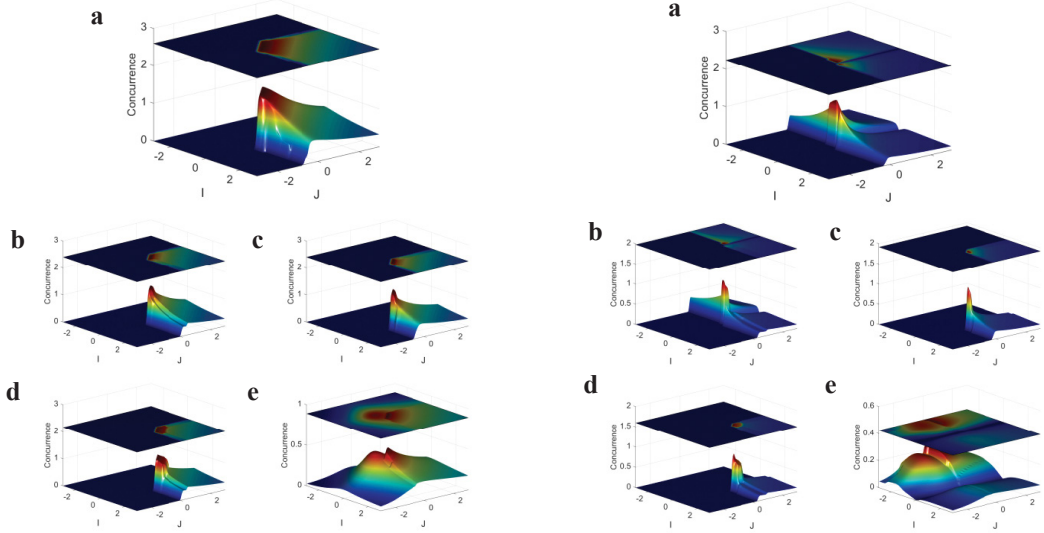


Figure 1. **Left panel.** Entanglement  $C$  for intersubsystem exchange  $K \cdot \sum (S_i S_j)(T_i T_j)$  with negative  $K = -1$  and external fields. The  $C$ -maximum occurs at a segment of the diagonal line. **a**  $H_s = H_t \ll 1$ , **b**  $H_s = 1$ ,  $H_t \ll 1$ , **c**  $H_s \ll 1$ ,  $H_t = 1$ , **d**  $H_s = H_t = 1$ , **e** staggered fields  $|H_s| = |H_t| = 1$  in both subsystems. Here,  $H_s$  and  $H_t$  stand for external fields in spin and pseudospin subsystems. **Right panel.** Entanglement  $C$  for intersubsystem exchange  $K \cdot \sum (S_i S_j)(T_i^z T_j^z)$  with negative  $K = -1$  and external fields. The  $C$ -maximum occurs at a segment of the diagonal line. **a**  $H_s = H_t \ll 1$ , **b**  $H_s = 1$ ,  $H_t \ll 1$ , **c**  $H_s \ll 1$ ,  $H_t = 1$ , **d**  $H_s = H_t = 1$ , **e** staggered fields  $|H_s| = |H_t| = 1$  in both subsystems. Here,  $H_s$  and  $H_t$  stand for external fields in spin and pseudospin subsystems.

In all the calculations the maximum available size of the chain ( $N \sim 10$ ) for comprehensive estimate is determined by the computational resources, mainly by the RAM size, so we extrapolate the results to  $1/N \rightarrow 0$ .

The results are presented in [4], [5].

*V.E.V. and N.M.S. acknowledge the support of the Russian Science Foundation (project No. 18-12-00438) in the part concerning numerical calculations. K.I.K. acknowledge the support of the Russian Science Foundation (project No. 20-62-46047) in the part concerning the data analysis.*

*The computations were carried out on MVS-10P at Joint Supercomputer Center of the Russian Academy of Sciences (JSCC RAS). This work has been carried out using also computing resources of the Federal Collective Usage Center Complex for Simulation and Data Processing for Mega-Science Facilities at NRC “Kurchatov Institute”, <http://ckp.nrcki.ru/>.*

1. K.I. Kugel and D.I. Khomski, Sov. Phys. Uspekhi, **25**, 231 (1982).
2. A.M. Belemuk, N.M. Chtchelkatchev, A.V. Mikheyenkov, and K.I. Kugel, Phys. Rev. B, **96**, 094435 (2017); New J. Phys., **20**, 063039 (2018).
3. D. Gotfryd, E.M. Parschke, J. Chaloupka, A.M. Oles, and K. Wohlfeld, Phys. Rev. R, **2**, 013353 (2020).
4. V.E. Valiulin, A.V. Mikheyenkov, N.M. Chtchelkatchev, K.I. Kugel, Phys. Rev. B, **102**, 155125 (2020).
5. V.E. Valiulin, A.V. Mikheyenkov, N.M. Chtchelkatchev and K.I. Kugel, arXiv:2203.08254.

## ON THE GENERAL CONDITIONS FOR ITINERANT FERROMAGNETISM FOR NON-DEGENERATE HUBBARD MODEL ON A THREE-DIMENSIONAL LATTICE

*P.A. Igoshev*<sup>1\*</sup>, *A.A. Katanin*<sup>2,1\*\*</sup>

<sup>1</sup>Institute of Metal Physics, Ekaterinburg, Russia

<sup>2</sup>Center for Photonics and 2D Materials, Moscow Institute of Physics and Technology, Dolgoprudny, Moscow region, Russia

\*E-mail: [igoshev\\_pa@imp.uran.ru](mailto:igoshev_pa@imp.uran.ru); \*\*E-mail: [andrey.katanin@gmail.com](mailto:andrey.katanin@gmail.com)

The formulation of sufficient conditions for itinerant ferromagnetism is a classical and still unsolved problem. Thus, it is well known that the classical Stoner criterion leads to a significant (several times) overestimation of the Curie temperature and is based on the relation between the density of electronic states (DoES) at the Fermi level  $E_F$  in the paramagnetic phase and the parameter of the local Coulomb interaction  $U$ . Being a mean-field theory, the Stoner theory (and its dynamic counterpart, the random phase approximation (RPA), works much worse than the mean-field theory for the Heisenberg model, especially at finite temperatures. This is due to the neglecting of the influence of local and magnetic correlations and the competition of various electron scattering channels caused by the electron interaction. Different variants of taking into account local and spin fluctuations were carried out in the works of Hubbard and Korenman, but Moriya's theory, which allows to self-consistently describe the thermodynamics of spin fluctuations and the critical behavior of itinerant ferromagnets, is the most successful. Despite the significant improvement of the Moriya theory compared to RPA, it does not take into account the second important factor that can prevent the formation of ferromagnetic ordering, i.e., the competition of different scattering channels (in simple theories, the influence of other channels is taken into account through screening, which is not entirely inconsistent).

We have considered the formation of ferromagnetism (FCC) in the non-degenerate Hubbard model for a face-centered cubic lattice in the approximation of the first (hopping integral  $t$ ), second (integral  $t'$ ), and third (integral  $t''$ ) neighbors, and the ratio of these parameters is chosen so that the effective masses in the vicinity of the point L, the Brillouin zones were sufficiently large, which creates an extended van Hove singularity (vHS) in the DoES  $\rho(E)$ . The dependence of the

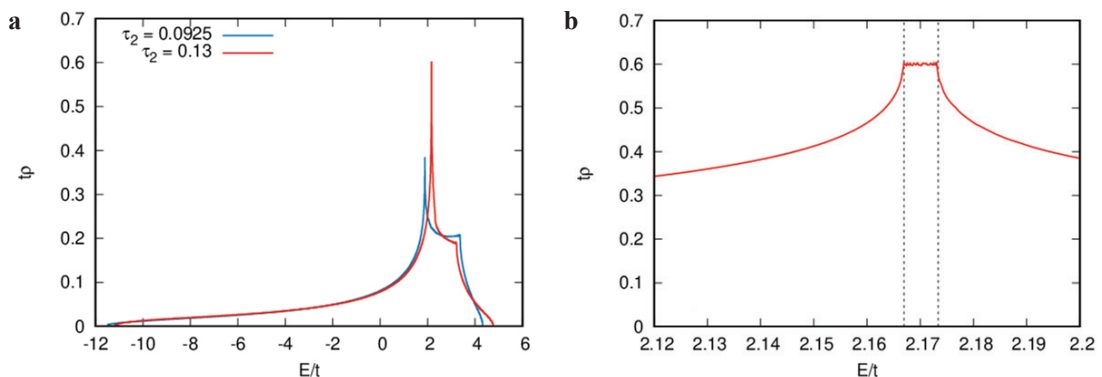


Figure 1. **a** DoES for FCC lattice at  $\tau_1 = -0.13$ ,  $\tau_2 = 0.0925$  и  $0.13$  in full energy interval; **b** this quantity in the vicinity of the peak  $\tau_2 = 0.13$ .

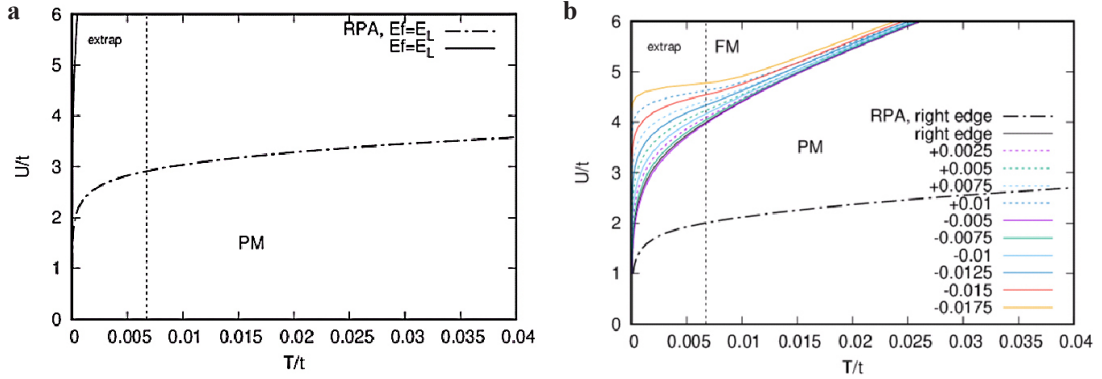


Figure 2. The phase diagram for ferromagnetic (FM)-paramagnetic (PM) transition in variables  $T_C-U$  obtained within one-loop fRG for  $\tau_1 = -0.13$  for different EF position. Dot-dashed line is FM-PM phase boundary in RPA approximation, solid black line corresponds to position  $E_F$  (a) at vHS, (b) at right edge of the plateau. a  $\tau_2 = +0.0925$ , b the Fermi level position measured from the right edge of the plateau is shown in the legend (dashed (solid) lines correspond to position of  $E_F$  to the left (right) of right plateau edge).

position of the vHSs of the electron spectrum on the transfer parameters  $\tau_1 = t'/t$ ,  $\tau_2 = t''/t$  was considered.  $\tau_1 = -0.13$  was chosen; (i) at  $\tau_2 = 0.0925$ , the vHS point L has two infinite effective masses; (ii) at  $\tau_2 > 0.0925$ , two van Hove points with very close energies  $E_1$  and  $E_2$  split off from the point L, between which the profile  $\rho(E)$  forms a plateau with a larger value of  $\rho(E)$  then in the case (i), see Fig. 1. In contrast to a single logarithmic peak of DoES in the case (i), the DoES peculiarity in the case (ii) is quite stable to changes of the spectrum parameters, see similar van Hove structures in ref. [1].

The temperature dependence of one-particle-irreducible (1PI) two-particle interaction vertices was studied within the framework of the functional renormalization group (fRG) method in the one-loop approximation [2], which allows to calculate directly the position of the Curie temperature  $T_C$  as a temperature of interaction vertex in magnetic channel turning to infinity. A phase diagram was constructed for the parameters corresponding to the formation of the logarithmic singularity of the DoES (case (i),  $\tau_2 = +0.0925$ ), and in the case (ii),  $\tau_2 = 0.13 > 0.0925$ , and the position of the Fermi level, which is at the level of the plateau and slightly to the left or to the right of it, see Fig. 2. In the case (i), the logarithmic singularity does not lead to the formation of ferromagnetic instability at not too low temperatures for the considered values of the parameter  $U$ ; in the case (ii), the formation of ferromagnetism is possible at not too low temperatures and moderate values of the parameter  $U$ .

Thus, for the formation of ferromagnetic ordering in the non-degenerate Hubbard model, it is necessary to have a sufficiently wide plateau in the density of electronic states (the giant van Hove singularity [1] can serve as an alternative), which significantly differs the situation from the two-dimensional case, see [3].

*The work was performed within the state assignment from the Ministry of Education of Russia (theme “Quant” AAAA-A18-118020190095-4) and partly supported by RFBR grant 20-02-00252a. The calculations were performed on the Uran supercomputer at the IMM UB RAS.*

1. P.A. Igoshev and V.Yu. Irkhin, *Physics of Metals and Metallography*, **120**, 1282–1290 (2019).
2. C. Husemann and M. Salmhofer, *Phys. Rev. B*, **79**, 195125 (2009).
3. A.A. Katanin and A.P. Kampf, *Phys. Rev. B*, **68**, 195101 (2003).

## ANISOTROPIC MAGNETORESISTANCE IN $RB_{12}$ ( $R = Ho, Er, Tm$ ) ANTIFERROMAGNETS WITH DYNAMIC CHARGE STRIPES

*K. Krasikov*<sup>1\*</sup>, *V. Glushkov*<sup>1</sup>, *S. Demishev*<sup>1</sup>, *A. Bogach*<sup>1</sup>, *A. Azarevich*<sup>1</sup>, *N. Shitsevalova*<sup>2</sup>,  
*V. Filipov*<sup>2</sup>, *S. Gabani*<sup>3</sup>, *K. Flachbart*<sup>3</sup>, *N. Sluchanko*<sup>1</sup>

<sup>1</sup>Prokhorov General Physics Institute of the Russian Academy of Sciences, Moscow, Russia

<sup>2</sup>Frantsevich Institute for Problems of Materials Science, National Academy of Sciences of Ukraine,  
Kyiv, Ukraine

<sup>3</sup>Institute of Experimental Physics, Slovak Academy of Sciences, Košice, Slovakia

\*E-mail: [krasikokirill@yandex.ru](mailto:krasikokirill@yandex.ru)

Rare Earth (RE) dodecaborides attract considerable attention, since, despite a relatively simple fcc lattice, some of them ( $HoB_{12}$ ,  $ErB_{12}$ ,  $TmB_{12}$ , etc.) exhibit a complex amplitude-modulated incommensurate  $4q$  antiferromagnetic (AF) structure in combination with electronic phase separation (dynamic charge stripes along the  $[110]$  direction) [1, 2]. Interplay between such instabilities often leads to a dramatic anisotropy of characteristics, so the study of scattering mechanisms of charge carriers in  $RB_{12}$  is of particular interest. Previously, it was shown [3] that in  $HoB_{12}$  the dependences of magnetoresistance (MR) on magnetic field  $\frac{\Delta\rho}{\rho}(H)$  can be described by a sum of linear positive and quadratic negative contributions

$$\frac{\Delta\rho}{\rho} = A(H - H_i) + B(H - H_i)^2,$$

where  $H_i$  are the magnetic field values of phase transitions between AF states with different magnetic structure that accompanied with sharp MR changes. The coefficients  $A$  and  $B$  determine different mechanisms of charge carrier scattering (i) by spin density waves and (ii) on local  $4f-5d$  spin fluctuations [3]. We performed here a comparative analysis with separation of MR contributions in the case of  $ErB_{12}$  and  $TmB_{12}$ , exploring the evolution of scattering mechanisms in dependence from temperature and applied magnetic field.

In the study we present results of field and angular dependences of resistivity of  $HoB_{12}$ ,  $ErB_{12}$  and  $TmB_{12}$  in the temperature range 1.7–10 K both in the paramagnetic and AF phases, in a magnetic field up to 80 kOe, directed along three principal directions in fcc lattice ( $\mathbf{H} \parallel [001]$ ,  $\mathbf{H} \parallel [110]$  and  $\mathbf{H} \parallel [111]$ ).

The observed strong anisotropy of the MR coefficients  $A$  and  $B$  of the linear and quadratic contributions, respectively, is extremely unusual for an fcc crystal. Since  $A$  and  $B$  values tied to the AF phase diagrams, we propose an explanation in terms of different magnetic ground states, which strongly depends of both strength and direction of an applied magnetic field  $\mathbf{H}$ . The origin of such a multicomponent phase diagram can presumably be related to the presence of dynamic charge stripes in the system with RKKY exchange, which lead to a renormalization of indirect exchange interaction (RKKY mechanism).

*This work was supported by the RSF grant № 22-22-00243.*

1. N.B. Bolotina et al., J. Phys. Condens. Matter, **30**(26), 265402 (2018).
2. N.E. Sluchanko et al., J. Phys. Condens. Matter, **31**, 065604 (2019).
3. K.M. Krasikov et al., Solid State Sci., **104**, 106253 (2020).

## MAGNETIC STATE OF $\text{Fe}_x\text{Mn}_{1-x}\text{S}$ , UNDER HYDROSTATIC AND CHEMICAL PRESSURE

*G. Abramova*<sup>1\*</sup>, *M. Boehm*<sup>2</sup>, *J. Schefer*<sup>3</sup>, *A. Piovano*<sup>2</sup>, *Yu. Knyazev*<sup>1</sup>, *O. Bajukov*<sup>1</sup>, *S.P. Kubrin*<sup>4</sup>

<sup>1</sup>Kirensky Institute of Physics, Federal Research Center KSC, SB RAS, Krasnoyarsk, Russia

<sup>2</sup>Institut Max von Laue – Paul Langevin, Grenoble, France

<sup>3</sup>Paul Scherrer Institute, CH-5232 Villigen, Switzerland

<sup>4</sup>Research Institute of Physics, Southern Federal University, Rostov-on-Don, Russia

E-mail: [agm@iph.krasn.ru](mailto:agm@iph.krasn.ru)

The  $\alpha$ -MnS-based  $\text{Fe}_x\text{Mn}_{1-x}\text{S}$  ( $0 < x < 0.3$ ) solid solutions are Mott materials with the rock salt structure. Investigation of such materials is interesting for both fundamental study of the interrelation between the magnetic, electrical, and structural properties in MnO-type strongly correlated electron systems and application. Pressure-induced metallization at hydrostatic and chemical pressure of these materials presented in [1]. Neutron diffraction data [3] show that the chemical-pressure ( $X$ ) induced Neel temperature shift from 150 ( $x = 0$ ) to  $200 \pm 5$  K ( $x = 0.29$ ) in these materials with a decrease in the NaCl-type cubic lattice parameters under ambient pressure. This indicates the enhancement of the superexchange interaction constant with decreasing distance between magnetic ions upon substitution of Fe for Mn. Below Neel temperature  $T_N$  similar to  $\alpha$ -MnS,  $\text{Fe}_x\text{Mn}_{1-x}\text{S}$  ( $0 < x < 0.3$ ) exhibit the FCC II (AFM-II) antiferromagnetic order with ferromagnetic (FM) sheets of the (111) planes antiferromagnetically stacked along the [111] direction of FCC NaCl lattice. With increasing of Fe-substitution the additional nonequivalent magnetic states of iron  $\text{Fe}^{2+}$  are appeared in the samples and its formed the magnetic structures which can be described by the propagation vectors:  $\mathbf{k}_1 = (1/2, 1/2, 1/2)$ ,  $\mathbf{k}_2 = (1/2, 1/2, 0)$ , and  $\mathbf{k}_3 = (1/2, 0, 0)$ . These data are correlated with the results of the Mössbauer investigation [2]. Mössbauer spectra of  $\text{Fe}_x\text{Mn}_{1-x}\text{S}$  samples with  $0.12 \leq x \leq 0.29$  measured in the temperature range from 4.2 to 300 K were studied.  $\text{Fe}^{2+}$  ions were found to have a high-spin state in locally distorted octahedral positions of the solid solution. As the substitution degree grows in the paramagnetic state, the chemical shift decreases and a weak quadrupolar splitting of the main spectral line appears. In the samples with  $0.25 \leq x \leq 0.29$ , the chemical pressure leads to appearing of new  $\text{Fe}^{2+}$  states corresponding to the additional doublet with the IS value typical of LS  $\text{Fe}^{2+}$ . In the magnetically ordered phase of the sulfides  $\text{Fe}_x\text{Mn}_{1-x}\text{S}$  ( $0.12 \leq x \leq 0.29$ ), structural disorder increases as  $x$  grows, and this leads to formation of nonequivalent states with different values of the quadrupolar shift ( $\sim 2.5$ – $3.0$  mm/s) and hyperfine magnetic field ( $\sim 56$ – $95$  kOe). Increasing chemical pressure causes rotation of the magnetic moment, which is evidenced by the change in the polar angle  $\theta$  between the hyperfine magnetic field vector and the EFG axis from  $21^\circ$  for  $x = 0.12$  to  $33^\circ$  for  $x = 0.29$ . This is accompanied also by the change in the asymmetry parameter, which means that the symmetry of the lattice in the antiferromagnetic state is altered. The additional doublet in the semimetal samples with  $0.25 \leq x \leq 0.29$  is nonmagnetic in the whole studied temperature range.

The results of the neutron diffraction investigations of the magnetic state with the propagation vector  $\mathbf{k}_1 = (1/2, 1/2, 1/2)$ , typical for  $\alpha$ -MnS, under hydrostatic pressures up to 42 kbar in the temperature range from 65 to 300 K [4] for  $x = 0.27$  presented on Fig. 1. The Néel temperature of the  $\text{Fe}_x\text{Mn}_{1-x}\text{S}$  ( $x \sim 0.27$ ) sample at ambient pressure  $T_N = 205 \pm 5$  K. The shift of the Néel temperature up to  $280 \pm 5$  K was detected with increasing pressure up to 42 kbar (4.2 GPa). The mechanism of the increase in the Néel temperature can be associated with a NaCl-lattice compression and an

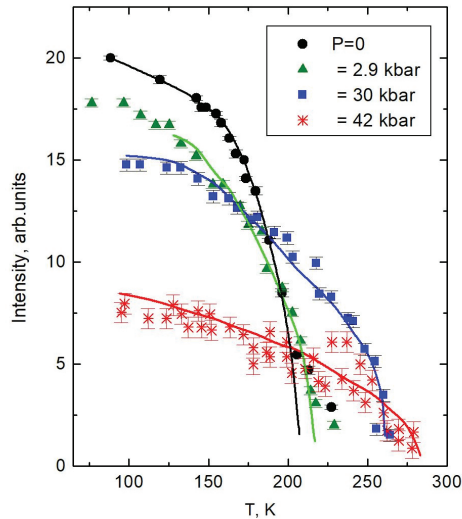


Figure 1. Change of integral intensity  $|F_{\text{mag}}|$  of the sublattice magnetization with  $k1 = (1/2, 1/2, 1/2)$  of  $\text{Fe}_x\text{Mn}_{1-x}\text{S}$  ( $x \sim 0.27$ ) under hydrostatic pressure up to 42 kbar.

increase in the exchange integral due to the increase in the degree of covalence and the metallization. Additional (see Fig. 1), we found a decrease in the sublattice magnetization ( $|F_{\text{mag}}| \sim \sqrt{I}$ ,  $I$  is the peak intensity) with increasing of hydrostatic pressure for  $\text{Fe}_x\text{Mn}_{1-x}\text{S}$ . For example, at 100 K the magnetization of the sample decreases nonlinearly by a factor of 2.5 with increasing pressure up to 42 kbar (4.2 GPa). Taken in to account the Mössbauer data [2], according which the chemical pressure leads to appearing of new  $\text{Fe}^{2+}$  states with the IS value typical of LS  $\text{Fe}^{2+}$ , we can supposed that the  $\text{Mn}^{2+}$  ions also have the coexistence of the HS and LS states with increasing of hydrostatic pressure due to spin crossover. For pure  $\alpha\text{-MnS}$  the spin state of  $\text{Mn}^{2+}$  ions is changed from HS to LS continuously in the pressure range from 10 to 40 GPa (400 kbar) [5].

*We acknowledge the beam time used at DIA and IN8 of the Institut Laue–Langevin Grenoble (ILL) and the single instrument ZEBRA at the Swiss Spallation Neutron Source SINQ/Paul Scherrer Institut, Villigen PSI. This study was in part supported by the INTAS project no. 06-100013-9002 and the CRDF-SB RAS project no. RUP1-7054-KR-11, N 16854.*

1. G.M. Abramova, A. Hanzawa, T. Kagayama, Y. Mita et al., *J. Mag. Mag. Mat.*, **465**, 775 (2018).
2. G.M. Abramova, Yu.V. Knyazev, O.A. Bayukov, S.P. Kubrin, *Physics of the Solid State*, **63**, 68 (2021).
3. G. Abramova, J. Schefer, N. Aliouane, M. Boehm et al., *J. Alloys and Compounds*, **632**, 563 (2015).
4. G. Abramova, M. Boehm, J. Schefer, A. Piovano et al., *JETP Letters*, **106**, 498 (2017).
5. Y. Wang, L. Bai, T. Wen, et al., *L. Angew. Chem. Int. Ed.*, **55**, 10350 (2016).

## AB INITIO STUDY OF PHYSICAL PROPERTIES OF MAGNETIC TETRABORATE CRYSTALS $\text{FeB}_4\text{O}_7$ AND $\text{MnB}_4\text{O}_7$

A.S. Shinkorenko

Kirensky Institute of Physics, Federal Research Center KSC SB RAS, Krasnoyarsk, Russia

E-mail: [shas@iph.krasn.ru](mailto:shas@iph.krasn.ru)

Borate compounds have a huge number of diverse crystal structures [1–4]. This diversity is explained by the variability of the boron-oxygen group; their basis is the structural elements  $-\text{BO}_3$  triangles and  $-\text{BO}_4$  tetrahedra. Depending on the structure formed, the physical parameters of the crystal vary considerably (hardness, optical and magnetic properties, etc.).

Depending on external effects tetraborates formed in structures with a symmetry group: *Pbca* ( $Z = 8$ ) and *Cmcm* ( $Z = 4$ ). The phase with the *Pbca* structure consists of  $-\text{BO}_3$  triangles and  $-\text{BO}_4$  tetrahedra in a 1:1 ratio, the phase with the *Cmcm* structure consist of tetrahedra only. The recently obtained  $\gamma\text{-NiB}_4\text{O}_7$  [5] phase with the  $P6_322$  symmetry group is also consist of tetrahedra and is of particular interest, since the compounds in this phase can show magnetoelectric properties. The aim of the present research is to establish the ground magnetic state of tetraborates  $\text{FeB}_4\text{O}_7$  [6] and  $\text{MnB}_4\text{O}_7$  [4], to study the electronic and magnetic properties, including the behavior of these compounds under pressure, and to construct phase diagrams.

At Fig. 1 the network of magnetic atoms in *Pbca* and *Cmcm* tetraborate phases are shown. In both cases, the magnetic structure is unusual. In the *Pbca* phase each magnetic ion has three neighbors, which is extremely unusual. In the *Cmcm* phase, the magnetic atoms are ordered into layers of irregular honeycombs. The magnetic and electronic structure of tetraborate compounds in various structures were calculated and analyzed.

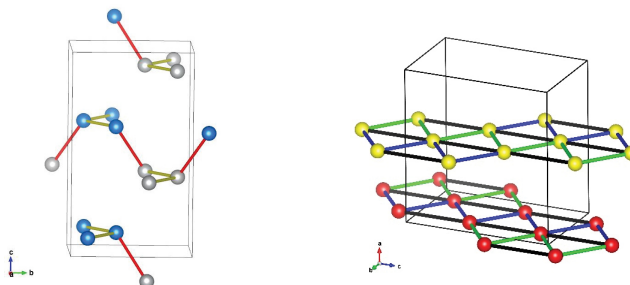


Figure 1. Network of magnetic atoms in compounds with space group *Pbca* and *Cmcm*.

The study was supported by the Russian Science Foundation grant No. 22-22-20024, <https://rscf.ru/project/22-22-20024/>.

1. P. Becker et al., *Adv. Mater.*, **10**, 13, 979 (1998).
2. M. Martinez-Rippol, S. Martinez-Carrera, S. Garcia-Blanco, *Acta Cryst.*, **B27**, 672 (1971).
3. R.D. Shannon et al., *Acta Cryst.*, **A32**, 751 (1976).
4. J.S. Knyrim et al., *Solid State Sciences*, **10**, 168 (2008).
5. M.K. Schmitt et al., *Inorg. Chem.*, **56**, 4217 (2017).
6. H. Huppertz, *Z. Anorg. Allg. Chem.*, 635 (2009).



**COMPETITIVE EFFECTS OF SUBSTITUTIONS  
 IN  $\text{La}_{1-x}\text{Sr}_x\text{Mn}_{0.9}(\text{Mg}_y\text{Ge}_z)_{0.1}\text{O}_{3+\gamma}$  SYSTEM**

*A.G. Badelin<sup>1\*</sup>, I.M. Derzhavin<sup>1</sup>, S.Kh. Estemirova<sup>2,1</sup>, V.K. Karpasyuk<sup>1</sup>*

<sup>1</sup>Astrakhan State University, Astrakhan, Russian Federation

<sup>2</sup>Institute for Metallurgy UB RAS, Ekaterinburg, Russian Federation

\*E-mail: alexey\_badelin@mail.ru

Structural, magnetic and electrical characteristics of  $\text{La}_{1-x}\text{Sr}_x\text{Mn}_{0.90}(\text{Mg}_{0.5}\text{Ge}_{0.5})_{0.10}\text{O}_{3+\gamma}$  ( $0.15 < x < 0.30$ ,  $\gamma = 0$ ,  $\gamma > 0$ ) and  $\text{La}_{0.91}\text{Sr}_{0.09}\text{Mn}_{0.90}\text{Mg}_{0.10}\text{O}_3$ ,  $\text{La}_{0.71}\text{Sr}_{0.29}\text{Mn}_{0.90}\text{Ge}_{0.10}\text{O}_3$  manganites are investigated.

Ceramic samples were sintered in air at 1473 K. They were then exposed to heat treatments at 1223 K and partial pressure of oxygen in the gas phase of  $P_{\text{O}_2} = 10^{-1}$  Pa and  $10^5$  Pa, which ensured the production of manganites with stoichiometric oxygen content ( $\gamma = 0$ ) and with  $\gamma > 0$  (containing cation vacancies), respectively. All synthesized manganites have rhombohedral crystal structure.

The values of non-stoichiometry index ( $\gamma$ ) of the studied samples are calculated from the data on unit cell volume according to algorithm proposed earlier [1, 2]. As follows from Table 1, the content of superstoichiometric oxygen and, accordingly, concentration of cation vacancies in manganites annealed in oxygen rise with an increase in Sr amount.

Table 1. Unit cell volume ( $V$ ) and non-stoichiometry index ( $\gamma$ ) of manganites: I – stoichiometric samples ( $\gamma = 0$ ); II – samples annealed in oxygen.

Compositions	I	II	
	$V, \text{Å}^3$	$V, \text{Å}^3$	$\gamma$
$\text{La}_{0.85}\text{Sr}_{0.15}\text{Mn}_{0.90}(\text{Mg}_{0.5}\text{Ge}_{0.5})_{0.10}\text{O}_{3+\gamma}$	354.619	353.197	0.021
$\text{La}_{0.83}\text{Sr}_{0.17}\text{Mn}_{0.90}(\text{Mg}_{0.5}\text{Ge}_{0.5})_{0.10}\text{O}_{3+\gamma}$	353.961	352.800	0.017
$\text{La}_{0.81}\text{Sr}_{0.19}\text{Mn}_{0.90}(\text{Mg}_{0.5}\text{Ge}_{0.5})_{0.10}\text{O}_{3+\gamma}$	353.569	352.783	0.012
$\text{La}_{0.70}\text{Sr}_{0.30}\text{Mn}_{0.90}(\text{Mg}_{0.5}\text{Ge}_{0.5})_{0.10}\text{O}_{3+\gamma}$	350.723	350.057	0.010

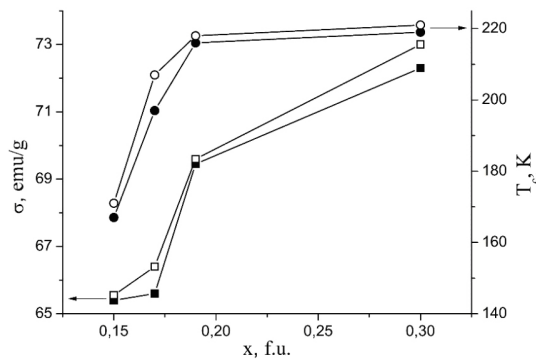


Figure 1. Dependencies of specific magnetization ( $\blacksquare$ ,  $\square$ ) and Curie point ( $\bullet$ ,  $\circ$ ) of  $\text{La}_{1-x}\text{Sr}_x\text{Mn}_{0.90}(\text{Mg}_{0.5}\text{Ge}_{0.5})_{0.10}\text{O}_{3+\gamma}$  manganites on the concentration of Sr: black symbols – stoichiometric samples, light symbols – samples annealed in oxygen.

Table 2. Parameters of manganites with double and mono-substitution for manganese.

No.	Stoichiometric samples	$\sigma$ , emu/g	$T_c$ , K
1	$\text{La}_{0.810}\text{Sr}_{0.190}\text{Mn}_{0.190}^{4+}\text{Mn}_{0.710}^{3+}(\text{Mg}_{0.5}^{2+}\text{Ge}_{0.5}^{4+})_{0.100}\text{O}_3$	68.5	216
2	$\text{La}_{0.910}\text{Sr}_{0.090}\text{Mn}_{0.190}^{4+}\text{Mn}_{0.710}^{3+}\text{Mg}_{0.100}^{2+}\text{O}_3$	61.0	171
3	$\text{La}_{0.710}\text{Sr}_{0.290}\text{Mn}_{0.190}^{4+}\text{Mn}_{0.710}^{3+}\text{Ge}_{0.100}^{4+}\text{O}_3$	76.7	263
4	$\text{La}_{0.810}\text{Sr}_{0.190}\text{Mn}_{0.190}^{4+}\text{Mn}_{0.710}^{3+}(\text{Zn}_{0.5}^{2+}\text{Ge}_{0.5}^{4+})_{0.100}\text{O}_3$	70.8	229

Table 3. Activation energy of conductivity ( $E_{act}$ ) and maximum resistivity ( $\rho_{max}$ , at  $T = 123$  K) of stoichiometric samples (I) and annealed in oxygen ones (II).

Compositions	$E_{act}$ , eV		$\rho_{max}$ , kOhm·cm	
	I	II	I	II
$\text{La}_{0.850}\text{Sr}_{0.150}\text{Mn}_{0.900}\text{Mg}_{0.050}\text{Ge}_{0.050}\text{O}_{3+\gamma}$	0.10	0.05	11.3	0.57
$\text{La}_{0.830}\text{Sr}_{0.170}\text{Mn}_{0.900}\text{Mg}_{0.050}\text{Ge}_{0.050}\text{O}_{3+\gamma}$	0.09	0.04	4.1	0.30
$\text{La}_{0.810}\text{Sr}_{0.190}\text{Mn}_{0.900}\text{Mg}_{0.050}\text{Ge}_{0.050}\text{O}_{3+\gamma}$	0.07	0.02	1.6	0.12

Specific magnetization ( $\sigma$ ) in magnetic field of 5600 Oe and Curie point ( $T_c$ ) of these manganites increase as a function of strontium content (Fig. 1), and the samples annealed in oxygen have higher values of magnetic parameters than stoichiometric ones.

Properties of  $\text{La}_{0.81}\text{Sr}_{0.19}\text{Mn}_{0.19}^{4+}\text{Mn}_{0.71}^{3+}(\text{Mg}_{0.5}^{2+}\text{Ge}_{0.5}^{4+})_{0.10}\text{O}_3$  manganite are compared with analogous parameters of  $\text{La}_{0.91}\text{Sr}_{0.09}\text{Mn}_{0.19}^{4+}\text{Mn}_{0.71}^{3+}\text{Mg}_{0.10}^{2+}\text{O}_3$ ,  $\text{La}_{0.71}\text{Sr}_{0.29}\text{Mn}_{0.19}^{4+}\text{Mn}_{0.71}^{3+}\text{Ge}_{0.10}^{4+}\text{O}_3$  and  $\text{La}_{0.81}\text{Sr}_{0.19}\text{Mn}_{0.19}^{4+}\text{Mn}_{0.71}^{3+}(\text{Zn}_{0.5}^{2+}\text{Ge}_{0.5}^{4+})_{0.10}\text{O}_3$  manganites having identical concentrations of substituents for Mn and equivalent concentrations of  $\text{Mn}^{4+}$ ,  $\text{Mn}^{3+}$  ions (Table 2). Composition of the sample No. 1 can be represented as a solid solution of compositions No. 2 and No. 3, and the values of  $\sigma$  and  $T_c$  calculated according to the additivity rule are close to the experimental values.

Zinc-containing manganite (No. 4) has higher magnetic parameters than magnesium-containing manganite (No. 1) of analogous composition, although ionic radius of  $\text{Zn}^{2+}$  (0.74 Å) is greater than the radius of  $\text{Mg}^{2+}$  (0.72 Å).

Manganites  $\text{La}_{1-x}\text{Sr}_x\text{Mn}_{0.9}(\text{Mg}_{0.5}\text{Ge}_{0.5})_{0.1}\text{O}_{3+\gamma}$  at  $0.15 \leq x \leq 0.19$  have semiconductor-type conductivity in the temperature range from 123 to 293 K. Activation energy of conductivity and maximum resistivity of stoichiometric and oxygen-annealed samples (Table 3) decrease with increasing strontium content, and manganites with superstoichiometric oxygen content have significantly lower  $E_{act}$  and  $\rho_{max}$  values.

In manganites  $\text{La}_{0.70}\text{Sr}_{0.30}\text{Mn}_{0.90}(\text{Mg}_{0.5}\text{Ge}_{0.5})_{0.10}\text{O}_{3+\gamma}$  there is a metal-semiconductor transition: at  $T = 186$  K in stoichiometric sample and at 179 K in manganite with  $\gamma = 0.01$ .

Peculiarities of the dependences of studied manganites properties on the composition are considered taking into account a number of competitive effects and factors [2]: influence of strontium, manganese substituents and oxygen content on the ratio of  $\text{Mn}^{4+}$ ,  $\text{Mn}^{3+}$  ions concentrations; violation of exchange bonds between  $\text{Mn}^{4+}$ ,  $\text{Mn}^{3+}$ ; role of cation vacancies; electron configuration, charge and radius of manganese substituents; inhomogeneous distribution of  $\text{Mg}^{2+}$  and  $\text{Ge}^{4+}$  ions, shielding of  $\text{Mn}^{4+}$  by magnesium ions.

1. D. Merkulov, A. Badelin, S. Estemirova and V. Karpasyuk, Acta Phys. Pol. A, **127**, 248–250 (2015).
2. V.K. Karpasyuk and A.G. Badelin, The Structure and Magnetic Characteristics of Lanthanum-Strontium Manganites with Substitution of Manganese by Different Valence Ions, IP Sorokin R.V., Astrakhan (2016) [in Russian].

## NEGATIVE PHOTOCONDUCTIVITY OF THE HETEROSTRUCTURE $\text{Ba}_{0.8}\text{Sr}_{0.2}\text{TiO}_3/\text{LaMnO}_3$

*A.O. Chibirev*<sup>1\*</sup>, *A.V. Leontiev*<sup>1</sup>, *N.N. Garig'yanov*<sup>1</sup>, *M.I. Bannikov*<sup>1,2</sup>, *R.F. Mamin*<sup>1</sup>

<sup>1</sup>Zavoisky Physical-Technical Institute, FRC Kazan Scientific Center, Russian Academy of Sciences, Kazan, Russia

<sup>2</sup>P.N. Lebedev Physical Institute, Moscow, Russia

\*E-mail: [chibirev12@mail.ru](mailto:chibirev12@mail.ru)

Unique properties of functional materials are achieved due to the effects associated with the complex composition of the interface structure. A high-mobility electron gas has been discovered at the interface between two oxide insulators  $\text{LaAlO}_3$  (LAO) and  $\text{SrTiO}_3$  (STO) [1]. The effect of infrared, green, and ultraviolet laser radiation on the electrical resistance of the heterostructure  $\text{Ba}_{0.8}\text{Sr}_{0.2}\text{TiO}_3/\text{LaMnO}_3$  was investigated here.

Dependencies of the electrical resistance on temperature were studied for  $\text{Ba}_{0.8}\text{Sr}_{0.2}\text{TiO}_3/\text{LaMnO}_3$  heterostructure and  $\text{Ba}_{0.8}\text{Sr}_{0.2}\text{TiO}_3/\text{LaMnO}_3/\text{Ba}_{0.8}\text{Sr}_{0.2}\text{TiO}_3$  on  $\text{MgO}$ -substrate heterostructure. An unfocused laser beam with a diameter of 4 mm, with a Gaussian shape, irradiated the space between the contact pads through the optical window of the cryostat. We observed an increase in resistance when exposed to light at all wavelengths used and a recovery of resistance in the dark state. In 80-200K range this transient component is positive and up to 15% of the steady-state resistance, the time constant associated with the transient component is ~4–20 s. The response to green light exposure was the most prominent. It was found that when illuminated with light of different wavelengths, there was a cumulative effect, a change in resistance over several on/off cycles green and infrared light. The observed effect cannot be explained by direct heating of the sample by laser pulses, because the laser pulse repetition rate is low and, therefore, the cumulative thermal effects should be negligible. This example shows that quasi-two-dimensional high conductance at ferroelectric/dielectric interfaces can be controlled by a relatively simple technique.

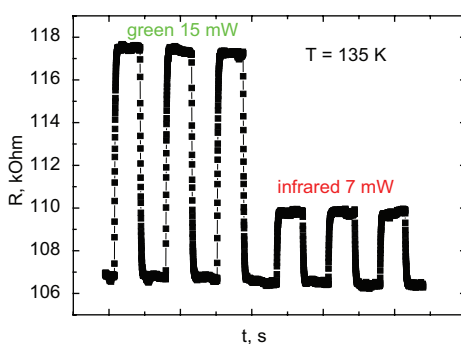


Figure 1. Multiple on-off switching of electrical resistance of the  $\text{Ba}_{0.8}\text{Sr}_{0.2}\text{TiO}_3/\text{LaMnO}_3$  heterostructure at 135 K by green and infrared illumination.

*The Hall measurement was done at P.N. Lebedev Physical Institute. The main reported study was funded by Russian Science Foundation according to the research project No. 21-12-00179.*

1. A. Ohtomo and H. Y. Hwang, *Nature*, **427**, 423 (2004).

## DIAMIC AND STATIC PROPERTIES OF A NON-HEISENBERG FERRIMANET WITH A SINGLE-ION ANISOTROPY

*O.A. Kosmachev, Ya.Yu. Matyunina\*, Yu.A. Fridman*

Institute of Physics and Technology, V.I. Vernadsky Crimean Federal University, Simferopol,  
 Republic of Crimea, Russian Federation

\*E-mail: [yurifridman@gmail.com](mailto:yurifridman@gmail.com)

In recent years, new and actively developing fields of applied magnetism physics, spintronics, and magnonics have emerged, which are based on the use of magnetic degrees of freedom of magnetically ordered crystals. To increase the speed of spintronics devices, the use of compensated magnets, primarily antiferromagnets, was proposed. However, antiferromagnets have a high sensitivity of the magnetic order to the presence of defects that violate the sublattice structure of the crystal sample. This fact makes it difficult to use them in spintronics. Consequently, ferrimagnets located near the compensation point can be used for various ultrafast spintronics devices [1]. Thus, the question of the properties of non-Heisenberg ferrimagnets, taking into account the influence of one-ionic anisotropy of the “easy plane” type, is not only of academic interest, but also of important applied importance.

In the mean field approximation, we consider a two-lattice anisotropic magnet with the magnetic ion spin of the first sublattice  $S = 1$  and the second one  $\sigma = 1/2$ , and a non-Heisenberg exchange interaction for the sublattice with  $S = 1$ . At the same time, the first sublattice takes into account both bilinear and biquadratic exchange interactions, as well as single-ionic anisotropy of the “light plane” type. The Hamiltonian of such a system can be represented as:

$$H = -\frac{1}{2} \sum_{n,n'} [J^{(2)}(n-n')(\mathbf{S}_n \mathbf{S}_{n'}) + K(n-n')(\mathbf{S}_n \mathbf{S}_{n'})^2] - \frac{1}{2} \sum_{m,m'} J^{(1)}(m-m')(\sigma_m \sigma_{m'}) - \frac{1}{2} \sum_{n,m} A(n-m)(\sigma_m \mathbf{S}_n) + \frac{\beta}{2} \sum_n (S_n^x)^2,$$

where  $J^{(1)} > 0$  is the exchange interaction constant for a sublattice with spin  $\sigma = 1/2$ ;  $J^{(2)} > 0$ ,  $K > 0$  – constants of bilinear and biquadratic exchange interactions for  $S = 1$ ;  $A < 0$  – intersublattice interaction constant,  $\beta > 0$  – single-ion anisotropy constant of the “easy plane” type (ZOY basal plane). The consideration is carried out for low temperatures ( $T \ll T_N$ ,  $T_N$  – the Néel temperature).

The studies performed have shown that taking into account even a small single-ion anisotropy of the “easy plane” type in a non-Heisenberg ferrimagnet with sublattices  $S = 1$  and  $\sigma = 1/2$  leads to coordinate changes in both the static and dynamic properties of the system, in comparison with the case of an isotropic non-Heisenberg ferrimagnet [2, 3]. In an anisotropic non-Heisenberg ferrimagnet, depending on the ratios of the exchange integrals, it is possible to realize both a phase characterized by a dipole order parameter (FiM phase) and a phase characterized by both vector and tensor order parameters (QFiM phase). However, in contrast to the isotropic case, the region of existence of the QFiM phase increases, which is associated with the influence of single-ion anisotropy, which, like the biquadratic exchange interaction, tends to establish a quadrupole (or nematic) order.

In addition, as shown by the thermodynamic analysis of the free energy and the analysis of the spectra of elementary excitations, taking into account single-ion anisotropy leads to the fact that the QFiM–FiM phase transition is a first-order transition, in contrast to the case of an isotropic ferrimagnet, in which a similar phase transition is a second-order transition. We have also shown that

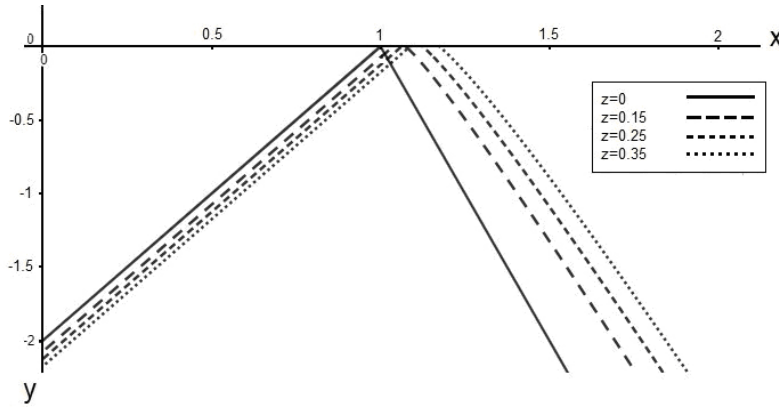


Figure 1. Cross section of the phase diagram of an easy-plane non-Heisenberg ferrimagnet for different values of the single-ion anisotropy constant.

in the vicinity of the sublattice spin compensation line, the spectrum of “longitudinal” excitations has an “antiferromagnetic” behavior.

It should be noted that our results are consistent with the results of studies in which the properties of isotropic and exchange-anisotropic non-Heisenberg ferrimagnets with  $S = 1$  and  $\sigma = 1/2$  sublattices were studied. As noted earlier, taking into account the easy-plane single-ion anisotropy in the sublattice with  $S = 1$  significantly expands the stability region of the QFiM phase in comparison with an isotropic ferrimagnetic, and, most interestingly, makes the QFiM-FiM transition a first-order phase transition.

1. B.A. Ivanov and A.L. Sukstanski, Zh. Eksp. Teor. Fiz., **84**, 370 (1983).
2. A.V. Krivtsova, Ya.Yu. Matyunina, E.A. Polyanskaya, O.A. Kosmachev, Yu.A. Fridman, JMMM, **513**, 167178 (2020).
3. A.V. Krivtsova, Ya. Yu. Matyunina, and Yu. A. Fridman JETP, **131**, 302 (2020).

## ANISOTROPIC THERMAL EXPANSION IN $\text{Co}_3\text{BO}_5$ LUDWIGITE

*Yu.S. Gokhfeld*<sup>1\*</sup>, *N.V. Kazak*<sup>1</sup>, *M.S. Molokeev*<sup>1</sup>, *V.A. Dudnikov*<sup>1</sup>, *L.A. Solovyov*<sup>2</sup>,  
*S.G. Ovchinnikov*<sup>1</sup>

<sup>1</sup>Kirensky Institute of Physics, Federal Research Center KSC SB RAS, Krasnoyarsk, Russia

<sup>2</sup>Institute of Chemistry and Chemical Technology, Federal Research Center KSC SB RAS Krasnoyarsk, Russia

\*E-mail: [gokhfeld@kirensky.ru](mailto:gokhfeld@kirensky.ru)

Recently, it was found that the oxyborate  $\text{Co}_3\text{BO}_5$  undergoes a spin-state transformation of a  $\text{Co}^{3+}$  ion [1]. The compound has orthorhombic symmetry with space group  $Pbam$  (No. 55) and belongs to the ludwigite borate family. The crystal structure consists of a network of edge-sharing octahedra and planar  $\text{BO}_3$  triangles, lying in the  $ab$ -plane. The cobalt ions are located at non-equivalent positions M1 (2a), M2 (2b), M3 (4g), and M4 (4h) (Fig. 1). Although the spin-state crossover provides the essential features for understanding the magnetic behavior of  $\text{Co}_3\text{BO}_5$  [2, 3], its impact on the electronic properties and charge ordering is still unclear, as well as the exact nature of the local mechanisms responsible for these transitions.

In the present work the crystal structure of  $\text{Co}_3\text{BO}_5$  was investigated using powder X-ray diffraction at high temperatures. The orthorhombic symmetry (Sp. gr.  $Pbam$ ) was established at 300 K and no evidence of structural phase transitions was found up to 1000 K. The compound shows a strong anisotropy of the thermal expansion. A large negative thermal expansion along the  $a$ -axis is observed over a wide temperature range ( $T = 300\text{--}600$  K) with  $\alpha_a = -35 \text{ MK}^{-1}$  at  $T = 500$  K. It is accompanied simultaneous expansion along  $b$ - and  $c$ -axis with  $\alpha_b = 70 \text{ MK}^{-1}$  and  $\alpha_c = 110 \text{ MK}^{-1}$ , respectively (Fig. 2).

The present study revealed that the ludwigite framework can be considered as infinite  $[\text{Co}^{2+}\text{O}_6]_\infty$  layers along the  $bc$  plane, connecting along  $a$ -axis via the intermediated  $\text{BO}_3$  and  $\text{M4O}_6$  polyhedra (Fig. 1). This consideration differs from the well-known representation of the zigzag walls formed by the edge-sharing metal-oxygen octahedra, but it adequately describes the crystal structure behaviour upon heating. The strong anisotropy of the thermal expansion can be explained by the orientation of the rigid  $\text{BO}_3$  triangles and flexibility of  $[\text{Co}^{2+}\text{O}_6]_\infty$  framework. The decrease of the bond-angles involving the M4 site correlates with the negative thermal expansion along  $a$ -axis, assuming the crucial role of the given metal site in the anomalous thermal expansion of the ludwigites.

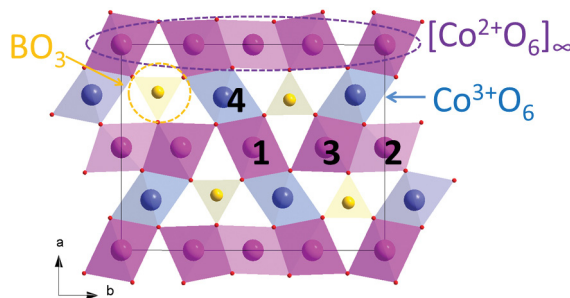


Figure 1. The crystal structure of  $\text{Co}_3\text{BO}_5$  presented in the  $ab$ -plane. The  $[\text{Co}^{2+}\text{O}_6]_\infty$  layers in the  $bc$  plane are shown by pink. The planar  $\text{BO}_3$  triangles and  $\text{Co}^{3+}\text{O}_6$  octahedra are shown by yellow and blue, respectively. The numbers correspond to the symmetry non-equivalent metal sites.

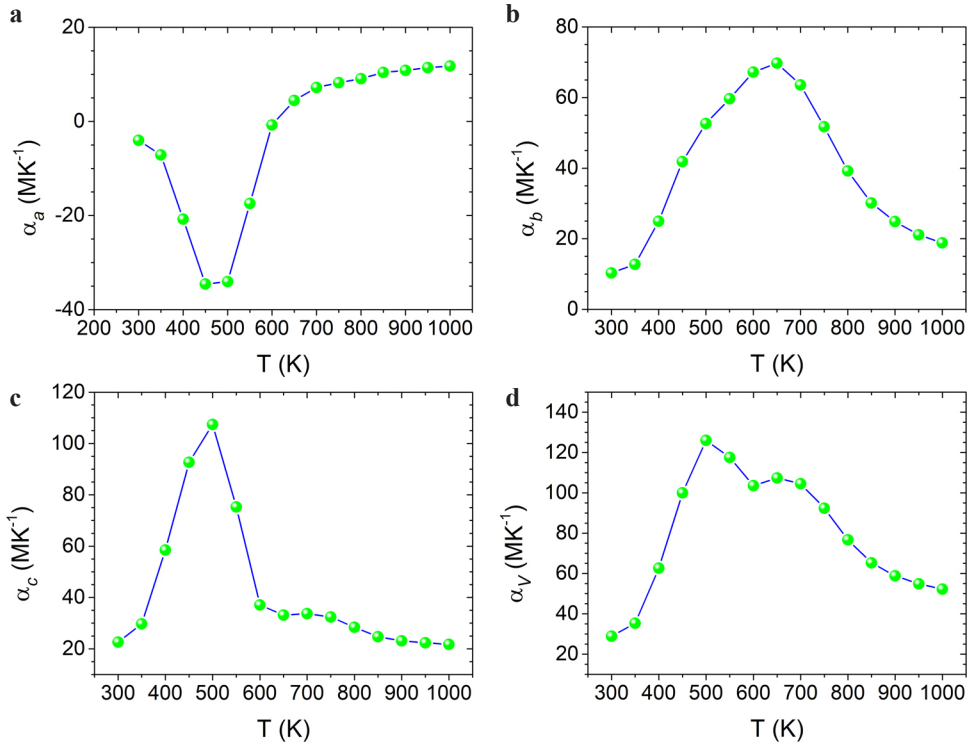


Figure 2. **a–c** Thermal expansion coefficients of *a*-, *b*-, and *c*-lattice parameters and **d** unit cell volume of  $\text{Co}_3\text{BO}_5$  as a function of the temperature.

A strong interrelation of the crystal structure and electronic properties was found. We conclude that with the temperature increase, the lattice parameters are changed not only due to conventional thermal expansion, but also due to the electronic processes associated with the spin-state and charge-ordering transitions.

*Support by RFBR 20-02-00559 and 21-52-12033 HHIIO\_a is acknowledged.*

1. N.V. Kazak, M.S. Platonov, Yu.V. Knyazev, M.S. Molokeev, M.V. Gorev, S.G. Ovchinnikov, Z.V. Pchelkina, V.V. Gapontsev, S.V. Streltsov, J. Bartolomé, A. Arauzo, V.V. Yumashev, S.Yu. Gavrilkin, F. Wilhelm, and A. Rogalev, *Phys. Rev. B*, **103**, 094445 (2021).
2. C.W. Galdino, D.C. Freitas, C.P.C. Medrano, R. Tartaglia, D. Rigitano, J.F. Oliveira, A.A. Mendonça, L. Ghivelder, M.A. Continentino, D.R. Sanchez, and E. Granado, *Phys. Rev. B*, **100**, 165138 (2019).
3. C.W. Galdino, D.C. Freitas, C.P.C. Medrano, D.R. Sanchez, R. Tartaglia, L.P. Rabello, A.A. Mendonça, L. Ghivelder, M.A. Continentino, M.J.M. Zapata, C.B. Pinheiro, G.M. Azevedo, J.A. Rodríguez-Velamazán, G. Garbarino, M. Núñez-Regueiro, and E. Granado, *Phys. Rev. B*, **104**, 19515 (2021).

## A THEORY OF MAGNETIC PHASE SEPARATION IN METALS AND ITS IMPACT ONTO THE MAGNETOCALORICAL EFFECT

*P.A. Igoshev*

Institute of Metal Physics, Ekaterinburg, Russia

Ural Federal University, Ekaterinburg, Russia

E-mail: [igoshev\\_pa@imp.uran.ru](mailto:igoshev_pa@imp.uran.ru)

Magnetocalorical effect (MCE) attracts a lot of attention in the last decade due to its possible technological applications for perspective use in refrigeration based on the new grounds. Despite intensive experimental and theoretical investigations in the past a lot of its aspects are still unclear. One of such aspects is a correct explanation of first-order transitions thermodynamics and corresponding phase separation caused by these transitions in the context of MCE.

A great scientific interest is devoted to compounds, where a ferromagnetic order coexists with antiferromagnetic (AFM) one. A coexistence can be achieved in two ways, they either join forming ferrimagnetic order, or sample spatially separates in two distinct phases (or both ways simultaneously). There are many materials exhibiting a ferrimagnetic order:  $\text{Ni}_{45}\text{Co}_5\text{Mn}_{37}\text{In}_{13}$ ,  $\text{MnRhAs}$ ,  $\text{Ni}_{1.68}\text{Co}_{0.32}\text{Mn}_{1.20}\text{Ga}_{0.8}$  or phase separation (PS):  $\text{MnFeP}_{0.8}\text{Ge}_{0.2}$  (PM–FM phase separation),  $\text{La}_{0.27}\text{Nd}_{0.40}\text{Ca}_{0.33}\text{MnO}_3$  (FM–charge-order phase separation),  $\text{Mn}_{0.99}\text{Cu}_{0.01}\text{As}$ ,  $\text{Gd}_5\text{Ge}_{2.3}\text{Si}_{1.7}$  (FM–AFM phase separation).

The origin of magnetic first-order transition in metals can be very different: accompanying structural phase transition, van Hove singularities of the electronic spectrum and a competition of magnetically ordered phase with antiferromagnetic one. All these cases have a common consequence, magnetic phase separation due to redistribution of itinerant electrons of competing phases which are connected by a common Fermi level. However a response for phases participating in PS onto an applying a magnetic field can be very different. Net MCE effect is in this case equal to weighed sum of separate phase contributions with weights proportional to volume of each phase.

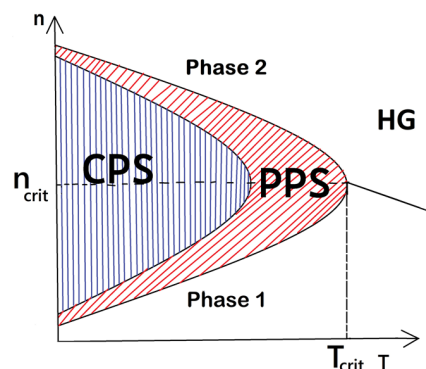


Figure 1. Schematic representations of a vicinity of a tricritical point ( $n_{\text{crit}}$ ,  $T_{\text{crit}}$ ) on the phase diagram in terms of temperature ( $T$ )–filling ( $n$ ): CPS – phase separation region “Phase 1 + Phase 2” in both zero and finite magnetic field, PPS – phase separation only exists in finite or zero magnetic field, HG – homogeneous phase (phase 1 or phase 2) in both zero and finite magnetic field. Black line corresponds to a 2nd order transition between Phase 1 and Phase 2.



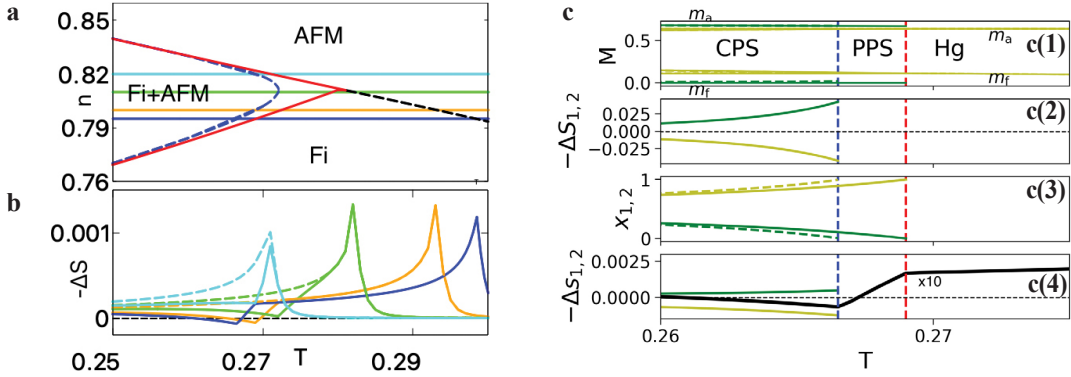


Figure 2. The results for the Hubbard model on a Bethe lattice at  $U = W$ ,  $W$  being a bandwidth. **a** Phase diagram corresponding to the vicinity of tricritical point; horizontal lines:  $n = 0.795$ ,  $n = 0.80$ ,  $n = 0.81$ ,  $n = 0.82$ . **b**  $\Delta S(T)$  for a fixed filling, line colors correspond to horizontal lines above. Dashed lines represent calculations without accounting for phase separation. **c** Temperature dependence of phase quantities for  $n = 0.795$ . Green lines correspond to AFM phase, yellow lines correspond to ferrimagnetic phase. Blue vertical dashed line corresponds to transition in homogeneous state in finite magnetic field, red vertical dashed line corresponds to transition in homogeneous phase in  $h = 0$ . **c(1)** Magnetization amplitudes, dashed lines correspond to finite magnetic field; **c(2)**  $\Delta S_{\text{AFM}\rightarrow\text{Fi}}$ ; **c(3)** phase volumes  $x_{\text{AFM}}$ ,  $x_{\text{Fi}}$ ; dashed lines correspond to finite magnetic field; **c(4)** black color  $\Delta S \cdot 10$ , and differences in specific phase entropies  $\Delta S_{\text{AFM}\rightarrow\text{Fi}}$ .

We show analytically that magnetically ordered phase typically exhibits inverse MCE contribution in the vicinity of tricritical point.

Schematic phase diagram in the vicinity of tricritical point, where the phase transition changes its order is shown in Fig. 1. An applying of the magnetic field shifts the boundaries of PS occurring as a consequence of first-order transition.

We derive a consistent treatment of MCE with an account of PS within the framework of Hubbard model [1, 2] on the square and Bethe lattice. It is found that an account of phase separation substantially changes a MCE behavior. A temperature region of partial phase separation occurs with drastically different MCE behavior compared with typical behavior for the vicinity of second order phase transition. We found that phases participating in PS exhibit entropy change  $\Delta S$  of different sign (inverse effect – magnetically ordered phase, direct effect – non-magnetic phase), see details in Fig. 2 and ref. [3].

*The work was partly supported by RSF grant 18-72-10098. The calculations were performed on the Uran supercomputer at the IMM UB RAS.*

1. P.A. Igoshev, M.A. Timirgazin, A.A. Katanin, A.K. Arzhnikov, and V.Y. Irkhin, Phys. Rev. B, **81**, 094407 (2010).
2. P.A. Igoshev, M.A. Timirgazin, V.F. Gilmutdinov, A.K. Arzhnikov, and V.Y. Irkhin, Journal of Physics: Condensed Matter, **27**, 446002 (2015).
3. V.V. Ivchenko and P.A. Igoshev, Phys. Rev. B, **104**, 024425 (2021).

**MAGNETIC PROPERTIES OF  $\text{Fe}_{1.21}\text{Ga}_{0.79}\text{O}_3$**

*I.V. Yatsyk*<sup>1\*</sup>, *R.M. Eremina*<sup>1</sup>, *E.M. Moshkina*<sup>2</sup>

<sup>1</sup>Zavoisky Physical-Technical Institute, FRC Kazan Scientific Center, Russian Academy of Sciences, Kazan, Russia

<sup>2</sup>Kirensky Institute of Physics, Federal Research Center KSC SB RAS, Krasnoyarsk, Russia

\*E-mail: [I.Yatsyk@gmail.com](mailto:I.Yatsyk@gmail.com)

The multiferroic materials, which exhibit coexistence and coupling of magnetic and electric orders, have emerged as promising candidates for basic understanding of the coupling between magnetic and electronic properties and uses of the materials in magnetoelectric devices, such as memory, logic devices, sensors, and voltage-driven magnetic tunnel junctions [1–6]. The integration of naturally existing or artificially designed multiferroic materials into devices opens up a new field to achieve the energy-saving and miniaturization of the devices [7]. Some transition metal oxides ( $\text{BiFeO}_3$ ,  $\text{TbMnO}_3$ ,  $\text{BiMnO}_3$ ,  $\text{HoMnO}_3$ ,  $\text{DyFeO}_3$ , and  $\text{GaFeO}_3$ ) have shown multiferroic properties [1–7] and majority of these oxides showed magnetic order at low temperatures.

The aim of this work is to study by ESR, magnetometry methods magnetic properties of  $\text{Fe}_{1.21}\text{Ga}_{0.79}\text{O}_3$ . The angular dependence of the ESR linewidth and the resonant field is shown in Fig. 1. At 70 °C, there is a sharp increase in the ESR linewidth and resonant field up to 700 mT. We believe that this is the ferromagnetic lines.

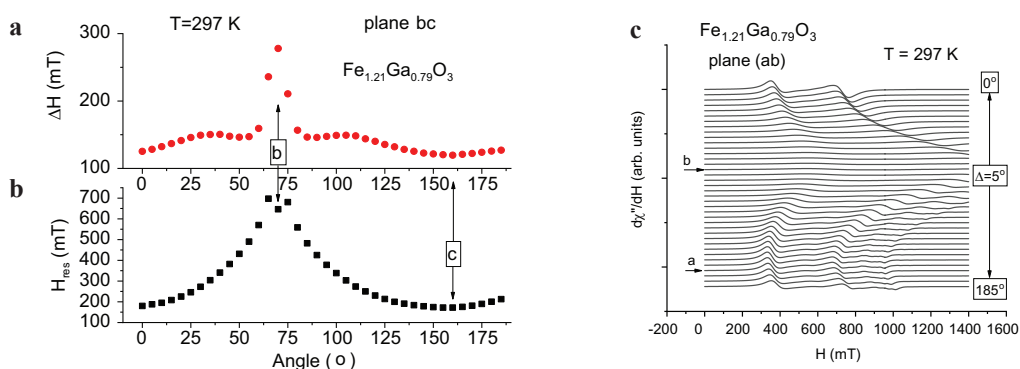


Figure 1. Angular dependence of the ESR linewidth (a) and resonance field (b) for  $\text{Fe}_{1.21}\text{Ga}_{0.79}\text{O}_3$  at room temperature (297 K) in the (bc) plane, (c) dependence of magnetic resonance spectra from angle in (ab) plane.

*I.V.Y. and R.M.E. acknowledge the financial support from the government assignment for FRC Kazan Scientific Center of RAS.*

1. A.G. Lone, R.N. Bhowmik, Journal of Alloys and Compounds, **905**, 164164 (2022).
2. M. Fiebig, T. Lottermoser, D. Meier, M. Trassin, Nat. Rev. Mater., **1**, 16046 (2016).
3. C. Lu, M. Wu, L. Lin, J.M. Liu, Natl. Sci. Rev., **6**, 4 (2019).
4. N.A. Spaldin, Proc. R. Soc. A, **476**, 20190542 (2020).
5. G. Catalan, J.F. Scott, Adv. Mater., **21**, 2463–2485 (2009).
6. Y.J. Wang, J.F. Li, D. Viehland, Mater. Today, **17**, 269–275(2014).
7. A.P. Pyatakov, A.K. Zvezdin, Phys. Usp., **55**, 557–581 (2012).

## IMPURITY FERROMAGNETISM IN Pd-Fe AND Pd-Co ALLOYS

*A.Y. Korableva*<sup>1\*</sup>, *I.I. Gumarova*<sup>1,2</sup>, *A.I. Gumarov*<sup>1,2</sup>, *I.V. Yanilkin*<sup>1,2</sup>, *R.I. Khaibullin*<sup>2</sup>

<sup>1</sup>Institute of Physics, KFU, Kazan, Russia

<sup>2</sup>Zavoisky Physical-Technical Institute, FRC Kazan Scientific Center, Russian Academy of Sciences, Kazan, Russia

\*E-mail: [alkorablewa@yandex.ru](mailto:alkorablewa@yandex.ru)

The first studies of impurity ferromagnetism of strongly paramagnetic palladium were made in the middle of the XX century. It aroused a great interest among theoreticians and experimentalists since the effective magnetic moment per one magnetic impurity, for example, iron, turned out to be anomalously large, up to 12 Bohr magnetons [1–3]. The revival of interest in such alloys was associated with the possibility of their use as a weak bond in superconducting hybrid structures that are promising for cryoelectronic devices [4], as well as a weak ferromagnet in superconducting magnetic random-access memory (MRAM) based on Josephson junctions [5–8].

At present, most of the theoretical and experimental studies of such systems are devoted to the study of the properties of alloys with iron impurities. Also, the region of low impurity concentrations has not yet been sufficiently studied.

Recently, it was demonstrated that density functional theory (DFT) calculations can reproduce the main experimental results obtained for Pd<sub>1-x</sub>Fe<sub>x</sub> alloys [9]. The impurity of Fe induces ferromagnetism in the Pd matrix persists down to low concentrations ( $x = 0.03$ ).

In this work, we study and compare the structural and magnetic properties of Pd<sub>x</sub>A<sub>1-x</sub> alloys ( $x \leq 10$  at.%, A = Fe and Co) using computer simulation within DFT framework. Calculations of the magnetic properties for such systems have shown that impurity atoms have a significant effect on the magnetic properties of the palladium matrix. In particular, the maximum magnetization for the Pd<sub>1-x</sub>Co<sub>x</sub> system turned out to be ~12  $\mu$ B calculated per Co impurity atom at a concentration  $x = 0.03$ , while for the most studied Pd<sub>1-x</sub>Fe<sub>x</sub> alloy, the maximum value of magnetization was found to be ~8  $\mu$ B per iron atom at  $x = 0.07$ .

The calculation results were verified by experiment. Implantation of iron (Fe<sup>+</sup>) or cobalt (Co<sup>+</sup>) ions with various doses (which determine the impurity concentration) into Pd epitaxial films was carried out. Magnetic properties of implanted Pd films were investigated by Vibrating Sample Magnetometer (VSM) in the temperature range from 5 K to 300 K. It was found that the experimental data are in qualitative agreement with the ab initio calculations: the values of the magnetic moments for Pd films implanted with Fe<sup>+</sup> (and Co<sup>+</sup>) ions are close to the calculated values for the corresponding impurity concentrations.

*Experimental part of this work was supported by RFBR Grant No. 20-02-00981. Theoretical calculations were supported by the Kazan Federal University Strategic Academic Leadership Program (Priority-2030).*

1. J. Crangle, *Philos. Mag.*, **5**, 335–342 (1960).
2. G.J. Nieuwenhuys, *Adv. Phys.*, **24**, 515–591 (1975).
3. E.P. Wohlfarth, *Handbook of Magnetic Materials*, vol. 1, North-Holland Publishing Company: London, UK, p. 75 (1980).
4. A. Esmacili, I.V. Yanilkin, A.I. Gumarov, *Thin Solid Films*, **669**, 338–344 (2019).
5. V.V. Ryazanov, *Uspekhi Fiz. Nauk*, **42**, 825–827 (1999).
6. T.I. Larkin, V.V. Bol'ginov, V.S. Stolyarov et al., *Appl. Phys. Lett.*, **100**, 222601 (2012).
7. V.V. Ryazanov, V.V. Bol'ginov, D.S. Sobanin et al., *Phys. Procedia*, **36**, 35–41 (2012).
8. I.V. Vernik, V.V. Bol'ginov, S.V. Bakurskiy et al., *IEEE Trans. Appl. Supercond.*, **23**, 1701208 (2013).
9. I. Piyanzina, A. Gumarov, R. Khaibullin, L. Tagirov, *Crystals*, **11**, 1257 (2021).

**HYPERFINE INTERACTIONS IN HIGH-PRESSURE-SYNTHESIZED COMPOUNDS OF 3D-METALS WITH RARE-EARTH AND ALKALINE-EARTH ELEMENTS**

*M.V. Magnitskaya*<sup>1,2\*</sup>, *A.V. Bokov*<sup>1</sup>, *D.A. Salamatin*<sup>1</sup>, *N.M. Chtchelkatchev*<sup>1</sup>,  
*V.I. Krylov*<sup>3</sup>, *A.V. Tsvyashchenko*<sup>1</sup>

<sup>1</sup>Vereshchagin Institute of High Pressure Physics, RAS, Troitsk, Moscow, Russia

<sup>2</sup>Lebedev Physical Institute, RAS, Moscow, Russia

<sup>3</sup>Skobeltsyn Institute of Nuclear Physics, Lomonosov MSU, Moscow, Russia

\*E-mail: [magma@yandex.ru](mailto:magma@yandex.ru)

Topologically close-packed Laves phases with the general chemical formula AB<sub>2</sub> are rather common among intermetallic compounds. Materials based on them are used as containers for hydrogen storage, as magneto-mechanical sensors and drives, as well as for wear-resistant and corrosion-resistant coatings in aggressive environments and at high temperatures [1]. Here, we present a joint theoretical and experimental study of the magnetic properties and hyperfine interactions in the Laves-phase-based compounds R(T<sub>1-*x*</sub>T<sub>2-*x*</sub>)<sub>2</sub>, where R is an alkaline-earth or rare-earth element and T = Fe, Co, Ni. Several continuous series R(T<sub>1-*x*</sub>T<sub>2-*x*</sub>)<sub>2</sub> were synthesized under high pressure *P* ~ 8 GPa over a wide range of concentrations, 0 ≤ *x* ≤ 1 (the synthesis method is described, e.g., in [2]). The obtained phases are found to crystallize in a cubic structure of the MgCu<sub>2</sub> type (C15). Note that some of them can only be formed under high-pressure–high-temperature conditions relevant to the Earth interior.

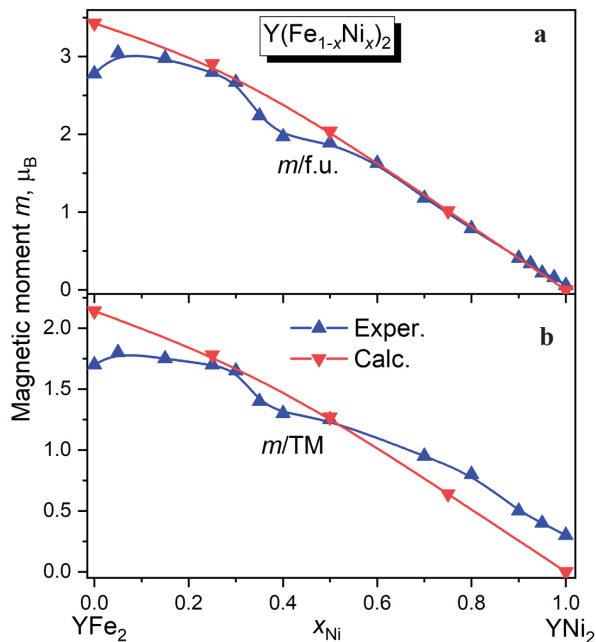


Figure 1. The measured (blue) and calculated (red) spin moment per formula unit (a) and per transition-metal atom (b) for Y(Fe<sub>1-*x*</sub>Ni<sub>*x*</sub>)<sub>2</sub>.

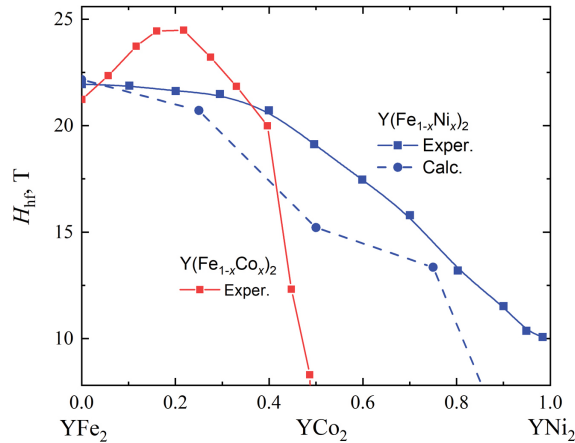


Figure 2. Variation of the hyperfine field at the iron nucleus,  $H_{\text{hf}}$ , with the Ni/Co concentration  $x$ : The experimental data for  $\text{Y}(\text{Fe}_{1-x}\text{Ni}_x)_2$  and  $\text{Y}(\text{Fe}_{1-x}\text{Co}_x)_2$  are shown in blue and red, respectively. The results of calculations for  $\text{Y}(\text{Fe}_{1-x}\text{Ni}_x)_2$  are shown by the dashed line.

Experimentally, we performed Mössbauer effect measurements at  $^{57}\text{Fe}$ . We also conducted *ab initio* density-functional-theory calculations using the Wien2k package [3]. The calculations of the partially disordered pseudo-binary alloys were done by simulating their electronic structure by that of hypothetical ordered ternary compounds with the same stoichiometry. The evaluated magnetic moments and hyperfine magnetic fields are consistent with experiment. Figure 1 presents the concentration dependence of the spin moment per formula unit and per transition-metal atom for  $\text{Y}(\text{Fe}_{1-x}\text{Ni}_x)_2$  (yttrium is usually considered as a rare-earth element due to its physico-chemical properties). Some of the compounds under consideration could not be synthesized either at normal pressure or at moderate pressures of the order of 8 GPa. Simple empirical assumptions, taking into account the ordering of materials in the “chemical space” according to atomic properties (such as size and electronegativity), led us to the conclusion that higher pressures are required for their formation. To theoretically predict the pressure ranges in which they are stable with respect to decomposition into components, an effective approach was used that significantly simplifies this task: an evolutionary search for energetically favorable phases using the USPEX code [4] in combination with the VASP package [5].

The high-pressure synthesis and investigation of new iron-containing compounds will expand the list of systems promising for modern technological applications. These studies are also related to the problem of the structure and chemical composition of the Earth’s core, to the construction of its thermal, magnetic and dynamical models.

*Support by the Russian Science Foundation under Grant RSF 22-22-00806 is acknowledged.*

1. F. Stein and A. Leineweber, *J. Mater. Sci.*, **56**, 5321–5427 (2021).
2. A.V. Tsyvashchenko, V.A. Sidorov, L.N. Fomicheva, V.N. Krasnorussky, R.A. Sadykov, J.D. Thompson, K. Gofryk, F. Ronning, and V.Y. Ivanov, *Solid State Phenom.*, **190**, 225–228 (2012).
3. P. Blaha, K. Schwarz, F. Tran, R. Laskowski, G.K.H. Madsen, and L.D. Marks, *J. Chem. Phys.*, **152**, 074101 (2020).
4. A.R. Oganov and C.W. Glass, *J. Chem. Phys.*, **124**, 244704 (2006).
5. G. Kresse and J. Furthmüller, *Phys. Rev. B*, **54**, 11169 (1996).

## CHARGE SUBSYSTEM RESPONSE TO PHASE TRANSITIONS IN DOUBLE MANGANITES $\text{LnBaMn}_2\text{O}_6$

*E.V. Mostovshchikova*<sup>1\*</sup>, *E.V. Sterkhov*<sup>2</sup>, *S.A. Uporov*<sup>2</sup>, *S.V. Pryanichnikov*<sup>2</sup>, *Ya.Ya. Pyzhyanov*<sup>1</sup>, *S.G. Titova*<sup>2</sup>

<sup>1</sup>M.N. Miheev Institute of Metal Physics of UB RAS, Ekaterinburg, Russia

<sup>2</sup>Institute of Metallurgy UB RAS, Ekaterinburg, Russia

\*E-mail: [mostovsikova@imp.uran.ru](mailto:mostovsikova@imp.uran.ru)

Double manganites  $\text{LnBaMn}_2\text{O}_6$  with alternating ordered Ln-O and Ba-O layers attract attention due to the strong increase in phase transition temperatures (up to room temperature and above) in comparison with equivalent disordered manganites  $\text{Ln}_{0.5}\text{Ba}_{0.5}\text{MnO}_3$ , as well as the appearance of additional orbital and charge ordering [1]. High temperatures of magnetic phase transitions and a large magnetoresistance found near  $T_C$  (similar to disordered hole-doped manganites) indicate the possibility of practical use of these materials. At present, there is a question about the relationship between magnetic phase transitions and structural transitions from one the hand and transitions to a state with charge and/or orbital ordering on the other hand, as well as with changes in the charge subsystem. In this regard, the structural, magnetic, transport, and optical properties of  $\text{LnBaMn}_2\text{O}_6$ , Ln = Pr and  $\text{Nd}_{1-x}\text{Sm}_x$ ,  $x = 0.25, 0.50, 0.70$  powders were studied. The ordered state was confirmed by the presence of a superstructural peak in the XRD patterns of the samples at  $2\theta = 11.4^\circ$ .

The magnetic data indicate that the temperature of the magnetic phase transition depends on the type of rare earth ion Ln and the degree of ordering of the Ln and Ba ions in the planes (Fig. 1). Systems with Ln = Pr and Ln =  $\text{Nd}_{1-x}\text{Sm}_x$  differ in the types of phase transitions that occur with decreasing temperature. In ordered  $\text{PrBaMn}_2\text{O}_6$  near 300 K, an increase in the magnetization  $M$  is observed, which is associated with the transition to the ferromagnetic (FM) state, and then the magnetization decreases at  $T < 240$  K due to the transition to the antiferromagnetic (AF) state. Near the temperature, which corresponds to the end of the region of decreasing magnetization  $T = 200$  K, a structural transition is observed, which is attributed to an orbital ordering [2]. A decrease in the degree of Pr and Ba ions ordering reduces both the value of  $T_C$  and the magnitude of the magnetization (Fig. 1a). For the Nd-Sm system, a cooling first leads to the appearance of a weak

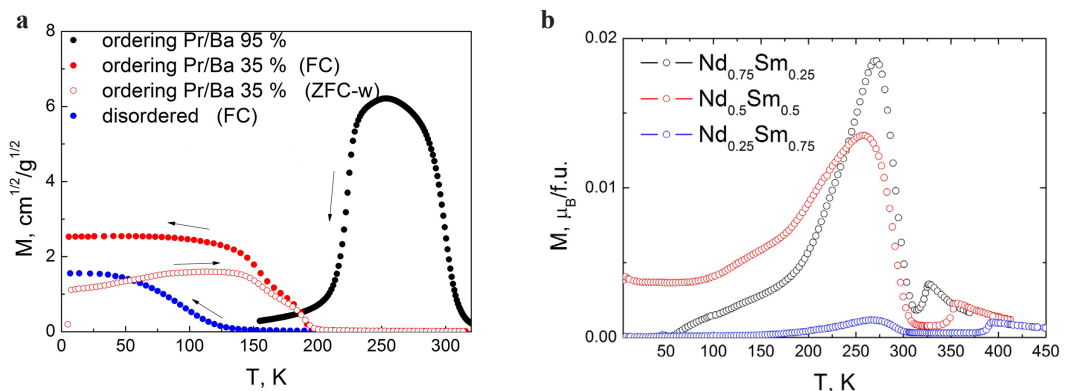


Figure 1. Temperature dependence of magnetization of  $\text{PrBaMn}_2\text{O}_6$  with different degree of ordering of Pr and Ba ions (a) and  $(\text{Nd}_{1-x}\text{Sm}_x)\text{BaMn}_2\text{O}_6$  (b).

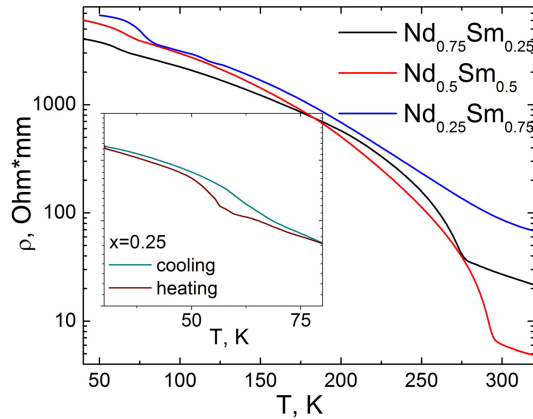


Figure 2. Temperature dependence of resistivity of  $(\text{Nd}_{1-x}\text{Sm}_x)\text{BaMn}_2\text{O}_6$ .

feature on the  $M(T)$  curve in the region of 400–320 K (depending on the ratio of Nd and Sm ions), which is associated with charge ordering, and then to an increase in magnetization below 300 K, which is significant for manganites with  $\text{Nd}_{0.75}\text{Sm}_{0.25}$  and  $\text{Nd}_{0.5}\text{Sm}_{0.5}$  and weak for  $\text{Nd}_{0.25}\text{Sm}_{0.75}$ . Further cooling leads to (i) a decrease in the magnetization  $T < 270$  K, (ii) to additional transition to charge ordered state near 200 K, and (iii) to a transition to the AF state near 120 K.

For samples with  $\text{Ln} = \text{Nd}_{1-x}\text{Sm}_x$ , the temperature dependences of the resistance  $\rho$  were also measured, which show the semiconductor nature of conductivity in the temperature range of 50–350 K and the manifestation of the charge ordering as a kink the  $\rho(T)$  curve (Fig. 2).

To obtain additional information about changes in the charge subsystem, we measured the optical density spectra  $D = \ln(1/t)$  being an analogous to the absorption spectra without taking into account the sample thickness and the temperature dependences of the light transmission  $t$ . For manganites with Pr, a response to magnetic phase transitions in the form of a metal-insulator transition (change of the sign of  $dt/dT$ ) was found, and for ordered manganite, a peculiarity in  $t(T)$  was found not only near  $T_C$ , as previously observed in disordered hole-doped manganites, but also near

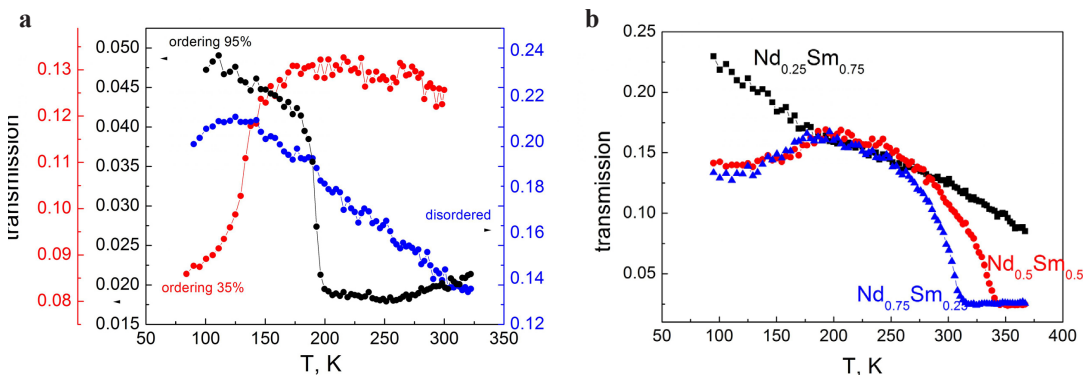


Figure 3. Temperature dependence of transmission measured at 0.1–0.3 eV for  $\text{PrBaMn}_2\text{O}_6$  with different degree of ordering of Pr and Ba ions (a) and  $(\text{Nd}_{1-x}\text{Sm}_x)\text{BaMn}_2\text{O}_6$  (b).

the temperature of structural ordering. In a series of ordered manganites with  $\text{Nd}_{1-x}\text{Sm}_x$ , magnetic and structural transitions also appear as metal-insulator transitions or a kink in the curve, respectively. For  $\text{Nd}_{0.25}\text{Sm}_{0.75}$  manganite, the transmission has a semiconductor character ( $t$  increases upon cooling), which is consistent with the  $\rho(T)$  dependence. The appearance of a “metallic” behavior of the temperature dependence of the transmission below 200 K is observed for the  $\text{Nd}_{0.75}\text{Sm}_{0.25}$  and  $\text{Nd}_{0.5}\text{Sm}_{0.5}$  samples, for which there is a noticeable contribution to the magnetization in the region of 200–300 K, although  $d\rho/dT < 0$  in the entire measured temperature range. Probably, the metal-insulator transition occurs in separate isolated regions. It should be noted that both in the manganite with Pr and in the manganites  $\text{Nd}_{0.75}\text{Sm}_{0.25}$  and  $\text{Nd}_{0.5}\text{Sm}_{0.5}$ , the temperature region below the structural transition corresponds to the metallic character of transmission (“metallic” conductivity in local regions), although the magnetization already significantly decreases. This is in agreement with the conclusion of [3], the results of which show coexistence of FM and AF regions due to the first-order-like formation of the AF phase inside the FM phase; FM region is microscopically identical to the bulk disordered  $\text{La}_{0.5}\text{Ba}_{0.5}\text{MnO}_3$  manganite.

*The research was supported by RSF (project no. 22-22-00507).*

1. T. Nakajima et al., J. Phys. Soc. Japan, **72**, 3237–3242 (2003).
2. E.V. Sterkhov et al., J. All. Comp., **892**, 162034–162042 (2022).
3. Y. Kawasaki et al., Phys. Rev. L, **96**, 037202 (2006).



## CHARGE ORDERING AND MAGNETIC TRANSITIONS IN $\text{Fe}_{1.75}\text{V}_{0.25}\text{BO}_4$ WARWICKITE

*N. Belskaya*<sup>1\*</sup>, *N. Kazak*<sup>2</sup>, *D. Velikanov*<sup>2</sup>, *S. Gromilov*<sup>3</sup>, *A. Sukhikh*<sup>3</sup>, *V. Rudenko*<sup>2</sup>, *S. Ovchinnikov*<sup>2</sup>

<sup>1</sup>Ioffe Institute, RAS, Saint-Petersburg, Russia

<sup>2</sup>Kirensky Institute of Physics, FRC SB PAS, Krasnoyarsk, Russia

<sup>3</sup>Nikolaev Institute of Inorganic Chemistry, SB RAS, Novosibirsk, Russia

\*E-mail: [nbels@mail.ioffe.ru](mailto:nbels@mail.ioffe.ru)

Oxyborates  $\text{Me}^{2+}\text{Me}^{3+}\text{BO}_4$  belong to the warwickite family and are of current interest due to the structural, electronic and magnetic transitions. The transition metal ions of mixed valent  $\text{Me}=\text{Mn}$  [1],  $\text{Fe}$  [2],  $\text{V}$  [3] occupy sites of octahedral symmetry with an interionic distance less than 3 Å. The formula unit contains equal amounts of  $\text{Me}^{2+}$  and  $\text{Me}^{3+}$  ions and therefore the warwickites might undergo a charge ordering in a similar manner to  $\text{Fe}_3\text{O}_4$ . Indeed, the charge ordering has been found thoroughly studied in  $\text{Mn}_2\text{BO}_4$ ,  $\text{Fe}_2\text{BO}_4$  and  $\text{V}_2\text{BO}_4$ , using Mössbauer spectroscopy, neutron diffraction, X-ray synchrotron diffraction, etc [4–6].

In this work, we present the results of the crystal structure, electronic and magnetic properties studies of  $\text{Fe}_{2-x}\text{V}_x\text{BO}_4$  warwickite ( $x = 0.25$ ), with a partial substitution of the iron ions by vanadium. Due to both Fe and V ions are mixed valence, a wide spectrum of electronic states is realized in a new compound. As a result,  $\text{Fe}_{1.75}\text{V}_{0.25}\text{BO}_4$  demonstrates the charge-ordering and magnetic ordering transitions.

Single crystals  $\text{Fe}_{1.75}\text{V}_{0.25}\text{BO}_4$  were grown by a flux method in the  $\text{Fe}_2\text{O}_3\text{-V}_2\text{O}_3\text{-B}_2\text{O}_3\text{-(70 PbO+30 PbF}_2\text{ wt.%)}$  [7]. The crystals are of a needle shape with a length up to 10 mm and  $0.10\times 0.15\text{ mm}^2$  in a cross-section. X-ray diffraction measurements at 100 and 390 K showed that the compound does not undergo structural transitions (sp. gr.  $Pnma$ ) in contrast to  $\text{Fe}_2\text{BO}_4$ , which exhibits an orthorhombic to monoclinic transition at  $T_{\text{CO}} = 340\text{ K}$  associated with the charge-ordering of iron ions [2] (Table 1). Refinement of the site occupation revealed that vanadium ions are equally occupy the crystallographically non-equivalent positions M1 and M2 (Fig. 1). Mössbauer effect measurements shown an electronic transition associated with the charge-ordering the type of  $\text{Fe}^{2+} + \text{Fe}^{3+} \rightarrow \text{Fe}^{2.5+}$  near  $T_{\text{CO}} = 240\text{ K}$ . The concentration of the delocalized electronic states progressively increases with temperature increase and reaches 70% at  $T = 505\text{ K}$  [7].

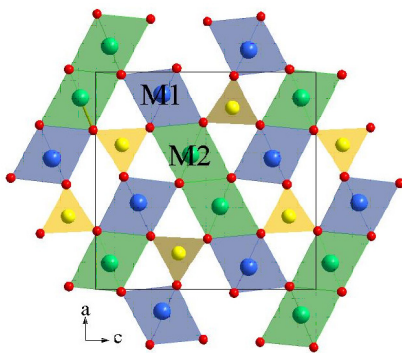


Figure 1. Crystal structure of the  $\text{Fe}_{1.75}\text{V}_{0.25}\text{BO}_4$ .

Table 1. Lattice parameters of the Fe-containing warwickites.

	$\text{Fe}_2\text{BO}_4$ [2]		$\text{Fe}_{1.75}\text{V}_{0.25}\text{BO}_4$ [7]	
	355 K	100 K	390 K	100 K
$a$ (Å)	3.1759	6.3333	9.2550	9.2410
$b$ (Å)	9.2538	9.3803	3.1786	3.1672
$c$ (Å)	9.4019	9.2469	9.401	9.3833
$V$ (Å)	276.31	549.34	276.6	274.63
Sp. gr.	$Pmnb$	$P2_1/c$	$Pnma$	$Pnma$

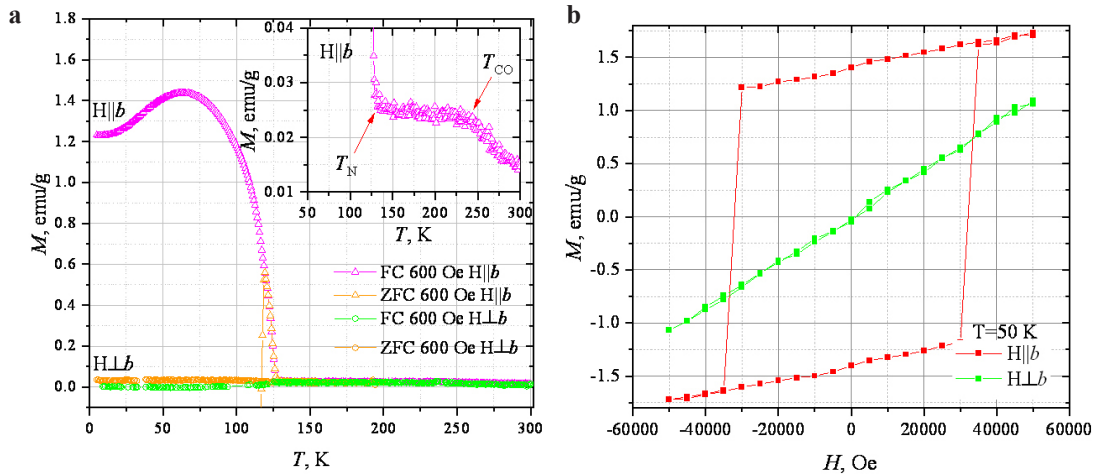


Figure 2. **a** Temperature dependence of magnetization of  $\text{Fe}_{1.75}\text{V}_{0.25}\text{BO}_4$ , inset shows electronic transition at  $T_{\text{CO}} = 240$  K and magnetic transition at  $T_{\text{N}} = 125$  K. **b** Field dependences of magnetization measured at 50 K for two directions of the external field relative EMD.

The magnetic properties of  $\text{Fe}_{1.75}\text{V}_{0.25}\text{BO}_4$  single crystal were measured in a wide temperature range  $T = 4.2\text{--}300$  K and magnetic field up to 50 kOe. A strong magnetic anisotropy was found with an easy magnetization direction (EMD)  $b$ -axis (Fig. 2). As the temperature decreases, an electronic transition first occurs, which manifests itself in a change of the magnetization slope at  $T_{\text{CO}} = 240$  K. The ferrimagnetic transition is clearly observed at  $T_{\text{N}} = 125$  K. In addition, a weak anomaly is seen at 116 K, which was earlier reported for  $\text{Fe}_2\text{BO}_4$  at 120 K.

The magnetic moments are fully compensated in the direction of  $H \perp b$  giving rise a linear dependence of  $M(H)$ . On contrary, there is a large uncompensated magnetic moment  $M_{\text{r}} = 0.05 \pm 0.01 \mu_{\text{B}}/\text{f.u.}$  along  $b$ -axis. The complex shape of the hysteresis loops and the temperature and field induced transformation of  $M(H)$  indicate that the  $\text{Fe}_{1.75}\text{V}_{0.25}\text{BO}_4$  is a multi-sublattice ferrimagnetic. The magnetic moments of several sublattices are directed along the  $b$ -axis, making it an EMD.

In summary, the vanadium substitution causes a shift of both electronic and magnetic transitions towards lower temperatures. The magnetic and electronic properties inherent in  $\text{Fe}_2\text{BO}_4$  are preserved despite of the structural disorder induced by the vanadium.

*This work was supported by RFBR №20-02-00559, №21-52-1203.*

1. N.V.Kazak, M.S. Platonov, Yu.V. Knyazev et al., JMMM, **393**, 316 (2015).
2. M. Angst, P. Khalifah, R.P. Hermann et al., PRL, **99**, 086403 (2007).
3. E.M. Carnicom, K. Górnicka, T. Klimeczuk, and R. Cava, J. Solid State Chem., **265**, 319 (2018).
4. A.P. Douvalis et al., J. Phys.: Condens. Matter, **12**, 177–188 (2000).
5. J.P. Attfield, A.M.T. Bell, L. M. Rodriguez-Martinez et al., J. Mater. Chem., **9**, 205 (1999).
6. N.V. Kazak, M.S. Platonov, Yu.V. Knyazev et al., Physica B: Condensed Matter, **560**, 228–235 (2019).
7. Yu.V. Knyazev, O.A. Bayukov, M.S. Shustin et al., JETP Lett., **113**, 279 (2021).

ALTERATION OF MAGNETIC PROPERTIES OF  $(\text{Mg}_{1-x}\text{Ni}_x)_3\text{Si}_2\text{O}_5(\text{OH})_4$   
( $x = 0.67, 1$ ) NANOSCROLLS AFTER HYDROGEN TREATMENT

*N. Belskaya\**, A. Krasilin, E. Khrapova, D. Chikurov, M. Volkov

Ioffe Institute, RAS, Saint-Petersburg, Russia

\*E-mail: [nbels@mail.ioffe.ru](mailto:nbels@mail.ioffe.ru)

$\text{Mg}_3\text{Si}_2\text{O}_5(\text{OH})_4$  phyllosilicate nanoscrolls with chrysotile structure alone of wide-spread minerals that can be synthesized via hydrothermal method in the laboratory. Chrysotile layer scrolls due to the size difference between octahedral ( $\text{MgO}_6$ ) and tetrahedral ( $\text{SiO}_4$ ) sheets in the structure. One way to change the physical, in particular, magnetic properties of chrysotile is to replace Mg ions with *d* element ions, such as Fe, Co, and Ni. Reduction of these elements from phyllosilicate structure paves the way for their application as catalysts and magnetically controlled adsorbents. This work reports on research of the magnetic properties of composition  $(\text{Mg}_{1-x}\text{Ni}_x)_3\text{Si}_2\text{O}_5(\text{OH})_4$  ( $x = 0.67, 1$ ) phyllosilicate before and after metal reduction with hydrogen.

Nanotubular phyllosilicate  $(\text{Mg}_{1-x}\text{Ni}_x)_3\text{Si}_2\text{O}_5(\text{OH})_4$  ( $x = 0.67, 1$ ) were synthesized by hydrothermal method at  $T = 350$  °C и  $P = 22$  MPa [1]. The obtained particles were in the form of scrolls up to several microns long and 30–50 nm in diameter. Nickel was reduced to metal by the heat treatment in Ar+H<sub>2</sub> (4 vol.%) at 600 °C, which resulted in the formation of a composite with Ni nanoparticles (Fig. 1).

The magnetic properties of the powder samples were investigated in a wide temperature interval  $T = 4.2$ –300 K and in the field range up to 60 kOe for all samples. Temperature dependence of magnetization experienced a kink at  $T = 20$  K, and the FC FH mode lines overlapped well in the whole temperature range in the case ( $x = 0.67$ ) before reduction. For the case  $x = 1$  magnetic transition to the ferromagnetic state was observed near  $T_c = 24.9$  K even in a small magnetic field of 100 Oe. It is worth noting that the value of the magnetic transition temperature correlated well with earlier magnetic experiments for  $\text{Ni}_3\text{Si}_2\text{O}_5(\text{OH})_4$  [2] and increased with decrease in nickel concentration.

For the samples after reduction a kink was observed in the temperature dependences of magnetization around 22 K (inset in Fig. 2a). In the case  $x = 0.67$  (Fig. 2a), the mode lines diverged at low temperatures; this may be related to the relaxation of the magnetic moment during prolonged

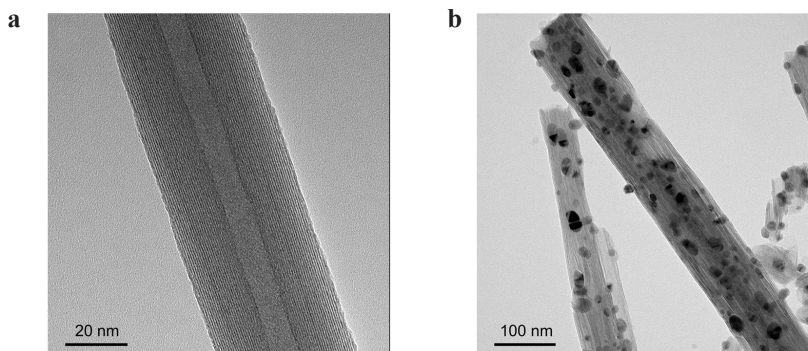


Figure 1. Nanotubular  $(\text{Mg}_{1-x}\text{Ni}_x)_3\text{Si}_2\text{O}_5(\text{OH})_4$  ( $x = 0.67$ ) phyllosilicate: **a** before reduction of nickel, **b** after reduction of nickel at 600 °C [1].

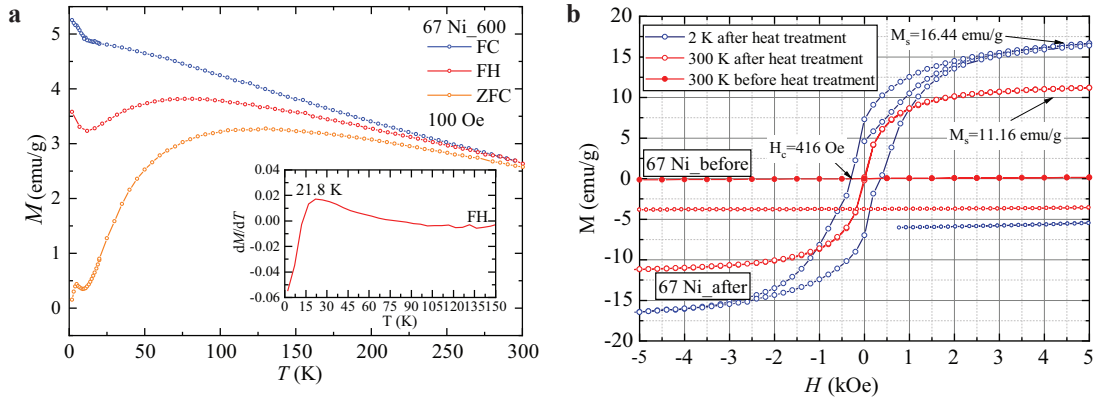


Figure 2. **a** Temperature dependence of magnetization for  $(\text{Mg}_{1-x}\text{Ni}_x)_3\text{Si}_2\text{O}_5(\text{OH})_4$  ( $x = 0.67$ ) after reduction, the inset to the figure shows the first derivative of magnetization. **b** Field dependence of magnetization for  $(\text{Mg}_{1-x}\text{Ni}_x)_3\text{Si}_2\text{O}_5(\text{OH})_4$  ( $x = 0.67$ ) before and after reduction of metal.

exposure of the sample at a low temperature. Regarding field dependencies for the case  $x = 0.67$  below the magnetic transition temperature, the coercive force is 416 Oe, and the saturation magnetization reached a value of 16.44 emu/g. At room temperature, the value of saturation magnetization corresponded to 11.16 emu/g. For the case  $x = 1$  at room temperature the value of saturation magnetization and coercive force were 19.76 emu/g and 78 Oe, respectively. In conclusion, we would like to emphasize that hysteresis loops were detected at room temperature for samples after reduction with hydrogen.

*The research was partially supported by RSF grant № 19-13-00151.*

1. E. Khrapova et al., ChemNanoMat., **7**, 257–269 (2021).
2. A.A. Krasilin et al., EPL, **113**, 47006 (2016).

**METAL-INSULATOR TRANSITION AND MAGNETIC PROPERTIES  
 $\text{NdBaCo}_2\text{O}_{5+\Delta}$ ,  $0.37 \leq \Delta \leq 0.65$**

*N.I. Solin, S.V. Naumov\**

M.N. Mikheev Institute of Metal Physics of the Ural Branch RAS

\*E-mail: [solin@imp.uran.ru](mailto:solin@imp.uran.ru)

Currently, layered cobaltites  $\text{RBaCo}_2\text{O}_{5+\delta}$  are well studied, where  $\delta \approx 0.5$  is the oxygen content,  $\text{R}^{3+}$  is a rare earth ion, there are only  $\text{Co}^{3+}$  ions. The effect of  $\text{Co}^{4+}$  ions on the magnetic and electrical properties of  $\text{RBaCo}_2\text{O}_{5+\delta}$  at  $\delta \neq 0.5$  is poorly understood. The nature of the unusual magnetic properties of  $\text{RBaCo}_2\text{O}_{5+\delta}$  with the largest ion sizes  $\text{R} = \text{La}, \text{Pr}$  is not clear [1, 2]. The work is aimed at elucidating the role of  $\text{Co}^{4+}$  ions in the metal-insulator transition, on the magnetic properties and spin state of  $\text{Co}^{3+}$   $\text{NdBaCo}_2\text{O}_{5+\delta}$  ions.

Figure 1 shows the temperature dependences of the magnetization  $M(T)$  of  $\text{NdBaCo}_2\text{O}_{5+\delta}$  samples. As  $\delta$  increases, the magnetization peak  $M_{\text{max}}(\delta)$  at the Neel temperature  $T_N$  changes nonmonotonically with a minimum at  $\delta = 0.60$ . The volume of the unit cell  $V_{\text{fu}}$  decreases with increasing  $\delta$ , which is associated with lattice contraction when  $\text{Co}^{3+}$  ions are replaced by smaller  $\text{Co}^{4+}$  ions and changes in the spin states of  $\text{Co}^{3+}$  and  $\text{Co}^{4+}$  ions. The Neel temperature  $T_N(\delta)$  slightly changes up to  $\delta = 0.53$ , at  $\delta > 0.60$  it sharply decreases by  $\sim 100$  K, and has a dependence on  $\delta$  similar to  $V_{\text{fu}}(\delta)$  (Fig. 1 inset).

Surprisingly, in  $\text{NdBaCo}_2\text{O}_{5+\delta}$  the ferromagnetic (FM) interactions are present in the antiferromagnetic (AFM) phase at all temperatures below  $T_N$ . The  $M(T)$  data below 175 K for  $\delta = 0.37-0.53$  are not shown in Fig. 1, but the FM magnetization remains below  $T_N$ , as for  $\delta = 0.60-0.65$ . The results are explained in the metamagnetic model. The compound is a layered AFM structure in which layers of  $\text{Co}^{3+}$  ions are separated by  $\text{Nd}^{3+}$  layers. It is assumed that the FM bond inside the Co layers remains strong, while the AFM bond between the Co layers is weakened due to the large size of the  $\text{Nd}^{3+}$  ions. Below  $T \sim 20$  K, in the absence of a magnetic field,  $\text{NdBaCo}_2\text{O}_{5.50}$  is in the AFM state, and in a small magnetic field of 10–20 kOe, it becomes metamagnetic, i.e. mixed FM+AFM state [3]. The FM state below  $T_N$  in  $\text{RBaCo}_2\text{O}_{5+\delta}$  with the largest ion sizes  $\text{R} = \text{La}, \text{Pr}$  [1, 2] and Nd, and its absence in the compound with a smaller ionic radius [4] confirms the model.

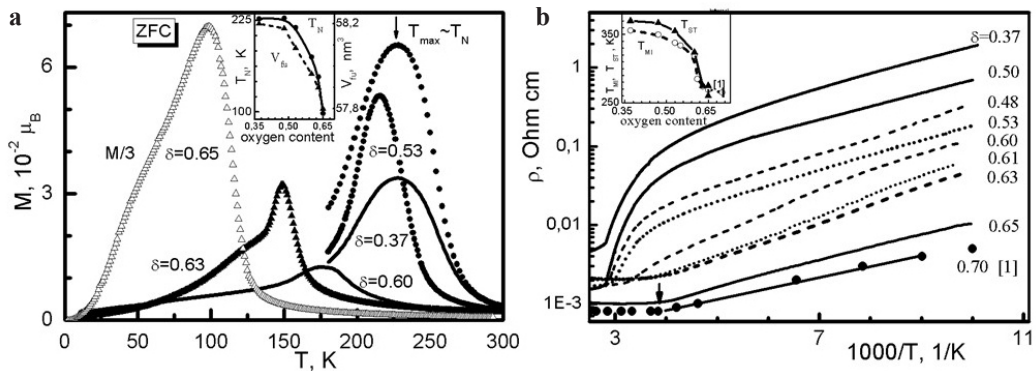


Figure 1. Temperature dependences of magnetization (a) and electrical resistance (b)  $\text{NdBaCo}_2\text{O}_{5+\delta}$ . The insets show the dependences of the phase volume ( $V_{\text{fu}}$ ), the Néel temperatures ( $T_N$ ), the metal-insulator transition ( $T_{\text{MI}}$ ), and the spin transition ( $T_{\text{ST}}$ ) on the oxygen content.

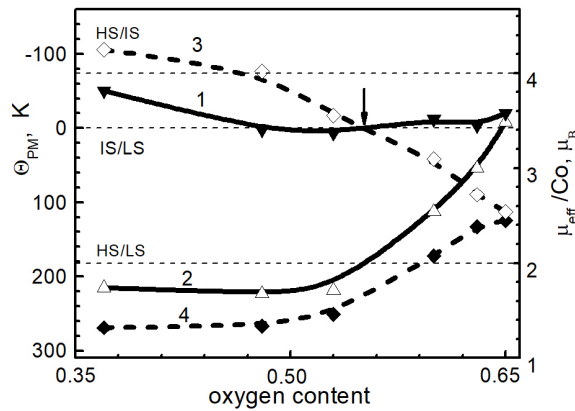


Figure 2. Influence of the oxygen content  $\delta$  on the effective magnetic moment  $\mu_{\text{eff}}/\text{Co}$  (curves 1 and 2) and the Weiss temperature  $\Theta_{\text{PM}}$  of cobaltite  $\text{NdBaCo}_2\text{O}_{5+\delta}$  (curves 3 and 4) in the metallic (curves 1 and 3) and semiconductor (curves 2 and 4) phase. The PM contribution of the  $\text{Nd}^{3+}$  ion is subtracted.

Features at  $\delta \sim 0.60$  are also manifested in the temperature dependence of the electrical resistance  $\rho(T)$  (Fig. 1b). The electrical resistance of  $\text{NdBaCo}_2\text{O}_{5+\delta}$  up to  $\delta < 0.60$  sharply increases at  $T > T_{\text{MI}}$ , at  $\delta > 0.60$  there is no sharp jump in  $\rho(T)$ . At values of  $\delta \sim 0.65$ , a smooth transition of the “heavily doped semiconductor – bad metal” type occurs without changing the spin state of  $\text{Co}^{3+}$  ions. The values of  $T_{\text{MI}}(\delta)$ ,  $T_{\text{N}}(\delta)$ ,  $T_{\text{ST}}(\delta)$  (insets in Figs. 1a and b) differ in magnitude by  $\sim 100$  K, but have approximately the same dependence on  $\delta$ . The results are explained by the influence of  $\text{Co}^{4+}$  ions on the electrical resistance.

From measurements of the paramagnetic susceptibility  $\chi^{-1}(T)$ , the dependences of  $\mu_{\text{eff}}/\text{Co}^{3+}$  (taking into account  $\text{Co}^{4+}$  ions) and the Weiss temperature  $\Theta_{\text{PM}}$  on the oxygen content were determined. In the metallic phase (curves 1 Fig. 2), at all values of  $\delta$ , the  $\text{Co}^{3+}$  ions are in the HS/LS state, the deviations from this state are in reasonable agreement with the influence of the  $\text{Co}^{2+}$  and  $\text{Co}^{4+}$  ions. In the paramagnetic phase,  $\text{Co}^{3+}$  ions up to  $\delta = 0.53$  are located in the IS/LS state, with an increase in  $\delta > 0.53$  they pass into the HS/LS state (curves 2 Fig. 2).

In the semiconductor phase, the values of  $\Theta_{\text{PM}}$  decrease with increasing  $\delta$  (curve 4 in Fig. 2). In the metallic phase (curve 3 in Fig. 2), the values of  $\Theta_{\text{PM}}$  change sign at  $\delta \sim 0.55$ , increase and take values close to those in the semiconductor phase at  $\delta = 0.65$ . The non-monotonic behavior of  $M_{\text{max}}(\delta)$  is evidence of the presence of competing FM and AFM interactions in these compounds. The change in sign of  $\Theta_{\text{PM}}$  at  $\delta \approx 0.55\text{--}0.6$  means that the character of exchange interactions changes from AFM+FM to FM exchange and the FM exchange becomes stronger with increasing  $\delta$ .

It is assumed that the decrease in  $T_{\text{N}}$ ,  $T_{\text{C}}$ ,  $T_{\text{MI}}$  and  $T_{\text{ST}}$  by  $\sim 100\text{--}150$  K, the non monotonic behavior of the magnetization  $M_{\text{max}}(T = T_{\text{N}})$  and its increase at  $\delta > 0.53\text{--}0.6$  are caused by a change in the indirect exchange interactions of  $\text{Co}^{3+}$  and  $\text{Co}^{4+}$  from AFM+FM to FM exchange when the proportion of the  $\text{Co}^{4+}$  ion changes. The FM behavior of  $\text{NdBaCo}_2\text{O}_{5+\delta}$  below  $T_{\text{N}}$  is explained in the metamagnetic model by the influence of the  $\text{Nd}^{3+}$  ion size on the AFM state of  $\text{NdBaCo}_2\text{O}_{5+\delta}$ .

*Support state assignment of Ministry of Science and Higher Education of the Russian Federation (theme “Spin” No. 122021000036-3), supported in part by RFBR (project No. 20-02-00461).*

1. S. Ganorkar, K.R. Priolkar, P.R. Sarode et al., J. Appl. Phys. **110**, 053923 (2011).
2. E.-L. Rautama, V. Caignaert, P. Boullay et al., Chem. Mater., **21**, 102 (2009).
3. N.I. Solin, S.V. Naumov, JETP Letters, **114**, No. 3, 150 (2021).
4. A.A. Taskin, A.N. Lavrov, Yoichi Ando, Phys. Rev. B, **71**, 134414 (2005).

**EFFECT OF THE ELECTRON-PHONON INTERACTION ON THE FORMATION OF THE EXCITON PHASE IN STRONGLY CORRELATED SYSTEMS WITH THE SPIN CROSSOVER**

*Yu.S. Orlov<sup>1,2</sup>, S.V. Nikolaev<sup>1,2\*</sup>, V.I. Kuz'min<sup>2</sup>, S.G. Ovchinnikov<sup>1,2</sup>*

<sup>1</sup>Siberian Federal University, Krasnoyarsk, Russia

<sup>2</sup>Kirensky Institute of Physics, Federal Research Center KSC SB RAS, Krasnoyarsk, Russia

\*E-mail: [svinikolaev@sfu-kras.ru](mailto:svinikolaev@sfu-kras.ru)

The formation and condensation of electron-hole pairs (excitons) in semimetals and semiconductors was predicted more than half a century ago. The weak coupling theory of the excitonic insulators has been developed analogously to the Bardeen-Cooper-Schrieffer (BCS) theory of superconductivity [1]. Later the ideas of excitonic condensation were discussed for strongly correlated materials within the Hubbard-type models. Within the multiband Hubbard-type model the interrelation of the excitonic condensation and the high spin (HS)–low spin (LS) crossover takes place [2].

The minimal model which contains the multiorbital physics and excitonic effects is the two-band Hubbard-type model both in the strong coupling and weak coupling regimes. In the strong coupling limit we have suggested [3] the similar approach as the Hubbard's original one that starts with the exact diagonalization of the local part of the Hamiltonian and construction the Hubbard X-operators. Within such approach the effective Hamiltonian has been obtained that was used to study the phase diagram and the HS-LS crossover under external pressure. A spin gap between the LS and the HS is an external parameter of our model that may be varied by pressure.

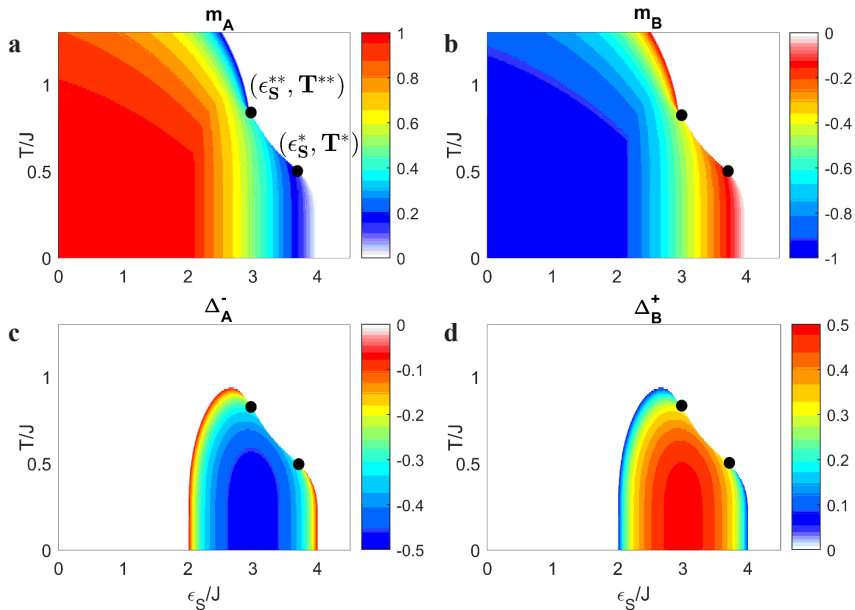


Figure 1. Phase diagrams of **a**, **b** magnetization  $m$ , and **c**, **d** exciton order parameter components  $\Delta$  for sublattices A (on the left) and B (on the right).

The mean-field phase diagram in the plane spin gap–temperature (or pressure–temperature) contains the HS antiferromagnetic and paramagnetic, excitonic, and nonmagnetic LS phases. The excitonic phase appears in the spin crossover region and coexists with the HS AFM phase (Fig.1) [4].

Two cases can be distinguished. In the first (weakly correlated) case, we have a two-band semiconductor or a semimetal (depending on the model parameters), in which an exciton condensate can form according to the BCS or Bose-Einstein condensation scenario. In the second case (strongly correlated), when the energy of the Coulomb interaction of electrons is larger than their kinetic energy and becomes comparable with the energy of the crystal field, the spin crossover and the formation of localized magnetic excitons become possible. In this study we showed using the two-band Hubbard-Kanamori model that there is a condensation of such excitons near the spin crossover, which, in turn, leads to the opening of a dielectric gap in the electronic spectrum and the occurrence of the antiferromagnetic ordering. The emergence of the magnetism induced by the condensation of excitons was found.

Effect of the electron-phonon interaction on formation of the exciton phase was studied. Our calculation showed that the diagonal electron-phonon interaction suppresses the exciton phase, while the off-diagonal electron-phonon interaction supports it.

*The study was supported by the Russian Scientific Foundation, the Krasnoyarsk Regional Fund of Science, grant No. 22-22-20007.*

1. L.V. Keldysh and Y.V. Kopaev, Sov. Phys. Solid State, **6**, 2219 (1965).
2. J. Kunes and P. Augustinsky, Phys. Rev. B, **89**, 115134 (2014).
3. V.I. Kuz'min, Yu.S. Orlov, and et al., Phys. Rev. B, **100**, 144429 (2019).
4. Yu.S. Orlov, S.V. Nikolaev, and et al., Phys. Rev. B, **104**, 195103 (2021).



## LIGHT-INDUCED ULTRAFAST QUANTUM RELAXATION DYNAMICS OF MAGNETICALLY ORDERED SPIN CROSSOVER SYSTEMS

*Yu.S. Orlov<sup>1,2\*</sup>, S.V. Nikolaev<sup>1,2</sup>, S.G. Ovchinnikov<sup>1,2</sup>*

<sup>1</sup>Siberian Federal University, Krasnoyarsk, Russia

<sup>2</sup>Kirensky Institute of Physics, Federal Research Center KSC SB RAS, Krasnoyarsk, Russia

\*E-mail: [jso.krasn@mail.ru](mailto:jso.krasn@mail.ru)

The development of the ultrafast magneto-optics during the last 15 years results in a new fundamental knowledge on the ultrafast interaction of light and magnetic materials and also in a very important practical possibility to increase the speed of writing/reading processes in computers in  $10^5$ – $10^6$  times. Several groups in the world have found long-living magnetic oscillations after femtosecond laser pump, for example in  $\text{FeBO}_3$  [1]. Within a phenomenological approach this effect has been explained as the inverse Faraday effect. In our work we demonstrate such oscillations within the microscopic model of the magnetic insulator with two possible multielectron terms at each cation site. The terms have different spin values and forms local polarons due to electron-phonon interactions with vibrations of local anions. We assume that femtosecond pumping by the very fast charge-transfer excitations results in a switching of the initial high spin term of cation into the excited low spin term, and the dynamics of the excited state is studied within the master equation for the reduced density matrix. In the Fig. 1 we demonstrate the dynamics of 3 material parameters: the concentration of high spin terms (blue line), sublattice magnetization (red line), and variation of the cation-oxygen bond length (black line). The time scale is given in ps ( $10^{-12}$  sec). We can see the generation of vibrations during the relaxation. After 1 ps all parameters reach their equilibrium values typical for the high spin state, and magnetization demonstrates long-living oscillations.

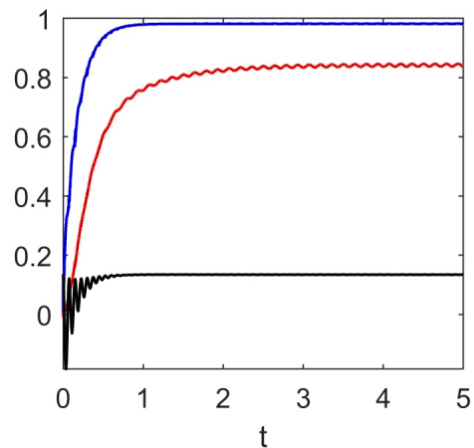


Figure 1. Temporal dynamics of the concentration of high spin terms (blue line), sublattice magnetization (red line), and variation of the cation-oxygen bond length (black line). The time scale is given in ps ( $10^{-12}$  sec).

*The study was supported by the Russian Scientific Foundation, the Krasnoyarsk Regional Fund of Science, grant No. 22-22-20007.*

1. A.M. Kalashnikova, A.V. Kimel, R.V. Pisarev, V.N. Gridnev, A. Kirilyuk, Th. Rasing, Phys. Rev. Lett., **99**, 167205 (2007).

**STRAIN-INDUCED CHARGE ORDERING  
IN Pr-Sr MANGANITES ( $x \leq 0.4$ )**

*Yu.E. Samoshkina<sup>1</sup>, M.V. Rautskii<sup>1</sup>, D.S. Neznakhin<sup>2</sup>, E.A. Stepanova<sup>2</sup>,  
N.V. Andreev<sup>3</sup>, V.I. Chichkov<sup>3</sup>, A.V. Chernichenko<sup>4</sup>*

<sup>1</sup>Kirensky Institute of Physics, Federal Research Center KSC SB RAS, Krasnoyarsk, Russia

<sup>2</sup>Institute of Natural Sciences and Mathematics, Ural Federal University, Yekaterinburg, Russia

<sup>3</sup>National University of Science and Technology (NUST “MISIS”), Moscow, Russia

<sup>4</sup>Krasnoyarsk Rail Transport Institute, Irkutsk State Transport University, Krasnoyarsk, Russia

\*E-mail: [uliag@iph.krasn.ru](mailto:uliag@iph.krasn.ru)

In recent years, strain manganite films of  $R_{1-x}A_xMnO_3$  have been actively studied [1–3]. Due to the strain and the tendency to phase separation, various spin structures can form in them and unique properties can manifest themselves. The strain engineering is one of routes to optimize the physical properties of the manganite films [4, 5]. In turn, the charge ordering (CO), which is the spatial ordering of the  $Mn^{3+}$  and  $Mn^{4+}$  ions, is closely related to the phase separation. Besides, the CO is one of the most interesting phenomena observed in the mixed valence manganites. The samples in the CO state can exhibit multiferroic and magnetoelectrical properties [6, 7]. For applications, it is important to induce the CO state in the manganite at room temperature and above. Currently, known mixed manganites doped with rare earth elements exhibit a pronounced state of CO below room temperature.

In this work, the behavior of the magnetic susceptibility and electronic magnetic resonance of  $Pr_{1-x}Sr_xMnO_3/YSZ$  ( $x = 0.2$  and  $x = 0.4$ ) polycrystalline films in a wide temperature range have been studied. The Curie temperature ( $T_C$ ) of the films is 115 K for  $x = 0.2$  and 215 K for  $x = 0.4$ . At high temperatures exceeding room temperature, the samples showed CO signs (Fig. 1). The CO state is determined by the martensitic nature and is caused by an internal strain in the films. Such strain is responsible for a phase separation in the films, which reduces the  $T_C$  value and expands the boundaries of the Griffiths-like phase as well as the CO state. The key to the appearance of the internal strain in polycrystalline manganite films lies in the crystallites size and the boundary between them.

The obtained results provide the basis for the development of new research and technological tasks for the CO generation at high-temperatures in various polycrystalline manganites doped with rare earth elements.

1. L. Marin et al., Nano Lett., **15**, 492–497 (2015).
2. A.S. McLeod et al., Nat. Mater., **19**, 397–404 (2020).
3. G.M. Pierantozzi et al., Phys. Chem. C, **125**, 14430–14437 (2021).
4. L. Abad et al., Adv. Funct. Mater., **17**, 3918–3925 (2007).
5. F.J. Wong et al., J. Appl. Phys., **111**, 063920 (2012).
6. C.R. Serrao et al., Bull. Mater. Sci., **33**, 169–178 (2010).
7. I. Ouni et al., RSC Adv., **9**, 35599–35607 (2019).

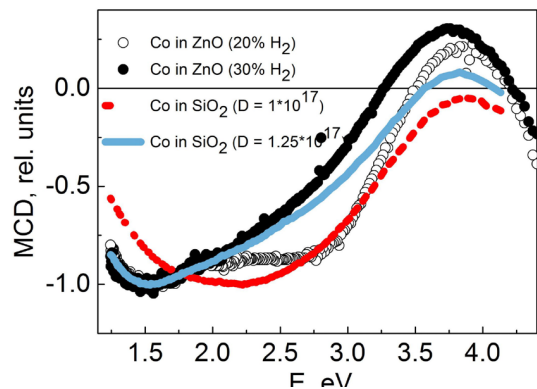


Figure 1. FC-FH temperature dependences of the inverse magnetic susceptibility for the films with  $x = 0.2$  at  $H = 500$  Oe (squares) and  $x = 0.4$  at  $H = 100$  Oe (circles). The substrate contribution is deducted. Inset: inverse thermoremanent magnetization (ITRM) of the film with  $x = 0.2$  after cooling in  $H = 500$  Oe and warming in  $H = 0$ .

## MAGNETIC INTERACTIONS IN FeBO<sub>3</sub> UNDER HIGH PRESSURE

S.I. Polukeev<sup>1\*</sup>, V.A. Gavrichkov<sup>1</sup>, S.G. Ovchinnikov<sup>1,2</sup>

<sup>1</sup>Kirensky Institute of Physics, Krasnoyarsk, Russia

<sup>2</sup>Siberian Federal University, Krasnoyarsk, Russia

\*E-mail: [psi@iph.krasn.ru](mailto:psi@iph.krasn.ru)

In high-pressure experiments iron borate behaves in an unusual way [1]. At pressure  $P_C = 60$  GPa corresponding to the spin crossover on the iron ion  $\text{Fe}^{3+}$  the magnetic ordering temperature  $T_N(P_C) = 500$  K drops to almost zero. A further increase in pressure does not lead to the appearance of magnetic order. In this case, the dielectric gap decreases to values  $E_g = 0.5$  eV and the overlaps of all atomic orbitals obviously increase. As a result, the absence of magnetic bonding of  $\text{Fe}^{3+}$  ions at high pressure looks strange.

In [2], where the dependence of the exchange interaction on the applied pressure was studied, ions with the electronic configuration  $d^5$  ( $\text{Fe}^{3+}$ ,  $\text{Mn}^{2+}$ ) and  $d^7$  ( $\text{Ni}^{3+}$ ,  $\text{Co}^{2+}$ ) were singled out. The magnetic interaction in materials with these ions can change its character from AFM at normal pressure to FM at high pressure. However, this does not explain the results of the experimental study of iron borate. In order to give an acceptable explanation for the observed facts, it is necessary to study the magnetic interaction in  $\text{FeBO}_3$  in more detail. The scheme of superexchange interaction indicates the presence of two types of magnetic bonds of  $\text{Fe}^{3+}$  ions with the nearest environment. The first are exchange links with six neighbors at an angle of  $\sim 120^\circ$ . The second are  $180^\circ$  bonds in the chain of  $\text{Fe}^{3+}$  iron ions. As can be seen from Fig. 1, at normal pressure, both types of magnetic bonds  $J_{5E^5E}(180^\circ)$  and  $J_{5E^5T_2}(120^\circ)$  have an AFM character, since the spins of virtual electron and hole states in the corresponding exchange loops are equal to each other  $S_e = S_h = 3/2$  [2]. With an increase in pressure, when the crystal field reaches value  $10Dq = 3J_H$ , a spin crossover occurs, and the state  $|^6A_1\rangle$  of the  $\text{Fe}^{3+}$  ion changes to  $|^2T_2\rangle$ . In this case, the  $e_g$  orbitals disappear in the ( $180^\circ$ ) magnetic bonds, and the ( $120^\circ$ ) magnetic bonds with six nearest neighbors change their character very much. Indeed, in Fig. 1, four main contributions  $J_{3T_1^3T_2}^{AFM}(120^\circ)$ ,  $J_{3T_1^1T_1}^{FM}(120^\circ)$  and  $J_{1T_2^3T_2}^{FM}(120^\circ)$ ,  $J_{1T_2^1T_1}^{AFM}(120^\circ)$  can be distinguished, two of which are FM, and the other two are AFM. All contributions

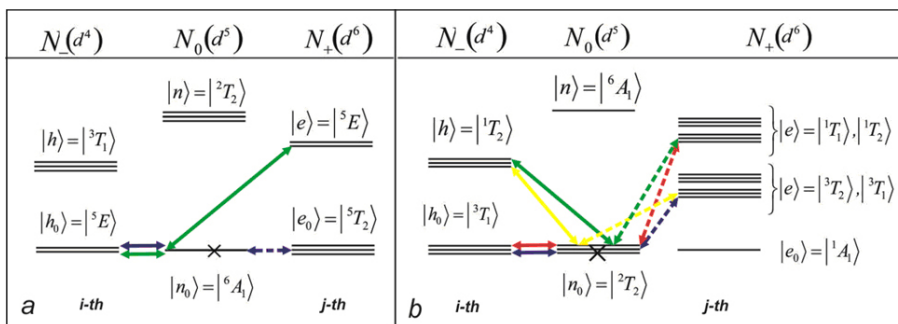


Figure 1. Scheme of exchange loops for  $120^\circ$  superexchange. **a** At normal pressure. The blue and green colors indicate  $J_{5E^5T_2}^{FM}(120^\circ)$ ,  $J_{5E^5E}^{FM}(180^\circ)$  AFM interaction. The dashed and solid lines correspond to  $t_{2g}$  and  $e_g$  virtual electrons and holes. **b** At high pressure  $P > P_C$ . FM contributions  $J_{3T_1^1T_1}^{FM}(120^\circ)$ ,  $J_{1T_2^3T_2}^{FM}(120^\circ)$  are marked in red and yellow, AFM contributions  $J_{3T_1^3T_2}^{AFM}(120^\circ)$ ,  $J_{1T_2^1T_1}^{AFM}(120^\circ)$ , are marked in blue and green.

are identical in terms of the overlap integrals of the  $t_{2g}$  and  $e_g$  orbitals involved in the magnetic bond. Therefore, the total superexchange interaction is determined by their simple superposition  $J_{\text{tot}}(120^\circ) = (J_{3T_2^3T_2}^{\text{AFM}} - J_{3T_1^1T_1}^{\text{FM}}) + (J_{1T_2^1T_1}^{\text{AFM}} - J_{1T_2^3T_2}^{\text{FM}})$ .

At  $10Dq = 3J_H$  and critical pressure, we have an upper bound for  $J_{\text{tot}}(120^\circ)$  in the form

$$J_{\text{tot}}(120^\circ) \approx \frac{2t_{ij}^2(120^\circ)}{(U + J_H)} \left( \frac{J_H}{U + J_H} \right)^2. \quad (1)$$

Now we can evaluate the reasons for the absence of magnetic ordering at high pressure in iron borate and the prospects for its detection with decreasing temperature to very low values. If at normal pressure

$$J_{5E^5T_2}^{\text{AFM}}(120^\circ) = \frac{2t_{ij}^2(120^\circ)}{\Delta_{5E^5T_2}}, \quad \text{where } \Delta_{5E^5T_2} = U - 10Dq + 4J_H, \quad (2)$$

then, at and critical pressure, their ratio is

$$\frac{J_{\text{tot}}(120^\circ)}{J_{5E^5T_2}^{\text{AFM}}(120^\circ)} \approx \left( \frac{J_H}{U + J_H} \right)^2 \approx 10^{-2}. \quad (3)$$

Then the ratio of the critical temperatures of magnetic ordering before and after the spin crossover is

$$\left. \frac{T_N^{\text{LS}}}{T_N^{\text{HS}}} \right|_{P=P_C} \approx \frac{1/2(1/2+1)}{5/2(5/2+1)} \frac{J_{\text{tot}}(120^\circ)}{J_{5E^5T_2}^{\text{AFM}}(120^\circ)} \approx 10^{-3}, \quad (4)$$

i.e. taking into account  $T_N^{\text{HS}}|_{P=P_C} \approx 500$ , the temperature of magnetic ordering  $T_N^{\text{LS}}$  at high pressure less than one Kelvin. Moreover, with a further increase in pressure, despite the increase in the overlap of orbitals,  $T_N$  only decreases, because when  $10Dq \gg 3J_H$

$$J_{\text{tot}}(120^\circ) \approx \frac{2t_{ij}^2(120^\circ)}{(U + 10Dq)} \left( \frac{J_H}{U + 10Dq} \right)^2 \quad (5)$$

and the magnetic bonding of  $\text{Fe}^{3+}$  iron ions in the nearest environment is practically absent.

*Support by RFBR grant №21-52-12033 is acknowledged.*

1. A.G. Gavriluk, I.A. Trojan, S.G. Ovchinnikov, I.S. Lyubutin, and V.A. Sarkisyan, J. Exp. Theor. Phys., **99**, 566 (2004).
2. V.A. Gavrichkov, S.I. Polukeev, S.G. Ovchinnikov, Phys. Rev. B, **101**, 094409 (2020).

## NMR STUDY OF ELECTRONIC STATES IN CHALCOGENIDES $\text{Cr}_x\text{NbSe}_2$ ( $x \leq 0.5$ )

*V.V. Ogloblichev*<sup>1\*</sup>, *N.V. Baranov*<sup>1</sup>, *Yu.V. Piskunov*<sup>1</sup>, *A.Y. Germov*<sup>1</sup>, *N.M. Nosova*<sup>2</sup>,  
*E.M. Sherokalova*<sup>2</sup>, *N.V. Selezneva*<sup>2</sup>

<sup>1</sup>M.N. Mikheev Institute of Metal Physics, Ural Branch, Russian Academy of Sciences, Ekaterinburg, Russian Federation

<sup>2</sup>Institute of Natural Science, Ural Federal University, Ekaterinburg, Russian Federation

\*E-mail: [ogloblichev@imp.uran.ru](mailto:ogloblichev@imp.uran.ru)

Transition metal dichalcogenides and their intercalates have become the subject of active studies of physics, chemistry, materials science and nanotechnology due to their intriguing physical and chemical properties. Compounds  $2\text{H-NbX}_2$  ( $X = \text{S}, \text{Se}$ ) exhibit metallic type of conductivity and superconducting transition when at the temperatures below 5.7 K and 7.2 K in sulfide and selenide compounds, respectively [1]. It was found that the intercalation of 3d-metal atoms in  $2\text{H-NbS}_2$  and  $2\text{H-NbSe}_2$  not only suppresses superconductivity, but also generates different magnetic states depending on the type and concentration of intercalated atoms. Additionally, in the compound  $\text{Cr}_{0.33}\text{NbS}_2$  intercalated with chromium, a long-period helimagnetic structure was found which can be transformed into a chiral soliton lattice under magnetic field effect [2]. However, selenide compounds  $\text{Cr}_x\text{NbSe}_2$  with  $x = 0.33$  usually exhibit ferromagnetic ordering. In contrast to the sulfide compound  $\text{Cr}_{0.33}\text{NbS}_2$ , there are insufficient literature data on the features of the electronic structure and the distributions of charge and spin density in  $\text{Cr}_x\text{NbSe}_2$  selenide compounds intercalated with Cr atoms. Taking into account that the charge and spin density distributions are the key to understanding of the mechanisms responsible for the changes in the structural, magnetic, and transport properties of intercalated compounds, the aim of this study is to investigate  $\text{Cr}_x\text{NbSe}_2$  compounds with chromium concentrations  $x = 0.33$  and  $x = 0.55$  using  $^{53}\text{Cr}$  and  $^{93}\text{Nb}$  NMR spectroscopy.

Figure 1 demonstrates the NMR spectra of  $^{53}\text{Cr}$  and  $^{93}\text{Nb}$  of  $\text{Cr}_{0.5}\text{NbSe}_2$  in a zero external magnetic field at a temperature of  $T = 4.2$  K. The  $^{53}\text{Cr}$  NMR spectrum split into three lines is due to the interaction of the quadrupole moment of chromium nuclei with the electric field gradient cre-

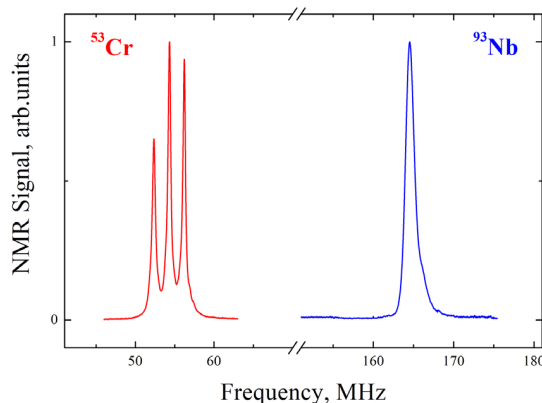


Figure 1.  $^{53}\text{Cr}$  and  $^{93}\text{Nb}$  NMR spectrum in  $\text{Cr}_{0.5}\text{NbSe}_2$  at temperature  $T = 4.2$  K in zero external magnetic field.

ated by the charge environment. The quadrupole frequencies has been experimentally determined as  $^{53}\nu_Q = 3.82(6)$  MHz and  $^{93}\nu_Q = 0.264(10)$  MHz. Local hyperfine fields  $|h_{loc}| = \nu_{res}/\gamma$  (where  $\gamma$  is gyromagnetic ratio) correspond to Larmor frequencies  $^{53}\nu_{res}$  and  $^{93}\nu_{res}$  of chromium and niobium atoms, correspondingly. Estimates of the dipole field contribution have shown that its contribution to the local hyperfine field is negligible in a magnetically ordered state. The main contribution to local hyperfine field  $|h_{loc}|$  is due to their own unpaired d-electrons. From the analysis of the local hyperfine fields of  $^{53}\text{Cr}$  nuclei, the average value of the magnetic moment of chromium is determined as  $\mu_{\text{NMR}} \approx 2.2 \mu_B$  which is less than the theoretical value  $\mu = 3\mu_B$  of  $\text{Cr}^{3+}$  and close to  $\mu = 2\mu_B$  of  $\text{Cr}^{4+}$ . We experimentally determined the value of local hyperfine field  $|h_{loc}| \approx 160$  kOe of  $^{93}\text{Nb}$  nuclei. The decrease in the average value of the magnetic moment of chromium and the presence of a non-zero local hyperfine field  $|h_{loc}|$  on niobium nuclei can be explained by a high degree of hybridization of the  $a_{1g}$  and  $e_g$  orbitals of 3d-shell of Cr with  $4d_{2-}$  and  $5s$ -orbitals of Nb. A similar transfer of electron densities from chromium ions to niobium ions is most likely occurs in compounds  $\text{Cr}_{0.33}\text{NbS}_2$ , where  $^{53}\text{Cr}$  NMR signal is also observed at the frequency range from 48 to 52 MHz with the local hyperfine field value  $|h_{loc}| = 207.7(2)$  kOe and magnetic moment of chromium  $\mu = 2.1\mu_B$  [3]. It should be noted that the values of the magnetic moment obtained by neutron diffraction for other intercalated compounds with long-range magnetic order of intercalated atoms turned out to be less than corresponding theoretical spin value [4, 5]. Decrease of the magnetic moment of atoms  $M$  in  $M_x\text{MX}_2$  was attributed to the hybridization of 3d-electrons of intercalated atoms with electronic states of the main lattice  $\text{MX}_2$ . In  $\text{Fe}_x\text{TiSe}_2$ , the presence of a small induced magnetic moment on the Ti atoms has been proposed to describe the antiferromagnetic structure of these compounds [5].

*This work was supported by the Russian Science Foundation (project no. 22-12-00220).*

1. I. Guillamón, H. Suderow, S. Vieira, L. Cario, P. Diener, P. Rodiere, PRL, **101(16)**, 166407 (2008).
2. Y. Togawa, T. Koyama, K. Takayanagi, S. Mori, Y. Kousaka, J. Akimitsu, S. Nishihara, K. Inoue, A.S. Ovchinnikov, J. Kishine, PRL, **108**, 107202 (2012).
3. V.V. Ogloblichev, Yu.V. Piskunov, F.B. Mushenok, JETP, **125**, 317 (2017).
4. N.V. Selezneva, N.V. Baranov, V.G. Pleshchev, N.V. Mushnikov, and V.I. Maksimov, Phys. Solid State, **53**, 329 (2011).
5. N.V. Baranov, E.M. Sherokalova, N.V. Selezneva, A.V. Proshkin, L. Keller, A.S. Volegov, and E.P. Proskurina, J. Phys.: Condens. Matter, **25**, 066004 (2013).

## A SIMPLE EXACTLY SOLVABLE SPIN-REORIENTATION MODEL IN RARE-EARTH ORTHOFERRITES

*E.V. Vasinovich*<sup>1\*</sup>, *A.S. Moskvina*<sup>1,2</sup>, *A.V. Shadrin*<sup>1</sup>

<sup>1</sup>Ural Federal University, Ekaterinburg, Russia

<sup>2</sup>Institute of Metal Physics UB RAS, Ekaterinburg, Russia

\*E-mail: [e.vasinovich@gmail.com](mailto:e.vasinovich@gmail.com)

Rare-earth orthorhombic perovskites, orthoferrites  $R\text{FeO}_3$  and orthochromites  $R\text{CrO}_3$  (where  $R$  is a rare-earth ion and yttrium), exhibit many important features, such as weak ferro- and antiferromagnetism, which are an overt and hidden canting of magnetic sublattices, magnetization reversal, anomalous circular magneto-optics and the phenomenon of spontaneous spin reorientation. Spin reorientation (SR) is one of their unique properties that attracted a lot of attention back in the 1970s [1], though their exact microscopic origin is still a challenge to theorists and experimentalists.

In this work, we consider a simple microscopic theory of the SR transition in a certain plane of the rare-earth orthoferrite induced by the 4f–3d interaction, more specifically, the interaction of the well-isolated ground-state Kramers doublet or non-Kramers quasidoublet of the 4f ion with an effective magnetic field induced by 3d sublattice. For instance, a thermodynamic potential of the model for the SR transition  $G_x$ – $G_z$  in the  $ac$  plane ( $\mathbf{G}$  is the antiferromagnetic vector of the 3d sublattice) can be written as

$$\Phi(\theta) = K_1 \cos 2\theta + K_2 \cos 4\theta - kT \ln 2 \cosh \frac{\Delta(\theta)}{2kT}, \quad (1)$$

where  $K_1$  and  $K_2$  are the first and second anisotropy constants of the 3d sublattice [2],  $\theta$  is the orientation angle,  $\Delta(\theta)$  is the lower doublet (quasi-doublet) splitting of the 4f ion. Minimizing  $\Phi(\theta)$  leads to two equations:

$$\begin{aligned} \sin 2\theta &= 0 \text{ (phases } G_x \text{ and } G_z), \\ \alpha\mu + \beta\mu^3 &= \tanh(\mu/\tau) \text{ (angular phase } G_{xz}), \end{aligned} \quad (2)$$

where  $\tau = T/T_{\text{sr}}$ ,  $T_{\text{sr}} = [\Delta^2(0) - \Delta^2(\pi/2)]/16kK_1$ ,  $\mu = \Delta(\theta)/2kT_{\text{sr}}$ , and  $\alpha$ ,  $\beta$  are the parameters, which depend on the  $K_1$ ,  $K_2$ ,  $\Delta(0)$ , and  $\Delta(\pi/2)$ .

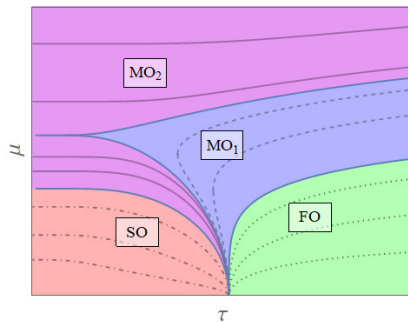


Figure 1. The  $\mu$ – $\tau$  phase diagram of the model.

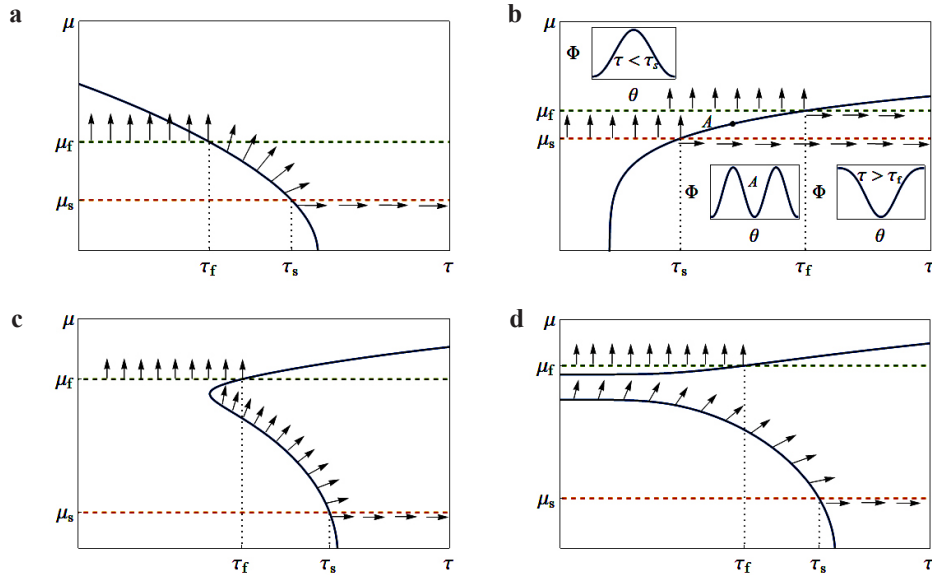


Figure 2. Illustrations of typical (a, b) and unconventional (c, d) SR transitions predicted by the model. The arrows indicate the direction of the antiferromagnetic vector  $\mathbf{G}$  in the  $ac$  plane.

Figure 1 shows typical solutions for the master equation (2). This model can describe a variety of the SR scenarios including rather typical smooth SR via one or two second-order phase transitions (see SO region in Fig. 1), sharp first-order phase transition (see FO region), and unconventional “mixed” SR via combination of the second and first-order phase transitions (see  $MO_{1,2}$  regions).

Figure 2 shows detailed examples of the phase diagram. Figure 2a describes a typical smooth SR transition with two second-order phase transitions  $G_x-G_{xz}$  at the beginning ( $\tau_s$ ) and  $G_{xz}-G_z$  at the end ( $\tau_f$ ) of the spin reorientation. Figure 2b describes an abrupt first-order SR transition: for  $\tau > \tau_f$  there is the  $G_x$ -phase, which can remain stable up to  $\tau_s$  when cooled; for  $\tau < \tau_s$  there is the  $G_z$ -phase, which can remain stable up to  $\tau_f$  when heated.

Figures 2c and d describe the more interesting cases when the model predicts the existence of mixed-type SR transitions. At  $\tau_s$ , there is the smooth second-order phase transition  $G_x-G_{xz}$ . At  $\tau \leq \tau_f$ , we have two stable phases,  $G_z$  and  $G_{xz}$ : at those temperatures the sharp first-order phase transition  $G_x-G_{xz}$  can happen, or the system could stay in the angular  $G_{xz}$ -phase.

The main results have been published in [3].

*The work was supported by RSF project № 22-22-00682.*

1. K.P. Belov, A.K. Zvezdin, A.M. Kadomtseva and R.Z. Levitin, Orientation Phase Transitions in Rare Earth Magnetic Materials, Nauka, Moscow (1979) [in Russian].
2. A. Moskvina, Magnetochemistry, **7**, 111 (2021).
3. A. Moskvina, E. Vasinovich and A. Shadrin, Magnetochemistry, **8**, 45 (2022).



## CHARGE AND MAGNETIC CORRELATIONS IN GRAPHENE NANOFLEAKS WITH SCREENED LONG-RANGE COULOMB POTENTIAL

*V.S. Protsenko*<sup>1,2\*</sup>, *A.A. Katanin*<sup>3,1</sup>

<sup>1</sup>M.N. Mikheev Institute of Metal Physics of Ural Branch of Russian Academy of Sciences, Ekaterinburg, Russia

<sup>2</sup>Ural Federal University n.a. the first President of Russia B.N. Yeltsin, Ekaterinburg, Russia

<sup>3</sup>Center for Photonics and 2D Materials, Moscow Institute of Physics and Technology, Dolgoprudny, Moscow region, Russia

\*E-mail: [protsenko.vladimir15@mail.ru](mailto:protsenko.vladimir15@mail.ru)

Graphene nanoflakes (GNFs) are structures obtained by restricting the size of graphene plane. Due to their interesting electronic properties, arising from the properties inherited from the graphene sheets and dimension reduction, GNFs are considered as one of the most promising candidates for fabrication of nanoelectronic and spintronic devices.

It is well known that long-range Coulomb interactions in graphene sheets play a crucial role, favoring the formation of spin density wave (SDW) or charge density wave (CDW) states. From this point of view the study of the role of long-range interactions in GNFs represents an important task whose consideration has been to date mostly limited to the account of only the on-site and nearest-neighbor electron-electron interactions or restricted to the  $1/r$  dependence of the non-local potential on distance  $r$ .

We investigate charge and magnetic properties of hexagonal GNFs of different sizes (an example of hexagonal GNF for  $N = 96$  atoms is shown in Fig. 1) with the screened realistic long-range electron interaction of refs. [1, 2] and compare the results to those for the uniformly screened long-range Coulomb potential  $\propto 1/r$ . By using the functional renormalization group (fRG) method we calculate [3] the dependencies of the staggered magnetization and the difference between the average occupation numbers of the sublattices on  $U$  and  $\epsilon_{n1}$ , where  $U$  is the local (on-site) interaction and the dielectric permittivity  $\epsilon_{n1}$  accounts for the screening of non-local interactions. By extracting from the above dependencies the critical values of  $U$  and  $\epsilon_{n1}$ , corresponding to SDW and CDW

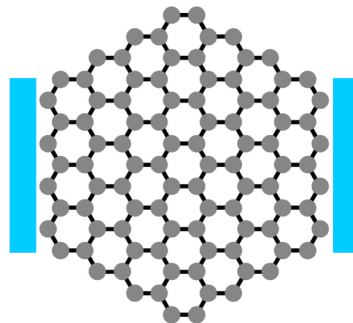


Figure 1. Hexagonal GNF system with  $N = 96$  atoms. Rectangles represent left and right leads, which are connected to the GNF to study its electron transport properties (not presented; see ref. [3] for the results on transport properties).

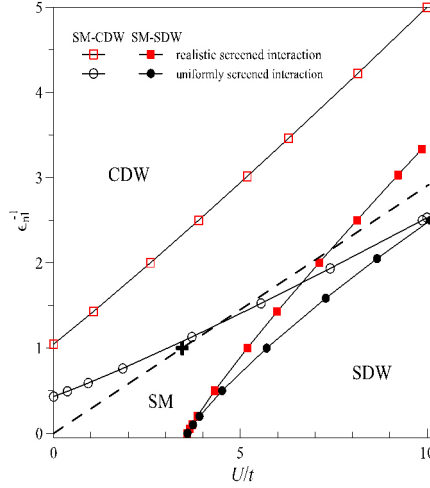


Figure 2. Phase diagram of the zigzag-edge GNF system with  $N = 96$  atoms with the realistic screened  $U_{ij}^* = U_{ij}^*/\epsilon_{n1}$  (red squares) and uniformly screened  $U_{ij} = e^2/\epsilon_{n1}\epsilon_{\text{eff}}r_{ij}$  (black circles) form of non-local interaction in the  $U/t, \epsilon_{n1}^{-1}$  coordinates: SM-SDW phase transitions are denoted by solid lines with filled symbols, SM-CDW phase transitions are marked by solid lines with open symbols. The dashed line  $U = U_r/\epsilon_{n1}$  corresponds to simultaneous screening of local and non-local interaction. The point  $\epsilon_{n1} = 1$  and  $U = U_r = 9.3 \text{ eV} \approx 3.4t$ , corresponding to freely suspended graphene, is marked by the plus symbol. Here  $U_{ij}^*$  is the realistic non-local potential of refs. [1, 2],  $t = 2.7 \text{ eV}$  is the nearest-neighbor hopping parameter, and  $\epsilon_{\text{eff}} \approx 1.41\epsilon_{\text{eff}}$  is the effective dielectric permittivity, resulting from the screening of interaction by  $\sigma$  orbitals [2].

order, we obtain [3] the ground-state phase diagrams at half-filling in the  $(U/t, \epsilon_{n1}^{-1})$  coordinates (the corresponding phase diagram for the GNF system with  $N = 96$  is presented in Fig. 2).

We obtain [3] that for  $U < U_c^N$ , where  $U_c^N$  is the critical local interaction for SDW order in  $N$ -atom GNF in the absence of non-local interaction ( $\epsilon_{n1}^{-1} = 0$ ), the GNF system undergoes the semimetal (SM) to the CDW phase transition with increasing the non-local interaction strength (i.e. decrease of  $\epsilon_{n1}$ ). When  $U > U_c^N$ , GNFs systems undergo two quantum phase transitions with decrease of  $\epsilon_{n1}$ : first, from the SDW to the SM phase and, second, from the SM to the CDW phase. For the realistic non-local interactions all obtained SM-CDW phase transition lines (except the one for the GNF with  $N = 6$ ) are very close to each other and are well fitted by linear dependencies. Critical value of the  $\epsilon_{n1}$  (as well as  $U_c^N$ ) for the SM-SDW phase transition decreases with increasing of the size of the system  $N$ . As can be seen from Fig. 2, the realistic screening of Coulomb interaction leads to moderate (strong) enhancement of critical long-range interaction strength, needed for the SDW (CDW) instability, compared to the results for the uniformly screened Coulomb potential. This is caused by the significant difference between the realistic potential of refs. [1, 2] and the uniformly screened long-range Coulomb potential at intermediate distances due to the screening of interaction by  $\sigma$  orbitals. One can see from Fig. 2 that for the uniformly screened long-range Coulomb potential freely suspended graphene nanoflakes (corresponding to the parameters marked by plus symbol in Fig. 2) would be on the verge of the charge instability. The above-discussed enhancement of critical long-range interaction strength, needed for the CDW instability, in the case of the realistic Coulomb interaction gives rise to a wide region of stability of the SM phase for realistic interaction, such that freely suspended GNFs are far from both SM-SDW and SM-CDW phase-transition boundar-

ies and correspond to the SM phase. At the same time, we find that the corresponding GNFs are characterized by an enhanced staggered susceptibility, and therefore, substantial SDW correlations.

To provide an insight into the effects of disorder in GNFs we compare the above results on the magnetic instability of the GNF system with  $N = 96$  to those obtained for this system in the presence of two randomly placed vacancies in the GNF lattice (one vacancy for each sublattice). We calculate the dependence of the average relative staggered magnetization on  $U$  for different values of  $\epsilon_{n1}$  by statistically averaging over random distribution of vacancies (we use set of 10 disorder realizations). We found that the presence of only two vacancies in GNF system with  $N = 96$  atoms (corresponding to about 2% of vacant sites) leads to a notable enhancement (up to about 20–40% depending on  $\epsilon_{n1}$ ) of the staggered magnetization induced by the staggered magnetic field, which reflects strong enhancement of magnetic correlations in the SM state.

*The work was partly supported by RFBR grant 20-02-00252a. The calculations were performed on the Uran supercomputer at the IMM UB RAS.*

1. T.O. Wehling, E. Şaşıoğlu, C. Friedrich, A.I. Lichtenstein, M.I. Katsnelson, and S. Blügel, Phys. Rev. Lett., **106**, 236805 (2011).
2. M.V. Ulybyshev, P.V. Buividovich, M.I. Katsnelson, and M.I. Polikarpov, Phys. Rev. Lett., **111**, 056801 (2013).
3. V.S. Protsenko and A.A. Katanin, Phys. Rev. B, **104**, 245139 (2021).

## MAGNETIC AND ELECTRONIC PROPERTIES OF $Mn_3Z$ ( $Z = Ga, Ge, In, Sn$ ): *AB INITIO* STUDIES

*M.A. Zagrebina\**, *M.A. Obambi*, *V.D. Buchelnikov*

Physics Department, Chelyabinsk State University, Chelyabinsk, Russia

\*E-mail: [miczag@mail.ru](mailto:miczag@mail.ru)

The complex magnetic behavior of the isostructural intermetallic compounds with nominal compositions  $Mn_3Z$  ( $Z = Ga, Sn$  and  $Ge$ ) has been the subject of a number of studies. The  $Mn_3Z$  ( $Z = Ga, Sn$  and  $Ge$ ) type Heusler compounds can have three different structural phases, where each phase exhibits different magnetic properties [1–6]. The hexagonal phase has been known for decades. Mn atoms in the hexagonal structure have a triangular antiferromagnetic coupling with a weak net magnetic moment [1, 2]. The cubic phase is the standard full Heusler structure. In this phase, Mn atoms are present in two unique lattice sites; these different sites have magnetic moments with opposite directions, leading to ferrimagnetic (FIM) order [4]. The tetragonal phase can be treated as a cubic phase with a distortion along the  $z$  direction. This distortion makes the magnetic moments favor the  $c$  axis, meaning the system possesses perpendicular magnetocrystalline anisotropy [5], which promises great potential for future high-density spin-transfer torque applications [6]. The aim of this work is *ab initio* study of magnetic and electronic properties of the  $Mn_3Z$  ( $Z = Ga, Ge, In, Sn$ ) compound.

In order to investigate the electronic structure and the magnetic and structural ground state properties of  $Mn_3Z$  ( $Z = Ga, Ge, In, Sn$ ) alloys, we used the projector augmented wave (PAW) method and the Korringa–Kohn–Rostoker Green’s function method as implemented in VASP (Vienna *ab initio* simulation program) [7, 8] and SPR-KKR (spin-polarized-relativistic Korringa–Kohn–Ros-

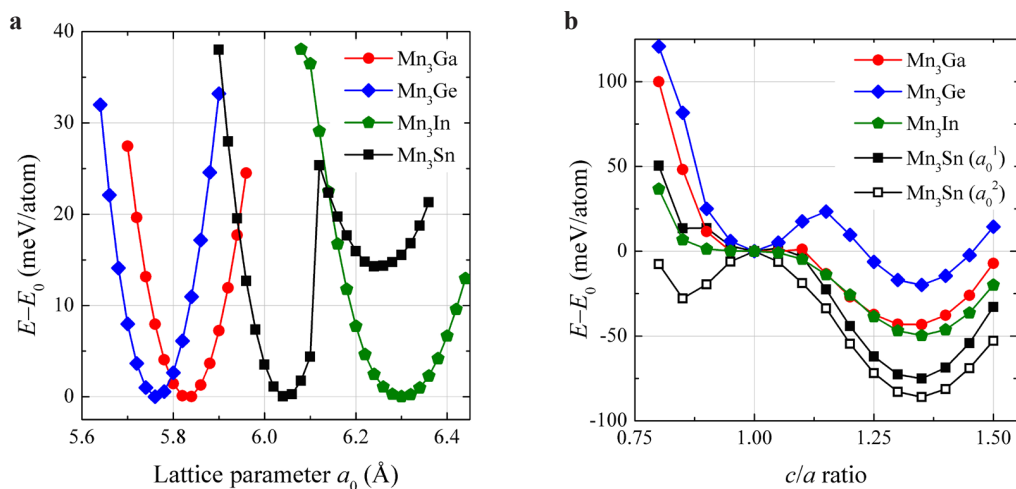


Figure 1. The total energy differences with respect to equilibrium value for a series of  $Mn_3Z$  ( $Z = Ga, Ge, In, Sn$ ) compounds in FIM magnetic state as functions of **a** lattice parameter and **b** tetragonal distortion.

Table 1. Calculated lattice parameter  $a_0$  (in Å) spin polarization  $P$  (in %), Curie temperature  $T_C$  (in K) and energy of magnetocrystalline anisotropy  $E_{MCA}$  (in meV) for austenite and martensite phases for a series of  $Mn_3Z$  ( $Z = Ga, Ge, In, Sn$ ) compounds in FIM magnetic state.

Compound	Austenite			Martensite		
	$a_0$	P	$T_C$	P	$T_C$	$E_{MCA}$
$Mn_3Ga$	5.831	91.2	86	53.7	593	0.751
$Mn_3Ge$	5.763	86.9	90	43.4	394	0.705
$Mn_3In$	6.151	28.7	1513	65.0	193	1.243
$Mn_3Sn$	6.046	83.2	36	2.1	228	0.452
	6.250	25.7	1448	23.0	637	0.776

token code) [9], respectively. In both cases, the exchange correlation effects were described by the Perdew–Burke–Ernzerhof formulation of the generalized gradient approximation [10]. The optimization for the geometrical structure of the austenite phase was carried out using the VASP package in combination with the 16-atom supercell approach.

To perform the crystal structure optimization, we used the  $L2_1$  structure (space group  $Fm-3m$ , No. 225,  $Cu_2MnAl$  as the prototype). To determine the possibility of martensitic transformation in studied alloys, we performed total energy calculations for tetragonal distortion of the cubic structure along  $z$  axis. In our calculations we considered two magnetic reference states labelled as FM and FIM. In the first one all magnetic moments of  $Mn_1$  and  $Mn_2$  atoms are parallel, while in the second one the magnetic moment of  $Mn_2$  atoms is reversed. Here,  $Mn_1$  denotes Mn atoms located at the  $8c$  ( $(1/4, 1/4, 1/4)$  and  $(3/4, 3/4, 3/4)$ ), and  $Mn_2$  denotes Mn atoms located at the  $4b$  ( $1/2, 1/2, 1/2$ ) Wyckoff positions. The optimized lattice parameters further used to calculate the exchange coupling constants ( $J_{ij}$ ), total and partial DOS and magnetic moments by using the SPR-KKR package. Energy of magnetocrystalline anisotropy  $E_{MCA}$  have been calculated by using of magnetic torque method, implemented in SPR-KKR code [9]. Obtained  $J_{ij}$  allowed us to estimate Curie temperatures ( $T_C$ ) by using Heisenberg model in the framework of mean field approximation [11].

From our calculations lead that for all compounds under consideration (both in austenite and martensite) the ferrimagnetic state is preferred. The further analysis will be given for FIM states. In the Fig. 1a we depicted the total energy difference curves,  $\Delta E(a)$ , relative to equilibrium energies of all studied alloys. From figure it is seen that  $Mn_3Ge$  alloys has smallest equilibrium lattice parameter while  $Mn_3In$  has largest one. It should be noted, that in the case of  $Mn_3Sn$  there are two minima on the  $E(a)$  dependence. This fact indicates the presence of two stable austenitic structures with different lattice parameters. The total energy differences between the tetragonal distorted and cubic phases for alloys as functions of  $c/a$  ratio are depicted in Fig. 1b. We can observe that alloys exhibit the possibility of austenite-martensite transformation. Calculated properties of the considered compounds are collected in Table 1.

The largest value of spin polarization is obtained for  $Mn_3Ga$  alloy in austenitic state, and the largest value of magnetocrystalline anisotropy is obtained for  $Mn_3In$  alloy.

It was found that the obtained properties agree with existent experimental and theoretical data [4, 12]. We suppose that  $Mn_3Z$  ( $Z = Ga, Ge, In, Sn$ ) alloys might be promising for the technological applications.

*Support by Russian Science Foundation (Project No. 22-12-20032) is acknowledged.*

1. S. Tomiyoshi, Y. Yamaguchi, J. Magn. Magn. Mater., **31-34**, 629–630 (1983).
2. P.J. Brown et al., J. Phys.: Condens. Matter, **2**, 9409–9422 (1990).
3. D. Zhang et al., J. Phys.: Condens. Matter, **25**, 206006 (2013).
4. S. Wurmehl et al., J. Phys.: Condens. Matter, **18**, 6171 (2006).
5. J. Winterlik et al., Adv. Mater., **24(47)**, 6283–6287 (2012).
6. H. Kurt et al., Appl. Phys. Lett., **101**, 132410 (2012).
7. G. Kresse, J. Furthmüller, Phys. Rev. B, **54**, 11169–11186 (1996).
8. G. Kresse, D. Joubert, Phys. Rev. B, **59**, 1758–1775 (1999).
9. H. Ebert et al., Rep. Prog. Phys., **74**, 96501 (2011).
10. J.P. Perdew et al., Phys. Rev. Lett., **77**, 3865 (1996).
11. P.W. Anderson, Solid State Phys., **14**, 99–214 (1963).
12. B. Balke et al., Appl. Phys. Lett., **90**, 152504 (2007).

## PRESSURE EFFECT ON THE ELECTRONIC AND MAGNETIC PROPERTIES OF NOVEL IRON OXIDE Fe<sub>4</sub>O<sub>5</sub>

*V.S. Zhandun\**, *N.V. Kazak*

Kirensky Institute of Physics, Federal Research Center KSC SB RAS, Krasnoyarsk, Russia

\*E-mail: [jvc@iph.krasn.ru](mailto:jvc@iph.krasn.ru)

Iron oxides are attracting a lot of attention due to their complex structural properties and fundamental aspects from the point of view of natural sciences and industrial applications [1, 2]. In the last decade, studies at high temperatures and high pressures have revealed the existence of new binary iron oxides with unusual stoichiometry, such as Fe<sub>4</sub>O<sub>5</sub> [3] and Fe<sub>5</sub>O<sub>6</sub> [4]. The discovery of new compounds motivated the study of their physical properties and potential for innovative applications [2]. While data on the crystal structure and some physical properties at ambient pressure are available, the electronic and magnetic properties under extreme pressure/temperature conditions are still poorly investigated. This knowledge is important for both solid state physics and earth sciences.

At the present work, we theoretically studied the pressure effect on the electronic and magnetic properties and phase stability of novel Fe<sub>4</sub>O<sub>5</sub> oxide using the DFT+GGA approach. The optimized crystal structure of Fe<sub>4</sub>O<sub>5</sub> contains three nonequivalent metal positions: the octahedral positions Fe1 (4a) and Fe2 (8a) and triangular prism Fe3 (4c). The ground magnetic state was found to be ferrimagnetic with the large magnetic moments of the iron atoms  $\mu(\text{Fe1}) = 3.6\mu_B$ ,  $\mu(\text{Fe2}) = 4.3\mu_B$ ,  $\mu(\text{Fe3}) = 3.7\mu_B$ . To study the phase stability, the enthalpy of the Fe<sub>4</sub>O<sub>5</sub> formation was calculated in combination with the linear optimization procedures and considering the competitive phases. The Fe<sub>4</sub>O<sub>5</sub> is thermodynamically unstable at zero pressure. However, a rather low pressure of about 13 GPa is able to stabilize Fe<sub>4</sub>O<sub>5</sub> phase (Fig. 1a). The pressure behavior of the iron magnetic moments is the site-dependent (Fig. 2b). The magnetic moments of the octahedral sites Fe1 and Fe2 collapse in the pressure range  $P_c = 50\text{--}60$  GPa, whereas the magnetic moment of Fe3 atom undergoes a spin-state crossover at higher pressures.

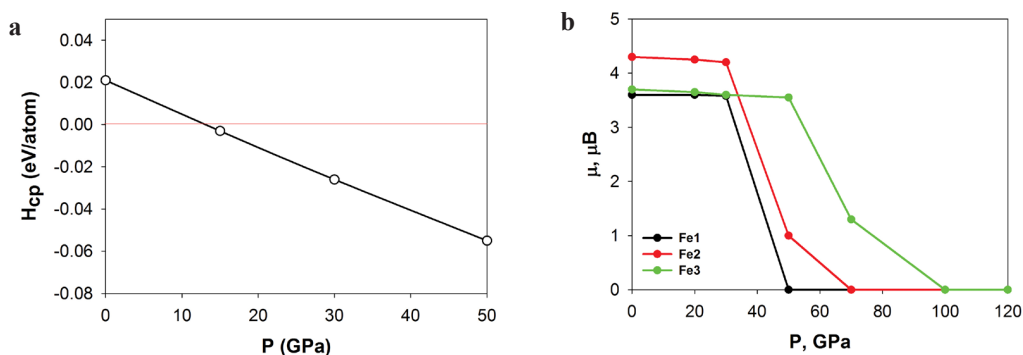


Figure 1. **a** Dependence of the formation enthalpy of Fe<sub>4</sub>O<sub>5</sub> on the pressure; **b** The pressure dependence of the iron magnetic moments.

*This work is funded by the Russian Foundation for Basic Research (project no. 21-52-12033).*

1. C. Delacotte, Y. Bréard, V. Caignaert et al., *Solid State Chem.*, **247**, 13–19 (2017).
2. S.V. Ovsyannikov, M. Bykov, E. Bykova et al., *Nat. Commun.*, **9**, 4142 (2018).
3. B. Lavina, P. Dera, E. Kim et al., *Proc.Natl.Acad.Sci. U.S.A.*, **108**, 17281–5 (2011).
4. B. Lavina, Y. Meng, *Sci. Adv.*, **1**, e1400260–e1400260 (2015).

## THE SPIN-STATE TRANSITION IN $ACo_2O_4$ OXIDES (A = Be, Mg, Ca, Cd, Zn)

V.S. Zhandun

Kirensky Institute of Physics – Federal Research Center “Krasnoyarsk Science Centre,  
Siberian Branch of the Russian Academy of Sciences”, Krasnoyarsk, Russia

E-mail: [jvc@iph.krasn.ru](mailto:jvc@iph.krasn.ru)

H.P24

We have performed the investigation of magnetic and electronic properties of the cobaltite oxides  $ACo_2O_4$  (A = Be, Mg, Ca, Zn, Cd). Based on our calculations, all compounds have the cubic unit cell, except for Ca-based oxide which has an orthorhombic structure in agreement with the experiment. The lattice parameter increases with an increase of the atomic number of the A-site cation. In all compounds, the octahedrally coordinated cobalt ion  $Co^{3+}$  is in a low-spin state due to the crystal field splitting of  $t_{2g}$ - and  $e_g$ -states. This leads to all compounds being in a non-magnetic state. We found that the spin state of the  $Co^{3+}$  ion can be tuned by pressure. At a critical pressure of about  $P = (-10)–(-20)$  GPa, a sharp appearance of the magnetic moment on  $Co^{3+}$  occurs (Fig. 1), which corresponds to the spin-state transition of the  $Co^{3+}$  ion into the high-spin state due to the redistribution of d-electrons. This pressure-induced spin-state transition leads to the  $ACo_2O_4$  oxides becoming ferromagnetic. The formation of low-spin state and high-spin state are discussed in terms of inter-atomic distances between  $Co^{3+}$  ion and its nearest environment. The magnetic (ferromagnetic) state turns out to be favorable by energy in thin films also. All compounds are insulators with the energy band gap varying from 1.95 to 2.67 eV. The applied tensile pressure leads to the abrupt increase of the majority spin bandgap and the decrease of the minority spin band gap at the critical pressure of the spin-state transition. The mechanism of such behavior is related to the shift of the  $t_{2g}$ - and  $e_g$ -states under applied pressure. Thus, our theoretical predictions can stimulate experimenters and technologists to develop new spintronic materials based on  $ACo_2O_4$  oxides.

*The study was supported by the Russian Science Foundation grant No. 22-22-20024, <https://rscf.ru/project/22-22-20024/>.*

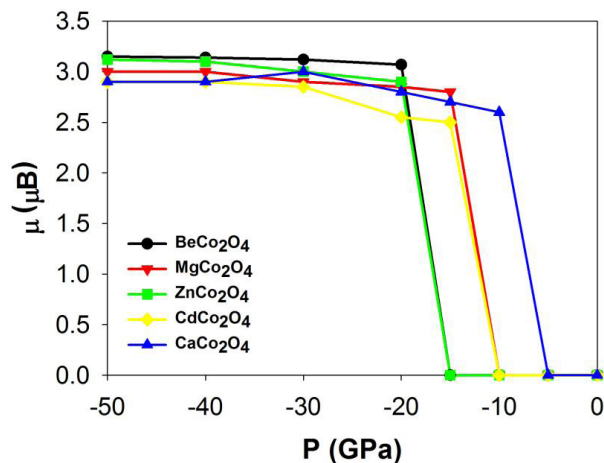


Figure 1. The pressure dependence of  $Co^{3+}$  ion magnetic moments.



**SYNTHESIS AND MAGNETIC PROPERTIES OF NANOSTRUCTURAL COMPOSITE  $(\text{CaCu}_3\text{Ti}_4\text{O}_{12})_{1-x}(\text{SrFe}_{12}\text{O}_{19})_x$  ( $x = 0.01, 0.03, 0.07$  AND  $0.1$ )**

*Yu. A. Deeva<sup>1,2\*</sup>, T.I. Chupakhina<sup>1,3</sup>, T.P. Gavrilova<sup>4</sup>, R.M. Eremina<sup>4</sup>*

<sup>1</sup>Institute of Solid State Chemistry of RAS (UB), Ekaterinburg, Russia

<sup>2</sup>The Ural Federal University named after the first President of Russia B.N. Yeltsin, Ekaterinburg, Russia

<sup>3</sup>Ural State Mining University, Ekaterinburg, Russia

<sup>4</sup>Zavoisky Physical-Technical Institute, FRC Kazan Scientific Center, Russian Academy of Sciences, Kazan, Russia

\*E-mail: [juliahik@mail.ru](mailto:juliahik@mail.ru)

Magnetoelectric materials have tempting prospects for use in various devices of solid -state electronics. To obtain them, composite structures of the “core-shell” type containing two or more ferromagnetic and paramagnetic phases mechanically interconnected are intensively examined. Interest in these materials is due to the fact that the magnetoelectric effect arising in them is a new property that is absent in the original components.

In this study we investigated the materials, which consist of two inorganic phases. One of the components of the composite material is  $\text{CaCu}_3\text{Ti}_4\text{O}_{12}$  (CCTO), which dielectric behavior exhibits an extraordinarily high dielectric constant and shows good thermal stability in a wide temperature range. As the second component of the composite material, we chose ferromagnetic material is strontium hexaferrite  $\text{SrFe}_{12}\text{O}_{19}$  (SFO) [1, 2].

The initial step of the formation of  $(\text{SrFe}_{12}\text{O}_{19})_x(\text{CaCu}_3\text{Ti}_4\text{O}_{12})_{1-x}$  nanocomposite was the synthesis of  $\text{SrFe}_{12}\text{O}_{19}$  (SFO) strontium hexaphaferrite, synthesized by the standard method of solid-phase synthesis. To obtain SFO, a stoichiometric amount of chemically pure  $\text{SrCO}_3$  and  $\text{Fe}_2\text{O}_3$  reagents were taken. The resulting mixture was annealing at 1000 °C for 8 hours.

At the second stage of the formation of the  $(\text{SrFeO})_x(\text{CCTO})_{1-x}$  ( $x = 0.01, 0.03, 0.07$  and  $0.1$ ) composite, the resulting SFO was used, in which the presence of impurities was not observed, and the stoichiometric amount of  $\text{CaO}$ ,  $\text{CuO}$  and  $\text{TiO}$  oxides. The annealing of the resulting mixture was carried out at 1000 °C for 24 hours with an intermediate grinding.

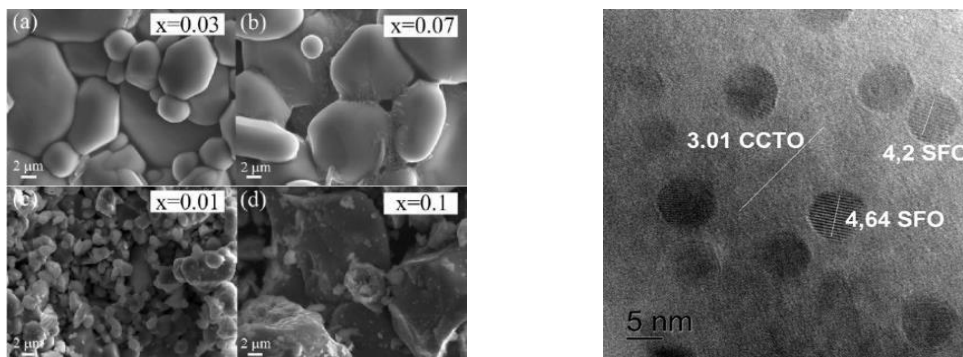


Figure 1. SEM image (left)  $\text{SFO}_x\text{CCTO}_{1-x}$  for  $x = 0.03$  (a),  $x = 0.07$  (b),  $x = 0.01$  (c),  $x = 0.1$  (d) and TEM image (right) for  $(\text{SrFe}_{12}\text{O}_{19})_x(\text{CaCu}_3\text{Ti}_4\text{O}_{12})_{1-x}$  ( $x = 0.07$ ).

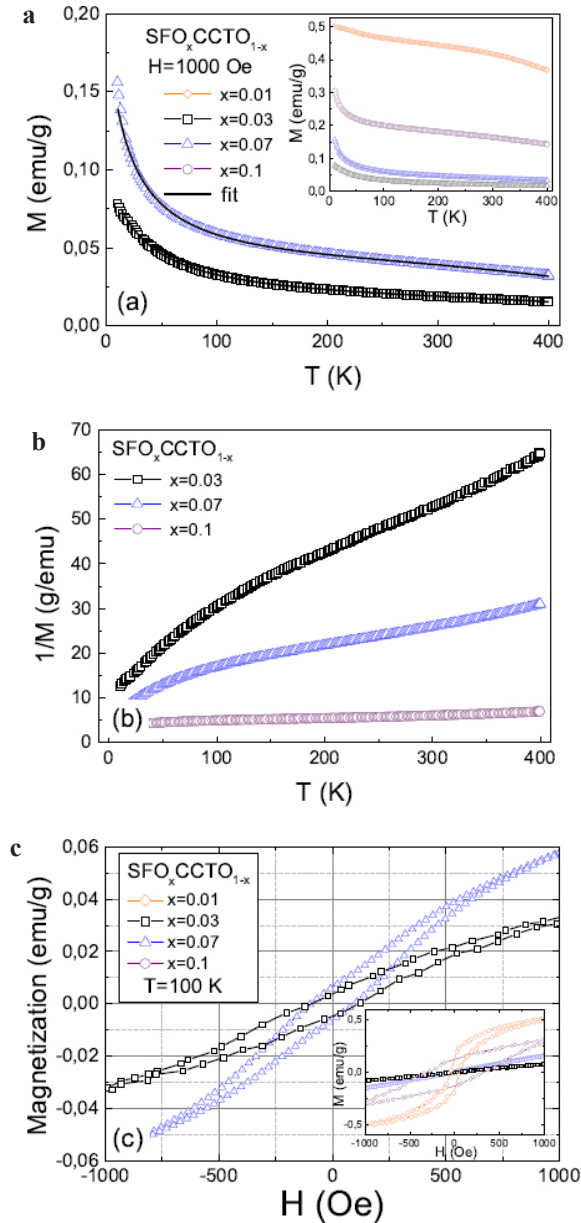


Figure 2. Temperature dependences of magnetization (a) and reverse magnetization in  $\text{SFO}_x\text{CCTO}_{1-x}$  (b), field dependence of magnetization in  $\text{SFO}_x\text{CCTO}_{1-x}$  at  $T = 100$  K (c)

The surface of the composites  $(\text{SFO})_x(\text{CCTO})_{1-x}$  by SAM and the internal structure of the composite with 7% content of SFO by TEM were investigated (Fig. 1).

From the SEM images, we can see that the composites with  $x = 0.03$  and  $x = 0.07$  have a granular structure, while at  $x = 0.01$  and  $0.1$  there is no granular structure, and the powder particles have an irregular shape. The TEM images show that the nanocrystalline inclusions in the CCTO matrix are the SFO phase based on the calculated interplanar spacings.

The results of the study of the magnetization of composites with the composition  $\text{SFO}_x\text{CCTO}_{1-x}$  are shown in Fig. 2.

When studying the magnetization of composites, it was found that the absolute value of the magnetization strongly depends on the concentration  $x$ . It increases with increasing SFO content over the entire temperature range, except for the concentration  $x = 0.01$ . The increase in coercivity at  $x = 0.1$  and in saturation magnetization at  $x = 0.01$  can be explained by the presence of  $\text{CaCu}_3\text{Ti}_{1-y}\text{Fe}_y\text{O}_{12-\delta}$  solid solutions in the samples. The temperature dependence of the magnetization does not follow the Curie-Weiss law, which is confirmed by the non-linear temperature dependence of the inverse magnetic susceptibility (Fig. 3b). The presence of ferromagnetism in the  $\text{SFO}_x\text{CCTO}_{1-x}$  composites is confirmed by a well-defined loop hysteresis loop up to room temperature (Fig. 3c).

Based on the analysis of X-ray diffraction, SEM and TEM, it can be concluded that nanostructured composites in which SFO nanoinclusions are inside the CCTO matrix were formed only for  $x = 0.03$  and  $x = 0.07$ . The mutual influence of the ferromagnetic and paramagnetic phases on the dielectric and magnetic properties of the resulting composites, which differ from the properties of individual components, has been established.

*Support by RSF (IEEE, ARC, ARCNN, DFG, NSF etc.) is acknowledged.*

1. R.M. Eremina, K.R. Sharipov, I.V. Yatsyk et al., JETP, **123** (1), 127–133 (2016).
2. T.P. Gavrilova, J.A. Deeva, I.V. Yatsyk et al., Physica B, **536**, 303–309 (2018).

## SPIN DYNAMICS AND MAGNETIC PROPERTIES IN RARE-EARTH ORTHOFERRITES $TmFeO_3$ AND $TbFeO_3$

*S.A. Skorobogatov*<sup>1,2\*</sup>, *K.A. Shaykhutdinov*<sup>1,2</sup>, *D.A. Balaev*<sup>1,2</sup>, *M.S. Pavlovskii*<sup>1,2</sup>, *A.A. Krasikov*<sup>1</sup>,  
*K.Yu. Terentjev*<sup>1</sup>

<sup>1</sup>Kirensky Institute of Physics, Federal Research Center KSC SB RAS, Krasnoyarsk, Russia

<sup>2</sup>Siberian Federal University, Krasnoyarsk, Russia

\*E-mail: [sgsas13@gmail.com](mailto:sgsas13@gmail.com)

Rare-earth orthoferrites with the general composition  $RFeO_3$  ( $R$  – rare-earth ion) are oxide magnetic materials, they belong to space group №62 ( $Pbnm$ ,  $Pnma$ ). These compounds were researched more than half a century and, in this time, many unique properties were obtained, such as: spontaneous spin-reorientation transition [1], laser-pulse induced ultrafast spin rotation [2], anisotropic magnetic entropy evolution [3] and appearance of soliton lattices [4]. Manifold of magnetic properties is a consequence 3d-4f interaction, which emerges between subsystems of  $Fe^{3+}$  and  $R^{3+}$  ions, however a low symmetry of the materials makes it difficult to construct a realistic microscopic magnetic model.

In this research, we attempt to address this problem by studying magnetic properties of an orthoferrite compounds with different rare-earth ions (Yb, Ho, Tm and Tb), for it uses inelastic neutron scattering and empirical methods. Neutron scattering measurements were performed in different energy ranges:  $Fe^{3+}$  ions subsystem ( $\sim 60$  meV) for rare-earth ions subsystem  $Tm^{3+}$  ( $>12$  meV) and  $Tb^{3+}$  ( $>40$  meV). Experiments with inelastic neutron scattering were held in the Oak Ridge National Laboratory.

We described the high-energies magnetic excitation, use linear spin-wave theory (LSWT) and found constants of exchange interaction for  $Fe^{3+}$  ions subsystem in compounds:  $TmFeO_3$  [5, 6],  $YbFeO_3$  [7] and  $TbFeO_3$  [8]. Fig. 1 shows an energy-momentum plot along three high-symmetry directions.

Our results (summarized in Table 1) show considerable anisotropy between exchange interactions in  $ab$ -plane and along  $c$ -axis in space group  $Pbnm$ . Spectra of magnetic excitation associated with rare-earth ions consist of several excitations of crystalline electric field (CEF) levels. For  $Tm^{3+}$  ions subsystem transition energies are located on  $\sim 2$  meV and  $\sim 5$  meV, while  $Tb^{3+}$  have transition energies located on  $\sim 17$ ,  $\sim 25$  and  $\sim 35$  meV. Calculations based on the point charge model (PCM) reproduce well the experimentally observed transition energies for  $Tm^{3+}$  and  $Tb^{3+}$  ions subsystem, respectively. In this model, the magnetization of the rare-earth ions subsystem and the magnon dispersion were calculated and plotted.

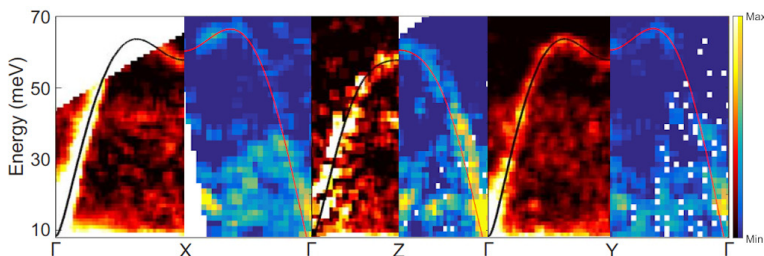


Figure 1. Magnon dispersion in compound  $TmFeO_3$  and  $TbFeO_3$  in three main directions of reciprocal space, solid line shows calculation in LSWT model, black and red color for  $TmFeO_3$  and  $TbFeO_3$  respectively.

Table 1. Values of exchange interaction constants ( $J$ ) and constant of anisotropy ( $K_c$ ) for  $\text{Fe}^{3+}$  ions subsystem in  $\text{TmFeO}_3$  and  $\text{TbFeO}_3$  compounds.

	$J_{ab}$	$J_c$	$J_{2ab}$	$J_{2c}$	$K_c$
$\text{TmFeO}_3$ [6]	4.74	5.15	0.15	0.3	-0.09
$\text{TbFeO}_3$ [8]	4.74	4.96	0.02	0.2	-0.2

*This study was supported by the Russian Foundation for Basic Research, project no. 20-32-90142.*

*We acknowledge A. Podlesnyak for help with INS experiments and S. E. Nikitin for stimulating discussion.*

1. R.L. White, J. Appl. Phys., **40**, 1061 (1969).
2. A.V. Kimel et al., Nature (London), **435**, 655 (2005).
3. Y.J. Ke et al., Sci. Rep., **6**, 19775 (2016).
4. S. Artyukhin et al., Nature materials, **11.8**, 694–699 (2012).
5. S.M. Shapiro et al., Phys. Rev. B, **10**, 2014 (1974).
6. S.A. Skorobogatov et al., Phys. Rev. B, **101**, 014432 (2020).
7. S.E. Nikitin et al., Phys.Rev. B, **98**, 064424 (2018).
8. S.A. Skorobogatov et al., arXiv:2204.03239 (2022)

Section I.  
**Magnetism and superconductivity**

---

## MULTITERMINAL JOSEPHSON STRUCTURES WITH QUASIPARTICLE INJECTION

*V.V. Ryazanov\**, *T.E. Golikova*, *I.V. Bobkova*, *A.M. Bobkov*

Institute of Solid State Physics, Russian Academy of Science, Chernogolovka, Russia

\*E-mail: [ryazanov@issp.ac.ru](mailto:ryazanov@issp.ac.ru)

Multiterminal coherent hybrid nanostructures based on superconductors, normal metals and ferromagnets have been fabricated using modern nanotechnological methods. Joint influence of two proximity effects both on the superconductor (S)/normal metal (N) interface and the ferromagnet (F)/normal metal (N) one in hybrid Josephson S-N/F-S structures with a two-layer N/F barrier has been theoretically and experimentally investigated. The Josephson characteristic changes under the action of spin diffusion and spin injection from a single-domain ferromagnet into the Josephson barrier are studied. The control of the critical current, the inverse population of states carrying supercurrent are demonstrated. For the first time, a double transition from the conventional state to the state with the phase difference inversion ( $\pi$ -state) and *vice versa* (Fig. 1) was observed under the influence of nonequilibrium quasiparticle injection [1]. We ascribe this effect to the appearance of two zero-crossing points in the supercurrent-carrying density of states (SCDOS) caused by the Zeeman splitting of the superconducting correlations in the N/F interlayer. The model taking into account SCDOS of a S-N/F-S structure and spin injection into the N layer is developed to describe the observed effect.

1. T.E. Golikova et al., Supercond. Sci. Technol., **34**, 095001 (2021).

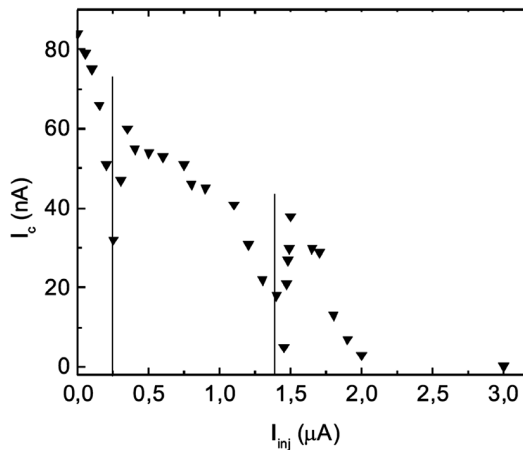


Figure 1. Critical current  $I_c$  of the crosslike submicron-scale Al-Cu/Fe-Al junction as a function of the injection current  $I_{inj}$  across the junction at  $T = 0.3$  K.

## MAGNETOCHIRAL EFFECT IN SUPERCONDUCTING HYBRID STRUCTURES

*A.S. Mel'nikov<sup>1\*</sup>, A.A. Kopasov<sup>1</sup>, A.G. Kutlin<sup>2</sup>*

<sup>1</sup>Institute for Physics of Microstructures RAS, Nizhny Novgorod, Russia  
<sup>2</sup>Max Planck Institute for Physics of Complex Systems, Dresden, Germany

\*E-mail: [melnikov@ipmras.ru](mailto:melnikov@ipmras.ru)

Electrical magnetochiral anisotropy is known to arise in the systems with the broken time reversal and inversion symmetries. This phenomenon can naturally appear in so-called Rashba systems where the spatial inversion is uniaxially broken along a certain  $\mathbf{n}$  direction due to the spin-orbit interaction. Applying an external magnetic field  $\mathbf{H}$  to a conducting Rashba system one can obviously expect the observation of a nonlinear resistance which can be phenomenologically written in the form:  $R = R_0(1 + [\mathbf{nH}]\mathbf{I})$ , where  $\mathbf{I}$  is the electric current. Recently these nonreciprocal phenomena attracted considerable interest in the context of superconducting charge transport. For the case of superconducting hybrid structures the magnetochiral anisotropy should reveal itself in the appearance of the spontaneous momentum of the Cooper pairs proportional to the vector product  $[\mathbf{nH}]$ . Note that for the case of a ferromagnet-superconductor hybrid structure the magnetic field  $\mathbf{H}$  in the above expression can be replaced by the exchange field of a ferromagnet. Experimentally the nonreciprocal phenomena in superconducting systems can be observed, e.g., in the measurements of the anisotropy of the critical current characterizing the threshold of the stability of the superconducting state as well as in the measurements of the critical supercurrent in various Josephson systems depending on the direction of the applied current.

In this report we review the recent experimental and theoretical works devoted to the superconducting nonreciprocal effects. Based on a microscopic description of the proximity effect for layered superconductor-ferromagnet systems with the Rashba interaction, we analyze the microscopic origin of the spontaneous momentum of the Cooper pairs and its behavior with respect to the band structure parameters of the ferromagnet and the energy of the spin-orbit interaction. Then we focus on the study of the magnetochiral effects in the hybrid structures with topologically nontrivial superconducting correlations, namely Majorana nanowires.

In the latter part of the report the nonreciprocal effects in superconducting transport are analyzed for the particular case of semiconducting nanowires with the induced superconductivity which are considered to be a perspective platform for the search of Majorana quasiparticle states and real-

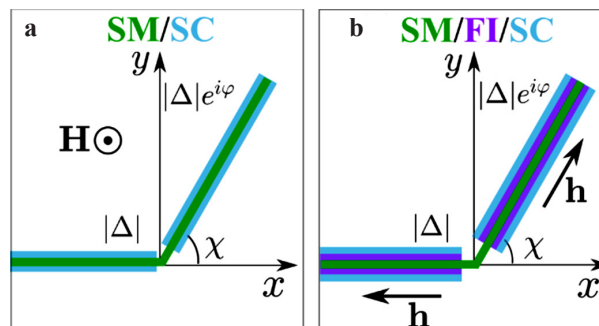


Figure 1. Two configurations of the Josephson junctions based on the curved Majorana nanowires.



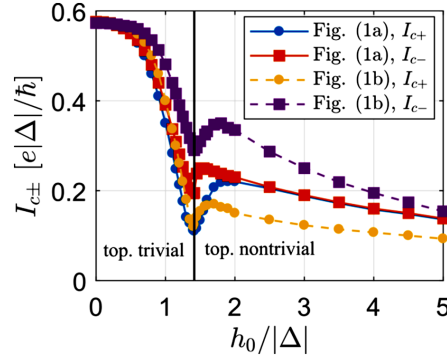


Figure 2. Josephson critical current as a function of the spin splitting field  $h_0$ , normalized at the induced superconducting gap  $\Delta$  for  $\chi = \pi/2$ .

ization of topologically protected quantum computations. The magnetochiral phenomena in these systems can be used for the characterization of the topologically nontrivial superconducting phases. We discuss here two exemplary configurations of the Josephson junctions based on the curved Majorana nanowires shown in Fig. 1. In the first configuration the Josephson junction is placed in the external magnetic field  $\mathbf{H}$  directed perpendicular to the substrate. For the second configuration the spin splitting of quasiparticle spectrum is caused by the exchange field  $h$  which appears due to the spin dependent tunneling through the layer of a ferromagnetic insulator placed between the superconducting film and semiconducting nanowire.

Based on numerical simulations and analytical estimates within the framework of the Bogoliubov-de Gennes equations we reveal the magnetic field driven crossover from conventional to anomalous Josephson effect as the system undergoes the topological phase transition. Calculating the quasiparticle spectra and supercurrent-phase relations we find the energetically favorable phase difference as a function of the Zeeman (or exchange) field and the geometrical offset angle. The nonreciprocal effect in the current phase relation appears to be most pronounced in the vicinity of the transition between the topologically trivial and nontrivial phases (see Fig. 2). The resulting tunable phase battery can be used as a probe of topological transitions in Majorana networks and can become a useful element of various quantum computation devices.

*This work was supported by the Russian Science Foundation (Grant No. 20-12-00053).*

## PROXIMITY EFFECT AT SUPERCONDUCTOR/ANTIFERROMAGNET INTERFACES

G.A. Bobkov<sup>1</sup>, I.V. Bobkova<sup>2,1,3\*</sup>, A.M. Bobkov<sup>2,1</sup>, Akashdeep Kamra<sup>4</sup>

<sup>1</sup>Moscow Institute of Physics and Technology, Dolgoprudny, Russia

<sup>2</sup>Institute of Solid State Physics of RAS, Chernogolovka, Russia

<sup>3</sup>National Reserch University Higher School of Economics, Moscow, Russia

<sup>4</sup>Condensed Matter Physics Center (IFIMAC) and Departamento de Fisica Teorica de la Materia Condensada, Universidad Autonoma de Madrid, Madrid, Spain

\*E-mail: [bobkova.iv@phystech.edu](mailto:bobkova.iv@phystech.edu)

The proximity effect in the bilayer heterostructures superconductor (S)/ferromagnetic insulator (FI) is well-studied: the exchange field at the S/FI interface suppresses superconductivity via the partial conversion of the singlet superconducting correlations to triplet correlations, which do not contribute to the superconducting order parameter in the singlet channel. Naively, one can expect that fully compensated antiferromagnet with zero average interface magnetization does not produce triplet correlations, which suppress singlet superconductivity. We demonstrate that it is not the case. We consider proximity effect in a bilayer heterostructure consisting of a conventional superconductor and a fully compensated antiferromagnetic insulator (AF). The calculations are based on two approaches. The first one is the numerical calculation in the framework of the BdG equations. The second one is the analytical consideration in the framework of the quasiclassical Eilenberger equations, which we have generalized to properly account for the Neel-type staggered quantities.

The main physical result, obtained in the framework of both approaches is the Neel-type staggered triplet correlations induced in the superconductor by the proximity to the antiferromagnetic insulator. The 2D plot of the Neel-type triplet correlations calculated numerically in the framework of BdG equations is presented in Fig. 2.

The influence of the antiferromagnetic insulator on the superconductor can be described by the staggered effective exchange field, induced at the AF/S interface. It produces staggered Neel-type triplets in the superconductor at the length scale of the order of the superconducting coherence length. The Neel-type triplets suppress the critical temperature of the thin-film S/AF bilayer and superconductivity at S/AF interfaces analogously to the ordinary triplets induced by the well-known proximity effect with ferromagnets in spite of the fact that the average exchange field induced in

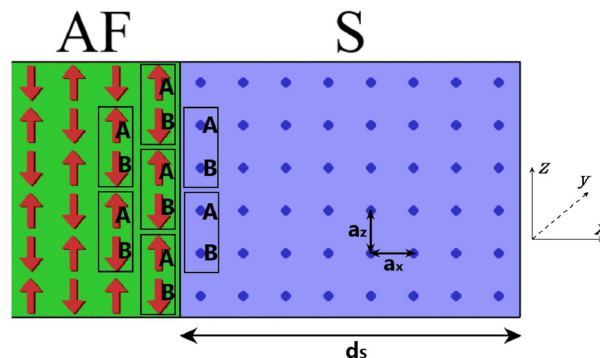


Figure 1. Sketch of the AF/S bilayer under consideration.

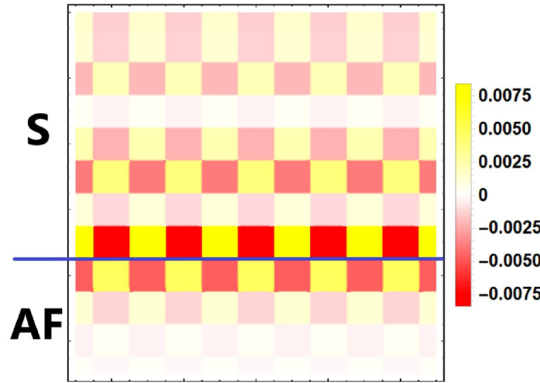


Figure 2. 2D-plot of the Neel triplet correlations. Each square represents one site of the lattice and its color codes the amplitude of the triplet correlations at the corresponding site.

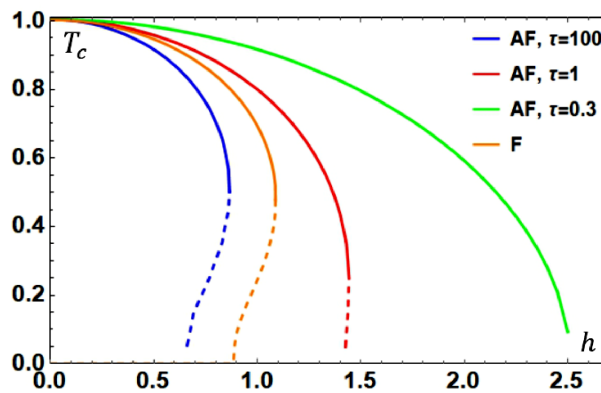


Figure 3. Critical temperature of the AF/S bilayer as a function of the effective exchange field induced by the antiferromagnet in the superconductor for different values of the impurity scattering time  $\tau$ , which is measured in units of the inverse superconducting critical temperature of the bulk superconductor.

the superconductor by the antiferromagnet is zero for the case under consideration. We investigate the dependence of the Neel-type triplet amplitude on the impurity concentration in the superconductor and find that the Neel-type triplets are suppressed by the impurities. It results in the highly nontrivial dependence of the critical temperature of the thin film S/AF bilayer on the impurity concentration: the critical temperature grows upon increasing the impurity concentration. Thus, the critical value of the staggered exchange field in the superconductor, which is able to fully suppress superconductivity, increases with impurity concentration.

Orange line in Fig. 3 represents the critical temperature for an S/F bilayer with a ferromagnetic insulator producing the same value of the effective exchange field (but homogeneous, not staggered) in the superconductor. The S/F interface is not sensitive to impurities, for this reason only one line is shown for the ferromagnetic case.

*Support by RSF project № 22-22-00522 is acknowledged.*

## FUNCTIONAL BASE ELEMENTS FOR ARTIFICIAL NEURAL NETWORK

*A. Sidorenko*<sup>1,2\*</sup>, *N. Klenov*<sup>3</sup>, *I. Soloviev*<sup>3</sup>, *S. Bakurskiy*<sup>3</sup>, *A. Vakhrushev*<sup>2,4</sup>,  
*V. Boian*<sup>1</sup>, *A. Prepelitsa*<sup>1</sup>, *A. Iacuin*<sup>1</sup>, *M. Lupu*<sup>1</sup>, *A. Denisov*<sup>5</sup>

<sup>1</sup>Institute of Electronic Engineering and Nanotechnologies, Chisinau, Moldova

<sup>2</sup>I.S. Turgenev Orel State University, Orel, Russia

<sup>3</sup>M.V. Lomonosov Moscow State University, Skobeltsyn Institute of Nuclear Physics, Moscow, Russia

<sup>4</sup>Nanotechnology and Microsystems Department, Izhevsk State Technical University, Izhevsk, Russia

<sup>5</sup>“NanoAnalytics” Integrated Laboratory, Kazan National Research Technological University, Kazan, Russia

\*E-mail: [anatoli.sidorenko@kit.edu](mailto:anatoli.sidorenko@kit.edu)

Energy efficiency and the radical reduction of the power consumption level becomes a crucial parameter constraining the advance of supercomputers. The most promising solution is design and development of the non-von Neumann architectures, first of all – the Artificial Neural Networks (ANN) based on superconducting elements. Superconducting ANN needs elaboration of two main elements – nonlinear switch (neuron) [1] and linear connecting element (synapse) [2]. We present results of our design and investigation of superconducting spin-valves and superconducting synapse, based on layered hybrid structures superconductor-ferromagnet.

Results of our theoretical and experimental study of the proximity effect in a stack-like superconductor/ferromagnet (S/F) superlattice with Co-ferromagnetic layers of different thicknesses and coercive fields, and Nb-superconducting layers of constant thickness equal to coherence length of niobium, are presented.

The superlattices Nb/Co demonstrate change of the superconducting order parameter in thin s-films due to switching from the parallel to the antiparallel alignment of neighboring F-layers. We argue that such superlattices can be used as tunable kinetic inductors for ANN synapses design.

*The study was supported by the Russian Science Foundation by Grant (RSF) No. 20-62-47009 “Physical and engineering basis of computers non-von Neumann architecture based on superconducting spintronics” (theory development, samples measurements, results evaluation), and by the Moldova State Program Project «Nanostructuri și nanomateriale funcționale pentru industrie și agricultură» no. 20.80009.5007.11 (samples fabrication).*

1. N. Klenov, Y. Khaydukov, S. Bakurskiy, R. Morari, I. Soloviev, V. Boian, T. Keller, M. Kupriyanov, A. Sidorenko, B. Keimer, Beilstein J. Nanotechnol., **10**, 833–839 (2019). <https://doi.org/10.3762/bjnano.10.83>.
2. S. Bakurskiy, M. Kupriyanov, N. Klenov, I. Soloviev, A. Schegolev, R. Morari, Yu. Khaydukov, A. Sidorenko, Beilstein J. Nanotechnol., **11**, 1336–1345 (2020). <https://doi.org/10.3762/bjnano.11.118>.

SUPERCONDUCTIVITY, MAGNETIC INTERACTIONS,  
AND DISORDER IN IRON-BASED MATERIALS*M.M. Korshunov*<sup>1\*</sup>, *V.A. Shestakov*<sup>1</sup>, *L.V. Begunovich*<sup>2</sup>, *Yu.N. Togushova*<sup>2</sup><sup>1</sup>Kirensky Institute of Physics, Federal Research Center KSC SB RAS, Krasnoyarsk, Russia<sup>2</sup>Siberian Federal University, Krasnoyarsk, Russia\*E-mail: [mkor@iph.krasn.ru](mailto:mkor@iph.krasn.ru)

Unconventional superconductivity is a wide field of novel phenomena. Here we show how the short-range magnetic interactions (i.e. spin fluctuations) in iron pnictides and chalcogenides [1–3] results in an unconventional superconducting state that is characterized by a complicated order parameter structure taking the form of nodal, nodeless, sign-changing, or sign-preserving gap [4, 5]. Its particular type results from the mixture of factors like Fermi surface topology, orbital content of bands, and the balance of intra- vs interband interactions [6, 7].

For the most iron-based superconductors, spin resonance peak that is the hallmark of the sign-changing  $s_{\pm}$  gap [8–10] was observed in the inelastic neutron scattering. One of the features of the  $s_{\pm}$  state is possibility to transform to the sign-preserving  $s_{++}$  state with the increase of the nonmagnetic disorder [11, 12]. Here we discuss the London magnetic penetration depth within the two-band model for the  $s_{\pm}$  and  $s_{++}$  superconductors. By solving Eliashberg equations for the spin-fluctuation-mediated pairing and nonmagnetic impurities in the T-matrix approximation, we derived a set of specific signatures of the  $s_{\pm} \rightarrow s_{++}$  transition in the temperature dependence of the penetration depth and the superfluid density [13].

Metal-organic compounds are a recent trend in functional materials design. One can use organic molecules as electron donors and structure stabilizers to control the features of a metallic subsystem. Organic EMIM cations were inserted into FeSe during the liquid-ion-gating process and superconductivity with  $T_c$  of about 44 K was discovered [14]. To make a first step towards understanding the nature of superconductivity in  $(\text{EMIM})_x\text{FeSe}$ , we calculated its band structure and Fermi surface using density functional theory. We show that the bands near the Fermi level are formed primarily by Fe-d orbitals. Although there is no direct contribution of EMIM orbitals to the near-Fermi level states, the presence of organic cations leads to a shift of the chemical potential that results in the appearance of small electron pockets in the quasi-two-dimensional Fermi surface of  $(\text{EMIM})_x\text{FeSe}$  [15].

1. M.V. Sadovskii, Phys. Usp., **51**, 1201 (2008).
2. Y.A. Izyumov, E.Z. Kurmaev, Phys. Usp., **51**, 1261 (2008).
3. G.R. Stewart, Rev. Mod. Phys., **83**, 1589 (2011).
4. P.J. Hirschfeld, M. M. Korshunov, I.I. Mazin, Rep. Prog. Phys., **74**, 124508 (2011).
5. M.M. Korshunov, Phys. Usp., **57**, 813 (2014).
6. S. Maiti, M.M. Korshunov, T.A. Maier, P.J. Hirschfeld, A.V. Chubukov, Phys. Rev. Lett., **107**, 147002 (2011).
7. S. Maiti, M.M. Korshunov, T.A. Maier, P.J. Hirschfeld, A.V. Chubukov. Phys. Rev. B, **84**, 224505 (2011).
8. M.M. Korshunov, I. Eremin, Phys. Rev. B, **78**, 140509 (2008).
9. T.A. Maier, D.J. Scalapino, Phys. Rev. B, **78**, 020514 (2008).
10. M.M. Korshunov, Phys. Rev. B, **98**, 104510 (2018).
11. D.V. Efremov, M.M. Korshunov, O.V. Dolgov, A.A. Golubov, P.J. Hirschfeld, Phys. Rev. B, **84**, 180512 (2011).
12. M.M. Korshunov, Y.N. Togushova, O.V. Dolgov, Phys. Usp., **59**, 1211 (2016).
13. V.A. Shestakov, M.M. Korshunov, Yu.N. Togushova, O.V. Dolgov, Supercond. Sci. Technol., **34**, 075008 (2021).
14. J. Wang, Q. Li, W. Xie, G. Chen, X. Zhu, H.H. Wen, Chin. Phys. B, **30**, 107402 (2021).
15. L.V. Begunovich and M.M. Korshunov, Materials, **15**, 1856 (2022).

## THE MAGNETIC FLUX STRUCTURE $\text{EuFe}_2\text{As}_2$ SINGLE CRYSTALS DOPED BY RUBIDIUM

*M.S. Sidelnikov<sup>1</sup>, A.V. Palnichenko<sup>1</sup>, A.A. Avtandilyan<sup>2</sup>, K.S. Pervakov<sup>3</sup>, V.A. Vlasenko<sup>3</sup>,  
I.A. Golovchanskiy<sup>2</sup>, V.M. Pudalov<sup>3</sup>, V.S. Stolyarov<sup>2</sup>, L.Ya. Vinnikov<sup>1\*</sup>*

<sup>1</sup>Institute of Solid State Physics, Russian Academy of Sciences, Chernogolovka, Russia

<sup>2</sup>Center for Advanced Mesoscience and Nanotechnology Moscow Institute of Physics and Technology, Dolgoprudny, Moscow, Russia

<sup>3</sup>Lebedev Physical Institute, Russian Academy of Sciences, Moscow, Russia

\*E-mail: [vinnik@issp.ac.ru](mailto:vinnik@issp.ac.ru)

A family of Fe-based superconductors with Eu ions are of great interest in connection with the problem of the coexistence of superconductivity and ferromagnetism. The  $\text{EuFe}_2\text{As}_2$  parent compound is the basic structure, which exhibits a wide range of magnetic transitions when doped [1]. Namely, when arsenic ions are partially replaced by P ions in  $\text{EuFe}_2(\text{As}_{1-x}\text{P}_x)_2$  single crystals, an antiferromagnetic state for  $x < 0.13$  and temperature  $T < 15$  K and ferromagnetism for  $x > 0.25$  and  $T < 18$  K were observed, whereas in the narrow range at  $x = 0.2$ , the coexistence of superconductivity and ferromagnetism was discovered [1]]. Magnetic flux structure in  $\text{EuFe}_2(\text{As}_{1-x}\text{P}_x)_2$  single crystals was investigated in [2, 3]. In  $\text{EuRbFe}_4\text{As}_4$  single crystals, the coexistence of superconductivity ( $T_{\text{SC}} = 35$  K) and ferromagnetism ( $T_{\text{m}} = 15$  K) with the magnetization vector lying in the base plane was found, [4]. Whereas in  $\text{EuFe}_2(\text{As}_{1-x}\text{P}_x)_2$  single crystals, the magnetization vector is perpendicular (parallel to the  $c$  axis) [2, 3]. To date, for the perfect  $\text{EuRbFe}_4\text{As}_4$  single crystals, no any features in the vortex structure on the base plane was detected in the region of coexistence of superconductivity and ferromagnetism ( $T < 15$  K) [4]. The synthesis of perfect single crystals of  $\text{EuRbFe}_4\text{As}_4$  is quite complex and, therefore synthesized crystals often turn out to be non-superconducting and inhomogeneous with presence of the 122-phase. In the present work the single crystals were synthesized by the self-flux crystal growth technique [5]. It should be noted that on all the studied crystals – both non-superconducting (Fig. 1a) and superconducting (Fig. 1b) – the magnetic features were observed at temperatures of 15 and 20 K (Fig. 1a and 1b, respectively).

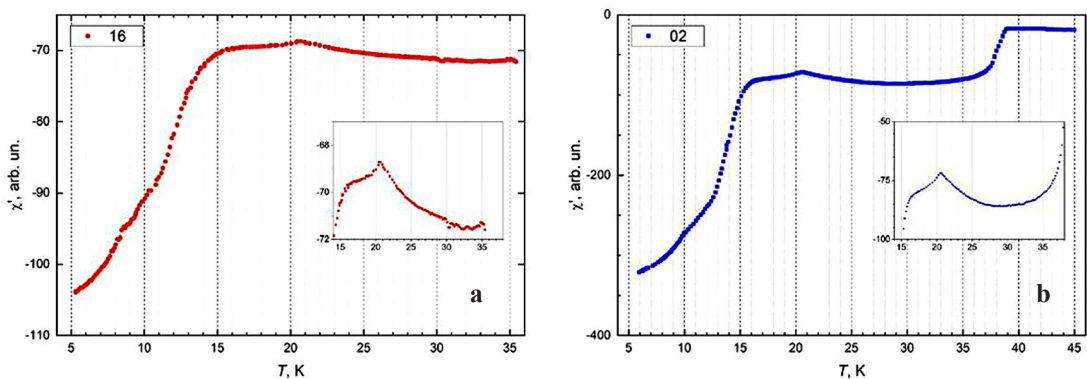


Figure 1. Real part of the dynamic magnetic susceptibility on temperature for crystals: **a** nonsuperconducting, **b** superconducting ( $T_{\text{SC}} = 37$  K)  $\text{EuRbFe}_4\text{As}_4$ . The insets have increased the scale along the ordinate axis. (Amplitude of the excitation magnetic field 3.5 mOe, frequency 1.5 Hz.)

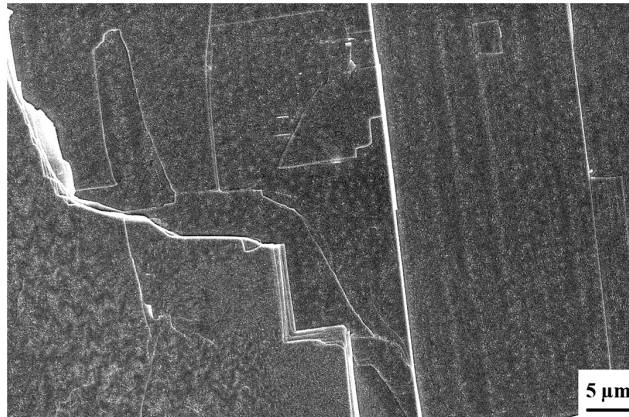


Figure 2. Magnetic flux structure superconducting  $\text{EuRbFe}_4\text{As}_4$  single crystal on basal plane at temperature 8 K and magnetic field 20 Oe.

The structure of the magnetic flux was studied by the method of high-resolution low-temperature decoration with magnetic nanoparticles [6]. On a significant part of the studied surface of the base plane of a superconducting single crystal, the magnetic susceptibility of which is shown in Fig. 1b, vortex structures were observed due to pinning on the internal crystal growth defects. Figure 2 shows a fragment of the picture of the inhomogeneous distribution of the magnetic flux on the surface of the basic plane, where, in addition to the Abrikosov vortices, a labyrinth domain structure is observed (lower left corner in Fig. 2). Perhaps the observed structures are associated with local heterogeneity of the Eu and Rb ions concentration and the formation of intermediate magnetic phases. The singularities in Fig. 1a near  $T = 15$  K are associated with the helicoidal ordering of Eu ions, while the the another one near  $T = 20$  K attributed to the antiferromagnetic or ferromagnetic ordering. At that, the corresponding magnetization vector is oriented perpendicularly to the base plane.

1. S. Nandi, W.T. Jin, Y. Xiao et al., *Phys. Rev. B*, **89**, 014512 (2014).
2. I.S. Veshchunov, L.Ya. Vinnikov, V.S. Stolyarov et al., *JETP Letters*, **105**(2), 98 (2017).
3. L.Ya. Vinnikov, I.S. Veshchunov, M.S. Sidelnikov et al., *JETP Lett.*, **109**(8), 521 (2019).
4. V.S. Stolyarov, A. Casano, M.A. Belyanchikov et al., *Phys. Rev. B*, **98**, 140506(R) (2018).
5. V. Vlasenko, K. Pervakov, S. Gavrilkin, *Supercond. Sci. Technol.*, **33**, 084009 (2020).
6. L.Ya. Vinnikov, I.S. Veshchunov, M.S. Sidelnikov and V.S. Stolyarov, *Instruments and Experimental Techniques*, **62**(4), 587 (2019).

## SUPERCONDUCTING HYBRID SPIN-VALVE WITH SPIN-ORBIT INTERACTION

A. Neilo<sup>1</sup>, N. Klenov<sup>1</sup>, I. Soloviev<sup>2</sup>, M. Kupriyanov<sup>2</sup>, S. Bakurskiy<sup>2</sup>

<sup>1</sup>Faculty of Physics, Lomonosov Moscow State University, Moscow, Russia

<sup>2</sup>Skobeltsyn Institute of Nuclear Physics, Lomonosov Moscow State University, Moscow, Russia

E-mail: r4zz@mail.ru

Superconducting spin valves with ferromagnetic layers are promising devices for implementing non-volatile memory and logic elements. Conventional spin-valves contain two or more ferromagnetic layers with control due to the changing the relative magnetization direction [1, 2]. At the same time, devices with a single ferromagnetic layer have significant advantages [3, 4]. One of the possible implementations of this type of device is hybrid structure that include metal layers with significant spin-orbit interaction.

We have investigated the proximity effect in hybrid structures with superconducting S, ferromagnetic F, and normal metal layers with significant spin-orbit interaction  $N_{SO}$ . In such hybrid structures, the superconducting order parameter is affected by both magnetic and spin-orbit interactions, which leads to a change of the pairing amplitude and the appearance of triplet components with a nonzero spin projection.

We have considered the proximity effect in structures of different types of spin-orbit interaction: Rashba, Dresselhaus and mixed type. It was shown that a metal layer with significant spin-orbit interaction effectively suppresses the triplet components of the pairing amplitude, which leads to an increase in the critical temperature of the superconductor. In the case of a mixed spin-orbit interaction, the suppression efficiency also on the direction of the magnetization, which makes it possible to use such structures as a spin valve.

*This work was supported by grants from the Russian Science Foundation 20-12-00130 (theory and calculations of basic hybrid structures, as well as Josephson junctions), and from Russian Ministry of Science and Education Grant No. 075-15-2021-1353 (study of multilayer structures with multiply repeating groups of layers).*

1. V.I. Zdravkov, J. Kehrle, G. Obermeier, D. Lenk, H.A.K. von Nidda, C.K.M.Y. Müller, ... & L.R. Tagirov, Phys. Rev. B, **87**(14), 144507 (2013).
2. Y.V. Fominov, A.A. Golubov, T.Y. Karminskaya, M.Y. Kupriyanov, R.G. Deminov, L.R. Tagirov, JETP Lett., **91**(6), 308–313 (2010).
3. I.I. Soloviev, N.V. Klenov, S.V. Bakurskiy, V.V. Bol'ginov, V.V. Ryazanov, M.Y. Kupriyanov, A.A. Golubov, Appl. Phys. Lett., **105**(24), 242601 (2014).
4. S.V. Bakurskiy, N.V. Klenov, I.I. Soloviev, M.Y. Kupriyanov, A.A. Golubov, Appl. Phys. Lett., **108**(4), 042602 (2016).



## MAGNON-COOPARONS IN MAGNET-SUPERCONDUCTOR HYBRIDS

*I.V. Bobkova<sup>1,2,3\*</sup>, A.M. Bobkov<sup>1,2</sup>, A. Kamra<sup>4</sup>, W. Belzig<sup>5</sup>*

<sup>1</sup>Moscow Institute of Physics and Technology, Dolgoprudny, Russia

<sup>2</sup>Institute of Solid State Physics of RAS, Chernogolovka, Russia

<sup>3</sup>National Research University Higher School of Economics, Moscow, Russia

<sup>4</sup>Condensed Matter Physics Center (IFIMAC) and Departamento de Física Teórica de la Materia Condensada, Universidad Autónoma de Madrid, Madrid, Spain

<sup>5</sup>Fachbereich Physik, Universität Konstanz, Konstanz, Germany

\*E-mail: [bobkova.iv@phystech.edu](mailto:bobkova.iv@phystech.edu)

Generation and detection of spinfull Cooper pairs in conventional superconductors has been intensely pursued by designing increasingly complex magnet-superconductor hybrids. We demonstrate theoretically that magnons with nonzero wavenumbers in a ferromagnetic insulator (FI) universally induce a cloud of spinfull triplet Cooper pairs around them in an adjacent conventional superconductor [1]. The resulting composite quasiparticle, termed magnon-cooparon, consists of a spin flip in the magnet screened by a cloud of the spinfull superfluid condensate. The sketch of this composite quasiparticle is presented in Fig. 1.

Magnon-cooparon inherits a large effective mass, which can be measured experimentally. The effective mass of the composite quasiparticle is expressed via the FI spin stiffness  $m_{\text{eff}} = 1/2\tilde{D}_m = 1/(2D_m + 2\delta D_m)$ . The correction  $\delta D_m$  to the stiffness produced by the cloud of triplet Cooper pairs accompanying the magnon is demonstrated in Fig. 2.

As it is seen from Fig. 2,  $\delta D_m$  is negative and is quite large for typical experimental parameters. It means that the effective mass of the composite quasiparticle is enhanced as compared to that of a magnon. The spin of the magnon is screened by the triplet pairs. Our estimates suggest that the reduction of the net composite particle spin as compared to the spin 1 of the bare magnon can be of the order of about a few tenths.

Furthermore, we demonstrate that two magnetic wires deposited on a superconductor serve as a controllable magnonic directional coupler mediated by the nonlocal and composite nature of magnon-cooparons. The sketch of the proposed device is presented in Fig. 3.

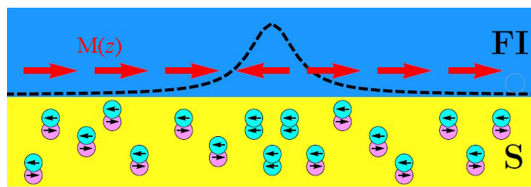


Figure 1. A localized spin-flip or magnon wave packet induces a surrounding cloud of spinfull triplet Cooper pairs in an adjacent conventional spin-singlet superconductor. The spatially varying magnetization or spin profile (depicted via dashed line) associated with the excitation induces spinfull condensate, that screens the magnon spin, in the otherwise spinless superconductor.

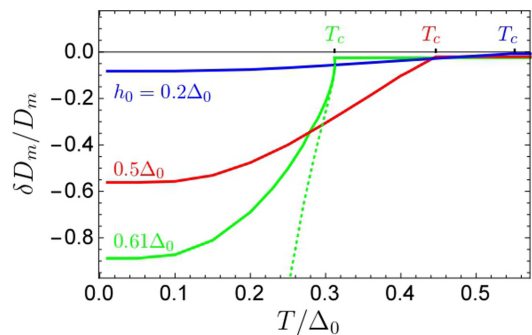


Figure 2. Relative change in the spin stiffness as a function of temperature for different values of the static exchange field  $h_0$  induced in S by the proximity to FI.

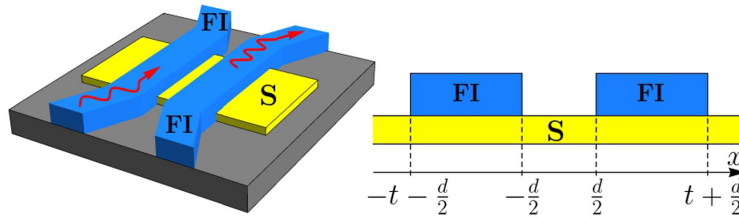


Figure 3. Schematic depiction of a magnonic directional coupler based on magnon-cooperons. A spin wave propagating through one FI wire is controllably transferred to the second FI wire.

Therefore, our analysis predicts a quasiparticle that enables generation, control, and use of spinfull triplet Cooper pairs in the simplest magnet-superconductor heterostructures.

*Support by RSF project № 22-42-04408 is acknowledged.*

1. I.V. Bobkova, A.M. Bobkov, A. Kamra, W. Belzig, arXiv:2203.05336.

## TRANSPORT AND MICROWAVE STUDIES OF MAGNETIC FLUCTUATION IMPACT ON THE CONDUCTIVITY AND SUPERCONDUCTING TRANSITION OF IRON CHALCOGENIDES

I. Gimazov<sup>1</sup>, D. Chareev<sup>2</sup>, A. Vasiliev<sup>3</sup>, A. Sadakov<sup>4</sup>, Yu. Talanov<sup>1\*</sup>

<sup>1</sup>Zavoisky Physical-Technical Institute, RAS, Kazan, Russia

<sup>2</sup>Institute of Experimental Mineralogy RAS, Chernogolovka, Russia

<sup>3</sup>M.V. Lomonosov Moscow State University, Moscow, Russia

<sup>4</sup>P.N. Lebedev Physical Institute RAS, Moscow, Russia

\*E-mail: [talanov@kfti.knc.ru](mailto:talanov@kfti.knc.ru)

The interactions responsible for the pairing of electrons in the superconducting state, affect the scattering of current carriers above the critical temperature. A good illustration of this statement is conventional superconductors. The formation of Cooper pairs in them occurs through lattice vibrations (phonons). The same phonons determine the resistance of the material at  $T > T_c$ . The situation is similar in HTSC materials. An interaction that claims to be a connecting element in Cooper pairs can manifest itself in the transport parameters in the normal state. Therefore, an important task is to find a relationship between the transport properties of materials (in particular, resistance), and superconducting parameters, such as critical temperature. The use of high-frequency methods for studying scattering processes, such as microwave absorption (MWA), provides more information than low-frequency methods due to greater sensitivity to short-lived electronic and magnetic excitations.

In this paper, the problem is solved through studying the transport properties and microwave absorption of iron dichalcogenides  $\text{FeTe}_{1-x}\text{Se}_x$ . It is known that at extreme values of selenium concentration  $x$ , the compounds exhibit incomparable states at low temperatures. While  $\text{FeTe}$  ( $x = 0$ ) is an antiferromagnet with  $T_N = 73$  K,  $\text{FeSe}$  ( $x = 1$ ) is a superconductor with a critical temperature  $T_c = 9$  K. Moreover,  $\text{FeSe}$  is in a state of nematic order in the temperature range from  $T_c$  to the structural transition temperature  $T_s = 90$  K [1]. All the above-listed states and phase transitions are reflected in the temperature dependence of the resistance of these compound crystals. In  $\text{FeSe}$ ,  $R(T)$  has a metallic character with a kink at  $T = T_s$  and a sharp drop to zero upon transition to the superconducting state. The  $\text{FeTe}$  resistance exhibits a semiconductor behavior with lowering the temperature from 300 K to  $T_N$ , where it is largely determined by antiferromagnetic fluctuations. In a magnetically ordered state, the influence of fluctuations weakens, and the resistance acquires a metallic character, that is, it decreases with lowering temperature [2]. At temperature  $T = T_N$ , the dependence  $R(T)$  has a maximum. When a small amount of selenium is added to  $\text{FeTe}$  ( $x < 0.08$ ), this maximum shifts down in temperature, its height decreases, and it gradually disappears. At  $x > 0.08$ , magnetic ordering does not occur over the entire temperature range  $T > T_c$ , and only a weak local maximum, characteristic of scattering by magnetic fluctuations, remains on the  $R(T)$ -dependence [2].

Our study, carried out with the help of the MWA measurements of the  $\text{FeTe}_{1-x}\text{Se}_x$  crystals with  $0.09 < x < 1.00$ , revealed the presence of magnetic fluctuations in a wide temperature range with a maximum amplitude at about  $T \sim 80$  K. While the  $R(T)$  dependence obtained in DC measurements has a weak local maximum near  $T = 33$  K.

*This work was supported in part by the government assignment for FRC Kazan Scientific Center of RAS. The magnetization measurements were performed by A.V.S. in the Ginzburg Center for High Temperature Superconductivity and Quantum Materials, P.N. Lebedev Physical Institute of RAS in the frame of the RSF project no. 21-72-20153. D.A.C. and A.N.V. acknowledge the support of RFBR (project no. 20-02-00561).*

1. M.A. Tanatar, A.E. Boehmer, E.I. Timmons et al., Phys. Rev. Lett., **117**, 127001 (2016).
2. A. Martinelli, A. Palenzona, M. Tropeano et al., Phys. Rev. B, **81**, 094115 (2010).

## SPIRAL AND FERRO-MAGNETS IN THE INVERSE PROXIMITY EFFECT

*N.G. Pugach*<sup>1\*</sup>, *D.V. Seleznev*<sup>1</sup>, *V.O. Yagovtsev*<sup>1</sup>, *N.A. Gusev*<sup>2,3</sup>

<sup>1</sup>HSE University, Moscow, Russia

<sup>2</sup>V.I. Vernadsky Crimean Federal University, Simferopol

<sup>3</sup>Russian Quantum Center, Moscow, Russia

\*E-mail: [pugach@magn.ru](mailto:pugach@magn.ru)

In this work we theoretically investigate the influence of magnetization orientation and reorientation in a spiral magnetic material on the superconducting properties of the adjacent superconducting layer, i.e. the inverse proximity effect (IPE). The IPE induced by a ferromagnetic insulator is also presented. The IPE exhibits in the critical superconducting temperature or in the density of states.

Basing on the possibility of the magnetic spiral reorientation we propose a superconducting spin valve (SSV), which consists of a superconductor and a spiral antiferromagnet. The last one is an itinerant magnetic material, with an intrinsic non-collinear magnetic order characterized by a wave vector that may be aligned in a few equivalent directions in the ground state under the control of a weak external magnetic field pulse. The magnetic layer may be made from a helimagnetic layer of B20 family compounds, for example spiral antiferromagnetic MnSi. Thanks to unique properties of B20 family magnets – i.e. its cubic crystal lattice, there are few ground state magnetic configurations with different directions of the magnetic spiral, divided by a potential barrier [1]. Superconductivity in such a bilayer is controlled by the spiral vector reorientation in the MnSi layer, which leads to a change in the critical temperature of the Nb superconducting layer due to the inverse proximity effect [2–4]. Another possibility may be bilayer with a helimagnetic metal like Er or Ho magnetized to the saturation in an external magnetic field [4].

The change of magnetic configuration allows one to controllably modify long-range spin-triplet superconducting correlations, leading to spin-valve switching behavior. We developed a control method of such a bilayer SSV non-perturbing superconductivity and suitable for energy saving cryogenic electronics. The switching is proposed to be carried out by a several hundred ps in duration magnetic field pulse of several kOe of magnitude. Such a pulse does not destroy the superconducting state of the Nb layer by itself but leads to the excitation of magnons in the MnSi layer, which triggers the process of reorientation of the magnetic spiral. Inverse switching returns the spiral to the initial state, opening the valve and turning on the superconducting state. The system can be switched there and back by a magnetic field of opposite signs along one direction in the layers plane, which allows easy control. Such SSV may be used as an element of superconducting memory for energy-efficient digital and quantum electronics [5].

*The numerical experiments were financially supported by the Russian Ministry of Education and Science, Megagrant project N 075-15-2019-1934, analytical calculations were supported by the Basic Research Program of the HSE University via the Mirror Laboratories collaboration project.*

1. S.V. Grigoriev et al., Phys. Rev. B, **76**, 092407 (2007).
2. N.G. Pugach et al., Appl. Phys. Lett., **111**, 162601 (2017).
3. N.G. Pugach, D. Heim, D.V. Seleznev, A.I. Chernov, D. Menzel, Supercond. Sci. Technol., **35**, 025002 (2022).
4. N.G. Pugach, M.O. Safonchik, V.I. Belotelov, T. Ziman, T. Champel, cond-mat:arXiv:2110.00369 (2021).
5. N. Gusev, D. Dzheparov, N. Pugach, and V. Belotelov, Appl. Phys. Lett., **118**, 232601 (2021).

## PROXIMITY INDUCED SUPERCONDUCTIVITY IN ORGANIC DIELECTRIC

*K.Yu. Arutyunov*<sup>1,2\*</sup>, *K.A. Belyaev*<sup>1</sup>, *A.N. Lachinov*<sup>3,4</sup>, *A.P. Yusupov*<sup>4</sup>

<sup>1</sup>MIEM HSE, Moscow, Russia

<sup>2</sup>Kapitza Institute RAS, Moscow, Russia

<sup>3</sup>Institute of physics of molecules and crystals RAS, Ufa, Russia

<sup>4</sup>Bashkir State Pedagogic University, Ufa, Russia

\*E-mail: [karutyunov@hse.ru](mailto:karutyunov@hse.ru)

Layered thin-film lead-polydiphenylphthalide (PDF)-lead sandwich heterostructures on various dielectric substrates were studied. It is known that under the influence of an external electrostatic field and/or mechanical stresses, the electrical conductivity of a PDP polymer can significantly increase [1]. In particular, it was found that when mechanical deformations and/or an electrostatic field are applied in this (dielectric) material, the local electrical conductivity sharply increases, reaching a value of  $10^5$  ( $\Omega\cdot\text{cm}$ )<sup>-1</sup>, and the current density can reach impressive values of the order of  $10^6$  A/cm<sup>2</sup>. The observed effect was interpreted as a stimulated metallic state of the polymer [2].

A number of samples were fabricated, which consisted of two crossed thin-film strips of lead (Pb) with a width of about 1 mm, between which there was a PDP polymer film. Two materials were chosen as substrates: silicon (Si) and glass. The indicated geometry makes it possible to study the voltage-temperature  $V(T, I = \text{const})$  and current-voltage characteristics  $I(V, T = \text{const})$  of both lead films and the PDP polymer film itself, sandwiched between lead electrodes. Lead is a classical superconductor with bulk critical temperature  $T = 7.2$  K. The shape of  $R(T)$  and  $V(I)$  characteristics of the studied samples (Fig. 1) can be interpreted as the presence of superconducting correlations induced in an organic polymer film sandwiched between two superconductors (proximity effect).

*The work was supported by the Mirror Lab project of HSE and DSPU Universities.*

1. A.N. Lachinov, V.M. Kornilov, T.G. Zagurenko, A.Yu. Zsherebov, JETP, **129**, 728 (2006).
2. A.N. Lachinov, N.V. Vorob'eva, Uspekhi Fizicheskikh Nauk, **176**(12), 1249 (2006).

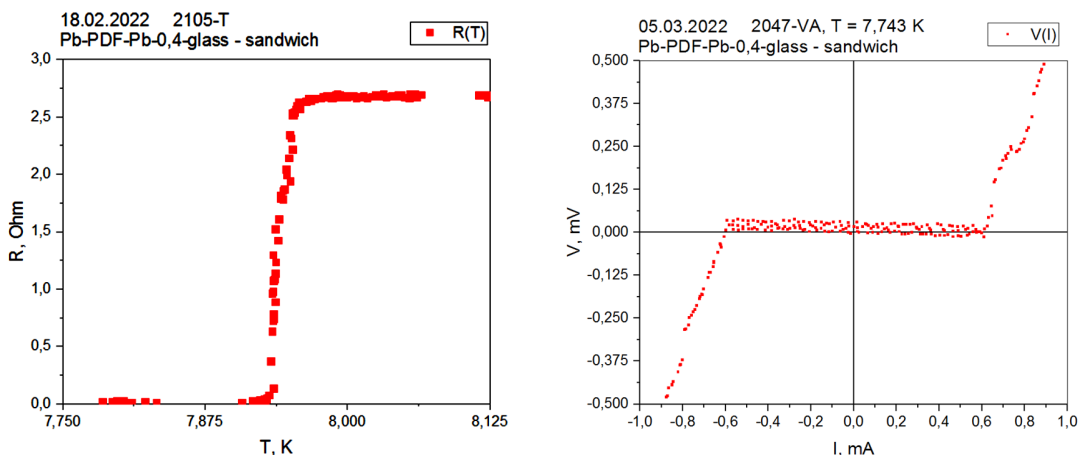


Figure 1.  $R(T)$  and  $V(I)$  characteristics of Pb-PDF-Pb “sandwich” heterostructure on glass substrate with 400 nm-thick PDF intermediate layer.

## DYNAMICAL PROPERTIES OF SUPERCONDUCTOR/ FERROMAGNETIC-INSULATOR HYBRID STRUCTURES UNDER FERROMAGNETIC RESONANCE CONDITION

*Y.V. Turkin\**, *N.G. Pugach*

HSE University, Moscow, Russia

\*E-mail: [turkin.yaroslav@gmail.com](mailto:turkin.yaroslav@gmail.com)

Spin transport in superconductor/ferromagnetic-insulators hybrid structures have been studied for long time. This great research interest originates from possibility of using such hybrid structures as energy-efficient sources of the spin current injection due to long lifetime of the spin-dependent correlations in superconductor [1]. Moreover, interactions between magnetic oscillations in ferromagnetic insulators and superconductive correlations play a crucial role in the dynamics of ferromagnetic Josephson junctions [2]. Ferromagnetic resonance assisted spin current injection into superconductor from ferromagnetic insulator has already been demonstrated [3]. Most theoretical works describe this phenomenon using microscopic framework in momentum space. This formalism ignores spatiotemporal dynamics of correlations inside superconductor layer.

In this work we theoretically investigate the influence of magnetization excitations in ferromagnetic insulator on the dynamics of the attached superconducting layer. To correctly describe periodic time-dependent dynamics in the dirty limit we derive so-called Usadel-Floquet equation [4]. Floquet formalism allows us to transform time-dependent differential equations to stationary equations for different Fourier harmonics of quasiclassical Green functions. Usadel-Floquet equations system was linearized to obtain uncoupled equations for the different Fourier harmonics. The system of linearized Usadel-Floquet equations was solved numerically and analytically for different precession frequencies and angles between the interface normal and the magnetization precession axis. Numerical solution is obtained using the finite-difference collocation method. Boundary conditions on the interface between ferromagnetic insulator and superconductor are derived in the limit of small spin mixing angle. We use adiabatic approximation for to describe time-dependent boundary conditions because the energy scale of magnetization precession field is much smaller than energy scale of order parameter in superconductor [5, 6].

Obtained results allow us to predict how the dynamics and spectrum of superconducting correlations depend on the uniform magnetization precession in the attached ferromagnetic insulator thin film. Fourier harmonics of the quasiclassical Green functions demonstrate slightly different behavior in comparison to the constant part of the solution. It is shown that amplitudes of the order parameter harmonics strongly depend on the angle between interface normal and magnetization precession axis.

*The numerical experiments were financially supported by the Russian Ministry of Education and Science, Megagrant project N 075-15-2019-1934, analytical calculations were supported by the Basic Research Program of the HSE University via the Mirror Laboratories collaboration project.*

1. J. Linder, Nat. Phys., **11**, 307–315 (2015).
2. M. Houzet, Phys. Rev. Lett., **101**, 057009 (2008).
3. M. Umeda, et al., App. Phys. Lett., **112**, 232601 (2018).
4. A. Brinkman, et al., Phys. Rev. B, **68**, 224513 (2003).
5. M. Eschrig, et al., New J. Phys., **17**, 083037 (2015).
6. M. Silaev, Phys. Rev. B, **102**, 180502 (2020).

## MAJORANA AND SUBGAP VORTEX-BOUND STATES IN SPIN-SINGLET CHIRAL SUPERCONDUCTORS WITH NONCOLLINEAR SPIN ORDERING

*A.O. Zlotnikov*

Kirensky Institute of Physics, Federal Research Center KSC SB RAS (Russia)

\*E-mail: [zlotn@iph.krasn.ru](mailto:zlotn@iph.krasn.ru)

Majorana modes (MM) that are localized at the ends of quantum wires have been actively studied in recent years both theoretically and experimentally [1] due to their applications to topologically protected quantum computations. Nevertheless, the similar modes propagate along the edges in 2D topological superconductors (TSCs), thus preventing their use in braiding. On the other hand, well separated MM in 2D TSCs can be localized on topological defects, such as Abrikosov vortices, magnetic skyrmions, corners in higher-order TSCs, and so on (see review [2]).

MM were predicted in the vortex state in triplet  $p_x + ip_y$  superconductors [3], in spin-singlet superconductors with spin-orbit interaction [4], topological insulator/superconductor heterostructures [5], iron chalcogenide  $\text{FeTe}_{0.55}\text{Se}_{0.45}$  [6].

It was proved over 20 years ago that a chiral  $d_{x^2-y^2} + id_{xy}$  superconductor is TSC with zero energy edge states which are not Majorana states due to the presence of the only spin-singlet component of the order parameter [7]. Moreover, the vortex-bound states in the  $d_{x^2-y^2} + id_{xy}$ -wave superconductor exist only at finite energy [8]. On the other hand, it is known that helical long-range magnetic order in spin-singlet superconductors can also lead to TSC and, namely, such spin ordering leads to appearance of the Majorana vortex modes with zero energy [9].

In this study topologically nontrivial edge and vortex bound states are described in the coexistence phase of chiral  $d_{x^2-y^2} + id_{xy}$  superconductivity and noncollinear spin ordering on a triangular lattice. Since chiral superconductivity is nodeless in a wide range of parameters, the obtained bound states are separated from trivial bulk states. Even though nearby excitation energies of subgap states including the edge-localized and vortex-localized states are very close to each other, the energy dif-

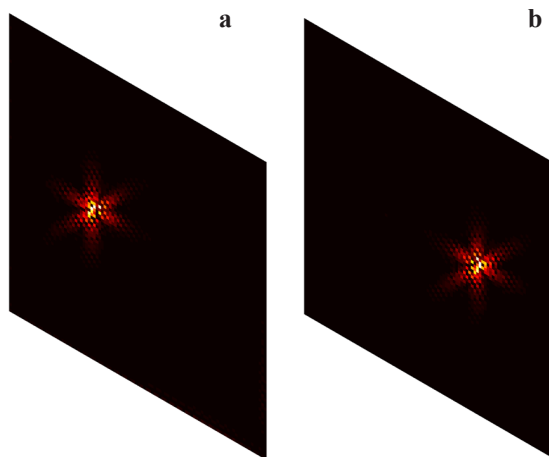


Figure 1. Majorana vortex modes (**a** and **b**) localized on different vortices. Black color corresponds to near zero values of the probability density, the brightest color is for maximum values  $\approx 0.125$ .

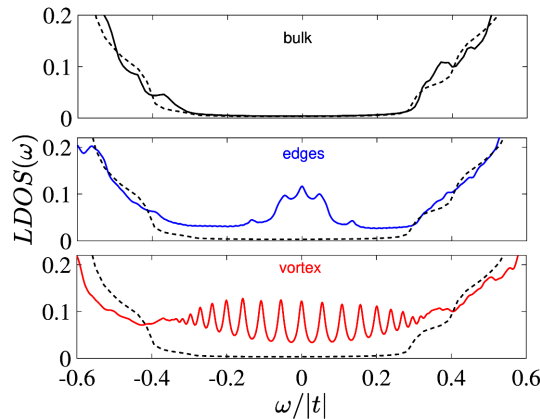


Figure 2. Local density of states (LDOS) in the vicinity of the vortex (solid line on the lower graph), near the edges (solid line on the middle graph), and far from inhomogeneities (solid line on the upper graph). The dashed line is DOS calculated for comparison in the homogeneous case with periodic boundary conditions.

ference between different vortex bound states is an order of magnitude higher. It opens the way to experimentally detect the zero energy MM localized at vortex cores by using methods measuring local density of states (LDOS) such as tunneling experiments.

The existence of spatially separated Majorana vortex modes localized on different vortices in the considered structure is demonstrated in Fig. 1. The map of MM probability density is shown. The parameters are  $\Delta = 0.2|t|$  (superconducting order parameter),  $h = |t|$  (exchange field),  $h_z = 0.1|t|$  (Zeeman splitting),  $\mu \approx -0.4|t|$  (chemical potential), and  $t$  is hopping integral. In this case the dependencies of LDOS on energy near the vortex, edges, and far from inhomogeneities are shown in Fig. 2. For the triangular lattice with open boundary conditions in the Shubnikov phase the edge and vortex bound states appear. Notably, Majorana vortex modes with zero energy are separated from finite-energy vortex states. On the other hand, a band of overlapping edge states appears in the superconducting gap for LDOS near edges with the broadening parameter  $\delta = \Delta/20$ . Such broadening is comparable with experimental STM resolution [5].

For a few pairs of vortices, the vortex-bound states with near zero energy can appear. Nevertheless, they are localized on different vortices in comparison with the localization of Majorana vortex modes. In this case the zero modes are still separated in energy and space from the other states in the LDOS results. The difference between density of states near the vortex and near the antivortex with MM is also demonstrated.

*Support by the Theoretical Physics and Mathematics Advancement Foundation “BASIS” is acknowledged.*

1. J. Shen et al., Phys. Rev. B, **104**, 045422 (2021).
2. A.O. Zlotnikov, M.S. Shustin, and A.D. Fedoseev, J. Supercond. Nov. Magn., **34**, 3053 (2021).
3. Y.E. Kraus, A. Auerbach, H.A. Fertig, and S.H. Simon, Phys. Rev. B, **79**, 134515 (2009).
4. K. Björnson and A.M. Black-Schaffer, Phys. Rev. B, **88**, 024501 (2013).
5. R.S. Akzhanov, A.L. Rakhmanov, A.V. Rozhkov, and F. Nori, Phys. Rev. B, **94**, 125428 (2016).
6. V. Pathak, S. Plugge, and M. Franz, Annals of Physics, 168431 (2021).
7. G.E. Volovik, JETP Lett., **66**, 522 (1997).
8. Y.-M. Lu and Z. Wang, Phys. Rev. Lett., **110**, 096403 (2013).
9. D. Lee and A.P. Schnyder, Phys. Rev. B, **93**, 064522 (2016).



## SUPERCONDUCTING BIO-INSPIRED NEURONS FOR SPIKING NETWORKS

*A.E. Schegolev<sup>1\*</sup>, N.V. Klenov<sup>2</sup>, I.I. Soloviev<sup>1</sup>, M.Yu. Kupriyanov<sup>1</sup>*

<sup>1</sup>Skobeltsyn Institute of Nuclear Physics, Lomonosov Moscow State University, Moscow, Russia

<sup>2</sup>Faculty of Physics, Moscow State University, Moscow, Russia

\*E-mail: [tanuioir@gmail.com](mailto:tanuioir@gmail.com)

Modeling the processes in the brain of living beings is a complex and urgent task [1–9]. One of the main problems in this area is an insufficient number of neurons and synapses in modern Complementary-Metal-Oxide-Semiconductor (CMOS) neuromorphic processors. Their complexity is closely tightened by large power consumption and heat dissipation of the circuits. The best CMOS neuromorphic systems simulate the networks consisting of about 1 million neurons and a quarter of a billion synapses [10–12]. However, the most ambitious biological projects state the goals of  $10^{10}$  neurons and  $10^{14}$  synapses [13]. The demand for such a high complexity makes important the consideration of novel physical principles for signal transmission and processing. The application of superconducting materials allows to compete CMOS also in the implementation of artificial neurons. Josephson junction (JJ) switching provides the generation of picosecond-width quantized voltage spike of  $\sim$  mV amplitude accompanied by  $\sim$  sub-aJ energy dissipation [14, 15]. The shape of this spike can be quite close to the one produced in neurophysiological processes.

A conventional SQUID cell can be naturally used for the implementation of the SQUID-based neuron proposed in [16]. However, more useful circuit may be developed using 3JJ cell, see Fig. 1. The advantage of the proposed topology of an artificial neuron is the ability to simulate several operation modes of a biological neuron, such as regular mode or bursting mode. This circuit was analyzed using the RSJ model with capacitance of Josephson junctions.

The circuit dynamics are governed mainly by two parameters at fixed bias current value. They are the normalized critical current of the third junction,  $\eta$ , determining the neuron firing threshold, and the normalized capacitance of the junctions,  $\beta$ , responsible for the refractory period. The first and second JJs play the role of sodium ( $\text{Na}^+$ ) and potassium ( $\text{K}^+$ ) ion channels in the neuron membrane [1, 17], respectively. The voltage across the cell,  $v_{\text{out}}$  (see Fig. 1), reflects the processes during the neuron firing typical for biological one.

The proposed neuron is capable of mimic the biological activity corresponding to the modes partially presented in Fig. 2: regular mode shows the typical response of a neuron to external stimula-

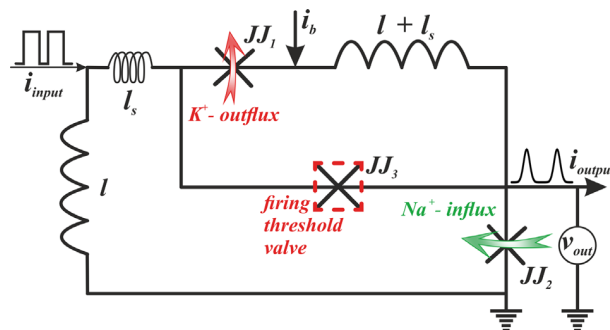


Figure 1. Schematic of the proposed klen bio-inspired neuron for spiking neural networks.

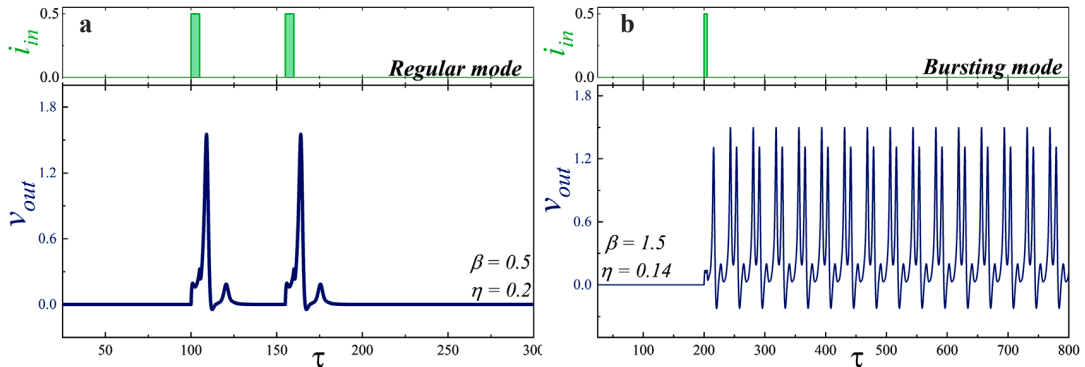


Figure 2. Simulations of the superconducting bio-inspired neuron dynamics in the various operation modes: **a** regular mode ( $\beta = 0.5$ ,  $\eta = 0.2$ ) and **b** bursting mode ( $\beta = 1.5$ ,  $\eta = 0.14$ ). The circuit parameters are  $i_b = 1.9$ ,  $l = 5$ ,  $I_S = 3.85$ .

tion. A short input current pulse of a sufficient amplitude causes single spike, whereafter the system returns to a stable state. The interspike interval is determined by a neuron refractory period, which, in consequence, is related to the recovery of  $\text{Na}^+$  channels; bursting mode demonstrates generation of a series of spikes in response to single stimulating current pulse. Such behavior may be the result of the complex neuron interaction in the network. Bursting behavior in *in vivo* neurons plays an important role in synaptic plasticity, synchronization of big neuron groups, information encoding, and reliability of synaptic transmission, which may be crucial for processing of important stimuli.

Numerical simulations show that the proposed 3JJ cell is capable of mimic specific biological neuron activity missed in previously presented superconducting artificial neurons. In this mode of operation, regular and irregular spike sequences are generated as activation patterns occurring *in vivo* in many cases including stereotypical motor programs, neural coding, and neuropathologies.

*Support by RSF grant No. 20-12-00130 is acknowledged.*

1. A.L. Hodgkin, A.F. Huxley, *The Journal of Physiology*, **117**(500) (1952).
2. M.D. Forrest, *BMC Neuroscience*, **16**, 1–23 (2015).
3. Y. Deng, H. Liu, G. Uhlmann, *J. Differential Equations*, **267**, 2471–2502 (2019).
4. M.J. Sætra, G.T. Einevoll, G. Halnes, *PLoS Computational Biology*, **16**, e1007661 (2020).
5. M.J. Sætra, G.T. Einevoll, G. Halnes, *PLoS Computational Biology*, **17**, e1008143 (2021).
6. F. Chance, *IEEE Spectrum*, **58**, 28–33, (2021).
7. A.M. Jürgensen, A. Khalili, E. Chicca, G. Indiveri, M.P. Nawrot, *Neuromorphic Computing and Engineering*, **1**, 024008 (2021).
8. D. Ham, H. Park, S. Hwang, K. Kim, *Nature Electronics*, **4**, 635–644 (2021).
9. E. Toomey, K. Segall, M. Castellani, M. Colangelo, N. Lynch, K.K. Berggren, *Nano Letters*, **20**, 8059–8066 (2020).
10. H. Markram, E. Muller, S. Ramaswamy et al., *Cell*, **163**, 456–492 (2015).
11. S. Furber, *J. Neural Engineer.* **13**, 051001 (2016).
12. I. Sourikopoulos, S. Hedayat, C. Loyez, F. Danneville, V. Hoel, E. Mercier, A. Cappy, *Frontiers in Neuroscience*, **11**, 123 (2017).
13. F.A. Azevedo, L.R. Carvalho, L.T. Grinberg, J.M. Farfel, R.E. Ferretti, R.E. Leite, W.J. Filho, R. Lent, S. Herculano-Houzel, *J. Compar. Neurology*, **513**, 532–541 (2009).
14. K.K. Likharev, *Dynamics of Josephson Junctions and Circuits*. Routledge (2022).
15. A. Barone, G. Paterno, *Physics and Applications of the Josephson Effect*, vol. 1. Wiley Online Library, (1982).
16. P. Crotty, D. Schult, K. Segall, *Phys. Rev. E*, **82**, 011914 (2010).
17. A.L. Hodgkin, B. Katz, *J. Physiol.* **108**(37), (1949).

## MODEL OF CHARGE TRIPLETS FOR UNCONVENTIONAL HTSC SYSTEMS

*A.S. Moskvin*<sup>1,2\*</sup>, *Yu.D. Panov*<sup>1</sup>

<sup>1</sup>Ural Federal University, Ekaterinburg, Russia

<sup>2</sup>Institute of Metal Physics UB RAS, Ekaterinburg, Russia

\*E-mail: [alexander.moskvin@urfu.ru](mailto:alexander.moskvin@urfu.ru)

Explanation of the unconventional HTSC phenomenon in cuprates, nickelates, and ferropnictides should involve some fundamentally new physics that requires going beyond the standard Fermi liquid description of the normal state and BCS paradigm of the superconducting state. In this regard, we would like to draw attention to the undeservedly forgotten “glueless” disproportionation mechanism (see [1] and references therein), especially popular in the “chemical” community, that leads to bosonic superconductivity in nominally insulating 3d compounds. It was addressed earlier by many authors, however, by now it was not properly developed theoretically, and perhaps that is why it has not yet been a worthy competitor to the traditional BCS approach.

A simple view of the disproportionated system such as  $3d^n + 3d^n \rightarrow 3d^{n+1} + 3d^{n-1}$  implies the electron(hole) center  $3d^{n+1}(3d^{n-1})$  to be composed of hole(electron) center plus electron(hole) coupled pair  $3d^2(3d^2)$  that seems to constitute a composite electron(hole) local boson. In other words, the disproportionated system is anticipated to be a system of local bosons moving in a lattice formed by electron(hole) centers. It is easy to see that the optimal conditions for the superconductivity are expected for parent  $3d^n$  systems with  $3d^{n+1}$  configurations which correspond either empty, or filled and half-filled  $t_{2g}$  and  $e_g$  orbitals. Second, to minimize the reduction effect of the electron-lattice interaction and avoid the localization, we need the S-type ( $A_{1g}$ ,  $A_{2g}$ ) orbital symmetry of the local boson that provides the conservation of the orbital degeneracy when it moves on the lattice. Third, to minimize the reduction effect of the spin degrees of freedom, we need spin-singlet local bosons. Fourth, to maximize the transfer integral we need a participation of the strongest  $\sigma$  bonds.

The most effective S-type ( $A_{1g}$ ,  $A_{2g}$ )  $e_g^2$  configuration of the local composite boson providing maximal values of the boson transfer integral without strong reduction effects of the electron-lattice coupling is realized only for several optimal  $d^n$  configurations: HS- $d^4$ , LS- $d^7$ ,  $d^9$  given octahedral crystal field, and  $d^1$ , HS- $d^6$  configurations given tetrahedral crystal field (HS = high spin, LS = low spin) [1]. All these bare systems are characterized by E-type orbital degeneracy, i.e. these are prone to a strong Jahn-Teller effect. In all the instances the disproportionation reaction lifts the bare orbital degeneracy, that is it has a peculiar “anti-Jahn-Teller” character. These bare JT-systems are characterized by a strong localization due to a vibronic reduction of the one-particle (electron or hole) transport, while after disproportionation these are characterized by an effective two-particle (local boson) transport. Undesirable spin-triplet structure of the local composite bosons appears to be a common feature of all the above mentioned disproportionated systems with a high symmetry crystal field. Furthermore, the  $d^4$ - and  $d^6$ -systems reveal unavoidable coexistence of the spin-triplet bosons and a magnetic lattice. The most optimal conditions for HTSCs with spinless local bosons and a spinless lattice can only be achieved for low-symmetry quasi-two-dimensional  $d^9$ -systems such as cuprates and nickelates. All these results are summarized in Table 1 where we have added examples of 3d-systems with optimal  $3d^n$  configurations.

Following the spin-magnetic analogy proposed by Rice and Sneddon [2] to describe the three charge states ( $Bi^{3+}$ ,  $Bi^{4+}$ ,  $Bi^{5+}$ ) of the bismuth ion in  $BaBi_{1-x}Pb_xO_3$  as a  $S = 1$  pseudospin triplet, we develop a unified non-BCS spin-pseudospin model to describe the main phase states

Table 1.  $3d^n$  and  $4d^n$  JT-systems optimal for the “anti-JT” disproportionation driven superconductivity. Real HTSC systems, cuprates, nickelates, and ferropnictides are highlighted in color.

Electron configuration	Symm.	LS/HS	Local boson	Lattice	Parent compound	SC
$3d^1(e_g^1):^2E$ $Ti^{3+}, V^{4+}$	tetra	—	$e_g^{2,3}A_{2g}$ , $s = 1$	$S = 0$	—	—
$3d^4(t_{2g}^3e_g^1):^5E$ $Mn^{3+}, Fe^{4+}$	octa	HS	$e_g^{2,3}A_{2g}$ , $s = 1$	$S = 3/2$	$(Ca,Sr)FeO_3$ $RMnO_3$	Local
$3d^6(e_g^3t_{2g}^3):^5E$ $Fe^{2+}, Co^{3+}$	tetra	HS	$e_g^{2,3}A_{2g}$ , $s = 1$	$S = 3/2$	$LaFeAsO_3, \dots$ $LiFeAs$	$T_c \leq 56$ K
$3d^7(t_{2g}^6e_g^1):^2E$ $Co^{II+}, Ni^{III+}$	octa	LS	$e_g^{2,3}A_{2g}$ , $s = 1$	$S = 0$	$RNiO_3$ $AgNiO_2$	?
$3d^9, 4d^9(t_{2g}^6e_g^3):^2E$ $Cu^{2+}, Ni^{+}, Ag^{2+}$	octa	—	$e_g^{2,3}A_{2g}$ , $s = 1$	$S = 0$	$KCuF_3, \dots$ $AgO$ $(Ag^{1+}Ag^{3+}O_2)$	?
$3d^9(t_{2g}^6e_g^3):^2B_{1g}$ $Cu^{2+}, Ni^{+}$	octa* square	—	$b_{1g}^{2,1}A_{1g}$ , $s = 0$	$S = 0$	$La_2CuO_4, \dots$ $Nd_2CuO_4$ $RNiO_2$	$T_c \leq 135$ K
$4d^9(t_{2g}^6e_g^3):^2B_{1g}$ $Ag^{2+}$	square	—	$b_{1g}^{2,1}A_{1g}$ , $s = 0$	$S = 0$	$AgF_2$	?

of HTSC cuprates and nickelates starting with a minimal model for the  $CuO_2/NiO_2$ -planes with the on-site Hilbert space reduced to a charge triplet of the three effective valence centers  $[CuO_4]^{5-,6-,7-}/[NiO_4]^{6-,7-,8-}$  (nominally  $Cu^{3+,2+,1+}/Ni^{2+,1+,0+}$ ) with different conventional spin [1, 3–5]. The effective spin-pseudospin Hamiltonian of the charge triplet model takes into account local and nonlocal correlations, correlated one-particle and two-particle (bosonic) transport, and Heisenberg spin exchange. In accordance with experimental data for apexless cuprates and nickelates [6, 7] we argue that not only antiferromagnetic insulating (AFMI), but charge ordered (CO), superconducting (BS), and Fermi-liquid (FL) phases are possible phase states of a model parent cuprate/nickelate, while typical phase state of a doped system, in particular, mysterious pseudogap phase in cuprates, is the result of a phase separation (PS) [4, 5].

Superconductivity of cuprates/nickelates is not the consequence of the pairing of doped holes, but the result of the quantum transport of on-site composite hole bosons, whereas the main peculiarities of normal state can be related to an electron-hole interplay for unusual Fermi-liquid phase and features of the PS. Simplified, the local on-site composite hole boson in cuprates is a pair of holes coupled by local correlations both with each other and with the “core”, that is, the electronic center  $[CuO_4]^{7-}$  (nominally  $Cu^{1+}$ ). In fact, such a local boson exists only as an indivisible part of the Zhang-Rice hole center  $[CuO_4]^{5-}$  (nominally  $Cu^{3+}$ ).

Our supposition of ferropnictide as the system of local spin-triplet bosons with the  $e_g^2$ -configuration moving in the lattice of  $Fe^{1+}$  centers with spin 3/2 (see Table 1) is fundamentally different from the currently accepted BCS “multiorbital” paradigm of the pairing of band carriers with  $t_{2g}$ -symmetry. Based on the analysis of the effective spin-pseudospin Hamiltonian of the charge triplet model [1, 3] and direct analogy with the “double exchange” model, we have considered the main phases and phase states of ferropnictides and other iron-based superconductors.

*Support from the Ministry of Science and Higher Education of the Russian Federation (project # FEUZ-2020-0054) is acknowledged.*

1. A.S. Moskvina, J. Phys.: Condens. Matter, **25**, 085601 (2013).
2. T.M. Rice and L. Sneddon, Phys. Rev. Lett., **47**, 689 (1981).
3. A.S. Moskvina, Phys. Rev. B, **79**, 115102 (2009); *ibid* **84**, 075116 (2011).
4. A.S. Moskvina, Y.D. Panov, Condens. Matter, **6**, 24 (2021).
5. A.S. Moskvina, Yu.D. Panov, JMMM, **550**, 169004 (2022).
6. M. Naito, Y. Krockenberger, A. Ikeda et al., Physica C, **523**, 28 (2016).
7. D.Li, K. Lee, B.Y. Wang et al., Nature, **572**, 624 (2019).

**PECULIAR PROPERTIES OF 0- $\pi$  TRANSITION  
 IN SF-F-FS VARIABLE THICKNESS BRIDGES**

*V.I. Ruzhickiy<sup>1,2\*</sup>, S.V. Bakurskiy<sup>1</sup>, N.V. Klenov<sup>1,2</sup>, I.I. Soloviev<sup>1,2</sup>, M.Yu. Kupriyanov<sup>1</sup>, A.A. Golubov<sup>3,4</sup>*

<sup>1</sup>Lomonosov Moscow State University Skobeltsyn Institute of Nuclear Physics, Moscow, Russia

<sup>2</sup>Physics Department of Moscow State University, Moscow, Russia

<sup>3</sup>Moscow Institute of Physics and Technology, Dolgoprudny, Moscow Region, Russia

<sup>4</sup>Faculty of Science and Technology and MESA+ Institute for Nanotechnology, University of Twente, The Netherlands

\*E-mail: [vi.ruzhickiy@physics.msu.ru](mailto:vi.ruzhickiy@physics.msu.ru)

Recently, interest has been renewed in the study of Josephson structures of variable thickness bridges. The calculations carried out in Refs. [1–3] indicated the possible prospect of their use as basic elements of digital and analog superconducting devices.

Josephson variable thickness bridges were first proposed by Likharev [4] and were intensively studied both theoretically [5–9] and experimentally [10–14] until the end of the 80s. The structure (see Fig. 1) consists of two superconducting (S) electrodes with a thickness  $d_s$  connected by a structured film of a weak link material with a thickness  $d_f$ .

In SN-N-NS and SF-F-FS Josephson junctions the final interface transparency leads to violation of the rigid boundary conditions used in the above estimates [15] and delocalization of the weak coupling region [1]. In the limit  $L_b \ll \xi$  both critical current  $I_c$  and  $I_c R_N$  product are mainly determined in these junctions by suppression parameter  $\gamma_{BM}$  rather than on bridge geometrical factors  $L_b$  and  $W$ . There is no need for additional structuring of the width of the bridge film [1]. Its width may coincide with the width of the composite electrode and be determined by the requirements for the line width of a technological process.

To find the required dependencies  $I(\varphi)$  and  $J_{Fx}(x, \varphi)$ , it is necessary to solve in the F-film the Usadel equations. In case of low film thickness,  $d_f \ll \xi_f$ , Usadel Green’s functions  $\Phi$  independent of the coordinate  $y$ . Figure 2a shows the dependence of the current,  $I(x)$ , in the F,N-layer for different values of the normalized on  $\pi T_c$  exchange energy  $H$ . It can be seen that there are Josephson junctions with positive (0-junction) and negative ( $\pi$ -junction) critical current ( $I_c = I(0)$ ). In addition, the presence of a vortex can be observed in both cases. It makes the existence of junctions with the bistable phase-current relation.

From Usadel equation in the S-electrodes it follows that in this approximation phases of order parameter  $\Delta(x,y)$  and anomalous Usadel Green’s functions,  $\Phi_s(x,y)$  coincide with each other, while their modules equal to their equilibrium values in a superconductor at a given temperature,  $T$ :  $\Phi_s(x,y) = \Delta(x,y) = \Delta \exp\{\chi(x,y)\}$ . Here  $\Delta$  is normalized on  $\pi T_c$  magnitude of superconductors order

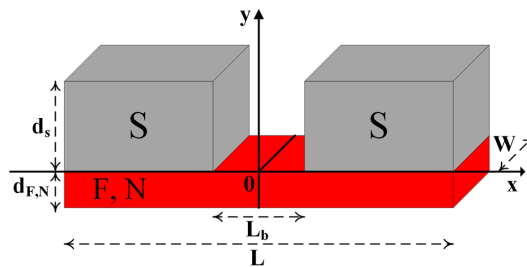


Figure 1. Sketch of SF-F-FS Josephson junction with variable thickness bridge geometry.

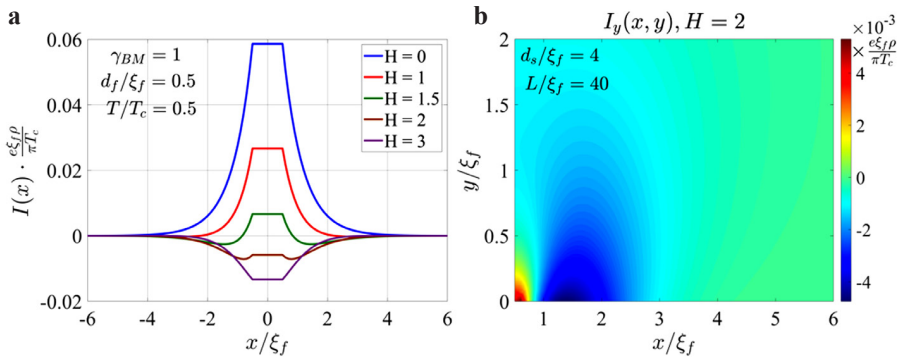


Figure 2. **a** Dependence of the current,  $I(x)$ , in the F,N layer for different values of the normalized exchange energy  $H$ ; **b** Spreading of the  $y$ -component of the current,  $I_y$ , in the superconducting electrode S for  $H = 2$ .

parameter. The phase  $\chi(x,y)$  obeys the Laplas equation with Neumann boundary conditions. Figure 2b shows the calculation of the spreading of the  $y$ -component of the current,  $I_y$ , in the superconducting electrode S for  $H = 2$ . In the vicinity of F-FS corner the vortex character of current spreading in the S-electrode is observed. When moving away from the bridge by a value of about  $3\xi_F$  the current is evenly distributed along of coordinate  $y$ .

In summary, we assert that SF-F-FS junction with variable thickness bridge geometry can have a different sign of the critical current (0 or  $\pi$  junctions). In addition, we have shown that in the presence of Zeeman splitting in a weak link material, these supercurrent configurations can be even of a vortex nature. Another important feature is the absence of the critical current oscillations when the film thickness  $d_F$  or the S electrode thickness  $d_S$  changes.

*The work is supported by Grant No. 20-12-00130 of the Russian Science Foundation. M.Yu.K. and N.V.K. are grateful to the Interdisciplinary Scientific-Educational School of the Moscow State University “Photonic and Quantum Technologies. Digital Medicine.”*

1. I. Soloviev, S. Bakurskiy, V. Ruzhickiy, N. Klenov, M. Kupriyanov, A. Golubov, O. Skryabina, and V. Stolyarov, *Phys. Rev. Applied*, **16**, 044060 (2021).
2. P.M. Marychev and D.Y. Vodolazov, *Beilstein J. Nanotechnol.*, **11**, 858{865 (2020).
3. V. Bosboom, J.J.W.V. der Vegt, M.Y. Kupriyanov, and A.A. Golubov, *Supercond. Sci. Technol.*, **34**, 115022 (2021).
4. K.K. Likharev, *Zh. Eksp. Teor. Fiz.*, **61**, 1700 (1971).
5. K.K. Likharev, *Pis'ma Zh. Tekh. Fiz.*, **2**, 29 (1976), [*Sov. Tech. Phys. Lett.*, **2**, 12 (1976)].
6. M.Y. Kupriyanov, K.K. Likharev, and V.F. Lukichev, *Zh. Eksp. Teor. Fiz.*, **83**, 431 (1982), [*Sov. Phys. JETP*, **56**, 235–240 (1982)].
7. A.A. Golubov, M.Y. Kupriyanov, and V.F. Lukichev, *Soviet Microelectronics*, **12**, 180 (1983).
8. P. Dubos, H. Courtois, B. Pannetier, F.K. Wilhelm, A.D. Zaikin, and G. Schon, *Phys. Rev. B*, **63**, 064502 (2001).
9. J.M. Warlaumont, J.C. Brown, T. Foxe, and R.A. Buhrman, *Phys. Rev. Lett.*, **43**, 169 (1979).
10. R.B. van Dover, A. de Lozanne, and M.R. Beasley, *J. Appl. Phys.*, **52**, 7327 (1981).
11. O. Liengme, P. Lerch, W. Liu, and P. Martinoli, *IEEE Tran. Magn.*, **19**, 995 (1983).
12. H. Nakano and T. Aomine, *Jap. J. Appl. Phys.*, **26**, 304 (1983).
13. J. Sauvageau, R. Ono, A. Jain, K. Li, and J. Lukens, *IEEE Tran. Magn.*, **21**, 854 (1985).
14. Y. Baryshev, A. Dmitriev, A. Krivospitsky, V. Lukichev, A. Orlikovsky, and K. Valiev, *Microelectronic Engineering*, **9**, 385 (1989).
15. V.K. Semenov, Y.A. Polyakov, and S.K. Tolpygo, *IEEE Trans. Appl. Supercond.*, **29**, 1302809 (2019).

## EFFECT OF WEAK HUBBARD REPULSION ON SPECTRUM AND TRANSPORT IN HIGHER-ORDER TOPOLOGICAL SUPERCONDUCTOR

*S.V. Aksenov\**, *A.D. Fedoseev*, *M.S. Shustin*, *A.O. Zlotnikov*

Kirensky Institute of Physics, Federal Research Center KSC SB RAS, Russia

\*E-mail: [asv86@iph.krasn.ru](mailto:asv86@iph.krasn.ru)

One of the actively developing areas of modern condensed matter physics is the study of the topological properties of low-dimensional superconducting systems and the search for Majorana states [1]. These states, due to their separation in space, are stable with respect to local perturbations, which makes them natural candidates for the implementation of quantum computing. In this regard, two-dimensional higher-order topological superconductors (HOTSCs) *a priori* look more attractive than one-dimensional structures (i.e., first-order topological superconductors) due to the initially available possibility of rearranging Majorana modes without crossing their trajectories (braiding operation), which is necessary for unitary transformation of the qubit wave function [2].

From a technological point of view two-dimensional HOTSCs also have a number of advantages, since there is an energy gap not only between Majorana and bulk excitations, but also between Majorana and edge excitations [3]. Moreover, the values of these gaps do not depend significantly on the ratio of the structure geometric dimensions (i.e. sides). In addition, Majorana modes in such systems are localized strictly in the corners, which greatly simplifies the control of their position during braiding (in comparison, for example, with the Abrikosov vortices). However, despite the significant interest in Majorana corner modes, they have not yet been experimentally detected, which makes it necessary to go beyond basic models and analyze additional factors that can affect the HOTSC properties.

Here we investigate the effect of weak local Coulomb interactions on spectrum and transport in a square-shape lattice featuring the Rashba spin-orbit coupling and superconducting pairing with two orbitals per site [4]. Such a system models HOTSC, namely, a 2D topological insulator proximitized by an  $s_{\pm}$ -wave superconductor. The corresponding Hamiltonian is

$$\mathcal{H} = \mathcal{H}_0 + \mathcal{H}_1,$$

$$\mathcal{H}_0 = \sum_{f\eta\sigma} (-\mu + \eta\Delta\epsilon) c_{f\eta\sigma}^{\dagger} c_{f\eta\sigma} + U \sum_{f\eta} c_{f\eta\uparrow}^{\dagger} c_{f\eta\uparrow} c_{f\eta\downarrow}^{\dagger} c_{f\eta\downarrow} + V \sum_{f\eta\sigma\sigma'} c_{f\eta\sigma}^{\dagger} c_{f\eta\sigma} c_{f\eta\sigma'}^{\dagger} c_{f\eta\sigma'},$$

$$\mathcal{H}_1 = \sum_{\langle fm \rangle_x \sigma \eta} t_x \eta c_{f\eta\sigma}^{\dagger} c_{m\eta\sigma} + \sum_{\langle fm \rangle_y \sigma \eta} t_y \eta c_{f\eta\sigma}^{\dagger} c_{m\eta\sigma} + i\alpha \sum_{\langle fm \rangle_{\eta\eta'\sigma\sigma'}} (\vec{\sigma}^{\sigma\sigma'} \times \vec{d}_{fm})_z c_{f\eta\sigma}^{\dagger} c_{m\eta'\sigma'} + \sum_{\langle fm \rangle} \Delta_I c_{f\eta\uparrow}^{\dagger} c_{m\eta\downarrow} + \text{h.c.}$$

To obtain the spectrum and properties of the lowest-energy excitations the many-body interactions are treated in the generalized mean-field approximation where the Bogoliubov coefficients have to be calculated self-consistently [5]. Further, employing the nonequilibrium Green's functions linear-response transport features of the system related to the presence of Majorana corner modes are analyzed.



*The study was supported by Russian Science Foundation, project 22-22-20076, and Krasnoyarsk Regional Fund of Science.*

1. V.V. Val'kov, M.S. Shustin, S.V. Aksenov, A.O. Zlotnikov, A.D. Fedoseev, V.A. Mitskan, M.Yu. Kagan, *Phys. Usp.*, **65**, 2 (2022).
2. W.A. Benalcazar, B.A. Bernevig, T.L. Hughes, *Science*, **357**, 61 (2017).
3. A.O. Zlotnikov, M.S. Shustin, A.D. Fedoseev, *J. Sup. Nov. Mag.*, **34**, 3053 (2021).
4. Q. Wang, C.-C. Liu, Y.-M. Lu and F. Zhang, *Phys. Rev. Lett.*, **121**, 186801 (2018).
5. B.G. Kukhareenko, *JETP*, **42**, 321 (1975).

## BROADENED YU-SHIBA-RUSINOV STATES IN DIRTY SUPERCONDUCTING FILMS

*S.S. Babkin<sup>1,2\*</sup>, A.A. Lyublinskaya<sup>1,2</sup>, I.S. Burmistrov<sup>2,3</sup>*

<sup>1</sup>L.D. Landau Institute for Theoretical Physics, Chernogolovka, Russia

<sup>2</sup>Moscow Institute of Physics and Technology, Dolgoprudnyi, Russia

<sup>3</sup>Laboratory for Condensed Matter Physics, HSE University, Moscow, Russia

\*E-mail: [babkin.ss@phystech.edu](mailto:babkin.ss@phystech.edu)

The interplay of a potential and magnetic disorder in superconductors remains an active field of research for decades. Within the framework of the Usadel equation [1], we study the local density of states near a solitary classical magnetic impurity in a dirty superconducting film [2]. We find that a potential disorder results in broadening of the delta-function peak in the local density of states at the Yu-Shiba-Rusinov (YSR) energy [3–5]. This broadening is proportional to the square root of a normal-state spreading resistance of the film. We demonstrate that modification of multiple scattering on the magnetic impurity due to intermediate scattering on surrounding potential disorder affects crucially a profile of the local density of states in the vicinity of the YSR energy.

1. K.D. Usadel, Phys. Rev. Lett. **25**, 507 (1970).
2. S.S. Babkin, A.A. Lyublinskaya and I.S. Burmistrov, arXiv:2201.11723 (2022).
3. L. Yu, Acta Phys. Sin. **21**, 75 (1965).
4. H. Shiba, Prog. Theor. Phys. **40**, 435 (1968).
5. A.I. Rusinov, Zh. Eksp. Teor. Fiz. **56**, 2047 (1969).

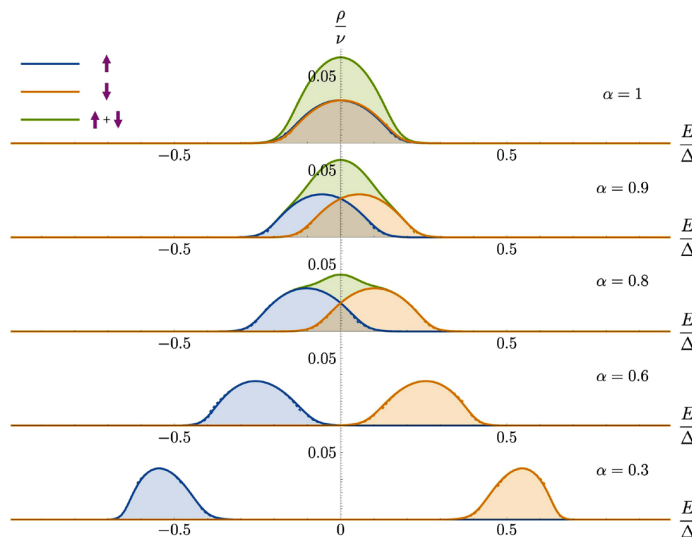


Figure 1. Dependence of the LDoS on the energy at the position of the magnetic impurity for different values of  $\alpha$  (dimensionless effective strength of the magnetic impurity). The total LDoS is shown in green, whereas LDoS for electron's spin with negative (positive) projection on magnetic impurity is shown in orange (blue) color. The analytical (numerical) result is depicted as a solid (dotted) line. The LDoS is normalized on the density of states at the Fermi level in the normal state (per one spin projection), the energy is normalized on the order parameter.

## MAGNETIC AND THERMAL PROPERTIES OF POLYCRYSTALLINE YBCO SUPERCONDUCTOR

D.Z. Gabadulin, A.G. Kiiamov, M.A. Cherosov, R.G. Batulin\*

Institute of Physics, Kazan Federal University, Kazan, Russia

\*E-mail: [tokamak@yandex.ru](mailto:tokamak@yandex.ru)

Here we present the investigation of polycrystalline samples  $\text{YBa}_2\text{Cu}_3\text{O}_{7-\delta}$  made by a solid-state reaction method.  $\text{BaCO}_3$  (Alfa Aesar, 99.8%),  $\text{Y}_2\text{O}_3$  (Alfa Aesar, 99.9%),  $\text{CuO}$  (Alfa Aesar, 99%) oxides were used as starting reagents. The thoroughly grinded and mixed in stoichiometric ratio mixture was put into the crucible and in the preheated up to 500 °C furnace.  $\text{YBa}_2\text{Cu}_3\text{O}_{7-\delta}$  was synthesized for 12 hours at 920 °C, a homogeneous black color powder after the reaction was obtained. A small amount of powder sample were examined with powder X-ray diffraction (Bruker D8 ADVANCE,  $\text{Cu}_{K\alpha}$ ) and found to be a phase-pure material with lattice parameters and space group symmetry corresponding to the structure of  $\text{YBa}_2\text{Cu}_3\text{O}_7$ . The data were analyzed by a standard Rietveld refinement using the FullProf software [1]. All diffraction peaks were well described within the known ( $\text{YBa}_2\text{Cu}_3\text{O}_7$ ) structure model. As grown crystal  $\text{YBa}_2\text{Cu}_3\text{O}_{7-\delta}$  were annealed in an oxygen atmosphere using vertical furnace and various temperatures.

The magnetic properties (zero-field cooled (ZFC) magnetization curve and magnetization  $M(H)$  curves) of as grown and annealed samples were studied using PPMS (Quantum Design) by means of a vibrating sample magnetometer within the temperature range 5–120 K. The heat capacity was measured using PPMS option by two tau model (Quantum Design) within the temperature range 5–300 K.

*This paper has been supported by the Kazan Federal University Strategic Academic Leadership Program (PRIORITY-2030).*

1. J. Rodriguez-Carvajal, Phys. B Condens. Matter, **192**, 55–56 (1993).

## QUASICLASSICAL THEORY OF PROXIMITY EFFECT AT SUPERCONDUCTOR/ANTIFERROMAGNET INTERFACES

*G.A. Bobkov<sup>1</sup>, I.V. Bobkova<sup>2,1,3\*</sup>, A.M. Bobkov<sup>2,1</sup>, V.M. Gordeeva<sup>1</sup>, Akashdeep Kamra<sup>4</sup>*

<sup>1</sup>Moscow Institute of Physics and Technology, Dolgoprudny, Russia

<sup>2</sup>Institute of Solid State Physics of RAS, Chernogolovka, Russia

<sup>3</sup>National Research University Higher School of Economics, Moscow, Russia

<sup>4</sup>Condensed Matter Physics Center (IFIMAC) and Departamento de Física Teórica de la Materia Condensada, Universidad Autónoma de Madrid, Madrid, Spain

\*E-mail: [bobkova.iv@phystech.edu](mailto:bobkova.iv@phystech.edu)

The quasiclassical theory in terms of the Eilenberger equations for the Green's functions is one of the most powerful methods for treating inhomogeneous superconducting hybrids. It has been extremely successful for theoretical description of proximity phenomena in superconductor/ferromagnet hybrids [1, 2]. At the same time proximity effect at superconductor (S)/antiferromagnet (AF) interfaces and, in particular, structure of triplet correlations and critical temperature of S/AF bilayers are largely unexplored yet and the quasiclassical theory is highly desirable in this field. The staggered magnetization of antiferromagnets prevents its direct implementations to AF/S hybrids owing to the rapid oscillations of the magnetization at the atomic scale. In order to be applicable to such heterostructures the quasiclassical theory should be modified. One of the methods to solve the problem is to divide the system into two sublattices. It allows for avoiding the rapid oscillations of the magnetization by doubling the matrix structure of the Green's functions. Basing on the idea we develop the corresponding quasiparticle approach. The unit cell is introduced as shown in Fig. 1.

The quasiclassical Green's function is defined in the sublattice space as

$$\check{g} = \begin{pmatrix} \hat{g}^{AA} & \hat{g}^{AB} \\ \hat{g}^{BA} & \hat{g}^{BB} \end{pmatrix},$$

where each of the components has additional matrix structure in the particle-hole and spin spaces. The Green's function obeys the following Eilenberger equation

$$[(i\omega_m \tau_z + \mu + \tau_z \check{\Delta} - \mathbf{h}\sigma\tau_z \rho_x) \rho_x - \check{\Sigma}_{\text{imp}}, \check{g}(\mathbf{p})] + i v_F \nabla \check{g}(p) = 0,$$

$$\check{\Sigma}_{\text{imp}} = \frac{i}{\tau} (\rho_+ \check{g} \rho_- + \rho_- \check{g} \rho_+),$$

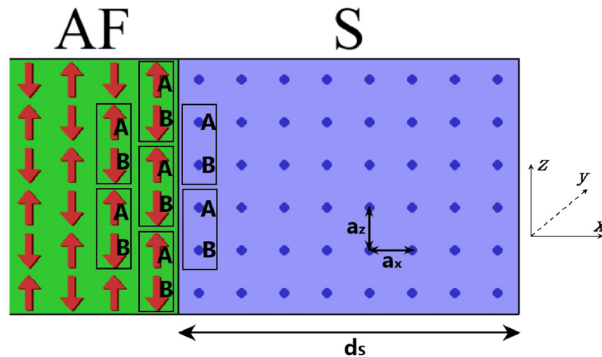


Figure 1. Sketch of the AF/S bilayer under consideration.

where  $\rho_i$  are Pauli matrices in the sublattices space. The boundary conditions for the quasiclassical Green's function at the interfaces between a superconductor and an antiferromagnetic insulator are also discussed. The theory is applied to study the critical temperature of AF/S bilayer structures.

*Support by RSF project № 22-22-00522 is acknowledged.*

1. A.I. Buzdin, Rev. Mod. Phys., **77**, 9352 (2005).
2. F. Bergeret, A. Volkov, and K. Efetov, Rev. Mod. Phys., **77**, 1321 (2005).

**MODELLING OF THE SUPERCONDUCTING TRIPLET SPIN VALVE WITH SEVERAL SUPERCONDUCTOR LAYERS**

*R.R. Gaifullin\**, *R.G. Deminov*<sup>1</sup>, *V.N. Kushnir*<sup>2,3</sup>, *M.Yu. Kupriyanov*<sup>4</sup>,  
*A.A. Golubov*<sup>5</sup>, *L.R. Tagirov*<sup>1,6</sup>

<sup>1</sup>Kazan Federal University, Institute of Physics, Kazan, Russia

<sup>2</sup>Belarus State University of Informatics and Radioelectronics, Minsk, Belarus

<sup>3</sup>Theoretical Physics Department, Belarusian State University, Minsk, Belarus

<sup>4</sup>Skobeltsyn Institute of Nuclear Physics, Moscow State University, Moscow, Russia

<sup>5</sup>Faculty of Science and Technology and MESA+ Institute of Nanotechnology,  
 University of Twente, AE Enschede, The Netherlands

<sup>6</sup>Zavoisky Physical-Technical Institute, FRC Kazan Scientific Center of RAS, Kazan, Russia

\*E-mail: [gaifullin.rashid@gmail.com](mailto:gaifullin.rashid@gmail.com)

We study the critical temperature  $T_c$  and distribution of the singlet pairing components of symmetric S/F/S, asymmetric S1/F/S2 and S1/F1/S2/F2 structures (S, is a singlet superconductor, F<sub>i</sub> is a ferromagnetic metal), where the long-range triplet superconducting component is generated at the canted magnetizations of the F-layers [1]. The dependences of  $T_c$  of the SFS structure in 0 and  $\pi$  phase states [2] were obtained by the matrix method [3] for the parameters of materials and boundaries from the work [4]. The distribution of components characterizes the phase state and behavior of  $T_c$  depending on the thickness  $d_F$  (Fig. 1a–4a).

The normalizing denominator  $\Sigma f_0$  of the singlet components of asymmetric S1/F/S2 structure of the larger  $T_c$  belongs to the thicker layer S in Fig. 2b–3b.

In the S1/F/S2 structure, the  $\pi$ -state with the phase difference  $\pi$  between S-layers may have higher  $T_c$  than the 0-state with the zero phase difference (see Figs. 1–3). It is likely that the S1/F1/S2/F2 structure contains spin-valve modes in the  $\pi$ -state with higher  $T_c$  than in the S/F1/F2 structure. The distribution of the components is discussed as the main reason for the behavior of the  $T_c$  of the S1/F1/S2/F2 structure as a function of the angle  $\alpha$  between the magnetic moments of the ferromagnetic layers. The triplet mode is realized by transition from  $\pi$ -states to the 0-states in Fig. 4b.

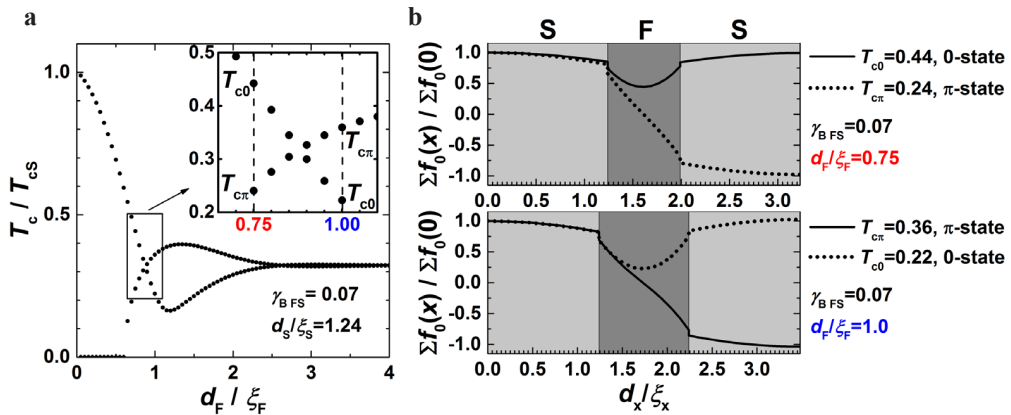


Figure 1. **a**  $T_c$  as a function of the thickness  $d_F$  of the symmetric S/F/S structure. **b** The spin singlet  $\Sigma f_0(x)/\Sigma f_0(0)$  distributions of the superconducting pairing components for **a**.

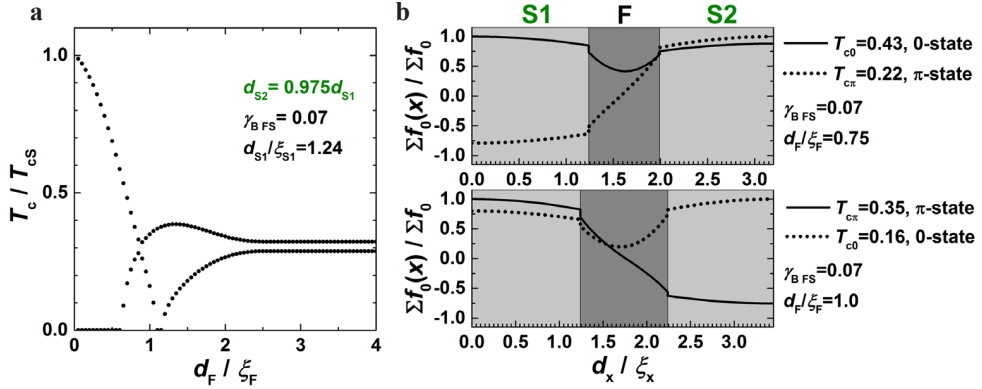


Figure 2. **a**  $T_c$  as a function of thickness  $d_F$  of the asymmetric S1/F/S2 structure. **b** The spin singlet  $\Sigma f_0(x) / \Sigma f_0(0)$  distributions of the superconducting pairing components for **a**.

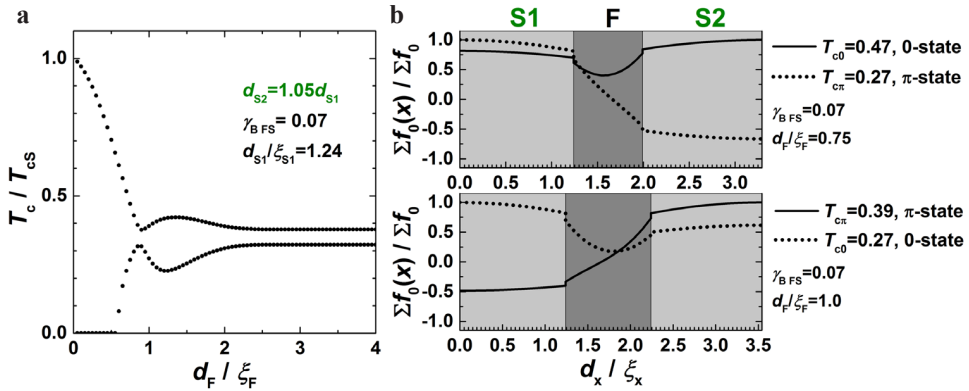


Figure 3. **a**  $T_c$  as a function of the thickness  $d_F$  of the asymmetric S1/F/S2 structure. **b** The spin singlet  $\Sigma f_0(x) / \Sigma f_0(0)$  distributions of the superconducting pairing components for **a**.

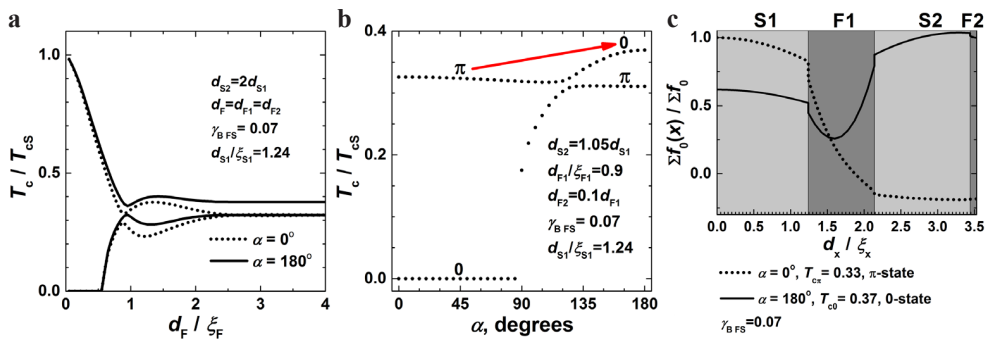


Figure 4. **a**  $T_c$  as a function of the thickness  $d_F$  for parallel and antiparallel configuration magnetic moments of the ferromagnetic layers of the S1/F/S2/F structure. **b** Critical temperature  $T_c$  of the S1/F1/S2/F2 structure versus the angle  $\alpha$ . **c** The spin singlet  $\Sigma f_0(x) / \Sigma f_0(0)$  distributions of the superconducting pairing components for the S1/F1/S2/F2 structure.

Thus, a phase transition from  $\pi$ - to 0-state is obtained with a change of the angle  $\alpha$  between the magnetizations of the ferromagnetic layers in the S1/F1/S2/F2 heterostructure.

*Support by the Priority-2030 Program of KFU is acknowledged. V.N.K. thanks the GPNI “Convergence-2025” (2021-2025), subprogram “Interdisciplinary investigations and incipient technologies”, project “Spin ordering in the heterostructures of Superconductor-Graphene type”.*

1. F.S. Bergeret, A.F. Volkov, and K.B. Efetov, Rev. Mod. Phys., **77**, 1321 (2005).
2. T. Karabassov, V.S. Stolyarov, A.A. Golubov, V.M. Silkin, V.M. Bayazitov, B.G. Lvov and A.S. Vasenko, Phys. Rev. B, **100**, 104502 (2019).
3. V.N. Kushnir, S.L. Prischepa, C. Cirillo, A. Vecchione, C. Attanasio, M.Yu. Kupriyanov, and J. Aarts, Phys. Rev. B, **84**, 214512 (2011).
4. Ya.V. Fominov, N.M. Chtchelkatchev, and A.A. Golubov, Phys. Rev. B, **66**, 014507 (2002).



## GAP STRUCTURE OF MULTIBAND SUPERCONDUCTORS WITH A SPIN-FLUCTUATION INTERACTION

*A.E. Karakozov\**, *M.V. Magnitskaya*

L.F. Vereshchagin Institute for High Pressure Physics, RAS, Troitsk, Moscow, Russia

\*E-mail: [chkara@rambler.ru](mailto:chkara@rambler.ru)

The study of the properties of iron-containing superconductors (FeSCs) makes it possible, in principle, to determine the magnitude of the correlation effects in FeSCs, which are directly related to the non-phonon part of the pairing interaction  $V(k, k')$ , the spin-fluctuation interaction (SFI). For a correct study of the role of SFI, it is necessary to take into account up to five bands on the Fermi surface (FS) (and too many theory parameters). The simplifications that are inevitable because of this can lead to directly opposite estimates of SFI in different approaches, so there is a need to use simplified versions of the theory, which, nevertheless, make it possible to describe reliably established general properties of FeSCs, including the doping evolution (phase diagram) of FeSCs.

Previously, many papers have already discussed the insufficiency for these purposes of the standard “minimal” model, which takes into account only two interacting isotropic s-bands (see, for example, [1, 2]). We considered a simple three-band model of FeSC with a low carrier density: a quasi-two-dimensional superconductor with FS consisting of two hole (h) circles around the point  $\Gamma$  and electron (e) circles around the points  $X = (\pi, 0)$  and  $Y = (0, \pi)$  of small diameter. It can be shown that for such a FS-geometry, to the extent of smallness of the e- and h-pockets, the anisotropic pairing interaction  $V(\mathbf{k}, \mathbf{k}')$ , including the interaction with phonons  $U(k, k')$  and electronic fluctuations  $G(k, k')$ , has a very simple view and is defined by just two parameters. For interband e-h scattering on large wave vectors  $\mathbf{k}_e - \mathbf{k}_h \sim$  antiferromagnetic (AFM) vectors  $\mathbf{Q} = (\pi, 0), (0, \pi)$ ,  $V(\mathbf{k}_e, \mathbf{k}_h) = G(\mathbf{k}_e, \mathbf{k}_h) \approx G$ . The intraband electron-phonon interaction (EPI)  $U(\mathbf{k}_e, \mathbf{k}_e) \approx u$  is the same in all bands, and the intraband interaction in the e-band  $V(\mathbf{k}_e, \mathbf{k}_e) = U(1 \pm d \cos 2\varphi_{XY})(1 \pm d \cos 2\varphi'_{XY})$ , where  $\varphi$  and  $\varphi'$  are polar angles measured from  $\mathbf{k}_{XY}$ , anisotropy coefficient  $d = (2G/U)^{1/2}$ . The ratio  $x = G/U$  of interband SFI  $G$  to intraband EPI  $U$  has the meaning of a measure of proximity to an AFM-transition or doping dependence in FeSCs. The behavior of the pairing interaction  $V(\mathbf{k}, \mathbf{k}')$  at large and small wave vectors  $\mathbf{q}$  qualitatively coincides with the behavior of the spectra of electronic fluctuations in FeSCs: observed at large  $q \sim Q$  interband isotropic spin and at small  $q$  intraband quadrupole  $d_{x^2-y^2}$  charge (orbital) electronic fluctuations. Solutions of the three-band system of equations with interaction  $V(\mathbf{k}, \mathbf{k}')$  for  $t = T/T_c$  have the form  $\Delta_{1h,2h}(t)$  for the h-gaps and  $\Delta_e(\varphi, t) = \Delta_e(t)(1 + D(t)\cos 2\varphi)$  for the e-gap. Due to renormalization by interband s-interactions, the e-gap anisotropy coefficient  $D(t)$  differs from the anisotropy of the pairing interaction  $d$ . The three-band model with strong coupling corrections (see [1, 2]) can be used to analyze the experimental data of FeSCs.

Here, we will focus on the analysis of the unconventional deviation of the dependence of the dimensionless dominant L-gap  $\delta_L(t) < \delta_0(t)$  from

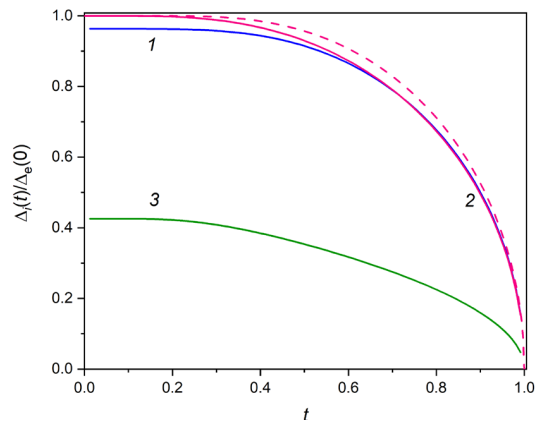


Figure 1. See text for notation.

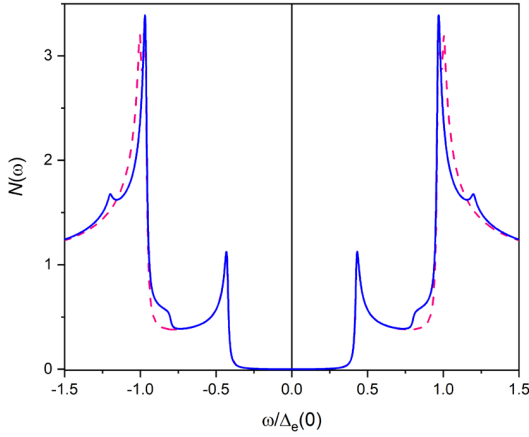


Figure 2.

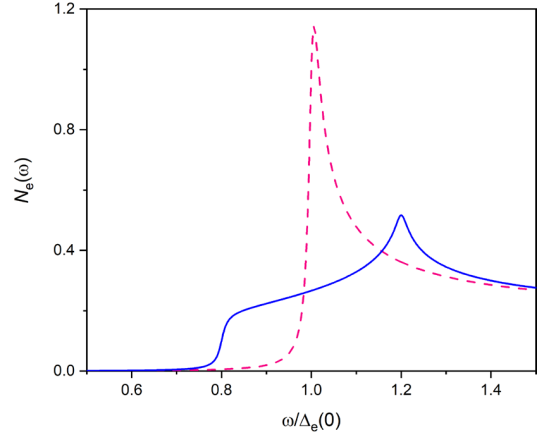


Figure 3.

the universal BCS function  $\delta_0(t)$  observed in tunneling experiments in optimally (with maximum SFI) doped FeSCs (see, e.g., [3]). The dependence of the form  $\delta_L(t) < \delta_0(t)$  in pure superconductors takes place only in multiband systems and in FeSCs is related to SFI. In the two-band model with independent parameters, the deviation  $\delta_L(t) < \delta_0(t)$  is explained by a weak interband interaction with coupling constants  $\lambda_{SL}, \lambda_{LS} \ll \lambda_{LL}, \lambda_{SS}$ , provided that the density of states in the S-band is much higher, than in the L-band ( $\gamma_S \gg \gamma_L$ ) and  $\lambda_{LL} \sim \lambda_{SS}$ . However, the first relation contradicts to the experimental data, and the second one means that the intraband pairing in the S-band is anomalously small ( $V_{SS} \ll V_{LL}$ ), which is hardly possible for small L- and S-pockets. Therefore, in our opinion, the formal application of the minimal model for determining the parameters of superconducting pairing in FeSCs is not very reliable. In our model, the behavior of gaps similar to [3] takes place in the case of a sufficiently strong SFI interaction  $G \sim U$ ,  $x = 0.9$  at almost coinciding e- and h-gaps, an anisotropy of the e-gap  $\sim 20\%$ , and a low density of states in the e-band. Figure 1 shows the dependence of the normalized gaps  $\Delta_i(t)/\Delta_e(0)$  (1, 3 – the hole gaps, 2 – the electron gap, dotted line –  $\delta_0(t)$ ) for this case in comparison with the normalized total density of states (Fig. 2) and the density of states in the e-band (Fig. 3) at  $t \rightarrow 0$  for isotropic (dotted line) and anisotropic superconductors with the same gaps. The maximum in  $N_e(\omega)$  (and its temperature dependence) do not coincide with  $\Delta_e(t)$  by an order of magnitude of the e-gap anisotropy. The figures show that the anomaly  $\delta_L(t) < \delta_0(t)$  can also take place for a strong anisotropic SFI (as in optimally doped FeSCs), and also point to the ambiguity in the interpretation of tunneling spectra of FeSC with close e- and h-gaps and an anisotropic electron gap in the two-band approach.

*Support by the Russian Science Foundation under Grant RSF 22-22-00806 is acknowledged.*

1. A.E. Karakozov, S. Zapf, B. Gorshunov, Ya.G. Ponomarev, M.V. Magnitskaya, E. Zhukova, A.S. Prokhorov, V.B. Anzin, and S. Haindl, Phys. Rev. B, **90**, 014506 (2014).
2. A.E. Karakozov, M.V. Magnitskaya, L.S. Kadyrov, and B.P. Gorshunov, Phys. Rev. B, **99**, 054504 (2019).
3. T.E. Kuzmicheva, A.V. Muratov, S.A. Kuzmichev, A.V. Sadakov, Yu.A. Aleshchenko, V.A. Vlasenko, V.P. Martovitskii, K.S. Pervakov, Yu.F. El'tsev, and V.M. Pudalov, Phys.-Usp., **60**, 419 (2017).

## EFFECTIVE INTERACTIONS IN HIGHER-ORDER TOPOLOGICAL SUPERCONDUCTORS WITH STRONG ELECTRON CORRELATIONS

*S.V. Aksenov, A.D. Fedoseev, M.S. Shustin\*, A.O. Zlotnikov*

Kirensky Institute of Physics, Federal Research Center KSC SB RAS, Russia

\*E-mail: [mshustin@yandex.ru](mailto:mshustin@yandex.ru)

In recent years, higher-order topological superconductors (HOTSCs) have been actively investigated [1, 2]. Unlike ordinary topological superconductors, both bulk and edge excitations in HOTSCs are gapped, while excitations localized at higher-order boundaries (corners in 2D-systems, edges and corners in 3D systems) are gapless. Such excitations are called Majorana corner modes (MCMs) and they are robust against to local perturbations. It is known that chiral Majorana modes in ordinary topological superconductors propagate along the edges and cannot be used for braiding operations. At the same time, the localization of MCMs in 2D HOTSCs makes it possible to consider them as more promising for topological quantum computations [3].

To give rise to HOTSC a system with first-order gapless edge states is usually used, and a perturbation is introduced that breaks the symmetry responsible for the topological protection of the edge states. This leads to the opening of a gap in the edge spectrum. Then, if the effective (Dirac) mass of edge states has a different sign at two adjacent boundaries, the corner between such edges acts as a domain wall on which MCMs arise. Although the principle of formation of HOTSC is general, the specific mechanisms for its implementation can vary greatly [2]. Most of the proposed mechanisms for the formation of HOTSC are based on the consideration of free fermions. Meanwhile, it is known that the Coulomb interactions between fermions can lead to the formation of new topological classes [4]. Thus, it is desirable to study the influence of Coulomb interactions, including strong ones, on the mechanisms of HOTSC formation.

We study the conditions of implementation of Majorana-type excitations in HOTSC with strong electron correlations. The problem is solved in the framework of the 2D two-band HOTSC model on a square lattice [5], considering local Coulomb interactions. The Hamiltonian has the form:

$$\mathcal{H} = \mathcal{H}_0 + \mathcal{H}_1,$$

$$\mathcal{H}_0 = \sum_{\substack{f\eta\sigma=A,B \\ \sigma=\uparrow,\downarrow}} (-\mu + \eta\Delta\epsilon) c_{f\eta\sigma}^+ c_{f\eta\sigma} + U \sum_{f\eta} n_{f\eta\uparrow} n_{f\eta\downarrow} + V \sum_{f,\sigma\sigma'=\uparrow,\downarrow} c_{fA\sigma} c_{fB\sigma'},$$

$$\mathcal{H}_1 = \sum_{\langle\tilde{f}\tilde{m}\rangle_x, \sigma\eta} t_x \eta c_{f\eta\sigma}^+ c_{m\eta\sigma} + \sum_{\langle\tilde{f}\tilde{m}\rangle_y, \sigma\eta} t_y \eta c_{f\eta\sigma}^+ c_{m\eta\sigma} + i\alpha \sum_{\langle\tilde{f}\tilde{m}\rangle_{\eta\eta'\sigma\sigma'}} (\vec{\sigma}^{\sigma\sigma'} \times \vec{d}_{f\tilde{m}})_z c_{f\eta\sigma}^+ c_{m\eta'\sigma'} + \sum_{\langle\tilde{f}\tilde{m}\rangle} \Delta_1 c_{f\eta\uparrow}^+ c_{m\eta\downarrow}^+ + \text{h.c.}$$

For such a system, in the second order of the perturbation theory, effective interactions are obtained when the parameters of the intraband ( $U$ ) and interband ( $V$ ) repulsion significantly exceed the other parameters. Based on the analysis of such interactions, the low-energy dynamics of the system is projected onto the basis of effective operators using the Zwanzig-Mori technique [6, 7]. Further, with the use of irreducible Green's functions based on these operators, the excitation spectrum and distribution of quasiparticles on the lattice are studied in the ensemble of Hubbard fermions.

*The study was supported by Russian Science Foundation, project 22-22-20076, and Krasnoyarsk Regional Fund of Science.*

1. W.A. Benalcazar, B.A. Bernevig, T.L. Hughes, *Science*, **357**, 61 (2017).
2. A.O. Zlotnikov, M.S. Shustin, A.D. Fedoseev, *J. Sup. Nov. Mag.* **34**, 3053 (2021).
3. C. Nayak, S.H. Simon, A. Stern, M. Freedman, S. Das Sarma, *Rev. Mod. Phys.* **80**, 1083 (2008).
4. K. Kudo K., T. Yoshida, Y. Hatsugai, *Phys. Rev. Lett.* **123**, 196402 (2019).
5. Q. Wang, C.-C. Liu, Y.-M. Lu and F. Zhang, *Phys. Rev. Lett.* **121**, 186801 (2018).
6. R. Zwanzig, *Phys. Rev.* **124**, 983 (1961).
7. H. Mori, *Prog. Theor. Phys.* **33**, 423 (1965).

## QUANTUM MONTE-CARLO STUDY OF HARDCORE BOSONS IN TWO DIMENSIONS

*V.S. Ryumshin\**, *V.A. Ulitko*, *Y.D. Panov*

Ural Federal University, Ekaterinburg, Russia

\*E-mail: [vitaliy.ryumshin@urfu.ru](mailto:vitaliy.ryumshin@urfu.ru)

Lattice boson models are extensively employed for the description of systems demonstrating nontrivial phase diagram with competing or mixed states. Various variants of this model are currently used for the description of the characteristics of a large number of physical systems including high-temperature superconductors [1], magnetic insulators in external field [2] and many others. An interest in these models has grown in recent years after discovery of the coexistence of charge ordering and superconductivity in cuprates [3].

We consider the two dimensional hardcore bosons model, with the Hamiltonian:

$$\mathcal{H} = V \sum_{i,\bar{j}} n_i n_{\bar{j}} - t \sum_{i,\bar{j}} (a_i^\dagger a_{\bar{j}} + a_{\bar{j}}^\dagger a_i) - \mu \sum_i n_i, \quad (1)$$

where  $a_i^\dagger$ ,  $a_i$  is the creation (annihilation) operator for hard-core bosons,  $n$  is the number operator,  $V$  is the nearest neighbor Coulomb repulsion,  $t$  is the hopping parameter and  $\mu$  is the chemical potential.

This model is equivalent to an anisotropic spin-1/2 XXZ model in magnetic field. The boson Hamiltonian has been studied as a model of the superconductor-insulator transition [4], of spin-flop transitions in quantum spin systems in external magnetic fields [5], of supersolid behavior [6] and many others. Boson model explores the role of correlations in inducing ordered phases of many quantum mechanical particles, and the nature of the quantum phase transitions between these phases.

However, there is a problem related on the appearance of the phase separation region between superfluid and solid phases [7]. Calculations within the framework of the mean field and the Bethe approximation do not predict the appearance of the phase separation region [8] and, respectively, the “critical line”, in contrast to quantum Monte-Carlo simulations. Therefore, the question is whether this is a feature of the quantum Monte-Carlo calculation or this is a new type of phase transition?

The purpose of this study is to construct phase diagrams and refine the results obtained in earlier works [7, 9], which studied boson model in different variations of quantum Monte-Carlo simulations, in particular, to study the phase separation region observed between superfluid and solid phases.

The study was performed using quantum Monte-Carlo simulations in the framework of Stochastic Series Expansion method with a loop update algorithm [10]. The algorithm has been adapted to conserve charge in order to explain and define the boundaries and the presence of the phase separation region. The simulations were performed for lattices up to size  $96 \times 96$ .

*This work was supported by the Ministry of Science and Higher Education of the Russian Federation, project FEUZ-2020-0054.*

1. N.H. Lindner, A. Auerbach. Phys. Rev. B, **81**, 054512 (2010).
2. T. Giamarchi et al., Nat. Phys., **4**, 198 (2008).
3. G. Ghiringhelli et al., Science, **337**, 821 (2012).
4. V.F. Elesin et al., JETP Lett., **60**, 177 (1994).
5. M. Kohno, M. Takahashi, Phys. Rev. B, **56**, 3212 (1997).
6. G.G. Batrouni et al., Phys. Rev. Lett., **74**, 2527 (1995).
7. G. Schmid et al., Phys. Rev. Lett., **88**, 167208, (2002).
8. E.L. Spevak et al., Phys. Solid State, **1**, (2021).
9. F. Hebert et al., Phys. Rev. B, **65**, 014513 (2001).
10. A.W. Sandvik. Phys. Rev. B, **59**, R14157, (1999).

## INDUCEMENT OF SUPERCONDUCTIVITY IN ANTIFERROMAGNETIC IRON TELLURIDE BY DOPING WITH TITANIUM CHALCOGENIDES

*E.V. Kislov<sup>1\*</sup>, N.V. Selezneva<sup>1</sup>, N.V. Baranov<sup>1,2</sup>*

<sup>1</sup>Institute of Natural Sciences and Mathematics, Ural Federal University, Ekaterinburg, Russia

<sup>2</sup>Institute of Metal Physics, Ekaterinburg, Russia

\*E-mail: [evgny.kislov@urfu.ru](mailto:evgny.kislov@urfu.ru)

It is known that substitutions in the iron and chalcogen sublattices in FeX (X = Se, Te) compounds with a tetragonal crystal structure of the PbO type and P4/nmm space group can affect their properties. For example, the replacement of selenium by tellurium in the FeSe compound having a transition to the superconducting state at  $T_C \approx 8$  K leads to an increase in the critical temperature up to a maximal value 15 K in FeSe<sub>0.5</sub>Te<sub>0.5</sub> [1]. In contrast to superconducting FeSe, the isostructural FeTe compound with a slight excess of iron does not exhibit a transition to the superconducting state [2] and shows an antiferromagnetic order below the Neel temperature  $T_N = 70$  K.

In this work, we study the possibility of inducement of superconducting transition in antiferromagnetic iron telluride by doping with titanium dichalcogenides. It was assumed that upon doping, sulfur or selenium atoms would occupy tellurium positions, while titanium atoms would occupy iron positions in the FeTe tetragonal structure. In addition, it was expected that in the presence of a superconducting transition titanium atoms would affect the pinning of superconducting vortices and the critical currents of the compounds.

Samples of the Fe<sub>1.1</sub>Te(TiX<sub>2</sub>)<sub>y</sub> system were synthesized in two stages: at the first stage, Fe<sub>1.1</sub>Te matrices were prepared by melting at 920 °C followed by quenching; then the matrices were doped with titanium chalcogenides (TiX<sub>2</sub>)<sub>y</sub> (X = S, Se; y = 0.1, 0.2), remelted and cooled down slowly for homogenization and stabilization of superconducting phase. The phase composition and structure of the samples were examined using a Bruker D8 Advance diffractometer. The temperature dependences of the electrical resistance were measured by the standard 4-probe method.

The initial Fe<sub>1.1</sub>Te sample obtained of single-phase and has a PbO-type tetragonal structure described by the P4/nmm space group. Doped samples of Fe<sub>1.1</sub>Te(TiX<sub>2</sub>)<sub>y</sub> (X = S, Se; y = 0.1, 0.2) turned out to be inhomogeneous: in addition to the initial phase, they may contain foreign phases, in particular, pyrrhotite-like Fe<sub>7</sub>Se<sub>8</sub> phase, FeTe<sub>2</sub> and the  $\delta$ -FeTe<sub>1.5</sub> phase depending on the composition, as well as on the conditions of heat treatment and cooling.

It was assumed that the admixture of a small amount of titanium dichalcogenides TiX<sub>2</sub> (X = S, Se) into the initial matrix would lead to the replacement of tellurium by chalcogens of smaller ionic radius and, as a consequence, to compression of the crystal lattice along the c axis and improvement of the superconducting properties. This assumption, in turn, is related to the fact that the FeSe<sub>0.5</sub>Te<sub>0.5</sub> compound with the parameter  $c = 5.942$  Å of the tetragonal lattice demonstrates the highest critical temperature in the FeSe<sub>x</sub>Te<sub>1-x</sub> system [1]. Indeed, we obtained that the addition of TiS<sub>2</sub> and TiSe<sub>2</sub> led to a decrease in the values of the c lattice parameter, while the parameter a remained practically unchanged. The temperature dependences of the resistance of all doped Fe<sub>1.1</sub>Te(TiX<sub>2</sub>)<sub>y</sub> (X = S, Se; y = 0.1, 0.2) samples, in contrast to the initial Fe<sub>1.1</sub>Te, demonstrate a sharp decrease in the electrical resistance, which indicates the onset of superconducting transition, however, the transition was completed not for all samples. It was found that the width of the superconducting transition depends on the value of the current during the measurement, which can

be associated with the granular nature of superconductivity, inhomogeneity of the samples and the presence of additional phases.

*This work was supported financially by the Ministry of Education and Science of the Russian Federation (Project No. FEUZ-2020-0054).*

1. Y. Takano, Y. Mizuguchi, J. Phys. Soc. Jpn., **79**, 102001 (2010).
2. P.K. Maheshwari, R. Jha, B. Gahtori, V.P.S. Awana, J. Supercond. Nov. Magn., **28**, 2893–2897 (2015).

## CRITICAL TEMPERATURE OF SUPERCONDUCTOR/FERROMAGNET NANOSTRUCTURE NEAR A MAGNETIC SKYRMION

*Yu.N. Proshin, V.E. Zayceva, V.A. Tumanov\**

Theoretical Physics Department, Kazan Federal University, Kazan, Russia

\*E-mail: [tumanvadim@yandex.ru](mailto:tumanvadim@yandex.ru)

This research addresses the proximity effect of a superconductor with a chiral ferromagnetic metal. We theoretically study the effect of skyrmions and chiral bobbles [1] on a critical temperature of superconductor/ferromagnet (S/F) heterostructure. In recent years many very small scale (1–100 nm) magnetic skyrmions and skyrmion lattices have been experimentally discovered in specially created materials [2–4]. In contrast to the previously discovered micron-scale spin vortices, such structures can have a significant effect on the critical temperature of the superconducting transition.

We have studied the S/F systems in the dirty limit, since this approximation is consistent with most experimental systems. Based on the Usadel equations for inhomogeneous magnetization obtained in [5] we started with rotation of the matrix Usadel function in spin space. The rotation matrix is chosen in such a way that in the transformed equations the term responsible for the interaction with localized spins becomes diagonal. After transformation the gradient transforms into the extended derivative in the Usadel equations and boundary conditions. Self-consistency equation is invariant under such transformations and has conventional form (see, for example [6]).

We use a generalization of the approach when the order parameter is constant within the layer, so this procedure simplifies the boundary value problem in many practical cases. For complex spin textures, such as spin vortices and domain walls, the Usadel equations do not reduce to a system of equations with constant coefficients after the unitary rotation. However, the transformed Usadel function phase changes much weaker along the SF boundary. This allows us to use an approximate approach to solving the boundary value problem by neglecting some terms in the Usadel equation for the ferromagnetic layer. Within this framework we can obtain a quantitative estimation of the

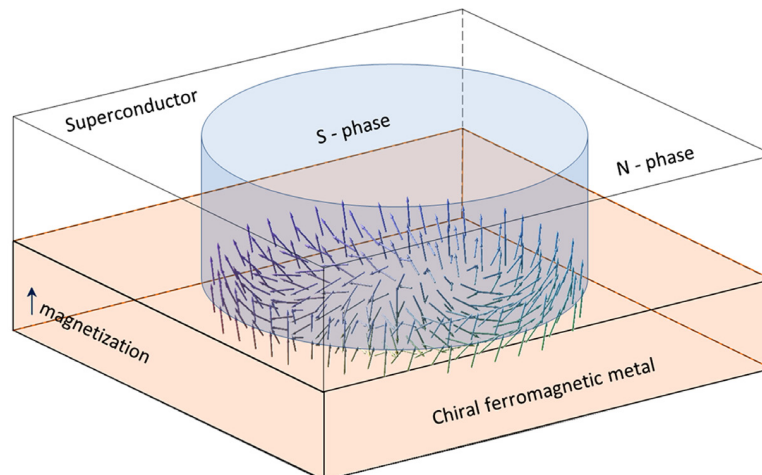


Figure 1. Schematic representation of a superconducting phase localized near a chiral skyrmion.



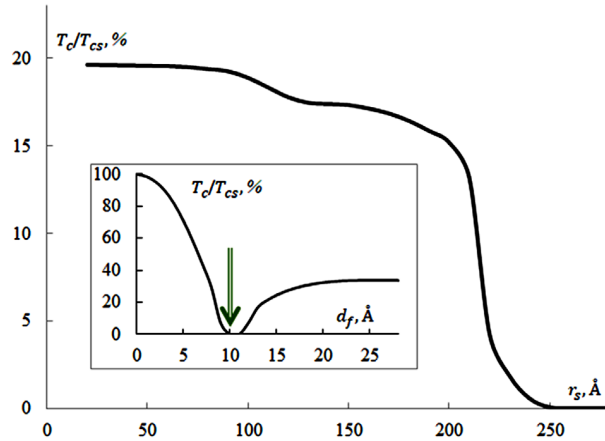


Figure 2. A superconductor/chiral magnetic contact is considered. Main panel: dependence of the critical temperature  $T_c$  of superconducting island of the contact on the radius  $r_s$  [4] of the isolated skyrmion. Inset: dependence of the critical temperature  $T_c$  of the S/F contact on the thickness  $d_f$  of the ferromagnetic layer for uniform magnetization. Here green arrow shows the position of the parameters considered on main panel in the diagram  $T_c(d_f)$ . Parameters of the system: superconductor thickness  $d_s = 111$  Å, free path length  $l_s = 120$  Å, superconducting coherence length  $\xi_s = 125$  Å, product of the mean free path effective exchange field  $2l\tau_f = 0.3$ , transparency parameter  $\sigma_s = 4$ ,  $n_{sf} = 4$  ( $n_{sf} = (v_s N_s)/(v_f N_f)$ , where  $v$  and  $N$  are velocity and density of states at the Fermi level, respectively),  $d_f = 10$  Å.

effect on the superconducting critical temperature for almost any spin texture. Using our approach, we calculated the critical temperature for S/F systems containing conical magnetization, Neel, Bloch, chiral skyrmions, and chiral bobsbers.

As expected, the impact on critical temperature near the magnetic inhomogeneity is determined by its scale compared to the superconducting coherence length. According to our calculations, the described effect is very sensitive to the thickness of the superconducting layer and the border transparency. By special choice of layer thicknesses, it is possible to achieve that superconductivity occurs only in the spin vortex localization region (see Fig. 1). In this case the critical temperature is about 10-20% of the bulk superconductor critical temperature. The scale of effect on the local critical temperature  $T_c$  is strongly depends on the relation between the skyrmion radius and the superconducting coherence length (see Fig. 2).

The significant effect of nanoscale spin vortices on the critical temperature, combined with topological stability and low current density required for their movement [3,7], makes it possible to use such systems as superconducting spin valves. For example, the superconducting island tied to a skyrmion can be placed between two superconductors as a movable bridge for supercurrent.

*This work has been supported by the Kazan Federal University Strategic Academic Leadership Program.*

1. A.B. Borisov, Physics-USpekhi, **63**, 269–288 (2020).
2. N. Romming et al., Science, **341**, 636–639 (2013).
3. J. Baumard et al., Phys. Rev. B, **99**, 014511 (2019).
4. A.O. Leonov et al., New J. Phys., **18**, 065003 (2016).
5. Y.V. Fominov, A.F. Volkov, K.B. Efetov, Phys. Rev. B, **75**, 104509 (2007).
6. K.B. Efetov et al., Springer Tracts in Modern Physics, **227**, 251–290 (2008).
7. A.P. Petrović et al., Phys. Rev. Lett., **126**, 117205 (2021).

## CLASSICAL MONTE CARLO ALGORITHM FOR SIMULATION OF A PSEUDOSPIN MODEL FOR CUPRATES

*V.A. Ulitko\**, *Yu.D. Panov*, *A.S. Moskvina*

Institute of Natural Sciences and Mathematics, Ural Federal University, Ekaterinburg, Russia

\*E-mail: [vasiliy.ulitko@urfu.ru](mailto:vasiliy.ulitko@urfu.ru)

To account for the exotic electronic properties of cuprates in the normal state and to reveal the nature of unconventional superconductivity [1] various theoretical models have been developed. The presence of heterogeneity due to non-isovalent substitution, as well as to the internal electronic tendency to heterogeneity [2] makes the development of pseudospin approaches to the description of cuprates and the use of the real-space numerical simulations especially attractive.

We develop a pseudospin model of cuprates where the  $\text{CuO}_2$  planes are considered as lattices of  $\text{CuO}_4$  clusters, which are the main element of the crystal and electronic structure of cuprates. The on-site Hilbert space [3, 4] is formed by four states. Three effective valence states of the cluster,  $[\text{CuO}_4]^{7-}$ ,  $[\text{CuO}_4]^{6-}$ , and  $[\text{CuO}_4]^{5-}$ , have different spin states: formally one-hole  $[\text{CuO}_4]^{6-}$  center is the  $s = 1/2$  doublet, while the  $[\text{CuO}_4]^{7-}$  and  $[\text{CuO}_4]^{5-}$  centers are the spin singlets. As a result, the basis  $|SM; s\mu\rangle$  on a given site is the quartet of states  $\{|11;00\rangle, |10;1/2\ 1/2\rangle, |10;1/2\ -1/2\rangle, |1\ -1;00\rangle\}$ . Earlier, we investigated a simplified static version of the spin-pseudospin model, for which phase diagrams of the ground state and at a finite temperature were constructed, both analytically, in the mean field approximation [5], and as a result of Monte Carlo simulations [6].

In the present work, we use the following [7] effective spin-pseudospin Hamiltonian (1) for the model cuprate which takes into account both local and nonlocal charge correlations (2), Heisenberg spin-exchange interaction (3), as well as single and two-particle transport (4), (5):

$$\hat{\mathcal{H}} = \hat{\mathcal{H}}_{\text{pot}} + \hat{\mathcal{H}}_{\text{ex}} + \hat{\mathcal{H}}_{\text{kin}}^{(1)} + \hat{\mathcal{H}}_{\text{kin}}^{(2)}, \quad (1)$$

$$\hat{\mathcal{H}}_{\text{pot}} = \sum_i (\Delta \hat{S}_{iz}^2 - \mu \hat{S}_{iz}) + \frac{1}{2} V \sum_{i \neq j} \hat{S}_{iz} \hat{S}_{jz}, \quad (2)$$

$$\hat{\mathcal{H}}_{\text{ex}} = Js^2 \sum_{i < j} \hat{\mathbf{s}}_i \cdot \hat{\mathbf{s}}_j, \quad (3)$$

$$\hat{\mathcal{H}}_{\text{kin}}^{(1)} = - \sum_{i < j} \sum_v [t_p \hat{P}_i^v \hat{P}_{j-}^v + t_n \hat{N}_{i+}^v \hat{N}_{j-}^v + \frac{i}{2} t_{pn} (\hat{P}_{i+}^v \hat{N}_{i-}^v + \hat{P}_{i-}^v \hat{N}_{j+}^v) + \text{h.c.}], \quad (4)$$

$$\hat{\mathcal{H}}_{\text{kin}}^{(2)} = -t_b \sum_{i < j} (\hat{S}_{i+}^2 \hat{S}_{j-}^2 + \hat{S}_{i-}^2 \hat{S}_{j+}^2). \quad (5)$$

Here, the pseudospin  $S = 1$  operators  $S_{iz}$ ,  $S_{iz\pm}$  act on the charge triplet  $|SM\rangle$ , operators  $\hat{\mathbf{s}} = \hat{P}_0 \hat{\mathbf{s}}/s$  take into account the on-site spin density  $\hat{P}_0 = 1 - \hat{S}_z^2$  and the spin  $s = 1/2$  operators  $\hat{\mathbf{s}}$  act on the spin states  $|s\mu\rangle$ . Operators  $\hat{P}_{\pm}^v$  and  $\hat{N}_{\pm}^v$  change not only the local charge (pseudospin), but also the spin states, e.g.,  $\hat{P}_+^v |10; 1/2\ -v\rangle = |11; 00\rangle$ ,  $\hat{N}_-^v |10; (1/2)v\rangle = |1\ -1; 00\rangle$  and in fact,  $\hat{P}_{\pm}^v$  and  $\hat{N}_{\pm}^v$  are the operators of the creation/destruction of an electron/hole in the multi-electron state of the ‘‘parent’’  $[\text{CuO}_4]^{6-}$  center.

We implement the classical Monte Carlo algorithm in a framework of the real space pseudospin formalism for the spin-charge quartets. As a key feature, we formulate a state selection rule in the classical Monte Carlo algorithm for a given quasi-classical parameterization of the wave function in order to ensure a uniform distribution of states in the phase space taking into account the conservation of the total  $z$ -component of the pseudospin.

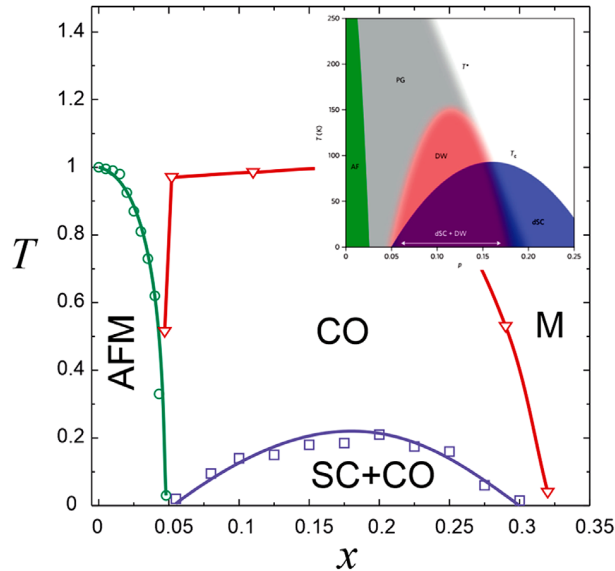


Figure 1. The  $T$ - $x$  ( $x$  – the charge doping) phase diagram for the model cuprate calculated with the classical Monte Carlo algorithm. Parameters of the model (1–5) have the following values:  $\Delta = 0.8$ ,  $V = 0.625$ ,  $J = 1$ ,  $t_p = 0.35$ ,  $t_n = 0$ ,  $t_{pn} = -0.24$ , (all in units of the  $t_b$ ). The insert shows a schematic phase diagram of hole-doped cuprates [8].

To identify the phase states of a model cuprate shown in Fig. 1, we calculated the structure factors of different type for the antiferromagnetic ordering (AFM), charge ordering (CO), superconducting (SC) ordering and the “metal” phase (M). The critical temperatures for these phases were determined from the jump in the structure factor from zero to a certain finite value.

The main problems in the implementation of our modeling, such as inhomogeneous phase states and the associated difficulties in identifying them, are predetermined by the enhanced role of fluctuations in low-dimensional systems. But at the same time, the obtained phase diagrams show promising possibilities to describe the coexistence and competition of various phase orders in cuprates.

*This work was supported by the Ministry of Education and Science of the Russian Federation, project FEUZ-2020-0054.*

1. I. Božović, X. He, J. Wu and A.T. Bollinger, *Nature*, **536**, 309–311 (2016).
2. A.S. Moskvina and Y.D. Panov, *JSNM*, **32**, 61–84 (2019).
3. A.S. Moskvina, *Phys. Rev. B*, **84**, 075116 (2011).
4. A.S. Moskvina, *J. Phys.: Condensed Matter*, **25**, 085601 (2013).
5. Y.D. Panov, V.A. Ulitko, K.S. Budrin, A.A. Chikov, A.S. Moskvina, *JMMM*, **477**, 162–166 (2019).
6. D.N. Yasinskaya, V.A. Ulitko, Y.D. Panov, *Phys. Solid State*, **62**, 1713–1718 (2020).
7. A.S. Moskvina and Y.D. Panov, *JMMM*, **550**, 169004 (2022).
8. M.H. Hamidian, S.D. Edkins, C.K. Kim, J.C. Davis, A.P. Mackenzie, H. Eisaki, S. Uchida, M.J. Lawler, E.-A. Kim, S. Sachdev, K. Fujita, *Nat. Phys.*, **12**, 150–156 (2016).

## SUPERCURRENT-INDUCED LONG-RANGE TRIPLE CORRELATIONS AND CONTROLLABLE JOSEPHSON EFFECT IN SUPERCONDUCTOR/FERROMAGNET HYBRIDS WITH EXTRINSIC SOC

*A.A. Mazanik*<sup>1,2\*</sup>, *I.V. Bobkova*<sup>3,1,4</sup>

<sup>1</sup>Moscow Institute of Physics and Technology, Dolgoprudny, Russia

<sup>2</sup>BLTP, Joint Institute for Nuclear Research, Dubna, Moscow Region, Russia

<sup>3</sup>Institute of Solid State Physics, Chernogolovka, Moscow Region, Russia

<sup>4</sup>National Research University Higher School of Economics, Moscow, Russia

\*E-mail: [mazanik@theor.jinr.ru](mailto:mazanik@theor.jinr.ru)

We predict that long-range triplet correlations (LRTC) in superconductor/ferromagnet (S/F) hybrids with extrinsic impurity spin-orbit coupling can be generated and manipulated by supercurrent flowing in the superconducting leads along the S/F interfaces. The LRTC appear via two basic mechanisms. The essence of the first one is the generation of triplets by the superconducting spin Hall effect. These pairs are long range in the ferromagnet under the appropriate mutual orientation of the condensate momentum and the ferromagnet magnetization. The second mechanism is based on the singlet-triplet conversion at the S/F interface followed by the rotation of the spin of the obtained short-range opposite-spin pairs via the spin current swapping mechanism. The structure of the supercurrent-induced LRTC is studied both for S/F bilayers and superconductor/ferromagnet/superconductor (S/F/S) Josephson junctions. We demonstrate that in S/F/S junctions, where the Josephson coupling is realized via the supercurrent-induced LRTC, the ground state phase can be switched between 0 and  $\pi$  in a controllable manner. The switching is performed by reversing the supercurrent in one of the superconducting leads, thus realizing a physical principle of the 0- $\pi$  shifter.

The presentation is based on Ref. [1].

*We are thankful to Mikhail Silaev for valuable discussions. The work of I.V.B. has been supported by Russian Foundation for Basic Research Grant No. 19-02-00466. I.V.B. and A.A.M. also acknowledge financial support by the Foundation for the Advancement of Theoretical Physics and Mathematics “BASIS”.*

1. A.A. Mazanik, I.V. Bobkova, Phys. Rev. B, **105**, 144502 (2022).

Section J.  
**Soft and hard magnetic materials**

---

## FIELD-INDUCED MAGNETIC PHASE TRANSITIONS IN HIGHLY ANISOTROPIC $RFe_5Al_7$ FERRIMAGNETS

*N.V. Mushnikov<sup>1\*</sup>, E.V. Rosenfeld<sup>1</sup>, D.I. Gorbunov<sup>2</sup>, A.V. Andreev<sup>3</sup>*

<sup>1</sup>Institute of Metal Physics UB RAS, Ekaterinburg, Russia

<sup>2</sup>High Magnetic Field Laboratory, Dresden, Germany

<sup>3</sup>Institute of Physics, Academy of Sciences, Prague, Czech Republic

\*E-mail: [mushnikov@imp.uran.ru](mailto:mushnikov@imp.uran.ru)

Intermetallic compounds of rare earth and 3d-transition metals can combine high magnetic ordering temperatures typical of 3d metals and strong magnetic anisotropy of rare earth ions. The study of the interaction between delocalized 3d electrons and localized 4f electrons in 4f-3d intermetallics is of both fundamental and practical interest. Experimentally, this interaction can be studied in ferrimagnets with oppositely directed magnetic sublattices.

We have studied magnetic properties of  $RFe_5Al_7$  ( $R = Tb, Dy, Ho, Tm$ ) ferrimagnetic single crystals. The compounds have a tetragonal crystal structure. The magnetization vectors of both magnetic sublattices are oriented in the basal plane. At the temperature dependences of the magnetization of the compounds, compensation points are observed (Fig. 1), in which total magnetization vanishes.

When a magnetic field is applied along the easy magnetization direction in the basal plane at the temperature near the magnetic compensation temperature in compounds with  $R = Dy, Ho,$  and  $Tb$ , we found magnetization jumps in a critical field, the value of which tends to zero at the compensation point [1, 2]. The jumps indicate a first-order phase transition induced by the magnetic field.

In order to explain the observed magnetic phase transitions, a phenomenological theory of magnetization of an anisotropic ferrimagnet with two weakly interacting magnetic sublattices, one of which has large magnetic anisotropy, is developed. It is assumed that, under the application of a magnetic field, a spin-reorientation transition occurs in the direction of the easy magnetization axis of the tetragonal crystal, which is perpendicular to the applied magnetic field direction. Analytical

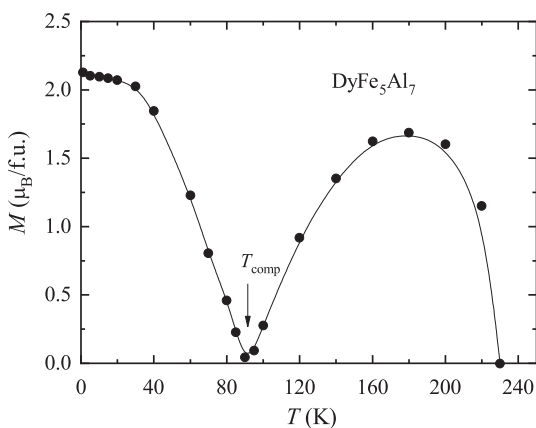


Figure 1. Temperature dependence of the spontaneous magnetic moment of  $DyFe_5Al_7$ . The arrow indicates the compensation point  $T_{comp}$ .

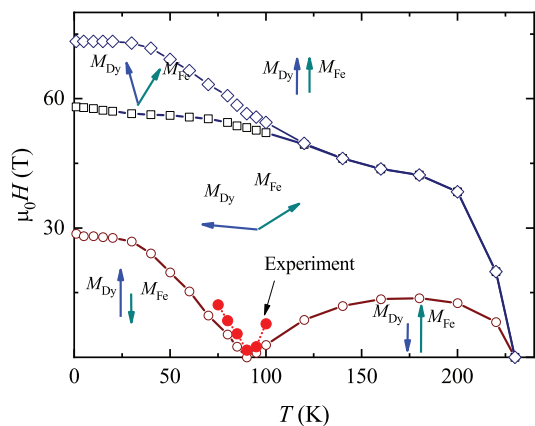


Figure 2. Calculated magnetic phase diagram in the  $T$ - $H$  plane for  $DyFe_5Al_7$  in the field applied along the  $[100]$  easy magnetization direction. Closed symbols are experimental data.

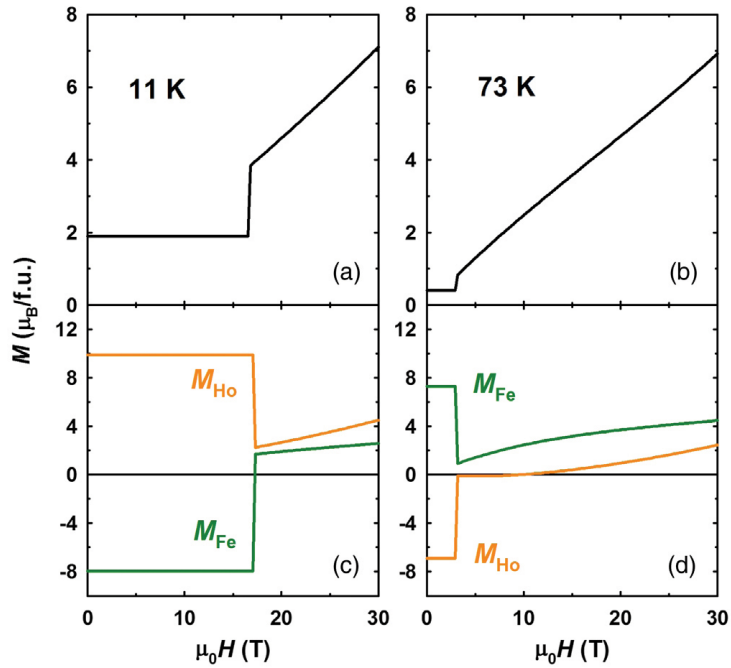


Figure 3. Calculated field dependences of magnetization of  $\text{HoFe}_5\text{Al}_7$ , and magnetic moments of Fe and Ho sublattices at temperatures below (11 K) and above (73 K) the compensation temperature.

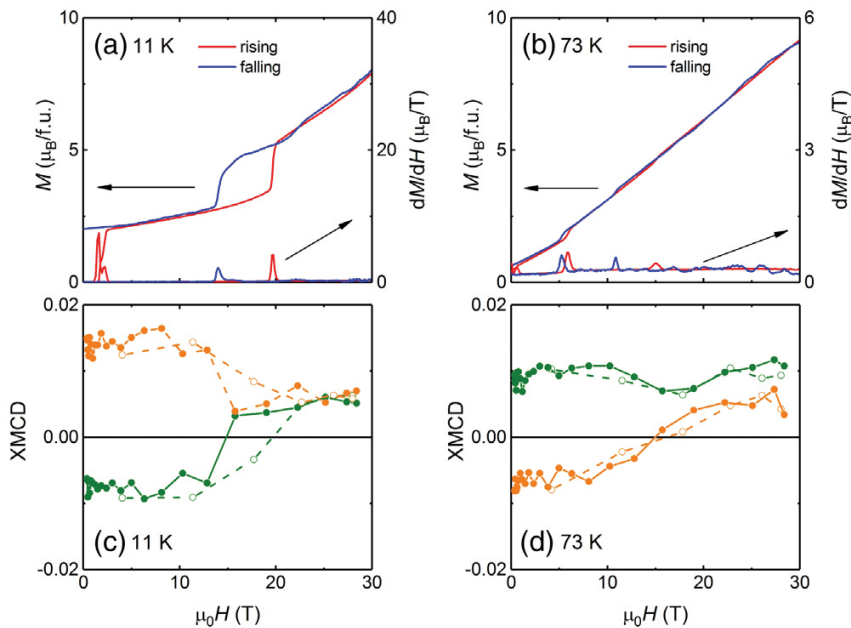


Figure 4. Measured field dependences of magnetization and XMCD signal from Fe sublattice (green color) and Ho sublattice (yellow color) of  $\text{HoFe}_5\text{Al}_7$  single crystal.

expressions are obtained for the magnetization curve and the critical field of the spin-reorientation transition. It is predicted that in addition to experimentally observed magnetic field-induced phase transition, in strong magnetic fields one more transition should be observed, after which the orientation of the magnetic moments will be close to collinear ferromagnetic. A magnetic phase diagram is constructed (Fig. 2) and the magnetic structures that are realized in different magnetic fields at different temperatures are determined.

Experimental verification of the magnetization model of the  $RFe_5Al_7$  ferrimagnets was carried out with the study of X-ray magnetic circular dichroism at the Desy (Germany) and SPring-8 (Japan) synchrotrons in high pulsed magnetic fields [3–5]. The method makes it possible to track the rotation of the magnetization separately for the R and Fe sublattices. In Figs. 3 and 4 we compare the calculated and measured field dependences of the  $H_0$  and Fe sublattices of  $HoFe_5Al_7$ . The experiments confirmed the presence of a magnetic field-induced first order phase transition in the direction perpendicular to the applied field both above and below the compensation point. It is found that the model of nonrigid magnetic sublattices gives a more adequate description of the field dependence of the magnetization above the compensation temperature.

*The research was carried out within the state assignment of Ministry of Science and Higher Education of the Russian Federation (theme “Magnet”).*

1. N.V. Mushnikov, E.V. Rosenfeld, D.I. Gorbunov, A.V. Andreev, Phys. Met. Metallogr., **115**, 257–267 (2014).
2. D.I. Gorbunov, S. Yasin, A.V. Andreev, Y. Skourski, N.V. Mushnikov, E.V. Rosenfeld, S. Zherlitsyn, J. Wosnitza, J. Magn. Magn. Mater., **383**, 208–214 (2015).
3. D.I. Gorbunov, C. Strohm, M.S. Henriques, P. van der Linden, B. Pedersen, N.V. Mushnikov, E.V. Rosenfeld, V. Petriček, O. Mathon, J. Wosnitza, A.V. Andreev, Phys. Rev. Lett., **122**, 127205 (6 p.) (2019).
4. Sh. Yamamoto, D.I. Gorbunov, H. Akai, H. Yasumura, Y. Kotani, T. Nakamura, T. Kato, N.V. Mushnikov, A.V. Andreev, H. Nojiri, J. Wosnitza, Phys. Rev. B, **101**, 174430 (6 p.) (2020).
5. Sh. Yamamoto, D.I. Gorbunov, I.F. Diaz-Ortega, A. Miyata, T. Kihara, Y. Kotani, T. Nakamura, N.V. Mushnikov, A.V. Andreev, H. Nojiri, J. Wosnitza, Phys. Rev. B, **104**, 064405 (7 p.) (2021).



## SELECTIVE LASER SINTERING OF HIGH-COERCIVITY PERMANENT MAGNETS

*A.S. Volegov\**, *S.V. Andreev*, *N.V. Selezneva*, *N.M. Nosova*, *I.A. Ryzhikhin*,  
*N.V. Kudrevatykh*, *V.E. Maltseva*

Institute of Natural Sciences and Mathematics, UrFU, Ekaterinburg, Russia

\*E-mail: [Alexey.Volegov@urfu.ru](mailto:Alexey.Volegov@urfu.ru)

The development of energetics and robotics, miniaturization of high-tech devices as well as electric vehicles require an increase in the production of permanent magnets and at the same time improvement or tuning of their magnetic properties. Due to eddy currents, the temperature of permanent magnets used in generators and electric motors, exceeds room temperature, and often reaches up to 400–450 K. Since, Curie temperature of the  $\text{Nd}_2\text{Fe}_{14}\text{B}$  compound is relatively low and coercivity strong dependent of temperature, it is necessary to increase the coercivity at all temperatures. The NdFeB magnets are mainly produced by sintering that enables simple shapes. Application of additive manufacturing technologies allowed to create magnets of more complex shapes and, thus, to abandon application of soft magnetic “ballast” in magnetic cores of magnetic system.

The aim of the work is to prove the concept of additive manufacturing process of permanent magnets with high coercivity without heavy rare-earth metals. For this purpose, the low-melting eutectic alloy powder based on 3d-4f metals was mixed with the NdFeB-based alloy. The eutectic alloy performs two functions, namely, (i) a binder function to create a permanent magnet body from the powder and (ii) an effective separation function of nanoscale grains of the  $\text{Nd}_2\text{Fe}_{14}\text{B}$  phase that suppresses the exchange interaction between the grains. For this purpose, two powder mixtures consisting of the MQP-B alloy powder and 20 wt.% of the  $(\text{Pr,Nd})_{75}(\text{Cu}_{0.25}\text{Co}_{0.75})_{25}$  eutectic alloy were prepared.

The implementation of the proposed approach allowed to obtain permanent magnets with coercivity up to 19.5 kOe in single-layer samples and 12 kOe in bulk samples. Detailed results of the phase composition, microstructure, and magnetic properties of the obtained samples will be given in the talk.

*The research was financially supported by Russian Science Foundation (Grant Number 21-72-10104).*

## INVESTIGATION OF NANOPARTICLES OF MATERIALS WITH HIGH MAGNETIC ANISOTROPY IN STRONG PULSED MAGNETIC FIELDS

*D.A. Balaev*

Kirensky Institute of Physics, Federal Research Center “Krasnoyarsk Scientific Center”,  
Siberian Branch, Russian Academy of Sciences, Krasnoyarsk, Russia

E-mail: [dabalaev@iph.krasn.ru](mailto:dabalaev@iph.krasn.ru)

Study of the magnetic properties of magnetic nanoparticle systems is an essential part of their characterization and make it possible to determine fundamental parameters that are important both from the point of view of physical materials science and for specific applications. These parameters include the magnitudes of the particle magnetic moment  $\mu_p$  and the effective (particle size-dependent) magnetic anisotropy constant  $K_{\text{eff}}$  etc. Also, mentioned parameters reflect the important role of surface and size effects in the formation of the magnetic state of nanoscale particles [1, 2]. However, not always the data obtained from the analysis of magnetic properties can give objective information. This is largely due to the standardization of the installations used and the difficulty of performing experiments in strong magnetic fields; for DC magnetization, these are fields exceeding the range of 60–150 kOe, and for AC magnetization (hysteresis loop in an alternating field  $H = H_0 \cdot \sin(\omega t)$ ) these are  $H_0$  values of the order of several kOe. For the first case (i), the maximum field value of 60–150 kOe may not be sufficient to correctly determine the magnitude  $\mu_p$  (even taking into account the particle distribution by values  $\mu_p$ ) when processing the magnetization curve  $M(H)$  by the Langevin function. In the second case (ii), if the material particles have high magnetic anisotropy, the AC loop of magnetic hysteresis will only be a minor loop if the value of  $H_0$  is less than the anisotropy field (or  $H_0$  does not significantly exceeds the coercive field  $H_C$ ).

The report will review the results of the study of the magnetic properties of nanoparticles with high magnetic anisotropy obtained in strong pulsed magnetic fields using the installation [3] (working at the Kirensky Institute of Physics, laboratory of High Magnetic Fields). This setup allows measurements of magnetization in two modes: (i) – dependence of  $M(H)$  with a maximum field of 250–350 kOe; (ii) – measurement of the hysteresis loop with a maximum field up to  $\sim \pm 130$ –150 kOe (3/4 of the hysteresis loop is measured here). (The pulse length  $\tau_{\text{pulse}}$  is within the range  $\sim 4$ –32 ms).

Using the described approach, the following results were obtained. For systems of antiferromagnetic (AFM) NiO nanoparticles (with average sizes of 4.5, 8 and 23 nm) [4–7], the contributions of several magnetic subsystems formed in AFM nanoparticles are correctly determined from magnetization curves in fields up to 250 kOe. These are the uncompensated magnetic moment of the particles  $\mu_p$  due to decompensation of ferromagnetic planes within the particle [8], the subsystem of surface spins (the spins of Ni atoms located on the edges of the particles – “paramagnetic” behavior), and, for extremely small particles (4.5 nm), the contribution caused by superantiferromagnetic susceptibility [7, 9–11].

The study of the dynamic magnetic hysteresis loops (the behavior of the coercive force  $H_C$  when the rate of change of the external field  $dH/dt$  varies up to 60 MOe/s) of nanoscale ferrimagnetic nanoparticles  $\epsilon\text{-Fe}_2\text{O}_3$  (average size 6–8 nm) [12] and  $\text{CoFe}_2\text{O}_4$  (average size 6 nm) [13] allowed, when analyzed within the framework of theoretical concepts [13–15], to identify the contribution of surface magnetic anisotropy and obtain it estimates. Also, the difference in the behavior of the dependence of the coercive force on the rate of change of the magnetic field  $H_C(dH/dt)$  for ferrimagnetic and AFM nanoparticles [16–19] is discussed.

1. R.H. Kodama, A.E. Berkowitz, *Phys. Rev. B*, **59**, 6321 (1999).
2. S. Mørup, D.E. Madsen, C. Fradsen, C.R.H. Bahl, and M.F. Hansen, *J. Phys.: Condens. Matter*, **19**, 213202 (2007).
3. A.A. Bykov, S.I. Popkov, A.M. Parshin, A.A. Krasikov, *Journal of Surface Investigation. X-ray, Synchrotron and Neutron Techniques*, **9**, 111 (2015).
4. D.A. Balaev, A.A. Dubrovskiy, A.A. Krasikov, S.I. Popkov, A.D. Balaev, K.A. Shaikhutdinov, V.L. Kirillov, and O. N. Mart'yanov, *Phys. Solid State*, **59**, (no. 8), 1547 (2017).
5. S.I. Popkov, A.A. Krasikov, A.A. Dubrovskiy, M.N. Volochaev, V.L. Kirillov, O.N. Martyanov, D.A. Balaev, *J. Appl. Phys.*, **126**, 103904 (2019).
6. D.A. Balaev, A.A. Krasikov, S.I. Popkov, A.A. Dubrovskiy, S.V. Semenov, D.A. Velikanov, V.L. Kirillov, O.N. Martyanov, *J. Magn. Magn. Mater.*, **515**, 167307 (2020).
7. D.A. Balaev, A.A. Krasikov, S.I. Popkov, S.V. Semenov, M.N. Volochaev, D.A. Velikanov, V.L. Kirillov, O.N. Martyanov, Uncompensated magnetic moment and surface and size effects in few-nanometer antiferromagnetic NiO particles, *J. Magn. Magn. Mater.*, **539**, (2021) 168343.
8. L. Néel, *C.R. Acad. Sci. Paris*, **252**, 4075 (1961).
9. L. Néel, *C.R. Acad. Sci. Paris*, **253**, 1286 (1961).
10. C. Gilles, P. Bonville, H. Rakoto, J.M. Broto, K.K.W. Wong, S. Mann, *J. Magn. Magn. Mater.*, **241**, 430 (2002).
11. N.J.O. Silva, A. Millan, F. Palacio, E. Kampert, U. Zeitler, V. S. Amaral, *Phys. Rev. B*, **79**, 104405 (2009).
12. D.A. Balaev, I.S. Poperechny, A.A. Krasikov, K.A. Shaikhutdinov, A.A. Dubrovskiy, S.I. Popkov, A.D. Balaev, S.S. Yakushkin, G.A. Bukhtiyarova, O.N. Martyanov, and Yu.L. Raikher, *J. Appl. Phys.*, **117**, 063908 (2015).
13. D.A. Balaev, I.S. Poperechny, A.A. Krasikov, S.V. Semenov, S.I. Popkov, Y.V. Knyazev, V.L. Kirillov, S.S. Yakushkin, O.N. Martyanov, and Yu.L. Raikher, *J. Phys. D: Appl. Phys.*, **54**, 275003 (2021).
14. I. S. Poperechny, Yu. L. Raikher, and V. I. Stepanov, *Phys. Rev. B*, **82**, 174423 (2010).
15. I. S. Poperechny and Yu. L. Raikher, *Physica B*, **435**, 58–61 (2014).
16. D.A. Balaev, A.A. Krasikov, A.A. Dubrovskiy, A.D. Balaev, S.I. Popkov, V.L. Kirillov, O.N. Martyanov, *J. Supercond. Nov. Magn.*, **32**, 405 (2019).
17. S.I. Popkov, A.A. Krasikov, S.V. Semenov, A.A. Dubrovskii, S.S. Yakushkin, V.L. Kirillov, O.N. Mart'yanov, D.A. Balaev, *Phys. Solid State*, **62**, (no. 9), 1518–1524 (2020).
18. S.I. Popkov, A.A. Krasikov, D.A. Velikanov, V.L. Kirillov, O.N. Martyanov, D.A. Balaev, *J. Magn. Magn. Mater.*, **483**, 21 (2019).
19. I. S. Poperechny, *Phil. Trans. R. Soc. A.*, **380**, (2021) doi.org/10.1098/rsta.2020.0312.

## MAGNETIC STRUCTURES IN $(\text{La}_{1-x}\text{Tb}_x)\text{Mn}_2\text{Si}_2$

*P.A. Borisova*<sup>1</sup>, *V.P. Glazkov*<sup>1</sup>, *Haneen M Alsafi*<sup>1</sup>, *M.A. Semkin*<sup>2,3</sup>, *E.G. Gerasimov*<sup>2,3</sup>,  
*P.B. Terentev*<sup>2,3</sup>, *N.V. Mushnikov*<sup>2,3</sup>, *A.N. Pirogov*<sup>2,3\*</sup>

<sup>1</sup>National Research Center “Kurchatov Institute”, Moscow, Russia

<sup>2</sup>Institute of Natural Sciences and Mathematics, Ural Federal University, Ekaterinburg, Russia

<sup>3</sup>M.N. Miheev Institute of Metal Physics UB RAS, Ekaterinburg, Russia

\*E-mail: [pirogov@imp.uran.ru](mailto:pirogov@imp.uran.ru)

Intermetallic compounds of the  $\text{RMn}_2\text{X}_2$  (where R is rare-earth element, X is Si or Ge) crystallize in a body-centered tetragonal structure of the  $\text{ThCr}_2\text{Si}_2$  type belonging to the space group  $I4/mmm$  [1]. The R, Mn and X atoms occupy the  $2a$ ,  $4d$  and  $4e$  positions respectively and they form layers are stacked along the crystallographic  $c$ -axis in the strict sequence  $-M-X-R-X-M-$ . The Mn-Mn interlayer distance along the  $c$ -axis is about two times as longer than that intralayer one. So, it is expected that extremely interesting magnetic behavior will originate from two-dimensional arrangement of Mn atoms. Indeed, various magnetic phase transitions are observed in  $\text{RMn}_2\text{X}_2$  compounds.

In this work, we studied the magnetic structures and magnetic phase transitions in the  $(\text{La}_{1-x}\text{Tb}_x)\text{Mn}_2\text{Si}_2$  compounds by neutron powder diffraction.

The  $(\text{La}_{1-x}\text{Tb}_x)\text{Mn}_2\text{Si}_2$  alloys with the concentration  $0 \leq x \leq 1.0$  were prepared by induction melting of the constituents in an argon atmosphere followed by annealing at 900 °C for one week. Neutron powder diffraction measurements have been carried out with the diffractometers DISK of the reactor IR-8, Kurchatov Institute and D-3 of the reactor IVV-2M, Zarechny.

At 4.2 K for  $\text{LaMn}_2\text{Si}_2$  a canted ferromagnetic structure within the Mn layers takes a place. Ferromagnetic interlayer arrangement of axial components of the Mn moments is directed along the  $c$ -axis. For the concentrations  $x = 0.27$  and  $0.4$  the interlayer ordering of the manganese moments is antiferromagnetic. The magnetic structure of the compound with  $x = 0.2$  and  $0.4$  is interpreted as a mixture of phases with ferromagnetic and antiferromagnetic interlayer Mn-Mn. coupling. For  $\text{TbMn}_2\text{Si}_2$ , the interlayer Mn-Mn ordering is found to be ferromagnetic again for the Mn sublattice. Within the manganese layer, a canted magnetic structure with antiferromagnetic ordering of the basal-plane components of Mn moments is realized for all the studied compounds.

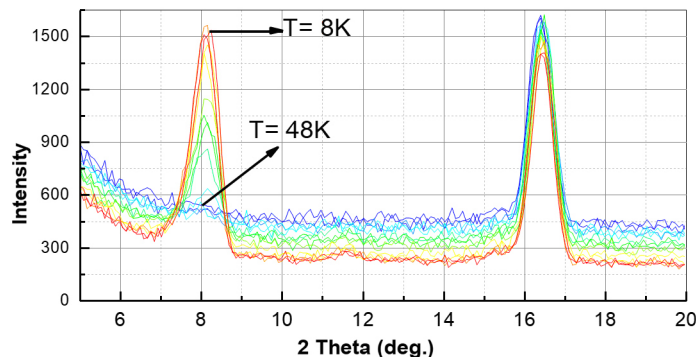


Figure 1. Neutron powder diffraction patterns of  $\text{La}_{0.2}\text{Tb}_{0.8}\text{Mn}_2\text{Si}_2$  over temperature interval (8–48) K.

At 8 K the neutron diffraction patterns for concentrations  $x = 0.6, 0.8$  and  $1.0$  show an intensive (001) reflection. The origin of this reflection is due to a ferromagnetic interplane coupling of the axial components of the ferromagnetically aligned Mn moments in the layers and antiferromagnetic interplane coupling of the planar components. When temperature increases the (001) reflection disappears. This temperature is maximal in the sample with  $x = 1.0$  and minimal for  $x = 0.6$ . As the example, Fig. 1 shows that the (001) reflection disappears at 48 K in  $\text{La}_{0.2}\text{Tb}_{0.8}\text{Mn}_2\text{Si}_2$ .

*The reported study was funded by the state assignment of Minobrnauki of Russia (theme “Flux”) and was supported in part by MES of RF (contract No. FEUZ-2020-0051).*

1. G. Venturini, R. Welter, E. Ressouche, and B. Malaman, *J. Magn. Magn. Mater.*, **150**, 197–212 (1995).

## INVESTIGATION OF THE ULTRA-HIGH FIELD-INDUCED PHASE TRANSITION IN THE $(\text{Nd,Dy})_2\text{Fe}_{14}\text{B}$

*N.V. Kostyuchenko*<sup>1\*</sup>, *I.S. Tereshina*<sup>2</sup>, *O.M. Surdin*<sup>3,4</sup>, *D.A. Maslov*<sup>3,4</sup>, *I.S. Strelkov*<sup>3</sup>,  
*R.V. Kozabaranov*<sup>3,4</sup>, *A.S. Korshunov*<sup>3</sup>, *Yu.B. Kudasov*<sup>3,4</sup>, *V.V. Platonov*<sup>3,4</sup>, *I.V. Makarov*<sup>3</sup>,  
*A.I. Bykov*<sup>3</sup>, *A.V. Filippov*<sup>3</sup>, *S.V. Galanova*<sup>3</sup>, *A.K. Zvezdin*<sup>1</sup>

<sup>1</sup>Moscow Institute of Physics and Technology (National Research University), Dolgoprudny, Moscow Region, Russia

<sup>2</sup>Faculty of Physics, Lomonosov Moscow State University, Moscow, Russia

<sup>3</sup>Russian Federal Nuclear Center – All-Russian Research Institute of Experimental Physics, Sarov, Russia

<sup>4</sup>Sarov Institute of Physics and Technology NRNU MEPhI, Sarov, Russia

\*E-mail: [nvkost@gmail.com](mailto:nvkost@gmail.com)

The intrinsic properties of the substituted  $(\text{R,R}')_2\text{Fe}_{14}\text{B}$  (R or R' – heavy rare-earth ion) compounds in the vicinity of the transition from ferri- to ferromagnetic state are of prime importance for investigation of such systems. We perform the study of substituted compound  $(\text{Nd}_{0.5}\text{Dy}_{0.5})_2\text{Fe}_{14}\text{B}$  using a combination of several methods. Firstly, we carried out the experimental investigation of magnetization, including unique measurements in ultra-high magnetic fields up to 165 T [1, 2]. Then we performed the analytical study of the magnetization curves. The suggested models successfully explained all existing critical features of the magnetization behavior in the high-field region, including transition from ferri- to ferromagnetic state. The experimental and theoretical results were compared with those previously obtained (up to 60 T), in which these phase transition has not yet been observed [3].

To create magnetic fields with maximum induction values of  $\sim 600$  T, we used a “small” magnetocumulative generator of the MK-1 type [1]. Powder samples were cooled to 5 K in a helium flow cryostat. Ultra-high field magnetization curves were measured up to 165 T (see Fig. 1). We report on the critical fields' evaluations, which values allows us to clarify the magnetization behavior in the

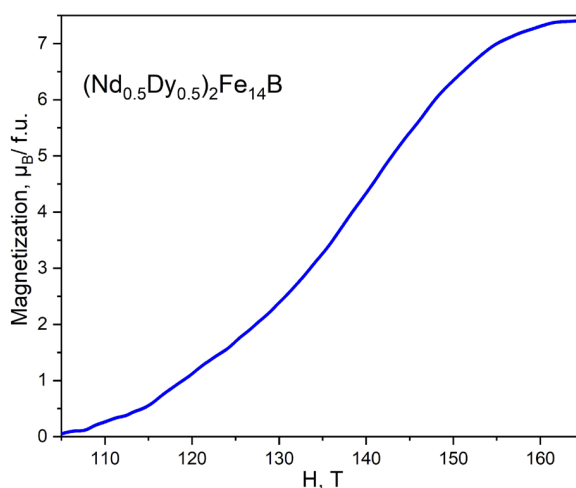


Figure 1. Magnetization curves of the  $(\text{Nd}_{0.5}\text{Dy}_{0.5})_2\text{Fe}_{14}\text{B}$  compound measured at  $T = 4.2$  K in pulsed ultra-high magnetic fields.

region of the magnetic transitions. The forced-ferromagnetic state becomes at 160 T. The obtained information is essential both for the progress in fundamental physics of the magnetic phenomena and for modern practical applications.

*This work was supported by the Ministry of Science and Higher Education of the Russian Federation (No. FSMG-2021-0005). We express our gratitude to the professor A.V. Andreev for providing the samples.*

1. M.I. Dolotenko, Magnetocumulative generators MK-1 of superstrong magnetic fields, Sarov, RFNC-VNIIEF, 2015.
2. S. Takeyama et al., J. Phys. E, **21**, 1025 (1998).
3. N.V. Kostyuchenko et al., Intermetallics, **124**, 106840 (2020).

## SUPERPARAMAGNETISM AND HYSTERESIS CHARACTERISTICS OF COMPOSITES $\text{Fe}_3\text{O}_4\text{-Fe}_{3-x}\text{Ti}_x\text{O}_4$ : MICROMAGNETIC MODELING

*P.V. Kharitonskii<sup>1</sup>, A.Yu. Ralin<sup>2</sup>, E.S. Sergienko<sup>3</sup>, N.A. Zolotov<sup>1,4</sup>,  
K.G. Gareev<sup>1\*</sup>, Yu.A. Anikieva<sup>1</sup>*

<sup>1</sup>Saint Petersburg Electrotechnical University “LETI”, Saint Petersburg, Russia

<sup>2</sup>Far Eastern Federal University, Vladivostok, Russia

<sup>3</sup>Saint Petersburg State University, Saint Petersburg, Russia

<sup>4</sup>Institute of Precambrian Geology and Geochronology of RAS, Saint Petersburg, Russia

\*E-mail: [kggareev@etu.ru](mailto:kggareev@etu.ru)

Theoretical works devoted to the study of ensembles of superparamagnetic (SP) particles often use the “non-interacting particles” approximation and the assumption of their chemical homogeneity. The authors [1, 2] studied composites, in which the presence of a significant fraction of SP particles was found. It was shown that the magnetic properties of the studied samples cannot be explained without taking into consideration the chemical inhomogeneity of individual particles and the magnetostatic interaction between them.

Synthesis of composites based on the  $\text{Fe}_m\text{O}_n\text{-TiO}_2$  system was carried out by magnetite precipitation in suspension of  $\text{TiO}_2$  powder [1, 2]. Samples T05L, T10L, and T20L were obtained by dispersing  $\text{TiO}_2$  powder (0.5, 1.0, and 2.0 g, respectively) into solution, followed by hydrothermal treatment (240 °C, 50 MPa) for 4 hours. Sample T05H was treated under 470 °C and 42 MPa. Sample T20R was not subjected to temperature treatment.

Table 1 shows the characteristics of the samples:  $M_s$  is the saturation magnetization and  $M_{rs}$  is the saturation remanence,  $\mu_0H_c$  is the coercive force and  $\mu_0H_{cr}$  is the remanence coercivity. According to magnetic granulometry [3], it can be assumed that the first group of samples is dominated by single- and low-domain particles, whereas in T20R by SP particles.

For the modeled samples, the presence of three groups of particles was assumed: 1) the fraction of chemically inhomogeneous two-phase particles (magnetite–titanomagnetite), 2) the weakly magnetic fraction (hematite), and 3) SP particles of the first two fractions. The first fraction is an ensemble of cubic two-phase particles [4]. Each phase is a homogeneously magnetized crystallographically uniaxial ferrimagnet. The characteristic size of particle  $a$  ranged from 20 to 80 nm, and the thickness of the second phase  $\varepsilon$  ranged from 0.05 to 0.20.

Table 1. Hysteresis characteristics of the samples [1, 2].

Sample	$M_s$ , A · m <sup>2</sup> /kg	$M_{rs}$ , A · m <sup>2</sup> /kg	$\mu_0H_c$ , mT	$\mu_0H_{cr}$ , mT	$M_{rs}/M_s$	$H_{cr}/H_c$
T05L	26.37	2.95	5.62	14.92	0.11	2.66
T10L	19.53	2.06	4.77	12.61	0.11	2.65
T20L	14.11	1.92	5.97	13.77	0.14	2.31
T05H	23.79	4.15	8.78	18.32	0.18	2.09
T20R	28.95	0.35	0.51	1.90	0.01	3.73



To find the magnetic states and critical fields of remagnetization, the free magnetic energy was minimized. The magnetostatic energy was calculated considering the constancy of surface magnetic charge densities of mutually parallel and mutually perpendicular rectangles [4, 5]. In this case, the two-phase particle can be in four states: the magnetic moments of the phases are parallel to each other along ( $n_1$ ) or against ( $n_2$ ) the external magnetic field  $H$  or antiparallel to each other ( $n_3$  and  $n_4$ ). In the case of non-interacting particles in the absence of an external field, it is possible to determine their relative number in the  $m$ -th state:

$$n_m|_{H=0} = A \exp(-E_m/(kT)). \quad (1)$$

Then the magnetization of the ensemble of two-phase ferrimagnetic particles is [4]:

$$M(a, \varepsilon, H) = C_1 [I_{sM}(1 - \varepsilon)(n_1 - n_2 + n_3 - n_4) + I_{sT}\varepsilon(n_1 - n_2 - n_3 + n_4)]. \quad (2)$$

Here  $C_1 = N \cdot v/V$  is the volume concentration of the first fraction ( $N$  and  $v$  are the number and the average volume of two-phase particles,  $V$  is the sample volume),  $I_{sM}$  and  $I_{sT}$  are the effective spontaneous magnetizations of the first and second phases, respectively. If we assume that the random fields of magnetostatic interaction  $H_i$  are uniformly distributed in the interval from  $-H_{\max}$  to  $+H_{\max}$ , the calculation of the magnetization in the first approximation is reduced to the case of non-interacting particles with a shift of the critical fields by  $-H_{\max}$  [4].

During modeling, the saturation remanence was provided by the two-phase particles and the weakly magnetic fraction. However, it was possible to agree the theoretical values of the saturation magnetization with the experimental data only in the assumption of the presence of a large number of SP particles in the samples. Then for the first four samples (Table 1)

$$M_s = M_{s1} + M_{s2} + M_{sSP}, \quad M_{rs} = M_{rs1} + M_{rs2}, \quad (3)$$

$M_{s1}$  and  $M_{rs1}$ ,  $M_{s2}$  and  $M_{rs2}$ ,  $M_{sSP}$  are the magnetizations of the corresponding three fractions.

Judging by the hysteresis characteristics (Table 1), the fifth sample (T20R) contains mainly SP particles. Therefore, the average particle size of this sample varied in the range of 20–30 nm. The contribution of all particles to the saturation magnetization was taken into consideration, and only the particles blocked due to the magnetostatic interaction were included in the remanence. The interaction results in that a particle with the volume  $v > v_b(H_i)$  can contribute to the remanence. Here  $v_b(H_i)$  is the critical volume of a particle whose magnetic moment remains stable when the particle is exposed to the field  $H_i$  [6]. For interacting SP particles, the magnetic moment contributing to the remanence is [6]:

$$m = vI_s \tanh[v_b H_i I_s |H + H_i|/kT] = vI_{sSP}, \quad (4)$$

where  $I_{sSP}$  is the effective spontaneous magnetization of two-phase SP particles blocked due to interaction ( $I_{sSP} \ll I_s$  at  $H = 0$ ). Then for the superparamagnetic sample T20R

$$M_s = M_{s1b} + M_{s2b} + M_{snb}, \quad M_{rs} = M_{rs1b} + M_{rs2b}, \quad (5)$$

where  $M_{s1b}$  and  $M_{rs1b}$ ,  $M_{s2b}$  and  $M_{rs2b}$  correspond to the blocked particles and  $M_{snb}$  to the unblocked particles. Having calculated the critical fields of remagnetization  $H_0$  of the strong magnetic fraction using the two-phase particle model and assuming that  $H_0 = H_{cr1}$ , we estimated the coercive force of this group of particles  $H_{c1}$ . Then, using the experimental values (Table 1), we fitted  $H_{cr2}$  and  $H_{c2}$ .

Table 2. Theoretical values of magnetizations,  $A \cdot m^2/kg$ .

Sample	$M_{s1}$	$M_{s2}$	$M_{sSP}$	$M_{rs1}$	$M_{rs2}$
T05L	10.07	0.26	16.04	2.89	0.06
T10L	7.26	0.24	12.03	2.02	0.04
T20L	6.20	0.30	7.61	1.84	0.08
T05H	22.14	0.60	1.05	3.79	0.36
Sample	$M_{s1b}$	$M_{s2b}$	$M_{snb}$	$Mr_{s1b}$	$Mr_{s2b}$
T20R	23.74	0.51	4.70	0.23	0.12

Taking into consideration the shares of the fractions, the average theoretical values of  $H_c$  and  $H_{cr}$  of the samples coincided with the experimental ones. Table 2 shows the calculated magnetization values, which in total are equal to the experimental  $M_s$  and  $M_{rs}$  of the samples (Table 1).

The hysteresis characteristics of the simulated composites are well explained within the model of an ensemble of magnetostatically interacting two-phase particles. The superparamagnetic fraction largely determines the magnetic properties of the samples and its consideration makes it possible to agree their theoretical and experimental characteristics.

1. P. Kharitonskii, S. Kirillova, K. Gareev et al., IEEE Trans. Magn., **56**, 7200209 (2020).
2. P. Kharitonskii, A. Kosterov, A. Gurylev et al., Phys. Solid State, **62**, 1691–1694 (2020).
3. J.L. Kirschvink, D.S. Jones, B.J. MacFadden, Magnetite Biomineralization and Magnetoreception in Organisms. A New Biomagnetism, Plenum Press, New York, (1985).
4. L. Afremov, A. Ralin, P. Kharitonskiy, Izv. Phys. Solid Earth, **31**, 533–537 (1996).
5. P.V. Kharitonskii, A.M. Frolov, Izv. vuzov. Fizika, **3/2**, 197–200 (2010) [in Russian].
6. P. Kharitonskii, K. Gareev, S. Ionin et al., J. Magn., **20**, 221–228 (2015).

## HIGH FREQUENCY MAGNETOIMPEDANCE (MI) IN AMORPHOUS MICROWIRES WITH DIFFERENT ANISOTROPY NEAR THE CURIE TEMPERATURE

*J. Alam<sup>1</sup>, A. Zedan<sup>1</sup>, D. Mosharov<sup>1</sup>, M.G. Nematov<sup>1</sup>, N.A. Yudanov<sup>1</sup>,  
L.V. Panina<sup>1,2\*</sup>, V.G. Kostishin<sup>1</sup>*

<sup>1</sup>National University of Science and Technology, MISiS, Moscow, Russia

<sup>2</sup>Immanuel Kant Baltic Federal University, Kaliningrad, Russia

\*E-mail: [drpanina@gmail.com](mailto:drpanina@gmail.com)

This paper investigates the temperature behavior of magnetoimpedance (MI) in amorphous microwires with different anisotropies near the Curie temperature,  $T_C$ , which can be used for temperature sensing and for investigations of the critical behavior of various magnetic parameters. The investigation of the MI behaviour near  $T_C$  also presents a fundamental interest related to the exchange interaction and the magnetic anisotropy of amorphous systems.

There is an interest to realize a controllable change in impedance in a moderate temperature range (so-called industrial range) of  $-20$  to  $+100$  °C. The addition of Ni and Cr in Co/Fe amorphous alloys results in a decrease in  $T_C$  placing it in a desirable range [1]. Near  $T_C$  the magnetic properties such as the saturation magnetization, magnetostriction, and anisotropy experience considerable variations. This will cause the modification in MI when approaching  $T_C$  [2]. Depending on the anisotropy type (near circumferential in  $\text{Co}_{27.4}\text{Fe}_5\text{B}_{12.26}\text{Si}_{12.26}\text{Ni}_{43.08}$  wires with  $T_C = 48$  °C (Fig. 1a) and near axial in  $\text{Co}_{64.82}\text{Fe}_{3.9}\text{B}_{10.2}\text{Si}_{12}\text{Cr}_9\text{Mo}_{0.08}$  wires with  $T_C = 62$  °C (Fig. 2a)), the MI vs temperature characteristics are different. In the case of a circumferential anisotropy, a substantial change in impedance with temperature requires the use of a dc bias field since the transverse permeability is small at zero field for any temperatures as demonstrated in Fig. 1b. For a frequency of 0.9 GHz and a bias field of 3 Oe the impedance drops by 100% when the temperature increases to  $T_C$ . For axial anisotropy, the initial permeability is maximal at zero field and for relatively high frequencies, the permeability

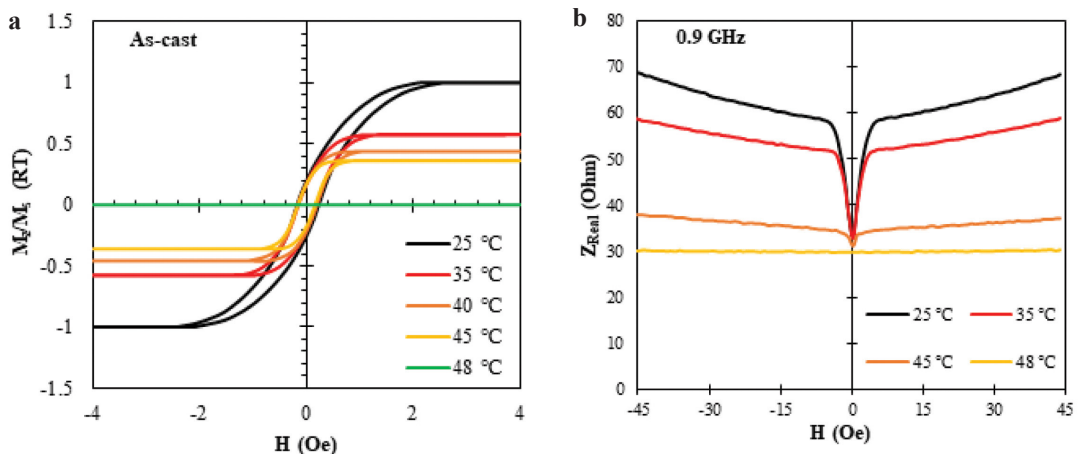


Figure 1. Hysteresis loops (a) and MI plots for a frequency of 0.9 GHz (b) of amorphous  $\text{Co}_{27.4}\text{Fe}_5\text{B}_{12.26}\text{Si}_{12.26}\text{Ni}_{43.08}$  wires with  $T_C = 48$  °C at different temperatures.

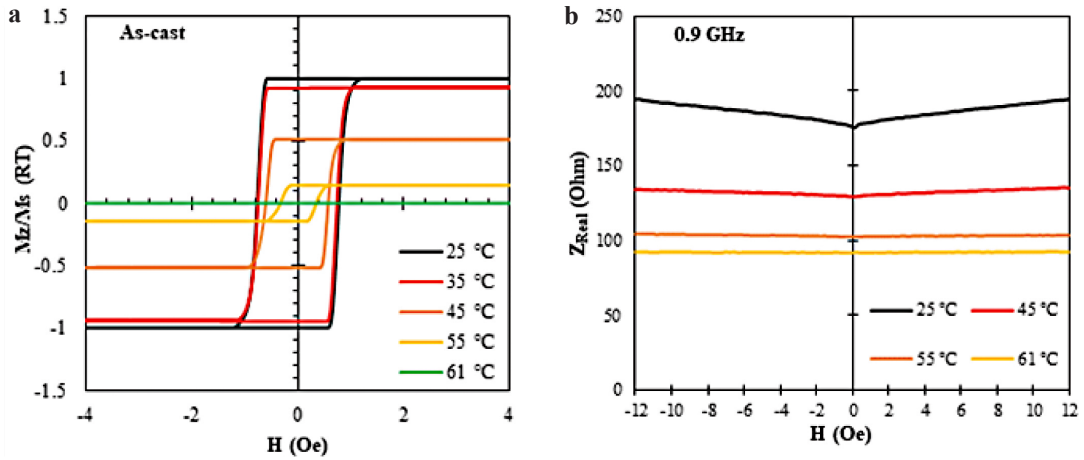


Figure 2. Hysteresis loops (a) and MI plots for a frequency of 0.9 GHz (b) of amorphous  $\text{Co}_{64.82}\text{Fe}_{3.9}\text{B}_{10.2}\text{Si}_{12}\text{Cr}_9\text{Mo}_{0.08}$  wires with  $T_C = 62$  °C at different temperatures.

decreases near  $T_C$  resulting in a decrease in impedance for any field (see Fig. 2b). It is interesting to notice that at lower frequencies the permeability may increase with temperature before a sharp drop near  $T_C$  leading to a non-monotonic temperature dependence of the impedance, which is not useful for sensor application. However, this present interest for the investigation of the critical behavior of the magnetic parameters.

*The work was supported by the Russian Foundation for Basic Research (RFBR project No. 20-31-70001).*

1. V. Zhukova, M. Ipatov, A. Zhukov, R. Varga, A. Torcunov, J. Gonzalez, and J. M. Blanco, *J. Magn. Magn. Mat.*, **300**, 16 (2006).
2. P. Sarkar, A. BasuMallick, R.K. Roy, A.K. Panda, A. Mitra, *J. Magn. Magn. Mater.*, **324**, 1551 (2012).
3. L.V. Panina, A. Dzhumazoda, S.A. Evstigneeva, A.M. Adam, A.T. Morchenko, N.A. Yudanov, V.G. Kostishyn, *J. Magn. Magn. Mater.*, **459**, 147–153 (2018).

## ELECTROMAGNETIC PROPERTIES OF COMPOSITE MATERIAL BASED ON ABC100.30 IRON CAPSULATED BY PHOSPHORUS OXIDE

*O.F. Demidenko<sup>1\*</sup>, A.O. Larin<sup>1</sup>, G.A. Govor<sup>1</sup>, A.L. Zhaludkevich<sup>1</sup>,  
T.V. Shoukavaya<sup>1</sup>, A.R. Normirzaev<sup>2</sup>*

<sup>1</sup>Scientific–Practical Materials Research Centre NASB, Minsk, Belarus

<sup>2</sup>Namangan Engineering–Construction Institute, Namangan, Uzbekistan

\*E-mail: [demiden@physics.by](mailto:demiden@physics.by)

For the efficient operation of electrical devices, including electric vehicles, it is necessary to maintain a balance between the energy stored by the batteries and the power consumed by the electric motors. Actually, electromagnetic motors are used in electric vehicles, and in addition to traction motors [1, 2]. The scientific and technical task of developing new highly efficient magnetic materials is creation of motors of various sizes that will correspond to their functional purpose in the overall system of an electric vehicle is relevant. It is possible to improve the characteristics of electric motors by using new materials based on metal powders coated with an insulating layer in the manufacture of magnetic circuits [3]. The manufacture of magnetic circuits by powder metallurgy allows to reduce eddy current losses due to the fact that each particle of the material is isolated from others, as well as to reduce production waste, thus increasing the environmental friendliness of production.

Composite was received by applying an insulating layer  $P_2O_5$  to the surface of the iron ABC100.30 particles, and subsequent pressing under a pressure of  $7-8 \text{ t} \cdot \text{cm}^{-2}$ . Density of composite is  $7.7 \text{ g/cm}^3$ . Crystalline structure of investigated materials it was studied by X-ray analysis in  $\text{CuK}\alpha$ -radiation in the  $20^\circ \leq 2\theta \leq 90^\circ$  angle range at room temperature. X-ray patterns was analyzed using the FullProf Suite program. The phase composition of obtained composite materials does not differ from the composition of the initial ABC100.30 powder and contain one cubic  $\alpha$ -Fe main phase. The lattice parameter is equal  $0.2868 \pm 0.0003 \text{ nm}$ .

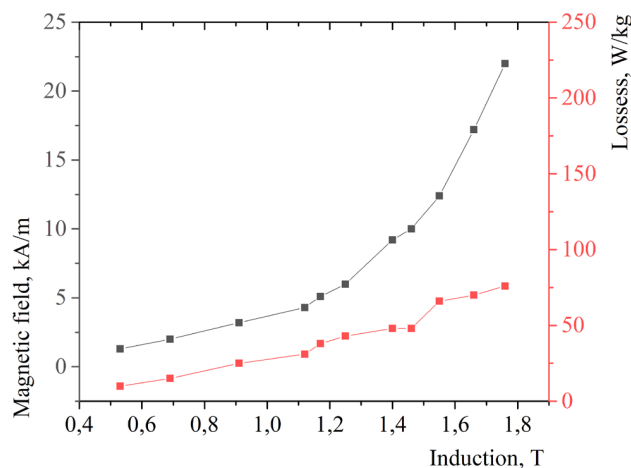


Figure 1. Electromagnetic characteristics of composite based on capsulated by phosphorus oxide ABC100.30 powder.

Electromagnetic properties were measured on an express magnetometer, where losses and other magnetic parameters were determined from the magnetization reversal curves of the samples. On Fig. 1 are presented dependences of magnetic field and losses vs. magnetic induction for composite materials based on ABC100.30 powder capsulated by phosphorus oxide. Developed materials can be used for production of high-efficiency inverter electric motors, transformers, inductors and other devices.

*This work was financial supported by Belarusian Republican Foundation for Basic Research as part of the projects No. T21UZBG-006.*

1. A. Saxenaa, and S.S. Godara, AIP Conf. Proc., **2148**, 30–35 (2019).
2. Z. Birčáková et al., J. of Mag. and Mag. Mater., **485**, 1–7 (2019).
3. A. Vetcher, O. Demidenko, V. Constantin, and A.-M. Popescu, Chem. Res. Chin. Univ., **36**, 1326–1331 (2020).

## ACID ETCHING EFFECTS ON THERMAL STABILITY OF $\Delta E$ -EFFECT IN Cr-DOPED IRON-BASED AMORPHOUS RIBBONS

*E.A. Golygin*<sup>1\*</sup>, *Y.S. Chen*<sup>2</sup>, *J.G. Lin*<sup>2,3</sup>, *A.A. Gavriluk*<sup>1</sup>

<sup>1</sup>Department of Physics, Irkutsk State University, Irkutsk, Russia

<sup>2</sup>Center for Condensed Matter Sciences, National Taiwan University, Taipei 10617, Taiwan

<sup>3</sup>Center for Atomic Initials for New Materials, National Taiwan University, Taipei 10617, Taiwan

\*E-mail: [egolygin2011@gmail.com](mailto:egolygin2011@gmail.com)

We study the thermal stability of  $\Delta E$ -effect and field sensitivity on the  $\text{Fe}_{67}\text{Co}_{10}\text{Cr}_3\text{Si}_5\text{B}_{15}$  (FCCSB) ribbons with different acid-etching time. The testing temperature ( $T$ ) range is from 30 to 240 °C. For all samples, we observed a general feature of  $\Delta E$ -effect increasing with magnetic field up to a saturation value.

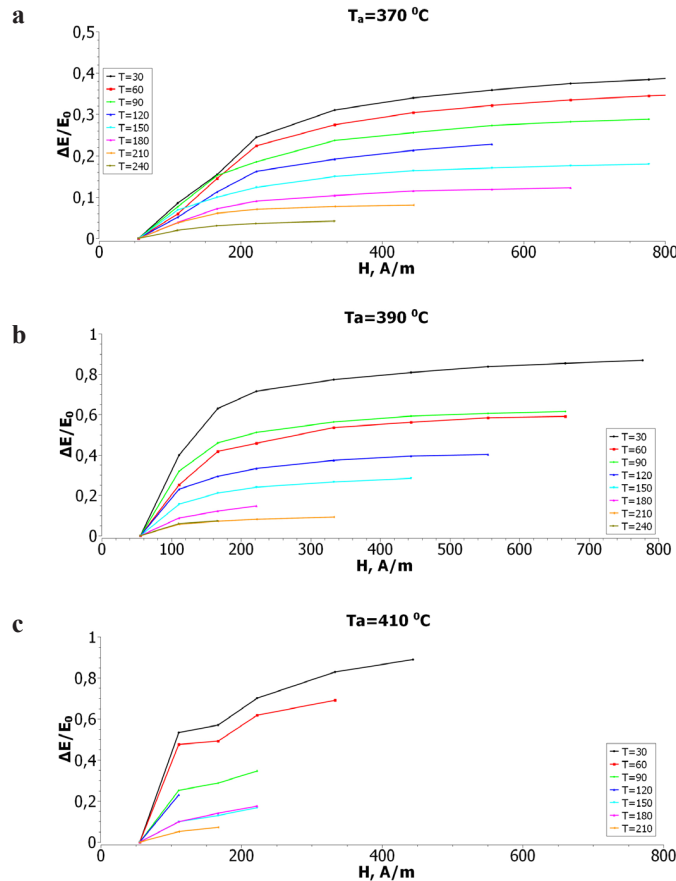


Figure 1. Field dependence of  $\Delta E$ -effect for FCCSB ribbons with various  $T_a$ : **a**  $T_a = 370$  °C, **b**  $T_a = 390$  °C and **c**  $T_a = 410$  °C. Different curve represents the data at different  $T$ : 30 °C ( $\blacklozenge$ ), 60 °C ( $\blacksquare$ ), 90 °C ( $\blacktriangle$ ), 120 °C ( $\times$ ), 150 °C ( $*$ ), 180 °C ( $\circ$ ), and 210 °C ( $+$ )

Amorphous iron based metal alloys are promising materials for modern industry since they have a number of unique magnetic and magnetoelastic properties together with excellent strength characteristics. Such materials have been characterized with high magnetostriction, high magnetic permeability, low coercive force, and significant fatigue strength [1]. The combination of these properties allows the amorphous metal alloys to act as sensing elements in various devices to detect magnetic field and deformation. Since the industrial operation requires the devices to against aggressive environments, the study of the magnetic and magnetostriction properties of amorphous metal alloys and their stability in highly corrosive media (usually acid or alkali environment [2]) is particularly important.

The as-made samples of  $\text{Fe}_{67}\text{Co}_{10}\text{Cr}_3\text{Si}_5\text{B}_{15}$  (FCCSB) ribbons were obtained by rapid quenching from a melting state and cut out from the original wide strip along the rolling axis in the form of narrow strips with a width of  $\sim 10^{-3}$  m. The thickness of the samples was around  $3 \cdot 10^{-5}$  m, and the length was 0.05 m. The choice of this specific composition is because of its high magnetization and high magnetoelastic ( $M_s = 1.3$  to  $1.8 \cdot 10^6$  A/m,  $\lambda_s = 20$  to  $35 \cdot 10^{-6}$ ). The adding of 3% Cr is for the resistance of anti-corrosion. Two post-treatment parameters are the duration of acid-etching ( $t$ ) and the post annealing temperature ( $T_a$ ). The concentration of hydrochloric acid (HCl) is 0.20 N. The samples were first acid etched, and then post annealed in vacuum at different annealing temperature ( $T_a$ ) of 370, 390 and 410 °C for 20 minute. An in-plane magnetic field of 2000 Oe was applied during the thermal annealing along the direction transversal to the axis of ribbon..

For comparison, the obtained  $\Delta E$  value is normalized to its initial value at zero field ( $E_0$ ). Figure 1a to 1c plot the field dependences of  $\Delta E/E_0$  for the FCCSB ribbons without acid-etching but with post annealed at  $T_a = 370$  °C to 410 °C. Each curve represents the data measured at different  $T$  (30 to 240 °C). The observed general trend is that  $\Delta E/E_0$  increases with increasing field and saturates at certain field, but its magnitude decreases with increasing  $T$ . In comparison with the samples without Cr [3, 4], it is evident that the Cr-adding leads to a change in the sign of field dependence of the  $\Delta E$ -effect from a negative to positive. Although the exact mechanism of Cr-induced change of the field driven lattice-response from shrinking to expansion is still unknown, we tentatively attribute it to the domain reorientation.

Thus, we attribute the etching enhanced thermal stability of magnetostriction properties to the modification of interfacial stress. This study provides useful information for the application of FCCSB ribbons as a field sensor with anti-corrosion properties.

*This work is financially supported by the NIR 091-20-116, Goszadanie of Russian Federation (Project No. 3.1941.2017/Pch); and part by the Ministry of Science and Technology and National Taiwan University in Taiwan under the projects of MOST 108-2112-M-002-022 and NTU-109L900803 respectively.*

1. C. Suryanarayana, A. Inoue, Iron-based bulk metallic glasses, *International Materials Reviews*, **58**(3), 131–166 (2013).
2. W. Dandana, M.A. Yousfi, K. Hajlaoui, F. Gamaoun, A.R. Yavari, Thermal stability and hydrogen-induced softening in  $\text{Zr}_{57}\text{Al}_{10}\text{Cu}_{15.4}\text{Ni}_{12.6}\text{Nb}_5$  metallic glass, *Journal of Non-Crystalline Solids*, **456**, 138–142 (2017).
3. C.A.C. Souza, D.V. Ribeiro, C.S. Kiminami, Corrosion resistance of Fe-Cr-based amorphous alloys: An overview, *Journal of Non-Crystalline Solids* **442**, 56–66 (2016).
4. A.A. Gavriluk, A.L. Semenov, E.A. Golygin, A.R. Gafarov, and A.A. Zinchenko, Influence of Temperature on  $\Delta E$  Effect in Amorphous  $\text{Fe}_{64}\text{Co}_{21}\text{B}_{15}$  Ribbons, *The Physics of Metals and Metallography* **114**(4), 295–298 (2013).



## NANOSTRUCTURED FeNi-C FILMS REDUCED BY CARBOHYDRATES: SYNTHESIS AND MAGNETIC PROPERTIES

*E.A. Chekanova*<sup>1</sup>, *E.A. Denisova*<sup>1,2\*</sup>, *S.V. Komogortsev*<sup>1</sup>, *O.A. Li*<sup>2</sup>, *R.S. Iskhakov*<sup>1</sup>,  
*D.A. Velikanov*<sup>1</sup>, *A.L. Suhachev*<sup>1</sup>, *I.V. Nemtsev*<sup>2,3</sup>

<sup>1</sup>Kirensky Institute of Physics, FRC KSC SB RAS, Krasnoyarsk, Russia

<sup>2</sup>Siberian Federal University, Krasnoyarsk, Russia

<sup>3</sup>Krasnoyarsk Scientific Center, FRC KSC SB RAS Krasnoyarsk, Russia

\*E-mail: [len-den@iph.krasn.ru](mailto:len-den@iph.krasn.ru)

Soft magnetic films have been widely used in the fields of magnetic recordings, magnetic sensors, microwave absorption [1, 2]. As a kind of typical soft magnetic materials, FeNi alloy films exhibit superior magnetic properties such as low coercivity, low magneto-crystalline anisotropy, high permeability and high saturation magnetization. A variety of chemical and physical techniques could be used for synthesis of Fe-based alloys films. However, these methods are fraught with many problems with the use of toxic solvents or high energy consumption. So, there is a growing need to prepare environmentally friendly magnetic materials that do not produce toxic wastes in their process synthesis protocol. A promising approach to achieve this objective is to use the polysaccharides (e.g. chitosan, cellulose) as environmental alternative to conventional reducing agents [3]. Herein, we introduce a very promising eco-friendly processing technique based on the electroless deposition of FeNi-C thick films with carbohydrates as reducing and stabilizing agents.

The FeNi-C thick films were prepared by electroless reduction of metals from aqueous solutions of the corresponding salts at 80 °C on glass or copper substrate. We used several types of carbohydrates as reducing agents: arabinogalactan – natural polysaccharide, corn starch and sucrose. The

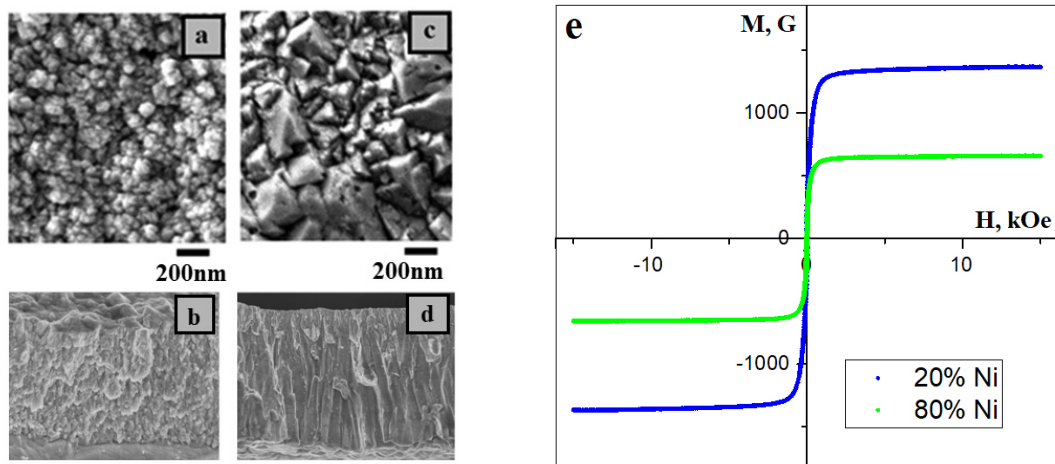


Figure 1. SEM images of the surface morphology and cross section of the FeNi-C films prepared with different reducing agent: arabinogalactan (a, b), sucrose (c, d). Hysteresis loops for FeNi-C films produced with different Ni content (e).

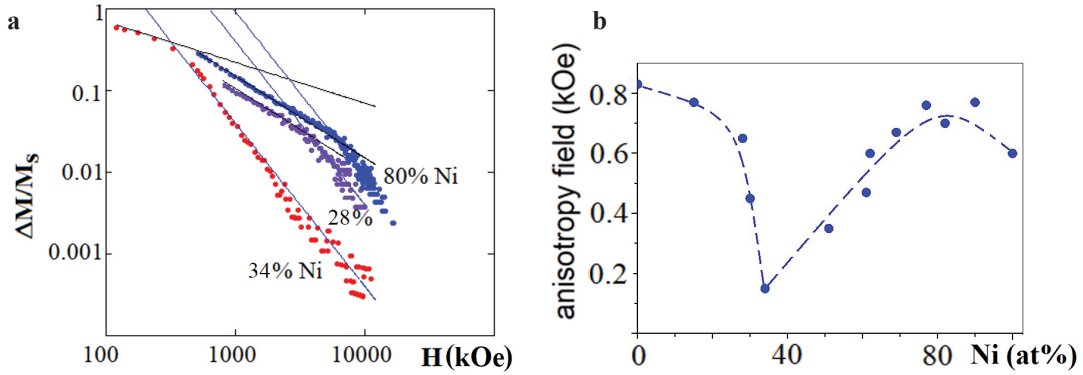


Figure 2. Approach magnetization to saturation for the FeNi-C films produced with different Ni content (a). The local anisotropy field  $H_a$  as a functions of Ni content for FeNi-C films (b).

thickness of deposited films was in range 0.2–4  $\mu\text{m}$ . The nanostructured thick films were characterized electron microscopy, X-ray photoelectron spectroscopy, and X-ray diffraction. Magnetic parameters such as the saturation magnetization, the exchange constant, the coercivity of the films were studied as a function of Fe content. The data of X-ray photoelectron spectroscopy studies show that carbon concentration in FeNi(C) alloy does not exceed  $\sim 1.5$  at.% for all film series and remaining carbon quantity ( $\sim 12\%$ ) is contributed by graphitic carbon, carboxyl, and carbonyl groups. According to X-ray data the  $\text{Fe}_{100-X}\text{Ni}_X\text{-C}$  films with  $X < 12$  have bcc structure, with  $12 < X < 40$  consist of mixture bcc and fcc phases, and FeNi-C alloy with greater than 40 at.% Ni has fcc structure. The average crystallite size calculated using the Scherrer formula for the all types of reducing agents was in range 10–27 nm. It was found that Fe content and type of reducing agent affect the surface morphology (Fig. 1a–d). The coercive force values range from 8 up to 30 Oe and the saturation magnetization from 50 to 196 emu/g depending on the bath composition and deposition parameters. The shape of the hysteresis loop is determined by the columnar microstructure of the films. It was found that exchange coupling constant values for FeNi-C films were in range  $(3.5\div 9.5) \cdot 10^{-7}$  erg/cm. Information on local magnetic anisotropy field  $H_a$  was obtained from investigation of approach magnetization to saturation law [4]. Figure 1e show the typical experimental magnetization curves for FeNi-C films with different Ni content. For all film series, the high-field part of magnetization curves satisfies the dependence (Fig. 2a):

$$M = M_s \left( 1 - \left( \frac{aH_a}{H} \right)^2 \right),$$

where  $H_a = 2K/M_s$  is magnetic anisotropy field,  $a$  is a coefficient equal to  $(2/105)^{0.5}$  for cubic anisotropy. The latter enabling us to determine the local anisotropy field  $H_a$ , which contains contributions of magnetocrystalline anisotropy and anisotropy of internal stresses (Fig. 2b). The invar feature manifests on dependence of local anisotropy field on Ni content. We observe the minimum of  $H_a$  value at 34 at.% Ni.

The magnetic properties of the films are discussed in relation with the microstructure. A comparison between the magnetic properties of the FeNi-C films produced by electroless plating with different reducing agent was carried out.

*The authors thank the Krasnoyarsk Regional Center of Research Equipment of Federal Research Center KSC SB RAS for the provided equipment. The research was funded by RFBR, Krasnoyarsk Territory and Krasnoyarsk Regional Fund of Science, project number 20-43-240003.*

1. Y. Cheng, G. Ji, Zh. Li, et al., Journal of Alloys and Compounds, **704**, 289–295 (2017).
2. M. Alper, H. Kockar, T. Sahin, O. Karaagac, IEEE Transaction on magnetic, **46**, 390 (2010).
3. P.R. Chang, J. Yu, X. Ma, D. P. Anderson, Carbohydr. Polym., **83**, 640 (2011).
4. S.V. Komogortsev, R.S. Iskhakov, J. Magn. Mater., **440**, 213–216 (2017).

INFLUENCE OF HYDROGENATION ON THE STRUCTURAL AND MAGNETIC PROPERTIES OF  $\text{Tb}(\text{Fe},\text{Co})_{11}\text{Ti}$ 

*A.A. Makurenkova*<sup>1\*</sup>, *N.Y. Pankratov*<sup>1</sup>, *I.S. Tereshina*<sup>1</sup>, *M. Zhelezny*<sup>2</sup>, *S.A. Nikitin*<sup>1</sup>

<sup>1</sup>Faculty of Physics, Moscow State University, Moscow, Russia

<sup>2</sup>Baikov Institute of Metallurgy and Materials Science, Moscow, Russia

\*E-mail: [makurenkova@physics.msu.ru](mailto:makurenkova@physics.msu.ru)

Recently much attention has been paid to structural and magnetic properties research of iron rich rare-earth (RE) intermetallic compounds with tetragonal  $\text{ThMn}_{12}$ -type structure [1].  $\text{RFe}_{11}\text{Ti}$  compounds are convenient model for studying fundamental problems of magnetic phenomena due to the features of the crystal and magnetic structure. RE atom occupies only symmetrical 2a site, while iron and titanium atoms have three non-equivalent sites (8i; 8j; 8f). The magnetic structure of  $\text{RFe}_{11}\text{Ti}$  compounds consist of two sublattice (RE and 3d). In case of light RE elements, the ferromagnetic ordering of the magnetic moments of both sublattices occurs, while for the heavy RE elements it is ferrimagnetic. The main contribution to the MCA of RE intermetallic compounds is single-ion, so the MCA constants are defined by the crystal electric field in the RE ion's site. At low temperatures the RE sublattice's contribution to magnetocrystalline anisotropy (MCA) is dominant, while at high temperatures on the contrary the contribution from the 3d-sublattice predominates. Partial substitution of Fe to Co in  $\text{RFe}_{11}\text{Ti}$  compounds together with hydrogenation leads to an increase in Curie temperature and changes in the MCA of 3d-sublattice, which makes it possible to obtain new magnetic materials with unique properties [2, 3]. The aim of this work is a comparative study of structural and magnetic properties of  $\text{Tb}(\text{Fe},\text{Co})_{11}\text{Ti}$  compounds and their hydrides.

In  $\text{TbFe}_{11}\text{Ti}$  compound an easy axis is orthogonal to the crystallographic direction [001] at low temperatures [4]. With temperature increase the first order spin-reorientation transition (SRT) occurs at 325 K when the easy magnetization direction re-orientes along the tetragonal direction. Partial substitution of iron on cobalt in  $\text{TbFe}_{11}\text{Ti}$  leads to decrease of the SRT temperature and to increase of the Curie temperature and expands the uniaxial state area.  $\text{Tb}(\text{Fe},\text{Co})_{11}\text{TiHy}$  hydrides were synthesized at 670 K in high pressure reactor chamber under pressure of 1.2 MPa. Hydrogen content ( $y = 1.0 \pm 0.1$ ) in the samples was calculated by the change in hydrogen pressure. The field and temperature dependencies of a magnetization along main crystallographic directions were obtained at magnetic fields up to 70 kOe for the 5–300 K temperature range. Based on the single-ion anisotropy model values of the magnetic anisotropy constants  $K_1$  and  $K_2$  were calculated from the experimental data.

Comparison of obtained results of hydrides with the MCA constants of the initial  $\text{Tb}(\text{Fe},\text{Co})_{11}\text{Ti}$  compounds reveals that the hydrogenation changes the signs of both MCA constant  $K_1$  and  $K_2$ . At the same time the hydrogenation increases the saturation magnetization.

*The reported study was funded by RFBR, project number № 20-32-90236.*

1. A.A. Makurenkova, D. Ogawa, P. Tozman, S. Okamoto, S. Nikitin, S. Hirose, K. Hono, Y.K. Takahashi, **861**, 158477 (2021).
2. T.P. Kaminskaya, I.S. Tereshina, Moscow University Physics Bulletin, **75**, 629–635 (2020).
3. I.S. Tereshina, S.A. Nikitin, V.N. Nikiforov, L.A. Ponomarenko, V.N. Verbetsky, A.A. Salamova, K.P. Skokov, J. Alloys Comp., **345**, 16–19, (2002).
4. S.A. Nikitin, I.S. Tereshina, V.N. Verbetsky, A.A. Salamova, K.P. Skokov, N.Y. Pankratov, Y.V. Skourski, N.V. Tristana, V.V. Zubenko, I.V. Telegina, J. Alloys Comp., **322**, 42–44 (2001).

## MAGNETIC PROPERTIES AND ELECTRONIC STRUCTURE OF Gd(Co,Ru)Si TERNARY INTERMETALLICS

*A.V. Lukoyanov*<sup>1,2\*</sup>, *R.D. Mukhachev*<sup>1,2</sup>, *S.P. Platonov*<sup>1</sup>, *A.G. Kuchin*<sup>1</sup>

<sup>1</sup>M.N. Mikheev Institute of Metal Physics UB RAS, Ekaterinburg, Russia

<sup>2</sup>Ural Federal University, Ekaterinburg, Russia

\*E-mail: [lukoyanov@imp.uran.ru](mailto:lukoyanov@imp.uran.ru)

Ternary intermetallic compounds Gd(TM)Si, where TM are various d elements, such as: Ti, V, Cr, Mn, Fe, Co, and others, attract the attention of researchers with a variety of physical properties and the possibility of applications [1]. The crystal structure of these compounds is a tetragonal type with space group  $P4/nmm$ . The ferromagnetic intermetallic compound GdFeSi is characterized by a Curie temperature of 118 K [2]. The Curie temperature of 167 K was experimentally determined in GdCoSi [1]. Several magnetic transitions were found in GdMnSi at temperatures of 50, 275, 310–325 K [3].

Theoretical calculations of the magnetic properties and electronic structure of Gd(TM)Si were carried out using the Quantum ESPRESSO software package [4] within the DFT+U method based on the Perdew-Burke-Ernzerhof version of the generalized gradient correction approximation. The lattice constants corresponding to the equilibrium volumes show the most stable structure, the atomic coordinates in the calculations were preliminarily optimized. To take into account strong electron correlations in the 4f shell of gadolinium ions, the values of the Coulomb parameter of 6.7 eV and the exchange interaction parameter of 0.7 eV were used.

In our work, the theoretical studies of the GdRuSi and GdCoSi compounds in the  $P4/nmm$  tetragonal structure were carried out. The obtained densities of states are plotted in Fig. 1. For Gd

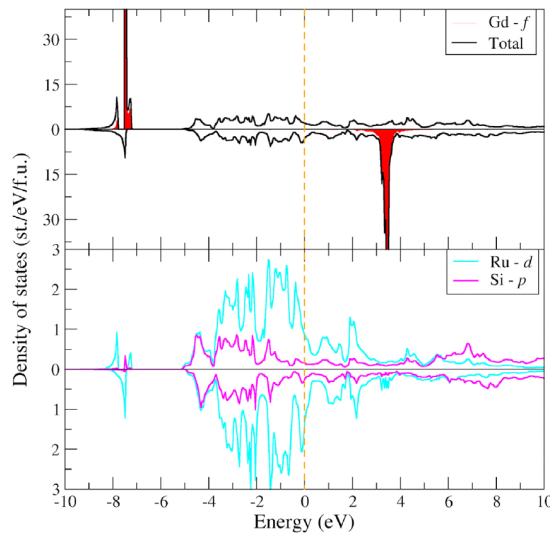


Figure 1. Electronic structure of the GdRuSi compound. The Fermi energy at zero energy is shown as a vertical dashed line. The densities of states are plotted for the majority ( $\uparrow$ ) and minority ( $\downarrow$ ) spin projections.

ions, the spin polarization values obtained from our self-consistent calculations correspond to an effective magnetic moment of  $7.1 \mu_B$ . The Si, Co and Ru ions are non-magnetic. The electronic states near the Fermi level are determined mainly by the d electronic states of the Ru or Co ions. Both compounds are calculated to have a ferromagnetic ordering of the magnetic moments. The calculated magnetic properties are found in a good agreement with the available experimental data.

*This research was supported by Russian Science Foundation project RSF 18-72-10098.*

1. S. Gupta and K.G. Suresh, *J. Alloys Compd.*, **618**, 562–606 (2015).
2. A.G. Kuchin et al., *Intermetallics*, **133**, 107183 (2021).
3. S.A. Nikitin et al., *J. Magn. Magn. Mater.*, **157/158**, 387–388 (1996).
4. P. Giannozzi et al., *J. Phys.: Condens. Matter.*, **29**, 465901 (2017).

## INVESTIGATION OF THE MAGNETIC PROPERTIES OF AMORPHOUS IRON-BASED MICROWIRES WITH A PARTIALLY CRYSTALLIZED SURFACE LAYER

*A.A. Fuks<sup>1,2</sup>, A.S. Aronin<sup>1</sup>, O.I. Aksenov<sup>1\*</sup>*

<sup>1</sup>Institute of Solid State Physics, RAS, Chernogolovka, Russia

<sup>2</sup>National Research University Higher School of Economics, Moscow, Russia

\*E-mail: [oleg\\_aksenov@inbox.ru](mailto:oleg_aksenov@inbox.ru)

Amorphous microwires are one of the most promising soft magnetic materials at the moment. The amorphous structure of microwires determines the predominant effect of magnetoelastic anisotropy on their magnetic properties and magnetic domain structure. That is, almost all magnetic properties of microwires depend on their internal or applied external mechanical stresses. Small sizes, a wide range of magnetic and high-frequency properties (giant magnetic impedance effect, bistable magnetization reversal, natural ferromagnetic resonance) and the relationship of these properties with the stressed state of the material determine a significant interest in the use of microwires as sensors [1, 2]. Efforts are constantly being made to improve the current properties of microwires. This is achieved by varying the composition, heat treatment, changing internal and external stresses [3]. One of the most promising areas is the optimization of the giant magnetic impedance (GMI) effect in microwires. At present, the best values of the GMI effect have been obtained in Co-based microwires (650%). The key factors for achieving the best values of the GMI effect in amorphous microwires are high magnetic permeability, low values of resistivity and magnetostriction. Such indicators are typical both for amorphous cobalt-based alloys and for an amorphous-nanocrystalline alloy with  $\text{Fe}_{73.8}\text{Cu}_1\text{Nb}_{3.1}\text{B}_{9.1}\text{Si}_{1.3}$  (FINEMET) composition. Microwires based on this alloy became the object of study in the framework of this work.

It is generally accepted that in the central part of the microwires (obtained by the Ulitovsky-Taylor method) tensile stresses of the order of hundreds of MPa predominate. In this case, compressive stresses of the order of a few GPa dominate in the surface layer of a microwire [4]. This can lead to different crystallization rates in the central and surface parts of the microwire. Moreover, the crystallization rate in the surface part can be higher than in the central part for microwires of the FINEMET composition. This is due to the fact that the resulting nanocrystals have a higher density than the original amorphous matrix leading to a negative volume effect. With a negative volume effect the Gibbs energy of the critical nucleus decreases with increasing compressive stresses and conversely increases with tension. As a result, the formation of nanocrystals should be facilitated in the region of compressive stresses (surface). As mentioned above the nanocrystallization of the FINEMET alloy leads to a significant increase in its magnetic permeability. During crystallization the increase in magnetic permeability in the surface layer of the microwire can be higher than in the central part. In addition, the decrease in magnetostriction during nanocrystallization of the FINEMET alloy should also proceed nonuniformly. Near-zero magnetostriction can be achieved in the surface layer of the microwire faster than in the central part. In this case the microwire can be some kind of composite. The surface layer of the microwire will have a high magnetic permeability, and its magnetic properties will weakly depend on external mechanical stresses. In this case in the central part of the microwire the magnetic permeability will be lower than in the surface layer and the magnetostriction will be positive. A microwire with such a structure may be of interest as a sensitive element of a sensor. On the one hand, it should have high GMI values due to the high

magnetic permeability of the surface layer, and on the other hand, its core remains magnetically sensitive to mechanical stresses.

In the framework of this work, we tested the hypothesis about the predominant crystallization of the surface layer of the microwire at the early stages of heat treatment. A comparison was made with ribbons of a similar composition. It has been established that the volume fraction and size of nanocrystals precipitated in microwires is higher than in ribbons. The surface crystalline layer was removed from the microwire. X-ray studies of microwires with a removed crystalline layer confirmed that the core of the microwire remained amorphous at the initial stages of heat treatment. Hysteresis loops of partially crystallized microwires were measured. The effect of partial crystallization on size of the domain layers of microwires and the nature of their magnetization reversal has been established.

*The research is carried out within the state task of ISSP RAS.*

1. H. Chiriac, T.A. Ovari, ProgMater Sci., **40**, 333–407 (1996).
2. O.I. Aksenov, A.A. Fuks, A.S. Aronin, J. Alloys Compd., **836**, 155472 (2020).
3. A. Zhukov, M. Ipatov, P. Corte-León, L. Gonzalez-Legarreta, M. Churyukanova, J.M. Blanco, J. Gonzalez, S. Taskaev, B. Hernando, V. Zhukova, J. Alloys Compd., **814**, 152225 (2020).
4. H. Chiriac, T.A. Ovari, G. Pop, Physical Review B, **52**, 10104–10113 (1995).



## SYNTHESIS AND MAGNETIC PROPERTIES OF Co, Ni AND COMPOUNDS OF CoFe, NiFe NANOWIRES

*A.E. Dryagina*<sup>1\*</sup>, *A.N. Gorkovenko*<sup>1</sup>, *N.A. Kulesh*<sup>1</sup>, *V.O. Vas'kovskiy*<sup>1,2</sup>

<sup>1</sup>Ural Federal University named after the First President of Russia B. N. Yeltsin, Ekaterinburg, Russia

<sup>2</sup>M.N. Mikheev Institute of Metal Physics, Ural Branch of the Russian Academy of Sciences, Ekaterinburg, Russia

\*E-mail: [dryagina.nastya@list.ru](mailto:dryagina.nastya@list.ru)

Magnetic nanowires are of great interest in various fields of science and technology. The possibility of varying their shape, size, and composition, can potentially be useful for different applications including sensors, optical elements, information recording, etc. [1]. Arrays of magnetic nanowires embedded into thin alumina films have significant potential for applications since they can potentially be obtained in the framework of standard MEMS fabrication technologies and can be included as an active element of electric circuit. In this work we focused on the development of a technology allowing synthesis of magnetic nanowires of different compositions: Co, Ni, and Co-Fe, Ni-Fe alloys in thin alumina film deposited onto the glass substrate. Magnetic properties of the synthesized samples were analyzed and compared.

High-purity aluminum films deposited by ion sputtering onto the glass substrates were used anodized and used as templates. The anodization was performed in aqueous electrolyte solution containing oxalic acid (0.3 M) at room temperature and constant voltage of 40 V [2]. The partial dissolution of the barrier layer for a subsequent electrodeposition was carried out by limiting current in a stepwise manner. Pure metals Co, Ni and compounds Ni-Fe and Co-Fe were electrodeposited from corresponding aqueous electrolyte solutions containing boric acid and corresponding salts.

The composition of the Fe-Co compound was varied by increasing the iron content in the electrolyte solution, the Fe-Ni compound – by increasing the nickel content in the electrolyte solution. The final composition of the samples was controlled using total reflection X-ray fluorescence spectrometer. As a result, dependences of iron concentration in Fe-Co and Fe-Ni samples on the

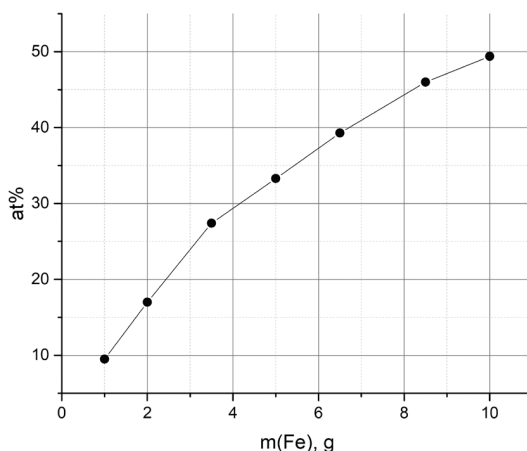


Figure 1. Dependence of iron concentration in Fe-Co nanowires (in at.%) on the content of  $\text{FeSO}_4$  in the electrolyte solution (in grams).

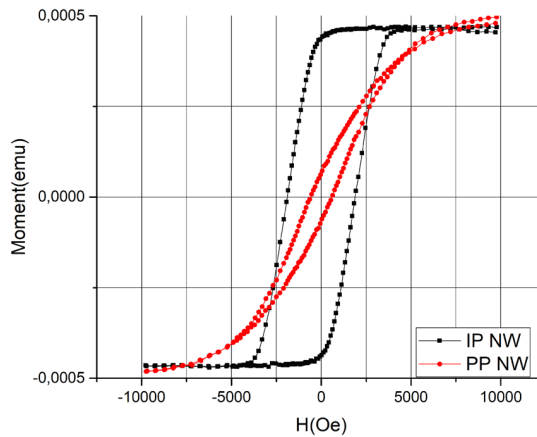


Figure 2. Hysteresis loops obtained for  $\text{Fe}_{9.5}\text{Co}_{90.5}$  sample parallel (black) and perpendicular (red) to the nanowires axis.

content of iron salts in electrolyte solutions were obtained. One of the corresponding dependencies obtained for Fe-Co sample is shown in Fig. 1.

Magnetic properties of the synthesized samples were studied using LakeShore vibrating sample magnetometer at room temperature. Measurements were performed in two directions: parallel and perpendicular to the nanowires axis, which correspond to the application of external magnetic field perpendicular and parallel to the surface of alumina film respectively. As a result of analysis of hysteresis loops, the values of residual magnetization, coercivity, and magnetic moment of the samples under study were obtained.

As an example, Fig. 2 shows hysteresis loops obtained on the  $\text{Fe}_{9.5}\text{Co}_{90.5}$  sample parallel (black) and perpendicular (red) to the axis of nanowires. It can be seen from the graph that the easy magnetization axis lies perpendicular to the film, i.e., parallel to the nanowires array axis, and the hard magnetization axis lies perpendicular to the nanowires array axis, which corresponds to the theory. The shape of the hysteresis loops and the high value of the coercivity when measured along the axis of the array of nanowires indicate the presence of a strong uniaxial magnetic anisotropy, which confirms the prevailing contribution of the shape anisotropy. Analysis of the morphology by scanning electron microscopy showed that the average pore diameter was 50 nm, and the length of the nanowires was 200–300 nm (can be adjusted by choosing an appropriate deposition time).

As a result of this work, a technique for obtaining nanowires in a thin layer of aluminum oxide was developed and arrays of Ni, Co nanowires, Fe-Ni, Fe-Co compounds were obtained and their compositions were determined. The dependences of the concentration of iron in Fe-Co and Fe-Ni compounds on the content of iron and nickel in the corresponding electrolyte solutions (in grams) are obtained. An analysis of the hysteresis properties of the obtained arrays of nanowires perpendicular and parallel to the axis of the array of nanowires is performed.

*The research funding from the Ministry of Science and Higher Education of the Russian Federation (Ural Federal University project within the Priority-2030 Program) is gratefully acknowledged.*

1. A. Dryagina, N. Kulesh, V.O. Vas'kovskiy and E. Patrakov, Synthesis and Magnetic Properties of Co Nanowires/PVDF Composites, *IEEE Magnetics Letters*, **13**, 1–4 (2022).
2. W. Lee and S.J. Park, Porous Anodic Aluminum Oxide: Anodization and Templated Synthetic of Functional Nanostructures, *Chem. Rev.*, **114**, 7487–7556 (2014).

MAGNETOCALORIC EFFECT IN  $R_2Fe_{10}Al_7$  COMPOUND*N.Yu. Pankratov*<sup>1\*</sup>, *A.Yu. Karpenkov*<sup>1,2</sup>, *S.A. Nikitin*<sup>1</sup>, *I.S. Tereshina*<sup>1</sup><sup>1</sup>Faculty of Physics, M.V. Lomonosov Moscow State University, Moscow, Russia<sup>2</sup>Faculty of Physics, Tver State University, Moscow, Russia\*E-mail: [pankratov@phys.msu.ru](mailto:pankratov@phys.msu.ru)

The magnetocaloric effect (MCE), which is considered as a foundation in technical applications of magnetic refrigeration, has attracted a considerable attention in recent years [1]. The MCE is an important phenomena of magneto-thermodynamics which manifests itself as magnetic entropy change ( $\Delta S$ ) or an adiabatic temperature change ( $\Delta T$ ) when the magnetic material is exposed to a varying magnetic field. It is intensively studied due to several factors: first, to obtain significant data on the magnetic entropy, which varies greatly in the region of the magnetic phase transitions; second, in order for further applications of the magnetocaloric materials in the magnetic refrigerator [2]. Many efforts are under-way to discover materials showing large magnetocaloric effect under moderate applied magnetic fields, so that magnetic cooling technology may become a reality in the near future. In the case of the ferromagnet the thermodynamic formulation of the MCE predicts  $\Delta S < 0$  and  $\Delta T > 0$ , i.e. the sample heats up when the external magnetic field is applied adiabatically. On the other hand, in case of positive temperature derivative of the magnetization the inverse MCE occurs, i.e.  $\Delta S > 0$  and  $\Delta T < 0$ , the sample cools down when the magnetic field is applied adiabatically. The inverse MCE exists for example in antiferromagnetic and ferrimagnetic near phase transition [3]. So, the important physical characteristics of the ferromagnetic materials could be obtained due to MCE study.

$R_2Fe_{17}$  compounds (R is rare-earth) have the highest Fe content among the R-Fe series of binary intermetallic compounds. Most of these compounds have ferro- (for light RE) or ferrimagnetic (for heavy RE) order with rather moderate Curie temperatures near room temperature. The magnetic properties of these compounds depend on three types of exchange interaction: R-R, R-Fe and Fe-Fe. The addition of 3d-, 3p-, and 4p-elements provokes drastic changes of the Curie temperature. In the  $R_2Fe_{17-x}Al_x$  system the magnetic moment of Fe sublattice is dropped with Al concentration and for compounds with  $x > 5$  the magnetization of the RE sublattice is larger than that of the iron sublattice. In  $Dy_2Fe_{10}Al_7$  compound there exists a compensation of the magnetic moments of the R and Fe sublattices at compensation temperature ( $T_{comp}$ ) [4]. It was established, that the abrupt change of magnetization may appear around the compensation temperature, where MCE should be expected. The investigation of the MCE in the vicinity of  $T_{comp}$  is of significant interest because of the fact that the magnetic features of the ferrimagnetic compounds are exhibited most clearly at this temperature.

In this work, we set a goal to investigate the influence of ferrimagnetic structure on MCE of  $R_2Fe_{10}Al_7$  compounds (R = Gd, Tb, Dy, Ho, Y). To do this, we synthesized the compositions of the  $R_2Fe_{10}Al_7$ . All obtained samples were certified by X-ray diffraction phase analysis and optical metallography. Experimental data on the features of the field and temperature dependences of the magnetocaloric effect have been obtained and analyzed. MCE and magnetization measurements were performed using special equipment (automated complex for studying the magnetic properties of materials “MagEq MMS” manufactured by LLC “AMT&C”) in magnetic field up to 18 kOe.

To solve the above mention problem the magnetization and MCE of  $R_2Fe_{10}Al_7$  compounds with magnetic RE were held on the same samples in similar condition (magnetic fields, temperatures and e.g.). The MCE of the ferromagnetic  $Y_2Fe_{10}Al_7$  compound was also studied and these data were used for calculation the contribution of 3d-sublattice on the MCE and magnetization. It was allow

us first to find the contribution in MCE of the RE sublattice in ferromagnetic compounds at forced magnetization. The study of the contribution of the RE sublattice to the magnetization and MCE allows in the future to search the compounds with a high inverse MCE (caused by RE sublattice).

The magnetic order degree in both ferrimagnetic and ferromagnetic materials increases under an applied magnetic field in a forced magnetization region, which results in a maximum positive value of the MCE in a region of the ferromagnetic-paramagnetic and ferrimagnetic-paramagnetic transitions. The experimental results and theoretic estimations of the MCE and magnetization of the  $R_2(\text{Fe,Al})_{17}$  compound show that the temperature and field dependencies of the MCE in RE ferrimagnetic intermetallic materials differ strongly from those in ferromagnetic materials. The both positive and inverse MCE in the region of forced magnetization and the change in the MCE sign from positive to negative in a region of the compensation temperature were found. We are suggested that the physical mechanism determining the temperature and field dependencies of the MCE of the ferrimagnetic structure is the inducing of both magnetic order and disorder of the sublattices in an external magnetic field depending on the field direction in relation to the sublattices magnetization.

Our results show the course of further search for rare-earth materials with high MCE in temperature region below room temperature. These materials should possess optimal effective field value (acting upon rare-earth sublattice) in a certain temperature region.  $R_2(\text{Fe,Al})_{17}$  compounds with inverse MCE can be useful for devices that stabilize the temperature when it deviates from the specified values.

*The study was supported by the Russian Science Foundation grant No. 22-29-00773, <https://rscf.ru/project/22-29-00773/>.*

1. A.M. Tishin and Y.I. Spichkin, The magnetocaloric effect and its applications, Institute of Physics Publishing, Bristol and Philadelphia (2003).
2. V. Franco, et al., Prog. Mater. Sci., **93**, 112–232 (2018).
3. H. Zu, W. Dai, A.T.A.M. de Waele, Cryogenics, **121**, 103390 (2022).
4. S. A. Nikitin, N.Y. Pankratov, A.I. Smarzhenskaya et al., J.Alloys Comp., **854**, 156214 (2021).

## MAGNETIC STRUCTURE OF Tb(Ni<sub>0.9</sub>Mn<sub>0.1</sub>)<sub>2</sub>Si<sub>2</sub>

*Haneen M. Alsafi*<sup>1\*</sup>, *E.G. Gerasimov*<sup>1,2</sup>, *A.E. Teplykh*<sup>1</sup>, *P.B. Terentev*<sup>1,2</sup>,  
*N.V. Mushnikov*<sup>1,2</sup>, *A.N. Pirogov*<sup>1,2</sup>

<sup>1</sup>Institute of Metal Physics, of UB of RAS, Ekaterinburg, Russia

<sup>2</sup>Institute of Natural Science and Mathematics, Ekaterinburg, Russia

E-mail: [haneenalsafi.1991@gmail.com](mailto:haneenalsafi.1991@gmail.com)

The rare-earth compounds TbNi<sub>2</sub>Si<sub>2</sub> and TbMn<sub>2</sub>Si<sub>2</sub> belong to the family of ternary intermetallic compounds of the RM<sub>2</sub>X<sub>2</sub> type, where M = Ni, Mn, Fe, and X = Si, Ge. These compounds crystallize in the body-centered tetragonal ThCr<sub>2</sub>Si<sub>2</sub> type tetragonal structure, the space group *I4/mmm*. The structure consists of atomic layers perpendicular to the *c*-axis are stacked with the sequence R-X-M-X-R. The layered structure of these compounds is considered to be responsible for quite an exciting variety of magnetic orders and phase transitions. For example, in TbMn<sub>2</sub>Si<sub>2</sub> the Tb-ion magnetic moments are ordered ferromagnetically below 65 K while the Mn-atom moments are arranged mutually antiferromagnetically. The TbNi<sub>2</sub>Si<sub>2</sub> compound undergoes at 15 K successive the magnetic phase transition to an amplitude modulated antiferromagnetic structure.

The present report represents the results of neutron diffraction study of the effect of Mn doping on the magnetic order in TbNi<sub>2</sub>Si<sub>2</sub>.

The neutron powder diffraction (NPD) patterns have been recorded with the D-3 diffractometer (reactor IVV-2M). The incident neutron length was equal to 0.243 nm. An analysis of the NPD patterns was performed using “Fullprof” program.

Angle positions of magnetic reflections and satellites point to the propagation vector of the magnetic structure  $\{\mathbf{k}_8\} = 2\pi/a((1 - 2\delta)/2, (1 + 2\delta)/2, 0)$ ;  $\delta = 0.082$ . The composition of a magnetic representation for the Tb ions: *2a* position: (0, 0, 0) and (0.5, 0.5, 0.5) is

$$d_m(2a) = \tau_2 + \tau_3 + \tau_4,$$

where  $\tau_2$ ,  $\tau_3$ , and  $\tau_4$  are the irreducible representations (in Kovalev’s notations [1]) of space group *I4/mmm*. The basic functions of all these representations describe antiferromagnetic orientation of the

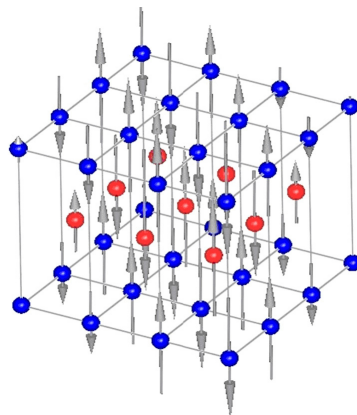


Figure 1. Magnetic structure of Tb(Ni<sub>0.9</sub>Mn<sub>0.1</sub>)<sub>2</sub>Si<sub>2</sub> at 4.2 K.

Tb spins. The best description of observed NPD patterns achieved for  $\tau_3$  irreducible representation that means an amplitude – modulated magnetic structure with the Tb – ion spins along the  $c$ -axis and with a magnitude  $7.4(1) \mu_B$ . The Ni/Mn sublattice magnetization is nonmagnetic.

*The research funding from the Ministry of Science and Higher Education of the Russian Federation (Ural Federal University Program of Development within the Priority-2030 Program) is gratefully acknowledged*

1. O.V. Kovalev, Irreducible representations and corepresentations of Fedorov groups, Nauka, Moscow (1981) [in Russian].

## MAGNETISM IN Fe<sub>3</sub>Se<sub>4</sub> UNDER THE ISOTROPIC COMPRESSION

*L.V. Begunovich*<sup>1\*</sup>, *M.M. Korshunov*<sup>1,2</sup>, *S.G. Ovchinnikov*<sup>1,2</sup>

<sup>1</sup>Siberian Federal University, Krasnoyarsk, Russia

<sup>2</sup>L.V. Kirensky Institute of Physics, Krasnoyarsk, Russia

\*E-mail: [lyuda.illuzia@gmail.com](mailto:lyuda.illuzia@gmail.com)

Many insulator transition metal oxides demonstrate magnetic collapse under high pressure, that results in the disappearance of magnetic moments in 3d ions. In this case the spin crossover between the high-spin and low-spin states of the cation takes place [1]. Here the high-pressure magnetic states of metallic Fe<sub>3</sub>Se<sub>4</sub> have been investigated within the density functional theory. Fe<sub>3</sub>Se<sub>4</sub> is a monoclinic structure with ordered iron vacancies located in every second iron layer [2, 3]. The presence of Fe vacancies leads to the ferrimagnetic ground state of Fe<sub>3</sub>Se<sub>4</sub>. We calculated the magnetic moment changes with increasing isotropic compression along the lattice constant. The values of the magnetic moments decrease nonmonotonically and eventually vanish. The total magnetic moment changes qualitatively correlate with nonmonotonic dependence of the density of states at the Fermi level  $N(E_F)$ . A decrease in the magnetic moment is accompanied by a decrease in the  $N(E_F)$ . The magnetic order changes from the ferrimagnetic to the ferromagnetic one at 7% compression and becomes nonmagnetic at 14% compression. The total magnetic moment of ferrimagnetic and ferromagnetic states are 2.128  $\mu_B$ , and 1.061  $\mu_B$  per formula unit, respectively. For all compression values the metallic state remains stable. This magnetic collapse cannot be represented as the energy-level crossing of the high-spin and low-spin cation states, because Fe<sub>3</sub>Se<sub>4</sub> has metallic properties. In this case, the magnetic collapse is caused by the alignment of the numbers of spin-up and spin-down electrons on each cation, so this can be called the itinerant analogue of the spin crossover.

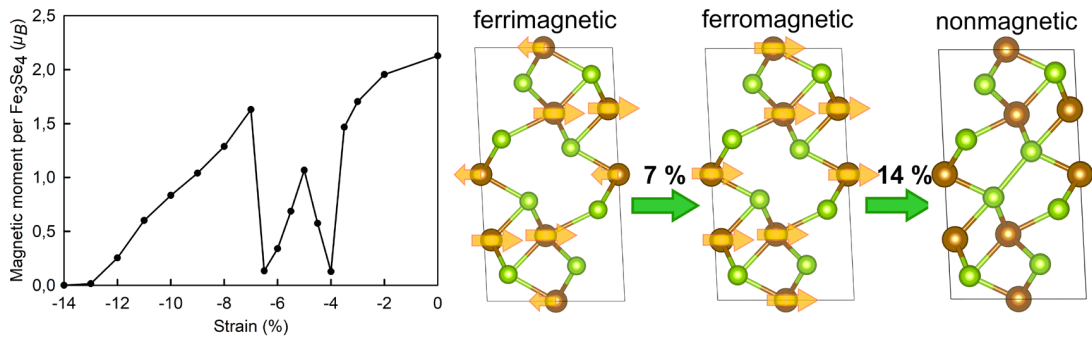


Figure 1. The dependence of magnetic moment on isotropic compression and the illustration of change in the magnetic ordering under isotropic compression. Brown and yellow-green colors correspond to iron and selenium atoms, respectively. Arrows indicate the directions of magnetic moments on Fe atoms.

*This work is supported by the Russian Science Foundation (Project 18-12-00022-II). L.V.B. would like to thank Information Technology Center, Novosibirsk State University, for providing the access to supercomputer facilities.*

1. I.S. Lyubutin and A.G. Gavriluk, *Uspekhi Fiz. Nauk*, **179**, 1047 (2009).
2. R. Pohjonen, O. Mustonen, M. Karppinen, and J. Lindén, *J. Alloys Compd.*, **746**, 135 (2018).
3. A.F. Andresen, *Asta Chem. Scand.*, **22**, 827 (1968).

## MODELING AND ANALYSIS OF FREQUENCY DEPENDENCES OF SOFT MAGNETIC AMORPHOUS WIRES IMPEDANCE

*D.A. Bukreev\**, *M.S. Derevyanko*, *A.A. Moiseev*, *V.O. Kudryavtcev*, *A.V. Semirov*

Irkutsk State University, Irkutsk, Russia

\*E-mail: [da.bukreev@gmail.com](mailto:da.bukreev@gmail.com)

The magnetic structure of amorphous soft magnetic Co-based wires is described, as a rule, within the framework of the model “axially magnetized core – circularly magnetized shell” [1]. This makes it possible to explain the main features of the magnetoimpedance effect (MI) at different ac frequencies. However, some experimental data point to a more complex distribution of magnetization inside the wire [2].

Direct study of the magnetic structure of the amorphous wires is difficult. Nevertheless, detailed information about it can be obtained by analyzing the frequency dependences of the impedance and MI (this approach can be called magnetoimpedance tomography). When the ac frequency  $f$  increases, the skin depth  $\delta$  decreases. So, the contribution of the deep regions of the wire to the impedance modulus  $Z$  decreases, while the contribution of the regions closer to the surface increases. If these regions have different magnetic permeabilities (we assume that they have the same electrical conductivity), then some features in the form of, for example, inflections should appear in the  $Z(f)$  dependency. Then, it will be possible to estimate the position of the boundaries of the above-mentioned regions by calculating the skin depth corresponding to these features.

We believe that the best way to test these assumptions is a computer modeling and analysis of the impedance frequency dependences and further comparison with experimental results. This work is devoted to modeling and analysis.

The impedance response of the wire was modeled by the finite element method using the COMSOL Multiphysics software package (license no. 9602434). The length of the wire model was 24 mm, its radius  $r_0 = 90 \mu\text{m}$ , and the shell thickness  $a = 15 \mu\text{m}$  (Fig. 1a, inset). Thus, the core radius was  $75 \mu\text{m}$ . The electrical conductivity of both wire regions  $\sigma$  was  $870 \text{ kS/m}$ , the magnetic permeability of the core  $\mu_{\text{core}}$  was 1500. The magnetic permeability of the shell  $\mu_{\text{shell}}$  was varied from 1 to 1500. The wire impedance response was simulated in the AC frequency range from 0.01 to 100 MHz. The frequency dispersion of electrical conductivity and magnetic permeability was not considered. We made sure that the size of the element did not exceed  $\delta$  when constructing a finite element mesh.

Figure 1 shows the  $Z(f)$  dependencies obtained for different values of  $\mu_{\text{shell}}$ . Both axes are given on a logarithmic scale. In all dependencies, one can see an inflection at ac frequencies less than 0.1 MHz. The dependencies obtained when  $1 < \mu_{\text{shell}} < \mu_{\text{core}}$  also have a second inflection at higher frequencies.

The noted features of the dependencies  $Z(f)$  are well revealed using the second derivative  $D = d^2(\ln Z)/d(\ln f)^2$ , which was calculated by the three-point method (Fig. 1b). There are  $D$  maxima at the inflection points. The greater difference between  $\mu_{\text{shell}}$  and  $\mu_{\text{core}}$ , the better the second maximum is expressed.

The skin depth  $\delta$  was calculated using the expression for the cylindrical conductor impedance [3]. We found that the first maximum of the  $D(f)$  dependency corresponds to  $\delta \approx r_0$ , and the second one corresponds to  $\delta \approx a$ .

In our opinion, it is a promising result. Using this approach, it is possible to estimate the position of the boundaries of the wire regions with different magnetic permeabilities, obtaining detailed information about the magnetic structure of the wire.



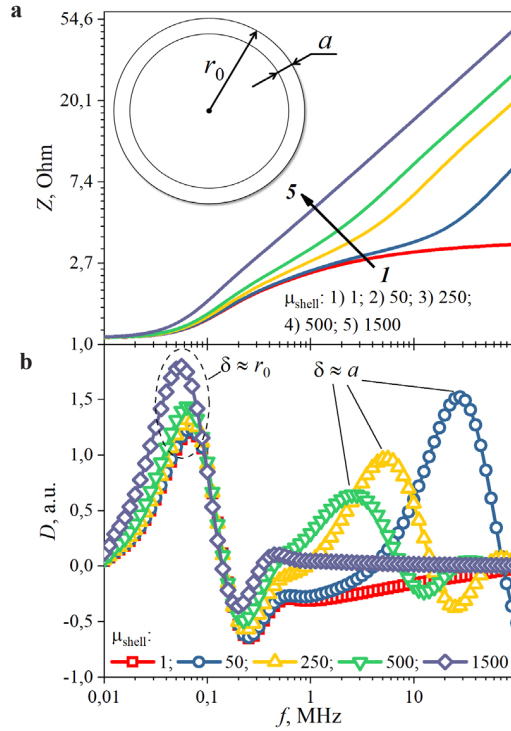


Figure 1. Frequency dependencies of the impedance modulus  $Z$  (a) and the second derivative  $D = d^2(\ln Z)/d(\ln f)^2$  (b).

In the future, we plan to compare the results of the modeling with experimental data, as well as simulate the impedance response when the wire has more than two regions with different magnetic permeability values.

*Support by RSF (project No 22-22-00709, <https://rscf.ru/project/22-22-00709/>) is acknowledged.*

1. N.A. Usov, A.S. Antonov, A.N. Lagar'kov, JMMM., **185**, 159–173 (1998).
2. A.V. Semirov, A.A. Moiseev, D.A. Bukreev et al., PMM., **118**, 535–540 (2017).
3. L.D. Landau, E.M. Lifshitz, Electrodynamics of Continuous Media, Pergamon Press, Oxford (1960).

## EFFECT OF SURFACE LAYER TEMPERATURE ON MAGNETIC HYSTERESIS PROPERTIES OF Nd-Fe-B PERMANENT MAGNETS

*A.S. Cherepanova<sup>1,2\*</sup>, V.E. Maltseva<sup>1</sup>, S.V. Andreev<sup>1</sup>, A.S. Volegov<sup>1</sup>*

<sup>1</sup>Institute of natural sciences and mathematics, UrFU, Ekaterinburg, Russia

<sup>2</sup>Institute of Metal Physics of Ural Branch of Russian Academy of Science, Ekaterinburg, Russia

\*E-mail: [A.S.Cherepanova@inbox.ru](mailto:A.S.Cherepanova@inbox.ru)

The manufacturing of hard magnetic materials by selective laser melting (SLM) is of great interest. An important feature of hard magnetic materials is their microstructure which provides magnetic properties. The samples microstructure obtained by additive manufacturing differs from the microstructure of samples obtained by sintering. In the SLM process, the temperature of the top powder layer contributes significantly to the formation of the microstructure of this layer as well as those below it. In the SLM process temperature control is necessary for the desired microstructure. This problem led to the development of a non-contact temperature sensing system for the 3D printing process.

In this work, we developed and calibrated a device for determining the temperature, and the temperature of the powder layer in the SLM was determined.

Web cameras are one of the devices available for this investigation. However, the autotuning of the camera settings and the lack of manual setting is a problem for its future use. Subsequently, it was chosen the digital camera Levenhuk M500 Base. An optical system including a 12.5 magnification lens and camera body was made to get images. The camera was mounted on a monopod in the build chamber of the 3D printer (Fig. 1).

The measuring unit was calibrated to determine the temperature by the signal intensity of the three color channels (RGB). The oven and a halogen bulb were used for calibration. The internal volume of the furnace was imaged through an observation aperture in the temperature range from 600 to 1100 °C. The RGB intensity values were then determined using the Pipette program. When comparing the color temperature of the furnace with the color temperature of the powder layer in the 3D printing process, the powder layer was found to heat above 1100 °C. Further calibration of the measurement setup was carried out using the induction oven. For calibration used gadolinium with a melting temperature of 1311 °C. The RGB intensities values versus the furnace temperature were plotted in the graph (Fig. 2). The linear fitting was plotted to temperatures above 1100 °C.

The next step was the single-layer sample 3D printing process. Laser beam parameters were variate in the experiment such as power, scan velocity, and laser beam diameter. As a result of exposure to the laser beam, the powder heating process was shot by the camera. Analysis of the image showed



Figure 1. Camera Levenhuk M500 Base in the built chamber of the 3D printer.

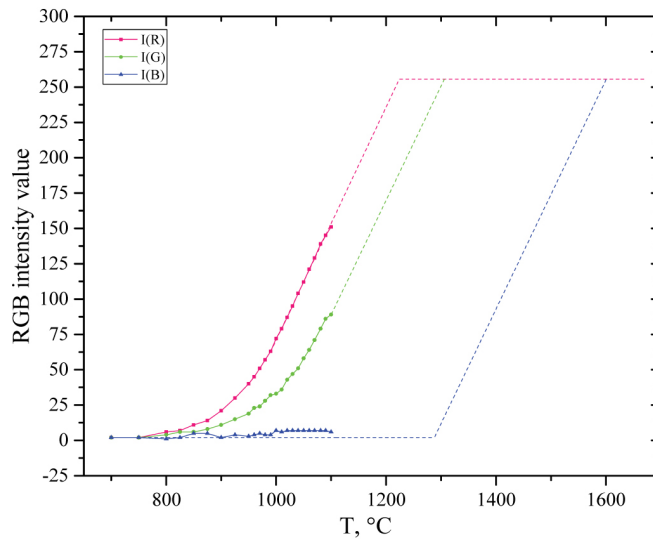


Figure 2. The graph of RGB intensities values versus the oven heating temperature.

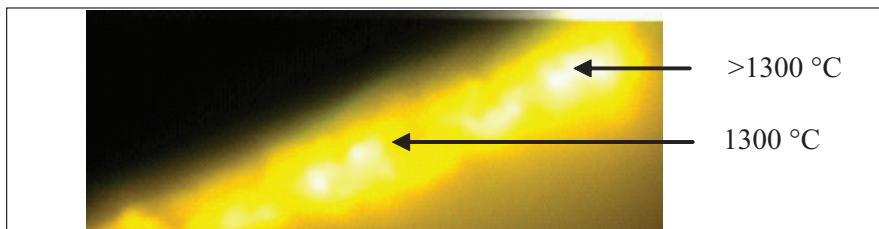


Figure 3. The irregularity of powder layer heating.

that the first line of laser scanning cannot always be detected on the build surface. It depends on the first line temperature and exposure time. If the first line temperature is below 750 °C and the exposure time of the camera is minimal, no glow of the powder layer is observed. After several scanning lines, the data obtained from the camera become more reliable because the powder heating temperature is 1100 °C or more. When determining the surface temperature of the powder layer, the difficulty lies in the non-uniformity of the powder heating (Fig. 3). The studies show the irregularity of the powder heating (Fig. 3) due to the different thermal contact of the powder particles.

The report will demonstrate the effect of temperature on the magnetic properties of magnetically hard materials, as well as the results of simulation the temperature distribution in the layer of powder and permanent magnet.

*A.S.C. is grateful that the research was financially supported under the state assignment of the Ministry of Science and Higher Education of the Russian Federation (topic “Additivity” No. 121102900049-1) – computer simulation. V.E.M., S.V.A., and A.S.V. are grateful to Russian Science Foundation Grant Number 21-72-10104 – powder preparation, additive manufacturing, measurement setup build and calibration, magnetic properties measurements.*

**MAGNETIC PROPERTIES OF HIGH-ENTROPY CERAMICS  $(\text{SmEuGd})_{1-x}\text{M}_x\text{MnO}_3$  ( $\text{M} = \text{LaBa, SrBa AND SrBaCa}$ ) WITH PEROVSKITE STRUCTURE**

*N.A. Cherkasova*<sup>1\*</sup>, *V.E. Zhivulin*<sup>1</sup>, *S.V. Taskaev*<sup>2</sup>, *D.A. Vinnik*<sup>1</sup>, *O.V. Zaitseva*<sup>1</sup>, *E.A. Trofimov*<sup>1</sup>,  
*D.A. Zhrebtsov*<sup>1</sup>, *S.A. Gudkova*<sup>1</sup>

<sup>1</sup>South-Ural State University, SUSU, Chelyabinsk, Russia

<sup>2</sup>Chelyabinsk State University, CSU, Chelyabinsk, Russia

\*E-mail: [Cherkasova.N.A.@yandex.ru](mailto:Cherkasova.N.A.@yandex.ru)

Perovskites with the general formula  $\text{ABO}_3$  attracts much attention due to their physical properties. High-entropy perovskites form a novel group of such substances. Various elements and their combinations can act as cations A and B.

High-entropy manganites with the general formula  $\text{Ln}_{1-x}\text{M}_x\text{MnO}_3$  where Ln – rare earth metal (Sm, Eu, Gd, La and others), M – alkaline earth Sr, Ca, Ba can be expected by the presence of colossal magnetoresistance, inhomogeneous magnetic and charge state, isotopic shift, etc., and also giant magneto-optical effects in IR-range of the spectrum, and therefore deserve careful study.

This work is devoted to the study of the magnetic properties of high-entropy manganites  $(\text{SmEuGdLaBa})\text{MnO}_3$ ,  $(\text{SmEuGdSrBa})\text{MnO}_3$ ,  $(\text{SmEuGdSrBaCa})\text{MnO}_3$ , having equal atomic fractions of each element in the A position.

The synthesis of samples was carried out by the solid-phase sintering. The oxides of manganese ( $\text{MnO}_2$ ), lanthanum ( $\text{La}_2\text{O}_3$ ), samarium ( $\text{Sm}_2\text{O}_3$ ), gadolinium ( $\text{Gd}_2\text{O}_3$ ), europium ( $\text{Eu}_2\text{O}_3$ ), calcium ( $\text{CaO}$ ), as well as barium and strontium carbonates ( $\text{BaCO}_3$ ,  $\text{SrCO}_3$ ) were chosen as the initial components of the charge. The weighed portions of the initial components corresponded to the stoichiometric ratios given by the formula  $(\text{SmEuGd})_{1-x}\text{M}_x\text{MnO}_3$  (where M is a combination of Ba, Sr, Ca). The resulting mixture of oxides and carbonates was ground with an agate mortar for 30 minutes. After

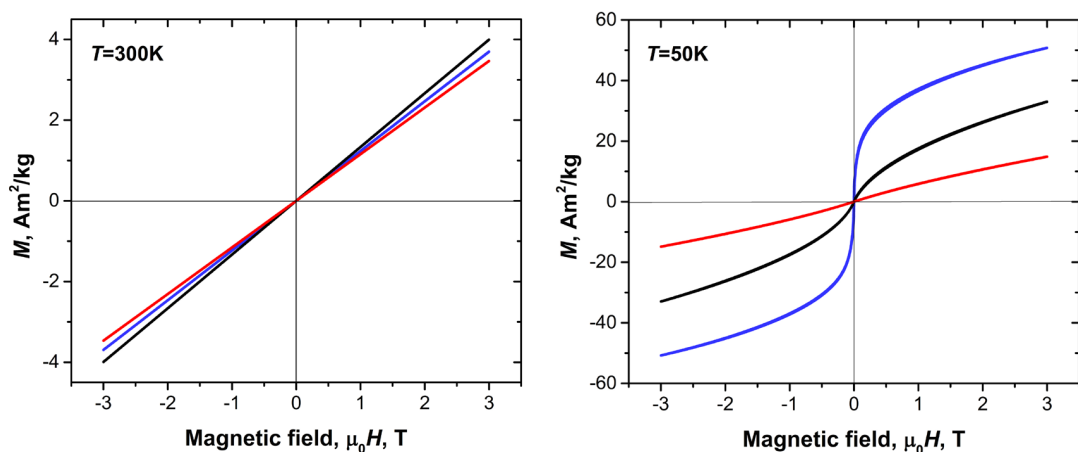


Figure 1. The field dependences of the magnetization of the samples at temperatures of 300 (left) and 50 (right) K. Different colors indicate data for:  $(\text{SmEuGdLaBa})\text{MnO}_3$  (blue),  $(\text{SmEuGdSrBa})\text{MnO}_3$  (black) and  $(\text{SmEuGdSrBaCa})\text{MnO}_3$  (red).

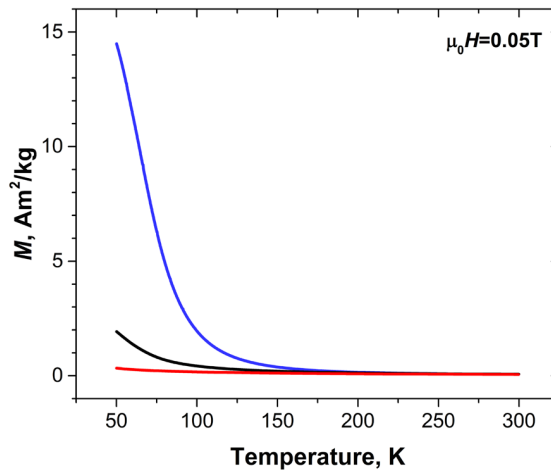


Figure 2. Dependences of magnetization of samples on temperature. Different colors indicate data for: (SmEuGdLaBa)MnO<sub>3</sub> (blue), (SmEuGdSrBa)MnO<sub>3</sub> (black), (SmEuGdSrBaCa)MnO<sub>3</sub> (red).

Table 1. Magnetic characteristics of samples.

Chemical formula	$T_C$ , K	M (50 K), Am <sup>2</sup> /kg
(SmEuGdLaBa)MnO <sub>3</sub>	66	50
(SmEuGdSrBa)MnO <sub>3</sub>	55	30
(SmEuGdSrBaCa)MnO <sub>3</sub>	<50	–

grinding, the mixture was pressed into tablets using a die with a diameter of 8 mm under pressing force of 5 tons. The resulting tablets were sintered at a temperature of 1400 °C for 5 hours.

X-ray phase analysis confirm that all 3 samples are single phase perovskites. The study of the chemical composition showed that the quantitative ratio of the elements is in a good agreement with the initially specified composition.

The magnetic properties were measured using a Versa Lab Quantum Design vibrating magnetometer in the magnetic field range of 0–3 T. Magnetic measurements were carried out in the temperature range of 50–300 K. 300 K (right). Figure 1 shows that at a temperature of 300 K all the samples under study are in the paramagnetic state. When the temperature is lowered to 50 K, two samples pass into the ferromagnetic state. According to the measurement data of the temperature dependence of the magnetic moment (Fig. 2) the temperatures of the magnetic phase transition (Curie temperature) were determined as well as saturation magnetization at a temperature of 50 K (Table 1).

New high-entropy oxides with the perovskite structure were obtained for the first time by the solid-phase sintering. Their magnetic characteristics have been studied. The temperatures of the magnetic phase transition and the saturation magnetization are diminishing upon increasing of average oxidation state of Mn from (SmEuGdLaBa)MnO<sub>3</sub> to (SmEuGdSrBaCa)MnO<sub>3</sub>.

*This work was supported by the Russian Science Foundation (project no. 19-73-10046).*

## INTERLAYER COUPLING AND COERCIVITY OF SANDWICH STRUCTURES PRODUCED BY CHEMICAL DEPOSITION

*A.V. Chzhan*<sup>1\*</sup>, *V.A. Orlov*<sup>2,3</sup>

<sup>1</sup>Krasnoyarsk State Agrarian University, Krasnoyarsk, Russia

<sup>2</sup>Siberian Federal University, Krasnoyarsk, Russia

<sup>3</sup>Kirensky Institute of Physics, Federal Research Center KSC SB RAS, Krasnoyarsk, Russia

\*E-mail: [avchz@mail.ru](mailto:avchz@mail.ru)

As established in sandwich structures with two Co-P magnetic layers, obtained by chemical deposition [1], an anomalous decrease of coercivity  $H_C$  is observed at small thicknesses of the non-magnetic layer of amorphous Ni-P [2]. The  $H_C$  drop is observed both in asymmetric films containing hard magnetic-soft magnetic layers and in the symmetric films with two soft magnetic layers (Fig. 1).

The loop shift  $H_D$  disappears in the thickness range of 2–4 nm. In the same area a minimum of the coercivity is observed. In this paper, we propose a theoretical justification of the mechanism for changing the loop shift and coercivity, which is associated with interlayer coupling.

Let us consider a model of a three-layer ferromagnetic-nonmagnetic-ferromagnetic system with a paramagnetic layer thickness  $t$ . The energy functional of such a system can be represented as:

$$E = \frac{1}{2} \int \left[ \frac{J_1}{a} (\nabla M)^2 + \frac{J_2}{a^3} M^2 \right] dV = \frac{1}{2} S \int \left[ \frac{J_1}{a} (\nabla M)^2 + \frac{J_2}{a^3} M^2 \right] dx, \quad (1)$$

where  $S$  is the interface area,  $J_1$  is the exchange constant,  $a$  is the interatomic distance,  $J_2$  is the intraatomic exchange constant, and  $M$  is the magnetization.

Integration (1) should be carried out over the volume of the entire sample. But, if we assume that  $t \ll \sqrt{S}$ , then calculation (1) can be reduced to a single integral over the  $x$  coordinate.

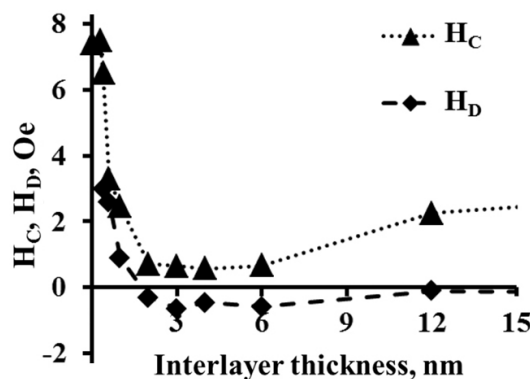


Figure 1. The dependence of coercivity and loop shift of symmetric films on the nonmagnetic layer thickness.

The extremum of functional (1) is realized when the magnetization distribution is described by the function:

$$M(x) = m_{01}e^{\xi x} + m_{02}e^{-\xi x}, \quad (2)$$

where the constants  $m_{01}$  and  $m_{02}$  are determined by the boundary conditions.

To estimate the effective exchange coupling parameter between the magnetic subsystems of ferromagnetic layers, two extreme cases are considered: 1) the magnetizations of the magnetic layers are parallel, 2) the magnetizations are antiparallel. The magnetization distributions in the paramagnetic layer for these cases take the form:

$$M_{\text{fm}} = M_0 \frac{\cosh(\xi x)}{\cosh\left(\xi \frac{t}{2}\right)}, \quad M_{\text{afm}} = M_0 \frac{\sinh(\xi x)}{\sinh\left(\xi \frac{t}{2}\right)}, \quad (3)$$

where  $\xi^2 = \frac{J_2}{J_1 a^2}$ .

Then for the energies from (1) we get:

$$E_{\text{fm}} = \frac{SJ_1 \xi M_0^2}{a} \tanh\left(\xi \frac{t}{2}\right), \quad E_{\text{afm}} = \frac{SJ_1 \xi M_0^2}{a} \frac{1}{\tanh\left(\xi \frac{t}{2}\right)}. \quad (4)$$

The effective exchange constant is estimated from the relationship:

$$J_{\text{eff}} = \frac{E_{\text{eff}}}{S} \approx E_{\text{afm}} - E_{\text{fm}} = \frac{J_1 \xi M_0^2}{a} \left[ \frac{1}{\tanh\left(\xi \frac{t}{2}\right)} - \tanh\left(\xi \frac{t}{2}\right) \right] = \frac{2J_1 \xi M_0^2}{a \sinh(\xi t)}. \quad (5)$$

Taking into account (5), the expression for the loop shift is obtained:

$$H_D(t) = \frac{J_{\text{eff}}}{M_0 t_F} \approx \frac{2J_1 \xi M_0}{t_F a} \frac{1}{\sinh(\xi t)}. \quad (6)$$

Qualitative dependence (6) agrees with the experimental results (see Fig. 1). Here is also quantitative agreement. Indeed, the parameter is of the order of [3] and for nickel compounds, respectively  $\xi \approx 1/0.35 \text{ nm}^{-1}$ . The characteristic thickness of the paramagnetic layer  $t_0$ , on which HD drops by about a factor of three, is determined from the equation:  $\sinh(\xi t_0) = 3$ . In this case  $t_0 \approx 0.64 \text{ nm}$ , which is in good agreement with the measurement results (Fig. 1).

Summing up, we note that the interaction of ferromagnetic layers in the three-layer system under consideration has the nature of an exchange arising due to the interaction between the nearest atoms in the interlayer. Despite the short-range and weak nature of this interaction, a large number of atoms involved in bonds in the ferromagnetic-paramagnetic interface makes this interaction noticeable [4].

1. A.V. Chzhan, V.A. Serezhkin, T.N. Patrusheva, S.A. Podorozhnyak, G.N. Bondarenko, Bulletin of the Russian Academy of Sciences: Phys., **80**, 692–694 (2016).
2. A.V. Chzhan, S.A. Podorozhnyak, A.N. Shahov, D.A. Velikanov, G.S. Patrjn, J. of Phys.: Conference Series, **1389**, 012118 (2019).
3. I.I. Oleinik, E.Y. Tsybmal, D.G. Pettifor, Phys. Rev. B, **62**, 3952–3959 (2000).
4. R. Skomski, A. Kashyap, Y. Qiang, D.J. Sellmyer, J. Appl. Phys., **93**, 6477–6479 (2003).

**TEMPERATURE DEPENDENCE OF ELECTRIC IMPEDANCE OF THE COBALT-BASED SOFT MAGNETIC WIRE NEAR THE FERROMAGNETIC PHASE TRANSITION**

*M.S. Derevyanko\**, D.A. Bukreev, A.A. Moiseev, A.V. Semirov

Department of Physics, Pedagogical Institute, Irkutsk State University, Irkutsk, Russia

\*E-mail: [mr.derevyanko@gmail.com](mailto:mr.derevyanko@gmail.com)

Amorphous and nanocrystalline soft magnetic alloys based on iron and cobalt are of interest for study from both applied and fundamental points of view. Of particular interest is due to the unique combination of high-frequency electrical and soft magnetic properties in them. For example,

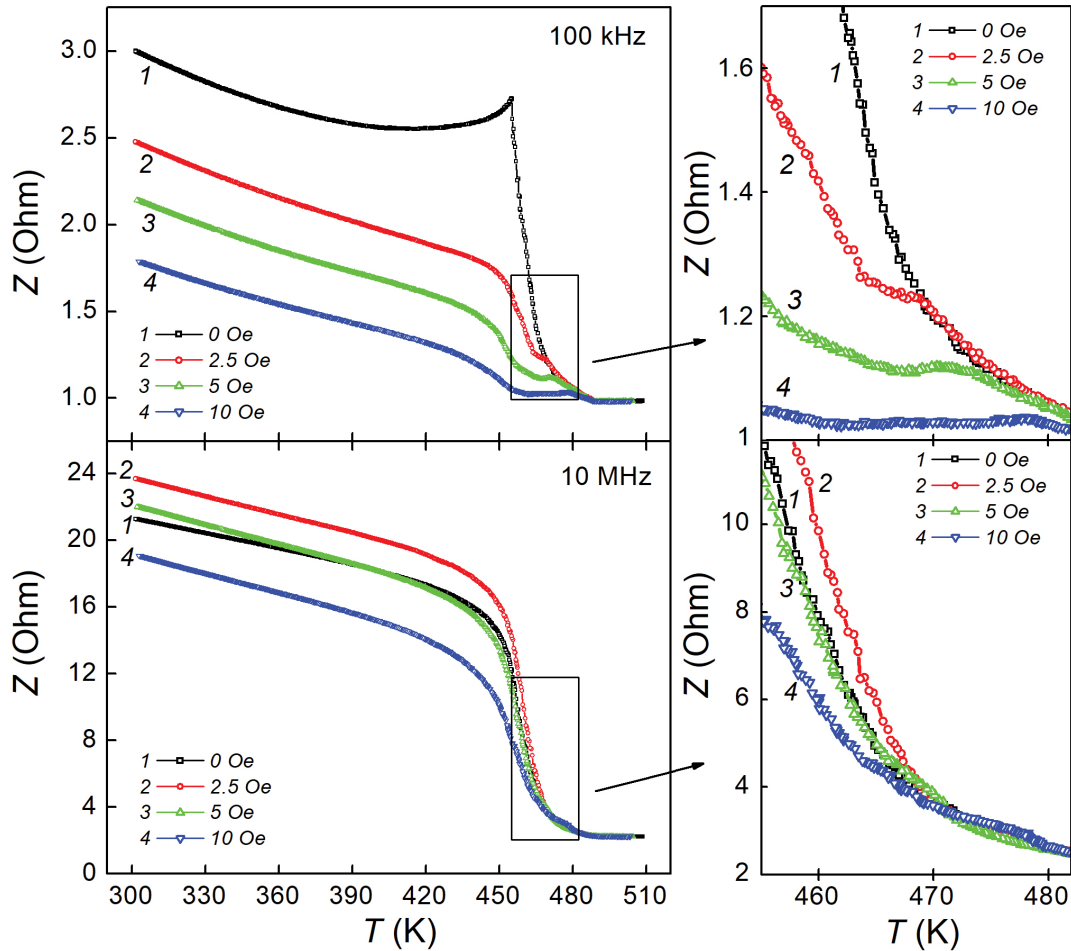


Figure 1. Temperature dependences of the impedance of  $\text{Co}_{66}\text{Fe}_4\text{Nb}_{2.5}\text{Si}_{12.5}\text{B}_{15}$  wires obtained in the external magnetic field of 0, 2.5, 5, and 10 Oe at frequencies of 0.1 and 10 MHz.



the giant magnetoimpedance effect (the change in impedance,  $Z$ , under the action of an external magnetic field) reaches hundreds of percent in such materials [1], which opens up great application prospects. However, in addition to the strong influence of the external magnetic field, the impedance of some ferromagnetic alloys undergoes significant changes when exposed to a temperature. Moreover,  $Z$  reaches the greatest changes in the region of thermally induced phase transitions inherent in alloys [2, 3].

The results of studies of the amorphous alloy  $\text{Co}_{66}\text{Fe}_4\text{Nb}_{2.5}\text{Si}_{12.5}\text{B}_{15}$  samples in the form of segments of cylindrical wires 30 mm long and 180  $\mu\text{m}$  in diameter are presented. The wires are obtained by fast quenching technique from the melt. The saturation magnetization and magnetostriction constant of the samples were about 320 kA/m and  $10^{-7}$ , respectively.

The impedance modulus  $Z$  of the samples was measured in a previously developed automated setup based on Agilent impedance analyzer 4294A and described in [4]. Measurements of  $Z$  were carried out with an alternating current frequency range,  $f$ , of (0.1–100) MHz. The effective value of the current was 1 mA. The impedance measurements were carried out with decreasing temperature in the range from 510 to 295 K. In the same way, the magnetic hysteresis properties were studied by the inductive method.

During the  $Z(T)$  measurements an external magnetic field  $H$  was applied along the longitudinal direction of the wire. Its strength in the experiment was varied from 0 to 10 Oe (Fig. 1).

Figure 1 shows that temperature has a strong effect on the electrical impedance of the wires over the entire frequency range. However, the degree of this influence varies depending on the strength of the applied external magnetic field.

It can be seen that in most cases the impedance undergoes the greatest changes in the temperature range (455–467) K (Fig. 1). This is especially pronounced in the absence of  $H$  at a frequency of 100 kHz. As the frequency increases, this effect also displays itself well in the  $Z(T)$  dependencies obtained with the application of  $H$ .

The inflection observed in the  $Z(T)$  dependencies in the region  $T = 467$  K deserves special attention. This inflection becomes most pronounced when the sample is exposed to the external magnetic field, which is clearly observed in the case of  $f = 100$  kHz (Fig. 1). As the  $H$  increases,

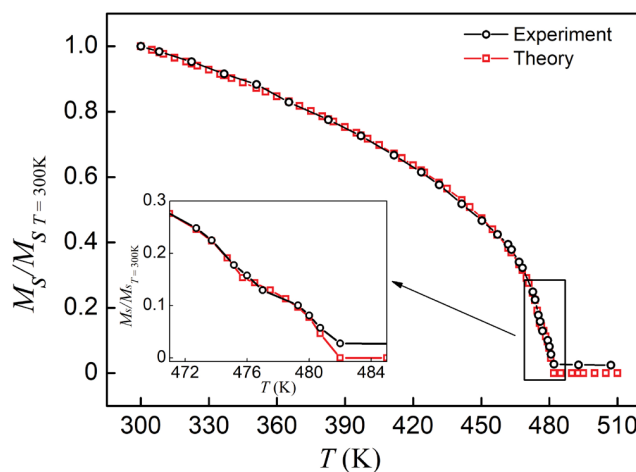


Figure 2. Temperature dependence of the wire saturation magnetization.

the temperature range in which the inflection is observed also increases. But the increase in the ac frequency leads to the decrease in the influence of  $H$  on the inflection.

The change in the impedance of the wires under the action of temperature is due to the temperature change in its magnetization and an effective anisotropy field [2]. In the temperature range under study, their competing influence on the impedance changes. At a frequency of 100 kHz, when the thickness of the skin depth is commensurate with the wire radius, the contribution to the temperature change in the impedance from the magnetization,  $M_S$ , of the entire wire volume will prevail, especially in the presence of  $H$ . Therefore, the inflection in the  $Z(T)$  dependencies can be associated with the presence of two magnetic phases with different Curie temperatures,  $T_C$ .

This conclusion agrees well with the experimental temperature dependence of the wire saturation magnetization (Fig. 2, black markers). It also shows the inflection.

Within the framework of the two-phase model, the experimental dependence  $M_S(T)$  was approximated by a curve described by the expression:

$$M_S(T) = \sum_{i=1}^2 v_i M_{S0i} \left( 1 - \frac{T}{T_{Ci}} \right)^{\beta_i},$$

where  $v_i$ ,  $M_{S0i}$ ,  $T_{Ci}$ ,  $\beta_i$  – volume fraction, saturation magnetization at 0 K, Curie temperature and critical exponent of the  $i$ -th phase, respectively. The maximum value of the correlation coefficient between the experimental and theoretical dependences is 0.9997. It is achieved at a ratio of the volume fraction of the phases of 0.4 and 0.6, while the Curie temperatures of these phases are 475 K and 481 K, respectively.

*Support by RSF (project No 22-22-00709, <https://rscf.ru/project/22-22-00709/>) is acknowledged.*

1. G.V. Kurlyandskaya, A. García-Arribas, J.M. Barandiarán, E. Kisker, Sensors Actuators, A Phys., **91**, 116–119 (2001).
2. M. Kurniawan, R.K. Roy, A.K. Panda, D.W. Greve, P. Ohodnicki, M.E. McHenry, J. Electron. Mater., **43**, 4576–4581 (2014).
3. D.A. Bukreev, M.S. Derevyanko, A.A. Moiseev, A.S. Kuz'mina, G.V. Kurlyandskaya, A.V. Semirov, Phys. Met. Metallogr., **121**, 949–954 (2020).
4. D.A. Bukreev, M.S. Derevyanko, A.A. Moiseev, A.V. Semirov, P.A. Savin, G.V. Kurlyandskaya, Materials (Basel), **13**, 3216 (2020).

## MANUFACTURING OF PERMANENT MAGNETS BASED ON $\text{SmFe}_{11}\text{Ti}$ PHASE BY SELECTIVE LASER SINTERING

*D.S. Neznakhin*<sup>1\*</sup>, *V.E. Maltseva*<sup>1</sup>, *S.V. Andreev*<sup>1</sup>, *N.V. Selezneva*<sup>1</sup>, *E.I. Patrakov*<sup>2</sup>,  
*O.A. Golovnia*<sup>1,2</sup>, *A.S. Volegov*<sup>1</sup>

<sup>1</sup>Ural Federal University, Ekaterinburg, Russia

<sup>2</sup>M.N. Miheev Institute of Metal Physics, Ekaterinburg, Russia

\*E-mail: [D.S.Neznakhin@urfu.ru](mailto:D.S.Neznakhin@urfu.ru)

Permanent magnets are increasingly used in various technical devices. Therefore, the properties of already available materials are constantly being improved to meet the industrial needs. The promising material for permanent magnets are alloys based on the  $\text{SmFe}_{11}\text{Ti}$  phase, which has higher Curie temperature and better intrinsic magnetic properties compared with that of  $\text{Nd}_2\text{Fe}_{14}\text{B}$  phase. Additive technology is a modern and perspective technology for manufacturing of permanent magnets that now attracts more and more attention.

$(\text{Sm}_{1-x}\text{Zr}_x)\text{Fe}_{11}\text{Ti}$  alloys with  $x = 0, 0.1$  and  $0.2$  were obtained from chemically pure elements (99.9%) by induction melting in Ar atmosphere as described in the ref. [1]. The selective laser sintering (SLS) was used as an additive technology. Two powders of  $(\text{Sm}_{1-x}\text{Zr}_x)\text{Fe}_{11}\text{Ti}$  with  $x = 0-0.2$  and the  $\text{Sm}_{75}(\text{Cu},\text{Co})_{25}$  low-melting additive were used for 3D-printing. The additive is used as metallic binder of the hard magnetic particles.

The best results of magnetic properties were obtained for samples based on the  $\text{Sm}_{0.8}\text{Zr}_{0.2}\text{Fe}_{11}\text{Ti}$  alloy (Fig. 1).

SLS allows permanent magnet production based on the  $\text{SmFe}_{11}\text{Ti}$  phase with coercivity close to that obtained in melt-spun ribbons. Heating and cooling that are substantially nonequilibrium and accompanied with high temperature gradients favors the formation of a variety of phases. Some

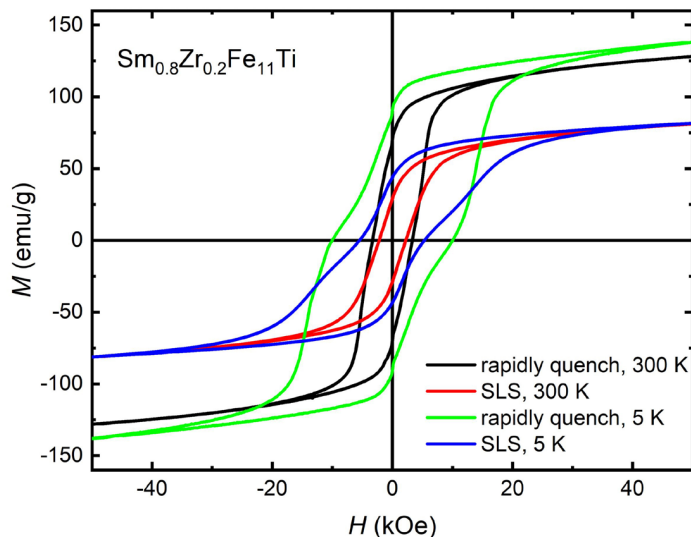


Figure 1. Magnetic hysteresis loops of  $\text{Sm}_{0.8}\text{Zr}_{0.2}\text{Fe}_{11}\text{Ti}$  alloy sample.

of these phases cause deterioration of coercivity. The use of a highly coercive initial powder with an optimally matched binder composition can help manufacturing bulk permanent magnets with industrial values of coercivity.

Detailed results on the phase composition, microstructure, and magnetic properties of the obtained samples will be given in the report.

*The research was financially supported by RSF (Grant Number 21-72-10104).*

1. I.A. Ryzhikhin, S.V. Andreev, M.A. Semkin, N.V. Selezneva, A.S. Volegov, N.V. Kudrevatykh, Journal of Physics: Conference Series, **1389**, 012117 (2019).

## MAGNETIC STATE OF $\text{Fe}_{0.33}\text{TiS}_2$ WITH TRIANGULAR NETWORK OF INTERCALATED Fe ATOMS

*E.M. Sherokalova*<sup>1\*</sup>, *N.V. Selezneva*<sup>1</sup>, *A.S. Volegov*<sup>1</sup>, *N.V. Baranov*<sup>1,2</sup>

<sup>1</sup>Institute of Natural Sciences and Mathematics, Ural Federal University, Ekaterinburg, Russia

<sup>2</sup>M.N. Miheev Institute of Metal Physics, UB of RAS, Ekaterinburg, Russia

\*E-mail: [ElizavetaSherokalova@urfu.ru](mailto:ElizavetaSherokalova@urfu.ru)

The transition-metal (T) dichalcogenides  $\text{TX}_2$  ( $X = \text{chalcogen}$ ) are known as quasi-two-dimensional systems characterized by the strong bonding within  $X\text{-T-X}$  tri-layers and the weak coupling between tri-layers, which makes possible the intercalation by various atoms and molecules and creation of new materials with interesting properties [1]. Intercalation of  $\text{TX}_2$  by M atoms with a magnetic moment can lead to the appearance of various magnetic orderings depending on the type and concentration of intercalated atoms, on the type of matrix compound, and on the distribution of M atoms and vacancies in layers. The indirect RKKY type interaction via conduction electrons and super-exchange interaction via chalcogen atoms are suggested to determine the different magnetic orderings in  $\text{M}_x\text{TX}_2$ .

The present work aims to study how the distribution of Fe atoms and vacancies affects the magnetic state and magnetoresistance behavior of  $\text{Fe}_{0.33}\text{TiS}_2$ . Polycrystalline samples of  $\text{Fe}_{0.33}\text{TiS}_2$  were synthesized by the two-stage solid-phase reaction method. Structural characterization of the obtained samples was done using a Bruker D8 Advance X-ray diffractometer. Neutron powder diffraction (NPD) measurements were performed in magnetic fields up to 5 T by using WAND diffractometer installed at the High Flux Isotope Reactor at Oak Ridge National Laboratory (ORNL). The transversal magnetoresistance was measured by a four-contact *ac* method in magnetic fields up to 10 T.

According to the X-ray analysis the Bragg peaks on diffraction pattern for the  $\text{Fe}_{0.33}\text{TiS}_2$  compound can be indexed in the trigonal singony (space group  $P\bar{3}1c$ ), which indicates the presence of the triangular network and  $\sqrt{3}a_0 \times \sqrt{3}a_0 \times 2c_0$  superstructure ( $a_0$  and  $c_0$  are the lattice parameters of the  $\text{CdI}_2$  type unit cell). The formation of such a superstructure in this compound has also recently been observed using transmission electron microscopy [2]. The magnetic susceptibility of the  $\text{Fe}_{0.33}\text{TiS}_2$  compound is found to exhibit the large difference between ZFC and FC curves below  $\sim 44$  K and the magnetization isotherms show quite smooth behavior. The neutron diffraction measurements on the  $\text{Fe}_{0.33}\text{TiS}_2$  sample at  $T = 2$  K did not reveal any additional magnetic Bragg reflections and substantial changes in the intensity of Bragg nuclear peaks compared to the NPD patterns obtained in the paramagnetic state. Only a broad diffuse maximum was revealed. The absence of a long-range magnetic order in the subsystem of intercalated Fe atoms in  $\text{Fe}_{0.33}\text{TiS}_2$  may be attributed to the frustrations of exchange interactions of different signs due to the formation of a triangular Fe network in the *ab*-plane. This magnetic state of  $\text{Fe}_{0.33}\text{TiS}_2$  differs from that observed in  $\text{Fe}_x\text{TiS}_2$  compounds with lower ( $x = 0.25$ ) and higher ( $x = 0.5$ ) iron concentrations, which exhibit a long-range antiferromagnetic (AFM) order [3, 4] since Fe atoms form chains in these compounds.

The field dependences of MR observed for  $\text{Fe}_{0.33}\text{TiS}_2$  below  $T_f = 44$  K turned out to be quite typical for cluster glass materials unlike AFM ordered compounds which showed a drastic decrease in the resistivity at the field-induced phase transition from AFM to the ferromagnetic state [3, 4].

The results obtained show a strong structural conditionality of the magnetic and transport properties of these quasi two-dimensional compounds.

*The present work was supported by the Russian Science Foundation (Grant No 22-13-00158).*

1. Z. Wang et al., *SmartMat.*, **1**, e1013 (2020).
2. A. Yamasaki et al., *Surface Rev. Lett.*, **9**, 961 (2002).
3. N.V. Baranov et al., *J. Phys.: Condens. Matter*, **25**, 066004 (2013).
4. N.V. Selezneva et al., *Phys. Rev. B*, **104**, 064411 (2021).

## PHASE TRANSITIONS UPON SINTERING OF Nd-Dy-Fe-B POWDERS STUDIED BY IN-SITU DSC

*O.A. Golovnia*<sup>1,2\*</sup>, *L.A. Stashkova*<sup>1</sup>, *A.V. Protasov*<sup>1,2</sup>, *A.V. Ogurtsov*<sup>3</sup>, *M.K. Sharin*<sup>3</sup>, *A.G. Popov*<sup>1,2</sup>,  
*K.A. Kruchinina*<sup>2</sup>, *A.V. Shitov*<sup>1,4</sup>

<sup>1</sup>Mikheev Institute of Metal Physics, Ural Branch, Russian Academy of Sciences, Ekaterinburg, Russia

<sup>2</sup>Ural Federal University, Ekaterinburg, Russia

<sup>3</sup>POZ-Progress Ltd., V. Pyshma, Sverdlovsk region, Russia

<sup>4</sup>Urals Electromechanical Plant, Joint-Stock Company, Ekaterinburg, Russia

\*E-mail: [golovnya@imp.uran.ru](mailto:golovnya@imp.uran.ru)

The sintering processes are an integral part of the powder metallurgy, including modern highly perspective technologies such as additive technology of production of bulk magnets. The main driving force of the sintering is the surface energy. The final density of green compacts is reached by minimization of surface energy. As is known, upon the sintering of the NdFeB and PrFeB magnets, liquid phase appears at 655 and 690 °C, respectively. The formation of this phase favours sintering and increases the rate of compacts densification. First time, the sintering was studied *in-situ* by the dilatometry in 2000s [1]. The sintering consists of the following stages: (1) the abrupt densification by capillary forces after the liquid phase formation; (2) the dissolution of the fraction of small particles, which is accompanied by the active diffusion; (3) the formation of coarse grain carcass due to the large grain growth. Such division is based on the liquid surface tension changes in the liquid phase, which is attributed to the specifics of the dilatometry measurements tracing the sample volume.

The phase formation was studied indirectly after sintering, e.g., by widely spread methods of temperature measurements of structure sensitive properties, i.e., DSC and thermomagnetic analysis [2]. However, the main problem of this methods is that they study already sintered sample, i.e., the phase formation has already finished. The study of the phase formation in powder samples upon the full heating-cooling cycle has not been carried out because of the complexity of sample preparation.

In 2008, M. Sagawa et al. [3] suggested new pressless process which excludes pressing stage (PLP). The combination of this technology with DSC allows study of the sintering and phase formation upon the primary cycle of heating-cooling *in-situ*, as well as numerical characterization of the process, e.g., enthalpy estimation.

In this work, the possibilities of PLP in DSC measurements for *in-situ* study of magnet sintering are demonstrated. Two alloys with different Dy content were studied by DSC, X-ray diffractometry and magnetic properties measurements (Table 1). Magnets were prepared from these alloys by PLP technology and by conventional technology by POZ-Progress Ltd. In addition, a fraction was used to carry out *in-situ* PLP sintering in DSC equipment.

Figure 1 shows two consequent cycles of heating and cooling of a powder Nd-Fe-B sample. Apparently, the primary heating has four characteristic temperatures, i.e., the Curie temperature of the main Nd<sub>2</sub>Fe<sub>14</sub>B phase  $T_C = 318$  °C, melting temperature  $T_M = 867$  °C, temperature of densifica-

Table 1. Alloy content.

Alloys	Nd	Dy	Pr	Fe	Co	B	Al	Ti
11–16	35	0	0	63.48	0	1.02	0.2	0.3
12–16	15	18	0	65.48	0	1.02	0.2	0.3

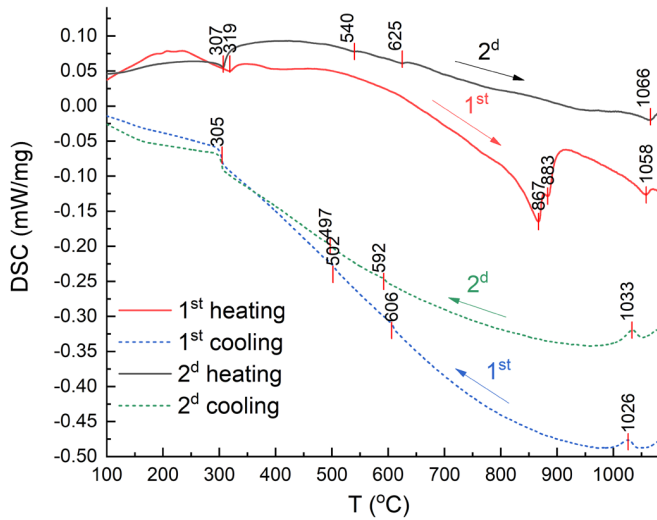


Figure 1. *In-situ* sintering in DSC and secondary cycle of heating and cooling.

tion  $T_D = 883$  °C, melting temperature of fine particles of the main phase  $T_2 = 1058$  °C [1]. The shape of the endothermic peak of the main melting is complex and at least includes two peaks, i.e., in the temperature range 700–800 °C and at 867 °C. The secondary heating has peaks typical of sintered permanent  $\text{Nd}_2\text{Fe}_{14}\text{B}$  magnets: the Curie temperature of  $\text{Nd}_2\text{Fe}_{14}\text{B}$   $T_C = 305$  °C, eutectic peak  $T_{E1} = 540$  °C, triple eutectic peak  $T_{E2} = 625$  °C [4], and melting peak of the main grain phase  $T_4 = 1066$  °C.

Apparently, primary and secondary DSC heating cycles are different processes. The former describes powder sintering, and the latter, permanent magnet heating. Compared to dilatometric measurements, DSC provides more detailed information, precise temperatures of phase transitions, and enthalpies.

*The work is performed within the state assignment of Ministry of Science and Higher Education of the Russian Federation (theme Magnet No. 122021000034-9).*

1. B.E. Davies, R.S. Mottram, and I.R. Harris, *Mater. Chem. Phys.*, **67**, 272 (2001).
2. A.G.G. Popov, O.A.A. Golovnia, and V.A.A. Bykov, *J. Magn. Magn. Mater.*, **383**, 226 (2015).
3. M. Sagawa and Y. Une, in 20th Int. Work. Rare Earth Perm. Magnets Their Appl., (Knossos-Crete, 2008), pp. 103–105.
4. F. Vial, F. Joly, E. Nevalainen, M. Sagawa, K. Hiraga, and K. T. Park, *J. Magn. Magn. Mater.*, **242–245**, 1329 (2002).

## MAGNETIC PROPERTIES OF IRON-DOPED $\text{WTe}_2$ , A WEYL SEMIMETAL

*A.Sh. Khachatryan*<sup>1\*</sup>, *E.V. Charnaya*<sup>2</sup>, *V.V. Marchenkov*<sup>3,4</sup>

<sup>1</sup>Ioffe Institute, St. Petersburg, Russia

<sup>2</sup>Institute of Physics, St. Petersburg State University, St. Petersburg, Russia

<sup>3</sup>Ural Federal University, Ekaterinburg, Russia

<sup>4</sup>Mikheev Institute of Metal Physics, Ekaterinburg, Russia

\*E-mail: [maizr@yandex.ru](mailto:maizr@yandex.ru)

Recently, type II Weyl semimetals  $\text{WTe}_2$  doped with potassium [1] and chromium [2] have been investigated and demonstrated interesting magnetic and transport properties. Low doping with magnetic ions allows the topological properties of the Weyl semimetals to be retained. This can lead to exotic quantum phenomena such as the anomalous or quantum anomalous Hall effects. It attracts close attention to studies of magnetic properties induced by magnetic ions in the diamagnetic matrix of Weyl semimetals.

In our work the magnetic properties of single crystalline  $\text{Fe}_{0.03}\text{W}_{0.97}\text{Te}_2$ , annealed (1 hour) and non-annealed, were studied in comparison with an undoped  $\text{WTe}_2$  single crystal using a Quantum Design MPMS (SQUID-VSM) magnetometer. The field and temperature dependences of dc magnetization were measured. The measurements were performed under the ZFC and FCC protocols at two sample orientations  $c \parallel H$  and  $c \perp H$ . The heat capacity of the  $\text{Fe}_{0.03}\text{W}_{0.97}\text{Te}_2$  crystal was also measured using Quantum Design PPMS-9 + Ever-Cool-II within the temperature range 1.9–302 K in magnetic fields of 0 Oe, 500 Oe, and 1 kOe.

A significant influence of annealing on magnetic properties of the  $\text{Fe}_{0.03}\text{W}_{0.97}\text{Te}_2$  crystal was found. The coexistence of different types of magnetic ordering (ferromagnetic, antiferromagnetic and possibly metamagnetic) was revealed at different temperatures. Temperature-dependent diamagnetism was found in the undoped  $\text{WTe}_2$  crystal, apparently induced by Weyl fermions. In the temperature region corresponded to the paramagnetic state of the iron-doped annealed crystal in the field of 60 kOe the temperature dependence of the magnetic susceptibility was described by the Curie-Weiss law. The negative Weiss temperature was  $-123$  K and the evaluated effective spin indicated the  $+2$  valence state for iron. Heat capacity studies have shown that the Debye temperature for  $\text{Fe}_{0.03}\text{W}_{0.97}\text{Te}_2$  equal to 161 K is close to that for the  $\text{WTe}_2$  single crystal. Magnetic fields 500 Oe and 1 kOe did not noticeably affect the electronic component of the heat capacity.

1. Li Zhu, Qi-Yuan Li et al., *Nano Lett.*, **18**, 6585 (2018).

2. L. Yang, H. Wu et al., *Adv. Funct. Mater.*, **31**, 2008116 (2021).



## TUNING THE MAGNETIC PROPERTIES OF NANOWIRES MADE OF IRON GROUP METALS

*D.R. Khairetdinova*<sup>1,2\*</sup>, *I.M. Doludenko*<sup>2</sup>, *S.A. Lukkareva*<sup>1</sup>, *D.L. Zagorskiy*<sup>2</sup>, *L.V. Panina*<sup>1</sup>

<sup>1</sup>NUST “MISIS”, Moscow, Russia

<sup>2</sup>FSRC “Crystallography and Photonics”, Russian Academy of Sciences, Moscow, Russia

\*E-mail: [hairetdr@gmail.com](mailto:hairetdr@gmail.com)

Ferromagnetic nanowires (NWs) are perspective for various applications, including magnetic memory and spintronics elements, rare-earth-free micromagnets and sensors [1]. Such structures can improve the compactness of devices and can also be used in flexible electronics. Solid solutions based on iron group metals (iron, cobalt, and nickel) in their bulk forms have soft magnetic properties and high values of the saturation magnetization [2]. Decreasing the size and forming 1D-structures can lead to the increase in coercive force ( $H_c$ ), converting them to semihard and hard-magnetic material, while the saturation magnetization ( $M_s$ ) practically remains unchanged. This happens because of shape anisotropy in NWs with axially ordered crystallites.

NWs of various compositions  $\text{Fe}_x\text{Ni}_{1-x}$  and  $\text{Fe}_x\text{Co}_{1-x}$  were synthesized in PETF ion track membranes. To investigate the effect of diameter on magnetic properties of NWs, they were deposited into membranes with different pore size: 30, 65 and 100 nm. The pore density was  $10^8 \sim 1.2 \cdot 10^9$  pore/cm<sup>2</sup> for membranes with 100 nm pore diameter,  $\sim 4.6 \cdot 10^9$  pore/cm<sup>2</sup> for membranes with 65 nm pore diameter, and  $\sim 9 \cdot 10^9$  pore/cm<sup>2</sup> for membranes with 30 nm pore diameter. To control the alloy composition in NWs, the concentrations of metal ions in electrolyte were altered – the technique was given in [3]. The magnetic properties were investigated with the help of vibrating sample magnetometer VM-07. Two orientations of magnetization field were used: field parallel ( $H_{\parallel}$ ) and perpendicular ( $H_{\perp}$ ) to NWs’ axis.

The behaviour of  $H_c$  of NWs of  $\text{Fe}_x\text{Co}_{1-x}$  solid solutions in all the cases had a non-monotonic dependency on Fe content (Fig. 1). For NWs with the diameter of 100 nm, the maximum values of coercivity (340 Oe) were obtained for alloys with approximately 50 at.% of Fe. In the case of

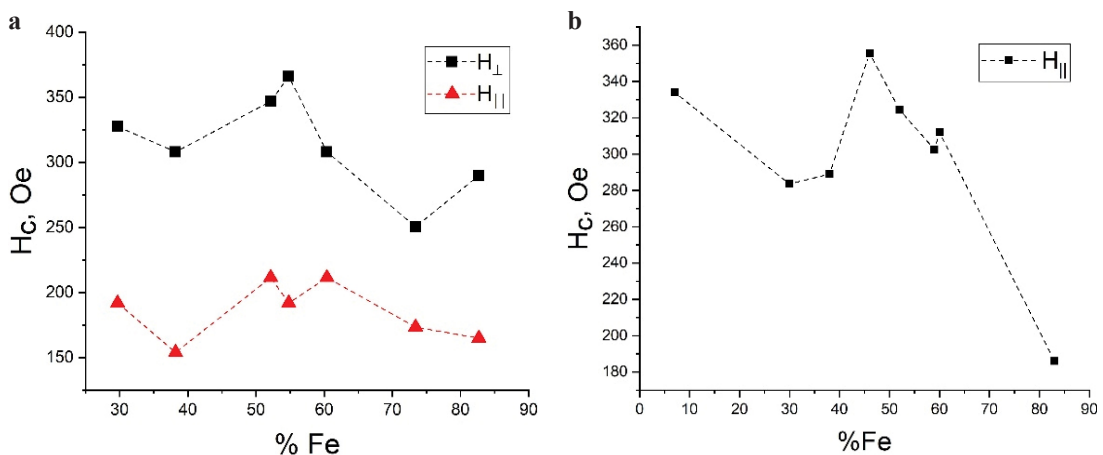


Figure 1.  $H_c$  dependency on Fe content in 100 nm  $\text{Fe}_x\text{Co}_{1-x}$  NWs grown in **a** membranes with the pore density of  $10^9$  pore/cm<sup>2</sup>; **b** membranes with the pore density of  $10^8$  pore/cm<sup>2</sup>.

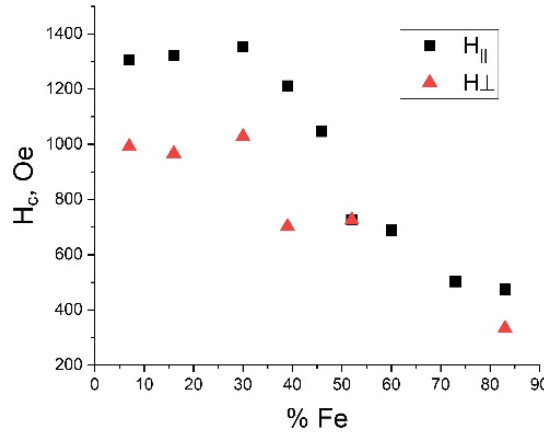


Figure 2.  $H_c$  dependency on Fe content in 30 nm  $Fe_xCo_{1-x}$  NWs.

arrays of NWs with the pore density of  $10^9$  pore/cm<sup>2</sup>, there was no distinct easy magnetization axis and larger values of  $H_c$  were observed for the magnetizing field in the direction, perpendicular to the NWs' axis, while the squareness coefficient ( $M_r/M_s$ ,  $M_r$  is the remanence magnetization) was below 0.25. This can be explained by the effect of magnetostatic interaction between the NWs prevailing over the shape anisotropy.

For the case of NWs of 30 nm in diameter,  $H_c$  values drastically increased (Fig. 2), and the maximum value of 1350 Oe was observed for NWs of 30 at.% of Fe for the parallel field magnetization. In this case, higher squareness coefficients were obtained and pronounced easy and hard magnetization axes were formed, confirming the dominating role of the shape anisotropy in overall magnetic anisotropy.

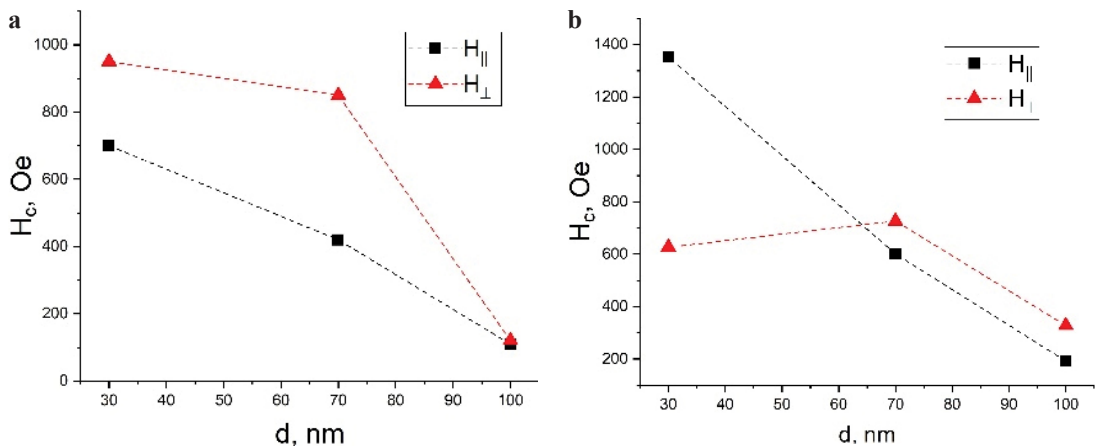


Figure 3.  $H_c$  dependency on diameter of NWs for **a**  $Fe_{0.3}Co_{0.7}$ ; **b**  $Fe_{0.24}Ni_{0.76}$ .

The decrease in the NW diameter of both compositions  $\text{Fe}_x\text{Ni}_{1-x}$  and  $\text{Fe}_x\text{Co}_{1-x}$  led to an increase in  $H_c$  (Fig. 3). For NWs of  $\text{Fe}_{0.24}\text{Ni}_{0.76}$ , the value of  $H_c$  increased from 120 Oe to 950 Oe when the diameter decreased from 100 nm to 30 nm (for the perpendicular magnetization).

For both cases such an effect can be explained by the axial structure, the dominance of shape anisotropy and remagnetisation by a coherent rotation. However, in  $\text{Fe}_{0.24}\text{Ni}_{0.76}$  samples there was no change in the orientation of the easy magnetization axis: larger values of  $H_c$  were obtained when the field was applied perpendicular to the axis, while for  $\text{Fe}_{0.3}\text{Co}_{0.7}$  samples the formation of a distinct easy magnetization axis was formed for NWs with a diameter of 30 nm. This may be due to the differences of the crystalline structure of materials. The other factor is related with the highest value of  $M_s$  for this composition, and hence, more pronounced shape anisotropy.

In conclusion, the maximum  $H_c$  in NWs of  $\text{Fe}_x\text{Co}_{1-x}$  and  $\text{Fe}_x\text{Ni}_{1-x}$  compositions was obtained when the diameter was decreased down to 30 nm presumably owing to the axial orientation of crystallites, shape anisotropy and rotational mode of remagnetization.

*The obtaining of nanowires was done within State task of FRSC “Crystallography and Photonics”. The analysis of magnetic measurements was supported by Russian Science Foundation (Project No. 21-72-30032). The magnetic measurements were held on the base of NUST “MISIS”.*

1. X.F. Han, S. Shamaïla and R. Sharif, in N. Lupu (ed.), *Electrodeposited Nanowires and Their Applications*, InTech, p. 228, (2010)
2. N. Mansouri, N. Benbrahim-Cherief, E. Chainet et al., *J. Magn. Magn. Mater.*, **493**, 165746 (2020).
3. I. Doludenko, D. Zagorski, K. Frolov et al., *Phys. Solid State*, **62**, 1639–1646 (2020).

## MAGNETIC PROPERTIES AND MICROSTRUCTURE OF $\text{Sm}_2\text{Fe}_{17}\text{N}_3$ POWDERS AFTER MILLING IN DIFFERENT TYPE MILLS

*D.A. Kolodkin*<sup>1\*</sup>, *A.G. Popov*<sup>1,2</sup>

<sup>1</sup>M.N. Miheev Institute of Metal Physics of Ural Branch of Russian Academy of Sciences, Ekaterinburg, Russia

<sup>2</sup>Institute of Natural Sciences and Mathematics, Ural Federal University, Ekaterinburg, Russia

\*E-mail: [kolodkin@imp.uran.ru](mailto:kolodkin@imp.uran.ru)

Anisotropic  $\text{Sm}_2\text{Fe}_{17}\text{N}_3$  powders are the most promising materials for the production of resin-bonded magnets or spark plasma-sintered magnets [1–3]. Such powders are synthesized by nitriding of initial  $\text{Sm}_2\text{Fe}_{17}$  alloys made by strip-casting method or by the reduction diffusion method. To manufacture an anisotropic Sm-Fe-N magnet with a high residual magnetic induction  $B_r$  and coercivity  $H_c$ , submicron powders with a particle size approaching the critical single domain size ( $D_c \sim 0.3 \mu\text{m}$ ) are usually required. Thus, the milling process becomes a key one for obtaining anisotropic ultrafine Sm-Fe-N powders. In this work, a comparative study of the influence of the milling process parameters of Sm-Fe-N powders on their magnetic properties and microstructure during milling in three types of ball mills: vibratory (VM), centrifugal (CM) and planetary (PM) is carried out. The milling processes in these mills differ in terms of both the predominant deformation mechanism (impact for VM, shear for CM, and impact-shear for PM) and degree of energy impact.

The initial alloy  $\text{Sm}_2\text{Fe}_{17}$  was produced by the strip-casting method. To obtain a nitrided powder, the alloy was preliminarily mechanically crushed to an average particle size of  $\sim 50 \mu\text{m}$  and then nitrided in  $\text{H}_2$  and  $\text{N}_2$  mixture at  $500 \text{ }^\circ\text{C}$  [4]. Nitrided  $\text{Sm}_2\text{Fe}_{17}\text{N}_3$  powders were milled in VM, CM and PM in a protective medium of acetone with the addition of surfactants (mixture of methyl caproate  $\text{C}_7\text{H}_{14}\text{O}_2$  and siloxane  $\text{Si}(\text{OC}_2\text{H}_5)_4$ ) [5].

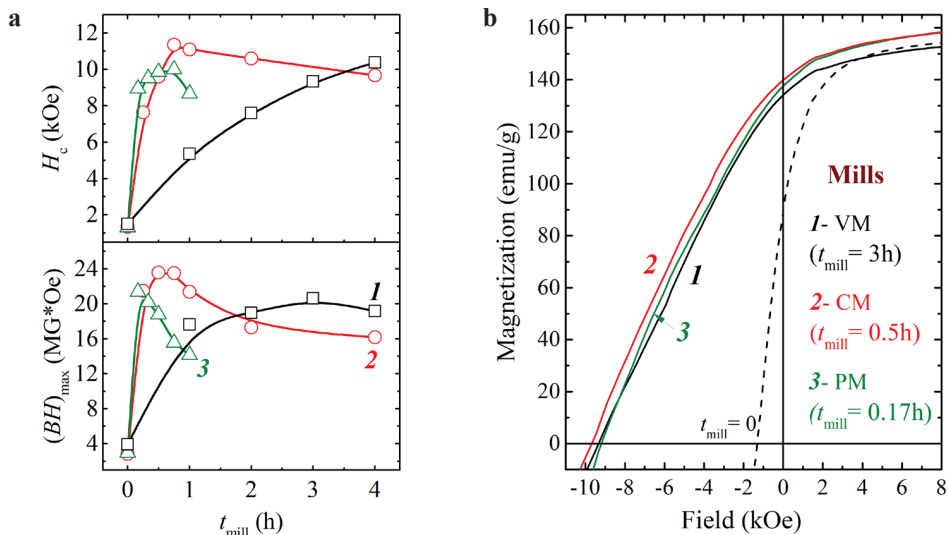


Figure 1. Dependences of  $H_c$  and  $(BH)_{\text{max}}$  on milling time  $t_{\text{mill}}$  (a) and magnetization reversal curves (b) of  $\text{Sm}_2\text{Fe}_{17}\text{N}_3$  powders after milling in VM (1), CM (2) and PM (3).

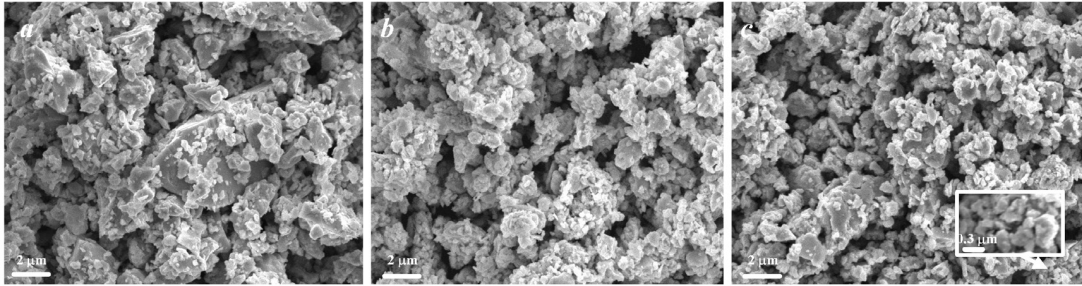


Figure 2. SEM images of milled powder in acetone medium with addition of surfactants: 1% methyl caproate + 1% siloxane. **a** VM (3 h); **b** CM (0.75 h); **c** PM (0.17 h).

Figure 1a shows the dependences of  $H_c$  and the maximum energy product  $(BH)_{\max}$  of  $\text{Sm}_2\text{Fe}_{17}\text{N}_3$  powders on the milling time  $t_{\text{mill}}$  in VM, CM and PM. The maxima of  $(BH)_{\max}$  shift towards lower values of  $t_{\text{mill}}$  with an increase in the energy intensity of the mills. For VM, CM and PM the maximum values  $(BH)_{\max} = 20.6, 23.6$  and  $21.4 \text{ MG}\cdot\text{Oe}$  were obtained for  $t_{\text{mill}} = 3 \text{ h}, 0.75 \text{ h}$  and  $0.17 \text{ h}$ , respectively. Magnetization reversal curves of powders with maximum values of  $(BH)_{\max}$  are shown in Fig. 1b.

Figure 2 shows SEM images of the microstructure of  $\text{Sm}_2\text{Fe}_{17}\text{N}_3$  powders which show the maximum values of  $(BH)_{\max}$  after milling in VM, CM and PM. From the comparison of SEM images it follows that the most uniform powder milling is achieved in CM. The powder milled in VM (Fig. 2a) contains a large number of particles larger than  $2 \mu\text{m}$ . This is the reason for low  $H_c$  values after long milling times (Fig. 1a). On the other hand, milling in PM is accompanied by the formation of a large number of conglomerates of very small particles (inset in Fig. 2c) despite the fact that the most intensive milling of the powder in PM makes it possible to obtain the maximum value  $(BH)_{\max}$  in a short time (0.17 h). However, with an increase in the milling time the formation of conglomerates and increasing particle defects become more active. Both of these factors prevent the rotation of the easy magnetization axes of powder particles along the direction of the magnetic field during texturing and, thereby, significantly worsen the squareness of the magnetization reversal curves.

Thus, as a result of a comparative study of the milling of Sm-Fe-N powders in vibratory, centrifugal and planetary mills, it was shown that the most uniform distribution of powder particles in size and the lowest content of particle conglomerates in the total volume is achieved for milling in a centrifugal mill. In this case, the proportion of powder particles with a size close to the size of a single-domain state exceeds 70%. Milling with the addition of a two-component surfactant yielded powders with a modified particle surface having a coercive force  $H_c \geq 9.6 \text{ kOe}$ , a saturation magnetization  $4\pi M_s \geq 140 \text{ emu/g}$  and a maximum energy product  $(BH)_{\max} \geq 23.6 \text{ MG}\cdot\text{Oe}$ .

*This work was supported by the state assignment of Ministry of Science and Education of Russia [topic “Magnet” No. AAAA-A18-118020290129-5].*

1. M. Matsuura, Y. Nishijima, N. Tezuka, S. Sugimoto, T. Shoji, N. Sakuma, *J. Magn. Magn. Mater.*, **467**, 64 (2018).
2. D. Prabhu, H. Sepehri-Amin, C.L. Mendis, T. Ohkubo, K. Hono, S. Sugimoto, *Scripta Materialia*, **67**, 153 (20X.B. Ma, L.Z. Li, S.Q. Liu, B.Y. Hu, J.Z. Han, C.S. Wang, H.L. Du, Y.C. Yang, J.B. Yang, *J. Alloys Compd.*, **612**, 153103 (2014).
3. D.A. Kolodkin, A.G. Popov, A.V. Protasov, V.S. Gaviko, D.Yu. Vasilenko, S. Kavita, D. Prabhu, R. Gopalan, *J. Magn. Magn. Mater.*, **518**, 167416 (2021).
4. D.A. Kolodkin, A.G. Popov, V.S. Gaviko, *Physics of Metals and Metallography*, **122**, 547 (2021).

**CANTED FERROMAGNETS IN DOPED GdTSi SYSTEMS**

*A.G. Kuchin<sup>1\*</sup>, S.P. Platonov<sup>1</sup>, R.D. Mukhachev<sup>1,2</sup>, A.V. Lukoyanov<sup>1,2</sup>,  
 A.S. Volegov<sup>1,2</sup>, V.S. Gaviko<sup>1,2</sup>, M.Yu. Yakovleva<sup>1</sup>*

<sup>1</sup>Institute of Metal Physics UB RAS, Ekaterinburg, Russia

<sup>2</sup>Ural Federal University, Ekaterinburg, Russia

\*E-mail: [kuchin@imp.uran.ru](mailto:kuchin@imp.uran.ru)

The GdTSi intermetallic compounds crystallize in the tetragonal CeFeSi-type structure ( $P4/nmm$ ) which is built from alternating (001) layers with the sequence: Gd-Si-T2-Si-Gd-Gd-Si-T2-Si-Gd (T = Ti, Mn, Fe, Co) [1]. The hybridization between Si p and T 3d states causes the absence of

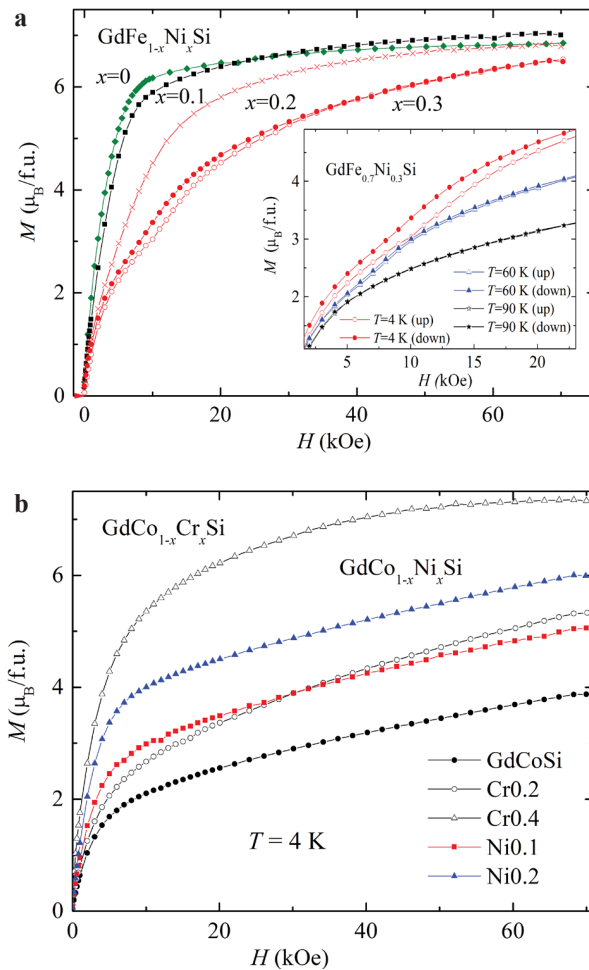


Figure 1. Magnetization curves  $M(H)$  at  $T = 4$  K of free powder samples of the compounds: **a**  $\text{GdFe}_{1-x}\text{Ni}_x\text{Si}$ ,  $x = 0-0.3$  and **b**  $\text{GdCo}_{1-x}\text{Cr}_x\text{Si}$ ,  $x = 0-0.4$ ,  $\text{GdCo}_{1-x}\text{Ni}_x\text{Si}$ ,  $x = 0.1, 0.2$ . The Inset in **a** shows the low-field part of  $M(H)$  for  $x = 0.3$  at  $T = 4, 60, 90$  K on a larger scale.

the magnetic moment of Fe or Co in the GdTSi compound. It is of interest to study the magnetic and magnetothermal properties of the  $\text{GdM}_{1-x}\text{T}_x\text{Si}$  substitutional alloys with  $M = \text{Co}, \text{Fe}, \text{T} = \text{Ti}, \text{Cr}, \text{V}, \text{Ni}$  with different atomic radii and the number of 3d electrons.

It was found that the Curie temperature  $T_C$  sharply increases from 130 K to 255 K and 250 K for  $\text{GdFe}_{1-x}\text{Cr}_x\text{Si}$  and  $\text{GdFe}_{1-x}\text{V}_x\text{Si}$  and decreases to 98 K for  $\text{GdFe}_{1-x}\text{Ni}_x\text{Si}$  when  $x$  changes from 0 to 0.5, 0.3, and 0.3, respectively. This result is explained within the framework of the mechanism proposed to explain a similar sharp increase of  $T_C$  up to 185 K in the  $\text{GdFe}_{1-x}\text{Ti}_x\text{Si}$ ,  $x = 0-0.1$  system [2]. Calculations of the electronic structure indicated that the Fermi level  $E_F$  for GdFeSi is localized on the right slope of the density of states  $N(E)$  peak [2]. In the rigid band shift method, when Fe is replaced by Ti [2], V, Cr or Ni in GdFeSi,  $E_F$  shifts to the left or to the right along the slope due to the smaller or larger number of 3d electrons in the Ti (2), V (3), Cr (5) or Ni (8) atoms compared to the Fe (6) atom. As a result, the density of states at the Fermi level  $N(E_F)$  and, therefore,  $T_C$  in the  $\text{GdFe}_{1-x}\text{T}_x\text{Si}$  systems increases with  $\text{T} = \text{Ti}, \text{V}, \text{Cr}$  or decreases with  $\text{T} = \text{Ni}$ , within the framework of the model of effective d–f exchange interaction in R-3d metal intermetallics, in which  $T_C \sim N(E_F)$  [3]. The Curie temperature decreases from 167 K to 145 K and 150 K for  $\text{GdCo}_{1-x}\text{Cr}_x\text{Si}$  and  $\text{GdCo}_{1-x}\text{Ni}_x\text{Si}$  when  $x$  changes from 0 to 0.6 and 0.2, respectively. Presumably, a canted ferromagnetic structure is formed in the  $\text{GdFe}_{1-x}\text{Ni}_x\text{Si}$  ( $x = 0.2, 0.3$ ),  $\text{GdCo}_{1-x}\text{Cr}_x\text{Si}$  ( $x = 0 [4] - 0.3$ ),  $\text{GdCo}_{1-x}\text{Ni}_x\text{Si}$  ( $x = 0.1, 0.2$ ) systems, while  $\text{GdCo}_{1-x}\text{Cr}_x\text{Si}$ ,  $x = 0.4$  is almost collinear ferromagnet as is seen from Fig. 1. This structure can be caused by chaotic localization of crystal electric fields arising due to different electric charges of Fe, Co, Cr, Ni ions. The weakening of the Gd-Gd exchange interactions in the  $\text{GdFe}_{1-x}\text{Ni}_x\text{Si}$ ,  $\text{GdCo}_{1-x}\text{Ni}_x\text{Si}$ ,  $\text{GdCo}_{1-x}\text{Cr}_x\text{Si}$  systems contributes to the appearance of the canted ferromagnetic structure.

*Support by RSF 18-72-10098, <https://rscf.ru/en/project/18-72-10098/> is acknowledged.*

1. S. Gupta, K. Suresh, J. Alloys Compd., **618**, 562–606 (2015).
2. A.G. Kuchin, S.P. Platonov, A.V. Lukoyanov, A.S. Volegov, V.S. Gaviko, R.D. Mukhachev, M.Yu. Yakovleva, Intermetallics, **133**, 107183 (6) (2021).
3. A. Cyrot, M. Lavagna, J. de Phys., **40**, 763–771 (1979).
4. S.A. Nikitin, T.I. Ivanova, I.G. Makhro, Yu.A. Tskhadadze, J. Magn. Magn. Mater., **157/158**, 387–388 (1996).

## MAGNETIC PROPERTIES AND STRUCTURE OF THE ALLOY $\text{Fe}_{63.5}\text{Ni}_{10}\text{Cu}_1\text{Nb}_3\text{Si}_{13.5}\text{B}_9$ WITH INDUCED MAGNETIC ANISOTROPY

*V.A. Lukshina\**, *N.V. Dmitrieva*, *E.G. Volkova*, *D.A. Shishkin*

Miheev Institute of Metal Physics, UB RAS, Ekaterinburg, 620108 Russia

\*E-mail: [lukshina@imp.uran.ru](mailto:lukshina@imp.uran.ru)

In the alloy  $\text{Fe}_{63.5}\text{Ni}_{10}\text{Cu}_1\text{Nb}_3\text{Si}_{13.5}\text{B}_9$ , which is conventional FINEMET with Fe replaced by 10 at.% Ni, the effects of the temperature and time of nanocrystallizing annealing (NA) in the presence of tensile stresses (stress annealing, SA) on the magnetic properties, magnetic anisotropy, and structure are considered. The magnetic state of ribbon samples 100 mm in length was controlled with hysteresis loops measured in fields up to the 16 kA/m along the long side of the sample in open magnetic circuit with an F-190 galvanometric compensation microfluxmeter. The alloy structure was studied via transmission electron microscopy (TEM) with a JEM 200CX electron microscope. The data for the calculation of the average grain size and grain-size-distribution histograms were determined from dark-field images. The grain size was determined with the linear-intercept method; 300 grains were counted for each sample.

It is known [1, 2] that the addition of 10 at.% nickel to the nanocrystalline  $\text{Fe}_{73.5}\text{Cu}_1\text{Nb}_3\text{Si}_{13.5}\text{B}_9$  alloy does not affect the magnetic anisotropy induced during SA. As in conventional FINEMET, transverse magnetic anisotropy of the easy-plane type is induced. After NA and SA at 520 °C, the phase composition of the considered samples is determined by the treatment duration. Upon crystallization, nanocrystals of the  $\alpha$ -(Fe,Ni)Si solid solution and  $\text{Fe}_3\text{Si}$  form in the alloy, both in the presence and absence of tensile stresses, upon an increase in the annealing duration from 10 min to 1 h. Further annealing for 1–4 h facilitates the formation of the tetragonal  $\text{Fe}_3\text{NiSi}_{1.5}$  phase. It was demonstrated that there is a correlation between the structural state (phase composition) of the  $\text{Fe}_{63.5}\text{Ni}_{10}\text{Cu}_1\text{Nb}_3\text{Si}_{13.5}\text{B}_9$  alloy and its magnetic properties and type of induced magnetic anisotropy (IMA). Thus, the formation of nanocrystals of  $\alpha$ -(Fe,Ni)Si solid solution and  $\text{Fe}_3\text{Si}$  with negative magnetostriction is the reason for the appearance of transverse magnetic anisotropy in the alloy upon nanocrystallizing annealing in the presence of tensile stresses. The tetragonal  $\text{Fe}_3\text{NiSi}_{1.5}$  phase, which appears in the course of annealing for 1–4 h, increases the coercivity of the considered alloy samples. The goal of this work was to study the magnetic properties, magnetic anisotropy, and structure of the alloy  $\text{Fe}_{63.5}\text{Ni}_{10}\text{Cu}_1\text{Nb}_3\text{Si}_{13.5}\text{B}_9$ , which was nanocrystallized in the presence of tensile stresses ( $\sigma$ ) in a temperature range of 480–550 °C. Magnetic properties after SA at different temperature and time of treatment are shown in Table 1.

Table 1. Values of  $H_c$  and  $K_u$  of alloy samples after SA at  $\sigma = 200$  MPa with respect to the temperature  $T$  and time of treatment.

Time of SA, $t$	SA temperature, $T$ , °C									
	480		500		520		540		550	
	$H_c$ , A/m	$K_u$ , J/m <sup>3</sup>	$H_c$ , A/m	$K_u$ , J/m <sup>3</sup>	$H_c$ , A/m	$K_u$ , J/m <sup>3</sup>	$H_c$ , A/m	$K_u$ , J/m <sup>3</sup>	$K_u$ , J/m <sup>3</sup>	$K_u$ , J/m <sup>3</sup>
10 min					25	1240	90	1920	67	2320
1 h	2	10	32	960	44	1680	2320	1650	3500	1280
4 h	16	200	62	1280	1250	1700				



Analysis of the structural images and selected area-electron diffraction (SAED) patterns of the alloy after SA at 480 °C for 1 h and 4 h indicates that nanocrystals of the  $\alpha$ -(Fe,Ni)Si solid solution developed; they are probably accompanied by  $\text{Fe}_3\text{Si}$  phase formation. Since rings characteristic of the  $\text{Fe}_3\text{Si}$  phase are not found in the SAED patterns after the treatment, this is evidence of the small size of these precipitations. In [2], we showed that these phases were responsible for the formation of transverse IMA in the studied alloy upon SA at 520 °C. After SA at 480 °C for 1 h, the structure images and SAED patterns show a relatively large amount of amorphous phase. After SA at 480 °C for 4 h, the structural images and SAED patterns show that the proportion of crystallites increases. However, the amorphous phase apparently still exists. After SA at 500 °C, the IMA constant is 100 and 6 times higher than that after SA at 480 °C for 1 h and 4 h, respectively (see Table 1). This suggests that the amount of the nanocrystalline phase increases with an increase in the treatment temperature. In the studied alloy, SA at 520 °C is efficient even for a duration of 10 min. Its effects on the magnetic properties, magnetic anisotropy, and structure of the alloy were described in [1, 2].

An increase in the temperature of the 10-min SA up to 540–550 °C makes it possible to obtain the maximum IMA constant ( $\sim 2000 \text{ J/m}^3$ ) in comparison with other SA modes. In this case,  $H_c$  remains less than 100 A/m (see Table 1). However, with an increase in SA time up to 1 h at 540 and 550 °C, the coercivity increases by factors of 26 and 52 and  $K_u$  decreases by 16 and 45%, respectively. After SA at 550 °C for 1 h, the SAED patterns demonstrate single reflections that can be attributed to  $\text{Fe}_3\text{NiSi}_{1.5}$  phase. The appearance of tetragonal phase in the alloy structure can lead to an increase its  $H_c$  similar to that shown for the alloy after SA at 520 °C with an increase in treatment time up to 4 h. Thus, after SA at 550 °C for 1 h, the alloy contains nanocrystals of the  $\alpha$ -(Fe,Ni)Si solid solution, as well as  $\text{Fe}_3\text{Si}$  and  $\text{Fe}_3\text{NiSi}_{1.5}$  phases, i.e., as with SA at 520 °C, the  $\alpha$ -(Fe,Ni)Si solid solution and  $\text{Fe}_3\text{Si}$  phases are responsible for the IMA. The IMA is controlled by the volume of these phases and their magnetoelastic properties. Since the  $K_u$  constant decreases with an increase in SA duration from 10 min to 1 h, it can be suggested that the volume of these phases decreases and the volume of the phases increases with positive magnetostriction. One of the possible reasons for this may be the change in the mechanism of the formation of tetragonal phase at 550 °C in comparison with that at lower temperatures (e.g., 520 °C) [3]. It is suggested that the diffusion of nickel into the  $\text{Fe}_3\text{Si}$  phase begins upon an increase in the temperature up to 550 °C, which destabilizes the latter and favors the transformation to the tetragonal phase [3].

*Conclusion:* At SA temperatures lower than 520 °C, the IMA constant of the  $\text{Fe}_{63.5}\text{Ni}_{10}\text{Cu}_1\text{Nb}_3\text{Si}_{13.5}\text{B}_9$  alloy decreases upon a decrease in the treatment temperature, and the time to reach its maximum value increases. In addition, the IMA constant of the studied alloy is less than that of conventional FINEMET prepared under the same treatment conditions. This is due to the decreased crystallization rate of the studied alloy in comparison with that of conventional FINEMET.

At SA temperatures of 520–550 °C, tetragonal phase develops in the alloy upon an increase in treatment time, and this increases its coercivity.

At SA temperatures of 540–550 °C, unlike the temperature of 520 °C, the IMA constant in the alloy decreases with an increase in treatment time. This suggests that the volume fractions of the structural components of the alloy changes with negative and positive magnetostriction.

*Support by the state Assignment of the Ministry of the Education and Science (theme “Magnet” No. AAAA-A18-118020290129-5) is acknowledged.*

1. V.A. Lukshina, N.V. Dmitrieva, E.G. Volkova, and D.A. Shishkin, Phys. Met. Metallogr., **120(4)**, 320–324 (2019).
2. V.A. Lukshina, N.V. Dmitrieva, E.G. Volkova, and D.A. Shishkin, Phys. Met. Metallogr., **120(12)**, 1145–1151 (2019).
3. P. Duhaj, P. Švec, J. Sitec, and D. Janičkovič, Mater. Sci. Eng. A, **304–306**, 178–186 (2001).

## MAGNETIC CHARACTERISTICS OF NdFeB 3D-PRINTED PERMANENT MAGNETS OBTAINED BY SELECTIVE LASER SINTERING

*V.E. Maltseva\**, *A.N. Urzhumtsev*, *S.V. Andreev*, *A.S. Volegov*

Ural Federal University, Institute of Natural Science and Mathematics, Ekaterinburg, Russia

\*E-mail: [viktoria.maltseva@urfu.ru](mailto:viktoria.maltseva@urfu.ru)

Hard magnetic materials belong to the class of functional materials, which are the base of modern technological processes, devices for everyday use, electrical transport, etc. The rate of improvement of the magnetic hysteresis properties of permanent magnets is constantly decreasing, since the potential of the  $\text{Nd}_2\text{Fe}_{14}\text{B}$  compound in industrial production is already almost completely realized [1]. To further improve the functional properties of products with permanent magnets, it is necessary to apply new approaches to the design of such products. One of the options for creating magnets of complex shape as well as local variation of material properties is the use of additive manufacturing technologies [2].

This work is devoted to the study of additive manufacturing methods used for 3D-printing of permanent magnets, establishing the relationship between the magnetic hysteresis properties of samples of single-layer permanent magnets of the NdFeB and conditions of their synthesis by selective laser sintering experimentally. Since additive manufacturing involves building an object layer by layer, understanding the potential of magnetic properties in a single layer will allow predicting the upper limit of magnetic hysteresis properties of a bulk permanent magnet sample.

The obtained samples are in the form of squares, with linear dimensions equal to  $10 \times 10 \text{ mm}^2$  and a thickness of less than 1 mm. A photo of the obtained samples is shown in Fig. 1.

For 3D-printing, a mechanical mixture of two powders was used: MQP-B (Magnequench Int. production) and the low melting eutectic alloy  $\text{Pr}_{75.0}\text{Cu}_{6.2}\text{Co}_{18.8}$  in an 80% to 20% weight ratio. The alloys were milled using a ball mill in alcohol to prevent oxidation of the powders. 3D-printing was carried out by means of the additive system of selective laser melting Orlas Creator RA: a specially chiseled platform made of brass was inserted into the build chamber, on which the powder was evenly distributed in a recess with a depth of 1 mm. The printing process was carried out in an argon atmosphere with an oxygen content in the build chamber of no more than 0.5%.

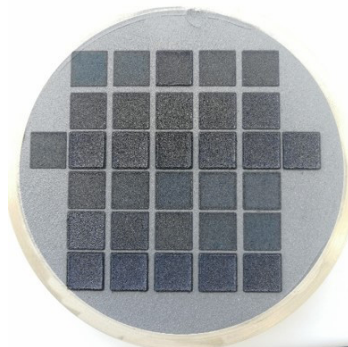


Figure 1. Appearance of printed samples.

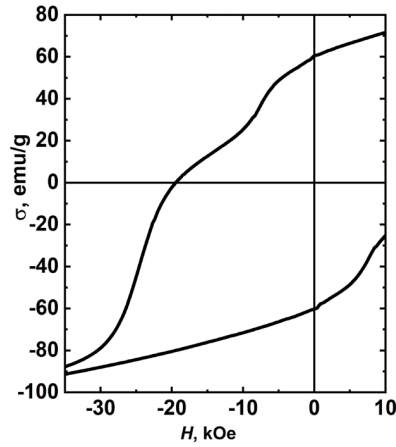


Figure 2. Major hysteresis loop of 3D-printed sample.

To obtain optimal mechanical and magnetic properties, the following parameters were varied: laser beam power ( $P$ , W), number of laser beam passes over the sintered sample ( $N$ , times), distance between the subsequent and the previous laser beam passages ( $h$ ,  $\mu\text{m}$ ), laser beam speed ( $v$ , mm/s), direction of laser beam passage ( $\alpha$ , deg.), laser beam diameter ( $d$ ,  $\mu\text{m}$ ). All magnetic hysteresis properties were measured at room temperature by means of a KVANS-1 vibrating sample magnetometer and at  $T = 300$  K by a PPMS DynaCool T9 magnetometer with the VSM option (Quantum Design, USA). The possibility of obtaining the coercivity of 19.5 kOe on single-layer magnets without the use of heavy rare-earth metals was shown (Fig. 2).

More details about the results obtained and methods of obtaining permanent magnets by additive manufacturing will be presented in the report.

*This work was financially supported by RSF grant № 21-72-10104.*

1. Vasilenko D.Yu. et al., Phys. Metals Metallogr., **122**, 12, 1173–1182 (2021).
2. Volegov A.S. et al., Acta Materialia, **188**, 733–739 (2020).

## MAGNETIC PROPERTIES AND MAGNETIC HYSTERESIS IN HIGH-COERCIVE $\text{Fe}_{0.25}\text{TaS}_2$ : EFFECT OF Se FOR S SUBSTITUTION

*N.M. Nosova*<sup>1\*</sup>, *N.V. Baranov*<sup>1,2</sup>, *E.M. Sherokalova*<sup>1</sup>, *A.S. Volegov*<sup>1</sup>

<sup>1</sup>Institute of Natural Sciences and Mathematics, Ural Federal University, Ekaterinburg, Russia

<sup>2</sup>M.N. Miheev Institute of Metal Physics, UB of RAS, Ekaterinburg, Russia

\*E-mail: [toporova.natalia@urfu.ru](mailto:toporova.natalia@urfu.ru)

Transition metal dichalcogenides (TMDCs) are a broad class of layered materials with a variety of structural, electronic, and magnetic properties. The intrinsic properties of the bulk materials can be further expanded by the intercalation of atoms and small molecules between the layers. In particular, the incorporation of 3d transition metal atoms results in the onset of new magnetic states and properties which can be tuned by the intercalant concentration, the choice of intercalated species, and the host lattice [1]. In total, the range of magnetic states and properties in the intercalated TMDCs is enormous, providing a platform on which to study magnetism and create new materials.

It is well known that, in the crystal structure of  $\text{Fe}_{0.25}\text{TaS}_2$ , the Fe atoms are intercalated in the van der Waals gap of the  $\text{TaS}_2$  crystals and maintain 2H-type layer stacking. The properties of  $\text{Fe}_x\text{TaS}_2$  compounds are established in its bulk form, where  $\text{Fe}_x\text{TaS}_2$  shows ferromagnetic ordering accompanied by strong perpendicular magnetic anisotropy when  $x$  ranges between 0.15 and 0.45. The ferromagnetic ordering is strongest at  $x \sim 0.25$  due to the formation of the Fe superstructure. Thus, the highest ferromagnetic transition temperature  $T_C$  of 160 K can be achieved at this Fe content [2]. Single crystals of  $\text{Fe}_{0.25}\text{TaS}_2$  were observed to exhibit a large magnetic hysteresis upon magnetization reversal (coercive field  $H_c \sim 37\text{--}55$  kOe) and a huge magnetocrystalline anisotropy (anisotropy field  $H_a \sim 500$  kOe) at low temperatures [3]. Significant magnetic hysteresis and field-induced magnetic phase transitions were observed in other intercalated system  $\text{Fe}_{0.5}\text{Ti}(\text{S},\text{Se})_2$ , in which sulfur was replaced by selenium [4].

In the present work, we aimed to perform a study of the effect of substitution in the anionic sublattice on the crystal structure and magnetic properties of the  $\text{Fe}_{0.25}\text{TaS}_{2-y}\text{Se}_y$  system with  $y \leq 2$ . The  $\text{Fe}_{0.25}\text{TaS}_{2-y}\text{Se}_y$  compounds were prepared by solid-state reactions using a single-stage technology at a temperature of  $T = 700$  °C. The X-ray certification was carried out by using a Bruker D8 Advance diffractometer. The magnetization was measured by using a SQUID-magnetometer at temperatures from 2 K to 350 K and in magnetic fields up to 70 kOe.

In this work, for the first time, we synthesized a system of compounds  $\text{Fe}_{0.25}\text{TaS}_{2-y}\text{Se}_y$ ,  $y \leq 2$ . According to the X-ray diffraction measurements, all the synthesized  $\text{Fe}_{0.25}\text{TaS}_{2-y}\text{Se}_y$  samples are single-phase. The replacement of sulfur with selenium in  $\text{Fe}_{0.25}\text{TaS}_{2-y}\text{Se}_y$  dramatically influences the magnetization behavior with temperature and magnetic field. It was found that the substitution of selenium for sulfur leads to an increase in the interatomic distance and a significant decrease in the magnetic ordering temperature. A jump-like behavior of the magnetization at 2 K is observed for substituted compounds with the whole concentration range. The decrease in the coercive field with increasing temperature follows the exponential function for all samples. Similar results were obtained earlier for a single crystal  $\text{Fe}_{0.25}\text{TaS}_2$  [5] and other systems with a high local magnetic anisotropy.

*The research was carried out with the financial support of the Competitiveness Enhancement Program – CEP 3.1.1.1-20.*

1. S.S.P. Parkin and R.H. Friend, *Phil. Mag. B*, **41**, 65–93 (1980).
2. M. Arai et al., *Appl. Phys. Lett.*, **107**, 103107 (2015).
3. Will J. Hardy et al., *Physical Review B*, **91**, 054426 (2015).
4. N.V. Baranov et al., *Phys. Rev. B*, **100**, 024430 (2019).
5. E. Morosan et al., *Phys. Rev. B*, **75**, 104401 (2007).

## STRUCTURAL TRANSITIONS AND MAGNETIC RESPONSE OF SUPRAMOLECULAR MAGNETIC POLYMER-LIKE STRUCTURES WITH BIDISPERSE MONOMERS

*E.S. Pyanzina*<sup>1</sup>, *E.V. Novak*<sup>1\*</sup>, *M. Gupalo*<sup>1</sup>, *S.S. Kantorovich*<sup>1,2</sup>

<sup>1</sup>Ural Federal University, Ekaterinburg, Russia

<sup>2</sup>University of Vienna, Wien, Austria

\*E-mail: [ekaterina.novak@urfu.ru](mailto:ekaterina.novak@urfu.ru)

Construction of supracolloidal magnetic polymers (polymer-like structures in which magnetic nanoparticles are playing the role of monomers) has recently been made possible. They combine the flexibility of polymeric conformations and controllability of magnetic nanoparticles. However, up to now, making supracolloidal magnetic polymers with perfectly monodisperse monomers is a challenge. Thus, the open problem in the application of supracolloidal magnetic polymers is the missing understanding of the polydispersity impact on their structural and magnetic properties. In this contribution, extensive Langevin dynamics simulations combined with parallel tempering method is used to investigate supracolloidal magnetic polymers of four different types – chain-, Y-, X- and ring-like ones – composed by monomers of two different sizes on cooling. Our investigation reveal that the presence of small particles dramatically changes not only the structural transitions happening in magnetic supracolloidal magnetic polymers on cooling, but also affects magnetic response of those systems. The presence of small particles in supracolloidal magnetic polymers making those structures surprisingly more magnetically responsive than their monodisperse counterparts.

*The work was supported by RSF (Grant No. 19-72-10033). Calculations were performed at the Ural Federal University cluster.*

## DESIGN OF LAMINATED NANOCOMPOSITES FOR MICROWAVES

*A.V. Osipov\**, *S.Y. Bobrovskii*, *A.N. Lagarkov*, *S.A. Maklakov*, *S.S. Maklakov*,  
*K.N. Rozanov*, *I.A. Ryzhikov*, *P.A. Zezyulina*

Institute for Theoretical and Applied Electromagnetics RAS, Moscow, Russia

\*E-mail: [avosipov@mail.ru](mailto:avosipov@mail.ru)

Some problems of microwave technology needs in materials with high values of magnetic permeability [1]. It is known from the theory of ferromagnetic resonance that the limiting values of microwave magnetic permeability are achievable with use of soft magnetic ferromagnets, first, possessing high saturation magnetization, second, having the form of thin magnetic films with planar magnetic anisotropy, and these can exceed the values of currently used materials by 1–2 orders in magnitude [2]. Meanwhile, in practice, bulk magnetic materials with a thickness of several millimeters and higher are more often required, whereas the use of thin films in microwave is limited by the fact that their thickness cannot exceed several submicrometers due to eddy currents and deviation of the magnetic structure from the optimal one [3]. These difficulties can be avoided by applying some ferromagnetic layers of extreme thickness through thin dielectric layers. Thus, design of laminated nanocomposites, which are structured bulk materials based on thin ferromagnetic films, is considered as one of the promising direction in solving the problem of creating highly efficient materials with magnetic properties optimized in the microwave range [4].

This report is devoted to this type of composite materials. The report presents practical results of the study of the dependence of the microwave magnetic permeability of laminates based on various ferromagnets on the parameters of laminates: the thickness of magnetic and dielectric layers, their number, geometric dimensions of elements, etc. Optimization of these parameters allows obtaining materials with extremely high values of magnetic permeability for the microwave range; for example, Fig. 1 shows the effective magnetic permeability of a material based on Permalloy with a ferromagnetic volume fraction of 23%.

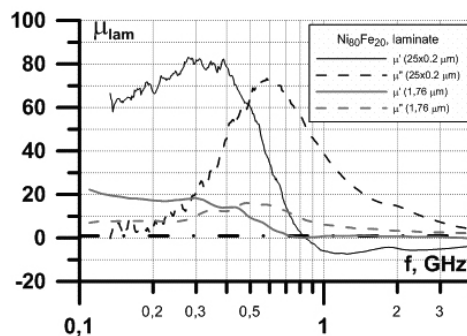


Figure 1. Frequency dependence of the magnetic permeability of laminate based on permalloy.

*This study was financially supported by the Russian Science Foundation (RSF) under project No. 21-19-00138.*

1. O. Acher, CLEFS CEA, **56**, 19–28 (Winter 2007-2008).
2. A.N. Lagarkov et al., J. Communicat. Technol. Electron., **54**(5), 625–633 (2009).
3. S.Y. Bobrovskii et al., J. Magn. Magn. Mater., **459**, 20–25 (2018).
4. I.T. Iakubov et al., AIP Adv., **4**, 107143 (2014).

## NEGATIVE ANISOTROPY IN Ni-Fe FILMS

*P.A. Savin*<sup>1\*</sup>, *O.A. Adanakova*<sup>1</sup>, *V.N. Lepalovskij*<sup>1</sup>, *E.V. Kudyukov*<sup>1</sup>, *V.O. Vas'kovskiy*<sup>1,2</sup>

<sup>1</sup>Ural Federal University, Ekaterinburg, Russia

<sup>2</sup>Institute of Metal Physics UB RAS, Ekaterinburg, Russia

\*E-mail: [Peter.Savin@urfu.ru](mailto:Peter.Savin@urfu.ru)

The author of [1] showed the existence in some FeNi films of small regions with “negative anisotropy”. The name of the effect comes from the possibility of describing uniaxial anisotropy by a free energy density  $E_k = K_{\pm} \sin^2 \varphi$ , where  $\varphi$  is the angle between the magnetization  $M$  and the deposition field  $H_{\text{dep}}$ . The anisotropy constant  $K_{\pm}$  can be chosen positive or negative in accordance with the direction of the induced anisotropy, along the field or across.

For the controlled formation of an easy axis during film deposition, a deposition magnetic field  $H_{\text{dep}}$  is usually applied in the substrate plane and the easy axis is formed along this direction [2].

The authors of [3] proposed a model to explain the effect of negative anisotropy. The model is based on a negative magnetostriction and inhomogeneous stresses.

Since, in accordance with the model, one of the factors in the formation of the “negative anisotropy” is a stresses, we were interested to observe the dependence of the anisotropy on the additional stresses. We proceeded from the assumption that the resulting anisotropy consists of the action of two mechanisms, each of which generates mutually perpendicular directions of anisotropy. The first mechanism comes from the shape anisotropy of crystallites and crystal chains, and the second is provided by mechanical stresses and magnetostriction [3]. Consequently, the competition between these two mechanisms can change both the magnitude and the sign of the anisotropy constant, that is, “negative anisotropy” can be “turned off” for example.

The samples were prepared by means of magnetron sputtering using ATC Orion system. The films were deposited onto square-shaped (22×22) mm Corning glass substrates placed on a non-heated and rotating substrate holder at a speed of 32 rpm. The film deposition occurred in the presence of “in plane” magnetic field of 250 Oe and RF substrate bias at Ar pressure of 1.6 mTorr. Fe<sub>19</sub>Ni<sub>81</sub> and Fe<sub>10</sub>Ni<sub>90</sub> alloy disks were used as targets. The film deposition rate was 1.2 Å/s and the thicknesses were 40 and 70 nm. To study the magnetic properties of the films, a Kerr magnetometer Evico magnetics was used.

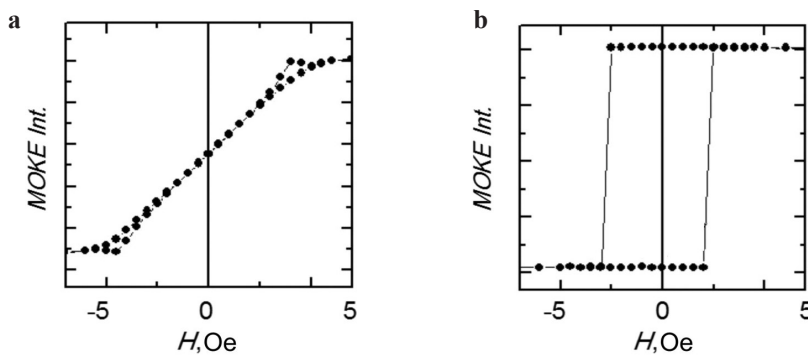


Figure 1. Hysteresis loops taken along the deposition field direction for the films of different compositions: **a** Fe<sub>10</sub>Ni<sub>90</sub> film (hard magnetization axis), **b** Fe<sub>19</sub>Ni<sub>81</sub> film (easy magnetization axis). Longitudinal magneto-optical Kerr effect.

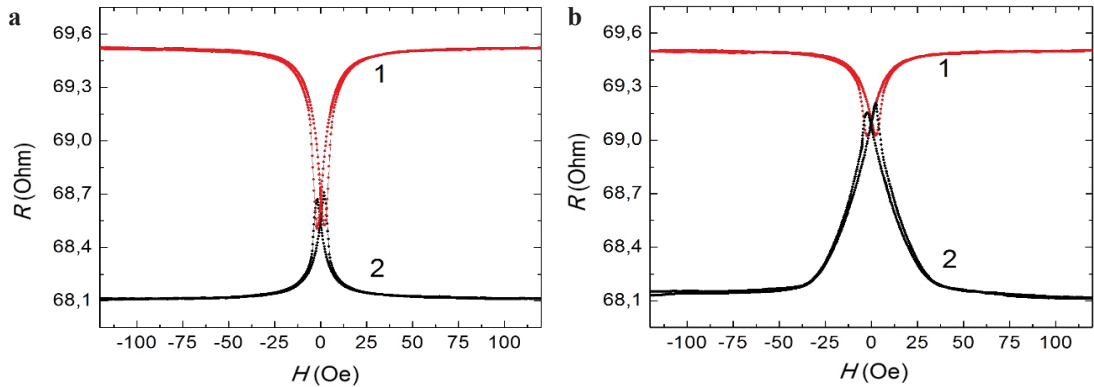


Figure 2.  $R$ - $H$  curves for the strips cut out along the deposition field direction (“crystallite chains” along the strip): **a** without deforming load, **b** with deforming load.

If the model assumptions are correct, then the application of additional stresses along or across the “crystallite chains” should affect the anisotropy. When, for example, a compressive stress is applied along the “crystallite chains”, the tensile stress is compensated. And the anisotropy mechanism associated with magnetostriction becomes disabled. Then the “crystallite chains” form anisotropy dominates and, as a consequence, the easy magnetization axis is rotated 90 degrees.

The described situation corresponds to Fig. 2 which shows the  $R$ - $H$  curves for the sample cut out from the original  $\text{Fe}_{10}\text{Ni}_{90}$  film along the deposition field direction. In accordance with the model, this corresponds to the orientation of the “crystallite chains” along the strip. From Fig. 2a (without deforming load), we can see that the application of the field along the strip ( $H_{\parallel}$ , red curve – 1) significantly changes (increases) the resistance, while the transverse application of the field ( $H_{\perp}$ , black curve – 2) changes the resistance not so much. In other words, the application of the field along the strip rotates the magnetization from the initial perpendicular orientation (at  $H_{\parallel} = 0$  Oe) to the parallel orientation (with increasing the field  $H_{\parallel}$  to saturation), while the transverse application of the field rotates the magnetization slightly. From this, it can be concluded that the orientation of the easy magnetization axis is predominantly transverse to the strip.

In accordance with the tested model, the effect of “negative anisotropy” can be caused by the competition of two anisotropy mechanisms acting in mutually perpendicular directions. By applying additional stresses, we acted on one of the mechanisms, changing their ratio, which led either to an increase in the effect or to its “off”. Thus, at least in relation to the described impacts, the model demonstrated its adequacy.

The model can be used to study the mechanisms of the formation of induced magnetic anisotropy, as well as to control it, in products of planar technology [4] and glass-coated ferromagnetic microwires [5].

1. D.O. Smith, Appl. Phys. Lett., **2**, 191 (1963).
2. R. Soohoo, Czech. J. Phys., **21**, 494 (1971).
3. P.A. Savin, O.A. Adanakova, V.N. Lepalovskij, E.V. Kudyukov, K.V. Polozov and V.O. Vas’kovskiy, J. Phys.: Conf. Ser., **1389**, 012122 (2019).
4. L. Jogschies, D. Klaas, R. Kruppe, J. Rittinger, P. Taptimthong, A. Wienecke, L. Rissing and M.C. Wurz, Sensor, **15**, 28665 (2015).
5. A. Zhukov, J. González, J.M. Blanco, M. Vázquez and V. Larin, J. Mater. Res., **15**, 2107 (2000).



## DETERMINATION OF THE 3d-4f ELECTRONIC STATES DISTRIBUTION IN THE VALENCE BAND IN COMPOUNDS WITH LAVES PHASE STRUCTURE $\text{ErCo}_2$ AND $\text{ErCo}_2\text{Mn}_{0.4}$ BY RESONANT PHOTOEMISSION

*E.A. Ponomareva*<sup>1\*</sup>, *V.I. Grebennikov*<sup>1,2</sup>, *E.G. Gerasimov*<sup>1,3</sup>,  
*P.B. Terent'yev*<sup>1,3</sup>, *A.A. Inishev*<sup>1</sup>, *N.V. Mushnikov*<sup>1,3</sup>, *T.V. Kuznetsova*<sup>1,3</sup>

<sup>1</sup>M.N. Miheev Institute of Metal Physics UB RAS, Ekaterinburg, Russia

<sup>2</sup>Ural State University of Railway Transport, Ekaterinburg, Russia

<sup>3</sup>Ural Federal University, Ekaterinburg, Russia

\*E-mail: [ponomareva@imp.uran.ru](mailto:ponomareva@imp.uran.ru)

The non-stoichiometric intermetallic  $\text{RCo}_2\text{Mn}_x$  compounds with Laves phase structure of the  $\text{MgCu}_2$ -type (space group  $Fd3m$ ) attract attention with their changing magnetic properties depending on transition metal amount and the choice of rare-earth element, which allows expanding the scope of their application [1]. In addition to the magnetic properties, the electronic structure also changes, which currently requires clarification, in particular, the contribution of the rare-earth f-states to the valence band (VB).

The electronic structure of  $\text{ErCo}_2\text{Mn}_x$  ( $x = 0, 0.4$ ) compounds with Laves phase structure are studied by resonant X-ray photoemission spectroscopy (RPES). To determine the excitation energies near the Mn  $L_{2,3}$ , Co  $L_{2,3}$  and Er  $N_{4,5}$  edges of  $\text{ErCo}_2$  and  $\text{ErCo}_2\text{Mn}_{0.4}$ , the corresponding absorption spectra were taken. This method makes it possible to study not only the ground state, but also the lifetime of the excited state (a core level-hole – VB electron), determine the energies of VB single-particle states and two-hole states on selected atoms see reactions to the sudden appearance of the core-level photo-hole. Resonance photoemission in narrow-gap materials is described by the sum of first- and second-order transitions, their quantum-mechanical interference leads to an increase in the spectrum from the valence bands and the appearance of an asymmetric dependence on the photon energy. Recently, these effects were studied experimentally on the example of ternary intermetallic compounds  $\text{ErNi}_2\text{Mn}_x$  [2] and  $\text{DyNi}_2\text{Mn}_x$  [3]. The competition between the elastic and inelastic photoemission channels leads to different dependences of the photoemission spectra in our case from cobalt and manganese on the photon energy. The amount of manganese affects the intensity of the rare-earth peaks in the VB, which confirms the need to determine the d-f interactions in such systems.

*The research was supported by RFBR project № 20-02-00541.*

1. E.G. Gerasimov, N.V. Mushnikov, A.A. Inishev, P.B. Terentev, and V.S. Gaviko, *J. Alloys Compd.*, **680**, 359–365 (2016).
2. K. Balinski, T.V. Kuznetsova, E.G. Gerasimov, A.V. Protasov, V.V. Marchenkov, N.V. Mushnikov, V.R. Galakhov, V.V. Mesilov, S.N. Shamin, V.S. Gaviko, B.V. Senkovskiy, M. Fijałkowski, L. Schneider, A. Ślebarski, A. Chrobak, and K. Kuepper, *AIP Advances*, **8**, 105225 (2018).
3. V.V. Marchenkov, N.V. Mushnikov, T.V. Kuznetsova, A. Buling, E.G. Gerasimov, V.S. Gaviko, V.I. Grebennikov, K.A. Fomina, H.W. Weber, C. Derks, M. Neumann, *Journal of Physics: Conference Series*, **400** 032050 (2012).

**MICROSTRUCTURE AND MAGNETIC PROPERTIES  
OF STRIP-CASTED (Sm,Zr)(Fe,Co)<sub>10</sub>Ti<sub>0.7</sub> ALLOY**

*A.V. Protasov<sup>1,2\*</sup>, O.A. Golovnya<sup>1,2</sup>, A.G. Popov<sup>1,2</sup>, A.S. Volegov<sup>1,2</sup>, V.S. Gaviko<sup>1,2</sup>, A.V. Shitov<sup>1,3</sup>*

<sup>1</sup>M.N. Miheev Institute of Metal Physics of Ural Branch of Russian Academy of Sciences, Ekaterinburg, Russia

<sup>2</sup>Ural Federal University, Ekaterinburg, Russia

<sup>3</sup>Urals Electromechanical Plant, Joint-Stock Company, Ekaterinburg, Russia

\*E-mail: [protasov@imp.uran.ru](mailto:protasov@imp.uran.ru)

Tetragonal Sm(Fe,M)<sub>10–12</sub> alloys ThMn<sub>12</sub>-type structure (space group *I4/mmm*) have long history; however, there are few reports in the literature on the problem of sintering bulk magnets [1–5]. In the manufacturing of permanent magnets, the content of the magnetically ThMn<sub>12</sub> hard phase has to be high. However, the high temperature heating is accompanied by evaporation and oxidation of Sm, which causes the formation of the soft magnetic α-(Fe,M) phase and has to be eliminated.

The aim of this work was to produce (Sm,Zr)(Fe,Co)<sub>10</sub>Ti<sub>0.7</sub> alloy by strip casting. The strip casting method ensures a dispersed crystalline structure of the samples and simplifies the solid-solution treatment; it also facilitates production of the fine-grained powder with a uniform size distribution of single-crystal particles.

Strip-casted alloy was prepared by Urals Electromechanical Plant. The linear velocity of a water-cooled copper cylinder was 2 m/s. The alloy plates had a thickness of 0.2–0.3 mm and a width of 3–4 cm. The chemical composition of the alloy is presented in Table 1.

Figure 1 shows scanning microscopy images of cross-sections of strip-casted plates. The structure contains three types of areas of different phase contrast. Dark gray areas A correspond to ThMn<sub>12</sub> structures. Light gray regions B correspond to the (Sm)(Fe<sub>0.87</sub>Co<sub>0.13</sub>)<sub>9</sub>Ti<sub>0.44</sub> composition. Since the

Table 1. The chemical composition of alloy.

	Sm	Zr	Fe	Co	Ti
at. %	7.61	0.76	75.92	8.97	6.04

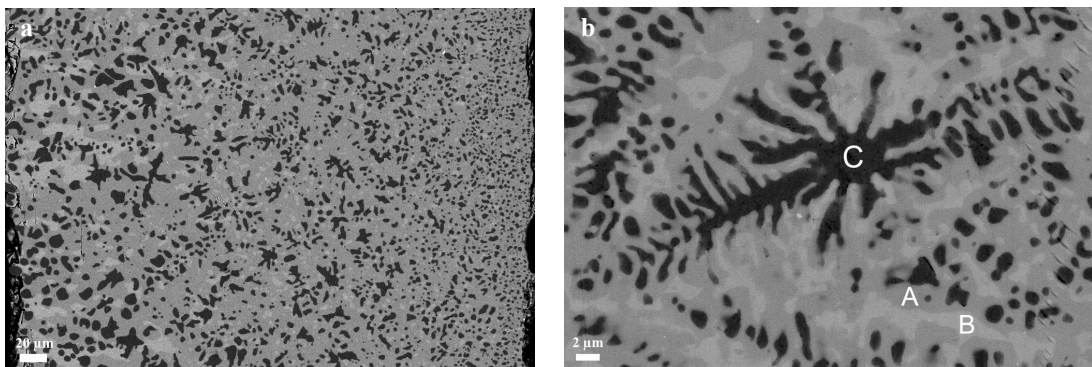


Figure 1. Microstructure of strip-casted alloy.

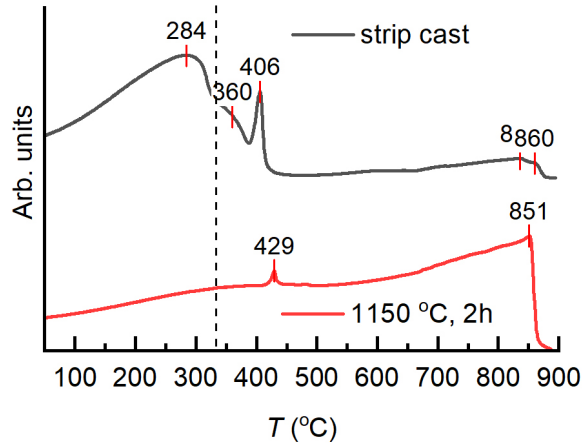


Figure 2. AC susceptibility of (–) initial and (–) homogenous alloy.

contents of Fe and Co in regions A and B are close, the contrast in this case is controlled by the content of Ti and Sm. The black regions C represent the  $\alpha$ -Fe phase with partial substitution for Co and Ti.

The temperature dependence of the *ac* magnetic susceptibility  $\chi(T)$  of the  $(\text{Sm}_{0.91}\text{Zr}_{0.09})(\text{Fe}_{0.9}\text{Co}_{0.1})_{10.14}\text{Ti}_{0.72}$  strip-casted alloy is shown in Fig. 2a (line 1). The Curie temperature  $T_C$  of the  $\text{ThMn}_{12}$ -type phase is 406 °C. Heating over 406 °C does not cause  $\chi(T)$  to vanish, indicating the likely presence of the  $\alpha$ -(Fe,Co) phase. In addition, in the temperature range of 250–400 °C, two broad peaks are visible, the corresponding Curie temperatures are 284 and 360 °C. To optimize the microstructure and determine the region of temperature stability of additional phases, we studied the effect of solid-solution treatment at temperatures of 950–1150 °C for 1–4 h.

After solid solution treatment at 1150 °C, the dependence of magnetic susceptibility has one peak corresponding to the main  $\text{ThMn}_{12}$  phase, and in the temperature range 250–400 °C the peaks of other phases disappear; however, the relative intensity of the iron peak increases strongly. In addition, the Curie temperature of the  $\text{ThMn}_{12}$  phase increases by 23 °C, which can be attributed to the element redistribution in the alloy upon heat treatment.

First time ever, the  $(\text{Sm,Zr})(\text{Fe,Co})_{10}\text{Ti}_{0.7}$  alloy was produced by strip casting method. The optimum solid-solution treatment temperature is 1150 °C.

*The research was supported by the state assignment of Ministry of Science and Higher Education of the Russian Federation [theme “Magnet” No. 122021000034-9].*

1. F.E. Pinkerton and D.J. Van Wingerden, *IEEE Trans. Magn.*, **25**, 3306 (1989).
2. J. Yang and Y. Yang, in *Handb. Adv. Magn. Mater.* (Springer US, Boston, MA, 2006), pp. 1414–1451.
3. K. Otsuka, M. Kamata, T. Nomura, H. Iida, and H. Nakamura, *Mater. Trans.*, **62**, 887 (2021).
4. J.S. Zhang, X. Tang, H. Sepehri-Amin, A.K. Srinithi, T. Ohkubo, and K. Hono, *Acta Mater.*, **217**, 117161 (2021).
5. I. Dirba, J. Li, H. Sepehri-Amin, T. Ohkubo, T. Schrefl, and K. Hono, *J. Alloys Compd.*, **804**, 155 (2019).

**Cu DOPED HARD MAGNETIC POWDERS BASED ON Nd(FeCo)B.  
MICROMAGNETIC PROPERTIES AND STRUCTURE**

*A.V. Ognev\**, *V.Yu. Samardak*, *V.N. Kharitonov*, *A.A. Belov*, *O.O. Shichalin*, *E.K. Papynov*,  
*A.S. Samardak*

Institute of High Technologies and Advanced Materials, Far Eastern Federal University,  
Vladivostok, Russia

\*E-mail: [ognev.av@dvfu.ru](mailto:ognev.av@dvfu.ru)

*Introduction.* The development of modern technologies for robotics, automobile transport, small aircraft, electric transport, clean energy, and other areas requires strong and compact permanent magnets, which are used in electric drives and generators [1]. Composites from polymer materials with magnetic powders (magnetoplastics) are also used in numerous applications, including electromagnetic drives for micropumps [2]. Intensive research has focused on new methods for synthesis and optimal microstructure formation since the discovery of superior Nd<sub>2</sub>Fe<sub>14</sub>B hard magnetic alloys [3].

The aim of this work is to investigate the influence of the Cu additive on the structure and magnetic properties of powders, which was obtained from the melt-spun of ribbons of the Nd-(Fe,Co)-B alloy. Copper was incorporated by mechanical synthesis during powder milling. The influence of a relatively high concentration of Cu (1 wt.%) on the structure, reversal magnetization, and energy product of Nd-(Fe,Co)-B neodymium magnets were investigated.

*Experiment.* Hard magnetic powders were obtained by ball milling of the commercial rapidly quenched Nd-(Fe,Co)-B alloy (product No. 04821610, Jovi International, China) using a Tencan XQM-0.4A planetary ball mill (China), regime: 700 rpm in one 6-hour cycle in an inert gas atmosphere (argon) and acetone. Powder samples with Cu incorporation were synthesized by adding 1 wt.% of Cu powder in the initial alloy before ball milling. Furthermore, powders without additives and with 1 wt.% Cu incorporation were annealed at 750 °C for 10 minutes for thermal stability investigation.

*Results and discussions.* The XRD of the initial powder of Nd-(Fe,Co)-B alloy and its milled form, as well as after doping with 1 wt.% of Cu, are shown in Fig. 1. The main phase of the powders is the tetragonal phase Nd<sub>2</sub>Fe<sub>14</sub>B (2-14-1) with the spatial symmetry group *P42/mnm*. Miller indices of the phase are shown in Fig. 1a. The lines of the (2-14-1) phase are very broad, which

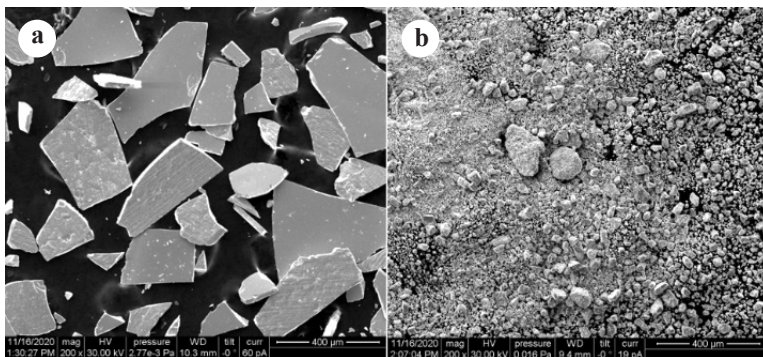


Figure 1. SEM images of the morphology of the Nd-(Fe,Co)-B alloy particles in the initial state (a), after being milled without copper (b).

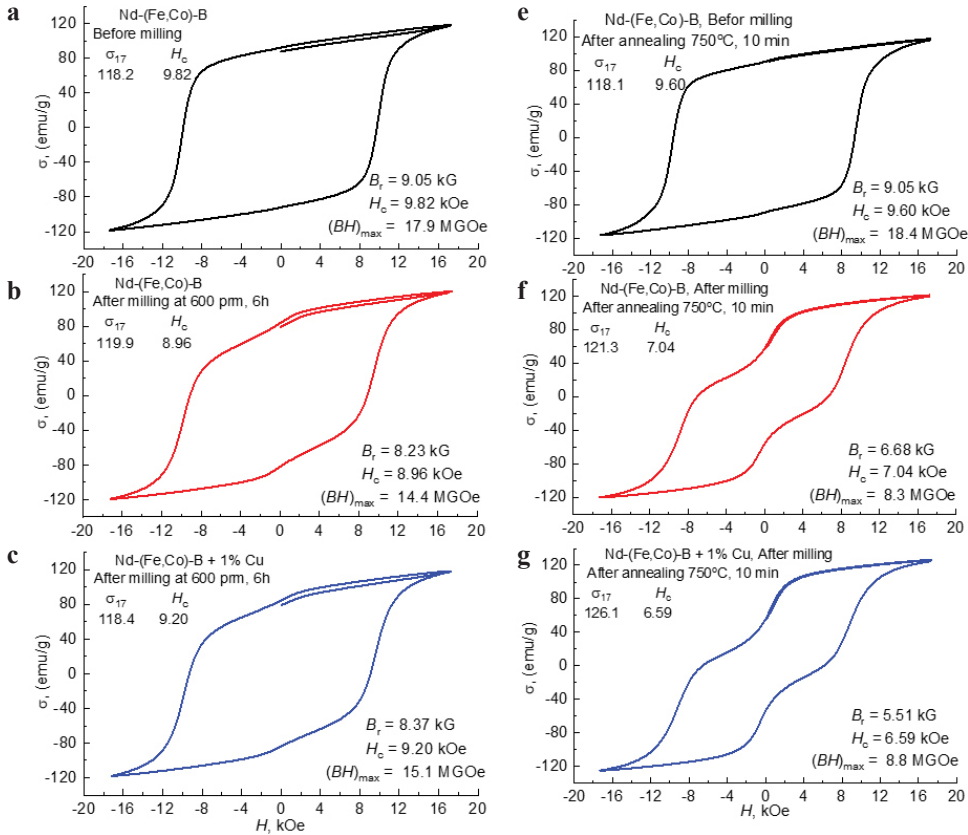


Figure 2. Hysteresis loops of the initial Nd-(Fe,Co)-B alloy powders (a), after milling (b), with 1 wt% Cu additive (c), and the same powders after annealing at 750 °C for 10 minutes (e, f, g).

allows for an estimate of the coherent scattering regions (CSRs) size of about 30 nm. The grain deformation of the initial powder is 0.1%, and after milling it increases several times. Intensive lines of NdO oxide and  $\alpha$ -phase Fe-Co phases appear in XRD diffractograms for milled powders after annealing. This explains the decrease in  $H_c$  for the powders.

Figure 1a shows SEM images of the initial powder of Nd-(Fe,Co)-B alloy. The powder particles are plate-shaped with sharp edges. The thickness of the particles is about 20  $\mu\text{m}$  with an average in-plane size of about 370  $\mu\text{m}$ . Figs. 1b and c show SEM images of the powder of the Nd-(Fe,Co)-B alloy after milling. These powders contain agglomerates, as well as individual particles of different sizes and irregular shapes. The average grain size is 2  $\mu\text{m}$ .

Figure 2 shows the magnetic hysteresis loops for Nd-(Fe,Co)-B alloy powders measured by a vibrating magnetometer. Figures 2e–g shows hysteresis loops of annealed powders. The magnetic characteristics of the initial powders did not change significantly after annealing (Fig. 2a, e). The coercivity decreased considerably for milled powders, indicating significant powder contamination after milling and increased contributions of surface effects. The coercivity and energy product are higher for samples with 1 wt.% Cu additive than for those without Cu. This trend persists even after annealing. The improvement in magnetic characteristics for Nd-(FeCo)-B alloy powders with

the 1 wt.% Cu additive is probably due to the segregation of Cu in the intergranular phase region and the stabilization of the magnetically stiff phase.

*Conclusions.* In the study, it was found that the initial fast quenched Nd-(Fe,Co)-B alloy powder has a composition of approximately 28 Nd, 66 Fe, 5 Co, 1 B (wt.%). The main phase of the alloy is the Nd<sub>2</sub>Fe<sub>14</sub>B structure. The high powder coercivity up to 9.82 kOe is due to the presence of nanocrystalline grains of about 30-60 nm inside the powder particles with an average size of about 370 μm. The particle size of the powder is reduced to an average size of approximately 2 μm after milling. The coercivity for the milled powders decreases slightly but remains at a fairly high level (8.96 and 9.20 kOe). The addition of 1 wt.% of Cu leads to an increase in coercivity and energy ratio compared to the powder without Cu.

*The research was carried out with the support of the Russian Science Foundation (project 19-72- 20071).*

1. J.M. Coey, Magnetism in future, J. Magn. Magn. Mater., **226-230**, 2107–2112 (2001).
2. C. Yamahata, C. Lotto, E. Al-Assaf, M.A.M. Gijs, A PMMA valveless micropump using electromagnetic actuation, Microfluid. Nanofluidics, **1**, 197 (2005).
3. M. Sagawa, S. Fujimura, N. Togawa, H. Yamamoto, Y. Matsuura, New material for permanent magnets on a base of Nd and Fe (invited), J. Appl. Phys., **55**, 2083–2087 (1984).

## MAGNETIC PROPERTIES OF MN-DOPED $\text{Fe}_{3+x}\text{Si}_{1-x}$ FILMS SYNTHESIZED ON SOI SUBSTRATE BY LOW TEMPERATURE ANNEALING

*A.V. Lukyanenko<sup>1,2</sup>, A.S. Tarasov<sup>1,2</sup>, I.A. Tarasov<sup>1</sup>, M.V. Rautskii<sup>1</sup>, I.A. Yakovlev<sup>1</sup>,  
N.N. Kosyrev<sup>1</sup>, V.A. Komarov<sup>1,2</sup>, L.V. Shanidze<sup>1,3\*</sup>, S.N. Varnakov<sup>1,3</sup>,  
S.G. Ovchinnikov<sup>1,2</sup>, G.S. Patrin<sup>1,2</sup>, N.V. Volkov<sup>1</sup>*

<sup>1</sup>Kirensky Institute of Physics, Federal Research Center KSC SB RAS, Krasnoyarsk, Russia

<sup>2</sup>Institute of Engineering Physics and Radio Electronics, SFU, Krasnoyarsk, Russia

<sup>3</sup>Federal Research Center KSC SB RAS, Krasnoyarsk, Russia

\*E-mail: [shanidze.l.v@mail.ru](mailto:shanidze.l.v@mail.ru)

Obtaining manganese-doped  $\text{Fe}_3\text{Si}$  directly on the SOI substrate is a very important technology for the further introduction of spintronic devices in the traditional semiconductor industry. There are works on lateral spin valves (LSV) on SOI using mainly Fe and 3d metals as FM contacts [1–4], as well as works on  $\text{Fe}_{1-x}\text{Mn}_x\text{Si}$  films prepared on traditional Si or other semiconducting substrates [5, 6]. Here we demonstrate a simple method for obtaining Mn-doped  $\text{Fe}_{3+x}\text{Si}_{1-x}$  films on SOI by Mn and Fe co-deposition and subsequent annealing. We present the results of studying the magnetic properties as a function of Mn concentration.

The samples were fabricated using SOI substrate with a boron-doped Si(100) 100 nm thick device layer with a resistivity of  $18 \Omega \cdot \text{cm}$ . Fe and Mn films were deposited onto the SOI device layer by thermal evaporation in ultrahigh vacuum. Prior to deposition, the Si layer was reduced to a thickness of 30 nm using reactive ion etching (RIE) in  $\text{CF}_4$  gas plasma. Fe and Mn was depositing with  $x$  axis gradient of sample (Fig. 1a). The thickness of the layers and in the center of the substrate is 17.6 nm and 38 nm for Fe and Mn, respectively. The thickness was chosen to achieve the stoichiometric composition of  $\text{Fe}_2\text{MnSi}$  (Fe – 17.6 nm / Mn – 38 nm / Si – 30 nm) in the central region. Prior to the evaporation of iron, substrate was annealed to clean the Si surface. After deposition of Fe and Mn films annealing was carried out to initiate the process of formation of Mn-doped  $\text{Fe}_{3+x}\text{Si}_{1-x}$  films of various compositions over the area of the substrate.

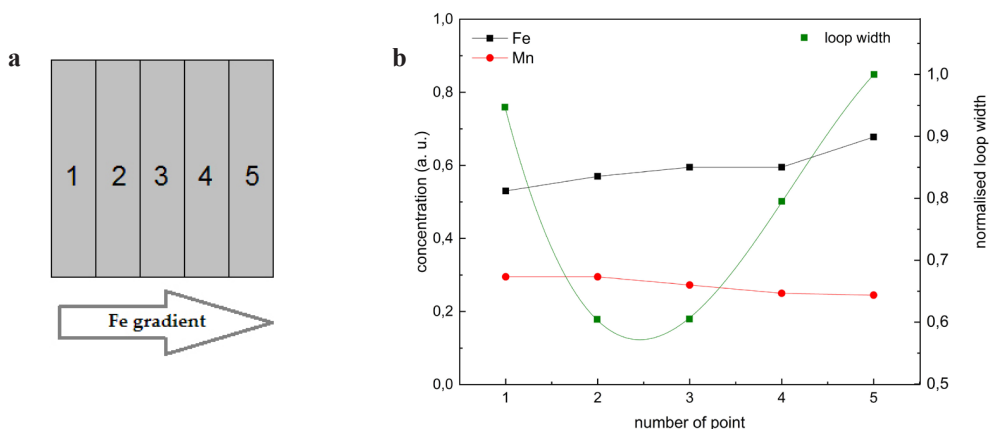


Figure 1. **a** Schematic representation of the deposition process and sample numbering. **b** Plot of element concentration distribution according to EDS data (left axis) and plot of hysteresis loop width (right axis).

Structural characterization was carried out using scanning electron microscopy (SEM). The composition of the films was analyzed using energy dispersive X-ray spectroscopy (EDS). The magnetic properties were studied by the methods of the magneto-optical Kerr effect (MOKE). EDS mode makes it possible to judge the distribution of the element gradient over the substrate surface. Quantitative estimates are difficult because the film thickness is less than the depth of analysis of the EDS method. Local elemental mapping of the surface was performed that confirm gradient of Mn and Fe content. Qualitative composition of the film over the  $x$  axis is shown on Fig. 1b. The proportion of iron increases, and manganese decreases. MOKE measurements were carried out along the sample, the point numbers correspond to the designations given in the diagram (Fig. 1a). Normalized width of magnetic hysteresis loop  $\delta H$  was chosen as main parameter to compare magnetic properties of samples with different stoichiometry. It was found nonmonotonic dependence of  $\delta H$  with increasing of iron content. This experimental fact can be associated with transition of Mn-doped  $\text{Fe}_{3+x}\text{Si}_{1-x}$  alloy to  $\text{Fe}_2\text{MnSi}$ . More detailed studies are needed.

*The research was funded by Krasnoyarsk Regional Fund of Science.*

1. M. Ishikawa, H. Sugiyama, T. Inokuchi, T. Tanamoto, K. Hamaya, N. Tezuka, and Y. Saito, *J. Appl. Phys.*, **114**, 243904 (2013).
2. S. Sato, M. Ichihara, M. Tanaka, and R. Nakane, *Phys. Rev. B*, **99**, 165301 (2019).
3. S. Sato, M. Tanaka, and R. Nakane, *Phys. Rev. B*, **102**, 035305 (2020).
4. T. Tahara, H. Koike, M. Kamenno, T. Sasaki, Y. Ando, K. Tanaka, S. Miwa, Y. Suzuki, and M. Shiraishi, *Appl. Phys. Express*, **8**, 113004 (2015).
5. L. Pal, K.G. Suresh, and A.K. Nigam, *J. Appl. Phys.*, **113**, 093904 (2013).
6. M. Tang, C. Jin, and H.L. Bai, *J. Appl. Phys.*, **116**, 173909 (2014).



## CORRELATION OF THE CHEMICAL COMPOSITION AND MAGNETIC PROPERTIES OF Ni-Zn-Co FERRITE

*D.A. Vinnik<sup>1</sup>, D.P. Sherstyuk<sup>1\*</sup>, V.E. Zhivulin<sup>1</sup>, D.A. Zherebtsov<sup>1</sup>, S.A. Gudkova<sup>1</sup>, N.S. Perov<sup>2,3</sup>, Yu.A. Alekhina<sup>2</sup>, K.A. Astapovich<sup>4</sup>, A.V. Trukhanov<sup>1,4</sup>*

<sup>1</sup>South Ural State University (National Research University), Chelyabinsk, Russia

<sup>2</sup>Lomonosov Moscow State University, Moscow, Russia

<sup>3</sup>Baltic Federal University, Kaliningrad, Russia

<sup>4</sup>SSPA “Scientific and Practical Materials Research Centre of NAS of Belarus”, Minsk, Belarus

\*E-mail: [sherstiukd@susu.ru](mailto:sherstiukd@susu.ru)

Nickel-zinc-cobalt ferrites (NZCF) have attracted considerable research attention due to their magnetic properties, low coercive force, low eddy current losses, high mechanical hardness, relatively high Curie temperature, high magnetic permeability, high operating frequency and extremely high electrical resistivity. Ferrites have many potential applications, such as high density devices, microwave devices, transformers, magnetic fluids, etc [1].

A series of samples with the general formula  $\text{Co}_{0.3}\text{Zn}_{0.7-x}\text{Ni}_x\text{Fe}_2\text{O}_4$ , where  $x = 0-0.7$  with a step of 0.3, was obtained by solid-phase synthesis. The sintering of samples was carried out at 1150 °C with the isothermal holding time of 5 h in a tubular high-temperature furnace. Elemental analysis and surface morphology of the samples were studied using a Jeol JSM 7001F electron microscope (Oxford INCA X-max 80 energy dispersive spectrometer). Based on the data obtained as a result of elemental analysis, it can be concluded that the given and actual formulas are consistent.

The phase composition and structure of Ni-Zn-Co ferrite samples were studied on a Rigaku Optima IV powder diffractometer. The diffraction patterns of the studied samples are shown in Fig. 1, which shows that each of the samples contains only one phase. The refinement of the crystal lattice parameters was carried out using reflections (111), (220), (311), (222), (400), (422), (511), (440), (620), (522), (622), (642), belonging to the cubic system [2]. Their crystal structure can be well described in the framework of cubic SG Fd-3m (No. 227).

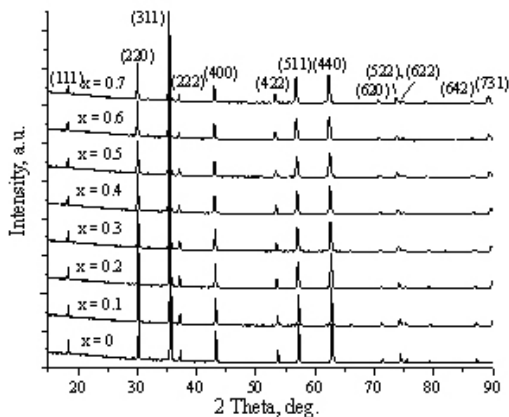


Figure 1. XRD patterns of NZCF samples.

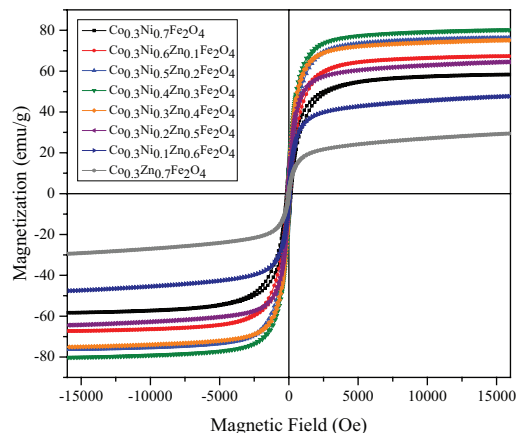


Figure 2. Hysteresis loops of NZCF samples.

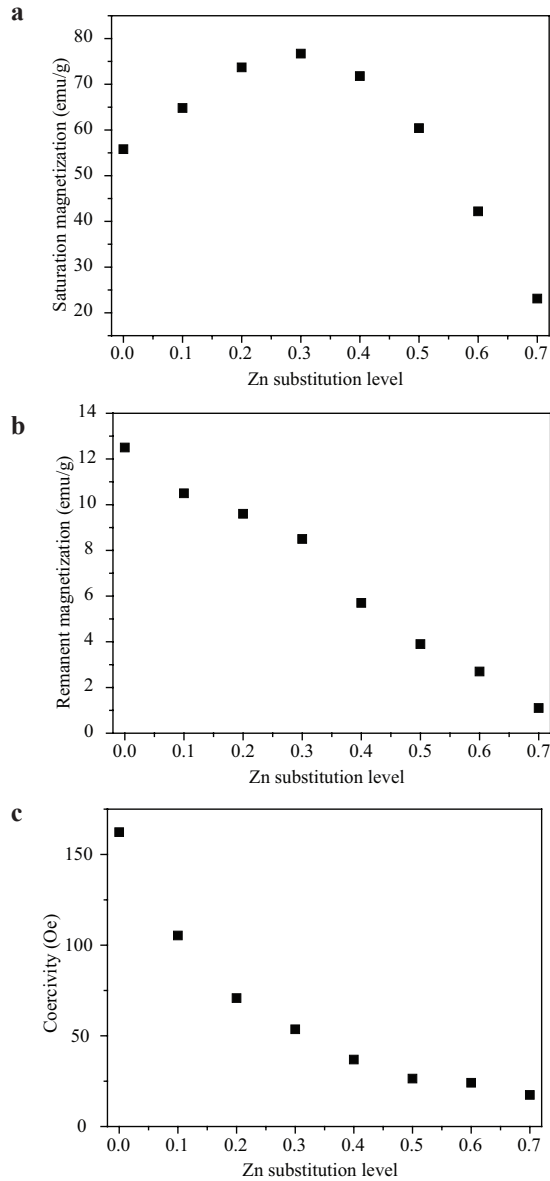


Figure 3. Concentration dependences of the main magnetic parameters of NZCF obtained from VSM: magnetization saturation –  $M_s$  (a); remnant magnetization –  $M_r$  (b) and coercivity  $H_c$  (c).

The measurements of magnetic properties were carried out using a vibrating sample magnetometer Lakeshore 7400 series in the magnetic field range of  $\pm 16$  kOe at room temperature. Figure 2 shows the hysteresis loops for the series of samples.

Spinels as soft magnetic materials can be characterized by high magnetization saturation, low coercivity and remnant magnetization at temperatures near room temperature. In Fig. 2, magnetization dependences vs. magnetic field for NZCF samples are shown.

Almost all investigated NZCF samples have non-linear behavior on concentration dependences of the main magnetic characteristics. Based on field dependences, we determined the main magnetic parameters ( $M_s$  – magnetization saturation,  $M_r$  – remnant magnetization,  $H_c$  – coercivity and graphically represent their dependence on the degree of substitution of Zn atoms (Fig. 3). This nature of the dependence of parameters on substitution can be associated with the differences in the magnetic moment of the  $Zn^{2+}$  is  $0 \mu B$  (there are no unpaired electrons with diamagnetic behavior) compared to  $2 \mu B$  for the  $Ni^{2+}$  (there are two unpaired electrons on 3d-shell). The general trend towards a monotonic decrease in  $H_c$  can be explained by a decrease in the anisotropy associated with the addition of nonmagnetic  $Zn^{2+}$  ions and the displacement of magnetic  $Ni^{2+}$  ions.

Summarizing, experimental samples of  $Co_{0.3}Zn_{0.7-x}Ni_xFe_2O_4$ , ( $0.7-x$ , where  $0 \leq x \leq 0.7$ ) was obtained by solid state synthesis from initial oxides. The correlation of the chemical content and magnetic characteristics was investigated. Almost all investigated NZCF samples have nonlinear behavior on concentration dependences of the main magnetic characteristics. It was observed that in the range of low Co-concentration ( $0.0 \leq x \leq 0.4$ ) in NZCF the values  $M_s$  increase till  $\sim 76.7$  emu/g (for  $x = 0.4$ ).

*This work was supported by the RFBR (project No 20-08-00716) and President's grants for young doctors of science (MD-5612.2021.4).*

1. M.I.A. Abdel Maksoud, Ramy Amer Fahim, A.G. Bedir et al., Environmental Chemistry Letters (2022).
2. U. Koenig, G. Chol, J. Appl. Crystallogr., **1**, (1968).

## STUDY OF ALIGNMENT DEGREE OF Nd-Dy-Fe-B SINTERED MAGNETS BY DIFFERENT METHODS

*A.V. Shitov*<sup>1,2\*</sup>, *O.A. Golovnia*<sup>2,3</sup>, *V.S. Gaviko*<sup>2,3</sup>, *A.G. Popov*<sup>2,3</sup>, *D.Yu. Vasilenko*<sup>1</sup>

<sup>1</sup>Urals Electromechanical Plant, Joint-Stock Company, Ekaterinburg, Russia

<sup>2</sup>Mikheev Institute of Metal Physics, Ural Branch, Russian Academy of Sciences, Ekaterinburg, Russia

<sup>3</sup>Ural Federal University, Ekaterinburg, Russia

\*E-mail: [matan.usu@gmail.com](mailto:matan.usu@gmail.com)

The remanence  $B_r$  and maximum energy density product  $(BH)_{\max}$  of sintered Nd-Fe-B magnets are greatly affected by easy axis alignment of each individual  $\text{Nd}_2\text{Fe}_{14}\text{B}$  grain, which is determined by alignment degree  $\alpha_r$ :

$$B_r = J_s \cdot V \cdot \alpha_p \cdot \alpha_r$$

where  $J_s$  is the saturation polarization,  $V$  is the volume fraction of the  $\text{Nd}_2\text{Fe}_{14}\text{B}$  phase,  $\alpha_p$  is the magnet relative density.

This work studies the alignment degree of the 25.08Nd-5.67Dy-67.02Fe-0.98B-1.02Co-0.11Cu-0.12Ga (wt.%) magnets, produced by low-oxygen technology [1]. Two production methods of these magnets were used. The first method includes loading powder into metallic mold, alignment in magnetic field followed by transverse pressing (TP). In the second method, the powder is loaded into a rubber mold with subsequent application of a pulse magnetic field, and subjected to hydraulic pressing (the rubber hydrostatic pressing (RHP)). An isotropic magnet was also produced by the RHP. After pressing green compacts were sintered and subjected to two-stage heat treatment. For magnetization reversal measurement rectangular samples were cut out from the magnets. Figure 1 shows an example of magnetization reversal curve. The main magnetic properties of the TP- and RHP-magnets measured along and perpendicular to the alignment axis are listed in Table 1 together with magnetic properties of an isotropic magnet.

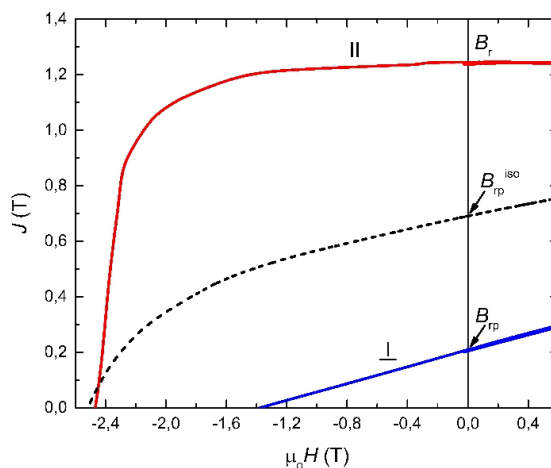


Figure 1. Magnetization reversal of the RHP isotropic magnets, the RHP magnets measured along and perpendicular to the alignment axis.

Table 1. Magnetic properties of the TP and RHP magnets measured along and perpendicular to alignment axis.

Sample	$B_r$ , T	$\mu_0 H_{cB}$ , T	$\mu_0 H_{cJ}$ , T	$(BH)_{max}$ , kJ/m <sup>3</sup>
TP-magnet				
Along alignment axis	1.225	1.20	2.46	293.7
Perpendicular to alignment axis	0.250	0.22	1.54	10.7
RHP-magnet				
Along alignment axis	1.257	1.23	2.42	307.3
Perpendicular to alignment axis	0.209	0.18	1.39	7.5
Isotropic	0.690	0.62	2.54	85.2

Alignment degree of TP- and RHP-magnets are estimated by three methods. The first method determines the alignment degree ( $\alpha_T$ ) from the ratio of remanence of an anisotropic magnet  $B_r^{\parallel}$  and  $J_s$ , where  $J_s$  is equal to the remanence of isotropic magnet  $B_r^{iso}$  multiplied by 2. Thus,  $\alpha_T$  is determined as follows:

$$\alpha_T = B_r^{\parallel} / 2B_r^{iso}.$$

The second method calculates the alignment degree ( $\alpha_{TM}$ ) from magnetic measurements by the Fernengel method [2] as follows:

$$\alpha_{TM} = \cos\theta = \cos(\arctg(2B_r^{\perp} / B_r^{\parallel})),$$

where  $\theta$  is the average angle between easy axes of each individual  $Nd_2Fe_{14}B$  grain and the texture axis of a magnet.  $B_r^{\perp}$  and  $B_r^{\parallel}$  are the remanences of magnets, which are determined from the magnetization reversal curves along and perpendicular to the alignment axis, respectively.

The third method determines alignment degree ( $\alpha_{TX}$ ) as the ratio of peak intensities with the same  $hkl$  indices of the diffraction pattern taken from the surfaces of anisotropic and isotropic magnets [3].

Alignment degrees of the TP- and RHP-magnets determined by different methods are listed in Table 2. According to Table 1,  $B_r$  of the RHP-magnet is 2.5% higher than that of the TP-magnet. The differences of the alignment degree between the two groups of magnets for each of 3 methods are listed in the last column of Table 2.

The difference in  $\alpha_T$  which is determined for the TP- and RHP-magnets is only 0.5%. The best correlation between  $B_r$  and alignment degree of the TP- and RHP-magnets is shown by the second method [2], and  $\alpha_{TM}$  is about 2.5%. However, the third method shows no correlation between magnetic properties and alignment degree.  $\alpha_{TX}$  are too low for the TP- and RHP-magnets, which

Table 2. Alignment degrees determined by different methods.

Alignment degree	TP-magnet	RIP-magnet	$\Delta$ of alignment degree, %
$\alpha_T$	0.921	0.925	0.5
$\alpha_{TM}$	0.926	0.949	2.5
$\alpha_{TX}$	0.73	0.86	15

contradicts  $B_r$  and  $(BH)_{\max}$  results. When the alignment degree is determined by the X-ray method, an equal contribution of all grains into axes distribution is assumed. In this case, only one Gaussian distribution describes the alignment of  $\text{Nd}_2\text{Fe}_{14}\text{B}$  grains. The difference between  $\alpha_{\text{TM}}$  and  $\alpha_{\text{TX}}$  most probably indicates the presence of two fraction of grains with different Gaussian distributions of easy axes. It leads to low  $\alpha_{\text{TX}}$ .

Thus, the Fernengel method has the best correlation with magnetic properties of the sintered magnets. To establish correlation between magnetic properties and alignment degree  $\alpha_{\text{TX}}$ , additional sample preparation and statistical data are required.

1. D.Yu. Vasilenko, A.V. Shitov, A.G. Popov, V.S. Gaviko, D.Yu. Bratushev, K.I. Podkorytov, O.A. Golovnya, *Physics of Metals and Metallography*, **123**, 145 (2022).
2. W. Fernengel, A. Lehneret, M. Katter, W. Rodewald, B. Wall, *J. Magn. Magn. Mater.*, **157/158**, 19 (1996).
3. D. Givord, A. Lignard, R. Perrier de la Bzthie, P. Tenaud, T. Viadieu, *Journal de Physique*, **46**, C6-313 (1985).

## EFFECT OF ION SUBSTITUTIONS ON THE MAGNETIC PROPERTIES OF BARIUM HEXAFERRITE

*I.A. Solizoda*<sup>1\*</sup>, *V.E. Zhivulin*<sup>1</sup>, *E.A. Trofimov*<sup>1</sup>, *S.V. Taskaev*<sup>1,2,3</sup>, *D.A. Vinnik*<sup>1</sup>

<sup>1</sup>Sout Ural State University, Chelyabinsk, Russia

<sup>2</sup>Chelyabinsk State University, Chelyabinsk, Russia

<sup>3</sup>National University of Science and Technology “MISIS”, Moscow, Russia

\*E-mail: [Solehzoda-i@email.ru](mailto:Solehzoda-i@email.ru)

We investigated the effect of substitution of magnetic Fe<sup>3+</sup> ions, with a magnetic moment of 5 μ<sub>B</sub>, with non-magnetic Al<sup>3+</sup>, Ti<sup>4+</sup> and Al<sup>3+</sup>-Ti<sup>4+</sup> ions on the magnetic properties of barium hexaferrite. BaFe<sub>12-x</sub>Al<sub>x</sub>O<sub>19</sub> (BaM:Al<sub>x</sub>, x = 0, 0.5, 1, 1.5, 2, 2.5, 3, 3.5) and BaFe<sub>11.5-x</sub>Ti<sub>0.5</sub>Al<sub>x</sub>O<sub>19</sub> (BaM:Ti<sub>0.5</sub>Al<sub>x</sub>, x = 0, 0.5, 1, 1.5, 2, 2.5, 3) powders were fabricated from the BaCO<sub>3</sub>, Fe<sub>2</sub>O<sub>3</sub>, Al<sub>2</sub>O<sub>3</sub> and TiO<sub>2</sub> precursors through a conventional ceramic technique [1].

The magnetic properties ( $M_s$ ,  $H_c$ ) of the samples were measured at room temperature using a VersaLab Quantum Design magnetometer, and the phase transition temperatures ( $T_c$ ) were measured using a differential scanning calorimeter STA 449 F1 Jupiter NETZCH.

Figures 1 and 2 show the dependence of the coercive force ( $H_c$ ) and saturation magnetization ( $M_s$ ) on the concentration of the substituted ions for BaM:Al<sub>x</sub> and BaM:Ti<sub>0.5</sub>Al<sub>x</sub> samples. By increasing concentration of Al<sup>3+</sup> in BaM:Al<sub>ex</sub>,  $H_c$  increases and  $M_s$  decreases (Fig. 1). While, as shown in Fig. 2, by increasing concentration of Al<sup>3+</sup> in BaM:Ti<sub>0.5</sub>Al<sub>x</sub> up to x = 0.5,  $H_c$  decreases and  $M_s$  increases. Starting from BaM:Ti<sub>0.5</sub>Al<sub>0.5</sub>, an increase in the concentration of Al<sup>3+</sup> leads to a monotonous decrease in  $M_s$  and an increase in  $H_c$ . In addition, there is a monotonous decrease in the temperature of the phase transitions for the studied samples (Fig. 3).

The decrease in  $M_s$  and  $E_c$  compared to BaM is due to the magnetic moments of the replaced ions. Substitution of the magnetic Fe<sup>3+</sup> ion (5 mB) with non-magnetic Al<sup>3+</sup> and Ti<sup>4+</sup> ions leads to a weakening of the exchange interaction between Fe<sup>3+</sup>-O-Fe<sup>3+</sup> ions, which reduces the value of  $M_s$  and  $T_c$ .

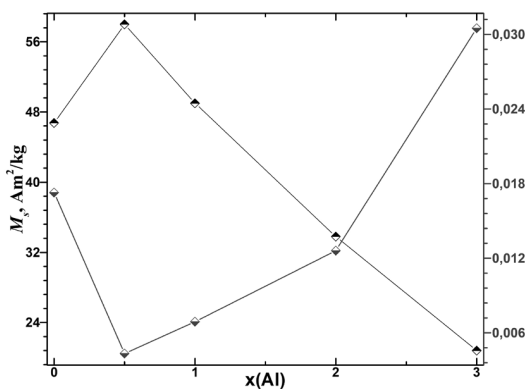


Figure 1. Dependence of  $H_c$  and  $M_s$  on the substitution level of Al<sup>3+</sup> for BaM:Al<sub>x</sub>.

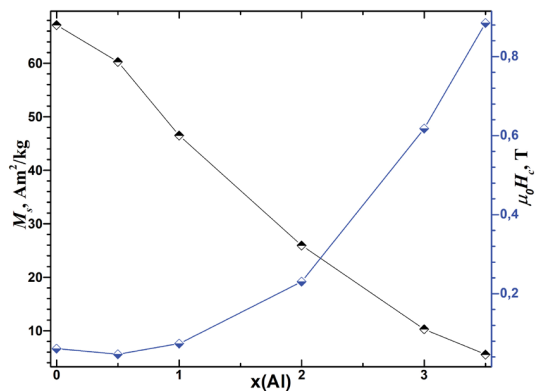


Figure 2. Dependence of  $H_c$  and  $M_s$  on the substitution level of Al<sup>3+</sup> for BaM:Ti<sub>0.5</sub>Al<sub>x</sub>.

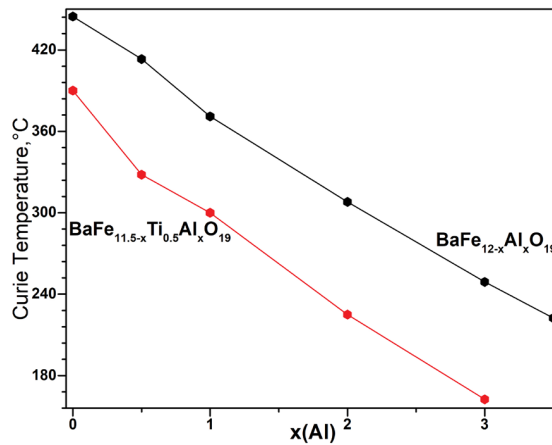


Figure 3. Dependence of  $T_c$  on the degree of substitution of  $Al^{3+}$  for samples  $BaM:Al_x$  and  $BaM:Ti_{0.5}Al_x$ .

The increase in the coercive force is explained by the particle size of the magnetic material. Substitution of  $Fe^{3+}$  ions with an ionic radius of [0.645 Å] with  $Al^{3+}$  ions with a smaller ionic radius of [0.545 Å] [2] leads to a decrease in the particle size from a multi-domain structure to a single-domain structure, which in turn leads to an increase in the coercive force [3].

*This work was supported by Russian Foundation for Basic Research (RFBR), grant No. 20-08-00716 and President's grants for young doctors of science (MD-5612.2021.4).*

1. V.E. Zhivulin, I.A. Solizoda et al., J. Mater. Res. Technol., **11**, 2235–2245 (2021).
2. R.D. Shannon, C.T. Prewitt, Acta Crystallogr., **A32**, 925–946 (1969).
3. C.-J. Li, B.-N. Huang and J.-N. Wang, J. Mater. Sci., **48**, 1702–1710 (2012).



**INVESTIGATION OF THE MAGNETIC AND DIELECTRIC PROPERTIES OF BARIUM-TITANIUM HEXAFERRITE**

*S.V. Trukhanov*<sup>1,2,3</sup>, *T.I. Zubar*<sup>1,2</sup>, *V.A. Turchenko*<sup>2,4,5</sup>, *An.V. Trukhanov*<sup>1,2,3</sup>, *L. Matzui*<sup>6</sup>,  
*O. Yakovenko*<sup>6</sup>, *D.A. Vinnik*<sup>2</sup>, *A.Yu. Starikov*<sup>2\*</sup>, *V.E. Zhivulin*<sup>2</sup>, *A.V. Trukhanov*<sup>1,2,3</sup>

<sup>1</sup>Scientific Practical Materials Research Centre of NAS of Belarus, Minsk, Belarus  
<sup>2</sup>South Ural State University, Chelyabinsk, Russia  
<sup>3</sup>National University of Science and Technology “MISiS”, Moscow, Russia  
<sup>4</sup>Frank Laboratory of Neutron Physics, Joint Institute for Nuclear Research, Dubna, Russia  
<sup>5</sup>Donetsk Institute for Physics and Engineering named after O.O. Galkin of the NASU, Kiev, Ukraine  
<sup>6</sup>Physics Department, Taras Shevchenko National University, Kiev, Ukraine  
 \*E-mail: [starikov-andrey@mail.ru](mailto:starikov-andrey@mail.ru)

Due to specific crystal structure with several cation positions different in coordination, the BaFe<sub>12</sub>O<sub>19</sub> type ferrites are characterized by great capacity for the accommodation of different metals at high doping levels that provides a possibility for wide tuning of physical properties by cation substitution. Hexagonal ferrites from the BaFe<sub>12</sub>O<sub>19</sub> family are highly attractive for the application

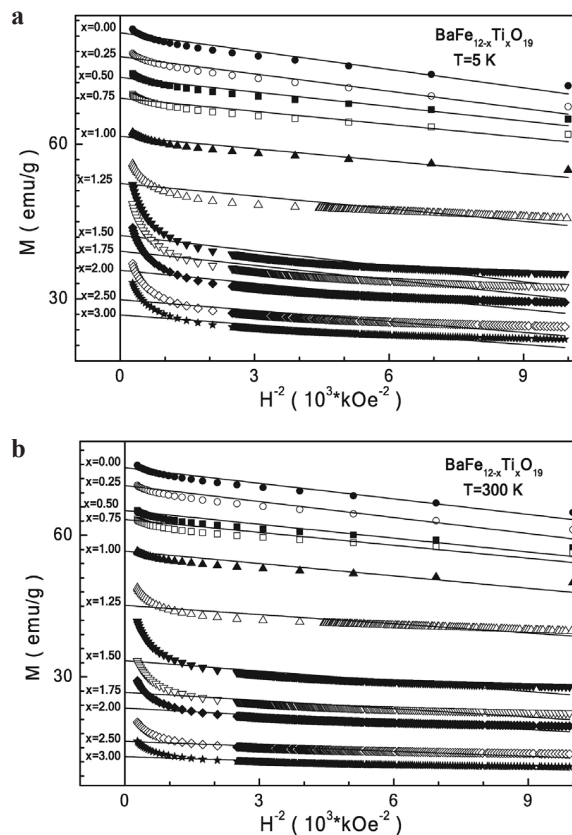


Figure 1.  $M(H^{-2})$  magnetization vs. field inverse square for the titanium-barium hexaferrites at 5 K (a) and 300 K (b). Straight line is for eye guide.

in microwave technology due to high chemical and thermal stability and strong magnetic anisotropy [1]. The relevance of the properties of the compositions under consideration is explained by the distribution of the electron density [2].

Substitution by  $\text{Ti}^{4+}$  ( $S = 0$ ) titanium cations is always very exciting since it leads to a change in the charge state of iron cations, which in turn can change the magnetic structure of the sample. The question of filling positions remains open up to this day [3]. In addition, interesting facts are that the iron cation  $\text{Fe}^{2+}$  in octahedral coordination can undergo a transition to the low-spin state (LS,  $S = 0$ ) at low temperatures [4] while in tetrahedral coordination it is a Jahn-Teller ion [5].

The main objective of this work was to optimize the magnetic and dielectric performance of the barium hexaferrites by substituting titanium cations at high concentrations. It was necessary to clarify the positions occupied by titanium cations on the basis of the already known data given above. The importance of this study is explained by the fact that with a favorable distribution of titanium cations over positions, it is possible to increase the magnetic and dielectric characteristics, which cause high microwave absorption.

So, in this investigation, the range of the titanium-barium hexaferrites is extended up to 3.00. The crystal structure parameters were received with the Rietveld method from X-ray powder diffraction data. The occupation mechanism was confirmed at high substitutional concentrations. The spontaneous magnetization, remanent magnetization, the magnetocrystalline anisotropy coefficient and the anisotropy field are investigated at temperatures of 5 K and 300 K. The electrical ac-resistivity, the real part of the permittivity and the tangent loss are investigated in a wide temperature range at different frequencies.

The titanium-barium  $\text{BaFe}_{12-x}\text{Ti}_x\text{O}_{19}$  hexaferrites up to  $x = 3.00$  were produced with common ceramic technology. The Mossbauer investigations at different temperatures and zero magnetic field confirm the localization of  $\text{Ti}^{4+}$  cations in the  $2a$  and  $4f_{\text{VI}}$  octahedrally coordinated positions,  $4f_{\text{IV}}$  tetrahedrally coordinated positions and  $2b$  pentahedrally coordinated positions. The  $M_s$  spontaneous magnetization was determined with the law of approach to saturation from the field magnetization measured at 5 K and 300 K. The  $K_{\text{eff}}$  effective magnetic crystal anisotropy coefficient and  $H_a$  anisotropy field were calculated. These values decrease almost monotonically with substitution and temperature. The  $M_s$  spontaneous magnetization decrease from  $\sim 81.63$  emu/g for the  $x = 0.00$  down to  $\sim 26.89$  emu/g for the  $x = 3.00$  at 5 K whereas at 300 K it decreases from  $\sim 74.31$  emu/g for the  $x = 0.00$  down to  $\sim 13.10$  emu/g for the  $x = 3.00$ . With an increase in the doping concentration, both the magnitude of the  $\rho$  electrical ac-resistivity and the  $T_{\text{cl}}$  temperature of transition to the activation type of conductivity increase non-monotonically. For the  $x = 0.50$ , the lowest electrical resistivity of  $\rho \sim 5.10 \cdot 10^3$  Ohm·cm is observed at room temperature. At  $x = 3.00$ , the maximum electrical resistivity of  $\rho \sim 9.70 \cdot 10^6$  Ohm·cm is observed. The  $\epsilon'$  real part of the permittivity increases constantly with increasing temperature and decreases with increasing frequency for all the compositions. The concentration dependence of the  $\epsilon'$  real part of the permittivity is not monotonic with a maximum at  $x = 0.50$ . The temperature peak of the  $\text{tg}(d)$  loss tangent with the doping concentration changes nonmonotonically in magnitude and position. An interpretation of the magnetic and dielectric properties of the titanium-barium hexaferrites is performed in frame of magnetic dilution and breakdown of  $\text{Fe}^{3+}\text{-O}^{2-}\text{-Fe}^{3+/2+}(\text{Ti}^{4+})$  indirect superexchange interactions taking into account the positions occupation

*This work was supported by Russian Foundation for Basic Research (RFBR), grant No. 20-08-00716 and President's grants for young doctors of science (MD-5612.2021.4).*

1. R. Pullar, Prog. Mater. Sci., **57**, 1191–1334 (2012).
2. Yim, Y. Youn et al., npj Comput mater., **4**, 17 (2018).
3. D.A. Vinnik, V.E. Zhivulin et al., J. Alloys Compd., **859**, 158365 (2021).
4. P. Gütllich, A. Hauser and H. Spiering, Angew. Chem. Int. Ed. Engl., **33**, 2024–2054 (1994).
5. S.V. Trukhanov, A.V. Trukhanov et al., J. Exp. Theor. Phys., **113**, 819–825 (2011).

**INFLUENCE OF THERMAL TREATMENTS ON THE MAGNETIC PROPERTIES OF SOFT MAGNETIC MATERIALS PRODUCED BY SLS METHOD FROM IRON POWDER**

*E.A. Stepanova\**, D.A. Razueva, V.E. Maltseva, S.V. Andreev, A.S. Volegov

Ural Federal University, Ekaterinburg, Russia

\*E-mail: [elena.stepanova@urfu.ru](mailto:elena.stepanova@urfu.ru)

New technologies, including 3D printing, are used to obtain a high level of magnetic properties. The method of 3D printing provides an opportunity to obtain magnetic cores of unique configurations in accordance with the specific demands of consumers [1]. However, A.S. Zhukov et al. [2] showed that it is impossible to obtain the required properties immediately after manufacturing. Therefore, thermal treatment (TT) is recommended to improve magnetic properties. Considering that the properties are strongly determined by the initial condition (powder size, laser power and speed), it is necessary to undertake studies to establish the optimal mode of TT.

In this paper, the influence of TT at different temperatures on the magnetic properties of the torus produced by 3D printing from carbonyl iron powder was studied. Samples were obtained by

Table 1. Magnetic properties of 3D-torus after different thermal treatment.

	B, T			m	HL $H_m = 2000$ A/m	
	$H_m = 500$ A/m	$H_m = 1000$ A/m	$H_m = 2000$ A/m		$H_c$ , A/m	$B_r$ , T
Initial state	0.027	0.06	0.17	70	10	0.01
TT 900 °C	0.12	0.47	0.78	379	560	0.58
TT 1000 °C	0.14	0.55	0.90	440	560	0.64
TT 1200 °C	0.33	0.70	0.94	590	400	0.69

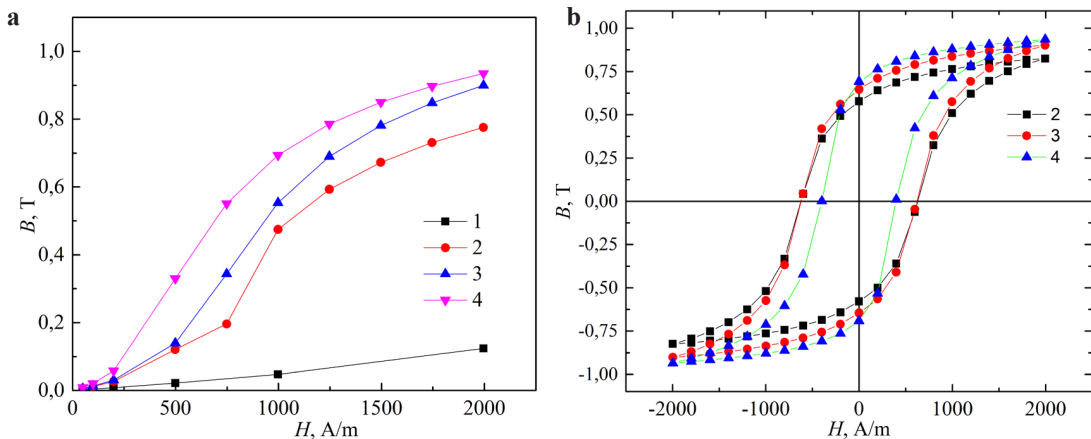


Figure 1. Magnetization curves (a) and hysteresis loops (b) after TT: 1 – initial state, 2 – at 900 °C, 3 – at 1000 °C, 4 – at 1200 °C.

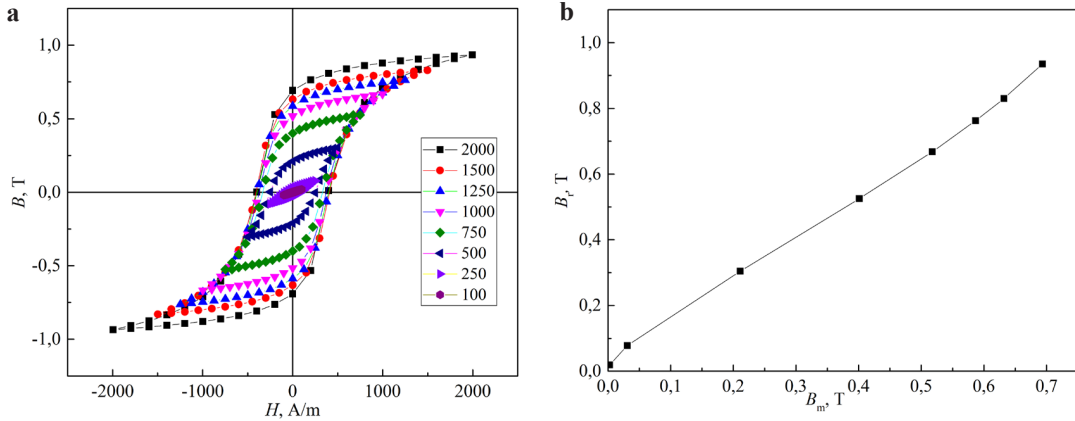


Figure 2. Hysteresis loops at different magnetic fields (a) and dependent  $B_r(B_m)$  (b) after TT 1200 °C.

selective laser sintering (SLS) at the Orlas Creator RA. The laser beam power was 158 W, the speed of laser beam spot on the powder surface was 1000 mm/s. TT were performed in a vacuum at temperatures of 900, 1000, and 1200 °C.

Magnetization curves and hysteresis loops were obtained on measuring complex MMKS-0.5-100 (SRI STT, Smolensk) with an error not exceeding 3%.

Magnetization curves and hysteresis loops (HL) for  $H_m = 2$  kA/m are shown in Fig. 1. Several magnetic properties are presented in Table 1. TT lead to significant changes in magnetic properties, including the increase of maximum magnetic permeability and residual induction, the decrease of magnetic coercivity. The best properties were received after TT at 1200 °C. In the study [2] a mechanism for improving the properties by increasing the grain size as a result of TT was proposed.

Figure 2b shows the  $B_r(B_m)$  dependence for TT at 1200 °C obtained from partial hysteresis loops (Fig. 2a). Based on the study [3] and the linear nature of the dependency, it was suggested that the magnetization processes occur by displacement of the domain boundaries walls.

In the result of the study, the best magnetic properties of the samples were achieved at an annealing temperature of 1200 °C, which is most likely explained by grain enlargement during TT [2]. According to linear dependence  $B_r(B_m)$  (on Fig. 2b) it was assumed that the magnetization processes occur due to the displacement of the domain boundaries walls [3].

*Support by RSF № 21-72-10104 is acknowledged.*

1. A.R. Safin, Ranjan Kumar Behera, Problemy energeticy, **23**, no. 3, 14–33 (2021) [in Russian].
2. A.S. Zhukov, B.K. Barakhtin, V.V. Bobyr, P.A. Kuznetsov, I.V. Shakirov, J. of Physics: Conference Series, **1791**, p. 012122 (2021).
3. N.A. Skulkina, O.A. Ivanov, A.K. Mazeeva, P.A. Kuznetsov, E.A. Stepanova, O.V. Blinova, E.A. Mikhailitsyna, Physics of Metals and Metallography, **119**, no. 2, 127–133 (2018).

## PREDICTIONS OF THE MAGNETIC PROPERTIES OF NANOCRYSTALLINE FINEMET-TYPE ALLOYS USING MACHINE LEARNING

*K.A. Stepanova\**, *V.A. Kataev*

Department of magnetism and magnetic nanomaterials, UrFU, Ekaterinburg, Russia

\*E-mail: [ksenia.stepanova@urfu.ru](mailto:ksenia.stepanova@urfu.ru)

In 1988 Yoshizawa et al. introduced a new soft magnetic material based on the Fe-Si-B alloy doped with small amount of Cu and Nb elements [1]. The appropriate chemical composition and heat treatment resulted in ultrafine Fe-Si grains embedded in an amorphous matrix. Such a nanostructure yielded excellent soft magnetic properties that can be maintained even at high-frequency range. This achievement defined the microstructural concept for the design of next-generation soft magnetic materials. However, the traditional approach of developing new compositions is laborious and indirect, i.e. the “trial and error” method is used quite often. Machine learning (ML) can overcome this issue and boost the development of new soft magnetic materials substantially. In particular, ML can summarize extensive experimental data on FINEMET-type alloys and train regressors to predict magnetic properties based on chemical composition and processing conditions.

Thus, the aim of our work is to develop ML models that are capable to predict the magnetic properties of Fe-based nanocrystalline FINEMET-type alloys based on the chemical compositions and heat treatment conditions.

The database for ML containing the experimental information about 1440 samples was collected from the articles in ref. [2]. Data was split into train and test datasets with proportion 80/20 %, respectively. The main constituent chemical elements of the samples and details of processing are shown in Fig. 1. They are:

- Groups 4, 5 and 6 of elements that inhibit grain growth.
- Groups 11 and 12 of elements that providing nucleation centers.
- Groups 13, 14, 15 of elements forming the amorphous phase.

group 1																		18																													
H																	He																														
Li	Be											B	C	N	O	F	Ne																														
Na	Mg	3	4	5	6	7	8	9	10	11	12	13	14	15	16	17																															
K	Ca	Sc	Ti	V	Cr	Mn	Fe	Co	Ni	Cu	Zn	Ga	Ge	As	Se	Br	Kr																														
Rb	Sr	Y	Zr	Nb	Mo	Tc	Ru	Rh	Pd	Ag	Cd	In	Sn	Sb	Te	I	Xe																														
Cs	Ba		Hf	Ta	W	Re	Os	Ir	Pt	Au	Hg	Tl	Pb	Bi	Po	At	Rn																														
		<table border="1"> <tr> <td>La</td> <td>Ce</td> <td>Pr</td> <td>Nb</td> <td>Pm</td> <td>Sm</td> <td>Eu</td> <td>Gd</td> <td>Tb</td> <td>Dy</td> <td>Ho</td> <td>Er</td> <td>Tm</td> <td>Yb</td> <td>Lu</td> </tr> <tr> <td>Ac</td> <td>Th</td> <td>Pa</td> <td>U</td> <td>Np</td> <td>Pu</td> <td>Am</td> <td>Cm</td> <td>Bk</td> <td>Cf</td> <td>Es</td> <td>Fm</td> <td>Md</td> <td>No</td> <td>Lr</td> </tr> </table>																La	Ce	Pr	Nb	Pm	Sm	Eu	Gd	Tb	Dy	Ho	Er	Tm	Yb	Lu	Ac	Th	Pa	U	Np	Pu	Am	Cm	Bk	Cf	Es	Fm	Md	No	Lr
La	Ce	Pr	Nb	Pm	Sm	Eu	Gd	Tb	Dy	Ho	Er	Tm	Yb	Lu																																	
Ac	Th	Pa	U	Np	Pu	Am	Cm	Bk	Cf	Es	Fm	Md	No	Lr																																	
<b>Details of processing</b>		Annealing temperature (K)		Annealing time (s)		Crystallization temperatures (K)			Direction of annealing magnetic field			Ribbon thickness (nm)																																			
						$T_{onset}$ $T_{(I)peak}$ $T_{(II)peak}$																																									

Figure 1. Used dataset: chemical elements and alloys processing.

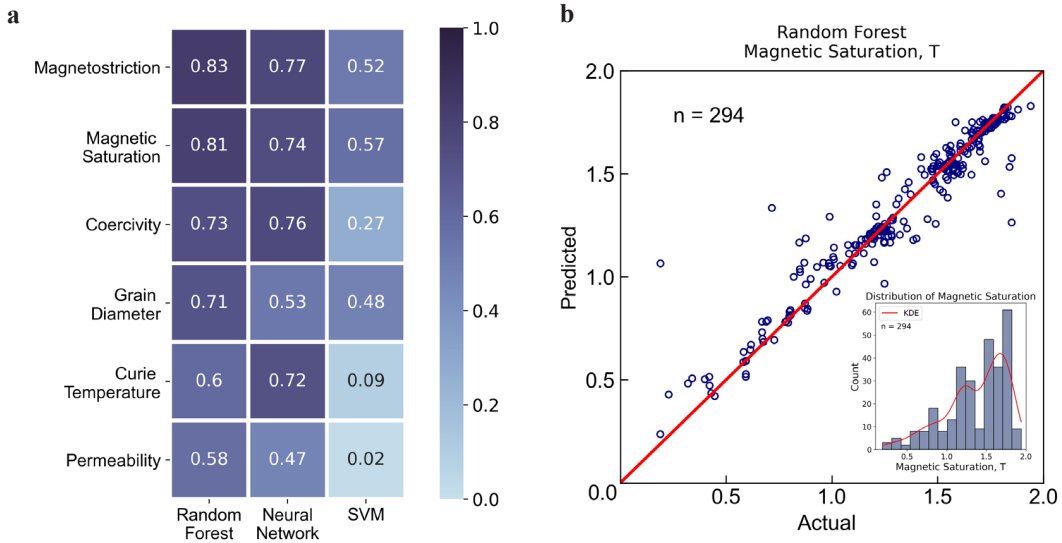


Figure 2. Evaluation of Machine Learning Algorithms: **a** comparison of algorithms' predictions by  $R^2$  and **b** comparison of Random Forest predictions and measured values of saturation induction.

We built ML models using a Scikit Python library that included several algorithms: Random Forest, Neural Network and Support Vector Machine regressor (SVM). Algorithms' parameters were found by grid search to obtain the best scoring metrics. Such principally different algorithms were selected to examine and compare their ability to predict the magnetic properties of FINEMET-type alloys as targets, i.e.. magnetostriction, magnetic saturation, coercivity, curie temperature, permeability, grain size that shown in Fig. 2a.

The coefficient of determination ( $R^2$ ) was used to compare the performance of the algorithms while Root Mean Square Error (RMSE) was selected as a scoring metric of predicting magnetic properties.

According to preliminary assessment, the Random Forest model has benefits over other algorithms and can predict magnetostriction and magnetic saturation the best way (Fig. 2a). In Fig 2b in range 1,5–2,0 Random Forest algorithm described magnetic saturation with small value of RMSE.

After developing ML algorithms, we performed validation with new data obtained from articles not included in the original database. For the new data, magnetic characteristics were predicted and then compared with the values reported in the papers.

According to obtained results, we made conclusions about the quality of the predictions and about the possibility of using this model in future to create new FINEMET-type alloys.

A special gratefulness to the authors of ref. [2] for providing the database.

1. Y. Yoshizawa, S. Oguma, K. Yamauchi, New Fe-based soft magnetic alloys composed of ultrafine grain structure, *J. Appl. Phys.*, **64**, (10), 6044–6046 (1988).
2. Y. Wang, Y. Tian, T. Kirk, O. Laris, J.H. Ross Jr., R.D. Noebe, V. Keylin, R. Arroyave, Accelerated design of Fe-based soft magnetic materials using machine learning and stochastic optimization. *Acta Materialia*, **194**, 144–155 (2020).

**EASY PLANE TYPE OF MAGNETIC ANISOTROPY  
IN LAYERED  $GdMn_2Si_2$  COMPOUND WITH EASY AXIS TYPE  
OF MAGNETOCRYSTALLINE ANISOTROPY**

*P.B. Terentev<sup>1,2\*</sup>, E.G. Gerasimov<sup>1,2</sup>, A.F. Gubkin<sup>1,2</sup>, N.V. Mushnikov<sup>1,2</sup>*

<sup>1</sup>M.N. Mikheev Institute of Metal Physics of Ural Branch of Russian Academy of Sciences, Ekaterinburg, Russia

<sup>2</sup>Institute of Natural Sciences and Mathematics, Ural Federal University, Ekaterinburg, Russia

\*E-mail: [terentev@imp.uran.ru](mailto:terentev@imp.uran.ru)

Magnetic properties and magnetic structures of layered  $GdMn_2Si_2$  compound were studied using quasi-single crystal, high magnetic fields up to 520 kOe, and neutron powder diffraction experiment designed for high absorbent systems (Fig. 1). It was shown that  $GdMn_2Si_2$  has strong easy plane type magnetic anisotropy at temperatures  $T_{Gd} < 52$  K at which Gd atoms are magnetically ordered. At temperatures  $52$  K  $< T < 453$  K, the compound has antiferromagnetic ordering of Mn layers and easy axis type magnetic anisotropy with the easy axis directed along the tetragonal  $c$ -axis. The exchange-induced in-plane magnetic anisotropy of layered  $GdMn_2Si_2$  at low temperatures arises to prevent magnetic frustration in Gd layers. Magnetic properties of  $GdMn_2Si_2$  at temperatures below 52 K can be described within a three-sublattice model based on the Yafet-Kittel approximation.

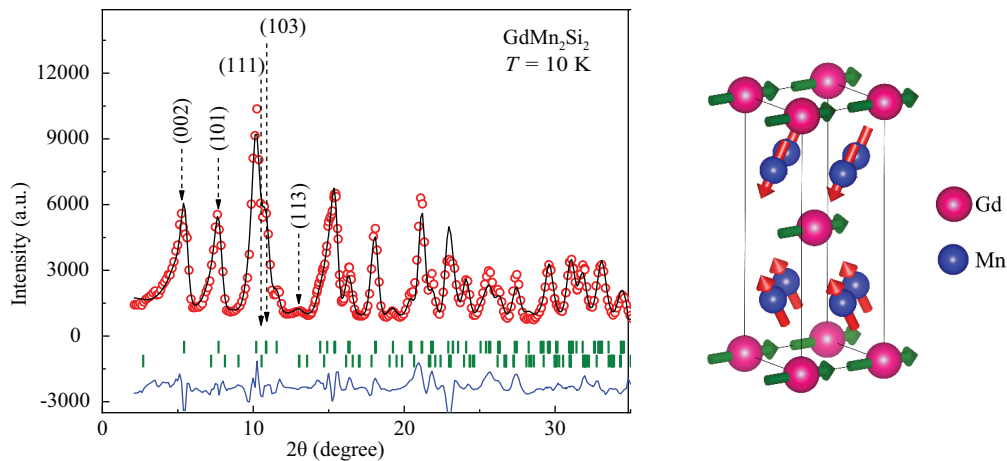


Figure 1. Neutron diffraction patterns of  $GdMn_2Si_2$  at 10 K (left side). Points are experimental data, bold lines are Rietveld refinement with FullProf. Below the patterns, vertical lines point to the positions of magnetic and nuclear reflections, thin solid line at the bottom shows the difference between experimental and calculated profiles. Schematic visualization of the noncollinear magnetic structure refined at  $T = 10$  K (right side).

**MAGNETIZATION REVERSAL PROCESSES IN Nd<sub>2</sub>Fe<sub>14</sub>B AND Sm(Co, Fe, Zr, Cu)<sub>6.63</sub> PERMANENT MAGNETS**

*A.N. Urzhumtsev\*, V.E. Maltseva, A.S. Volegov*

The Institute of Natural Sciences and Mathematics, Ural Federal University, Ekaterinburg, Russia

\*E-mail: [andrei.urzhumtsev@urfu.ru](mailto:andrei.urzhumtsev@urfu.ru)

In the modern industry, the usage of rare earth permanent magnets (PM), such as Nd<sub>2</sub>Fe<sub>14</sub>B and Sm(Co, Fe, Zr, Cu)<sub>z</sub>, is widespread in the field of energy, electric vehicles and green technologies. Despite almost half a century history of their research and development of technologies for their production, a number of fundamental questions about the mechanisms of their magnetization reversal processes are still controversial [1]. A detailed understanding of the mechanisms of formation of a high-coercivity state in this class of PMs will expand the possibilities for optimizing their magnetic properties. This will apply these materials for use as the basis for 3D printing of PMs using selective laser melting technology (SLM) [2].

To date, the question of the key mechanism of the high-coercivity state in sintered Nd<sub>2</sub>Fe<sub>14</sub>B and Sm(Co, Fe, Zr, Cu)<sub>z</sub> magnets remains open. Previously, it was believed that the key mechanism in Nd<sub>2</sub>Fe<sub>14</sub>B magnets is the nucleation [3]. Later, it was suggested that in such magnets a different type of magnetization reversal is pinning [4]. For Sm(Co, Fe, Zr, Cu)<sub>z</sub> magnets, the pinning mechanism is mainly determined, which is provided by the microcellular structure of this class of magnets [5, 6]. However, it was shown in [1, 7] that it is more complex than pure pinning mechanism. We have proposed an approach based on the analysis of magnetometric methods, in particular, on the analysis of the angular dependences of the coercivity  $H_c(\theta)$  and of the magnetic ac susceptibility  $\chi(H)$  to estimate the formation mechanism of a high-coercivity state [7].

Sintered permanent magnets NdFeB (N48) and Sm(Co, Fe, Zr, Cu)<sub>6.63</sub> (KS-25) were obtained by the sintering technology at the POZ-Progress LLC in Verkhnyaya Pyshma town. Samples of PMs were cut into discs 5 mm in diameter and 1 mm high and fixed in paraffin wax into copper containers. Magnetic measurements were carried out in magnetic field up to 90 kOe and up to 70 kOe at the temperature  $T = 300$  K using the PPMS DynaCool with VSM option (Quantum Design)

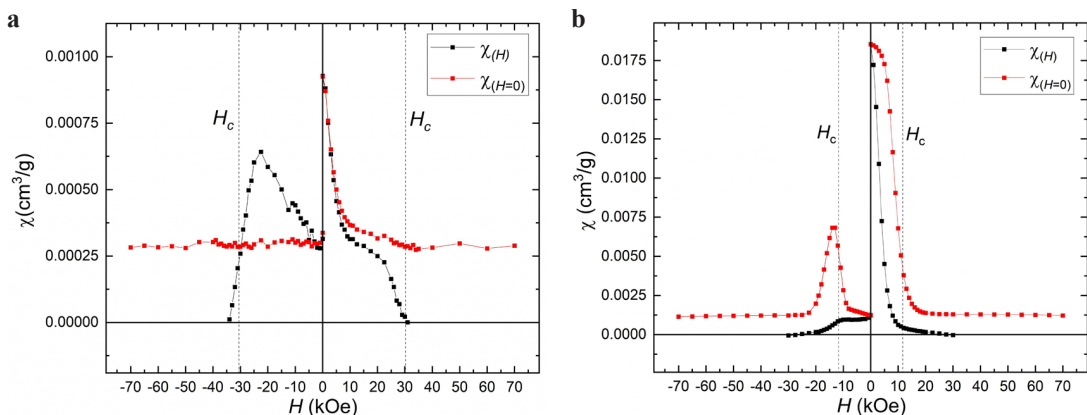


Figure 1. Magnetic ac susceptibility  $\chi(H)$  for Nd<sub>2</sub>Fe<sub>14</sub>B (a) and Sm(Co, Fe, Zr, Cu)<sub>6.63</sub> (b).



and MPMS XL 7 (Quantum Design), respectively. Magnetization curves were measured from the thermally demagnetized state. The magnetic susceptibility was measured in an alternating magnetic field with a strength of  $H = 3.7$  Oe and at a frequency of 7 Hz. The susceptibility  $\chi(H)$  was measured in an external magnetic field and after this was turned off ( $\chi(H = 0)$ ).

Measurements of the angular dependences coercivity  $H_c(\theta)$  showed that for  $\text{Sm}(\text{Co}, \text{Fe}, \text{Zr}, \text{Cu})_z$  magnets these dependences are well described within the framework of the Stoner-Wohlfahrt model, which indirectly indicates that the magnetization reversal mechanism is the nucleation. At the same time, for  $\text{Nd}_2\text{Fe}_{14}\text{B}$  magnets, the dependences  $H_c(\theta)$  of the Kondorsky type were obtained, which indicates the predominance of domain wall pinning.

From the ac susceptibility curves  $\chi(H)$  in Fig. 1, it can be seen that the initial susceptibility for PMs is quite high. This result is because there are practically no defects in these PMs in the grains and the domain walls (DW) is easily displaced under the external magnetic field.

In NdFeB magnets magnetization reversal processes plausible proceed as follows: in the thermally demagnetized state, the DWs are inside the grains; when the magnetizing field is turned on, they begin to move perpendicular to the easy magnetization axis of the grains. This state corresponds to a fairly high level of magnetic susceptibility. After the field is turned off, under the action of its own demagnetizing field, the DWs return to their original state. This continues until the external field exceeds its own demagnetizing field, and the DWs passes to the grain boundary. During magnetization reversal, demagnetization channels are formed, which capture part of the grains. As a result, domain walls are formed in grains. Domain walls are easily displaced, which manifests itself in a high value of ac susceptibility.

A model of the magnetization reversal mechanism is proposed to explain the entire set of properties of the  $\text{Sm}(\text{Co}, \text{Fe}, \text{Zr}, \text{Cu})_z$  PMs [7]. The essence of the model is as follows. In a demagnetizing field, the lamellar of the Zr-rich phase, which are exchange-coupled with the main phase of  $\text{Sm}_2\text{Co}_{17}$ , act as a region for the formation of a magnetization reversal nucleus of the main phase. In this case, the motion of the domain wall turns out to be limited by precipitates of the Zr-rich or  $\text{Sm}(\text{Cu}, \text{Co})_5$  phase. As a result of the grain magnetization reversal, the DWs passes through the grain as a whole and annihilates at the grain boundary; as a result, there is practically no contribution to the susceptibility  $\chi(H = 0)$  on Fig. 1b. The proposed model makes it possible to explain the features of the strong dependence of the coercivity of the  $\text{Sm}(\text{Co}, \text{Fe}, \text{Zr}, \text{Cu})_z$  magnets from the heat treatment regimes, which has not yet been satisfactorily done under the assumption of the only pinning model [6].

A more detailed description of the processes of magnetization and magnetization reversal in permanent magnets  $\text{Nd}_2\text{Fe}_{14}\text{B}$  and  $\text{Sm}(\text{Co}, \text{Fe}, \text{Zr}, \text{Cu})_z$  based on magnetometric measurements will be presented in the report.

*This work was financially supported by RSF grant № 21-72-10104.*

1. D. Givord, P. Tenaud, T. Viadieu, Coercivity mechanisms in ferrites and rare earth transition metal sintered magnets ( $\text{SmCo}_5$ , Nd-Fe-B), IEEE Trans. on Magn., **24**(2), 1921–1923 (1988).
2. A.S. Volegov et al., Additive manufacturing of heavy rare earth free high-coercivity permanent magnets, Act. Mater., **188**, 733–739 (2020).
3. H. Kronmüller, K.-D. Durst, M. Sagawa, Analysis of the magnetic hardening mechanism in RE-FeB permanent magnets, J. Magn. Magn. Mater., **74**(3), 291–302 (1988).
4. J. Li, H. Sepehri-Amin et al., Most frequently asked questions about the coercivity of Nd-Fe-B permanent magnets, Science and Technology of Advanced Materials, **22**(1), 386–403 (2021).
5. O. Gutfleisch et al., Evolution of magnetic domain structures and coercivity in high performance  $\text{SmCo}_2$ :17-type permanent magnets, J. Act. Mater., **54**(4), 997–1008 (2006).
6. L. Pierobon et al., Unconventional magnetization textures and domain-wall pinning in Sm-Co magnets, Sci. Rep., **10**(1) (2020).
7. A. Urzhumtsev et al., Magnetization reversal processes in sintered permanent magnets  $\text{Sm}(\text{Co}, \text{Fe}, \text{Zr}, \text{Cu})_z$ , J. Magn. Magn. Mater., **551**, 169143 (2022).

## STRUCTURAL FEATURES OF MAGNETIC METAL-DIELECTRIC FILMS (CoFeB + SiO<sub>2</sub>)

*L.N. Kotov\*, V.A. Ustyugov, V.S. Vlasov*

Syktyvkar State University, Syktyvkar, Russia

\*E-mail: [kotovln@mail.ru](mailto:kotovln@mail.ru)

Material science of composite nanostructured materials is an actively developing field today. Experimental studies and modeling of the structural parameters, chemical composition of thin metal-dielectric films, and the search for a connection between the material parameters and magnetic properties will allow us in the future to optimize the processes of industrial synthesis of such materials for specific practical applications [1–3].

In the present work the characteristics of metal-dielectric composite films of composition  $\{(Co_{0.44}Fe_{0.36}B_{0.2})_x + (SiO_2)_{(1-x)/3}\}$  were investigated. The structure of the films is characterized by high metal concentration gradient within  $0.42 \pm 0.85$  atomic fraction along a 48 mm long sheet of lamsan. The thicknesses and chemical composition of the samples were determined using a TESCAN MIRA3 scanning electron microscope. The surface topography as well as the magnetic structure of the film surface was investigated using an ARIS-3500 atomic force microscope.

To analyze the topographic structure of the surface of the samples, the distributions of the average densities of points with different heights relative to the base level (the lowest point in the atomic force microscopy image) were plotted. From the obtained graphs (Fig. 1) it is clear that at low concentrations of metallic phase, the film surface is characterized by compactness in height: the maximum height difference does not exceed 25 nm, with the highest density of points with a height of about 10 nm. This degree of surface homogeneity may indicate the formation of a dielectric matrix in which small metal granules are embedded. On the contrary, when the metal concentration is high, apparently, due to the fusion of metal particles into large formations, a wider and smoother distribution of points in height is observed in the plot.

Important data for the construction of theoretical models are information about the thickness and chemical composition of the films (Fig. 2). The graphs show that the thickness of the films

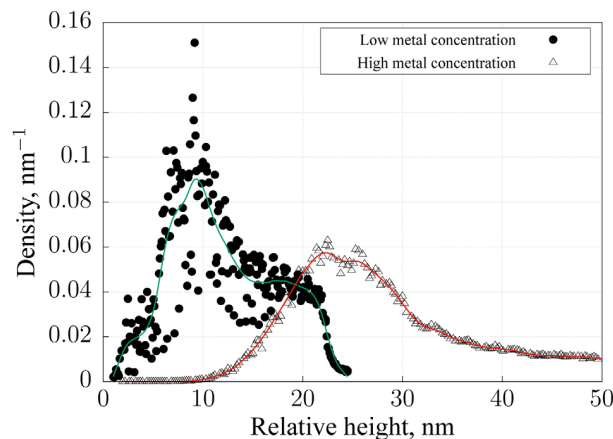


Figure 1. Atomic force microscopy image point distributions of samples by height.

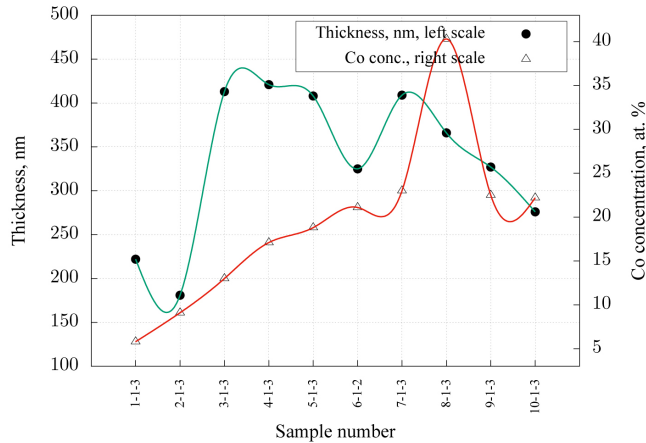


Figure 2. Sample thicknesses and percent cobalt content (metal concentration in the samples increases from left to right).

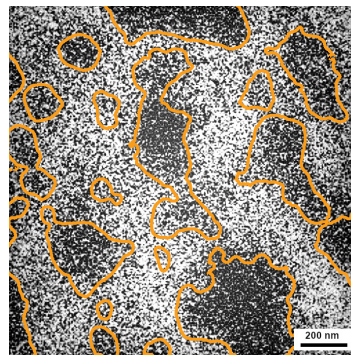


Figure 3. Overlaying topographic elevation boundaries on the magnetic phase contrast image.

decreases as the metal concentration increases, which is primarily due to the geometry of the sputtering machine, and probably needs to be corrected in the future. The content of cobalt, a component of the metallic phase, obviously increases with increasing concentration of the latter, which can also be seen in the graph. The maximum in the right part of the graph seems to be related to the percolation transition and the formation of the metallic matrix on the film surface.

A comparison of magnetic phase contrast images and surface topography (Fig. 3) shows that the topographic elevations are reliably associated with magnetized matter, i.e., metal grains.

The obtained data on material parameters are used to build theoretical models of film formation and manifestation of their magnetic high-frequency properties.

*Support by RSF (project №21-72-20048) is acknowledged.*

1. A. Sarychev, V. Shalaev. *Electrodynamics of metamaterials*, World Scientific (2007).
2. L.N. Kotov, V.S. Vlasov, V.A. Ustyugov et al., *IOP Conf. Series: Materials Science and Engineering*, **175**, 012021 (2017).
3. L.N. Kotov, V.S. Vlasov, V.K. Turkov et al., *JNN*, **12** (2), 1696 (2012).

UNIQUE MAGNETIC PROPERTIES OF NANOCRYSTALLINE  
CO-BASED GLASS-COATED HYBRID ALLOY

*V. Kolesnikova*<sup>1\*</sup>, *N. Andreev*<sup>1,2</sup>, *A. Omelyanchik*<sup>1</sup>, *I. Baraban*<sup>1</sup>, *M. Gorshenkov*<sup>2</sup>, *V. Rodionova*<sup>1</sup>

<sup>1</sup>Immanuel Kant Baltic Federal University, Kaliningrad, Russia

<sup>2</sup>National University of Science and Technology “MISiS”, Moscow, Russia

\*E-mail: [VGKolesnikova1@kantiana.ru](mailto:VGKolesnikova1@kantiana.ru)

Glassy ferromagnetic metals poses unique magnetic properties such as small coercive field versus high remanent magnetization [1–3] and can be kinetically metastable and thermodynamically unstable materials. But they could be transferred into a more stable nanocrystalline phase by, for example, thermal treatment. It was shown that metallic are the most suitable candidates for nanocrystallization [4, 5]. The development of complex nanocrystalline alloys from their metastable amorphous precursors became the state-of-art topic in creating new materials for high-temperature applications [6, 7].

This work offers a novel simple approach of producing nanocrystalline metallic glasses in the shape of glass-coated microwires using the modified Taylor–Ulitovsky method [8] by eliminating a water quenching from the manufacturing process. This modification allows us to prepare the multi-phase metallic glasses which consist of nanocrystallites embedded in an amorphous matrix without an additional step of annealing. The soft magnetic hybrid nanocrystalline alloy and its structural and magnetic characterization are performed on cylindrical  $\text{Co}_{77.5}\text{Si}_{7.5}\text{B}_{15}$  glass-coated microwire (diameter of the metallic core  $d \sim 21 \mu\text{m}$ , outer diameter  $D \sim 27 \mu\text{m}$ ). The structural properties (crystalline phase, crystal size, shape and orientation) were studied by X-Ray diffractometry and transmission electron microscopy analysis.

The magnetization reversal processes in a complex system are studied through vibration sample magnetometry at different temperatures and FORC-analysis. FORC-analysis presents a powerful tool for analysis of the internal magnetic interactions of complex granular systems. The aim to use this method was the evaluation of the interactions between the amorphous matrix and the crystallites and among the crystallites. The FORC diagram shows the presence of the positive interactions in the microwire nucleus caused by the exchange coupling among the mixed hcp and fcc Co nanocrystallites. The FORC diagram also renders a minor trace of the residual matrix as a third magnetic phase with near-zero coercive field distribution. The FORC analysis has shown that the modified Taylor–Ulitovsky method lead to the formation of the robust extra-granular exchange coupling through the metal glass matrix in hybrid Co-based nanocrystalline alloy.

1. P. Corte-León et al., *Applied Materials Today*, 101263 (2021).
2. M.G. Nematov et al., *Journal of Alloys and Compounds* **890**, 161740 (2022).
3. I. Alekhina et al., *Nanomaterials*, **11**, 274 (2021).
4. M.E. McHenry et al., *Amorphous and Nanocrystalline Materials for Applications as Soft Magnets* (1999).
5. K. Lu, *Mater. Sci. Eng. Reports*, **16**, 161 (1996).
6. G. Herzer, *Acta Mater.*, **61**, 718 (2013).
7. N. Zhou, T. Hu, J. Huang, and J. Luo, *Scr. Mater.*, **124**, 160 (2016)
8. V.S. Larin, et al., *J. Magn. Magn. Mater.*, **249**, 39 (2002).

## APPLICATION OF MACHINE VISION IN DILATOMETRY TECHNIQUE

*V. Rodionov\*, D. Borov*

Immanuel Kant Baltic Federal University, Kaliningrad, Russia

\*E-mail: [rodionov\\_vlad@mail.ru](mailto:rodionov_vlad@mail.ru)

Dilatometers are used to measure the changes in linear dimensions of the samples. In this work, we have developed a setup to measure the size changes of the ferroelectric composites caused by an external magnetic field. The experimental setup consists of a primary coil, precision lever system of non-magnetic material (aluminum), mirror, translucent screen and high definition camera. The main distinguishing feature of developed approach is the use of computer vision. The lever system releases a laser beam, which, reflecting from the mirror, falls on a translucent screen, where it is snapping by the camera. When the linear dimensions of the sample change, the laser spot on the screen shifts, so that 1 mm on the screen corresponds to a change in the size of the sample by about 10 nm. A high-resolution camera connected to a computer and used to accurately measure the movement of a laser spot on the screen. A real-time object tracking program was developed in the LabVIEW development environment.

To perform the measurements, the system is calibrated and the initial dimensions of the sample are measured. The incoming video stream is processed by several filters and then the pattern matching process is applied. The pattern matching process consists of two stages: learning and matching. During the learning stage, the algorithm extracts gray value and edge gradient information from the template image. The algorithm organizes and stores the information in a manner that facilitates faster searching in the inspection image. The information learned during this stage is stored as part of the template image. Then, the algorithm finds the matches by locating regions in the inspection image where the highest cross-correlation is observed and outputs the coordinates of the center of this region.

In the case of measurement of magnetic materials together with tracking the object, the program supplies voltage to the magnetic coil and reads data from the Hall sensors. Thus, at the output of the program, we have data on the dependence of the change in the linear dimensions of the sample on the magnitude of the magnetic field. This allows us to draw conclusions about the size changes of the studied sample. In the case of the magnetoelectric composites the size changes goes thought the magnetic materials shiftless in the piezoelectric matrix.

Otherwise, it is possible to measure changes in the linear dimensions of polymers, including polymer filaments, without the influence of a magnetic field. It is possible to find defects or damages in elongated threads with an accuracy about 10 nanometers.

*This work was supported by the Russian Science Foundation No. 21-72-30032.*

**SYNTHESIS OF HIGH-ENTROPY PHASE  
WITH THE MAGNETOPLUMBITE STRUCTURE  
BY THE NITRATE-CITRATE METHOD**

*V.E. Zhivulin\**, N.A. Cherkasova, D.A. Vinnik, O.V. Zaitseva, D.A. Zherebtsov, E.A. Trofimov

South-Ural State University, SUSU, Chelyabinsk, Russia

\*E-mail: [zhivulinv@susu.ru](mailto:zhivulinv@susu.ru)

Barium hexaferrite  $\text{BaFe}_{12}\text{O}_{19}$  is widely used due to its high magnetic properties. Substitution of iron in the structure of barium hexaferrite  $\text{BaFe}_{12-x}\text{Me}_x\text{O}_{19}$  by other metals (Al, Cr, In, Ga, Ti etc.) significantly changes the magnetic properties of the substance. Thus, the replacement of iron with aluminum causes an increase in magnetic anisotropy, as a result of which there is a strong change in the coercive force and a shift in the frequency of the ferrimagnetic resonance towards higher frequencies. The substitution of iron for titanium leads to a decrease in the saturation magnetization and a slight increase in the coercive force. In this case the material also becomes a semiconductor.

The solubility of individual alloying elements in the hexaferrite structure, their ability to occupy the positions of iron atoms, is usually limited. The high configurational entropy of mixing of atoms within the framework of the sublattice, which iron atoms form in hexaferrites, can contribute to the production of stable crystalline structures with a high degree of substitution. High values of this quantity should contribute to an increase in the entropy of the phase as a whole, which will lead to a decrease in its Gibbs energy, and thus make the process of formation and existence of this phase more thermodynamically beneficial than the formation of other phases from the same elements.

This work is devoted to the production of oxides with the magnetoplumbite structure, the composition of which reflects the formula  $\text{BaFe}_6\text{Al}_{1.5}\text{Cr}_{1.5}\text{In}_{1.5}\text{Ga}_{1.5}\text{O}_{19}$  and  $\text{BaFe}_{2.4}\text{Al}_{2.4}\text{Cr}_{2.4}\text{In}_{2.4}\text{Ga}_{2.4}\text{O}_{19}$ . In

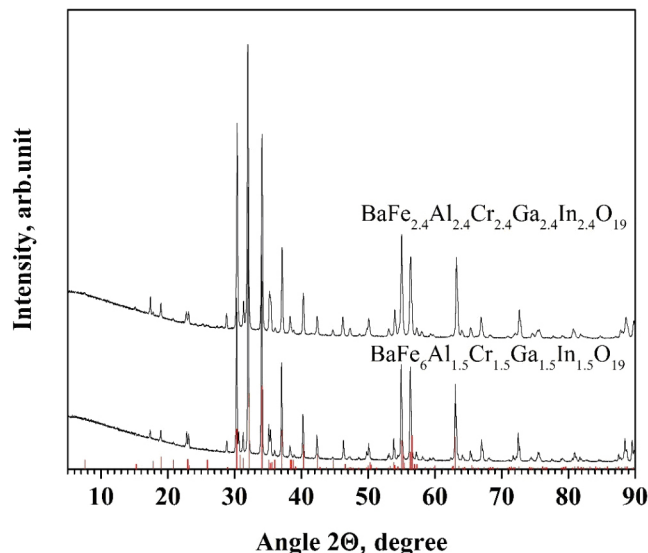


Figure 1. X-ray diffraction patterns of the synthesized samples. The vertical lines indicate the literature data for  $\text{BaFe}_{12}\text{O}_{19}$ .

Table 1. Elemental composition of the obtained samples.

№	Batch formula	Atomic % found						Calculated formula
		Al	Cr	Fe	Ga	In	Ba	
1	$\text{BaFe}_6\text{Al}_{1.5}\text{Cr}_{1.5}\text{In}_{1.5}\text{Ga}_{1.5}\text{O}_{19}$	4.3	5.0	19.4	5.4	4.0	3.4	$\text{BaFe}_{6.1}\text{Al}_{1.3}\text{Cr}_{1.6}\text{In}_{1.3}\text{Ga}_{1.7}\text{O}_{19}$
2	$\text{BaFe}_{2.4}\text{Al}_{2.4}\text{Cr}_{2.4}\text{In}_{2.4}\text{Ga}_{2.4}\text{O}_{19}$	6.8	7.9	7.9	9.2	6.0	3.5	$\text{BaFe}_{6.1}\text{Al}_{1.3}\text{Cr}_{1.6}\text{In}_{1.3}\text{Ga}_{1.7}\text{O}_{19}$

the iron sublattice, there are also four more elements: Al, Cr, In, Ga. Such a composition provides a high configurational entropy of mixing  $S_{\text{mix}}$ . The maximum entropy value will be reached when the concentration of all cations in the iron sublattice is identical. The configurational entropy values within the iron sublattice for named formulas are 1.386294 and 1.609438, respectively.

The nitrate-citrate method was chosen as the synthesis method. The starting components for the synthesis were barium nitrate ( $\text{Ba}(\text{NO}_3)_2$ ), iron nitrate nonahydrate ( $\text{Fe}(\text{NO}_3)_3 \cdot 9\text{H}_2\text{O}$ ), aluminum nitrate octahydrate ( $\text{Al}(\text{NO}_3)_3 \cdot 8\text{H}_2\text{O}$ ), chromium nitrate nonahydrate ( $\text{Cr}(\text{NO}_3)_3 \cdot 9\text{H}_2\text{O}$ ) and citric acid. Indium and gallium nitrates were obtained by dissolution of indium oxide  $\text{In}_2\text{O}_3$  and gallium oxide  $\text{Ga}_2\text{O}_3$  in concentrated nitric acid at a temperature of 75 °C. The initial components were weighed in stoichiometric ratios and dissolved. The solutions were mixed. Neutralization of the resulting solution was carried out by adding an ammonia solution to pH = 7 with control using universal indicator paper. After neutralization, the resulting solution was evaporated on a water bath until a viscous gel was formed. The resulting gel was calcined in two stages. At the first stage, heating was carried out for 5 hours to a temperature of 300 °C and kept at this temperature for 5 hours. At the second stage, heating was performed for 3 hours to a temperature of 500 °C with isothermal holding at this temperature for 5 hours. The products obtained as a result of calcination without additional grinding were subjected to final ferritization at a temperature of 1300 °C for 5 hours.

Figure 1 shows the X-ray powder patterns of the obtained samples. Strait lines indicate literature data for pure barium hexaferrite. It can be seen from the figure that all the peaks in the X-ray diffraction patterns coincide with the peaks given in the literature, which indicates the similarity of the structures under study to the structure of barium hexaferrite. Table 1 presents the results of studying the elemental composition of the obtained samples using EDS and the gross formulas calculated on the basis of these data. It can be seen from the table that the composition of the obtained samples is in a good agreement with the initially specified one.

Thus, samples of high-entropy oxides with the structure of barium hexaferrite were synthesized for the first time by the nitrate-citrate method.

*The work was supported by Russian Science Foundation (project No. 18-73-10049).*

**EFFECT OF PLASTIC DEFORMATION ON THE MAGNETIC PROPERTIES OF RAPIDLY QUENCHED CoFeNbSiB WIRES**

*N.A. Lyu-yu, N.V. Morozova, E.A. Golygin, A.V. Gavrilyuk, S.M. Zubritskii\*, A.A. Gavrilyuk*

Irkutsk State University, Irkutsk, Russia

\*E-mail: [zubr@api.isu.ru](mailto:zubr@api.isu.ru)

There is a known technique [1, 2] for determining the distribution of magnetization in rapidly quenched ferromagnetic materials by investigating of partial hysteresis loops. The method is based on the analysis of the dependence of the residual induction of the sample  $B_r$  on the magnitude of the induction on the magnitude of the maximum magnetic field  $B_m$  for a partial hysteresis loop.

In this work, for the first time, the technique developed for rapidly quenched ribbons was applied to rapidly quenched CoFeNbSiB wires after plastic deformation treatment. Rapidly quenched metal wires  $\text{Co}_{66}\text{Fe}_4\text{Nb}_{2.5}\text{Si}_{12.5}\text{B}_{15}$ , 0.09 m length, 155  $\mu\text{m}$  diameter, were obtained and certified at Central Research Institute of Ferrous Metallurgy (Moscow). The values of the magnetostriction constant  $\lambda_s \sim 10^{-7}$  for wires in the undeformed state (without plastic deformation treatment).

The plastic deformation of the wires was carried out by a treatment with direct electric current with a density  $j = 38.7 \text{ MA/m}^2$  in air for 2 min with the simultaneous application of tensile stresses with value from 5.3 to 106 MPa. The value of the residual plastic deformation of the wires  $\Delta l/l_0$  under the application of tensile stresses  $\sigma$ ; varied in the range from 0.23 ( $\sigma = 5.3 \text{ MPa}$ ) to 4.47% ( $\sigma = 106 \text{ MPa}$ ) depending on the value of tensile stresses applied during direct electric current treatment. The purpose of treatment was to achieve the maximum values of plastic deformation in the wires, which do not lead to the destruction of the samples. After application of plastic deformation, partial hysteresis loops were measured. Dependences  $B_r(B_m)$  were determined.

Figure 1 shown partial hysteresis loops of undeformed wires and plastically deformed wires with different value  $\Delta l/l_0 = 4.47$  ( $l_0$  is the length of the undeformed wire,  $\Delta l = l - l_0$  is the change of the length of the wire under the deformation).

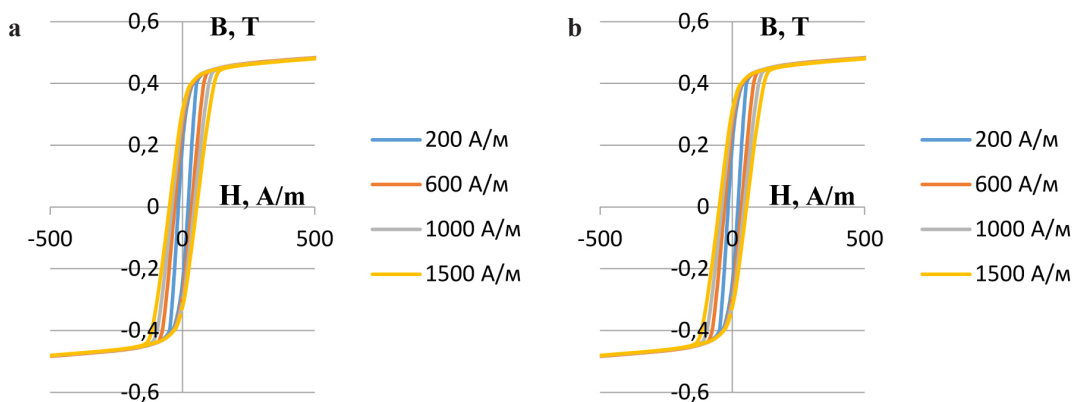


Figure 1. Partial hysteresis loops  $\text{Co}_{66}\text{Fe}_4\text{Nb}_{2.5}\text{Si}_{12.5}\text{B}_{15}$  wires: **a** without plastic deformation treatment, **b** plastic deformation treatment with value  $\Delta l/l_0 = 4.47\%$ . Maximum magnetic field applied to wires along their length: 200 A/m, 600 A/m, 1000 A/m, 1500 A/m.



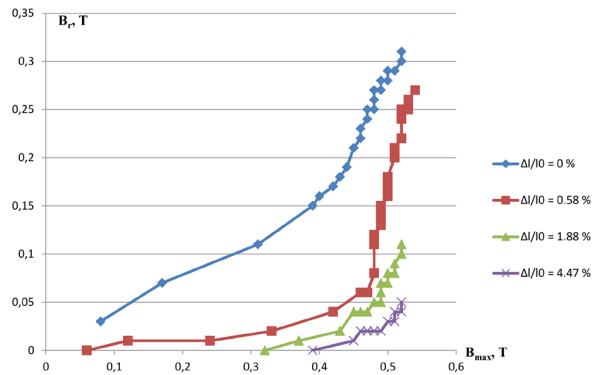


Figure 2. Dependences of the residual magnetic induction  $B_r$  on the value of the maximum magnetic induction of partial hysteresis loops  $\text{Co}_{66}\text{Fe}_4\text{Nb}_{2.5}\text{Si}_{12.5}\text{B}_{15}$  wires after plastic deformation treatment.

Plastic deformation changes the course of the hysteresis loop. The hysteresis of wires after a plastic deformation treatment become narrower, and their magnetic permeability decreases. This may indicate that the main processes of magnetization in wires after plastic deformation treatment are the processes of magnetization rotation. Figure 2 shown plots of the dependence  $B_r(B_m)$  for wires with different values of  $\Delta l/l_0$ .

As follows from the dependences (Fig. 2), there are two pronounced sections with different inclination angles with respect to the magnetic field axis. This indicates a change in the dominant magnetization process with an increase the value of the external magnetic field. It can be assumed that the first section of dependence, can be connected with the processes of rearrangement of the domain structure in the near-surface region of the wire according to the domain structure model, and the second section of dependence (sharper) can be connected with the processes of displacement of domain walls in the core region of the wire. Plastic deformation leads to a qualitative change in the distribution of magnetization in rapidly quenched Co-bases wires due to increasing the volume of near-surface region of wires and a decreasing core volume. It should be noted that at high values of plastic deformation, the residual magnetic induction is close to zero value, and the processes domain walls displacement begin to occur in high magnetic fields. By using plastic deformation, it is possible to purposefully change the magnetic properties of rapidly quenched soft Co-based ferromagnetic wires.

1. N.A. Skulkina, O.A. Ivanov, A.K. Mazeeva, P.A. Kuznetsov, E.A. Stepanova, O.V. Blinova, E.A. Mikhailitsyna, Magnetization processes in amorphous ribbons soft magnetic alloys, *Physics of metals and metallography*, **119**, no. .2, 137–143 (2018).
2. N.A. Skulkina, O.A. Ivanov, N.D. Denisov, V.I. Chekis, Cooling rate upon in air heat treatment and magnetic properties of amorphous soft magnetic alloys, *Journal of Magnetism and Magnetic Materials*, **470**, 156–158 (2019).

**STRUCTURE AND MORPHOLOGY OF TITANIUM DIOXIDE  
ENCAPSULATED IRON POWDER**

*A.L. Zhaludkevich*<sup>1\*</sup>, *O.F. Demidenko*<sup>1</sup>, *A.O. Larin*<sup>1</sup>, *G.A. Govor*<sup>1</sup>, *U.T. Berdiev*<sup>2</sup>,  
*U.B. Suleimanov*<sup>2</sup>, *F.F. Hasanov*<sup>2</sup>

<sup>1</sup>Scientific–Practical Materials Research Centre NASB, Minsk, Belarus

<sup>2</sup>Tashkent State Transport University, Tashkent, Uzbekistan

\*E-mail: [zheludkevich27@gmail.com](mailto:zheludkevich27@gmail.com)

Recently many the international scientific community has been searching for new magnetically soft composite materials for their use in electrical products. One of them are composite materials based on magnetically soft particles, usually pure metal powder, the particles of which are coated with an electrically insulating coating [1, 2]. Based on such composite soft magnetic materials, highly efficient inverter motors, transformers, inductors, and other devices are created [3]. In this regard, the main properties of encapsulated iron powder particles, such as crystal structure and developed morphology, are very important for their practical application.

Iron powder ABC100.30 manufactured by Hoeganaes was chosen as the basis. A protective coating about 15 nm thick was obtained by depositing a layer of TiO<sub>2</sub> on the surface of iron particles and subsequent annealing in an inert atmosphere at 500 °C for 1 hour.

After encapsulation, the powders were examined by X-ray diffraction analysis on a DRON-3M automated apparatus in CuK $\alpha$ -radiation in the angle range  $20^\circ \leq 2\theta \leq 90^\circ$  at room temperature. The X-ray diffraction patterns were processed using the FullProf Suite program, which is based on the Rietveld method to refine the parameters of the crystal cell. The morphology of the powders was studied by scanning electron microscopy (SEM) on a Hitachi SEM, Zeiss apparatus.

It was revealed that the composite has one cubic  $\alpha$ -Fe phase with a unit cell parameter of  $0.2865 \pm 0.0003$  nm. The TiO<sub>2</sub> phase (particle coating) was clearly not detected, this is due to the small thickness of the coating compared to the particle size, since the particle size is in the range of 50–100 microns. Powder particles have a complex geometry (Fig. 1), this is important from

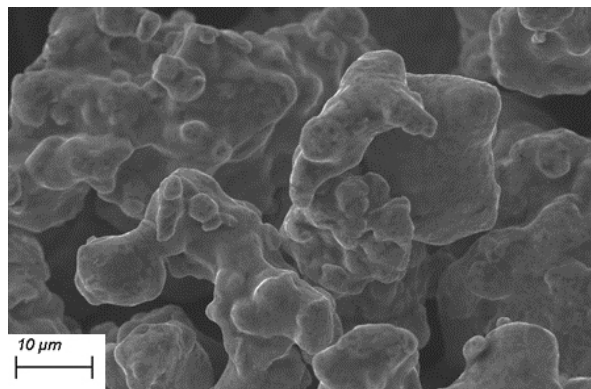


Figure 1. SEM of encapsulated iron particles.

the point of view of the practical application of such particles in pressing and creating dense composites, the density of which will make it possible to obtain electrical products with good functional properties.

*This work was financial supported by Belarusian Republican Foundation for Basic Research as part of the projects No. T21UZBG-023.*

1. M. Bingyang, H. Jiexin et al., *J. Magn. Magn. Mat.*, **492**, 165651 (2019).
2. L. Jingxin, Y. Jing et al., *J. Magn. Magn. Mat.*, **454**, 103–109 (2018).
3. Y. Xinran, L. Yongjian, Y. Qingxin, *IEEE Trans. on Mag.*, **55**, 2, 1–5 (2019).

## BEHAVIOR OF ELECTRICAL RESISTANCE OF FERROMAGNETIC MICROWIRES HEATED BY EXTERNAL SOURCE AND DIRECT CURRENT

*A.A. Pahomova\**, *A.A. Samokhvalov*, *A.T. Morchenko*

National University of Science and Technology MISiS, Moscow, Russia

\*E-mail: [m1808458@edu.misis.ru](mailto:m1808458@edu.misis.ru), [dratm@mail.ru](mailto:dratm@mail.ru)

Amorphous ferromagnetic microwires in a glass shell are promising functional materials for creating various devices of microsystem technology and magnetoelectronics [1, 2].

Revealing potential for the practical use of this type of materials in some cases is difficult due to the lack of a number of factual data on their main characteristics and parameters of the processes used in the modification of the wire material during subsequent processing [3, 4]. In particular, during current annealing of wires, the influencing factors are heating and the circular magnetic field of the current. Direct measurement of the temperature of the microwires in these conditions is an almost impossible task.

The study of the correlation of the resistance of microwires of various compositions and geometric characteristics when heated from an external source and due to the thermal action of the current allows us to identify the regularities of the process of heating the wire with current and use these data to characterize the thermomagnetic treatment mode.

In the first case, a change in the resistance of a piece of microwire placed in a furnace with a controlled heating temperature is recorded (Fig. 1). In the second case, the resistance of a piece of microwire is measured when the voltage applied to its ends changes (Fig. 2). At the same time, the different spatial arrangement of the wire and the dependence of the results obtained on the environment are discussed.

It is analyzed the dependence of resistance of microwires, differing in the composition of the core and geometric parameters, on temperature and on the current flowing through them. Areas with characteristic features of resistance behavior have been identified. Considerations are made

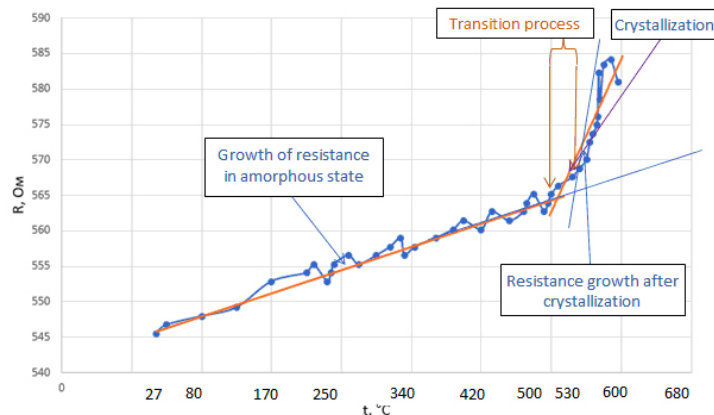


Figure 1. A characteristic type of dependence of the resistance of the microwire ( $R$ ) on the temperature ( $t$ ) when it is heated in the furnace.

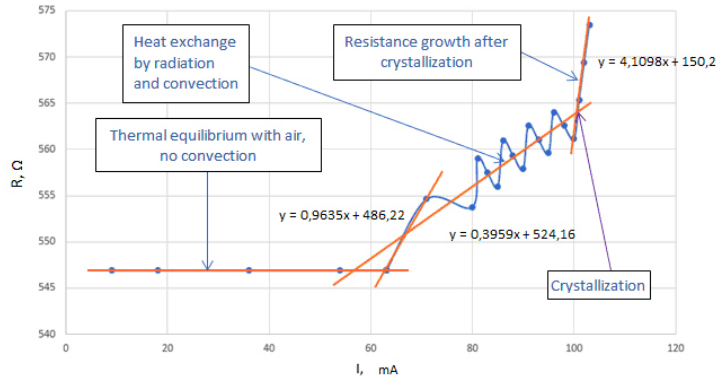


Figure 2. A characteristic type of dependence of the resistance of the microwire ( $R$ ) on the flowing current ( $I$ ) with the horizontal method of its fixing near the vertical wall.

about the processes occurring in the core material at different sections of the curves, and about the correlation of the results obtained under different heating conditions.

1. L. Panina, L. Dzhumazoda, M. Nematov, J. Alam, A. Trukhanov, N. Yudanov, A. Morchenko, V. Rodionova, A. Zhukov, Soft Magnetic Amorphous Microwires for Stress and Temperature Sensory Applications, *Sensors*, **19**(23), 5089 (2019).
2. V.S. Larin, A.V. Torcunov, A. Zhukov, J. Gonzalez, M. Vazquez, L. Panina, Preparation and properties of glass-coated microwires, *J. Magn. and Magn. Mat.*, **249**(1-2), 39–45 (2002).
3. S.A. Baranov, Dependence of magnetic properties of micro- and nanowires on stress and magnetic heat treatment, *Surface Engineering and Applied Electrochemistry*, **53**(1), 77–88 (2017).
4. A. Gonzalez, V. Zhukova, P. Corte-Leon, A. Chizhik, M. Ipatov, J.M. Blanco, A. Zhukov, Tuning of Magnetoimpedance Effect and Magnetic Properties of Fe-Rich Glass-Coated Microwires by Joule Heating, *Sensors*, **22**(3), 1053 (2022).

Section K.  
**Magnetic semiconductors, multiferroics,  
topological insulators**

---

## MAGNETOELECTRIC EFFECT IN PARAMAGNETIC RARE-EARTH LANGASITES

*A.A. Mukhin\**, *V.Yu. Ivanov*, *A.M. Kuzmenko*, *A.Yu. Tikhonovskii*

Prokhorov General Physics Institute of the Russian Academy of Sciences, Moscow, Russia

\*E-mail: [mukhin@ran.gpi.ru](mailto:mukhin@ran.gpi.ru)

In recent years, magnetoelectric effects, in particular magnetic field-induced electric polarization, were observed not only in magnetically ordered but also in paramagnetic compounds, for example in rare earth aluminoborates  $\text{RAl}_3(\text{BO}_3)_4$  ( $\text{R} = \text{Ho}, \text{Yb}, \dots$ ) [1, 2] and in some rare earth pure [3] or doped langasites [4]. The latter compounds belongs to the  $\text{R}_3\text{Ga}_5\text{SiO}_{14}$  family, which has a non-centrosymmetric crystal lattice (space group  $\text{P}321$ ), and are not magnetically ordered up to lowest temperatures. The study of magnetoelectricity in langasite crystals is of significant interest due to new mechanisms of magnetoelectric effect. In these systems consideration of local symmetry of the magnetic ion environment ( $\text{C}_2$ ) and global (higher) crystal symmetry is especially important as it determines new features of their magnetoelectric properties observed recently in Ho-doped langasite [4]. In particular, it was revealed an unusual combination of linear and highly non-linear magnetoelectric responses when electric polarization along  $c$ -axis grows linearly with the magnetic field but oscillates upon rotation of the magnetic field around  $\text{C}_3$ -axis.

In this work we also studied magnetoelectric effect in Ho-doped langasite  $\text{La}_{3-x}\text{Ho}_x\text{Ga}_5\text{SiO}_{14}$  in other geometry as compare to [4], i.e. for the electric polarization  $P_a, P_b$  in the basal plane. The single crystals were grown by the Czochralski technique (B. Mill),  $x = 0.045$ , and by the floating zone method (A.M. Balbashov),  $x = 0.09$ . The measurements were carried out by means the MPMS-5 (Quantum Design) installation at temperatures from 1.9 K. Figure 1 shows the dependences of the electric polarization induced along the crystallographic axis  $a$  by a magnetic field applied along the axes  $a$  and  $b$  of the  $x = 0.045$  sample. According to the phenomenological relations for crystals of trigonal symmetry, the allowed components of the induced electric polarization along the  $x||a$  and  $y||b^*$  axes in the lowest order on magnetic field are:

$$P_x = \alpha_1 H_y H_z + \alpha_2 (H_x^2 - H_y^2) + \dots, P_y = -2\alpha_2 H_x H_y - \alpha_1 H_x H_z + \dots \quad (1)$$

According to (1),  $P_a (P_x)$  should depend quadratically on the magnetic field  $H$ , and have the same absolute value and different signs, respectively, for the  $H||a$  and  $H||b$ . These rules are fulfilled at temperatures above  $\approx 25$  K, while at low temperatures the dependence of polarization on field very quickly becomes quasi-linear (Fig. 1). In addition, the absolute value of polarization in the field along the  $a$ - and  $b$ -axes differs noticeably at low temperatures. The reason for this behavior is a saturation of the magnetization of  $\text{Ho}^{3+}$  ions with an increase of the magnetic field, which requires a more complicated description of the observed effects taking into account nonequivalent ion sites.

The coefficients  $\alpha_1$  and  $\alpha_2$  in (1) might be considered as quadratic magnetoelectric susceptibilities; they can be found by the differentiation of polarization over the  $H^2$ . While the  $\alpha_2$  is easily determined from  $H||a$  and  $H||b$  curves (Fig. 1), to find the  $\alpha_1$ , the  $P_b (P_y)$  component of polarization was measured in a magnetic field applied in the  $ac$ -plane at angles of  $+45^\circ$  and  $-45^\circ$  to the  $c$ -axis (Fig. 2). The behavior of the  $P_b(H)$  is similar: a quasi-linear dependence at low temperatures which transforming into a quadratic one with increasing temperature.

To describe the observed effects, a quantum-phenomenological approach has been developed which takes into account the quasi-doublet structure of the ground state of the  $\text{Ho}^{3+}$  ion in a crystal

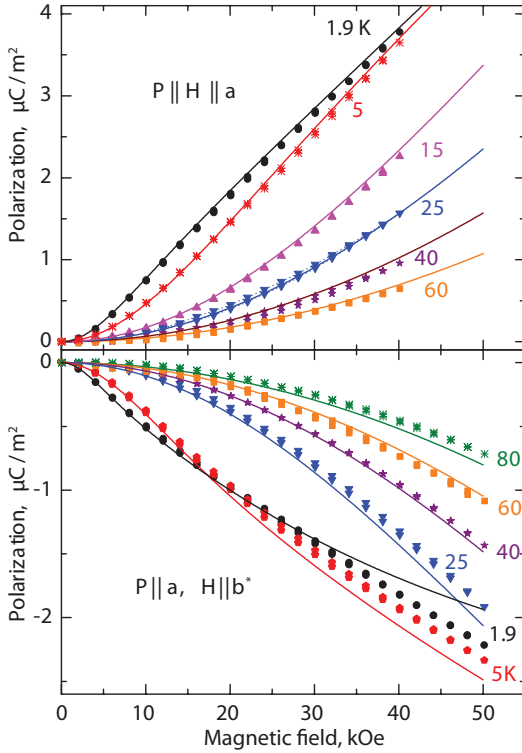


Figure 1. Dependences of electric polarization  $P_a$  along the  $a$ -axis on the magnetic field directed along the  $a$ -axis (top) and along the  $b$ -axis (bottom) in  $\text{La}_{2.957}\text{Ho}_{0.043}\text{Ga}_5\text{SiO}_{14}$ . Points – experiment, lines – theory (see text).

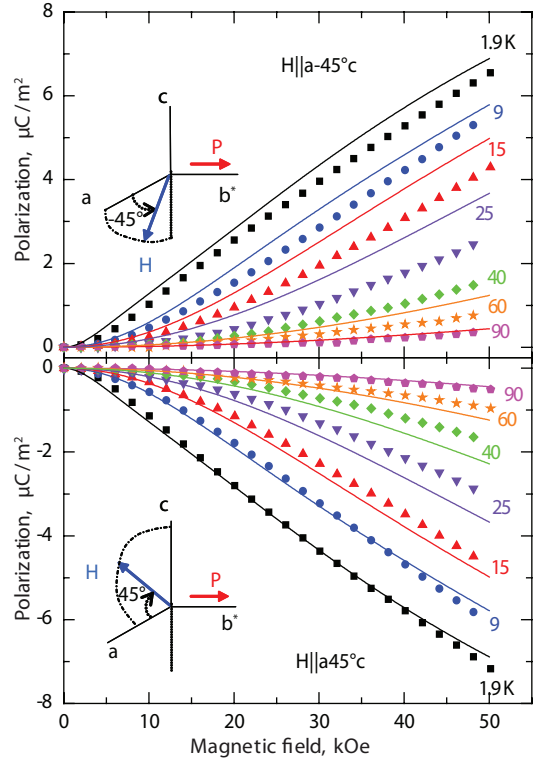


Figure 2. Dependences of electric polarization  $P_b$  along the  $b^*$ -axis on the magnetic field directed at an angle of  $-45^\circ$  (top) and  $+45^\circ$  (bottom) to the  $c$  axis in the  $ac$ -plane in  $\text{La}_{2.957}\text{Ho}_{0.043}\text{Ga}_5\text{SiO}_{14}$ . Points – experiment, lines – theory.

field of low local symmetry ( $C_2$ ), which allows magnetoelectric coupling. As a result the  $P_{x,y}$  can be represented in the following general form

$$\begin{aligned}
 P_x = & \chi[L_1 H_y H_z + L_1 (H_x^2 - H_y^2)] + L_3[\chi_{123} H_y H_z - \chi_{23} (-H_x H_z)] \\
 & + L_4[\chi_{123} (H_x^2 - H_y^2) - \chi_{23} (-2H_x H_y)] + \chi_{123}[L_5 (H_x^2 + H_y^2) + L_6 H_z^2], \\
 P_y = & \chi[L_1 (-H_y H_z) + L_1 (-2H_x H_y)] + L_3[-\chi_{123} (-H_x H_z) - \chi_{23} H_y H_z] \\
 & + L_4[-\chi_{123} (-2H_x H_y) - \chi_{23} (H_x^2 - H_y^2)] + \chi_{23}[L_5 (H_x^2 + H_y^2) + L_6 H_z^2],
 \end{aligned} \tag{2}$$

where  $\chi$ ,  $\chi_{123}$ ,  $\chi_{23}$  are symmetrized combinations of local effective susceptibilities of  $\text{Ho}^{3+}$  ions in different sites, which depend on temperature and splitting of the ground quasidoublet in magnetic field,  $L_i$  are phenomenological constants. The Eqs. (2) made it possible to quantitatively describe the polarization behavior in a wide range of fields and temperatures. At low temperatures, they give a quasi-linear dependence on the magnetic field, while at high temperatures – a quadratic one. We obtained similar results for a sample with a higher concentration of holmium.



*This work was supported by the Russian Science Foundation (No. 22-42-05004).*

1. Liang K.-C., Chaudhury R.P., Lorenz B. et al., Phys. Rev. B, **83**, 180417(R) (2011).
2. V.Yu. Ivanov, A.M. Kuzmenko, A.A. Mukhin, JETP Lett., **105**, 435 (2017).
3. A.A. Mukhin, V.Yu. Ivanov, B.V. Mill, Book of Abstracts, Moscow International Symposium on Magnetism, 1–5 July 2017, M.V. Lomonosov Moscow State University. Moscow 2017, p.663.
4. L. Weymann, L. Bergen, T. Kain, A. Shuvaev, E. Constable, D. Szaller, A. Pimenov, B.V. Mill, A.M. Kuzmenko, V.Yu. Ivanov, N.V. Kostyuchenko, A.I. Popov, A.K. Zvezdin, A.A. Mukhin, and M. Mostovoy et al., npj Quantum Mater., **5**, 61 (2020).

## EFFECT OF BaTiO<sub>3</sub> AND Zn<sub>0.25</sub>Co<sub>0.75</sub>Fe<sub>2</sub>O<sub>4</sub> FILLERS ON MECHANICAL AND MAGNETOELECTRIC PROPERTIES OF PVDF-TrFE-BASED COMPOSITES

K.V. Sobolev<sup>1</sup>, V.G. Kolesnikova<sup>1</sup>, A.S. Omelyanchik<sup>1</sup>, Yu.A. Alekhina<sup>2</sup>, L.A. Makarova<sup>2</sup>,  
V.N. Antipova<sup>1</sup>, K.V. Levada<sup>1</sup>, A.A. Amirov<sup>1</sup>, V.V. Rodionova<sup>1\*</sup>

<sup>1</sup>Immanuel Kant Baltic Federal University, IKBFU, Kaliningrad, Russia

<sup>2</sup>Lomonosov Moscow State University, Moscow, Russia

\*E-mail: [VRodionova@kantiana.ru](mailto:VRodionova@kantiana.ru)

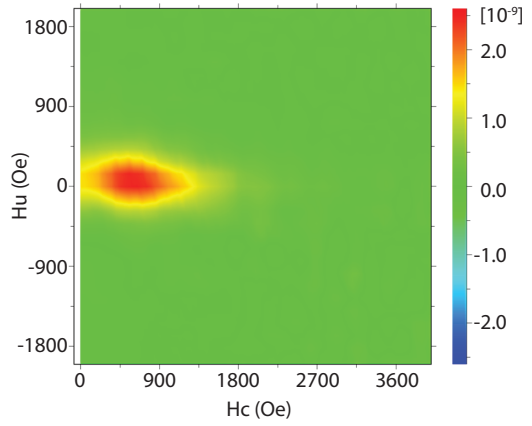
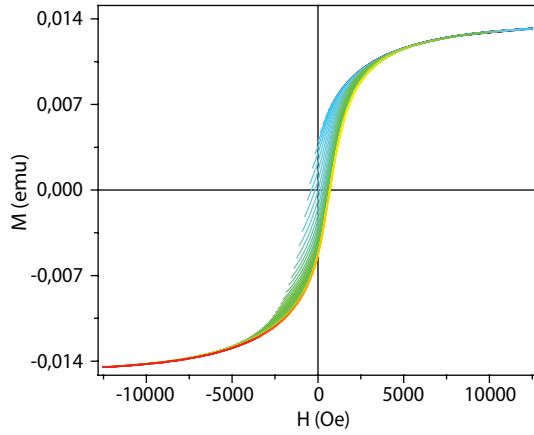
The development of new composite multiferroic materials with interrelated piezoelectric and ferromagnetic properties has received a great deal of attention in recent years [1]. The development of this technology creates the general demand for the miniature, light-weight, flexible elements, made of easily processed materials, thus enhancing the interest in polymer-based composite multiferroics. One of the intriguing representatives consists of a piezoelectric matrix with embedded magnetic particles. The magnetoelectric conversion in such structures occurs due to mechanical stresses, induced by magnetostriction or magnetostatic interactions of the filler, inducing piezoresponse of the piezopolymer matrix [2]. Polymer-based multiferroic materials can be used in biomedicine as functional scaffolds to promote stem cells differentiation [3]. To reproduce the optimal conditions for differentiation of stem cells *in vitro/in vivo* on scaffolds it is necessary to take into account the structural features of bones (stiffness, internal nanostructure, mechanical properties), and also to ensure the action of various biophysical signals, such as piezoelectric, pyroelectric, ferroelectric, etc., since they play a key role in the regulation of the cell activity: promote adhesion, proliferation and differentiation of stem cells [4, 5].

Polyvinylidene fluoride (PVDF) and its copolymers, for example PVDF-TrFE, are the most common piezopolymer for creating composite structures. It has several different phases, among which the polarized  $\beta$ -phase is the best in terms of ferroelectric properties [6, 7]. Previously there were several reports, aiming to enhance piezoelectric performance via such approaches as: the addition of the ceramic filler (as the interaction of the PVDF polar molecules with the charged surface of the inclusion particles causes the polymer ordering and the nucleation of the electroactive  $\beta$ -phase) or the polymerization of PVDF with other polymers, like PVDF-TrFE (it promotes the higher formation of the electroactive  $\beta$ -phase due to the appearance of the extra fluorine molecule in the composition) [8]. In this work we study PVDF-TrFE-based nano-composites with embedded magnetic and piezoelectric fillers. The change in the magnetoelectric and mechanical properties in such systems can be of the great importance for the future use in bioactive scaffolds.

First of all, the composite materials, based on PVDF-TrFE polymer matrix with micro-size piezoelectric (BaTiO<sub>3</sub>) and/or nanosize ferrimagnetic (Zn<sub>0.25</sub>Co<sub>0.75</sub>Fe<sub>2</sub>O<sub>4</sub>) filler inclusions, were successfully synthesized and characterized using doctor blade protocol. We studied the samples using X-ray computed tomography. It was shown that the presence of BTO microparticles induce the linear orientation of the whole filler (BTO + ZCFO) subsystem and the higher formation of the electroactive polar PVDF  $\beta$ -phase. The linear orientation leads to the preservation of the mechanical properties (Young's modulus, stiffness) of the polymer matrix (mechanical properties were estimated by AFM in hybrid mode). At the same time, it was shown that the addition of BTO to the composites does not change the magnetic interactions among ZCFO particles which can be seen from the FORC diagrams in Fig. 1. Finally, BTO/ZCFO/PVDF-TrFE sample demonstrates the highest value of the magnetoelectric coefficient – 18.6 mV/cm·Oe, see the graphs in Fig. 2. All together with the suit-

K.12

ZCFO/PVDF-TrFE



BTO/ZCFO/PVDF-TrFE

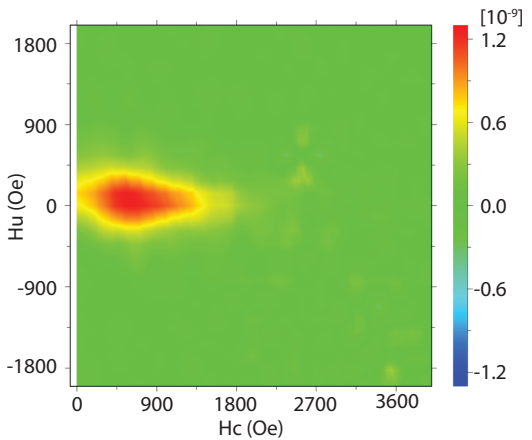
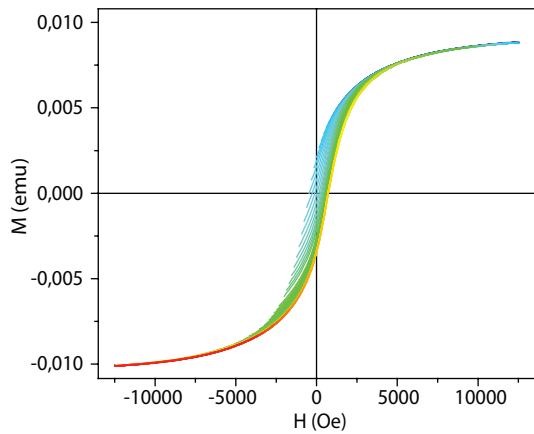


Figure 1. First order reversal curves (FORCs) and FORC-diagrams for ZCFO/PVDF-TrFE and BTO/ZCFO/PVDF-TrFE samples.

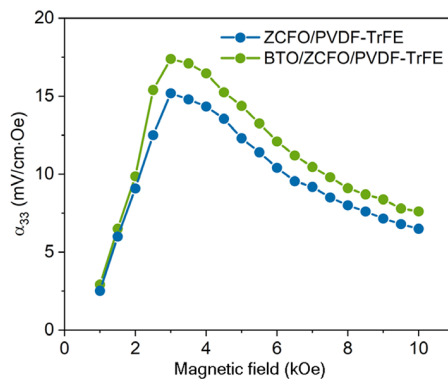


Figure 2. Dependence of ME voltage coefficients ( $\alpha_{ME}$ ) of ZCFO/PVDF-TrFE and BTO/ZCFO/PVDF-TrFE on the DC external magnetic field ( $H_{DC}$ ) at room temperature.

able mechanical properties and biocompatibility it makes the material of particular interest in the field of multiferroic-based scaffolds.

*The authors would like to acknowledge the RSF grant № 21-72-30032 for the financial support of this work.*

1. N.A. Spaldin, M. Fiebig, *Science*, **309**(5733), 391–392 (2005).
2. S. Kopyl, R. Surmenev, M. Surmeneva, Y. Fetisov, A. Kholkin, *Materials Today Bio* 100149, (2021).
3. Alaribe, Franca & Manoto, Sello & Motaung, Shirley, *Biologia*, 71 (2016).
4. A.R. Del Bakhshayesh, N. Asadi, A. Alihemmati, H. Tayefi Nasrabadi, A. Montaseri, S. Davaran, S. Saghati, A. Akbarzadeh, A. Abedelahi, *J. Biol. Eng.*, **13**, 85 (2019).
5. Y. Yang, K. Wang, X. Gu, K.W. Leong, *Engineering (Beijing)*, **1**, 36–54 (2017).
6. P. Martins, A.C. Lopes, S. Lanceros-Mendez, *Progress in Polymer Science*, **39**(4), 683–706 (2014).
7. F. He, M. Sarkar, S. Lau, *Polymer Testing*, **30**(4), 436–441 (2011).
8. M.R. Liu, *Materials Science Forum – Trans Tech Publications Ltd.*, **977**, 277–282 (2020).

## TERAHERTZ INDUCED DYNAMICS OF ANTIFERROMAGNETS

*E.A. Mashkovich*

University of Nizhny Novgorod, Nizhny Novgorod, Russia

\*E-mail: [eamashkovich@gmail.com](mailto:eamashkovich@gmail.com)

Progress in development of strong terahertz (THz) radiation sources opened up new pathways in the ultrafast magnetism. For example, if THz photon energy matches an antiferromagnetic mode (AFM) energy, it can open efficient energy transfer from THz photons to spins. In my talk I will show multiple examples of THz-spin coupling in the magnets with antiferromagnetic exchange interaction including cobalt fluoride [1], iron borate [2], hematite [3], thulium and yttrium iron garnets [4]. The experiments were performed using THz-pump optical-probe technique in a liquid helium cryostat. Optical pulses from Ti:sapphire amplifier with 4 mJ energy, 110 fs duration and repetition rate of 1 kHz were used to generate THz radiation by using tilted front optical rectification technique in LiNbO<sub>3</sub> crystal [5]. The generated THz beam was broadened by the pairs of parabolic mirrors and tightly focused onto the studied crystal. To minimize water absorption and dispersion the THz path was purged with nitrogen. The low intense optical probe beam was overlapped with the THz beam on the studied crystal. THz-induced magnetization dynamics were strobed by measuring probe pulse polarization changes acquired upon propagating via the studied crystal. For example, we were able to excite magnetization dynamics at THz-scale in an yttrium iron garnet thin film, see Fig. 1a. The Fourier spectrum plotted in Fig. 1b reveals the peak at  $\approx 250$  GHz, which can be attributed to the exchange mode between octahedral and tetrahedral iron sites.

In case of CoF<sub>2</sub>, we have shown that the excited AFM spins can mediate nonlinear coupling between THz light and a lattice [1]. High-intense THz pulse resonantly interacts with a coherent magnon state (1.14 THz at 5 K) in CoF<sub>2</sub> and excites the Raman-active  $B_{1g}$  phonon (1.97 THz at 5 K). The phonon amplitude scales quadratically with the THz field strength clearly evidencing the

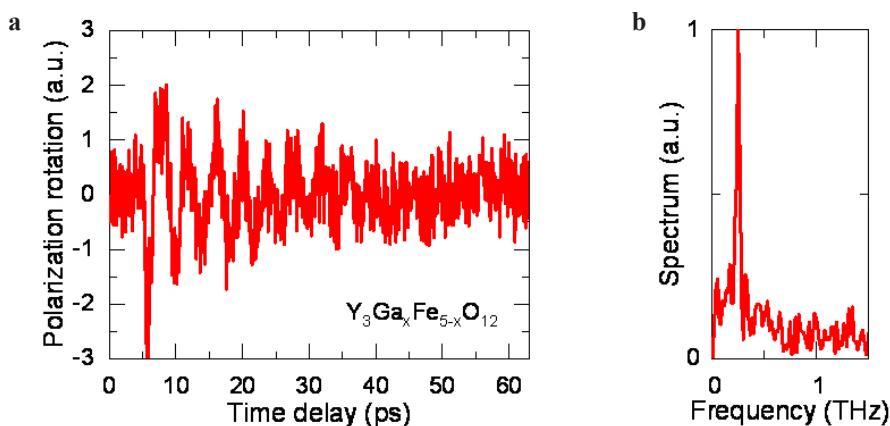


Figure 1. **a** THz induced probe polarization rotation in yttrium iron garnet at room temperature. **b** Corresponding Fourier spectrum.

K.13

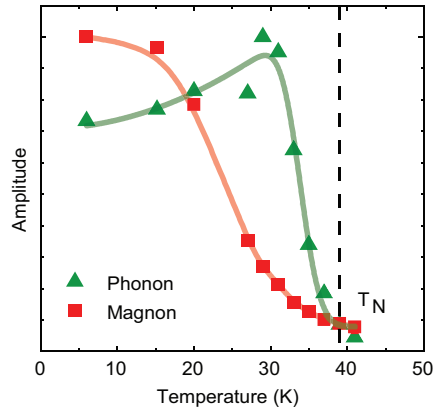


Figure 2. The magnon and the  $B_{1g}$  phonon amplitudes vs. temperature.

nonlinear excitation mechanism. Interestingly, that the phonon amplitude reaches maximum near a special temperature at which the magnon frequency matches half of the phonon frequency. At the same time the magnon amplitude monotonically decreases with temperature. Above the Néel temperature, the magnon disappears, while the phonon amplitude considerably drops (see Fig. 2).

Moreover, we have performed unique measurements combining high-intense THz pulses and high static magnetic fields (up to 10 T) in TELBE facility (Dresden, Germany). The  $B_{1g}$  phonon excitation shows resonance behaviour while tuning the frequency of the magnon with the help of external magnetic field (see Fig. 3a). Interestingly that the magnon frequency at this resonance is close to earlier mentioned frequency matching condition: the magnon frequency matches half of

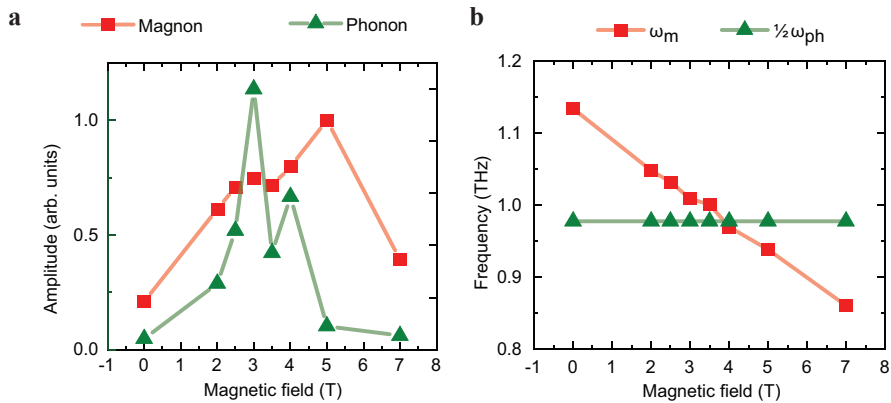


Figure 3. **a** The magnon and the  $B_{1g}$  phonon amplitudes induced by the superradiant THz TELBE source centered at 1 THz vs. an external static magnetic field. **b** The corresponding magnon and the half of the  $B_{1g}$  phonon frequencies vs. an external static magnetic field. Temperature is 8 K.

the phonon frequency (see Fig. 3b). The results demonstrate that the magnon mediated coupling between THz light and a lattice can be controlled by an external magnetic field.

*Support by Ministry of Science and Higher Education of the Russian Federation (FSWR-2021-011) is acknowledged.*

1. E.A. Mashkovich et al., *Science*, **374**, 1608 (2021).
2. E.A. Mashkovich et al., *Phys. Rev. Lett.*, **123**, 157202 (2019).
3. K.A. Grishunin et al., *Phys. Rev. B*, **104**, 024419 (2021).
4. T.G.H. Blank et al., *Phys. Rev. Lett.*, **127**, 037203 (2021).
5. J. Hebling et al., *Opt. Express*, **10**, 1161 (2002).

## MAGNETOELECTRIC COUPLING IN $\text{FeCr}_2\text{O}_4$ , $\text{FeV}_2\text{O}_4$ , $\text{DyCrO}_4$ AND $\text{Fe}_2\text{Mo}_3\text{O}_8$

*M.V. Eremin*

Kazan (Volga region) Federal University, Institute of Physics, Russian Federation

E-mail: [meremin@kpfu.ru](mailto:meremin@kpfu.ru)

Magnetolectric coupling in  $\text{FeCr}_2\text{O}_4$ ,  $\text{FeV}_2\text{O}_4$ ,  $\text{DyCrO}_4$  and  $\text{Fe}_2\text{Mo}_3\text{O}_8$  was discovered relatively recently. The first two compounds are ferromagnetic and therefore interesting for technical applications, since they are magnetized already in the absence of an external field. Strict antiparallel ordering of spins in  $\text{DyCrO}_4$  and  $\text{Fe}_2\text{Mo}_3\text{O}_8$  means that the known mechanisms of coupling of exchange-coupled spins with an electric field containing a vector product of spins (such as the spin-current mechanism) are not related to the origin of the linear magnetolectric effect in these compounds. The analysis of the origin of magnetolectric coupling is carried out in two stages. In the first stage, the effective coupling operator of 3d electrons to an external electric field is derived taking into account the mixing of the states of the  $3d^n$  and  $3d^{n-1}4p$  configurations as well as the so-called charge-transfer configuration, in which an oxygen electron (from the 2p or 2s shell) is carried into the 3d shell. Then the effective coupling operator for the orbital momentum of the 3d electron  $\hat{H}_E$  obtained in this manner is combined with the operators of the exchange interaction, spin-orbit coupling, and external magnetic field in the third order of perturbation theory with respect to the energy levels of the  $3d^n$  configuration [1, 2].

In the case of  $\text{FeCr}_2\text{O}_4$  and  $\text{FeV}_2\text{O}_4$ , two mechanisms dominate [3]. The one-ion mechanism is obtained by combining the interaction operator of the 3d electron orbital states with the electric field and the spin-orbital interaction operator in the third order of perturbation theory. In this case, the magnetolectric coupling operator is proportional to the square of the spin-orbit coupling parameter. The expression for the magnetolectric coupling energy by the two-ion mechanism is also derived in the third order of perturbation theory by combining three operators: the interaction of the orbital states of the 3d electron with the electric field, the spin-orbit coupling operator, and the energy operators of the exchange interaction with neighboring magnetic ions.

The large linear magnetolectric effect in an external magnetic field in the collinear antiferromagnet  $\text{DyCrO}_4$  results from the combined effect of spin-orbit coupling and the interaction of the Cr orbital moment with magnetic field induction. The magnetic field acting on the spins of chromium ions is enhanced by the factor  $(1 + 4\pi\chi) \sim 7$ . The dominant contribution to spin susceptibility  $\chi$  is associated with dysprosium ions, since they have a large magnetic moment ( $9.7\mu_B$ ).

Iron ions in  $\text{Fe}_2\text{Mo}_3\text{O}_8$  are in tetrahedral and octahedral positions. The octahedral positions of iron ions are distorted quite strongly and have no inversion symmetry. The magnetic moments of  $\text{Fe}^{2+}$  ions in the antiferromagnetic phase  $\text{Fe}_2\text{Mo}_3\text{O}_8$  are collinearly ordered. Magnetolectric coupling mechanisms, which are proportional to the vector product of spins, do not appear in this compound. The exchange striction mechanism and the one-ion mechanism related to action of odd crystal fields on the iron ions are discussed. Effective operators of magnetolectric coupling taking into account the orbital degeneracy of the ground states of iron ions are constructed. The ground state in the tetrahedral position is orbitally degenerate  $\text{Fe}^{2+}({}^5E_g)$ ; in the octahedral position, the ground state is  $\text{Fe}^{2+}({}^5T_2)$ .

The support by the Russian Science Foundation (project no. 19-12-00244) is acknowledged.

1. M.V. Eremin, Phys. Rev. B, **100**, 140404(R) (2019).
2. M.V. Eremin, Phys. Rev. B, **102**, 104107 (2020).
3. K.V. Vasin and M.V. Eremin, J. Phys.: Condens. Matter, **33**, 225501 (2021).



**TEMPERATURE BEHAVIOR OF MAGNETIC AND MAGNETOELECTRIC PROPERTIES IN Fe LANGASITES**

*A.Yu. Tikhanovskii*<sup>1\*</sup>, *V.Yu. Ivanov*<sup>1</sup>, *A.M. Kuzmenko*<sup>1</sup>,  
*Yu.F. Popov*<sup>2</sup>, *G.P. Vorobev*<sup>2</sup>, *A.A. Mukhin*<sup>1</sup>

<sup>1</sup>Prokhorov General Physics Institute of the Russian Academy of Sciences, Moscow, Russia  
<sup>2</sup>Lomonosov Moscow State University, Moscow, Russia  
 \*E-mail: [tikhanovskii@phystech.edu](mailto:tikhanovskii@phystech.edu)

Recently, iron-containing langasites ( $\text{Ba}_3\text{NbFe}_3\text{Si}_2\text{O}_{14}$ ,  $\text{Ba}_3\text{TaFe}_3\text{Si}_2\text{O}_{14}$ , and  $\text{Sr}_3\text{TaFe}_3\text{Si}_2\text{O}_{14}$ ), which are emerging as a new class of compounds exhibiting magnetoelectric properties, were synthesized [1]. They have attracted attention due to their nontrivial magnetic structure and the presence of magnetoelectric effect [2, 3]. The crystal structure of Fe langasites belongs to the non-centrosymmetric P321 space group. Below  $T_N = 27$  K, they order antiferromagnetically into a structure with double chirality (in-plane triangular ordering of the  $\text{Fe}^{3+}$  spins rotating along  $c$ -axis) [1]. In the articles [2, 3], the magnetoelectric effect was experimentally investigated. Later in [4], a detailed experimental and theoretical study of the magnetic and magnetoelectric properties of Fe langasites was presented and the electric polarization occurrence mechanisms were proposed. However, the temperature behavior of the magnetic susceptibility and electric polarization has not been explained yet. In the current work we propose a description of the magnetic susceptibility and electric polarization temperature dependences for various orientations and values of the external magnetic field.

According to the theory [5], the susceptibility of the magnetic spiral structure for  $T < T_N$  and the magnetic field directed perpendicular to the spiral’s plane ( $\mathbf{H}||c$ ) does not depend on temperature (Fig. 1b). It defines as  $\chi_{\perp} = 1/(J(k) - J(0))$ , where  $J(k) = \sum_i J_i \exp(-i(kR + \phi_i)) + \text{c.c.}$  is the sum over all exchange integrals. However, the susceptibility in field  $\mathbf{H}||c$  increases with temperature lowering, which we associate with contribution of defects.

The weak external magnetic field directed in the magnetic helix plane ( $\mathbf{H}||b^*$ ) distorts the magnetic helix and induces the second harmonic. It determines the magnitude of the magnetic susceptibility at low temperatures [5]. At a strong magnetic field ( $\mathbf{H}||b^*$ ), the helix plane rotates perpendicular to the field, and the electric polarization appears [4]. In this case, the spin-flop transition field is defined as  $H_{\text{sf}}^2 = K\sigma^2/(\chi_{\perp} - \chi_{||})$ , where  $K$  – the easy-plane anisotropy constant,  $\sigma(T)$  – the normalized magnetization determined by the Brillouin function,  $\chi_{||}$  – the susceptibility in the

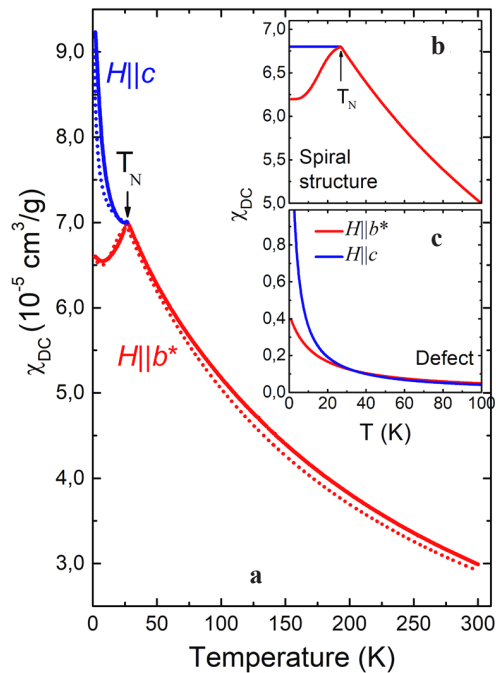


Figure 1. **a** Temperature dependences of DC susceptibility in  $\text{Ba}_3\text{NbFe}_3\text{Si}_2\text{O}_{14}$  along the crystallographic directions  $b^*$  (red line) and  $c$  (blue line) measured in field  $\mu_0 H = 0.1$  T. (Dotted lines – model simulation). **b** The susceptibility of the spiral structure and **c** of the defects.

field lying in the helix plane. We determined the temperature dependence of the spin-flop transition field (Fig. 2b) from the electric polarization  $P_{a(b^*)}$  ( $H_{b^*(a)}$ ) field dependences inflection at  $T < T_N$ . With temperature increase, the spin-flop transition field also increases, which leads to the decrease of the helix deviation from the basal plane. The parallel susceptibility  $\chi_{\parallel} = \chi_{\perp} - K(\sigma/H_{sf})^2$ , thus,  $\sigma(T)$  and  $H_{sf}(T)$  determine its temperature dependence.

To describe additional contribution to the susceptibility of Fe langasites (Fig. 1a), we propose a model in which superparamagnetic defects with  $\text{Fe}^{3+}$  spins have an anisotropic g-factor. Interaction between defects and the helical structure of Fe langasite results in an anisotropic effective exchange field. Thus, the contribution to the magnetic susceptibility from defects is anisotropic in the magnetic field directed in the basal plane and perpendicular to it (Fig. 1c). The Curie-Weiss law with the parameters  $g_x = 2.3$ ,  $g_z = 2$ ,  $\theta_x = -12.8$  K,  $\theta_z = -1.5$  K, and the defects concentration of  $\sim 0.3\%$  together with the susceptibility of the helical magnetic structure suitably describe experimental data (Fig. 1a).

Using the temperature dependence of the magnetic helix orientation and field-induced magnetization representing as order parameters [4] and determining by  $H_{sf}(T)$ ,  $\sigma(T)$  and  $\chi(T)$ , we simulated the temperature dependences of the electric polarization for various orientations of the magnetic field (Fig. 2). At low temperatures and in a field  $H = 60$  kOe, which is close to spin-flop transition field value, the electric polarization  $P_{a(b^*)}$  is determined by the helix deviation from the basal plane (inverse Dzyaloshinskii-Moriya interaction) and the quadratic field-induced contribution  $M_y M_z$  ( $-M_x M_z$ ) of the opposite sign (single-ion contribution). The spin-flop transition field increases rapidly near Neel temperature, which leads to decrease of the magnetic helix deviation. Thus, the contribution from the inverse Dzyaloshinskii-Moriya interaction decreases. As a result, only single-ion contribution determines the electric polarization in the paramagnetic region.

*This work was supported by the Russian Science Foundation (Project No. 22-42-05004).*

1. K. Marty, V. Simonet, E. Ressouche, R. Ballou, P. Lejay, and P. Bordet, Phys. Rev. Lett., **101**, 247201 (2008).
2. N. Lee, Y. J. Choi, and S. W. Cheong, Appl. Phys. Lett., **104**, 072904 (2014).
3. H. Narita, Y. Tokunaga, A. Kikkawa, Y. Taguchi, Y. Tokura, and Y. Takahashi, Phys. Rev. B, **94**, 094433 (2016).
4. A.Y. Tikhonovskii, V.Y. Ivanov, A.M. Kuzmenko, A.M. Balbashov, Z. Wang, V. Skumryev, A.A. Mukhin, Phys. Rev. B, **105**, 104424 (2022).
5. T. Nagamiya, Solid State Phys., **20**, 305 (1968).

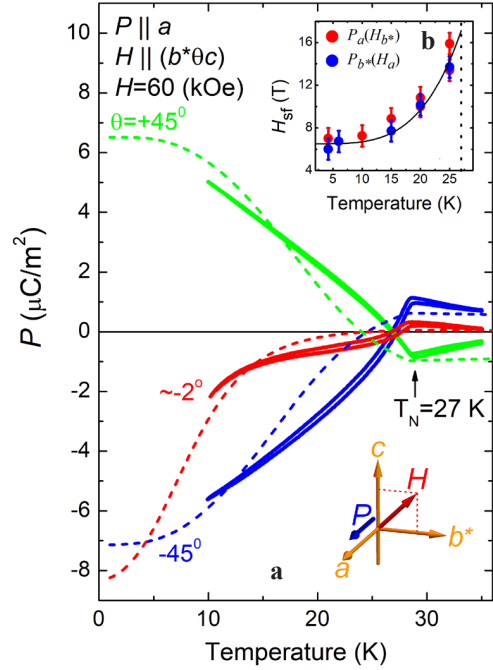


Figure 2. **a** The temperature dependence of the a component of the electric polarization in magnetic field  $\mathbf{H}$ .  $\theta$  indicates the field deviation from the  $b^*$ -axis towards the  $c$ -axis. The insets show the corresponding orientations of the magnetic field vector and the polarization. Solid lines: experiment; dotted lines: model simulations. **b** Spin-flop field dependence on temperature derived from  $P_a(H_{b^*})$  and  $P_{b^*}(H_a)$  pulsed field experiment.

## DETECTION OF ELECTRIC POLARIZATION IN TERBIUM ORTHOFERRITE

*V.Yu. Ivanov\**, *A.M. Kuzmenko*, *A.A. Mukhin*

Prokhorov General Physics Institute, RAS, Moscow, Russia

\*E-mail: [ivanov@ran.gpi.ru](mailto:ivanov@ran.gpi.ru)

Rare-earth orthoferrites  $RFeO_3$  belong to the centrosymmetric space group  $D_{2h}^{16} - Pbnm$ , which forbids the existence of the magnetoelectric effect. However, this effect can arise in the case of intrinsic antiferromagnetic ordering of the rare-earth subsystem into the noncentrosymmetric modes. A symmetry analysis of magnetoelectric interactions in rare-earth orthoferrites and orthochromites was carried out in [1], where, in particular, the possibility of the existence of electric polarization in  $TbFeO_3$  was predicted for certain configurations of  $Fe^{3+}$  spins and  $Tb^{3+}$  magnetic moments. Besides  $Tb$  orthoferrite, antiferromagnetic ordering of the rare earth subsystem occurs in  $Gd$  and  $Dy$  orthoferrites, where the existence of electric polarization (spontaneous in  $GdFeO_3$  [2] and induced by a magnetic field in  $DyFeO_3$  [3]) was found experimentally. In both cases, polarization appears along the  $c$ -axis of the crystals. In this paper, we report the discovery of magnetic field-induced  $\mathbf{H}||b$ -axis electric polarization along the  $a$ -axis in  $TbFeO_3$  at a temperature of 1.8 K, i.e., below the antiferromagnetic ordering temperature of the terbium subsystem.

The measurements were carried out on an  $a$ -cut plate of a single crystal grown by A.M. Balbashov by means of zone melting. The electric charge was measured using a Keithley 6517A electrometer with a Quantum Design MPMS XL5 setup. To obtain reproducible results, it is essential that an electrical voltage be applied to the sample during measurements (usually  $E \sim 1.5$  kV/cm), and magnetic field scanning should be carried out up to certain field values. The  $P_a(H_b)$  curves are mainly determined by the initial state of the sample: the signs and magnitudes of the electric and magnetic fields applied to the sample during its cooling down to  $T = 1.8$  K.

It is known [4] that the magnetization curve of  $TbFeO_3$  at low temperatures has a two-step character, shown in Fig. 1, where the configurations of the magnetic moments of  $Fe^{3+}$  and  $Tb^{3+}$  ions (4 ions per unit cell) are also depicted. In the initial state ( $H = 0$ ), iron ions have the  $\Gamma_4(G_xF_z)$  configuration, and strongly anisotropic (Ising)  $Tb^{3+}$  ions have the noncentrosymmetric  $\Gamma_8(a_xg_y)$  configuration, i.e. their moments form a cross in the  $ab$ -plane with a deviation from the  $a$ -axis by an angle of  $\sim \pm 360^\circ$ . At  $H_{cr1} \sim 0.5$  T the simultaneous reorientation of the magnetic moments of iron to the  $\Gamma_2(G_zF_x)$  configuration and the reversal of one of the antiferromagnetically ordered  $Tb^{3+}$  moments (moment 3 in Fig. 1) take place. In this case, the magnetization increases noticeably. When the magnetic field reaches a value of  $H_{cr2} \sim 1.8$  T, the remaining  $Tb^{3+}$  moment 4 reverses close to the field accompanying magnetization increasing and the  $Fe^{3+}$  spins return to the initial configuration  $\Gamma_4(G_xF_z)$ .

Figure 2 shows the field dependence of the electric polarization of the sample which was previously cooled down from 5 to 1.8 K in an electric field of 1.5 kV/cm and magnetic field  $H = 1.2$  T. The measurements were carried out in  $E = 1.5$  kV/cm. The polarization depends almost linearly versus the magnetic field below  $H_{cr1}$ , and its sign and slope are determined by the direction of the field scan. The polarization retains also in the intermediate range of magnetic fields between  $H_{cr1}$  and  $H_{cr2}$ ; however, in this region, it depends nonmonotonically on the magnetic field and exhibits hysteresis phenomena, but does not change its sign, which is determined by the sign of the electric field applied during cooling. For  $H > H_{cr2}$ , the polarization completely disappears.

Symmetry analysis based on [1] showed that the electric polarization along the  $a$ -axis can exist in the low-field and intermediate phases and can be described by the expression:

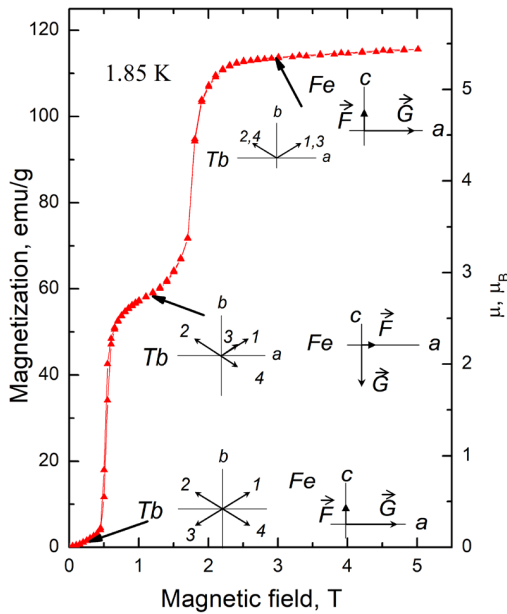


Figure 1. Magnetisation curve of TbFeO<sub>3</sub> crystal along *b*-axis at 1.85 K. Inserts illustrate magnetic moments configurations of Fe<sup>3+</sup> and Tb<sup>3+</sup> ions in various magnetic fields.

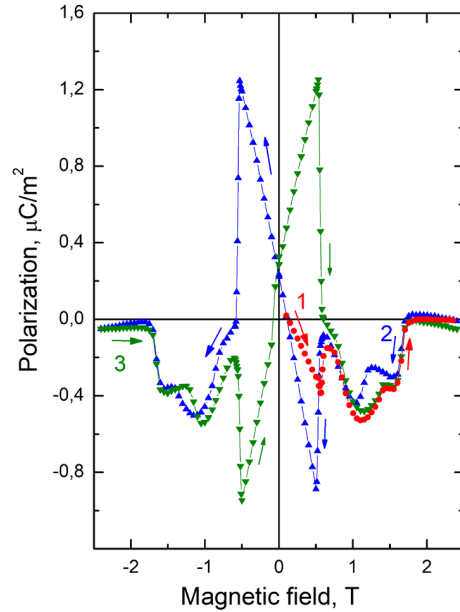


Figure 2. Field dependence of electric polarization  $P_d(H_b)$  in the TbFeO<sub>3</sub> at  $T = 1.8$  K after cooling in  $E = 1.5$  kV/cm and  $H = 1.2$  T. Arrows show the direction of the magnetic field change: curve 1 (red) – from 0 to 2.4 T; 2 (blue) –2.4 T — 0 — -2.4 T; 3 (olive) — -2.4 T — 0 — +2.4 T.

$$P_x \sim \lambda_1 a_x H_y + \lambda'_1 a_x f_y + \lambda_2 a_y G_z + \lambda'_2 a_y f_x, \quad (1)$$

where  $a_i, f_i$  are the projections of the basis vectors of the magnetic moments of the Tb subsystem,  $G_z$  is *z*-component of the main antiferromagnetic mode of Fe subsystems,  $\lambda_i, \lambda'_i$  are the magnetoelectric constants. In the ZFC state (cooling in  $H = 0, E = 0$ ) the sample is in a multi-domain degenerate state. The fourfold degeneracy is also preserved in the intermediate phase. Cooling in an electric field, or its application in the high-field phase, partially removes the degeneracy, which leads to the appearance of an electric polarization of certain sign. The first term of in Eq. (1) is responsible for the behavior of the polarization, which resembles a “butterfly”, which provides a linear dependence of the polarization on the field and jumps to another branches corresponding to different signs of  $a_x$  after the magnetization reversal of the sample.

The measurements of electric polarization in the fields do not exceeding  $H_{cr2}$  and at  $E = 0$  (after preliminary poling) revealed the manifestation of specific “memory effects” to be further studied.

*Support by RSF (Project No. 22-12-00375) is acknowledged.*

1. A.K. Zvezdin and A.A. Mukhin, JETP Lett., **88**, 505–510 (2008).
2. Y. Tokunaga, S. Iguchi, T. Arima and Y. Tokura, Phys. Rev. Lett., **101**, 097205 (2008).
3. Y. Tokunaga, N. Furukawa, H. Sakai et al., Nature Materials, **8**, 558 (2009).
4. K.P. Belov, A.K. Zvezdin, A.M. Kadomtseva, N.B. Krynetskii and A.A. Mukhin, JETP, **49**, 723–728 (1979).

## THE ROLE OF MANGANESE SUBSTITUTION IN CHANGING THE MAGNETIC AND DIELECTRIC PROPERTIES OF BULK MAGNETOELECTRICS $\text{BiFe}_{1-x}\text{Mn}_x\text{O}_3$ ( $x = 0.05$ AND $0.15$ )

*T.N. Tarasenko*<sup>1\*</sup>, *V.I. Mikhaylov*<sup>1</sup>, *Z.F. Kravchenko*<sup>1</sup>, *V.V. Burkhovetskiy*<sup>1</sup>, *A.I. Izotov*<sup>1</sup>,  
*Yu.A. Legenki*<sup>2</sup>, *A.M. Zyvulko*<sup>3</sup>, *K.I. Yanushkevich*<sup>3</sup>, *S.S. Aplesnin*<sup>4</sup>

<sup>1</sup>Public Institution “Donetsk Institute for Physics and Engineering named after A.A. Galkin”, Donetsk, DPR

<sup>2</sup>Donetsk National University, Donetsk, DPR

<sup>3</sup>SSPA “Scientific-Practical Materials Research Center of NAS of Belarus”, Minsk, Belarus

<sup>4</sup>Reshetnev Siberian State University of Science and Technology, Krasnoyarsk, Russia

\*E-mail: [t.n.tarasenko@mail.ru](mailto:t.n.tarasenko@mail.ru)

$\text{BiFeO}_3$  bismuth ferrite (BFO), due to its high ferroelectric ( $T_C = 1083$  K) and magnetic ( $T_N = 643$  K) ordering temperatures, is of considerable practical interest as a model object for creating magneto-optical materials. The presence of a spatially modulated spin structure in BFO does not allow for the linear magnetoelectric effect and spontaneous magnetization, which, however, are allowed by crystal symmetry [1]. An effective method to improve the magnetic and ferroelectric properties of BFO is to produce solid solutions based on BFO. X-ray diffraction studies of  $\text{BiFe}_x\text{Mn}_{1-x}\text{O}_3$  samples ( $x = 0, 0.05$ , and  $0.15$ ) synthesized by the sol-gel method [2] show that with increasing manganese content the percentage of impurity phases decreases and the main phase (space group R3c) stabilizes with decreasing lattice distortions.

The purpose of this work is to study the effect of the substitution of  $\text{Fe}^{3+}$  cations by  $\text{Mn}^{3+}$  cations in BFO on the magnetic and dielectric properties of  $\text{BiFe}_x\text{Mn}_{1-x}\text{O}_3$  multiferroic samples synthesized by sol-gel method.

The results of the study of the temperature dependences of specific magnetisation  $\sigma(T)$  (Fig. 1) suggest that in the  $\text{BiFe}_x\text{Mn}_{1-x}\text{O}_3$  system in the concentration range  $0.05 < x < 0.15$  the samples have magnetic characteristics typical for ferromagnetics (FM). It is assumed that there is a contribution to magnetization from impurity phases. The temperature of the magnetic phase transition were deter-

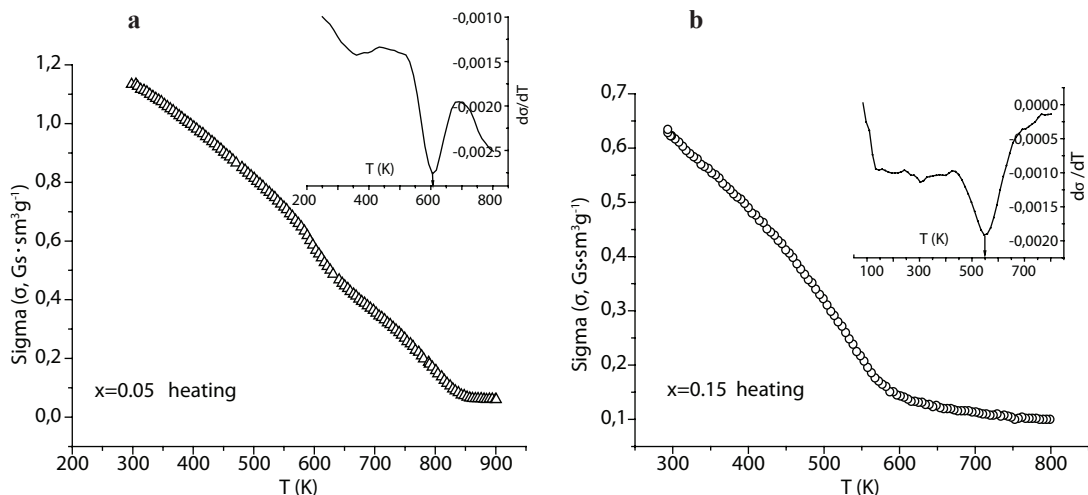


Figure 1. Temperature dependences of the specific magnetization  $\sigma$  and  $d\sigma/dT$  of  $\text{BiFe}_x\text{Mn}_{1-x}\text{O}_3$  and impurity phases.

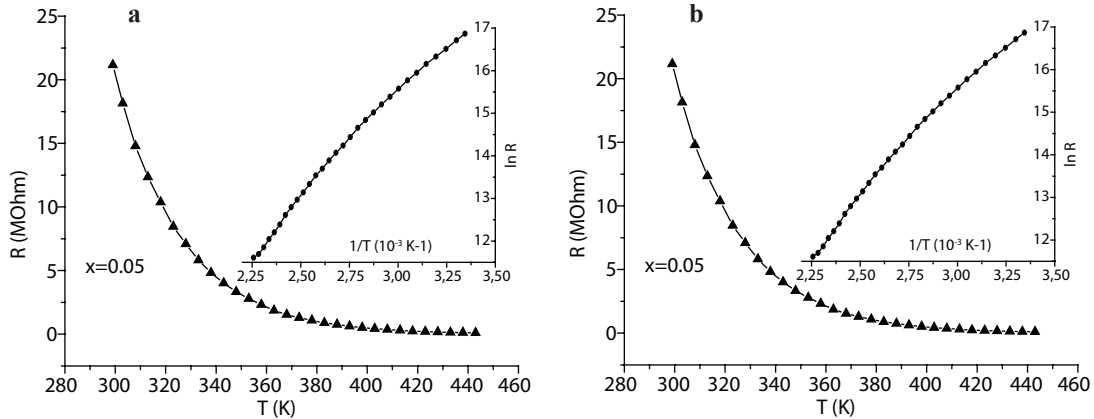


Figure 2. Temperature dependences of the resistance  $R$  and  $\ln R(1/T)$  of  $\text{BiFe}_x\text{Mn}_{1-x}\text{O}_3$ .

mined from the temperature derivative of the specific magnetization  $\sigma(T)$  (smoothed curves on the insets to Fig. 1). For compositions with  $x = 0.05$   $T_C = 605$  K, and for  $x = 0.15$  value  $T_C = 550$  K.

The electrical resistance was measured in the temperature range  $T_{\text{room}} \leq T \leq 523$  K. It follows from the analysis of the measurement results that  $\text{BiFeO}_3$  is a dielectric over the entire temperature range. Compounds containing manganese exhibit semiconductor type of conductivity in the entire temperature range (Fig. 2a). The width between conductivity band and the impurity subband was determined from dependence  $\ln R(1/T)$  (insets to Fig. 2):  $\Delta E = 1.03$  eV for  $\text{BiFe}_{0.95}\text{Mn}_{0.05}\text{O}_3$  and  $\Delta E = 0.8$  eV for  $\text{BiFe}_{0.85}\text{Mn}_{0.15}\text{O}_3$ . With the increase of  $x$  increase of dielectric permittivity is observed.

The results of measurements of dielectric parameters of  $\text{BiFe}_x\text{Mn}_{1-x}\text{O}_3$  samples ( $x = 0; 0.05; 0.15$ ) measured at 1 kHz and 1 MHz are presented in Table 1. At 1 kHz an increase in dielectric permittivity with increasing manganese content is observed: 1.8 times for  $x = 0.05$  and 7.2 times for  $x = 0.15$  compared to  $\epsilon = 17.5$  for BFO. At 1 MHz, a slight increase in dielectric permittivity.

Table 1. Dielectric parameters of  $\text{BiFe}_x\text{Mn}_{1-x}\text{O}_3$  samples ( $0 \leq x \leq 0.15$ ).

$x$	1 κΓЦ (E7-8)			1 МΓЦ (E7-12)		
	$\text{tg}\delta$	G, $\mu\text{S}$	$\epsilon \pm \Delta\epsilon$	$\text{tg}\delta$	G, $\mu\text{S}$	$\epsilon \pm \Delta\epsilon$
0	0.2	3.3	$17.5 \pm 0.5$	0.019	1.97	$11.8 \pm 0.5$
0.05	0.17	1.5	$30.75 \pm 0.5$	0.022	3.15	$20.4 \pm 0.5$
0.15	0.1	2.05	$126.6 \pm 1.0$	0.025	3.37	$24.1 \pm 0.5$

Thus, it is revealed that in the concentration range  $0.05 < x < 0.15$  the investigated compositions possess specific magnetization peculiar to substances with magnetic ordering. The  $T_C$  temperature for the compositions with concentration  $x = 0.05$  has a value of  $T_C = 605$  K, and for  $x = 0.15$  –  $T_C = 550$  K. Compounds containing manganese exhibit semiconductor type of conductivity in the entire temperature range. The gap width between conductivity band and the impurity subband is determined:  $\Delta E = 1.03$  eV for  $\text{BiFe}_{0.95}\text{Mn}_{0.05}\text{O}_3$  and  $\Delta E = 0.8$  eV for  $\text{BiFe}_{0.85}\text{Mn}_{0.15}\text{O}_3$ . With the increase of  $x$  increase of dielectric permittivity is observed.

The presence of “magnetic order-magnetic disorder” phase transformations at temperatures above room temperature in combination with semiconducting properties makes the use of  $\text{BiFe}_x\text{Mn}_{1-x}\text{O}_3$  compositions ( $x = 0, 0.05$  and  $0.15$ ) in microelectronic devices promising.

1. A.P. Pyatakov and A.K. Zvezdin, Phys. Usp., **55**, 557–581 (2012).
2. T.N. Tarasenko et al., Bull. Russ. Acad. Sci.: Phys., **84**, 1113–1115 (2020).

## EFFECT OF DOPING IMPURITIES ON THE SENSITIVITY OF DIAMAGNETIC CdTe CRYSTALS TO PULSED MAGNETIC ACTION

*I.S. Volchkov\**, *P.L. Podkur*, *M.D. Pavlyuk*, *V.B. Kvartalov*, *V.M. Kanevskii*

IC RAS, FSRC “Crystallography and Photonics” RAS, Moscow, Russia;

\*E-mail: [volch2862@gmail.com](mailto:volch2862@gmail.com)

Progress in the field of semiconductor materials and technologies contributes to their widespread use in electronics and energy. Increasingly important is the production of high-quality semiconductor crystals on a large scale, in particular, semiconductor crystals based on CdTe. These crystals are the most promising materials for the development of X-ray and gamma detectors operating at room temperature and photoelectric converters. The creation of perfect crystals with desired properties based on cadmium telluride crystals is a very difficult task, regardless of the field of application: obtaining a high-quality high-resistance material necessary for use as a detector material or a low-resistance high-quality material with a strict control of the band gap for photoelectric converters. Improving growth methods, although promising, is only possible to a limited extent. In this regard, methods for improving the characteristics of already grown crystals are of interest. Such methods may include the impact on already grown crystals of “weak” ( $\mu_B B \ll kT$ ) magnetic fields.

The effects of changes in the real structure and properties of diamagnetic materials after exposure to “weak” magnetic fields have been known for a relatively long time [1–3]. These effects can be conventionally divided into three types: effects observed only in a magnetic field, effects with slow relaxation, and effects of an irreversible change in properties after exposure to a magnetic field, including a pulsed one. The latter are of particular interest.

It should be noted that these effects are observed on diamagnetic materials, which is especially interesting. It is generally accepted that they occur due to spin-dependent rearrangement reactions of defective complexes of the material triggered by the action of a pulsed magnetic field. Thus, materials based on CdTe are wide-gap semiconductors with a band gap  $E_g > 1$  eV, which in theory have low conductivity and are diamagnetic. However, the real situation is such that all II–VI compounds are nonstoichiometric and the deviation from the ideal structure is due to the presence of intrinsic defects: vacancies ( $V_A$  and  $V_B$ ) and interstitial atoms ( $A^i$  and  $B^i$ ). When impurities are added during crystal growth, impurities are added to intrinsic defects. The appearance of defects during growth leads to a significant change in the physical properties and makes the material sensitive to “weak” pulsed magnetic action. Moreover, it is interesting that crystals close to stoichiometry and grown without the addition of alloying components turn out to be weakly sensitive to this effect, or insensitive at all. At the same time, on lightly doped semiconductor crystals based on CdTe, changes in properties are very clearly

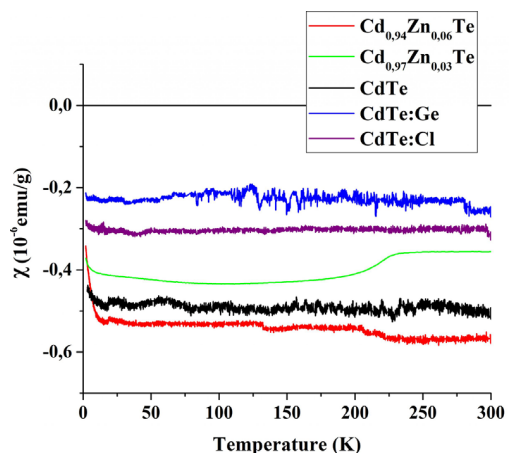


Figure 1. Temperature dependence of  $\chi$  measured at 1000 Oe.



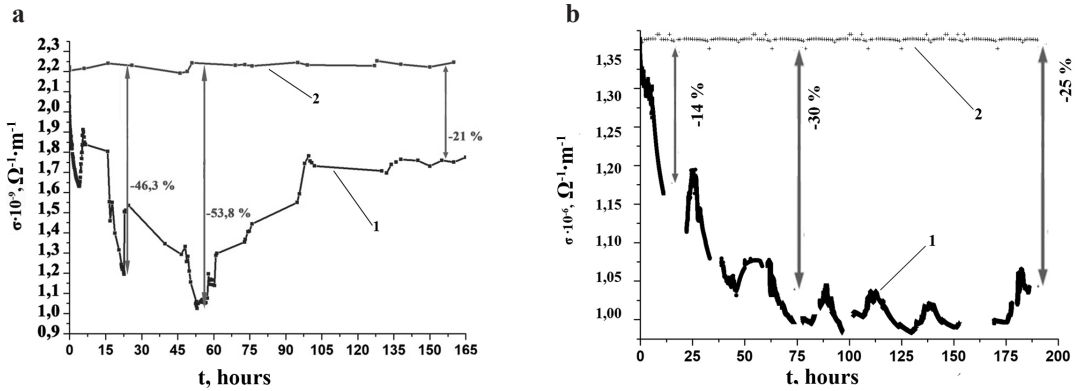


Figure 2. Electrical conductivity versus time, after magnetic treatment. **a** CdTe:Cl, **b** CdTe:Ge.

observed after magnetic exposure [4, 5]. In this regard, studies were carried out on the sensitivity of CdTe-based crystals to pulsed magnetic action depending on the type and amount of the dopant.

CdTe, Cd<sub>1-x</sub>Zn<sub>x</sub>Te, CdTe:Cl and CdTe:Ge samples grown by the modified Obreimov-Shubnikov method at the Institute of Crystallography of the Federal Research Center “Crystallography and Photonics” of the Russian Academy of Sciences were used as the material under study. The impurity composition and structure of the samples were controlled by mass spectrometry, EDS analysis, and X-ray phase analysis. Magnetic properties (Fig. 1) was measured with a SQUID MPMS XL magnetometer (Quantum Design). Changes in the properties of the studied samples were recorded by changes in the electrical and mechanical characteristics. The electrical properties of the samples were studied by two-contact and four-contact methods (Cresbox, Napson) before exposure to a magnetic field and repeatedly over time after (Fig. 2). The mechanical characteristics were studied by the nanoindentation method. The samples were exposed to a pulsed magnetic field (amplitude  $B = 1$  T, frequency  $\nu = 12$  Hz) for  $t_{\text{exp}} = 10$  min. Some samples, with the subtraction of the diamagnetic contribution of the crystal lattice, showed ferromagnetic properties.

It has been determined that the sensitivity of CdTe-based diamagnetic crystals depends on their band gap and electrical properties, as well as on the magnetic properties of their impurity component.

1. V.M. Kanevsky, V.P. Vlasov, A.A. Purtskhvanidze, *Solid State Physics*, **33**, 2194–2197 (1991) [in Russian].
2. Yu.I. Golovin and R.B. Morgunov, *Dokl. Akad. Nauk*, **354**(5), 632 (1997).
3. V.I. Al’shits, E.V. Darinskaya, O.L. Kazakova, *JETP Lett.*, **62**, 375 (1995).
4. E.V. Darinskaya, E.A. Petrzhik, Yu.M. Ivanov, S.A. Erofeeva, M.R. Raukhan, *Phys. Stat. Sol. (c)*, **2**(6), 1873–1877 (2005).
5. I.S. Volchkov, V.M. Kanevskii, M.D. Pavlyuk, *JETP Lett.*, **107**(4), 269–272 (2018).

## MAGNETIC RESONANCE IN Ho-DOPED RARE-EARTH LANGASITE

*A.M. Kuzmenko*<sup>1\*</sup>, *A.A. Mukhin*<sup>1</sup>, *V.Yu. Ivanov*<sup>1</sup>, *A.Yu. Tikhanovskii*<sup>1</sup>,  
*L. Weymann*<sup>2</sup>, *A. Shuvaev*<sup>2</sup>, *A. Pimenov*<sup>2</sup>

<sup>1</sup>Prokhorov General Physics Institute of the Russian Academy of Sciences, Moscow, Russia

<sup>2</sup>Institute of Solid State Physics, Vienna University of Technology, Vienna, Austria

\*E-mail: [artem.kuzmenko.gpi@gmail.com](mailto:artem.kuzmenko.gpi@gmail.com)

This study is devoted to magnetoelectric materials based on the well-known langasite crystal  $\text{La}_3\text{Ga}_5\text{SiO}_{14}$ . The original material exhibits piezoelectric properties due to its trigonal structure with non-centrosymmetric crystallographic space group P321. This symmetry leads to the appearance of magnetoelectric properties when magnetic ions are introduced into the crystal structure. Replacing nonmagnetic La ions with magnetic ones leads to the creation of a new magnetoelectric crystal. In this work, we studied  $(\text{Ho}_{0.03}\text{La}_{0.97})_3\text{Ga}_5\text{SiO}_{14}$  langasite lightly doped with strongly magnetic holmium ions. The small ionic radius of the Ho ion compared to La leads to a loss of crystal lattice stability; therefore, crystal growth is impossible at high Ho concentrations.

In [1], the magnetic and magnetoelectric properties of langasite doped with holmium were studied. In this compound, the rare-earth Ho subsystem remains paramagnetic down to lowest temperatures. This Ho-doped langasite exhibits an unusual combination of linear and highly non-linear magnetoelectric responses in a paramagnetic state: its electric polarization increases along  $c$ -axis linearly with the magnetic field, but oscillates as the magnetic field vector rotates in  $ab$ -plane. Low local symmetry ( $C_2$ ) of  $\text{Ho}^{3+}$  positions in the crystal of higher (trigonal) symmetry provides such magnetoelectric response that does not require special magnetic orders, and occurs already in the paramagnetic state.

Both magnetic and magnetoelectric properties depend on electron structure of  $\text{Ho}^{3+}$  ion in langasite crystal field (CF), the main contribution is determined by the lower CF levels, especially at low temperatures. To reveal the structure of the ground state of the  $\text{Ho}^{3+}$  ion, in this work, terahertz spectroscopic studies of the transmission and phase shift spectra of the transmitted radiation in an external magnetic field up to 7 T were carried out. Direct transitions between the components of the ground quasi-doublet of the  $\text{Ho}^{3+}$  ion split by the CF and an external magnetic field are discovered and studied. The resonant modes of the paramagnetic Ho subsystem have a weak intensity due to a low concentration of Ho ions and are usually not visible in the quasi-optical transmission spectra in a frequency scanning mode at a constant external magnetic field. However, sweeping the magnetic field at a fixed frequency makes it possible to detect these weak resonance lines (Fig. 1a-d). The ability to measure at a fixed frequency is provided by a quasi-optical backward wave oscillator (BWO) spectrometer, which allows to tune the frequency in a wide range from 50 to 1000 GHz using a set of BWO generators.

The theoretical model used in Ref. [1] takes into account the local  $C_2$  symmetry of the Ising-like Ho ion, in which the magnetization axis is directed perpendicular to the local  $a$ -axis of the crystal. However, this approach does not describe the behavior of the observed resonance lines and experimental values of the magnetization anisotropy in a magnetic field, which is apparently associated with local distortions of the CF on holmium ions. The study of magnetic resonance makes it possible to obtain additional information about the local environment of the rare-earth ion in order to refine the ground state and its contribution to the magnetic, magnetoelectric, and resonance properties. We propose a model that takes into account the presence of local symmetry distortions which lead to the deviation of the Ising axes from the allowed position corresponding  $C_2$  local symmetry. Thus,

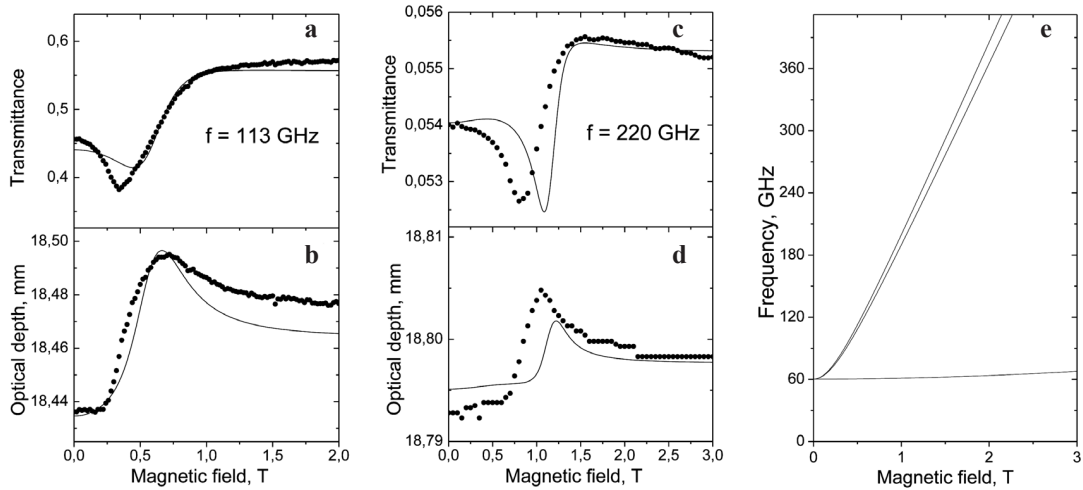


Figure 1. Dependencies of transmittance (a, c) and optical thickness (reflects the phase shift) (b, d) on magnetic field at frequencies of 113 and 220 GHz at temperature 1.8 K. Block e shows the calculated dependences of the resonance frequencies for six positions (the frequencies of some positions coincide). All data are given for geometry  $\mathbf{H}\parallel b^*$ ,  $\mathbf{h}\parallel b^*$ ,  $\mathbf{e}\parallel c$ .

in the initial non-distorted state, the  $\text{Ho}^{3+}$  easy axes lie in the  $b^*c$ -plane ( $b^*$ -axis is perpendicular to crystallographic axes  $a$  and  $c$ ), while CF distortions result in its random deviation from the  $b^*c$ -plane and the appearance of two positive/negative components along the local  $a$ -axis. Taking into account three  $a$ -axes in the crystal, the model includes six types of the Ising axes.

First of all, we used this model to describe the anisotropic magnetic properties of holmium-doped langasite. Then all the same parameters of the model (CF splitting, local magnetization of six holmium sites) were used to simulate the observed resonant spectra, which are in a good agreement with experiment (Fig. 1a-d). The only additional fitting parameter was the linewidth.

Figure 1 shows examples the spectra description and the dependence of the resonance lines on the external magnetic field ( $\mathbf{H}$ ) for the  $\mathbf{H}\parallel b^*$ ,  $\mathbf{h}\parallel b^*$ ,  $\mathbf{e}\parallel c$  geometry ( $\mathbf{h}$ ,  $\mathbf{e}$  are ac magnetic and electric fields, respectively). To describe the spectra, we calculated both the dependences of the frequencies (Fig. 1e) and intensities of the resonance modes on the magnetic field. The mode contributions to the magnetic susceptibility strongly depend on the splitting of the ground  $\text{Ho}^{3+}$  quasi-doublet in the CF; they decrease rapidly with increasing external magnetic field. It should be noted an important role of the CF splitting in the  $\text{Ho}^{3+}$  ground quasi-doublet (besides magnetic moment) which determines intensities of the resonance modes as well as excitation in geometries where ac magnetic field is parallel to the external magnetic field.

*Support by Russian Science Foundation (No. 22-42-05004) is acknowledged.*

I. L. Weymann, L. Bergen, T. Kain et al., npj Quantum Mater., 5, 61 (2020).

## POLYMER MAGNETOELECTRIC COMPOSITES BASED ON PVDF

*A.A. Amirov<sup>1,2\*</sup>, V.V. Rodionova<sup>1</sup>, A.M. Aliev<sup>2</sup>*

<sup>1</sup>Immanuel Kant Baltic Federal University, Kaliningrad, Russia

<sup>2</sup>Amirkhanov Institute of Physics, Dagestan Federal Research Center,  
Russian Academy of Sciences, Makhachkala, Russia

\*E-mail: [amiroff\\_a@mail.ru](mailto:amiroff_a@mail.ru)

Recently, the scientific interest has focused on the design and studies of smart materials for biomedical and energy applications. Among them multiferroics are on the advanced smart materials due to the coexistence of magnetism and ferroelectricity. Multiferroic composites due to the large magnetoelectric (ME) coupling are more prospective for practical applications in magnetic (biomagnetic) field sensors, energy transfer and harvesting, spin memory/logic devices, and scaffolds for tissue engineering and etc. In focus of biomedical applications, composites based on biocompatible polymers are more prospective [1].

The ME composites have various connectivity schemes and basis information about them are summarized in [2]. In general, connectivity schemes divide into the following types: 0-3 type – for particulate composites of piezoelectric and magnetic grains, 2-2 type – for layered composites consisting of piezoelectric and magnetic layers, and 1-3 type – for composites with fibers of one phase embedded in the matrix of another phase.

Polyvinylidene fluoride (PVDF) is a thermoplastic fluoropolymer and has four crystalline phases  $\alpha$ ,  $\beta$ ,  $\gamma$  and  $\delta$  depending on the chain conformation. Among them the polar  $\beta$ -phase has the most interest due to its spontaneous polarization and piezoelectric effect. For practical applications, the most interesting is electroactive PVDF, which is used in piezoelectric generators, and sensors. PVDF is biocompatible, non-toxic, flexible, has a good chemical resistance, and is suitable for biomedical applications (sensors, scaffolds and etc.).

The present work is devoted to the design, fabrication and studies of new multiferroic composites with different connectivity schemes (0-3, 1-3, 2-2) based on piezoelectric polymer. As the ferroelectric component, a PVDF polymer is suggested. In order to develop the “smart” effects, we propose to use magnetic materials with large magnetostriction and magnetocaloric effects (MCE). In results of applying of magnetic field, we can observe as ME effect as well as MCE. Thus, in proposed new polymer composite we are expected two output smart effects: electric voltage generated in results of ME effect and temperature changes due to the MCE.

The 0-3 type polymer ME composite Fe-Rh/PVDF, consisting of microparticles of a magnetocaloric powder  $\text{Fe}_{50}\text{Rh}_{50}$  embedded in a polymer piezoelectric matrix of polyvinylidene fluoride, has been manufactured by solvent casting method using modified technological protocol (Fig. 1.). The

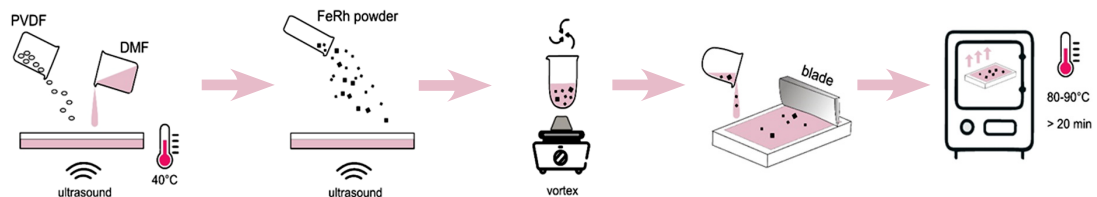


Figure 1. Fabrication scheme of 0-3 type PVDF based composite.

microparticles  $\text{Fe}_{50}\text{Rh}_{50}$  used for the composite fabrication were obtained from the ingot of the same composition by mechanical filing. The average size of the  $\text{Fe}_{50}\text{Rh}_{50}$  microgranules obtained as a result of filing was 50 microns. X-ray diffraction analysis showed the presence of an electroactive  $\beta$ -phase of polyvinylidenefluoride and an ordered B2 phase corresponding to a crystal structure with a bcc volume-centered crystal lattice, which can exhibit magnetoelectric and multicaloric effects.

It was shown that the temperature of the transition from the antiferromagnetic to the ferromagnetic state for  $\text{Fe}_{50}\text{Rh}_{50}$  microparticles as a result of mechanical processing is shifted towards high temperatures, as a result of mechanical action in the process of obtaining Fe-Rh powder, and in the region of  $\sim 670$  K, a transition from the ferromagnetic state to the paramagnetic state is observed. It was demonstrated that annealing of the  $\text{Fe}_{50}\text{Rh}_{50}$  microparticles at a temperature of  $\sim 1000$  °C for 20 min is able to recover the magnetic properties close to the bulk sample with a same composition. For the Fe-Rh/PVDF composite, a wide magnetic phase transition of  $\sim 387$  K (AFM-FM) in the heating mode and  $\sim 364$  K (FM-AFM) in the cooling mode is observed, which coincides with the results of magnetic measurements obtained for the heat-treated  $\text{Fe}_{50}\text{Rh}_{50}$  microparticles. Preliminary experiments on samples with mass fractions of the magnetic fillers 10% observed the presence of a ME interaction in the vicinity of the magnetic phase transition temperature of the magnetocaloric component of the composite, which can be used for applications in smart composites.

The 2-2 type ME composite of PVDF/Fe-Rh samples has the bi-layer structure and consisted PVDF layer coated on substrate of magnetocaloric alloy  $\text{Fe}_{49}\text{Rh}_{51}$  (FeRh). The polymer coating were performed based on solvent casting method with help of doctor blade technique [1]. The substrate material of  $\text{Fe}_{49}\text{Rh}_{51}$  (FeRh) was synthesized by arc melting of pure elements Fe (99.98 %), Rh (99.8 %) in helium atmosphere ( $10^{-4}$  mbar) with further annealing at 1000 °C for 7 days and air quenching. Strong ME coupling and large MCE were observed at 310 K corresponded the metamagnetic phase transition of Fe-Rh.

The 1-3 type ME composite of Ni-Mn-Ga/PVDF were consisted of Heusler-type magnetic microwires embedded in PVDF polymer matrix fabricated based on modified solvent casting technique. The maximum in adiabatic temperature change  $\Delta T$  about  $\sim 0.04$  K were observed around 276 K with narrow hysteresis accompanied with maximum of magnetoelectric coefficient. Observed temperature dependences of magnetocaloric and ME effects could be associated with both magnetic (paramagnetic-ferromagnetic) and structural (austenite-martensite) phase transitions. The measurements of MCE in modes with different frequencies of modulated magnetic field exhibit the reduction of  $\Delta T$  about 38% with increase of frequency from 0.5 to 20 Hz.

In summary, the composites with three differ connectivity schemes were designed, fabricated and investigated. The MCE effect corresponded large ME coupling were observed in all types of composites. The proposed approaches can be used for the design of new smart composites with magnetoelectric and caloric effects.

*The reported study was funded by the Russian Science Foundation, Project No. 21-72-30032.*

1. A. Omelyanchik et al., *Nanomaterials*, **11**, 1154 (2021).
2. Ce-Wen Nan, M. I. Bichurin, Shuxiang Dong, D. Viehland, and G. Srinivasan, *J. Appl. Phys.*, **103**, 031101-1–031101-35 (2008).

## NÉEL TRANSITION TEMPERATURES AS A FUNCTION OF LATTICE PARAMETER FOR LITHIUM METAL ORTHOPHOSPHATES

*M.A. Semkin*

M.N. Miheev Institute of Metal Physics UB RAS, Ekaterinburg, Russian Federation

E-mail: [semkin@imp.uran.ru](mailto:semkin@imp.uran.ru)

Olivine structured  $\text{LiMPO}_4$  ( $M = \text{Mn, Fe, Co, Ni}$ ) phosphates are of great interest from both practical and fundamental points of view. On the one hand they are the applied materials of the cathodes of lithium-ion batteries. On the other hand, they exhibit unique magnetic and magnetoelectric properties [1]. The presence of the magnetoelectric effect, the coincidence of the Néel transitional and polarization temperatures and a variety of magnetic structures forms a fundamental interest in studying the physical properties of the doped  $\text{LiNi}_{1-x}\text{Co}_x\text{PO}_4$  solid states [2].

Both for practical applications and fundamental research it is important to know the peculiarities of the crystal structure and physical properties of the material under study. The X-ray diffraction and magnetic measurements have been carried out to study the polycrystalline samples  $\text{LiNi}_{1-x}\text{Co}_x\text{PO}_4$  prepared by the glycerol-nitrate synthesis method.

The  $\text{LiMPO}_4$  orthophosphates crystallize in the orthorhombic olivine crystal structure (space-group  $Pnma$ ). In the crystal structure of  $\text{LiMPO}_4$  the A-site ( $\text{Li}^+$  and  $\text{M}^{2+}$ ) cations occupy 4a and 4c Wyckoff positions, which are surrounded by oxygen anions in the  $\text{LiO}_6$  and  $\text{MO}_6$  octahedrons. The B-site ( $\text{P}^{5+}$ ) cation occupying the 4c Wyckoff position is surrounded by oxygen anions in the  $\text{PO}_4$  tetrahedron.

The ground state of  $\text{LiNiPO}_4$  ( $x = 0$ ) is characterized by the antiferromagnetic (AFM) ordering ( $T_N = 20.8$  K) of components of the Ni-ion magnetic moments along  $c$ -axis  $\mu_z = 2.2\mu_B$ . The  $\text{LiCoPO}_4$  ( $x = 1$ ) orthophosphate undergoes the magnetic phase transition from an AFM ordering of Co-ion

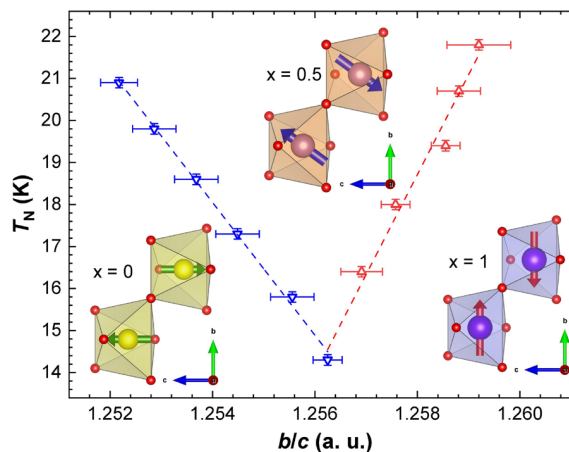


Figure 1. Néel transition temperatures as a function of lattice parameter for orthorhombic  $\text{LiNi}_{1-x}\text{Co}_x\text{PO}_4$  ( $x = 0-1$ ) taken from X-ray diffraction and magnetic measurements. The dashed lines are a linear fit thorough  $0 \leq x \leq 0.5$  and  $0.5 \leq x \leq 1$  of the data. Cartoon labeling the oxygen (red) position defining the orthorhombic surrounding the Ni (yellow) or Co (violet) species.

magnetic moments to a paramagnetic state at  $T_N = 21.6$  K. The average Co-ion magnetic moment has projections on the  $b$ -axis  $\mu_y = 3.5\mu_B$ .

In Fig. 1 the Néel transition temperatures for series of orthorhombic  $\text{LiNi}_{1-x}\text{Co}_x\text{PO}_4$  solid states ( $x = 0-1$ ) are shown as a function of the ratio of the  $b/c$  lattice parameters.

A linear expansion of the cell volume depends on concentration of the Co-ions and is anisotropic: parameter  $a$  shows the largest increase, parameter  $b$  increases too, while parameter  $c$  increases slightly and all obey the Vegard's law. This is associated with the size effect: the ionic radius of Co is larger than the ionic radius of Ni in 1.145 times [3].

The  $\text{LiNi}_{0.5}\text{Co}_{0.5}\text{PO}_4$  ( $x = 0.5$ ) orthophosphate undergoes the magnetic phase transition at  $T_N = 14.3$  K. The average Ni/Co-ion magnetic moment has projections on the  $b$  and  $c$  axes (at 7 K):  $\mu_y = 1.1\mu_B$ ,  $\mu_z = 1.6\mu_B$  and total magnetic moment is equal to  $1.9\mu_B$ . Moments in positions  $(1/4 + \varepsilon; 1/4; 1 - \delta)$  and  $(3/4 + \varepsilon; 1/4; 1/2 + \delta)$  are oriented antiparallel to moments in the positions  $(3/4 - \varepsilon; 3/4; \delta)$  and  $(1/4 - \varepsilon; 3/4; 1/2 - \delta)$ , where  $\varepsilon \approx 0.026$ ;  $\delta \approx 0.017$ .

Interestingly, we find a linear trends that are thorough  $0 \leq x \leq 0.5$  and  $0.5 \leq x \leq 1$  regions of the data. The critical point ( $x = 0.5$ ) at minimum  $T_N$  are changes linear trends from decrease to increase values of antiferromagnetic-paramagnetic transition temperature with an increase  $b/c$  parameter. We can assume that for  $x \geq 0.5$  the increase  $T_N$  because a Co-ion spin is larger a Ni-ion spin.

In summary, in series of  $\text{LiNi}_{1-x}\text{Co}_x\text{PO}_4$  orthophosphates the magnetic moments of 3d-transition ions are oriented along the  $c$ -axis and  $b$ -axis (i.e., in the  $bc$ -plane). The orientations and magnetic moment magnitudes are defined by Ni/Co-O-Ni/Co strong antiferromagnetic interaction.

*The reported study was funded by RFBR (project No. 19-32-60011).*

1. N. Nitta, F. Wu, J.T. Lee and G. Yushin, Mater. Today, **18**, 252–264 (2015).
2. M.A. Semkin, N.V. Urusova, A. Hoser, D.S. Neznakhin and A.N. Pirogov, J. Phys.: Condens. Matter, **34**, 165801–7 (2022).
3. R.D. Shannon and C.T. Prewitt, Acta Cryst., **25**, 925–945 (1969).

## EFFECTIVE MASS ANISOTROPY AND SPIN-ORBIT COUPLING IN 2D ELECTRON GAS OF GaN/AlN HIGH-ELECTRON-MOBILITY TRANSISTOR HETEROSTRUCTURES

*N.K. Chumakov<sup>1</sup>, I.S. Ezubchenko<sup>1</sup>, I.A. Chernykh<sup>1</sup>, I.V. Belov<sup>1</sup>, M.L. Zanaevskina<sup>1</sup>,  
 L.L. Lev<sup>2,3</sup>, V.N. Strocov<sup>4</sup>, V.G. Valeev<sup>1\*</sup>*

<sup>1</sup>National Research Centre “Kurchatov Institute”, Moscow, Russia

<sup>2</sup>Moscow Institute of Physics and Technology, Dolgoprudny, Russia

<sup>3</sup>P.N. Lebedev Physical Institute of the Russian Academy of Sciences, Moscow, Russia

<sup>4</sup>Swiss Light Source, Paul Scherrer Institute, Villigen-PSI, Switzerland

\*E-mail: [Valeev\\_VG@nrcki.ru](mailto:Valeev_VG@nrcki.ru)

Wurtzite GaN/AlN high electron mobility transistor (HEMT) heterostructures are widely studied for the last decades in the interest of the next generation high-power, high-temperature and microwave electronics. This activity is conditioned by their ability to provide current density, operating temperatures, breakdown voltage and cut-off frequencies, much higher compared to the existing GaAs, Si and Ge functional systems. A significant progress in the development of III-nitride functional systems is based on a thorough study of the physical properties of this family of materials.

Recently we explore 2D electron gas (2DEG) of GaN/AlN HEMT heterostructures with an ultrathin barrier layer, accessing its electronic structure is with soft-X-ray angle-resolved photoelectron spectroscopy [1]. The experiment yielded first direct  $k$ -space images of the electronic structure fundamentals of this system – the Fermi surface, band dispersions and occupancy, allowing, in particular, to discover significant planar anisotropy of the 2DEG electron Fermi surface and effective mass, which translates into nonlinear (high-field) transport properties of the GaN/AlN heterostructures as an anisotropy of the saturation drift velocity of the carriers. A possible reason for this fact, though valid for the case of quasiclassic perturbations of the crystal field only, was associated there with relaxation of the interfacial GaN atomic positions. Another reason, which in contrast is of fundamental nature, is discussed in what follows.

Bulk GaN has a hexagonal crystal structure with nonsymmorphic space group  $C_{6v}^4$ . Our point is that in the presence of a (0001) interface the symmetry of the crystal is reduced to  $C_{3v}$ , which consists of a threefold rotation  $C_3$  around the trigonal  $c$ -axis and a mirror operation  $x \rightarrow -x$  where  $x$  is in  $\Gamma K$  direction. Simple analyses shows, that the anisotropic 2DEG Fermi surface [1] can be explained by account for the third order terms in the  $kp$ -Hamiltonian,  $\hat{H}(\mathbf{k})$  breaking the U(1) rotational symmetry of the bare

$$\hat{H}_0 = \hbar^2 k^2 / 2m^* + V(z),$$

where  $z$  is coordinate, normal to the heterointerface,  $m^*$  is isotropic effective mass of the 2DEG electrons at the origin of the Brillouin zone and  $V(z)$  is the confining potential.

The  $C_{3v}$ -system symmetry dictates the following choice, [2]:

$$\hat{H}(\mathbf{k}) = \hat{H}_0 + v_k (k_x \hat{\sigma}_y - k_y \hat{\sigma}_x) + \frac{\lambda}{2} [(k_x + ik_y)^3 + (k_x - ik_y)^3] \hat{\sigma}_z. \quad (1)$$

Here  $\hat{\sigma}_i$ ,  $i = 1, 2, 3$  are the standard Pauli matrices in the spin subspace,  $v_k = v(1 + \alpha k^2)$  the circular-symmetric second term is Rashba spin-orbit contribution and the  $\lambda$ -term stands for cubic Dresselhaus spin-orbit coupling in the  $C_{3v}$ -symmetric system.



The 2DEG band dispersion of the Hamiltonian, given by Eq. (1), is

$$E_{n,\sigma}(\mathbf{k}) = E_n + \frac{1}{2m^*} \hbar^2 k^2 + \sigma \sqrt{v_k^2 k^2 + \lambda^2 k^6 \cos^2(3\theta)}, \quad (2)$$

where  $E_{n,\sigma}$  is energy of the  $\sigma$ -th spin subband of the  $n$ -th quantum well state (QWS),  $\theta$  – the azimuth angle of the electron momentum  $\mathbf{k}$  with respect to the  $x$ -axis (sketched on Fig. 1a, where the dispersions of only two lowest spin subbands ( $n = 1, \sigma = \pm 1$ ) are given for clarity). Notice that due to time reversal symmetry the band structure, Eq. (2), is six-fold symmetric with respect to  $\theta \rightarrow \theta + \pi/3$ .

The hexagonal warping model, presented above, is qualitatively confirmed by our first-principles calculations for GaN/AlN HEMT heterostructure, carried out in the DFT framework as implemented in the VASP code [45–47] with spin, v. 5.4.4. The (PAW) [3, 4] generalization of the US-PP [5] and LAPW [6] methods was employed with the Ceperly-Alder parametrization [7] for the xc-potential. Self-consistent calculations were performed with a plane wave cutoff energy of 400 eV. The initial supercell structure of 106 atoms (7 AlN layers and 19 GaN layers passivated by NH) and a vacuum gap was obtained by relaxation of the ionic degrees of freedom of the system, supercell shape and volume were the same as those in the bulk GaN,  $z$ -coordinates of atoms are fixed. The relaxation is stopped when the norms of all Hellmann-Feynman forces on each atom are smaller than  $\text{EDIFFG} = 3 \cdot 10^{-2}$  eV/Å. The energy was found from the variational principle written in terms of the electron density, stopped under the condition that the Helmholtz free energy change between two iteration steps was less than  $\text{EDIFF} = 10^{-6}$  eV. Figure 2 presents the DFT-result for the 2DEG Fermi surface (FS) with an electron density of  $2.5 \cdot 10^{13}$  cm $^{-2}$ , superimposed on the ARPES data [1]. with parameter  $a$  standing for the GaN lattice period in the 2DEG localization plane.

Comparison of the above results with the ARPES data allows one to estimate the Rashba and Dresselhaus constants characterizing the SOI of electrons in the 2DEG of GaN/AlN HEMT heterostructures, while future observation of the 2DEG FS spin texture would definitely clarify the situation further.

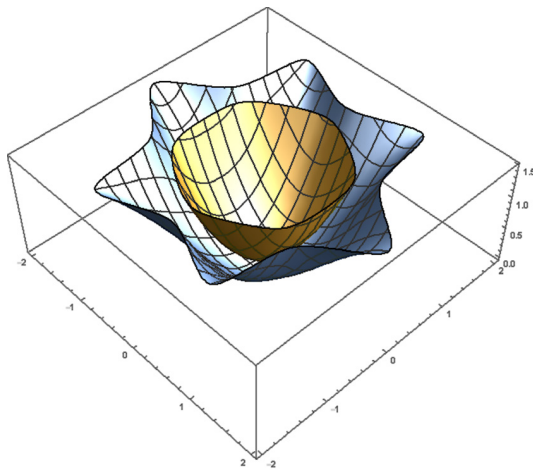


Figure 1. The lowest GaN/AlN 2DEG QWS dispersion with account for SOC.

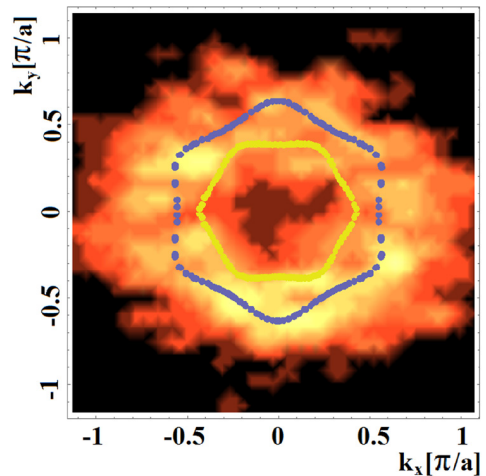


Figure 2. DFT-result for the 2DEG Fermi surface with an electron density of  $2.5 \cdot 10^{13}$  cm $^{-2}$ , superimposed on the ARPES data [1].

*N.K. Chumakov, I.A. Chernykh, I.V. Belov and V.G. Valeyev were partially supported by the Russian Foundation for Basic Research under grant no. 20-07-00813. The work was performed in part with the computing resources of the federal collective usage center “Complex for Simulation and Data Processing for Mega-Science Facilities” (<http://ckp.nrcki.ru>) at the National Research Center Kurchatov Institute.*

1. L.L. Lev et al., Nat. Comm., **9**, article number: 2653 (2018).
2. Liang Fu, Phys. Rev. Lett., **103**, 266801 (2009).
3. P.E. Blochl, Phys. Rev. B, **50**, 17953 (1994).
4. D. Hobbs, G. Kresse and J. Hafner, Phys. Rev. B, **62**, 11 556 (2000).
5. G. Kresse, J. Hafner, J. Phys: Cond. Matt., **6**, 8245 (1994).
6. O.K. Andersen, Phys. Rev. B, **12**, 3060 (1975).
7. D.M. Ceperley, B.J. Alder, Phys. Rev. Lett., **45**, 566 (1980).

## FERROMAGNETISM AND TWO MAGNETIC PHASES IN COBALT ION IMPLANTED RUTILE: EFFECT OF SUBSTRATE TEMPERATURE

*E.M. Begishev*<sup>1\*</sup>, *I.R. Vakhitov*<sup>2</sup>, *N.M. Lyadov*<sup>1</sup>, *V.I. Nuzhdin*<sup>1</sup>, *V.F. Valeev*<sup>1</sup>,  
*V.V. Bazarov*<sup>1</sup>, *D.M. Kuzina*<sup>2</sup>, *R.I. Khaibullin*<sup>1</sup>

<sup>1</sup>Zavoisky Physical-Technical Institute, FRC Kazan Scientific Center of RAS, Kazan, Russia

<sup>2</sup>Kazan Federal University, Kazan, Russia

\*E-mail: [begishev.evg@gmail.com](mailto:begishev.evg@gmail.com)

Titanium dioxide (TiO<sub>2</sub>) with rutile structure is a wide-gap semiconductor ( $E_g = 3$  eV) and diamagnetic. Rutile doped with magnetic impurity of 3d elements is a promising material for spintronics and non-volatile memory applications [1]. Previously [2, 3], we found that two magnetic phases are observed in Co-ion implanted rutile. The first phase was related to the formation of cobalt nanoparticles in the implanted region. The second phase was formed due to the solid solution substitution of Ti<sup>4+</sup> ions by paramagnetic Co<sup>2+</sup> ions. However, the properties of these two magnetic phases had not been studied in detail. In this work we implanted Co ions into rutile plates at different substrate temperatures to obtain the samples where one phase would dominate over the other, and then to determine magnetic parameters of these two phases (magnetization, coercivity, magnetic anisotropy and Curie temperature).

The samples were obtained by implantation with 40 keV Co<sup>+</sup> ions into monocrystalline (100)- and (001)-face oriented plates of rutile (TiO<sub>2</sub>) to the fluence of  $1.5 \cdot 10^{17}$  ions/cm<sup>2</sup> at various substrate temperatures during implantation: 300, 570, 720 and 900 K. In addition, subsequent stepwise annealing of the samples was carried out in air atmosphere in the temperature range 420–720 K and then in high vacuum conditions at 870 K to establish the influence of the annealing on two magnetic phases formation. Magnetic properties of cobalt-implanted rutile were studied by vibrating sample magnetometer (VSM) with a magnetic field sweep 500 mT and differential thermomagnetic analysis (DTMA) in the temperature range 300–1100 K. Magnetic measurements at room temperature were performed after every step of annealing procedure. Magnetic studies were supported by structural measurements: scanning electron microscopy (SEM) and X-ray photoelectron spectroscopy (XPS).

VSM studies have shown that every sample exhibits ferromagnetism at room temperature. Saturation magnetization decreases from 1.5 to  $1.0 \mu_B$ /(Co atom) for (100)-face oriented and from 1.2 to  $0.9 \mu_B$ /(Co atom) for (001)-face oriented plates Co-implanted TiO<sub>2</sub> with increasing implantation temperature. The coercive force first increases until 570 K implantation temperature and then decreases with further increasing implantation temperature. Two components hysteresis loop related two magnetic phases were observed for (100)-face oriented samples implanted at 300 and 570 K temperature (Fig. 1a). Also, Co-implanted TiO<sub>2</sub> plates exhibit magnetocrystalline 2-fold and 4-fold in-plane anisotropy for (100)- and (001)-TiO<sub>2</sub> samples, respectively. However, (001)-TiO<sub>2</sub> implanted with Co at 900 K reveals isotropic magnetic response. All Co-ion implanted samples show out-of-plane shape anisotropy (easy plane) that is typical for thin magnetic films.

DTMA studies have shown that almost all samples exhibit two-phase ferromagnetism, with the exception of (001)-plates implanted at substrate temperatures of 570 or 900 K (Fig. 1b). Ferromagnetism completely disappears after first heating of the sample in air during DTMA measurements as it is clearly demonstrated by second heating DTMA curves. However, temperatures of the observed magnetic-nonmagnetic transitions during DTMA heating differ for samples implanted at different substrate temperatures.

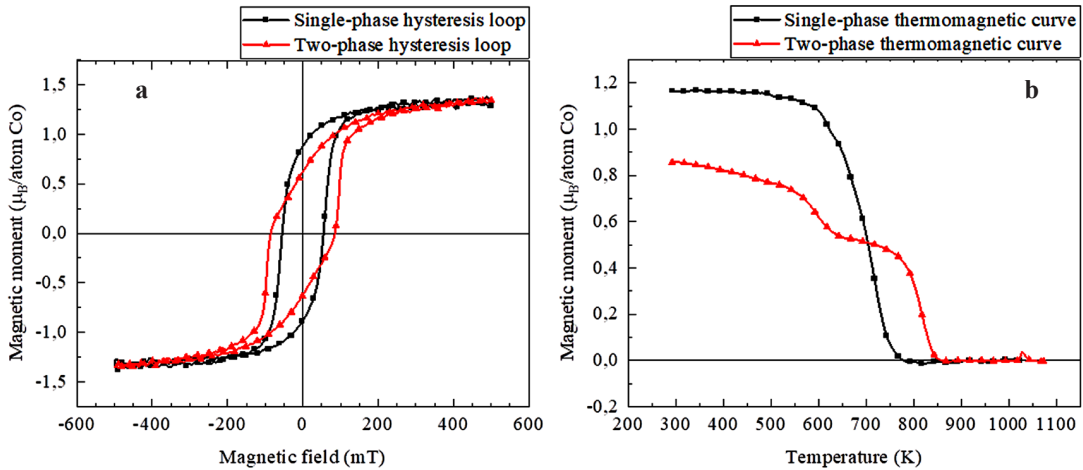


Figure 1. Magnetic studies for Co-implanted rutile plates: **a** dependences of magnetization on the applied external magnetic field and **b** dependences of magnetization on the temperature. The figures show graphs for a single-phase and two-phase magnetic systems.

Gradual decrease in saturation magnetization and anisotropy down to zero values was observed during stepwise annealing in air atmosphere. It is important to note that the repeated reduction annealing of those samples under vacuum conditions leads to the restoration of the isotropic phase in all the studied samples, where ferromagnetism was first suppressed by stepwise annealing in air.

SEM studies have shown that cobalt concentration in surface layer decreases monotonically after annealing procedures. This fact suggests the diffusion of the impurity deep into the plate. XPS studies have shown that cobalt in rutile plates implanted at room temperature is in both metallic and 2+ oxidation states, but it is only in 2+ state after air or vacuum annealing.

We suppose that anisotropic ferromagnetic phase in Co-ion implanted  $\text{TiO}_2$  can be relate to cobalt metal nanoparticles coherently embedded in rutile lattice. On the other hand, isotropic ferromagnetic phase is due to the fact that cobalt in 2+ oxidation state is in  $\text{Ti}^{4+}$  substitution position and is bound by indirect exchange through oxygen vacancies. Implantation at room temperature lead to the growth of metallic cobalt nanoparticles, but implantation at high temperature (900 K) lead to cobalt diffusion deep into rutile structure and to form substitution solid solution. Ferromagnetism disappears during air annealing due to oxidation cobalt nanoparticles and recombination oxygen vacancies by oxygen. In the first case, antiferromagnetic cobalt oxide nanoparticles are formed. In the second case, oxygen from atmosphere or from the depth of rutile plate fills vacancies. That is why indirect exchange disappears and ferromagnetism destroys. After additional vacuum annealing isotropic magnetic phase restores because oxygen atoms leave  $\text{TiO}_2$  crystal matrix and oxygen vacancies are forming again in cobalt implanted region of rutile.

*The study was supported by the Russian Science Foundation (project number 22-19-00712, <https://rscf.ru/project/22-19-00712/>).*

1. U. Diebold, Surf. Sci. Rep., **48**, 53–229 (2003).
2. R.I. Khaibullin, Sh.Z. Ibragimov, L.R. Tagirov, V.N. Popok and I.B. Khaibullin, Nucl. Inst. Meth. Phys. Res. B, **257**, 369–373 (2007).
3. R.I. Khaibullin, L.R. Tagirov, Sh.Z. Ibragimov, V.F. Valeev, V.I. Nuzhdin, Y.N. Osin, A.A. Achkeev, I.A. Faizrahmanov and N.A. Cherkashin, Uchenie zapiski Kazanskogo universiteta **149**, 31–41 (2007) [in Russian].

## FREQUENCY DEPENDENCES OF ELECTRICAL RESISTANCE OF MANGANITES WITH MANGANESE REPLACEMENT BY $(\text{Ni}_{0.5}^{2+}\text{Ge}_{0.5}^{4+})$ COMBINATION

*A.G. Badelin, I.M. Derzhavin\*, V.K. Karpasyuk, E.A. Korneeva, D.I. Merkulov*

Astrakhan State University, Astrakhan, Russia

\*E-mail: [derzh\\_igor@mail.ru](mailto:derzh_igor@mail.ru)

In the present work experimental data are shown for the electrical resistance of manganites with paired substitution of donor and acceptor dopants for manganese depending on frequency and amplitude of electrical measuring field at different temperatures.

Bulk  $\text{La}_{1-c}\text{Sr}_c\text{Mn}_{0.9}(\text{Ni}_{0.5}\text{Ge}_{0.5})_{0.1}\text{O}_3$  manganites ( $c = 0.15\text{--}0.30$ ) were prepared by solid state reactions in air with final sintering step performed at 1473 K. In order to provide stoichiometric oxygen content, the samples were processed at 1223 K and partial pressure of oxygen in the gas phase of  $P_{\text{O}_2} = 10^{-1}$  Pa. Compositions with  $c = 0.15, 0.17, 0.19$  reveal semiconducting type of temperature dependence of dc-resistance at 120–295 K, and the sample with  $c = 0.30$  have “metal-semiconductor” transition point at 270 K.

Figure 1 shows frequency dependences of relative resistance  $R(f)/R_0$  of the samples under various conditions, where  $R(f)$  is the resistance at the frequency  $f$ , and  $R_0$  is dc resistance ( $f = 0$ ) at electrical field strength  $E = 8$  V/cm and corresponding temperature.

At low frequency range ( $f < 0.7$  MHz) at 273 K (Fig. 1a) the plateau is observed in the relative resistance plots. Plateau region extends to higher frequencies with the increase of temperature and electrical field strength (Fig. 1b). As the frequency increases in the studied range, resistance of all samples decreases monotonically. The most significant decline of  $R(f)$  is observed in manganites with strontium content  $c = 0.3$ , and in other samples the values of  $R(f)/R_0$  merge when the frequency is approaching 2.5 MHz (at 273 K, Fig. 1a).

At a temperature of 295 K and a field strength of 16 V/cm, the low-frequency values of  $R(f)/R_0$  are lower than at 273 K and  $E = 8$  V/cm, but the decline of relative resistance with increasing frequency is more gradual.

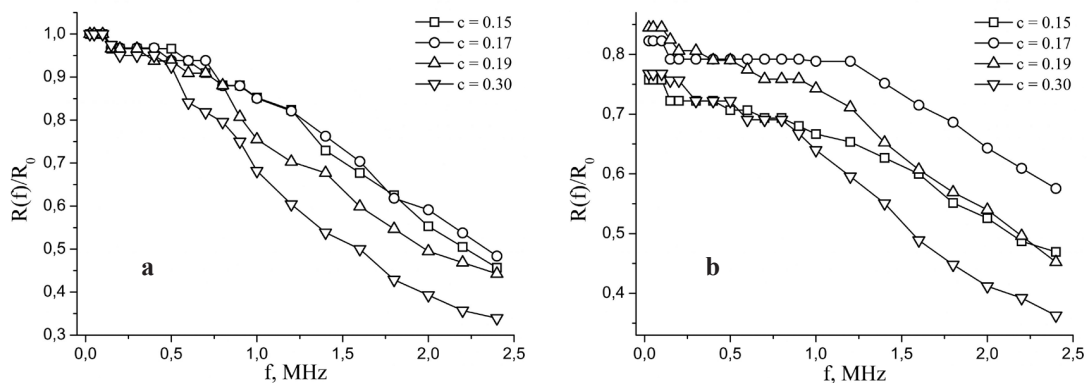


Figure 1. Relative resistance of  $\text{La}_{1-c}\text{Sr}_c\text{Mn}_{0.9}(\text{Ni}_{0.5}\text{Ge}_{0.5})_{0.1}\text{O}_3$  manganites as a function of frequency at various temperatures  $T$  and electrical field strength amplitude  $E$ : **a**  $T = 273$  K,  $E = 8$  V/cm; **b**  $T = 295$  K,  $E = 16$  V/cm.

Possible approach to the interpretation of obtained experimental data is discussed in terms of variable-range-hopping and universal dielectric response models [1, 2].

1. P. Lunkenheimer, F. Mayr and A. Loidl, *Ann. Phys. (Leipzig)*, **15**(7-8), 498–507 (2006).
2. A. Jonscher, *Nature*, **267**, 673–679 (1977).

**DIRECT AND REVERS MAGNETOELECTRIC EFFECT  
 IN NdFe<sub>3</sub>(BO<sub>3</sub>)<sub>4</sub>**

*E.V. Eremin\*, A.L. Freydmann, I.A. Gudim*

Kirensky Institute of Physics, Federal Research Center KSC SB RAS, Krasnoyarsk, Russia

\*E-mail: [eev@iph.krasn.ru](mailto:eev@iph.krasn.ru)

In recent years, the multiferroic materials combining the magnetic and electric orderings have been attracting much attention. The interplay of electric and magnetic subsystems in these materials can result in the giant magnetoelectric effect, which is of great importance for application in micro-electronics, magnetic memory, and sensor engineering, since the problem of mutual transformation of static magnetic and electric fields must now be solved at a new miniature scale.

A magnetoelectric material can exhibit two types of magnetoelectric effect: the direct ME<sub>H</sub> effect, which consists in changing the electric polarization of the sample in an external magnetic field ΔP(H); the reverse ME<sub>E</sub> effect is a change in the magnetic moment of the sample in an external electric field ΔM(E). In the vast majority of cases, the ME<sub>H</sub> effect is experimentally investigated in the works, while the ME<sub>E</sub> effect is insufficiently covered in the literature. This is due to the difficulties associated with the construction of experimental facilities for measuring the ME<sub>E</sub> effect.

In this paper, the dependencies of the study of direct ME<sub>H</sub> (Fig. 1) and reverse ME<sub>E</sub> (Fig. 2) effects are presented.

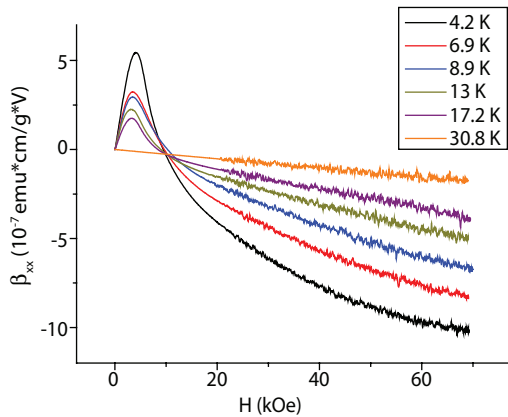


Figure 1. Dependence of the magnetoelectric susceptibility of the longitudinal ME<sub>E</sub> effect.

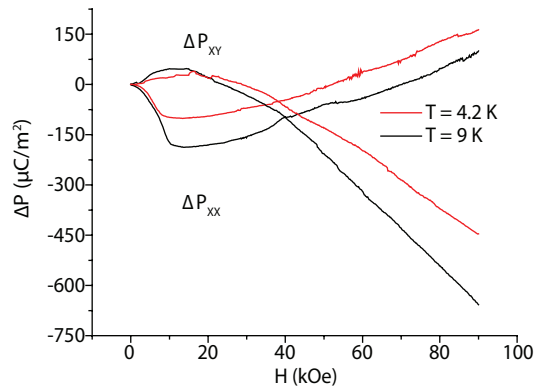


Figure 2. Field dependence of the reverse ME<sub>H</sub> effect.

*Support by RSF-KRFS №22-1220019 is acknowledged.*

## MAGNETIC FIELD SPECTRUM ANALYZER USING MAGNETO-ELECTRIC EFFECT OF FREQUENCY MIXING IN COMPOSITE FERROMAGNET-PIEZOELECTRIC STRUCTURE

*L.Y. Fetisov, D.V. Chashin, D.V. Saveliev, D.A. Burdin, Y.K. Fetisov, F.A. Fedulov\**

Research and Educational Center “Magnetoelectric materials and devices”,  
MIREA – Russian Technological University, Moscow, Russia

\*E-mail: [ostsilograf@ya.ru](mailto:ostsilograf@ya.ru)

Over recent years, much attention has been paid to the development of low-frequency magnetic fields sensors generated by natural and man-made sources [1, 2]. Perspective application areas of magnetic sensors are as follows: the study of the Earth’s magnetic field and fields of moving magnetic objects [3, 4]; measurement of magnetic fields created by industrial machines and household appliances with frequencies up to 100 kHz [5] etc. In this regard, the major issue lies in the development of low-frequency magnetic field spectrum analyzers working in the frequency range up to 100 kHz.

In this paper, we present a low-frequency magnetic field spectrum analyzer of a new type that uses the nonlinear magnetoelectric (ME) effect of magnetic field frequency mixing in a composite resonator containing mechanically coupled ferromagnetic (FM) and piezoelectric (PE) layers.

The suggested ME spectrum analyzer belongs to the swept-tuned analyzers [6]. The key element of the device is an ME frequency-selective mixer, which is tuned in frequency to select the spectral components of measured field in a sequential way [7]. By placing into a measured magnetic field with a spectrum  $h_1(f)$  and an exciting harmonic magnetic field with a frequency  $f_2$ , the mixer generates an output electric voltage  $v$  with frequency  $f_0$ , which corresponds to the resonant frequency of the mixer, only when the frequency synchronism condition is satisfied  $f_1 \pm f_2 = f_0$  (where  $f_1$  is the frequency of the spectrum component of the measured field  $h_1$ ). The frequency of the exciting field is tuned linearly during the measurement.

The mixer represents a three-layer composite FM-PE-FM structure. The PE layer of the structure is made of a Czochralski-grown  $\text{La}_3\text{Ga}_{5.5}\text{Ta}_{0.5}\text{O}_{14}$  (LGT) langatate single crystal (Fomos Materials, Moscow, Russia), with dimensions in the plane of 30 mm×7 mm and thickness  $a_p = 0.5$  mm. The

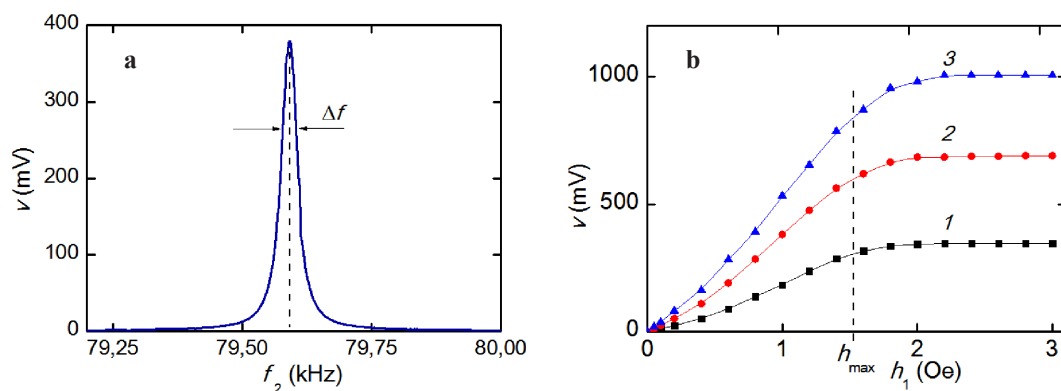


Figure 1. Dependence of the ME voltage  $v$  on the field frequency  $f_2$  at  $h_1 = 0.5$  Oe,  $f_1 = 5$  kHz,  $h_2 = 1$  Oe and  $H = 0$  (a); dependence of the ME voltage  $v$  on the field  $h_1$  at  $f_1 = 20$  kHz,  $f_2 = 64.592$  kHz,  $H = 0$  and different amplitudes of the second field  $h_2$ , Oe: 1 – 0.25, 2 – 0.5, and 3 – 0.75 Oe (b).



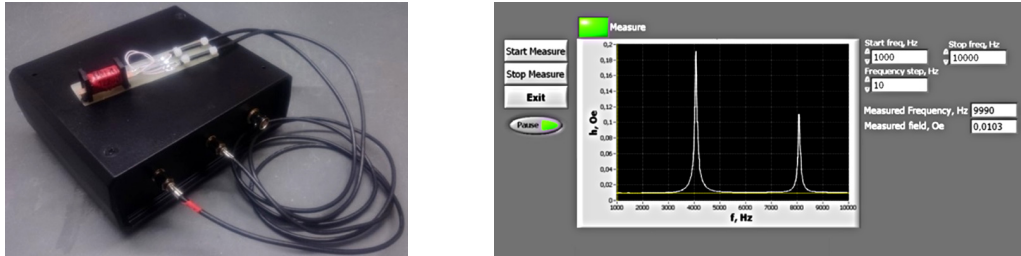


Figure 2. The appearance of the ME magnetic field spectrum analyzer and the user interface of the software for the hardware control and the data acquisition.

FM layers of the structure are made of a ribbon of an amorphous ferromagnetic alloy FeBSiC (Metglas 2605SA1, Metglas Inc., USA) and have dimensions in the plane of 30 mm×7 mm, thickness  $a_m = 25 \mu\text{m}$ , saturation magnetostriction  $\lambda_s \approx 22 \cdot 10^{-6}$  in the saturation field  $H_s \sim 50 \text{ Oe}$ . The layers of the structure are bonded together by soldering.

During the investigations, the linear and nonlinear ME effects of frequency mixing were studied using the standard method of the low-frequency magnetic field modulation [8]. The resonant frequency of the ME mixer is  $f_0 = 84.59 \text{ kHz}$ .

Figure 1a shows the dependence  $v(f_2)$  at a fixed frequency  $f_1 = 5.00 \text{ kHz}$  and an amplitude  $h_1 = 0.5 \text{ Oe}$  of the measured field, sweeping the frequency  $f_2$  of the exciting field with an amplitude  $h_2 = 1 \text{ Oe}$  and  $H = 0$ . One can see the Lorentzian-shaped voltage peak with an amplitude of  $v_m = 310 \text{ mV}$  with  $Q \approx 210$  near the frequency  $f_2 \approx 79.59 \text{ kHz}$ .

Figure 1b shows the dependences of the voltage  $v_m$  generated by the structure upon magnetic field mixing with frequencies  $f_1 = 20 \text{ kHz}$  and  $f_2 \approx 64.59 \text{ kHz}$  on the measured field amplitude  $h_1$  at different amplitudes of the exciting field  $h_2$ . One can see that the dependences are approximately linear in the range of  $h_1$  from zero to  $h_{\text{max}} \approx 1.5 \text{ Oe}$ . With a further increase in  $h_1$ , the output voltage saturates and stops growing. The slope of the  $v(h_1)$  in the linear section increases for all curves with increasing  $h_2$ . Thus, there is a possibility to control the efficiency of the magnetic field mixing process by changing the amplitude of the exciting field.

An appearance of the magnetic field spectrum analyzer are shown in Fig. 2. To demonstrate the operability of the ME analyzer, the frequency spectrum of the lab made magnetic field was measured. The hardware control, data acquisition and display was performed using the LabVIEW software. The lab made field was created using Helmholtz coils connected simultaneously to two oscillators generated currents with frequencies of 4 kHz and 8 kHz of different amplitudes. The measured frequency spectrum of the magnetic field is shown in Fig. 2. It can be seen that the spectrum contains two harmonic components with frequencies of 4 kHz and 8 kHz and amplitudes of 0.19 Oe and 0.1 Oe, respectively.

The analyzer operates in the frequency range of 0.1–85 kHz, has a frequency resolution of  $\sim 44 \text{ Hz}$ , a sensitivity threshold of 50 nT, and a dynamic range of 35 dB. The analyzer can be used to measure the spectra of magnetic fields generated by industrial machines, household appliances, biological objects for contactless diagnostics of their condition.

*This work was supported by the Russian Science Foundation, grant № 19-79-10128.*

1. J. Lenz, S. Edelstein, IEEE Sens. J., **6**, 631–649 (2006).
2. P. Ripka, M. Janosek, IEEE Sens. J., **10**, 1108–1116 (2010).
3. M. Diaz-Michelena, Sensors, **9**, 2271–2288 (2009).

4. C. Li, S. Huang, D. Wei, Y. Zhong, K.Y. Gong, *J. of Engin. Sci. & Techn. Review*, **8**, 105–110 (2015).
5. S. Tofani, L. Anglesio, P. Ossoia, J. d’Amoro, *Bioelectromagnetics*, **16**, 356–364 (1995).
6. S. Louis, O. Sulymenko, V. Tiberkevich, J. Li, D. Aloï, O. Prokopenko, I. Krivorotov, E. Bankowski, T. Meitzler, A. Slavin, *Appl. Phys. Lett.*, **113**, 112401 (2018).
7. D.A. Burdin, D.V. Chashin, N.A. Ekonomov, Y.K. Fetisov, L.Y. Fetisov, *J. Appl. Phys.*, **113**, 033902 (2013).
8. D.A. Burdin, D.V. Chashin, N. A. Ekonomov, L. Y. Fetisov, G. Sreenivasulu, G. Srinivasan, *JMMM*, **358**, 98–104 (2014).

## MAGNETOELECTRIC FREQUENCY DOUBLER

*F.A. Fedulov, D.V. Saveliev, L.Y. Fetisov\**

Scientific and Educational center “Magnetolectric materials and devices”,  
MIREA – Russian Technological University, Moscow, Russia

\*E-mail: [fetisovl@yandex.ru](mailto:fetisovl@yandex.ru)

Nonlinear magnetolectric (ME) effects in layered ferromagnetic-ferroelectric composite structures have been intensively studied in recent years [1, 2]. To date, such effects as the generation of the ME voltage harmonics, frequency doubling, frequency mixing of the generated voltage, etc. have been discovered. These effects are primarily appearing due to the nonlinear dependence of the magnetostriction of the magnetic layer on a constant magnetic field. The interest of this kind of research is due not only to theoretical studies of nonlinear ME phenomena in composite structures, but also from a practical point of view. The interest of this kind of research is due not only to theoretical studies of nonlinear ME phenomena in composite structures, but also because of its promising practical applications in microelectronics and microsystem technology. In particular, recently it has been proposed to use the nonlinear effect to create sensors of a constant magnetic field [3]. It was proposed to increase the sensitivity of ac magnetic fields sensors, based on nonlinear ME effects, which operate at low frequencies, by reducing the  $1/f$  noise in the low-frequency region [4]. In this work, a frequency doubler based on the nonlinear ME frequency doubling effect of the voltage generated by the layered structure is fabricated and studied.

The frequency doubler was implemented on the basis of a three-layer symmetrical Metglas-LGT-Metglas structure. A rectangular plate of single-crystal langatate composition  $\text{La}_3\text{Ga}_{5.5}\text{Ta}_{0.5}\text{O}_{14}$  (FOMOS-Materials, Moscow, Russia) was used as a piezoelectric layer. Metglas 2605SA1 amorphous magnetic alloy ribbon (Metglas Co, USA) was used as material for magnetic layers. The in plane dimensions of the structure were  $30\text{ mm} \times 7\text{ mm}$ . The Metglas and LGT layers thicknesses were 25 and  $500\text{ }\mu\text{m}$ , respectively. Ti-Pt electrodes with the thickness of  $0.5\text{ }\mu\text{m}$  were deposited on the crystal surface by magnetron sputtering. All layers were connected by soldering using Zn50%-Pb32%-Cd18% solder with a melting point of  $145\text{ }^\circ\text{C}$ . In the investigated structure, the linear and nonlinear ME effects were observed using the standard method of the low-frequency magnetic field modulation [1]. The operation of the doubler is based on the nonlinear ME effect of frequency doubling. The piezoelectric layer of the structure generates an alternating ME voltage when the structure is excited by an alternating magnetic field with a half resonant frequency.

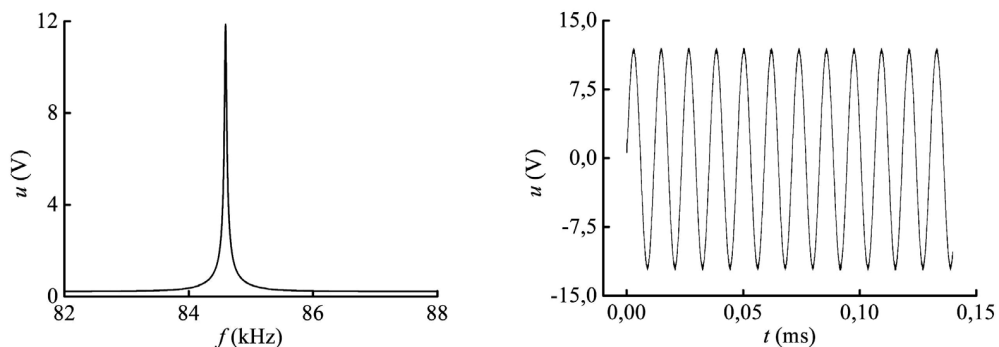


Figure 1. Frequency dependence and oscillogram of the ME voltage in case of a linear ME effect.

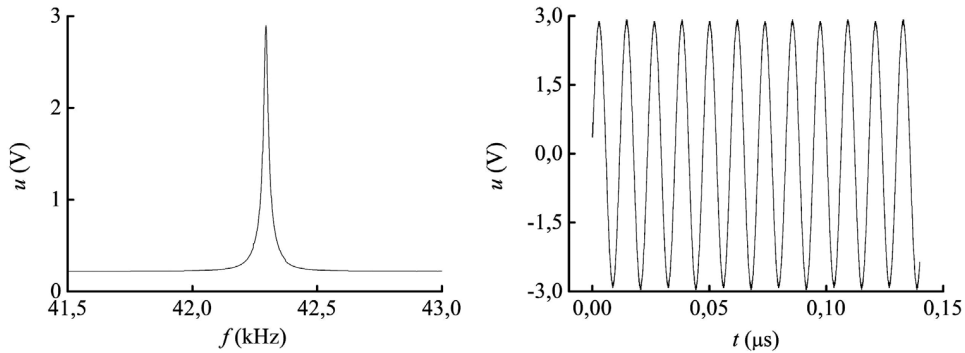


Figure 2. Frequency dependence and oscillogram of the ME voltage in case of a nonlinear ME effect.

Figure 1 shows the frequency dependence of the ME voltage and the oscillogram obtained for the structure when measuring the linear ME effect. The resonant frequency of the structure was  $f = 84.592$  kHz. The linear ME effect was measured in a constant field of  $H = 5$  Oe and at an excitation alternating magnetic field amplitude  $h = 2.15$  Oe. The ME coefficient value at the resonant frequency was  $\alpha \approx 110.4$  V/(Oe cm). The quality factor of the structure resonance was  $Q \approx 2563$ .

Figure 2 shows the frequency dependence of the ME voltage and the oscillogram obtained for the structure when observing the nonlinear doubling effect. The frequency dependence shows a maximum at the frequency  $f = f_r/2 = 42.296$  kHz. The frequency dependences of the ME voltage of the structure were measured in a field  $H = 2$  Oe and at  $h = 2.75$  Oe. The ME coefficient value at the resonant frequency for this structure in the nonlinear regime was  $\alpha \approx 5.4$  V/(Oe<sup>2</sup> cm). The quality factor of this resonance was  $Q \approx 2820$ .

The load characteristics of the frequency doubler were also measured. The load resistance  $R$  was connected in parallel with the doubler. It follows from the measured dependences of the output power  $P_{out}$  and efficiency  $\eta$  on the load resistance  $R$  that with an increase in the load resistance from 1 to 1000 k $\Omega$ , both the output power and the efficiency decrease. The maximum output power of 0.07 mW achieved at load resistance 1 k $\Omega$ , and the efficiency was 0.6%. Both values at 1000 k $\Omega$  decreased almost to 0.

Thus, a frequency doubler based on the nonlinear ME doubling effect in the Metglas-LGT-Metglas structure was fabricated and studied. The maximum output power of this doubler was 0.07 mW, and the efficiency was 0.6%.

It is possible to increase the efficiency of the doubler by manufacturing higher quality ME structures, which will have a higher quality factor at resonance, which will make it possible to increase the efficiency of the structure by an order of magnitude. In addition, the use of film technologies will lead to a significant increase in the ME coefficient, which will also improve the characteristics of the doubler.

*This work was supported by the Russian Science Foundation, grant number 19-79-10128.*

1. D.A. Burdin, D.V. Chashin, N.A. Ekonomov, L.Y. Fetisov, G. Sreenivasulu, G. Srinivasan, *JMMM*, **358**, 98–104 (2014).
2. D.A. Burdin, D.V. Chashin, N.A. Ekonomov, L.Y. Fetisov, G. Sreenivasulu, G. Srinivasan, *J. Appl. Phys.*, **113**, 033902 (2013).
3. D.A. Burdin, D.V. Chashin, N.A. Ekonomov, L.Y. Fetisov, Y.K. Fetisov, M. Shamonin, *J. Phys. D: Appl. Phys.*, **49**, 375002 (2016).
4. J. Petrie, D. Viehland, D. Gray, S. Mandal, G. Sreenivasulu, G. Srinivasan, A.S. Edelstein, *J. Appl. Phys.*, **110**, 124506 (2011).

## THE INFLUENCE OF RARE EARTH ION SUBSTITUTION ON MAGNETOELECTRIC PROPERTIES IN ORTHORHOMBIC SINGLE CRYSTALS $\text{Dy}_{1-x}\text{Ho}_x\text{MnO}_3$

*I.N. Horoshiy<sup>1,2</sup>, M.I. Kolkov<sup>1</sup>, K.Yu. Terent'ev<sup>1</sup>, A.L. Freydmann<sup>1,2\*</sup>*

<sup>1</sup>Kirensky Institute of Physics, Federal Research Center KSC SB RAS, Krasnoyarsk, Russia

<sup>2</sup>Institute of Engineering Physics and Radio Electronics, Siberian Federal University, Krasnoyarsk, Russia

\*E-mail: [fss4@yandex.ru](mailto:fss4@yandex.ru)

The topic of multiferroism is one of the most discussed, since it opens up the possibility of implementing many new spintronic devices. Among the known multiferroics, orthorhombic compounds  $\text{RMnO}_3$ , in which the magnetic properties depend on the rare-earth ion, attract much attention. In orthorhombic single crystals with  $R = \text{Gd}, \text{Tb}, \text{Dy}$ , a magnetoelectric effect is observed, and a magnetoelectric response has been reported in conjunction with  $R = \text{Ho}$ ; however, measurements have been performed on polycrystalline samples. Furthermore, the magnetic ordering in  $\text{DyMnO}_3$  and  $\text{HoMnO}_3$  is different, the spin cycloid and the E-type antiferromagnetic ordering, respectively. The latter means that the transition compositions  $\text{Dy}_{1-x}\text{Ho}_x\text{MnO}_3$  open up great prospects for studying the magnetoelectric effect, since they are a connecting bridge between two types of magnetic ordering. In this work, we focused on the evolution of the magnetoelectric response as  $\text{Dy}^{3+}$  ions are replaced by  $\text{Ho}^{3+}$  ions in  $\text{Dy}_{1-x}\text{Ho}_x\text{MnO}_3$  single crystals with  $x = 0-0.4$ .

Figure 1a shows the relative permittivity  $\epsilon_a$  as a function of the applied magnetic field  $H_b$ . Obvious anomalies are observed for  $\text{Dy}_{1-x}\text{Ho}_x\text{MnO}_3$  compounds with substitution values  $x = 0.2$  and  $0.3$ , for  $x = 0.4$ , the anomaly is almost not noticeable, for  $x = 0$ , the data can be found in [1]. As the substitution  $x$  in the compound increases, the magnetic field leading to the reorientation of the polarization vector increases. At  $x = 0$ ,  $H_c \sim 13$  kOe ( $T = 2$  K) [1], for  $x = 0.2, 0.3$ , the field at which the anomaly is observed is  $H_c \sim 19, 22$  kOe ( $T = 4.2$  K), respectively. For  $x = 0.4$ , the field  $H_c$  is also about 22 kOe. The plots of the  $\epsilon_a(H_b)$  dependence also clearly show hysteresis, which is related to the sequence of  $P_c \rightarrow P_a \rightarrow P_c$  transitions. The arrows in the figure show the direction of the field change. The permittivity anomalies correspond to a transition consisting in the overturning of the plane of the cycloid of  $\text{Mn}^{3+}$  ion spins from  $bc$  to  $ba$  with a simultaneous rotation of the spontaneous polarization vector  $P_c \rightarrow P_a$ .

Figure 1b shows the dependences of the electric polarization on the external magnetic field  $H_b$ . Some of the above data were already published by us earlier [2] for a pure  $\text{DyMnO}_3$  crystal; in this work, we supplement them and present a more complete picture with the substitution of Dy for Ho. As can be seen from the dependences  $P(H)$ , as the substitution  $x$  increases, the polarization decreases, and the magnetic field of the  $P_c \rightarrow P_a$  transition also increases. In general, it can be argued that the polarization plots are in complete agreement with the dependences  $\epsilon(H)$ .

In general, it can be concluded that the substitution of  $\text{Ho}^{3+}$  for  $\text{Dy}^{3+}$  ions has a suppressive effect on the magnetoelectric effect in this compound. As the substitution  $x$  increases, a decrease in the polarization  $P_a$  is observed, a decrease in the susceptibility of the inverse magnetoelectric effect  $\alpha_{ba}$ , in addition, the field  $H_b$  increases, at which the  $P_c \rightarrow P_a$  transition is observed, and the temperature range of existence of the magnetoelectric response decreases.

The measurement results also indicate that the applied electric field is capable of prolonging the  $P_a$  state and, consequently, the magnetic state with the cycloid lying in the  $ab$ -plane. Also, the data obtained indicate the possible presence of nonlinear effects associated with the electric field dependence of the susceptibility of the linear term of the magnetoelectric effect.

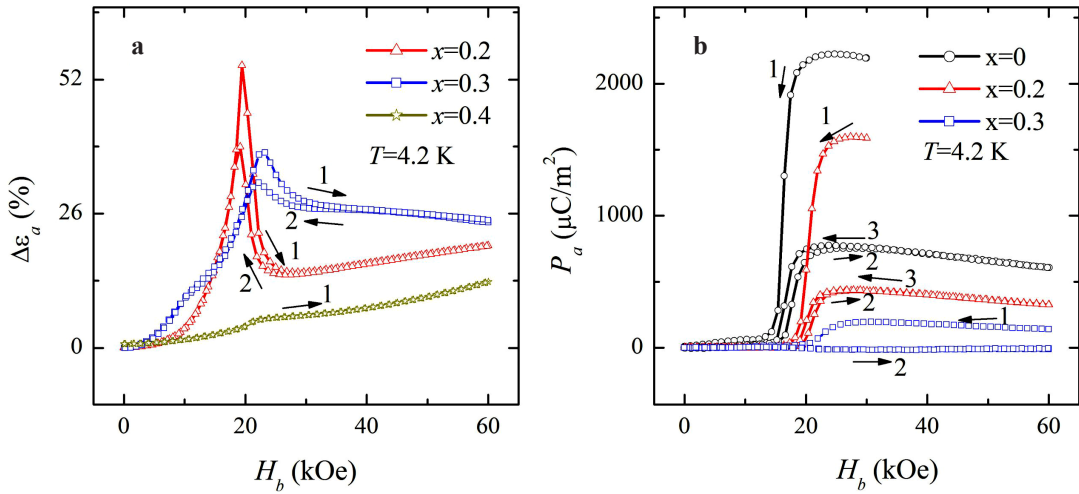


Figure 1. Dependence of the relative change in permittivity  $\epsilon_a$  (a) and polarization  $P_a$  (b) on the external magnetic field  $H_b$  for different  $\text{Dy}_{1-x}\text{Ho}_x\text{MnO}_3$  compositions ( $x = 0-0.4$ ) at a temperature  $T = 4.2$  K.

This work was supported by Russian Foundation for Basic Research, Government of Krasnoyarsk Territory, Krasnoyarsk Regional Fund of Science to the research project number 20-42-243008.

1. T. Kimura, G. Lawes, T. Goto, Y. Tokura, A.P. Ramirez, Phys. Rev. B, **71**, 224425 (2005).
2. A.L. Freidman, S.V. Semenov, M.I. Kolkov, K.Yu. Terent'ev, N.S. Pavlovskiy, D.M. Gokhfeld, K.A. Shaykhutdinov, D.A. Balaev, J. Appl. Phys., **128**, 094102 (2020).

## MAGNETIC PROPERTIES OF TWIN TRIGONAL OXIBORATE WITH HUNTITE STRUCTURE. EFFECT OF ANNEALING

*I.A. Gudim*<sup>1\*</sup>, *E.V. Eremin*<sup>1</sup>, *V.R. Kuchesheva-Titova*<sup>1,2</sup>

<sup>1</sup>Kirensky Institute of Physics, Krasnoyarsk, Russia

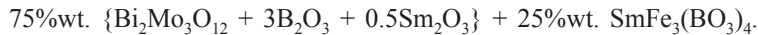
<sup>2</sup>Siberian Federal University, Krasnoyarsk, Russia

\*E-mail: [irinagudim@mail.ru](mailto:irinagudim@mail.ru)

Recently, multiferroic crystals have attracted great interest due to the ability to control the electrical properties of a crystal using a magnetic field and/or temperature and *vice versa*. Single crystals of trigonal oxyborates (RM<sub>3</sub>(BO<sub>3</sub>)<sub>4</sub> (R – rare-earth element, M = Al, Ga, Sc, Fe) with the huntite structure are multiferroics. They have the space group R32 [1]. This structure is characterized by the presence of helicoidal chains M-ions along the trigonal axis of the crystal. These chains can rotate both to the right and to the left. X-ray measurements have shown that the ratio of left and right chains, even in one crystal, can vary in different parts of the crystal.

Consider the effect of twinning and the possibility of changing it using the example of SmFe<sub>3</sub>(BO<sub>3</sub>)<sub>4</sub>.

The crystals were grown by the group method (several crystals grew simultaneously under the same conditions) from melt solutions based on bismuth trimolybdate [2]. A solution-melt system for growing single crystals can be represented in a quasi-binary form



The saturation temperatures of such solutions-melts were 960±10 °C.

The magnetoelectric effect for the left and right chains have opposite signs (Fig. 1) and are subtracted as a result. Table 1 shows the ratios of the left and right chains (*F*, %rt.) for different crystals of the same composition and the corresponding magnetoelectric polarization.

It was shown in our works [3, 4] that twinning can be different even in separate parts of the crystal. The traditional method of dealing with crystal imperfections is annealing. Therefore, we annealed several crystals at a temperature of 950 °C for 10 hours, followed by slow cooling. The results are shown in Table 2.

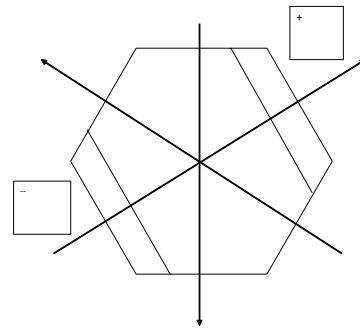


Figure 1. Dependence of the sign of the induced electric polarization on the sample faces relative to the direction of the polar axis in it.

Table 1. Dependence of the magnetoelectric polarization vs *F*(rt).

Composition of crystals	<i>R/r</i>	<i>F</i> , %rt.	<i>P<sub>a</sub></i> ( <i>H<sub>b</sub></i> ), mK/M <sup>2</sup>	<i>P<sub>max</sub></i> , recalculation for 100%
SmFe <sub>3</sub> (BO <sub>3</sub> ) <sub>4</sub>	1.485	17	98	600
SmFe <sub>3</sub> (BO <sub>3</sub> ) <sub>4</sub>	1.485	100	500(10 Oe)	500
SmFe <sub>3</sub> (BO <sub>3</sub> ) <sub>4</sub>	1.485	100	492(10 Oe)	
SmFe <sub>3</sub> (BO <sub>3</sub> ) <sub>4</sub>	1.485	34	154	452
SmFe <sub>3</sub> (BO <sub>3</sub> ) <sub>4</sub>	1.485	0	495	

Table 2. Change in twinning after annealing.

Composition of crystals	$F$ , %rt., initial	$F$ , %rt., result
$\text{SmFe}_3(\text{BO}_3)_4$	17	68
$\text{SmFe}_3(\text{BO}_3)_4$	100	100
$\text{SmFe}_3(\text{BO}_3)_4$	100	59 !
$\text{SmFe}_3(\text{BO}_3)_4$	34	100

As can be seen from the table, the results of annealing are ambiguous. In one case, the ratio of left and right spirals improved, in the other it worsened or remained unchanged.

Crystal annealing can be recommended only in the case of the worst results in the measurement of integral twinning.

*The work on this study was supported by RSF-KRFS No. 22-12-20019.*

1. A.D. Mills, Inorg. Chem. **1**, 960 (1960).
2. I.A. Gudim, E.V. Eremin and V.L. Temerov, J. Cryst. Growth, **312**, 2427–2430 (2010).
3. E. Eremin, I. Gudim, V. Temerov, D. Smolyakov, M. Molokeyev, J. Cryst. Growth, **518**, 1 (2019).
4. M.S. Platunov, I.A. Gudim, E.N. Ovchinnikova et al., Crystals, **11**(1), 1050531 (2021).



THE PHENOMENON OF MAGNETIC COMPENSATION  
IN THE MULTICOMPONENT (Sm, Gd, Y)Fe<sub>2</sub> COMPOUNDS

*M.R. Khomenko*<sup>\*</sup>, *N.Yu. Pankratov*<sup>1</sup>, *Z.S. Umhaeva*<sup>2,3</sup>, *I.M. Aliev*<sup>2,3</sup>,  
*A.Yu. Karpenkov*<sup>4</sup>, *I.S. Tereshina*<sup>1</sup>

<sup>1</sup>Faculty of Physics, Lomonosov Moscow State University, Moscow, Russia

<sup>2</sup>Complex Research Institute named after Kh. I. Ibragimov, Russian Academy of Sciences, Grozny, Russia

<sup>3</sup>Faculty of Physics, Chechen State University, Grozny, Russia

<sup>4</sup>Department of Condensed Matter Physics, Tver State University, Tver, Russia

\*E-mail: [khomenko.mr17@physics.msu.ru](mailto:khomenko.mr17@physics.msu.ru)

The compounds of rare earth (RE) and 3d-transition metals form a comprehensive class of materials widely known in science and technology due to their unique physical properties. Intermetallic compounds RFe<sub>2</sub> (R – RE ion), having the structure of Laves phases C15, demonstrate high Curie temperatures and large magnetostriction in a wide temperature range. Binary compounds SmFe<sub>2</sub> and TbFe<sub>2</sub> have the highest values of saturation magnetostriction at room temperature ( $\lambda_s = -1.5 \cdot 10^{-3}$  and  $1.7 \cdot 10^{-3}$ , respectively) [1]. It is well known that in R-Fe intermetallics the magnetic moment of light RE atoms is collinear to the magnetic moment of the iron sublattice. The magnetic moment of heavy RE on the contrary is antiparallel to the moment of the iron sublattice.

The phenomenon of magnetic compensation in the multisublattice rare earth (R) ferrimagnets consists in mutual cancellation of magnetic moments of individual sublattices so the resulting net magnetic moment is zero. The principal factors for observing this effect are the chemical composition of the compounds and the temperature. The composition and temperature at which the compensation effect occurs is called the compensated composition and the compensation temperature, respectively. This phenomenon is of great practical importance: by varying the concentrations of substitution atoms near the compensated composition, it is possible to change the value of spontaneous magnetization in a controllable way. The study of fundamental properties of new ferrimagnetic materials demonstrating magnetic compensation is essential for the determination of their functional characteristics. Thus, at a certain ratio of concentrations of heavy and light rare earth elements, the phenomenon of complete magnetic compensation is possible, as, for example, in the system (Tb, Y, Sm)Fe<sub>2</sub> [2]. By diluting the rare-earth sublattice with non-magnetic atoms (Y, Lu or La) the magnetic moments of the sublattices could be compensated. In order to observe this phenomenon and possibly to control it.

The structural and magnetostrictive characteristics of SmFe<sub>2</sub> and Sm<sub>0.2</sub>Y<sub>0.8</sub>Fe<sub>2</sub> compounds have been investigated yearly [3]. The magnetic moments of Sm and Gd ions are oppositely directed and a phenomenon of magnetic compensation is possible. Moreover, two spin-reorientation transitions are found in SmFe<sub>2</sub>, as well as in Sm<sub>0.2</sub>Y<sub>0.8</sub>Fe<sub>2</sub> [3]. The aim of the work was to investigate the structural and magnetic properties of the Sm<sub>0.2</sub>(Gd, Y)<sub>0.8</sub>Fe<sub>2</sub>, where gadolinium is partially replaced by non-magnetic yttrium, as well as to find magnetic compensation point depending on temperature and concentration of Y.

Sm<sub>0.2</sub>(Gd<sub>1-x</sub>Y<sub>x</sub>)<sub>0.8</sub>Fe<sub>2</sub> alloys ( $x = 0, 0.2, 0.4, 0.6, 0.8, \text{ and } 1$ ) were obtained by high-frequency induction melting in an atmosphere of pure argon, after that the ingots were subjected to homogenizing annealing for 2 weeks [4]. Rietveld analysis showed that the alloys in this system have a cubic structure of the Laves phase C15 and contain no more than 5% of RFe<sub>3</sub> phase (with a crystal structure of the PuNi<sub>3</sub> type). The magnetization was studied in the temperature range 80–340 K in fields up to 18 kOe by using the induction magnetometer (MagEQ) and in range 300–700 K in a field up to 5 kOe on the pendulum magnetometer.

According to our data, in compounds  $\text{Sm}_{0.2}(\text{Gd}, \text{Y})_{0.8}\text{Fe}_2$ , with an increase in the concentration of Y, the cubic lattice parameter decreases linearly, because the metallic radius of Y is smaller than metallic radiuses of Sm and Gd. The Curie temperatures were obtained from the results of thermomagnetic analysis. TC also decreases linearly with an increase in the concentration of Y. The Curie temperatures of  $\text{RFe}_2$  are defined primarily by the Fe-Fe exchange, and also by contribution of the inter-sublattice R-Fe interaction. Dilution of the rare-earth sublattice of  $\text{Sm}_{0.2}\text{Gd}_{0.8}\text{Fe}_2$  by yttrium leads to a monotonious decrease of  $T_C$  with the Y concentration increase due to decreasing R-Fe exchange interaction.

The magnetic structure of  $\text{Sm}_{0.2}(\text{Gd}_{1-x}\text{Y}_x)_{0.8}\text{Fe}_2$  compounds can be considered in the model of three sublattices Sm, Gd and Fe, whose magnetic moments are oriented collinearly. The magnetic moment on atoms of heavy rare-earth Gd is  $\mu_{\text{Gd}} = 7\mu_{\text{B}}/\text{ion}$  and is ordered antiparallel to the magnetic moment of iron, while the magnetic moment on atoms of Sm is  $\mu_{\text{Sm}} = 0.7\mu_{\text{B}}/\text{ion}$  and is ordered parallel to the magnetic moment of iron. Diluting a rare-earth sublattice with non-magnetic Y, one can observe the phenomenon of magnetic compensation and determine the compensation composition. The theoretical calculations were carried out in the model of collinear moments of three sublattices (Sm, Gd and Fe) without accounting thermal fluctuations. The magnitude of the total magnetic moment is determined by the equation:

$$\mu_{\text{calc}} = 2\mu_{\text{Fe}} + 0.2\mu_{\text{Sm}} - 0.8(1 - x)\mu_{\text{Gd}}, \quad (1)$$

where  $\mu_{\text{Fe}} = 1.45\mu_{\text{B}}/\text{Fe}$  is the magnetic moment in the Fe ion determined from the magnetization of  $\text{YFe}_2$ . According to this calculation, the value of Y concentration in the compensation composition, where  $\mu_{\text{calc}} = 0$ , is near  $x \approx 0.46$ .

The temperature dependencies of magnetization for  $\text{Sm}_{0.2}(\text{Gd}_{1-x}\text{Y}_x)_{0.8}\text{Fe}_2$  compositions with  $x = 0, 0.2, 0.4, 0.8$  show a minimum in temperature range 200–300 K, corresponding to the points of the magnetic compensation. For the composition with  $x = 0.6$  the  $M(T)$  curve on the contrary demonstrates a maximum near 400 K.  $\text{Sm}_{0.2}\text{Gd}_{0.8}\text{Fe}_2$  has a temperature dependence of magnetization with monotonically decrease till  $T_C$ .  $\text{Sm}_{0.2}\text{Y}_{0.8}\text{Fe}_2$  shows a ferromagnetic behavior of magnetization.

Apparently, in the  $\text{Sm}_{0.2}(\text{Gd}_{1-x}\text{Y}_x)_{0.8}\text{Fe}_2$  with  $x < 0.46$  the rare-earth sublattice magnetic moment exceeds the Fe-sublattice moment in the low-temperature region and such compound can be considered as a ferrimagnet with a “weak” magnetic sublattice according to Neel’s classification. Since the R and Fe sublattices’ magnetization  $M_{\text{R}}$  and  $M_{\text{Fe}}$  depend differently on the temperature, and  $M_{\text{R}}$  declines faster than  $M_{\text{Fe}}$  with the temperature increase, their compensation takes place at 300, 240 and 280 K, for  $x = 0, 0.2,$  and  $0.4,$  respectively. For the compound with  $x = 0.6$ , the minimum on the  $M(T)$  curve should be occur near temperature of absolute zero. The anomaly of magnetization at 175 K in low field  $H \sim 200$  Oe was found in  $\text{Sm}_{0.2}\text{Y}_{0.8}\text{Fe}_2$  and in  $\text{Sm}_{0.2}(\text{Gd}_{1-x}\text{Y}_x)_{0.8}\text{Fe}_2$ . These anomalies of magnetization behavior are due to magneto-structural deformations caused by spin-reorientation transition.

This studies demonstrate that substitution of Gd by Y atoms is efficient tool to vary the strength of the R-Fe exchange coupling in case of multicomponent  $\text{RFe}_2$ -type compounds. The structure and magnetic properties of the  $\text{Sm}_{0.2}(\text{Gd}_{1-x}\text{Y}_x)_{0.8}\text{Fe}_2$  intermetallic compounds were compared with the same properties of the  $\text{SmFe}_2$  compound. It was found that the spin-reorientation transitions demonstrated by  $\text{SmFe}_2$ , is preserved within substitution Sm by Gd and Y. We observed the decrease in the temperatures corresponding to the onset and the end of the transition region with the simultaneous appearance of magnetic compensation temperature near room temperature.

*The research was carried out at the expense of the grant of the Russian Science Foundation № 22-22-00313, <https://rscf.ru/project/22-22-00313/>.*

1. X. Liu, K. Lin, Q. Gao et al., *Inorg. Chem.*, **57**(2), 689–694 (2017).
2. A.S. Ilyushin, I.S. Tereshina, N.Yu. Pankratov et al., *J. Alloys Comp.*, **847**, 155976–156001 (2020).
3. N.Yu. Pankratov, I.S. Tereshina, G.A. Politova et al., *J. Magn. Magn. Matter.*, **521**, 167728–167753 (2021).
4. I.S. Tereshina, D.I. Gorbunov, A.Yu. Karpenkov et al., *IEEE Magn. Lett.*, **13**, 2504605 (2022).

## MAGNETOELECTRIC EFFECT IN YIG-GGG-PZT STRUCTURE

*K.V. Lambrianidi\**, *D.A. Burdin*, *Y.K. Fetisov*, *N.A. Ekonomov*, *D.V. Chashin*

<sup>1</sup>The Institute for Advanced Technologies and Industrial Programming  
MIREA – Russian technological university, Moscow, Russia

\*E-mail: [k.v.lambrianidi@gmail.com](mailto:k.v.lambrianidi@gmail.com)

The magnetoelectric (ME) effect in composite structures containing magnetostrictive (MS) and piezoelectric (PE) layers results from the combination of magnetostriction and piezoelectricity due to mechanical coupling of the layers [1]. The ME-effect is used to create various devices, such as magnetic field sensors, controlled inductors, memory elements, and others. MS-layers for ME-structures are usually made of polycrystalline alloys or amorphous ferromagnetic alloys. However, these materials have high eddy current losses, low acoustic quality factor, and a high level of magnetization reversal noise [2], which limits the frequency range and sensitivity of ME-devices. To overcome the above drawbacks, single-crystal yttrium iron garnet (YIG) films can be used as the MS layer of the structure. YIG-films demonstrate low levels of conductivity and magnetic losses, as well as low excessive magnetization reversal noise, and at the same time have noticeable magnetostriction [3]. This work is devoted to the experimental study of the ME-effect in the YIG-PZT structure.

A structure (Fig. 1) was made of  $Y_3Fe_5O_{12}$  (YIG) layer, 20  $\mu\text{m}$  thick, on a  $Ga_3Gd_5O_{12}$  (GGG) substrate, 500  $\mu\text{m}$  thick, and a plate of PZT-46 piezoceramic with a thickness  $d = 230 \mu\text{m}$  and in-plane dimensions 5 mm×28 mm. The PZT-plate with electrodes was polarized perpendicular to its plane. The YIG-film and the PZT-plate were connected under the press with cyanoacrylate adhesive. The direct ME-effect was studied by the method of harmonic modulation of the magnetic field. The sample was fixed at one end and placed in a coil with a 9 mm×19 mm cross section and an 18 mm length, containing 10 turns. The coil was powered by an Agilent 33210a generator, creating an exciting magnetic field  $h\cos(2\pi ft)$  with an amplitude up to  $h = 5$  Oe and a frequency  $f = 0\text{--}100$  kHz. At the same time, a constant magnetic field  $H = 0\text{--}100$  Oe was applied along the long side of the structure using Helmholtz coil. The voltage  $u$  generated between the electrodes of the PZT-layer was recorded with an SR-770 spectrum analyzer.

Figure 2 shows the dependence of the ME voltage  $u$  on the excitation field frequency  $f$  at  $h = 0.4$  Oe and  $H = 9$  Oe. The maximum values of  $u_1 = 1$  mV and  $u_2 = 2.5$  mV near the frequencies  $f_1 = 4.9$  kHz and  $f_2 = 92$  kHz respectively correspond to the excitation of the main mode of flexural and longitudinal acoustic oscillations in the structure. The values of the resonance ME coefficient were  $\alpha_E(f_1) = u_{me}/dh = 170$  mV/(cm·Oe) and  $\alpha_E(f_2) = 400$  mV/(cm·Oe).

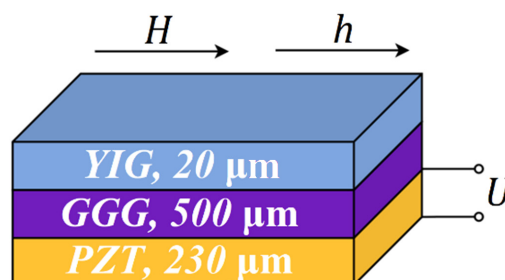


Figure 1. A schematic representation of the ME structure.

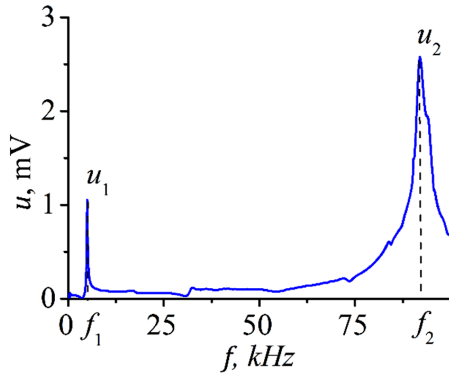


Figure 2. The dependence of the voltage  $u$  generated by the PE layer of the structure on the frequency of the alternating magnetic field at  $h = 0.4$  Oe,  $H = 9$  Oe.

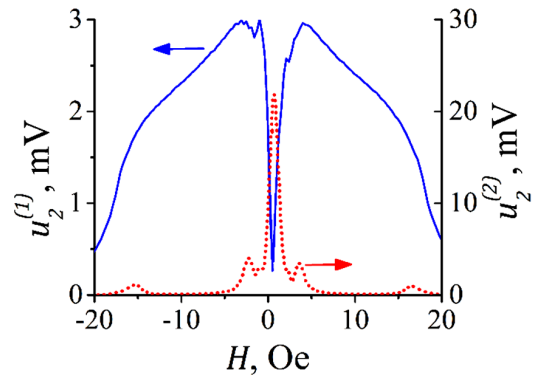


Figure 3. The dependence of the ME voltage on the bias field  $H$  at the longitudinal resonance frequency  $f_2$  and  $h = 0.4$  Oe: curve 1 (blue)  $f = f_2$ , curve 2 (red)  $f = f_2/2$ .

Curve 1 (blue) in Fig. 3 shows the dependence  $u_2^{(1)}(H)$  of the ME-voltage  $u_2$  on the constant field  $H$  at  $h = 0.4$  Oe and excitation frequency  $f_2$ . It can be seen that  $u_2^{(1)} = 0$  at  $H = 0$ , then monotonically increases with increasing field, reaching a maximum of  $u_2^{(1)} = 3$  mV at  $H_m \approx 4$  Oe. As the field increases further,  $u_2^{(1)}$  monotonically decreases and vanishes at  $H \approx 40$  Oe.

The frequency spectrum of the ME-voltage contained a large number of harmonics, which indicates the nonlinearity of the ME-effect. Curve 2 (red) in Fig. 3 demonstrates the field dependence of the voltage  $u_2^{(2)} = u(f_2)$  generated by the PE layer of the structure at frequency  $f_2$  when excited by a field with frequency  $f = f_2/2$  (frequency doubling effect [4]). The curve has the form characteristic of the field dependence of the nonlinear piezomagnetic coefficient  $q(H) = \delta\lambda/\delta H$ :  $u_2^{(2)}$  is maximal at  $H = 0$ , vanishes at the  $H_m$  field, then reaches the maximum again and drops to zero with a further increase in  $H$ .

Thus, the direct low-frequency ME-effect in a composite layered structure containing a YIG film and a PZT piezoceramic plate was discovered and studied for the first time. At the acoustic resonance frequency, the ME coefficient  $\alpha_E = 0.4$  V/(cm·Oe) was achieved at a constant magnetic bias field  $H = 4$  Oe. A nonlinear ME-effect of second harmonic generation was found in the structure. The results we obtained can be used to design new ME-devices.

*This work was supported by Russian Science Foundation, project № 22-29-01093.*

1. Z. Chu, M. J. PourhosseiniAsl, S. Dong, J. Physics D: Appl. Phys., **51**, 243001 (2018).
2. J. Zhai, Z. Xing, S. Dong, J. Li, D. Viehland, J. Am. Ceram. Soc., **91**(2), 351–358 (2008).
3. A. Nakamura, Y. Sugiura, J. Phys. Sic. Japan, **15**, 1704 (1960).
4. D.A. Burdin, D.V. Chashin, N.A. Ekonomov et al., JMMM, **358-359**, 98–104 (2014).

## INFLUENCE OF SPACERS AND NANOSTRUCTURING ON THE MAGNETOELECTRIC PROPERTIES OF METAL/PVDF FILM COMPOSITES

*K.G. Balymov<sup>1\*</sup>, E.V. Kudyukov<sup>1</sup>, A.A. Feshenko<sup>1</sup>, M.A. Kalinin<sup>1</sup>, V.O. Vas'kovskiy<sup>1,2</sup>*

<sup>1</sup>Ural Federal University, Ekaterinburg, Russia

<sup>2</sup>Institute of Metal Physics, Ural Branch of Russian Academy of Sciences, Ekaterinburg, Russia

\*E-mail: [k.g.balymov@urfu.ru](mailto:k.g.balymov@urfu.ru)

Composite multiferroics with a magnetoelectric effect continue to arouse the interest of researchers and developers of technical devices. One of the promising objects for practical applications are film structures of the Metal/Polymer-type, where polyvinylidene fluoride (PVDF) can act as a ferroelectric polymer medium [1], in which the formation of a ferroelectric  $\beta$ -phase is achieved by spin-coating. The metal layers of such composites can be metals and alloys characterized by a high value of magnetostriction, for example, alloys based on classical ferromagnets Fe, Co, and Ni [2, 3]. In such composites, the value of the magnetoelectric effect is greatly affected by the interlayer interface and the value of the magnetostriction. This work is devoted to the study of the effect of nanostructuring of metal layers and the introduction of interlayer spacers on the magnetoelectric properties of film composites of the metal/PVDF-type.

The studied samples were Metal/PVDF and Metal/Spacer/PVDF sandwiches deposited on Corning glass substrates, where Metal =  $\text{Fe}_{10}\text{Ni}_{90}$  (50–200 nm) and  $[\text{Fe}_{10}\text{Ni}_{90}$  (1000 nm)/Cu (30 nm)]<sub>x</sub>, Spacer = Ta, Cu (5–100 nm). PVDF layers were obtained using spin-coater method. Thickness of PVDF layers varied within 200–1000 nm. Metal layers were deposited by RF-magnetron sputtering. In this work, FTIR reflection spectra in the wave number range of 7000–400  $\text{cm}^{-1}$  were obtained using a Thermo Nicolet 6700 spectrometer. XRD-data of PVDF were obtained by Bruker D8 diffractometer. Piezoelectric properties of the samples were measured using the method of piezoresponse force microscopy (PFM). Magnetic properties were measured using Kerr-microscope Evico Magnetics. Magnetoelectric properties were measured using lock-in Amplifiers Zurich Instruments MFLI 500 kHz/5 MHz. AC field magnitude was 20 Oe.

In all the studied samples, a magnetoelectric effect was detected (Fig. 1). It is shown that nanostructuring with ultrathin nonmagnetic spacers promotes an increase of the effective thickness

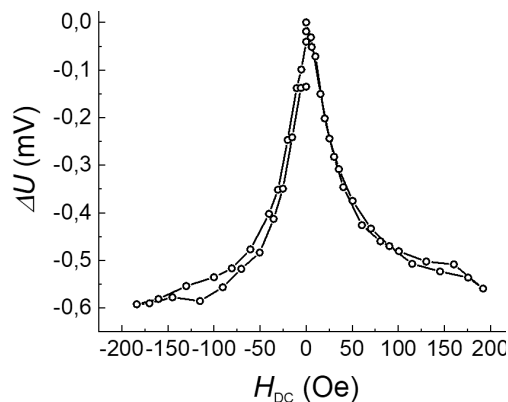


Figure 1. Magnetoelectric effect of  $[\text{Fe}_{10}\text{Ni}_{90}/\text{Cu}]_4/\text{Fe}_{10}\text{Ni}_{90}/\text{PVDF}$  film.

of the magnetostrictive layer without increasing the magnetic hysteresis due to the formation of a “hypercritical” magnetic structure and the fixing effect of the substrate, which in complex leads to an increase of the magnetostrictive deformation and, as a consequence, an increase of the value of the magnetoelectric effect compared with samples without nanostructuring. It has been established that the introduction of metal spacers also contributes to a more efficient interaction between the ferroelectric and magnetostrictive layers.

1. E. Kudyukov et al., Prog. Org. Coat., **147**, 105857 (2020).
2. D. Hunter, Nature Commun., **2**, 518 (2011).
3. R. Bonin, J. Appl. Phys., **98**, 123904 (2005).

**SYNTHESIS AND MAGNETIC PROPERTIES  
OF TbCr<sub>3</sub>(BO<sub>3</sub>)<sub>4</sub> SINGLE CRYSTALS**

A.I. Pankrats<sup>1</sup>, I.A. Gudim<sup>1</sup>, M.S. Molokeev<sup>1</sup>, N.V. Mikhashenok<sup>2\*</sup>

<sup>1</sup>Kirensky Institute of Physics, Federal Research Center KSC SB RAS, Krasnoyarsk, Russia

<sup>2</sup>Federal Research Center KSC SB RAS, Krasnoyarsk, Russia

\*E-mail: natali\_sapronova@mail.ru

A class of crystals of rare-earth metal compounds with the general formula RM<sub>3</sub>(BO<sub>3</sub>)<sub>4</sub>, where R is a rare-earth metal and M = Fe, Cr, Al, Ga, and Sc [1–4], has received much attention last decades. Extensive studies have been concerned with the growth of Fe-containing crystals [5, 6] and their structure and properties, whereas considerably less data have been reported for the rare-earth chromium borates.

Rare-earth chromium borate TbCr<sub>3</sub>(BO<sub>3</sub>)<sub>4</sub> single crystal with huntite-like structure were grown from fluxes based on two different solvents. When using Li<sub>2</sub>WO<sub>4</sub> as a solvent, the single crystals of trigonal symmetry with non-centrosymmetric sp. gr. R32 crystallized. Whereas, when Bi<sub>2</sub>Mo<sub>3</sub>O<sub>12</sub> as a solvent was used, the single crystals grown in a series of syntheses predominantly belonged to the monoclinic sp. gr. C2/c. The cell parameters of both crystals defined by powder X-Ray analysis are presented in Table 1.

Table 1. Cell parameters of TbCr<sub>3</sub>(BO<sub>3</sub>)<sub>4</sub>.

Symmetry	Cell parameters
R32	$a = b = 9.47 \text{ \AA}; c = 7.49 \text{ \AA};$
C2/c	$a = 7.41 \text{ \AA}; b = 9.65 \text{ \AA}; c = 11.31 \text{ \AA}; \beta = 103.42^\circ.$

Magnetic properties were studied on the single crystal with the R32 symmetry; the results are shown on Fig. 1.

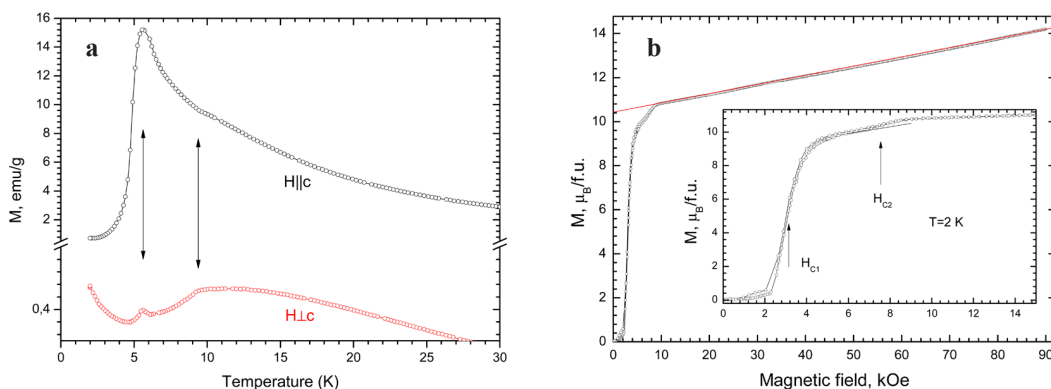


Figure 1. The temperature dependences (a) and the field dependences of magnetization (b) for c-axis of TbCr<sub>3</sub>(BO<sub>3</sub>)<sub>4</sub> single crystal.



The temperature dependences of magnetization show that most likely there are two critical temperatures:  $\sim 5.5$  K and  $\sim 9.5$  K. The upper temperature, apparently, is the Néel temperature corresponding to the magnetic ordering of the Cr subsystem, which polarizes the Tb subsystem due to the f-d exchange interaction. At the lower temperature, the spontaneous spin-reorientation transition from an “easy plane” antiferromagnetic state to an “easy axis” one occurs. For both directions of the magnetic field,  $\mathbf{H} \parallel c$  and  $\mathbf{H} \perp c$ , broad peaks of the magnetization are observed above the Néel temperature, indicating the establishment of a short-range magnetic order.

The field dependence of the magnetization (Fig. 1b) measured at  $T = 2$  K and  $\mathbf{H} \parallel c$  shows two anomalies. A sharp jump of the magnetization occurring at  $H_{C1} \approx 3$  kOe is most likely due to a metamagnetic transition in the antiferromagnetically ordered Tb subsystem. This jump ends with the saturation of the magnetization, which level is close to the saturation magnetization  $M_s = 8.3\mu_B/\text{f.u.}$  of the Tb subsystem in the crystal of the isomorphous diamagnetic analogue  $\text{TbAl}_3(\text{BO}_3)_4$ . The weak hysteresis observed upon this reorientation suggests that this is a first-order transition.

Another anomaly observed at  $H_{C2} \approx 7.5$  kOe is most likely due to the spin-flop transition occurring in the Cr subsystem. Both anomalies exist only in the easy-axis state and disappear at temperatures above 5.5 K.

The magnetization study of the single crystals with monoclinic symmetry are in progress.

*This work is supported by RSF-KRFS, grant no. 22-12-20019.*

1. A.D. Mills, Inorg. Chem., **1**, 960 (1962).
2. G. Blasse and A. Bril, Phys. Status Solidi, **20**, 551 (1967).
3. V.I. Chani, M.I. Timoshechkin, K. Inoue et al., Inorg. Mater., **30**, 1466 (1992).
4. N.I. Leonyuk and L.I. Leonyuk, Prog. Cryst. Growth Charact. Mater., **31**, 179 (1995).
5. L.N. Bezmaternykh, V.L. Temerov, I.A. Gudim, and N.A. Stolbovaya, Crystallogr. Rep., **50**, suppl. 1, S97 (2005).
6. L.N. Bezmaternykh, S.A. Kharlamova, and V.L. Temerov, Crystallogr. Rep., **49**, 855 (2004).

## STRONTIUM IRIDATE THIN FILMS – MATERIAL FOR SUPERCONDUCTING CRYOELECTRONICS AND SPINTRONICS

*I.E. Moskal*<sup>1,2\*</sup>, *Yu.V. Kisilinski*<sup>1</sup>, *A.M. Petrzhik*<sup>1</sup>, *K.Y. Constantinian*<sup>1</sup>,  
*A.V. Shadrin*<sup>1,3</sup>, *G.A. Ovsyannikov*<sup>1</sup>

<sup>1</sup>V.A. Kotelnikov Institute of Radio Engineering and Electronics,  
Russian Academy of Sciences, Moscow, Russia;

<sup>2</sup>Russian Technological University – MIREA Moscow, Russia

<sup>3</sup>Moscow Institute of Physics and Technology (National Research University),  
Moscow region, Dolgoprudny, Russia.

\*E-mail: [ivan.moscal@yandex.ru](mailto:ivan.moscal@yandex.ru)

5d iridates are interesting for their unusual properties, which, in particular, are associated with a strong spin-orbit interaction. Strontium iridate films of different compositions differ significantly, so, for example, SrIrO<sub>3</sub> demonstrates the properties of a paramagnetic metal, and Sr<sub>2</sub>IrO<sub>4</sub> is an antiferromagnetic dielectric. A feature of the synthesis of iridate thin films by laser ablation and cathod sputtering methods is the possibility of obtaining different phases, as well as their mixture, from the same target. In a number of works from metal target SrIrO<sub>3</sub> by laser ablation method films of composition SrIrO<sub>3</sub>, Sr<sub>2</sub>IrO<sub>4</sub> and Sr<sub>3</sub>Ir<sub>2</sub>O<sub>7</sub> were obtained [1]. SrIrO<sub>3</sub>, Sr<sub>2</sub>IrO<sub>4</sub> and Sr<sub>3</sub>Ir<sub>2</sub>O<sub>7</sub> films were obtained from Sr<sub>3</sub>Ir<sub>2</sub>O<sub>7</sub> target [2].

Due to the close lattice parameters in the *ab*-plane, epitaxial growth of heterostructures consisting of SrIrO<sub>3</sub> or Sr<sub>2</sub>IrO<sub>4</sub> iridate and superconducting cuprate is possible. It should be noted that the crystal structure of Sr<sub>2</sub>IrO<sub>4</sub> is similar to that of the cuprate superconductor La<sub>2</sub>CuO<sub>4</sub>.

Heterostructures superconductor-SrIrO<sub>3</sub> can be of interest from a practical point of view as low resistance contacts with YBa<sub>2</sub>Cu<sub>3</sub>O<sub>x</sub> for promising cryoelectronic devices, in a number of works the contacts YBa<sub>2</sub>Cu<sub>3</sub>O<sub>x</sub>-SrIrO<sub>3</sub> with very small contact resistances are obtained: 10<sup>-8</sup>–10<sup>-7</sup> Ω, which is several orders of magnitude lower than when using traditional Au and Pt for cryogenic electronics [3].

Heterostructure Sr<sub>2</sub>IrO<sub>4</sub>-cuprate superconductor is of scientific interest. Previously in the heterostructure Nb/Sr<sub>2</sub>IrO<sub>4</sub>/YBa<sub>2</sub>Cu<sub>3</sub>O<sub>x</sub> was registered superconducting current at the thickness of the intermediate layer Sr<sub>2</sub>IrO<sub>4</sub> *d* = 5 and 7 nm [4]. “Zero bias peak” on *I-V* curve was detected and described. Unusual Fiske steps were registered for samples with *d* = 5 nm [5]. It is known that in the superconductor-ferromagnetic-superconductor junctions, the Josephson effect is enhanced by the formation of triplet Cooper pairs, in which the directions of the spins of both carriers coincide. Such pairs appearance requires special conditions, such as a strong spin-orbit interaction in the interlayer material [6].

In this work we describe the properties of strontium iridate films of SrIrO<sub>3</sub> and Sr<sub>2</sub>IrO<sub>4</sub> grown on different substrates and by different methods: laser ablation and cathod DC sputtering. Along with the traditional characterization of the quality of the grown films by the sharpness of diffraction peaks, the dependences of the resistance on temperature are also compared. Figure 1 shows *R(T)* curves for Sr<sub>2</sub>IrO<sub>4</sub> films sputtered by laser ablation on a single-crystal SrTiO<sub>3</sub> substrate at different sputtering temperatures and operating atmospheres: one film was produced in an argon atmosphere, the other – in oxygen.

The obtained samples can also be characterized by the activation energy  $\Delta E_A$ , which corresponds to the dielectric band gap width; based on the value of the parameter it is possible to identify the most high-quality and defect-free samples. The activation energy can be calculated as a derivative of  $\Delta E_A = d(\ln \rho)/d(1/T)$ , where  $\rho$  is the film resistivity and *T* is the temperature. As in the case with

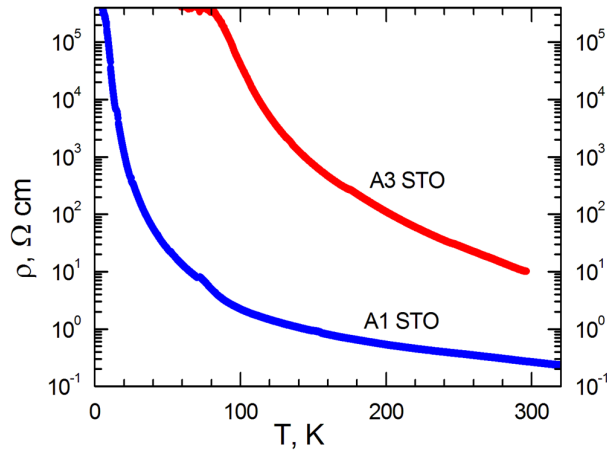


Figure 1. Dependence of resistivity of strontium iridate  $\text{Sr}_2\text{IrO}_4$  on temperature. The sample A1 STO was deposited at oxygen pressure of 0.05 mbar and temperature 770–730 °C. Sample A3 STO was deposited at 0.5 mbar Ar pressure and temperature 800–760 °C.

the dependence of resistivity on temperature, the activation energy varies for samples deposited in different conditions, and its behavior also changes.  $\Delta E_A$  is significantly different for samples deposited in pure argon or pure oxygen. For films obtained by laser ablation in oxygen, the  $E_A$  was 50–70 meV, while in argon it was 200–260 meV.

In dielectrics the activation energy depends on temperature weakly [7, 8]. The activation energies for all our samples were calculated according to the method described in [8].

*This work was carried out within the framework of the state task of the Kotel'nikov IRE RAS. The study was carried out using the Unique Science Unit "Cryointegral" (USU #352529), Project No. 075-15-2021-667.*

1. K. Nishio, H.Y. Hwang, APL Mater., **4**, 036102 (2016).
2. A. Gutierrez-Llorente, L. Iglesias, B. Rodríguez-González, and F. Rivadulla APL Materials, **6**, 091101 (2018).
3. Yu.V. Kislinskii, K.Y. Constantinian, G.A. Ovsyannikov, et al., Extended abstracts of V International conference "Fundamental problems of High Temperature Superconductivity", p. 144. Moscow, October (2015).
4. A.M. Petrzhik, K.Y. Constantinian, G.A. Ovsyannikov, A.V. Zaitsev, A.V. Shadrin, A.S. Grishin, Yu.V. Kislinski, G. Cristiani, and G. Logvenov, Phys. Rev. B, **100**, 024501 (2019).
5. A.M. Petrzhik, K.Y. Constantinian, G.A. Ovsyannikov, A.V. Shadrin, Yu.V. Kislinskii, G. Cristiani and G. Logvenov, J. Surf. Inv., **14**(3), 547–550 (2020).
6. I.V. Bobkova and A.M. Bobkov, Phys. Rev. B, **95**, 184512 (2017).
7. C. Lu, A. Quindeau, H. Deniz, D. Preziosi, D. Hesse, and M. Alexe, Appl. Phys. Lett., **105**, 082407 (2014).
8. N.G. Bebenin, R.I. Zainullina, N.S. Chusheva, V.V. Ustinov and Ya.M. Mukovskii, Phys. Rev. B, **69**, 104434 (2004).

**SENSITIVITY OF Cd<sub>1-x</sub>Zn<sub>x</sub>Te DIAMAGNETIC SEMICONDUCTOR CRYSTALS (x = 0.06; 0.03; 0) TO THE INFLUENCE OF A PULSED MAGNETIC FIELD**

*P.L. Podkur, I.S. Volchkov\*, V.B. Kwartalov, M.V. Pavlyuk, V.M. Kanevskii*

IC RAS, FSRC “Crystallography and Photonics” RAS, Moscow, Russia

\*E-mail: [volch2862@gmail.com](mailto:volch2862@gmail.com)

Progress in the area of semiconductor materials and technologies contributes to their widespread used in electronics and energy. The production of high-quality semiconductor crystals on a large scale, in particular, CdTe and Cd<sub>1-x</sub>Zn<sub>x</sub>Te, is becoming increasingly important. These crystals are the most promising materials for the development of X-ray and gamma detectors operating at room temperature. The creation of a sufficiently high-resistivity material based on the data of crystals, which is necessary for the development of active detector elements of various devices, is very difficult, but extremely urgent task of materials science of semiconductors. Due to the complexity of obtaining high-quality CdTe and Cd<sub>1-x</sub>Zn<sub>x</sub>Te crystals, methods for improving the characteristics of already grown crystals are of interest. It is known that “weak” magnetic fields (fields for which the condition  $\mu_B B \ll kT$  is satisfied, where  $\mu_B$  – the Bohr magneton,  $k$  – the Boltzmann constant,  $T$  – the temperature, and  $B$  – the magnetic field induction) affect the defect impurity structure of semiconductors, which leads to many cases, to an irreversible change in the defective structure and properties [1, 2]. Thus, a “weak” magnetic field is a promising method for controlling the characteristics of semiconductor materials.

Wide-gap semiconductors with a band gap  $E_g > 1$  eV, which include CdTe and Cd<sub>1-x</sub>Zn<sub>x</sub>Te, should have low conductivity and be diamagnetic. However, the real situation is such that all AIIIBVI compounds are non-stoichiometric and the deviation from the ideal structure is caused by the presence of its own defects: vacancies ( $V_A$  and  $V_B$ ) and interstitial atoms ( $A_i$  and  $B_i$ ). In the case of adding dopants during crystal growth, impurities are added to intrinsic defects. The appearance of defects during growth leads to significant change in physical properties.

The phase diagram of Cd<sub>1-x</sub>Zn<sub>x</sub>Te imposes stringent requirements on the temperature regimes of crystal growth and the contents of the Zn component [3, 4]. At the same time, when the Zn content changes, the magnetic and electrical properties of the crystals change [5]. In connection with this, as well as with the known influence of a weak pulsed magnetic field (PMF) on the properties of CdTe crystals, studies were carried out to find a correlation between the Zn content on the properties of the Cd<sub>1-x</sub>Zn<sub>x</sub>Te material and its sensitivity to PMF.

CdTe and Cd<sub>1-x</sub>Zn<sub>x</sub>Te samples grown by the modified Obreimov-Shubnikov method at the Institute of Crystallography of the FSRC “Crystallography and Photonics” RAS were used as the material under study. The impurity composition and structure of the samples were controlled by mass spectrometry, EDX analysis, and X-ray phase analysis. Magnetic hysteresis was recorded by a SQUID MPMS XL (Quantum Design) magnetometer. Changes in the properties of the studied samples were recorded by changing the electrical characteristics. The electrical properties of the samples were studied by two-contact and four-contact methods (Cresbox, Napson) before exposure to a magnetic field and, repeatedly in time, after. The samples were subjected for  $t_{\text{exp}} = 10$  min to the pulsed magnetic field (amplitude of  $B = 1$  T, frequency of  $\nu = 12$  Hz).

All samples under study are diamagnetic (Fig. 1). However, the Cd<sub>0.94</sub>Zn<sub>0.6</sub>Te sample has some anomaly in the dependence of magnetization. The magnetization values are more than 2 times higher than for other samples. In addition, the magnetization itself has a slight bend, at low fields,

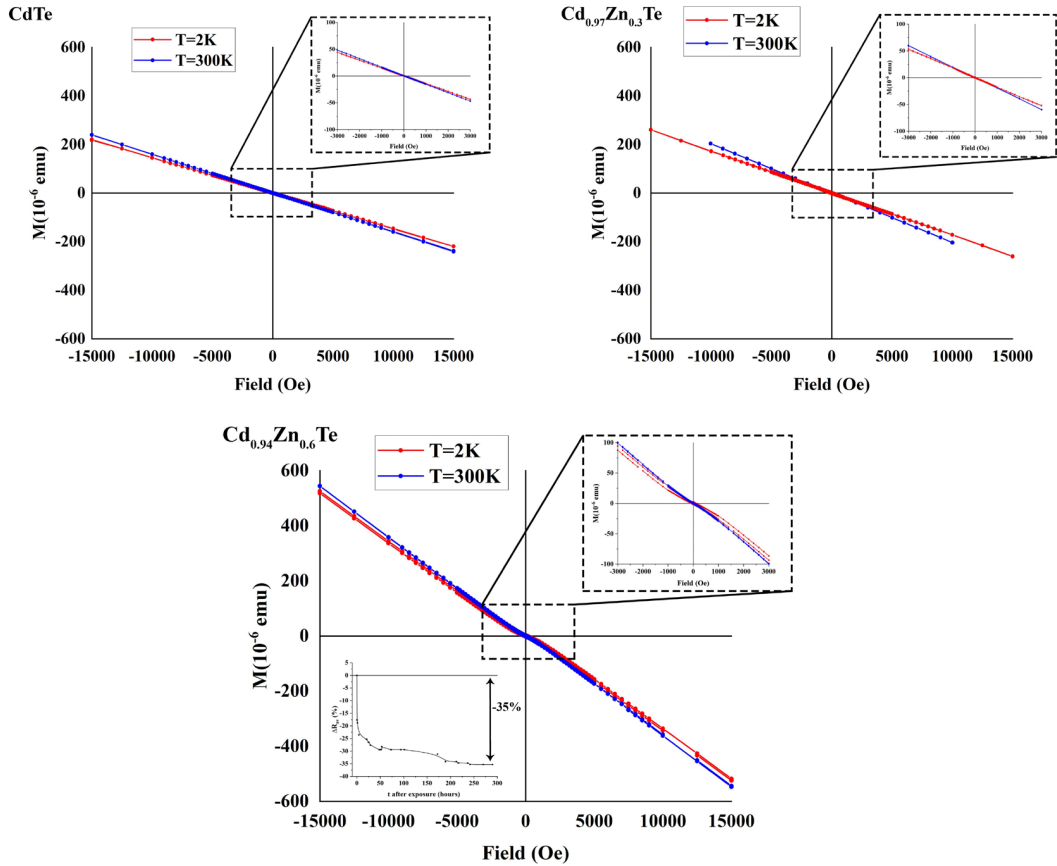


Figure 1. Magnetic hysteresis loops recorded at 300 and 2 K. The inset of the graph for the Cd<sub>0.94</sub>Zn<sub>0.6</sub>Te sample shows the dependence of the change in the average value of the resistance of the sample after a pulsed magnetic effect.

which is characteristic of ferromagnetic. Indeed, when the diamagnetic contribution of the lattice is subtracted, the dependence of the magnetization on the field takes the form of a ferromagnetic loop. Changes in electrical properties after exposure to a pulsed magnetic field are most noticeable for Cd<sub>0.94</sub>Zn<sub>0.6</sub>Te samples (Fig. 1).

The observed changes in properties are associated with the influence of a pulsed magnetic field on defect complexes formed by intrinsic CdTe defects and impurity defects: Cl, in the case of a CdTe sample; Zn in the case of the Cd<sub>0.97</sub>Zn<sub>0.3</sub>Te sample. In the case of the Cd<sub>0.94</sub>Zn<sub>0.6</sub>Te sample, the observed changes, which exceed those for other samples, are associated both with a greater sensitivity to a magnetic field and with a greater “metastability” of the sample, associated with the presence of phase alternations of CdTe and Cd<sub>0.94</sub>Zn<sub>0.6</sub>Te.

1. E.V. Darinskaya, E.A. Petrzhik, Yu.M. Ivanov, S.A. Erofeeva, M.R. Raukhan, *Phys. Stat. Sol. (c)*, **2**(6), 1873–1877 (2005).
2. I.S. Volchkov, V.M. Kanevskii, M.D. Pavlyuk, *JETP Lett.*, **107**(4), 269–272 (2018).
3. Yu.M. Ivanov, *J. Cryst. Growth*, **194**, 309–316 (1998).
4. I.C. Avetisov, Ph.D. Thesis. Moscow D. Mendeleev Institute of Chemical Technology, 2011.
5. Yu.V. Shaldin, I. Warchulska, M.Kh. Rabadanov, V.K. Komar', *Semiconductors*, **38**, 288–292 (2004).

## STRUCTURAL, MAGNETIC AND TRANSPORT PROPERTIES THULIUM-SUBSTITUTED MANGANESE SELENIDE

*O.B. Romanova*<sup>1\*</sup>, *S.S. Aplesnin*<sup>1,2</sup>, *L.V. Udod*<sup>1,2</sup>, *K.I. Yanushkevich*<sup>3</sup>,  
*A.I. Galays*<sup>3</sup>, *A.M. Zhivulko*<sup>3</sup>

<sup>1</sup>Kirensky Institute of Physics, Federal Research Center KSC SB RAS, Krasnoyarsk, Russia

<sup>2</sup>Reshetnev Siberian State University of Science and Technology, Krasnoyarsk, Russia

<sup>3</sup>Scientific-Practical Materials Research Center NAS, Minsk, Belarus

\*E-mail: [rob@iph.krasn.ru](mailto:rob@iph.krasn.ru)

The systems doped with variable-valence rare-earth elements form an intriguing group of compounds with the unique combination of the magnetic and electrical properties depend of temperature, pressure, composition, and other factors [1–3]. Structural, electronic, and magnetic phase transitions, as well as magnetotransport effects, are realized in these compounds [4, 5]. The aim of this work was to synthesize a new  $Tm_xMn_{1-x}Se$  chalcogenide system and study structural, magnetic, acoustic, and transport properties.

The  $Tm_xMn_{1-x}Se$  ( $0 \leq x \leq 0.2$ ) polycrystalline samples were synthesized by the solid-phase reaction. According to X-ray diffraction data, the synthesized samples of the  $Tm_xMn_{1-x}Se$  system have a cubic face-centered structure of the NaCl type of the space group  $Fm\bar{3}m$ . With an increase in the degree of cationic substitution of manganese with thulium, the unit cell parameter  $a$  increases linearly, according to Vegard's law, which indicates the formation of solid solutions of the  $Tm_xMn_{1-x}Se$  system.

The morphology of polycrystalline samples and their microstructure were studied using scanning electron microscopy (SEM) and energy dispersive X-ray spectroscopy (EDS). The results of these studies showed that the samples of the  $Tm_xMn_{1-x}Se$  system are homogeneous and their composition corresponds to the chemical composition of the parameters of the load.

The magnetic properties of these compounds were measured by the ponderomotive method in the temperature range of 80–900 K and in a magnetic field with an induction of 0.86 T. At a temperature of  $\sim 80$  K, when the thermal vibrations of atoms in the nodes of the unit crystal cell are significantly weakened, the value of the specific magnetization increases from 0.64 emu/g for a sample with a concentration of  $x = 0.05$  to 1.25 emu/g for a sample with a concentration of  $x = 0.2$ . An increase in the concentration of substitution of manganese with thulium in  $Tm_xMn_{1-x}Se$  leads to an increase in the ferromagnetic interaction and a decrease in the Néel temperature from 134 K (for MnSe) to 100 K (for  $x = 0.2$ ). Above the temperature  $T > 300$  K, an anomalous behavior of the dependences of the specific magnetization and magnetic susceptibility is observed in all concentrations studied, which correlates with the anomalies found in the temperature dependences of the electrical resistance, sound attenuation coefficient, and thermal expansion coefficient. These anomalies are caused by changes in the electronic structure due to the shift of the chemical potential towards the conduction band.

The temperature dependences of the electrical resistance and thermopower of the  $Tm_xMn_{1-x}Se$  polycrystals were investigated on cylindrical samples in the range of 80–320 K in zero magnetic field by a four-probe method. Studies of the transport properties have shown that the synthesized  $Tm_xMn_{1-x}Se$  samples are hole-type semiconductors. The growth of the substitution concentration ( $0 \leq x \leq 0.2$ ) leads to an increase in the resistivity as compared with the parameter for the initial manganese monoselenide. Activation energy  $E_a$  determined from the relation  $\ln R = \ln R_0 - E_a/kT$  decreases above the percolation concentration  $x_c = 0.17$  of the FCC cubic lattice. The kink in the concentration dependence of the activation energy of the  $Tm_xMn_{1-x}Se$  system is probably caused by the change in the valence of Tm ions.

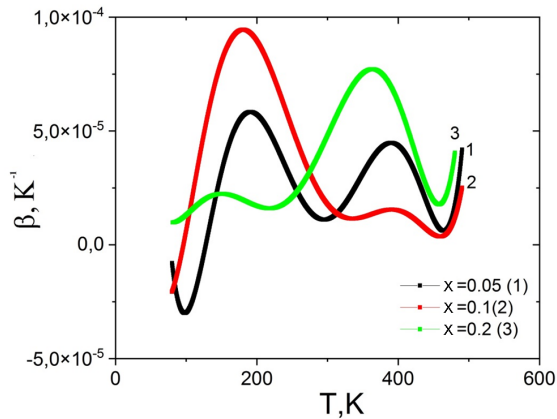


Figure 1. Temperature dependence of the thermal expansion coefficient of the  $Tm_xMn_{1-x}Se$  system.

The structural deformation and structural transitions can be observed from the temperature dependence of the sound attenuation coefficient ( $\alpha$ ) and thermal expansion coefficient ( $\beta$ ) which is proportional to the lattice compressibility. The temperature range of the anomalous compressibility was determined for the  $Tm_xMn_{1-x}Se$  samples. The  $\beta(T)$  dependence for each concentration contains two temperature regions with the maximum values of the thermal expansion coefficient at  $T_1 = 188\text{--}146$  K and  $T_2 = 389\text{--}361$  K (Fig. 1). Anomalies in the thermal expansion coefficient at  $T_1$  are related to the lattice strain. With an increase in the concentration of thulium above the concentration of the percolation of  $x_c = 0.17$  the ratio between these maxima changes. The electronic phase transition in the  $Tm_{0.2}Mn_{0.8}Se$  samples at temperature  $T_2$  is associated with the electronic compressibility determined by a change in the valence of thulium ions upon temperature variation. In the region of structural and electronic phase transitions, anomalies were found in the temperature dependence of the sound attenuation coefficient, which are associated with fluctuations in the density of the material. A correlation of structural, magnetic, electrical and acoustic properties has been established.

*This study was supported by the Russian Foundation for Basic Research and the Belarusian Republic Foundation for Basic Research (project no. 20-52-00005) and (project no. T20P-052).*

1. C. Celandia, A.-V. Mudring, J. Solid State Chem., **274**, 243–258 (2019).
2. Zheshan Zhang, Hongyang Zhao, Chao Zhang, Feng Luo, Yaping Du, InfoMat, **2**, 466–482 (2020).
3. S. Aplesnin, M. Sitnikov, O. Romanova, A. Kharkov, O. Begisheva, F. Zelenov, Eur. Phys. J. Plus, **137**, 226–238 (2022).
4. S. Aplesnin, O. Romanova, V. Korolev, M. Sitnikov, K. Yanushkevich, J. Appl. Phys., **121**, 075701–7 (2017).
5. S.S. Aplesnin, A.M. Harkov, E.V. Eremin, O.B. Romanova, D.A. Balalev, V.V. Sokolov, A.Yu. Pichugin, IEEE Trans. Magn., **47**, 4413–4416 (2011).

## FEATURES OF THE ELECTRONIC STATE OF $\text{Cu}^+$ IONS IN DELAFOSSITE COMPOUNDS $\text{CuBO}_2$ ( $\text{B} = \text{Al}, \text{Cr}, \text{Fe}$ ) ACCORDING TO NMR- AND NQR-DATA

*A.G. Smolnikov\**, *V.V. Ogloblichev*, *A.F. Sadykov*, *Yu.V. Piskunov*, *R.V. Skoryunov*

Mikheev Institute of Metal Physics, Ural Branch, Russian Academy of Sciences, Ekaterinburg, Russia

\*E-mail: [Smolnikov@imp.uran.ru](mailto:Smolnikov@imp.uran.ru)

Not so long ago, delafossite oxides  $\text{CuBO}_2$  ( $\text{B} = \text{Cr}, \text{Fe}$ ) attracted the attention of researchers as multiferroics with a frustrated spin structure [1–3]. The ferroelectricity in  $\text{CuBO}_2$  has a strong correlation with incommensurate spin magnetic helicoids that appear at low temperature on triangular crystalline layers of  $\text{B}^{3+}$  cations with AF-interaction.

Development of modern optoelectronics based on p-n junctions has led to exploration materials with high electrical conductivity and optical transparency in the visible region [4]. Some wide-gap simple metal oxides ( $\text{In}_2\text{O}_3$ ,  $\text{SnO}_2$ ,  $\text{ZnO}$ ) can be doped for n-type conductivity. In contrast, obtaining p-type transparent conducting oxides (TCO) is difficult. The delafossite family  $\text{CuBO}_2$  was the first p-type TCO with a wide band gap. [5] In the report, we present new NQR  $^{63,65}\text{Cu}$  data for paramagnetic  $\text{CuCrO}_2$  analyzed in combination with NMR/NQR, neutron diffraction, and magnetometer data for the  $\text{CuBO}_2$  ( $\text{B} = \text{Al}, \text{Cr}, \text{Fe}$ ) series.

In works [6–8], the parameters of the electric field gradient tensor (EFG) (quadrupole frequency  $\nu_Q$ , asymmetry parameter  $\eta$ , direction of the main axis of the tensor  $Z_q$ ) were measured at the position  $^{63,65}\text{Cu}$  on a series of single crystals and powders  $\text{CuBO}_2$  ( $\text{B} = \text{Al}, \text{Cr}, \text{Fe}$ ). For the entire series of samples, the EFG tensor is axially symmetric ( $\eta \approx 0$ ), and the direction of the main axis of its tensor coincides with the  $c$ -axis of the crystal ( $Z_q \parallel c$ ), while the quadrupole frequency differs by no more than 7% (Table 1). These data allow us to state the general similarity of the local charge environment of copper nuclei in the entire series of samples studied.

In the case of an axially symmetric EFG, the quadrupole frequency coincides with the frequency of the nuclear quadrupole resonance NQR. Figure 1 shows the temperature dependence of the NQR frequency ( $^{63,65}\nu_{\text{NQR}}$ ) measured in the paramagnetic state of  $\text{CuCrO}_2$ . There is an increase in frequency with decreasing temperature. If the copper ions  $\text{Cu}^+$  have  $3d^{10}$  completely closed electron orbitals, then the main contribution to the EFG will be made by the lattice ions ( $q_c$ ). However, according to the neutron diffraction data [9], the distances  $\text{Cu-O}$  increase with decreasing temperature (inset in Fig. 1), which should lead to a decrease lattice contribution to the EFG. Thus, we assume the presence of a significant valence contribution to the EFG ( $q_v > q_c$ ) directed against the lattice one ( $q = q_v - q_c$ ). The valence contribution to the EFG can arise due to the openness of the  $3d_{z^2-r^2}$  orbitals of the copper ion.

Table 1. EFG parameters at the position  $^{63,65}\text{Cu}$  in  $\text{CuBO}_2$  ( $\text{B} = \text{Al}, \text{Cr}, \text{Fe}$ ).

Sample	$^{63}\nu_Q$ , MHz	$^{63}\eta$	article link
$\text{CuAlO}_2$	28.46(4)	0.00(3)	[6]
$\text{CuCrO}_2$	26.85(2)	0.00(1)	[7]
$\text{CuFeO}_2$	26.60(3)	0.00(1)	[8]



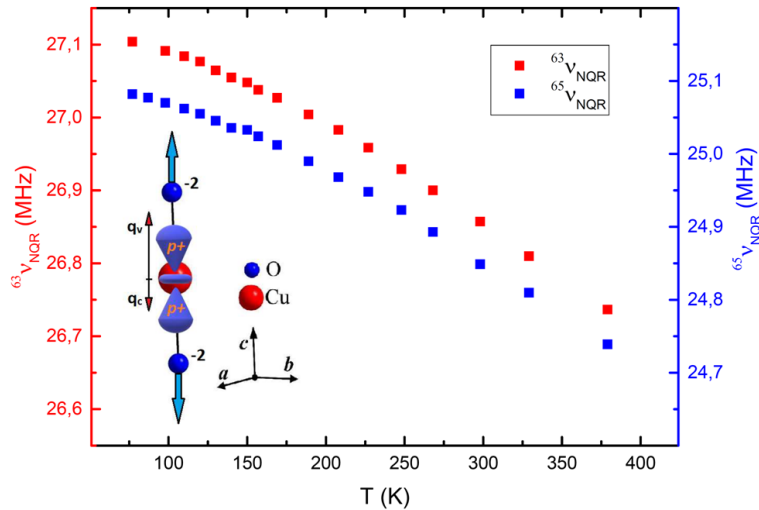


Figure 1. The temperature dependence of the  $^{63,65}\text{V}_{\text{NQR}}$  in the paramagnetic state of  $\text{CuCrO}_2$ . The inset shows the nearest charge environment of copper.

An analysis of the magnetic susceptibility data and NMR line shifts leads to the conclusion that there is a hole in the hybridized  $|3d4s\rangle$  copper orbitals for the whole class of copper deloffosites. In this case, a pair of electrons in these  $|3d4s\rangle$  orbitals have a predominantly antiparallel ( $\uparrow\downarrow$ ) state of spins.

*The work was carried out with the support of a grant from the President RF for young scientists No. MK-6094.2021.1.2.*

1. S. Seki, Y. Onose, and Y. Tokura, Phys. Rev. Lett., **101**, 067204 (2008).
2. Yu.A. Sakhratov, L.E. Svistov, P.L. Kuhns, H.D. Zhou, and A.P. Reyes, Phys. Rev. B, **94**, 094410 (2016).
3. T.T.A. Lummen, C. Strohm, H. Rakoto, and P.H.M. van Loosdrecht, Phys. Rev. B, **81**, 224420 (2010).
4. D.S. Hecht, L. Hu, G. Irvin, Adv. Mat., **23**(13), 1482 (2011).
5. T. Minami, Semicond. Sci. Tech., **20**(4), 35 (2005).
6. V.V. Ogloblichev, A.G. Smolnikov, A.L. Buzlukov et al., JETP, **133**, 567–573 (2021).
7. A.G. Smol'nikov, V.V. Ogloblichev, S.V. Verkhovskii et al., Phys. Metals Metallogr., **118**, 134–142 (2017).
8. A.G. Smol'nikov, V.V. Ogloblichev, A.Y. Germov et al. JETP Lett., **107**, 134–138 (2018).
9. M. Poienar, F. Damay, C. Martin, V. Hardy, A. Maignan, G. Andre, Phys. Rev. B, **79**, 177201 (2009).

REFLECTION AND MAGNETOREFLECTION SPECTRUM  
OF THE  $\text{MnFe}_2\text{O}_4$  FERRITE-SPINEL*E.A. Surzhikov\**, Yu.P. Sukhorukov, S.V. Naumov, A.V. Telegin

Institute of Metals Physics M.N. Mikheev UB of RAS, Ekaterinburg, Russia

\*E-mail: [surzhikov@imp.uran.ru](mailto:surzhikov@imp.uran.ru)

In connection with the intensive development of a new direction in the physics of magnetic phenomena – strain magneto-optics, there is a problem of searching for new materials with a strong correlation of magneto-optical and magnetoelastic properties. It is assumed that one of these materials can be ferrimagnetic spinel  $\text{MnFe}_2\text{O}_4$ , which is similar in its physicochemical properties to  $\text{CoFe}_2\text{O}_4$ , in which unique strain-magneto-optical properties have been found [1, 2]. The aim of this work was to study the spectrum of the reflection coefficient of the  $\text{MnFe}_2\text{O}_4$  single crystals in the absence and presence of an external magnetic field in a wide infrared (IR) spectral range from 1 to 30  $\mu\text{m}$ .

Single crystals of the  $\text{MnFe}_2\text{O}_4$  was synthesized by the method of crucibleless zone melting with radiation heating. By using EDAX and XRD it has been confirmed that the samples are single-phase, and their chemical composition corresponds to the formula unit.

All optical measurements were carried out at room temperature by using the IR prism monochromator in magnetic fields of up to  $H = 3$  kOe directed in-plane to the sample surface and along various crystallographic axes of the  $\text{MnFe}_2\text{O}_4$  crystal. It was shown the existence of the magnetoreflexion effect in  $\text{MnFe}_2\text{O}_4$  crystals. This effect was observed within a wide IR wavelength range, but it was most clearly pronounced near the absorption edge and impurity-type bands. The magnetoreflexion in  $\text{MnFe}_2\text{O}_4$  changes its sign as a function of the magnetic field and reaches 2% at a magnetic field of 3 kOe at wavelength  $\lambda = 3.9$   $\mu\text{m}$ . According to [1, 2] it is suggested the magnetoreflexion effect in  $\text{MnFe}_2\text{O}_4$  is related to the absorption edge shift and to magnetoelastic strains. The magnetorefractive and magnetoabsorption effects in  $\text{MnFe}_2\text{O}_4$  spinel was also estimated using the Kramers-Kronig analysis of reflectivity data. The geometry of the experiment made it possible to estimate the anisotropy of the magnetoreflexion effect in spinel. The observed effect could help in understanding the strain-magneto-optics phenomena and developing novel optical devices.

*The work is carried out within the framework of the state task of the Ministry of Science and Higher Education of Russia (subject “Spin” No. 122021000036-3).*

1. Yu.P. Sukhorukov, A.V. Telegin, A.P. Nosov et al., JETP Lett., **104**(6), 384–387 (2016).
2. Yu.P. Sukhorukov, A.V. Telegin, N.G. Bebenin et al., J. Appl. Phys., **128**, 195103 (2020).

## ROOM TEMPERATURE FERROMAGNETISM IN ORGANIC-INORGANIC LEAD IODIDE PEROVSKITE SINGLE CRYSTALS

*I.V. Zhevstovskikh<sup>1\*</sup>, T.B. Charikova<sup>1</sup>, A.S. Klepikova<sup>1</sup>, M.R. Popov<sup>1</sup>,  
E.A. Stepanova<sup>2</sup>, O.I. Semenova<sup>3</sup>*

<sup>1</sup>M.N. Mikheev Institute of Metal Physics, Ural Branch of Russian Academy of Sciences,  
Ekaterinburg, Russia

<sup>2</sup>Ural Federal University, Ekaterinburg, Russia

<sup>3</sup>A.V. Rzhanov Institute of Semiconductor Physics, Siberian Branch of Russian Academy of Sciences,  
Novosibirsk, Russia

\*E-mail: [zhevstovskikh@imp.uran.ru](mailto:zhevstovskikh@imp.uran.ru)

In the past few years, hybrid organic-inorganic halide perovskites have been investigated intensively due to their unique properties such as a high absorption coefficient, a low exciton binding energy, a long charge carrier diffusion length, and a tunable bandgap. They are promising materials for various applications, including photovoltaic devices, light-emitting diodes, photodetectors, microlasers [1–3]. Methylammonium lead triiodide  $\text{CH}_3\text{NH}_3\text{PbI}_3$  ( $\text{MAPbI}_3$ ), which consists of the organic cation  $(\text{CH}_3\text{NH}_3)^+(\text{MA})^+$  and the inorganic anion  $(\text{PbI}_3)^-$  is the most investigated compound among hybrid perovskites because it exhibits the best properties for solar cells. The recently observed ferromagnetic ordering in a direct band gap semiconductor  $\text{MAPbI}_3$  [4] may provide the potential application of hybrid perovskites in spintronic application.

The temperature (in the range of 5–300 K) and magnetic field (up to 50 kOe) dependences of the magnetization of the high quality  $\text{CH}_3\text{NH}_3\text{PbI}_3$  single crystals at different directions of the magnetic field were investigated. We have found an anisotropic behavior of the magnetic properties. When the magnetic field is applied perpendicular to (001) crystallographic plane, the diamagnetic behavior of the magnetic susceptibility is detected (Fig. 1, curve 2), whereas of the parallel orientation magnetic field with respect to the (001) plane the ferromagnetic behavior is found (Fig. 1, curve 1). At the temperature 5 K, the saturation of the magnetization is about 15.5 emu/mol, as the temperature rises to 300 K, the magnetization decreases to 9.3 emu/mol. These values are higher than obtained earlier in [4] for polycrystalline samples of  $\text{CH}_3\text{NH}_3\text{PbI}_3$ . The temperature of the transition from the ferromagnetic state to the paramagnetic state is equal 115 K (Fig. 1, insert at the bottom). The Curie-Weiss temperature determined from the fitting in the paramagnetic region is approximately 280 K, which is higher than the magnetic transition temperature (Fig. 1, insert at the top). This indicates on the presence of a structural disorder in the hybrid perovskite  $\text{CH}_3\text{NH}_3\text{PbI}_3$ . At temperatures below 50 K, we revealed the features of the magnetic susceptibility likely due to antiferromagnetic correlations.

In addition, we found the influence of the structural transition from the tetragonal (I4/mcm s.g.) to the orthorhombic phase (Pnma) at  $T_c = 160$  K on the magnetization of  $\text{CH}_3\text{NH}_3\text{PbI}_3$  single crystals. Under the phase transition from the tetragonal to orthorhombic phase, the rotation of the octahedra  $\text{PbI}_6$  with angles Pb-I-Pb changes and the final ordering of  $(\text{CH}_3\text{NH}_3)^+$  cations takes place with the alignment of the C-N bond along the  $\langle 110 \rangle$  axis in a distorted primitive cell (Fig. 1). These changes lead to a rearrangement of the magnetic moments and therefore to a change of the magnetization. We have estimated the value of the effective magnetic moment  $\mu_{\text{eff}}$  for our samples in different temperature ranges from the Curie constant. In the tetragonal phase,  $\mu_{\text{eff}}$  is equal  $0.76\mu_B$ , but in the orthorhombic phase is equal  $0.39\mu_B$ . The value  $0.76\mu_B$  well agree with the previously obtained from first principle calculation of the value  $\sim 0.74\mu_B$  [4]. Authors of [4] explained the origin of the

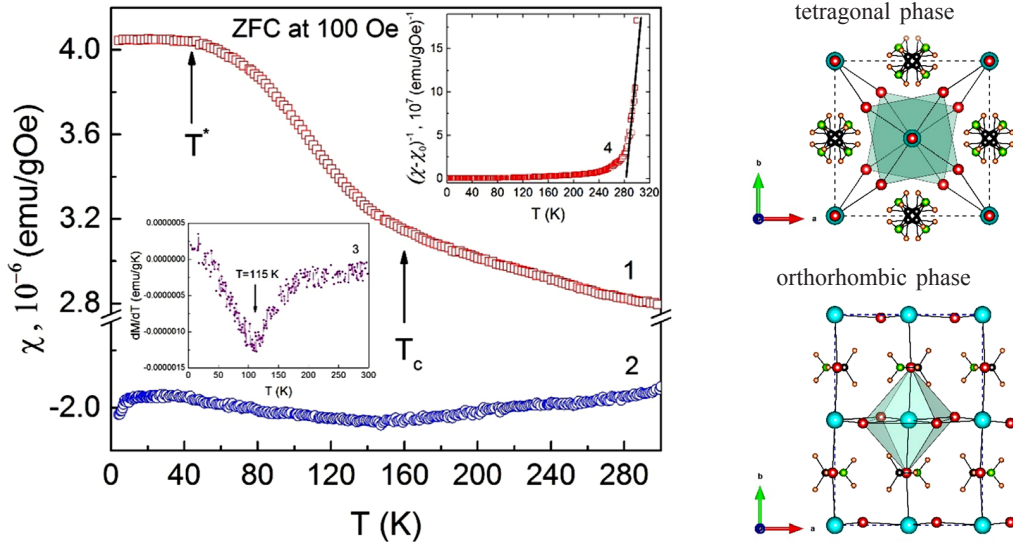


Figure 1. Temperature dependence of the magnetic susceptibility in  $\text{CH}_3\text{NH}_3\text{PbI}_3$  single crystal. Curve 1 is obtained at the parallel orientation of the magnetic induction vector with respect to the (001) plane, curve 2 – at the perpendicular orientation of the magnetic induction vector with respect to the (001) plane, curve 3 is the derivative  $dM/dT$ , curve 4 is the inverse susceptibility with the Curie-Weiss fitting.

ferromagnetism in  $\text{CH}_3\text{NH}_3\text{PbI}_3$  hybrid perovskite due to the presence iodine or lead vacancies. The pristine system has a symmetric spin polarized DOS, and hence, the system is diamagnetic. In the presence of Pb or I vacancies, the total DOS becomes asymmetric resulting in a net magnetic moment in the system. We suggest that the lead vacancies cause the ferromagnetism in  $\text{CH}_3\text{NH}_3\text{PbI}_3$  single crystals, since we detected their presence in the low-temperature photoluminescence spectra obtained on the same samples [5].

*This work was carried out as part of the state assignment on the topic “Electron” no. AAAA-A18-118020190098-5 and was supported by the Russian Foundation for Basic Research and the Sverdlovsk region as part of the scientific project no. 20-42-660004.*

1. Z. Chen, B. Turedi, A.Y. Alsalloum, C. Yang, X. Zheng, I. Gereige, A. AlSaggaf, O.F. Mohammed and O.M. Bark, ACS Energy Lett., **4**, 1258–1267 (2019).
2. S. Stranks and H.J. Snaith, Nat. Nanotechnol., **10**, 391–402 (2015).
3. J.S. Manser, J.A. Christians and P.V. Kamat, Chem. Rev., **116**, 12956–3008 (2016).
4. B. Bandyopadhyay, H. Luitel, S. Sil, J. Dhar, M. Chakrabarti, P. Nath, P. P. Ray, D. Sanyal, Phys. Rev. B, **101**, 094417 (2020).
5. I.V. Zhevstovskikh, N.S. Averkiev, M.S. Sarychev, O.I. Semenova, O.E. Tereshchenko, J. Phys. D: Appl. Phys., **55**, 095105 (2022).

## TOPOLOGICAL FEATURES IN BAND STRUCTURE OF GdNiSb COMPOUND

*S.T. Baidak*<sup>1,2\*</sup>, *A.V. Lukoyanov*<sup>2,1</sup>

<sup>1</sup>Ural Federal University, Ekaterinburg, Russia

<sup>2</sup>M.N. Mikheev Institute of Metal Physics of Ural Branch of RAS, Ekaterinburg, Russia

\*E-mail: [baidak@imp.uran.ru](mailto:baidak@imp.uran.ru)

RNiSb intermetallic compounds (R = rare earth elements) belong to the RTX (T = 3d/4d/5d transition metals, and X = p-elements) family [1] with a variety of properties and phenomena promising for functional applications. In RNiSb with some R, high mobility ratio and high-temperature power factor are found [2]. The intermetallic compounds are crystalized in the MgAgAs-type (space group F-43m) half-Heusler structure [3]. In this work, the band structure and magnetic properties of these RNiSb for R = Gd, Er compounds are investigated in the framework of the DFT+U method based on density functional theory and accounting for strong electron correlations in the 4f shell of the R ions [1]. All compounds are found to be narrow gap semiconductors with the indirect gap in the electronic structure in both spin projections. The energy gap ( $E_g$ ) in the studied RNiSb was found to be 0.21–0.26 eV due to the occupied and empty electronic states in the minority spin projection with the largest value of the band gap in GdNiSb. At the same time, in the majority spin projection of GdNiSb, the gap at the Fermi energy is 0.52 eV. The band structure exhibits the presence of occupied bands which can form a hole pocket near  $\Gamma$  point (L- $\Gamma$ -X, K- $\Gamma$ ) at the Fermi energy. The occupied bands have the nonsymmetric band near X point ( $\Gamma$ -X-W) and another band near K-point at higher energies. The calculated magnetic properties are solely caused by the magnetic moments of the Gd ions and provide a good agreement with the experimental data [3].

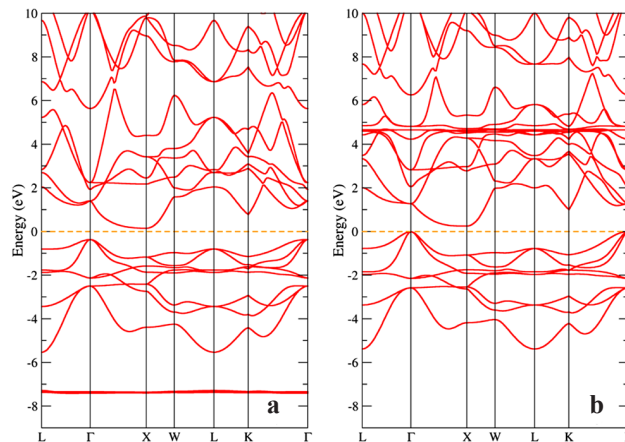


Figure 1. Band structure of GdNiSb for majority (a) and minority (b) spin projections.

*This study was supported by the grant of Russian Science Foundation No 22-42-02021.*

1. S. Gupta, A.V. Lukoyanov, Yu.V. Knyazev, Yu.I. Kuz'min, and K.G. Suresh, *J. Alloys Compd.*, **888**, 161493 (2021).
2. K. Ciesielski, K. Synoradzki, I. Wolańska, P. Stachowiak, L. Kepiński, A. Jeżowski, T. Toliński, and D. Kaczorowski, *J. Alloys Compd.*, **816**, 152596 (2020).
3. K. Hartjes and W. Jeitschko, *J. Alloys Compd.*, **226**, 81–86 (1995).

## MAGNETOELECTRIC EFFECT IN A HEMATITE-PIEZOELECTRIC HETEROSTRUCTURE

*V.V. Borichok\**, *D.A. Burdin*, *Y.K. Fetisov*, *N.A. Ekonomov*, *D.V. Chashin*

MIREA – Russian technological university, Moscow

\*E-mail: [fsdaga@yandex.ru](mailto:fsdaga@yandex.ru)

Recently, the magnetoelectric (ME) effect in composite layered structures has been intensively studied. This effect results from elastic interaction between mechanically coupled magnetostrictive (MS) and piezoelectric (PE) layers [1]. As a rule, magnetically soft metals and alloys with a high value of saturation magnetostriction ( $\lambda_s > 10^{-5}$ ) are used as the material of MS-layers. Of interest is using dielectric magnetically ordered single crystals in such structures. One of these materials is a single-crystal hematite  $\alpha\text{-Fe}_2\text{O}_3$  [2], which has a low conductivity  $\sim 10^{-7}$  S and a noticeable saturation magnetostriction  $\lambda_s \approx 3 \cdot 10^{-6}$ . In this work, we experimentally studied the direct ME-effect in the hematite-piezoelectric structure.

The structure is shown schematically in Fig. 1. A PZT-5 piezoceramic plate, 230  $\mu\text{m}$  thick and 15 mm $\times$ 13 mm in size, with Ag-el electrodes deposited on its surface is used as a PE-layer. A plate of single-crystal hematite of a thickness 330  $\mu\text{m}$  and dimensions of 15 mm $\times$ 11 mm is used as the MS-layer. The layers were connected together using COSMO CA-500.200 cyanoacrylate glue. The sample was placed in a solenoid 27 mm in diameter, containing 200 turns. The solenoid was fed by an Agilent 33210A generator and created ac magnetic field with a frequency  $f = 0\div 50$  kHz. A dc magnetic field  $H = 0\div 400$  Oe was created by the Helmholtz coils. The signal from electrodes of the PE-layer was registered by an SR844 lock-in amplifier.

Figure 2 shows measured dependence of the voltage  $u$  generated by the PE layer on the frequency of ac magnetic field  $h$ . Near the frequencies of 8.5, kHz and 29 kHz, resonance peaks are visible. The peak with a frequency of 8.5 kHz, a height of  $u_r = 45$  mV, and a quality factor of  $Q \approx 20$ , as shown by the calculation, corresponds to the main mode of bending vibrations of the structure.

Figure 3 shows the dependence of the ME-voltage  $u_r$ , generated by the structure at the resonance frequency  $f_r$ , on the field  $H$ , when excited by ac magnetic field with frequency  $f_r$  (linear ME-effect,  $u_r$  – curve 1) and at half frequency  $f_r/2$  (nonlinear frequency doubling [3],  $u_r^{(2)}$  – curve 2). As the field increases from zero,  $u_r$  first increases linearly, reaches a maximum of 45 mV at  $H_m \approx 2.5$  Oe, and then decreases monotonically and vanishes at the field of  $H = 400$  Oe. The amplitude of the second harmonic is maximum  $\sim 23$  mV at  $H = 0$  and decreases monotonically with increasing field, turning to zero already at  $H \approx 5$  Oe.

As can be seen from the research results, despite the small value of  $\lambda_s$ , a rather strong ME-transformation is observed in the hematite-PZT structure. Apparently, this is due to large value of the piezomagnetic modulus of hematite  $q = \partial\lambda(H)/\partial H$  (where  $\lambda(H)$  is the field dependence of the magnetostriction) in the magnetic fields range of  $-2.5$  Oe  $< H < 2.5$  Oe.

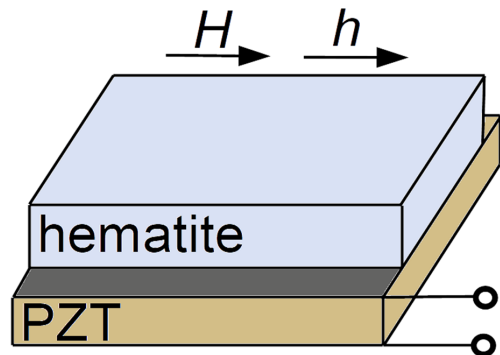


Figure 1. Schematic view of the sample.

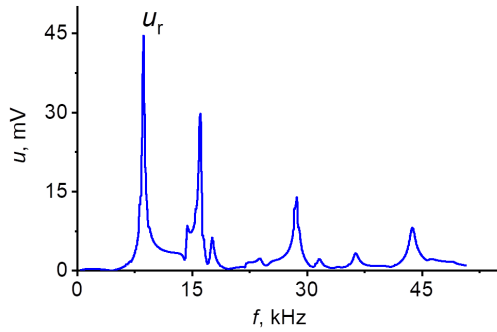


Figure 2. Dependence of the ME-voltage  $u$ , generated by the structure, on the ac magnetic field frequency  $f$  at  $h = 4$  Oe and  $H = 2$  Oe.

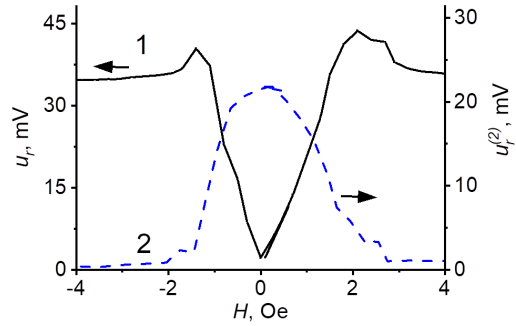


Figure 3. Field dependence of the ME-voltage, generated by the structure at the resonance frequency  $f_r = 8620$  Hz, when excited by ac field  $h = 4$  Oe with a frequency: 1 –  $f_r$ , 2 –  $f_r/2$ .

Thus, for the first time, linear and nonlinear ME-effects in the hematite-PZT layered structure were experimentally observed and investigated. The linear ME-coefficient at the resonance frequency of the fundamental mode of flexural acoustic oscillations of the structure was  $\alpha_E = 4.9$  V/(cm Oe<sup>2</sup>), and the nonlinear ME-coefficient was  $\alpha_{E2} = 0.6$  V/(cm Oe<sup>2</sup>). The results obtained can be used in the development of new solid-state electronic devices.

*This work was supported by the Russian Science Foundation, project No 22-29-01093.*

1. Y. Wang, J. Li, D. Viehland, *Materials Today*, **17**(6), 269–275 (2014).
2. R.Z. Levitin, A.S. Pakhomov, and V.A. Shchurov, *Soviet Phys. JETP*, **29**(4), 667–674 (1969).
3. D.A. Burdin, D.V. Chashin, N.A. Ekonomov et al., *JMMM*, **358-359**, 98–104 (2014).

## EFFECT OF A MELT-SOLUTION ON THE MAGNETIC PROPERTIES OF A SINGLE CRYSTAL WITH THE HUNTITE STRUCTURE

*V.R. Kuchsheva-Titova, I.A. Gudim, E.V. Eremin*

Kirensky institute of Physics, Federal Research Center KSC SB RAS, Krasnoyarsk, Russia

E-mail: [bb1995@mail.ru](mailto:bb1995@mail.ru)

In recent decades, crystals, one of the promising groups of compounds of rare-earth oxyborates with the huntite structure  $RM_3(BO_3)_4$  ( $R = Y, La - Lu$ ;  $M = Fe, Al, Cr, Ga, Sc$ ), which has a rhombohedral structure, have been actively studied. This structure is described by the space group R32 or P3121. The noncentrosymmetric structure makes these materials promising candidates for optical applications.

$RAI_3(BO_3)_4$  demonstrate giant values of magnetoelectric polarization. These compounds in the entire temperature range have a crystalline structure with space group R32. An increase in the magnetoelectric effect is also observed when ions in  $HoFe_3(BO_3)_4$  are replaced from  $Fe^{3+}$  to  $Ga^{3+}$ .

Taking into account that the replacement of the magnetic subsystem (Fe) in  $RM_3(BO_3)_4$  by the nonmagnetic subsystem (Al, Ga) leads to the fact that the magnetoelectric effect reaches gigantic values, it seems promising to study other subclasses of oxyborates with the huntite structure with one magnetic subsystem: for example, rare earth scandoborates  $RSc_3(BO_3)_4$ .

In this paper, we present data on the magnetic properties  $NdSc_3(BO_3)_4$  single crystals. In this compound, the system of small cations is represented by  $Sc^{3+}$  ions with a large ionic radius compared to  $Al^{3+}$  and other electronic structures.  $NdSc_3(BO_3)_4$  single crystals were grown from fluxes based on bismuth trimolybdate. Methods for growing crystals are described in detail in [1].

The magnetic properties were investigated on a vibrating magnetometer PPMS QuantumDesign (Shared Use Center of the FRC KSC SB RAS) in the temperature range 4.2–300 K and magnetic fields up to 9 T, and also on and also on the vibrating magnetometer of the original design [2].

Studies of magnetic properties were carried out in magnetic fields  $B = 0.1, 1, 3, 5, 6$  and 9 T, when the magnetic field is oriented along the  $c$ -axis of the third order and along the  $a$ -axis of the second order, perpendicular to the  $c$ -axis. Figure 1 shows the temperature dependences of the magnetization in the direction of the magnetic field along and perpendicular to the threefold axis.

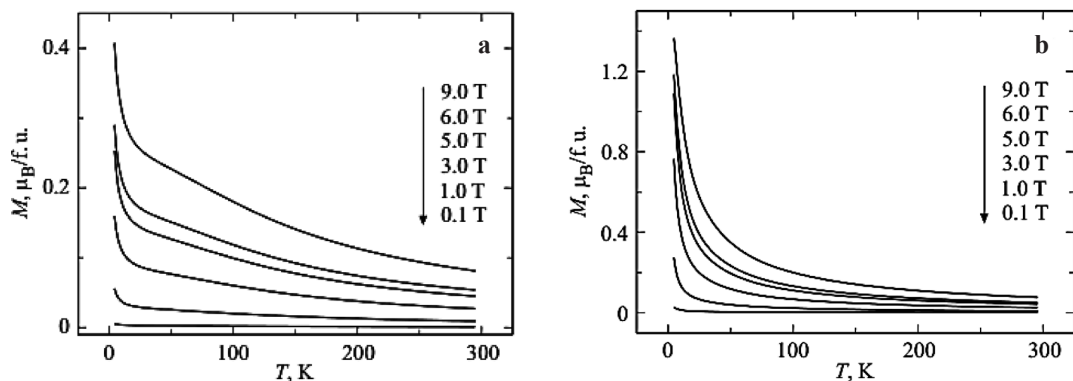


Figure 1. Temperature dependences of the magnetization of  $NdSc_3(BO_3)_4$  measured in various magnetic fields in the geometry  $B \parallel c$  (a) and  $B \perp c$  (b).



From Fig. 1 it can be seen that for all curves the dependences  $M(T)$  have a similar form typical for a paramagnet and differ only in magnitude.

*The study was supported by RSF-KRFS, project no. 22-12-20019.*

1. I.A. Gudim, E.V. Eremin, and V.L. Temerov, J. Crystal Growth, **312**, (2010) 2427.
2. A.D. Balaev, Yu.V. Boyarshinov, M.I. Karpenko, B.P. Khrustalev, PTE, **3**, 167 (1985).

## IRON OXIDATION STATE IN $\text{La}_{0.7}\text{Sr}_{1.3}\text{Fe}_{0.7}\text{Ti}_{0.3}\text{O}_4$ AND $\text{La}_{0.5}\text{Sr}_{1.5}\text{Fe}_{0.5}\text{Ti}_{0.5}\text{O}_4$ LAYERED PEROVSKITES: DIELECTRIC AND MAGNETIC PROPERTIES

*T.P. Gavrilova<sup>2</sup>, T.I. Chupakhina<sup>1\*</sup>, Yu.A. Deeva<sup>1</sup>, I.F. Gilmutdinov<sup>2</sup>, M.A. Cherosov<sup>2</sup>,  
I.V. Yatsyk<sup>2,3</sup>, F.G. Vagizov<sup>2</sup>, A.R. Yagfarova<sup>2</sup>, R.M. Eremina<sup>2,3</sup>*

<sup>1</sup>Institute of Solid State Chemistry of RAS (UB), Ekaterinburg, Russia

<sup>2</sup>Zavoisky Physical-Technical Institute, FRC Kazan Scientific Center of RAS, Kazan, Russia

<sup>3</sup>Institute of Physics, Kazan Federal University, Kazan, Russia

\*E-mail: [Chupakhina@yandex.ru](mailto:Chupakhina@yandex.ru)

Layered perovskite structures with the chemical formula  $\text{A}_2\text{BO}_4$ , (where A is a rare earth or alkaline earth element, and B is d-metals of the IV period of the periodic table), are widely known and intensively studied, since they possess a multifunctional set of properties that are promising for practical applications. Strontium titanate  $\text{Sr}_2\text{TiO}_4$  is considered as a dielectric material with a high Q-factor.

From the point of view of dielectric properties  $\text{Sr}_{2-x}\text{La}_x\text{Ti}_{1-x}\text{Fe}_x$  ( $x = 0.5$  и  $0.7$ ) are materials with a high dielectric constant  $\varepsilon \approx 10^5$  (Fig. 1).

One of the reasons for the high values of the dielectric constant of these oxides is small polaron hopping conduction mechanism presumably due to the different valence state of Fe. One can suggest that observed in strontium titanate (with conjugated La/Fe substitution in positions A and B) effects can be due to the presence of half-filled d-orbitals of  $\text{Fe}^{3+}$  ions, which are usually in a high spin state, as well as the probability of the existence of mixed-valence iron ions. Thus a deep understanding and explanation of high dielectric constant in  $\text{Sr}_{2-x}\text{La}_x\text{Ti}_{1-x}\text{Fe}_x$  ( $x = 0.5$  и  $0.7$ ) oxides requires a detailed investigation of their magnetic properties.

Magnetization measurements of  $\text{La}_{0.5}\text{Sr}_{1.5}\text{Fe}_{0.5}\text{Ti}_{0.5}\text{O}_4$  and  $\text{La}_{0.7}\text{Sr}_{1.3}\text{Fe}_{0.7}\text{Ti}_{0.3}\text{O}_4$  were reported in Ref. [1] and suggested that the investigated samples are in the paramagnetic state with strong antiferromagnetic correlation between spins of magnetic ions, because above  $T > 200$  K the  $M$ - $T$  curve (FC regime  $H = 0.1$  T) can be fitted by the Curie-Weiss law with negative values of the Weiss constant. Moreover, in the sample with a higher iron content  $\text{La}_{0.7}\text{Sr}_{1.3}\text{Fe}_{0.7}\text{Ti}_{0.3}\text{O}_4$  the sharp feature was clearly

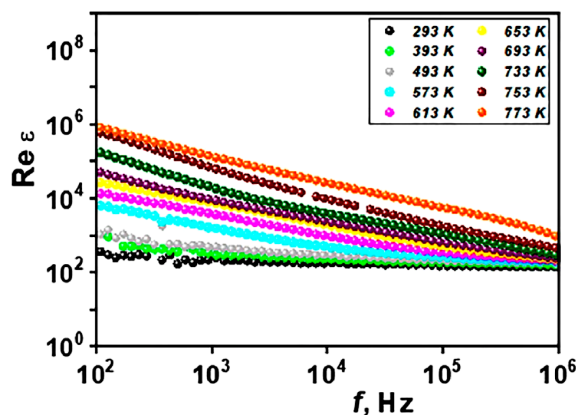


Figure 1. Frequency dependences of the dielectric constant for  $\text{Sr}_{2-x}\text{La}_x\text{Ti}_{1-x}\text{Fe}_x$  ( $x = 0.5$ ) at fixed temperatures.

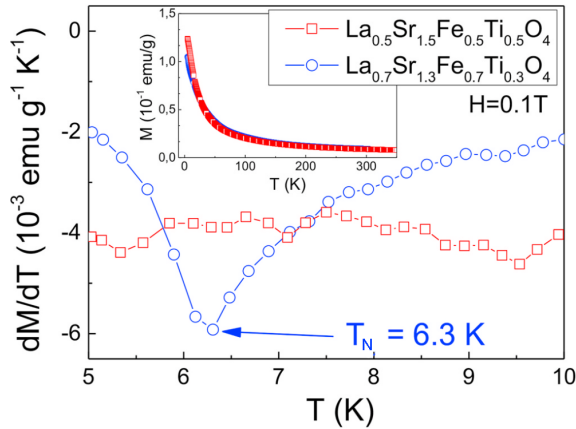


Figure 2. Temperature dependencies of the first derivative of the magnetization for  $\text{La}_{0.7}\text{Sr}_{1.3}\text{Fe}_{0.7}\text{Ti}_{0.3}\text{O}_4$  and  $\text{La}_{0.5}\text{Sr}_{1.5}\text{Fe}_{0.5}\text{Ti}_{0.5}\text{O}_4$  measured in FC regime in the external magnetic field  $H = 0.1$  T. Inset shows the temperature dependence of the magnetization of both samples [1].

detected at the temperature about 6 K (Fig. 1), that most probably corresponds to the phase transition to the antiferromagnetically (AFM) ordered state. The phase transition to AFM state is confirmed by further ESR experiments, where the drop decrease in the integral intensity of the paramagnetic line is observed below  $T = 50$  K. In addition to above mentioned experiments the magnetization measurements in FC-ZFC regimes in low magnetic field  $H = 10$  mT were performed to determine the temperature below which magnetic correlations become dominant over thermal fluctuations. The ZFC-FC splitting was already observed in  $\text{La}_{0.7}\text{Sr}_{1.3}\text{Fe}_{0.7}\text{Ti}_{0.3}\text{O}_4$  below  $T_{\text{split}} = 150$  K, while in  $\text{La}_{0.5}\text{Sr}_{1.5}\text{Fe}_{0.5}\text{Ti}_{0.5}\text{O}_4$  it was observed only below  $T_{\text{split}} = 120$  K. This splitting suggests the presence of short-range magnetic correlations in the investigated samples that can be proved at the next step by isothermal magnetization measurements as a function of the external magnetic field below 120–150 K. Nonlinear behavior of  $M$ - $H$  curves was observed for both samples at  $T = 10$  K, while the ferromagnetic hysteresis loops were clearly detected in  $M$ - $H$  curves at temperatures 5 and 2 K.

The observed shift of the magnetic hysteresis loop is the typical manifestation of exchange bias effect, so one can suggest the presence of two different types of magnetic phases, which are exchange coupled to each other. We can suggest that in the investigated here  $\text{La}_{0.5}\text{Sr}_{1.5}\text{Fe}_{0.5}\text{Ti}_{0.5}\text{O}_4$  and  $\text{La}_{0.7}\text{Sr}_{1.3}\text{Fe}_{0.7}\text{Ti}_{0.3}\text{O}_4$  layered perovskites iron ions can be in different valence states, that is confirmed by Mössbauer experiments. The exchange interaction between  $\text{Fe}^{3+}(3d^5)$  and  $\text{Fe}^{4+}(3d^4)$  have the complex nature and lead to the electronic phase separation – the simultaneous existence of the paramagnetic phase and magnetically correlated regions, which form due to the mixed-valence iron ions. The paramagnetic phase with strong antiferromagnetic correlation exists in both samples, while the second phase is ferromagnetically and ferrimagnetically correlated regions in  $\text{La}_{0.5}\text{Sr}_{1.5}\text{Fe}_{0.5}\text{Ti}_{0.5}\text{O}_4$  and  $\text{La}_{0.7}\text{Sr}_{1.3}\text{Fe}_{0.7}\text{Ti}_{0.3}\text{O}_4$ , respectively.

1. T.I. Chupakhina, N.V. Melnikova, N.I. Kadyrova, Y.A. Deeva, A.A. Mirzorakhimov, T.P. Gavrilova, I.F. Gilmudtinov, R.M. Eremina, J. Solid State Chem., **292**, 21687 (2020).

## FABRICATION AND ANALYZIS OF 2D COMPOSITE MATERIALS BASED ON PIEZOELECTRIC POLYMERS AND FERROMAGNETIC NANOPARTICLES

*S.A. Vorontsov\**, *K.V. Sobolev*, *V.G. Kolesnikova*, *A. Omelyanchik*, *V.V. Rodionova*, *K. Levada*

Immanuel Kant Baltic Federal University, Kaliningrad, Russia

\*E-mail: [stanisvorontsov@gmail.com](mailto:stanisvorontsov@gmail.com)

In the recent years the interest in composite materials studies has grown. Due to their molecular structure, polymers have a wide range of physical and chemical properties, among which are elasticity, thermoplasticity and mechanical strength. In the manufacturing sector the use of polymers allows to solve the set of problems for a wide range of industries, including materials for medicine and medical applications [1]. Today the most perspective polymers for industry and biomedical applications are piezoelectric polymers, such as polyvinylidene fluoride (PVDF) and polylactide (PLA) [2]. To increase the effectivity of the polymer-based composites in biomedicine the ferromagnetic fillers, such as nanoparticles based on iron salts ( $\text{CoFe}_2\text{O}_4$ ), are used [3]. By adding the ferromagnetic powder to the piezoelectric polymer a unique composite with increased magneto-electric effect is formed.

This work studies the series of samples based on PVDF polymer, containing ferromagnetic nanoparticles ( $\text{CoFe}_2\text{O}_4$ ) in mass percentages of 5%, 10%, 15%, and 20%, obtained by the Doctor Blade method. We used a scanning electron microscope (SEM) to study the thickness of the polymer composites and detect defects on the composites surface; the atomic force microscopy (AFM) was used to study the surface topology and mechanical (determination of the stiffness and Young's modulus) and piezoelectric properties of the polymer film. X-ray powder diffractometer (XRD) was used for the study of the crystal and phase structure of the polymer films. A protocol for obtaining 2D composites based on PVDF with the addition of ferromagnetic nanoparticles was also developed.

Thus, a new technique for the fabrication of composite films was developed, and the technology for obtaining reproducible 2D composites with the constant parameters of thickness, dimensionality and surface roughness was worked out. Adhesive properties and Young's modulus were measured for each sample. The effect of the concentration of the ferromagnetic powder on the strength of the composite was established. In future, with the positive results of biological studies of polymer films as substrates for the growth of the cell cultures, it is proposed to use these materials for the development and creation of biomedical applications.

Acknowledge financial support of the Russian Science Foundation, project No. 21-72-30032, as a part of the development and research of multi-materials with magnetic nanocomponents for additive 3d-5d technologies.

1. P. Saxena, & P. Shukla, A comprehensive review on fundamental properties and applications of poly(vinylidene fluoride) (PVDF), *Advanced Composites and Hybrid Materials*, **4**(1), 8–26 (2021).
2. F.S. Senatov et al., Mechanical properties and shape memory effect of 3D-printed PLA-based porous scaffolds, *Journal of the Mechanical Behavior of Biomedical Materials*, **57**, 139–148 (2016).
3. A. Omelyanchik et al., Boosting magnetoelectric effect in polymer-based nanocomposites, *Nanomaterials*, **11**(5) (2021).

Section L.  
Magnetic soft matter

---

## TISSUE-MIMETIC MAGNETOACTIVE ELASTOMERS BASED ON BOTTLEBRUSH POLYMER MATRICES

S.A. Kostrov<sup>1</sup>, S.S. Sheiko<sup>2</sup>, E.Yu. Kramarenko<sup>1\*</sup>

<sup>1</sup>Faculty of Physics, Lomonosov Moscow State University, Moscow, Russian Federation  
<sup>2</sup>Department of Chemistry, University of North Carolina at Chapel Hill, Chapel Hill, USA

\*E-mail: [kram@polly.phys.msu.ru](mailto:kram@polly.phys.msu.ru)

Magnetoactive polymer materials, in particular, magnetoactive elastomers (MAEs) based on polymer networks filled with ferromagnetic micro- and/or nanoparticles are attracting considerable attention nowadays. A synergetic combination of polymer viscoelasticity and magnetic properties of filler particles produces unique phenomena in these composites, namely, significant changes in the mechanical, viscoelastic, deformational, magnetic, dielectric, surface and other properties of MAEs [1, 2] in magnetic fields. Due to their magnetic response, MAEs are promising for a wide range of practical applications as elements of damping and sealing devices, lubricants, polishing agents, sensors, etc [4].

The magnetic response of the MAEs is largely determined by the properties of the polymer matrices. The softer the matrix is, the more pronounced rearrangement of magnetic particles takes place in magnetic field, leading to higher changes in physical properties of MAEs. In this talk, we report on new polymer media based on so-called bottlebrush macromolecules, i.e. polymers with densely grafted side chains, which allow to produce super-soft, solvent-free MAEs with a giant magnetorheological effect.

In the first type of MAEs, bottlebrush polymers are covalently cross-linked forming 3d chemical networks. We demonstrate that the combination of bottlebrush network architecture and magnetically responsive microparticles empowers synergistic enhancement on MAE performance, allows to finely tune the MAE mechanical properties in a broad range even without a magnetic field, and mimic the stress-strain response of assorted skin tissues. In the presence of a magnetic field, additional control over MAE's mechanical properties enables not only three orders of magnitude modulus enhancement but also fundamentally changes the viscoelastic nature of bottlebrush MAEs due to almost 10-fold decrease of the damping factor.

The MAEs of the second type are based on bottlebrush copolymers with a small fraction of segregating side chains. The micellar aggregates formed in the course of copolymer self-assembly act as physical crosslinks, ensuring the formation of bottlebrush elastomers at room temperature. The destruction of the physical network takes place upon heating, and the medium response switches from highly elastic to viscous. In the viscous state, a free rearrangement of magnetic particles in an applied magnetic field becomes possible, and the new magnetic structures can be fixed within the material after cooling. Reversible transitions between the elastomeric and viscous states of the dispersion medium make it possible to repeatedly reconfigure the aggregates of magnetic particles and, therefore, *in situ* control the physical properties of composites combining temperature and magnetic field effects. The developed MAEs give new opportunities in the design of actuators and active vibration insulation systems.

*Financial support by RSF (grant no. 19-13-00340-II) is gratefully acknowledged.*

1. M. Shamonin, E.Yu. Kramarenko. In: Novel Magnetic Nanostructures, Elsevier, 2018, pp. 221–245.
2. E.Yu. Kramarenko, G.V. Stepanov, A.R. Khokhlov, INEOS OPEN, **2**, 178–184 (2019).
3. Y. Li, J. Li, J.; W. Li, H. Du., Smart Mater. Struct., **23**, 123001 (2014).
4. S.A. Kostrov, E. Dashtimoghadam, A.N. Keith, S.S. Sheiko, E.Yu. Kramarenko, ACS Appl. Mater. Interfaces, **13**, 38783–38791 (2021).

## MATHEMATICAL AND COMPUTER MODELLING OF THE EFFECTS OF INTERACTIONS, STRUCTURE FORMATION, AND POLYDISPERSITY ON THE DYNAMIC MAGNETIC SUSCEPTIBILITY AND MAGNETIC RELAXATION OF FERROFLUIDS

*A.O. Ivanov<sup>1\*</sup>, P.J. Camp<sup>2</sup>*

<sup>1</sup>Department of Theoretical and Mathematical Physics, Institute of Natural Sciences and Mathematics, Ural Federal University, Ekaterinburg, Russian Federation

<sup>2</sup>School of Chemistry, University of Edinburgh, Edinburgh, Scotland, United Kingdom

\*E-mail: [Alexey.Ivanov@urfu.ru](mailto:Alexey.Ivanov@urfu.ru)

Linear response theory relates the decay of equilibrium magnetization fluctuations in a ferrofluid to the frequency-dependent response of the magnetization to a weak ac external magnetic field. The characteristic relaxation times are strongly affected by interactions between the constituent particles. Similarly, the relaxation of an initially magnetized system towards equilibrium in zero field occurs on a range of timescales depending on the structure of the initial state, and the interactions between the particles. The topic of this contribution is the relationship between the time scales for the linear response, and the time scales for relaxation from an initially aligned state.

In this work, ferrofluids are modelled as colloidal suspensions of spherical particles carrying point dipole moments, and undergoing Brownian motion. Recent theoretical and simulation work [1] on the relaxation and linear response of these model ferrofluids is reviewed, and the effects of interactions, structure formation, and polydispersity on the characteristic time scales are outlined.

It is shown that:

(i) in monodisperse ferrofluids, the timescale characterizing the collective response to weak fields increases with increasing interaction strength and/or concentration;

(ii) in monodisperse ferrofluids, the initial, short-time decay is independent of interaction strength, but the asymptotic relaxation time is the same as that characterizing the collective response to weak fields;

(iii) in the strong-interaction regime, the formation of self-assembled chains and rings introduces additional timescales that vary by orders of magnitude; and

(iv) in polydisperse ferrofluids, the instantaneous magnetic relaxation time of each fraction varies in a complex way due to the role of interactions; the interactions cause the small (fast) particles to relax asymptotically at a rate dictated by the large (slow) particles, which dominate the instantaneous magnetization to which the small particles are coupled.

*Support by the Ministry of Science and Higher Education of the Russian Federation (Ural Mathematical Center project, Agreement No. 075-02-2022-877) is acknowledged.*

1. A.O. Ivanov and P.J. Camp, *J. Mol. Liq.*, **356**, 119034 (2022).

## MAGNETIC PROPERTIES OF MAGNETIC ELASTOMERS FILLED WITH SPHERICAL AND FLAKE-LIKE PARTICLES

*A.B. Dobroserdova*<sup>1\*</sup>, *S.S. Kantorovich*<sup>1,2</sup>

<sup>1</sup>Department of Theoretical and Mathematical Physics, Institute of Natural Sciences and Mathematics, Ural Federal University, Ekaterinburg, Russia

<sup>2</sup>Computational Physics, Faculty of Physics, University of Vienna, Vienna, Austria

\*E-mail: [Alla.Dobroserdova@urfu.ru](mailto:Alla.Dobroserdova@urfu.ru)

In this study we focus on magnetic response of magnetic elastomers which are systems consisting of magnetisable particles embedded in a non-magnetic elastomeric matrix. Such systems have wide range of applications, from technical applications to medicine. For example, the design of magnetically controlled adaptive damping devices, stiffness tunable mounts, vibrational absorbers, force sensors and artificial muscles, soft actuators and micromanipulators. The mechanical and rheological behaviour of such materials, their shape and physical properties can be controlled using an applied external magnetic field. It is important to note that in the case of magnetoactive elastomers, sufficiently weak fields can be used in contrast to natural soft magnetic materials, which is an undoubted advantage of such systems.

We study magnetoactive elastomers using Molecular Dynamics Simulations and consider two types of magnetic filler. We have modeled elastomers filled with magnetic particles, which are represented by spherical particles with point magnetic dipoles located in the center of the particles. Magnetic particles interact via a magnetic dipole-dipole potential, which describes the attraction of magnetic particles. The short-range repulsion is described by the Weeks-Chandler-Andersen potential. We use Zeeman energy to take into account the interaction between magnetic particles and an applied external magnetic field. In order to consider elastic interactions in the system we can use the classical harmonic potential. In computer simulations, such an interaction can be represented as a harmonic spring that holds the particles. It is possible to change the elasticity of a non-magnetic matrix by changing the rigidities of the springs.

The second type of the magnetic filler is magnetic particles with the shape anisotropy. In order to model such complex particles, we need to surround magnetic particle with non-magnetic ones, the centers of which are located in one plane which is perpendicular to the dipole moment of the magnetic particle (the base of a particle is an ellipse). As a result, the particle will have a shape close to the shape of flakes. After that we need to model an elastic matrix (where magnetic particles with a flake-like shape in the form of flakes are suspended). In this case we use four harmonic springs to constraint the translational and rotational motion. Two of them will hold the extreme non-magnetic particles located on the major axis of the ellipse, the others – the extreme non-magnetic particles on the small axis.

For such systems we can measure magnetisation curves, radial distribution functions and other characteristics. All measurements will be carried out for different values of the magnetic field strength, spring rigidities. Also we plan to plot the First Order Reversal Curves (FORCs) distribution diagrams using the classical approach by Ch. Pike [3] for several systems under study.

Computer simulations are performed using the Vienna Scientific Cluster (VSC) and the cluster of Ural Federal University.

*Support by RSF 19-12-00209 is acknowledged.*

1. J. Carlson, M.R. Jolly, Mr fluid, foam and elastomer devices, *Mechatronics*, **10** (2000) 555–569.
2. Y. Li, J. Li, W. Li, H. Du, A state-of-the-art review on magnetorheological elastomer devices, *Smart Mater. Struct.*, **23**, 123001 (2014).
3. C. R. Pike et al., *J. Appl. Phys.*, **85**, 6660 (1999).



## MAGNETICALLY INDUCED STRUCTURAL TRANSITIONS IN LIQUID CRYSTALS DOPED WITH CARBON NANOTUBES: BRIDGING FROM MOLECULAR-STATISTICAL TO CONTINUUM THEORY

*D.A. Petrov*

Physics of Phase Transitions Department, Perm State University, Perm, Russia

E-mail: [petrovda@bk.ru](mailto:petrovda@bk.ru)

In the physics of liquid crystals (LC) and composite materials based on them, the continuum theory [1, 2] has proved to be useful. Due to its relatively simple nature, the theory enables a good description of experimentally observed magneto-orientational transitions. However, the weak point of the continuum theory is the lack of consideration for the temperature effect on the orientational structure of both the LC carrier medium and the impurity subsystem. In this approach, all material parameters of the LC composite are considered constant. In turn, the molecular-statistical theory allows taking into account both temperature and field dependences of the ordering degree in the composite components. We have proposed an approach based on the mean-field theory for a suspension of carbon nanotubes in a nematic matrix that makes it possible not only to describe the possible structural transitions associated with temperature changes but also to consider the orientation transitions induced by the influence of the magnetic field. Thus, we can indicate a connection between the molecular-statistical and continuum theories.

As the object of the study, we consider a composite material, which is a suspension of carbon nanotubes in a nematic LC with a negative anisotropy of the diamagnetic susceptibility. Since carbon nanotubes have an abnormally high and positive value of the diamagnetic susceptibility anisotropy (compared to an impurity-free LC, the difference is several orders of magnitude), the magnetic field can induce orientation phases with a biaxial ordering of the LC and the impurity subsystem. This happens because the long axes of nanotubes tend to orient in the field direction, and the long axes of LC molecules, due to the negative diamagnetic anisotropy, in the direction orthogonal to the field. To describe the magneto-orientational response of the LC composite, we used a previously proposed tensor form of the free energy record [3]. There, in addition to the dispersion interactions, the steric repulsions of the carbon nanotubes were taken into account, i.e., the excluded volume effects were taken into account.

It was found that three orientational phases (planar, homeotropic, and angular) are possible in the spatially homogeneous suspension, depending on the magnetic field strength. The planar phase corresponds to the state with the parallel orientation of the major nematic order axes, i.e. the LC and nanotube directors. The homeotropic phase corresponds to the orthogonal mutual orientation of the LC and nanotube directors. The angular phase corresponds to an intermediate state between the planar and homeotropic phases. It was found that with an increasing magnetic field, the sequence of the planar phase – angular phase – homeotropic phase transitions can be realized. We found the dependences of the transition fields between the orientational phases in the composite on the nanotube concentration, temperature, and energy of the orientational coupling between the impurity and the LC matrix. The temperature and field dependences of the order parameters of the LC and impurity subsystems were constructed, and the degree of biaxiality of the suspension components in each orientation phase was determined. It is found that when the orientation coupling of the LC matrix and carbon nanotubes is weak, a direct transition from the planar to the homeotropic phase, bypassing the angular phase, may occur as the magnetic field increases.

The proposed approach is the most universal and will make it possible to describe further the effect of temperature on orientation transitions in LC suspensions of dipole particles, which has not been done before.

*This research was supported by the Foundation for the Advancement of Theoretical Physics and Mathematics “BASIS”.*

1. K. Koch, M. Kundt, A. Eremin, H. Nadasi, A.M. Schmidt, *Phys. Chem. Chem. Phys.*, **22**, 2087 (2020).
2. S. Burylov, D. Petrov, V. Lacková, K. Zakutanská, N. Burylova, A. Voroshilov, V. Skosar, F. Agresti, P. Kopčanský, N. Tomašovičová, *J. Mol. Liq.*, **321**, 114467 (2021).
3. D.A. Petrov, A.N. Zakhlevnykh, *J. Mol. Liq.*, **287**, 110901 (2019).

## MAGNETIC AND STRUCTURAL EQUILIBRIUM PROPERTIES OF A SUSPENSION OF MAGNETIC MULTICORE NANOPARTICLES

*A.A. Kuznetsov*<sup>1\*</sup>, *E.V. Novak*<sup>1</sup>, *E.S. Pyanzina*<sup>1</sup>, *S.S. Kantorovich*<sup>1,2</sup>

<sup>1</sup>Ural Federal University, Ekaterinburg, Russia

<sup>2</sup>University of Vienna, Wien, Austria

\*E-mail: [andrei.kuznetsov@urfu.ru](mailto:andrei.kuznetsov@urfu.ru)

Magnetic multicore nanoparticles (MMNPs) are dense clusters of single-domain magnetic nanocrystals embedded in a rigid non-magnetic matrix. Recently, MMNPs have attracted a lot of research attention due to their wide range of potential biomedical and biotechnological applications [1]. In this work, we combine Langevin dynamics simulations and statistical theory of dipolar systems to study equilibrium properties of a weakly concentrated suspension of MMNPs in a non-magnetic liquid. We model MMNPs as spherical impenetrable particles filled randomly and uniformly with spherical magnetic grains. Each grain has a magnetic moment of constant magnitude which can freely rotate under the action of applied magnetic fields and thermal fluctuations. All grains interact with each other via the dipole-dipole interaction potential. The system is subjected to a uniform magnetic field and maintained at a constant temperature. ESPResSo simulation package [2] is used for simulations. Theoretical treatment is based on the modified mean-field approach [3].

Simulation results demonstrate that equilibrium magnetic properties of the suspension depend crucially on the dipolar coupling constant  $\lambda = \mu^2/\sigma^3k_B T$ , which is the ratio between the characteristic dipolar interaction energy of two grains and the thermal energy ( $\mu$  is the grain magnetic moment,  $\sigma$  is its diameter). Increasing  $\lambda$  leads to a non-linear increase in the suspension initial magnetic susceptibility. For small and moderate values of  $\lambda$ , this behavior can be accurately described theoretically, but at  $\lambda \sim 10$  the theory strongly underestimates numerical results. At non-zero field, the discrepancies between theory and simulations arise even at smaller dipolar constants (Fig. 1a).

We interpret the anomalous magnetic response as a results of self-aggregation processes in the ensemble of MMNPs. For  $\lambda < 10$ , magnetic interactions between superparamagnetic MMNPs in

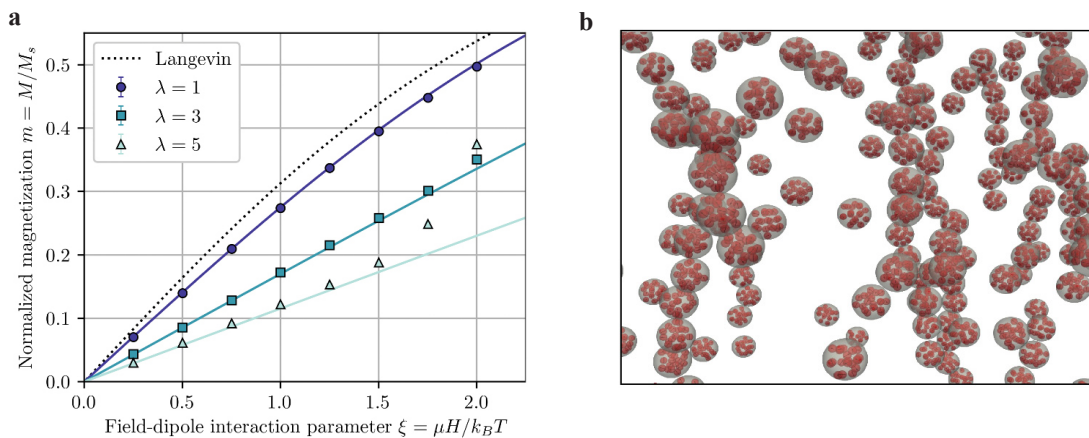


Figure 1. **a** Magnetization curves of a MMNP suspension at different dipolar coupling constants. Symbols – simulation results, solid lines – theory, dotted line – Langevin function (magnetization of an ideal paramagnetic gas). **b** Snapshot of a simulated system at  $\lambda = 5$  and  $\xi = 2$ , the field is directed vertically.

zero-field are insignificant and do not lead to the formation of aggregates. However, in large enough fields chain-like structures can be observed (Fig. 1b). It is shown based on a systematic cluster analysis of the simulation data that MMNPs constituting these structures are magnetized by the field much stronger than isolated ones.

*The work was supported by RSF (Grant No. 19-72-10033). Calculations were performed at the Ural Federal University cluster.*

1. S. Dutz, IEEE Trans. Magn., **52** (2016).
2. <https://espressomd.org/>
3. A.O. Ivanov, O.B. Kuznetsova, Phys. Rev. E, **64**, 041405 (2001).

## FORMATION OF RING-SHAPED DEPOSITS DURING THE EVAPORATION OF DROPS OF MAGNETIC COLLOIDS IN MAGNETIC AND ELECTRIC FIELDS

*S.A. Semenova<sup>1</sup>, A.S. Drozdov<sup>2</sup>, Yu.I. Dikansky<sup>1\*</sup>*

<sup>1</sup>Department of Experimental Physics, NCFU, Stavropol, Russia

<sup>2</sup>ITMO University, Saint-Petersburg, Russia

\*E-mail: [dikansky@mail.ru](mailto:dikansky@mail.ru)

In this paper, we present the results of studying the features of deposit formation during the evaporation of magnetic colloid droplets placed on a solid substrate. We examined a water-based ferrofluid sample. In addition, we studied a sample of a ferrofluid based on kerosene. The average size of colloidal particles in both samples was about 10 nm.

We applied drops of magnetic fluid with a syringe onto the surface of a horizontal glass plate pretreated with a mixture of acetone and ethyl alcohol. Droplet evaporation occurred at room temperature in the room. When studying the features of the formation of ring deposits under the additional action of a magnetic field, glass with a drop was placed above the conical pole of an electromagnet. In this case, the tip of the electromagnet pole was located directly under the glass substrate opposite the center of the flat drop. When studying the influence of an electric field on the nature of the structure of the formed deposit, a needle electrode was lowered into a drop located on a conducting substrate. The voltage between the electrode and the conductive substrate was created using a stabilized power source. The analysis of the shape of the precipitates formed was carried out on the basis of the obtained images; to construct profiles of the relative thickness of the precipitate of the dried drop, a technique similar to that described in [1] was used.

Studies have shown that the evaporation of drops of both samples of magnetic colloids located on a solid substrate leads to the formation of ring structures similar to those studied earlier in a number of works (for example, in [2–4]). As an example, Fig. 1a shows a photograph of such a deposit formed during the evaporation of a drop of a water-based sample.

The impact of an inhomogeneous magnetic field with the configuration described above significantly changes the deposit structure: in this case, the formation of a ring around the drop perimeter was not observed, while a round spot with a greater thickness was formed around the drop center than at the drop edges (Fig. 1b).

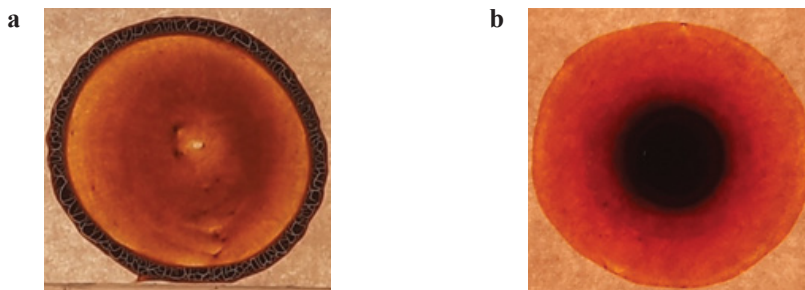


Figure 1. Photos of ring-shaped deposit after the drop of magnetic fluid has dried: **a** without a magnetic field, **b** under the action of a non-uniform magnetic field.

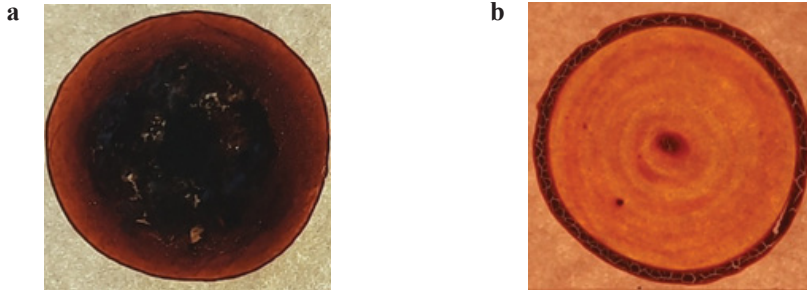


Figure 2. Photos of ring-shaped deposit after drops evaporation in electric field: **a** substrate has a negative potential, **b** substrate has a positive potential.

The control of deposit formation was also possible with an electric field. On Fig. 2 shows photographs of deposits formed in an electric field at a potential difference between the electrodes of 5 V. In Fig. 2a the substrate has a negative potential, in Fig. 2b – positive potential. The additional action of the electric field during the drying of the drop in a nonuniform magnetic field leads to a change in the shape and structure of the deposit. The deposit structure depends on the direction of the electric field. The results obtained for the formation of sediment architecture were discussed using the methods of dissipative dynamics previously used in [5].

*Support by the Ministry of Science and Higher Education of Russia (project No. 0795-2020-0007) is acknowledged.*

1. Y.I. Dikanskii, A.R. Zakinyan, L.I. Khalupovskaya, V.I. Goncharov, N.V. Demidova, *Colloid J.*, **81**(5), 501–506 (2019).
2. R.G. Deegan, *Phys. Rev. E*, **61**, 475–485 (2000).
3. H. Siringhaus, T. Kawase, R.H. Friend, T. Shimoda, M. Inbasekaran, W. Wu, E.P. Woo, *Science*, **290**, 2123–2126 (2000).
4. V.V. Vysotskii, O.Y. Uryupina, I.N. Senchikhin et al., *Colloid J.*, **75**, 142–149 (2013).
5. P.V. Lebedev-Stepanov, R.M. Kadushnikov, S.P. Molchanov et al., *Nanotechnol. Russia*, **8**, 137–162 (2013).

## DYNAMIC RESPONSE OF AN ENSEMBLE OF INTERACTING MAGNETIC PARTICLES: THE INFLUENCE OF AC MAGNETIC FIELD AMPLITUDE

*E.A. Elfimova\**, *M.S. Rusanov*, *V.C. Zverev*

Ural Federal University, Ekaterinburg, Russia

\*E-mail: [Ekaterina.Elfimova@urfu.ru](mailto:Ekaterina.Elfimova@urfu.ru)

Based on numerical results of dynamic susceptibility, a simple theory of the dynamic response of an ensemble of interacting magnetic particles to an ac magnetic field is obtained that includes both the effects of interparticle dipole-dipole interactions and the dependence on field amplitude. We assume that particles undergo Brownian relaxation only. Interparticle interactions are incorporated in the theory using the so-called first-order modified mean-field approach. The new theory has the following important characteristics: in noninteracting regime at a weak ac field, it gives the correct single-particle Debye theory results; it expands the applicability of known theories valid for high concentrations [1] or large values of ac field amplitudes [2]. The susceptibility spectra are analyzed in detail. It is demonstrated that interparticle dipole-dipole interactions and an increase in field amplitude have an opposite effect on the dynamic response of the system, so that at certain field amplitudes, relaxation processes in the system of interacting particles are determined by the characteristic relaxation times for an ideal paramagnetic gas. The new theory correctly predicts the dynamic susceptibility and characteristic relaxation times of an ensemble of interacting magnetic particles at high ac field amplitudes as long as the Langevin susceptibility  $\chi_L \leq 1$ , which is a complex characteristic of the particle density and the intensity of dipole-dipole interactions.

1. A.O. Ivanov, V.S. Zverev, S.S. Kantorovich, *Soft Matter*, **12**, 3507–3513 (2016).
2. T. Yoshida, K. Enpuku, *Japanese Journal of Applied Physics*, **48**, 127002 (1-7) (2009).

## MAGNETIC PROPERTIES OF FRACTIONED FERROFLUID

*S.A. Kunikin\**, *A.G. Ispiryanyan*, *N.V. Gorkovenko*, *D.I. Dmitryevskaya*

Faculty of Physics and Technology, NCFU, Stavropol, Russia

\*E-mail: [skunikin@ncfu.ru](mailto:skunikin@ncfu.ru)

Magnetic nanoparticles are of great technological importance because of their use in ferrofluid, information storage system, medical applications and their interest in fundamental science, especially for addressing the fundamental relationships between magnetic properties and its structure [1, 2].

Recently, several methods were used to synthesize highly crystalline and uniformly sized magnetic nanoparticles of cobalt ferrite [3–6]. Most of these methods cannot be applied to a large scale and economic production because they require expensive and toxic reagents, complicated synthetic steps, high temperature for synthesis and long reaction time.

The aim of this investigation to clarify magnetic properties of magnetite fine particles. Samples for the study were made by fractioning of ferrofluid in high g centrifuge [3]. Ferrofluid was synthesized via co-precipitation method. Particles were stabilized by oleic acid surfactant and dispersed in dodecane carrier. Surfactant for the particles was oleic acid. The process of centrifuging produced at 7000 g for 30 minutes. Then sample was separated into 2 part: 1 – bottom, 2 – top. Magnetization was investigated via Cryogenic S700x SQUID magnetometer in temperature range from 10 to 300 K.

Magnetization investigations were performed through analysis of ZFC/FC curves. The main protocol for this measurement follows next step. Initially the sample was placed in magnetic gap of magnetometer at room temperature in liquid state. To reduce effect of Earth magnetic field the sample was demagnetized in field up to 0.01 of Earth magnetic field magnitude. After that it was cooled to 10 K. Then FC/ZFC data was acquired at 5 Oe field.

The results obtained in this way are shown in Fig. 1. Magnetization is standardized on the magnetization of the sample at a temperature of 290 K.

The data presented are of a fairly classical nature. At the same time, there are a number of features. First of all, it is worth noting a sharp drop in FC magnetization when reaching a temperature of 263 K. The indicated temperature corresponds to the crystallization temperature of the carrier – dodecane. The recession is most likely due to the unblocking of the Brownian degrees of freedom of individual particles. Another feature is the different position of the maximum on the ZFC

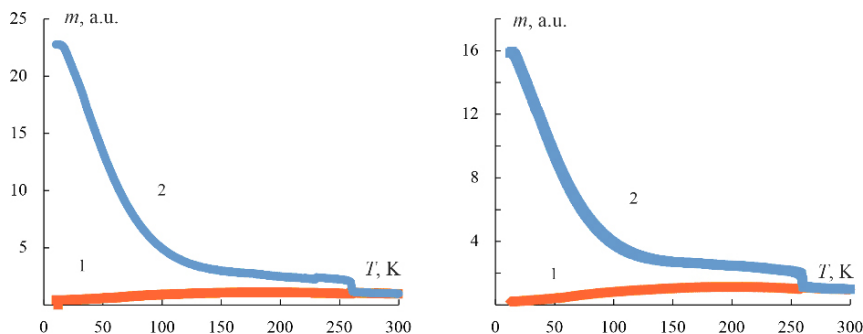


Figure 1. Magnetization of the sample No. 1 on the left and No. 2 on the right (1 – ZFC, 2 – FC).



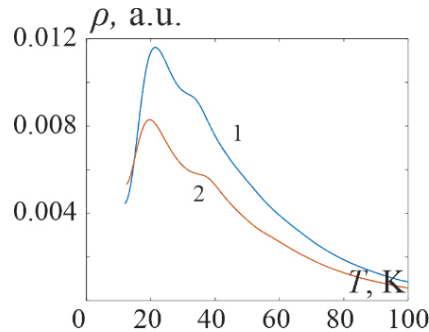


Figure 2. Magnetocrystalline anisotropy energy distribution in the studied samples.

magnetization dependence. For sample No. 1 – the lower fraction, it corresponds to a temperature of 250 K, for sample No. 2 – the upper fraction – 260 K.

Consider the process of magnetizing the sample in these measurement modes. On the one hand, the measurement of magnetization is carried out in a constant magnetic field. At the same time, the process is associated with a change in temperature – a change in the macroscopic state of the system. In papers [4–6] authors analyze the dynamics of changes in magnetization no longer over time, but in connection with changes in temperature. The solution of this model depends on the initial state of the system. Analysis of the model made it possible to determine energy distribution function (Fig. 2) due to magnetic energy of fine particles. One can find, the distributions are clearly different. The dependence for sample No. 2 shows that the maximum corresponds to higher temperatures, and therefore to higher energies. It is known that the energy of magnetocrystalline anisotropy is proportional to the volume of the particle. Therefore, we conclude that in sample No. 2 the fraction of particles with a large volume exceeds that for sample No. 1.

Thus, ultracentrifugurization allows fractionation of the magnetic colloid. With relatively simple magnetic measurements, we can confirm the separation of the original sample into fractions. At the same time, the obtained results can be subjected to significant criticism associated with the possible dependence of the parameters of magnetic anisotropy of nanoparticles on the temperature and particle size.

*Support by MSHE (proj. 0795-2020-0007 and RF 2296.61321X0029 (075-15-2021-687)) is acknowledged.*

1. E.A. Périgo, B. Weidenfeller, P. Kollár, J. Füzér, Past, present, and future of soft magnetic composites, *Appl. Phys. Rev.*, **5**, no. 3, 031301 (2018).
2. P. Biehl, M. von der Lühe, S. Dutz, F.H. Schacher, Synthesis, characterization, and applications of magnetic nanoparticles featuring polyzwitterionic coatings, *Polymers*, **10**, no. 1 (2018).
3. G. Kronkalns, M. Kodols, M.M. Maiorov: Structure, composition and magnetic properties of ferrofluid nanoparticles after separation, *Latv. J. Phys. Tech. Sci.*, **50**, no. 4, 56–61 (2013).
4. F. Tournus, A. Tamion, Magnetic susceptibility curves of a nanoparticle assembly II. Simulation and analysis of ZFC/FC curves in the case of a magnetic anisotropy energy distribution, *J. Magn. Magn. Mater.*, Elsevier, **323**, no. 9, 1118–1127 (2011).
5. F. Tournus, A. Hillion, A. Tamion, V. Dupuis, Effect of nonlinear superparamagnetic response on susceptibility curves for nanoparticle assemblies, *Phys. Rev. B – Condens. Matter Mater. Phys.*, **87**, no. 17 (2013)
6. F. Tournus, E. Bonet: Magnetic susceptibility curves of a nanoparticle assembly, I: Theoretical model and analytical expressions for a single magnetic anisotropy energy, *J. Magn. Magn. Mater.*, Elsevier, **323**, no. 9, 1109–1117 (2011).

## DYNAMICS OF MULTIPHASE MAGNETIC FLUID SYSTEMS UNDER VARIOUS EXTERNAL INFLUENCES

*P.A. Ryapolov\**, *E.V. Shel'deshova*, *E.A. Sokolov*, *D.A. Kalyuzhnaya*, *A.O. Vasilyeva*

Department of Nanotechnology, Microelectronics, General and Applied Physics,  
Southwest State University, Kursk, Russia

\*E-mail: [r-piter@yandex.ru](mailto:r-piter@yandex.ru)

Magnetic fluids have been known for a long time, but they still have not lost their relevance due to the unique combination of magnetic properties, fluidity and colloidal stability. One of their features is the ability to control its physical properties using various combinations of magnetic influences. The possibilities of “classical” magnetic fluids can be significantly expanded by adding one or more dispersed phases, which can be a gas bubble, drops of immiscible liquids, as well as solid magnetic and non-magnetic inclusions. Combined external influences on such multiphase magnetic systems with various flow options make it possible to achieve controlled dynamics both in millimeter-sized channels and in microchannels, which is of undoubted interest for microfluidics, where the usual methods of flow control do not work.

This report shows that the size of the formed non-magnetic inclusions in such a magnetic fluid system does not depend on the flow rate and hydrostatic pressure. The ability to control the size of non-magnetic liquid and gas inclusions by changing the parameters of the magnetic fluid and magnetic field can be used for microdosers or gas meters in microfluidic systems [1].

Also in this paper, we study the dynamics of the volume of a magnetic fluid levitating in a uniform magnetic field of an electromagnet experiencing an oscillatory shift. Samples with different physical parameters are considered, and the dependence of the magnetoviscous effect is studied. It is shown that the greatest influence on the dynamics of a magnetic fluid that experiences vibrational-shear and magnetoviscous effects is exerted by the microstructure of the sample and the presence of large magnetic particles. The results of the work can be used to develop a method for rapid testing of magnetic fluid samples, as well as to develop acceleration and vibration sensors based on magnetic fluids [2].

*The study was supported by the Russian Science Foundation grant No. 22-22-003113.*

1. P.A. Ryapolov, E.A. Sokolov, and E.B. Postnikov, *JMMM*, **549**, 169067 (2022).
2. P.A. Ryapolov, V.M. Polunin, E.V. Shel'deshova, *JMMM*, **496**, 165924 (2020).

## SUPERPARAMAGNETIC EFFECTS IN LONGITUDINAL DYNAMIC MAGNETIC SUSCEPTIBILITY OF UNIAXIAL NANOPARTICLES SUSPENDED IN A LIQUID

*A.V. Lebedev<sup>1</sup>, M.A. Koskov<sup>1</sup>, I.S. Poperechny<sup>1,2\*</sup>*

<sup>1</sup>Institute of Continuous Media Mechanics UB of RAS, Perm, Russia

<sup>2</sup>Perm State National Research University, Department of Phase Transitions Physics, Russia

\*E-mail: [poperechny@icmm.ru](mailto:poperechny@icmm.ru)

The properties of ensembles of magnetic nanoparticles, dispersed in various media, have been actively studied for several decades. Nevertheless, interest in these systems is only increasing. One of the main reasons is technological prospects. The list of possible applications of magnetic nanoparticles is constantly expanding. If earlier they were considered, mainly, as base elements for data storage devices with a high recording density, now a variety of biomedical applications are in focus: from immunoassay to controlled drug delivery [1]. Effective use of magnetic nanoparticles requires a clear understanding of their response to the applied magnetic field. The important thing is that ultradisperse magnets have specific, atypical for massive samples, properties. First of all, this is the orientation thermal fluctuations of the magnetic moment.

A desire to correctly take into account thermal effects has instigated the development of kinetic theories of the magnetic response of nanoparticles. In result, a significant progress in description of magnetization reversal in mechanically fixed superparamagnets has been achieved [2]. However, the theory of remagnetization of suspensions of nanoparticles is much less developed. This applies even to low-concentrated samples, in which the interparticle interaction can be considered negligible. Superparamagnetic particles suspended in a liquid obviously have rotational degrees of freedom. Therefore, their magnetic moment has not one, but two mechanisms of reorientation with respect to a given direction: random rotations relative to the crystallographic axes of the particle and rotation together with its “skeleton”. Thus, the kinetics of the system’s magnetization in this case represents random walks in a multidimensional configuration space. The fundamentals of the theory of this process were created in [3], where an equation was obtained for the joint distribution function of the directions of the magnetic moment of a particle and its anisotropy axis. In the particular case when the internal (also called superparamagnetic) diffusion of the magnetic moment is not taken into account, this equation corresponds to the so-called “hard dipole” approximation. It is well known that the latter predicts a simple Debye expression for the dynamic susceptibility of a dilute suspension of nanoparticles if there is no stationary magnetizing (bias) field. The Cole-Cole diagram in this case is just a semicircle.

Application of the bias field, together with AC component, allow one to obtain additional information about the kinetic properties of a magnetic suspension. Our calculations showed that in the presence of a static magnetic field the linear response of an ensemble of noninteracting hard magnetic dipoles becomes multimode: the dynamic susceptibility of such a system is a superposition of several Debye-type terms. The relaxation times corresponding to these modes are close to each other; they decrease with the growth of the magnetizing field, so the maximum of the imaginary part of the dynamic susceptibility shifts to higher frequencies. However, the left (high-frequency) intersection point of the Cole-Cole curve with the abscissa axis does not depend on the value of the bias field.

To clarify the applicability of these results, we developed a more general theory of the linear response of superparamagnetic particles suspended in a liquid, taking into account the internal diffusion of the magnetization vector. For this purpose, we extended a method, presented in [4], to

solve the complete kinetic equation for the joint distribution function. In the constructed scheme, a kinetic operator that determines the evolution of the distribution function is introduced, and a representation in which it has a block-diagonal form is selected. The basis in this representation consists of bipolar harmonics, composed as an irreducible tensor product of two spherical functions, the arguments of which are the angular coordinates of the magnetic moment of the particle and its anisotropy axis. The kinetic equation written in matrix form was linearized and subjected to Fourier transformation. The numerical solution of the obtained algebraic equation by the matrix sweep method made it possible to find the frequency spectra (away from the microwave range) of the dynamic susceptibility of a dilute suspension of superparamagnetic particles at different temperatures and magnitudes of the bias field. It turned out that even in the absence of the latter, the response of the system was a superposition of plenty of modes and was not described by a simple Debye formula. Each mode is defined by the eigenvector and corresponding eigenvalue (it determines the inverse relaxation time) of the kinetic matrix. The analysis shows that all modes can be divided into two qualitatively different types. The first one includes modes that describe relaxation processes associated with random transitions of the magnetic moment of the particle over the energy barrier, that is, with the reorientation of the magnetization vector relative to the anisotropy axis. These reversals of the magnetic moment, certainly, accompanied the Brownian rotation of the particle in a surrounding liquid. The second type is formed by modes that correspond to superparamagnetic relaxation inside each of the energy wells. For a finite ratio of anisotropy energy to temperature, the reference relaxation times for the mentioned types of modes may differ by several orders of magnitude. Therefore, the imaginary part of the dynamic magnetic susceptibility generally has two frequency-separated maxima. For the same reason, Cole-Cole diagrams, when taking into account the superparamagnetic properties of particles, comprise not one, but two characteristic arcs. With an increase of the bias field, both of the indicated maxima shift to higher frequencies, and the junction point of the two arcs in the Cole-Cole diagram is displaced.

To verify these conclusions, we measured at room temperature dynamic magnetic susceptibility of two magnetic fluids with distinguishable properties. The first one had been prepared on basis of magnetite nanoparticles, while the second – cobalt ferrite nanoparticles. Note that the effective anisotropy constants for these ferrites differ at least by an order of magnitude. For both fluids magnetic phase had been dispersed in water and stabilized by a double surfactant layer. For the magnetic suspension of cobalt ferrite particles, the Cole-Cole diagram turned out to be of the quasi-Debye type, and position of its high frequency edge was independent of the bias field – in accordance with the rigid dipole model. However, for the magnetite suspension the results were beyond the scope of that theoretical approximation. In particular, it was found that the left edge of the Cole-Cole diagram was shifted with increase of the bias field, which means that superparamagnetic relaxation of magnetite nanoparticles plays an essential role in this case.

*Support by Russian Science Foundation (grant No. 22-22-00288) is acknowledged.*

1. Fei Xiong et al., *Drug Deliv. Industr. Pharm.*, **44**, 697–706 (2018).
2. W. T. Coffey, Yu. P. Kalmykov and S. V. Titov, *Thermal Fluctuations and Relaxation Processes in Nanomagnets*, World Scientific, Singapore (2020).
3. V. Stepanov, M. Shliomis, *Bull. Acad. Sci. USSR. Ph. Ser.*, **55**, 1042–1049 (1991) [in Russian].
4. I. Poperechny, *J. Mol. Liq.*, **299**, Art. no. 112109 (2020).

**MODELING OF THE PSEUDO-PLASTICITY EFFECT  
 INDUCED BY FORCED DEFORMATION OF A MAGNETOACTIVE  
 ELASTOMER UNDER EXTERNAL FIELD**

*O.V. Stolbov\*, Yu.L. Raikher*

Laboratory Dynamics of Disperse Systems, Institute of Continuous Media Mechanics,  
 Russian Academy of Sciences, Ural Branch, Perm, Russia

\*E-mail: [sov@icmm.ru](mailto:sov@icmm.ru)

In the framework of mesoscopic approach, a numerical experiment is performed on a magnetoactive elastomer (MAE) with magnetically soft filler. In the initial (field- and stress-free) state the tested sample is a regular elongated bar with 150 spherical particles spread randomly over its volume. The particle radius is distributed lognormally with the mean value 1 and dispersion 0.1. This mean value is taken for a unit of length, the sample dimensions are  $7.6 \times 7.6 \times 38$ , see Fig. 1a.

The simulation is accomplished similarly to those described in ref. [1]: the matrix is assumed to be a Hooken elastic continuum whereas the interparticle interaction is taken in the point dipole approximation. In result of minimization of the joint (magnetic+elastic) energy together with the work of the externally applied force – this is done for the given values of magnetic field and exerted force – one obtains the spatial distribution of the particles (they are movable) and their actual magnetic moments.

The pseudo-plasticity effect is demonstrated as follows. First, in step-by-step manner a uniform magnetic field is applied. Then in the field is set to halt, and according to the same protocol the external load is exerted on one of the end-walls of the sample, the other one is fixed on an unmovable plane. The mechanical stress may be varied both ways: it either increases or decreases. The results of simulation come out as the stress-strain dependences under a given field strength.

Two situations have been considered: the sample is stretched along its longest axis from its initial state (positive strain) and the sample is compressed along the same direction (negative strain). Each quasistatic process is cyclic: the stress is applied and then reduced to zero.

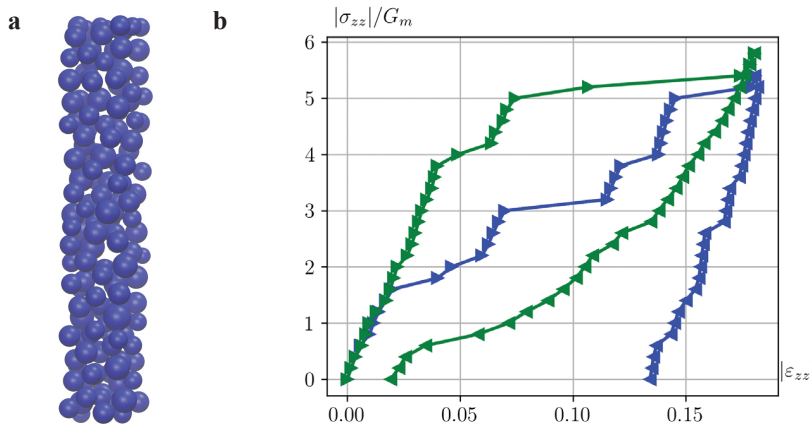


Figure 1. **a** Initial distribution of the particles; the bar faces are made invisible; **b** stress-strain cycles for the compression (green) and stretching (blue) protocols performed on the sample subject to a uniform magnetic field.

In both cases, the initial parts of the stress-strain curves (Fig. 1b) have the same slope. Further on, however, they become distinctively different: (i) the yield stress under compression is far higher than that under stretching; (ii) the hardening modulus for stretching exceeds that for compression; (iii) the residual strain that accompanies compression is greater than that caused by stretching.

1. O.V. Stolbov and Yu.L. Raikher, IOP Conference Series: Material Sci. and Eng., **581**, art. no. 012003 (2019).

## GMI DETECTION OF EPOXY COMPOSITES WITH VARIOUS CONCENTRATIONS OF IRON OXIDE MICROPARTICLES

*G.Yu. Melnikov*<sup>1\*</sup>, *L. Media Ranero*<sup>2</sup>, *A.P. Safronov*<sup>1</sup>, *A. Larrañaga*<sup>3</sup>, *A.V. Svalov*<sup>1</sup>,  
*G.V. Kurlyanskaya*<sup>1,2</sup>

<sup>1</sup>Ural Federal University, Ekaterinburg, Russia

<sup>2</sup>Depto Electricidad y Electrónica, Universidad del País Vasco UPV/EHU, Bilbao, Spain

<sup>3</sup>SGIKER, Basque Country University UPV/EHU, Leioa, Spain

\*E-mail: [grisha2207@list.ru](mailto:grisha2207@list.ru)

Giant magnetoimpedance effect (GMI) – is the change of the impedance of ferromagnetic conductor in the external magnetic field when the high frequency current flows through it [1]. This effect has very high sensitivity to a magnetic field useful for sensor applications. Multilayered films based on FeNi/Cu or FeNi/Ti layers demonstrate sensitivities up to 300 %/Oe [2]. Epoxy magnetic composites with Fe<sub>3</sub>O<sub>4</sub> magnetic particles are required in many applications: recording media, medicine and magnetic absorbers [3]. It is easily processed and obtained material with adjustable magnetic properties by selection the concentration of magnetic particles. Non-contact GMI detection of magnetic composites with various concentrations of magnetic particles is interesting task for non-destructive testing. It is also a method for evaluation of the properties of magnetic composites, including distribution of magnetic particles or even shape of the composite sample. In this work, magnetoimpedance thin film sensitive element was tested for evaluation of the properties of epoxy composites various concentration of iron oxide microparticles.

The composites were prepared with the commercial epoxy resin based on diglycidyl ether of bisphenol A (DGEBA, ED-20, Chimex Ltd., RF) filled with magnetite (Alfa Aesar, USA) submicron sized particles (Fe<sub>3</sub>O<sub>4</sub> phase – 94 wt.%; Fe<sub>2</sub>O<sub>3</sub> phase – 1 wt.%; FeO(OH) phase – 5 wt.%). ED-20 resin was mixed with triethylenetetramine (DOW Chemical, USA) in 6:1 weight proportion and with different loads of magnetite particles. Curing was done at room temperature for 24 hrs. The X-ray diffraction technique (BrukerD8 Discover) was employed for structural evaluation and scanning electron microscopy (SEM, JEOL JSM-640) was used for evaluation of the properties of microparticles and composites [4]. Cylindrical samples of epoxy composites were 5 mm in diameter (d), 4 mm in height (h). The content of magnetite filler was 0, 1, 2, 5, 9, 20 and 30 wt.%. Rectangular (0.5 × 10 mm) GMI [Fe<sub>21</sub>Ni<sub>79</sub>(100 nm)/Cu(3 nm)]<sub>5</sub>/Cu(500 nm)/[Cu(3 nm)/Fe<sub>21</sub>Ni<sub>79</sub>(100 nm)]<sub>5</sub> element was deposited by dc magnetron sputtering. The GMI was measured by Agilent HP E 4991. The magnetic composite cylinder inside the non-ferromagnetic tube was placed at a distance of 1.1 ± 0.2 (mm) above the GMI element surface (Fig. 1a) and its axis was perpendicular to the long side of the element. Magnetic cylinder was displaced along the axis perpendicular to the long side of the GMI element (OX axis). The magnetization of the magnetic cylinders was directed along the OY axis being close to remanent magnetization. For GMI effect description GMI ratio was used:  $\Delta Z/Z(H) = 100\% \cdot (Z(H) - Z(H_{\max})) / Z(H_{\max})$ , where  $H_{\max} = 100$  Oe. GMI response on magnetic cylinders was calculated as:  $\Delta(\Delta Z/Z(H)) = \Delta Z/Z_{\text{control}} - \Delta Z/Z_{\text{position}}$ , where  $\Delta Z/Z_{\text{control}}$  is the total impedance GMI ratio with the control (concentration of 0%);  $\Delta Z/Z_{\text{position}}$  is the total impedance GMI ratio with the magnetic cylinder located in the certain position. Magnetic properties of magnetic composite were measured by VSM magnetometer.

The structure of the epoxy composites depends on the microparticles concentrations. Figure 1b shows some selected examples. As the concentration of magnetic particles in composites increases, specific magnetic moment linearly increases. The specific magnetic moment of saturation of magnetic microparticles, calculated from the magnetic measurements of the composite ( $m_s = 65$  emu/g) is consistent with the values for pure magnetic particles. Remnant magnetization of all composites

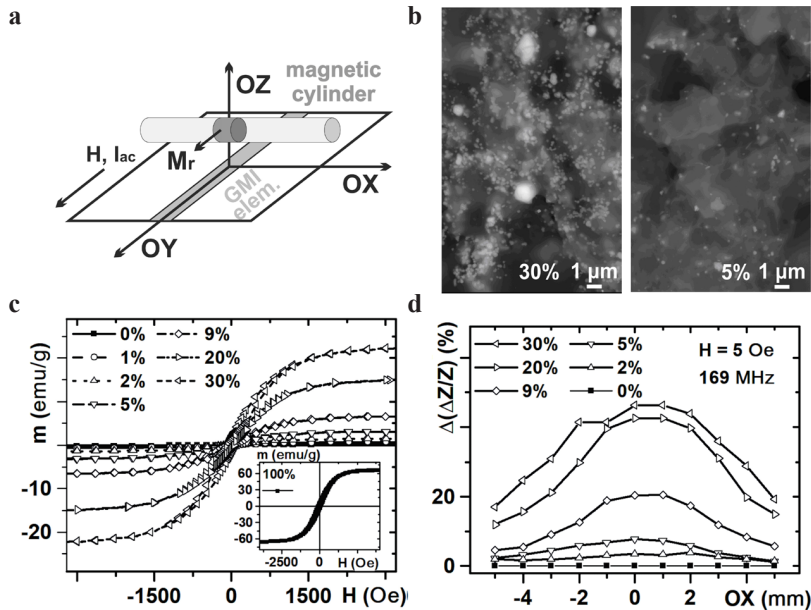


Figure 1. Scheme of magnetic cylinders GMI detection (a); SEM images of magnetic composites with 5% and 30% concentration of magnetic particles (b); magnetic moment of magnetic composite (c); GMI response of GMI element on position of magnetic cylinders with various iron oxide concentrations (d).

was non-zero being important for GMI detection as the sensor detects the stray magnetic fields (Fig. 1c). Optimum current frequency was defined as 169 MHz, where element had the highest sensitivity of 42 %/Oe, in the range 3–6 Oe (Fig. 1b). Maximum GMI response corresponds to position of the center of magnetic cylinder exactly above the GMI element. For 30% concentration GMI response is about 50%. Lowest detectable concentration FeO is 5%, where GMI response value is close to 8%. None-zero response at 5 mm position characterized concentrations of 20 and 30%. It means the GMI sensitivity was sufficient for the detection of the magnetic object at this distance. GMI detection allowed defining magnetic cylinder shape as well as position. For (9, 20 and 30% of filler concentration) shapes of the GMI curves were close to each other and GMI response peak width was about 4 mm (close to the height of cylinder (Fig. 1d)).

*This research was in part founded by the Ministry of Science and Higher Education of the Russian Federation (project No. FEUZ -2020-0051). Selected studies were performed at SGIKER services of the Basque Country University UPV-EHU. We thank V.N. Lepalovskij, I. Orue and S. Suarez for support.*

1. G.V. Kurlyandskaya, S.O. Volchkov, D. De Cos. Russ. J. Nondestr. Test., **45**, 377–398 (2009).
2. A. García-Arribas, E. Fernández, A. Svalov, G.V. Kurlyandskaya, J.M. Barandiaran. J. Magn. Magn. Mater., **400**, 321–326 (2016).
3. L.A. Ramajo, A.A. Cristybal, P.M. Botta, J.M. Porto Lypez, M.M. Reboredo, M.M. Reboredo, M.S. Castro. Composites: Part A, **40**, 388–393 (2009).
4. G.V. Kurlyandskaya, A.P. Safronov, S.M. Bhagat, S.E. Loffland, I.V. Beketov, L. Marcano Prieto. J. Appl. Phys. **117**, 123917 (2015).
5. G.Y. Melnikov, V.N. Lepalovskij, A.V. Svalov, A.P. Safronov, G.V. Kurlyandskaya. Sensors, **21**, 3621 (2021).



## DYNAMIC REMAGNETIZATION OF CLUSTERED FERROGELS

*A.Y. Zubarev*

Ural Federal University, Ekaterinburg, Russia

E-mail: [A.J.Zubarev@urfu.ru](mailto:A.J.Zubarev@urfu.ru)

Magneto-polymer composites (ferrogels, magnetic elastomers, etc) consist of a polymer host media and embedded nano- or micron-sized magnetic particles. These systems attract considerable interest of researchers and engineers due to rich set of unique physical properties valuable for progressive industrial and bio-medical applications. Their macroscopical properties and behavior are determined by combination of magnetic and mechanical characteristics of the embedded particles, the host medium, coupling between the medium and the particles, the particles spatial arrangement, etc.

Dynamic remagnetization of biological tissues with magnetic nanoparticles play a key role, for instance, in the effect of magnetic hyperthermia – a progressive method of oncological diseases therapy [1]. It also presents interest from the viewpoint of development of technology of magnetically controlled scaffolds for tissues engineering and regeneration [2].

The classical model of the dynamics of single-domain ferromagnetic particle remagnetization [3] deals with isolated particles; any interaction between them is not taken into account. However, in reality the interparticle interaction can play significant role on the dynamic response of the composites. Recently models of dynamic susceptibility of systems with chaotically (gas-like) spatially distributed single domain ferromagnetic particles, immobilized in a host medium, were proposed in [4, 5]. In the real systems, because of the magnetic, Van der Waals and adhesion interactions, the particles very often unite into various heterogeneous structures. Because of diversity of these structures and clusters, a general mathematical model for all their types hardly can be proposed. The most reasonable and realistic way is to consider the different types of the clusters separately.

We propose a model of the simplest cluster consisting of two single-domain ferromagnetic particles immobilized in a carrier medium. Theoretical analysis is based on the Fokker-Plank equation for the density of probability of the dimer particles magnetic moments orientation. Assuming that both dimensionless parameters  $\lambda$  of the particles dipole-dipole interaction and  $\sigma$  of the particle magnetic anisotropy are much more than one, what is typical for the clustered particles, we have used modification, for the two particles dynamics, of the mathematically regular Kramers saddle-point method. The results show that initial susceptibility of the dimer exceeds the mutual susceptibility of the isolated particles – this is a consequence of the interparticle magnetic interaction. Because of the dipole-dipole interaction, characteristic time of the dimer remagnetization is much more than the time of remagnetization of the single particle. The internal ways of the dimer remagnetization are determined by the relation between the parameters  $\lambda$  and  $\sigma$ . If the inequality  $3\lambda > 2\sigma$  is held, the most probable way corresponds to the passage through the configuration when the particles magnetic moments have diametrically opposite orientations perpendicular to their axes of easy magnetization. In the situation  $3\lambda < 2\sigma$ , the most probable way is successive passage the particles through potential barrier of their magnetic anisotropy.

Despite the physical simplicity of this approach, the results, obtained for the dimer, as well as the way of the mathematical study of this problem, can be a robust basement for consideration of

effect of more complicated internal structures on the dynamic remagnetization of magneto-polymer composites and biological tissues with the embedded magnetic particles.

*This work has been supported by the RFBR, grants 20-02-00022, 21- 36552-12013, Ministry of Education and Science of the Russian Federation, project FEUZ-2020-0051.*

1. L. Trahms, in: Colloidal Magnetic Fluids (2009), ed. S. Odenbach, Springer: Berlin, Germany, 327–358
2. M.T. Lopez-Lopez, G. Scionti, A.C. Oliveira, J.D.G. Duran et al., PLoS ONE **10**(7):e0133878 (2015)
3. W.F. Brown, Phys. Rev., **130**, 1677 (1963)
4. A.Yu. Zubarev, Physical Review E, **99**, 062609 (2019)
5. A.V. Ambarov, V.S. Zverev, E.A. Elfimova, Journal of Magnetism and Magnetic Materials, **497**, 166010 (2020)

## SUSPENSION AGGREGATION KINETICS IN A UNIFORM STATIONARY MAGNETIC FIELD

*A.R. Zakinyan*

North-Caucasus Federal University, Stavropol, Russia

E-mail: [zakinyan.a.r@mail.ru](mailto:zakinyan.a.r@mail.ru)

The complex anisotropic structure formation in the external uniaxial magnetic or electric field is characteristic of many functional disperse media. These structures reflect on the media's macroscopic properties. The kinetics of structure formation determines the speed of system response after a field is applied, and is therefore worthy of investigation [1]. The aggregation kinetics can be analyzed by studying the time evolution of the physical characteristics of a macroscopic suspension sample in the process of field-induced structure formation. The aim of this research is to experimentally study the aggregation kinetics in a suspension by analyzing the change in its macroscopic electrical properties during structure formation caused by the action of a homogeneous stationary magnetic field. Here, an athermal (non-Brownian) model magnetic suspension will be considered. The obtained results can then be transferred to a wide range of physical properties of similar suspensions, mathematically described by the formally identical functional relations.

In this research, a magnetic fluid emulsion is used as a convenient model suspension (see, e.g., [1]). To create an emulsion, a kerosine-based magnetic fluid with oleic acid-stabilized magnetite nanoparticles was used. Water droplets were mechanically dispersed in a magnetic fluid. Polyglyceryl-3 polyricinoleate was used as an emulsifier. The densities of the magnetic fluid and the water were matched to each other to avoid sedimentation stratification. The emulsion was polydisperse, and the mean droplet diameter was about 23  $\mu\text{m}$ . Since the size of magnetic nanoparticles of magnetic fluid (10 nm) is much smaller than the size of emulsion microdrops, the magnetic fluid can be considered as a continuous liquid magnetizable medium.

Optical microscopy observations have shown, that under the action of external uniform magnetic field, the emulsion microdrops keep spherical shape (owing to their large capillary pressure) and organize into ordered chain-like structures (Fig. 1). The microdrops, coalescence was not observed in the entire range of magnetic field strength used.

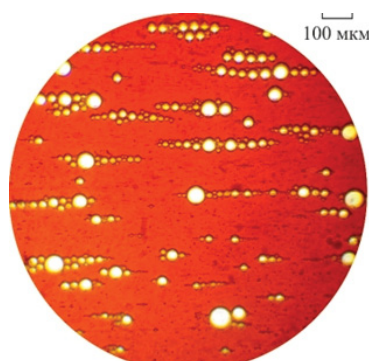


Figure 1. Microstructure of magnetic fluid emulsion in a uniform magnetic field.

The measured emulsion sample filled a 5 mm thick and 2 cm diameter capacitor whose conductivity and capacitance were measured. These parameters were measured using a digital alternating current LCR-meter (GW Instek LCR 7811OG). The measuring signal value was small and did not induce structural changes in the sample. To create microstructural ordering, the capacitor with emulsion sample inside was placed into an external stationary homogeneous magnetizing field directed along the measuring electrical field. The magnetizing field was created by a Ruben coil system of five square coils. The macroscopic properties evolution determined by the kinetics of structure formation in the magnetic fluid emulsion has been measured.

It is a major challenge to scale the data so that all plots of a permeability relative change as a function of time would collapse together, regardless of the experimental conditions. As a result of this study, it was shown that the aggregation kinetics in a 3-D sample of an athermal suspension in a uniaxial field has a definite time scale. The collapse of the time dependence curves of the sample macroscopic parameters in the process of structure formation occurs when these dependences are normalized to their maximum value and at the corresponding time scaling. The obtained results can be applied to a number of structurally sensitive properties of composite materials, such as, for example, thermal conductivity and magnetic susceptibility.

*Support by Grants Council of the President of the Russian Federation is acknowledged (project MD-2683.2022.1.2).*

1. G. Bossis, P. Lançon, A. Meunier, L. Isakova, V. Kostenko, A. Zubarev, *Phys. A*, **392**, 1567–1576 (2013).
2. A. Zakinyan and I. Arefyev, *Colloid Polym. Sci.*, **298**, 1063–1076 (2020).

## STRAIN-MAGNETO-OPTICS OF MAGNETOSTRICTIVE FERRITE-SPINELS

*Yu.P. Sukhorukov\**, *A.V. Telegin*, *N.G. Bebenin*, *S.V. Naumov*, *E.A. Surzhikov*

Institute of Metals Physics M.N. Mikheev UB of RAS, Ekaterinburg, Russia

\*E-mail: suhorukov@imp.uran.ru

Strain-magneto-optics is a new section of straintronics which studies the relationship between the magneto-optical and magnetoelastic properties of magnets. The relationship between the magneto-optical and magnetoelastic properties of the ferrite spinels is clearly manifested in the similarity of the field dependences of magnetostriction and the effects of magneto-reflection and magneto-absorption (magneto-transmission) of unpolarized light in the infrared region of wavelengths  $1 \leq \lambda \leq 30 \mu\text{m}$ . This relationship also manifests itself in the similarity of magnetoelastic and magneto-optical properties depending on the orientation of the magnetic field relative to the axes of the crystal and the direction of the field relative to the plane of the crystal plate, the so-called Voigt and Faraday geometry of the experiment. The strain-magneto-optical properties have been found in ferrimagnetic spinels  $\text{CoFe}_2\text{O}_4$ , and  $\text{MnFe}_2\text{O}_4$  which have a large magnetostriction at room temperatures, as well as low optical losses in the IR. The spectral region of the strain magneto-optics in these spinels includes the fundamental absorption edge, impurity absorption of light, and the region of interaction of light with residual rays. It has been found that the mechanism responsible for the correlation of the magneto-optical and magnetoelastic properties in  $\text{CoFe}_2\text{O}_4$  and  $\text{MnFe}_2\text{O}_4$  is indirect. It is due to the fact that magnetostriction makes an anomalously large contribution to the magnetic anisotropy constant, comparable to the value of the constant itself. Thus, the magnetic field leads to a strong deformation of the crystal lattice, which in turn affects the change in the electronic configuration of the sample and, as a consequence, its optical properties. It was shown that in the Faraday geometry of the experiment, the influence of the classical Faraday effect on the magnetoabsorption is possible and can reach 15%, due only to the optical characteristics of the experimental installation.

The obtained effects are important for the creation of a large number of functional magneto-optical materials for the IR, visible and terahertz regions of the spectrum, the optical properties of which can be controlled by a magnetic field.

*The work was carried out within the framework of the state task of the FASO of Russia (subject "Spin" No. AAAA-A18-118020290104-2)*

## THE INFLUENCE OF THE SHEAR FLOW AND TOPOLOGY ON THE MAGNETORHEOLOGICAL PROPERTIES OF CLUSTERS FORMED BY STOCKMAYER SUPRACOLLOIDAL MAGNETIC POLYMERS

*V.S. Zverev<sup>1\*</sup>, E.V. Novak<sup>1</sup>, I. Novikau<sup>2</sup>, S.S. Kantorovich<sup>1,2</sup>*

<sup>1</sup>Department of theoretical and mathematical physics, UrFU, Ekaterinburg, Russia

<sup>2</sup>University of Vienna, Vienna, Austria

\*E-mail: [vladimir.zverev@urfu.ru](mailto:vladimir.zverev@urfu.ru)

Construction of magnetic filaments or supracolloidal magnetic polymers (SMPs, polymer-like structures in which magnetic nanoparticles are playing the role of monomers) has recently been made possible. The advantage of such SMPs is that they keep their structure independently from the temperature and can be potentially used as an alternative to nanoparticles in magnetic fluids to obtain a desired and easily controlled magnetic or rheological response. This is important for predicting behavior in closed geometries, such as microchannels used in microfluidic devices. Microchannels are tubes whose size does not exceed hundreds of microns, and has several advantages, for example, a high speed of heat and mass transfer.

We assume SMPs formed by monodisperse magnetic colloids, modeled as identical spherical beads. We consider SMPs of four different topologies: chain-, Y-, X- and ring-like ones. Using Langevin dynamics simulations, we pay our attention to solutions of filaments, the magnetic nanoparticles in which are not only interacting via dipole-dipole potential but also via short-range attractive forces (Lennard-Jones type). Such filaments tend to aggregate in dense spherical droplet-like clusters. The resulting composite soft colloid is placed in the microchannel, where its behavior in the shear flow under influence of an external field is investigated, varying a wide range of system parameters.

We consider the influence of hydrodynamic interactions and long-range magnetic forces on the transport of nanocomposite particles in the channel during shear flow. It was found that the external magnetic field enhances the deformation of the cluster in the microchannel in a flow. The shear flow stabilises the shape of the clusters not letting them extend in the direction of the field and disintegrate. The stabilising effect depends on topology of clusters and it is particularly strong for clusters made of linear SMPs. It was found that clusters can demonstrate oscillating in time magnetic response. The mutual orientation of the flow and the direction of the external field, along with the ratio of the flow velocity to the field strength, can stabilize the movement of clusters and suppress oscillations.

*The work was supported by RSF 19-12-00209*

1. W. Liu, J. Halverson and Y. Tian, *Nature chemistry*, **8**, 867 (2016).
2. Y. Tian, Y. Zhang and T. Wang, *Nature Materials*, **15**, 654 (2016).
3. V.S. Zverev, M.A. Gupalo, N.J. Mauser, S.S. Kantorovich, and E.V. Novak, *J. Magn. Magn. Mater.*, **521** (2021).

## SPHERICAL MAGNETIZABLE BODY IN A DROP OF FERROFLUID IN A UNIFORM HORIZONTAL MAGNETIC FIELD

*K.L. Sogomonyan<sup>1</sup>, A.S. Vinogradova<sup>2\*</sup>, O.A. Sharova<sup>1,2</sup>, D.A. Pelevina<sup>1,2</sup>, V.A. Naletova<sup>2</sup>*

<sup>1</sup>Faculty of Mechanics and Mathematics, Lomonosov Moscow State University, Moscow, Russia

<sup>2</sup>Institute of Mechanics, Lomonosov Moscow State University, Moscow, Russia

\*E-mail: [vinogradova-as@mail.ru](mailto:vinogradova-as@mail.ru)

Stable levitation of a magnet immersed in a ferrofluid (FF) was for the first time demonstrated experimentally in 1966 by R.E. Rosensweig [1]. Since then, many works have shown that not only magnets but also magnetizable bodies immersed in a FF can levitate in special-shaped vessels in strong enough uniform magnetic fields. And they can also float on a surface of a small volume of FF. In [2], an equilibrium of a spherical magnetizable body floating in a drop of FF situated on a horizontal plane in a uniform vertical applied magnetic field was observed experimentally and considered theoretically in the non-inductive approximation, without regard to surface tension forces. By analogy, in this paper we raise the following question: Can such a body float in a drop of FF if a horizontal rather than a vertical field is applied?

In the experiment, the applied uniform horizontal magnetic field is created by a Helmholtz coil. A water-based FF (of density  $1.2 \text{ g/cm}^3$  and with magnetic permeability of 1.42) and a transformer oil (of density  $0.93 \text{ g/cm}^3$ ) as a surrounding medium are used. A drop of FF is placed at the horizontal bottom of a rectangular plexiglas container (5 cm in length, 2 cm in width, 3 cm in height) filled with an oil. The spherical body made of a magnetizable elastomer (of radius 0.215 cm, mass 0.15 g and with magnetic permeability of 3.62) or a bearing steel (of radius 0.157 cm and mass 0.13 g) is immersed in the drop of FF in the maximum magnetic field of 450 Oe that the coil can produce. Then the magnitude of the field is stepwise decreased to zero. Thus, a series of 11 experiments was performed for the elastomeric body with FF volumes from 0.02 ml to 0.41 ml and a series of 5 experiments was carried out for the steel body with FF volumes from 0.04 ml to 0.2 ml, see Fig. 1. In all the experiments performed, the spherical magnetizable body did not float in a FF drop in a horizontal field.

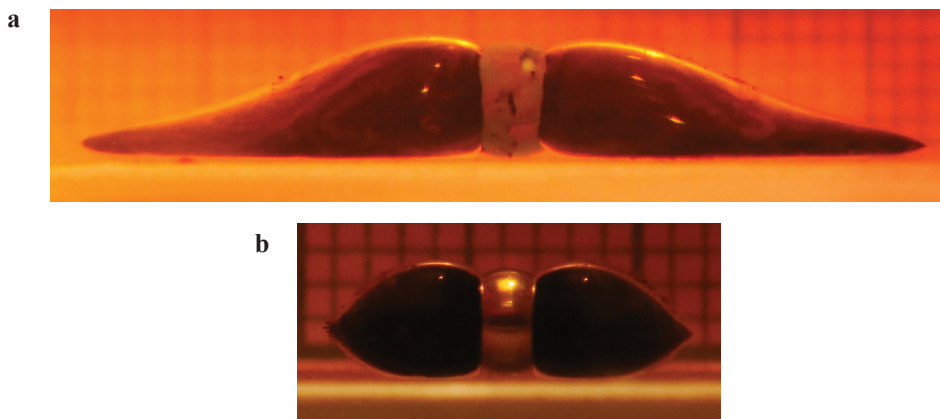


Figure 1. Spherical body made of **a** magnetizable elastomer; **b** bearing steel in a FF volume of 0.32 ml (**a**); 0.06 ml (**b**) in a uniform horizontal magnetic field of 450 Oe.

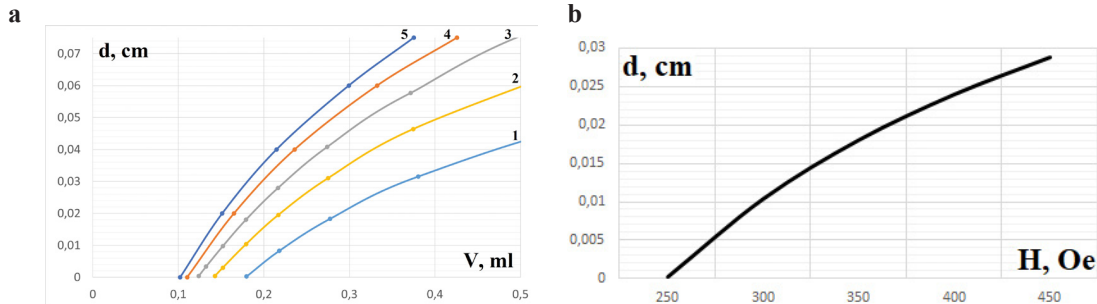


Figure 2. The dependences of the floating height of the elastomeric body **a** on the FF volume for the field of 1 – 250 Oe, 2 – 300 Oe, 3 – 350 Oe, 4 – 400 Oe, 5 – 450 Oe; **b** on the magnitude of the field for the FF volume of 0.18 ml.

An equilibrium of a spherical magnetizable body in a drop of FF situated on a horizontal plane in a uniform horizontal applied magnetic field is also studied theoretically in the non-inductive approximation, without regard to surface tension forces. The FF surface shape is determined from the equilibrium equation for a heavy, incompressible, homogenous, isothermal FF and dynamic boundary condition. An analytical expression for the force acting on the body from the surrounding media is found. The floating height of the body and the volume of FF are numerically calculated to satisfy the equilibrium equation for the body. The dependences of the floating height on the volume of FF and on the magnitude of the field are obtained for the experimental parameters, see Fig. 2. It is found that for a fixed magnetic field there exist a minimum volume of FF at which the body can float and a maximum volume of FF at which the calculated FF surface shape no longer resembles that of a drop and the FF completely fills a container. It is also found that for a fixed volume of FF there is a minimum magnitude of the field required for the body to float.

Numerical simulations show that, in contrast to a vertical magnetic field [2], in which the body can float at a height of several millimeters in small volumes of FF and in weak fields, in a horizontal field, the body should float only at a height of several tenths of millimeter, and it happens only at relatively large volumes of FF and in strong enough fields, see Fig. 2. Such a difference in the floating height of the body in a vertical and horizontal field may be due to the position of the FF: in a horizontal field, the FF is located not under the body (as in a vertical field), but on opposite sides of the body (left and right), see Fig. 1.

It is possible that a qualitative difference between the results of the proposed theory and the experiments performed in a horizontal magnetic field (in the experiment the body does not float, but according to the theory it can float) is since the theory does not describe well enough the shapes of the FF surface observed in the experiment. And the force acting on the body strongly depends on the surface shape. Most likely, the reason lies in the non-inductive approximation in which the problem is solved, namely, in the fact that in such an approach the theory does not describe the normal-field surface instability. In a horizontal field, the magnetic field strength vector is perpendicular to the FF surface at the extreme left and right points: instability peaks appear there, see Fig. 1 (as in the Rosensweig instability). In the experiment, the peaks stretch the FF surface, and it ceases to resemble the surface shape predicted by theory.

*The research was supported by the RSF Grant № 20-71-10002.*

1. R.E. Rosensweig, *Nature*, **210** (5036), 613–614 (1966).
2. D.A. Pelevina, O.A. Sharova, D.I. Merkulov et al., *JMMM*, **494**, 165751 (2020).



## THE DYNAMIC MAGNETIC RESPONSE OF IMMOBILIZED SUPERPARAMAGNETIC NANOPARTICLES TO AN AC FIELD WITH ARBITRARY AMPLITUDE

*A.V. Ambarov\**, *E.A. Elfimova*, *V.S. Zverev*

Ural Federal University, Ekaterinburg, Russia

\*E-mail: [alexander.ambarov@urfu.ru](mailto:alexander.ambarov@urfu.ru)

Magnetic nanoparticles already proved their applicability in different areas. Embedding magnetic nanoparticles into polymer matrix makes it possible to control the properties of a composite material using an external magnetic field. Such materials, so-called magnetic soft matters, include magnetic elastomers, ferrogels, and various biocompatible magnetic filling. In the last decade, a new wave of interest to magnetic soft matter appears due to their connection with using such material in diagnostics and therapy.

In this work the dynamic magnetic response of immobilized superparamagnetic nanoparticles to an ac magnetic field with an arbitrary amplitude is studied using numerical simulations. It is assumed that the nanoparticles are randomly distributed within an implicit solid matrix, but the easy axes of the particles are aligned parallel or perpendicular to the ac magnetic field. The calculation of the dynamic response is based on the Fokker-Planck equation in which the interparticle dipole-dipole interactions are included within the framework of the modified mean-field theory [1]. The numerical solution of Fokker-Planck equation is based on an unconditionally stable scheme for convection-diffusion problems [2]. The effects of the magnetic crystallographic anisotropy barrier, the ac field amplitude, and the interparticle interactions on the dynamic magnetization, susceptibility,

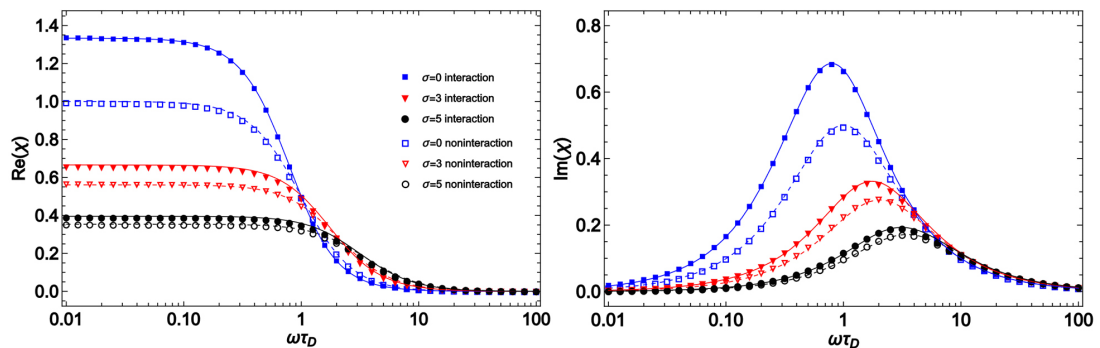


Figure 1. The real and imaginary parts of susceptibility for noninteracting (dashed lines and open symbols) and interacting (solid lines and filled symbols) particles in the system with the Langevin susceptibility  $\chi_L = 1$  at magnetic field amplitude  $\alpha = 0.01$  ( $\alpha$  is the Langevin parameter). Lines correspond to analytical expression from [3] obtained for small field amplitudes. Symbols are from numerical solution of the Fokker-Planck equation. The anisotropy constants are  $\sigma = 0$  (blue squares),  $\sigma = 3$  (red triangles),  $\sigma = 5$  (black circles).

and relaxation time are analyzed. The numerical results are compared against a theory [3] reliable in a weak ac field, and the excellent agreement is obtained.

The obtained results represent essential information in the design and synthesis of new functional materials.

*The study was funded by RFBR, project number 20-32-90209 aspirant.*

1. A.O. Ivanov, V.S. Zverev, S.S. Kantorovich, *Soft Matter*, **12(15)**, 3507–3513 (2016).
2. N.M. Afanasyeva, P.N. Vabishchevich, M.V. Vasilyeva, *Russian Mathematics*, **57**, 1 (2013).
3. A.V. Ambarov, V.S. Zverev, E.A. Elfimova, *Journal of Magnetism and Magnetic Materials*, **497**, 166010 (2020).

## TEMPERATURE DEPENDENCE OF THE MAGNETO-OPTICAL EFFECT IN A MAGNETIC EMULSION

*S.S. Belykh\*, C.V. Yerin, V.V. Fursova*

Department of Experimental Physics, NCFU, Stavropol, Russia

\*E-mail: [sergeyb.stav@mail.ru](mailto:sergeyb.stav@mail.ru)

Magnetic colloidal systems are a special type of artificial smart materials that have no analogues in nature. Their characteristic feature is a significant response to a magnetic field, which is expressed as a change in the magnetic, rheological, and optical properties [1]. Magnetic fluids have been known since the late 1970s and have been fairly well studied, but multicomponent systems synthesized on their basis are of considerable interest. One of such promising media are magnetic emulsions, in which suspended microdroplets of a magnetic fluid of micron or submicron size can easily be deformed under the influence of a low-strength magnetic field, which leads to the appearance of interesting physical effects [2–4].

In this paper, we present the results of experimental studies of the magneto-optical effect of changing the transparency of a magnetic emulsion with low interfacial tension depending on the sample temperature.

The sample was an emulsion of drops of kerosene magnetic fluid with a magnetic phase concentration of 10%. The magnetic fluid was mechanically mixed in AMG-10 oil at a ratio of 1:20 without the addition of stabilizers and emulsifiers, after which it was exposed to a pulsed magnetic field for some time, which made it possible to obtain a stable emulsion with a volume concentration of magnetic phase droplets of 5% [4]. The droplet size in the magnetic emulsion is in the range of 1–20  $\mu\text{m}$ . The magneto-optical effect of changing the transparency of a magnetic emulsion under the influence of a magnetic field codirectional with the light beam was studied. For research, an experimental setup similar to that described in [5] was used.

Under the action of a pulsed magnetic field, magnetic emulsion drops are elongated in the direction of the lines of tension, which leads to a change in the transparency of the sample (Fig. 1). An increase in the sample temperature leads both to an increase in the amplitude of the magneto-optical effect and to an increase in the transparency of the emulsion without the action of the field. The

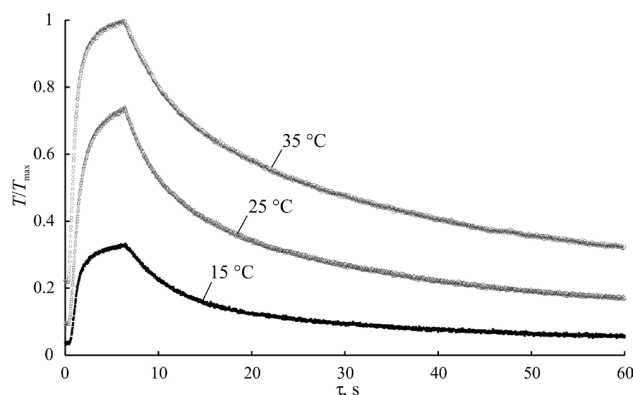


Figure 1. Magneto-optical responses of a magnetic emulsion to the action of an 8-second magnetic field pulse at various temperatures.

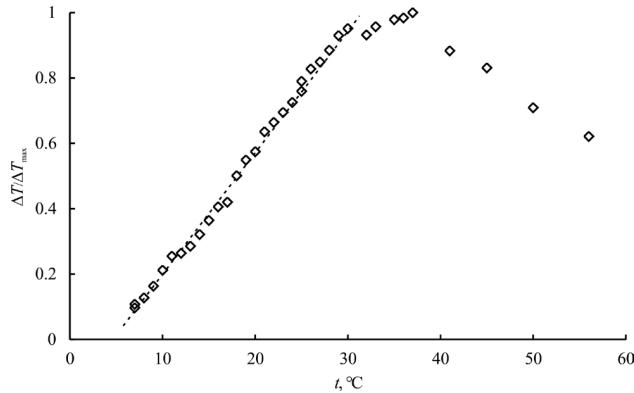


Figure 2. Temperature dependence of the amplitude of the magneto-optical effect.

dependence of the amplitude of the magneto-optical effect on temperature has a non-monotonic character (Fig. 2) with a maximum in the region of 30–35 °C. At lower temperatures, this dependence is linear, while at higher temperatures, the amplitude of the effect somewhat decreases.

The interpretation of the magneto-optical effect in magnetic emulsions can be constructed taking into account the complex temperature dependence of microdroplet deformation at a constant magnetic field strength. In this case, it is necessary to take into account both the change in the magnetic energy of the microdroplet with temperature and the change in the interfacial tension, as well as the possible partial dissolution of the emulsion microdroplets with increasing temperature.

*Support by the Ministry of Science and Higher Education of Russia (project No. 0795-2020-0007) is acknowledged.*

1. S. Odenbach, Adv. Coll. Int. Sci., **46**, 263–282 (1993).
2. J. Liu, E.M. Lawrence, A. Wu, M.L. Ivey et al., Phys. Rev. Lett., **74**, No. 14, 2828–2831 (1995).
3. K.V. Erin, S.A. Kunikin, Optics and Spectroscopy, **104**, No. 2, 277–281 (2008).
4. A.R. Zakinyan, Yu.I. Dikansky Magnetic and electrical properties of magnetic emulsions. Saarbrücken-Moscow, LAP Lambert Academic Publishing, 2011. 146 p.
5. S.S. Belykh, C.V. Yerin, IEEE Magnetics Letters, **13**, 7100605 (2022).

## THEORETICAL STUDY OF THE MAGNETIC PROPERTIES OF THE DIMER

*A.Yu. Zubarev, D.N. Chirikov\**

Institute of Natural Sciences and Mathematics, Ural Federal University, Ekaterinburg, Russia

\*E-mail: [d.n.chirikov@urfu.ru](mailto:d.n.chirikov@urfu.ru)

Magnetic polymer materials (ferrogels, magnetic elastomers, etc.) are composites, consisting of fine magnetic particles embedded in a host polymer media. These materials are interesting, first, because of combination of their high magnetic and elastic properties.

Magnetic interaction between the embedded particles significantly affects magnetization of both liquid ferrofluids and cured magnetic polymers[1–3]. These theoretical works deal with homogeneous, “gas-like” spatial distribution of the magnetic particles in a carrier medium. However, experiments and computer simulations demonstrate, that this distribution can take place only if the energy of magnetic interaction between the particles is quite low, not more than two-three  $kT$ . If this energy significantly exceeds  $kT$ , various heterogeneous aggregates (linear chains, bulk “drops”, etc.) appear in the system of the particles [1, 4].

Analysis shows that calculation of magnetization of the chain with an arbitrary number of the particles presents very cumbersome problem. However, some results of quite general physical character can be obtained by considering the simplest cluster, consisting of two particles (dimer).

We consider a dimer, consisting of two identical single-domain ferromagnetic particles which are in direct physical contact. We suppose that the particle has a single axis of easy magnetization.

The equilibrium distribution function over orientations of the unit vectors of the particles magnetic moments before the field application  $\boldsymbol{\mu}_{1,2}^0$  and the corresponding unit vectors of the particles axes of easy magnetizations  $\mathbf{v}_{1,2}$  must obey the Boltzmann law. Therefore, the equilibrium function of distribution over the vectors  $\mathbf{v}_{1,2}$  can be presented as:

$$f^0(\mathbf{v}_1, \mathbf{v}_2) = \frac{1}{Z^0} \int \exp(-u^0) d\boldsymbol{\mu}_1^0 d\boldsymbol{\mu}_2^0, \quad Z^0 = \int \exp(-u^0) d\boldsymbol{\mu}_1^0 d\boldsymbol{\mu}_2^0 d\mathbf{v}_1 d\mathbf{v}_2,$$

$$u^0 = -\sigma[(\boldsymbol{\mu}_1^0 \cdot \mathbf{v}_1)^2 + (\boldsymbol{\mu}_2^0 \cdot \mathbf{v}_2)^2] + u_{dd},$$

$$u_{dd} = \lambda[\sin\theta_1^0 \sin\theta_2^0 \cos(\varphi_1^0 - \varphi_2^0) - 2\cos\theta_1^0 \cos\theta_2^0]. \quad (1)$$

Here  $u_{dd}$  is the dimensionless, with respect to  $kT$ , energy of the dipole-dipole interaction between the particles;  $\lambda$  is dimensionless parameter of the particles dipole-dipole interaction. The term proportional  $\sigma$  in  $u^0$  presents the dimensionless energy of the particles magnetic anisotropy.

Let us suppose now that the magnetic field is switched on. We will denote the unite vectors of the magnetic moments of the dimer particles in the field, as  $\boldsymbol{\mu}_1$  and  $\boldsymbol{\mu}_2$  without the superscript 0. The average component  $\mu_h(\psi)$  of the vector  $\boldsymbol{\mu}_1$  in the field  $\mathbf{H}$  direction is:

$$\mu_h(\psi) = \frac{1}{Z} \int \frac{(\mathbf{h} \cdot \boldsymbol{\mu}_1)}{h} e^{-u} f^0 d\boldsymbol{\mu}_1 d\boldsymbol{\mu}_2 d\mathbf{v}_1 d\mathbf{v}_2, \quad Z = \int e^{-u} f^0 d\boldsymbol{\mu}_1 d\boldsymbol{\mu}_2 d\mathbf{v}_1 d\mathbf{v}_2,$$

$$u = -(\mathbf{h} \cdot \boldsymbol{\mu}_1) - (\mathbf{h} \cdot \boldsymbol{\mu}_2) - \sigma[(\boldsymbol{\mu}_1 \cdot \mathbf{v}_1)^2 + (\boldsymbol{\mu}_2 \cdot \mathbf{v}_2)^2] + u_{dd}, \quad \mathbf{h} = \mu_0 \frac{m\mathbf{H}}{kT}. \quad (2)$$

Here  $\psi$  is the angle between the field and the dimer axis;  $u$  is the dimer energy in the field;  $\mathbf{h}$  is the dimensionless magnetic field; its absolute value  $h$  is often called as the Langevin parameter.

At the random orientations of the dimer axis with respect to the field  $\mathbf{H}$ , the mean value of the vector  $\boldsymbol{\mu}_1$  projection onto the field direction is:

$$\langle \mu_h \rangle = \int_0^{\pi/2} \mu_h(\psi) \sin \psi d\psi . \quad (3)$$

Some estimates can be obtained in the frames of the approximation  $\lambda, \sigma \gg 1$  and  $\lambda, \sigma \gg h$  (the condition  $h < 1$  is not necessary for our analysis). In this situation, using the saddle-point method in the asymptotic  $\lambda, \sigma \rightarrow \infty$  after cumbersome transformations, one gets:

$$\langle \mu_h \rangle = \int_0^1 x \tanh(2hx) dx . \quad (4)$$

Another simplification of the general approach (1–3) can be obtained if to suppose that the particles axes of easy magnetization are directed strictly along the dimer axis:

$$\mu_h(\psi) = \frac{1}{Z} \int \frac{(\mathbf{h} \cdot \boldsymbol{\mu}_1)}{h} e^{-u} d\boldsymbol{\mu}_1 d\boldsymbol{\mu}_2 , \quad Z = \int e^{-u} d\boldsymbol{\mu}_1 d\boldsymbol{\mu}_2 . \quad (5)$$

$$u = -(\mathbf{h} \cdot \boldsymbol{\mu}_1) - (\mathbf{h} \cdot \boldsymbol{\mu}_2) - \sigma[(\boldsymbol{\mu}_1 \cdot \mathbf{v}_1)^2 + (\boldsymbol{\mu}_2 \cdot \mathbf{v}_2)^2] + u_{dd} ,$$

We have calculated the component  $\langle \mu_h \rangle$  for the dimer within the framework of the general strict model (1–3), within the framework of the simplified model (5) and by using the asymptotic relation (4). The calculation results are shown in the Fig. 1.

This figure illustrates the small discrepancy between the results obtained within these approaches. Therefore, to avoid cumbersome calculations, at large  $\lambda$  and  $\sigma$  one can recommend using the either the asymptotic formula (4) or the simplified model (5) with the magnetic anisotropy axes directed along the dimer axis.

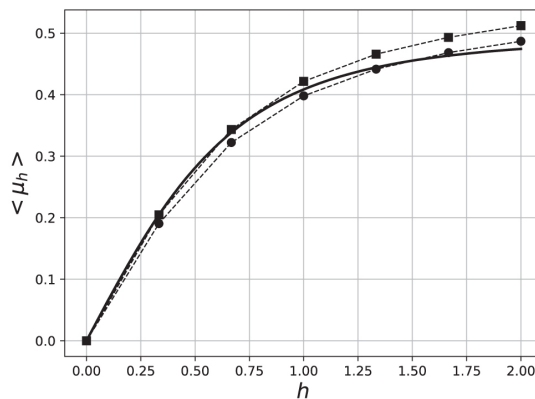


Figure 1. The dependence of the orientation of the magnetic moment of the dimer  $\langle \mu_h \rangle$  vs. the magnetic field  $h$ . Dimensionless magnetic anisotropy parameter  $\sigma = 10$ ; dipole-dipole interaction parameter  $\lambda = 8$ . Solid line – result by the formula (4); square dots – numerical integrations according to Eqs. (1–3); circle dots – according to Eq. (5).

We believe that the presented results can serve as a robust basis for theoretical modelling of ferrogels with more complicated structures.

*This work has been supported by Russian Fund of Fundamental Investigation, grants 20-02-00022; 21-52-12013 and Ministry of Science and Education of the Russian Federation, project FEUZ-2020-0051*

1. E. Blums, A. Cebers, M. Maiorov, Magnetic Fluids (Berlin, New York: Walter de Gruyter), (1997).
2. A. Ivanov, O. Kuznetsova, Physical Review E, **64**, 041405 (2001).
3. E.A. Elfimova, L.Y. Iskakova, A.Y. Solovyova, A.Y. Zubarev, Physical Review E, **00**, 004600, (2021).
4. A.O. Ivanov, A.Yu. Zubarev, Materials **13**, 3956, (2020).

**MATHEMATICAL MODELING OF THE POLYMER FERROCOMPOSITE MAGNETIC PROPERTIES TAKING INTO ACCOUNT DIPOLAR INTERACTIONS**

*D.I. Radushnov, A.Yu. Solovyova, E.A. Elfimova\**

Ural Mathematical Center, Department of Theoretical and Mathematical Physics,  
 Ural Federal University, Ekaterinburg, Russia

\*E-mail: [Ekaterina.Elfimova@urfu.ru](mailto:Ekaterina.Elfimova@urfu.ru)

This work is devoted to the theoretical study of the structural and magnetic properties of an ensemble of single-domain interacting magnetic nanoparticles immobilized in a non-magnetic medium. This model is typical for the description of polymer ferrocomposites. It is assumed that the ferrocomposite is obtained by solidification of the carrier medium in a ferrofluid under the applying magnetic field, the intensity of which is determined by the Langevin parameter  $\alpha_p$ ; after solidification of the carrier liquid, the nanoparticles retain the spatial distribution and orientation of their easy magnetization axes, which they had before solidification of the carrier medium. The features of the orientational texture formed in the sample are analyzed depending on the intensity of the magnetic field  $\alpha_p$  and interparticle dipole-dipole interactions. The further reaction of the polymerized composite with immobilized magnetic nanoparticles to the magnetic field  $\alpha_p$  has superparamagnetic nature, i.e., the change in the orientation of the magnetic moment occurs inside the body of the nanoparticle according to the Néel mechanism due to the deviation of the magnetic moments from the magnetic anisotropy axis of the particles.

To determine the magnetization, we used the virial expansion of the one-particle distribution function, which shows the directions of the easy magnetization axes. The second virial coefficient was determined within an accuracy of  $\chi_L^1$ , which characterizes the Langevin susceptibility. Computer simulation of the system under study was also carried out using the Monte Carlo (MC) method.

Figure 1 shows the cosine of the polar angles of the magnetic moment vectors depending on  $\alpha_p$  and  $\alpha$ . It can be seen that the orientational structure of the ferrocomposite is very sensitive to the field  $\alpha_p$  in which the sample was polymerized. Under the same magnetic field  $\alpha = 1$  a sample polymerized at  $\alpha_p = 1$  (Fig. 1a) has very wide distribution of magnetic moments while for the

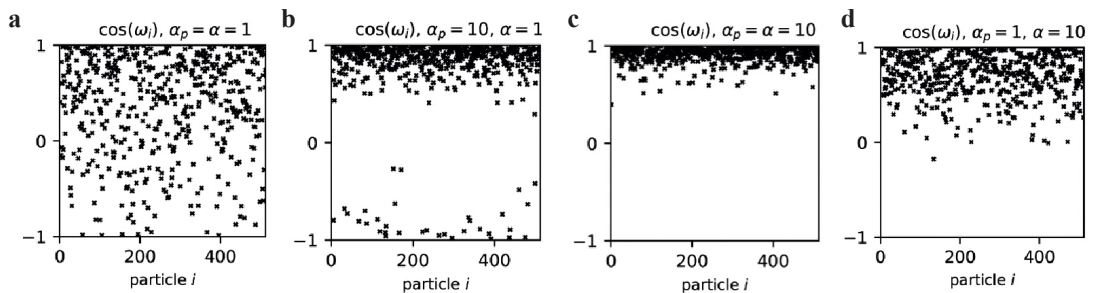


Figure 1. The value of the polar angles of the magnetic moment vectors  $\cos\omega_i$  for each particle  $i$  in typical configuration of simulated polymer ferrocomposite with  $\chi_L = 1$ , volume concentration  $\phi = 0.125$ , anisotropy constant  $\sigma = 15$  in applied magnetic field: **a**  $\alpha_p = \alpha = 1$ , **b**  $\alpha_p = 10$ ,  $\alpha = 1$ , **c**  $\alpha_p = 1$ ,  $\alpha = 10$ , **d**  $\alpha_p = \alpha = 10$ .



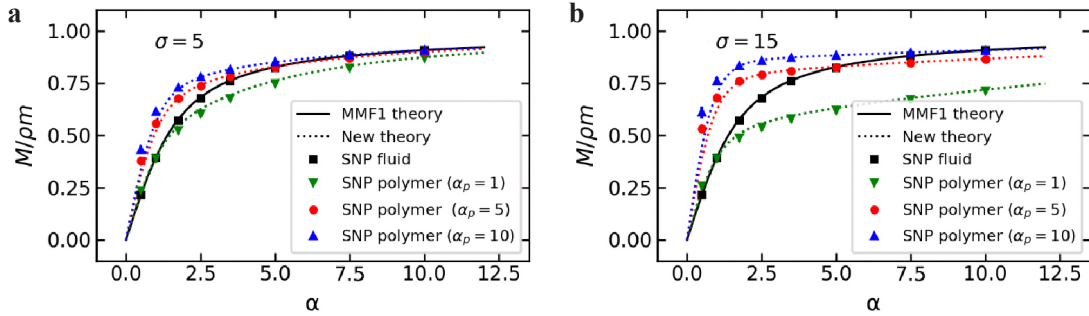


Figure 2. The normalized magnetization  $M/\rho m$  ( $\rho$  – concentration of the SNP,  $m$  – magnetic moment SNP) as a function of the Langevin parameter  $\alpha$ . Lines are from theory, points are computer simulation results.

sample polymerized at a field of  $\alpha_p = 10$  (Fig. 1b) the most of the magnetic moments are oriented along the field. Thus, a ferrocomposite polymerized at  $\alpha_p = 10$  will exhibit a significantly higher magnetization compared to a sample polymerized at  $\alpha_p = 1$ . In Fig. 1c and d a similar behavior is observed under the field  $\alpha = 10$ .

Figure 2 presents theoretical results (dashed lines) and MC simulation data (symbols) for magnetization of ferrocomposites with  $\chi_t = 1$ , volume concentration  $\phi = 0.125$ , anisotropy constant  $\sigma = 15\phi$  depending on the intensity of the magnetizing field  $\alpha$ . The magnetization of ferrocomposites is compared with the magnetization of ferrofluid indicated in the Fig. 2 in black. The black squares are the results of computer simulation, the solid line is a modified first-order mean field theory [1]. In fields  $\alpha < \alpha_p$ , ferrocomposites are magnetized much more efficiently than ferrofluids due to the polymerization texture that is currently forming. The value of the magnetization of the ferrocomposite at  $\alpha = \alpha_p$  coincides with the magnetization of the ferrofluid, since with these parameters the ferrocomposite has a similar internal structure of the ferrofluid. In fields  $\alpha > \alpha_p$  ferrocomposite is magnetized worse than ferrofluid. This is due to the absence of translational degrees of freedom in the ferrocomposite.

*The work was funded by the Ministry of Science and Higher Education of the Russian Federation within the framework of the Ural Mathematical Center project (agreement N 075-02-2022-877).*

1. A. Pshenichnikov, V. Mekhonoshin and A. Lebedev, Journal of Magnetism and Magnetic Materials, **161**, 12, 94–102. (1996).

## DEFORMATION OF A STRUCTURED MAGNETICALLY ACTIVE ELASTOMER WITH MAGNETICALLY HARD INCLUSIONS IN A 2D FORMULATION

*A.A. Ignatov<sup>1\*</sup>, O.V. Stolbov<sup>2</sup>, V.V. Rodionova<sup>1</sup>*

<sup>1</sup>Immanuel Kant Baltic Federal University, Kaliningrad, Russia

<sup>2</sup>Institute of Continuum Mechanics, Ural Branch of the Russian Academy of Sciences, Perm, Russia

\*E-mail: [artem.ignatov98@gmail.com](mailto:artem.ignatov98@gmail.com)

In the last few years, there has been an increased interest in “smart” materials based on a polymer with magnetic inclusions [1, 2]. Numerical methods are used to study the quantitative properties of such materials [3]. This work is devoted to the calculation of deformations in an external field of a structured magnetically active elastomer with magnetically hard inclusions in a 2D formulation by the finite element method using the FEniCS package.

In the initial state, the particles (Fig. 1) were located at the nodes of a 4×4 rectangular grid with square cells and had a “checkerboard” orientation of magnetic moments – any neighboring particles in a vertical column or horizontal row have an antiparallel orientation of magnetic moments.

Another simulated series of configurations (Fig. 2) was a rectangular parallelogram with an aspect ratio of varying from 6 to 12. The particles were located at the nodes of a 2×12 rectangular grid. 12 particles were located along the long side. The distance between particles located along the short side ( $r_x$ ) did not change. Only the distance between the particles located along the long side ( $r_y$ ) changed from  $r_x = r_y$  to  $r_x = 2r_y$ . In the initial state, the magnetic moments of all particles were codirectional and oriented along the long side. In the course of the experiment, the dependences of the relative strain on the applied field were obtained for configurations with different  $r_y$ .

The Neo-Hooke potential [4] was used to describe the hyperelastic matrix material. In modeling, the shape of the particles was assumed to be an ideal circle, and the particles themselves were considered to be single-domain. Also, during the simulation, the possibility of destruction of the matrix-particle boundary was excluded, i.e. full adhesion of particles and matrix was assumed.

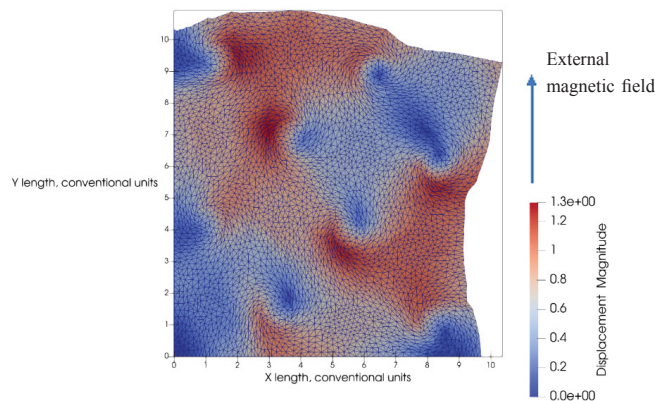


Figure 1. Deformation of an elastic matrix with hard magnetic particles.

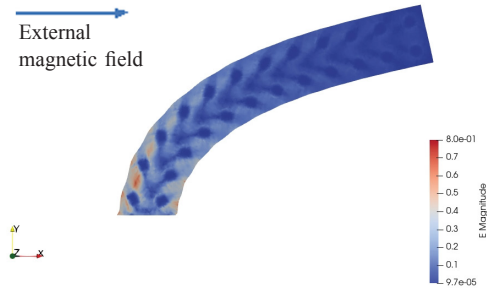


Figure 2. Deformation of an elastic matrix by hard magnetic particles in an external magnetic field.

As a result, the deformations of the material were calculated depending on the initial orientation of the magnetization of the particles and the magnitude of their magnetic moments.

*The reported study was funded by Russian Science Foundation, project number 21-72-30032.*

1. A. Allue, P. Corte-León, K. Gondra, V. Zhukova, M. Ipatov, J. Maria Blanco, A. Zhukov. Smart composites with embedded magnetic microwire inclusions allowing non-contact stresses and temperature monitoring. *Composites Part A: Applied Science and Manufacturing* (2019).
2. Z. Varga, G. Filipcsei, M. Zrínyi, Smart composites with controlled anisotropy. *Polymer*, **46**(18), 7779–7787 (2005).
3. Germain Sossou, Frédéric Demoly, Hadrien Belkebir, H. Jerry Qi, Samuel Gomes, Ghislain Montavon, Design for 4D printing: Modeling and computation of smart materials distributions, *Materials and Design*, **181**, 108074 (2019)
4. A.I. Lurie, *Theory of elasticity*, Science, 1970, published in Russian.

**PROBLEM OF MAGNETOSTATIC SKYRMION STABILIZATION  
 IN FERROMAGNET/X (X = PARAMAGNET, SUPERCONDUCTOR)  
 HYBRID SYSTEMS**

*M.A. Kuznetsov<sup>1\*</sup>, K.R. Mukhamatchin<sup>2</sup>, A.A. Fraerman<sup>1</sup>*

<sup>1</sup>Institute for Physics of Microstructures, Nizhny Novgorod, Russian Federation

<sup>2</sup>Lobachevsky State University, Nizhny Novgorod, Russian Federation

\*E-mail: [kuznetsov@ipmras.ru](mailto:kuznetsov@ipmras.ru)

As is known, the Dzyaloshinskii-Moriya (DM) interaction [1, 2] in magnetic structures leads to the removal of the chiral degeneracy and the stabilization of a magnetic skyrmion (MS) [3]. The DM interaction has a spin-orbit nature and is clearly manifested for ferromagnet (FM)/heavy metal systems [4]. However, the DM interaction is not the only mechanism that makes it possible to control the chirality of an FM. It was shown that the magnetostatic interaction also affects the chirality of distributions in an FM film on a paramagnetic [5] or superconducting [6, 7] substrate. This interaction can lead to the instability of a homogeneous state in an FM, while modes with a certain chirality are the first to lose their stability [8]. It was also shown that the magnetostatic interaction in such systems leads to the appearance of the nonreciprocity in the spin wave spectrum [9, 10]. In this work, we theoretically investigate the problem of a magnetostatic MS stabilization in an FM on a substrate from a paramagnet (PM) (an FM above the critical temperature) or from London superconductor (SC). The MS induces an image MS in the substrate, which can stabilize the original one due to interaction with it. We have shown that only the PM stabilizes the MS, which radius is temperature sensitive near the Curie point of the PM. Our results provide a new way to control and stabilize the MS without Dzyaloshinskii-Moriya interaction.

We place the FM film at  $0 < z < h$ , while a PM or SC substrate is at  $z < 0$  and the external magnetic field  $\mathbf{H}_{\text{ext}}$  is directed against the  $z$  axis. We consider the film to be thin enough, so that the dependence of the MS magnetization  $\mathbf{M}$  on the coordinate  $z$  could be discarded. Then  $\mathbf{M} = \mathbf{M}(\rho)$ , where  $\rho$  is the coordinate measured from the MS center, i.e.,

$$\mathbf{M}(\rho) = M_0(\cos\psi\sin\Theta(\rho), \sin\psi\sin\Theta(\rho), \cos\Theta(\rho)) , \tag{1}$$

where  $M_0$  is the saturation magnetization,  $\Theta(\rho)$  is some function of  $\rho$  and  $\psi$  ( $0 < \psi < \pi$ ) is the constant.

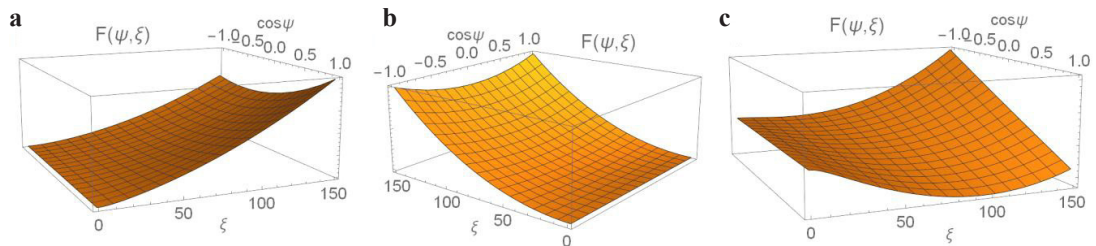


Figure 1. Free energy  $F(\psi, \xi)$  for the cases  $\kappa = -1$  (a),  $\kappa = 0$  (b),  $\kappa = 1$  (c).

Equation (1) describes an axially symmetric MS of a general form. For example,  $\psi = 0, \pi$  or for  $\psi = \pm\pi/2$  we have Neel- and Bloch-type MS, respectively. The free energy of the film  $F$  has the form

$$F = E_{MS} + 2\pi M_0^2 h \int_0^\infty \left[ \frac{L_0^2}{2} \left( \left( \frac{\partial \Theta}{\partial \rho} \right)^2 + \frac{1}{\rho^2} \sin^2 \Theta \right) - \frac{1}{2} K_a \cos^2 \Theta + \frac{H_{ext}}{M_0} \cos \Theta \right] d\rho, \quad (2)$$

where  $K_a > 0$  is the constant of magnetic anisotropy,  $L_0$  is the exchange constant,  $E_{MS}$  is the total magnetostatic energy, including the energy of the film  $\omega$  and the interaction energy of the film and substrate  $W$ , i.e.,  $E_{MS} = \omega + W$ . The energies  $\omega$  and  $W$  have the form

$$\omega = S^2 \int_0^\infty \left[ \frac{1}{q^2} (qh - (1 - e^{-qh})) \operatorname{div}^2 \mathbf{M}(q) + (1 - e^{-qh}) (\mathbf{e}_z \mathbf{M}(q))^2 \right] dq, \quad (3)$$

$$W = \frac{hS^2}{2\pi} \int_0^\infty D_{\text{eff}}(q) [\operatorname{div} \mathbf{M}(q) + q \mathbf{e}_z \mathbf{M}(q)]^2 dq, \quad (4)$$

where  $S$  is the system area,  $\mathbf{M}(q)$  and  $\operatorname{div} \mathbf{M}(q)$  are Fourier transforms of  $\mathbf{M}(\rho)$  and  $\operatorname{div} \mathbf{M}(\rho)$ , respectively,  $D_{\text{eff}}(q) = -\pi \kappa(q) (1 - e^{-qh})^2 / q^2 h$  is the effective DM constant [10], and  $\kappa(q)$  is dimensionless constant, which distinguishes PM from SC, i.e.,

$$k(q) = \begin{cases} 2\pi\chi / (1 + 2\pi\chi), & \text{FM/PM} \\ -(\sqrt{q^2 l_s^2 + 1} - q l_s) / (\sqrt{q^2 l_s^2 + 1} + q l_s), & \text{FM/SC} \end{cases} \quad (5)$$

In Eq. (5)  $\chi = C/(T - T_C)$  is the PM susceptibility,  $l_s = l_{s0}(1 - T/T_C)^{-1/2}$  is the SC London penetration depth,  $T$  is the system temperature,  $T_C$  is the critical temperature for the FM-PM or normal metal-SC transition,  $C$  is the Curie constant,  $l_{s0}$  is  $l_s$  when  $T = 0$ . For the ideal PM (SC) case, when  $\chi \rightarrow \infty$  ( $l_s = 0$ ), the constant  $\kappa$  tends to 1 (−1). We use the simplest linear ansatz for  $\Theta(\rho)$ , i.e.,  $\Theta(\rho) = \pi\rho\theta(R - \rho)/R + \pi\theta(\rho - R)$  [3], where  $\theta(\rho)$  is the Heaviside step function,  $R$  is the MS radius. Thus, we have two independent parameters,  $\xi = 2R/h$  and  $\psi$ , characterizing the MS. We can find the local minimum of the  $F$  as a function of  $\xi$ . After that, by changing the parameter  $\psi$ , we can find the global minimum. Figure 1 shows the  $F(\psi, \xi)$  for  $H_{ext} = 0$  and for the cases  $\kappa = -1, 0, 1$ , which correspond to FM/ideal SC, FM/ideal PM, and FM without substrate, respectively. We can see that

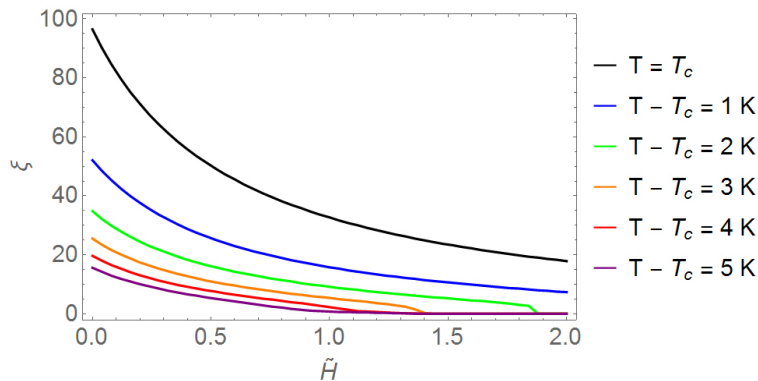


Figure 2. Parameter  $\xi$  vs.  $\tilde{H}$  for various temperatures. The following parameters were used in these calculations:  $L_0/h = 0.2$ ,  $K_a/4\pi = 1.1$ ,  $C = 0.4$  K.

only PM stabilizes the MS, and this MS is a Neel type and has a certain chirality corresponding to  $\psi = 0$ . Figure 2 shows the dependences of  $\xi$  on  $\tilde{H} = H_{\text{ext}}/M_0$  at various temperatures in FM/PM. As can be seen, a temperature change of a few degrees results in a dramatic decrease in the MS radius, which allows control of the MS state by changing temperature.

*The work was supported by Russian Foundation for Basic Research (Grant No. 20-02-00356). One of us (M.A. K.) thanks to the Foundation for the Advancement of Theoretical Physics and Mathematics “BASIS”.*

1. I.E. Dzialoshinskii, Sov. Phys. JETP, **5**, 1259 (1957).
2. T. Moriya, Phys. Rev., **120**, 91 (1960).
3. A.N. Bogdanov and D.A. Yablonskii, Zh. Eksp. Teor. Fiz., **95**, 182 (1989).
4. A. Crepieux and C. Lacroix, J. Magn. Magn. Mater., **182**, 341 (1998).
5. N. Mikuszeit, S. Meckler, R. Wiesendanger, and R. Miranda, Phys. Rev. B, **84**, 054404 (2011).
6. K.R. Mukhamatchin and A.A. Fraerman, JETP. Lett., **93**, 716 (2011).
7. I.M. Nefedov, A.A. Fraerman, and I.A. Shereshevskii, Phys. Solid State, **58**, 503 (2016).
8. A.A. Fraerman and K.R. Mukhamatchin, J. Exp. Theor. Phys., **131**, 963 (2020).
9. I.A. Golovchanskiy, N.N. Abramov, V.S. Stolyarov et al., J. Appl. Phys., **124**, 233903 (2018).
10. R.A. Gallardo, T. Schneider, A.K. Chaurasiya et al., Phys. Rev. Applied, **12**, 034012 (2019).

**THE SPECIFIC LOSS POWER IN THE SYSTEMS OF MOBILE AND IMMOBILIZED MAGNETIC PARTICLES IN APPLIED AC MAGNETIC FIELD**

*A.A. Kuznetsova\**, *E.A. Elfimova*, *A.V. Ambarov*

Institute of Natural Sciences and Mathematics, Ural Federal University, Ekaterinburg, Russia

\*E-mail: [anastasia.kuznetsova@urfu.ru](mailto:anastasia.kuznetsova@urfu.ru)

Magnetic hyperthermia is a progressive method of treatment of tumor diseases. The idea of this method is the injection of a ferroparticles into the region with the diagnosed tumor. Then the particles and, therefore, the tumor cells, are heated by an ac magnetic field. Numerous investigations show that in the temperature range  $\sim 42\text{--}50\text{ }^\circ\text{C}$  the tumor cells die, whereas the healthy cells, being more temperature resistive, survive. The specific loss power (SLP) is a characteristic of the effectiveness of the magnetic hyperthermia method. In this work, we calculate the SLP for the cases of mobile and immobilized particles in order to find the frequency and amplitude ranges of the magnetic field which give the best hyperthermic effect. It should be noted that some restrictions are imposed on the characteristics of the magnetic field since a person can experience a pain in some ranges of the frequencies and amplitudes of the field. We consider and compare the cases of mobile and immobilized particles because magnetic particles injected into the human body can be placed in liquid (blood, cerebrospinal fluid etc.) or solid (epithelium, muscles etc.) media. For the case of the immobilized particles, we assume that the easy magnetization axes of the particles are aligned parallel to the ac magnetic field. The rotational motion of a magnetic moment is described by the probability distribution function which is the solution of the Fokker-Planck equation (FPE). Interparticle dipole-dipole interactions are included to the FPE within the framework of modified

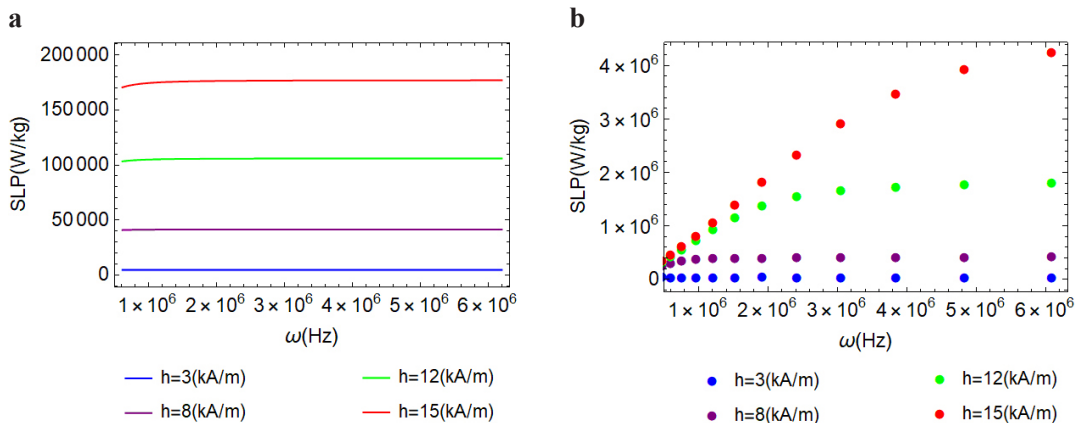


Figure 1. The SLP as a function of the frequency  $\omega$  of the magnetic field with different values of the amplitude  $h$  for the ensemble of interacting mobile particles (a) and interacting immobilized magnetic particles (b).

mean-field theory [1]. The solution of the FPE is used for calculation of the dynamic susceptibility and then SLP:

$$\text{SLP} = \frac{\mu_0 \pi f h^2 \chi''}{\rho \phi},$$

where  $\mu_0$  is the magnetic constant,  $f$  is the frequency of the alternating magnetic field,  $h$  is the amplitude of the alternating magnetic field,  $\rho$  is the particle material density,  $\phi$  is the volume concentration of particles in the magnetic material,  $\chi''$  is the imaginary part of the dynamic susceptibility. Figure 1 shows SLP for the mobile particles (Fig. 1a) and immobilized particles (Fig. 1b) in the range of amplitudes and frequencies of the ac magnetic field used in magnetic hyperthermia: we consider magnetic field amplitudes not exceeding 15 kA/m and angular frequencies from 620 to 6200 kHz. The results were obtained on the basis of analytical [2] and numerical [3] calculations of the dynamic susceptibility. It can be seen that it is possible to control the release of energy in ensemble of magnetic particles by changing the amplitudes of the magnetic field. In the case of immobilized magnetic particles, an increase in the field frequency leads to an increase in the SLP. If magnetic particles are placed in a liquid and have translational degrees of freedom, then the amount of energy released does not change in the considered frequency range of the magnetic field for the fixed value of the field amplitude.

*The study was funded by RFBR, project number 20-02-00358.*

1. A.O. Ivanov, V.S. Zverev, S.S. Kantorovich, *Soft Matter.*, **12**, 3507 (2016).
2. A.V. Ambarov, V.S. Zverev, E.A. Elfimova, *Modelling and Simulation in Materials Science and Engineering*, **28**, 085009-(1-15) (2020).
3. E.A. Elfimova, M.S. Rusanov, V.S. Zverev, *Physical Review E*, **104**, 044604-(1-11) (2021).



## THE MAGNETIC CHARACTERISTICS INHOMOGENEITY OF AMORPHOUS COBALT-BASED ALLOY IN AS-QUENCHED STATE

*E.S. Nekrasov, N.A. Skulkina\**

Ural Federal University, Ekaterinburg, Russia

\*E-mail: [nadezhda.skulkina@urfu.ru](mailto:nadezhda.skulkina@urfu.ru)

The structure of amorphous alloys obtained by rapid quenching is nonequilibrium, which affects on the level of magnetic characteristics. The inhomogeneity of internal stresses in the as-quenched state does not allow one to obtain the optimal level of magnetic characteristics and their uniformity after heat treatment, since the relaxation of stresses of different levels calls for isothermal holdings differing in the duration [1, 2]. For example, heat treatments of samples that has not the same properties in the initial state showed that after heat treatments at 380 and 400 °C with an isothermal holding time of 10 minutes, the values of  $\mu_{\max}$  are in the ranges 248000–396000 and 221000–60000, respectively. This work presents the results of studies of the magnetic characteristics inhomogeneity in the as-quenched state of the amorphous soft magnetic cobalt-based alloy in order to ascertain opportunities for the optimization of its service characteristics.

The samples of the amorphous alloy Co-Ni-Fe-Cr-Mn-Si-B (AMAG-172) were in a form of strips  $110 \times 10 \times 0.022$  mm, which were cut from an industrial ribbon 20 mm wide manufactured in the JSC NIIMET (Kaluga). Two series of samples were formed, which were prepared by cutting a ribbon 2 cm wide in two parts along the width; the parts cut was sequentially numbered along the ribbon length. The total length of studied parts was  $\sim 4$  m. Numbers of the studied samples correspond to the numbers of ribbon parts. The magnetic permeability was determined by the induction-pulse method, the relative volume of domains with orthogonal magnetization ( $V_{\text{orth}}$ ) – by the correlation curve obtained by mössbauer studies [3, 4] with errors not exceeding 3 and 5%, respectively.

The study results showed that there is a significant inhomogeneity of magnetic characteristics along the ribbon width: the values of  $\mu_{\max}$  and  $V_{\text{orth}}$  for the same parts of different series differ by three and 2.5 to 3 times, respectively. Figure 1 shows the results of changing the magnetic characteristics along the ribbon length for a series of samples with large  $\mu_{\max}$  and smaller  $V_{\text{orth}}$ . For another series of samples, there is a similar dependence with significantly lower  $\mu_{\max}$  and higher  $V_{\text{orth}}$ .

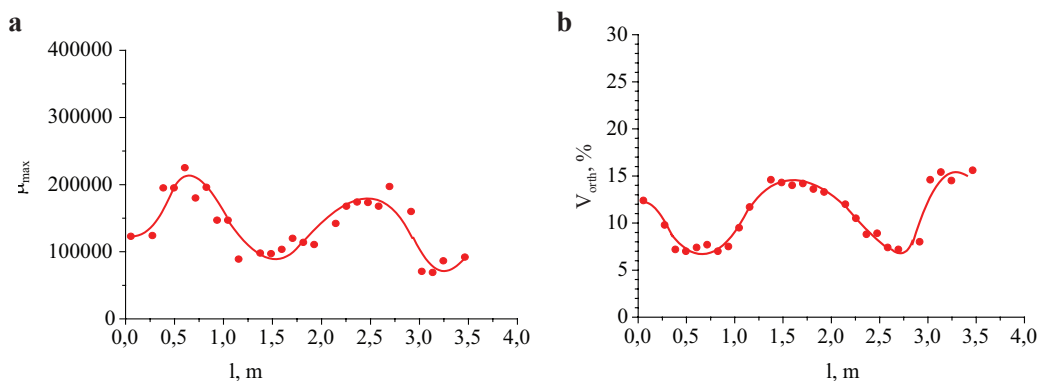


Figure 1. Nonuniformity of the **a** maximum magnetic permeability and **b** volume of domains with orthogonal magnetization along the ribbon length for second-series samples.

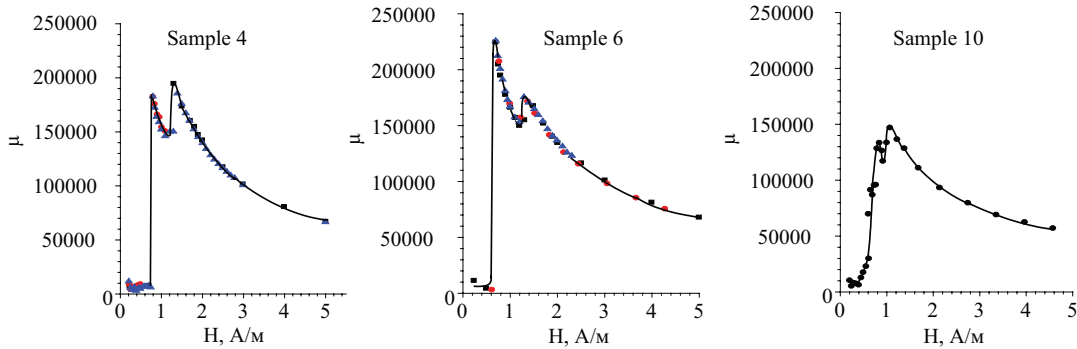


Figure 2. Field dependences of the magnetic permeability of second-series samples corresponding to areas characterized by minimum values of the volume of domains with orthogonal magnetization. The different symbols correspond to multiple numerous clarifying measurements, including was performed on different installations.

The observed behavior of the maximum magnetic permeability is periodic and sinusoidal in shape. The character of the dependence  $V_{\text{orth}}$  is analogous. The difference consists in the fact that, with respect to variations of the maximum magnetic permeability, the volume of domains with the orthogonal magnetization component varies in antiphase. A correlation between the period of variations of the magnetic characteristics and size of a cooling disk of standard installations used for manufacturing ribbons is observed. For this series of samples in areas with minimal values of the volume of domains with orthogonal magnetization were found a bimodal field dependence of the magnetic permeability (Fig. 2). In passing from one to another ribbon area, changes in the maximum heights and their relationship are observed. The transformation of the field dependence of the magnetic permeability in this area is realized as follows. At first, an additional peak appears in the area of weak fields, the height of which is less than the main one. Then, when moving to subsequent sections, the height of the additional peak increases, becomes greater than the height of the main peak, and then it changes in reverse order. In this case, the field range ( $\Delta H$ ) between the first and second maxima on the field dependence of the magnetic permeability decreases; in the end, merging the maxima takes place. For the another-series samples corresponding to interval with minimum values of  $\mu_{\text{max}}$ , no double maximum on the field dependence of the magnetic permeability is observed. The bimodal field dependence of the magnetic permeability can be related to the ribbon-thickness inhomogeneity because of different levels of internal stresses, which are due to the temperature gradient across the thickness during ribbon manufacturing.

The results reported in this study completely agreed with those obtained in previous studies. The most probable reasons for the high inhomogeneity of the magnetic characteristics in the as-quenched state of the ribbon are related to the technology of its manufacture, the optimization of which can help in increasing the uniformity of its properties,

*The study was supported in part by the Ministry of Science and Higher Education of the Russian Federation, project no. FEUZ-2020-0051.*

1. Skulkina N.A., Ivanov O.A., Pavlova I.O., Minina O.A., Phys. Met. Metallogr., **112**, 583–588 (2011).
2. Skulkina N.A., Ivanov O.A., Shubina L.N., Blinova O.V., Phys. Met. Metallogr., **117**, 1085–1091 (2016).
3. Skulkina N.A., Ivanov O.A., Mazeeva A.K., Kuznetsov P.A., Stepanova E.A., Izv. Ross. Akad. Nauk, Ser. Fiz., **65**, 1483–1486 (2001).
4. Skulkina N.A., Ivanov O.A., Mazeeva A.K., Kuznetsov P.A., Stepanova E.A., Blinova O.V., Mikhaliysyna E.A., Denisov N.D., Chekis V.I. Phys. Met. Metallogr., **118**, 1182–1189 (2017).

## DEMAGNETIZING FACTOR CONTRIBUTION TO THE FUNCTIONAL PROPERTIES OF COBALT-BASED AMORPHOUS RIBBONS WITH HIGH GIANT MAGNETIC IMPEDANCE

*A.A. Pasyukova<sup>1,2\*</sup>, A.V. Timofeeva<sup>2</sup>, V.A. Lukshina<sup>2</sup>, G.V. Kurlyandskaya<sup>2,3</sup>*

<sup>1</sup>Institute of Metal Physics, Ural Branch of Russian Academy of Sciences, Ekaterinburg, Russia

<sup>2</sup>Institute of Natural Sciences and Mathematics, Ural Federal University, Ekaterinburg, Russia

<sup>3</sup>Depto Electricidad y Electrónica, Universidad del País Vasco UPV/EHU, Bilbao, Spain

\*E-mail: [pasyukova\\_a@imp.uran.ru](mailto:pasyukova_a@imp.uran.ru)

Modern technological applications are based on miniature devices and highly sensitive detectors that monitor the main parameters. The physical size is important parameter for the sensitive elements of sensors based on the giant magnetoimpedance effect (GMI). The effect consists in a change in the total impedance of a ferromagnetic conductor in an external magnetic field when an alternating current flows through it [1]. The properties of a ferromagnet can vary significantly over the cross section as it happens for rapidly quenched amorphous ribbons. In this work, a comparative analysis of the contribution of size effects to the GMI properties of cobalt-based amorphous ribbons obtained experimentally and theoretically.

Rapidly quenched amorphous ribbons of  $\text{Fe}_3\text{Co}_{67}\text{Cr}_3\text{Si}_{15}\text{B}_{12}$  composition were studied. Samples without additional treatments (after rapid quenching), after post-preparation relaxation annealing (at the temperature of 350 °C during 1 hour) or thermomechanical treatment (350 °C, 1 hour and 250 MPa specific load) were considered. The width and the thickness of the ribbons were either 0.8 mm and 0.024 mm or 2 mm or 0.032 mm respectively. Differences in the geometry were associated with the technology of ribbon fabrication. Magnetic properties were studied by the induction method and by vibrating sample magnetometry. GMI effect was studied by an automated complex (Agilent HP e4991A impedance analyzer). The GMI ratio of the total impedance  $Z$  was calculated as follows:  $\Delta Z/Z = 100\% \cdot (Z(H) - Z(H_{\max}))/Z(H_{\max})$ ,  $H_{\max} = 110$  Oe (the real and imaginary components were also analyzed). An approach of the demagnetizing factor [2] was proposed for comparison of

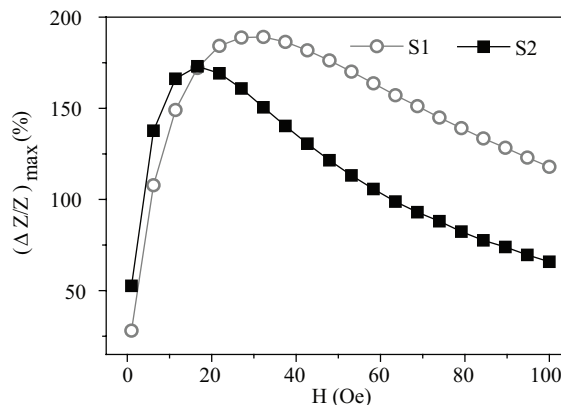


Figure 1. Frequency dependence of the GMI ratio for samples after thermomechanical treatment with equal length to width ratio.

magnetic and GMI studies. In this regard, samples with a length of 18 (0.8 mm wide, S1) and 45 mm (2.0 mm wide, S2) were considered.

The demagnetizing factor as well as the stray fields associated with the shape anisotropy were noticeably higher for narrow than for wide ribbons according to the calculation. Regardless of the type of processing, the GMI ratio of the imaginary component was higher for the S1 sample. As a result, the GMI ratio of sample S1 was also slightly higher, which can be seen from the values of the absolute maximum of the GMI ratio (Fig. 1). The contribution of the imaginary component to the dynamic magnetic permeability can be determined by a lower dispersion both over the width and thickness of the S1 ribbon. The maximum value  $(\Delta Z/Z)_{\max}$  was reached at higher frequencies for S1 ribbons.

*This work was financially supported by the grant of President of Russian Federation MK-2080.2022.1.2.*

1. G.V. Kurlyandskaya, J.M. Barandiaran, M. Vazquez, D. Garcia, N.V. Dmitrieva, JMMM, **215-216**, 740–742 (2000).
2. D.-X. Chen, E. Pardo, A. Sanchez, IEEE Trans. Magn., **41(6)**, 2077–2088 (2005).

## MAGNETOACTIVE ELASTOMERS WITH MAGNETICALLY HARD PARTICLES: THE EFFECT OF PARTICLE/MATRIX ADHESION FAILURE ON THE MAGNETIZATION

*M.V. Vaganov<sup>1</sup>, D.Yu. Borin<sup>2</sup>, S. Odenbach<sup>2</sup>, Yu.L. Raikher<sup>3\*</sup>*

<sup>1</sup>Clarendon Laboratory, Department of Physics, University of Oxford, UK

<sup>2</sup>Magnetofluidynamics, Measuring and Automation Technology,  
Institute of Mechatronic Engineering, TU Dresden, Germany

<sup>3</sup>Institute of Continuous Media Mechanics, Russian Academy of Sciences, Ural Branch,  
Perm, Russia

\*E-mail: [raikher@icmm.ru](mailto:raikher@icmm.ru)

Magnetoactive elastomers (MAEs) – the composites where a polymeric matrix is filled with micron-size ferromagnet particles are quite new and highly promising smart materials, see recent reviews [1–3] and many others. For some time, the one and only type of MAEs under study was represented by the systems filled with the particles of iron-like substances, i.e., magnetically soft metals or alloys. Later on, the MAE family was qualitatively extended by introducing into it magnetically hard (MH) particles, NdFeB in particular [4–8]. The materials of that type differ significantly from ‘classical’ MAEs. Due to that, their applicational prospects extend yet more since, unlike ‘classical’ prototypes, MH-MAEs are able to possess permanent magnetization – tuned in the production process – and, hence, can produce magnetic fields of their own both inside and outside the samples made of these materials.

This new chapter in the MAE material science claimed for new theoretical approaches capable of handling the specific fundamental properties of such easily deformable magnetic composites. Indeed, considering the MH-MAEs from the viewpoint of nomenclature of magnetic materials, one easily finds out that they are undoubtedly unique. Namely:

1. their micron-size particles are magnetically hard but not single-domain. In fact, each particle is a tight solid assembly (clot) of single-domain grains, which are uniaxial and whose axes are distributed at random within the particle;
2. these particles dwell in a soft (mechanically compliant) matrix and because of that may move inside it under the action of their own (interparticle) and external magnetic fields;
3. unlike to what happens in ‘classical’ MAEs, the multigrain particles, once having been magnetized, acquire non-zero remanent magnetic moments that makes them to react to an applied field mostly via a rotational rather than translational mode. This is especially true in the case of a uniform external field.

As it follows from the above, the magnetomechanical (sometimes termed as mutiferroic) properties of MH-MAEs, i.e., the change in the shape and elasticity of the samples under the action of the field, are crucially dependent on the extent to what the magnetic torques imposed on the particles by the field, are transferred to the matrix. In other words, for the optimal control on the field-induced behavior of MH-MAEs, the particles should be unbreakably attached to the polymeric environment.

In view of that objective, the real quality of the particle/matrix contact is an important issue. And even from an *a priori* consideration one infers that an undesirable breakage of that contact is not at all impossible. Indeed, the surface of a particle where the metal abuts on silicone rubber is a customary contact pair in MH-MAEs. Such an interface does not produce chemical bonds, however, so that the major source of the particle/matrix attachment is provided by the van-der-Waals interaction that is not that strong. A simple estimate shows that application of a field of a few hundred kA/m

suffices to make an MH particle to get ‘unleashed’ and start to rotate relative to the wall of its cavity inside the elastomer [9]. Remarkably, in the majority of theoretical works on these composites this possibility is completely ignored, and the contact is assumed infinitely strong even though the hints to the breakage of the particle/matrix adhesion readily follow from the already accumulated experimental data: the magnetization loops of real MH-MAEs display the coercivities much lower than any estimates based on the Stoner-Wohlfarth model of the grains which constitute the particles.

In this work we develop a description that explicitly takes into account the fact that the interface between the matrix and magnetic particles might become unstable. If to go into more detail, when a field is applied, it exerts a torque on the particle magnetic moment which, due to a high internal magnetic anisotropy, transfers it to the particle anisotropy axis, i.e., to the particle body itself. At relatively low torques, the particle responds reversibly and deviates from its initial orientation fully dragging on the surrounding matrix with it. As soon as the resisting elastic torque generated by the matrix exceeds some critical value, the adhesion breaks, the particle ‘unleashes’ and begins torsional slipping motion inside the cavity that it occupies. Evidently, this process facilitates inversion of the sample magnetization and reduces the overall (macroscopically observed) coercivity.

The base of the developed model is a numerical description of magnetization of an MH multi-grain particle as such [10]. On that grounds, the mechanical behavior of the particle embedded in an elastic environment is considered. The occurrence of slippage is introduced as a transition which takes place after the particle deviation angle exceeds some reference threshold value. The latter is derived from the experimental data on cyclic magnetization measurements of several consecutive hysteresis loops under variation of the maximal field.

The simulation is performed on an assembly of 3600 particles within each of which the grain ‘population’ is generated at random. The results are compared with the experimental data obtained on MH-MAEs whose polymeric matrices are made of polydimethylsiloxane and the magnetic filler is NdFeB spherical particles of Magnequench brand. First place, the juxtaposition of the loops simulated under assumption of unbroken adhesion and the ones delivered by our model reveals qualitative difference of the loop shapes. Moreover, using the independent rheological data on the tested MH-MAEs and adopting them as material parameters for the numerical simulations on the above-described MH particle assembly, we, first, find a striking loop-shape resemblance and, second, obtain a fairly good quantitative agreement with the magnetic measurements.

*Support by RFBR project 19-52-12045 and projects Bo 3343/3-1 and Od 18/24-1 within SPP1681 and PAK907 programs is acknowledged.*

1. S. Samal, M. Škodová, L. Abate, and I. Blanco, Applied Sciences, **10**, Art. no. 4899 (2020).
2. D. Zhalmuratova and H.-J. Chung, ACS Applied: Polymer Materials, **2**, 1073–1091 (2020).
3. S. Lucarini, M. Hossain, and D. Garcia-Gonzalez, Composite Structures, **279**, Art. no. 114800 (2022).
4. P.R. von Lockette, J. Kadlowec, and J.-H. Koo, Proc. SPIE, **6170**, Smart Structures and Materials 2006: Active Materials: Behavior and Mechanics, 61700T (April 06, 2006); doi:10.1117/12.658750.
5. G.V. Stepanov, A.V. Chertovich, and E.Yu. Kramarenko, Journal of Magnetism and Magnetic Materials, **324**, 3448–3451 (2012).
6. D.Yu. Borin, G.V. Stepanov and S. Odenbach S, Journal of Physics: Conference Series, **412**, Art. no. 012040 (2013).
7. J.M. Linke, D.Yu. Borin, and S. Odenbach, RSC Advances, **6**, 100407–100416 (2016).
8. G.V. Stepanov, D.Yu. Borin, A.V. Bakhtiarov, and P.A. Storozhenko, Smart Materials and Structures, **26**, Art.no. 035060 (2017).
9. M.V. Vaganov, D.Yu. Borin, S. Odenbach, and Yu.L. Raikher, Advanced Theory and Simulations, **4**, Art. no. 2000327 (2021).
10. M.V. Vaganov, D.Yu. Borin, S. Odenbach, and Yu.L. Raikher, Soft Matter, **15**, 4947–4960 (2019).

## NUMERICAL CALCULATION OF THE CUBIC TERM OF THE DYNAMIC SUSCEPTIBILITY OF INTERACTING AND MOVING MAGNETIC PARTICLES

*M.S Rusanov\**, *E.A Elfimova*, *V.C. Zverev*

Department of Theoretical and Mathematical Physics, Institute of Natural Sciences and Mathematics, Ural Federal University, Ekaterinburg, Russia

\*E-mail: [rusanoff.mixail@yandex.ru](mailto:rusanoff.mixail@yandex.ru)

In this work we study the response of ferrofluid to an AC magnetic field of arbitrary amplitude. The response of ferrofluid can be determined by the coefficients in the expansion of the magnetization  $M$  by the magnetic field  $H$ :

$$M = \chi_1 H + \chi_3 H^3 + \dots$$

The coefficient at the first power of  $H$  is the linear magnetic susceptibility. The dependence of  $\chi_1$  on the interparticle dipole-dipole interactions and the AC magnetic field amplitude was studied in detail in ref. [1]. In this work, based on the results of numerical simulations, a simple approximate formula was obtained for the cubic term  $\chi_3$  taking into account interactions and different magnetic field amplitudes.

The ferrofluid is modeled by an ensemble of moving, interacting, spherical magnetic particles of the same size. Each particle has a constant magnetic moment. Relaxation of magnetic moments occurs by the Brownian mechanism with the Brownian rotation time  $\tau_B$ . The AC magnetic field  $\mathbf{H} = h \cos(\omega t) \hat{\mathbf{H}}$  is applied along the  $z$ -axis,  $\hat{\mathbf{H}} = (0, 0, 1)$ ,  $h$  is a magnetic field amplitude,  $\omega$  is a field frequency,  $t$  denotes time. The magnetic moment orientation probability density function  $W(t, x)$  is determined from the solution of the Fokker-Planck equation:

$$2\tau_B \frac{\partial W}{\partial t} = \frac{\partial}{\partial x} \left[ (1-x^2) \left( \frac{\partial W}{\partial x} + W \frac{\partial U}{\partial x} \right) \right],$$

where  $U$  is the potential energy of a dipole in units of the thermal energy  $k_B T$ ,  $x = \cos(\theta)$ ,  $\theta$  is polar angle which describes the orientation of each magnetic moment. Interparticle interactions in the Fokker-Planck equation are taken into account in the potential energy  $U$  at the level of a modified first-order mean field theory [2]. Magnetization is determined as the averaged projection of the magnetic moment orientations  $W(t, x)$  onto the magnetic field direction:

$$M(t) = \int_{-1}^1 x W(t, x) dx$$

The real  $\chi_3'$  and imaginary  $\chi_3''$  part of the cubic term of the dynamic susceptibility are defined as the third term of the Fourier series:

$$\chi_3'(\omega) = \frac{\omega}{\pi h^3} \int_0^{2\pi/\omega} M(t) \cos(3\omega t) dt,$$

$$\chi_3''(\omega) = \frac{\omega}{\pi h^3} \int_0^{2\pi/\omega} M(t) \sin(3\omega t) dt.$$

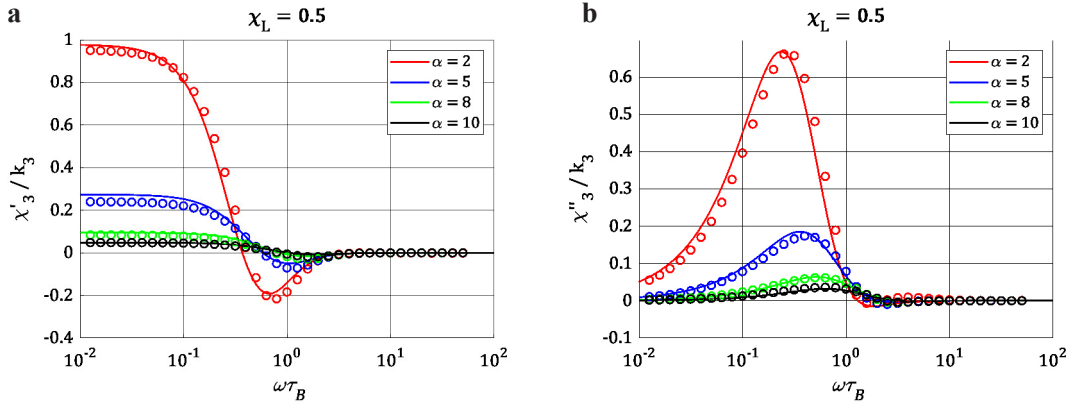


Figure 1. Real  $\chi'_3$  (a) and imaginary  $\chi''_3$  (b) parts of the susceptibility as a function of the dimensionless frequency of the AC field  $\omega\tau_B$  for different AC field amplitudes  $\alpha$ .  $k_3 = -\mu_0 m^4 n / 180 (k_B T)^3$  is the normalization factor, where  $\mu_0$  is the vacuum magnetic permeability,  $m$  is the magnetic moment,  $n$  is numerical concentration of the particles. Points are from numerical solution of the Fokker-Planck equation, lines are new simple approximation analytical formula. On the abscissa axis the logarithmic scale is used.

The Fokker-Planck equation was solved numerically by a finite-difference scheme suggested in [3]. The proposed in [3] the algorithm was developed for convection-diffusion problems. We changed this algorithm for the solution of the Fokker-Planck equation. Numerical simulations allowed us to obtain  $\chi_3$  for different values of the field amplitude, particle concentrations, intensity of dipole-dipole interactions. Using these numerical results, we found a simple approximation analytical formula for  $\chi_3$  with the help of the least square method.

Figure 1 shows the reduced real and imaginary parts of  $\chi_3$  as the functions of the field frequency  $\omega\tau_B$  for different values of the Langevin parameter  $\alpha$  which characterizes the field amplitude. The points are from the numerical solution of the Fokker-Planck equation. The lines represent new approximation analytical formula for  $\chi_3$ . The Fig. 1 shows the result for the system with the Langevin susceptibility  $\chi_L = 0.5$ . We can see that the greater the field amplitude, then smaller the value of  $\chi_3$ . Studies have shown that the new approximation analytical formula for  $\chi_3$  is valid for  $\chi_L \lesssim 1.5$ .

*This work was financially supported by the Ministry of Science and Higher Education of the Russian Federation within the project “Ural Mathematical Center” (agreement № 075-02-2022-877)*

1. M.S. Rusanov, E.A. Elfimova, V.S. Zverev, Phys. Rev. E, **104**, 044604 (2021).
2. A.O. Ivanov, V.S. Zverev, S.S. Kantorovich, Soft Matter, **12**, 3507 (2016).
3. N. Afanas'eva, P.N. Vabishchevich, M.V. Vasil'eva, Russian Mathematics, **57**, 1 (2013).



## COMPUTER SIMULATION OF JOINT MAGNETIC-STRUCTURAL-MECHANICAL RESPONSE OF MAGNETOSENSITIVE VESICLES

*A.V. Ryzhkov*

Institute of Continuous Media Mechanics, Perm Federal Research Center of the  
Ural Branch of the Russian Academy of Sciences, Perm, Russia  
E-mail: [ryzhkovalexandr@gmail.com](mailto:ryzhkovalexandr@gmail.com)

Magnetic nanosized particles (MNPs) show their promising powerful features for mostly biomedical applications during the last decades. To extend application area and to improve biocompatibility MNPs are generally coupled-with or embedded-into macromolecular structures. Hence, the wide range of *magnetic soft matter* entities that are explored experimentally and theoretically is available. Among other examples the so-called magnetosensitive vesicles (MSVs) – submicron-sized closed amphiphilic self-assemblies with decorated by MNPs bilayer membrane – attract the attention of researchers [1, 2]. The union of nature-inspired vesicular morphology and magnetosensitive components opens prospects for creating of artificial multifunctional remotely controlled nanovehicles with tunable properties for drug or another substance delivery and release. Synthesis methods in this sense allow to create MSVs of different sizes, shapes, membrane structures, but induced by external field MNPs rearrangements may keep them predictably deformable nanosurgery tools. The features of such a coupled magnetic, structural, and deformational response for vesicles of different geometries are proposed to study by means of coarse-grained molecular dynamics simulation [3] in ESPResSo software [4].

In model representation which is based on bead-spring notion for polymeric capsule the separate MSV consists of two concentric spherical shells (which imitate amphiphilic bilayer) made up of polymeric beads bonded by a set of potentials and one or several layers of equal-sized MNPs which are placed into intramembrane space (see Fig. 1 for the template of two-layered MSV as an example). The beads inside of outer or inner shell are connected by linear elastic springs and angle harmonic potential to specify stretching and bending properties. The beads of opposite shells are connected by the series of springs to keep thickness of the membrane approximately the same. The MNPs which are assumed to be soft dipolar spheres interact via magnetic dipolar coupling. The soft repulsion is also involved in the interaction between the MNPs and polymeric layers, so nanopar-

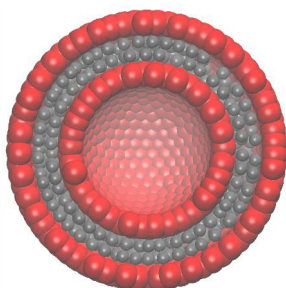


Figure 1. Schematic representation of two-layered MSV template (in cross-section): red particles are polymeric layers, grey ones are MNPs.

ticles turn out to be locked inside the membrane, although they can migrate within the confines of the intramembrane space. After the generating of two-component spherical template it may be reshaped into spheroid, ellipsoid, disc with one or two concavities. When the initial configuration of the model MSV (including the assignment of volume fraction of MNPs and number of MNP layers) is defined the equations of motion for every particle are solved numerically considering interparticle interactions, coupling with implicit solvent at constant temperature (Langevin thermostat conditions), and influence of applied external homogeneous magnetic field.

Several problems are calculated using the developing model. First, the response on growing magnetic field of spherical multilayered MSVs (with one, two, and three nanoparticles layers) is studied for three values of intramembrane volume fraction of MNPs. Another series of computational experiments is the magnetization of one-layered spheroidal vesicles under the field, which is applied parallel, perpendicular, and at an angle to the axis of spheroid. The change of shape and MNPs density rearrangements are analyzed. Then, one-layered MSVs of discocyte (biconcave disc) and stomatocyte (disc with one concavity) shapes are subjected to the external magnetic field strength which increases up to defined value and then decreases to zero during step-by-step computational experiment. The obtained data includes MNPs aggregates rearrangements during the cycle of magnetization-demagnetization as well as vesicle shape changes associated with field-induced response. Additionally, the case when intramembrane MNPs become attached to polymeric walls after the field switching-off is simulated as a part of synthesis procedure of non-spherical MSVs during cross-linking [5]. Furthermore, the upgraded model which includes particles of transportable inside the cavity substance in implicit way is planned for presentation.

*The research was funded by Russian Science Foundation grant number 20-71-00045.*

1. S. Lecommandoux et al., *Adv. Mater.*, **17** (6), 712–718 (2005).
2. H. Oliveira et al., *J. Control. Release.*, **169** (3), 165–170 (2013).
3. R. Weeber, P. Kreissl, C. Holm., *Arch. Appl. Mech.*, **89** (1), 3–16 (2019).
4. F. Weik et al., *Eur. Phys. J. Spec. Top.*, **227** (14), 1789–1816 (2019).
5. A.V. Ryzhkov, Y.L. Raikher. *IEEE Magn. Lett.*, **13**, 6100905 (2022).

## DYNAMICS OF MAGNETIC FLUIDS AND BIDISPERSE MAGNETIC SYSTEMS UNDERGOING OSCILLATORY SHEAR

*E.V. Shel'deshova\**, *P.A. Ryapolov*

Department of Nanotechnology, Microelectronics, General and Applied Physics,  
Southwest State University, Kursk, Russia

\*E-mail: [blackberry\\_\\_@mail.ru](mailto:blackberry__@mail.ru)

Magnetic fluids have a unique combination of magnetic properties, fluidity and colloidal stability, which has allowed them to find applications in a variety of technical devices, such as shock absorbers and sensors. One of the features of this smart material is the ability to control its physical properties using various combinations of magnetic influences. In this work, the dynamics of a magnetic fluid volume levitating in an uniform magnetic field of an electromagnet undergoing oscillatory shear is investigated. The samples with different physical parameters were considered, the dependence of magnetoviscous effect was investigated. It is shown that the microstructure of the sample and the presence of large magnetic particles have the greatest influence on the dynamics of the magnetic fluid undergoing oscillatory shear and magnetoviscous effect. The results of the work can be used to develop a method for express testing of magnetic fluid samples, as well as to develop acceleration and vibration sensors based on magnetic fluids [1].

The dependences of the viscosity for samples MF-1–MF-4 are plotted, shown in Fig. 1. The obtained dependences of the viscosity show an increase in its value by a factor of 5 for the MF-1 sample, with an increase in the field to 1000 kA/m, which can be explained by interparticle interactions and the formation of weakly bound aggregates in the near-wall layer in a more concentrated initial MF-1 sample. In a more diluted sample MF-2, such an increase in viscosity is not observed. The images MF-3, MF-4 are characterized by the presence of an excess free surfactant, which negatively affects the magnetoviscous effect.

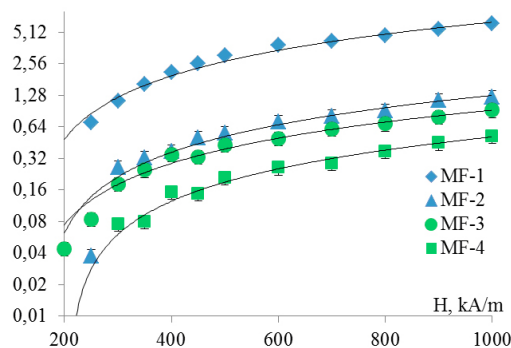


Figure 1. Dependences of viscosity for samples MF-1–MF-4.

*The study was supported by the Russian Science Foundation grant No. 22-22-003113.*

1. P.A. Ryapolov, V.M. Polunin, E.V. Shel'deshova, *JMMM*, **496**, 165924 (2020).

## MAGNETIC PROPERTIES OF Fe-Ga ALLOYS

*V.A. Lukshina<sup>1,2</sup>, D.A. Shishkin<sup>1,2\*</sup>, N.V. Ershov<sup>1,2</sup>, A.R. Kuznetsov<sup>2</sup>, Yu.N. Gornostyrev<sup>1</sup>*

<sup>1</sup>Mikheev Institute of Metal Physics, Ural Branch, Russian Academy of Sciences, Ekaterinburg, Russia

<sup>2</sup>Ural Federal University Named after the first President of Russia B.N. Yeltsin, Ekaterinburg, Russia

\*E-mail: [shishkin@imp.uran.ru](mailto:shishkin@imp.uran.ru)

The Fe-Ga alloys based on bcc Fe with a dopant concentration close to the two-phase region boundary attract considerable interest due to their extraordinary magnetic properties such as giant magnetostriction [1]. The phenomenon of induced magnetic anisotropy resulted from magnetic field annealing (MFA) was studied in detail for Fe-Si and Fe-Al alloys [2, 3], while for Fe-Ga alloys the effect of MFA on their magnetic properties remains obscure. Iron alloys with gallium belong to ordered substitutional solid solutions which contain anisotropic clusters of the B2 phase of sub-nanoscale size or modified D03 phase [4–6] at low alloying element concentrations. Therefore, it can be expected that thermomagnetic treatment will be efficient for these alloys, since this causes changes in atomic structures, hence, changes in magnetic properties.

The samples of iron-gallium alloys were casted in the form of rods with a diameter of about 10 mm. The size of crystalline grains varied from 1 to 4 mm. Disk samples of all compositions were used to measure hysteresis loops in a magnetic field to 640 kA/m using a vibrating sample magnetometer Lake Shore 7407 VSM (Center for Collective Use of IMP UB RAS). To study the effect of MFA on magnetic properties, the ring shape of samples was chosen to eliminate the effect of the demagnetizing factor on the behavior of magnetic properties. The concentration dependence of magnetic properties of iron alloys with 3–25% of gallium is studied. It was shown that the saturation induction monotonically decreases from 240 to 150 A·m<sup>2</sup>·kg<sup>-1</sup> with gallium content increasing from 3 to 25 at.% Ga, while the coercivity exhibits a step increase with a step from 85 to 135 A/m between 12 and 15 at.% Ga. The effect of MFA on the behavior of the residual induction and coercive force in alloy samples containing from 3 to 18 at.% Ga is studied. As a result of MFA, magnetic anisotropy is induced in the alloy: magnetic hysteresis loops become narrower, the

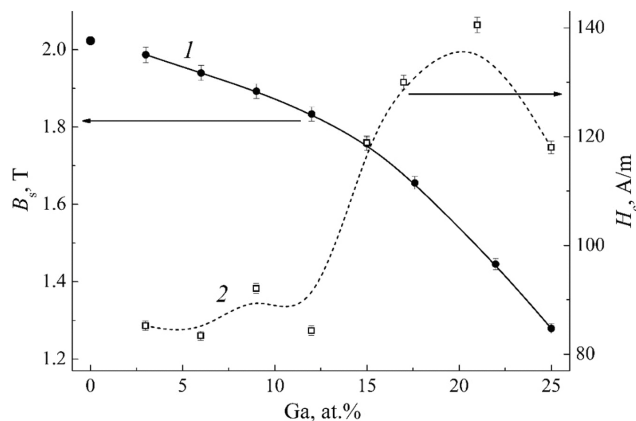


Figure 1. Saturation induction (1) and coercive force (2) of Fe-Ga samples as functions of the gallium content. The saturation induction of pure  $\alpha$ -iron is taken from [7].

residual induction increases, and the coercivity decreases. The MFA efficiency reaches a maximum at a Ga content of 15–18 at.%. The features of the structure state of iron-gallium alloys and their role in the formation of magnetic properties during annealing in a dc magnetic field are discussed.

*This work was financially supported by the Russian Science Foundation, project no. 22-12-00179.*

1. A.E. Clark, K.B. Hathaway, M. Wun-Fogle, J.B. Restorff, T.A. Lograsso, V.M. Keppens, G. Petculescu, and R.A. Taylor, *J. Appl. Phys.*, **93**, 8621–8623 (2003).
2. H.I. Birkenbeil and R.W. Cehn, *Proc. Phys. Soc.*, **79**, 831 (1962).
3. V.V. Gubernatorov, Yu.N. Dragoshanskii, and T.S. Sycheva, *Phys. Met. Metallogr.*, **120**, 723–728 (2019).
4. Yu.P. Chernenkov, N.V. Ershov, and V.A. Lukshina, *Phys. Solid State*, **60**, 2370–2380 (2018).
5. Yu.P. Chernenkov, N.V. Ershov, and V.A. Lukshina, *Phys. Solid State*, **61**, 1960–1968 (2019).
6. Y. Wu, Y. Chen, Ch. Meng, H. Wang, X. Ke, J. Wang, J. Liu, T. Zhang, R.Yu, J.M.D. Coey, Ch. Jiang, and H. Xu, *Phys. Rev. Mater.*, **3**, 033401 (2019).
7. R. Bozorth, *Ferromagnetism*, IEEE Magn. Soc., New York (1993).

## ORIENTATIONAL TRANSITIONS IN A LIQUID CRYSTAL SUSPENSION OF SPIRAL MAGNETIC PARTICLES UNDER WEAK SEGREGATION

*D.P. Sokolchik\**, *D.V. Makarov*

Perm State University, Perm, Russia

\*E-mail: [dsokolchik@rambler.ru](mailto:dsokolchik@rambler.ru)

One of the current trends in the development of soft matter physics is the synthesis of new soft magnetic materials with specified properties. The need to create such substances is primarily due to their practical application since many natural materials often do not have the necessary set of properties for their application. In particular, various suspensions based on liquid crystals are examples of such systems. Depending on the type of the liquid crystal that is the basis of the magnetic suspension, they can have different orientation structures. For example, cholesteric liquid crystals formed by chiral molecules have a helical (spiral) supramolecular structure.

The addition of anisometric impurity particles (rod-shaped or disk-shaped) into such an LC matrix makes it possible to prepare a liquid crystal suspension with a spiral structure [1]. However, a similar orientational structure can also be induced by helical particles embedded in a nematic liquid crystal [2] with a homogeneous orientational structure typical in the absence of external fields and constraining surfaces.

In this paper, we investigate theoretically a suspension based on a nematic liquid crystal containing helical magnetic particles. The paper proposes a phenomenological description [3] of such a suspension, taking into account the additional contribution that allows for the presence of achiral colloidal particles. The coupling between the liquid crystal and magnetic subsystems was assumed to be planar. Using the minimization of the total free energy functional, we obtained the equations of orientation equilibrium in the presence of an external homogeneous magnetic field. The ground state of a chiral ferronematic corresponds to a helicoidal orientation structure of the director and magnetization fields with a helical step depending on the concentration of impurity particles, the Frank constant, and the phenomenological coefficient of interaction between the subsystems. The inclusion of a magnetic field perpendicular to the axis of the helical structure leads to its unwinding. We studied the field-induced transitions to the uniform orientational state for the given suspension.

We considered the cases of homogeneous distribution of impurity over the volume and its weak segregation. It was found that in the approximation of the homogeneous distribution of helical particles, the chiral ferronematic behaves similarly to the ferrocholesteric [4] with the corresponding renormalization of their chirality parameters (wavenumbers of unperturbed helices). A closed system of orientational equations was obtained in the weak impurity segregation approximation. Critical fields of the system transition to the unwinding phase were obtained numerically and analytically. It is shown that the fields of transition to the unwinding phase decrease under weak magnetic segregation of helical particles. Under similar conditions in the ferrocholesteric LC, this led to an increase in the critical fields.

1. P.M. Rupnik, D. Lisjak, M. Copic et al., *Science Advances*, **3**, e1701336 (2017).
2. B. Senyuk, M.B. Pandey, Q. Liu et al., *Soft Matter*, **11**, 8758–8767 (2017).
3. S.V. Burylov, Y.L. Raikher., *Molecular Crystals and Liquid Crystals*, **258**, 107–122 (1995).
4. A.N. Zakhlevnykh, P.A. Sosnin, *Journal of Magnetism and Magnetic Materials*, **146**, 103–110 (1995).

**DYNAMICS OF NONMAGNETIC DROPS AND GAS BUBBLES  
 IN A MICROCHANNEL WITH A MAGNETIC FLUID  
 IN AN INHOMOGENEOUS MAGNETIC FIELD**

*E.A. Sokolov\**, *D.A. Kalyuzhnaya*, *A.O. Vasilyeva*, *P.A. Ryapolov*

Department of Nanotechnology, Microelectronics, General and Applied Physics,  
 Southwest State University, Kursk, Russia

\*E-mail: [evgeniysokolov1@yandex.ru](mailto:evgeniysokolov1@yandex.ru)

This work presents the results of studying the dynamics of non-magnetic bubbles and droplets in a magnetic fluid placed in an inhomogeneous magnetic field. Using a digital high-speed system for video recording, the mechanism of the detachment of a non-magnetic droplet from the major part of the magnetic fluid has been considered in detail. It is experimentally demonstrated that the size of formed non-magnetic inclusions in such a magnetic-fluid system does not depend on the flow rate and hydrostatic pressure. The possibility to control the size of non-magnetic liquid and gas inclusions by changing the parameters of magnetic fluid and magnetic field can be used for microdosers or gas meters in microfluidic systems [1].

The principal scheme of the setup’s configuration and results of the experiment are presented in Fig. 1. The stages of evolution of the surface of a volume consisting of a nonmagnetic liquid levitating in the magnetic fluid carrier are considered when a drop is detached from the former relatively to the distribution of isolines of the external magnetic field intensity modulus. It is established experimentally that the skittle-shaped envelope of the volume containing the non-magnetic liquid of interest is well-coordinated with these isolines that makes possible a quantitatively accurate production of desired microbubbles.

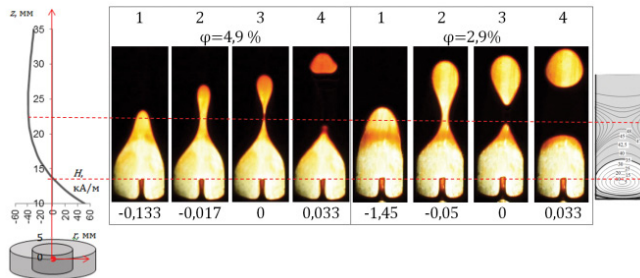


Figure 1. Frames of video recording of the interphase boundary position between non-magnetic liquid and magnetic fluid at the moment of and after detachment of the non-magnetic droplet in the inhomogeneous magnetic field created by the ring magnet.

*The study was supported by the Russian Science Foundation grant No. 22-22-003113.*

1. P.A. Ryapolov, E.A. Sokolov, E.B. Postnikov, JMMM, **549**, 169067 (2022).

## SPECTRA OF BIREFRINGENCE AND DICHROISM IN MAGNETIC COLLOIDS WITH SIZE-SORTED NANOPARTICLES

*E.I. Shevchenko, V.I. Vivchar, C.V. Yerin\**

Department of Experimental Physics, NCFU, Stavropol, Russia

\*E-mail: [exiton@inbox.ru](mailto:exiton@inbox.ru)

Magnetic fluids exhibit optical effects when exposed to a magnetic field: birefringence [1, 2], linear and circular dichroism [3], Faraday rotation and ellipticity [4], changes in the intensity of transmitted, scattered, and reflected light [5, 6], etc. Due to these effects, magnetic fluids find application in various magneto-optical devices: optical filters, limiters and shutters, waveguides and fiber-optic modulators, period-controlled diffraction gratings, optical magnetic field sensors, static and dynamic displays, etc. [7].

To establish the mechanisms of magneto-optical effects in magnetic fluids, it is necessary to study in detail the dependences of the magnitude of the effects on the field strength, concentration and size of particles, and also on the wavelength of light. In this paper, we present the results of a study of the spectral dependences of the effects of birefringence and dichroism for magnetic fluids with different particle sizes.

To determine the optical effects in magnetic fluids, an apparatus based on the Ellips-1891 spectral ellipsometric complex was used. The setup made it possible to measure the transparency and ellipsometric parameters of transmitted light in the wavelength range of 350–1050 nm. Measurements were taken of 2 samples of ferrofluid with a volume concentration of 0.01%. The samples were obtained by diluting two fractions of concentrated ferrofluid with pure kerosene. Fractions were obtained by long-term settling of one sample of ferrofluid in a tall vessel for many years. Fractions for dilution were taken from the bottom (sample S) and top (sample U) of the vessel. Studies of the samples by the method of dynamic light scattering showed that the particle size of the fraction taken from the upper part of the vessel is somewhat smaller than the particle size of the fraction from the lower part. Figure 1 shows particle size distribution curves for the samples we studied. The difference in average sizes between the two samples is about 2.5 nm (5.5 and 8 nm, respectively). To create a magnetic field, Helmholtz coils mounted on the sample table in the ellipsometer were used. The ellipsometric parameters of the samples  $\Psi$  and  $\Delta$ , which determine the state of the polarization ellipse of transmitted or reflected light, were studied. Using  $\Delta$ , the main parameter of birefringence

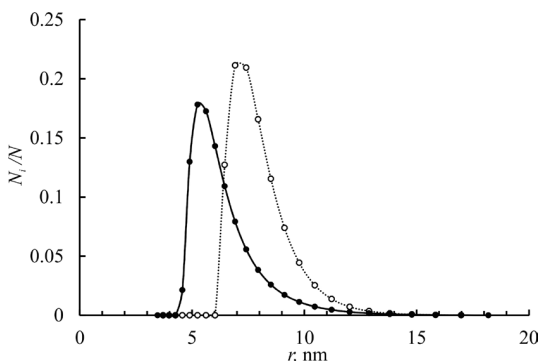


Figure 1. Particle size distributions for two samples (left, sample U, right, sample S).

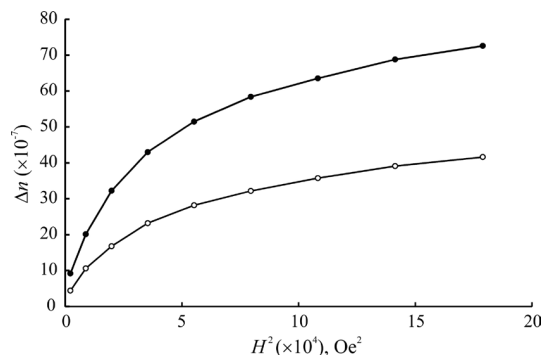


Figure 2. Field dependences of birefringence (bottom, sample U, top, sample S).



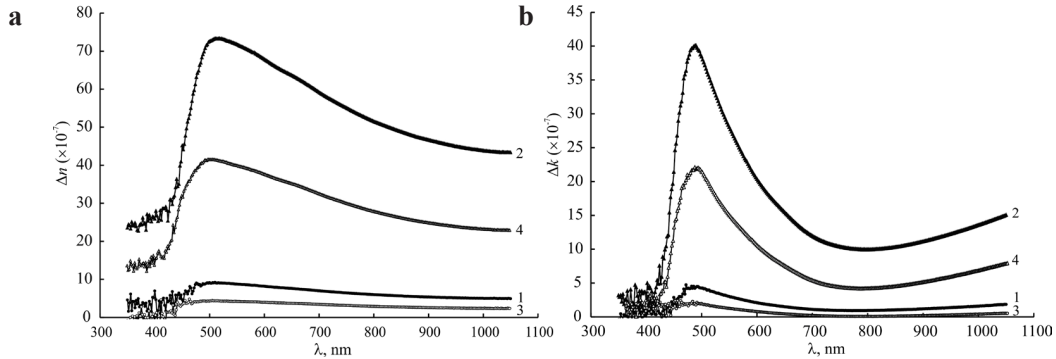


Figure 3. Spectra of birefringence (a) and dichroism (b) at magnetic field strengths of 50 Oe and 420 Oe: 1, 2 – sample S, 3, 4 – sample U.

was calculated – the difference between the refractive indices of the extraordinary and ordinary rays  $n_{\parallel} - n_{\perp} = \lambda \cdot \Delta / (2\pi L)$ , and according to  $\Psi$  – dichroism parameter  $k_{\parallel} - k_{\perp} = -\lambda \cdot \ln(\tan \Psi) / (2\pi L)$ . For research, the samples were placed in rectangular glass cuvettes 5 mm thick.

Figures 2 and 3 show the spectra of the effects of birefringence and dichroism in ferrofluid samples with different particle sizes exposed to a constant magnetic field. An analysis of the experimental dependences shows that the magnitude of the effects of birefringence and dichroism significantly depends on the particle size of the magnetic colloid. The values of the effects in the colloid with larger particles are significantly (more than 2 times) higher than the values obtained in the sample with smaller particles. The ratio of the average particle sizes is about 1.45. The shape of the spectral dependences of the birefringence and dichroism effects are similar and do not depend on the particle size. The spectral dependences are determined by the features of the refractive index of magnetite and the surrounding dispersion medium. The magneto-optical effects are most pronounced in the wavelength range of 480–520 nm, but the maximum transparency of magnetic colloids based on magnetite is in the near-IR region (730–760 nm). The study of the field dependence of the effects of magnetic birefringence and dichroism shows their form, which is common for such effects in colloidal solutions [8]. In weak magnetic fields, the magnitude of the effects is proportional to the square of the field strength, and in very strong fields it reaches saturation. On the whole, the magnitude of the effects for magnetically hard particles should be proportional to the square of the particle volume, i.e.  $\sim r^6$ . For superparamagnetic particles, the dependence should be stronger  $\sim r^9$  [9]. At the same time, such significant differences are not observed experimentally, which may be due to the polydispersity of the samples, as well as the presence of small aggregates of several tens of particles in the samples.

*Support by the Ministry of Science and Higher Education of Russia (project No. 0795-2020-0007) is acknowledged.*

1. H.W. Davies, J.P. Llewellyn, J. Phys. D: Appl. Phys., **13**, 2327–2336 (1980).
2. J.P. Llewellyn, Phys. D: Appl. Phys., **16**, 95–104 (1983).
3. B.R. Jennings, M. Xu and P.J. Ridler, Proc. Royal Soc. A, **456**, 891–907 (2000).
4. F. Donatini, S. Neveu, J. Monin JMMM, **162**, 69–74 (1996).
5. K.V. Yerin, S.A. Kunikin, Optics and Spectroscopy, **102**(5), 765–770 (2007).
6. C.V. Yerin, V.I. Vivchar, JMMM, **498**, 166144 (2020).
7. I. Torres-Diaz and C. Rinaldi, Soft Matter, **10**, 8584–8605 (2014).
8. A.A. Spartakov, A.A. Trusov, V.V. Vojtylov, E.V. Rudakova, Colloids and Surfaces A., **148**, 9–16 (1999).
9. E. Hasmonay, E. Dubois, J.-C. Bacri, R. Perzynski, Yu.L. Raikher, V.I. Stepanov, EPJ B, **5**, 859–867 (1998).

## MATHEMATICAL AND COMPUTER MODELING OF THE SYSTEMS OF THE IMMOBILIZED PARTICLES LOCATED IN THE NODES OF THE SIMPLE CUBIC LATTICE OR DISTRIBUTED RANDOMLY

*S.A. Sokolsky\**, *A.Yu. Solovyova*, *E.A. Elfimova*

Ural Mathematical Center, Ural Federal University, Ekaterinburg, Russian Federation

\*E-mail: [Sokolsky2304@gmail.com](mailto:Sokolsky2304@gmail.com)

This work presents a study of the effect of the interparticle dipole-dipole interaction on the magnetic, static and thermodynamic properties of the ensemble of the immobilized superparamagnetic particles in the external magnetic field.

The relaxation of the magnetic moment of the model ferroparticles occurred by the Néel mechanism. The directions of the easy axes of all particles were assumed to be parallel to each other, but at the same angle to the direction of the external magnetic field  $\mathbf{H}$ . The directions of the easy axes were described by vector  $\mathbf{n}$  using the polar angle  $\varphi$  and azimuth angle  $\theta$  (Fig. 1).

The potential energy of the system includes a single-particle dipole-axial interaction, a single-particle dipole-field interaction and long-range interparticle dipole-dipole correlations.

In the system, two variants of the distribution of ferroparticles over the volume of the container are considered: in the nodes of a simple cubic lattice and randomly (Fig. 2).

The described model was studied theoretically by expanding the Helmholtz free energy into a classical virial series up to the second virial coefficient with an addition transformation into the logarithmic form [1, 2]. With help of the new theory, the contribution of dipole-dipole interactions in the changes of the magnetic susceptibility, magnetization, and heat capacity of the system was estimated. The difference between the behavior of the Helmholtz free energy for the lattice and the random textures lies in the dependence on the polar angle of the easy axes  $\varphi$  in applied field except the state of magnetic saturation. In a zero external magnetic field, the contribution of the dipole-dipole interaction into the Helmholtz free energy depends clear on azimuthal angle  $\theta = \angle(\mathbf{H}, \mathbf{n})$ , whereas for a random distribution there is no such dependence.

To test the new theory, Monte Carlo simulations were carried out in the canonical ( $NVT$ ) ensemble of  $N = 512$  dipolar hard spheres which were placed in the cubic box in the simple cubic lattice nodes or by the random way. In the case of a random texture, ten independent realizations of the spatial distribution of particles were studied for each specific set of input parameters with further averaging of the results.

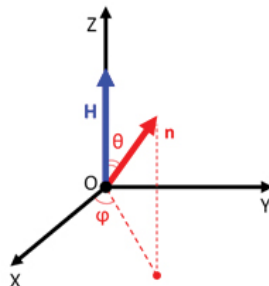


Figure 1. The coordinate system: the OZ-axis is parallel to the direction of the applied external magnetic field  $\mathbf{H}$ .

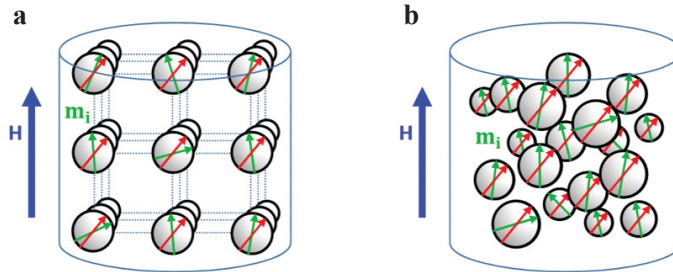


Figure 2. A monodisperse system of the stationary single-domain superparamagnetic ferroparticles in the external magnetic field  $\mathbf{H}$ : the distribution of the particles by the volume is assumed in the nodes of the simple cubic lattice (a) or randomly (b)

The analytical expressions of the static magnetization and the heat capacity were calculated as derivatives of the Helmholtz free energy, which allowed to investigate the region of the theory applicability by critical comparing with computer simulation data. At  $\varphi = 0$  it turned out that for low intensity of the dipole-dipole interactions (the Langevin susceptibility  $\chi_L \leq 1.25$  and anisotropy parameter  $\sigma \leq 5$ ) there is no essential difference between considered properties of the lattice and random textures. In a zero and moderate external magnetic fields, the new theory allows to describe the numerical calculations much more efficient than the ideal approximations, for which the inter-particle dipole-dipole interactions were neglected. The Helmholtz free energy of ideal system does not depend on the temperature, ferroparticles' concentration and their distribution in the sample.

*Support by RFBR (grant № 20-02-00358) is acknowledged.*

1. E.A. Elfimova, A.O. Ivanov and P.J. Camp., Phys. Rev. E, **86**(2), 021126, (2012).
2. E.D. Vtulkina, E.A. Elfimova, J. Magn. Magn. Mater., **431**, 218–221, (2017).

## ON THE THEORY OF MAGNETICALLY INDUCED FLOWS IN THROMBOSED CHANNELS

*A.Yu. Musikhin, A.Yu. Zubarev*

Department of Theoretical and Mathematical Physics, Institute of Natural Sciences and Mathematics,  
Ural Federal University, Ekaterinburg, Russia  
E-mail: [Antoniusmagna@yandex.ru](mailto:Antoniusmagna@yandex.ru)

We propose a mathematical model and a method of its approximate analysis for flows induced by a traveling magnetic field in a channel filled with a non-magnetic liquid and a drop of ferrofluid embedded in it. One end of the channel is assumed to be closed (thrombosed). The study was conducted as part of the development of the scientific basis of magnetically induced intensification of drug transport in thrombosed blood vessels.

The main problem of treatment of brain strokes is related to very slow diffusion of the thrombolytic drugs toward blood clots through blocked vessels. An American company Pulse Therapeutics has proposed a smart solution to this problem using magnetic micro- or nanoparticles entrained in motion by alternating magnetic fields and able to create recirculating flows in the blocked vessels [1]. These recirculating flows considerably enhance convective transport of the drug towards the clots.

Obviously, the practical application of this method requires a thorough study of the features of generating these flows, their structure, identifying the optimal configuration of the magnetic field and other physical characteristics of the system. Despite the research undertaken on this topic, now many important aspects of it have not been studied. Thus, in theoretical model [2], an infinitely long channel with a drop (cloud) of ferrofluid was considered and the influence of the thrombus itself on the generated flows was not considered.

In this paper, we propose a model of flows generated by a traveling oscillating field in a channel with a drop of ferrofluid located next to a thrombus, as well as an approximate method for solving emerging equations.

For the sake of maximum simplification of the mathematical side of the matter, as a model of a blood vessel, we will consider not a cylindrical channel, but a semi-infinite flat gap filled with a non-magnetic Newtonian fluid. Note that the transition to a cylindrical channel does not create fundamental difficulties but makes the calculations more cumbersome and less transparent. The left end of the gap is closed by a liquid-impermeable wall simulating a thrombus; a drop of soluble ferrofluid is located in the gap not far from the wall. It should be noted that from a practical point of view, the solubility of the implanted liquid seems to be a prerequisite, since an insoluble drop itself can thrombose a blood vessel. Within the framework of the proposed model, the fact that a drop of ferrofluid is soluble in a carrier medium will be considered by a smooth distribution of the concentration of nanoparticles in a drop without a clearly defined boundary.

This model allows us calculate the magnetic field inside the channel created by the solenoids using the Bio-Savart law. Using our solution method of the ferrohydrodynamic [3] equations, we plan to calculate the flow rate of ferrofluid depending on the external magnetic field.

*Support by RSF 20-12-00031 is acknowledged.*

1. Creighton, Francis M. 2012. "Magnetic-based systems for treating occluded vessels". U.S. Patent No. 8,308,628. 13 Nov.
2. A. Musickhin, A.Yu. Zubarev, M. Raboisson-Michel, G. Verger-Dubois and P. Kuzhir, Field-induced circulation flow in magnetic fluids, *Phil. Trans. R. Soc. A*, **378**, 20190250.
3. R. Rosensweig, *Ferrohydrodynamics* (Cambridge, New York), (1985).

Section M.  
**Magnetism in biology and medicine**

---

## MULTIFUNCTIONAL MAGNETORHEOLOGICAL MATERIALS AND THEIR APPLICATION PROSPECTS

*N.S. Perov<sup>1,2\*</sup>, L.A. Makarova<sup>1,2</sup>, D.A. Isaev<sup>1</sup>, Iu.A. Alekhina<sup>1,2</sup>, M.F. Khajrullin<sup>1</sup>,  
E.Yu. Kramarenko<sup>1</sup>*

<sup>1</sup>Faculty of Physics, Lomonosov MSU, Moscow, Russia

<sup>2</sup>REC SMBA, Immanuel Kant BFU, Kaliningrad, Russia

\*E-mail: [perov@magn.ru](mailto:perov@magn.ru)

Magnetorheological elastomers (MRE), or magnetoactive elastomers, have been studied by researchers for a long time. MRE represents the soft polymer medium with embedded ferro- (ferri-) magnetic micro- (nano-) particles. Attractive mechanical properties of the composites and their tunability with magnetic field were of prior interest for investigations and practical implementation. Magnetorheological effect, magnetodeformational effect, high bending properties, immediate response and remote control allows to use of MRE in a wide range of applications from engineering sensors and valves up to biomedical devices.

Recent advances in MRE and composites based on it show interesting peculiarities of electrical and magnetic properties. The possibility to control magnetic properties of MRE by varying concentration of particles became the direction of investigation for 3D-printing and tunable magnetization gradient. Their mechanical response to magnetic field can be also set by the shape of the particular element (pillars array, zig-zag structures, tubes, etc.) The multifunctional actuators based on such MRE elements were demonstrated [1]. Moreover, since the possible compositions of MRE vary in a wide range, their biocompatibility is easily achievable, making them promising for biomedical applications. One of the examples of biomedical implementation of MRE is the seal for complex retinal detachment treatment [2, 3]. Biocompatible element with excellent mechanical bending properties and magnetic susceptibility can be effectively held by a silicon-covered buckle of permanent magnets allowing good retina fixation.

Mechanical properties of the composite can be utilized for energy harvesting application. This can be achieved in layered composite based on MRE and piezopolymer substrate [4]. Due to gradient magnetic field bending deformation of the structure occurs which can be tuned by the rate of magnetic field switching and the value of magnetic field. The resonance of oscillations was also received in the AC magnetic field. Tunable energy utilization by novel composites allows to develop different types of sensors, energy harvesting devices and devices for mechanotronics.

Magnetodielectric effect (MDE) in MRE was studied experimentally and numerically and it revealed the increase of effective permittivity under an external magnetic field [5, 6]. The mechanism of MDE is associated with the displacement of microparticles in soft elastic medium. The movement of particles in polymers with relatively low values of Young's modulus can be essential under applied external fields. Rearrangement of conductive filler changes the effective capacitance of the MRE filled capacitor. Thus, each FM particle induces and, at the same time, is affected by an elastic force.

Particles displacement also allows the elastic coupling between different fillers, if several types of particles are used in the material. Any shift of the particles inside the polymer matrix produces internal stresses affecting the distribution and interactions of another filler type. Magnetoelectric effect was observed in three component MAE based on silicone matrix with a mixture of ferromagnetic and ferroelectric microparticles [7]. The stresses induced by ferromagnetic particles shifting under applied external magnetic fields affect the state of the second type of particles – ferroelectric,

changing the polarization state of the material. Shifting of ferroelectric particles under electric field cause the inverse magnetodeformational effect through elastic interactions. Thus, such materials can be considered as composite multiferroics.

The contribution of elastic interaction between particles of different types was investigated numerically [8]. The suggested results can be used for the optimization of structural properties of composite materials to achieve higher efficiency in magnetoelectrical transformation. This means that such materials can be used in various fields: ranging from biomedical, where the mutual influence of particle movements under applied external magnetic or electric fields as well as mechanical deformations of the matrix are required; to engineering for electromagnetic energy harvesting.

*Financial support of the Russian Science Foundation (grant No. 19-13-00340) is gratefully acknowledged*

1. W. Hu, G.Z. Lum, M. Mastrangeli, M. Sitti, *Nature*, **554** (7690), 81–85 (2018).
2. Y.A. Alekhina, L.A. Makarova, S.A. Kostrov et al., *Journal of Applied Polymer Science*, **136** (17), 47425–47425(9) (2019).
3. L.A. Makarova, T.A. Nadzharyan, Yu.A. Alekhina, G.V. Stepanov, E.G. Kazimirova, N.S. Perov, E.Yu. Kramarenko, *Smart Mater. Struct.*, **26**, 095054 (2017).
4. L.A. Makarova, Y.A. Alekhina, D.A. Isaev et al., *Journal of Physics D – Applied Physics*, **54** (1), 015003 (2021).
5. D. Isaev, A. Semisalova, Y. Alekhina et al., *International Journal of Molecular Sciences*, **20** (6), 1457–1457 (2019).
6. S.A. Kostrov, M. Shamonin, G.V. Stepanov, E.Yu. Kramarenko, *Int. J. Mol. Sci.*, **20**, 2230 (2019).
7. L.A. Makarova, Y.A. Alekhina, A.S. Omelyanchik et al., *Journal of Magnetism and Magnetic Materials*, **470**, 89–92 (2019).
8. L.A. Makarova, D.A. Isaev, A.S. Omelyanchik et al., *Polymers*, **14** (1), 153 (2022).

## REGISTRATION OF MAGNETIC NANOPARTICLES IN AQUEOUS USING MAGNETOMETERS

*L.P. Ichkitidze<sup>1,2\*</sup>, M.V. Belodedov<sup>3</sup>, A.Yu. Gerasimenko<sup>1,2</sup>, D.V. Telyshev<sup>1,2</sup>, S.V. Selishchev<sup>2</sup>*

<sup>1</sup>I.M. Sechenov First Moscow State Medical University, Moscow, Russia

<sup>2</sup>National Research University of Electronic Technology (MIET), Zelenograd, Moscow, Russia

<sup>3</sup>Bauman Moscow State Technical University Moscow, Russia

\*E-mail: [ichkitidze\\_ip@staff.sechenov.ru](mailto:ichkitidze_ip@staff.sechenov.ru); [ichkitidze@bms.zone](mailto:ichkitidze@bms.zone)

Magnetic nanoparticles (MNPs – average size  $\leq 100$  nm) are being actively studied for large-scale application in diagnostics and treatment (in theranostics) in oncology and orthopedics [1, 2]. In these areas, MNPs, the so-called superparamagnetic iron oxide nanoparticles (SPIONs), with sizes of 5–100 nm, are especially actively used.

It has been established that the effectiveness of theranostics of cancer, including its hyperthermia, significantly depends on many properties of SPIONs, in particular, on their size (5–100 nm), shape (spherical, rod, disk), coating material type, and magnetization value. The concentration of SPIONs and their distribution in the places of their localization in target tissues also matters. A similar situation is observed in cases of using SPIONs in theranostics for orthopedic diseases, including the treatment of osteoarthritis.

In this work, we study the possibility of non-invasive registration of MNPs, including SPIONs, at the sites of their localization in the biological environment. For this purpose, modern supersensitive magnetic field sensors (MFSs) are considered, which record external magnetic field disturbances caused by introduced magnetic particles, taking into account their accompanying parameters.

The calculation of the maximum possible distance between MNPs and MFS with the limiting threshold magnetosensitivity  $\delta B$ , at which non-invasive registration of MNPs in a biological medium becomes possible, has been carried out. In this case, various MNP parameters and  $\delta B$  values are taken into account in the calculations. It is assumed that MNPs have a spherical shape with a diameter  $\Delta$  and magnetization  $J$ . Let an external background magnetic field, for example, the Earth's magnetic field  $\mathbf{B}_b$ , be directed vertically along the  $z$  symmetry axis. Under the action  $\mathbf{B}_b$ , the magnetization vectors  $\mathbf{J}$  of individual particles will be directed parallel to the  $z$  axis, and at  $\mathbf{B}_b = 0$ , these vectors will have a chaotic orientation. Let us take into account the fact that MNPs can form accumulations (clusters) with a characteristic linear size  $D$  containing magnetic nanoparticles with a concentration  $n$ . It can be assumed that the magnetic particles in the cluster are far from each other and there are no interactions between them, and that they create a total magnetic field  $\mathbf{B}$  at a distance  $l$ . Taking into account the above conditions, MFS will register MNPs located at a distance not exceeding, according to the formulas:

$$l \leq \Delta D (\pi \mu_0 n J / 96 \delta B)^{1/3}, \quad (1)$$

$$l \leq 0.00428 D (C \rho_a p_m / \delta B)^{1/3}, \quad (2)$$

where  $\mu_0 = 1.256 \cdot 10^{-6}$  H/m is the magnetic constant,  $C = m_p / m_a$  is the ratio of the total mass of magnetic particles  $m_p$  to the entire mass of the medium  $m_a$ , i.e.  $C$  is the relative concentration of particles in a liquid (in a biological medium),  $\rho_a$  is the density of the biological medium,  $p_m = |\mathbf{p}| / m_p$  is the specific magnetic moment, and  $\mathbf{p}$  is the average value of the modulus of the particle's magnetic moment.

Non-invasive registration of MNPs was carried out with a Honeywell HMR2300 magnetometer in the magnetic field range of  $\pm 200$   $\mu$ T [3]. Aqueous suspensions of superparamagnetic SPIONs



Table 1. Parameters of magnetic particles.

Parameters	Sileks MagNA [4]		Sileks MagNA-G [4]		ML-131 [5]
$C$ , %	5	0.05	1	0.01	~30
$\Delta$ , nm	50	50	100	100	–
$D$ , mm	14	14	14	14	14
$p_m$ , $A \cdot m^2/kg$ ( $B_b = 43.1 \mu T$ )	$7 \cdot 10^{-3}$	$1 \cdot 10^{-4}$	$9 \cdot 10^{-3}$	$1.2 \cdot 10^{-4}$	45
$l_m$ , mm	24	4	28	5	272
$l$ , mm (according to formulas (1) and (2))	8	2	9	2	900

(Sileks) were used [4], and magnetic fluid MF-131 (AQUASIL – in Russian) served as the objects of study [5]. Sileks MagNA and Sileks MagNA-G particles are mainly iron oxide  $Fe_2O_3$  particles coated with  $SiO_2$  layer.

The measurements were carried out both in the Earth’s magnetic field compensation mode and without its compensation. At the same time, the projection of the  $z$  component of the magnetic field was several times higher than the values of its other horizontal projections. In the Earth’s magnetic field, a suspension of SPIONs particles from Sileks always had a remanent magnetization  $J$ , the value of which varied depending on the magnitude of the applied magnetic field (approximately proportional to its value). This property emphasized the superparamagnetism of these particles. Iron particles MF-131 exhibited a ferromagnetic behavior [5]. Some parameters of the studied magnetic particles are given in Table 1, where  $C$ ,  $\rho_a$  and  $\Delta$  are passport data,  $D$  is the test tube diameter of 14 mm,  $p_m$  and  $B_b$  are the measured data,  $l_m$  and  $l$  are the measured and estimated values, which were determined with an accuracy of  $\pm 1$  mm.

Satisfied agreement (in order of magnitude) was obtained between the estimated and measured values of the maximum distance at which noninvasive registration of magnetic particles is possible. It is obvious that using a magnetic field sensor with a lower will make it possible to noninvasively control particles located at a greater depth in the biological medium [6, 7].

Thus, non-invasive observation of magnetic particles will allow monitoring the effectiveness of theranostics methods of oncology and orthopedics, including cancer and osteoarthritis. In particular, this will make it possible to directly observe the distribution, properties, and behavior of magnetic particles in a biological medium. In this case, there is no need to take a biopsy or to derive biological objects from experience in order to establish a connection between the properties of magnetic particles and the degree of effectiveness of theranostics. This approach is becoming important, since a gradual transition from laboratory research to clinical trials of magnetic particles in theranostics of various diseases has now begun [8].

*This work is supported by the Ministry of Science and Higher Education of the Russian Federation (project No. 075-03-2020-216 of December 27, 2019).*

1. V. Manescu, G. Paltenea, I. Antoniac, and M. Vasilescu. *Materials*, **14**, art. no. 5948 (2021).
2. J. Guang-Zhen, *Nanomaterials*, **10**, art. no. 2368 (2020).
3. <https://www.farnell.com/datasheets/46088.pdf>
4. [https://sileks.com/ru/products/magnetic\\_particles\\_silica\\_covered-sileksmagna.html](https://sileks.com/ru/products/magnetic_particles_silica_covered-sileksmagna.html)
5. <https://www.akvasil.ru/>
6. L.P. Ichkitidze, N.A. Bazaev, D.V. Telyshev et al., *Biomedical Engineering*, **48**(6), 305–309 (2016).
7. F. Hadadeh, A. Solignac, M. Pannetier-Lecoecur et al., *IEEE Sensors Journal*, **19**(22), 10403–08 (2019).
8. M. Cerqueira, E Belmonte-Reche, J. Gallo et al., *Pharmaceutics*, **14**, art. 506 (2022).

## “MAGNETIC CORE-GOLD SHELL” NANOSTRUCTURES FOR PHOTOTHERMAL THERAPY

*A. Shumskaya*<sup>1</sup>, *A. Rogachev*<sup>1</sup>, *I. Korolkov*<sup>2</sup>, *M. Zdorovets*<sup>2</sup>, *A. Kozlov*<sup>3</sup>, *A. Ognev*<sup>3</sup>,  
*V.K. Belyaev*<sup>4</sup>, *V.V. Rodionova*<sup>4</sup>, *L.V. Panina*<sup>4,5\*</sup>

<sup>1</sup>Institute of Chemistry of New Materials, National Academy of Sciences of Belarus

<sup>2</sup>L.N. Gumilyov Eurasian National University

<sup>3</sup>School of Natural Sciences, Far Eastern Federal University, Vladivostok, Russia

<sup>4</sup>Immanuel Kant Baltic Federal University, Kaliningrad, Russia

<sup>5</sup>National University of Science and Technology, MISiS, Moscow, Russia

\*E-mail: [drpanina@gmail.com](mailto:drpanina@gmail.com)

Magnetoplasmonic nanostructures (NSs) are widely used in various fields such as energy conversion, sensing, and biomedicine due to their unique optical properties. When the energy of the incident light matches the resonant frequency of free electrons, metal nanoparticles exhibit strong localized plasmon resonance (LPR) [1]. Excitation of plasmonic oscillations in a metal nanoparticle causes strong absorption and scattering of incident light depending on the material composition, size and morphology, as well as the dielectric constant of the environment. The energy absorbed by plasmonic nanoparticles can then be released either by photon re-emission (luminescence) or by phonon generation (heat) in light. Plasmonic nanostructures can absorb light of a certain range of wavelengths, which induces LPR and causes the electrons to oscillate. The electrons go into an excited energy state, after which electron-electron scattering on sub-picosecond time scales thereby leading to a redistribution of hot electrons. Subsequently, heat is transferred to the metal lattice through the electron-phonon interaction and then dissipates from the lattice into the environment within nanoseconds due to the phonon-phonon interaction. Unlike conventional heating methods, these nanoscale metal heaters allow heat to be localized in the submicron space, which is of great interest in practical applications [2]. At the same time, the influence of the applied magnetic field on the position of the LPR is poorly studied, which is of considerable interest due to the enhancement of absorption in the field.

NSs, as Ni-nanotubes (prepared by the method of template synthesis [3]), covered with gold and gold/iron/gold nano- and microdisks (prepared by e-beam lithography and magnetron sputtering) were synthesized. The SEM images of the fabricated NSs are shown in Fig. 1.

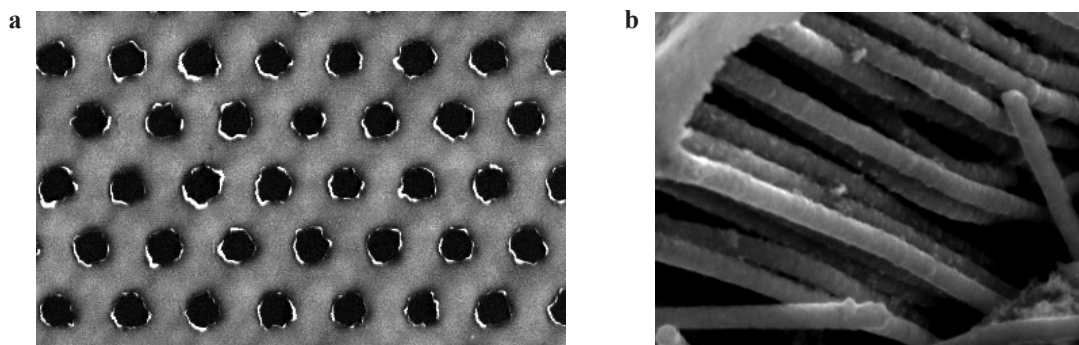


Figure 1. SEM images of fabricated gold/iron/gold nanodiscs on top of Si wafer (a) and of Ni@Au nanotubes (b).

The fabricated NSs were characterized by various methods to determine their morphology and dimensions, crystallographic structure, and magnetic and optical properties. Nanodisks were of  $0.8 \pm 0.05 \mu\text{m}$  in diameter and Ni@Au nanotubes were of  $8.1 \pm 0.2 \mu\text{m}$  in length and with the outer diameter of  $0.4 \pm 0.05 \mu\text{m}$ . The gold covering of Ni nanotubes consisted of nanostructured agglomerates of about 50 nm in size. The magnetic properties of NSs can be used for controlled particle delivery and for combined hyperthermia treatments. The magnetic properties of the both NSs are defined by the shape anisotropy and hence can be controlled by changing the morphology of nanostructures. The simulation of the magnetic properties was carried out, which showed the distribution of the magnetization vector for NSs with different morphology. The modelled absorption spectra of both structures demonstrated that the position of the LPR was red-shifted with respect to that of spherical gold particles. In particular, for a disc shaped particle, the position of LPR is about 750 nm for in-plane E-polarization, which is within the transparency window for tissues. The change in LSPR at different concentrations of nanostructures was also demonstrated. The recommendations are given on the possible application of the considered NSs for photothermal therapy.

*The work was supported by the Russian Science Foundation, grant № 21-72-20158.*

1. A. Motorzhina, S. Jovanović, V.K. Belyaev, D. Murzin et al., Processes, **9**(12), 2264 (2021).
2. L.V. Panina, D.L. Zagorskiy, A. Shymskaya, I.M. Doludenko et al., Phys. Status Solidi A, **219**(3), 2100538 (2022).
3. A. Shumskaya, L. Panina, A. Rogachev et al., Processes, **9**, 2279 (2021).

## EVALUATION OF CYTOTOXICITY OF GOLD COMPOSITES SUPPLEMENTED WITH METAL-DOPED CFO NANOPARTICLES USING JURKAT CELL LINE

A.V. Motorzhina<sup>1</sup>, S.E. Pshenichnikov<sup>1</sup>, V.V. Malashchenko<sup>2</sup>, S. Jovanović<sup>3,4</sup>, L.S. Litvinova<sup>2</sup>, L.V. Panina<sup>1,5</sup>, V.V. Rodionova<sup>1</sup>, K.V. Levada<sup>1\*</sup>

<sup>1</sup>Research & Education Center “Smart Materials & Biomedical Applications”, Immanuel Kant Baltic Federal University, Kaliningrad, Russia

<sup>2</sup>Center for Immunology and Cellular Biotechnology, Immanuel Kant Baltic Federal University, Kaliningrad, Russia

<sup>3</sup>Department of Physics, Vinča Institute of Nuclear Sciences – National Institute of the Republic of Serbia, University of Belgrade, Belgrade, Serbia

<sup>4</sup>Advanced Materials Department, Jožef Stefan Institute, Ljubljana, Slovenia

<sup>5</sup>National University of Science and Technology “MISIS”, Moscow, Russia

\*E-mail: [kateryna.levada@gmail.com](mailto:kateryna.levada@gmail.com)

Nanocomposites are of considerable interest as multiphase solid materials that combine various physical and structural properties. Regarding biomedical applications, they can provide a wide range of opportunities for theranostics, MRI, antibacterial therapy. In the current research we demonstrate three different nanocomposites (Table 1) as potential tools for biomedical applications.

The gold nanoparticle was used as a base for nanocomposite structure (Fig. 1). Gold nanoparticles were surrounded by cobalt ferrite (CFO) nanoparticles to implement magnetic properties. In addition, CFO nanoparticles substituted with Zn and Ga were used to modify the magnetic characteristics of composites.

Biocompatibility analysis of three types of nanocomposites was performed using WST-1 viability test. Well established and high proliferative T-lymphoblastic leukemia cell line (Jurkat, the Russian

Table 1. Nanocomposites.

Name	Description
Au(arg):CFO(DHCA)	composite of cobalt ferrite nanoparticles with dihydrocaffeic acid and gold nanoparticles with arginine
Au(arg):CFO_Zn(DHCA)	composite of cobalt ferrite nanoparticles substituted with zinc covered with dihydrocaffeic acid and gold nanoparticles with arginine
Au(arg):CFO_Ga(DHCA)	composite of cobalt ferrite nanoparticles substituted with gallium covered with dihydrocaffeic acid and gold nanoparticles with arginine

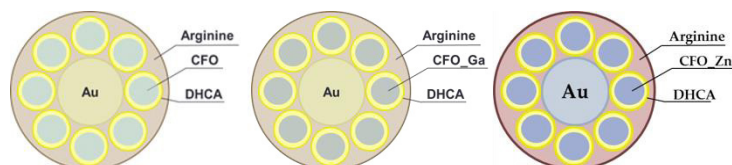


Figure 1. Structure of the Au(arg):CFO(DHCA), Au(arg):CFO\_Zn(DHCA), Au(arg):CFO\_Ga(DHCA) nanocomposites.

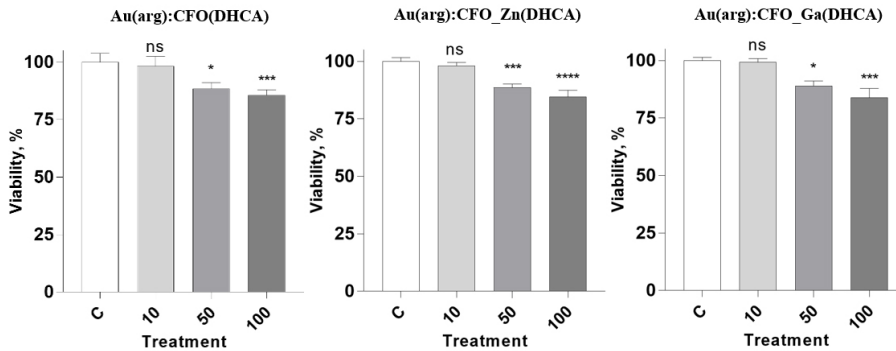


Figure 2. Jurkat cells viability was inhibited after 24 h treatment with Au(arg):CFO(DHCA), Au(arg):CFO\_Zn(DHCA) and Au(arg):CFO\_Ga(DHCA) nanocomposites. Cells were treated at three concentrations: 10 µg/ml (10), 50 µg/ml (50), 100 µg/ml (100). Data normalized to control cells viability (c) and shown as mean ±SE. Data values were analyzed using a one-way analysis of variance (one-way ANOVA) followed by Newman-Keuls test with Bonferroni correction. Statistical analysis was performed using GraphPad Prism 7.04 software (Graph Pad Software Inc., San Diego, CA, USA). All series of experiments were repeated three times.

Cell Culture Collection (Institute of Cytology RAS)) was used for experiments. Jurkat cells were incubated due to standard protocols (at 37 °C in humidified 5% CO<sub>2</sub> atmosphere). The cells were incubated in RPMI-1640 (Sigma, USA) nutrient medium. Nanocomposites were added to nutrient medium to obtain 10, 50, and 100 µg/ml treatment solutions. After 24 h cultivation, Jurkat cells were stained using WST-1 (Roche Diagnostics GmbH, Germany) and the absorbance was measured using a microplate reader Bio-Rad 680 (“Bio-Rad”, USA).

According to the biocompatibility analysis results (Fig. 2) Au(arg):CFO(DHCA), Au(arg):CFO\_Zn(DHCA) and Au(arg):CFO\_Ga(DHCA) nanocomposites induced dose-dependent cytotoxic effect in Jurkat cells after 24 h treatment. At 100 µg/ml, the composites demonstrated the greatest cytotoxicity effect and reduced the cells viability by more than 20% ( $p < 0.001$ ). At the same time, the treatment with 10 µg/ml did not affect cells viability.

At the next stage, the influence of nanocomposites on cell morphology was analyzed using Cell-IQ® v2 MLF integrated platform (CM Technologies Oy, Tampere, Finland). Hepatoma cell line (Huh7) was used. Cells were cultured in 24-well plates with nutrient medium (DMEM) in

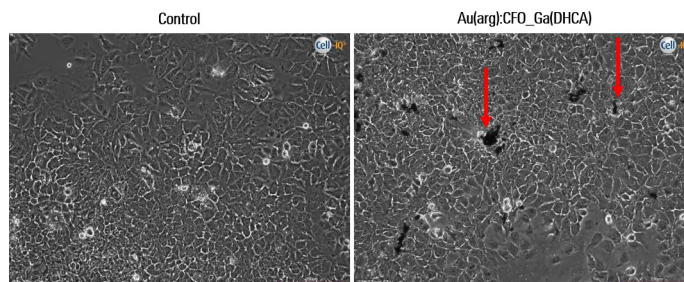


Figure 3. Huh7 cells morphology did not change after 24 h treatment with 100 µg/ml Au(arg):CFO\_Ga(DHCA). Red arrows show agglomerates in the nanocomposite. Scale bar – 200 µm.

standard conditions. After 24 h old media were removed and 100  $\mu\text{g/ml}$  of the composite DMEM solution was added. Next, the plate was transferred to Cell-IQ system for a cultivation (in standard conditions) and a continuous real-time phase-contrast imaging. Visualization was performed according to the manufacturer protocol. The results of continuous imaging demonstrated that Huh7 cells morphology did not change after 24 h treatment with Au(arg):CFO\_Ga(DHCA) (Fig. 3). The images demonstrated the formation of aggregates in the composite.

*The reported study was funded RSF grant number 21-72-20158. Authors are grateful to PhD N. Gazatova (Center for Immunology and Cellular Biotechnology, IKBFU) for helping in the realization of the experimental part of the project.*

**MAGNETIC NANOPARTICLES  $\text{Fe}_3\text{O}_4$ ,  $\text{Fe}_3\text{O}_4@\text{SiO}_2$ ,  $\text{Fe}_3\text{O}_4@\text{C}$ ,  
AND  $\text{Fe}_3\text{O}_4@\text{C}@\text{C}$  FOR THE ORGANIC DYES ADSORPTION**

*O.S. Ivanova*<sup>1\*</sup>, *I.S. Edelman*<sup>1</sup>, *A.E. Sokolov*<sup>1</sup>, *E.S. Svetlitsky*<sup>1</sup>, *Chun-Rong Lin*<sup>2</sup>, *Ying-Zhen Chen*<sup>2</sup>

<sup>1</sup>Kirensky Institute of Physics, FRC KSC SB RAS, Krasnoyarsk, Russia

<sup>2</sup>Department of Applied Physics, National Pingtung University, Pingtung City, Taiwan

\*E-mail: [osi@iph.krasn.ru](mailto:osi@iph.krasn.ru)

Adsorption of various water pollutants is one of the most common applications of magnetic magnetite nanoparticles (NPs). The number of publications on the study of the of organic dyes, heavy metals, waste of chemical and pharmaceutical industries adsorption by magnetic NPs is growing avalanche. In addition to the possibility of their easy extracting from the medium using magnetic field, an important advantage of the magnetite NPs is the ability of their surface to attach various substances. Selective adsorption of certain pollutants can be reached by different modifications of the NPs surface and the creation of the magnetic core-shell functionalized structures.

The present work is devoted to the comparative study of the adsorption capacity of  $\text{Fe}_3\text{O}_4$  NPs and  $\text{Fe}_3\text{O}_4$  NPs with various shells –  $\text{Fe}_3\text{O}_4@\text{SiO}_2$ ,  $\text{Fe}_3\text{O}_4@\text{C}$ , and  $\text{Fe}_3\text{O}_4@\text{C}@\text{C}$  in relation to various types of organic dyes: cationic methylene blue (MB), rhodamine C (Rh C)) and anionic Congo red (CR), methyl orange (MO), and eosin Y (EoY).

Different initial materials and procedures were used to synthesize different kinds of NPs. The core-shell  $\text{Fe}_3\text{O}_4@\text{SiO}_2$  NPs were produced in the two-stage regime. Firstly,  $\text{Fe}_3\text{O}_4$  NPs were prepared by co-precipitation using iron sulfate  $\text{FeSO}_4 \cdot 7\text{H}_2\text{O}$ ,  $\text{KNO}_3$  and  $\text{NaOH}$ ; the stirring process proceeded at 90 °C under Ar flow 1 h; washing with ethanol, the obtained precipitate was coated with silica via the Stöber process. The formed  $\text{SiO}_2$  shell with a thickness of about 7 nm is clearly visible in the TEM photo (Fig. 1a).

To synthesize  $\text{Fe}_3\text{O}_4@\text{C}$  nanoparticles, two-stage process was realized too but using other regimes and initial materials. At the first,  $\text{Fe}_3\text{O}_4$  NPs were obtained as a result of the thermal decomposition reaction of the iron-oleate complex (sodium oleate and iron (III) chloride hexahydrate), dissolved in a mixture of alcohol, deionized water, and n-hexane, at 70 °C in air for 4 h. After cooling to room temperature and the implementation of several rather complicated procedures,  $\text{Fe}_3\text{O}_4$  NPs were obtained, some of which were studied as independent objects, and the other part was covered with carbon in glucose dissolved in distilled water under stirring for 15 min at 90 °C. The final mixture was heated in autoclave at 200 °C for 12 h, and then allowed to cool to room temperature. The black products separated by a magnet and washed several times with water and ethanol were dried at 60 °C for 6 h (sample  $\text{Fe}_3\text{O}_4@\text{C}$ ).

Two stages were used to synthesize nanocomposites  $\text{Fe}_3\text{O}_4@\text{C}@\text{C}$ . In this case, the initial  $\text{Fe}_3\text{O}_4@\text{C}$  nanoparticles were synthesized by a one-step process using  $\text{Fe}(\text{NO}_3)_3 \cdot 9\text{H}_2\text{O}$ , oleic acid, and oleylamine. Obtained NPs were coated by the second carbon shell in glucose dissolved in distilled water just the same way as it was described above in the case  $\text{Fe}_3\text{O}_4@\text{C}$  NPs. The formed carbon shell is clearly visible in the TEM image of the obtained  $\text{Fe}_3\text{O}_4@\text{C}@\text{C}$  NPs (Fig. 1b).

So, we have three types of  $\text{Fe}_3\text{O}_4$  NPs obtained in different processes and core-shell NPs  $\text{Fe}_3\text{O}_4@\text{SiO}_2$ ,  $\text{Fe}_3\text{O}_4@\text{C}$ , and  $\text{Fe}_3\text{O}_4@\text{C}@\text{C}$ .

The NPs were single crystals with an average diameter of about 15–40 nm with the most intense X-ray peaks corresponding to the  $\text{Fe}_3\text{O}_4$  phase in all cases. The values of saturation magnetization 79 emu/g in magnetite NPs and 65–75 emu/g in coated NPs are close to the saturation magnetization of bulk magnetite – 84 emu/g.

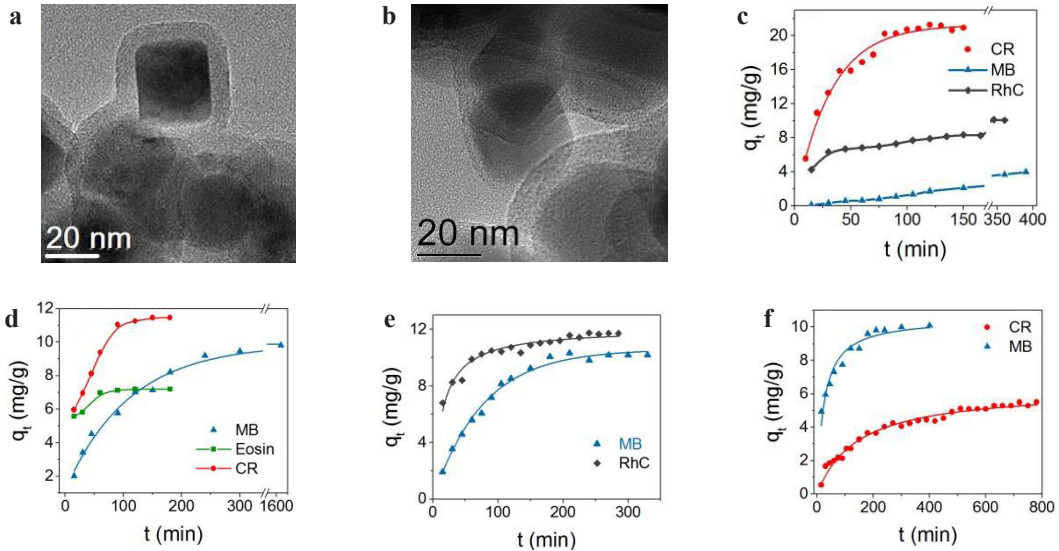


Figure 1. TEM images of  $\text{Fe}_3\text{O}_4@\text{SiO}_2$  (a) and  $\text{Fe}_3\text{O}_4@\text{C}@\text{C}$  (b) NPs. The kinetic adsorption curves different dyes for  $\text{Fe}_3\text{O}_4$  (c),  $\text{Fe}_3\text{O}_4@\text{SiO}_2$  (d),  $\text{Fe}_3\text{O}_4@\text{C}$  (e), and  $\text{Fe}_3\text{O}_4@\text{C}@\text{C}$  (f) NPs samples. Experimental conditions:  $C_0 = 30 \text{ mg/L}$ ,  $m(\text{NPs}) = 3 \text{ mg}$ ,  $V = 1.5 \text{ mL}$ .

To study the adsorption capacity, NPs were dispersed in aqueous dye solution in an ultrasonic bath for 10 minutes. Changes of the dyes concentration in the solution after their interaction with NPs were measured as the changes in the solution optical absorption at the wave length corresponding to the absorption maxima of the particular dye: 490 nm for eosin Y, 505 nm for CR, 500 nm for MO and 664 nm for MB. Then, NPs were removed from the solution using magnetic field, and the solution optical absorption spectrum was recorded. Then, the remaining solution was mixed again with magnetic particles, and the described procedure repeated several times. In such a way the kinetic curves for NPs adsorption capacity were obtained. The value of the adsorption capacity of NPs at any moment in time,  $q_t \text{ (mg/g)}$ , was calculated as follows:

$$q_t = \frac{(C_0 - C_t)V}{m}, \quad (1)$$

where  $C_0$  and  $C_t$  are the initial and in any time concentrations of the dye in the solution,  $V$  is the volume of the solution; and  $m$  represents the weight of the adsorbing NPs introduced into solution.

The  $q_t(t)$  dependencies for different dyes for all samples are shown in Figs. 1c–f. The higher values of the adsorption capacity and the short time to reach the equilibrium value for the CR indicate the preferred absorption of anionic dyes by  $\text{Fe}_3\text{O}_4$  NPs (Fig. 1b). The kinetic curve for CP is well described by the pseudo-first order kinetic model, and the isotherm shape is well described by Brunauer-Emmett-Teller (BET) theory isotherm equation for liquid phase adsorption for Case-3 – polymolecular adsorption model [1].

The adsorption capacity of the core shell  $\text{Fe}_3\text{O}_4@\text{SiO}_2$  NPs shows comparable absorption values of anionic CR and cationic MB dye, which can be used in solutions of complex contaminants. The adsorption capacity of the core shell  $\text{Fe}_3\text{O}_4@\text{C}$  of magnetic NPs has changed dramatically. The  $\text{Fe}_3\text{O}_4@\text{C}$  NPs showed selective sorption of only cationic dyes. Experiments carried out on anionic



dyes: CR, MO and EoY showed the same results – no adsorption. The  $\text{Fe}_3\text{O}_4@\text{C}@\text{C}$  NPs indicate the preferred absorption of cationic dyes, but they also adsorb anionic dyes, albeit with a lower capacity and speed. In all cases coating NPs, the kinetic data are well described by the pseudo first order kinetic mode and the concentration dependences of the equilibrium value of the adsorption capacity are described by the Langmuir equation, showing the formation of a homogeneous adsorbed monolayer, while the adsorbed molecules do not interact with each other.

Analysis of experimental data shows the key role of the surface properties of NPs formed during synthesis on the adsorption of various dyes.

*Support by Ministry of Science and Technology of Taiwan, Grants MOST № 108-2923-M-153-001-MY3 and № 109-2112-M-153-003- is acknowledged.*

1. A. Ebadi, J.S. Soltan Mohammadzadeh, A. Khudiev, *Adsorption*, **15**, 65 (2009).

## EFFECT OF PLASMA TREATMENT ON THE MORPHO-MECHANICAL AND ADHESIVE PROPERTIES OF MAGNETOELECTRIC NANOCOMPOSITES FOR BIOMEDICAL APPLICATIONS

*V. Antipova*<sup>1\*</sup>, *K. Sobolev*<sup>1</sup>, *E. Korepanova*<sup>1</sup>, *S. Vorontcov*<sup>1</sup>, *V. Malashchenko*<sup>2</sup>, *V.V. Shupletsova*<sup>2</sup>,  
*L. Litvinova*<sup>2</sup>, *K. Levada*<sup>1</sup>, *V. Rodionova*<sup>1</sup>

<sup>1</sup>Research and Education Center ‘‘Smart Materials & Biomedical Applications’’, IKBFU, Kaliningrad, Russia

<sup>2</sup>Basic Laboratory of Immunology and Cellular Biotechnology, Kaliningrad, Russia

\*E-mail: [VAntipova1@kantiana.ru](mailto:VAntipova1@kantiana.ru)

Magnetolectric polymer composites are a group of materials consisting of magnetic filler and a piezopolymer matrix, in which the magnetolectric coupling is associated with strain interactions between the filler and matrix [1]. The biocompatibility of the polymer backbone, along with the multiferroic properties of nanocomposites, makes them interesting for a number of biological applications. In particular, they can be used as interfaces for culturing stem cells, with the possibility to remotely control the physical parameters of the cell microenvironment by applying an external magnetic field, to control cell activity (adhesion, proliferation, cell differentiation, etc.) [2–3].

Poly(vinylidene fluoride) (PVDF) is a fluorine-containing semi-crystalline polymer derived from vinylidene fluoride, which has at least five different crystalline phases, of which the  $\beta$ -phase has the greatest piezoelectric response. The low surface energy of PVDF and its copolymers leads to high hydrophobicity and poor wettability of the polymer surface, which badly affects cell adhesion to the surface of substrates, based on them and limits their use in biomedical applications [4]. There are many different approaches to modify the PVDF surface, but cold plasma treatment is the most optimal method because it preserves the basic physicochemical bulk properties of the substrates, both for porous and non-porous polymer surfaces [5–6].

The main goal of this work was to investigate the effect of plasma treatment on the morpho-mechanical properties of biological interfaces. The nanocomposites were fabricated by the doctor blade method and then treated with cold plasma. PVDF modified with magnetic filler ( $\text{CoFe}_2\text{O}_4$ ) was used as the base for the nanocomposites. The structural and magnetic properties of the obtained samples were characterized using X-ray powder diffraction (XRD) and a vibrating magnetometer (VSM). The morpho-mechanical properties of the nanocomposites were investigated before and after plasma treatment by measuring the contact angle of the samples with water and by atomic force microscopy (AFM). The nanocomposites were additionally tested on human mesenchymal stem cell culture.



Figure 1. Water contact angle and wettability. **a** Large wetting angle: hydrophobic surface (untreated PVDF+ $\text{CoFe}_2\text{O}_4$  sample). **b**, **c** Small wetting angle: hydrophilic surface (PVDF+ $\text{CoFe}_2\text{O}_4$  samples treated for 60 and 90 seconds respectively).

In this study, it was demonstrated that plasma treatment at different time intervals reduces the mechanical properties of PVDF-based nanocomposites (Young's modulus, mechanical stiffness), while there is a decrease in the wetting angle of these substrates (Fig. 1) and improvement in their adhesive properties, which makes them promising for use in various biomedical applications, such as bone tissue engineering.

*The reported study was funded by I. Kant Baltic Federal University, project number 105-z-22.*

1. P. Martins, S. Lanceros-Méndez, Polymer-based Magnetolectric Materials, *Adv. Funct. Mater.*, **23**, 3371–3385 (2013).
2. C. Ribeiro, V. Sencadas, D.M. Correia et al., Piezoelectric polymers as biomaterials for tissue engineering applications, *Colloids Surfaces B Biointerfaces*, **136**, 46–55 (2015).
3. A.E. Stanton et al., Extracellular matrix type modulates mechanotransduction of stem cells, *Acta Biomater.*, **96**, 310–320 (2019).
4. M. Tavakoli, Surface modification of polymers to enhance biocompatibility, *Surfaces and Interfaces for Biomaterials*, 719–744 (2005).
5. S.M. Damaraju, S. Wu, M. Jaffe et al., Structural changes in PVDF fibers due to electrospinning and its effect on biological function, *Biomedical materials*, **8**, no. 4 (2013).
6. D.M. Correia et al., Surface wettability modification of poly(vinylidene fluoride) and copolymer films and membranes by plasma treatment, *Polymer*, **169**, 138–147 (2019).

## REMOVAL OF NONMAGNETIC PARTICLES FROM WATER BY USING MAGNETIC SYSTEM

*M.S. Filinkova*<sup>1\*</sup>, *Iu.A. Bakhteeva*<sup>1</sup>, *I.V. Medvedeva*<sup>1,2</sup>, *I.V. Byzov*<sup>1</sup>, *S.V. Zhakov*<sup>1</sup>, *M.A. Uimin*<sup>1</sup>

<sup>1</sup>M.N. Mikheev Institute of Metal Physics UB RAS, Ekaterinburg, Russia

<sup>2</sup>Ural State Mining University, Ekaterinburg, Russia

\*E-mail: [filinkova-ms@yandex.ru](mailto:filinkova-ms@yandex.ru)

A wide range of micro- and nanoparticles that are released into the environment in the course of human activity, such as TiO<sub>2</sub> nanoparticles from photocatalytic reactors during water treatment, micro- and nano- fragments from plastics degradation, etc., is of new potential threats to ecosystems. Ultimately, micro- and nanoparticles enter the food chains and end up inside many aqueous organisms (fish, shellfish [1]), damaging ecosystems and human health. Removal and prevention of micro- and nanoparticles contaminants in water is an urgent task. A promising approach is to use magnetic separation technology extended for nonmagnetic targets. This method provides removal nonmagnetic particles from water due to their aggregation with magnetic seeds and the subsequent separation of the heteroaggregates from water in a gradient magnetic field. Magnetic systems based on permanent magnets, are of particular interest, as magnetic field is generated without electrical energy consumption, which refers to a “green” technology concept [2].

An important stage in the development of equipment is the design of efficient magnetic systems. For effective separation of the particles, the magnetic system must produce a high magnetic induction and a high magnetic field gradient and have low maintenance costs. Two types of the magnetic systems depending on the separation process were designed and simulated, namely, for the magnetic sedimentation by gravitational and magnetic forces, and for the magnetic filtration by sticking particles from the water to the filler of the filter placed in a high gradient magnetic field.

The magnetic systems were made of permanent magnets NdFeB using soft magnetic steel to enhance the magnetic field gradient. Magnetic parameters ( $B_{\max}$  and  $\partial B/\partial z$ ) of the systems were

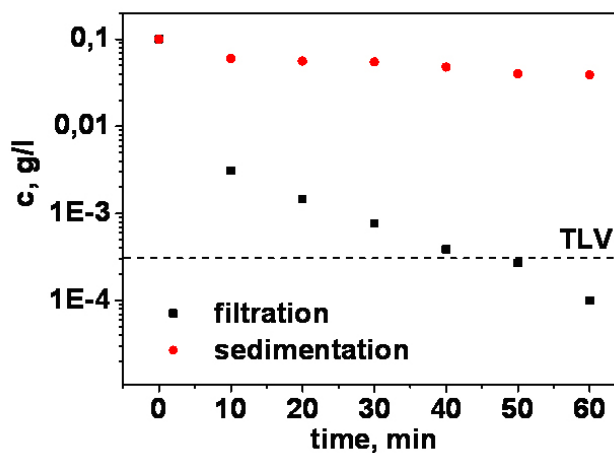


Figure 1. Time dependence of the residual concentration of magnetic nanoparticles in water by magnetic separation.

calculated using the Comsol Multiphysics program. The magnetic system for the sedimentation was a polyhedron of 6 trapezoid magnets, with the magnetization vector of each magnet directed to the center of the system. Inside internal space a cylindrical element made of magnetically soft steel was installed ( $B_{\max} = 0.8$  T,  $\partial B/\partial z = 90$  T/m) [3]. The magnetic system for the filtration was made of a ring-shaped magnet, and it was placed inside a plastic tube with steel wool filler ( $B_{\max} = 1.2$  T,  $\partial B/\partial z = 2\text{--}4 \cdot 10^3$  T/m).

The magnetic systems were used for the separation of composite Fe-C nanoparticles from aqueous suspensions. The core-shell Fe-C particles were synthesized by the gas-phase method [4, 5] and the stable aqueous suspension of these particles with a hydrodynamic diameter of 150 nm was obtained with a 1,2-distearoyl-sn-glycero-3-phosphoethanolamine-N-[amino (polyethylene glycol)-2000] (DSPE-PEG). The aggregates sizes and zeta potential values were determined by the Dynamic Light Scattering method. Spectrophotometric and Nuclear magnetic resonance relaxometry methods were used to detect the residual particles concentration in water after magnetic separation. For the spectrophotometric residual concentration determination of the partial components, a preliminary calibration based on the PLS method has been done. From these data the efficiency of the magnetic separation was estimated. The magnetic filtration process was more efficient compared to the magnetic sedimentation process (Fig. 1). In this case, the concentration of the nanoparticles Fe-C was decreased down to the threshold limit value (TLV), 0.3 mg/l for 40 minutes, while by the magnetic sedimentation it required more than 24 hours.

The magnetic filter was used to separate nonmagnetic  $\text{TiO}_2$  particles ( $d_h = 1 \mu\text{m}$ ) and polyethylene terephthalate (PET) particles ( $d_h = 10\text{--}30 \mu\text{m}$ ) from water by using a heteroaggregation with magnetic seeds containing Fe-C core. Preliminary, the surface of Fe-C nanoparticles was modified by diazotization reaction to obtain stable aqueous suspensions of Fe-C-COOH (used to remove  $\text{TiO}_2$ ) и Fe-C-NH<sub>2</sub> (used to remove PET). Various compositions of magnetic and nonmagnetic components were studied. It was found that the most efficient filtration occurs at the mass ratio  $\text{TiO}_2/\text{Fe-C-COOH} = 1:1$  and  $\text{PET}/\text{Fe-C-NH}_2 = 1:0.25$  at pH = 6. Under these conditions about 99 mass.% of plastic particles were removed.

The higher efficiency of the magnetic filtration compared to the magnetic sedimentation is due to the much higher magnetic field gradient. The effects of filler material, its shape, and the filling density on the efficiency of the magnetic filter system might be important, and it will require further research. The results obtained in this research can serve as a basis for designing magnetic separation devices for water purification and separation of nonmagnetic nano- and microparticles.

*The research was carried out within the state assignment of Ministry of Science and Higher Education of the Russian Federation (themes “Magnet” №122021000034-9 and “Pressure” №122021000032-5).*

1. Y. Lu, Y. Zhang, Y. Deng, W. Jiang, et al., Environ. Sci. Technol., **50**(7), 4054–4060, (2016).
2. C.T. Yavuz, J.T. Mayo, W. W. Yu, et al., Science, **314**, 964–967, (2006).
3. I.V. Medvedeva, M.A. Uimin, A.E. Yermakov et al., J. Nanopart., Res. **14**, 740, (2012).
4. I.A. Bakhteeva, I.V. Medvedeva, I.V. Byzov, et al., J. Sep. Pur., **188**, 341–347, (2017).
5. I.A. Bakhteeva, I.V. Medvedeva, I.V. Byzov, et al., Russ. Chem., Bull. **70**, 722–731, (2021).

## THE EFFECTIVENESS OF USING MAGNETIC PARTICLES IN CANCER HYPERTHERMIA

*L.P. Ichkitidze*<sup>1,2\*</sup>, *G.Yu. Galechian*<sup>1</sup>, *A.Yu. Gerasimenko*<sup>1,2</sup>, *D.V. Telyshev*<sup>1,2</sup>

<sup>1</sup>Institute of Bionic Technologies and Engineering, I.M. Sechenov First Moscow State Medical University, Moscow, Russia

<sup>2</sup>Institute of Biomedical Systems, National Research University of Electronic Technology, Moscow, Russia

\*E-mail: [ichkitidze\\_l\\_p@staff.sechenov.ru](mailto:ichkitidze_l_p@staff.sechenov.ru); [ichkitidze@bms.zone](mailto:ichkitidze@bms.zone)

Magnetic particles (MPs) having various configurations (spherical, rod-shaped, etc.), sizes (micron, submicron and nano) and physicochemical properties are actively investigated with the prospect of their large-scale application in medicine. Real uses of nanostructured materials in life sciences are common at the present time. The unique physicochemical properties of MNPs endow them with novel multifunctional capabilities for imaging, drug delivery and therapy, which are referred to as theranostics [1]. A new method of treatment based on magnetic nanoparticles is being developed – magnetic hyperthermia, in which oncological neoplasms are treated. The heating of the fabric occurs due to the release of heat during the magnetization of the MPs by an alternating magnetic field. In this case, irreversible thermal ablation of the pathological target occurs due to the release of heat and an increase in the local temperature in the suspension with magnetic particles of MPs, which are loaded with tissues. As a result, the viability of cancer cells is significantly reduced in the temperature range of 41–45 °C, while healthy cells can survive [2].

We analyzed the literature sources in which MPs was used for hyperthermia of an oncological tumor. Many researchers note that the effectiveness of hyperthermia therapy depends on many factors, the main of which are: the magnetic energy stored in the MPs and their residual magnetization  $M$ , the MPs dosage and the parameters of the alternating magnetic field. For biomedical applications, various factors like design strategies, synthesis process, coating and surface functionalization need to be considered. The most actively studied are spherical superparamagnetic iron oxide nanoparticles (SPIONs) with sizes  $d \sim 5\text{--}25$  nm, since they can act as multifunctional agents and combine diagnostic and therapeutic properties [3]. SPIONs from  $\gamma\text{-Fe}_2\text{O}_3$  exhibit lower toxicity compared to  $\text{Fe}_3\text{O}_4$  nanoparticles. However, the residual magnetization for the latter type of SPIONs is several times higher than for the former, and therefore the efficiency of hyperthermia based on them is expected to be higher [4]. For example, in the *in vitro* mode during hyperthermia on spherical  $\text{Fe}_3\text{O}_4$  MPs having large dimensions ( $d \geq 20$  nm) and low magnetization  $M \sim 10$  emu/g, the tissue temperature increased by  $\Delta t \sim 0.7$  °C, and at large  $M \sim 70$  emu/g per  $\Delta t \sim 2.0$  °C [5]. For this type of MPs with a particle diameter in the range of 30–80 nm, the maximum efficiency, defined as the heat released per unit mass of MPs, or the so-called specific absorption rate (SAR parameter), was at the level of SAR  $\sim 0.9$  kW/g [6]. For  $\gamma\text{-Fe}_2\text{O}_3$  SPIONs this parameter was of the order of SAR  $\sim 113$  W/g [7].

Based on the reviewed works, the following conclusions can be drawn.

To avoid the inductive heating of normal tissues due to dielectric losses and eddy current losses, the Brezovich criterion was formulated [8]. The threshold of biological discomfort, that is, the product of the amplitude of the alternating magnetic field  $H_{ac}$  by its frequency  $f_{ac}$  (Brezovich's criterion  $H_{ac} \cdot f_{ac} = 10^9$  A/(m·s) in the calculations of different works, it varied in the range  $H_{ac} \cdot f_{ac} = 2 \cdot 10^8\text{--}8 \cdot 10^9$  A/(m·s)). Apparently, this had a significant impact on the determination of SAR, which was observed in a wide range of SAR  $\sim 0.01\text{--}3.0$  kW/g.

In the *in vitro* mode, the maximum temperature increase by  $\Delta t \sim 20$  °C was realized under the conditions:  $H_{ac} = 237$   $\mu\text{T}$ ,  $f_{ac} = 3.0$  GHz and a constant magnetic field of 75 mT magnetization [9].

In the *in vivo* mode of heating of cancer tissue in laboratory mice  $\Delta t \sim 20$  °C was observed under conditions:  $H_{ac} = 247$   $\mu$ T,  $f_{ac} = 260$  kHz, which reduced the volume of the cancerous tumor by about half during several sessions of hyperthermia for 30 minutes [10].

The high-frequency alternating magnetic field  $f_{ac} \geq 100$  kHz negatively affects the state of healthy cells, therefore, the reduction of  $f_{ac}$ , the selection of the type of MPs, their size and other parameters allow you to adjust the SAR to acceptable values. In particular, for magnetic ferrite nanoparticles  $Zn_xMn_{1-x}Fe_2O_4$  at  $x = 0.2$ , the maximum SAR value of  $\sim 10$  W/g was realized at a small  $f_{ac} = 100$  kHz,  $H_{ac} = 10$  mT [11, 12]. This approach solves the dilemma of the negative impact of the high frequency of the alternating magnetic field on healthy tissues, and also simplifies the design of the solenoid that creates a magnetic field.

Undoubtedly, the high value of the residual magnetization of the MPs significantly increases the efficiency of hyperthermia, which is often observed in large particles or in aggregates from SPIONs. For example, large values of  $M \sim 86$  eme/g have been achieved in aggregates with dimensions of  $\sim 200$  nm containing numerous nanoparticles ( $d \sim 17$  nm) [13], magnetite  $M \sim 92$  eme/g [14].

The antitumor efficiency of purified bacterial magnetosomes is significantly higher than the efficiency of chemically synthesized magnetic particles [15].

Intracellular hyperthermia provides direct heating of cancer cells and additionally enhances the therapeutic effect when various ligands associated with MPs also act in tumor tissue [16, 17]. Localized temperature rise and selective heat dissipation in biological tissues using magnetic particles is a complex method of cancer treatment, which does not always give an unambiguous result. Unfortunately, a large number of results obtained in studies of the use of hyperthermia as a therapeutic method show that it is not yet optimized enough, this delays its active use in clinical settings. Although the stage of transition of the hyperthermia method from laboratory studies to clinical trials has already been passed.

*The research was funded by the Ministry of Science and Higher Education of the Russian Federation: grant No. 075-15-2021-596 (Sechenov University).*

1. X. Li, W. Li, M. Wang and Z. Liao, *Journal of Controlled Release*, **335**, 437–448 (2021).
2. L. Zhu, Z. Zhou, H. Mao, L. Yang. *Nanomedicine (Lond.)*, **12** (1), 73–87 (2017)
3. Z. Hashim, M. Green, P.H. Chung et al., *Nanoscale*, **6** (14), 8376–8386 (2014).
4. F.V. Gutierrez, A. De Falco, E. Yokoyama et al., *Nanomaterials*, **11**, 2197 (2021).
5. L. Yu, L. Yu, J. Liu, K. Wu et al. *Scientific Reports*, **4**, 7216 (2014).
6. K. Simeonidis, et al., *ACS Appl. Nano Mater.*, **3**, 4465–4476 (2020).
7. L. Dallet, D. Stanicki, P. Voisi et al., *Scientific Reports*, **11**, 3286 (2021).
8. I.A. Brezovich, R.F. Meredith, *Radio Clin. North Am.*, **27** (3) 589–602 (1989).
9. J.H. Lee, B. Kim, Y. Kim, S.K. Kim, *Scientific Reports*, **11**, 4969 (2021).
10. P.V. Gorelkin, A.S. Erofeev, A.O. Prelovskaya et al., Patent RU, no. 2742196.
11. N.N. Liu, A.P. Pyatakov, M.N. Zharkov et al., *Appl. Phys. Lett.*, **120**, art. no. 102403 (2022).
12. N.N. Liu, A.P. Pyatakov, A.M. Saletsky et al., *JMMM*, **555**, art. no. 169379 (2022).
13. B.D. Partain et al. *J Control. Release*, **321**, 259 –271 (2020).
14. N. Dudchenko, S. Pawar, I. Perelshtein and D. Fixler, *Materials*, **15** (7), art. no. 2601 (2022).
15. R. Le Fèvre, M. Durand-Dbief, I. Chebbi, C. Mandawala, *Theranostics*, **7** (18), 4618–4631 (2017).
16. K. El-Boubbou, *Nanomedicine (Lond.)*, **13** (8), 929–952 (2018).
17. K. El-Boubbou, *Nanomedicine (Lond.)*, **13** (8), 953–971 (2018).

## MAGNETIC STUDY OF THE DEFORMED MEDICAL GRADE 316L STEEL, MANUFACTURED WITH A LASER 3D PRINTER

*N.V. Kazantseva\**, *Yu.N. Koemets*, *I.V. Ezhov*, *D.I. Davydov*, *D.A. Shishkin*,  
*M.B. Rigmant*, *A.V. Kochnev*

Institute of Physics of Metals, Ural Branch of the Russian Academy of Sciences, Ekaterinburg, Russia

\*E-mail: [kazantseva@imp.uran.ru](mailto:kazantseva@imp.uran.ru)

The report demonstrates the application possibility of magnetic measurements for investigation of the deformation effect in the medical grade stainless steel manufactured by additive laser printing.

Stainless steels are used for medical implants and surgical tools due to the excellent combination of properties, such as cost, strength, and corrosion resistance. 316L stainless steel belongs to the class of stable austenitic steels, having a single-phase paramagnetic FCC composition over the operating temperature range. In convention steels of this class, the appearance of the ferromagnetic delta ferrite phase is practically not observed. Under deformation conditions, two types of martensite can form in 316L steel samples, namely: paramagnetic epsilon martensite with an HCP crystal lattice and ferromagnetic alpha prime martensite with a cubic crystal lattice. Strain-induced alpha prime martensite causes an embrittlement of the material, because of that this ferromagnetic phase is an undesirable one [1-2]. Local areas containing strain-induced martensite serve as sources of stress and are pre-fracture areas of material [3]. The difficulty of identifying such regions in austenitic steels is associated with a small percentage of the martensite phase, which makes it difficult to determine it by structural methods.

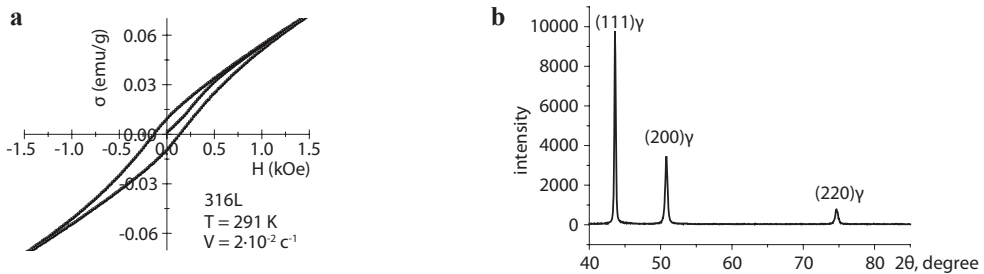


Figure 1. Results of the magnetic (a) and X-ray (b) studied for L-PBF sample after deformation.

A magnetic study of deformed samples of 316L austenitic steel manufactured by laser powder-bed fusion method (L-PBF) was done with a LakeShore 7407 vibrating-coil magnetometer in magnetic fields of up to 9 kOe at the Magnetic Measurement Department of the Institute of Metal Physics. Compression deformation at room temperature and at different rates ( $8 \cdot 10^{-4} \text{ c}^{-1}$ ;  $3 \cdot 10^{-3} \text{ c}^{-1}$ ;  $1 \cdot 10^{-2} \text{ c}^{-1}$ ;  $2 \cdot 10^{-2} \text{ c}^{-1}$ ) was performed. Figure 1a shows the presence of a ferromagnetic phase in the L-PBF deformed sample. Wherein, the diffraction reflections of only the paramagnetic FCC phase can be seen in the diffraction pattern of the same sample (Fig. 1b). The value of the coercive force calculated from the results of magnetic measurements indicates that a ferromagnetic martensite phase is present in this deformed sample. The obtained results are discussed and compared with the literature data.

*Support by RSF (project No. 22-29-01514) is acknowledged.*

1. M.J. Sohrabi, M. Naghizadeh, H. Mirzadeh. Archives of Civil and Mechanical Engineering, **20**, 124 (2020).
2. I. Meszaros, J. Prohaszka. Journal of Materials Processing Technology, **161**, 162–168 (2005).
3. M.B. Rigmant, M.K. Korkh, D.I. Davydov, D.A. Shishkin, Y.V. Korkh, A.P. Nichipuruk, N.V. Kazantseva, Russian journal of nondestructive testing, **51**, 680–691 (2015).



## HEAT RELEASE BY FERRIHYDRITE NANOPARTICLES AT FERROMAGNETIC RESONANCE

*S.V. Stolyar*<sup>1,2,3</sup>, *O.A. Li*<sup>1,3\*</sup>, *V.P. Ladygina*<sup>1</sup>, *E.D. Nikolaeva*<sup>1</sup>, *A.M. Vorotynov*<sup>2</sup>,  
*D.A. Velikanov*<sup>2</sup>, *V. F. Pyankov*<sup>1</sup>, *R.S. Iskhakov*<sup>2</sup>

<sup>1</sup>FRC KSC SB RAS, Krasnoyarsk, Russia

<sup>2</sup>Kirensky Institute of Physics, Federal Research Center KSC SB RAS, Krasnoyarsk, Russia

<sup>3</sup>Siberian Federal University, Krasnoyarsk, Russia

\*E-mail: [oali@sfu-kras.ru](mailto:oali@sfu-kras.ru)

Currently, searches are underway for safe and effective components for hyperthermia – one of the auxiliary methods of cancer treatment due to a general or local increase in temperature to 41–45 °C. In our work, we consider the heating of ferrihydrite particles by microwave field in the ferromagnetic resonance mode in comparison with nonresonant energy absorption.

Ferrihydrite nanoparticles were biogenically synthesized by the bacteria *Klebsiella oxytoca*. The average size of nanoparticles was 2.5 nm. Fig. 1 shows the ferromagnetic resonance (FMR) curve of ferrihydrite nanoparticles recorded at room temperature. The resonant field is  $H_r \approx 3.3$  kOe, the line width is  $\Delta H \approx 1.4$  kOe.

For practical applications, it is necessary to heat the particles in a narrow temperature range. The temperature increase depends on the absorbed power and duration of exposure. We have studied the time dependence of the temperature increment  $\Delta T$  of particles at different values of the constant magnetic field in the microwave field ( $f = 8.9$  GHz). Fig. 2 shows the results of these studies. In all cases, we observe a rapid increase in temperature at the initial moment of time, followed by a decrease in the rate of temperature increase with tendency to saturation. In a field close to resonant (with a strength of 3.34 kOe), the greatest increase in the temperature of the system of ferrihydrite nanoparticles is observed, which indicates the resonant nature of the absorption of microwave energy. Heating of magnetic powders at ferromagnetic resonance mode, in our opinion, can be used in medicine as a new method for implementing magnetic hyperthermia.

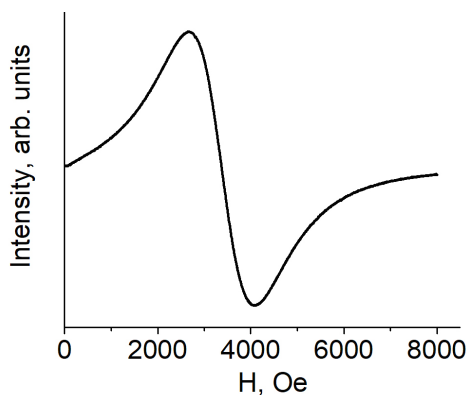


Figure 1. FMR spectrum of ferrihydrite nanoparticles.

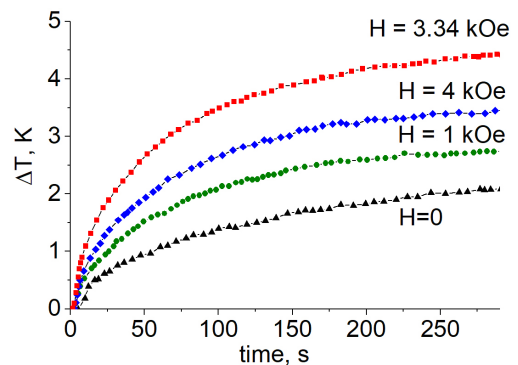


Figure 3. Temperature increment of ferrihydrite nanoparticles in a constant field  $H$ .

## COBALT FERRITE/GOLD NANOCOMPOSITE AS A POTENTIAL AGENT FOR PHOTOTHERMAL TREATMENT

*A.V. Motorzhina*<sup>1\*</sup>, *S.E. Pshenichnikov*<sup>1</sup>, *S. Jovanovic*<sup>2,3</sup>, *A.A. Anikin*<sup>1</sup>, *V.V. Rodionova*<sup>1</sup>,  
*L.V. Panina*<sup>1</sup>, *K.V. Levada*<sup>1</sup>

<sup>1</sup>REC SMBA, Immanuel Kant Baltic Federal University, Kaliningrad, Russia

<sup>2</sup>Department of Physics, Vinča Institute of Nuclear Sciences – National Institute of the Republic of Serbia, University of Belgrade, Vinca, Belgrade, Serbia

<sup>3</sup>Advanced Materials Department, Jožef Stefan Institute, Ljubljana, Slovenia

\*E-mail: [Amotorzhina1@kantiana.com](mailto:Amotorzhina1@kantiana.com)

A nanocomposite consisting of gold nanoparticles coated with arginine surrounded by cobalt ferrite nanoparticles coated with dihydrocaffeic acid was first synthesized and investigated as a potential agent for photothermal treatment of liver cancer cells Huh7.

A comprehensive study of the structural properties and morphology of nanocomposite particles shows a narrow size distribution, as well as structural and morphological stability over time [1]. Nanoparticles of cobalt ferrite determine the superparamagnetic properties of the nanocomposite, which decreases the aggregation in aqueous suspensions.

Before testing photothermal treatment the primary cytotoxic effect of nanocomposite was examined on Huh7 cell line using WST-1 test. The test results show an increase in the cytotoxic effect with increasing nanocomposite concentration and exposure time (Fig. 1).

Significant photothermal properties of nanocomposite were found at a wavelength of 800 nm which corresponds to the region of tissue optical transparency. The nanocomposite was dilute in cell medium DMEM and added to the cell suspension at 3 concentrations: 10, 50 and 100 µg/mL. After 24 h of exposure with nanocomposite, the cell suspension was illuminated by a laser with a wavelength of 800 nm and the increase in temperature of cell suspension was measured with the experimental setup. The effect of photothermal treatment on the cell suspension was measured using WST-1 test. It was found that the cytotoxic effect on cancer cells increased when combined with photothermal therapy.

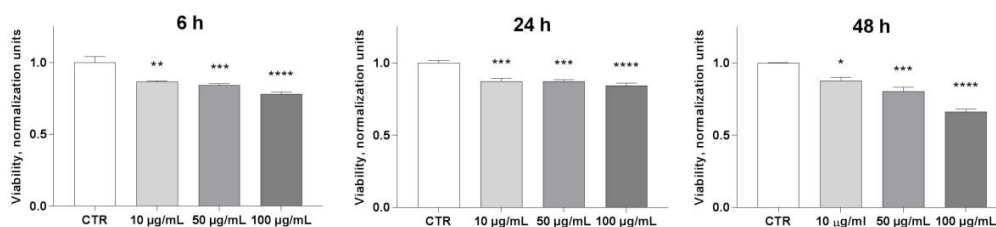


Figure 1. Relative viability of Huh7 cell line after nanocomposite exposure for 6, 24, 48 hours as a normalized units to the control data. The results shown are the mean  $\pm$  standard deviation. Columns marked with asterisks indicate the results that were statistically different from controls: \*  $P < 0.05$ , \*\*  $P < 0.01$ , \*\*\*  $P < 0.001$ , \*\*\*\*  $P < 0.0001$ . Statistical analysis was carried out using the One-way ANOVA.

Support by RSF, grant number 21-72-20158, is acknowledged.

1. A.V. Motorzhina et al., Processes, 9, 2264 (2021).

## CALCULATION OF TUNNEL MAGNETORESISTANCE OF MAGNETIC TUNNEL JUNCTION FOR MAGNETIC BIOSENSORS

*V.A. Paskal\*, N.Kh. Useinov*

Institute of Physics, Kazan Federal University, Kazan, Russian Federation

\*E-mail: [vapaskal@gmail.com](mailto:vapaskal@gmail.com)

Tunnelling magnetoresistance (TMR) is similar to GMR but has a non-magnetic insulating layer instead of a conducting one. The insulating layer is normally 1–2 nm thick, such that the electrons can tunnel through. These sensors are also known as magnetic tunnel junctions (MTJ). The materials of the insulating layer could be  $\text{Al}_2\text{O}_3$ ,  $\text{Ga}_2\text{O}_3$ ,  $\text{MgO}$ , grapheme, and etc. Several groups have demonstrated the capability of TMR sensors to detect micro to nano-sized magnetic beads [1]. MTJs are the most sensitive magnetoresistance sensors with a ratio of 20–50%, or, as more recently reported, over 200% when using a  $\text{MgO}$  tunnel barrier [2]. Instead of a Cu spacer like that found in the spin-valve construction, MTJs have a thin insulating layer ( $\leq 2$  nm thick), which acts as a tunnel barrier. The thickness of the insulating layer can be varied to effectively “tune” the device sensitivity. Additionally, the sensing current is directed perpendicular to the relatively large area MTJ layers rather than in the plane of the sensor as used in GMR structures. Wang et al. (2005) are pursuing this concept to produce a  $10^6$  sensor array, with the promise of each sensor detecting a single magnetic label attached to a single DNA fragment [3]. In a study by Albon et al. (2009) arrays of tunnel magnetoresistance sensors have been employed to detect magnetic microbeads. For single bead detection, elliptically shaped sensors of axis lengths of 400 and 100 nm are used [4]. A linear response of the sensor signal in a magnetic field range between  $-500$  and  $+500$  Oe has been reported. An elliptical element with a length of 400 nm on the longitudinal and 100 nm on the transverse axis has been used [5]. In addition, TMR sensors developed with low-noise amplifier circuits detected the magnetocardiography wave without averaging, and the QRS complex was clearly observed with averaging at a high signal-to-noise ratio [6].

Since the sensitivity varies between each sensor, we can introduce the relative resistance change

$$\text{TMR} = \left[ \frac{R_{\text{sample}} - R_{\text{sensor}}}{R_{\text{sensor}}} \right] \cdot 100\% \quad ,$$

where  $R_{\text{sample}}$  and  $R_{\text{sensor}}$  denote the resistance of the TMR sensor with and without sample, respectively. The resistance  $R$  is related of conductance  $G$  as  $R = 1/G$  and  $G$  is proportional to transmission coefficient  $T$ . We find this coefficient using the quantum mechanical and quasi- classical methods.

In this work are shown dependences of TMR on the ratio of radius contact to mean free path of conduction electrons and dependences of TMR on voltage. They can be used to interpret experimental data, see the articles above, obtained from biosensors based on MTJ.

*The work is funded by the Program of Competitive Growth of Kazan Federal University.*

1. V. Nabaei, R. Chandrawatib, H. Heidairi, Biosensors and Bioelectronics, **103**, 69–86 (2018).
2. S.S.P. Parkin, C. Kaiser et al., Nat. Mater., **3** (12), 862–867 (2004).
3. S.X. Wang, S.Y. Bae et al., J. Magn. Magn. Mater., **293** (1), 731–736 (2005).
4. C. Albon, A. Weddeman, et al., Appl. Phys. Lett., **95** (2), 023101 (2009).
5. M. Donolato, P. Vavassori et al., Adv. Mater., **22** (24), 2706 (2010).
6. K. Fujiwara et al., Appl. Phys. Express, **11**, 023001 (2018).

## CYTOTOXIC EFFECTS OF NANOCOMPOSITES OF GOLD AND GALLIUM-DOPED CFO NANOPARTICLES

*S.E. Pshenichnikov*<sup>1\*</sup>, *A.V. Motorzhina*<sup>1</sup>, *V.V. Malashchenko*<sup>2</sup>, *S. Jovanović*<sup>3,4</sup>, *L.S. Litvinova*<sup>2</sup>,  
*L.V. Panina*<sup>1,5</sup>, *V.V. Rodionova*<sup>1</sup>, *K.V. Levada*<sup>1</sup>

<sup>1</sup>Research & Education Center “Smart Materials & Biomedical Applications”, Immanuel Kant Baltic Federal University, Kaliningrad, Russia

<sup>2</sup>Center for Immunology and Cellular Biotechnology, Immanuel Kant Baltic Federal University, Kaliningrad, Russia

<sup>3</sup>Department of Physics, Vinča Institute of Nuclear Sciences – National Institute of the Republic of Serbia, University of Belgrade, Belgrade, Serbia

<sup>4</sup>Advanced Materials Department, Jožef Stefan Institute, Ljubljana, Slovenia

<sup>5</sup>National University of Science and Technology “MISIS”, Moscow, Russia

\*E-mail: [SPshnikov@gmail.com](mailto:SPshnikov@gmail.com)

Nanocomposites are multiphase materials, which can combine a wide range of physical and structural characteristics. Each constituent affects physical properties and potential applicability of a nanocomposite. The combination of different characteristics makes it possible to engineer multi-functional materials for solving specific biomedical problems.

In current research we propose nanocomposites with gold nanoparticles surrounded by gallium-doped Co-ferrite (CFO\_Ga) nanoparticles and covered with arginine (Au(arg):CFO\_Ga(DHCA), Fig. 1) as an innovative structure for using in biomedical applications. Gold nanoparticles were used as biocompatible component with potential applicability in MRI and photothermal therapy. Due to CFO\_Ga nanoparticles, the composite possesses magnetic properties, which are helpful for combined treatments. Nanocomposite was covered with arginine to decrease cytotoxicity. Structural characterization of the composite showed that the average size was 13.9±3.8 nm and 5.2±1.1 nm of gold and CFO\_Ga nanoparticles, respectively.

Biocompatibility of the Au(arg):CFO\_Ga(DHCA) composite was analyzed using WST-1 assay. The experiments were performed on peripheral blood mononuclear cells (PBMC), T-lymphoblastic leukemia cell line (Jurkat) and hepatoma cell line (Huh7). Cells were incubated in standard conditions (at 37 °C in humidified 5% CO<sub>2</sub> atmosphere) according to common established protocols. The cells were incubated in nutrient medium (RPMI-1640 or DMEM (Sigma, USA)) with three different concentrations (10, 50, 100 µg/ml) of the composite nanoparticles. After 24h treatment, the cells were stained using WST-1 (Roche Diagnostics GmbH, Germany) and the absorbance of cell suspensions was measured using a microplate reader Bio-Rad 680 (“Bio-Rad”, USA). In the

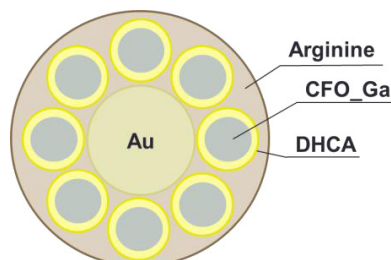


Figure 1. Structure of the Au(arg):CFO\_Ga(DHCA) composite.

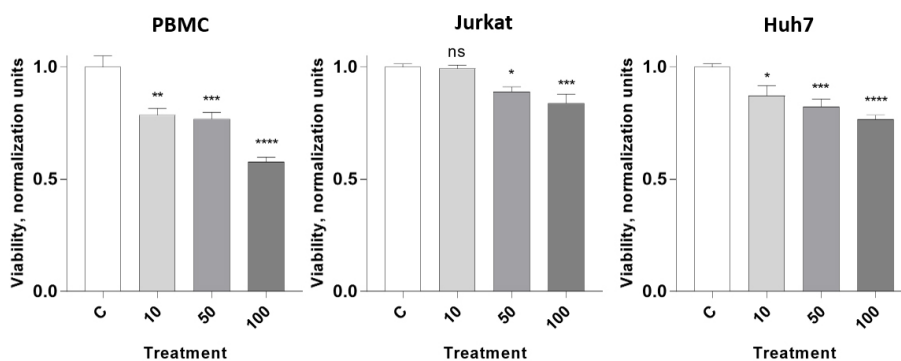


Figure 2. PBMC, Jurkat and Huh7 cells viability was inhibited after 24 h treatment with Au(arg):CFO\_Ga(DHCA) composite. The cells were treated at three concentrations: 10  $\mu\text{g/ml}$  (10), 50  $\mu\text{g/ml}$  (50), 100  $\mu\text{g/ml}$  (100). Data normalized to control cells viability and shown as mean  $\pm$ SE. Data values were analyzed using a one-way analysis of variance (one-way ANOVA) followed by Newman-Keuls test with Bonferroni correction. Statistical analysis was performed using GraphPad Prism 7.04 software (Graph Pad Software Inc., San Diego, CA, USA). All series of experiments were repeated three times.

next step, the effect of the composite on cell morphology was analyzed using confocal microscopy system (LSM 780, Zeiss, Germany). After 24 h treatment, Huh7 cells were stained using Calcein-AM (Sigma, USA) and Hoechst 33342 (Sigma, USA).

According to the results obtained with the cytotoxicity analysis, Au(arg):CFO\_Ga(DHCA) composite induced dose-dependent cytotoxic effect on three human cell lines (Fig. 2). The composite reduced the viability of PBMC and Huh7 at all three concentrations. At the same time, the viability of Jurkat cells was not suppressed by 10  $\mu\text{g/ml}$  treatment. Microscopy visualization showed that Huh7 morphology did not change after 24h treatment with 100  $\mu\text{g/ml}$  (Fig. 3).

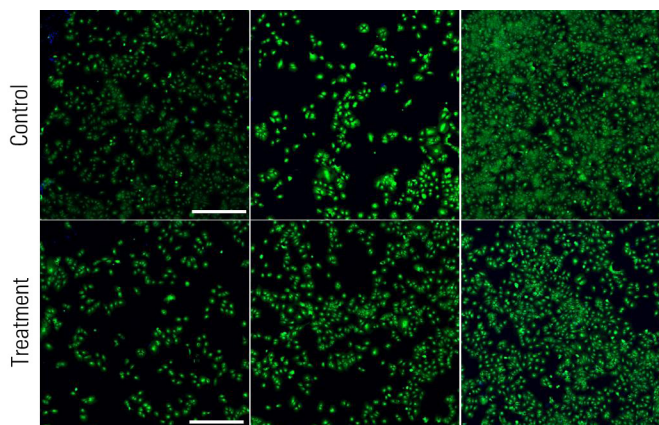


Figure 3. Huh7 cells after 24 h cultivation with 100  $\mu\text{g/ml}$  Au(arg):CFO\_Ga(DHCA). Cells were stained using Hoechst 33342 (nucleus, blue) and Calcein-AM (cytoplasm, green). Calcein positive stain indicates viable cells. Calcein negative and Hoechst positive stain indicate dead cells. Scale bar – 500  $\mu\text{m}$ .

Microscopy visualization showed that Huh7 morphology did not change after 24 h treatment with 100  $\mu\text{g/ml}$  (Fig. 3). The confluency of cell population did not change and only a few dead (Calcein negative and Hoechst positive stained) cells were found. The next stage of ongoing research is to determine the cytotoxic mechanisms in order to compare the toxic effect of the composite with structural characteristics.

*The reported study was funded by RSF grant number 21-72-20158. Authors are grateful to PhD N. Gazatova (Center for Immunology and Cellular Biotechnology, IKBFU) for helping in the realization of the experimental part of the project.*

## SYNTHESIS, OPTICAL AND MAGNETIC PROPERTIES OF Au-Fe<sub>3</sub>O<sub>4</sub> NANOHYBRIDS

*N.V. Volkov<sup>3</sup>, T.E. Smoliarova<sup>1,2\*</sup>*

<sup>1</sup>Siberian Federal University, Krasnoyarsk, Russia

<sup>2</sup>Laboratory for Controlled Digital Drugs and Theranostics, Federal Research Center

“Krasnoyarsk Science Center” SB RAS, Krasnoyarsk, Russia

<sup>3</sup>Kirensky Institute of Physics KSC SB RAS, Krasnoyarsk, Russia

\*E-mail: [smol.nano@yandex.ru](mailto:smol.nano@yandex.ru)

Over the years, magnetic nanoparticles have raised significant interest in many fields such as biological separation and protein purification [1–2], target delivery [3, 4], therapy [5, 6], biosensors [7, 8], and catalysis [9, 10]. Gold-magnetite nanohybrids composed of Fe<sub>3</sub>O<sub>4</sub> and Au nanoparticles (NPs) have attracted large attention due to the evident advantages of Au nanoparticles such as unique biocompatibility [11], facile surface modification [12], and high catalytic properties [13]. Herein, we report on the facile room-temperature synthesis approach for Au-Fe<sub>3</sub>O<sub>4</sub> nanohybrids preparation and their optical and magnetic properties investigation.

Au-Fe<sub>3</sub>O<sub>4</sub> nanohybrids were synthesized by chemical precipitation with a chemisorption process of Au nanoparticles (NPs) to the Fe<sub>3</sub>O<sub>4</sub> surface using polyvinylpyrrolidone (PVP) coverage. Octahedral Fe<sub>3</sub>O<sub>4</sub> NPs were prepared by mixing water solution of NaNO<sub>3</sub> and NaOH with 150 ml of 1:1 DI water and ethanol solution. Then, the water solution of Fe<sub>3</sub>SO<sub>4</sub>·7H<sub>2</sub>O was mixed with 0.01 M H<sub>2</sub>SO<sub>4</sub> solution and the resulting mixture was added to the total solution. The resulting solution

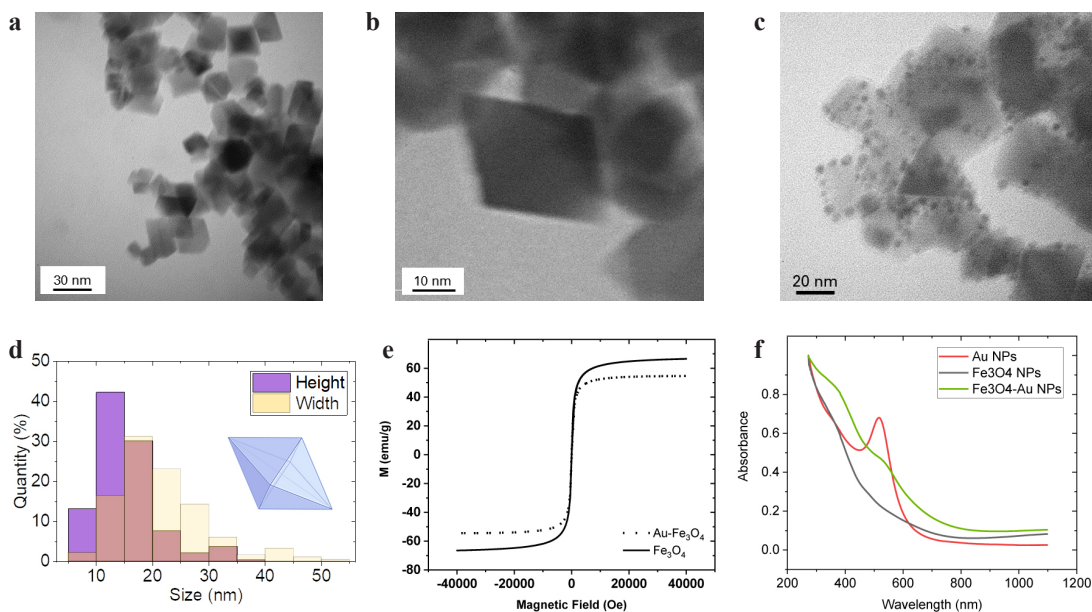


Figure 1. TEM results of synthesized **a, b** Fe<sub>3</sub>O<sub>4</sub> NPs and **c** Au-Fe<sub>3</sub>O<sub>4</sub> nanohybrids, **d** size distribution of Fe<sub>3</sub>O<sub>4</sub> NPs, **e** hysteresis loops of Fe<sub>3</sub>O<sub>4</sub> and Au-Fe<sub>3</sub>O<sub>4</sub> NPs, **f** absorbance spectra of the synthesized NPs.

was left for 2 h at  $T = 90\text{--}95\text{ }^{\circ}\text{C}$ . Then the solution was cooled to room temperature, the resulting NPs were separated from the solution by magnetic decantation and washed by centrifugation for 5 min (3000 rpm). Au NPs were prepared according to the procedure described in [14] and finally were attached to the PVP-covered  $\text{Fe}_3\text{O}_4$  surface. The results of transmission electron microscopy (TEM) and size distribution analysis are presented in Fig. 1a–d.

Magnetization loops of  $\text{Fe}_3\text{O}_4$  and Au- $\text{Fe}_3\text{O}_4$  NPs are shown in Fig. 1e. No coercivity or remanence existing at room temperature indicated the superparamagnetic behaviors of both samples. The saturation magnetization values of  $\text{Fe}_3\text{O}_4$  and Au- $\text{Fe}_3\text{O}_4$  NPs are 66.5 and 54.5 emu/g, respectively. This showed a significant decrease for Au- $\text{Fe}_3\text{O}_4$  NPs, which may be caused by the diamagnetic contribution of the Au nanoparticles in the hybrid NPs.

Absorbance spectra of Au,  $\text{Fe}_3\text{O}_4$ , and Au- $\text{Fe}_3\text{O}_4$  NPs are shown in Fig. 1f. Au NPs (red line) have the typical behavior with the plasmon peak at 520 nm. In comparison with the absorbance spectrum of  $\text{Fe}_3\text{O}_4$  NPs (black line), the spectrum for Au- $\text{Fe}_3\text{O}_4$  NPs (green line) demonstrates the presence of the light plasmon peak at 520 nm, which is an impact of attached Au NPs.

The obtained results seem to be the promising step for the core-shell Au- $\text{Fe}_3\text{O}_4$  NPs preparation, in the case of Au NPs will be considered as the seeds for the complete Au shell growth.

This research, especially synthesis procedure development, was funded by the Ministry of Science and Higher Education of the Russian Federation; project FWES-2022-0005. The study of magnetic and optical properties of the synthesized nanoparticles was funded by RFBR, project number 20-32-90134.

1. J. Bao et al., Bifunctional Au- $\text{Fe}_3\text{O}_4$  nanoparticles for protein separation, *ACS nano*, **1**, no. 4, 293–298 (2007).
2. S.V. Salihov et al., Recent advances in the synthesis of  $\text{Fe}_3\text{O}_4$ @Au core/shell nanoparticles, *Journal of magnetism and magnetic materials*, **394**, 173–178 (2015).
3. C. Xu, B. Wang, S. Sun, Dumbbell-like Au- $\text{Fe}_3\text{O}_4$  nanoparticles for target-specific platinum delivery, *Journal of the American Chemical Society*, **131**, no. 12, 4216–4217 (2009).
4. D.Z. Tulebayeva et al., Modification of  $\text{Fe}_3\text{O}_4$  nanoparticles with carboranes, *Materials Research Express*, **5**, no. 10, 105011 (2018).
5. C. Li et al., Gold-coated  $\text{Fe}_3\text{O}_4$  nanoroses with five unique functions for cancer cell targeting, imaging, and therapy, *Advanced functional materials*, **24**, no. 12, 1772–1780 (2014).
6. S. Rajkumar, M. Prabakaran. Multi-functional core-shell  $\text{Fe}_3\text{O}_4$ @Au nanoparticles for cancer diagnosis and therapy, *Colloids and Surfaces B: Biointerfaces*, **174**, 252–259 (2019).
7. W. Zhang et al., Multifunctional glucose biosensors from  $\text{Fe}_3\text{O}_4$  nanoparticles modified chitosan/graphene nanocomposites, *Scientific reports*, **5**, no. 1, 1–9 (2015).
8. L. Yu et al., Magnetic  $\text{Fe}_3\text{O}_4$ -reduced graphene oxide nanocomposites-based electrochemical biosensing, *Nano-Micro Letters*, **6**, no. 3, 258–267 (2014).
9. X. Cui et al., Synergistic catalysis by  $\text{Fe}_3\text{O}_4$ -biochar/peroxymonosulfate system for the removal of bisphenol, *Separation and Purification Technology*, **276**, 119351 (2021).
10. L. Tian et al., An ultrasensitive electrochemical cytosensor based on the magnetic field assisted binanozymes synergistic catalysis of  $\text{Fe}_3\text{O}_4$  nanozyme and reduced graphene oxide/molybdenum disulfide nanozyme, *Sensors and Actuators B: Chemical*, **260**, 676–684 (2018).
11. M. Ovais et al., Multifunctional theranostic applications of biocompatible green-synthesized colloidal nanoparticles, *Applied microbiology and biotechnology*, **102**, no. 10, 4393–4408 (2018).
12. Y. Chen, Y. Xianyu, X. Jiang Surface modification of gold nanoparticles with small molecules for biochemical analysis, *Accounts of chemical research*, **50**, no. 2, 310–319 (2017).
13. Y. Lee et al., Synthetic tuning of the catalytic properties of Au- $\text{Fe}_3\text{O}_4$  nanoparticles, *Angewandte Chemie International Edition*, **49**, no. 7, 1271–1274 (2010).
14. K.R. Brown, D.G. Walter, M.J. Natan, Seeding of colloidal Au nanoparticle solutions. 2. Improved control of particle size and shape, *Chemistry of Materials*, **12**, no. 2, 306–313 (2000).



## AMINATED MAGNETIC NANOPARTICLES FUNCTIONALIZED WITH ANTIBODIES FOR CELL SEPARATION

*A.V. Tyumentseva*<sup>1\*</sup>, *R.N. Yaroslavtsev*<sup>1,2</sup>, *S.V. Stolyar*<sup>1,2</sup>, *S.V. Komogortsev*<sup>2</sup>, *D.A. Velikanov*<sup>2</sup>,  
*Yu.V. Gerasimova*<sup>2</sup>, *Yu.V. Knyazev*<sup>2</sup>

<sup>1</sup>Krasnoyarsk Scientific Center, Federal Research Center KSC SB RAS, Krasnoyarsk, Russia

<sup>2</sup>Kirensky Institute of Physics, Federal Research Center KSC SB RAS, Krasnoyarsk, Russia

\*E-mail: [komivlann@yandex.ru](mailto:komivlann@yandex.ru)

The development of magnetic nanoparticles (MNPs) for cancer cell separation is a promising area. Conjugation with antibodies allows nanoparticles to bind highly specifically to cells and harvest them even when the concentration of the cells is low [1]. It may be very important for accurate diagnostics of tumor cells subpopulations studies (such as malignant lymphocytes in blood) or for detection small amounts of cells in a biological sample (such as bladder cancer cells in urine). The aim of the study was to develop magnetic nanoparticles conjugated with antibodies for cell separation.

Magnetic nanoparticles were synthesized by co-precipitation method using  $\text{FeCl}_3$  и  $\text{FeCl}_2 \cdot 4\text{H}_2\text{O}$  at the molar ratio 2:1 dissolved in 100 mL distilled water.  $\text{NH}_4\text{OH}$  (25%) solution was injected to reach pH 10–11. The solid  $\text{Fe}_3\text{O}_4$  was collected with magnet and washed several times with distilled water until pH became neutral. The MNPs were successively coated with tetraethyl orthosilicate (TEOS) and 3-aminopropyl triethoxy silane (APTES) to obtain a magnetic core shell of sufficient thickness and containing amino groups on the surface.

MNPs synthesized were visualized using light microscopy and high-resolution transmission electron microscopy (TEM). The structure of the MNPs was investigated by Mössbauer spectroscopy and Fourier transform infrared spectroscopy (FTIR). It was observed that the nanoparticles presented as magnetic cores with average size of 9.5 nm collected in aggregates and covered with  $\text{SiO}_2$  shell (Fig. 1a). The analysis of the IR spectrum showed the presence of the Fe–O ( $587\text{ cm}^{-1}$ ) and Si–O ( $1037\text{ cm}^{-1}$ ) bonds. A band at  $1568\text{ cm}^{-1}$  appears in the spectrum, corresponding to the N–H bond in primary amines. The absorption peak at  $2930\text{ cm}^{-1}$  refers to  $\nu_{\text{as}}$  vibrations of  $\text{CH}_2$ . The formation of the  $-\text{C}-\text{NH}_2$  bond (aliphatic primary amine) corresponds to an intense peak at  $3400\text{ cm}^{-1}$ .

$\text{NH}_2$ -groups density was studied by titration method [2] and estimated as  $9.4 \cdot 10^{17}$   $\text{NH}_2$ -groups per 1 mg of the nanoparticles.

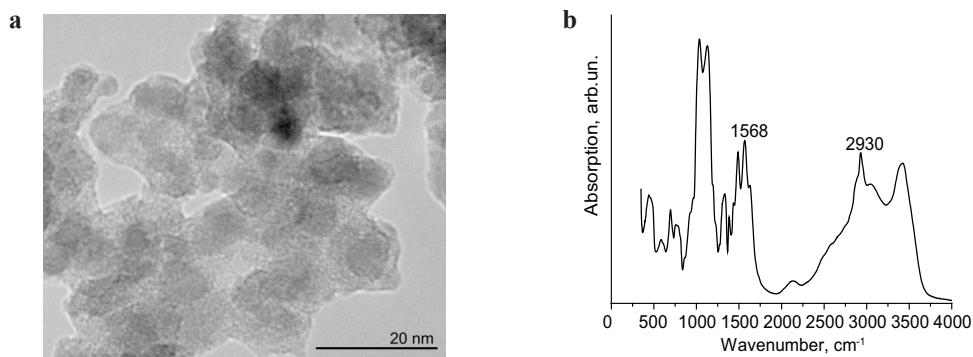


Figure 1. TEM-image (a) and FTIR-spectrum (b) of the nanoparticles.

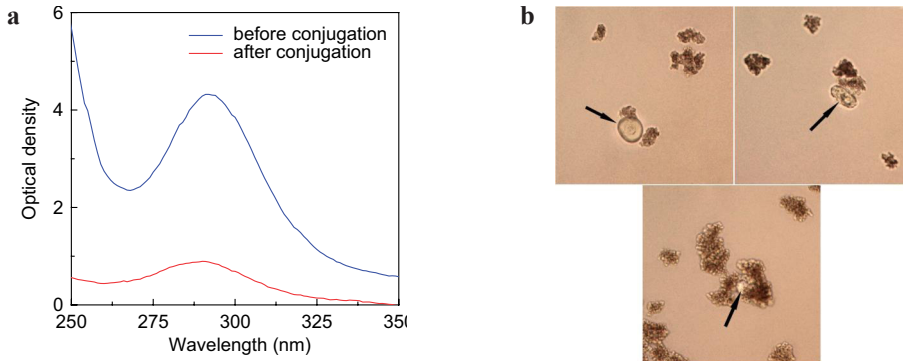


Figure 2. **a** Optical density of the IgG solution before and after conjugation with MNPs  $\text{Fe}_3\text{O}_4@\text{SiO}_2\text{-NH}_2$ ; **b** B-cells captured with anti-CD19-conjugated MNPs (200X magnification).

Two types of antibodies were tried to be immobilized on the MNPs' surfaces: anti-CD-19 (for B-lymphocytes separation) and anti-CD-326 (for epithelium cells isolation). Measurement of the optical density of the IgG solution at 280 nm (Fig. 2a) made it possible to estimate the protein concentration as 44  $\mu\text{g}$  before incubation, and 7.73  $\mu\text{g}$  after incubation with the aminated nanoparticles. This allows us to conclude the successful attachment of the protein to the nanoparticles.

The nanoparticles functionalized with anti-CD-19 were tested as sorbents for CD19+ cells in blood samples. Cells capture by the developed nanoparticles was visualized by light microscopy (Fig. 2b).

*The study was supported by the Russian Science Foundation and the Krasnoyarsk Region Science and Technology Support Fund, grant No. 22-14-20020.*

1. A. Saei, S. Asfia, H. Kouchakzadeh, and M. Rahmandoust, J. Biomed. Mater. Res. Part B Appl. Biomater., **108**, 2633 (2020).
2. O.I. Voroshilova, A.V. Kiselyov and Y.S. Nikitin, (in Russian), Colloid J., **2**, 223–229 (1980).

## A STUDY OF THE ANTI-TUMOUR ACTIVITY OF MAGNETIC HYPERTHERMIA USING BIOCOMPATIBLE IRON OXIDE NANOPARTICLES IN VIVO

*D.E. Yakobson*<sup>1\*</sup>, *M.N. Zharkov*<sup>1</sup>, *V.P. Ageev*<sup>1</sup>, *V.I. Shlyapkina*<sup>1</sup>, *O.A. Kulikov*<sup>1</sup>,  
*G.B. Sukhorukov*<sup>2</sup>, *N.A. Pyataev*<sup>1</sup>

<sup>1</sup>National Research Ogarev Mordovia State University, Saransk, Russia

<sup>2</sup>Queen Mary University of London, London, UK

\*E-mail: [ykbsn@mail.ru](mailto:ykbsn@mail.ru)

Regional magnetic hyperthermia (MHT) is a promising method in the treatment of tumours. MHT is based on introducing magnetically sensitive particles into tumour tissue and then exposing it to a high-frequency magnetic field [1]. However, currently there are few magnetic substances suitable for clinical applications. One of such substance is a “MagForce AG” composition based on iron oxide nanoparticles coated with aminosilane [2]. However, these particles have a low biodegradation rate, which is a major disadvantage.

In this work, we have obtained biocompatible magnetic iron oxide nanoparticles (MNPs Fe<sub>3</sub>O<sub>4</sub>@OA) which are stabilised with oleic acid and sodium oleate, which could be a successful therapeutic agent for regional hyperthermia. We present the result of a study of the anti-tumour activity of magnetic hyperthermia using a magnetic suspension of iron oxide nanoparticles (MNPs Fe<sub>3</sub>O<sub>4</sub>@OA).

Iron oxide nanoparticles were prepared by a modified method of co-precipitation of chlorides (Fe<sup>2+</sup>, Fe<sup>3+</sup>) (in a molar ratio of 1:2) in an alkaline ammonia medium. Oleic acid and sodium oleate were used as a particle stabiliser. For the production of nanoparticles, the sizes are determined, ζ-potential, iron concentration in suspension, magnetisation and specific absorption rate (SAR). The average size of the MNPs Fe<sub>3</sub>O<sub>4</sub>@OA nanoparticles according to transmission electron microscopy (TEM) is 8.7 ± 3.1 nm, from dynamic light scattering (DLS) data 25 ± 8 nm, ζ-potential –65 ± 3 mV at pH = 7.7, mass concentration of iron in suspension 112 mg/ml, magnetisation 79.5 emu/g, SAR 12 W/g Fe [3].

The toxicity of the MNPs Fe<sub>3</sub>O<sub>4</sub>@OA magnetic suspension was assessed for intramuscular and intraperitoneal administration prior to the anti-tumour activity study. Research of antitumour activity was carried out on Wistar rats. The carcinosarcoma strain Walker 256 was used as a transplanted tumour. The tumour cell suspension was implanted subcutaneously into the right thigh area. On the fourth day after tumour cell implantation, animals were randomly allocated into four groups (7 animals in each group). The first group of animals received no treatment (control group). The second group (starting on the fourth day of the experiment) was exposed to a magnetic field twice for 30 minutes at 24 h intervals (magnetic field group). In the third group, 0.5 ml of MNPs Fe<sub>3</sub>O<sub>4</sub>@OA was injected once into the tumour (control group with suspension). The fourth group, after injecting 0.5 ml of MNPs Fe<sub>3</sub>O<sub>4</sub>@OA into the tumour, was exposed to magnetic fields twice for 30 min at 24 h intervals (MHT group). An installation generating an alternating magnetic field with a frequency of 100 kHz and a maximum amplitude of 8 kA/m was used to irradiate the animals. The surface heating of the tumour tissue was monitored using a thermal imaging camera. The temperature inside of tumour was measured with a diamagnetic thermocouple sensor. The temperature of the tumour node was kept constant at 44–46 °C for the whole irradiation time by varying the field amplitude in the range of 5–8 kA/m. Tumour node volume was measured on the first day of treatment and then every two days thereafter. The presence of organ metastases was also detected. Histological examination of the tissues after therapy and biochemical blood tests were carried out.

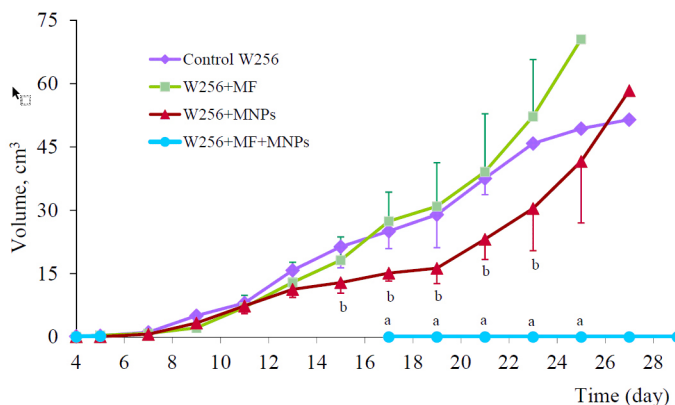


Figure 1. Tumour growth pattern of Walker carcinoma 256 in different experimental groups.

The results of a toxicity study of the nanoparticle suspension obtained allow them to be classified as low-toxic compounds when administered intraperitoneally and as virtually nontoxic or relatively harmless when administered intramuscularly [3]. Tumour growth curves are shown in Fig. 1.

Particular attention is drawn to the dynamics of tumour growth in the MHT group. In this group, severe swelling developed at the injection site, making it impossible to measure the tumour nodule until day 15 of the experiment. Healing of the ulcers in the MHT group took place within 30 days. A dense connective tissue scar remained at the healing site. In the other groups, growth of the tumour node was observed throughout the experiment. The tumour volume in the groups that did not undergo MHT for the first 7 days increased by a factor of 3–4 every 2 days. From day 11 onwards, there was a slowdown in growth, but it continued until the animals died.

The effectiveness of MHT assessed by the survival rate of animals with tumours in this experiment was 85%. If so, then the liquid does not require operations to remove nanoparticles after HT for a hard to-reach localisation, which is essential for brain tissue after treatments for glioblastoma. Therefore, the proposed fluid is a potential therapeutic agent for tumour HT.

*The work is supported by the Russian Foundation for Basic Research (grant 19-29-10013).*

1. Kheireddine El-Boubbou, Nanomedicine. Rev., **223** (2018).
2. N. Waldoefner, A. Jordan. Agglomerating Magnetic Alkoxysilane-Coated Nanoparticles. T.N.C. Magforce ag, the Nanotherm, Therapy. U.S. Patent 9,962,442 B2, (2018).
3. O.A. Kulikov, M.N. Zharkov et al. Magnetic Hyperthermia Nanoarchitectonics via Iron Oxide Nanoparticles Stabilised by Oleic Acid: Anti-Tumour Efficiency and Safety Evaluation in Animals with Transplanted Carcinoma. Int. J. Mol. Sci., **23**, 4234 (2022).

MAGNETIC PROPERTIES OF Fe<sub>3</sub>O<sub>4</sub>-Au NANOCOMPOSITES

*R.N. Yaroslavtsev<sup>1,2\*</sup>, S.V. Stolyar<sup>1,2</sup>, D.A. Velikanov<sup>2</sup>, M.N. Volochaev<sup>2</sup>*

<sup>1</sup>Krasnoyarsk Scientific Center, Federal Research Center KSC SB RAS, Krasnoyarsk, Russia

<sup>2</sup>Kirensky Institute of Physics, Federal Research Center KSC SB RAS, Krasnoyarsk, Russia

\*E-mail: [yar-man@bk.ru](mailto:yar-man@bk.ru)

Hybrid systems based on magnetite and gold nanoparticles are widely used as bifunctional materials for bio- and nanotechnologies. Due to the biocompatibility of Fe<sub>3</sub>O<sub>4</sub> and Au, they are materials of dual use (therapeutic and diagnostic). In recent years, a huge number of fluorescent markers, vector molecules, and drugs have been developed for the functionalization of Fe<sub>3</sub>O<sub>4</sub>@-Au [1, 2].

Magnetic particles were obtained via coprecipitation from solutions of FeCl<sub>3</sub> and FeCl<sub>2</sub> salts in 2:1 molar ratios at room temperature. Weighed portions of the chemicals were dissolved in distilled water and added to an NH<sub>4</sub>OH solution (25%) with stirring until the pH reached 10. Stirring continued for 30 min. Once the reaction was complete, the magnetic nanoparticles were collected using a magnet and washed several times in distilled water until the pH reached 7.0.

Fe<sub>3</sub>O<sub>4</sub>-Au composites were prepared as follows. 0.5 ml of a Fe<sub>3</sub>O<sub>4</sub> nanoparticles suspension with a concentration of 20 mg/ml was added to a 1 M sodium citrate solution with a volume of 100 ml. The solution was brought to a boil. Then 0.25 ml of 0.2 M HAuCl<sub>4</sub> solution was added. Boiling was continued for 15 min.

The nanoparticle samples were examined with a Hitachi HT7700 transmission electron microscope (accelerating voltage 100 kV) of the Center for Collective Use, Krasnoyarsk Scientific Center, Krasnoyarsk, Russia. Mössbauer spectra were measured on an MC-1104E5m spectrometer with the <sup>57</sup>Co(Cr) source at room temperature. Static magnetic measurements were carried out on a vibrating magnetometer in the field range up to 15 kOe and temperatures from 80 to 300 K.

Figure 1 shows an TEM-image of Fe<sub>3</sub>O<sub>4</sub>-Au nanocomposites. The average size of the magnetite core is ~10 nm.

The data of magnetic measurements (Fig. 2) provide information on the magnetic response of the particles, which is necessary for the analysis of the magnetic and magneto-mechanical response of the prepared composite particles.

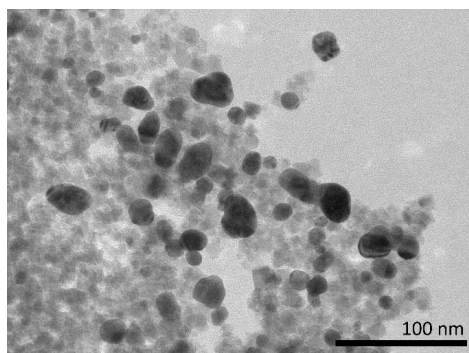


Figure 1. TEM-image of Fe<sub>3</sub>O<sub>4</sub>-Au nanoparticles.

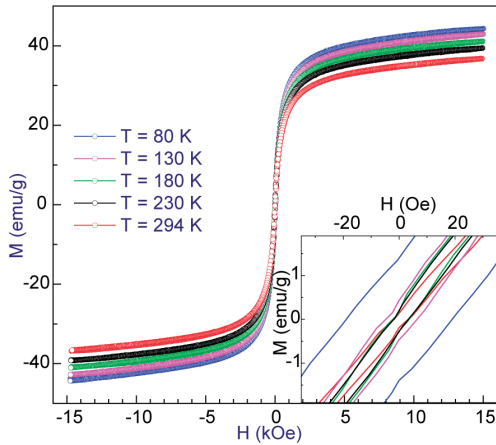


Figure 2. Hysteresis loops of  $\text{Fe}_3\text{O}_4@Au$  nanocomposites.

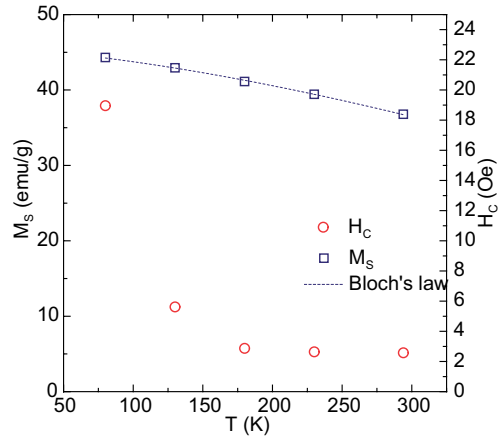


Figure 3. Temperature dependences of saturation magnetization and coercive force.

The magnetization curves measured in the range from  $-15$  to  $15$  kOe are symmetric relative to the origin of coordinates and contain a reversible part and an irreversible part, i.e., the hysteresis loop (Fig. 2). The coercive force, remanent magnetization, and magnetization in a field of  $15$  kOe decrease with increasing temperature. The low values of the coercive field indicate that particles of this size are close to the transition to the superparamagnetic state. Relatively low values of saturation magnetization of nanoparticles are due to inclusions of gold.

The change in the value of  $M_s$  with temperature is described by the Bloch law  $T^{3/2}$ :

$$M_s(T) = M_{s0}(1 - B \cdot T^{3/2}). \quad (1)$$

The best fit of experimental data by formula (1) corresponds to the following parameter values:  $M_{s0} = 45.48$  emu/g;  $B = 3.82 \cdot 10^{-5} \text{ K}^{-3/2}$

The study was supported by the Russian Science Foundation and the Krasnoyarsk Region Science and Technology Support Fund, grant No. 22-14-20020.

1. F. Yan and R. Sun, Mater. Res. Bull., **57**, 293 (2014).
2. T. Tarhan, A. Ulu, M. Sariçam, M. Çulha, and B. Ates, Int. J. Biol. Macromol., **142**, 443 (2020).

## AMOUNT OF MAGNETIC MATERIAL AND SIZE AS MAIN PARAMETERS OF DRUG CARRIERS FOR EFFECTIVE MAGNETIC TARGETING IN BLOOD MICROCIRCULATORY SYSTEM: THEORY AND EXPERIMENT IN VITRO/IN VIVO

M.A. Pyataev<sup>1</sup>, N.A. Pyataev<sup>1</sup>, D.E. Yakobson<sup>1</sup>, V.P. Ageev<sup>1</sup>, O.A. Kulikov<sup>1</sup>, G.B. Sukhorukov<sup>2</sup>,  
M.N. Zharkov<sup>1\*</sup>

<sup>1</sup>National Research Ogarev Mordovia State University, Saransk, Russia

<sup>2</sup>School of Engineering and Materials Science, Queen Mary University of London, London, UK

\*E-mail: [mikhail.zharkov.92@mail.ru](mailto:mikhail.zharkov.92@mail.ru)

The magnetically driven polyelectrolyte capsules are considered as a promising tool for targeted drug delivery. Investigation of the precipitation mechanism is necessary for correct choice of carrier parameters such as size, content of magnetic substance, magnetic field gradient and so on. At least roughly estimation of these parameters must be done to evaluate the ability of magnetic targeting.

In the present paper, we generalize this approach taking the diffusion process into account and obtain the partial differential equation for the concentration of capsules in the capillary. Based on our theory we have determined the parameters of carriers necessary for their precipitation. The results of calculation is compared to the *in vitro* experiment performed on a model of a blood vessel. The distribution of capsules in the lungs (*in vivo* experiment) in a magnetic field gradient was also studied.

The theoretical model is based on the analysis of particle motion in a liquid taking the diffusion into account. The equation of continuity in stationary mode is the basic equation in theoretical model. To find the velocity, we considered Newton's law of motion for a particle, taking into account the Stokes drag force and the magnetic force. Due to the very small particle size, the force of gravity and the Archimedes buoyant force can be neglected. We have obtained the final differential Eq. (1), solved it numerically and found the stationary distribution of particles.

$$\nabla c \cdot \left( \mathbf{v}_i + \frac{1}{6\pi r \eta} \mathbf{F}_m \right) + \frac{c}{6\pi r \eta} \nabla \mathbf{F}_m - D \nabla^2 c = 0 \quad (1)$$

Polymeric capsules were prepared by the “Layer by layer” method by alternately adsorption of oppositely charged polyelectrolytes and Fe<sub>3</sub>O<sub>4</sub> nanoparticles on spherical cores of CaCO<sub>3</sub>. Two types of capsules with different sizes and contents of magnetic nanoparticles were used in the experiment: 1)  $d \approx 0.7 \mu\text{m}$  and 0.65 pg Fe per capsules, 2)  $d \approx 2.3 \mu\text{m}$  and 3.2 pg Fe per capsules.

The experimental model of a blood capillary is made of a polyethylene tube with inner diameter of 1.4 mm. The capillary was located at a distance  $Z$  from the surface of a cylindrical permanent NdFeB-magnet with a maximum induction of 0.47 T at its base. The suspension of capsules was pumped through the capillary by the syringe infuser allowing precise control of the flow rate. After that the flow was stopped, the tube was frozen and then cut in pieces of 5 mm length. The content of capsules in each piece was determined by the amount of doxorubicin, which was measured by fluorimetry. The introduction of doxorubicin into capsules made it possible to increase the sensitivity of the method and to analyze biological media and tissues in comparison with the determination of iron concentration. In addition to quantitative analysis of the microcapsule concentration, the deposition process was visually observed in real time using an optical microscope.

The results of calculations and experimental measurements of concentration of capsules in different parts of the capillary are shown in Fig. 1.

The values are normalized so that the area under curve defines the total percentage of precipitated capsules. One can see that experimentally measured concentrations are smaller than theoretically

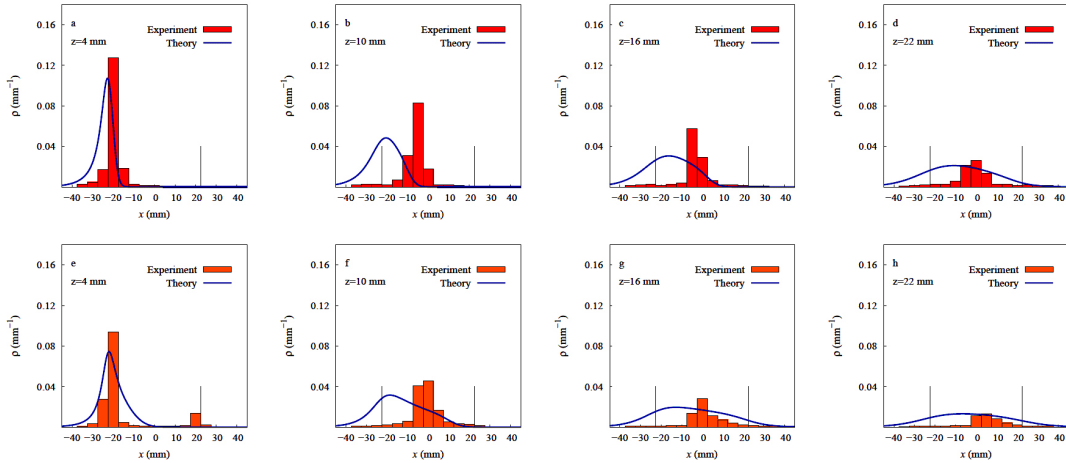


Figure 1. Distribution of precipitated capsules (red columns for 0.7  $\mu\text{m}$ , yellow for 2.3  $\mu\text{m}$ ) for different distances  $z$  from the magnet. Dashed lines show the  $x$ -position of the magnet edges.

calculated and shifted towards the direction of flow. The difference between the theory and experiment is most pronounced in the area of high capsules concentration. With the increase in distance, the capsules precipitate only partially, a significant part of them is carried out by the fluid flow from the area of the magnetic field.

For detailed investigation of the difference we have performed a real-time microscopic observation of the precipitation process. We have found that the precipitated capsules are forming the grass-like pillar structures. The formation of such structures can be explained by concentration of magnetic field inside ferromagnetic column that leads to appearance of high magnetic field gradient near the apex of the pillar and consequently strong attractive force driving the particle to the apex. We have seen with the microscope that some highest pillars are broken by the liquid flow and debris are carried away. As a result, the apex of the pillar from capsules are located in the flow region with a sufficiently high velocity and experience noticeable pressure of the flowing liquid. This pressure can make some of agglomerates to move in the direction of flow and precipitate at farther sites of the capillary. The quantitative description of this phenomenon requires information on the interaction of capsules with each other in a magnetic field and on their interaction with the capillary wall.

The basic rough estimation that can be made based on the theory is that the most of capsules will not precipitate in the magnetic field if they have not enough time to reach the wall of the capillary starting its motion in the axes of the capillary. In the framework of our model, the relative part of particles accumulated in the area of magnetic field depends on two dimensionless parameters  $g\tau/v_0$  and  $l/R$ , where  $R$  is the capillary radius,  $l$  is the typical length passed by the particle under the action of the field,  $\tau = m_0/(6\pi r\eta)$  is the relaxation time and  $g = F_m/m_0$  is the effective “magnetic gravity” i.e. the magnetic force per unit of magnetite mass  $m_0$ . In our experiment,  $l$  was determined by the diameter of magnet (45 mm), but in a living body, it is restricted by the geometry of capillary and the ratio  $l/R$  is of the order of 200. It is clear that the effective gravity  $g$  has to be at least an order of magnitude larger than the standard gravity. It leads to the following estimation for parameters of microcapsules: if the ratio  $m_0/r$  exceeds the value of 1  $\text{pg}/\mu\text{m}$  then the most of microcapsules will be precipitated in a magnetic field with  $g = 10^2 \text{m/s}^2$ .

*The work is supported by the Russian Foundation for Basic Research (grant № 19-29-10013).*



## DIAGNOSTIC TECHNIQUE FOR THE CROHN'S DISEASE USING FERROMAGNETIC $\text{Fe}_3\text{O}_4$ -Au NANOPARTICLES

Z.A. Grigoreva<sup>1</sup>, Ch.A. Gritsenko<sup>1</sup>, E.V. Levada<sup>1</sup>, V.V. Rodionova<sup>1</sup>, M.V. Efremova<sup>2</sup>

<sup>1</sup>Immanuel Kant Baltic Federal University, Kaliningrad, Russia

<sup>2</sup>Department of Chemistry, Lomonosov Moscow State University, Moscow, Russian Federation

\*E-mail: [grigoreva-zoja@rambler.ru](mailto:grigoreva-zoja@rambler.ru)

Crohn's disease is a chronic inflammatory disease in which the intercellular distance in the epithelial layer of the terminal fragment of the small and large intestine increases [1]. There are many methods available to diagnose Crohn's disease, for example, magnetic resonance imaging, computed tomography, confocal endoscopy, ultrasound, positron emission tomography, and biomarkers. [2]. Here we propose the method for diagnosing Crohn's disease based on using ferromagnetic  $\text{Fe}_3\text{O}_4$ -Au nanoparticles.

Wild-type mice were used in the experiment. There was a group of laboratory animals divided into: the group of control mice and the group of mice with intestinal infections simulating the symptoms of the Crohn's disease. The symptoms were induced by the use of the Dextran Sodium Sulfat Sigma Aldrich oral solution. Mice were separated into subgroups depending on a diameter of  $\text{Fe}_3\text{O}_4$  nanoparticles, which were used to estimate a possible penetration of nanoparticles into the intercellular distance in the intestinal wall. The aim of this work was to establish the metabolic excretion time of  $\text{Fe}_3\text{O}_4$ -Au hybrid nanoparticles into the feces, blood, and liver samples. Mice of both species received a solution of  $\text{Fe}_3\text{O}_4$ -Au nanoparticles at the concentration of 200  $\mu\text{g}/\text{ml}$  via gavage. Three types of nanoparticles depending on the diameter of  $\text{Fe}_3\text{O}_4$   $d = 5$  nm, 15 nm, and 25 nm were used.

Magnetic properties of dehydrated liver, blood and feces samples were studied by the vibration sample magnetometry (VSM). The feces samples of mice which did not receive a dose of nanoparticles show diamagnetic behavior typical for biological tissues. For the group of control mice, the highest magnetic moment of nanoparticles with the diameter  $d = 5$  nm in the feces was detected after 8 hours of their injection. For nanoparticles with the diameter  $d = 15$  nm – after 24 hours of their injection. For the samples with  $d = 25$  nm the highest magnetic moment is also observed after 24 hours. Nanoparticles were also found in the feces of sick mice. Preliminary results indicate penetration of nanoparticles into the intercellular space of the intestinal wall. No particle signal was detected in either the group of healthy mice or the group of sick mice in the liver samples.

1. D.C. Baumgart, W.J. Sandborn, Crohn's disease, *The Lancet*, **380**, no. 9853, 1590–1605 (2012).

2. L. Beaugerie et al., Predictors of Crohn's disease, *Gastroenterology*, **130**, no. 3, 650–656 (2006).

## THE MANIFESTATION OF STOICHIOMETRY DEVIATION IN SILICA-COATED MAGNETITE NANOPARTICLES

*S.V. Stolyar*<sup>1,2</sup>, *D.A. Velikanov*<sup>2\*</sup>, *A.V. Tyumentseva*<sup>1</sup>, *S.V. Komogortsev*<sup>2</sup>, *R.N. Yaroslavtsev*<sup>1,2</sup>,  
*Yu.V. Gerasimova*<sup>2</sup>, *M.V. Rautskii*<sup>2</sup>, *R.S. Iskhakov*<sup>2</sup>

<sup>1</sup>Krasnoyarsk Scientific Center, Federal Research Center KSC SB RAS, Krasnoyarsk, Russia

<sup>2</sup>Kirensky Institute of Physics, Federal Research Center KSC SB RAS, Krasnoyarsk, Russia

\*E-mail: [dponal@gmail.com](mailto:dponal@gmail.com)

In recent years, magnetic nanoparticles based on iron oxides have attracted interest in practical applications in the field of biotechnology and biomedicine [1]. Surface-modified magnetic nanoparticles can be used for selective isolation of certain biomolecules, such as nucleic acids and proteins. The method, commonly known as “magnetic separation”, has gained popularity in performing tests for diagnostic purposes [2].

The synthesis of magnetic nanoparticles was carried out by the method of chemical coprecipitation of iron salts  $\text{FeCl}_3$  and  $\text{FeCl}_2$  in a molar ratio of 2:1 in an aqueous solution. Tetraethoxysilane (TEOS) was used to coat magnetic nanoparticles with silicon oxide. Magnetic nanoparticles were coated in ethanol:water mixture in a 9:1 ratio with the addition of TEOS in two versions: 50 mg nanoparticles per 250  $\mu\text{l}$  TEOS (sample A  $\text{Fe}_3\text{O}_4:\text{SiO}_2 = 1:1.3$ ) and 50 mg nanoparticles per 800  $\mu\text{l}$  TEOS (sample B  $\text{Fe}_3\text{O}_4:\text{SiO}_2 = 1:4.5$ ).

The magnetization curves measured in the range from  $-15$  to  $15$  kOe are symmetric about the origin and contain a reversible part as well as an irreversible part – a hysteresis loop (Fig. 1). The coercive force, remanent magnetization, and magnetization in a field of 15 kOe decrease with increasing temperature. Low values of the coercive field indicate that particles with this size are close to the transition to the superparamagnetic state.

The relatively small values of the saturation magnetization of nanoparticles are due to the silica shell. This can be used for an independent assessment of the ratio of magnetite and silica, originally

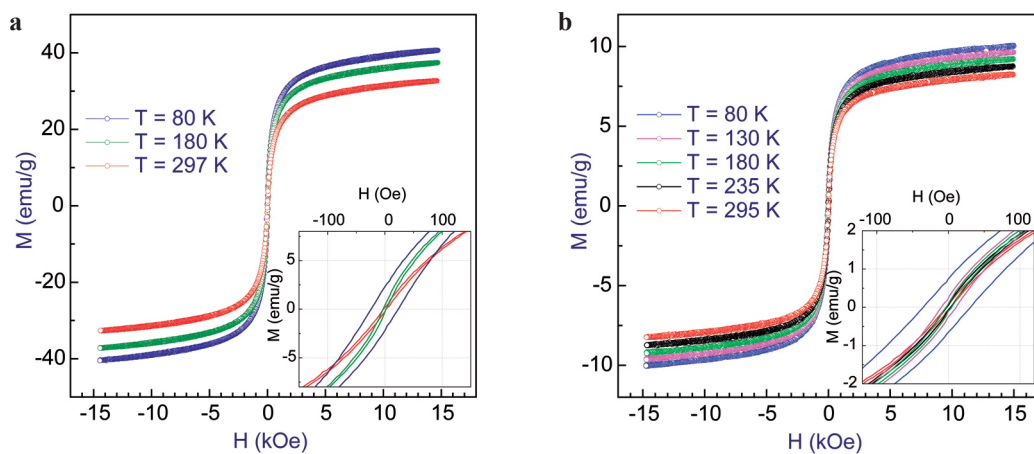


Figure 1. Hysteresis loops of magnetic nanoparticles. **a**  $\text{Fe}_3\text{O}_4:\text{SiO}_2 = 1:1.3$ , **b**  $\text{Fe}_3\text{O}_4:\text{SiO}_2 = 1:4.5$ .

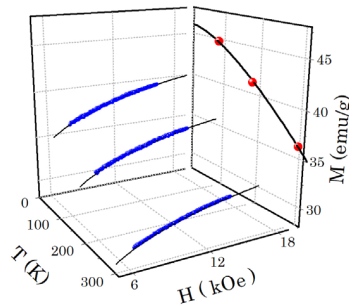


Figure 2. Determination of  $M_{s0}$  from the magnetization curves of particles in the region of approaching magnetization to saturation. Blue symbols – measured  $M(H)$ , thin black lines – fitting by Eq. (1), red symbols – saturation magnetization estimated from Eq. (1), black thick line – description of  $M_s(T)$  by Eq. (2).

made on the basis of the technological filling of the components during the synthesis. For such an estimate, we determined the magnetizations of the two studied samples of the composite material in a state of complete magnetic saturation and zero temperature ( $M_{s0}$ ). As can be seen from Fig. 2, the magnetization does not reach saturation even in the maximum fields used (15 kOe) and decreases with increasing temperature; therefore, we determined  $M_{s0}$  as follows. It was found that at a stabilized temperature in high fields, the magnetization of nanoparticles approaches saturation according to the equation [3]:

$$M(H) = M_s \left( 1 - \frac{1}{15} \frac{H_a^2}{H^{1/2}(H^{3/2} + H_R^{3/2})} \right), \quad (1)$$

where  $M_s$  – saturation magnetization,  $H_a$  – anisotropy field,  $H_R$  – exchange field in the core-shell system. Indeed, in our case, Eq. (1) makes it possible to describe the magnetization curves in high fields and estimate the quantitative values of  $M_s$  for different temperatures.

The change in the  $M_s$  value in magnetite nanoparticles with temperature is described by Bloch’s law  $T^{3/2}$ :

$$M_s(T) = M_{s0}(1 - B \cdot T^{3/2}). \quad (2)$$

Extrapolation of the data to 0 K according to Eq. (2) (Fig. 1) gives an estimate of  $M_{s0}$  (Table 1). Since the magnetization of silica is zero, the magnetization of the composite particle is related to the weight fraction of magnetite nanoparticles  $X_m$  and their magnetization  $M_{s0,m}$  as  $M_{s0} = X_m \cdot M_{s0,m}$ . Using the measured value  $M_{s0}$  and the weight fraction of magnetite  $X_m$ , we estimated the magnetization of nanoparticles reduced only to the weight of magnetite  $M_{s0,m}$  (see Table 1). As is known, the magnetization of pure quasi-spherical magnetite nanoparticles  $M_{s0,m}$  is lower than the

Table 1. Saturation magnetization of particles at 0 K.

Sample	$X_{Fe_3O_4}$ at synthesis	$M_{s0}$ , emu/g	Estimate of $M_{s0}$ of pure magnetite particles
A	$1/(1+1.3) \approx 0.435$	$46.0 \pm 0.2$	105
B	$1/(1+4.5) \approx 0.182$	$10.9 \pm 0.2$	60

magnetization of bulk magnetite crystals (92 emu/g) and depends on their size. For particles with an average size of 10 nm (our case), according to [4], the magnetization should be  $M_{s0,m} \approx 26$  emu/g. It can be seen from Table 1 that the magnetization of nanoparticles is significantly higher and that the magnetization of magnetite in the composition of the two studied samples is different. This can be interpreted as stoichiometric displacement in the composition of  $\text{Fe}_3\text{O}_4@\text{SiO}_2$  nanoparticles from standard  $\text{Fe}_3\text{O}_4$ . In addition, we also find an indication that this stoichiometric displacement is different in samples with different weights of magnetite and silica (the difference in magnetization in Table 1). Different stoichiometry in magnetite means that the stoichiometry of the silicate coating will also differ, i.e. it will have varying potencies in the isolation of nucleic acids.

*The study was supported by the Russian Science Foundation and the Krasnoyarsk Region Science and Technology Support Fund, grant No. 22-14-20020.*

1. P. Tartaj, M. a del P. Morales, S. Veintemillas-Verdaguer, T. Gonz lez-Carreño, and C. J. Serna, J. Phys. D. Appl. Phys., **36**, R182 (2003).
2. L. Borlido, A.M. Azevedo, A.C.A. Roque, and M.R. Aires-Barros, Biotechnol. Adv., **31**, 1374 (2013).
3. S.V. Komogortsev, S.V. Stolyar, L.A. Chekanova, R.N. Yaroslavtsev, O.A. Bayukov, D.A. Velikanov, M.N. Volochaev, P.E. Eroshenko, and R.S. Iskhakov, J. Magn. Magn. Mater., **527**, 167730 (2021).
4. A.P. Safronov, I.V. Beketov, S.V. Komogortsev, G.V. Kurlyandskaya, A.I. Medvedev, D.V. Leiman, A. Larrañaga, and S.M. Bhagat, AIP Adv., **3**, 052135 (2013).

## INVESTIGATION OF MAGNETITE NANOPARTICLES FOR MAGNETIC HYPERTHERMIA

*S.V. Stolyar*<sup>1,2,3\*</sup>, *O.A. Li*<sup>1,3</sup>, *D.A. Velikanov*<sup>2</sup>, *E.D. Nikolaeva*<sup>1</sup>, *A.M. Vorotynov*<sup>2</sup>,  
*V.F. Pyankov*<sup>1</sup>, *R.S. Iskhakov*<sup>2</sup>

<sup>1</sup>FRC KSC SB RAS, Krasnoyarsk, Russia

<sup>2</sup>Kirensky Institute of Physics, Federal Research Center KSC SB RAS, Krasnoyarsk, Russia

<sup>3</sup>Siberian Federal University, Krasnoyarsk, Russia

\*E-mail: [stol@iph.krasn.ru](mailto:stol@iph.krasn.ru)

In our work, we consider the heating of magnetite particles in the ferromagnetic resonance mode – selective absorption of microwave ( $f = 8.9$  GHz) radiation by magnetic particles at a constant magnetic field applied.

Magnetite nanoparticles 10–20 nm in size were synthesized by chemical deposition. Figure 1 shows the temperature dependence of the magnetization in the ZFC/FC mode in a field of 100 Oe. The particle blocking temperature is 270 K. Figure 2 shows the ferromagnetic resonance (FMR) curve of  $\text{Fe}_3\text{O}_4$  nanoparticles recorded at room temperature. The resonant field is  $H_r \approx 2.9$  kOe, the line width is  $\Delta H \approx 550$  Oe.

We have studied the time dependence of the particles temperature increment  $\Delta T$  for various values of the constant magnetic field  $H$  and the microwave field amplitude  $h$ . The temperature of the nanoparticles was measured with a T-type thermocouple: the positive electrode was made of copper (Cu), the negative electrode was made of constantan alloy (55% Cu + 45% Ni, Mn, Fe). When the thermocouple was placed in a resonator (without powder) with microwave pumping and a magnetic field sweep from 0 to 5 kOe, no temperature changes were recorded. Figure 3 shows the dependences of the particles temperature increment  $\Delta T$  on time for various values of the constant field  $H$  at a microwave attenuation of 2 dB. In a field close to resonant (with a strength of 2920 kOe), the greatest increase in the temperature of the system of particles is observed, which indicates the resonant nature of the absorption of microwave energy. Figure 4 shows the dependence of particles temperature increment  $\Delta T$  on the square of the microwave field amplitude and the approximation of

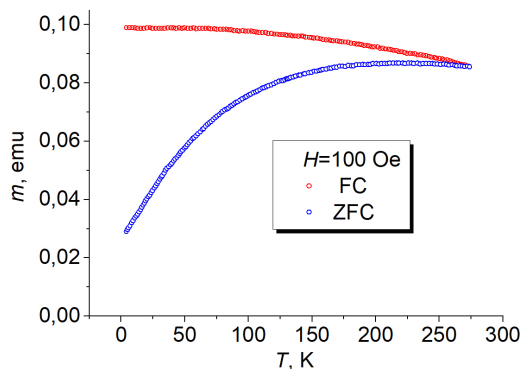


Figure 1. Temperature dependence of the magnetization of  $\text{Fe}_3\text{O}_4$  nanoparticles.

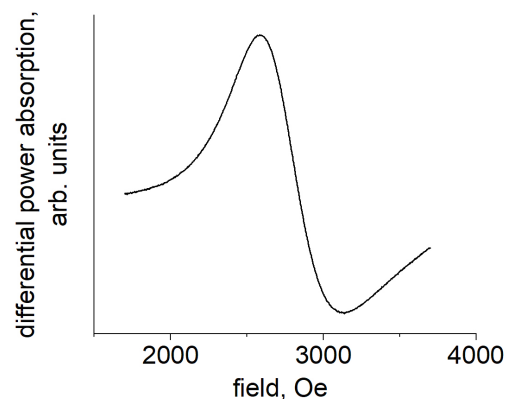


Figure 2. FMR spectrum of  $\text{Fe}_3\text{O}_4$  nanoparticles.

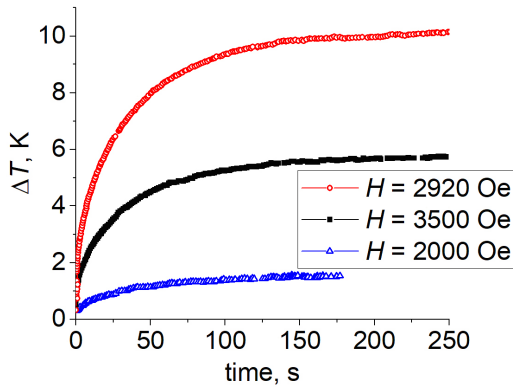


Figure 3. Temperature increment of nanoparticles in a constant field  $H$ .

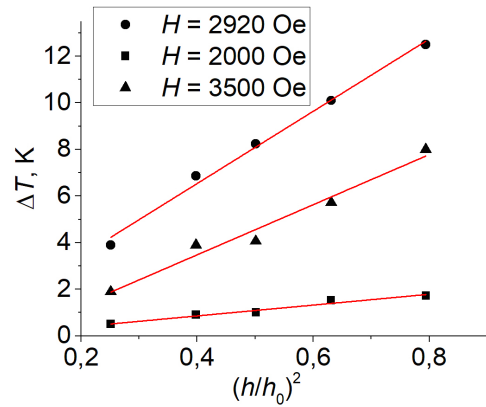


Figure 4. Dependence of the temperature increment of nanoparticles in a constant field  $H$  on the square of the microwave field amplitude.

this dependence by a straight line. As can be seen from the figure, the particle temperature increment is proportional to the square of the microwave amplitude.

Heating of magnetic powders in the ferromagnetic resonance mode, in our opinion, can be used in medicine as a new method for implementing magnetic hyperthermia. Hyperthermia is considered as one of the adjuvant methods of cancer treatment due to a general or local heating up to 41–45 °C. This effect is owing to the fact that tumor cells are more sensitive to temperature rise than healthy ones.

## CHARACTERISTICS OF EMR SIGNALS IN FAST-GROWING TARTARY BUCKWHEAT CALLUS CULTURES

*S.V. Yurtaeva*<sup>1</sup>, *I.V. Yatsyk*<sup>1</sup>, *A.I. Valieva*<sup>2</sup>, *E.A. Gumerova*<sup>2</sup>, *N.I. Rumyantseva*<sup>2</sup>

<sup>1</sup>Zavoisky Physical-Technical Institute, FRC Kazan Scientific Center, Russian Academy of Sciences, Kazan, Russia

<sup>2</sup>Kazan Institute of Biochemistry and Biophysics, FRC Kazan SC of RAS, Kazan, Russia

\*E-mail: [s.yurtaeva@kfi.knc.ru](mailto:s.yurtaeva@kfi.knc.ru)

Biogenic magnetism is studied since the discovery of biogenic magnetic nanoparticles (BMN). BMNs have been found in a wide variety of organisms including bacteria, fungi, fish, mammals, and plants [1]. Biogenic magnetites participate in different biological functions due to their specific physical properties including magnetotaxis and magnetoreception. However, many BMNs are detected in organs and tissues that are non-responsible for orientation of organisms in the earth's magnetic field. Recently, BMNs were detected in the cell walls of the plant vascular tissue (phloem) suggesting their possible role in transport processes [2]. In total, despite the establishment of BMN existence in many organisms, their involvement in specific biological processes remains poorly understood, especially in plants.

Electron paramagnetic resonance (EPR) is one of reliable methods to study biogenic magnetism and BMNs. The appearance of “broad electron spin resonance signal” presently called electron magnetic resonance (EMR) with simultaneous changes of static magnetic susceptibility was shown in the yeast cell culture at certain stages of its growth [3–5]. Magnetism in semi-synchronized yeast culture is observed immediately preceding the intensive budding; the EMR signal disappears when cell division is stopped [1–3]. It was supposed [5] that the EMR signal appears due to the iron clusters formed at the specific stage of the cell cycle. Later, it was shown that the nucleus is the cellular site of high concentration of iron which seems to play an important role in the process of cell division [6, 7].

The purpose of our study is to identify whether such a phenomenon is characteristic of plant cell cultures. We used fast-growing callus of Tartary buckwheat (*Fagopyrum tataricum*) cultured on agar medium RX in the dark with passage every 14 days [8].

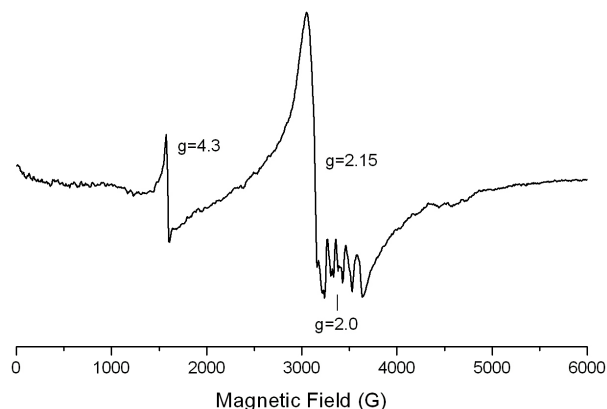


Figure 1. An example of EPR spectrum of callus cells at 4th day of culture.  $T = 150$  K.

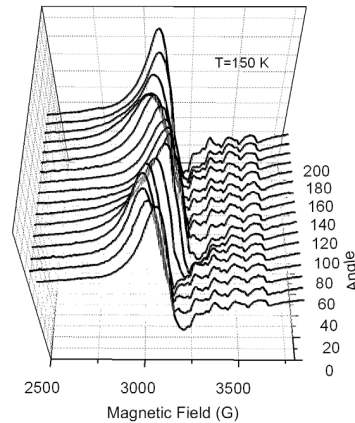


Figure 2. Angular dependence of EMR signal in callus at 4th day of culture.

To reveal EMR signals, we used samples of callus at the stationary phase of growth (14 days) and within the period from 1<sup>st</sup> till 6<sup>th</sup> day (with 1-day step) after the transfer of callus on fresh medium. At the early stage (2<sup>nd</sup>–4<sup>th</sup> day) at the exponential phase of the growth, the callus had the highest mitotic index (up to 5–6%) while after 5<sup>th</sup> day the mitotic index sharply decreased and at the stationary phase (10<sup>th</sup>–14<sup>th</sup> day) cell division ceased at all [8].

At the stationary phase (14<sup>th</sup> day), only two types of signals were recorded in EPR spectrum at 150 K: low intensity signal of non-heme Fe(III) rhombic center at  $g = 4.3$ , and 6 hyperfine lines centered at  $g = 2$  of Mn(II). These signals are often observed in biological tissues, and due to enzymes or other proteins with metal ions.

At 3<sup>rd</sup>–4<sup>th</sup> days of culture, the third signal appeared at  $g$ -value 2.1÷2.2 (Fig. 1) with the line width  $\Delta H$  100÷400 G. The resonance field  $H_{res}$  of this signal has a pronounced dependence on angle (Fig. 2). In some cases, we detected less intensive signals in lower fields ( $g$ -value 2.3÷2.5) also depended on angle. Such signals disappeared after 4–5 days of culture and were not detected later (at the stationary phase). Thus, we can conclude that the intensive wide signals with  $g > 2.1$  appear only when callus cells are in the mitotic cycle. For the best of our knowledge, this is the first observation of the considered phenomenon in plants.

In addition, the sample with the most intensive signal was studied in detail, including its dependence on the temperature (within 100 K–270 K) and on the orientation (Fig. 2). The parameters like the resonance field  $H_{res}$ , linewidth  $\Delta H$ , and integrated intensity were obtained. Comprehensive analysis of these parameters allows us to suppose that the observed phenomenon of the appearance of “broad electron spin resonance signal” in our experiment corresponds to the aggregated nano-sized magnetite ( $Fe_3O_4$ ) particles. Previously, we observed similar signals with the same characteristics in rat tissues [9]. The EMR signal observed can be a manifestation of BMNs appearing in different forms.

1. S.V. Gorobets, O.Yu. Gorobets, Yu.I. Gorobets et al., *Bioelectromagnetics*, **43**(2), 119–143 (2022).
2. S.V. Gorobets, O.Yu. Gorobets, A.V. Magerman et al., ArXiv:1901.07212 (2019).
3. O.P. Samoilova, L.A. Blumenfeld, *Biofizika*, **6**, 15–19 (1961) [in Russian].
4. A.I. Tsapin, O.P. Samoilova, L.A. Blumenfeld, *Biofizika*, **34**, 15–19 (1989) [in Russian].
5. O.P. Samoilova, A.I. Tsapin, L.A. Blumenfeld, *Biofizika*, **40**, 383–388 (1995) [in Russian].
6. H. Roschztardt, L. Grilletet et al., *J. of Biol. Chemistry*, **286**, 27863–27866 (2011).
7. A. Bertonchini, R. Meneghini et al., *J. of Cancer Science and Therapy*, **8**(8), 213–215 (2016).
8. G.V. Kamalova, A.N. Akulov, N.I. Rummyantseva, *Biochemistry(Moscow)*, **74**(6), 686–694 (2009).
9. S.V. Yurtaeva, V.N. Efimov, G.G. Yafarova et al., *Appl. Magn. Res.*, **47**(3), 555–565 (2016).



Section N.  
**Instruments and techniques for studying  
magnetism**

---

## Co-BASED AMORPHOUS MATERIALS: TOWARD HIGH FREQUENCY FUNCTIONAL COMPOSITES

*G.V. Kurlyandskaya*<sup>1,2\*</sup>, *I. Orue*<sup>3</sup>, *A.A. Pasyunkova*<sup>1,4</sup>, *A.V. Timofeeva*<sup>1</sup>, *S.O. Volchkov*<sup>1</sup>,  
*A. Larrañaga*<sup>3</sup>

<sup>1</sup>Ural Federal University, Ekaterinburg, Russia

<sup>2</sup>Depto Electricidad y Electrónica, Universidad del País Vasco UPV/EHU, Bilbao, Spain

<sup>3</sup>SGIKER, Basque Country University UPV/EHU, Leioa, Spain

<sup>4</sup>Institute of Metal Physics M.N. Mikheev of UD RAS, Ekaterinburg, Russia

\*E-mail: [galinakurlyandskaya@urfu.ru](mailto:galinakurlyandskaya@urfu.ru)

Rapidly quenched amorphous Co-based ribbons and wires are magnetically soft materials widely requested for technological applications [1–2]. Among others they are suitable for sensor applications in magnetoimpedance and magnetoelastic devices [2–4]. Magnetoimpedance effect (MI), i.e., the change of the high frequency impedance of ferromagnetic conductor under application of external magnetic field, was recently attracted special attention for the creation of functional composites consisting of ribbons with different coverings such as additional conductive, magnetic, graphene, polymer layers and polymer layers filled by nanoparticles of different kinds [5–6]. Co-based amorphous ribbons allow thorough control of their effective magnetic anisotropy by combination of appropriate shape anisotropy and induced anisotropy adjusted by post preparation treatments [7]. In this study we propose detailed comparison of the structure, static and dynamic magnetic properties (MI and ferromagnetic resonance (FMR) in the wide frequency range) of  $\text{Fe}_3\text{Co}_{67}\text{Cr}_3\text{Si}_{15}\text{B}_{12}$  rapidly quenched amorphous ribbons with different features of effective magnetic anisotropy.

Amorphous  $\text{Fe}_3\text{Co}_{67}\text{Cr}_3\text{Si}_{15}\text{B}_{12}$  ribbons were studied in as-quenched state (1), after relaxation annealing at 350 °C during 1 hour (2) and after stress annealing at 350 °C during 1 hour (3) for specific load of 230 MPa. The width and thickness of the ribbons were 0.8 mm and 0.024 mm respectively. The length for inductive measurements of the hysteresis loops  $M(H)$  and MI studies was 45 mm. For vibrating sample magnetometry (VSM) and FMR studies by standard cavity perturbation technique and broad band measurements in coaxial line the length was 5 mm. Both VSM and FMR by standard cavity perturbation technique were made for two configurations of the external magnetic field: in plane of the ribbons and out of plane of the ribbons. For the broad band measurements, we adapted previously developed technique for the measurements of the microwave properties of microwires in the coaxial line [8–9]. Here we show the possibility of accurate measurements of FMR of amorphous ribbons in a coaxial waveguide for the frequency range up to 12 GHz by the system based on a ZVA-67 (Rohde & Schwarz) vector network analyzer (VNA) using one port method. The power output of the signal of the ZVA analyzer was set at a level of 0.1 mW, based on the maximum signal-to-noise ratio criterion. ZVA-67 vector analyzer measures the amplitude, phase and power of the reflected signal. The value of the parameter S11 can be compensated for the length  $d$  of the SMA-adaptor with the holder.

According to X-ray diffraction analysis all samples were amorphous in all states. Figure 1a, b shows the hysteresis loops for long and short samples. One can see that for long as-quenched and annealed without stress samples the longitudinal effective anisotropy is evident but stress annealing results in the formation of well-defined transverse magnetic anisotropy with the anisotropy field about 3 Oe. MI measurements show very high sensitivity of the order of 200 %/Oe for the samples (3) in the field interval of 2 to 3 Oe useful for sensor applications. However, short samples of 5 mm show very similar features of the effective magnetic anisotropy (Fig. 1b due to the strong shape anisotropy contribution and very similar FMR characteristics. The results of the cavity perturbation

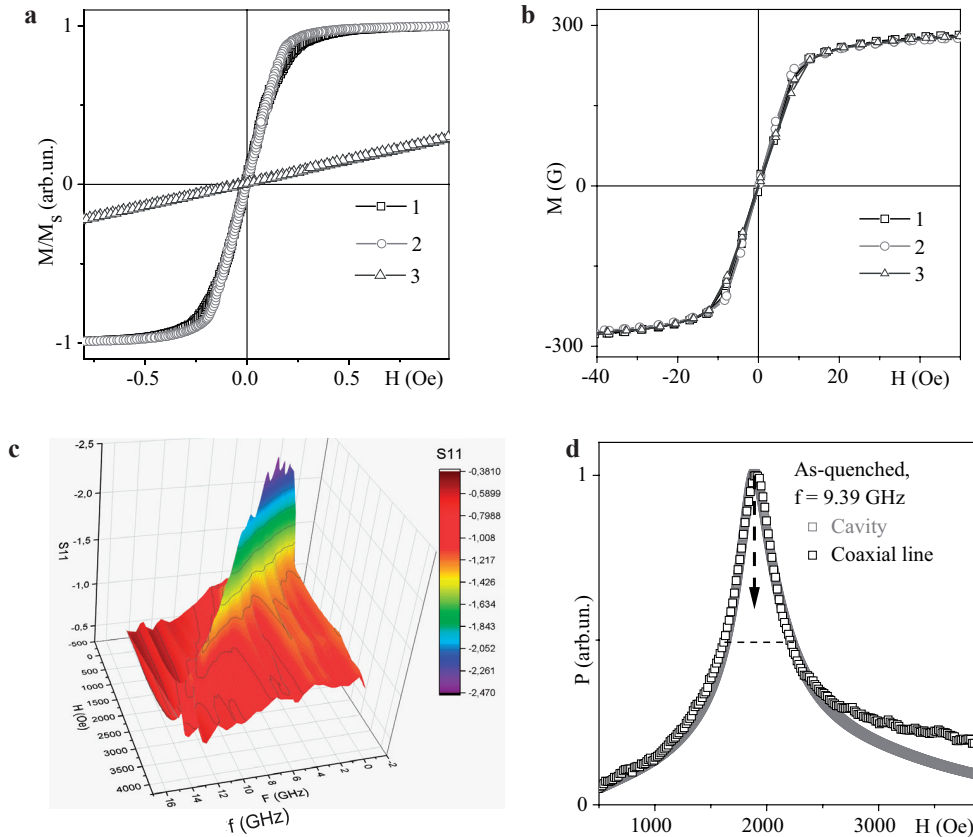


Figure 1. Hysteresis loops of amorphous ribbons after different treatments measured by inductive technique for 45 mm length (a) and by VSM for 5 mm length (b). S11 parameter values as functions of the applied magnetic field and microwave frequency for as-quenched amorphous ribbon (c). Comparison of the FMR spectra of as-quenched amorphous ribbon measured in plane of the ribbon by cavity perturbation technique and in broad band by ZVA-67 VNA: arrow indicates the FMR field value, dashed line – the FMR peak width (d).

and broad band measurements show (Fig. 1c, d) very good agreement for the frequency  $f = 9.39$  GHz confirming the validity of proposed the microwave absorption technique.

*This study was in part founded by the “Priority-2030” program. Selected measurements were performed at SGIKER services of UPV-EHU. We thank L. Lezama and V.A. Lukshina for support.*

1. D.A. Bukreev, M.S. Derevyanko, A.A. Moiseev, A.V. Semirov, P.A. Savin, G.V. Kurlyandskaya, *Materials*, **13**, 3216 (2020).
2. G.V. Kurlyandskaya, A. Garcia-Arribas, J.M. Barandiaran, E. Kisker, *Sens. Actuators A*, **91**, 116 (2001).
3. V.E. Makhotkin, B.P. Shurukhin, V.A. Lopatin, P.Y. Marchukov, Y.K. Levin, *Sens. Actuators A*, **27**, 759 (1991).
4. Z. Yang, H. Wang, P. Guo, Y. Ding, C. Lei, Y. Luo, *Sensors*, **18**, 1765 (2018).
5. D. Mukherjee, J. Devkota, A. Ruiz, M. Hordagoda, R. Hyde, S. Witanachchi, P. Mukherjee, H. Srikanth, M.H. Phan., *J. Appl. Phys.*, **116**, 123912 (2014).
6. G.V. Kurlyandskaya, R. El Kammouni, S.O. Volchkov, S.V. Shcherbinin, A. Larrañaga, *IEEE Trans. Magn.*, **53**, 200041 (2017).

## MAGNETIC NANOSTRUCTURES OF THE CORE/SHELL TYPE AND GRO-FERRITE NANOCOMPOSITES FOR BIOMEDICINE: SYNTHESIS AND CHARACTERIZATIONS

*A.S. Kamzin*

Ioffe institute RAS, St. Petersburg, Russia

E-mail: [ASKam@mail.ioffe.ru](mailto:ASKam@mail.ioffe.ru)

The work is devoted to the study of the magnetic structure, phase composition of the magnetic nanostructures (NS) Core/Shell (C/S) type and Graphene-Ferrite (G-F) nanocomposites (NC) and. Interest in these materials is determined by the prospects of their use in biomedicine (see [1, 2] and references therein). The main method used for research was Mössbauer spectroscopy (MS), because MS is a highly sensitive and effective means of studying the phase states and magnetic structure of both complex composites and individual components that make up complex magnetic structures as C/S. MS gives possibility to obtain information that is inaccessible to other methods.

The C/S type NS consist of a core, which can have high magnetic moment (for example, iron or others). The core is covered with a magnetic sheath with good biocompatibility. G-F NC consist of graphene and spinel ferrites (for ex.  $\text{Fe}_3\text{O}_4$ ,  $\text{CoFe}_2\text{O}_4$ ). Main advantage of such materials is their versatility, as well as the ability to optimize the physical and chemical properties of the material. Advances in nanotechnology make it possible to manufacture these multifunctional nanomaterials.

In this report describes the results of studies of graphene – various ferrites NC synthesized by the method of ball milling. As shown by Mössbauer studies the magnetic G-F NC synthesized by the ball milled method contain phases identified as spinels and as iron carbides and iron-depleted carbon clusters that were not detected by X-ray diffraction. Those G-F NC were able to retain the functional groups of graphene oxide. The efficacy of the magnetic nanocomposites for killing of cancerous cells is studied in vitro using HeLa cells in the presence of an Alternating Current magnetic field.

In the case of  $\text{Fe}_3\text{O}_4/\gamma\text{-Fe}_2\text{O}_3$  NS of the C/S type, it was established that they consist of a magnetite ( $\text{Fe}_3\text{O}_4$ ) core and a maghemite ( $\gamma\text{-Fe}_2\text{O}_3$ ) shell. On the surface of the shell is formed a layer, in which the spin magnetic moments are canted relative to the moments in-side the shell. Between the core and the shell is formed an intermediate layer in the spin-glass state.

As a result of this research, the dependence of the properties of G-F NC and C/S NS on the synthesis technology and particle size was shown, the interaction of the components and their influence on each other, as well as the phase state and magnetic structure, which significantly affect the properties of G-F NC and C/S NS.

1. A.S. Kamzin et al., Phys. Sol. State, **62**, 1933–1943 (2020).
2. A.S. Kamzin et al., Phys. Sol. State, **63**, 998–1008 (2021).

## MAGNETIC NON-DESTRUCTIVE TESTING USING A SCANNING GMI MAGNETOMETER

*S.A. Gudoshnikov*<sup>1,2\*</sup>, *G.E. Danilov*<sup>1</sup>, *V.P. Tarasov*<sup>1</sup>, *Yu.B. Grebenshchikov*<sup>2</sup>, *V.I. Odintsov*<sup>2</sup>,  
*A.V. Popova*<sup>2</sup>, *S.N. Venediktov*<sup>3</sup>

<sup>1</sup>National University of Science and Technology “MISIS”, Moscow, Russia

<sup>2</sup>Pushkov Institute of Terrestrial Magnetism, Ionosphere and Radio Wave Propagation, IZMIRAN, Troitsk, Moscow, Russia

<sup>3</sup>“Magnetic and Cryoelectronic Systems” Ltd., Troitsk, Moscow, Russia

\*E-mail: [gudosh@izmiran.ru](mailto:gudosh@izmiran.ru)

The amorphous glass coated ferromagnetic microwires with small metallic core diameters  $d \sim 5\text{--}30 \mu\text{m}$  are promising for various technological applications. In particular, the microwires with nearly zero magnetostriction show giant magnetoimpedance (GMI) effect with a very large GMI ratio [1]. This effect is used to design a new generation of sensitive magnetic field GMI sensors [2]. Due to the small diameter of the microwire, this magnetic sensor can be used as a measuring head of a scanning magnetometer. The important characteristics of this measuring system are a magnetic field sensitivity and a magnetic spatial resolution. These parameters are determined mainly by a GMI-sensor.

In this work a scanning GMI magnetometer [3] has been used in magnetic non-destructive testing of different characters and figures printed on a black and white laser printer. As the GMI-sensor we used a 4 mm long glass-coated microwire having  $13.5 \mu\text{m}$  core diameter with Co Fe Cr Si B composition and a pick-up coil of 70 turns wound around the microwire. The GMI-sensor was placed perpendicular to the sample surface so that the distance between the microwire’s tip and the sample surface  $z$  was of order of 0.2–0.5 mm. A configuration of the scanning GMI measurement system is shown in Fig. 1a. Relative movement of the sample and the GMI-sensor is performed by means of nonmagnetic  $X$ - $Y$ - $Z$  positioner. The maximum size of the scanning area was  $150 \times 150$  mm, the minimum scanning step in the  $X$ ,  $Y$  directions was 0.1 mm. During the scanning process, the perpendicular magnetic field component was recorded depending on  $X$ ,  $Y$  coordinates near the sample surface. Measurements were carried out within a magnetic shield to reduce the effects of external magnetic fields.

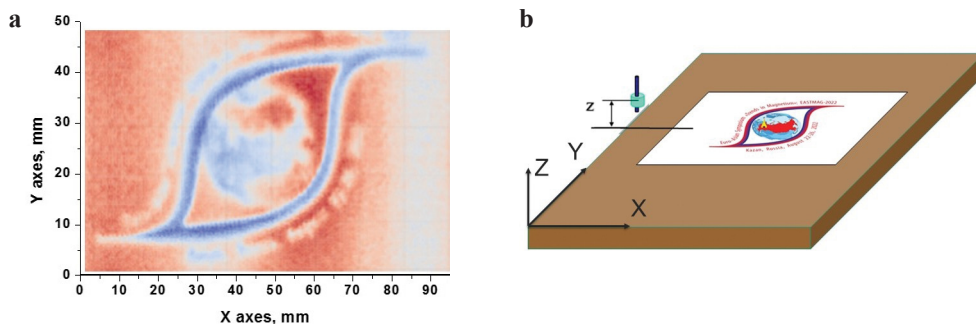


Figure 1. Schematic representation of the measuring part of the scanning GMI magnetometer (a) and color magnetic image of the Symposium logo printed by a black/white laser printer (b).

To check the main characteristics of the developed scanning GMI magnetometer, long two wire current lines were used as the samples. It was found that magnetic sensitivity (the minimum change in the magnetic field that is measured by the GMI magnetometer) corresponds to  $\sim 10$  nanoTesla, and the magnetic spatial resolution (the minimum distinguishable distance between two magnetic maxima) is of the order of 1.5 mm.

Using a scanning GMI magnetometer, we measured magnetic images of text characters and figures printed on various black and white laser printers. It is known that laser printer toners contain up to 10% magnetic iron oxide nanoparticles, so their residual magnetization can generate weak local magnetic fields. As an example, Fig. 1 shows a magnetic image of a figure in the form of a Symposium logo printed on a the HP Laser Jet 2200 printer. It was found that the value of the remnant magnetic moment of toner samples, determined by a scanning GMI magnetometer, is a quantitative magnetic characteristic of the toner and can be used in its identification in tasks of forensic examination. Further development of the method of scanning GMI is associated with an increase in its spatial resolution to 0.2–0.3 mm by improving the design of the GMI sensor.

*Support by NUST “MISiS”, grant K2-2022-018, is acknowledged.*

1. V. Zhukova, A. Chizhik et al., IEEE Trans. Magn., **38**, 3090 (2002).
2. S. Gudoshnikov, N. Usov et al., Phys. Status Solidi (A), **211** (5), 980 (2014).
3. S. Gudoshnikov, V. Tarasov, B. Liubimov et al., J. Magn. Magn. Mater, **510**, 166938 (2020).

## SCANNING GMI MAGNETOMETER FOR MEASURING STRAY MAGNETIC FIELDS OF AMORPHOUS FERROMAGNETIC MICROWIRES

*G.E. Danilov<sup>1\*</sup>, V.P. Tarasov<sup>1</sup>, Yu.B. Grebenschchikov<sup>2</sup>, V.I. Odintsov<sup>2</sup>, S.A. Gudoshnikov<sup>1,2</sup>*

<sup>1</sup>National University of Science and Technology “MISiS”, Moscow, Russia

<sup>2</sup>Pushkov Institute of Terrestrial Magnetism, Ionosphere and Radio Wave Propagation, IZMIRAN, Troitsk, Moscow, Russia

\*E-mail: [ge.danilov@physics.msu.ru](mailto:ge.danilov@physics.msu.ru)

The glass-coated amorphous ferromagnetic microwires (AFM) produced by Teylor-Ulitovsky method are very promising for application in magnetic sensors, for developing of new types of stress-tunable composite materials, for magnetic codification, etc. [1]. For these applications it is important to control the magnetization distribution within the wire in the remanent state and its response to a weak applied magnetic field. However, an experimental investigation of the domain structures in wires with diameters from 5 to 30  $\mu\text{m}$  turns out to be a rather complicated technical problem. As shown in [2], one of the possible approaches to the study of the AFM domain structure is the use of a highly sensitive scanning SQUID magnetometer. However, the disadvantage of this method is the need to conduct research at the boiling point of liquid nitrogen ( $-200\text{ }^\circ\text{C}$ ). In this paper, to measure the magnetic stray field of the AFM, it is proposed to use a scanning magnetometer based on a magnetic impedance (GMI) sensor.

When performing this study, a scanning GMI magnetometer, capable of registering weakly magnetic objects created magnetic fields of less than 10 nT, was used [3]. The measurements were carried out inside a magnetic screen. In the scanning magnetometer, a GMI sensor was used as a sensitive element, which measures the perpendicular component of the magnetic field. The sensor was mounted on a special holder in a vertical position (parallel to the  $Z$  axis) at a fixed distance  $h \sim 200\text{ }\mu\text{m}$  relative to the surface of the studied sample. During the measurements, the table with the sample was moved relative to the sensitive tip of the GMI sensor in the  $X$ - $Y$  directions using stepper motors. The maximum size of the scanning area was limited to  $180 \times 180\text{ mm}$ , the minimum scanning step along the  $X$  and  $Y$  axes was 0.1 mm.

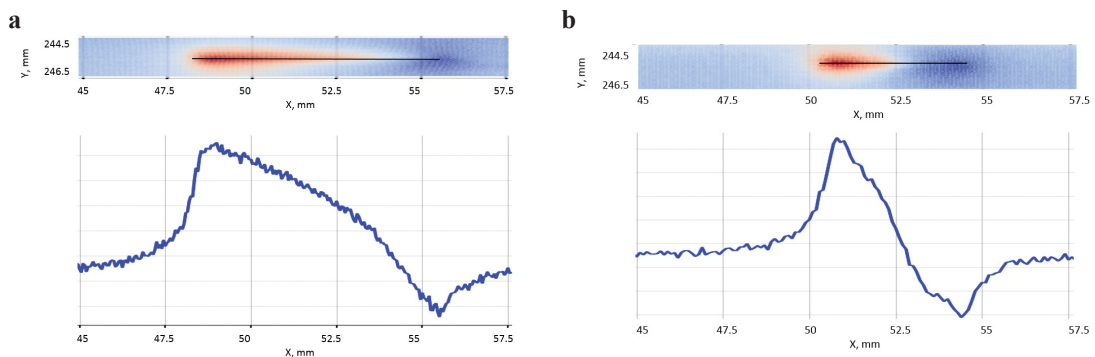


Figure 1. Magnetic images of the perpendicular component of the magnetic field over AFM samples  $\sim 7.5\text{ mm}$  long (a) and  $\sim 4.5\text{ mm}$  long (b). The graphs show the change in the magnetic field along the AFM axis in relative units.

The scanning GMI magnetometer was calibrated by measuring the magnetic fields of current-carrying samples with a known magnetic field distribution. In our experiments, long two-wire lines with oppositely directed currents (2-w line) were used as calibration samples. It was found that the experimental data are in good agreement with the data of numerical simulation of the magnetic field generated by the 2-w line, if we assume that the effective height between the GMI sensor and the plane of the sample with the current structure is  $\sim 0.5$  mm.

During research, using a scanning GMI magnetometer, experimental images of the perpendicular component of the stray magnetic fields of Co-rich AFM segments of various lengths were obtained. It was found that in the magnetic images of all studied AFM samples magnetic extremes of opposite signs are observed near the ends of the AFM segments, Fig. 1. The magnetic field strength in the region of extrema can reach amplitudes of over several hundreds of nanotesla. In low external longitudinal magnetic fields (up to  $\pm 2000$  A/m), AFM segments were easily remagnetized, which led to a change in the polarity of magnetic extrema. The magnetic images of AFM samples are compared with their hysteresis loops measured using a vibration magnetometer.

*Supports by RSF, grant 20-19-00607 and NUST “MISiS”, grant K2-2022-018, are acknowledged.*

1. M. Vazquez, H. Chiriac, A. Zhukov, L. Panina, T. Uchiyama, Phys. Status Solidi (a), **208**, 493–501 (2011).
2. S. Gudoshnikov, N. Usov, A. Zhukov et al., J. Magn. Magn. Mater., **316**, 188 (2006).
3. S. Gudoshnikov, V. Tarasov, B. Liubimov et al., J. Magn. Magn. Mater., **510**, 166938 (2020).



## DEVELOPMENT OF NON-CONTACT MECHANICAL STRESS SENSORS BASED ON NONLINEAR PROCESSES OF MAGNETIZATION REVERSAL IN AMORPHOUS MICROWIRES

*O.V. Lutsenko\**, *N.A. Yudanov*, *S.A. Evstigneeva*, *L.V. Panina*

National University of Science and Technology “MISiS”, Moscow, Russia

\*E-mail: [lucenkoolesya17@gmail.com](mailto:lucenkoolesya17@gmail.com)

Polymer composite materials are used in a wide variety of fields from medical technology to aircraft construction, and the problem arises of monitoring their structural parameters, such as mechanical stresses and dislocations. This is achieved through the inclusion of active sensor elements in the composite matrix, as well as the use of surface sensors. In this work, as sensor elements, it is proposed to use ferromagnetic microwires with a diameter of less than 30 microns, the magnetic structure of which is sensitive to mechanical stresses [1–3]. Amorphous magnetic microwires in a Pyrex glass shell are of particular interest for the development of biosensors due to their miniaturization, anisotropy, enhanced magnetic effects, and a protective biocompatible shell.

As a sensor element, an amorphous microwire of composition  $\text{Co}_{67.7}\text{Fe}_{4.3}\text{Si}_{11}\text{B}_{14}\text{Cr}_3$  was used, which has a small and negative magnetostriction constant of the order of  $-0.1$  ppm, which causes a significant effect of mechanical stresses on its magnetic structure. When no external stress is applied, the wire has an axial anisotropy and a nearly rectangular hysteresis loop due to the contribution of Co-clustering in overall anisotropy. When the wire is re-magnetized, a sharp voltage pulse is generated, the spectrum of which is characterized by a high-frequency harmonic. In the presence of an external tensile stress, the magnetostrictive contribution to the overall anisotropy increases and the magnetization loop becomes inclined, which strongly affects the harmonic spectrum of the induced voltage [3]. In this work, for detailed investigation, the wire remagnetization by a propagation of

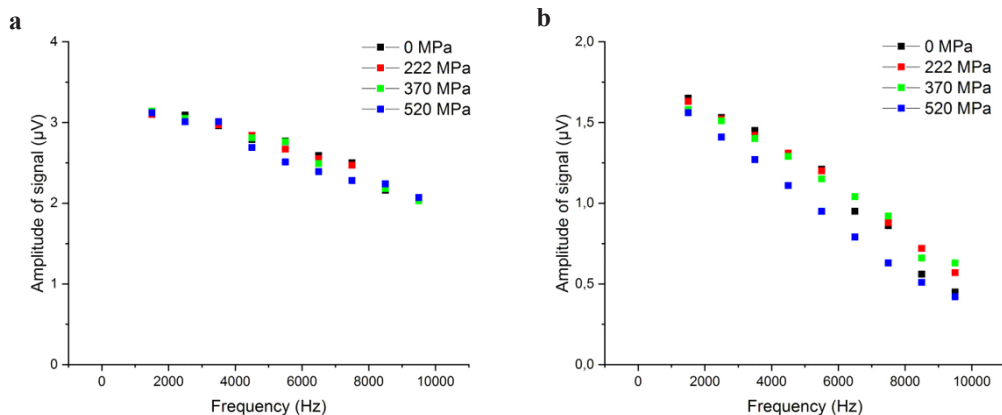


Figure 1. Harmonic spectrum of the signal of microwire’s remagnetization process under applied mechanical stresses, obtained using a flat coil, when generating an external magnetic field of a sinusoidal shape and amplitudes of **a** 200 A/m and **b** 800 A/m.

a single domain wall was realized in the presence of the external stress. The harmonic spectrum of the signal generated in the detection coil was measured when the wall passed through the coil.

For practical applications, it is necessary to develop an effective sensor system “microwire–magnetizing / detecting coils”, with which it would be possible to remotely remagnetize the wire and detect higher harmonics. This was achieved using a flat coil connected to a lock-in amplifier.

The amplitudes up to the 9th harmonic above 5  $\mu\text{V}$  (in fields of 200 A/m, Fig. 1a) and 9  $\mu\text{V}$  (in fields of 800 A/m, Fig. 1b) were realized by remote recording of spectral characteristics using the developed flat coil system with the microwire located at a distance of 0.1 cm. The application of mechanical stresses led to a change in the amplitudes of higher harmonics up to about 25% in both cases. Thus, a new non-contact method for determining mechanical loads using harmonic spectrum analysis has been demonstrated.

*The reported study was funded by RFBR according to the research project № 20-32-90145 and in the framework of federal academic leadership program Priority 2030 of NUST MISIS.*

1. M. Churyukanova, S. Kaloshkin, E. Shuvaeva et al., Journal of Alloys and Compounds, **748**, 199–205 (2018).
2. M.G. Nematov, I. Baraban, N.A. Yudanov et al., Journal of Alloys and Compounds, **837**, 155584 (2020).
3. L. Panina, A. Dzhumazoda, M. Nematov et al., Sensors, **19(23)**, 5089 (2019).

## DEVELOPMENT OF MAGNETIC CODING SYSTEM BASED ON FERROMAGNETIC MICROWIRE IN A GLASS-SHELL BASED ON Co ALLOY

*S.E. Medar*<sup>1\*</sup>, *S.A. Evstigneeva*<sup>1</sup>, *N.A. Yudanov*<sup>1</sup>, *L.V. Panina*<sup>1,2</sup>

<sup>1</sup>National University of Science and Technology, MISiS, Moscow, Russia

<sup>2</sup>Immanuel Kant Baltic Federal University, IKBFU, Kaliningrad, Russia

\*E-mail: [sveta.medar@yandex.ru](mailto:sveta.medar@yandex.ru)

Ferromagnetic microwires in a glass shell are promising for creating magnetic labels, owing to the combination of soft magnetic properties and bistable remagnetization process [1]. Magnetic tags with the possibility of their remote reading allow solving the problems of the logistics of objects, for example, in large warehouses or for verifying the authenticity of objects. The principle of operation of this type of labels is based on a specific response in the form of peaks of the induced voltage signal that is generated when the microwires are remagnetized by an external magnetic field varying in a small range.

The aim of the work was to develop a prototype coding system based on ferromagnetic microwires in a glass coat. Ferromagnetic microwires of Co-based composition with a diameter less than 40 m can demonstrate the magnetization flip in a small magnetic field (known as coercivity), and the value of coercivity depends on a number of factors such as composition and the technological regime of wire production. A number of such wires with different coercivity were chosen to create a prototype of a magnetic tag. Remote interrogation of selected microwires with different magnetization reversal fields was carried out using a system of two flat coils, one of which created a magnetizing magnetic field of a triangular waveform with a given frequency and amplitude, and the second coil was used for the detection of the induced voltage pulse appeared during the magnetization reversal of microwires. Figure 1 demonstrates a set of distinguishable peaks obtained from a label with two different microwires used as a magnetic label prototype.

*The reported study was funded by RFBR according to the research project № 20-32-90145 and in the framework of federal academic leadership program Priority 2030 of NUST MISiS.*

1. V. Zhukova, P. Corte-Leon, J.M. Blanco et al., *Chemosensors*, **9** (5), 100, p. 22 (2021).

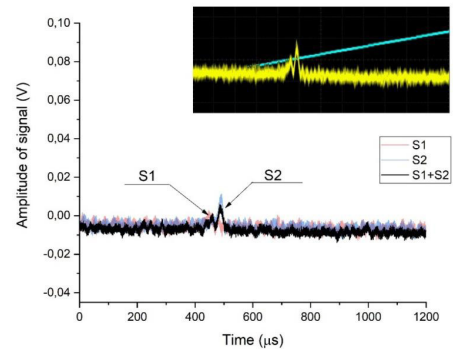


Figure 1. Signals received from magnetic tags incorporating a single microwire with different compositions (S1-Co<sub>67.7</sub>Fe<sub>4.3</sub>Si<sub>11</sub>B<sub>14</sub>Cr<sub>3</sub>,  $H_c \sim 3$  Oe and S2-Co<sub>66.6</sub>Fe<sub>4.28</sub>B<sub>11.51</sub>Si<sub>14.48</sub>Ni<sub>1.44</sub>Mo<sub>1.69</sub>,  $H_c \sim 13$  Oe). The insert shows the signal from the when usig a tag with two microwires S1 and S2 located at a distance about 1mm. The blue line corresponds to the magnetizing field. The amplitude of the magnetizing field was 1000 A/m and frequency was 500 Hz.

## NON-DESTRUCTIVE MAGNETO-OPTICAL ELLIPSOMETRY TESTING OF MAX MATERIALS

*O.A. Maximova*<sup>1,2\*</sup>, *S.A. Lyaschenko*<sup>1</sup>, *S.N. Varnakov*<sup>1</sup>, *S.G. Ovchinnikov*<sup>1,2</sup>

<sup>1</sup>Kirensky Institute of Physics, Federal Research Center KSC Siberian Branch

Russian Academy of Sciences, Krasnoyarsk, Russia

<sup>2</sup>Siberian Federal University, Krasnoyarsk, Russia

\*E-mail: [maximo.a@mail.ru](mailto:maximo.a@mail.ru)

MAX phases are layered ternary carbides and nitrides, where M is an early transition metal, A is a group A element, X is carbon or nitrogen [1–3], exhibiting combination of properties of metallic and ceramic materials [1, 3]. These materials have attracted huge interest of scientific society as they exhibit unique chemical, physical, electrical, and mechanical properties [2]. They have a unique combination of metallic and ceramic properties [1–3], such as low density, low hardness, good machinability, high strength and high Young's modulus at high temperature, high chemical resistance, excellent thermal shock resistance, as well as thermal and electrical conductivity [3]. The strength of MAX phases does not change with temperature, makes them highly attractive for high-temperature applications [3].

Recently much attention has been paid to magnetic MAX phases study. For example, such Mn-based MAX materials as  $Mn_2AlC$  and  $Mn_2SiC$  were investigated in [4],  $Mn_2GaC$  in [5] and [6]. Possibility of synthesis of magnetic Fe-based MAX phases is discussed [7–9], however these are only theoretical works which present the results of *ab initio* calculations. As far as such materials are predicted, it raises an issue of their experimental synthesis and complex investigation.

Thus we suggest applying the magneto-optical ellipsometry technique as an effective instrument for testing magnetic MAX phases. It can be implemented into the technological process of samples synthesis or be used after it both in ultrahigh vacuum and in the air. This is an optical technique which is highly sensitive and at the same time non-destructive which makes it promising for properties control during sample growth.

In the previous work [10] we discussed the case when MAX phases can be considered as bulk magnetic optically-anisotropic structures and reported a full algorithm of magneto-optical ellipsometry data processing.

This time we consider MAX phases as effective thin magnetic optically-anisotropic medium on a substrate. In order to analyse the light reflection, instead of conventional Fresnel coefficients we used reflection coefficients which take into account the sample's optical anisotropy which for MAX phases results in the difference in the components of dielectric permittivity tensor  $\epsilon_{xx} = \epsilon_{yy} \neq \epsilon_{zz}$ . Also the reflection coefficients in this study contained the second term, which corresponds to the magneto-optical contribution and is related to the off-diagonal  $\epsilon_{xy}$  element of dielectric permittivity tensor. In general, we obtained all necessary equations for finding out optical and magneto-optical properties of a thin MAX material on a substrate from spectral magneto-optical ellipsometry data.

*This work was supported by the grant from the Russian Science Foundation No. 21-12-00226, <http://rscf.ru/project/21-12-00226/>.*

1. N.C. Ghosh, S.P. Harimkar, in *Advances in Science and Technology of Mn+1AX<sub>n</sub> Phases*, Woodhead Publishing (2012).
2. X.K. Qian, in *Advances in Science and Technology of Mn+1AX<sub>n</sub> Phases*, Woodhead Publishing (2012).
3. W.K. Pang, I.M. Low, in *Advances in Ceramic Matrix Composites*, Woodhead Publishing (2014).

4. Ahmed Azzouz-Rached, M.A. Hadi, Habib Rached, Tariq Hadji, Djamel Rached, A. Bouhemadou, *Journal of Alloys and Compounds*, **885**, 160998 (2021).
5. S. Lyaschenko, O. Maximova, D. Shevtsov, S. Varnakov, I. Tarasov, U. Wiedwald, J. Rosen, S. Ovchinnikov, M. Farle, *JMMM*, **528**, 167803 (2021)
6. Andris Berzins, Janis Smits, Andrejs Petruhins, Hugo Grube, *Materials Chemistry and Physics*, **272**, 124972 (2021).
7. O.N. Draganyuk, V.S. Zhandun, N.G. Zamkova, *Mater. Chem. Phys.*, **271**, 124897 (2021).
8. O.N. Draganyuk, V.S. Zhandun, *International workshop on the properties of functional MAX-materials (2nd FunMax): Book of Abstracts*, p. 19. (2021).
9. V.S. Zhandun, N.G. Zamkova, O.N. Draganyuk et al., *Phys. Chem. Chem. Phys.*, **23**, Is. 46, 26376–26384 (2021).
10. O.A. Maximova, S.A. Lyaschenko, S.N. Varnakov, S.G. Ovchinnikov, *J. Exp. Theor. Phys.*, **133**, Is. 5, 581–590 (2021).

## STRESS-SENSITIVE MAGNETIC PARAMETERS OF EUTECTOID STEEL WITH DIFFERENT PEARLITE MORFOLOGY

*E.A. Schapova\**, *A.N. Stashkov*, *A.P. Nichipuruk*

M.N. Mikheev Institute of Metal Physics of the Ural Branch of the Russian Academy of Sciences  
(IMP UB RAS), Ekaterinburg, Russia

\*E-mail: [schapova@imp.uran.ru](mailto:schapova@imp.uran.ru)

Pearlitic steels are widely used in manufacture of rails, wire, reinforcement, and other tools [1]. To date, such steels attract much interest because their strength and other mechanical properties have not been fully realized [2–4]. Eutectoid steel with 0.8% carbon also belongs to pearlitic steels. Eutectoid steel is known to have the structure of lamellar or spheroidized pearlite depending on the technological operations performed (heat and thermomechanical treatments). Morphology determines the product properties. Thus, a product with a lamellar pearlite structure has increased strength, but low ductility and high fragility. Moreover, the properties largely depend on the interlamellar spacing. Spheroidized pearlite is characterized by low strength, while high plasticity. The structure of lamellar pearlite often is considered a defect of manufacture and needs special heat treatment to transform to spheroidized pearlite [1]. One of the main issues in research field is connected with stress state evaluation. It is well known that there are magnetic properties sensitive to the stress state. The aim of this research is to estimate the residual compressive stress of eutectoid steel with different pearlite morphology via magnetic parameters.

The experiments were carried out on samples of eutectoid steel with the chemical composition (by weight percent) 0.75–0.84 C; 0.17–0.33 Si; <0.03 P; <0.028 S; <0.2 Cr; <0.25 Ni, and <0.25 Ni. The samples were bars 270 mm long with a 2×3 mm<sup>2</sup> cross-section and with grippers for mechanical testing. The samples were divided into two batches according to the pearlite morphology: with the structures of spheroidized and lamellar pearlite. The lamellar pearlite structure was prepared by heat treatment of steel having a spheroidized pearlite structure under the following conditions: 1050 °C, 3 min → 650 °C, 1 h → air-cooling. The coercive force was measured by the magnetometric method under load. The magnetic incremental permeability was measured by the laboratory set-up before and after the plactical deformation. The description of the laboratory set-up and obtained results are given in [5].

The magnetoelastic fields  $H_e$  were calculated from the field dependences of the magnetic incremental permeability, after that the residual compressive stress was estimated. The minimum in the  $H_c(\sigma)$  dependence upon elastic extension [6] was found to appear in the case of the greatest degree of compensation of residual compressive stress by external tensile stress. This fact was used for estimation. The residual compressive stresses estimated via the magnetoelastic fields and the coercivity were found to be higher for the samples with lamellar pearlite than for the spheroidized pearlite samples with the equal elongations. The results of stress estimation via magnetoelastic field are in a good agreement with the results of X-ray diffraction analysis

*Funding:* The reported study was funded by Ministry of Science and Higher Education of the Russian Federation (theme “Diagnostics”, No. AAAA-A18-118020690196-3) and by RFBR, project number 20-32-90139.

1. C. Borchers and R. Kirchheim, Progress in Material Science, **82**, 405–444 (2016).
2. C. Zheng, L. Li, W. Yang and Z. Sun, Mater. Sci. Eng., A, **558**, 158–161 (2012).
3. J. Toribio, Procedia Structural Integrity, **26**, 360–367 (2020).
4. F. Zhang, Y. Zhao, Y. Tan, X. Ji and S. Xiang, Metals, **9**, 1133 (2019).
5. A.N. Stashkov, E.A. Schapova, S.V. Afanasiev, L.A. Stashkova, A.P. Nichipuruk, J. Magn. Magn. Mater, **546**, 168850 (2022).
6. V.G. Kuleev and T.P. Tsar’kova, Phys. Metals Metallogr., **104**, 461–468 (2007).

## MAGNETIC PROPERTIES OF 3D-PRINTING 09G2S STEEL BEFORE AND AFTER LOW-CYCLE TESTS

*A.N. Stashkov, E.A. Schapova\*, A.P. Nichipuruk*

M.N. Mikheev Institute of Metal Physics of Ural Branch of Russian Academy of Sciences,  
Ekaterinburg, Russia

\*E-mail: [schapova@imp.uran.ru](mailto:schapova@imp.uran.ru)

Recently, steel products manufactured using additive technologies on a 3D laser printer have found increasing use. The properties of such steels are different from steels of the same chemical composition, but made by “traditional” methods (casting, rolling) [1]. The purpose of this investigation was to study the behaviour of the magnetic properties of cast steel 09G2S and steel with the same chemical composition, but made using selective laser melting from the initial powder, before and after low-cycle tests in uniaxial tension.

The studies were carried out on samples of steel 09G2S (0.1% C; 1.5% Mn; <1% Si), made both by casting and on a laser 3D printer EOSINT M 280. Part of the cast samples was annealed at 650 °C for 2 hours, the other part was normalized at 980 °C for 30 minutes. Some 3D samples were annealed at 350 °C for 3 hours to relieve internal stress, other 3D samples were normalized from 980 °C for 30 minutes. Low-cycle tests were carried out according to the “soft” loading scheme. The load was tensile uniaxial, its value was stable throughout all test cycles, but the excess of the yield strength for each of the tested samples was different (from 20 to 70%). Measurements of magnetic properties (coercivity  $H_c$ , remanence  $B_r$ , maximum magnetic permeability  $\mu_{\max}$ ) before and during cyclic tests were carried out at room temperature on a Remagraph C-500 setup (an error of measuring magnetic field of 2%, of induction, 1%). The field dependencies of the incremental magnetic permeability were measured on unique laboratory setup [2].

As a result of the research work, it was found that 09G2S 3D steel after manufacturing on a laser 3D printer has high tensile strength 1057 MPa and low ductility ( $\delta = 6\%$ ), which is not typical for 09G2S steel manufactured using the “traditional” technology. Tests for low-cycle fatigue of such steel (when the yield strength was exceeded) were impossible due to the proximity of the values of the yield strength and strength. Normalization at 980 °C (30 min) reduces the tensile strength of 3D steel 09G2S by 2 times (up to 502 MPa) and increases the relative elongation by almost 6 times ( $\delta = 34.6\%$ ), bringing this steel closer in mechanical properties to cast steel 09G2S.

The main changes in the magnetic properties (coercivity  $H_c$ , remanence  $B_r$ , maximum magnetic permeability  $\mu_{\max}$ ) of both cast and 3D steel are observed at the initial stage of low-cycle tests (number of cycles <10). A further increase in the number of cycles (up to the destruction of the test samples) does not lead to a significant change in the magnetic properties. It is characteristic that, despite the different magnetic properties of undeformed steels, in the end of the low-cycle tests of the values of the magnetic properties of cast and 3D-steel become practically equal. The nature of the change in the magnetoelastic field  $H_{\sigma}$ , determined from the experimental field dependences of the incremental magnetic permeability, during low-cycle tests for cast and 3D steels is fundamentally different: for cast steel, the changes are small and ambiguous, for 3D steel, the changes are more significant and unambiguous (there is an increase in  $H_c$  with an increase in the number of cycles).

*The study was supported by Ministry of Science and Higher Education of the Russian Federation (theme “Diagnostics”, No. AAAA-A18- 118020690196-3) and by Russian Foundation for Basic Research Bel-a, Project number 20-58-00015.*

1. A.P. Nichipuruk, A.N. Stashkov, E.A. Schapova, N.V. Kazantseva and M.V. Makarova, *Fizika tverdogo tela*, **63**, 1719–1724 (2021) [in Russian].
2. A.P. Nichipuruk, A.N. Stashkov, V.G. Kuleev, E.A. Schapova and A.A. Osipov, *Russ. J. Nondestruct. Test*, **53**, 772–778 (2017).



## THE AUTOMATION OF THE SE/X-2544 EPR SPECTROMETER

*D.A. Velikanov*

Kirensky Institute of Physics, Federal Research Center KSC SB RAS, Krasnoyarsk, Russia

E-mail: [dponal@gmail.com](mailto:dponal@gmail.com)

Electron paramagnetic resonance (EPR) spectrometers are used to record the EPR spectra of diverse substances in various states of aggregation: crystals, powders, liquids, and gases. The SE/X-2544 spectrometer by Radiopan (Poznan, Poland) [1] with an operating frequency of 9400 MHz (X-band) is designed to observe and record the first or second derivative of the EPR absorption signal in a wide microwave power range (up to 400 mW) at high-frequency (100 kHz) or low-frequency (80 Hz) modulation of the magnetic field, measuring the number of paramagnetic centers in the test substance, as well as performing temperature studies in a wide temperature range. The distribution geography of the SE/X-2544 EPR spectrometers in Russia is quite extensive. They are operated both in research institutes and national universities [2], such as the Institute of Organic and Physical Chemistry (Kazan), the Ufa Institute of Chemistry, the Institute of Problems of Chemical Physics (Chernogolovka), the Baltic Federal University (Kaliningrad), Institute of Physics (Krasnoyarsk).

This device is widely used in both physicochemical and biomedical research [3, 4]. To display EPR spectra, SE/X-2544 spectrometers are factory-equipped with a built-in plotter, which in practice is not exactly comfortable, especially when conducting a large amount of research. Automation of the measurement process with saving data in electronic form can significantly improve the ergonomics and productivity of scientific research.

Data exchange between an IBM-compatible computer and the spectrometer is carried out using a specialized controller (Fig. 1). The controller is connected to an LPT port operating in the Nibble Mode, in which five status lines are used to enter data into the computer: ERROR, SELECT, PAPER OUT, ACKNLG, BUSY [5]. In this case, the incoming bits occupy positions from D3 to D7 in the information word. Numeric values are calculated in several stages using shift, masking and accumulation operations.

The magnetic field is scanned using the “Field scan unit type CUP-202” block. The control code comes from the controller via a 12-bit bus. The magnetic field strength is measured with a nuclear magnetic resonance (NMR) magnetometer included in the SE/X-2544 EPR spectrometer. The induction value is reflected on the digital indicator of the NMR magnetometer block and transmitted to

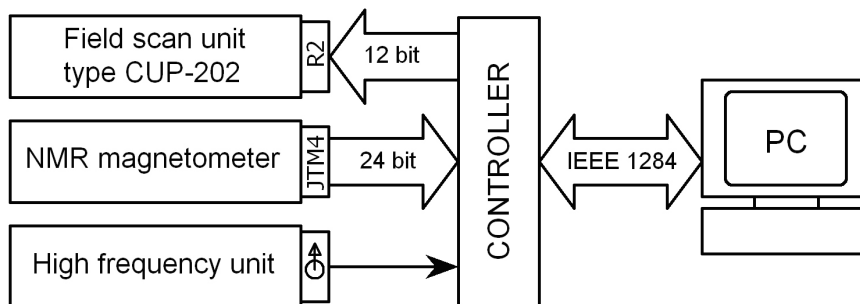


Figure 1. Scheme of data exchange between units of the SE/X-2544 EPR spectrometer and computer.

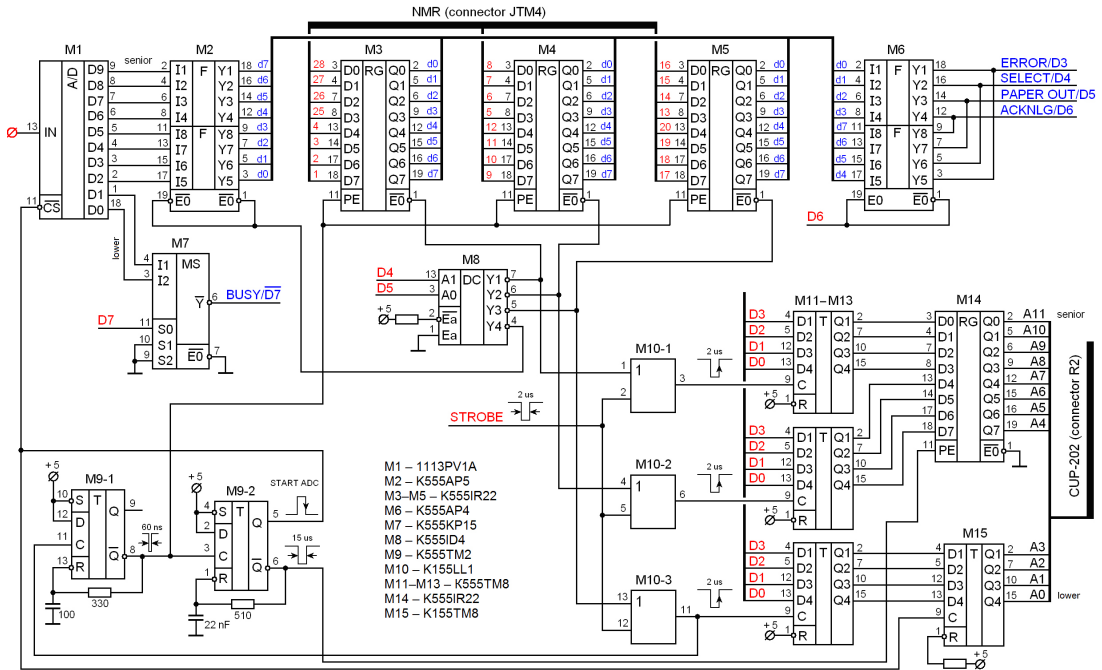


Figure 2. Schematic diagram of the controller.

the controller via a 24-bit bus. The controller also receives an analog signal from the block “High frequency unit”, which carries information about the EPR spectrum. The controller is made of chips of high and medium degree of integration.

Schematic diagram of developed controller is shown in Fig. 2. The 8-bit data bus D0–D7 of the LPT port is used both to transfer the information necessary to ensure the sweep of the magnetic field, and to control the controller when data is entered into the computer. Lines D0–D3 are responsible for the transfer of nibbles of a 12-bit binary number to quad D flip-flops M11–M13. The information is recorded on the positive edge of the clock pulses, which are fed through the STROBE line and distributed in turn between D flip-flops using decoder M8 and 2-input OR gates M10-1, M10-2, M10-3.

A sync pulse from the output of M10-3 starts a single pulse generator based on the D-type flip-flop M9-1, which in turn starts the one-shot M9-2. The first single vibrator is responsible for writing the readings of a 6-digit NMR magnetic induction meter into registers M3–M5. The second one-shot provides simultaneous data transfer from D flip-flops M11–M13 to register M14 and D flip-flop M15 with subsequent fixation of information. The 12-bit binary code formed in this way is fed via the A0–A11 bus to the magnetic field scanner of the EPR spectrometer, where it controls electronic switches that switch the n-2n transformer windings in the field setter [1]. In addition, the single vibrator M9-2 puts the analog-to-digital converter (ADC) M1 into the conversion mode. The high-speed 1113PV1A-type ADC M1 converts the voltage supplied to its input into a 10-bit parallel binary code. The two least bits of the code are fed to the inputs of the multiplexer M7, and all other bits are fed to the inputs of the microchip M2, which contains two four-channel drivers.

Lines D4–D7 of the LPT-port data bus are designed to control the multiplexer M7 and decoder M8 and to activate one by one the 3-states outputs of two drivers in the M6, which are connected

to the LPT-port status bus. In addition to distributing the strobe pulses, the decoder M8 switches the 3-states outputs of the microchips M2–M5 loaded on a common bus, which is connected to the inputs of the drivers of M6. The output of the multiplexer M7 is also connected to the BUSY line of the status bus. Such a circuitry solution makes it possible to transmit multi-bit numbers over buses with a limited number of lines.

The software is written in the DELPHI language. The magnetic field sweep is controlled both in one and in the opposite direction. Several different field scan speeds are available.

*The work was supported by the Russian Science Foundation and the Krasnoyarsk Region Science and Technology Support Fund, grant No. 22-14-20020.*

1. EPR spectrometer SE/X 2544. Instruction manual. Connection diagrams, component list, printed boards views, PDP Radiopan, Polska academia nauk, Poznań, (1986).
2. Magnetic resonance laboratories in Russia 2015–2016, Electronic resource URL: [http://cmr.spbu.ru/wp-content/uploads/Booklets/MR\\_laboratories\\_in\\_Russia\\_2015-2016.pdf](http://cmr.spbu.ru/wp-content/uploads/Booklets/MR_laboratories_in_Russia_2015-2016.pdf)
3. N.P. Piven, G.V. Simbirtseva, A.A. Arbuzov, D.P. Kiryukhin, S.D. Babenko, High Energy Chemistry, **53**, 6, 498 (2019) [in Russian].
4. R.K. Kadyrov, Bulletin of modern clinical medicine, **5**, 3, 15 (2012) [in Russian].
5. V.G. Solomenchuk, Hardware of personal computers, BHV-Petersburg, St. Petersburg (2003) [in Russian].

Section O.  
**MAX materials**

---

## HIGH TEMPERATURE PERFORMANCE EVOLUTION IN $(\text{Cr}_{1-x}\text{Mn}_x)_2\text{AlC}$ MAX-PHASE UPON MANGANESE DOPING

*K.V. Sobolev*<sup>1\*</sup>, *M.V. Gorshenkov*<sup>2</sup>, *V.V. Rodionova*<sup>1</sup>

<sup>1</sup>Immanuel Kant Baltic Federal University, IKBFU, Kaliningrad, Russia

<sup>2</sup>National University of Science and Technology “MISiS”, Moscow, Russia

\*E-mail: [Ksobolev1@kantiana.ru](mailto:Ksobolev1@kantiana.ru)

MAX-phases are the family of nano-lamellar compounds with the shared chemical formula  $\text{M}_{n+1}\text{AX}_n$ , where M is an early transition metal, A is a main group element (mostly of groups 13–15) and X is either C or N. MAX-phases possess the combination of the characteristic properties of both, metals and ceramics; MAX-phases are highly electrically and thermally conductive, elastically stiff and machinable like metals. At the same time, they are withstanding high temperatures, tolerant to high-temperature corrosion and harsh environments, like ceramics. Such an outstanding set of properties originates from the unique atomically layered crystal structure, consisting of al-

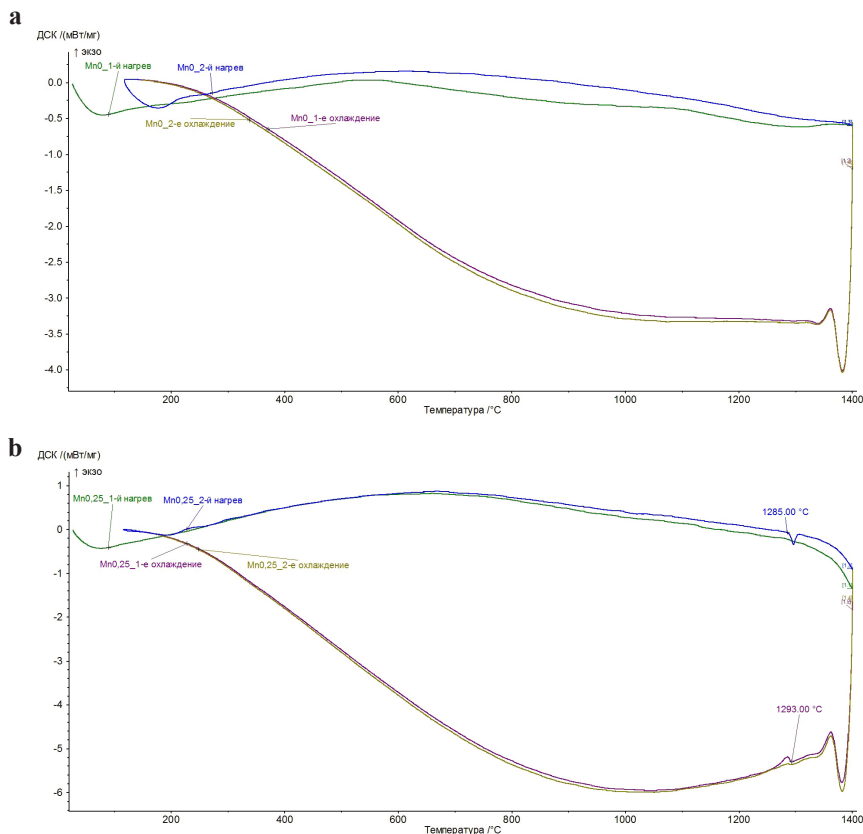


Figure 1. DSC curves for  $(\text{Cr}_{1-x}\text{Mn}_x)_2\text{AlC}$  MAX-phase samples with  $x = 0$  (a) and 15 at.% (b).

ternating layers of M6X octahedra and A atoms (space group  $P63/mmc$ ) [1]. Hence, MAX-phases are considered for a plethora of practical applications, from chemically stable electrical contacts to protective and shielding coatings, especially for high-temperature applications [2].

One of the promising MAX-phase compositions is  $(\text{Cr}_{1-x}\text{Mn}_x)_2\text{AlC}$ . This MAX-phase is of high interest not only due to its possible magnetic long-range order but also due to the ability to tune its properties by varying the Mn doping level [3]. Recently the synthesis approach to produce highly-doped phase-pure  $(\text{Cr}_{1-x}\text{Mn}_x)_2\text{AlC}$  MAX-phase powders was proposed [4]. Poor incorporation of Mn atoms into the crystal structure of  $(\text{Cr}_{1-x}\text{Mn}_x)_2\text{AlC}$  MAX-phase, accompanied by the dramatic worsening of its phase content (segregation of the parasite phases) has been the main problem, associated with this compound, for the long time [5]. However, highly-doped phase-pure synthesis is available now only for powder samples [4], while bulks can be higher applicable in the number of practical cases. To compress MAX-phase powders to bulks high temperature methods are required, like spark plasma sintering (SPS) [6]. Attempts to sinter  $(\text{Cr}_{1-x}\text{Mn}_x)_2\text{AlC}$  MAX-phase powders into bulks suffer from the growth of secondary phases in Mn-containing compounds. It was proposed that  $(\text{Cr}_{1-x}\text{Mn}_x)_2\text{AlC}$  MAX-phase becomes less stable with temperature upon the increment of the Mn doping level. It is necessary to study high temperature performance of this compound and its evolution with Mn concentration raise, as one of the most promising advantages of MAX-phases is their stability in the elevated temperature regime.

In the current study the degradation of  $(\text{Cr}_{1-x}\text{Mn}_x)_2\text{AlC}$  MAX-phase powders with  $x = 0\text{--}15$  at.% at high temperatures is illustrated by the results of their sintering using SPS protocol, previously described for the parental  $\text{Cr}_2\text{AlC}$  compound [6]. The pellets, obtained after SPS, were examined by SEM-EDX analysis. We observed the clear trend on the segregation of secondary phases in the samples with the higher Mn content. Afterwards, we studied  $(\text{Cr}_{1-x}\text{Mn}_x)_2\text{AlC}$  MAX-phase powder samples using DSC, XRD and TEM. The results of the DSC, obtained for  $(\text{Cr}_{1-x}\text{Mn}_x)_2\text{AlC}$  MAX-phase samples with  $x = 0$  and 15 at.%, are illustrated in Fig. 1. We observed that for the highest doped sample (with  $x = 15$  at.%) the reproducible peak at DSC curve around 1290 °C appears when cooling the sample and heating it for the second time. The peak cannot be seen at the curves, corresponding to  $\text{Cr}_2\text{AlC}$ , in the whole studied temperature range up to 1400 °C. Based on the results of XRD we associated this peak with the structural transformation of  $(\text{Cr}_{0.85}\text{Mn}_{0.15})_2\text{AlC}$  MAX-phase. Thus, we not only studied the high temperature performance in  $(\text{Cr}_{1-x}\text{Mn}_x)_2\text{AlC}$  MAX-phases upon Mn doping, but also collected the data, required to optimize current densification approaches (like SPS), which is of the significant value for the future studies.

1. M.W. Barsoum, Prog. Solid. State Ch., **28**(1-4), 201–281 (2000).
2. M. Sokol, V. Natsu, S. Kota and M.W. Barsoum, Trends in Chem., **1**(2), 210–223 (2019).
3. M. Dahlqvist, B. Alling, I. A. Abrikosov and J. Rosen, Phys. Rev. B, **84**(2), 220403 (2011).
4. K. Sobolev, H. Pazniak, M. Farle, V. Rodionova, U. Wiedwald, J. Mater. Chem. C, **9**(46), 16516–16522, (2021).
5. C.M. Hamm, J. D. Bocarsly, G. Seward, U.I. Kramm and C.S. Birkel, J. Mater. Chem. C, **23**(5), 5700–5708 (2017).
6. K. Sobolev, M. Gorshenkov, P. Manfrinetti, D. Peddis, A. Pazniak, V. Rodionova, Ceram. Int., **47**(15), 21069–21076 (2021).

## THE FORMATION OF FERROMAGNETIC ORDER IN THE Fe-DOPED MAX PHASE $Mn_2GaC$

*O.N. Draganyuk<sup>1\*</sup>, N.G. Zamkova<sup>1,2</sup>, V.S. Zhandun<sup>1</sup>*

<sup>1</sup>Kirensky Institute of Physics, Federal Research Center KSC SB RAS, Krasnoyarsk, Russia

<sup>2</sup>Siberian Federal University, Krasnoyarsk, Russia

\*E-mail: [dron060694@mail.ru](mailto:dron060694@mail.ru)

First-principle study of the functional materials makes it possible to predict the existence of new materials with promising properties. This allows to reduce research costs and to provide some recommendations regarding promising compositions and synthesis conditions to experimenters. MAX phases of  $Mn_2AX$  [1] are atomic layered materials where M is a transition metal, A is an A-group element, and X is carbon and/or nitrogen. MAX phases are actively used in spintronic and magnetic cooling devices. Recently much attention has been paid to the study of magnetic MAX phases, including those based on the Fe and Mn atoms.

The antiferromagnetic MAX phase of  $Mn_2GaC$  was experimentally synthesized [2] and the theoretical study [3] showed that the ferromagnetic and antiferromagnetic states of  $Mn_2GaC$  are energetically very close. Within the framework of DFT+GGA, the effect of the substitution of the Mn and Ga atoms in  $Mn_2GaC$  by Fe atoms has been studied and the stability of the obtained alloys has been calculated. The compound has been found to be stable (Fig. 1) aniferromagnet with 12.5% of the Mn atoms in the M-site being replaced by Fe atoms. While 25% substitution of the Mn atoms by Fe atoms makes it metastable.

The substitution of 12.5% Ga atoms in the A site by Fe atoms leads to the intriguing finding, namely, the formation of ferromagnetic order in the alloy is observed. Large values of the magnetic moment on the Fe and Mn atoms have been found to be equal to 2.8  $\mu_B$ , 1.7  $\mu_B$ , respectively. The compound  $Mn_2Fe_{0.125}Ga_{0.875}C$  is stable ferromagnetic and a promising candidate for synthesis and further practical applications. The further increasing in the Fe concentration results in increase of the magnetic moments. However, the MAX phase with the large Fe concentration at A-site has been shown to be unstable.

The temperature dependence of the magnetization for  $Mn_2GaC$  and  $Mn_2Fe_{0.125}Ga_{0.875}C$  has been obtained by Monte-Carlo method to estimate effect of Fe doping on the Curie temperature. As seen,  $Mn_2Fe_{0.125}Ga_{0.875}C$  has been shown to have the larger value of Curie temperature.

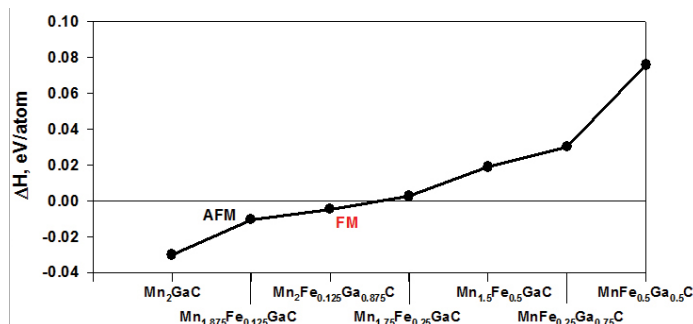


Figure 1. Dependence of the enthalpy of formation on the composition of the MAX phase.

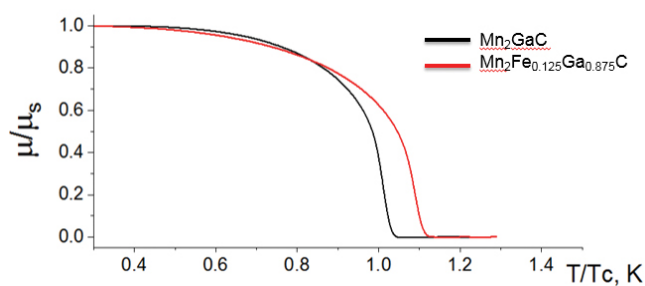


Figure 2. The temperature dependence of the magnetization of the MAX phase.  $\mu_s$  is magnetization at zero temperature,  $T_c$  is the Curie temperature of  $\text{Mn}_2\text{GaC}$  equal to 760 K.

*The reported study was funded by Russian Foundation for Basic Research, Government of Krasnoyarsk Territory, Krasnoyarsk Regional Fund of Science to the research project № 20-42-240004: “The effect of the composition, pressure, and dimension on the magnetic, electronic, optical, and elastic properties of the magnetic  $M_{n+1}AX_n$  ( $M = \text{Cr}, \text{Mn}; \text{Fe}, A = \text{Al}, \text{Ga}, \text{Si}, \text{Ge}, \text{P}, \text{In}; X = \text{C}, \text{N}; n = 1-3$ ) MAX-phases”. Participation in the Conference was funded by the Krasnoyarsk Regional Fund of Support of Scientific and Scientific-Technical Activities.*

1. M. Sokol, V. Natsu, S. Kota and M.W. Barsoum, Trends in Chemistry, **1** (2), 210–223 (2019).
2. A.S. Ingason, A. Petruhins, M. Dahlqvist, A. Mockute, B. Alling, L. Hultman, I.A. Abrikosov, P.O.A. Persson & J. Rosen, Materials Research Letter, **2**, 89–93 (2014).
3. V.S. Zhandun, N.G. Zamkova, O.N. Draganyuk, A.S. Shinkorenko, U. Wiedwald, S.G. Ovchinnikov and M. Farle, Phys. Chem. Chem. Phys., **23**, 26376–26384 (2021).



## AUGER ELECTRON SPECTROSCOPY OF THE Cr-Mn BASE MAX-PHASE SURFACE

*T.A. Andryushchenko*<sup>1\*</sup>, *S.A. Lyaschenko*<sup>1</sup>, *S.N. Varnakov*<sup>1</sup>, *U. Wiedwald*<sup>2</sup>, *M. Farle*<sup>2</sup>

<sup>1</sup>Kirensky Institute of Physics SB RAS, Krasnoyarsk, Russia

<sup>2</sup>Faculty of Physics, University of Duisburg-Essen, Duisburg, Germany

\*E-mail: [tanya.andryuchshenko@mail.ru](mailto:tanya.andryuchshenko@mail.ru)

MAX-phases are  $M_{n+1}AX_n$  ( $n = 1, 2, 3$ ) compounds which have nanolayered structure where layers of transition metals  $M$  carbides or nitrides ( $X = C$  or  $N$ ) alternate with layers of elements of XIII–XV groups in the periodic table ( $A = Al, Ge, Si, \text{etc.}$ ). This class of materials has many useful properties, such as stability at high temperatures [1], for example. This makes it possible to use these materials as the basis for thermostable coatings or details for many other purposes. But the main research at the present time is based on the synthesis of magnetic MAX-materials and the study of their properties [2].

The Auger electron spectra of MAX-phases can be used for its in-situ identification in the synthesis processes. In this work we describe the results of the Auger electron spectroscopy analysis of different thicknesses  $(Cr_{0.5}Mn_{0.5})_2GaC$  thin films on MgO (111) substrate [3].

The Auger electron spectra were measured using a low energy diffraction and Auger electron analysis system ErLEED 100 by SPECS with a retarding field energy analyzer. The primary electron energy was 3000 eV.

The Auger spectra of  $(Cr_{0.5}Mn_{0.5})_2GaC$  has changed during thermal annealing and ion etching. Figure 1 shows the Auger spectra of 10 nm  $(Cr_{0.5}Mn_{0.5})_2GaC$  thin film on MgO (111) substrate.

Temperature annealing makes it possible to eliminate the contribution of Auger electrons of adsorbed on the thin film surface carbon, after which the Auger signal describes the contribution of carbon atoms in the  $(Cr_{0.5}Mn_{0.5})_2GaC$  composition.

The intensity of the oxygen Auger peaks increases after thermal annealing and ion etching, which may be due to an increase of the substrate atoms Auger signal with a decrease of the thin film thickness.

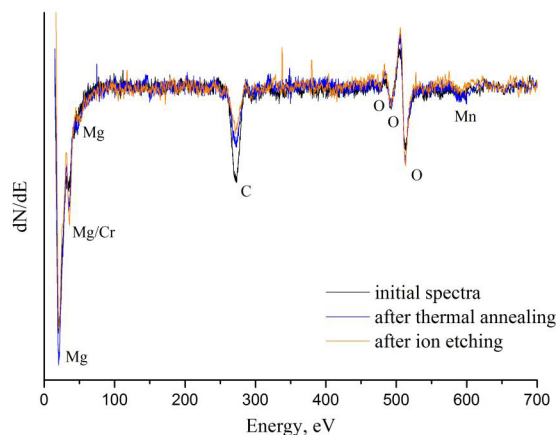


Figure 1. The Auger electron spectra of 10 nm  $(Cr_{0.5}Mn_{0.5})_2GaC$  thin film on MgO (111) substrate.

The Auger peaks of chromium atoms are difficult to distinguish against the peaks of magnesium atoms due to their low intensity (the energy of chromium Auger peak is 36 eV, Mg – 32 eV [4], experimental peak – 35 eV). The Auger peaks of manganese and oxygen are also located in the same energy region and are difficult to distinguish.

The results demonstrate the change in the spectra during the experiment and can be used for in-situ identification of the MAX-phases in synthesis processes.

*Sample synthesis was supported by the government of the Russian Federation (agreement No. 075-15-2019-1886). Measurements and analysis of samples were supported by the Russian Science Foundation (grant #21-12-00226, <http://rscf.ru/project/21-12-00226/>).*

1. M. Barsoum and T. El-Raghy, *Am. Sci.*, **89**, 334–343 (2001).
2. R. Salikhov, A.S. Semisalova, A. Petruhins, A.S. Ingason, J. Rosen, U. Wiedwald and M. Farle, *Materials Research Letters*, **3**(3), 156–160 (2015).
3. I.P. Novoselova, A. Petruhins, U. Wiedwald, D. Weller, J. Rosen, M. Farle and R. Salikhov, *Materials Research Letters*, **7**(4), 159–163 (2019).
4. L.E. Davis, N.C. MacDonald, P.W. Palmberg, G.E. Riach and R.E. Weber, *Handbook of Auger Electron Spectroscopy*, Physical Electronics, Minnesota (1976).

OPTICAL AND MAGNETOOPTICAL SPECTROSCOPY  
OF Mn-Cr BASED MAX-PHASES

*S.A. Lyaschenko*<sup>1\*</sup>, *O.A. Maximova*<sup>1,2</sup>, *S.G. Ovchinnikov*<sup>1,2</sup>, *S.N. Varnakov*<sup>1</sup>, *T.A. Andryushchenko*<sup>1</sup>,  
*D.V. Shevtsov*<sup>1</sup>, *U. Wiedwald*<sup>3</sup>, *M. Farle*<sup>3</sup>

<sup>1</sup>Kirensky Institute of Physics SB RAS, Krasnoyarsk, Russia

<sup>2</sup>Siberian Federal University, Krasnoyarsk, Russia

<sup>3</sup>Faculty of Physics, University of Duisburg-Essen, Duisburg, Germany

\*E-mail: [lsa@iph.krasn.ru](mailto:lsa@iph.krasn.ru)

MAX-materials are anisotropic atomic-layered structures in which layers of transition metal M carbides/nitrides ( $X = C$  or  $N$ ) alternate with layers of elements of groups XIII–XV of the periodic table ( $A = Al, Ga, Ge, Si, \text{etc.}$ ). The antiferromagnetic and weak ferromagnetic properties of atomic layered MAX materials based on Cr, Mn and Fe are very interesting for new spintronics devices and magnetically controlled coatings. Recently, new epitaxial magnetic MAX phases  $Mn_2GaC$  and  $(Cr_{0.5}Mn_{0.5})_2GaC$  on  $MgO(111)$  substrates have been synthesized [1, 2]. Epitaxial MAX phases of the  $(Cr,Mn)_2GeC$  system [3] on  $Al_2O_3(0001)$  and  $MgO(111)$  substrates are also known for which the mechanisms of the effect of chromium-manganese replacement on magnetic, structural and mechanical properties are investigated. These materials are also of interest for the analysis of changes in the electronic structure of atomic-layered samples during substitutions in the Cr-Mn system [4].

Optical spectroscopy is a promising method for the analysis of epitaxial thin magnetic films. However, its application for electronic structure analysis is limited due to the strong optical and magnetic anisotropy of the epitaxial MAX phase and the presence of a passivating oxide film.

In the presented work, we performed optical, magneto-optical, and electron spectroscopic analysis of the surface of  $(Cr_{0.5}Mn_{0.5})_2GaC$  and  $Cr_2GeC$  films of different thicknesses. We used spectral ellipsometry, the magneto-optical Kerr effect, and Auger-electron spectroscopy both before and after the etching of the oxide film with argon ions. Spectral ellipsometry was performed at various angles of incidence to identify the optical anisotropy of the films. The magneto-optical Kerr effect was measured in the transversal configuration with magnetization in the film plane.

As a result, we found the dependence of the electronic structure and optical properties of  $(Cr_{0.5}Mn_{0.5})_2GaC$  and  $Cr_2GeC$  thin films on thickness. We measured the optical properties of natural oxide films on the studied samples. Analysis of the temperature dependence of the spectral optical properties of MAX films in air allowed us to reveal the temperature of complete destruction of the structure of  $(Cr_{0.5}Mn_{0.5})_2GaC$  films.

*The synthesis of  $(Cr_{0.5}Mn_{0.5})_2GaC$  samples was supported by the government of the Russian Federation (agreement #075-15-2019-1886). This research was supported by the Russian Science Foundation (grant #21-12-00226, <http://rscf.ru/project/21-12-00226/>).*

1. A.S. Ingason, A. Petruhins, M. Dahlqvist, F. Magnus, A. Mockute, B. Alling, L. Hultman, I.A. Abrikosov, P.O.A. Persson & J. Rosen, *Materials Research Letters*, **2**(2), 89–93 (2014).
2. I.P. Novoselova, A. Petruhins, U. Wiedwald, D. Weller, J. Rosen, M. Farle and R. Salikhov, *Materials Research Letters*, **7**(4), 159–163 (2019).
3. A.S. Ingason, M. Dahlqvist and J. Rosen, *J. Phys.: Condens. Matter*, **28**, 433003 (2016).
4. I.P. Novoselova, A. Petruhins, U. Wiedwald, A.S. Ingason, T. Hase, F. Magnus, V. Kapaklis, J. Palisaitis, M. Spasova, M. Farle, J. Rosen & R. Salikhov, *Scientific Reports*, **8**, 2637 (2018).

## UHV SYSTEM FOR PRODUCING AND STUDYING OF MAX PHASES BY IN SITU SPECTRAL MAGNETO-OPTICAL ELLIPSOMETRY IN A WIDE TEMPERATURE RANGE

*D.V. Shevtsov<sup>1\*</sup>, S.A. Lyaschenko<sup>1</sup>, S.N. Varnakov<sup>1</sup>, S.G. Ovchinnikov<sup>1,2</sup>, O.A. Maximova<sup>1,2</sup>*

<sup>1</sup>Kirensky Institute of Physics SB RAS, Krasnoyarsk, Russia

<sup>2</sup>Siberian Federal University, Krasnoyarsk, Russia

\*E-mail: [snowman-82@mail.ru](mailto:snowman-82@mail.ru)

In recent years, researchers have been trying to create various new nanostructures with the required properties using various technologies. Layered structures “ferromagnetic metal/semiconductor”, where Fe, Co, Ni, Mn can be used as metal, and Si, Ge can be used as semiconductor layers, are a good example of new materials. MAX phases are also of great interest nowadays due to unusual combinations of chemical, physical, electrical and mechanical properties, a special layered structure and a unique combination of the most demanded properties of metal and ceramics [1].

In these structures, it is important to pay attention to the formation, composition and properties of interlayer interfaces. However, not only the properties of the final structure are of interest, but also diagnosing materials in the process of their creation, which would make it possible to obtain structures with the desired characteristics, to synthesize nanomaterials with composition, structure,

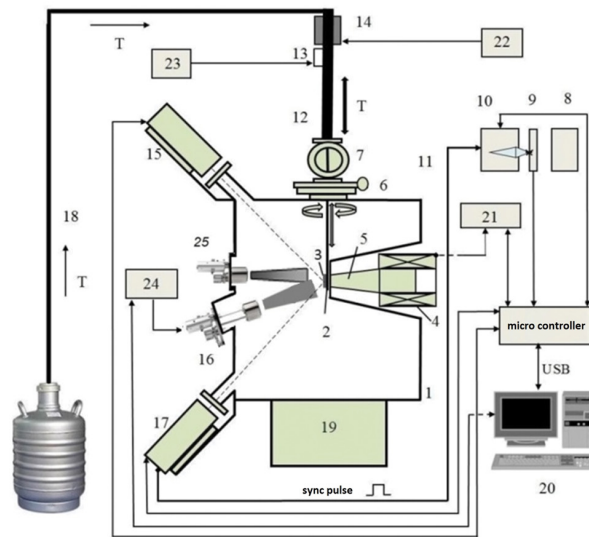


Figure 1. A block diagram of the ultrahigh-vacuum multifunctional apparatus: (1) vacuum chamber; (2) rod with the sample holder; (3) investigated sample; (4) electromagnet; (5) magnetic circuit; (6) slide gate; (7) lock chamber for sample recharging; (8) light source; (9) light chopper; (10) monochromator; (11) light guide; (12) linear bellows translator; (13) vacuum bellows three-degree-of-freedom manipulator; (14) flow-type evaporator–heater; (15) analyzer unit; (16) molecular source; (17) polarizer unit; (18) nitrogen supply system; (19) magnetic-discharge pump; (20) computer; (21) magnet power-supply unit; (22) flow-type heater power-supply unit; (23) sample-heater power-supply unit; (24) evaporator power-supply unit; (25) evaporator.

and properties controlled at the atomic and subatomic levels. The reflective spectral ellipsometry, being a non-destructive *in situ* method of surface analysis, is well suited for diagnostics [2–4]. This polarization optical technique allows one to obtain quantitative information about the structure and morphology of the surface of the sample under study, to find out its spectral optical and magneto-optical parameters directly during the formation of the structure, and to perform magneto-optical analysis of thin films when placing a ferromagnetic sample into an external magnetic field.

The ultra-high-vacuum setup is described in Fig. 1, which implements the joint use of ellipsometric measuring equipment and methods for setting the sample temperature with the application of an external magnetic field of a given value to it [5, 6].

The “ferromagnet/dielectric/semiconductor” structure was used to demonstrate the possibilities of the created ultrahigh-vacuum complex, i.e. to synthesize ferromagnetic nanostructures on the substrate surface with *in situ* non-destructive ellipsometric control and to carry out *in situ* studies of the obtained nanostructure by magneto-ellipsometry in the temperature range 85–1005 K in a single technological cycle.

The installation of additional sources of electron-beam evaporation will open up the possibility of synthesizing the Max-phases and carrying out *in situ* non-destructive analysis of the obtained structures by means of spectral-ellipsometric measurements and measurements of the surface Kerr effect in a wide temperature range.

*The work was supported by Scientific Grant No. 075-15-2019-1886 of the Government of the Russian Federation and by the Russian Science Foundation (grant no. 21-12-00226, <http://rscf.ru/project/21-12-00226/>).*

1. M.W. Barsoum, T. E-Raghy, Amer. Sci., **89**, 4, 336–345 (2001).
2. O.A. Maximova, N.N. Kosyrev, S.N. Varnakov, S.A. Lyaschenko, I.A. Yakovlev, I.A. Tarasov, D.V. Shevtsov, O.M. Maximova, S.G. Ovchinnikov, “In Situ Magneto-optical Ellipsometry Data Analysis For Films Growth Control”, Journal Of Magnetism And Magnetic Materials. Volume 440, 15 October 2017, Pages 196–198.
3. O.A. Maximova, *In situ* magneto-optical ellipsometry data analysis for films growth control / O.A. Maximova, N.N. Kosyrev, S.N. Varnakov, S.A. Lyaschenko, I.A. Yakovlev, I.A. Tarasov, D.V. Shevtsov, O.M. Maximova, S.G. Ovchinnikov, Journal of Magnetism and Magnetic Materials, **440**, 196–198 (2017).
4. O. Maximova, N. Kosyrev, I. Yakovlev, D. Shevtsov, S. Lyaschenko, S. Varnakov, S. Ovchinnikov, Magneto-ellipsometry as a powerful technique for investigating magneto-optical structures properties, Journal of Magnetism and Magnetic Materials, **440**, 153–156 (2017).
5. D.V. Shevtsov, S.A. Lyaschenko and S.N. Varnakov. An Ultrahigh-Vacuum Multifunctional Apparatus for Synthesis and *in situ* Investigation of Low Dimensional Structures by Spectral Magnetoellipsometry in the Temperature Range of 85–900 K, Instruments and Experimental Techniques, **60**, no. 5, 759–763 (2017).
6. D.V. Shevtsov, S.A. Lyaschenko and S.N. Varnakov, “Ultrahigh Vacuum Holder-positioner For *In situ* Studies Of Conductive Nanostructures In A Wide Temperature Range”, IOP Conference Series: Materials Science And Engineering, **155**, no. 1, 012028 (2016).

# SPONSORS

---

MTEON LIMITED

ЭМТИОН

ЭМТИОН - это российская компания, специализирующаяся на производстве и поставках аналитического и технологического оборудования.

Ведущие специалисты компании имеют 15-летний опыт работы в области приборостроения. ЭМТИОН может предложить Заказчикам как отдельные конкурентные решения, так и комплексное оснащение лабораторий, начиная с этапов проработки концепции и предпроектных работ и заканчивая вводом оборудования в эксплуатацию.

## Атомно-силовая микроскопия



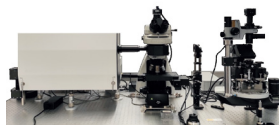
Поддержка всех существующих методик измерений (атомно-силовая микроскопия, магнитно-силовая микроскопия, электро-силовая микроскопия, силовая микроскопия пьезоотклика, измерения в вакууме, в жидкости, электрохимических средах и др.)

Прыжковая микроскопия для количественного нано-механического анализа

Диапазон сканирования 100x100x10 мкм

Разрешение по оси Z - 0,05 нм

## Комбинированные АСМ – Раман системы



Одновременные исследования образцов методами сканирующей зондовой микроскопии и конфокальной микроскопии/ спектроскопии комбинационного рассеяния (Раман)

Зондово-усиленная Рамановская/ флуоресцентная спектроскопия (TERS, EFS5, TERFS)

Одновременное использование до 5-ти лазеров, полная автоматизация

Быстрое сканирование (1000x1000 точек за 3 сек.)

## Конфокальная Рамановская микроскопия



Два автоматически переключаемых лазера в видимом диапазоне длин волн

Пространственное разрешение по XY 390 нм (при использовании лазера 473 нм, 100x, NA 0.95)

Спектральный диапазон 400-1100 нм

Спектральное разрешение 0.25 см<sup>-1</sup> (решётка 75 штр/мм Эшелле и лазер 532 нм)

Регулируемый пинхол

## Электронная микроскопия



Термоэмиссионный катод / катод типа Шоттки

Ускоряющее напряжение 0.1 - 30 кВ

Увеличение от 6 до 1 000 000X

Разрешение до 1 нм

Моторизованный по 5-ти осям предметный столик

Опции низкого вакуума и низкого ускоряющего напряжения

Система энергодисперсионного микроанализа

Широкий выбор дополнительных детекторов

## Оптическая микроскопия



Реализация режимов работы в светлом и темном поле, эпифлуоресценции, поляризации, дифференциально-интерференционного контраста. Доступные объективы 10x, 20x, 40x, 50x, 100x, 150x

Моторизованная турель для установки до бти объективов

Размер исследуемых образцов до 300мм в диаметре

Светодиодные широкополосные осветители

## Рентгеновские дифрактометры



Порошковые и монокристалльные дифрактометры

Высокопроизводительные детекторы Mythen (Швейцария)

Вращение образца на 360°

Диапазон сканирования -110°/161°

Минимальный шаг сканирования 0,0001°

Автосменщик образцов 6/8шт

Нагрев от -196°С до 1600°С

Опции для измерения тонких пленок

База данных спектров, программа обработки спектров Jade, совместимость с ПО заказчика

# Author Index

- Abdinov, D.S. 67  
 Abdullin, A.F. 72  
 Abramova, G. 79  
 Abuev, Ya.K. 21  
 Adanakova, O.A. 240  
 Ageev, V.P. 444, 448  
 Akramov, D.F. 19  
 Aksenov, O.I. 200  
 Aksenov, S.V. 153, 164  
 Alam, J. 188  
 Alekhina, Yu.A. 250, 283, 415  
 Aliev, I.M. 322  
 Aliev, A.M. 301  
 Alsafi, Haneen M. 181, 206  
 Ambarov, A.V. 378, 392  
 Amirov, A.A. 283, 301  
 Andreev, A.V. 175  
 Andreev, N. 107, 269  
 Andreev, S.V. 211, 220, 235, 260  
 Andriushchenko, P.D. 11  
 Andryushchenko, T.A. 482, 484  
 Anikieva, Yu.A. 185  
 Anikin, A.A. 435  
 Antipova, V.N. 283, 427  
 Aplesnin, S.S. 294, 335  
 Arauzo, A. 61  
 Aronin, A.S. 200  
 Arutyunov, K.Yu. 142  
 Arzhnikov, A.K. 72  
 Astapovich, K.A. 250  
 Ataeva, G.Ya. 21  
 Avtandilyan, A.A. 135  
 Azarevich, A. 78  
  
 Babaev, A.B. 21  
 Babaev, M.A. 21  
 Babkin, S.S. 155  
 Badelin, A.G. 67, 82, 310  
 Baidak, S.T. 342  
 Baisheva, A.H. 6  
  
 Bajukov, O. 79  
 Bakhteeva, Iu.A. 429  
 Bakurskiy, S. 133, 137, 151  
 Balaev, D.A. 125, 179  
 Balymov, K.G. 327  
 Bannikov, M.I. 84  
 Baraban, I. 269  
 Baranov, N.V. 110, 167, 222, 237  
 Bartolomé, J. 61  
 Batulin, R.G. 10, 15, 22, 29, 42, 156  
 Bazarov, V.V. 308  
 Bebenin, N.G. 374  
 Begishev, E.M. 308  
 Begunovich, L.V. 134, 208  
 Belodedov, M.V. 417  
 Belov, A.A. 245  
 Belov, I.V. 305  
 Belskaya, N. 98, 100  
 Belyaev, K.A. 142  
 Belykh, S.S. 380  
 Belzig, W. 138  
 Berdiev, U.T. 275  
 Bezmaternykh, L.N. 2, 25  
 Bobkov, A.M. 128, 131, 138, 157  
 Bobkov, G.A. 131, 157  
 Bobkova, I.V. 128, 131, 138, 157, 173  
 Bobrovskii, S.Y. 239  
 Boehm, M. 79  
 Bogach, A. 78  
 Boian, V. 133  
 Bokov, A.V. 93  
 Borichok, V.V. 343  
 Borin, D.Yu. 398  
 Borisova, P.A. 181  
 Borov, D. 270  
 Borus, A.A. 27, 61  
 Bovina, A.F. 25  
 Buchelnikov, V.D. 117  
 Bukreev, D.A. 217, 209  
 Burdin, D.A. 313, 325, 343



- Burkhovetskiy, V.V. 294  
 Burmistrov, I.S. 155  
 Bykov, A.I. 183  
 Byzov, I.V. 429
- Camp, P.J. 352  
 Chareev, D. 140  
 Charikova, T.B. 340  
 Charnaya, E.V. 225  
 Chashin, D.V. 313, 325, 343  
 Chausov, F.F. 4  
 Chekanova, E.A. 194  
 Chen, Y.S. 192  
 Chen, Ying-Zhen 424  
 Cherepanova, A.S. 211  
 Cherkasova, N.A. 213, 271  
 Chernichenko, A.V. 107  
 Chernykh, I.A. 305  
 Cherosov, M.A. 22, 29, 42, 156, 347  
 Chesnokov, M.A. 40, 43  
 Chibirev, A.O. 84  
 Chichkov, V.I. 107  
 Chikurov, D. 100  
 Chirikov, D.N. 382  
 Chtchelkatchev, N.M. 74, 93  
 Chumakov, N.K. 305  
 Chupakhina, T.I. 15, 56, 122, 347  
 Churyukanova, M.N. 17  
 Constantinian, K.Y. 331
- Danilov, G.E. 462, 464  
 Davydov, D.I. 433  
 Deeva, Yu.A. 56, 122, 347  
 Demidenko, O.F. 190, 275  
 Deminov, R.G. 159  
 Demishev, S. 78  
 Denisov, A. 133  
 Denisova, E.A. 194  
 Derevyanko, M.S. 209, 217  
 Derzhavin, I.M. 82, 310  
 Diep, H.T. 6  
 Dikansky, Yu.I. 358  
 Dmitrieva, N.V. 233  
 Dmitryevskaya, D.I. 361  
 Dobroserdova, A.B. 353  
 Dobyshcheva, L.V. 4, 72  
 Doludenko, I.M. 226  
 Draganyuk, O.N. 480
- Driagina, A.E. 202  
 Drozdov, A.S. 358  
 Dudnikov, V.A. 87  
 Dzebisashvili, D.M. 20
- Edelman, I.S. 424  
 Efremova, M.V. 450  
 Ekonomov, N.A. 325, 343  
 Elfimova, E.A. 360, 378, 385, 392, 400, 411  
 Elmanov, G.N. 17  
 Eremin, E.V. 2, 25, 312, 320, 345  
 Eremin, M.V. 65, 289  
 Eremina, R.M. 15, 56, 67, 91, 122, 347  
 Ershov, N.V. 405  
 Estemirova, S.Kh. 67, 82  
 Evstigneeva, S.A. 466, 468  
 Ezhov, I.V. 433  
 Ezubchenko, I.S. 305
- Farle, M. 482, 484  
 Fedoseev, A.D. 153, 164  
 Fedulov, F.A. 313, 316  
 Feshenko, A.A. 327  
 Fetisov, L.Y. 313, 316  
 Fetisov, Y.K. 313, 325, 343  
 Filinkova, M.S. 429  
 Filipov, V. 78  
 Filippov, A.V. 183  
 Flachbart, K. 78  
 Fraerman, A.A. 389  
 Freydmann, A.L. 312, 318  
 Fridman, Yu.A. 85  
 Fuks, A.A. 200  
 Fursova, V.V. 380
- Gabadulin, D.Z. 156  
 Gabani, S. 78  
 Gaifullin, R.R. 159  
 Galakhov, V.R. 53, 69  
 Galanova, S.V. 183  
 Galays, A.I. 335  
 Galechian, G.Yu. 431  
 Gareev, K.G. 185  
 Garig'yanov, N.N. 84  
 Gaviko, V.S. 231, 243, 253  
 Gavrichkov, V.A. 108  
 GavriloVA, T.P. 56, 122, 347  
 Gavrilyuk, A.A. 273

- Gavrilyuk, A.V. 273  
 Gerasimenko, A.Yu. 417, 431  
 Gerasimov, E.G. 181, 206, 242, 264  
 Gerasimova, Yu.V. 442, 451  
 Germov, A.Y. 19, 110  
 Gilmutdinov, I.F. 22, 29, 42, 56, 347  
 Gimazov, I. 140  
 Gizhevskii, B.A. 53, 69  
 Glazkov, V.N. 10  
 Glazkov, V.P. 181  
 Glushkov, V. 78  
 Gokhfeld, Yu.S. 27, 87  
 Golikova, T.E. 128  
 Golovchanskiy, I.A. 135  
 Golovnia, O.A. 220, 223, 243, 253  
 Golubov, A.A. 151, 159  
 Golygin, E.A. 192, 273  
 Gorbunov, D.I. 175  
 Gordeeva, V.M. 157  
 Gorkovenko, A.N. 202  
 Gorkovenko, N.V. 361  
 Gornostyrev, Yu.N. 405  
 Gorshenkov, M.V. 269, 478  
 Govor, G.A. 190, 275  
 Grebennikov, V.I. 242  
 Grebenshchikov, Yu.B. 462, 464  
 Grigoreva, Z.A. 450  
 Gritsenko, Ch.A. 450  
 Gromilov, S. 98  
 Gubkin, A.F. 47, 264  
 Gudim, I.A. 27, 312, 329, 320, 345  
 Gudkova, S.A. 213, 250  
 Gudoshnikov, S.A. 17, 462, 464  
 Gulenko, A.S. 63  
 Gumarov, A.I. 92  
 Gumarova, I.I. 92  
 Gumerova, E.A. 456  
 Gupalo, M. 238  
 Gusev, N.A. 141
- Hasanov, F.F. 275  
 Horoshiy, I.N. 318
- Iacunin, A. 133  
 Iafarova, A.F. 10  
 Iakovleva, M. 23  
 Ichkitidze, L.P. 417, 431  
 Ignatov, A.A. 387
- Igoshev, P.A. 76, 89  
 Inishev, A.A. 242  
 Isaev, D.A. 415  
 Iskhakov, R.S. 194, 434, 451, 454  
 Ispiryani, A.G. 361  
 Ivanov, A.O. 352  
 Ivanov, O.N. 58  
 Ivanov, V.Yu. 280, 292, 290, 299  
 Ivanova, A.G. 22, 29, 42, 72  
 Ivanova, O.S. 424  
 Izotov, A.I. 294
- Jovanović, S. 421, 435, 437
- Kalinin, M.A. 327  
 Kalyuzhnaya, D.A. 363, 408  
 Kamra, Akashdeep 131, 138, 157  
 Kamzin, A.S. 461  
 Kanevskii, V.M. 297, 333  
 Kantorovich, S.S. 238, 353, 356, 375  
 Kapitan, D.Yu. 11, 13  
 Kapitan, V.Yu. 11, 13  
 Karakozov, A.E. 162  
 Karpasyuk, V.K. 67, 82, 310  
 Karpenkov, A.Yu. 204, 322  
 Kataev, V.A. 262  
 Katanin, A.A. 76, 114  
 Kazak, N.V. 27, 61, 87, 98, 120  
 Kazantseva, N.V. 433  
 Khachatryan, A.Sh. 225  
 Khaibullin, R.I. 92, 308  
 Khairetdinova, D.R. 226  
 Khajrullin, M.F. 415  
 Kharitonov, V.N. 245  
 Kharitonskii, P.V. 185  
 Khomenko, M.R. 322  
 Khrapova, E. 100  
 Khudaiberdyev, A.A. 20  
 Kiiamov, A.G. 22, 29, 42, 156  
 Kislinski, Yu.V. 331  
 Kislov, E.V. 167  
 Klenov, N.V. 133, 137, 146, 151  
 Klepikova, A.S. 340  
 Knyazev, Yu.V. 79, 442  
 Kochnev, A.V. 433  
 Koemets, Yu.N. 433  
 Kokh, D. 25  
 Kolesnikova, V.G. 269, 283, 349

- Kolkov, M.I. 318  
 Kolodkin, D.A. 229  
 Komarov, V.A. 248  
 Komogortsev, S.V. 194, 442, 451  
 Kopasov, A.A. 129  
 Korableva, A.Y. 92  
 Korepanova, E. 427  
 Korneeva, E.A. 310  
 Korol, A.O. 11, 13  
 Korolyov, A.V. 72  
 Korshunov, M.M. 134, 208  
 Korshunov, A.S. 183  
 Koskov, M.A. 364  
 Kosmachev, O.A. 85  
 Kostishin, V.G. 188  
 Kostrov, S.A. 351  
 Kostyuchenko, N.V. 183  
 Kosyrev, N.N. 248  
 Kotov, L.N. 267  
 Kozabaranov, R.V. 183  
 Kozlov, I.V. 17  
 Kramarenko, E.Yu. 351, 415  
 Krasikov, A.A. 125  
 Krasikov, K. 78  
 Krasilin, A. 100  
 Kravchenko, Z.F. 294  
 Kruchinina, K.A. 223  
 Krylov, V.I. 93  
 Kubrin, S.P. 79  
 Kuchesheva-Titova, V.R. 2, 320, 345  
 Kuchin, A.G. 198, 231  
 Kudasov, Yu.B. 183  
 Kudrevatykh, N.V. 178  
 Kudryavtsev, V.O. 209  
 Kudyukov, E.V. 240, 327  
 Kugel, K.I. 74  
 Kulesh, N.A. 202  
 Kulikov, O.A. 444, 448  
 Kunikin, S.A. 361  
 Kupriyanov, M.Yu. 137, 146, 151, 159  
 Kurbanova, D.R. 30, 32  
 Kurlyandskaya, G.V. 368, 396, 459  
 Kushnir, V.N. 159  
 Kutlin, A.G. 129  
 Kuzina, D.M. 308  
 Kuzmenko, A.M. 280, 292, 290, 299  
 Kuz'min, V.I. 104  
 Kuznetsov, A.A. 356  
 Kuznetsov, A.R. 405  
 Kuznetsov, M.A. 389  
 Kuznetsova, A.A. 392  
 Kuznetsova, T.V. 242  
 Kvartalov, V.B. 297, 333  
 Lachinov, A.N. 142  
 Ladygina, V.P. 434  
 Lagarkov, A.N. 239  
 Lambrianidi, K.V. 325  
 Larin, A.O. 190, 275  
 Larrañaga, A. 368, 459  
 Lebedev, A.V. 364  
 Legenkii, Yu.A. 294  
 Leonov, I. 52  
 Leontiev, A.V. 84  
 Lepalovskij, V.N. 240  
 Lev, L.L. 305  
 Levada, E.V. 450  
 Levada, K.V. 283, 349, 421, 427, 435, 437  
 Li, O.A. 194, 434, 454  
 Lin, Chun-Rong 424  
 Lin, J.G. 192  
 Litvinova, L.S. 421, 427, 437  
 Lomova, N.V. 4  
 Lukkareva, S.A. 226  
 Lukoyanov, A.V. 198, 231, 342  
 Lukshina, V.A. 233, 396, 405  
 Lukyanenko, A.V. 248  
 Lupu, M. 133  
 Lutsenko, O.V. 466  
 Lyadov, N.M. 308  
 Lyaschenko, S.A. 469, 482, 485, 484  
 Lyublinskaya, A.A. 155  
 Lyu-yu, N.A. 273  
 Magnitskaya, M.V. 93, 162  
 Magomedov, M.A. 30, 32, 34  
 Makarov, D.V. 407  
 Makarov, I.V. 183  
 Makarova, L.A. 283, 415  
 Maklakov, S.A. 239  
 Maklakov, S.S. 239  
 Makurenkova, A.A. 197  
 Malashchenko, V.V. 421, 427, 437  
 Maltseva, V.E. 178, 211, 220, 235, 260, 265

- Mamin, R.F. 84  
 Marchenkov, V.V. 225  
 Martynov, A.S. 20  
 Martynov, S.N. 9  
 Mashera, V.S. 17  
 Mashkovich, E.A. 286  
 Maslov, D.A. 183  
 Matyunina, Ya.Yu. 85  
 Matzui, L. 258  
 Maximova, O.A. 469, 485, 484  
 Mazanik, A.A. 173  
 Medar, S.E. 468  
 Medvedeva, I.V. 429  
 Mel'nikov, A.S. 129  
 Melnikov, G.Yu. 368  
 Melnikov, N.B. 63  
 Merkulov, D.I. 310  
 Mikhailova, D. 8  
 Mikhalev, K.N. 19  
 Mikhashenok, N.V. 329  
 Mikhaylov, V.I. 294  
 Mikheyenkov, A.V. 74  
 Moiseev, A.A. 209, 217  
 Molokeev, M.S. 2, 25, 87, 329  
 Morchenko, A.T. 277  
 Morozov, O.A. 10  
 Morozova, N.V. 273  
 Mosharov, D. 188  
 Moshkina, E.M. 2, 25, 91  
 Moskal, I.E. 331  
 Moskvin, A.S. 112, 148, 171  
 Mostovshchikova, E.V. 53, 95  
 Motorzhina, A.V. 421, 437, 435  
 Mozgovykh, S.N. 19  
 Mukhachev, R.D. 198, 231  
 Mukhamatchin, K.R. 389  
 Mukhin, A.A. 280, 290, 299, 292  
 Murtazaev, A.K. 21, 30, 32, 34  
 Murtazaev, K.Sh. 32, 34  
 Mushnikov, N.V. 175, 181, 206, 242, 264  
 Musikhin, A.Yu. 413
- Nalbandyan, V. 23, 24  
 Naletova, V.A. 376  
 Nalivaiko, I.N. 40, 43  
 Naumov, S.V. 53, 69, 102, 339, 374  
 Nefedev, K. 40, 43, 45
- Neilo, A. 137  
 Nekrasov, E.S. 394  
 Nematov, M.G. 188  
 Nemtsev, I.V. 194  
 Neznakhin, D.S. 107, 220  
 Nichipuruk, A.P. 471, 472  
 Nidda, H.-A. Krug von 67  
 Nikitin, S.A. 197, 204  
 Nikolaev, S.V. 104, 106  
 Nikolaeva, E.D. 434, 454  
 Nori, F. 68  
 Normirzaev, A.R. 190  
 Nosova, N.M. 110, 178, 237  
 Novak, E.V. 238, 356, 375  
 Novikau, I. 375  
 Nugumanov, A.G. 6  
 Nurmukhametov, A.R. 65  
 Nuzhdin, V.I. 308
- Obambi, M.A. 117  
 Odenbach, S. 398  
 Odintsov, V.I. 17, 462, 464  
 Ogloblichev, V.V. 110, 337  
 Ogurtsov, A.V. 223  
 Omelyanchik, A.S. 269, 283, 349  
 Orlov, Yu.S. 104, 106  
 Orue, I. 459  
 Osipov, A.V. 239  
 Ovchinnikov, S.G. 61, 87, 98, 104, 106, 108, 208, 248, 469, 484, 485  
 Ovsyannikov, G.A. 331
- Pahomova, A.A. 277  
 Palnichenko, A.V. 135  
 Panina, L.V. 188, 226, 419, 435, 437, 466, 468  
 Pankratov, N.Yu. 197, 204, 322  
 Pankrats, A.I. 329  
 Panov, Y.D. 36, 49, 166  
 Panov, Yu.D. 148, 171  
 Papynov, E.K. 245  
 Paskal, V.A. 436  
 Pasyunkova, A.A. 396, 459  
 Patrakov, E.I. 220  
 Patrin, G.S. 248  
 Pavlovskii, M.S. 2, 125  
 Pavluyk, M.V. 297, 333  
 Pelevina, D.A. 376

- Perov, N.S. 250, 415  
Pervakov, K.S. 135  
Petrov, D.A. 354  
Petrzhik, A.M. 331  
Pimenov, A. 299  
Piovano, A. 79  
Pirogov, A.N. 181, 206  
Piskunov, Yu.V. 110, 337  
Platonov, S.P. 198, 231  
Platonov, V.V. 183  
Podkur, P.L. 297, 333  
Polukeev, S.I. 108  
Ponomareva, E.A. 242  
Poperechny, I.S. 364  
Popov, A.G. 223, 229, 243, 253  
Popov, D.V. 15  
Popov, M.R. 340  
Popov, Yu.F. 290  
Popova, A.V. 462  
Prepelitsa, A. 133  
Proshin, Yu.N. 169  
Protasov, A.V. 223, 243  
Protsenko, V.S. 114  
Pryanichnikov, S.V. 95  
Pshenichnikov, S.E. 421, 435, 437  
Pudalov, V.M. 135  
Pugach, N.G. 141, 143  
Pyankov, V.F. 434, 454  
Pyanzina, E.S. 238, 356  
Pyataev, M.A. 448  
Pyataev, N.A. 444, 448  
Pyzhyanov, Ya.Ya. 95
- Radushnov, D.I. 385  
Raikher, Yu.L. 366, 398  
Rakhmanov, A.L. 68  
Ralin, A.Yu. 185  
Ramazanov, M.K. 30, 32, 34  
Ranero, L. Media 368  
Rautskii, M.V. 107, 248, 451  
Razueva, D.A. 260  
Reser, B.I. 63  
Rigmant, M.B. 433  
Rodionov, V. 270  
Rodionova, V.V. 269, 283, 301, 349, 387, 421, 427, 435, 437, 450, 478  
Romanova, O.B. 335
- Romanova, I.V. 10  
Rosenfeld, E.V. 175  
Rozaev, K.N. 239  
Rozhkov, A.V. 68  
Rudenko, V. 98  
Rumyantseva, N.I. 456  
Rusanov, M.S. 360, 400  
Ruzhickiy, V.I. 151  
Ryapolov, P.A. 363, 404, 408  
Ryazanov, V.V. 128  
Ryumshin, V.S. 166  
Ryzhikov, I.A. 239  
Ryzhkov, A.V. 402
- Sadakov, A. 140  
Sadykov, A.F. 337  
Safronov, A.P. 368  
Salamatin, D.A. 93  
Salikhov, T. 23, 24  
Samardak, A.S. 245  
Samardak, V.Yu. 245  
Samokhvalov, A.A. 277  
Samoshkina, Yu.E. 107  
Sarakueva, A.E. 17  
Saveliev, D.V. 313, 316  
Savin, P.A. 240  
Sboychakov, A.O. 68  
Schapova, E.A. 471, 472  
Schefer, J. 79  
Schegolev, A.E. 146  
Seidov, Z.Y. 67  
Seleznev, D.V. 141  
Selezneva, N.V. 19, 110, 167, 220, 222  
Selishchev, S.V. 417  
Semenova, S.A. 358  
Semenova, O.I. 340  
Semirov, A.V. 209, 217  
Semkin, M.A. 181, 303  
Sergienko, E.S. 185  
Shabanova, K.A. 25  
Shadrin, A.V. 36, 112, 331  
Shanidze, L.V. 248  
Sharafullin, I.F. 6  
Sharin, M.K. 223  
Sharova, O.A. 376  
Shaykhutdinov, K.A. 125  
Sheiko, S.S. 351

- Shel'deshova, E.V. 363, 404  
 Sherokalova, E.M. 110, 222, 237  
 Sherstyuk, D.P. 250  
 Shestakov, A.V. 15, 134  
 Shevchenko, E.I. 409  
 Shevtsov, D.V. 484, 485  
 Shichalin, O.O. 245  
 Shinkorenko, A.S. 81  
 Shishkin, D.A. 19, 233, 405, 433  
 Shitov, A.V. 223, 243, 253  
 Shitsevalova, N. 78  
 Shlyapkina, V.I. 444  
 Shoukavaya, T.V. 190  
 Shukaev, I. 23  
 Shupletsova, V.V. 427  
 Shustin, M.S. 153, 164  
 Shustov, V.A. 67  
 Shuvaev, A. 299  
 Sidelnikov, M.S. 135  
 Sidorenko, A. 133  
 Skorobogatov, S.A. 125  
 Skoryunov, R.V. 337  
 Skulkina, N.A. 394  
 Sluchanko, N. 78  
 Smoliarova, T.E. 440  
 Smolnikov, A.G. 337  
 Sobolev, K.V. 283, 349, 427, 478  
 Sogomonyan, K.L. 376  
 Sokolchik, D.P. 407  
 Sokolov, A.E. 424  
 Sokolov, E.A. 363, 408  
 Sokolsky, S.A. 411  
 Soldatov, K.S. 40, 43  
 Solin, N.I. 102  
 Solizoda, I.A. 256  
 Soloviev, I.I. 133, 137, 146, 151  
 Solovyov, L.A. 27, 87  
 Solovyova, A.Yu. 385, 411  
 Solov'yov, S.V. 38  
 Sosin, S.S. 10  
 Starikov, A.Yu. 258  
 Stashkova, L.A. 223  
 Stashkov, A.N. 471, 472  
 Stepanova, K.A. 262  
 Stepanova, E.A. 107, 260, 340  
 Sterkhov, E.V. 95  
 Stolbov, O.V. 366, 387  
 Stolyar, S.V. 434, 442, 446, 451, 454  
 Stolyarov, V.S. 135  
 Strelkov, I.S. 183  
 Strocov, V.N. 305  
 Strongin, V.S. 40, 43  
 Suhachev, A.L. 194  
 Sukhikh, A. 98  
 Sukhorukov, G.B. 444, 448  
 Sukhorukov, Yu.P. 339, 374  
 Suleimanov, U.B. 275  
 Surdin, O.M. 183  
 Surzhikov, E.A. 339, 374  
 Svalov, A.V. 368  
 Svetlitsky, E.S. 424  
 Tagiev, M.M. 67  
 Tagirov, L.R. 159  
 Talanov, Yu. 140  
 Tarasenko, T.N. 294  
 Tarasov, A.S. 248  
 Tarasov, I.A. 248  
 Tarasov, V.P. 462, 464  
 Taskaev, S.V. 213, 256  
 Tayurskii, D.A. 22, 29, 42  
 Telegin, A.V. 339, 374  
 Telyshev, D.V. 417, 431  
 Teplykh, A.E. 206  
 Terent'ev, K.Yu. 318  
 Terentev, P.B. 181, 206, 264  
 Terentjev, K.Yu. 125  
 Terent'yev, P.B. 242  
 Tereshina, I.S. 183, 197, 322  
 Tereshina, I.S. 204  
 Tian, Y. 42  
 Tikhanovskii, A.Yu. 280, 290, 299  
 Timofeeva, A.V. 396, 459  
 Titova, S.G. 95  
 Titovets, I.A. 40, 43  
 Togushova, Yu.N. 134  
 Trofimov, E.A. 213, 256, 271  
 Trukhanov, A.V. 250, 258  
 Trukhanov, An.V. 258  
 Trukhanov, S.V. 258  
 Trukhin, V. 45  
 Tsvyashchenko, A.V. 93  
 Tumano, V.A. 169  
 Turchenko, V.A. 258

- Turkin, Y.V. 143  
 Tyumentseva, A.V. 442, 451
- Udintseva, M.S. 53, 69  
 Udod, L.V. 335  
 Uimin, M.A. 429  
 Ulitko, V.A. 49, 166, 171  
 Ulyanov, A.I. 4  
 Umhaeva, Z.S. 322  
 Uporov, S.A. 95  
 Urzhumtsev, A.N. 235, 265  
 Usatyy, I.M. 58  
 Useinov, N.Kh. 436  
 Ustyugov, V.A. 267  
 Uvin, D.S. 22
- Vaganov, M.V. 398  
 Vagizov, F.G. 56, 67, 347  
 Vakhitov, I.R. 308  
 Vakhrushev, A. 133  
 Valeev, V.F. 308  
 Valeyev, V.G. 305  
 Valieva, A.I. 456  
 Valiulin, V.E. 74  
 Varnakov, S.N. 248, 469, 482, 484, 485  
 Vasilchikova, T. 8, 23, 24  
 Vasilenko, D.Yu. 253  
 Vasiliev, A. 23, 24, 140  
 Vasiliev, E.V. 13  
 Vasilyeva, A.O. 363, 408  
 Vasin, K.V. 65  
 Vasinovich, E.V. 112  
 Vas'kovskiy, V.O. 202, 240, 327  
 Vaulin, A.A. 47  
 Vavilova, E. 8, 23, 24  
 Veligzhanin, A. 2  
 Velikanov, D.A. 25, 98, 194, 434, 442, 446, 451, 454, 474  
 Venediktov, S.N. 462  
 Vereshchagin, S.N. 27  
 Vinnik, D.A. 213, 250, 258, 256, 271  
 Vinnikov, L.Ya. 135  
 Vinogradova, A.S. 376  
 Vivchar, V.I. 409  
 Vlasenko, V.A. 135  
 Vlasov, V.S. 267  
 Volchkov, S.O. 459
- Volchkov, I.S. 297, 333  
 Volegov, A.S. 211, 220, 222, 231, 235, 237, 243, 260, 265  
 Volkov, N.V. 248, 440  
 Volkov, M. 100  
 Volkova, E.G. 233  
 Volochev, M.N. 446  
 Vorobev, G.P. 290  
 Voronina, E.V. 72  
 Vorontcov, S. 349, 427  
 Vorotynov, A.M. 434, 454
- Weymann, L. 299  
 Wiedwald, U. 482  
 Wiedwald, U. 484
- Yagfarova, A.R. 56, 347  
 Yagovtsev, V.O. 141  
 Yakobson, D.E. 444, 448  
 Yakovenko, O. 258  
 Yakovlev, I.A. 248  
 Yakovleva, M.Yu. 231  
 Yanilkin, I.V. 92  
 Yanushkevich, K.I. 294, 335  
 Yaroslavtsev, R.N. 442, 446, 451  
 Yasinskaya, D.N. 49  
 Yatsyk, I.V. 15, 56, 67, 91, 347, 456  
 Yerin, C.V. 380, 409  
 Yudanov, N.A. 188, 419, 466  
 Yuldasheva, A.R. 6  
 Yumashev, V.V. 61  
 Yurtaeva, S.V. 456  
 Yusupov, A.P. 142  
 Yusupov, R.V. 22, 29, 42
- Zagorskiy, D.L. 226  
 Zagrebin, M.A. 117  
 Zaitseva, O.V. 213, 271  
 Zakhvalinskii, V.S. 58  
 Zakinyan, A.R. 372  
 Zamkova, N.G. 480  
 Zaneskin, M.L. 305  
 Zayceva, V.E. 169  
 Zedan, A. 188  
 Zezyulina, P.A. 239  
 Zhakov, S.V. 429  
 Zhaludkevich, A.L. 190, 275

Zhandun, V.S. 120, 121, 480

Zharkov, M.N. 444, 448

Zhelezny, M. 197

Zherebtsov, D.A. 213, 250, 271

Zhevstovskikh, I.V. 340

Zhivulin, V.E. 213, 250, 256, 258, 271

Zhivulko, A.M. 335

Zlotnikov, A.O. 144, 153, 164

Zolotov, N.A. 185

Zubar, T.I. 258

Zubarev, A.Yu. 370, 382, 413

Zubritskii, S.M. 273

Zverev, N.N. 4

Zverev, V.C. 360, 400

Zverev, V.S. 375, 378

Zvereva, E. 23, 24

Zvezdin, A.K. 183

Zyvilko, A.M. 294





ISBN 978-5-94469-051-7



**VIII Euro-Asian Symposium «Trends in MAGnetism»**

**EASTMAG-2022**

**August 22–26, 2022, Kazan, Russia**

**BOOK OF ABSTRACTS. VOLUME II**

**Titles and abstracts are given in the author's edition**

The layout and design of EASTMAG-2022 Book of Abstracts – Polina A. Agzamova  
The editing of EASTMAG-2022 Book of Abstracts – Sergey G. L'VOV, Olga B. YANDUGANOVA



SiN (30)

Pb (20)

Cu (2)

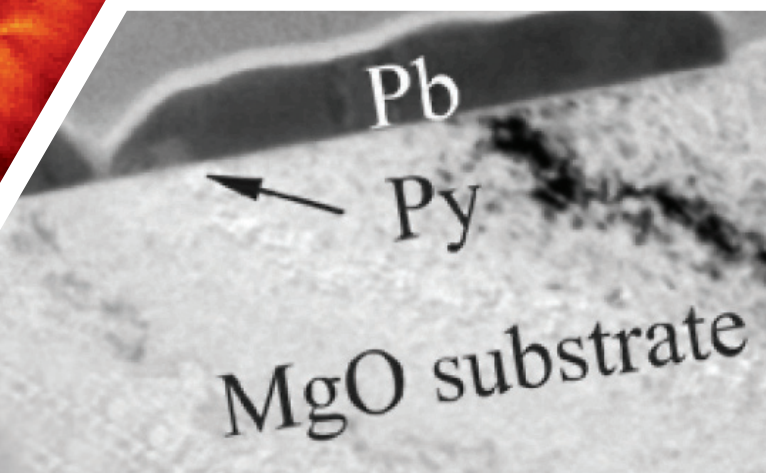
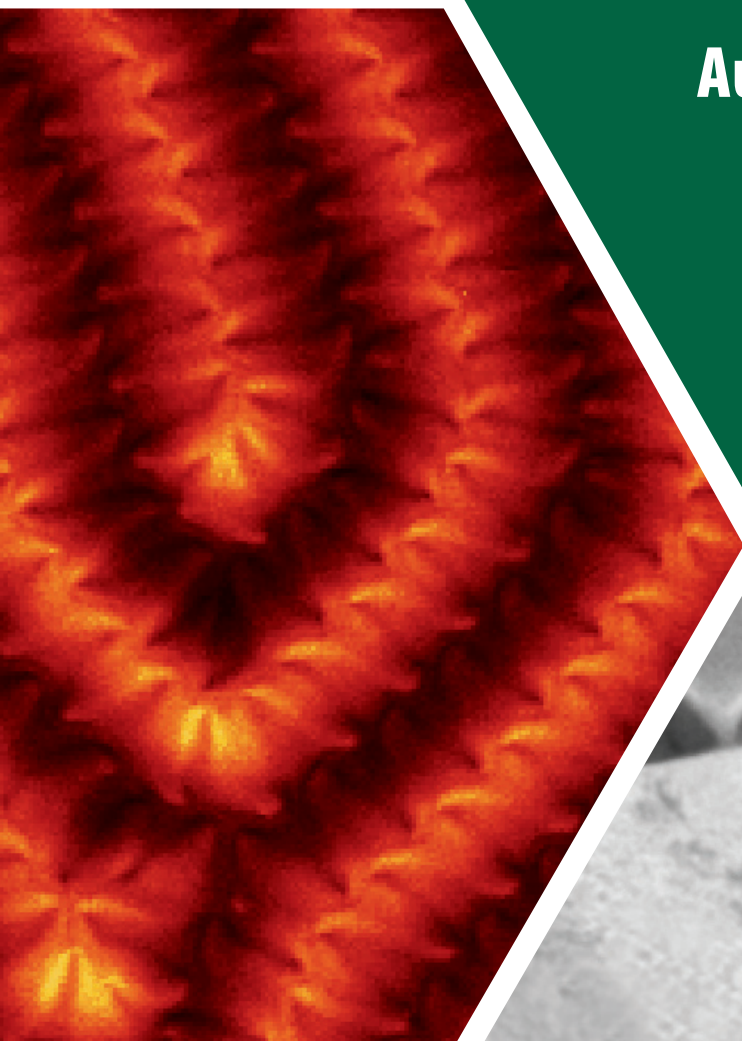
Heusler (12)



PdFe

VIII Euro-Asian Symposium  
«Trends in MAGnetism»

August 22–26, 2022,  
Kazan, Russia



Pb

Py

MgO substrate